Transactions of the ASME®

Technical Editor, **LEWIS T. WHEELER (1997)**

Department of Mechanical Engineering,
University of Houston,
Houston, TX 77204-4792

APPLIED MECHANICS DIVISION

Chairman, **C. T. HERAKOVICH**
Secretary, **T. HUGHES**
Associate Technical Editors,
R. ABEYARATNE (1997)
T. R. AKYLAS (1997)
J. L. BASSANI (1999)
R. BECKER (1998)
S. A. BERGER (1997)
I. M. DANIEL (1999)
W. J. DRUGAN (1997)
J. T. JENKINS (1999)
J. W. JU (1998)
V. KINRA (1999)
S. KYRIAKIDES (1997)
S. LICHTER (1998)
W. K. LIU (1999)
X. MARKENSCOFF (1997)
M. ORTIZ (1998)
N. C. PERKINS (1999)
J. N. REDDY (1998)
S. W. SHAW (1997)
M. SHINOZUKA (1997)
M. TAYA (1999)

BOARD ON COMMUNICATIONS

Chairman and Vice-President
R. MATES

OFFICERS OF THE ASME
President, **R. J. GOLDSTEIN**
Executive Director, **D. L. BELDEN**
Treasurer, **J. A. MASON**

PUBLISHING STAFF
Managing Director, Engineering
CHARLES W. BEARDSLEY
Director, Technical Publishing
PHILIP DI VIETRO
Managing Editor, Technical Publishing
CYNTHIA B. CLARK
Managing Editor, Transactions
CORNELIA MONAHAN
Production Coordinator
JUDITH SIERANT
Production Assistant
MARISOL ANDINO

Transactions of the ASME, Journal of Applied Mechanics (ISSN 0021-8936) is published quarterly (Mar., June, Sept., Dec.) for $210.00 per year by The American Society of Mechanical Engineers, 345 East 47th Street, New York, NY 10017.

Periodicals postage paid at New York, NY and additional mailing office. POSTMASTER: Send address changes to Transactions of the ASME, Journal of Applied Mechanics, c/o THE AMERICAN SOCIETY OF MECHANICAL ENGINEERS, 22 Law Drive, Box 2300, Fairfield, NJ 07007-2300.

CHANGES OF ADDRESS must be received at Society headquarters seven weeks before they are to be effective. Please send old label and new address. **PRICES:** To members, $40.00, annually: to nonmembers, $210.00. Add $30.00 for postage to countries outside the United States and Canada.

STATEMENT from By-Laws. The Society shall not be responsible for statements or opinions advanced in papers or . . . printed in its publications (B7.1, Para. 3), **COPYRIGHT © 1997** by The American Society of Mechanical Engineers. Authorization to photocopy material for internal or personal use under circumstances not falling within the fair use provisions of the Copyright Act is granted by ASME to libraries and other users registered with the Copyright Clearance Center (CCC). Transactional Reporting Service provided that the base fee of $3.00 per article is paid directly to CCC, Inc., 222 Rosewood Drive, Danvers, MA 01923. Request for special permission or bulk copying should be addressed to Reprints/Permission Department. **INDEXED** by Applied Mechanics Reviews and Engineering Information, Inc. Canadian Goods & Services Tax Registration #126148048.

Journal of Applied Mechanics

Published Quarterly by The American Society of Mechanical Engineers

VOLUME 64 • NUMBER 1 • MARCH 1997

TECHNICAL PAPERS

1 **The Kink Band Mechanism for the Compressive Failure of Fiber Composite Materials**
R. M. Christensen and S. J. DeTeresa

7 **Differential Equations Governing the Geometry of a Diamond Mesh Cod-end of a Trawl Net**
F. G. O'Neill

15 **Predicted Thermal Mismatch Stresses in a Cylindrical Bi-material Assembly Adhesively Bonded at Its Ends**
E. Suhir

23 **A Volume Integral Equation Technique for Multiple Inclusion and Crack Interaction Problems**
Jungki Lee and Ajit Mal

32 **Poroelastic Solution for an Inclined Borehole**
L. Cui, A. H-D. Cheng, and Y. Abousleiman

39 **Nonlinear Elasticity of Granular Media**
A. N. Norris and D. L. Johnson

50 **Seismic Waves in a Laterally Inhomogeneous Layered Medium, Part I: Theory**
Ruichong Zhang, Liyang Zhang, and Masanobu Shinozuka

59 **Seismic Waves in a Laterally Inhomogeneous Layered Medium, Part II: Analysis**
Ruichong Zhang, Liyang Zhang, and Masanobu Shinozuka

66 **Dynamic Crack Propagation in a Layered Medium Under Antiplane Shear**
Chien-Ching Ma and Yi-Shyong Ing

73 **Circular Rigid Punch With One Smooth and Another Sharp Ends on a Half-Plane With Edge Crack**
Norio Hasebe and Jun Qian

80 **Linear Complementary Formulations Involving Frictional Contact for Elasto-Plastic Deformable Bodies**
Maocheng Li, Desong Sha, and K. K. Tamma

90 **Minimum Weight Design of Symmetric Angle-Ply Laminates With Incomplete Information on Initial Imperfections**
S. Adali, A. Richter, and V. E. Verijenko

97 **Left Eigenvectors: Extraction From Measurements and Physical Interpretation**
I. Bucher and S. G. Braun

106 **Anisotropic Damage Effect Tensors for the Symmetrization of the Effective Stress Tensor**
G. Z. Voyiadjis and T. Park

111 **Elastothermodynamic Damping in Particulate Composites: Hollow Spherical Inclusions**
V. K. Kinra and J. E. Bishop

116 **Investigation of a New Formulation of the Lagrange Method for Constrained Dynamic Systems**
A. Rosen and E. Edelstein

123 **A Variable Sensitivity Displacement Interferometer With Application to Wave Propagation Experiments**
H. D. Espinosa, M. Mello, and Y. Xu

132 **Damping Characteristics of Laminated Thick Plates**
T. W. Taylor and A. H. Nayfeh

139 **Parametric Resonance of a Spinning Disk Under Space-Fixed Pulsating Edge Loads**
Jen-San Chen

144 **Contact Between Elastic Bodies With an Elliptic Contact Interface in Torsion**
J. F. Cuttino and T. A. Dow

149 **Stability of the Unison Response for a Rotating System With Multiple Tautochronic Pendulum Vibration Absorbers**
Chang-Po Chao, S. W. Shaw, and Cheng-Tang Lee

157 **Stochastic Averaging of Quasi-Nonintegrable-Hamiltonian Systems**
W. Q. Zhu and Y. Q. Yang

165 **A Nonclassical Vibration Analysis of a Multiple Rotating Disk and Spindle Assembly**
I. Y. Shen and C.-P. R. Ku

175 **Slaving the In-Plane Motions of a Nonlinear Plate to Its Flexural Motions: An Invariant Manifold Approach**
I. T. Georgiou and I. B. Schwartz

(Contents continued on Outside Back Cover)

Downloaded 04 May 2010 to 171.66.16.52. Redistribution subject to ASME license or copyright; see http://www.asme.org/terms/Terms_Use.cfm

CONTENTS (CONTINUED)

183 **Exact Solutions of Some Shear Dislocation Problems Involving a Stopping Effect**
Gwolong Lai and A. R. Robinson

193 **Strain-Rate Effects in the Dynamic Buckling of a Simple Elastic-Plastic Model**
D. Karagiozova and N. Jones

201 **An Orthotropic Viscoelastic Winding Model Including a Nonlinear Radial Stiffness**
W. R. Qualls and J. K. Good

209 **Equivalent Nonlinear System Method for Stochastically Excited and Dissipated Integrable Hamiltonian Systems**
W. Q. Zhu and Y. Lei

217 **Experiments on Nonlinear Dynamic Behavior of an Oscillator With Clearance and Periodically Time-Varying Parameters**
A. Kahraman and G. W. Blankenship

BRIEF NOTES

On the Motion of Lineal Bodies Subject to Linear Damping 227
M. F. Beatty

On the Thermal Response of Antisymmetric Angle-Ply Laminated Plates 229
A. A. Khdeir

Equilibrium of a Radially Symmetric Inhomogeneous Plate Under Tension and Load 233
A. R. Pineda and R. G. Root

236 On the Use of a Plane-Strain Model to Solve Generalized Plane-Strain Problems
Shoufeng Hu and N. J. Pagano

238 Modal Decoupling of Systems Described by Three Linear Operators
A. A. Renshaw

240 Effect of Mass Transfer on a Similar Flow in the Magnetohydrodynamic Squeeze Film
R. Usha and R. Sridharan

DISCUSSION

244 **A General Formulation of the Theory of Wire Ropes, by W. Jiang—Discussion by S. A. Velinsky**

245 **Bifurcation of Orthotropic Solids, by G. deBotton and K. Schulgasser—Discussion by A. Chattopadhyay and H. Gu**

247 **Stress and Strain Analysis in Molecular Dynamics Simulation of Solids, by P. A. Scagnetti, R. J. Nagem, G. V. H. Sandri, and T. G. Bifano—Discussion by O. R. Walton**

247 **A Critical Study of the Applicability of Rigid-Body Collision Theory, by D. Stoianovici and Y. Hurmuzlu—Discussion by A. Chatterjee and A. Ruina**

BOOK REVIEW

249 ***Stability Problems in Fracture Mechanics*, by Vladimir V. Bolotin . . .** Reviewed by **F. Ziegler**

ANNOUNCEMENTS AND SPECIAL NOTICES

22 Change of Address Form

38 Books Received by the Office of the Technical Editor

72 Finite Element Books Bibliography on the Internet

250 Worldwide Mechanics Meetings List

253 Information for Authors

254 Tenth International Conference on Numerical Methods for Laminar and Turbulent Flow—Call for Papers

255 Tenth International Conference on Numerical Methods for Thermal Problems—Call for Papers

Downloaded 04 May 2010 to 171.66.16.52. Redistribution subject to ASME license or copyright; see http://www.asme.org/terms/Terms_Use.cfm

R. M. Christensen
Lawrence Livermore National Laboratory,
Stanford University.

S. J. DeTeresa

Lawrence Livermore National Laboratory,
University of California,
P. O. Box 808,
Livermore, CA 94551-9900

The Kink Band Mechanism for the Compressive Failure of Fiber Composite Materials

A simple strain-based yield/failure criterion for fiber composite materials is incorporated into a kink band analysis of compressive failure. Under realistic conditions of fiber misalignment the analysis predicts compressive failure at load levels about one-fifth of the ideal value, and with kink band inclinations of about 20 deg. Some parametric variations of the relevant physical variables are given in simple graphical forms, and comparisons are made with newly obtained micrographs of kink bands.

Introduction

The compressive failure characteristic of fiber composite materials is in many cases the most limiting property. Generally, the stress at compressive failure in the fiber direction is much less in magnitude than the corresponding tensile stress at failure. A thorough theoretical and experimental understanding of this difficult property will be needed in order to improve the performance of these materials. That is certainly the goal of the present work, as well as that of other related studies in recent years.

There probably have been at least three landmark steps in the development of this subject. Rosen (1965) derived the ideal compressive strength of a stiff fiber composite given by

$$\sigma_{11} = -\sigma_c = -\mu_L$$

where μ_L is the longitudinal shear modulus. His instability analysis followed along classical lines. However, it became known that this prediction was far too large in size to model realistic cases. In the next major development, Argon (1972) recognized that the misalignment of fibers would have a large degrading effect on the compressive load at failure. Finally, Budiansky (1983) integrated Argon's treatment into a more general treatment that recovers both of the previous results. The effort probably would have ended at that point, had not the third and most general form still predicted one feature at variance with observations. Namely, this general treatment of Budiansky (1983), utilizing a kink band type of localization and instability, predicted a zero angle of inclination for the kink band. Otherwise the formulation was obviously realistic since it predicted load levels in the proper range.

Since the time of Budiansky's development, the problem has been much discussed, for example by Budiansky and Fleck (1993), and Fleck and co-workers such as Sutcliffe and Fleck (1993). Recently Kyriakides et al. (1994), Schapery (1994), and Moran et al. (1994) have made useful contributions, and in particular have predicted realistic ranges for kink band angles.

The present work has the same objective as other recent works, namely that of providing a theoretical framework that gives the major features of behavior including that of the kink band angle. The present work follows along the lines established by Budiansky (1983) and furthermore follows the apparent philosophy of Budiansky in seeking to circumscribe the problem in the simplest possible terms, in particular through the use of yield functions. Standard forms for the yield functions for high-fiber loading composites will be shown to render the problem quite transparent relative to the basic controlling mechanisms of compressive failure.

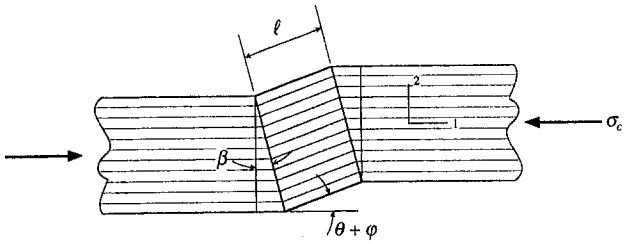


Fig. 1 Kink band geometry

Kink Analysis

The geometry of a kink under load is shown in Fig. 1. The initial and given fiber misalignment is designated by angle θ. Angle β gives the inclination of the kink from the direction normal to the gross fiber direction. Angle ϕ is the kink band distortional angle related to the deformation caused by the load.

Let ϵ be the transverse strain within the region of the kink, and let σ be the corresponding transverse stress. The corresponding shear stress is given by τ. Take $\sigma_{11} = -\sigma_c$ to be the applied axial stress in the fiber direction. Equilibrium of the kinked configuration in Fig. 1 under load gives the following condition:

$$\sigma_c = \{\tan\beta + \cot(\theta+\phi)\} \times \left\{\tau + \sigma\left[\frac{\tan\beta - \tan(\theta+\phi)}{1 + \tan\beta\tan(\theta+\phi)}\right]\right\} \quad (1)$$

where $\tau = \tau(\phi)$ and $\sigma = \sigma(\phi)$ which gives the dependence of the stresses upon the angle of shear deformation, ϕ. Equation (1) as well as Eq. (4) in the following is consistent with Budiansky and Fleck (1993).

Write the criterion expressing the yield or failure of the material in symbolic form as

Contributed by the Applied Mechanics Division of THE AMERICAN SOCIETY OF MECHANICAL ENGINEERS for publication in the ASME JOURNAL OF APPLIED MECHANICS.

Discussion on this paper should be addressed to the Technical Editor, Professor Lewis T. Wheeler, Department of Mechanical Engineering, University of Houston, Houston, TX 77204-4792, and will be accepted until four months after final publication of the paper itself in the ASME JOURNAL OF APPLIED MECHANICS.

Manuscript received by the ASME Applied Mechanics Division, Oct. 30, 1995; final revision, Aug. 26, 1996. Associate Technical Editor: S. Kyriadides.

Copyright © 1997 by ASME

Downloaded 04 May 2010 to 171.66.16.34. Redistribution subject to ASME license or copyright; see http://www.asme.org/terms/Terms_Use.cfm

$$\phi = \phi(\beta). \tag{2}$$

When relation (2) is given explicit form, then eliminating ϕ between (1) and (2) gives

$$\sigma_c = \sigma_c(\beta). \tag{3}$$

The final step will then be to minimize the applied load (stress) in (3) with respect to β in order to determine the kink angle and the corresponding load at the point of formation of the kink. This entire process will now be carried out.

The fiber misalignment angle, θ, and the angle of shear, ϕ, are very small within the realistic range of material behavior. Accordingly these nondimensional quantities will be taken to be small such that second-order quantities can be neglected compared with first-order terms, etc. The transverse strain is found to be

$$\epsilon = [\tan\beta - \theta(1 + \tan^2\beta)]\phi - \frac{\phi^2}{2} \tag{4}$$

where no restriction on the size of $\tan\beta$ is implied. The corresponding stress-strain relations are

$$\tau = \mu_L\phi$$

and

$$\sigma = \frac{2}{(1 - \nu_T)}\mu_T\epsilon \tag{5}$$

where μ_L is the axial shear modulus of the fiber composite and μ_T and ν_T are the transverse shear modulus and Poisson's ratio, respectively. Conditions of plane strain are implicit in (5), along with very stiff fibers.

Combining (1) at small θ and ϕ with (4) and (5) gives

$$\frac{\sigma_c}{\mu_L} = \frac{\phi}{\theta + \phi}\left\{1 + \frac{2}{(1 - \nu_T)}\left(\frac{\mu_T}{\mu_L}\right)\tan\beta[\tan\beta - 2(1 + \tan^2\beta)\theta - (\tfrac{3}{2} + \tan^2\beta)\phi]\right\}. \tag{6}$$

Now it is necessary to introduce yield (failure) criteria, which for simplicity will be called the yield criterion henceforth. The nature of the yielding of the composite material under kinking conditions is in a matrix dominated mode. The matrix-dominated yield criterion deduced by Christensen (1988) will be employed,

$$\alpha\epsilon_{kk} + e_{ij}e_{ij} \leq k^2 \tag{7}$$

where e_{ij} is the deviatoric strain and α and k are two parameters to be obtained from experimental data, as will be shown later with an application. This form was obtained from a polynomial expansion. In application to the present kink band under plane-strain conditions, (7) at yield becomes

$$\alpha\left[\phi\tan\beta - (1 + \tan^2\beta)\theta\phi - \frac{\phi^2}{2}\right] + \frac{\phi^2}{2} + \frac{2}{3}\phi^2\tan^2\beta = k^2. \tag{8}$$

Take yield parameters α and k to be of the same order as θ and ϕ. Then (8) becomes

$$\alpha\phi\tan\beta + \frac{\phi^2}{2} + \frac{2}{3}\phi^2\tan^2\beta = k^2 \tag{9}$$

Solving (9) for ϕ gives

$$\phi = \frac{1}{3 + 4\tan^2\beta}\left[-3\alpha\tan\beta + \sqrt{9\alpha^2\tan^2\beta + 6k^2(3 + 4\tan^2\beta)}\right]. \tag{10}$$

The governing relations are now (6) and (10). It is not difficult to show that for a consistent order of terms, the last two terms in (6) can be neglected giving

$$\frac{\sigma_c}{\mu_L} = \frac{\phi}{\theta + \phi}\left[1 + \frac{2}{1 - \nu_T}\left(\frac{\mu_T}{\mu_L}\right)\tan^2\beta\right]. \tag{11}$$

Rewriting (10) in slightly different form gives

$$\phi = \frac{1}{1 + \frac{4}{3}\tan^2\beta}\left[-\alpha\tan\beta + \sqrt{2k^2 + (\alpha^2 + \tfrac{8}{3}k^2)\tan^2\beta}\right]. \tag{12}$$

Relations (11) and (12) are the final results of the present derivation. Between them they give the load at kink formation, σ_c, as a function of kink angle, β. A minimum in this relation will be found, giving the critical load, σ_c, at the onset of the kink instability. Before proceeding with the application, however, a further approximation will be introduced to assess the scale of some effects.

Small Kink Angle Approximation

Take β and correspondingly $\tan\beta$ as being small such that expansions can be truncated at low-order terms. Then using the binomial theorem (12) becomes

$$\phi = \frac{\sqrt{2}k}{1 + \frac{4}{3}x^2}\left[1 - \frac{\alpha}{\sqrt{2}k}x + \left(\frac{2}{3} + \frac{1}{4}\frac{\alpha^2}{k^2}\right)x^2 + - - - -\right] \tag{13}$$

where

$$x = \tan\beta.$$

With (13), then (11) becomes

$$\frac{\sigma_c}{\mu_L} = \frac{1}{\tilde{\theta}}\left[1 - \frac{\alpha\theta}{2k^2\tilde{\theta}}x + \left(\zeta + \eta_1 - \eta_2 - \frac{\alpha^2\theta}{2\sqrt{2}k^3\tilde{\theta}^2}\right)x^2 + - - -\right] \tag{14}$$

where

$$\tilde{\theta} = 1 + \frac{\theta}{\sqrt{2}k}$$

$$\zeta = \frac{2}{(1 - \nu_T)}\left(\frac{\mu_T}{\mu_L}\right)$$

$$\eta_1 = \frac{2}{3} + \frac{1}{4}\frac{\alpha^2}{k^2}$$

$$\eta_2 = \frac{\frac{2}{3} + \frac{1}{4}\frac{\alpha^2}{k^2} + \frac{4}{3\sqrt{2}}\frac{\theta}{k}}{\tilde{\theta}}.$$

Truncating relation (14) at the explicit term shown, and minimizing σ_c with respect to $x = \tan\beta$ gives

Downloaded 04 May 2010 to 171.66.16.34. Redistribution subject to ASME license or copyright; see http://www.asme.org/terms/Terms_Use.cfm

$$\tan\beta = \frac{\dfrac{\alpha\theta}{4k^2}}{\left(1+\dfrac{\theta}{\sqrt{2}k}\right)\left(\dfrac{2}{1-\nu_T}\dfrac{\mu_T}{\mu_L}+\dfrac{2}{3}+\dfrac{1}{4}\dfrac{\alpha^2}{k^2}\right)-\left(\dfrac{2}{3}+\dfrac{1}{4}\dfrac{\alpha^2}{k^2}+\dfrac{4}{3\sqrt{2}}\dfrac{\theta}{k}\right)-\dfrac{\alpha^2\theta}{2\sqrt{2}k^3\left(1+\dfrac{\theta}{\sqrt{2}k}\right)}}. \quad (15)$$

Under the approximation that β is small, (15) gives the solution for the kink angle. Note that when yield parameter $\alpha = 0$ then $\beta = 0$ and when fiber misalignment angle $\theta = 0$ then $\beta = 0$, as expected.

Now introduce one further approximation. Take

$$\sqrt{2}k \ll \theta$$

which is fairly realistic within a range of data. Then (15) becomes

$$\tan\beta = \frac{\alpha}{2\sqrt{2}k\left[\dfrac{2}{1-\nu_T}\left(\dfrac{\mu_T}{\mu_L}\right)-\dfrac{2}{3}+\dfrac{1}{4}\dfrac{\alpha^2}{k^2}\right]}. \quad (16)$$

The corresponding stress at kink band formation is from (14)

$$\frac{\sigma_c}{\mu_L} = \frac{\sqrt{2}k}{\theta}\left[1-\frac{\alpha^2}{8k^2\left(\dfrac{2}{1-\nu_T}\dfrac{\mu_T}{\mu_L}-\dfrac{2}{3}+\dfrac{1}{4}\dfrac{\alpha^2}{k^2}\right)}\right]. \quad (17)$$

The formulas in this section will not be used to evaluate specific cases since in general the kink band angle cannot be taken to be small. However, these results do show limiting case behavior. For example, relation (16) is independent of θ, meaning that for a sufficiently large fiber misalignment angle, θ, relative to the yield parameter, k, the kink band angle approaches an upper limit. Despite this behavior, the stress for the kink band formation (17), remains inversely proportional to θ, no matter how large θ is relative to k. Yield parameter α in the yield criterion (7) is a measure of the eccentricity of tensile and compressive yield in transverse stress. That is, if $\alpha = 0$ then a Mises-type criterion results and the yield in transverse tension and compression are of equal magnitude. For $\alpha > 0$ the yield in transverse tension is less than the magnitude of the yield in transverse compression. Relation (16) shows that if $\alpha = 0$ then the kink angle $\beta = 0$. Thus the eccentricity of the yield in transverse tension and compression leads to the existence of inclined angle kink bands. Relation (17), however, shows that the sensitivity of the failure load to this eccentricity (through α) is not large.

Examples show that relations (16) and (17) are fairly accurate compared with the relations (11) and (12) from which they are derived; however, there is no advantage in using (16) and (17) thus the more exact relations will be used in the following assessments.

Yield Criterion

Under conditions of transverse normal stress and longitudinal shear stress, polymeric fiber composite have yield/failure functions of the type shown in Fig. 2. The distinguishing characteristic is the eccentricity of the transverse tensile and compressive yield levels. The tensile yield is generally far lower than the compressive yield stress, as much as by a factor of one-third. It is the characteristic form shown in Fig. 2 which when incorporated into the present theory will be shown to yield realistic results.

The strain yield function shown in (7) can be written in alternate form, at yield

$$\alpha\epsilon_{kk} - \tfrac{1}{3}\epsilon_{kk}^2 + \epsilon_{ij}\epsilon_{ij} = k^2. \quad (18)$$

Appropriate to a state of uniaxial transverse stress with $\sigma_{22} = \sigma \neq 0$ and all other stress components as vanishing, relation (18) becomes

$$\epsilon^2 + \tfrac{3}{7}\alpha\epsilon = \tfrac{6}{7}k^2 \quad (19)$$

where $\epsilon_{22} = \epsilon$, $\epsilon_{11} = 0$ for stiff fiber systems and $\epsilon_{33} = -\nu_T\epsilon = -\epsilon/2$ where transverse Poisson's ratio is taken as $\frac{1}{2}$, for stiff fiber systems. The problem now is to select the two parameters α and k to fit the three characteristics of transverse yield in tension, compression, and yield in longitudinal shear.

In examining data for graphite epoxy fiber composites, there is a very wide scatter in results for the above specific characteristics. Rather than fitting any one set of data of uncertain characteristics, an average of five sets of data have been used for different type graphite-epoxy systems. The data sets are shown below.

Material (Fiber/Resin)	ϵ_{12} (%)	ϵ_T (%)	ϵ_C (%)	Reference
IM7/8551-7	0.5	0.56	−1.9	[a]
IM7/8551-7A	0.65	0.66	−2.2	[b]
Type II/5605	0.65	0.64	−2.1	[c]
46-9A/DER	0.4	0.49	−1.4	[b]
AS4/3501-6	0.6	0.67	−1.9	[d]
AS4/PEEK*	0.6	0.89	−1.9	[e]

* Carbon Fiber/Thermoplastic Matrix composite.
[a] Colvin and Swanson (1990)
[b] Lyon et al. (1993)
[c] Halpin (1984)
[d] Grimes et al. (1987)
[e] Kyriakides et al. (1995)

Also included in the table, though not in the average are the failure strains for a carbon fiber/thermoplastic composite. The thermoplastic composite was excluded from this average for the reason that it exhibits a higher transverse tensile strain than the

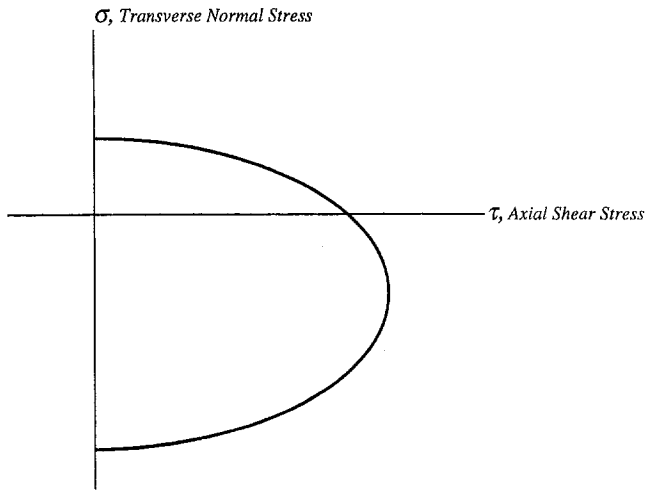


Fig. 2 Yield surface, transverse normal stress versus axial shear stress

Downloaded 04 May 2010 to 171.66.16.34. Redistribution subject to ASME license or copyright; see http://www.asme.org/terms/Terms_Use.cfm

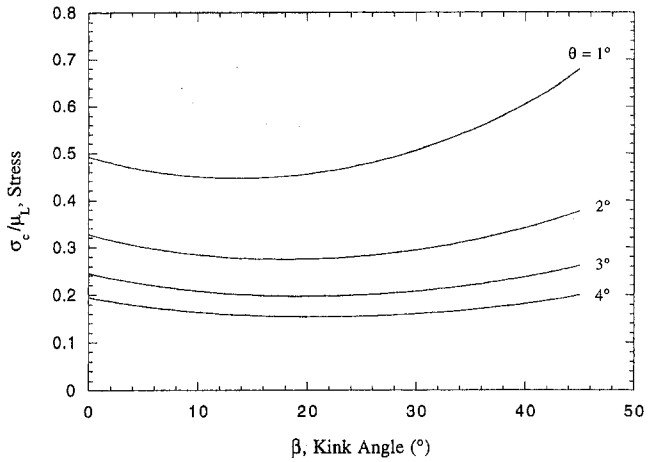


Fig. 3 Load versus kink angle, $\alpha = .028$, $k = .012$, $\zeta = 2.4$

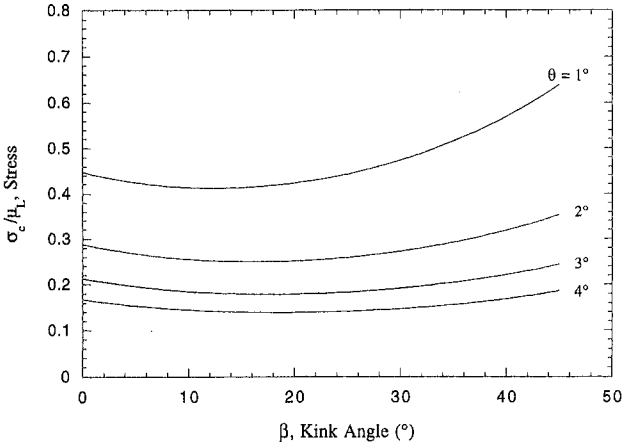


Fig. 4 Load versus kink angle, $\alpha = .02$, $k = .01$, $\zeta = 2.4$

epoxy systems. The implications of this will be discussed later. With the particular values of α and k shown below, the comparisons between (18) and the data are

Eq. (18) with $\alpha = 0.028$, $k = 0.012$	Data averages
$\epsilon_T = 0.0058$	$\epsilon_T = 0.0060$
$\epsilon_C = -0.018$	$\epsilon_C = -0.019$
$\epsilon_{12} = 0.0085$	$\epsilon_{12} = 0.0056$

where ϵ_T and ϵ_C refer to the transverse strains and ϵ_{12} is the shear strain. There is considerable latitude in the manner of specifying yield stress and yield strain in fiber composites. The method used with the above noted data was through the intersections of tangents to the stress strain curve at the initial and final (failure) points. Other methods could use offset definitions or area criteria. The variability is particularly acute with the longitudinal shear stress case where extreme nonlinearity is normally encountered. No attempt was made to optimize this process. The values of $\alpha = 0.028$ and $k = 0.012$ will be used in the first example that follows, thereafter "generic" values of α and k will be used.

Results

Relations (11) and (12) are used to eliminate angle ϕ between them to have the compressive stress σ_c at kink band formation as a function of kink band angle, β. The properties combination shown in (11) is taken as

$$\zeta = \frac{2}{1 - \nu_T}\left(\frac{\mu_T}{\mu_L}\right) = \frac{12}{5} \tag{20}$$

where μ_T/μ_L is taken with the realistic value of $\frac{3}{5}$ for graphite epoxy composites, and $\nu_T = \frac{1}{2}$. This value $\zeta = \frac{12}{5}$ will be used in all following examples.

Figure 3 shows the form of σ_c versus kink band angle β from (11) and (12) for various fiber misalignment angles θ at $\alpha = 0.028$ and $k = 0.012$. To the nearest half degree, the minimums in Fig. 3 are given by

θ	$\frac{\sigma_c}{\mu_L}$	β
1 deg	0.446	13.5 deg
2 deg	0.275	18.0 deg
3 deg	0.197	19.5 deg
4 deg	0.154	20.5 deg

It is seen that for these realistic values of the yield parameters, α and k, at a realistic value of fiber misalignment angle of 3 deg, the kink band angle is about 20 deg and the critical compressive stress at the instability is about $\frac{1}{5}$ of the ideal value of $\sigma_c = \mu_L$.

Next, take generally reasonable values of yield parameters α and k as

$$\alpha = 0.02$$

$$k = 0.01.$$

In transverse uniaxial stress, these give yield characteristics of $-\epsilon_C/\epsilon_T = 2.57$. The corresponding form of σ_C versus β is given in Fig. 4. The results are not greatly different from the results shown in Fig. 3. At $\theta = 3$ deg there results

$$\frac{\sigma_c}{\mu_L} = 0.179$$

at

$$\beta = 18.0 \text{ deg.}$$

With the values of $k = 0.01$ and $\theta = 3$ deg, σ_C versus β is given in Fig. 5 for various values of yield parameter α. At $\alpha = 0$ there is no minimum of σ_c versus β and a zero-angle kink band is the result. Parameter $\alpha = 0$ implies no eccentricity between tensile and compressive yield in transverse stress. The formation of finite angle kink bands is a consequence of the general eccentricity shown in Fig. 2. Also, note in Figs. 3, 4,

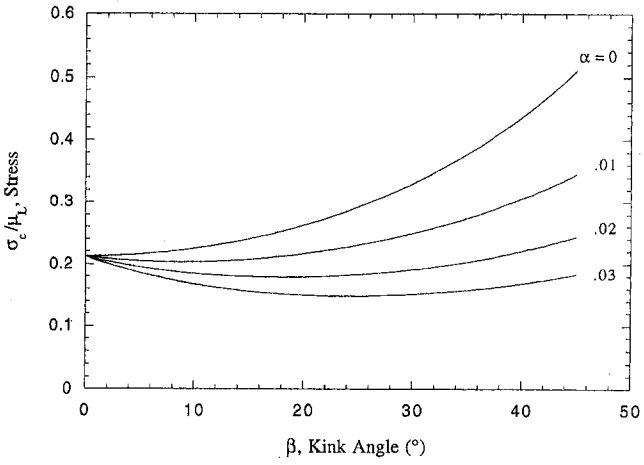


Fig. 5 Load versus kink angle, $k = .01$, $\theta = 3$ deg, $\zeta = 2.4$

Downloaded 04 May 2010 to 171.66.16.34. Redistribution subject to ASME license or copyright; see http://www.asme.org/terms/Terms_Use.cfm

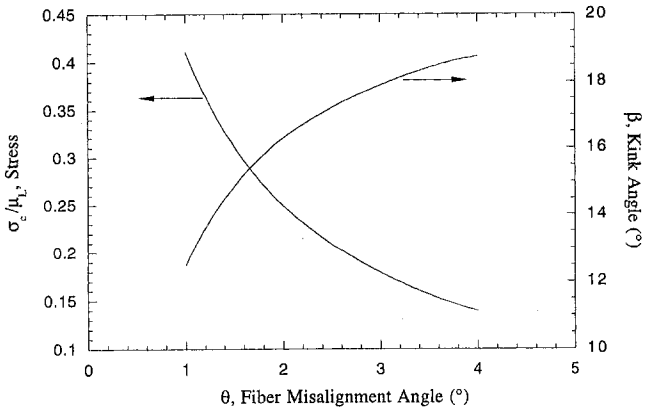


Fig. 6 Load and kink angle versus misalignment angle, α = .02, k = .01, ζ = 2.4

and 5 that the minimums in σ_c versus β are rather "shallow," suggesting that there would be expected a rather large scatter in the measurements of kink band inclinations.

A cross plot of data are given in Fig. 6 showing the values of σ_c and β at the minimum as a function of fiber misalignment angle, θ. It is seen that the angle of the kink band appears to approach an asymptote as θ increases, as discussed in the previous section on approximations. It may also be noted that the overall sensitivity of the kink band angle β to the fiber misalignment angle θ is at variance with the results of Kyriakides et al. (1995) and Fleck et al. (1995).

Attempts to generate well-defined compressive kink bands in carbon/epoxy composites are normally thwarted by an unstable fracture, which causes secondary failures such as delamination to occur upon failure in standard tests. In order to limit the fracture morphology to the kink band formed at the onset of compressive failure, well-aligned unidirectional cylindrical rods 1 mm in diameter were produced from a commercial carbon/epoxy prepreg tow (Fiberite 60U49 HyE). A single rod was embedded in an epoxy "dogbone" specimen in a manner similar to that described by Prandy and Hahn (1990). These specimens were compressed until failure occurred in the composite in the gage section—an event which was easily recognized by a significant load drop. Tested specimens were polished using standard metallographic techniques to expose the failed region of the composite rod.

Typical kink band morphologies for this carbon/epoxy system are shown in Fig. 7. All specimens exhibited several intersecting kink bands which were oriented at all directions with respect to the plane of the polished surface. Dark regions in the micrographs are locations where fractured material was expelled during polishing. Kink bands propagating within the plane of the polished surface were found to be inclined at approximately 20 deg.

To compare with model predictions, the compression strength of this material was measured using the Boeing-modified ASTM D695 test method and found to be 1.17 GPa. Furthermore, the longitudinal shear modulus was measured using a torsion test and found to be 4.83 GPa. In terms of the critical ratio for kinking (11), the measured strength ratio is 0.24. Comparison with strength and kink inclination angle predictions given earlier for averaged failure properties of typical carbon/epoxy systems shows that there is reasonable agreement with both of the corresponding measurements.

Due to the uniformity of failure properties for the carbon/epoxy systems, the predicted strength and kink angle for similar fiber misalignment angles will be the same. In contrast, the thermoplastic matrix composite APC-2 has different failure parameters and provides an interesting test of the model developed here. This material typically exhibits higher transverse tensile strength and strain than the epoxy-based systems. However, the transverse compression strain is comparable to the epoxy composites. Thus the failure parameter α is smaller for the thermoplastic system, resulting in the prediction that the kink band angle should be less inclined. Fortunately the inherently tough nature of the thermoplastic matrix leads to a more stable kink band development at failure and the geometry of well-defined bands have been reported. For APC-2, kink angles at smaller angles within the range 12–16 deg have indeed been measured (Kyriakides et al., 1995; Couque et al., 1993). Thus the reduced eccentricity between transverse tensile and compressive failure in thermoplastic systems yields smaller kink band angles than the epoxy-based materials as predicted by the model derived herein.

Acknowledgment

Work performed under the auspices of the U.S. Department of Energy by the Lawrence Livermore National Laboratory under contract number W-7405-ENG-48. The authors are appreciative to the Office of Naval Research, Dr. Y. D. S. Rajapakse monitor, for project support. S. J. DeTeresa gratefully acknowl-

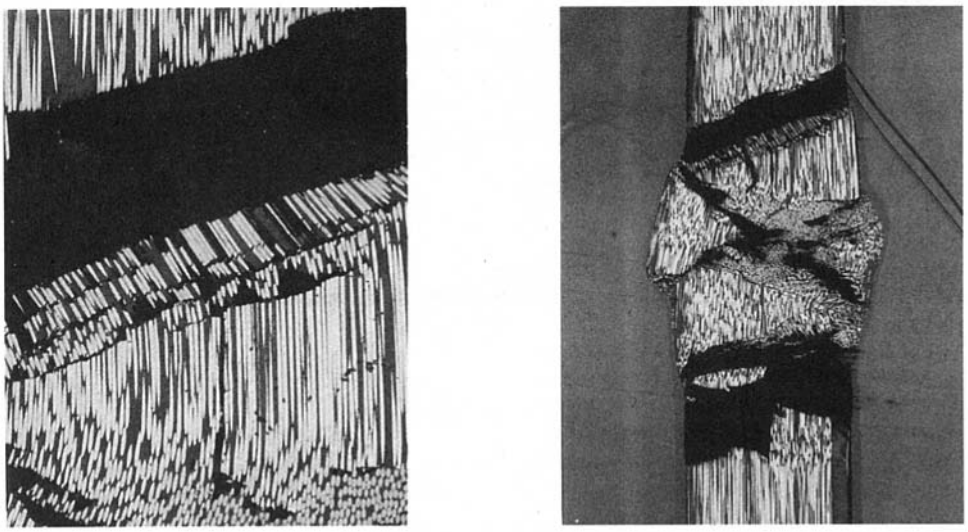


Fig. 7 Kink bands in 1-mm diameter unidirectional carbon fiber/epoxy composite rod

Downloaded 04 May 2010 to 171.66.16.34. Redistribution subject to ASME license or copyright; see http://www.asme.org/terms/Terms_Use.cfm

edges the support of the Joint DoD/DOE Office of Munitions Program.

References

Argon, A., 1972, "Fracture of Composites," *Treatise on Materials Science and Technology, 1,* Academic Press New York.

Budiansky, B., 1983, "Micromechanics," *Comput. Struct.,* Vol. 16, pp. 3–12.

Budiansky, B., and Fleck, N. A., 1993, "Compressive Failure of Fibre Composites," *J. Mech. Phys. of Sol.,* Vol. 41, pp. 183–211.

Christensen, R. M., 1988, "Tensor Transformations and Failure Criteria for the Analysis of Fiber Composite Materials," *J. Comp. Matls.,* Vol. 22, pp. 874–897.

Colvin, Jr., G. E., and Swanson, S. R., 1990, "Mechanical Characterization of IM7/8551-7 Carbon/Epoxy Under Biaxial Stress," ASME *Journal of Engineering Materials and Technology,* Vol. 112, p. 61.

Couque, H., Albertini, C., and Lankford, J., 1993, "Failure Mechanisms in a Unidirectional Fibre-Reinforced Thermoplastic Composite Under Uniaxial, In-Plane and Hydrostatically Confined Compression," *J. Mater. Sci. Letters,* Vol. 12, pp. 1953–1957.

Fleck, N. A., Deng, L., and Budiansky, B., 1995, "Prediction of Kink Width in Compressed Fiber Composites," ASME JOURNAL OF APPLIED MECHANICS, Vol. 62, pp. 329–337.

Grimes, G. C., Ranger, K. W., and Brunner, M. D., 1987, "Element and Subcomponent Tests," *Engineered Materials Handbook. Volume 1: Composites,* ASM International, pp. 313–345.

Halpin, J. C., 1984, *Primer on Composite Materials: Analysis,* Technomic, Lancaster, PA.

Kyriakides, S., Arseculeratne, R., Perry, E. J., and Liechti, K. M., 1995, "On The Compressive Failure of Fiber Reinforced Composites," *Int. J. Sol. Struct.,* Vol. 32, No. 6–7, pp. 689–738.

Lyon, R. E., Schumann, D. L., and DeTeresa, S. J., 1993, "Matrix-Dominated Mechanical Properties of a Fiber Composite Lamina," *Composite Materials: Testing and Design,* (11th Volume), ASTM STP 1206, E. T. Camponeschi, Jr., ed., ASTM, Philadelphia, PA, pp. 7–22.

Moran, P. M., Liu, X. F., and Shih, C. F., 1994, "Kink Band Formation and Band Broadening in Fiber Composites Under Compressive Loading," submitted for publication.

Prandy, J. M., and Hahn, H. T., 1990, "Compressive Strength of Carbon Fibers," *35th International SAMPE Symposium,* April 2–5, pp. 1657–1670.

Rosen, B. W., 1965, "Mechanics of Composite Strengthening" *Fiber Composite Materials,* ASM, Metals Park, OH, Chapter 3.

Schapery, R. A., 1994, "Prediction of Compressive Strength and Kink Bands in Composites Using a Work Potential," *Int. J. Sol. and Struct.,* in press.

Sutcliffe, W. S., and Fleck, N. A., 1993, "Effect of Geometry upon Compressive Failure of Notched Composites," *Int. J. Fract.,* Vol. 59, pp. 115–132.

Downloaded 04 May 2010 to 171.66.16.34. Redistribution subject to ASME license or copyright; see http://www.asme.org/terms/Terms_Use.cfm

Differential Equations Governing the Geometry of a Diamond Mesh Cod-end of a Trawl Net

F. G. O'Neill
SOAEFD Marine Laboratory,
P.O. Box 101
Victoria Road
Aberdeen AB11 9DB
Scotland

A new surface, made up of an infinite number of infinitesimal meshes, is defined to approximate the cod-end. The force balance on a mesh element of this surface is considered in the limit as the mesh size tends to zero and the differential equations governing the geometry of a diamond meshed cod-end of circular cross section are derived in cartesian coordinates. The parametric form of the equations in terms of a, *the distance along the cod-end profile, is then deduced and some special cases examined. In particular the case of a partially filled cod-end hanging under gravity is investigated and experimental measurements are compared with numerically obtained theoretical predictions. The numerical results are shown to provide a good description of the cod-end geometry except where the cod-end diameter is at its narrowest where there is a systematic departure of the predicted values from those measured. It is demonstrated that a probable explanation of this discrepancy is the assumption that the knots are simple points of intersection rather than finite well-defined structures.*

1 Introduction

To ensure that the conservation regulations which govern fishing gears are effective, they must be based on an understanding of the process by which fish are selected. Size selection of a fishing gear is the mechanism by which small fish escape through the meshes while the larger marketable fish are retained. The cod-end is that part of a trawl net where the catch accumulates and at which most fish selection is considered to take place (Fig. 1). It is the rearmost part of the net and is usually made up of two rectangular panels of netting joined at the sides to create a cylindrical section of netting (Figs. 2(*a*) and 2(*b*)). One end is joined to the net while the other is pulled closed by the codline, a rope fed through the last row of meshes, so that the only means of escape is through the meshes. The build up of catch at the back of the cod-end gives rise to the characteristic bulbous geometry (Fig. 2(*c*)).

In recent years changes in design and structure have been made in an effort to improve selectivity (Robertson and Ferro, 1988; Robertson and Stewart, 1988). It has become increasingly apparent, as a result, that mesh size is not the sole factor determining fish escape. The emphasis is now on the openness of the mesh and its dependence on mesh size and other design parameters such as number of meshes around, mesh shape, and twine thickness (Reeves et al., 1992; Lowry and Robertson, 1996). Furthermore, research is also directed at studying the roles of environmental parameters such as light intensity, water temperature, and water flow in modifying the behavioral responses of fish to their environmental and physical surroundings (Wardle, 1985). Essential to a study of any of these variables is a knowledge of the cod-end geometry which is determined by the interaction of the water flow, the catch size, and the design and physical characteristics of the netting.

This paper derives a set of differential equations which govern the geometry of an axisymmetric diamond mesh cod-end subject to applied forces which, due to the symmetry of the problem, are functions of one variable.

2 Basic Approach

The international standard ISO 1107-1974 defines a mesh to be "a designedly formed opening surrounded by netting material." However, for the purposes of this paper the definition of a mesh or mesh element will, in addition to the region specified by the ISO, also include the surrounding netting material and some of the area outside as marked in Fig. 3. Furthermore, the mesh size, M, is defined to be twice the "length of mesh side" as defined by ISO 1107-1974 (Fig. 3).

The standard approach in determining the set of differential equations governing a physical system is to examine the force balance on a differential element in the limit as the size of the element tends to zero. The success of such an approach depends on whether the differential element retains the mechanical properties of the system. With regard to a net, the mesh is the basic structural component and hence the smallest element capable of retaining these properties. Consequently the limiting approach is not readily applicable. By defining a series of surfaces, however, where the mesh size $M \to 0$, the number of meshes increases with $1/M^2$ and the tension in each mesh bar decreases with M, it is possible to apply a differential analysis to the force balance on a mesh element of the limiting surface.

This definition describes a surface to which the original piece of netting may be considered an approximation and is, in a sense, the reverse of the process employed in finite element analysis whereby a grid is defined to approximate a given surface.

2.1 Cod-end of Circular Cross-Section. For a cod-end of circular cross section, N meshes around and P meshes long the appropriate limiting regime is one where both NM and PM remain constant as $M \to 0$. Owing to the symmetry of the problem it is sufficient to restrict attention to a strip of meshes running the length of the cod-end and to determine from the position of these meshes a profile or outline of the cod-end (Fig. 4). This reduces the problem to one in one dimension. The approach will then be to examine the force balance on one of these meshes in the limit as the mesh size tends to zero.

It will be assumed that the meshes under investigation are bisected by the plane $z = 0$, that the x-axis is the axis of symme-

Contributed by the Applied Mechanics Division of THE AMERICAN SOCIETY OF MECHANICAL ENGINEERS for publication in the ASME JOURNAL OF APPLIED MECHANICS.

Discussion on this paper should be addressed to the Technical Editor, Professor Lewis T. Wheeler, Department of Mechanical Engineering, University of Houston, Houston, TX 77204-4792, and will be accepted until four months after final publication of the paper itself in the ASME JOURNAL OF APPLIED MECHANICS.

Manuscript received by the ASME Applied Mechanics Division, July 1995; final revision, Aug. 1996. Associate Technical Editor: W. K. Liu.

Copyright © 1997 by ASME

Downloaded 04 May 2010 to 171.66.16.34. Redistribution subject to ASME license or copyright; see http://www.asme.org/terms/Terms_Use.cfm

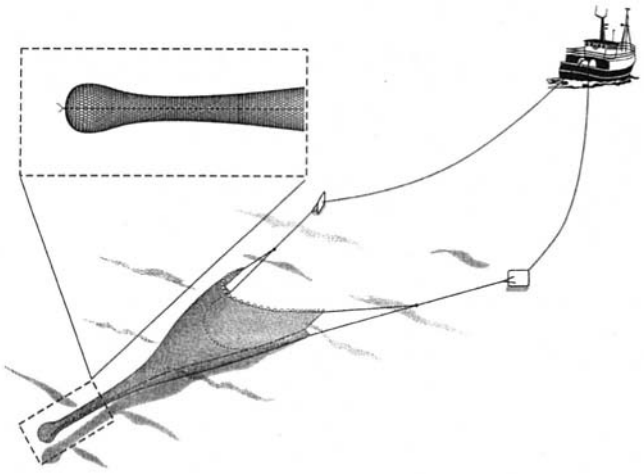


Fig. 1 A cod-end and its position on a demersal trawl

try and that y is the distance the knots (or nodes) of a mesh are from the axis of symmetry.

In Fig. 5 the nodes A and B of the mesh ACBD lie in the plane $z = 0$. The tensile forces acting on the mesh are

$$\tau^{+}_{A+},\ \tau^{-}_{A+},\ \tau^{+}_{B-},\ \tau^{-}_{B-},\ \tau^{+}_{C+},\ \tau^{+}_{C-},\ \tau^{-}_{D+},\ \tau^{-}_{D-}, \tag{1}$$

four of which are defined as follows:

$$\tau^{+}_{A+} = t_{A+}\begin{pmatrix} \cos\phi_{A+}\cos\theta_{A+} \\ \cos\phi_{A+}\sin\theta_{A+} \\ \sin\phi_{A+} \end{pmatrix}$$

$$\tau^{+}_{C-} = t_{C-}\begin{pmatrix} 1 & 0 & 0 \\ 0 & \cos\beta & -\sin\beta \\ 0 & \sin\beta & \cos\beta \end{pmatrix}\begin{pmatrix} -\cos\phi_{C-}\cos\theta_{C-} \\ -\cos\phi_{C-}\sin\theta_{C-} \\ \sin\phi_{C-} \end{pmatrix}$$

$$\tau^{-}_{B-} = t_{B-}\begin{pmatrix} -\cos\phi_{B-}\cos\theta_{B-} \\ -\cos\phi_{B-}\sin\theta_{B-} \\ -\sin\phi_{B-} \end{pmatrix}$$

$$\tau^{-}_{D+} = t_{D+}\begin{pmatrix} 1 & 0 & 0 \\ 0 & \cos\beta & \sin\beta \\ 0 & -\sin\beta & \cos\beta \end{pmatrix}\begin{pmatrix} \cos\phi_{D+}\cos\theta_{D+} \\ \cos\phi_{D+}\sin\theta_{D+} \\ -\sin\phi_{D+} \end{pmatrix} \tag{2}$$

where ϕ is half the angle between two adjacent mesh bars; θ the angle the plane they define makes with the plane $y = 0$; and where $\beta = \pi/N$, is half the angle made by the intersection of the radial lines through the two knots of a mesh either side of the plane $z = 0$ (Figs 6 and 7). The matrices are the 3×3 matrices of rotation of $\pm\beta$ radians about the x-axis and are required to give the correct form of the forces acting at C and D which are either side of the central line through A and B.

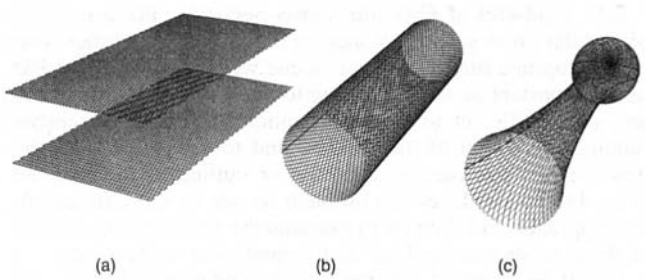


Fig. 2 A cod-end made from two rectangular pieces of netting

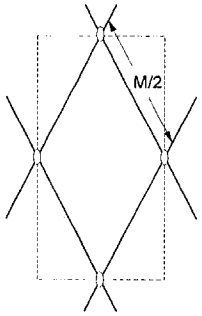


Fig. 3 The dotted line identifies the area of the surface element which is examined in the limit as the mesh size, $M \to 0$

The subscript identifies the node and the side of the node (in the x direction) on which the variable is evaluated and, in the case of the vector quantities, the superscript indicates whether the vector points to the right or the left of the xy-plane, i.e., the sign of the z component. The other four tensile vectors of (1) can be similarly defined.

It can be shown by examining the force balance of the four tensile vectors which act on a node, that $\theta_{\cdot+} = \theta_{\cdot-}$ and $t_{\cdot+}\cos\phi_{\cdot+} = t_{\cdot-}\cos\phi_{\cdot-}$ at each node.

2.2 Geometric Relationships. In Fig. 7 E bisects DC and $|AC| = |CB| = |BD| = |DA| = M/2$ implying that $\phi_{A-} = \phi_{B+} = \phi$. Hence $|AE| = |EB| = M/2\cos\phi$ and $|DC| = 2y_C \sin\beta = M\sin\phi$. The following relationships are easily derived from the geometry of the problem, the first two of which are equivalent and derived from Fig. 7 while the third follows from Fig. 6:

$$\sin\beta = \frac{M\sin\phi}{2y_C} \tag{3}$$

$$\tan\phi = \frac{2y_C\sin\beta}{\sqrt{M^2 - 4y_C^2\sin^2\beta}} \tag{4}$$

$$\Delta x = \frac{M}{2}\cos\phi(\cos\theta_A + \cos\theta_B) \tag{5}$$

3 Forces on a Mesh Element

3.1 Tensile Forces. Owing to symmetry, the subscripts C and D are interchageable, furthermore, $t_{C+}\cos\phi_{C+} = t_{C-}\cos$

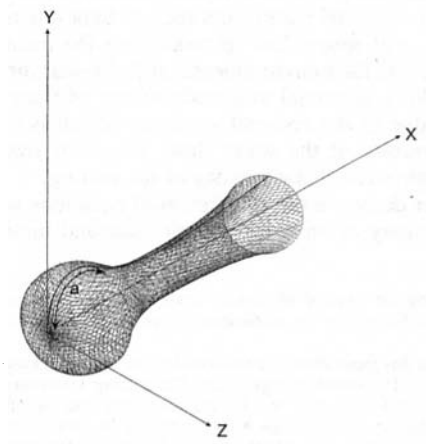


Fig. 4 Coordinate system and strip of meshes under investigation

Downloaded 04 May 2010 to 171.66.16.34. Redistribution subject to ASME license or copyright; see http://www.asme.org/terms/Terms_Use.cfm

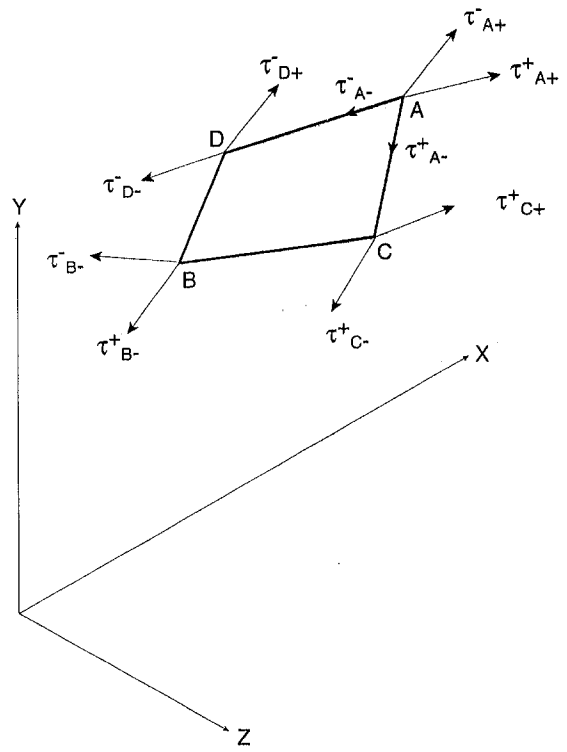


Fig. 5 The tensile forces acting on mesh ACBD

ϕ_{C-}. Hence the sum of the eight tensile forces of (1) can be shown to be

$$2t_{A+}\begin{pmatrix}\cos\phi_{A+}\cos\theta_A\\ \cos\phi_{A+}\sin\theta_A\\ 0\end{pmatrix}+2t_{B-}\begin{pmatrix}-\cos\phi_{B-}\cos\theta_B\\ -\cos\phi_{B-}\sin\theta_B\\ 0\end{pmatrix}$$

$$-2t_{C+}\begin{pmatrix}0\\ \sin\beta\sin\phi_{C+}\\ 0\end{pmatrix}-2t_{C-}\begin{pmatrix}0\\ \sin\beta\sin\phi_{C-}\\ 0\end{pmatrix}. \quad (6)$$

Let $T = 2Nt\cos\phi\cos\theta$ be the sum of the x-component of tension acting in each mesh across a cross section of the cod-end. $T_\cdot = 2Nt_{\cdot+}\cos\phi_{\cdot+}\cos\theta_\cdot = 2Nt_{\cdot-}\cos\phi_{\cdot-}\cos\theta_\cdot$ at each node so the sum of the tensile forces on a mesh are

$$\frac{T_A}{N}\begin{pmatrix}1\\ \tan\theta_A\\ 0\end{pmatrix}-\frac{T_B}{N}\begin{pmatrix}1\\ \tan\theta_B\\ 0\end{pmatrix}$$

$$-\frac{T_C}{N}\begin{pmatrix}0\\ \dfrac{\sin\beta\tan\phi_{C+}}{\cos\theta_C}\\ 0\end{pmatrix}-\frac{T_C}{N}\begin{pmatrix}0\\ \dfrac{\sin\beta\tan\phi_{C-}}{\cos\theta_C}\\ 0\end{pmatrix}. \quad (7)$$

3.2 Surface Forces. Figure 3 outlines the surface area of the mesh element which, from the geometric relationships of Fig. 7, is

$$\Delta s = y_C M\sin\beta\cos\phi + y_A\frac{M}{2}\sin\beta\cos\phi_{C+} + y_B\frac{M}{2}\sin\beta\cos\phi_{C-}. \quad (8)$$

With the force per unit area in the x and y directions given, respectively, by Q_C and R_C, the surface force vector is

$$\Delta s\begin{pmatrix}Q_C\\ R_C\\ 0\end{pmatrix}. \quad (9)$$

3.3 Force Balance. Gathering together the tensile and surface force terms the force balance is

$$\frac{T_A}{N}\begin{pmatrix}1\\ \tan\theta_A\\ 0\end{pmatrix}-\frac{T_B}{N}\begin{pmatrix}1\\ \tan\theta_B\\ 0\end{pmatrix}-\frac{T_C}{N}\begin{pmatrix}0\\ \dfrac{\sin\beta\tan\phi_{C+}}{\cos\theta_C}\\ 0\end{pmatrix}$$

$$-\frac{T_C}{N}\begin{pmatrix}0\\ \dfrac{\sin\beta\tan\phi_{C-}}{\cos\theta_C}\\ 0\end{pmatrix}+\Delta s\begin{pmatrix}Q_C\\ R_C\\ 0\end{pmatrix}=\begin{pmatrix}0\\ 0\\ 0\end{pmatrix} \quad (10)$$

which on multiplying through by $N/\Delta x$ gives

$$\frac{T_A}{\Delta x}\begin{pmatrix}1\\ \tan\theta_A\\ 0\end{pmatrix}-\frac{T_B}{\Delta x}\begin{pmatrix}1\\ \tan\theta_B\\ 0\end{pmatrix}-\frac{T_C}{\Delta x}\begin{pmatrix}0\\ \dfrac{\sin\beta\tan\phi_{C+}}{\cos\theta_C}\\ 0\end{pmatrix}$$

$$-\frac{T_C}{\Delta x}\begin{pmatrix}0\\ \dfrac{\sin\beta\tan\phi_{C-}}{\cos\theta_C}\\ 0\end{pmatrix}+\frac{N\Delta s}{\Delta x}\begin{pmatrix}Q_C\\ R_C\\ 0\end{pmatrix}=\begin{pmatrix}0\\ 0\\ 0\end{pmatrix}. \quad (11)$$

In the limit as $M \to 0$ each of the variables tends towards its nonsubscripted nonsuperscripted equivalent, which because of the symmetry of the problem will all be functions of x. The following relationships will also hold: $N\sin\beta \to \pi$, $\sin\beta/\Delta x \to \tan\phi/2y\cos\theta$, and $N\Delta s/\Delta x \to 2\pi y/\cos\theta$. The first follows directly from the definition of β, the second two from Eqs. (3), (5), and (8). When substituted into the above force vector balance equation the x and y component equations become

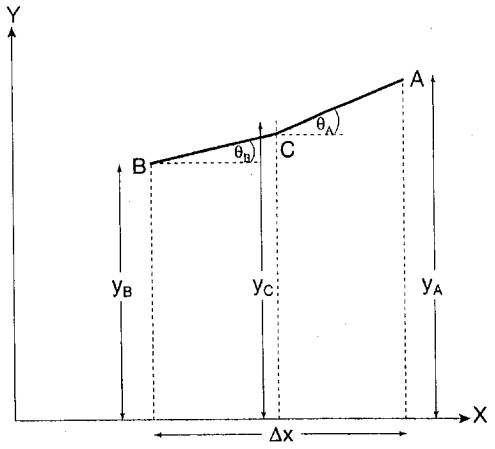


Fig. 6 Profile of mesh ACBD

Downloaded 04 May 2010 to 171.66.16.34. Redistribution subject to ASME license or copyright; see http://www.asme.org/terms/Terms_Use.cfm

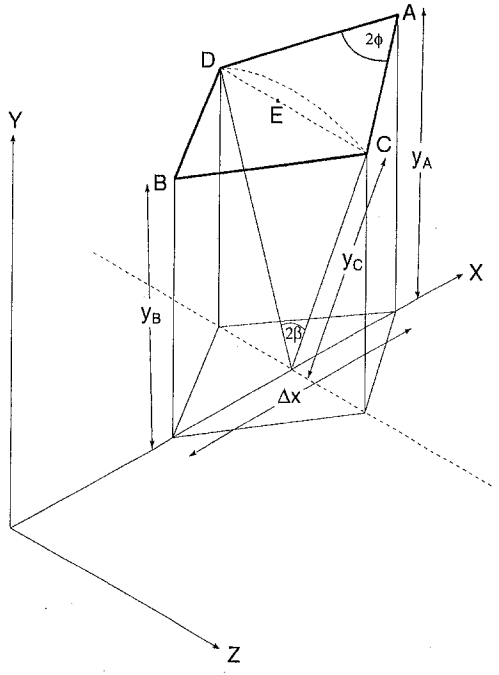


Fig. 7 Definition of geometric variables of mesh ACBD

$$\frac{dT}{dx} + \frac{2\pi y}{\cos\theta} Q(x) = 0 \tag{12}$$

$$\frac{d(T\tan\theta)}{dx} - \frac{T\tan^2\phi}{y\cos^2\theta} + \frac{2\pi y}{\cos\theta} R(x) = 0. \tag{13}$$

4 Governing Equations

4.1 Cartesian Formulation. It follows from Eq. (4) that in the limit

$$\tan\phi = \frac{2\pi y}{\sqrt{N^2M^2 - 4\pi^2y^2}}. \tag{14}$$

For a smooth curve with a continuous first derivative,

$$\tan\theta = \frac{dy}{dx}. \tag{15}$$

Substituting these two expressions into Eqs. (12) and (13) gives

$$\frac{d^2y}{dx^2} = \frac{4\pi^2y}{N^2M^2 - 4\pi^2y^2}\left(1 + \left(\frac{dy}{dx}\right)^2\right)$$

$$- \frac{2\pi y}{T(x)}\left(1 + \left(\frac{dy}{dx}\right)^2\right)^{1/2}\left(R(x) - Q(x)\frac{dy}{dx}\right) \tag{16}$$

$$\frac{dT}{dx} = -2\pi y Q(x)\left(1 + \left(\frac{dy}{dx}\right)^2\right)^{1/2}, \tag{17}$$

two equations in two unknowns: a second-order equation in y requiring two boundary conditions and a first-order equation in T requiring one. Thus this pair of equations governs the geometry of a cod-end N meshes around and of mesh size M subject to the surface force $(Q(x), R(x), 0)$ and prescribed boundary conditions.

It is shown in Appendix A that when the cod-end is P meshes long the maximum value of x must satisfy

$$\int_0^{x_{\max}} \frac{NM}{\sqrt{N^2M^2 - 4\pi^2y^2}}\left(1 + \left(\frac{dy}{dx}\right)^2\right)^{1/2} dx = PM. \tag{18}$$

4.2 Nondimensionalisation of Governing Equations. The following are suitable scales for the dimensional variables:

$$x' = x/NM \quad y' = y/NM \quad a' = a/NM$$

$$T' = T/T_0 \quad R' = R((NM)^2/T_0) \quad Q' = Q((NM)^2/T_0)$$

where T_0 is a representative T value. When substituted into Eqs. (16)–(18) and where for simplicity the superscripts are suppressed the result is the following:

$$\frac{d^2y}{dx^2} = \frac{4\pi^2y}{1 - 4\pi^2y^2}\left(1 + \left(\frac{dy}{dx}\right)^2\right)$$

$$- \frac{2\pi y}{T(x)}\left(1 + \left(\frac{dy}{dx}\right)^2\right)^{1/2}\left(R(x) - Q(x)\frac{dy}{dx}\right) \tag{19}$$

$$\frac{dT}{dx} = -2\pi y Q(x)\left(1 + \left(\frac{dy}{dx}\right)^2\right)^{1/2} \tag{20}$$

$$\int_0^{x_{\max}} \frac{N/P}{\sqrt{1 - 4\pi^2y^2}}\left(1 + \left(\frac{dy}{dx}\right)^2\right)^{1/2} dx = 1, \tag{21}$$

a system wholly dependent on the parameter N/P, the forces $Q(x)$ and $R(x)$ and the boundary conditions.

4.3 Parametric Form. For many practical problems the slope dy/dx will be infinite at one of the boundary points. This singularity, which would pose problems for numerical solutions, can be removed by using the equations of Appendix B to reformulate the problem in parametric form in terms of a, the arc length along the cod-end (Fig. 4), as follows:

$$\frac{d^2y}{da^2} = \frac{4\pi^2y}{1 - 4\pi^2y^2}\left(1 - \left(\frac{dy}{da}\right)^2\right)$$

$$- \frac{2\pi y R(a)}{T(a)}\left(1 - \left(\frac{dy}{da}\right)^2\right)^{3/2}$$

$$+ \frac{2\pi y Q(a)}{T(a)}\frac{dy}{da}\left(1 - \left(\frac{dy}{da}\right)^2\right) \tag{22}$$

$$\frac{dT}{da} = -2\pi y Q(a) \tag{23}$$

$$\frac{dx}{da} = \left(1 - \left(\frac{dy}{da}\right)^2\right)^{1/2} \tag{24}$$

$$\int_0^{a_{\max}} \frac{N/P}{\sqrt{1 - 4\pi^2y^2}}\,da = 1 \tag{25}$$

where a is the distance, from the codline, along the cod-end profile.

An alternative form of these governing equations is presented in Appendix C and employs forms of the variables that are intuitively more suited to the parameterization in a.

5 Particular Cases

When the surface forces are those due to the hydrodynamic flow through a cod-end $Q(a)$ and $R(a)$ represent the drag and lift components on a surface element of the cod-end. The func-

Downloaded 04 May 2010 to 171.66.16.34. Redistribution subject to ASME license or copyright; see http://www.asme.org/terms/Terms_Use.cfm

tional form of these forces, however, is not known and so to verify the model it is necessary to examine simpler cases where the surface forces can be fully described.

5.1 No Surface Forces. One such case is when there are no surface forces and $Q(a) = 0$ and $R(a) = 0$ and the only forces acting are the tensions in each mesh bar. This is the case for netting stretched between two circular rings. The governing equations are

$$\frac{d^2y}{da^2} = \frac{4\pi^2 y}{1 - 4\pi^2 y^2}\left(1 - \left(\frac{dy}{da}\right)^2\right) \tag{26}$$

$$T(a) = \text{constant} \tag{27}$$

$$\frac{dx}{da} = \left(1 - \left(\frac{dy}{da}\right)^2\right)^{1/2} \tag{28}$$

$$\int_0^{a_{\max}} \frac{N/P}{\sqrt{1 - 4\pi^2 y^2}}\, da = 1 \tag{29}$$

from which it is clear that the geometry of the netting stretched between two circular rings is independent of the force pulling the rings apart.

5.2 Pressure Forces. Another case is when the surface forces are pressure type and act normal to the netting surface. Here $Q(a)$ and $R(a)$ are the horizontal and vertical components of a pressure force $S(a)$ where $Q(a) = -S(a) \sin\theta$ and $R(a) = S(a) \cos\theta$ which, when substituted into the governing Eqs. (22)–(25), yield

$$\frac{d^2y}{da^2} = \frac{4\pi^2 y}{1 - 4\pi^2 y^2}\left(1 - \left(\frac{dy}{da}\right)^2\right) - \frac{2\pi y S(a)}{T(a)}\left(1 - \left(\frac{dy}{da}\right)^2\right) \tag{30}$$

$$\frac{dT}{da} = 2\pi y S(a)\frac{dy}{da} \tag{31}$$

$$\frac{dx}{da} = \left(1 - \left(\frac{dy}{da}\right)^2\right)^{1/2} \tag{32}$$

$$\int_0^{a_{\max}} \frac{N/P}{\sqrt{1 - 4\pi^2 y^2}}\, da = 1. \tag{33}$$

5.3 Cod-end Hanging Under Gravity. A partially filled cod-end hanging under gravity, shown in Figs. 8, 9, and 10, incorporates both these cases. The surface forces acting on the filled bulbous part of the cod-end act normal to the surface, and are of the form $S(a) = \rho g(h - x(a))$ where the origin is taken to be the codline and h is distance from the top of the "catch" (sealed polythene bags of water) to the origin. For $x(a) > h$, $S(a) = 0$ and the former set of equations holds.

These equations were solved numerically. An iterative finite difference scheme employing central differences solved Eq. (30), the integrations of Eqs. (31) to (33) were carried out by D01GAF (NAG, 1993) and $a_{\max}$ was estimated by the least squares minimization routine E04UPF (NAG, 1993). The continuous curve of Fig. 11 contains the numerical solution of the case where

the mesh size, $M = 38.2$ mm,
no meshes around, $N = 50$,
no meshes long, $P = 50$,
the volume of "catch" $= 0.0265$ m^3, and
the radius of the ring from which the cod-end hangs is 25 cm.

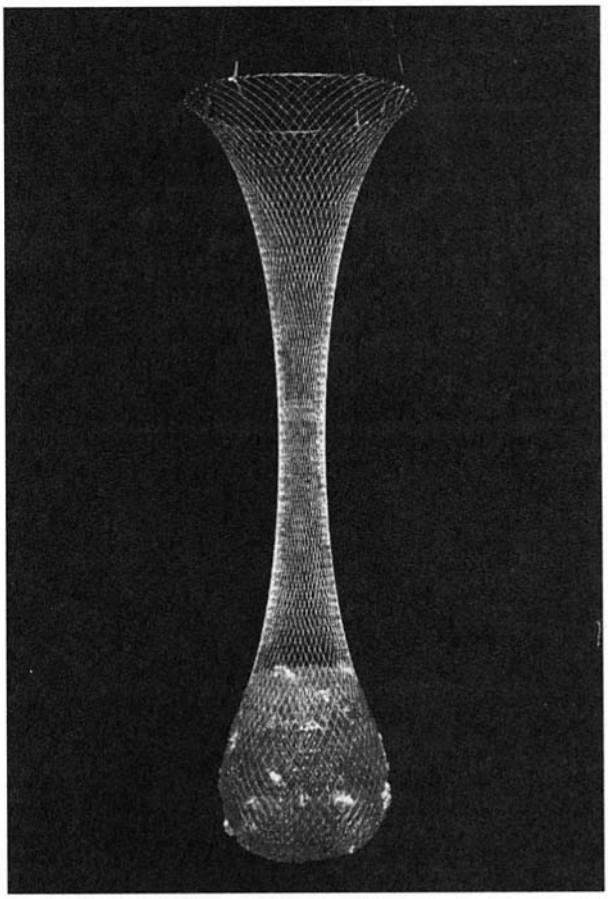


Fig. 8 The cod-end described in the text hanging with 31.5 kg of water filled polythene bags

The discrete points were measured from a video recording of such a cod-end. The camera was attached to a vertical stand and free to move the length of the cod-end. Individual frames were frozen and a digitized reading of the cross-sectional diameter of that part of the cod-end centred on the frame taken. The averaged unstretched mesh size was 37.6 mm (standard error 0.3 mm) and the averaged stretched mesh size, measured while the cod-end was hanging, was 38.2 mm (standard error 0.6 mm). The standard error of the stretched mesh size is larger because it not only measures the random variability of mesh size but also takes into account the different relative increases of mesh size when under tension.

It is clear from Fig. 11 that the numerical results provide a good description of cod-end geometry. However, where the cod-end diameter is at its narrowest there is a systematic departure of the predicted values from those measured. There are a number of potential explanations the most likely being as a result of the assumption, implicit in the derivation, that the knots are simple points of intersection rather than well-defined asymmetric finite structures. This structure and how the twine emerges from it will contribute to the openness of the mesh, and consequently to the cod-end geometry. One of the pairs of adjacent twines is separated by a twine width where it emerges from the knot, the effect of which will be more pronounced the more the mesh is closed. When the mesh is open the point definition of a mesh is probably sufficiently accurate and the predictions of the model reliable as the separating twine will not deflect those emerging. The minimum diameter measured was 9.8 cm whereas the predicted value was 8 cm giving a circumferential difference of 1.8 πcm or an increase of 0.11 cm per mesh. This is of the same order as the twine diameter which was approximately 0.09 cm.

Downloaded 04 May 2010 to 171.66.16.34. Redistribution subject to ASME license or copyright; see http://www.asme.org/terms/Terms_Use.cfm

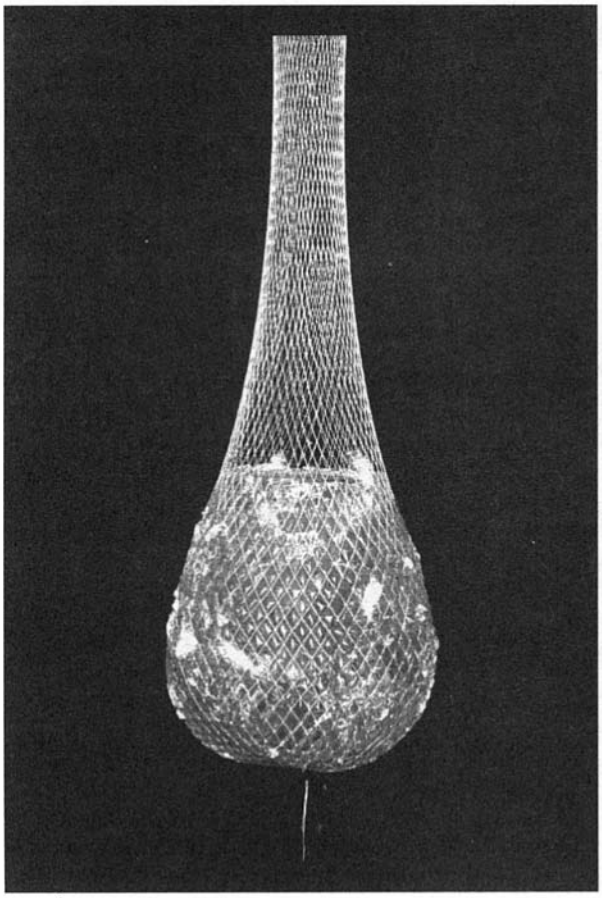


Fig. 9 The "catch" of Fig. 8 in greater detail

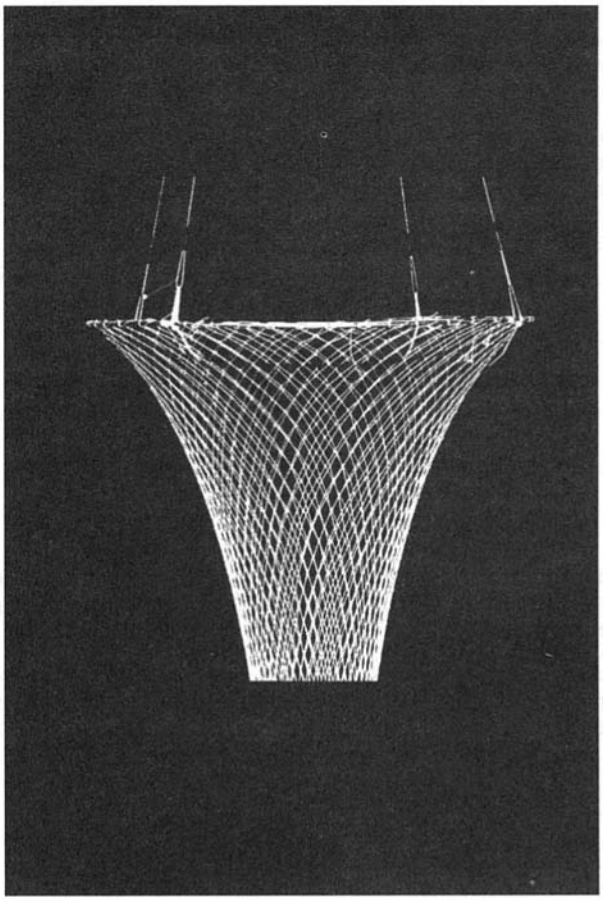


Fig. 10 The supporting ring of Fig. 8 in greater detail

The fact that the model uses an average mesh size and does not take into account twine elasticity may also be a contributory factor to the difference of predicted and measured values. The mesh bar tension, $t(x)$, is displayed in Fig. 12 for the case examined above where there are local maxima at the cod-end bulge and at the ring. It is shown in Appendix C that when the surface forces act normal to the surface the relationship between mesh bar tension and radial distance y can be expressed as follows:

$$t(a) \propto \frac{1}{1 - 4\pi^2 y^2}. \tag{34}$$

Mesh size extension will vary accordingly, though probably not enough to account solely for the discrepancies above. The other curve of Fig. 12 is that of $T(x)$ when read from the right-hand y-axis and $T(x)/2N$, the x-component of $t(x)$, when read from the left-hand axis.

The resistance of meshes to opening, due to twine flexural rigidity, will also affect cod-end geometry. This is particularly so for some of the cod-ends employed by the fishing industry (Lowry and Robertson, 1996). However, the nylon twine used in the construction of the netting of the experimental cod-end above has no effective flexural rigidity and consequently the resistance of meshes to opening is not a factor here.

6 Discussion

A series of experimental trials for cod-ends of different designs and of different twine to mesh size ratios would demonstrate whether the explanation put forward above accounts for the difference between the predicted and measured values of cod-end geometry If so, it will be necessary to investigate whether the effect of the knot can be incorporated into the mathematical model or whether an empirical approach will be required.

Nevertheless with regard to cod-end selectivity, the most important part of the cod-end is that immediately forward of the catch where the meshes unblocked by catch are most open. The predictions of the model in this area are very accurate for the case above of a cod-end hanging under gravity and should be more so for a cod-end being fished where the hydrodynamic forces acting will tend to open the cod-end further. Thus the model in its present form should prove very useful in studying and understanding the selection process. Initially it will enable a simple comparison of the amount the meshes are open, and hence potential selectivity, between cod-ends of different design (mesh size, no meshes around/long etc) and demonstrate the effect of catch size on selectivity. A more sophisticated model of cod-end geometry will incorporate the results of a study of the hydrodynamic forces, take into account factors such as twine elasticity and flexural rigidity and consider cod-ends of kite and

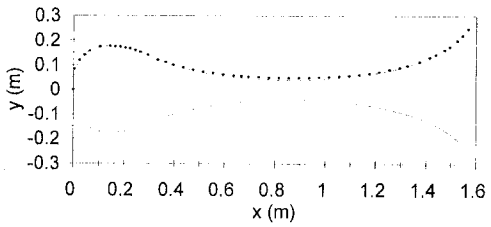


Fig. 11 The numerical predictions and measured values of the geometry of the cod-end described in the text filled with a "catch" of 26.5 kg

Downloaded 04 May 2010 to 171.66.16.34. Redistribution subject to ASME license or copyright; see http://www.asme.org/terms/Terms_Use.cfm

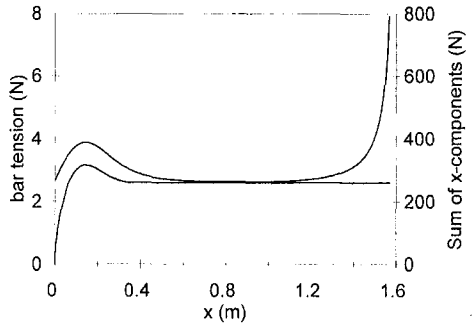


Fig. 12 The numerical predictions of bar tension $t(x)$, and $T(x) = 2Nt(x)$ cos ϕ cos θ

hexagonal shaped meshes. Such a model would be the basis of a predictive model of cod-end selectivity which would benefit fishing gear technologists and fisheries managers. To date very expensive sea trials have been necessary in the development of novel and more selective cod-ends and a capacity to evaluate, at the design stage, the influence of various parameters would permit the initial testing of new designs "on shore" and allow an assessment of their use by the fishing industry on future stocks.

References

ISO 1107-1974, 1974, "Fishing nets—Netting—Basic terms and definitions," International Standards Organisation.

Lowry, N., and Robertson, J. H. B., 1996, "The effect of twine thickness on cod-end selectivity of trawls for haddock in the North Sea," *Fisheries Research,* Vol. 26, pp. 353–363.

NAG, 1993, *NAG Fortan Library Manual Mark 16.* NAG Ltd., Oxford, UK.

Reeves, S. A., Armstrong, D. W., Fryer, R. J., and Coull, K. A., 1992, "The effects of mesh size, cod-end extension length and cod-end diameter on the selectivity of Scottish trawls and seines," *ICES Journal of Marine Science,* Vol. 49, pp. 279–288.

Robertson, J. H. B., and Ferro, R. S. T., 1988, "Mesh selection within the cod-ends of trawls. The effects of narrowing the cod-end and shortening the extension," Scottish Fisheries Research Report, Vol. 39.

Robertson, J. H. B., and Stewart, P. A. M., 1988, "A comparison of size selection of haddock and whiting by square and diamond mesh cod-ends," *J. Cons. Int. Explo. Mer,* Vol. 44, pp. 148–161.

Wardle, C. S., 1985, "Fish behaviour and fishing gears," *The Behaviour of Teleost Fishes,* T. J. Pitcher, ed., Croom Helm, pp. 463–495.

APPENDIX A

From Eq. (5)

$$M = \frac{2\Delta x}{\cos\phi(\cos\theta_A + \cos\theta_B)}$$

where Δx is the distance along the x-axis between the knots A and B. For a cod-end P meshes long

$$PM = \sum_{i=1}^{P} \left(\frac{2\Delta x}{\cos\phi(\cos\theta_A + \cos\theta_B)} \right)_i$$

where the term in brackets is evaluated at the ith mesh. In the limit as $M \to 0$, $P \to \infty$ and PM remains constant the summation becomes

$$PM = \int_0^{x_{\max}} \frac{1}{\cos\phi\cos\theta}\,dx = \int_0^{x_{\max}} \frac{NM}{\sqrt{N^2M^2 - 4\pi^2y^2}} \left(1 + \left(\frac{dy}{dx}\right)^2\right)^{1/2} dx$$

where $x_{\max}$ is the maximum value of x.

APPENDIX B

Using the following relationships between x, y, and a,

$$1 = \left(\frac{dx}{da}\right)^2 + \left(\frac{dy}{da}\right)^2 \quad \frac{dy}{dx} = \frac{dy}{da}\Big/\frac{dx}{da},$$

it can be shown that

$$\frac{dx}{da}\frac{d^2x}{da^2} = -\frac{dy}{da}\frac{d^2y}{da^2}$$

$$\frac{d^2y}{dx^2} = \left(\frac{dx}{da}\frac{d^2y}{da^2} - \frac{dy}{da}\frac{d^2x}{da^2}\right)$$

$$1 + \left(\frac{dy}{dx}\right)^2 = \left(1 - \left(\frac{dy}{da}\right)^2\right)^{-1},$$

the first two of which can be combined to give

$$\frac{d^2y}{dx^2} = \frac{d^2y}{da^2}\left(1 - \left(\frac{dy}{da}\right)^2\right)^{-2}.$$

APPENDIX C

The governing equations can again be reformulated in a slightly different way. Had the derivation of the equations from first principles initially employed the parametric variable a and resolved the force balance tangential and normal to the cod-end surface the most obvious characterization of tension would have been either $T_L(a) = 2Nt(a)\cos\phi$ or $T_N(a) = 2Nt(a)$ rather than $T(a) = 2Nt(a)\cos\phi\cos\theta$. Choosing the first of these and substituting $T(a) = T_L(a)\cos\theta$ into Eqs. (22)–(23) gives

$$\frac{d^2y}{da^2} = \frac{4\pi^2y}{1 - 4\pi^2y^2}\left(1 - \left(\frac{dy}{da}\right)^2\right) - \frac{2\pi yR(a)}{T_L(a)} \times \left(1 - \left(\frac{dy}{da}\right)^2\right) + \frac{2\pi yQ(a)}{T_L(a)}\frac{dy}{da}\left(1 - \left(\frac{dy}{da}\right)^2\right)^{1/2}$$

$$\frac{dx}{da}\frac{dT_L}{da} + T_L\frac{d^2x}{da^2} = -2\pi yQ(a).$$

Employing the formulae of Appendix B and substituting the first of these into the second gives the following expression for T_L:

$$\frac{dT_L}{da} = \frac{4\pi^2yT_L}{1 - 4\pi^2y^2}\frac{dy}{da} - 2\pi yQ(a)\left(1 - \left(\frac{dy}{da}\right)^2\right)^{1/2} - 2\pi yR(a)\frac{dy}{da}.$$

Expressing the surface forces in terms of forces acting normal and tangential to the surface provides the following alternative form of the scaled governing equations of diamond mesh cod-end geometry

$$\frac{d^2y}{da^2} = \frac{4\pi^2y}{1 - 4\pi^2y^2}\left(1 - \left(\frac{dy}{da}\right)^2\right) - \frac{2\pi yS(a)}{T_L(a)}\left(1 - \left(\frac{dy}{da}\right)^2\right)^{1/2}$$

$$\frac{dT_L}{da} = \frac{4\pi^2yT_L}{1 - 4\pi^2y^2}\frac{dy}{da} - 2\pi yV(a)$$

$$\frac{dx}{da} = \left(1 - \left(\frac{dy}{da}\right)^2\right)^{1/2}$$

$$\int_0^{a_{\max}} \frac{N/P}{\sqrt{1 - 4\pi^2y^2}}\,da = 1$$

where $S(a) = -Q(a)\sin\theta + R(a)\cos\theta$ and $V(a) = Q(a)\cos\theta + R(a)\sin\theta$.

Downloaded 04 May 2010 to 171.66.16.34. Redistribution subject to ASME license or copyright; see http://www.asme.org/terms/Terms_Use.cfm

For the case where the surface force acts only normally ($V(a) = 0$) the following analytic expression for T_L can be readily derived:

$$T_L = \frac{\text{constant}}{\sqrt{1 - 4\pi^2 y^2}}$$

which with $T_L(a) = 2Nt(a) \cos \phi$ and

$$\cos \phi = \sqrt{1 - 4\pi^2 y^2}$$

gives, for a given cod-end design specification,

$$t(a) \propto \frac{1}{1 - 4\pi^2 y^2} .$$

Clearly, if required, the governing equations can also be expressed in terms of $t(a)$.

Downloaded 04 May 2010 to 171.66.16.34. Redistribution subject to ASME license or copyright; see http://www.asme.org/terms/Terms_Use.cfm

Predicted Thermal Mismatch Stresses in a Cylindrical Bi-material Assembly Adhesively Bonded at Its Ends

E. Suhir
Bell Laboratories,
600 Mountain Avenue, Room ID-443,
Murray Hill, NJ 07974
Fellow ASME

A simple analytical stress model, based on the strength-of-materials approach, is developed for the evaluation of thermally induced shearing stresses in a long cylindrical bi-material assembly adhesively bonded at its ends and subjected to the change in temperature. The emphasis is on the interaction of the "global" thermal mismatch stresses, counted with respect to the mid cross section of the assembly as a whole, and the "local" stresses, counted with respect to the mid cross sections of the bonded regions. The effect of the coefficient of thermal expansion of the adhesive material itself is also considered. We show also how to evaluate the fundamental frequency of vibrations of the inner cylinder with consideration of the thermally induced tension, if any.

Introduction

An elongated bi-material assembly, adhesively bonded, soldered, welded, or brazed at the ends, is a useful analytical stress model which is able to provide valuable insight into the interaction of the "global" and "local" thermal expansion (contraction) mismatch stresses, as well as into the role of the compliance and the coefficient of expansion of the adhesive itself in some microelectronic and fiber optic structures. Typical examples are solder joint interconnections in flip-chip package designs, and optical glass fibers epoxy bonded or soldered into capillaries or ferrules. In this analysis, we use the term "global" to define the mismatch of the adherends (chip and substrate in an electronic package, or glass fiber and capillary in a fiber optic assembly), counted with respect to the mid cross section of the assembly as a whole, while the term "local" is used to define the mismatch, counted with respect to the mid cross sections of the bonded regions. This terminology, accepted in electronic packaging engineering (see, for instance, Clech et al., 1990, 1993; Suhir, 1995), should not be confused with similar terminology used in some other areas, such as, say, finite element analyses.

Mechanical behavior of, and thermally induced stresses in, adhesively bonded joints have been addressed by many investigators, primarily in application to the needs of the avionic industry and "high-technology" engineering (see, for instance, Volkersen, 1938; de Bruyne, 1944; Goland and Reissner, 1944; Hart-Smith, 1973a, b, c; Suhir, 1986, 1989, 1994a; Mishkevich and Suhir, 1993). The interaction of the global and the local thermal mismatch stresses in an elongated bi-material rectangular plate was analyzed by Suhir (1995) under an assumption that the adhesive layer is so thin and so compliant that its own coefficient of expansion need not be accounted for. The suggested model is a generalization of a theory developed earlier for a continuous bond (Suhir, 1986, 1989). In the analysis which follows, this model is modified for the case of a circular structure. In addition, when analyzing the effect of the local mismatch, i.e., the mismatch caused by the dissimilar materials within the bonded area, we consider a situation when the adhesive ring is not thin and therefore the coefficient of thermal expansion of the adhesive material, despite its low Young's modulus, should be taken into account.

Analysis

"Local" Mismatch

Axial Forces in the Midportion of a Long Bonded Area. Let a bi-material annular cylinder adhesively bonded at the ends (Fig. 1) be manufactured at an elevated temperature and subsequently cooled down to a low (room, operation, or testing) temperature. In this section, we consider local thermal contraction mismatch only, i.e., evaluate the effects of the thermal contraction mismatch of the dissimilar materials, including the adhesive material itself, within the bonded areas and disregard the forces, arising because of the thermal contraction mismatch of the adherends in the unbonded midportion of the assembly.

We start with a simplest model, aimed at the evaluation of the thermally induced forces in the inner region of a sufficiently long bonded area, where the interfacial shearing stresses are small. Note that a detailed analysis of the state of stress in the inner region of a tri-material composite cylinder has been carried out, on the basis of plane-strain approximation, in Suhir (1994b) in application to an optical glass fiber soldered into a ferrule.

The normal strains in the assembly components can be found as

$$\left.\begin{aligned} \epsilon_0 &= -\alpha_0\Delta t + \lambda_0 T_0 \\ \epsilon_1 &= -\alpha_1\Delta t - \lambda_1(T_0 + T_1) \\ \epsilon_2 &= -\alpha_2\Delta t + \lambda_2 T_1 \end{aligned}\right\}, \tag{1}$$

where the index "0" refers to the inner cylinder, "1"—to the adhesive ring, and "2"—to the outer cylinder. In the Eqs. (1), α_i is the coefficient of thermal expansion of the ith material,

$$\lambda_0 = \frac{1}{\pi r_0^2 E_0}, \quad \lambda_1 = \frac{1}{\pi(r_1^2 - r_0^2)E_1}, \quad \lambda_2 = \frac{1}{\pi(r_2^2 - r_1^2)E_2} \tag{2}$$

Contributed by the Applied Mechanics Division of THE AMERICAN SOCIETY OF MECHANICAL ENGINEERS for publication in the ASME JOURNAL OF APPLIED MECHANICS.

Discussion on this paper should be addressed to the Technical Editor, Professor Lewis T. Wheeler, Department of Mechanical Engineering, University of Houston, Houston, TX 77204-4792, and will be accepted until four months after final publication of the paper itself in the ASME JOURNAL OF APPLIED MECHANICS.

Manuscript received by the ASME Applied Mechanics Division, Dec. 18, 1995; final revision, May 15, 1996. Associate Technical Editor: R. Becker.

Copyright © 1997 by ASME

Downloaded 04 May 2010 to 171.66.16.34. Redistribution subject to ASME license or copyright; see http://www.asme.org/terms/Terms_Use.cfm

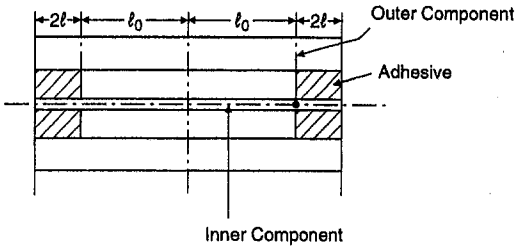


Fig. 1 Cylindrical bi-material assembly adhesively bonded at its ends

are the axial compliances of the constituent cylinders, r_i are the outer radii of the cylinders, E_i are Young's moduli of the materials, T_0 and T_1 are the axial thermally induced forces in the adherends (in the inner and the outer cylinders), and Δt is the change in temperature.

The strain compatibility condition $\epsilon_0 = \epsilon_1 = \epsilon_2$ results in the following equations for the forces T_0 and T_1:

$$\left.\begin{aligned}(\lambda_0 + \lambda_1)T_0 + \lambda_1 T_1 &= -(\alpha_1 - \alpha_0)\Delta t\\ -\lambda_0 T_0 + \lambda_2 T_1 &= (\alpha_2 - \alpha_0)\Delta t\end{aligned}\right\},$$

so that

$$\left.\begin{aligned}T_0 &= -\frac{\lambda_1(\alpha_2 - \alpha_0) + \lambda_2(\alpha_1 - \alpha_0)}{\lambda_0\lambda_1 + \lambda_1\lambda_2 + \lambda_0\lambda_2}\Delta t\\ T_1 &= \frac{\lambda_1(\alpha_2 - \alpha_0) - \lambda_0(\alpha_1 - \alpha_2)}{\lambda_0\lambda_1 + \lambda_1\lambda_2 + \lambda_0\lambda_2}\Delta t\end{aligned}\right\}. \quad (3)$$

The taken strain compatibility condition $\epsilon_0 = \epsilon_1 = \epsilon_2$ reflects the following assumptions:

1 Perfect adhesion exists between all the materials in the assembly.

2 The interfacial shearing stresses in the midportion of the assembly are next to zero, and the interaction of the assembly components is due to the shearing stresses which concentrate at the assembly ends.

3 The action of the interfacial shearing stresses can be substituted by the resultants T_0 and T_1, applied to the end planes of the adherends, and the resultant $T = -(T_0 + T_1)$, applied to the end planes of the adhesive ring.

Calculations based on these assumptions result in a sufficiently accurate prediction of the axial thermally induced forces in the midportion of sufficiently long assemblies (Suhir, 1986). The force in the adhesive ring can be computed as

$$T = -(T_0 + T_1) = \frac{\lambda_0(\alpha_1 - \alpha_2) + \lambda_2(\alpha_1 - \alpha_0)}{\lambda_0\lambda_1 + \lambda_1\lambda_2 + \lambda_0\lambda_2}\Delta t. \quad (4)$$

If the calculated force is positive, the component is subjected to tension, if the force is negative, the component experiences compression.

The axial stresses in the adherends, σ_0 and σ_2, and the adhesive, σ_1, can be computed by the formulas

$$\left.\begin{aligned}\sigma_0 &= \frac{T_0}{\pi r_0^2} = T_0\lambda_0 E_0\\ &= -\lambda_0 E_0\frac{\lambda_1(\alpha_2 - \alpha_0) + \lambda_2(\alpha_1 - \alpha_0)}{\lambda_0\lambda_1 + \lambda_1\lambda_2 + \lambda_0\lambda_2}\Delta t\\ \sigma_1 &= \frac{T}{\pi(r_1^2 - r_0^2)} = T\lambda_1 E_1\\ &= \lambda_1 E_1\frac{\lambda_0(\alpha_1 - \alpha_2) + \lambda_2(\alpha_1 - \alpha_0)}{\lambda_0\lambda_1 + \lambda_1\lambda_2 + \lambda_0\lambda_2}\Delta t\\ \sigma_2 &= \frac{T_1}{\pi(r_2^2 - r_1^2)} = T_1\lambda_2 E_2\\ &= \lambda_2 E_2\frac{\lambda_1(\alpha_2 - \alpha_0)\lambda_0(\alpha_1 - \alpha_2)}{\lambda_0\lambda_1 + \lambda_1\lambda_2 + \lambda_0\lambda_2}\Delta t\end{aligned}\right\}. \quad (5)$$

When the adhesive layer is very thin and, as a consequence of that, its axial compliance, λ_1, is substantially larger than the compliances, λ_0 and λ_2, of the adherends, the formulas (5) yield

$$\left.\begin{aligned}\sigma_0 &= -E_0\frac{\lambda_0(\alpha_2 - \alpha_0)}{\lambda_0 + \lambda_2}\Delta t\\ \sigma_1 &= E_1\frac{\lambda_0(\alpha_1 - \alpha_2) + \lambda_2(\alpha_1 - \alpha_0)}{\lambda_0 + \lambda_2}\Delta t\\ &= E_1\left(\alpha_1 - \frac{\lambda_0\alpha_2 + \lambda_2\alpha_0}{\lambda_0 + \lambda_2}\right)\Delta t\\ \sigma_2 &= E_2\frac{\lambda_2(\alpha_2 - \alpha_0)}{\lambda_0 + \lambda_2}\Delta t\end{aligned}\right\}. \quad (6)$$

If, in addition, the adherends have equal coefficients of thermal expansion ($\alpha_2 = \alpha_0$), then $\sigma_0 = \sigma_2 = 0$, and the stress in the adhesive is

$$\sigma_1 = E_1(\alpha_1 - \alpha_0)\Delta t.$$

When the adherends have equal coefficients of expansion ($\alpha_2 = \alpha_0$), the formulas (5) yield

$$\left.\begin{aligned}\sigma_0 &= -E_0\frac{\lambda_0\lambda_2(\alpha_1 - \alpha_0)}{\lambda_0\lambda_1 + \lambda_1\lambda_2 + \lambda_0\lambda_2}\Delta t\\ \sigma_1 &= E_1\frac{\lambda_1(\lambda_0 + \lambda_2)(\alpha_1 - \alpha_0)}{\lambda_0\lambda_1 + \lambda_1\lambda_2 + \lambda_0\lambda_2}\Delta t\\ \sigma_2 &= -E_2\frac{\lambda_0\lambda_2(\alpha_1 - \alpha_0)}{\lambda_0\lambda_1 + \lambda_1\lambda_2 + \lambda_0\lambda_2}\Delta t\end{aligned}\right\}. \quad (7)$$

If, in addition, the compliance, λ_2, of the outer cylinder is significantly smaller than the compliances, λ_0 and λ_1, of the inner cylinder and the adhesive layer, the formulas (7) yield

$$\left.\begin{aligned}\sigma_0 &= -E_0\frac{\lambda_2}{\lambda_1}(\alpha_1 - \alpha_0)\Delta t\\ \sigma_1 &= E_1(\alpha_1 - \alpha_0)\Delta t\\ \sigma_2 &= -E_2\frac{\lambda_2}{\lambda_1}(\alpha_1 - \alpha_0)\Delta t\end{aligned}\right\}. \quad (8)$$

In this case the adherends experience compressive stresses which are proportional to Young's moduli of the adherends and the axial compliance ratio, while the adhesive is subjected to a tensile stress which is proportional to Young's modulus of the material and is independent of the axial compliances of the adherends.

Shearing Stresses. Let us develop now a somewhat more complicated model which would enable one to evaluate not only the axial stresses in the assembly components, but the interfacial shearing stresses, $\tau_0(x)$ and $\tau_1(x)$, arising on the inner ($r = r_0$) and the outer ($r = r_1$) surfaces of the adhesive ring, as well. If these stresses were known, the longitudinal displacements of the inner cylinder, u_0, the inner boundary of the adhesive ring, u_{10}, the outer boundary of this ring, u_{12}, and the inner boundary of the outer cylinder, u_2, could be evaluated by the following approximate formulas:

$$\left.\begin{aligned}u_0(x) &= -\alpha_0\Delta t x + \lambda_0\int_0^x T_0(\xi)d\xi - \kappa_0\tau_0(x)\\ u_{10}(x) &= -\alpha_1\Delta t x\\ &\quad - \lambda_1\int_0^x [T_0(\xi) + T_1(\xi)]d\xi + \kappa_{10}\tau_0(x)\\ u_{12}(x) &= -\alpha_1\Delta t x\\ &\quad - \lambda_1\int_0^x [T_0(\xi) + T_1(\xi)]d\xi + \kappa_{12}\tau_1(x)\\ u_2(x) &= -\alpha_2\Delta t x + \lambda_2\int_0^x T_1(\xi)d\xi - \kappa_2\tau_1(x)\end{aligned}\right\}, \quad (9)$$

Downloaded 04 May 2010 to 171.66.16.34. Redistribution subject to ASME license or copyright; see http://www.asme.org/terms/Terms_Use.cfm

where

$$T_0(x) = 2\pi r_0 \int_{-l}^{x} \tau_0(\xi)d\xi, \quad T_1(x) = 2\pi r_1 \int_{-l}^{x} \tau_1(\xi)d\xi \quad (10)$$

are the forces produced by the shearing stresses $\tau_0(x)$ and $\tau_1(x)$, l is half the length of the bonded area, κ_0 is the shear compliance of the inner cylinder with respect to the longitudinal shearing forces distributed over its lateral surface, κ_2 is the shear compliance of the outer cylinder with respect to the shearing forces distributed over its inner lateral surface, κ_{10} is the shear compliance of the adhesive ring with respect to the forces acting along its inner lateral surface, and κ_{12} is the shear compliance of this ring with respect to the forces acting along its outer surface. The origin of the coordinate x is in the mid cross section of the bonded region at the cylinder axis.

In the formulas (9), the first terms are unrestricted (stress-free) thermal contractions of the assembly constituents. The second terms are the displacements due to the forces T_0 and T_1. These displacements are evaluated on the basis of Hooke's law, assuming that they are uniformly distributed over the components' cross sections. In reality, however, the interfacial displacements are somewhat larger than the displacements at the inner radii of the assembly components. This is accounted for by the third terms in the formulas (9). These terms reflect an assumption that the corresponding corrections are proportional to the shearing stress in the given cross section and are not affected by the stresses in the adjacent cross sections (Suhir, 1986).

In the further analysis we assume that the interfacial shear compliances, κ_0 and κ_2 of the adherends are significantly smaller than the compliances, κ_{10} and κ_{12}, of the adhesive. This is typically the case, since Young's modulus of the adhesive material is substantially smaller than Young's moduli of the adherends. With this assumption, Eqs. (9), after being introduced into the displacement compatibility conditions $u_0 = u_{10}$ and $u_{12} = u_2$, result in the following equations for the unknown shearing stress functions $\tau_0(x)$ and $\tau_1(x)$:

$$\left.\begin{aligned} \kappa_{10}\tau_0(x) - \lambda_{01}\int_0^x T_0(\xi)d\xi - \lambda_1 \int_0^x T_1(\xi)d\xi = \alpha_{10}\Delta t x \\ \kappa_{12}\tau_1(x) - \lambda_{12}\int_0^x T_1(\xi)d\xi - \lambda_1 \int_0^x T_0(\xi)d\xi = \alpha_{12}\Delta t x \end{aligned}\right\}, \quad (11)$$

where the following notation is used:

$$\lambda_{01} = \lambda_0 + \lambda_1, \quad \lambda_{12} = \lambda_1 + \lambda_2, \quad \alpha_{10} = \alpha_1 - \alpha_0, \quad \alpha_{12} = \alpha_1 - \alpha_2.$$

Based on the Appendix results, we use the following approximate formulas to evaluate the shear compliances κ_{10} and κ_{12}:

$$\kappa_{10} = \tfrac{1}{2} r_0\kappa, \quad \kappa_{12} = \tfrac{1}{2} r_1\kappa. \quad (12)$$

Here

$$\kappa = \frac{1}{G_1} \ln \frac{r_1}{r_0} \quad (13)$$

is the factor of the shear compliance and $G_1 = (E_1)/(2(1 + \nu_1))$ is the shear modulus of the adhesive material.

Differentiating the Eqs. (11) twice with respect to the coordinate x, we obtain

$$\left.\begin{aligned} \kappa_{10}\tau_0'(x) - \lambda_{01}T_0(x) - \lambda_1 T_1(x) = \alpha_{10}\Delta t \\ \kappa_{12}\tau_1'(x) - \lambda_{12}T_1(x) - \lambda_1 T_0(x) = \alpha_{12}\Delta t \end{aligned}\right\}, \quad (14)$$

and

$$\left.\begin{aligned} \kappa_{10}\tau_0''(x) - 2\pi r_0\lambda_{01}\tau_0(x) - 2\pi r_1\lambda_1\tau_1(x) = 0 \\ \kappa_{12}\tau_1''(x) - 2\pi r_1\lambda_{12}\tau_1(x) - 2\pi r_0\lambda_1\tau_0(x) = 0 \end{aligned}\right\}. \quad (15)$$

We seek the shearing stress functions $\tau_0(x)$ and $\tau_1(x)$ in the form

$$\left.\begin{aligned} \tau_0(x) = A_0 \sinh k_1 x + B_0 \sinh k_2 x \\ \tau_1(x) = A_1 \sinh k_1 x + B_1 \sinh k_2 x \end{aligned}\right\}. \quad (16)$$

Substituting these expressions into (15), we obtain the following algebraic equations for the constants of integration A_0, B_0, A_1, and B_1:

$$\left.\begin{aligned} (\kappa_{10}k_1^2 - 2\pi r_0\lambda_{01})A_0 - 2\pi r_1\lambda_1 A_1 = 0 \\ -2\pi r_0\lambda_1 A_0 + (\kappa_{12}k_1^2 - 2\pi r_1\lambda_{12})A_1 = 0 \end{aligned}\right\}, \quad (17)$$

and

$$\left.\begin{aligned} (\kappa_{10}k_2^2 - 2\pi r_0\lambda_{01})B_0 - 2\pi r_1\lambda_1 B_1 = 0 \\ -2\pi r_0\lambda_1 B_0 + (\kappa_{12}k_2^2 - 2\pi r_1\lambda_{12})B_1 = 0 \end{aligned}\right\}. \quad (18)$$

The Eqs. (17) and (18) indicate that the parameters k_1 and k_2 satisfy the same biquadratic equation

$$\kappa_{10}\kappa_{12}k^4 - 2\pi(r_0\kappa_{12}\lambda_{01} + r_1\kappa_{10}\lambda_{12})k^2 + (2\pi)^2 r_0 r_1(\lambda_0\lambda_1 + \lambda_1\lambda_2 + \lambda_0\lambda_2) = 0.$$

Considering (12), this equation can be written as

$$\kappa^2 k^4 - 4\pi\kappa(\lambda_{01} + \lambda_{12})k^2 + (4\pi)^2(\lambda_0\lambda_1 + \lambda_1\lambda_2 + \lambda_0\lambda_2) = 0. \quad (19)$$

The actual adhesively bonded structures, used in microelectronics and fiber optics, are characterized, as can be concluded from (13), by very low κ values. Therefore, in an approximate analysis, one can neglect the first term in (19), which is small in comparison with the two other terms. This results in the following simple formula for the k value:

$$k = \sqrt{\frac{4\pi D}{(\lambda_{01} + \lambda_{12})\kappa}}, \quad (20)$$

where the notation

$$D = \lambda_0\lambda_1 + \lambda_1\lambda_2 + \lambda_0\lambda_2 \quad (21)$$

is used.

Since only one k value, defined by the formula (20), is used, one can substitute the solutions (16) with the following simple expressions:

$$\tau_0(x) = A_0 \sinh kx, \quad \tau_1(x) = A_1 \sinh kx. \quad (22)$$

Introducing the first formula in (22) into the first formula in (10), we obtain the following expression for the thermally induced force in the inner adherend:

$$T_0(x) = -\frac{2\pi r_0 A_0}{k}(\cosh kl - \cosh kx). \quad (23)$$

In the midportion of a sufficiently long bonded area, the force $T_0(x)$ is constant (i.e., x independent) and is expressed by the first formula in (3). Then, by putting $x = 0$ in the Eq. (23), we obtain

$$A_0 = -\frac{kT_0}{2\pi r_0(\cosh kl - 1)} = -\frac{kT_0}{4\pi r_0 \cosh^2 \frac{kl}{2}}.$$

Similarly, we find

$$A_1 = -\frac{kT_1}{4\pi r_1 \cosh^2 \frac{kl}{2}},$$

and the formulas (22) yield

Downloaded 04 May 2010 to 171.66.16.34. Redistribution subject to ASME license or copyright; see http://www.asme.org/terms/Terms_Use.cfm

$$\tau_0(x) = -\frac{kT_0 \sinh kx}{4\pi r_0 \cosh^2 \frac{kl}{2}}, \quad \tau_1(x) = -\frac{kT_1 \sinh kx}{4\pi r_1 \cosh^2 \frac{kl}{2}}. \quad (24)$$

The maximum shearing stresses occur at the ends of the bonded area ($x = l$):

$$\tau_0 = -\frac{kT_0}{2\pi r_0} \tanh \frac{kl}{2}, \quad \tau_1 = -\frac{kT_1}{2\pi r_1} \tanh \frac{kl}{2}, \quad (25)$$

and, for long enough (large l values) and/or stiff enough (large k values) bonded regions (when $\tanh kl/2$ is approximately equal to unity), are expressed by the formulas

$$\tau_0 = -\frac{kT_0}{2\pi r_0}, \quad \tau_1 = -\frac{kT_1}{2\pi r_1}. \quad (26)$$

In an important special case, when the adhesive layer is thin and/or has a very low Young's modulus, and, because of that, the compliance, λ_1, of the adhesive layer is significantly larger than the compliances, λ_0 and λ_2, of the adherends, the formulas (3) yield: $T_0 = -T_1$. Then the stresses $\tau_0(x)$ and $\tau_1(x)$ are related by a simple equation:

$$r_0\tau_0(x) + r_1\tau_1(x) = 0. \quad (27)$$

Axial Forces in the Midportion of a Bonded Area of Finite Length. In the previous analysis we assumed that the bonded area is long enough, so that the axial thermally induced forces can be considered constant in the midportion of this area. In such a case these forces can be evaluated by the formulas (3) and (4). Let us assess the limitations of the taken assumption, i.e., the effect of the finite length of the bonded area on the axial forces.

The distributed axial forces $T_0(x)$ and $T_1(x)$ must be zero at the ends of the bonded area, $x = -l$ and $x = l$. Then the first of the formulas (14) results in the following boundary condition for the shearing stress $\tau_0(x)$:

$$\tau_0'(l) = \frac{\alpha_{10}}{\kappa_{10}} \Delta t,$$

and the first formula in (22) yields

$$A_0 = \frac{\alpha_{10}\Delta t}{k\kappa_{10} \cosh kl}.$$

Then the formula (23) results in the following expression for the axial force $T_0(x)$ in the inner cylinder:

$$T_0(x) = -2\pi r_0 \frac{\alpha_{10}\Delta t}{k^2\kappa_{10}} \chi(x),$$

where the factor

$$\chi(x) = 1 - \frac{\cosh kx}{\cosh kl}$$

considers the variability of the axial force along the bonded area, as well as the effect of the finite length of this area (Suhir, 1986). A similar result can be obtained for the force $T_1(x)$. The obtained formula for the factor χ indicates that the effect of the finite length $2l$ of the bonded area can be accounted for by multiplying the axial forces, computed by the formulas (3) and (4), by the factor

$$\chi_{\max} = 1 - \frac{1}{\cosh kl}.$$

Hence, the effect of the finite length of the bonded area need not be considered, if the kl value is sufficiently large, say, larger than five. Indeed, for $kl = 5$, the factor $\chi_{\max}$ is $\chi_{\max} = 0.9933$, i.e., quite close to unity. For smaller kl values, the effect of the finite length of the bonded area on the axial forces can be considered by multiplying the forces, computed using the formulas (3) and (4), by the factor $\chi_{\max}$.

"Global" Mismatch. The analysis, carried out in the previous section, was performed under an assumption that there were no external forces acting on the bonded portions of the assembly. In reality, however, if the adherends have different coefficients of expansion, these portions experience external forces, $\hat{T}_0$ and $\hat{T}_1$, which are due to the thermal expansion (contraction) mismatch of the materials of the adherends. In the analysis which follows, we evaluate these forces and the induced shearing stresses $\hat{\tau}_0(x)$ and $\hat{\tau}_1(x)$, assuming that no local mismatch exists, i.e., that the stresses, caused by the mismatch of the materials within the bonded areas, are zero.

The condition of the compatibility of displacements in the unbonded midportion of the assembly can be written as follows:

$$-\alpha_0\Delta t l_0 + \lambda_0\hat{T}_0 l_0 - \kappa_{10}\hat{\tau}_0 = -\alpha_2\Delta t l_0 + \lambda_2\hat{T}_1 l_0 - \kappa_{12}\hat{\tau}_1, \quad (28)$$

where l_0 is half the length of the midportion of the assembly. Since the adhesive ring does not experience any external loading, the resultant of the forces $T_0(x)$ and $T_1(x)$ acting on this ring from the adherends, must be zero:

$$T_0(x) + T_1(x) = 0,$$

and the formulas (10) lead to the relationship (27). Then, at the inner end of the bonded region, i.e., for $x = -l$ we have

$$\hat{T}_0 + \hat{T}_1 = 0, \quad r_0\hat{\tau}_0 + r_1\hat{\tau}_1 = 0,$$

and the compatibility condition (28) can be written, for the unknowns $\hat{T}_0$ and $\hat{\tau}_0$, as follows:

$$r_0\kappa\hat{\tau}_0 - (\lambda_0 + \lambda_2)\hat{T}_0 l_0 = (\alpha_2 - \alpha_0)\Delta t l_0. \quad (29)$$

We seek the shearing stress function $\hat{\tau}_0(x)$ in the form

$$\hat{\tau}_0(x) = C_1 \cosh kx + C_2 \sinh kx.$$

The corresponding axial force $\hat{T}_0(x)$ can be found by integration:

$$\hat{T}_0(x) = \frac{2\pi r_0}{k}(C_1 \sinh kx + C_2 \cosh kx). \quad (30)$$

This force must be zero at the end outer end of the bonded region, $x = l$. Then Eq. (30) results in the following relationship between the constants C_1 and C_2:

$$C_2 = -C_1 \tanh kl.$$

With this relationship, Eqs. (29) and (30) yield

$$\left.\begin{aligned} \hat{\tau}_0(x) &= C_1(\cosh kx - \tanh kl \sinh kx) \\ \hat{T}_0(x) &= \frac{2\pi r_0}{k} C_1(\sinh kx - \tanh kl \cos kx) \end{aligned}\right\}. \quad (31)$$

Putting $x = -l$ in these equations, we obtain the following formulas for the shearing stress and the axial force at the inner end of the bonded region:

$$\left.\begin{aligned} \hat{\tau}_0 &= C_1(\cosh kl + \tanh k \sinh kl) = C_1 \frac{\cosh 2kl}{\cosh kl}, \\ \hat{T}_0 &= -\frac{2\pi r_0}{k} C_1(\sinh kl - \tanh kl \cosh kl) \\ &= -\frac{2\pi r_0}{k} C_1 \frac{\sinh 2kl}{\cosh kl} \end{aligned}\right\}. \quad (32)$$

These formulas result in the following relationship between the unknowns $\hat{\tau}_0$ and $\hat{T}_0$:

Downloaded 04 May 2010 to 171.66.16.34. Redistribution subject to ASME license or copyright; see http://www.asme.org/terms/Terms_Use.cfm

$$\hat{T}_0 = -\frac{2\pi r_0}{k}\hat{\tau}_0 \tanh 2kl. \tag{33}$$

Introducing this relationship in the condition (29) and solving the obtained equation for the $\hat{\tau}_0$ value, we find

$$\hat{\tau}_0 = \frac{k\frac{l_0}{r_0}(\alpha_2 - \alpha_0)\Delta t}{2\pi(\lambda_0 + \lambda_2)l_0 \tanh 2kl + k\kappa}. \tag{34}$$

From the first formula in (32) we have

$$C_1 = \hat{\tau}_0 \frac{\cosh kl}{\cosh 2kl}.$$

Then the formulas (31) yield

$$\left.\begin{aligned} \hat{\tau}_0(x) &= \hat{\tau}_0 \frac{\cosh kl \cosh kx - \sinh kl \sinh kx}{\cosh 2kl} \\ &= \hat{\tau}_0 \frac{\cosh [k(l-x)]}{\cosh 2kl} \\ \hat{T}_0(x) &= \frac{2\pi r_0}{k}\hat{\tau}_0 \frac{\cosh kl \sinh kx - \sinh kl \sinh kx}{\cosh 2kl} \\ &= \frac{2\pi r_0}{k}\hat{\tau}_0 \frac{\sinh [k(l-x)]}{\cosh 2kl} \\ &= \hat{T}_0 \frac{\sinh [k(l-x)]}{\sinh 2kl} \end{aligned}\right\}, \tag{35}$$

where the interfacial shear stress $\hat{\tau}_0$ for the inner cylinder at the inner end of the assembly is given by the formula (34), and the "external" thermally induced force $\hat{T}_0$ is expressed by the formula (33).

When the unbonded portion of the assembly is long (large l_0 value) and the shear compliance of the bonded portion is small (small κ value), the formula (34) yields

$$\hat{\tau}_0 = \frac{k(\alpha_2 - \alpha_0)\Delta t}{2\pi r_0(\lambda_0 + \lambda_2)\operatorname{cotanh} 2kl}. \tag{36}$$

If, in addition to that, the bonded portion is also long, so that $\operatorname{cotanh} 2kl \simeq 1$, we obtain

$$\hat{\tau}_0 = \frac{k(\alpha_2 - \alpha_0)\Delta t}{2\pi r_0(\lambda_0 + \lambda_2)}. \tag{37}$$

In another extreme case, when a very compliant adhesive is used, and the κ value is large, the formula (34) yields:

$$\hat{\tau}_0 = \frac{l_0}{r_0}\frac{\alpha_2 - \alpha_0}{\kappa}\Delta t. \tag{38}$$

For the global shearing stress at the outer interface we have

$$\hat{\tau}_1 = -\hat{\tau}_0\frac{r_0}{r_1} = -\frac{l_0}{r_1}\frac{\alpha_2 - \alpha_0}{\kappa}\Delta t, \quad \hat{T}_1 = -\hat{T}_0,$$

so that

$$\hat{\tau}_1(x) = \hat{\tau}_1 \frac{\cosh [k(l-x)]}{\cosh 2kl},$$

$$\hat{T}_1(x) = \hat{T}_1 \frac{\sinh [k(l-x)]}{\sinh 2kl}.$$

These formulas are similar to the formula (35).

Total Shearing Stress. The total shearing stress at the inner interface, i.e., the stress on the surface of the inner cylinder, can be obtained as a sum of the local stress, expressed by the first formula in (24), and the global stress, given by the first formula in (35):

$$\tau_t^0(x) = -\frac{kT_0 \sinh kx}{4\pi r_0 \cosh^2 \frac{kl}{2}} + \hat{\tau}_0 \frac{\cosh [k(l-x)]}{\cosh 2kl}$$

$$= \tau_0 \frac{\sinh kx}{\sinh kl} + \hat{\tau}_0 \frac{\cosh [k(l-x)]}{\cosh 2kl}. \tag{39}$$

Here τ_0 is the local shearing stress, and $\hat{\tau}_0$ is the global stress at the inner end of the bonded region. The total stress at the outer end of this region ($x = l$) is the largest and, using (39), can be expressed by the formula:

$$\tau_{\max}^0 = \tau_0 + \frac{\hat{\tau}_0}{\cosh 2kl}. \tag{40}$$

This formula indicates that for long enough bonded areas (large kl values), the role of the global stresses is insignificant. For very short bonded areas, however, the contribution of both stress categories is comparable.

From the first formulas in (25) and (3), and the formula (34), we obtain the following relationship between the local, τ_0, and the global, $\hat{\tau}_0$, shearing stresses at the inner interface at the inner end of the bonded region:

$$\hat{\tau}_0 = \tau_0 \frac{2\pi D l_0 \alpha_{20} \operatorname{cotanh} \frac{kl}{2}}{[2\pi(\lambda_0 + \lambda_2)l_0 \tanh 2kl + k\kappa](\lambda_1\alpha_{20} + \lambda_2\alpha_{10})}. \tag{41}$$

Introducing this expression into the formula (40), we have

$$\tau_{\max}^0 = \tau_0\left[1 + \frac{2\pi D l_0 \alpha_{20} \operatorname{cotanh} \frac{kl}{2}}{(2\pi(\lambda_0 + \lambda_2)l_0 \sinh 2kl + k\kappa \cosh 2kl)(\lambda_1\alpha_{20} + \lambda_2\alpha_{10})}\right]. \tag{42}$$

In a special case, when the axial compliance λ_2 of the outer component is so small, that the terms, containing this compliance, can be disregarded, the formula (42) yields:

$$\tau_{\max}^0 = \tau_0\left(1 + \frac{\operatorname{cotanh} \frac{kl}{2}}{\sinh 2kl + \eta \cosh 2kl}\right). \tag{43}$$

Here the factor η is expressed as

$$\eta = \frac{k\kappa}{2\pi\lambda_0 l_0} = (1 + \nu_1)\frac{E_0}{E_1}\left(\frac{r_0}{l_0}\right)^2 kl_0 \ln\frac{r_1}{r_0}, \tag{44}$$

and the kl_0 value can be computed by the formula

$$kl_0 = l_0\sqrt{\frac{4\pi\lambda_1 G_1}{\left(1 + 2\frac{\lambda_1}{\lambda_0}\right)\ln\frac{r_1}{r_0}}}$$

$$= \frac{2l_0}{r_0}\sqrt{\frac{1}{2(1 + \nu_1)\left(\frac{r_1^2}{r_0^2} - 1 + 2\frac{E_0}{E_1}\right)\ln\frac{r_1}{r_0}}}. \tag{45}$$

After the stresses at the inner interface are found, calculation of the stresses at the outer interface does not cause any difficulties.

Downloaded 04 May 2010 to 171.66.16.34. Redistribution subject to ASME license or copyright; see http://www.asme.org/terms/Terms_Use.cfm

Numerical Example

Let, for instance, the radius of the inner component (the inner interface) be $r_0 = 6.25 \times 10^{-5}$ m = 0.0625 mm, the radius of the outer interface be $r_1 = 1.5 \times 10^{-4}$ m = 0.150 mm, and the outer radius of the outer component be $r_2 = 2.5 \times 10^{-4}$ m = 0.250 mm. Let the adherends have equal Young's moduli $E_0 = E_2 = 7.237 \times 10^{10}$ PA = 7385 kg/mm^2, but somewhat different coefficients of expansion: $\alpha_0 = 0.5 \times 10^{-6}$ 1/°C and $\alpha_2 = 0.4 \times 10^{-6}$ 1/°C. Young's modulus of the adhesive is $E_1 = 6.860 \times 10^9$ PA = 700 kg/mm^2, its Poisson's ratio is $\nu_1 = 0.40$, and the coefficient of expansion is $\alpha_1 = 70 \times 10^{-6}$ 1/°C. The change in temperature from the curing temperature to the operation temperature is $\Delta t = 100$°C. The lengths of the bonded and the unbonded areas are $2l = 0.01$ m = 10 mm, and $l_0 = 0.03$ m = 30 mm, respectively.

From the formulas (2) we find

$$\lambda_0 = 1.1260 \times 10^{-3}\ 1/\text{N} = 1.1034 \times 10^{-2}\ 1/\text{kg},$$

$$\lambda_1 = 2.4956 \times 10^{-3}\ 1/\text{N} = 2.4456 \times 10^{-2}\ 1/\text{kg},$$

$$\lambda_2 = 1.0990 \times 10^{-4}\ 1/\text{N} = 0.1077 \times 10^{-2}\ 1/\text{kg}.$$

Then, in accordance with (21), the determinant D is

$$D = 2.8100 \times 10^{-6} + 2.7427 \times 10^{-7} + 1.2375 \times 10^{-7} = 3.2080 \times 10^{-6}\ 1/\text{N}^2 = 3.0807 \times 10^{-4}\ 1/\text{kg}^2,$$

and the formulas (3) and (4) yield

$$T_0 = -0.2303\ \text{N} = -2.3504 \times 10^{-2}\ \text{kg},$$

$$T_1 = -2.4508\ \text{N} = -25.0082 \times 10^{-2}\ \text{kg},$$

$$T = -(T_0 + T_1) = 2.6811\ \text{N} = 27.3589 \times 10^{-2}\ \text{kg}.$$

The shear compliances factor, as predicted by the formula (13), is

$$\kappa = 3.5733 \times 10^{-10}\ 1/\text{PA} = 3.5019 \times 10^{-3}\ \text{mm}^2/\text{kg}.$$

The shear compliances, calculated by the formulas (12), are

$$\kappa_{10} = 1.1167 \times 10^{-14}\ \text{m}^3/\text{N} = 1.0943 \times 10^{-4}\ \text{mm}^3/\text{kg},$$

$$\kappa_{12} = 2.6801 \times 10^{-14}\ \text{m}^3/\text{N} = 2.6264 \times 10^{-4}\ \text{m}^3/\text{kg}.$$

The eigenvalue k, calculated by the formula (20), is $k = 4256.3$ 1/m = 4.2563 1/mm. Then the kl value is $kl = 127.7$, and the factor $\tanh kl/2$, considering the effect of the finite length of the bonded area on the maximum local shearing stresses, is practically equal to unity: $\tanh(1/2 \times 4256.3 \times 0.005) = \tanh 10.641 = 1$. Therefore the axial stresses in the adherends within the midportion of the bonded region and the local shearing stresses are not different from the stresses calculated for an infinitely long bonded region. The shearing stresses can be calculated by the formulas (26) as follows:

$$\tau_0 = 2.4963 \times 10^6\ \text{PA} = 0.2547\ \text{kg/mm}^2,$$

$$\tau_1 = 1.1067 \times 10^7\ \text{PA} = 1.1293\ \text{kg/mm}^2.$$

The global shearing stress at the inner end of the bonded area can be calculated for the inner interface by the formula (34), and, with $\tanh 2kl \simeq 1$, is as follows:

$$\hat{\tau}_0 = -8.7130 \times 10^4\ \text{PA} = -8.8908 \times 10^{-3}\ \text{kg/mm}^2.$$

For long enough unbonded areas, a simplified formula (36) can be used. This formula yields

$$\hat{\tau}_0 = -8.7698 \times 10^4\ \text{PA} = -8.9488 \times 10^{-3}\ \text{kg/mm}^2,$$

i.e., the difference is only 0.65 percent.

The global shearing stress at the inner end of the outer interface is

$$\hat{\tau}_1 = -\hat{\tau}_0 \frac{r_0}{r_1} = 3.6304 \times 10^4\ \text{PA} = 3.7045 \times 10^{-3}\ \text{kg/mm}^2.$$

The local shearing stresses at the outer end of the assembly ($x = l$) are

$$\tau_0 = -2.4963 \times 10^6\ \text{PA} = -0.2547\ \text{kg/mm}^2,$$

$$\tau_1 = -1.1067 \times 10^7\ \text{PA} = -1.1293\ \text{kg/mm}^2.$$

The global stresses at this end can be calculated by dividing the $\hat{\tau}_0$ and $\hat{\tau}_1$ at the inner end by $\cosh 2kl \simeq (1/2)e^{2kl} = 1.5270 \times 10^{18}$, i.e., are practically zero. The total shearing stresses at the inner and the outer interfaces are

$$\tau_t^0 = 2.4963 \times 10^6 - 0.0877 \times 10^6 = 2.4086 \times 10^6\ \text{PA} = 0.2458\ \text{kg/mm}^2,$$

$$\tau_t^1 = 1.1067 \times 10^7 + 0.036 \times 10^7 = 1.1103 \times 10^7\ \text{PA} = 1.1330\ \text{kg/mm}^2$$

at the inner end of the assembly, and

$$\tau_t^0 = -2.4963 \times 10^6\ \text{PA} = -0.2547\ \text{kg/mm}^2,$$

$$\tau_t^1 = -1.1067 \times 10^7\ \text{PA} = -1.1293\ \text{kg/mm}^2$$

at its outer end. Preliminary finite element calculations indicate that the results obtained on the basis of the suggested theory are in good agreement with the finite element data.

Note that a detailed comparison of a similar theory, developed for flat continuously bonded structures (Suhir, 1986, 1989), was carried out by Mishkevich and Suhir (1993) and showed good agreement between the finite element data and the results obtained on the basis of analytical modeling of the type applied in this paper.

Vibration Frequency

The fundamental natural frequency of the unbonded area of the inner component cylinder can be calculated as (Suhir, 1993)

$$\omega = \frac{\pi}{l_0}\sqrt{\frac{\hat{T}_0}{m} + \frac{\pi^2}{l_0^2}\frac{E_0 I_0}{m}},$$

where $m = \pi\rho r_0^2$ is the mass of the component per unit length, and $I_0 = \pi r_0^4/4$ is its moment of inertia. Then this formula can be written as

$$\omega = \frac{\pi}{l_0 r_0}\sqrt{\frac{\hat{T}_0}{\pi\rho}\left(1 + \frac{\pi^3}{4}\frac{E_0 r_0^4}{\hat{T}_0 l_0^2}\right)},$$

and, with $\hat{T}_0 = 8.0389 \times 10^{-3}$ N = 8.2029×10^{-4} kg, $\rho = 2200$ N sec^2/m^4 = 2.245×10^{-10} kg sec^2/mm^4, and the input data from the above numerical example, yields $\omega = 2670(1/\text{sec})$. The force $\hat{T}_0$ results in the following tensile stress in the inner cylinder:

$$\sigma_0 = \frac{\hat{T}_0}{\pi r_0^2} = 6.5507 \times 10^5\ \text{PA} = 0.06684\ \text{kg/mm}^2.$$

The corresponding strain is as low as $\epsilon_0 = \sigma_0/E_0 \simeq 9.05 \times 10^{-6}$. In the case $\hat{T}_0 = 0$, when the vibration frequency is due to the flexural rigidity of the inner component only, we obtain

$$\omega = \frac{\pi^2 r_0}{l_0^2}\sqrt{\frac{E_0}{\rho}} = 1956\frac{1}{\text{sec}}.$$

This value is by a factor of 0.733 lower than the frequency calculated with consideration of the tensile force.

Downloaded 04 May 2010 to 171.66.16.34. Redistribution subject to ASME license or copyright; see http://www.asme.org/terms/Terms_Use.cfm

Conclusion

Simple formulas are developed for the evaluation of the local and the global thermally induced shearing stresses in a long cylindrical bi-material assembly adhesively bonded at the ends, with consideration of the effect of the thermal coefficient of expansion of the adhesive itself. The developed analytical stress model can be helpful in the analysis and design of some fiber optic assemblies.

References

de Bruyne, N. A., 1944, "The Strength of Glued Joints," *Aircraft Engineering*, Vol. 16, pp. 115–118.

Clech, J.-P., et al., 1990, " 'Local' CTE Mismatch in SM Leaded Packages: A Potential Reliability Concern," *40th IEEE Electronic Component and Technology Conference Proceedings*, Vol. 1, Las Vegas, NV, pp. 368–376.

Clech, J.-P., et al., 1993, "Comprehensive SM Reliability Model Covering Several Generations of Packaging and Assembly Technology," *IEEE CHMT Transactions*, Vol. 16, No. 8, pp. 949–960.

Goland, M., and Reissner, E., 1944, "The Stresses in Cemented Joints," ASME JOURNAL OF APPLIED MECHANICS, Vol. 11, pp. A17–A27.

Hart-Smith, L. J., 1973a, "Adhesive-Bonded Single-Lap Joints," NASA, CR-112236.

Hart-Smith, L. J., 1973b, "Adhesive-Bonded Double-Lap Joints," NASA, CR-112235.

Hart-Smith, L. J., 1973c, "Adhesive-Bonded Scarf and Stepped-Lap Joints," NASA, CR-112237.

Mishkevich, V., and Suhir, E., 1993, "Simplified Approach to the Evaluation of Thermally Induced Stresses in Bi-Material Structures," *Structural Analysis in Microelectronic and Fiber-Optic Systems*, E. Suhir, ed., ASME Press, New York.

Oplinger, D. W., 1994, "Effects of Adherends Deflections in Single Lap Joints," *Int. J. of Solids and Structures*, Vol. 31, pp. 2565–2587.

Suhir, E., 1986, "Stresses in Bi-Metal Thermostats," ASME JOURNAL OF APPLIED MECHANICS, Vol. 53, pp. 657–660.

Suhir, E., 1989, "Interfacial Stresses in Bi-Metal Thermostats," ASME JOURNAL OF APPLIED MECHANICS, Vol. 56, pp. 595–600.

Suhir, E., 1993, "The Effect of the Nonlinear Stress-Strain Relationship on the Mechanical Behavior of Optical Glass Fibers," *Int. J. of Solids and Structures*, Vol. 30, No. 7, pp. 947–961.

Suhir, E., 1994a, "Approximate Evaluation of the Interfacial Shearing Stress in Circular Double Lap Shear Joints, with Application to Dual Coated Optical Fibers," *Int. J. of Solids and Structures*, Vol. 31, No. 23, pp. 3261–3283.

Suhir, E., 1994b, "Thermally Induced Stresses in an Optical Glass Fiber Soldered into a Ferrule," *IEEE/OSA J. of Lightwave Technology*, Vol. 12, No. 10, pp. 1766–1770.

Suhir, E., 1995, " 'Global' and 'Local' Thermal Mismatch Stresses in an Elongated Bi-Material Assembly Adhesively Bonded at the Ends," *Structural Analysis in Microelectronic and Fiber-Optic Structures*, E. Suhir, ed., ASME Press, New York, pp. 101–105.

Tsai, M. Y., and Morton, J., 1994, "An Evaluation of Analytical and Numerical Solutions to the Single-Lap Joint," *Int. J. of Solids and Structures*, Vol. 31, pp. 2537–2563.

Volkersen, O., 1938, "Die Niekraftverteilung in Zugbeanspruchten mit Konstanten Loschenquerschritten," *Luftfahrtforschung*, Vol. 15, pp. 41–47 (in German).

APPENDIX

Longitudinal Compliance of a Hollow Cylinder Subjected to Axial Shearing Forces Distributed Over Its Lateral Surfaces

The objective of the analysis which follows is to evaluate the longitudinal compliance of a hollow cylinder with respect to the shearing forces τ_0 and τ_1 uniformly distributed over its inner ($r = r_0$) and outer ($r = r_1$) lateral surfaces. The analysis is carried out under the following assumptions:

1 The radial, σ_r, and the tangential, σ_θ, normal stresses are zero throughout the cylinder.

2 The shearing stress, τ_{rz}, acting in the axial direction, z, depends on the radius, r, only (i.e., z independent), and the normal stress, σ_z, acting in the axial direction depends on the coordinate z only (i.e., r independent).

3 The end planes of the cylinder are stress free.

With these assumptions, the first equation of equilibrium

$$\frac{\partial \sigma_r}{\partial r} + \frac{\partial \tau_{rz}}{\partial z} + \frac{\sigma_r - \sigma_\theta}{r} = 0$$

is fulfilled automatically, and the second equation of equilibrium

$$\frac{\partial}{\partial r}(r\tau_{rz}) + r\frac{\partial \sigma_z}{\partial z} = 0$$

yields

$$\frac{1}{r}\frac{d}{dr}(r\tau_{rz}) = -\frac{d\sigma_z}{dz} = C,$$

so that

$$\tau_{rz} = \frac{1}{2}Cr + \frac{C_1}{r}, \quad \sigma_z = -Cz.$$

Introducing the obtained formula for the shearing stress, τ_{rz}, into the boundary conditions

$$\tau_{rz} = \tau_0, \quad \text{for} \quad r = r_0, \quad \tau_{rz} = \tau_1, \quad \text{for} \quad r = r_1,$$

we obtain the following equations for the constants of integration C and C_1:

$$\left.\begin{aligned} r_0^2 C + 2C_1 &= 2r_0\tau_0 \\ r_1^2 C + 2C_1 &= 2r_1\tau_1 \end{aligned}\right\}.$$

These equations yield

$$C = \frac{r_1\tau_1 - r_0\tau_0}{r_1^2 - r_0^2}, \quad C_1 = r_0 r_1 \frac{r_1\tau_0 - r_0\tau_1}{r_1^2 - r_0^2}.$$

The equilibrium condition for the external forces, acting on the cylinder, requires that

$$r_0\tau_0 = r_1\tau_1,$$

and therefore

$$C = 0, \quad C_1 = r_0\tau_0.$$

Thus, the axial normal stress, σ_z, is zero, and the shearing stress, τ_{rz}, in the cylinder is expressed by the formula

$$\tau_{rz} = \frac{r_0}{r}\tau_0.$$

The Hooke's law equations result in the following formulas for the strains:

$$\left.\begin{aligned} \epsilon_r = \frac{\partial u}{\partial r} &= \frac{1}{E}[\sigma_r - \nu(\sigma_\theta + \sigma_z)] = -\frac{\nu}{E}\sigma_z = 0 \\ \epsilon_0 = \frac{u}{r} &= \frac{1}{E}[\sigma_\theta - \nu(\sigma_r + \sigma_z)] = -\frac{\nu}{E}\sigma_z = 0 \\ \epsilon_z = \frac{\partial w}{\partial z} &= \frac{1}{E}[\sigma_z - \nu(\sigma_r + \sigma_\theta)] = \frac{1}{E}\sigma_z = 0 \\ \gamma_{rz} = \frac{\partial u}{\partial z} + \frac{\partial w}{\partial r} &= \frac{1}{G}\tau_{rz} = \frac{r_0}{r}\frac{\tau_0}{G} \end{aligned}\right\}.$$

The second of these equations yields $u = 0$, and the third equation indicates that the axial displacement, w, is z independent and therefore can be sought in the form $w = f(r)$. Then the fourth Hooke's equation results in the following formula for the function $f(r)$:

$$f'(r) = \frac{r_0}{r}\frac{\tau_0}{G}.$$

Then we have

$$w = f(r) = \frac{r_0\tau_0}{G}\ln r.$$

The displacement of the points, located at the outer surface

Downloaded 04 May 2010 to 171.66.16.34. Redistribution subject to ASME license or copyright; see http://www.asme.org/terms/Terms_Use.cfm

$(r = r_1)$, with respect to the points, located at the inner surface $(r = r_0)$, is

$$\Delta w = \frac{r_0 \tau_0}{G} (\ln r_1 - \ln r_0) = \frac{r_0 \tau_0}{G} \ln \frac{r_1}{r_0},$$

and the sought longitudinal shear compliance is

$$\kappa_0 = \frac{\Delta w}{\tau_0} = \frac{r_0}{G} \ln \frac{r_1}{r_0}. \quad \text{(A-1)}$$

If one is interested in the displacements with respect to the midsurface of the cylinder, then, in an approximate analysis, assuming linear distribution of the axial displacements across the thickness of the cylinder, one can take

$$\Delta w = \frac{r_0 \tau_0}{2G} \ln \frac{r_1}{r_0},$$

and the shear compliance will be half of the value defined by the formula (A-1):

$$\kappa_0 = \frac{r_0}{2G} \ln \frac{r_1}{r_0}. \quad \text{(A-2)}$$

Similarly, the displacement of the points located at the inner surface $(r = r_0)$, with respect to the points, located at the outer surface $(r = r_1)$, can be found as

$$\Delta w = \frac{r_1 \tau_1}{G} \ln \frac{r_1}{r_0},$$

and the longitudinal shear compliance in this case is

$$\kappa_1 = \frac{r_1}{G} \ln \frac{r_1}{r_0}. \quad \text{(A-3)}$$

The compliance with respect to the midsurface of the cylinder can be computed as half this value:

$$\kappa_1 = \frac{r_1}{2G} \ln \frac{r_1}{r_0}. \quad \text{(A-4)}$$

Downloaded 04 May 2010 to 171.66.16.34. Redistribution subject to ASME license or copyright; see http://www.asme.org/terms/Terms_Use.cfm

Jungki Lee
Department of Mechanical Design and Production Engineering,
Hong Ik University,
Jochiwon-Eup, Yeonki-Gun,
Chungnam, Korea 339800
Assoc. Mem. ASME

Ajit Mal
Department of Mechanical and Aerospace Engineering
University of California,
Los Angeles, CA 90095-1597
Fellow ASME

A Volume Integral Equation Technique for Multiple Inclusion and Crack Interaction Problems

A volume integral equation method is introduced for the solution of elastostatic problems in heterogeneous solids containing interacting multiple inclusions, voids, and cracks. The method is applied to two-dimensional problems involving long parallel cylindrical inclusions and cracks. The influence of interface layers on the interfacial stress field is investigated. The stress intensity factors for microcracks in the presence of interacting inclusions or voids are also calculated for a variety of model geometries. The accuracy and efficiency of the method are examined through comparison with results obtained from analytical and boundary integral methods.

1 Introduction

Calculation of the stress and strain fields in heterogeneous solids containing multiple inclusions, voids, and cracks and subject to external loads is of considerable interest in a variety of engineering problems. A notable example is the stress analysis of structural composites containing microcracks in order to predict their fracture and failure behavior under remotely applied loads. Clearly, a precise knowledge of the stress field near interacting fibers and microcracks could be extremely helpful in predicting crack initiation and propagation in these materials. However, realistic models of the problem are geometrically too complex to be accessible to analytical methods. Although numerical methods, e.g., Finite Element (FE) and Boundary Integral Equation (BIE) methods can, in principle, be used for highly complex geometries, the conventional finite element methods can not be directly applied to infinite domains and in hybrid methods the choice of the global functions is difficult (Zienkiewicz et al., 1981). If the inclusions themselves are inhomogeneous or if the number of interfaces is large, the boundary integral equation method becomes extremely cumbersome in dealing with the problem.

The volume integral equation method (VIEM) developed for elastodynamic problems (Lee and Mal, 1995) appears to be suitable for solving this class of problems. This is due to the fact that the continuity conditions at each interface are exactly satisfied in the formulation, and that the method requires discretization of the inclusions only, in contrast to finite element methods, where the full domain needs to be discretized. In this paper, the VIEM is applied to a class of two-dimensional elastostatic multiple inclusion and crack problems. The accuracy and efficiency of the method are examined through comparison with results obtained from analytical and boundary integral methods.

2 The Volume Integral Equation Method (VIEM) and the Boundary Integral Equation Method (BIEM)

2.1 The Volume Integral Equation Method (VIEM). The geometry of the general problem is shown in Fig. 1. Let $c^{(1)}_{ijkl}$ denote the elastic stiffness tensor of the inclusion and $c^{(2)}_{ijkl}$ those of the unbounded matrix material. The matrix is assumed to be homogeneous so that $c^{(2)}_{ijkl}$ is constant while $c^{(1)}_{ijkl}$ is arbitrary, i.e., the inclusions may, in general, be inhomogeneous. The interfaces between the inclusions and the matrix are assumed to be perfectly bonded insuring continuity of the displacement and stress vectors. The elastostatic problem can be formulated as a special case of the corresponding elastodynamic problem in the limiting case of zero frequency, resulting in the volume integral equation (Mal and Knopoff, 1967)

$$u_m(\mathbf{x}) = u^0_m(\mathbf{x}) - \int_R \delta c_{ijkl} g^m_{i,j}(\boldsymbol{\xi}, \mathbf{x}) u_{k,l}(\boldsymbol{\xi}) d\boldsymbol{\xi} \qquad (1)$$

where the integral is over whole space, $\delta c_{ijkl} = c^{(1)}_{ijkl} - c^{(2)}_{ijkl}$ and $g^m_i(\boldsymbol{\xi}, \mathbf{x})$ is the static Green's function (or, Kelvin's solution) for the unbounded matrix material, i.e., $g^m_i(\boldsymbol{\xi}, \mathbf{x})$ represents the ith component of the displacement at ξ due to unit concentrated force at $\mathbf{x}$ in the mth direction. In Eq. (1) the summation convention and comma notation have been used and the differentiations are with respect to ξ_i. It should be noted that the integrand is nonzero within the inclusions only, since $\delta c_{ijkl} = 0$, outside the inclusions. If $\mathbf{x}$ lies within the inclusions, then Eq. (1) is an integrodifferential equation for the unknown displacement vector $\mathbf{u}(\mathbf{x})$. It is extremely difficult, if not impossible to solve this coupled system analytically, except for unrealistically simple models of the general problem. In the case of well-separated spherical or ellipsoidal inclusions an approximate solution of the equation can be obtained under the assumption that the strains within the inclusions are uniform. This approach was used to calculate the effective elastic moduli of particulate composites for a random distribution of spherical inclusions by Mal and Knopoff (1967), and more recently, for periodic distributions of spherical as well as ellipsoidal inclusions by El Mouden and Molinari (1995). The constant strain assumption is clearly not valid for closely packed inclusions, for inclusions of nonellipsoidal shapes or for voids and cracks. In this paper we develop a numerical scheme for the solution of Eq. (1) to determine the local stress field in heterogeneous solids containing strongly interacting, arbitrarily shaped inclusions, voids, and cracks. We consider two-dimensional in-plane and antiplane problems for simplicity.

2.1.1 Two-Dimensional Problems. For plane-strain problems in the 1-2 plane, the volume integral Eq. (1) becomes

$$u_1(\mathbf{x}) = u^o_1(\mathbf{x}) - \int_R \{[\delta(\lambda + 2\mu) g^1_{1,1} u_{1,1} + \delta\lambda g^1_{1,1} u_{2,2} + \delta\mu g^1_{1,2}(u_{1,2} + u_{2,1})] + [\delta(\lambda + 2\mu) g^1_{2,2} u_{2,2} + \delta\lambda g^1_{2,2} u_{1,1} + \delta\mu g^1_{2,1}(u_{1,2} + u_{2,1})]\} d\xi_1 d\xi_2 \qquad (2)$$

Contributed by the Applied Mechanics Division of THE AMERICAN SOCIETY OF MECHANICAL ENGINEERS for publication in the ASME JOURNAL OF APPLIED MECHANICS.

Discussion on this paper should be addressed to the Technical Editor, Professor Lewis T. Wheeler, Department of Mechanical Engineering, University of Houston, Houston, TX 77204-4792, and will be accepted until four months after final publication of the paper itself in the ASME JOURNAL OF APPLIED MECHANICS.

Manuscript received by the ASME Applied Mechanics Division, Dec. 20, 1995; final revision, June 20, 1996. Associate Technical Editor: W. K. Liu.

Copyright © 1997 by ASME

Downloaded 04 May 2010 to 171.66.16.34. Redistribution subject to ASME license or copyright; see http://www.asme.org/terms/Terms_Use.cfm

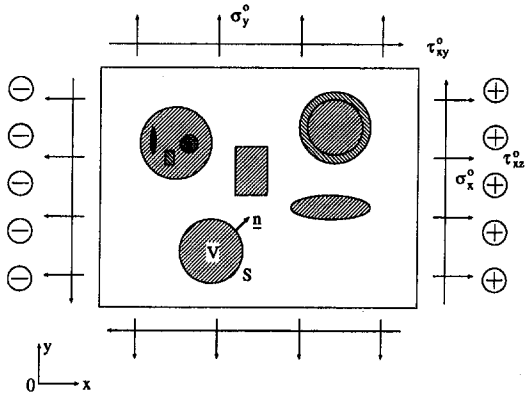


Fig. 1 Geometry of the general elastostatic problem

and

$$u_2(\mathbf{x}) = u_2^o(\mathbf{x}) - \int_R \{[\delta(\lambda + 2\mu)g_{1,1}^2 u_{1,1} + \delta\lambda g_{1,1}^2 u_{2,2} + \delta\mu g_{1,2}^2(u_{1,2} + u_{2,1})] + [\delta(\lambda + 2\mu)g_{2,2}^2 u_{2,2} + \delta\lambda g_{2,2}^2 u_{1,1} + \delta\mu g_{2,1}^2(u_{1,2} + u_{2,1})]\} d\xi_1 d\xi_2 \quad (3)$$

where $u_1(\mathbf{x})$, $u_2(\mathbf{x})$ are the in-plane displacement components, $\delta\mu = \mu_1 - \mu_2$, and $\delta\lambda = \lambda_1 - \lambda_2$, λ_1, μ_1 being the Lame' constants of the inclusions and λ_2, μ_2 are those for the unbounded matrix material. The Green's function is given by (Beskos, 1989)

$$g_\alpha^\beta = \frac{\lambda + 2\mu}{16\pi\mu(\lambda + \mu)}\left[-\frac{\lambda + 3\mu}{\lambda + \mu}\ln r\delta_{\alpha\beta} + r_{,\alpha}r_{,\beta}\right] \quad (4)$$

where $r = |\mathbf{x} - \xi|$ and $\alpha, \beta = 1, 2$.

For antiplane problems, the volume integral Eq. (1) becomes

$$u_3(\mathbf{x}) = u_3^o(\mathbf{x}) - \int_R \{\delta\mu[g_{3,1}^3(\xi, \mathbf{x})u_{3,1}(\xi) + g_{3,2}^3(\xi, \mathbf{x})u_{3,2}(\xi)]\} d\xi_1 d\xi_2 \quad (5)$$

and the Green's function is given by (Beskos, 1989)

$$g_3^3 = -\frac{1}{2\pi\mu}\ln r. \quad (6)$$

It should be noted that for uniformly applied remote stress the displacement vector $\mathbf{u}^o$ is of the form

$$u_1^o = C_1 x, \quad u_2^o = C_2 y, \quad u_3^o = C_3 x + C_4 y \quad (7)$$

where the constants $C_1 - C_4$ are related to the tensile and shear components of the applied remote stress.

2.2 The Boundary Integral Equation Method (BIEM). The integral equation on the outer surface S_+ of the inclusion can be expressed as (Beskos, 1989)

$$u_m(\mathbf{x}) = u_m^o(\mathbf{x}) + c_{ijkl}^{(M)} \int_{S_+} [g_{k,l}^{m(M)}(\xi, \mathbf{x})u_i(\xi) - g_i^{m(M)}(\xi, \mathbf{x})u_{k,l}(\xi)]n_j dS \quad (8)$$

while for the interior surface S_-

$$u_m(\mathbf{x}) = -c_{ijkl}^{(I)} \int_{S_-} [g_{k,l}^{m(I)}(\xi, \mathbf{x})u_i(\xi) - g_i^{m(I)}(\xi, \mathbf{x})u_{k,l}(\xi)]n_j dS \quad (9)$$

where $\mathbf{n}$ is the outward unit normal to S_+, and the superscripts (M) and (I) imply that the quantities involved are for the matrix and the inclusions, respectively. Equations (8) and (9), together with the continuity conditions across S, give rise to the so-called boundary integral equation for $\mathbf{u}(\mathbf{x})$. When the inclusion becomes a void, the integral equations reduce to the standard boundary integral equation

$$u_m(\mathbf{x}) = u_m^o(\mathbf{x}) + c_{ijkl}^{(M)} \int_S G_{k,l}^{m(M)}(\xi, \mathbf{x})u_i(\xi)n_j dS. \quad (10)$$

2.2.1 Two-Dimensional Problems. For plane problems in the 1-2 plane, the integral equations on the outer surface of the inclusion can be expressed as

$$u_1(\mathbf{x}) = u_1^o(\mathbf{x}) - \int_{S_+} [g_1^1(\xi, \mathbf{x})t_1(\xi) + g_2^1(\xi, \mathbf{x})t_2(\xi) - T_1^1(\xi, \mathbf{x})u_1(\xi) - T_2^1(\xi, \mathbf{x})u_2(\xi)]dS(\xi)$$

$$u_2(\mathbf{x}) = u_2^o(\mathbf{x}) - \int_{S_+} [g_1^2(\xi, \mathbf{x})t_1(\xi) + g_2^2(\xi, \mathbf{x})t_2(\xi) - T_1^2(\xi, \mathbf{x})u_1(\xi) - T_2^2(\xi, \mathbf{x})u_2(\xi)]dS(\xi)$$

$$u_3(\mathbf{x}) = u_3^o(\mathbf{x}) - \int_{S_+} \mu_2\left[g_3^3\frac{\partial u_3}{\partial n} - u_3\frac{\partial g_3^3}{\partial n}\right]dS \quad (11)$$

while for the interior surface, the equation is

$$u_1(\mathbf{x}) = \int_{S_-} [g_1^1(\xi, \mathbf{x})t_1(\xi) + g_2^1(\xi, \mathbf{x})t_2(\xi) - T_1^1(\xi, \mathbf{x})u_1(\xi) - T_2^1(\xi, \mathbf{x})u_2(\xi)]dS(\xi)$$

$$u_2(\mathbf{x}) = \int_{S_-} [g_1^2(\xi, \mathbf{x})t_1(\xi) + g_2^2(\xi, \mathbf{x})t_2(\xi) - T_1^2(\xi, \mathbf{x})u_1(\xi) - T_2^2(\xi, \mathbf{x})u_2(\xi)]dS(\xi)$$

$$u_3(\mathbf{x}) = \int_{S_-} \mu_1\left[g_3^3\frac{\partial u_3}{\partial n} - u_3\frac{\partial g_3^3}{\partial n}\right]dS \quad (12)$$

where

$$\begin{aligned} T_1^1 &= (\lambda + 2\mu)g_{1,1}^1 n_1 + \lambda g_{2,2}^1 n_1 + \mu(g_{1,2}^1 + g_{2,1}^1)n_2 \\ T_1^2 &= (\lambda + 2\mu)g_{1,1}^2 n_1 + \lambda g_{2,2}^2 n_1 + \mu(g_{1,2}^2 + g_{2,1}^2)n_2 \\ T_2^1 &= (\lambda + 2\mu)g_{2,2}^1 n_2 + \lambda g_{1,1}^1 n_2 + \mu(g_{1,2}^1 + g_{2,1}^1)n_1 \\ T_2^2 &= (\lambda + 2\mu)g_{2,2}^2 n_2 + \lambda g_{1,1}^2 n_2 + \mu(g_{1,2}^2 + g_{2,1}^2)n_1 \end{aligned} \quad (13)$$

and

$$\begin{aligned} t_1 &= (\lambda + 2\mu)u_{1,1}n_1 + \lambda u_{2,2}n_1 + \mu(u_{1,2} + u_{2,1})n_2 \\ t_2 &= (\lambda + 2\mu)u_{2,2}n_2 + \lambda u_{1,1}n_2 + \mu(u_{1,2} + u_{2,1})n_1. \end{aligned} \quad (14)$$

In the above equations we have dropped the superscripts (M) and (I) for convenience. As the observation point approaches the interface, $u_i(\mathbf{x})$ in Eqs. (11)–(12) are replaced by $(\frac{1}{2})u_i(\mathbf{x})$ for a smooth interface, and the derivatives of the Green's function must be interpreted in the Cauchy principal value sense. Applying the continuity conditions at the interface, followed by discretization, a system of four coupled algebraic equations for the in-plane case and two for the antiplane case for the interface displacements and tractions are obtained. The system of equations can be solved to give the displacements and stress components at the nodal points of the interface. Once the displacements and tractions at the interface are known, the displace-

Downloaded 04 May 2010 to 171.66.16.34. Redistribution subject to ASME license or copyright; see http://www.asme.org/terms/Terms_Use.cfm

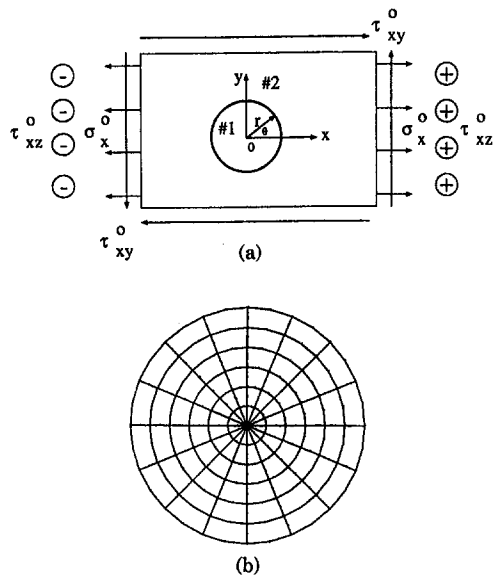


Fig. 2 (*a*) A cylindrical inclusion under arbitrary loading; (*b*) a typical discretized model in the volume integral equation method

ments and stresses everywhere can be calculated by evaluating the integral expressions Eqs. (11)–(12).

2.3 Numerical Formulation. Clearly, the integrands in Eqs. (2), (3), and (5), (11)–(12) contain singularities of different orders due to the singular nature of the Green's function at $\mathbf{x} = \boldsymbol{\xi}$. In general, g_i^m behaves as ln r and $g_{i,j}^m$ behaves as $1/r$ as $r \to 0$; these singularities are weaker than those in BIEM. We have used the direct integration scheme as introduced by Li et al. (1985) and Lu and Ye (1991) to handle the singularities; a brief description of the modified method used in the discretizations of the volume integral equation is given in the Appendix.

3 Inclusion Problems

In this section we consider inclusion problems of special interest in composite mechanics. In the first, a single inclusion in presence or absence of an "interphase" between the inclusion and the matrix is considered. In the second, the influence of the interaction between two closely spaced inclusions (e.g., fibers) on the stress field at the interface is studied.

3.1 The Single Inclusion (Plane-Strain). In order to check the accuracy of the volume integral equation method, the single homogeneous cylindrical inclusion shown in Fig. 2(*a*) under arbitrary loading is considered first. The matrix is assumed to be titanium and the inclusion is SiC fiber of radius 70 μm. The nominal material properties of the constituents are given in Table 1 (Cox et al., 1990). The remote applied loads are assumed to be $\sigma_x^o = 143.1$ GPa and $\tau_{xy}^o = \tau_{xz}^o = 37.88$ GPa.

Figure 2(*b*) shows a typical discretized model used in the VIEM. Since higher-order isoparametric elements allow a better

Table 1 Material properties of the constituents of SiC-6/Ti-15-3 composite

	E (GPa)	ν
SiC	440	0.25
Ti	100	0.32
Carbon	41	0.25

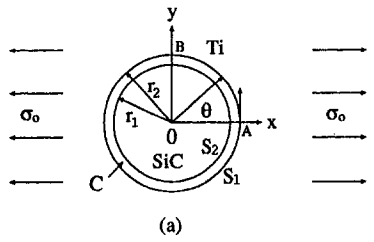
Table 2 Normalized stress components within a cylindrical inclusion due to remote loading

	Tensile Loading		In-plane Shear	Antiplane Shear
	σ_x / σ_x^o	σ_y / σ_x^o	τ_{xy} / τ_{xy}^o	τ_{yz} / τ_{yz}^o
Exact	1.2800	-0.1017	1.3817	1.6076
VIEM	1.2801	-0.1017	1.3813	1.6076

approximation of curved surfaces than do linear isoparametric elements, a total of 96 standard eight-node quadratic, quadrilateral and six-node quadratic, triangular elements were used in the VIEM. The number of elements, 96, was determined based on a convergence test. Table 2 shows the comparison between the well-known analytical solution (see, e.g., Mal and Singh, 1991) and the numerical solution using VIEM under different loading conditions. It can be seen that there is excellent agreement between the two sets of results.

3.2 The Single Inclusion With an Interphase (Plane-Strain). Consider a single cylindrical inclusion with an interphase under transverse loading, $\sigma_x^o = 143.1$ GPa, as shown in Fig. 3(*a*). The matrix is assumed to be titanium and the inclusion is a SiC fiber of 70-μm radius. The interphase is assumed to be a 5-μm thick homogeneous layer of carbon, with properties given in Table 1.

The formulation described in Section 2.2 for the BIEM can be applied to this problem in a straightforward manner. The integral representation of the displacement components must now be written in the three regions, namely, the matrix, interphase, and the inclusion. It should be noted that the displacement components must be written in terms of unknown displace-



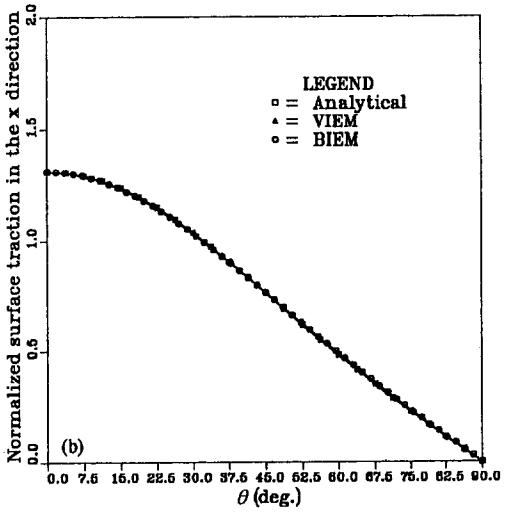
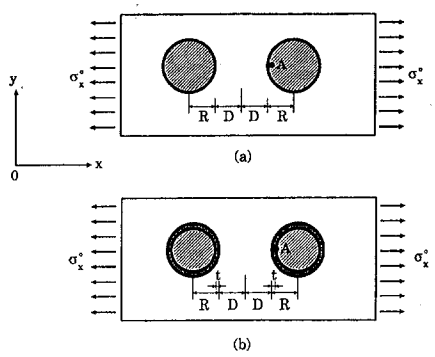


Fig. 3 Surface traction in the *x* direction at the fiber matrix interface

Downloaded 04 May 2010 to 171.66.16.34. Redistribution subject to ASME license or copyright; see http://www.asme.org/terms/Terms_Use.cfm



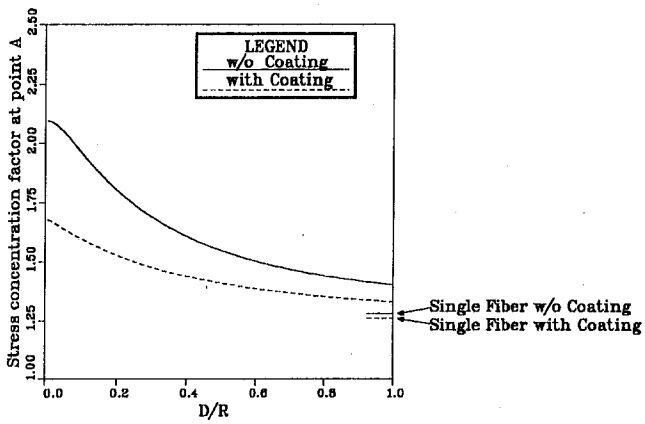


Fig. 4 Stress concentration factor at the fiber matrix interface

ments and tractions at the interfaces, S_1 and S_2, in the carbon interphase.

By applying the continuity conditions at the interfaces, S_1 and S_2, followed by discretization, a system of algebraic equations for the interface displacements and tractions can be obtained and solved. Once the displacements and tractions at the interfaces are obtained from the solution of these equations, the displacements and stresses everywhere can be calculated by evaluating the integral expressions of the displacement components in the three regions. A total of 50 standard three-node quadratic boundary elements (25 elements at S_1 and 25 elements at S_2; a total of 100 nodes) were used in the BIEM.

There is no change in the basic formulation for the VIEM from the homogeneous inclusion case except that δc_{ijkl} should be different in the interphase and the inclusion. Furthermore, only the Green's function for *Ti* matrix is needed for analysis. A total of 96 standard eight-node quadratic, quadrilateral and six-node quadratic, triangular elements (289 nodes) were used in the VIEM.

Figure 3(b) shows the normalized surface traction in the x direction on the surface S_1 in the carbon interphase from the analytical and the numerical solutions using BIEM and VIEM. It can be seen that there is excellent agreement in the results obtained by all three methods.

In the preceding examples, the number of boundaries involved is relatively small, so that both the VIEM and the BIEM are equally effective in formulating the discretized equations. Since two-dimensional elements are used in the VIEM while one-dimensional elements are used in the BIEM, it is expected that less number of nodes are needed in the BIEM than in the VIEM. However, as the number of boundaries increases, the VIEM becomes more efficient than the BIEM; the need to satisfy interface conditions at all the interfaces makes BIEM much more cumbersome to use. We consider a number of problems next where VIEM has a clear advantage over the BIEM.

3.3 The Inclusion-Pair. In order to determine the interaction effects between closely spaced fibers, the pairs shown in Fig. 4 are considered for a range of values of D/R where R is the radius of each fiber and D is their separation distance. To our knowledge the solution to this problem is not available in the literature. It can be seen that the stress concentration factor (σ_x/σ_x^o) at the point A (Fig. 4) is reduced significantly in presence of the interface layer and that the interaction between the fibers can be quite strong for small values of D/R. It should be noted that the linear elastic solution breaks down for $D/R \approx 0$. The results indicate that damage (e.g., matrix yielding or cracking) will be initiated in regions where inclusions are closely packed.

The VIEM results for a variety of other multiple inclusion problems are available in Lee (1994).

4 The Volume Integral Equation Method for Crack-Inclusion Interaction Problems

4.1 The Crack Model in VIEM. The volume integral equation method works very well for inclusion problems. The method, in its original form Eq. (1), breaks down for voids and cracks. However, as explained in Lee and Mal (1995), VIEM can be used for voids in a limiting sense with very small values of the material constants within the inclusions. This would, of course, introduce errors in the results for voids; however, as in the elastodynamic case, these errors can be made arbitrarily small by proper choice of the "material constants" of the void.

In order to apply VIEM to a crack, it is modeled as a thin elliptic inclusion with small values of the material constants. Figure 5 shows one quarter of a typical discretized crack model generated by PATRAN (1989). The calculated crack-opening displacement (COD) and the stress intensity factor (SIF) near the crack tip were compared with the analytical solutions for different aspect ratios of the ellipse. An aspect ratio of 40 for the ellipse was found to yield excellent agreement in the results obtained by the two methods.

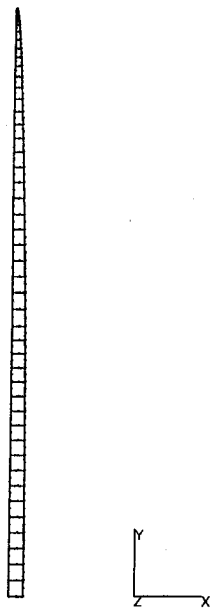


Fig. 5 One-quarter of a typical crack model in the VIEM

Downloaded 04 May 2010 to 171.66.16.34. Redistribution subject to ASME license or copyright; see http://www.asme.org/terms/Terms_Use.cfm

4.2 Determination of the Stress Intensity Factor by VIEM. Evaluation of the stress intensity factor for microcracks is very useful for predicting possible crack initiation and propagation near interacting inclusions or cracks. In most numerical techniques (e.g., FEM or BIEM), the stress intensity factors are computed from conventional or special crack-tip elements in a number of different ways. In one of these, the finite element or boundary element solution is equated to the analytical solution for displacements or stresses near the crack tip. In both FEM and BIEM, the procedure of equating displacements near the crack tip provides more accurate stress intensity factors than that of equating the stresses (Aliabadi and Rooke, 1991).

It is well known that the displacement field on the crack surfaces near the crack tip can be expressed as

$$u_2^+ - u_2^- = K_I \frac{(\kappa + 1)}{\mu} \sqrt{\frac{r}{2\pi}} + O(1)$$

$$u_1^+ - u_1^- = K_{II} \frac{(\kappa + 1)}{\mu} \sqrt{\frac{r}{2\pi}} + O(1)$$

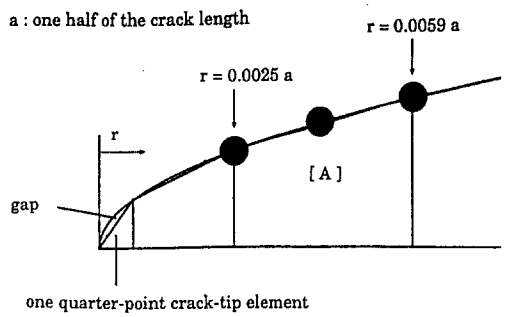
$$u_3^+ - u_3^- = K_{III} \left(\frac{4}{\mu}\right) \sqrt{\frac{r}{2\pi}} + O(1) \qquad (15)$$

where K_I, K_{II}, and K_{III} are the opening-mode (mode I), sliding-mode (mode II), and tearing-mode (mode III) stress intensity factors, $\kappa = 3 - 4\nu$ (plane strain), or $(3 - \nu)/(1 + \nu)$ (plane stress), r is the distance from the crack tip to the point of interest on the crack surface and $u_i^{\pm}$ denotes the displacement components on opposite surfaces of the crack.

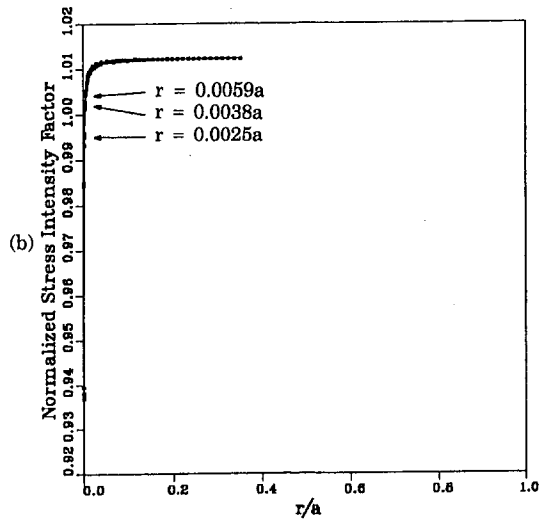
In VIEM, the procedure of equating the calculated displacements to the analytical solutions Eq. (15) on the crack surfaces was used to determine the stress intensity factor. It should be pointed out that in VIEM the crack is modeled as a limiting elliptical void rather than a surface of discontinuity of zero thickness used in the conventional FEM or BIEM. Thus, in VIEM, very accurate crack-opening displacements (COD) on the crack surface could be obtained without using any special crack-tip elements except at points very close to the crack tip.

In order to obtain accurate crack opening displacements (COD) near the crack tip, two different types of special crack-tip elements, originally developed for the finite element method, were explored. In one of these methods, (see e.g., Henshell and Shaw, 1975) the mid-side node of a quadratic element is moved to a quarter-point position, giving the desired $r^{1/2}$ variation in displacement on the crack surface. In the second method, Blackburn (1977) and Stern and Becker (1978) proposed a modified six node triangular element and the use of triangular polar co-ordinates in which the $r^{1/2}$ displacement field varies quadratically in the circumferential direction. The quarter-point crack-tip elements were found to provide more stable and accurate crack-opening displacements and stress intensity factors near the crack tip. Therefore, the quarter-point element was implemented at the crack tip in the VIEM. The stress intensity factor was determined by taking the average of three of its calculated values in the element closest to the crack tip (Fig. 6(a)). Figure 6(b) shows the normalized mode I stress intensity factor for five different crack lengths using this approach.

4.3 Comparison With Available Results. In this section, the stress intensity factors calculated by the VIEM are compared to those available in the literature for specific crack and inclusion configurations. A single crack of length $2a$ subject to either the uniaxial stress σ_y^o, a pure shear stress σ_{xy}^o, or an antiplane shear stress σ_{xz}^o at infinity was considered first. The normalized stress intensity factors, $K_I/\sigma_y^o\sqrt{\pi a}$, $K_{II}/\sigma_{xy}^o\sqrt{\pi a}$, and $K_{III}/\sigma_{xz}^o\sqrt{\pi a}$, for five different crack lengths



(a)



(b)

Fig. 6 (a) Enlarged view of the crack tip and (b) the crack-tip stress intensity factor calculated from the volume integral equation method

calculated by VIEM were compared with the exact solutions. The crack length $2a$ is assumed to be as 1, 1.33, 1.50, 1.75, or 2.0 in arbitrary units. In all cases, the maximum error in the numerical results from VIEM was found to be less than 0.2 percent for mode I, II cracks and less than 0.5 percent for mode III cracks; the results are not shown.

4.3.1 Multiple Crack Problems. Three collinear cracks, each of length $2a$, subjected to uniaxial stress σ_y^o at infinity (Fig. 7) is considered next. Let F_1 denote the normalized stress intensity factor, $F_I = K_I/\sigma_y^o\sqrt{\pi a}$. The calculated normalized stress intensity factors for different separation distances are compared with the exact solution given by Sih (1964) in Table 3. It can be seen that the solutions obtained from the VIEM are very close to the exact solution for all separation distances considered.

As another test of the accuracy of the present technique, a crack of length $2a$ located near another crack or multiple cracks and subjected to uniaxial stress σ_y^o at infinity (Fig. 8) is considered. The calculated normalized stress intensity factors defining through $F_I = K_I/\sigma_y^o\sqrt{\pi a}$ while $F_{II} = K_{II}/\sigma_y^o\sqrt{\pi a}$ are compared with the exact solution given by Isida (1970) and the semi-analytical solution by Lam and Phua (1991) in Table 4. It can be seen that the solutions obtained from the VIEM are very close to the known solutions for all crack configurations considered.

4.3.2 Crack-Inclusion Problems. We now consider crack of length $2a$ located near a cylindrical inclusion and subjected to uniaxial stress σ_y^o at infinity (Fig. 9(a)). The

Downloaded 04 May 2010 to 171.66.16.34. Redistribution subject to ASME license or copyright; see http://www.asme.org/terms/Terms_Use.cfm

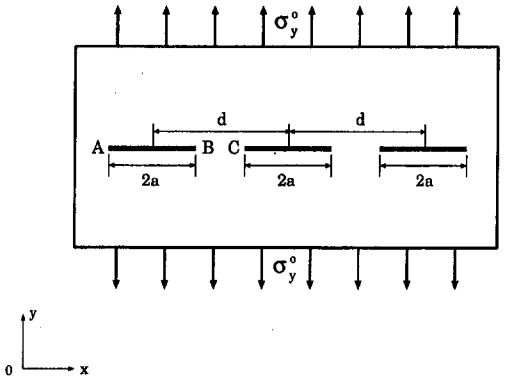


Fig. 7 Geometry of three-collinear-crack configuration

normalized stress intensity factor, F_I, calculated by VIEM is compared with the exact solution given by Erdogan and Gupta (1975) in Table 5(a). It can be seen that the solution obtained from the VIEM is very close to the exact solution even when the distance between the crack and the inclusion is very small. Erdogan and Gupta (1975) also considered a crack emanating from a cylindrical inclusion (Fig. 9(b)), for which the order of the stress singularity at the crack-tip A is no longer of the $r^{-1/2}$ type. For this problem, the stress intensity factors at crack-tip B was calculated by VIEM; the results are shown in Table 5(b). The agreement between the analytical solution and the present numerical solution can again be seen to be excellent.

Table 3 Comparison of the normalized mode I stress intensity factor for three collinear cracks in an infinite medium subjected to remote stress (Fig. 7). Analytical solution is from Sih (1964).

2a/d	F_I (A)			F_I (B)			F_I (C)		
	Exact	VIEM	Error (%)	Exact	VIEM	Error (%)	Exact	VIEM	Error (%)
0.8	1.1103	1.1100	0.027	1.2835	1.2808	0.210	1.3214	1.3119	0.719
0.9	1.1644	1.1654	0.086	1.5645	1.5535	0.703	1.6069	1.5938	0.815

Table 4(a) Comparison of the normalized mode I and II stress intensity factors for two cracks inclined at an angle α = 30 deg in an infinite medium subjected to remote stress (Fig. 8(a)). Analytical solution is from Isida (1970). $a = b$, $c = 1.5a$.

	Tip A		Tip B		Tip C		Tip D	
	F_I	F_{II}	F_I	F_{II}	F_I	F_{II}	F_I	F_{II}
Analytical	1.044	-0.023	1.099	-0.050	0.868	0.428	0.806	0.440
VIEM	1.044	-0.024	1.090	-0.052	0.867	0.440	0.797	0.441

Table 4(b) Comparison of the normalized mode I stress intensity factor of a central crack for the crack configuration shown in Fig. 8(b) in an infinite medium subjected to remote stress. Available solution is from Lam and Phua (1991). $b = a$, $c = h = 2a$.

F_I (A)		
Lam and Phua (1991)	VIEM	Difference (%)
0.9149	0.9133	0.175

Table 4(c) Comparison of the normalized mode I stress intensity factor of a central crack for the crack configuration shown in Fig. 8(c) in an infinite medium subjected to remote stress. Available solution is from Lam and Phua (1991). $b = a$, $c = h = 2a$.

e/a	α	F_I (A)		
		Lam and Phua (1991)	VIEM	Difference (%)
0.2	30°	1.0425	1.0432	0.067
1.0	30°	0.9657	0.9529	1.325
2.0	0°	0.9776	0.9861	0.869

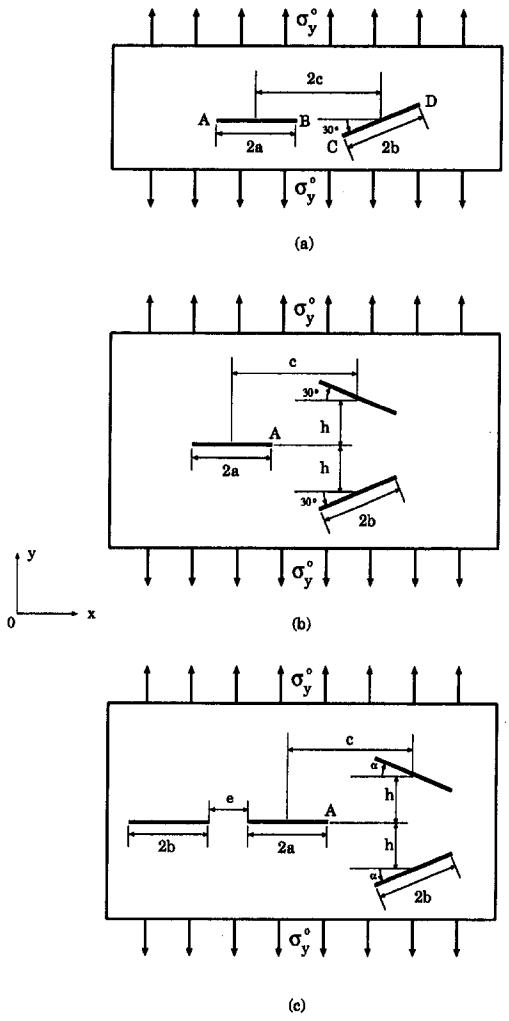


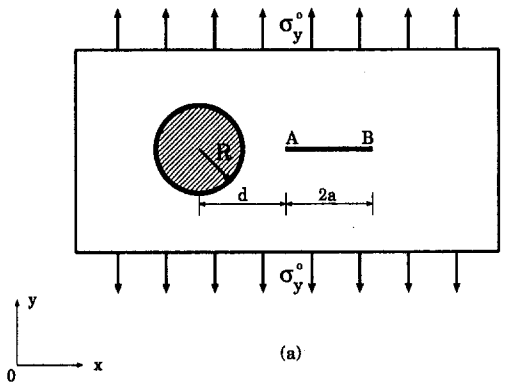
Fig. 8 Geometry of crack configuration

4.3.3 Crack-Hole Problems. A single crack of length $2a$ located near a cylindrical hole and subjected to anitplane stress σ_{xz}^o at infinity (Fig. 10) is considered first. The normalized stress intensity factor, $F_{III} = K_{III}/\sigma_{xz}^o\sqrt{\pi a}$, calculated by VIEM is compared with the exact solution given by Yokobori et al. (1971) in Table 6. It can be seen that the solution obtained from the VIEM is very close to the exact solution for different distances between the crack and the hole.

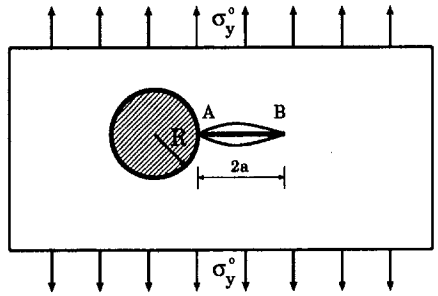
Two symmetrically placed collinear cracks of length $2a$ containing a cylindrical hole and subjected to uniaxial stress σ_y^o at infinity (Fig. 11) is considered next. The normalized stress intensity factor, $K_I/\sigma_y^o\sqrt{\pi a}$, calculated by VIEM is compared with the exact solution given by Nisitani et al. (1973) in Table 7. It can be seen that the solution obtained from the VIEM is very close to the exact solution.

The VIEM-based results were compared with known results for a number of other problems involving cracks, inclusions and voids. In all cases considered, the differences were less than 1.5 percent (Lee, 1994).

Downloaded 04 May 2010 to 171.66.16.34. Redistribution subject to ASME license or copyright; see http://www.asme.org/terms/Terms_Use.cfm



(a)



(b)

Fig. 9 Geometry of the crack-inclusion problem

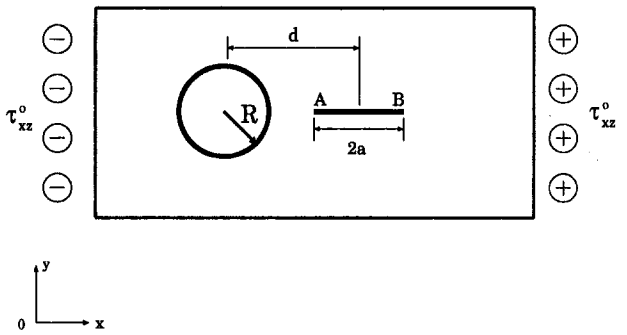


Fig. 10 Geometry of the crack (mode III)-hole problem

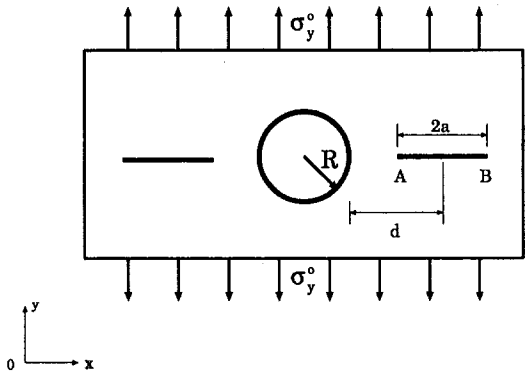


Fig. 11 Geometry of the crack-hole problem

Table 5(*a*) Comparison of the normalized mode I stress intensity factor for a crack near a cylindrical inclusion in an infinite medium subjected to remote stress (Fig. 9(*a*)). Exact solution is from Erdogan and Gupta (1975). $d/R = 1.1$, $(d + 2a)/R = 2.1$. $\kappa_1 = \kappa_2 = 2.0$, $\mu_1/\mu_2 = \frac{1}{3}$.

F_I (A)			F_I (B)		
Exact	VIEM	Error (%)	Exact	VIEM	Error (%)
1.482	1.486	0.270	1.160	1.158	0.172

Table 5(*b*) Comparison of the normalized mode I stress intensity factor for a crack emanating from a cylindrical inclusion in an infinite medium subjected to remote stress for $2a/R = 1$ (Fig. 9(*b*)). Exact solution is from Erdogan and Gupta (1975).

μ_1 / μ_2	$\kappa_1 = \kappa_2$	F_I (B)		
		Exact	VIEM	Error (%)
1/3	2.0	1.2330	1.2250	0.649
3	1.8	0.8610	0.8597	0.151
10	1.8	0.7969	0.7956	0.163
23	1.8	0.7796	0.7788	0.103

Table 6 Comparison of the normalized mode III stress intensity factor for a crack near a cylindrical hole in an infinite medium subjected to remote antiplane stress (Fig. 10). Analytical solution is from Yokobori et al. (1971).

a/R	a/d	F_{III} (A)		
		Exact	VIEM	Error (%)
0.50	1/5	1.2115	1.2143	0.230
0.50	2/9	1.2748	1.2761	0.106
0.50	1/4	1.3760	1.3813	0.387
0.50	2/7	1.5769	1.5847	0.496

Table 7 Comparison of the normalized mode I stress intensity factor for two symmetrically placed collinear cracks containing a cylindrical hole in an infinite medium subjected to remote stress (Fig. 11). Analytical solution is from Nisitani et al. (1973).

a/R	a/d	F_I (A)		
		Exact	VIEM	Error (%)
0.50	0.4	1.269	1.264	0.394
0.50	0.8	2.256	2.228	1.241

5 Concluding Remarks

The volume integral equation method is introduced for the solution of elastostatic problems involving multiple inclusions and cracks. The relative accuracy and efficiency of the method are examined through comparison with results obtained from analytical and boundary integral equation methods. In general, for strongly heterogeneous materials, the VIEM is found to give very accurate results, and is easier and more convenient to apply as compared to BIEM. Furthermore, the method is not sensitive to geometry, anisotropy and inhomogeneity of the inclusions.

Acknowledgment

This research was supported by the AFOSR under grant F49620-93-1-0320.

References

Aliabadi, M. H., and Rooke, D. P., 1991, *Numerical Fracture Mechanics*, Computational Mechanics Publications, Boston.

Beskos, D. E., ed., 1989, *Boundary Element Methods in Structural Analysis*, American Society of Civil Engineers, New York.

Blackburn, W. S., 1977, *The Mathematics of Finite Elements and Applications*, Brunel University.

Downloaded 04 May 2010 to 171.66.16.34. Redistribution subject to ASME license or copyright; see http://www.asme.org/terms/Terms_Use.cfm

Cox, B. N., Dadkhah, M. S., James, M. R., Marshall, D. B., Morris, W. L., and Shaw, M., 1990, "On Determining Temperature Dependent Interfacial Shear Properties and Bulk Residual Stresses in Fibrous Composites," *Acta metall. mater.*, Vol. 38, pp. 2425–2433.

El Mouden, M. E., and Molinari, A., 1995, "A cluster approach for the elastic interaction of inclusions," *C.R. Acad. Sci. Paris,* Vol. 321, pp. 355–361.

Erdogan, F., and Gupta, G. D., 1975, "The Inclusion Problem with a Crack Crossing the Boundary," *Int. J. Fract.,* Vol. 11, pp. 13–27.

Henshell, R. D., and Shaw, K. G., 1975, "Crack-Tip Finite Elements Are Unnecessary," *Int. J. Num. Meth. Engng.,* Vol. 9, pp. 495–507.

Isida, M., 1970, "Analysis of Stress Intensity Factors for Plates Containing Random Array of Cracks," *Bulletin of the JSME,* Vol. 13, pp. 635–642.

Lam, K. Y., and Phua, S. P., 1991, "Multiple Crack Interaction and its Effect on Stress Intensity Factor," *Engineering Fracture Mechanics,* Vol. 40, pp. 585–592.

Lee, J. K., 1994, "Micromechanics of Crack Extension in Composites," Ph.D. Dissertation, University of California, Los Angeles, CA.

Lee, J. K., and Mal, A. K., 1995, "A Volume Integral Equation Technique for Multiple Scattering Problems in Elastodynamics," *Applied Mathematics and Computation,* Vol. 67, pp. 135–159.

Li, H. B., Han, G. M., and Mang, H. A., 1985, "A New Method for Evaluating Singular Integrals in Stress Analysis of Solids by the Direct Boundary Element Method," *Int. J. Num. Meth. Engng.,* Vol. 21, pp. 2071–2098.

Lu, S., and Ye, T. Q., 1991, "Direct Evaluation of Singular Integrals in Elastoplastic Analysis by the Boundary Element Method," *Int. J. Num. Meth. Engng.,* Vol. 32, pp. 295–311.

Mal, A. K., and Knopoff, L., 1967, "Elastic Wave Velocities in Two Component Systems," *J. Inst. Math. Applics.,* Vol. 3, pp. 376–387.

Mal, A. K., and Singh, S. J., 1991, *Deformation of Elastic Solids,* Prentice-Hall, Englewood Cliffs, NJ.

Nisitani, H., Saito, K., and Hara, N., 1973, "Stress Concentration Due to an Elliptic Hole or Crack Existing near a Notch under Tension or Longitudinal Shear," *Trans. of the JSME,* Vol. 39, pp. 2312–2322.

Patran Plus User Manual, 1989, Vols. I and II, PDA Engineering, Costa Mesa, CA.

Sih, G. C., 1964, "Boundary Problems for Longitudinal Shear Cracks," *Proc. Conf. Theor. Appl. Mech.,* pp. 117–130.

Stern, M., and Becker, E. B., 1978, "A Conforming Crack Tip Element with Quadratic Variation in the Singular Fields," *Int. J. Num. Meth. Engng.,* Vol. 12, pp. 279–288.

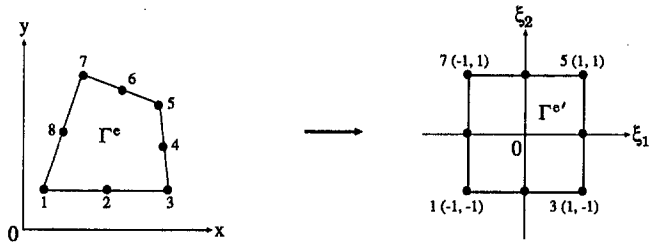
Yokobori, T., Ichikawa, M., Konosu, S., and Takahashi, R., 1971, "A Criterion for Brittle Fracture of Notched Solid," *J. Japan. Soc. Strength & Frac. Mater.,* Vol. 6, pp. 58–67.

Zienkiewicz, O. C., Bettess, P., Chiam, T. C., and Emson, C., 1981, "Numerical Methods for Unbounded Field Problems and a New Infinite Element Formulation," *Computational Methods for Infinite Domain Media-Structure Interaction,* A. J. Kalinowski, ed., ASME, New York, pp. 115–148.

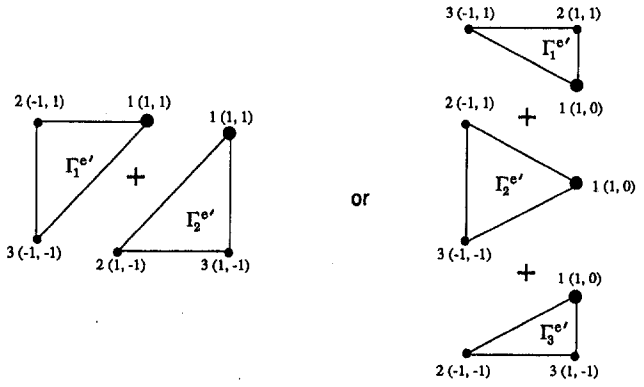
APPENDIX

Evaluation of the Singular Integrals

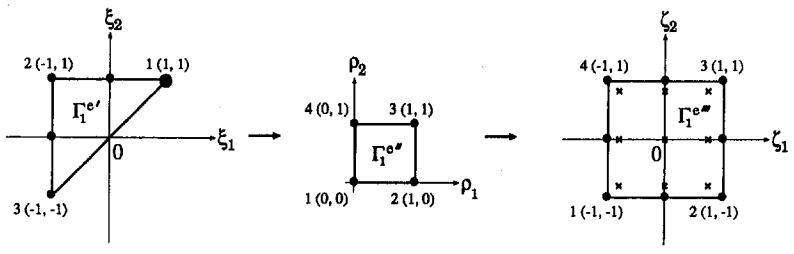
Triangular polar coordinates are used to reduce the order of singularity of the singular elements by one degree and to carry out the ingegration over the mappings of the singular elements onto plane squares (Li et al., 1985). This strategy results in good numerical approximations of singular integrals existing in



(a)Mapping of Γ^e onto $\Gamma^{e'}$



(b) Subdivision of $\Gamma^{e'}$ depending on the location of the singular point (point 1)



(c) Mapping of $\Gamma_1^{e'}$ onto $\Gamma_1^{e''}$ and of $\Gamma_1^{e''}$ onto $\Gamma_1^{e'''}$

Fig. 12 Quadratic, quadrilateral, isoparametric element with the singular point at a nodal point—sequence of coordinate mappings

Downloaded 04 May 2010 to 171.66.16.34. Redistribution subject to ASME license or copyright; see http://www.asme.org/terms/Terms_Use.cfm

the Cauchy principal value sense, and converts weakly singular integrals into integrals over smooth functions. As an example, the application of the special polar coordinates to quadratic, quadrilateral, isoparametric singular elements will be considered here.

1 First, the quadratic, quadrilateral element e, representing the part Γ^e of the surface Γ of the considered body, is mapped onto a square $\Gamma^{e'}$ of side-length 2 as shown in Fig. 12(a). While Γ^e is embedded in a global two-dimensional Cartesian space, $\Gamma^{e'}$ is associated with a local two-dimensional Cartesian space, characterized by the natural coordinates ξ_1 and ξ_2. For reference, Γ^e is embedded in a global three-dimensional Cartesian space in the three-dimensional boundary integral equation method.

2 The second step of the concept consists of a subdivision of $\Gamma^{e'}$ into two or three triangular subelements $\Gamma_g^{e'}$ depending on whether the singular point, designated locally as point 1, coincides with a corner or a midpoint node (Fig. 12(b)).

3 The third step involves the mapping of each one of the subelements onto a unit square, employing triangular polar coordinates. Figure 12(c) illustrates the mapping of the subelement $\Gamma_1^{e'}$ of the left-hand part of Fig. 12(b) into $\Gamma_1^{e''}$ and subsequently, the mapping of $\Gamma_1^{e''}$ onto $\Gamma_1^{e'''}$. The last mapping represents a linear transformation for the purpose of carrying out numerical integrations in a standard way. The right-hand part of Fig. 12(c) contains the integration points for a 3×3 Gaussian quadrature scheme. Similarly, all other subdomains $\Gamma_g^{e'}$ are to be mapped onto unit squares $\Gamma_g^{e''}$ which in turn must be mapped onto squares $\Gamma_g^{e'''}$.

Downloaded 04 May 2010 to 171.66.16.34. Redistribution subject to ASME license or copyright; see http://www.asme.org/terms/Terms_Use.cfm

L. Cui

A. H-D. Cheng

Department of Civil Engineering,
University of Delaware,
Newark, DE 19716

Y. Abousleiman

School of Engineering and Architecture,
Lebanese American University,
Byblos, Lebanon

Poroelastic Solution for an Inclined Borehole

The analytical solution for an infinitely long borehole in an isotropic, poroelastic medium, inclined to the far-field principal stresses, is presented. The solution utilizes a loading decomposition scheme which leads to three fundamental problems: a poroelastic plane-strain, an elastic uni-axial, and an elastic antiplane shear problem.

1 Introduction

The stress concentration near an excavated borehole is of critical interest to the oil and gas industry. Stress levels exceeding material limits can cause costly wellbore damage. For vertical borehole orientation, the linear elastic analysis based on the plane-strain assumption is well known (Hubert and Willis, 1957) and has been extensively applied. However, in petroleum engineering applications, the formation surrounding the borehole is often permeated with fluid. The pore pressure field near the borehole is perturbed by the excavation. Fluid diffusion leads to a time-dependent redistribution of total and effective stresses. These coupled effects should be examined within the framework of the Biot theory of poroelasticity (Biot, 1941; Detournay and Cheng, 1993).

Haimson and Fairhurst (1969) presented one of the first poroelastic borehole solutions based on an asymptotic analysis. The complete, time-dependent, poroelastic, plane-strain borehole solution was provided by Detournay and Cheng (1988). Several scenarios of poroelastic effects such as delayed compressive failure, inward migration of the critical shear failure region to inside the wall, and tensile failure under rapid depressurization, etc., were extensively discussed (Detornay and Cheng, 1988; Cheng et al., 1993). This plane-strain solution, however, was restricted to the physical conditions that the borehole axis coincides with one of the far-field principal in situ stresses, and that there is no displacement in the borehole-axis direction.

With the emergence of inclined and horizontal drilling technology, the inclined borehole problem has received considerable attention (Bradley, 1979; Aadnoy and Chenevert, 1987; Ong and Roegiers, 1993). These existing solutions are again based on elasticity, without rigorous consideration of the time-dependent pore fluid and solid matrix interaction. A poroelastic solution is needed.

The present paper provides an analytical solution for a circular, infinitely long borehole, embedded in a linear, poroelastic, homogeneous, and isotropic formation of infinite extent. In the far field, the stresses are uniform (but anisotropic) and pore pressure is a constant. The borehole axis is inclined to the principal axes of the far-field stresses. Under these conditions, a "generalized (or complete) plane-strain" condition naturally arises.

The solution technique is heuristic. Utilizing a loading decomposition scheme, the problem is separated into three fundamental problems, namely, a poroelastic plane-strain, an elastic uni-axial, and an elastic antiplane shear problem. Based on an understanding of the basic poroelastic mechanisms, the solution of each problem becomes known. The final solution is obtained by superposition. An effective stress analysis is then demonstrated and its consequence for failure illustrated.

2 Governing Equations

There are a number of ways that the poroelasticity governing equations can be presented (Detournay and Cheng, 1993). We choose the following form attributed to Rice and Cleary (1976):

- equilibrium equations

$$\sigma_{ij,j} = 0 \tag{1}$$

- compatibility equations

$$\nabla^2\sigma_{ij} + \frac{1}{1+\nu}\sigma_{kk,ij} + 2\eta\left(\delta_{ij}\nabla^2 p + \frac{1-\nu}{1+\nu}p_{,ij}\right) = 0 \tag{2}$$

- diffusion equation

$$\nabla^2\left(\sigma_{kk} + \frac{3}{B}p\right) = \frac{1}{c}\frac{\partial p}{\partial t} \tag{3}$$

where σ_{ij} is the total stress tensor (positive for tension), p the pore pressure, δ_{ij} the Kronecker delta, η the poroelastic stress coefficient, ν the drained Poisson ratio, B the Skempton pore pressure coefficient (Skempton, 1954), and c the generalized consolidation coefficient. The tensor differentiation notation and Einstein summation convention are adopted. The above system of Eqs. (1)–(3), is complete for the solution at the stress level.

3 Problem Definition

An inclined borehole is defined as a borehole drilled with its axis inclined to the far-field principal stress axes x'-y'-z' (Fig. 1). Borehole inclination can be a consequence of the natural oblique orientation of in situ stresses, an unintentional deviation in drilling, or a controlled directional drilling that leads to a horizontal well for production enhancement.

In Fig. 1(a), the Cartesian coordinate system $x'y'z'$ is chosen to coincide with the principal axes of the in situ compressive stresses, respectively designated as $S_{x'}$, $S_{y'}$ and $S_{z'}$. The virgin

Contributed by the Applied Mechanics Division of THE AMERICAN SOCIETY OF MECHANICAL ENGINEERS for publication in the ASME JOURNAL OF APPLIED MECHANICS.

Discussion on this paper should be addressed to the Technical Editor, Professor Lewis T. Wheeler, Department of Mechanical Engineering, University of Houston, Houston, TX 77204-4792, and will be accepted until four months after final publication of the paper itself in the ASME JOURNAL OF APPLIED MECHANICS.

Manuscript received by the ASME Applied Mechanics Division, Feb. 8, 1995; final revision, Mar. 1, 1996. Associate Technical Editor: J. T. Jenkins.

Copyright © 1997 by ASME

Downloaded 04 May 2010 to 171.66.16.34. Redistribution subject to ASME license or copyright; see http://www.asme.org/terms/Terms_Use.cfm

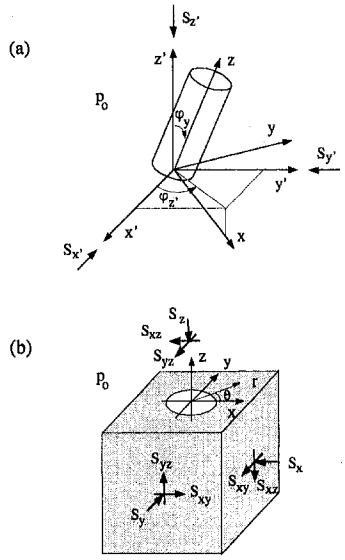


Fig. 1 Definition sketch of an inclined borehole problem

pore pressure is given by p_o. The borehole is defined by a local coordinate system xyz with the borehole axis coinciding with the z-axis. The local system is formed by a rotation of an azimuth angle $\varphi_{z'}$ about the z'-axis, and then by an inclination of a zenith angle φ_y toward the x-axis. See Fig. 1(a) for illustration.

For the convenience of solution presentation, the local (borehole) coordinate system xyz is chosen to portray the solution domain, as shown in Fig. 1(b). We note that the surfaces of the cube are presented for the purpose of easy visualization of far-field stresses. They otherwise do not exist as the domain is infinite. The in situ stresses can be converted to the local coordinate system via the transformation (Fjær et al., 1992)

$$\begin{Bmatrix} S_x \\ S_y \\ S_z \\ S_{xy} \\ S_{yz} \\ S_{xz} \end{Bmatrix} = \begin{bmatrix} l_{xx'}^2 & l_{xy'}^2 & l_{xz'}^2 \\ l_{yx'}^2 & l_{yy'}^2 & l_{yz'}^2 \\ l_{zz'}^2 & l_{zy'}^2 & l_{zz'}^2 \\ l_{xx'}l_{yx'} & l_{xy'}l_{yy'} & l_{xz'}l_{yz'} \\ l_{yx'}l_{zx'} & l_{yy'}l_{zy'} & l_{yz'}l_{zz'} \\ l_{zx'}l_{xx'} & l_{zy'}l_{xy'} & l_{zz'}l_{xz'} \end{bmatrix} \begin{Bmatrix} S_{x'} \\ S_{y'} \\ S_{z'} \end{Bmatrix} \tag{4}$$

where

$$\begin{bmatrix} l_{xx'} & l_{xy'} & l_{xz'} \\ l_{yx'} & l_{yy'} & l_{yz'} \\ l_{zx'} & l_{zy'} & l_{zz'} \end{bmatrix} = \begin{bmatrix} \cos\varphi_{z'}\cos\varphi_y & \sin\varphi_{z'}\cos\varphi_y & -\sin\varphi_y \\ -\sin\varphi_{z'} & \cos\varphi_{z'} & 0 \\ \cos\varphi_{z'}\sin\varphi_y & \sin\varphi_{z'}\sin\varphi_y & \cos\varphi_y \end{bmatrix}. \tag{5}$$

The conditions at the far field, $r \to \infty$, where r is the radial distance from the borehole axis, become

$$\sigma_{xx} = -S_x \tag{6a}$$

$$\sigma_{yy} = -S_y \tag{6b}$$

$$\sigma_{zz} = -S_z \tag{6c}$$

$$\sigma_{xy} = -S_{xy} \tag{6d}$$

$$\sigma_{yz} = -S_{yz} \tag{6e}$$

$$\sigma_{xz} = -S_{xz} \tag{6f}$$

$$p = p_o. \tag{6g}$$

At the borehole wall, $r = R$, where R is the borehole radius, surface tractions and pore pressure are assumed to vanish at the instant of excavation

$$\sigma_{rr} = -S_r H(-t) \tag{7a}$$

$$\sigma_{r\theta} = -S_{r\theta} H(-t) \tag{7b}$$

$$\sigma_{rz} = -S_{rz} H(-t) \tag{7c}$$

$$p = p_o H(-t). \tag{7d}$$

In the above, H denotes the Heaviside unit step function, S_r, $S_{r\theta}$, and S_{rz} are the far-field compressive stress components in cylindrical coordinates:

$$S_r = \frac{S_x + S_y}{2} + \frac{S_x - S_y}{2}\cos 2\theta + S_{xy}\sin 2\theta \tag{8a}$$

$$S_{r\theta} = S_{xy}\cos 2\theta - \frac{S_x - S_y}{2}\sin 2\theta \tag{8b}$$

$$S_{rz} = S_{xz}\cos\theta + S_{yz}\sin\theta. \tag{8c}$$

We note that $H(-t) = 1 - H(t)$ such that $H(-t) = 1$ for $t \leq 0$, and $H(-t) = 0$ for $t > 0$.

Owing to the linearity of the governing Eqs. (1) to (3), the boundary and far-field conditions (6) and (7) can be decomposed into three problems (see Fig. 2 for illustration):

Problem I. In the far-field ($r \to \infty$),

$$\sigma_{xx} = -S_x \tag{9a}$$

$$\sigma_{yy} = -S_y \tag{9b}$$

$$\sigma_{zz} = -\nu(S_x + S_y) - \alpha(1 - 2\nu)p_o \tag{9c}$$

$$\sigma_{xy} = -S_{xy} \tag{9d}$$

$$\sigma_{yz} = \sigma_{xz} = 0 \tag{9e}$$

$$p = p_o, \tag{9f}$$

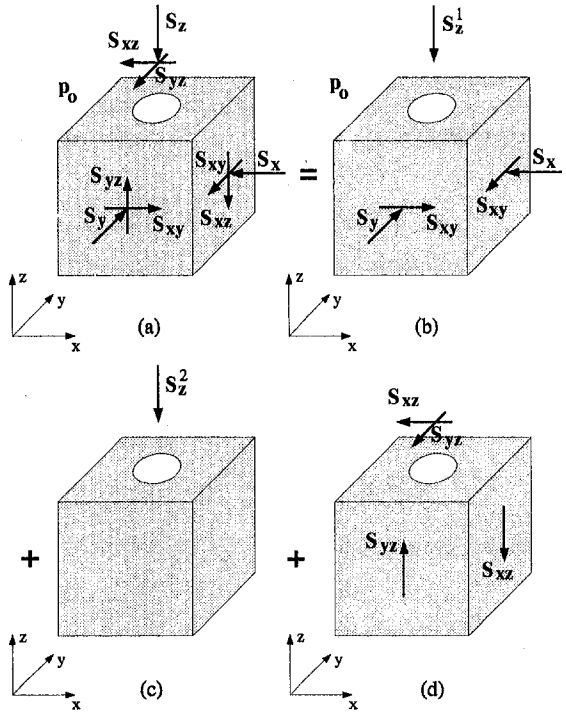


Fig. 2 Decomposition of the inclined borehole problem, where $S_z = S_z^1 + S_z^2$

Downloaded 04 May 2010 to 171.66.16.34. Redistribution subject to ASME license or copyright; see http://www.asme.org/terms/Terms_Use.cfm

at the borehole wall ($r = R$),

$$\sigma_{rr} = -S_r H(-t) \tag{10a}$$

$$\sigma_{r\theta} = -S_{r\theta} H(-t) \tag{10b}$$

$$\sigma_{rz} = 0 \tag{10c}$$

$$p = p_o H(-t). \tag{10d}$$

Problem II. In the far-field ($r \to \infty$),

$$\sigma_{zz} = -S_z + [\nu(S_x + S_y) + \alpha(1 - 2\nu)p_o] \tag{11a}$$

$$\sigma_{xx} = \sigma_{yy} = \sigma_{xy} = \sigma_{yz} = \sigma_{xz} = p = 0, \tag{11b}$$

at the borehole wall ($r = R$)

$$\sigma_{rr} = \sigma_{r\theta} = \sigma_{rz} = p = 0. \tag{12}$$

Problem III. In the far-field ($r \to \infty$),

$$\sigma_{xx} = \sigma_{yy} = \sigma_{zz} = \sigma_{xy} = p = 0 \tag{13a}$$

$$\sigma_{yz} = -S_{yz} \tag{13b}$$

$$\sigma_{xz} = -S_{xz}, \tag{13c}$$

at the borehole wall ($r = R$)

$$\sigma_{rr} = \sigma_{r\theta} = p = 0 \tag{14a}$$

$$\sigma_{rz} = -S_{rz} H(-t). \tag{14b}$$

In the above, α is the Biot effective stress coefficient. We note that (6) and (7) are reproduced by the summation of the above far-field and boundary conditions.

4 Solution

The decomposition presented above allows the solutions to be found elegantly as superposition of existing results, without a formal mathematical technique that can lead to lengthy, semi-analytical expressions.

4.1 Poroelastic Plane-Strain Problem. The first problem is designed to be a poroelastic plane-strain problem, namely that the out-of-plane displacement u_z and flux q_z vanish. We note that in a plane-strain problem, the far-field conditions of σ_{zz}, σ_{yz}, and σ_{xz} in (9), and the boundary condition of σ_{rz} in (10) are redundant. These conditions can be admitted only because they are fully compatible with the natural result of a plane-strain solution:

$$\sigma_{zz} = \nu(\sigma_{xx} + \sigma_{yy}) - \alpha(1 - 2\nu)p \tag{15a}$$

$$\sigma_{xz} = \sigma_{yz} = 0 \tag{15b}$$

Given those conditions, the poroelastic plane-strain solutions by Detournay and Cheng (1988) can be utilized.

To use the solution, we first perform a rotation of coordinates about the z-axis such that the x''-axis coincides with the minimum horizontal principal stress and y'' with the maximum. The angle of rotation, measured between the x and the x'' axes, is given by

$$\theta_r = \frac{1}{2} \tan^{-1} \frac{2S_{xy}}{S_x - S_y}. \tag{16}$$

The polar angle under the new coordinate system is

$$\theta'' = \theta - \theta_r. \tag{17}$$

The far-field conditions become, at $r \to \infty$,

$$\sigma_{x''x''} = -(P_o - S_o) \tag{18a}$$

$$\sigma_{y''y''} = -(P_o + S_o) \tag{18b}$$

$$\sigma_{x''y''} = 0 \tag{18c}$$

$$p = p_o, \tag{18d}$$

where P_o is the mean compressive stress and S_o the deviatoric stress given by

$$P_o = \frac{S_x + S_y}{2} \tag{19a}$$

$$S_o = \sqrt{\left(\frac{S_x - S_y}{2}\right)^2 + S_{xy}^2}. \tag{19b}$$

At the borehole wall, $r = R$, all surface tractions and the pore pressure vanish.

With the above far-field stresses, the solution of the first problem can be expressed as

$$\sigma_{rr}^{(I)} = -P_o + S_o \cos 2(\theta - \theta_r) + \sigma_{rr}^{(1)} + \sigma_{rr}^{(2)} + \sigma_{rr}^{(3)} \tag{20a}$$

$$\sigma_{\theta\theta}^{(I)} = -P_o - S_o \cos 2(\theta - \theta_r) + \sigma_{\theta\theta}^{(1)} + \sigma_{\theta\theta}^{(2)} + \sigma_{\theta\theta}^{(3)} \tag{20b}$$

$$\sigma_{zz}^{(I)} = \nu[\sigma_{rr}^{(I)} + \sigma_{\theta\theta}^{(I)}] - \alpha(1 - 2\nu)p^{(I)} \tag{20c}$$

$$\sigma_{r\theta}^{(I)} = -S_o \sin 2(\theta - \theta_r) + \sigma_{r\theta}^{(3)} \tag{20d}$$

$$\sigma_{rz}^{(I)} = \sigma_{\theta z}^{(I)} = 0 \tag{20e}$$

$$p^{(I)} = p_o + p^{(2)} + p^{(3)} \tag{20f}$$

where the superscript $^{(I)}$ is used to denote the solution for problem I, and the superscripts $^{(1)}$, $^{(2)}$, and $^{(3)}$ represent the solution of the three fundamental loading modes of a borehole, as explained in the following.

Following Detournay and Cheng (1988), the plane-strain borehole problem can be decomposed into three fundamental problems: a Lamé (elastic), a diffusion, and a poroelastic deviatoric stress loading problem, with the following boundary conditions at the borehole wall, $r = R$:

- mode 1

$$\sigma_{rr}^{(1)} = P_o H(t) \tag{21a}$$

$$\sigma_{r\theta}^{(1)} = 0 \tag{21b}$$

$$p^{(1)} = 0 \tag{21c}$$

- mode 2

$$\sigma_{rr}^{(2)} = 0 \tag{22a}$$

$$\sigma_{r\theta}^{(2)} = 0 \tag{22b}$$

$$p^{(2)} = -p_o H(t) \tag{22c}$$

- mode 3

$$\sigma_{rr}^{(3)} = -S_o H(t) \cos 2(\theta - \theta_r) \tag{23a}$$

$$\sigma_{r\theta}^{(3)} = S_o H(t) \sin 2(\theta - \theta_r) \tag{23b}$$

$$p^{(3)} = 0 \tag{23c}$$

At the far field, all stresses and pore pressure vanish.

The mode 1 loading does not cause any volumetric strain, hence no pore pressure is generated. The solution is purely elastic as given by the classical Lamé solution:

$$\sigma_{rr}^{(1)} = H(t)P_o \frac{R^2}{r^2} \tag{24a}$$

$$\sigma_{\theta\theta}^{(1)} = -H(t)P_o \frac{R^2}{r^2}. \tag{24b}$$

The mode 2 problem reduces to an uncoupled diffusion problem for pore pressure. The solution in time is in an integral form (Carslaw and Jaeger, 1959). For efficient evaluation and conciseness of presentation, the Laplace transform expressions are given instead:

Downloaded 04 May 2010 to 171.66.16.34. Redistribution subject to ASME license or copyright; see http://www.asme.org/terms/Terms_Use.cfm

$$\tilde{\sigma}_{rr}^{(2)} = -\frac{2\eta p_o}{s}\left[\frac{R}{r}\frac{K_1(\xi)}{\beta K_0(\beta)} - \frac{R^2}{r^2}\frac{K_1(\beta)}{\beta K_0(\beta)}\right] \quad (25a)$$

$$\tilde{\sigma}_{\theta\theta}^{(2)} = \frac{2\eta p_o}{s}\left[\frac{R}{r}\frac{K_1(\xi)}{\beta K_0(\beta)} - \frac{R^2}{r^2}\frac{K_1(\beta)}{\beta K_0(\beta)} + \frac{K_0(\xi)}{K_0(\beta)}\right] \quad (25b)$$

$$\tilde{p}^{(2)} = -\frac{p_o}{s}\frac{K_0(\xi)}{K_0(\beta)} \quad (25c)$$

in which $\tilde{}$ denotes the Laplace transform, s is the transform parameter, K_n is the modified Bessel function of the second kind of order n, and

$$\xi = r\sqrt{\frac{s}{c}} \quad (26a)$$

$$\beta = R\sqrt{\frac{s}{c}}. \quad (26b)$$

The solution in time is evaluated by a standard numerical inversion procedure such as the Stehfest algorithm (Stehfest, 1970; Cheng et al., 1994).

Mode 3 is a deviatoric loading and the solution involves a full poroelastic coupling. The solution in Laplace transform domain is shown below:

$$\tilde{\sigma}_{rr}^{(3)} = \frac{S_o}{s}\left\{\frac{B(1+\nu_u)}{3(1-\nu_u)}C_1\left[\frac{1}{\xi}K_1(\xi) + \frac{6}{\xi^2}K_2(\xi)\right] - \frac{1}{1-\nu_u}C_2\frac{R^2}{r^2} - 3C_3\frac{R^4}{r^4}\right\}\cos 2(\theta - \theta_r) \quad (27a)$$

$$\tilde{\sigma}_{\theta\theta}^{(3)} = \frac{S_o}{s}\left\{-\frac{B(1+\nu_u)}{3(1-\nu_u)}C_1\left[\frac{1}{\xi}K_1(\xi) + \left(1 + \frac{6}{\xi^2}\right)K_2(\xi)\right] + 3C_3\frac{R^4}{r^4}\right\}\cos 2(\theta - \theta_r) \quad (27b)$$

$$\tilde{\sigma}_{r\theta}^{(3)} = \frac{S_o}{s}\left\{\frac{2B(1+\nu_u)}{3(1-\nu_u)}C_1\left[\frac{1}{\xi}K_1(\xi) + \frac{3}{\xi^2}K_2(\xi)\right] - \frac{1}{2(1-\nu_u)}C_2\frac{R^2}{r^2} - 3C_3\frac{R^4}{r^4}\right\}\sin 2(\theta - \theta_r) \quad (27c)$$

$$\tilde{p}^{(3)} = \frac{S_o}{s}\left[\frac{B^2(1-\nu)(1+\nu_u)^2}{9(1-\nu_u)(\nu_u-\nu)}C_1K_2(\xi) + \frac{B(1+\nu_u)}{3(1-\nu_u)}C_2\frac{R^2}{r^2}\right]\cos 2(\theta - \theta_r) \quad (27d)$$

in which ν_u is the undrained Poisson ratio. The other constants appearing in (27) are

$$C_1 = -\frac{12\beta(1-\nu_u)(\nu_u-\nu)}{B(1+\nu_u)(D_2-D_1)} \quad (28a)$$

$$C_2 = \frac{4(1-\nu_u)D_2}{D_2-D_1} \quad (28b)$$

$$C_3 = -\frac{\beta(D_2+D_1) + 8(\nu_u-\nu)K_2(\beta)}{\beta(D_2-D_1)} \quad (28c)$$

where

$$D_1 = 2(\nu_u-\nu)K_1(\beta) \quad (29a)$$

$$D_2 = \beta(1-\nu)K_2(\beta). \quad (29b)$$

4.2 Elastic Uni-axial Stress Problem. For the second problem, an inspection shows that the solution is uni-axial and is given by a constant vertical stress everywhere. It is otherwise stress and pore pressure free:

$$\sigma_{zz}^{(II)} = -S_z + [\nu(S_x+S_y) + \alpha(1-2\nu)p_o] \quad (30a)$$

$$\sigma_{rr}^{(II)} = \sigma_{\theta\theta}^{(II)} = \sigma_{r\theta}^{(II)} = \sigma_{rz}^{(II)} = \sigma_{\theta z}^{(II)} = p^{(II)} = 0. \quad (30b)$$

This set of stresses and pore pressure satisfies all the governing Eqs. (1)–(3), boundary conditions (11) and far-field conditions (12), hence is an admissible poroelastic solution. Physically this solution can be envisioned as the following. The field is originally under a constant uni-axial stress without pore pressure. The removal of the borehole material sets the surface tractions and pore pressure on the borehole wall free, as indicated in (12). However, these conditions are identical with the earlier state, hence no disturbance is produced. The solution is time independent and is an elastic one.

4.3 Elastic Anti-plane Shear Problem. For the third problem, we notice that the disturbance is introduced by a sudden change of shear stress σ_{rz} from the value $-S_{rz}$ to zero at the borehole wall. This antiplane shear disturbance does not create any mean normal stress, hence no pore pressure will be generated by the Skempton effect. The solution is the same as the elastic one. Following Bradley (1979), the solution for problem III can be obtained as

$$\sigma_{rz}^{(III)} = -(S_{xz}\cos\theta + S_{yz}\sin\theta)\left[1 - H(t)\frac{R^2}{r^2}\right] \quad (31a)$$

$$\sigma_{\theta z}^{(III)} = (S_{xz}\sin\theta - S_{yz}\cos\theta)\left[1 + H(t)\frac{R^2}{r^2}\right] \quad (31b)$$

$$\sigma_{rr}^{(III)} = \sigma_{\theta\theta}^{(III)} = \sigma_{zz}^{(III)} = \sigma_{r\theta}^{(III)} = p^{(III)} = 0. \quad (31c)$$

4.4 Superposition. Finally, the solution of inclined borehole problem is obtained by the superposition

$$\sigma_{rr} = \sigma_{rr}^{(I)} \quad (32a)$$

$$\sigma_{\theta\theta} = \sigma_{\theta\theta}^{(I)} \quad (32b)$$

$$\sigma_{zz} = \sigma_{zz}^{(I)} + \sigma_{zz}^{(II)} \quad (32c)$$

$$\sigma_{r\theta} = \sigma_{r\theta}^{(I)} \quad (32d)$$

$$\sigma_{rz} = \sigma_{rz}^{(III)} \quad (32e)$$

$$\sigma_{\theta z} = \sigma_{\theta z}^{(III)} \quad (32f)$$

$$p = p^{(I)} \quad (32g)$$

in which components that are identically zero are omitted.

5 Borehole Stability Analysis

In this section, a simple stability analysis is carried out to demonstrate the potential use of the above solution. To fix ideas, the following far-field stress environment is selected (Woodland, 1990):

$$S_{z'} = 25 \text{ MPa/km}, \quad S_{x'} = 29 \text{ MPa/km},$$

$$S_{y'} = 20 \text{ MPa/km}, \quad p_o = 9.8 \text{ MPa/km}$$

We notice that the industry practice of using stress and pore pressure "gradients," instead of the stresses and pore pressure, is adopted. The borehole is drilled along the direction of azimuth angle $\varphi_{z'} = 30$ deg and zenith angle $\varphi_y = 60$ deg (see Fig. 1(a)). The radius of borehole is $R = 0.1$ m. The following set of material properties for a Gulf of Mexico Shale as reported in Abousleiman et al. are used:

Downloaded 04 May 2010 to 171.66.16.34. Redistribution subject to ASME license or copyright; see http://www.asme.org/terms/Terms_Use.cfm

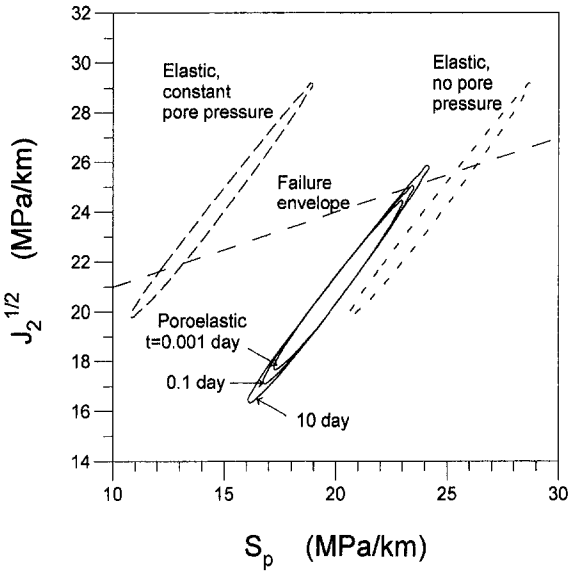


Fig. 3 Stress cloud at r/R = 1.0 and various times

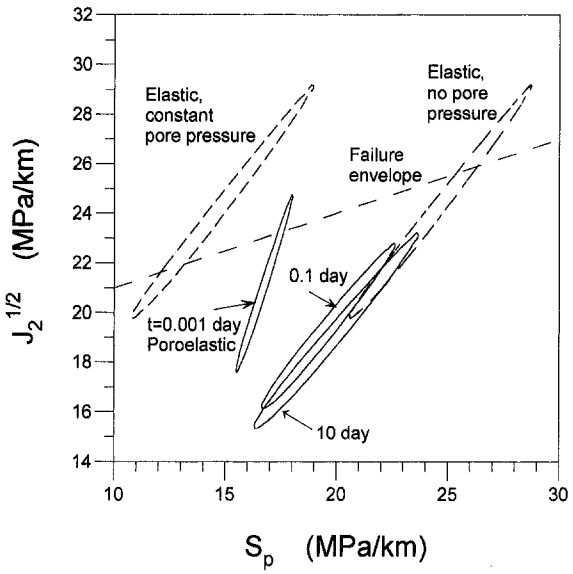


Fig. 4 Stress cloud at r/R = 1.05 and various times

$G = 7.6 \times 10^2$ MPa, $\nu = 0.219$, $\nu_u = 0.461$, $B = 0.915$, $\alpha = 0.968$, $\eta = 0.348$, $c = 1.54 \times 10^{-2}$ m^2/day.

In providing the above set, it is noted that only five poroelastic material coefficients can be independently given. All the rest must be consistently evaluated (Detournay and Cheng, 1993).

The "stress cloud" idea, as proposed by Bradley (1979) for visualization of failure potential, is used in conjunction with the Drucker-Prager criterion (Bradley, 1979; Desai and Siriwardane, 1984) for a shear failure analysis. The criterion is based on a mean shear stress $\sqrt{J_2}$ defined by

$$J_2 = \tfrac{1}{6}[(\sigma_{rr} - \sigma_{\theta\theta})^2 + (\sigma_{\theta\theta} - \sigma_{zz})^2 + (\sigma_{zz} - \sigma_{rr})^2] + \sigma_{r\theta}^2 + \sigma_{rz}^2 + \sigma_{\theta z}^2 \quad (33)$$

and an effective mean compressive stress S_p given as

$$S_p = -\frac{\sigma_{rr} + \sigma_{\theta\theta} + \sigma_{zz}}{3} - p. \quad (34)$$

In the above the definition has been modified to accommodate the Terzaghi effective stress, as it has been established that the relevant stress for shear and compressive failure of porous material is the Terzaghi effective stress.

For each set of fixed r and t value, a family of the pairs (S_p, $\sqrt{J_2}$) can be calculated for θ varying from 0 to 360 deg. Plotting these pairs in a graph of $\sqrt{J_2}$ versus S_p, a closed curve is formed, which is referred as the stress cloud. It delineates the range of stress state for potential failure. The Drucker-Prager criterion can be expressed as

$$\sqrt{J_2} = 3AS_p + D \quad (35)$$

where A and D are positive material constants (Desai and Siriwardane, 1984). It is known as the failure envelope in the $\sqrt{J_2}$ versus S_p space. For illustration, the following values are chosen as a reference:

$$A = 0.1, \quad D = 18 \text{ MPa/km}.$$

This envelope is shown in Figs. 3 to 5 as the long dashed straight line. If a stress cloud is entirely below the failure envelope, the borehole is stable. If a part of it is above the envelope, failure takes place in the corresponding region and time.

For comparison, the stress cloud based on Bradley's (1979) work is presented as the loops in short dashed lines in Figs. 3 to 5. First, if we totally ignore the existence of pore pressure, the stress cloud evaluated for $r = R$ based on the elastic solution is plotted as the dashed loop on the right. Realizing the existence of pore pressure, many earlier studies (Bradley, 1979; Aadnoy and Chenevert, 1987; Woodland, 1990) in fact have included that effect by regarding it as a constant given by the formation pressure p_o. The modified stress cloud based on the Terzaghi effective stress is shown as the left loop (dashed) in Figs. 3 to 5. We observe that the effect of pore pressure is to reduce the (effective) mean compressive stress S_p, while leaving the mean shear stress J_2 unchanged. The net result is to shift the stress cloud to the left, thus to increase the failure potential. Clearly, the use of a constant pressure is inappropriate as the pore pressure is time and space dependent. Moreover, the pore pressure near the well bore, where the failure potential is the greatest, is closer to zero than p_o. To more accurately describe the phenomenon, the poroelastic analysis is needed.

In Fig. 3, we illustrate the poroelastic stress cloud solution at the borehole wall, $r/R = 1.0$, and various times in solid lines. The curves are shifted down and to the left, as compared to the

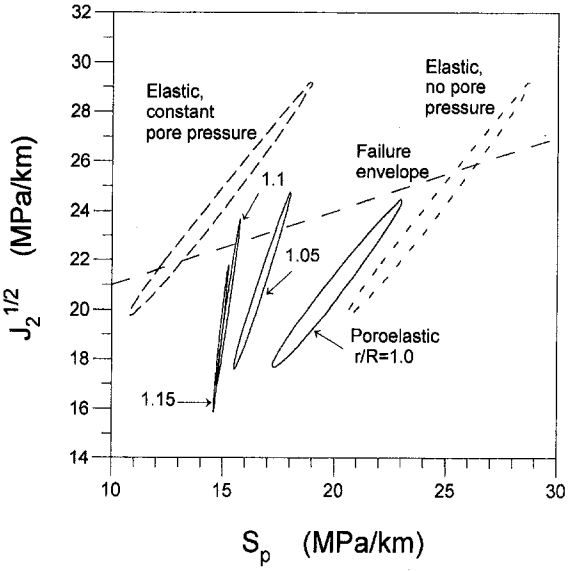


Fig. 5 Stress cloud at t = 0.001 day and various r/R

Downloaded 04 May 2010 to 171.66.16.34. Redistribution subject to ASME license or copyright; see http://www.asme.org/terms/Terms_Use.cfm

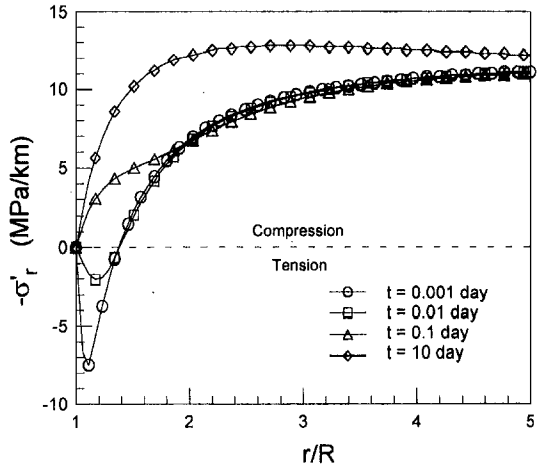


Fig. 6 Effective radial stress as a function of r/R at $\Theta = 70$ deg and various times

elastic, no pore pressure solution. We observe the expansion of the cloud with time along its long axis. At $t = 0.1$ day the borehole is at the threshold of failure. At $t = 10$ days the cloud is practically at steady state and a portion of the borehole wall has failed. This trend suggests that borehole failure potential increases with time. It is possible that a borehole does not fail at the time of excavation, but at a later time. Indeed, delayed failures have been observed in the field. This theoretical interpretation was first demonstrated by Detournay and Cheng (1988).

It is of interest to note that even at steady state, when pore pressure has vanished around the borehole, the poroelastic solution does not approach the elastic ones. This effect can be explained by the concept of an equivalent poroelastic stress ("backstress"). The draining of pore pressure in the near field while maintaining a pore pressure p_o at the far field is equivalent to the imposition of a uniform tensile stress $\sigma_{xx} + \sigma_{yy} + \sigma_{zz} = 4\eta p_o$ at the far field (Cheng, et al., 1993). At the borehole wall it brings a reduction in mean compressive stress as

$$\Delta S_p = \tfrac{4}{3}\,\eta p_o \tag{36}$$

Hence the poroelastic stress cloud at large time is shifted to the left by that amount as compared to the elastic-without-pore-pressure solution. This magnitude is nearly exactly reproduced by the $t = 10$ days stress cloud in Fig. 3. We note that (36) can also be formally obtained from the solution presented in the preceding sections by taking the limit $t \to \infty$. The same poroelastic effect exists for the mean shear stress which shifts the poroelastic cloud down. However, a simple formula for the difference as (36) cannot be worked out. From the relative positions of the clouds, it is obvious that the elastic solutions, with or without the consideration of pore pressure, overestimate the failure potential. Hence a careful borehole design by poroelastic theory allows a wider range of operation condition.

Next, we turn our attention to the failure potential at a small distance inside the wall, rather than at the wall. Figure 4 presents a result similar to Fig. 3, but at the distance $r/R = 1.05$. The transient location of the cloud is more complex than the earlier case. The trend is in fact the opposite of that shown in Fig. 3: The formation is more susceptible to failure at small times. In particular, we notice that failure will be initiated at a small time ($t = 0.001$ day) at $r/R = 1.05$. By this analysis, it is important to recognize that for the elasticity solution, the location of the highest failure potential is always located at the wall, $r/R = 1$. This is not the case for poroelasticity.

To further expound this phenomenon, Fig. 5 shows the stress clouds at different radial distances from the wall at $t = 0.001$ day. It is observed that the stress state is more critical at $r/R = 1.05$ and 1.1 than at the wall. However, away from a thin layer near the wall, the failure potential decreases, as shown by the loop marked by $r/R = 1.15$. It is reiterated that this critical state exists only at small time, as established in Fig. 4.

Another interesting phenomenon to examine is the borehole tensile failure. It has been reported (Paterson, 1986) that the sudden venting of an over-pressurized borehole can cause tensile failure known as "outburst." This tensile regime, which exists only at very small time, can be observed from the present solution. Figure 6 shows the effective radial stresses $\sigma'_{rr} = \sigma_{rr} + p$ as a function of r/R at $\theta = 70$ deg and various times. We note that it is presented in compression $-\sigma_{rr}$, hence a negative value in the figure corresponds to tension. It is clearly observed that at small times there exists a tensile region near the borehole wall. The region disappears as time increases. In Fig. 7 this region is visualized in a different way. The compressive effective radial stress is shown for the whole range of borehole azimuthal angle at $t = 0.001$ day and various r/R values. Again, the negative values marks region under tension. Since the tensile strength of all rock is typically weak, any development of tension implies failure.

6 Conclusion

By a heuristic decomposition technique, the analytical solution of an infinitely long borehole instantly drilled in a poroelastic medium is presented. The orientation of the borehole can be parallel or inclined to the principal directions of the in situ stresses. The poroelastic effects are examined using the stress cloud technique. The mathematical expressions are relatively simple and easy to evaluate. The solution can be a powerful design tool for the industry.

Acknowledgment

The work is supported by the Rock Mechanics Research Center at the University of Oklahoma, and the Oklahoma Center for Advancement of Science and Technology. The work has benefited from a discussion with Dr. J.-C. Roegiers in the early stages. His contribution is appreciated.

References

Aadnoy, B. S., and Chenevert, M. E., 1987, "Stability of Highly Inclined Boreholes," *SPE Drill. Eng.*, Vol. 2, pp. 364–374.

Abousleiman, Y., Cheng, A. H-D., Jiang, C., and Roegiers, J.-C., 1996, "Poro-viscoelastic Analysis of Borehole and Cylinder Problems," *ACTA Mechanica*, Vol. 109, pp. 199–219.

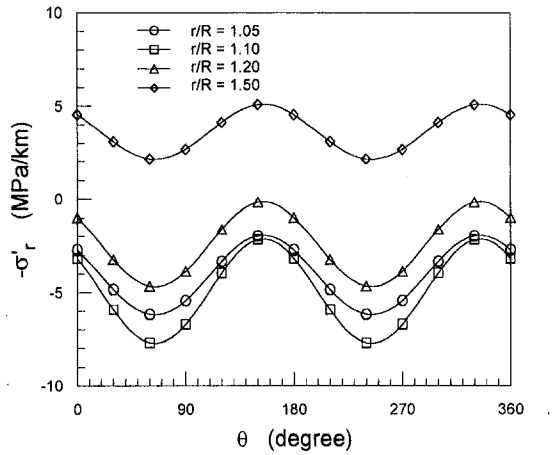


Fig. 7 Effective radial stress as a function of Θ at $t = 0.001$ day and various r/R values

Downloaded 04 May 2010 to 171.66.16.34. Redistribution subject to ASME license or copyright; see http://www.asme.org/terms/Terms_Use.cfm

Biot, M. A., 1941, "General Theory of Three-Dimensional Consolidation," *J. Appl. Phys.,* Vol. 12, pp. 155–164.

Bradley, W. B., 1979, "Failure of Inclined Boreholes," ASME *Journal of Energy Resources Technology,* Vol. 101, pp. 232–239.

Carslaw, H. S., and Jaeger, J. C., 1959, *Conduction of Heat in Solids,* 2nd ed., Oxford Univ. Press (Clarendon), London.

Cheng, A. H-D., Abousleiman, Y., and Roegiers, J.-C., 1993, "Review of Some Poroelastic Effects in Rock Mechanics," *Int. J. Rock Mech. Min. Sci. & Geomech. Abstr.,* Vol. 30, pp. 1119–1126.

Cheng, A. H-D., Sidauruk, P., and Abousleiman, Y., 1994, "Approximate Inversion of the Laplace Transform," *Mathematica J.,* Vol. 4, pp. 76–82.

Desai, C. S., and Siriwardane, H. J., 1984, *Constitutive Laws for Engineering Materials, with Emphasis on Geologic Materials,* Prentice-Hall, Englewood Cliffs, NJ.

Detournay, E., and Cheng, A. H-D., 1988, "Poroelastic Response of a Borehole in a Non-Hydrostatic Stress Field," *Int. J. Rock Mech. Min. Sci. Geomech. Abstr.,* Vol. 25, pp. 171–182.

Detournay, E., and Cheng, A. H-D., 1993, "Fundamentals of Poroelasticity," *Comprehensive Rock Engineering: Principles, Practice & Projects, Vol. 2, Analysis and Design Method,* C. Fairhurst, ed., Pergamon Press, pp. 113–171.

Fjær, E., Holt, R. M., Horsrud, P., Raaen, A. M., and Risnes, R., 1992, *Petroleum Related Rock Mechanics,* Elsevier, New York.

Haimson, B., and Fairhurst, C., 1969, "Hydraulic Fracturing in Porous-Permeable Materials," *Soc. Pet. Eng. J.,* pp. 811–817.

Hubbert, M. K., and Willis, D. G., 1957, "Mechanics of Hydraulic Fracturing," *Petroleum Trans., AIME.,* Vol. 210, pp. 153–168.

Ong, S. H., and Roegiers, J.-C., 1993, "Influence of Anisotropies in Borehole Stability," *Int. J. Rock. Mech. Min. Sci. Geomech. Abstr.,* Vol. 30, pp. 1069–1075.

Paterson, L., 1986, "A Model for Outbursts in Coal," *Int. J. Rock Mech. Min. Sci. Geomech. Abstr.,* Vol. 23, pp. 327–332.

Rice, J. R., and Cleary, M. P., 1976, "Some Basic Stress-Diffusion Solutions for Fluid Saturated Elastic Porous Media with Compressible Constituents," *Rev. Geophys. Space Phys.,* Vol. 14, pp. 227–241.

Skempton, A. W., 1954, "The Pore Pressure Coefficients A and B," *Géotechnique,* Vol. 4, pp. 143–147.

Stehfest, H., 1970, "Numerical Inversion of Laplace Transforms," *Comm. ACM.,* Vol. 13, pp. 47–49, 624.

Woodland, D. C., 1990, "Borehole Instability in the Western Canadian Overthrust Belt," *SPE Drill. Eng.,* Vol. 5, pp. 27–33.

Downloaded 04 May 2010 to 171.66.16.34. Redistribution subject to ASME license or copyright; see http://www.asme.org/terms/Terms_Use.cfm

Nonlinear Elasticity of Granular Media

A. N. Norris
Department of Mechanical and Aerospace Engineering, Rutgers University, Piscataway, NJ 08855-0909

D. L. Johnson
Schlumberger-Doll Research, Old Quarry Road, Ridgefield, CT 06877-4108

The finite and incremental elasticity of a random packing of identical spheres is derived using energy methods. We consider different models for the contact forces between spheres, all of which are based upon or related to the fundamental Hertz theory; we consider only the special cases of perfect friction (no tangential slip) or no tangential friction. The existence of a strain energy function for the medium depends critically upon the type of contact. If the tangential contact stiffness is independent of the normal force, then the energy is well defined for all values of the macroscopic strain. Otherwise, the strain energy of the system is path dependent, in general. However, the concept of a quadratic strain energy function is always well defined for incremental motion superimposed on large confining stress and strain. For all models considered, we derive the changes in wave speeds due to incremental strains. For the models based upon an energy function we derive expressions for the third-order elastic constants as a function of confining pressure.

1 Introduction

Consider a random packing of identical elastic spheres, which is a simple model for a granular medium. There are three basic problems of interest. First, we would like to know the dependence of the macroscopic stress, σ_{ij}, on the macroscopic strain, $\sigma_{ij} = \sigma_{ij}(e_{mn})$. We would also like the inverse relationship, $e_{ij} = e_{ij}(\sigma_{mn})$. This is linked with the issue of finding the finite forces between the particles. The second task is to calculate the incremental moduli for small motion superimposed upon the initial deformation. Finally, we would like to know how the associated speeds of small amplitude waves change upon the application of small additional stresses (Schwartz et al., 1994). The concept of strain energy density for a hyperelastic material allows one, in principle, to calculate all of these quantities. Thus, the large stress/strain behavior is governed by the finite elastic response. Incremental motion is then governed by the second-order elasticity theory, or the elastic stiffnesses C_{ijkl} at the prevailing finite strain e_{ij}. Finally, the linear variations in wave speeds for subsequent static deformation, Δe_{ij}, are linearly dependent on the third-order elasticities, C_{ijklmn} (Toupin and Bernstein, 1961).

However, the existence of a strain energy function is not always guaranteed nor even necessary for an elastic medium. Following Truesdell and Noll (1965) we use the term *hyperelastic* to refer to a medium for which there is a unique strain energy which is a function only of the current value of the strain tensor. We consider a medium to be *elastic* if there is a strain energy, which may be path dependent but which is not hysteretic along that path. In this paper we explore the concept of a strain energy function for the granular medium, both for finite deformation and for incremental motion. The key to the problem lies in the mechanics of a typical representative contact. Consider the following thought experiment: two solid spheres touch at a point but are otherwise separated. A normal force is applied, resulting in a finite contact zone, and a simultaneous approach of the two spheres. Then a shear is applied to the pair of contacting spheres, causing little or no further approach of their centers, but giving a lateral shift of the centers. Now consider the same initial configuration, subject to the same displacements, but in the reverse order. The energy expended in the two experiments may or may not be the same, even though the solid material is considered to be perfectly elastic (local deformations are reversible). The crux of the matter lies in the kinematic differences caused by the contact of the spheres. Thus, the energies are equal if there is no frictional resistance to the shear load. However, when the contact zone is rough, it induces a resistance to shearing, and the second experiment requires less energy than the first. This type of micromechanical picture must have an impact on the microscopic energy of an assemblage of spheres. In particular, it should be clear that frictional contacts will result in a macroscopic strain energy which depends upon the loading path, and is therefore not hyperelastic. The simple ideas exhibited in the two-grain experiment will be expanded upon in this paper, and the consequences discussed. Path-dependent effects are well known in granular media. For example, Deresiewicz (1958a, b) has discussed the effect in the context of simple cubic arrays of particles.

In Section 2 we review some general properties of the various contact forces which we use in Section 3 to derive expressions for the deformation energy of a single contact and, from that, the deformation energy of the ensemble of spheres. In this article we consider only the special cases of perfect friction (no tangential slip) or no tangential friction (perfect slip), although we briefly touch upon finite friction in the Appendix. For those models of contact forces which are derivable from a potential energy function, we are able to obtain explicit expressions for the stress, the second-order elastic constants, and the third-order elastic constants as a function of macroscopic strain. We restrict our consideration to those systems for which the change in stiffness is a much larger effect than the change in dimension, which is to say, systems for which the third-order constants are much larger than the second. This is a characteristic feature of weakly consolidated granular media, and is discussed further at the end of Section 3. For the contact forces which are not derivable from a potential energy function, we show, in Section 4, that the second-order elastic constants are still well defined, but not the third (or higher) order. Strictly speaking, for these elastic but not hyperelastic systems, one can still define third-order elastic constants simply as the second derivative of stress with respect to strain taken along a given path, and this, in effect, is what we do in Eq. (67). We derive the changes in wave speeds due to an incremental strain in Section 5 and we show an explicit

Contributed by the Applied Mechanics Division of THE AMERICAN SOCIETY OF MECHANICAL ENGINEERS for publication in the ASME JOURNAL OF APPLIED MECHANICS.

Discussion on this paper should be addressed to the Technical Editor, Professor Lewis T. Wheeler, Department of Mechancial Engineering, University of Houston, Houston, TX 77204-4792, and will be accepted until four months after final publication of the paper itself in the ASME JOURNAL OF APPLIED MECHANICS.

Manuscript received by the ASME Applied Mechanics Division, Feb. 24, 1995; final revision, May 28, 1996. Associate Technical Editor: J. T. Jenkins.

Copyright © 1997 by ASME

Downloaded 04 May 2010 to 171.66.16.34. Redistribution subject to ASME license or copyright; see http://www.asme.org/terms/Terms_Use.cfm

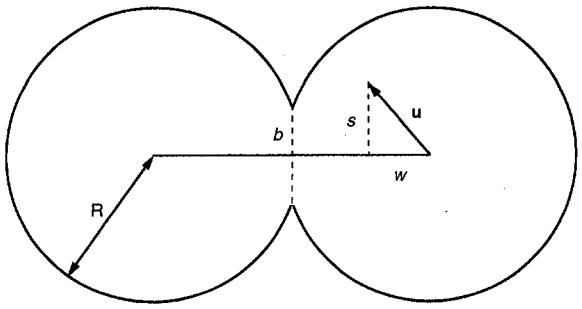


Fig. 1 Schematic of two spheres, each of radius R, in contact with each other. The radius of the initial unstressed circle of contact, b, may or may not be zero, depending on the model being considered. The center of one sphere is displaced relative to the other by a vector u which is resolved into the component along the line of centers, $2w$, and that perpendicular to it, $2s$. This deformation gives rise to a restoring force F (not shown) with component N along the line of centers, and T perpendicular to it.

example of hydrostatic confining pressure in Section 6. We present some numerical examples compared against experimental data in Section 7. Our concluding remarks appear in Section 8.

2 The Contact Forces

2.1 Contact Models. Consider two identical spheres each of radius R pressed together. The force between the spheres acts over a contact zone the radius of which is small compared with R. Let $2w(\geq 0)$ be the relative approach of the two spheres along the line joining their centers. The relative tangential displacement between the two spheres is $2\mathbf{s}$. See Figure 1. Similarly, the force may be decomposed into a normal force N and tangential force $\mathbf{T}$. We are interested in the finite and infinitesimal elasticity of an ensemble of spheres, for which the single pair in contact under normal and tangential loads describes the fundamental mechanics.

Our starting point is the incremental relations between the forces and the displacements,

$$\Delta N = D_n(w)\Delta w, \quad \Delta \mathbf{T} = D_t(w)\Delta \mathbf{s}, \tag{1}$$

where D_n and D_t are contact stiffnesses, in the notation of Digby (1981) and Winkler (1983). These are of the form

$$D_n = C_n a_n(w), \quad D_t = C_t a_t(w), \tag{2}$$

where C_n and C_t are actual stiffnesses (with units of pressure)

$$C_n = \frac{4\mu}{1-\nu} = \frac{8\mu(\lambda+\mu)}{\lambda+2\mu},$$

$$C_t = \frac{8\mu}{2-\nu} = \frac{16\mu(\lambda+\mu)}{3\lambda+4\mu}, \tag{3}$$

λ, μ are the Lamé constants of the spheres and the Poisson's ratio is ν. The lengths a_n and a_t depend upon the specific type of contact but do *not* depend upon the material properties of the spheres. Several models are discussed in the Appendix, and the functional forms for a_n and a_t are summarized in Table 1. All models considered in the present article either have smooth contacts with reversible slip or rough contacts with no relative slip. Both lengths are defined by the current value of w, but are independent of $\mathbf{s}$. Note also that the properties of each contact, though calculated within the approximations of ordinary linear elasticity theory, lead to nonlinear restoring forces. As we shall see, these nonlinear forces can, in turn, lead to extremely large nonlinear elastic constants for the aggregate media.

All the models in Table 1 have $a_t \leq a_n$, with equality for the infinitely rough contacts in models Ib, IIb, and IIIb. When $a_t = a_n$ the ratio D_n/D_t reduces to $C_n/C_t = 1 + \nu/(2-2\nu)$, which is approximately 1.17 for rocks ($\nu = 1/4$). This value is not consistent with the velocity data of Domenico (1977) on unconsolidated glass beads under pressure. Winkler (1983) demonstrated that Domenico's data yields a value for the ratio D_n/D_t ranging from 1.79 to 3.36, which is consistent with a contact model with $a_t < a_n$. This is one possible justification for a contact model that allows for frictionless sliding in tangential deformation, as in the Digby model IIa for which $a_t = 0$.

2.2 Path Dependence. The incremental rule for $\Delta\mathbf{T}$ in (1) does not hold for all deformation paths in the $w - \mathbf{s}$ space when the contact is not perfectly smooth. Generally, the increment in $\Delta\mathbf{T}$ depends upon whether w is increasing or decreasing, with different rules applicable in each case. However, it can be demonstrated (Johnson and Norris, 1995) that the distinction disappears for the models of Table 1 if the trajectory is self-repeating—that is, it retraces itself whenever w is decreasing. Therefore, to be specific, in this paper we only consider paths which are self-repeating in this sense.

Thus, $\mathbf{T}$ does not possess a unique functional form for models Ib, IIb, IIIb, and IV. Rather, it depends upon the path history of the loading, and is only defined along a given path in the $w - \mathbf{s}$ space. We distinguish the "path-dependent" models, Ib, IIb, IIIb, and IV, from the remaining models for which $\mathbf{T}$ is uniquely defined at all values of w and $\mathbf{s}$, i.e., it is a function of these parameters. The path dependence vanishes only for constant tangential stiffness. In order to integrate the force-displacement equations for a single contact with path dependence it is necessary to assume some relationship between w and $\mathbf{s} = \mathbf{s}(w)$. We can then rewrite the incremental force relations (1) as

$$dN = C_n a_n(w)dw, \quad d\mathbf{T} = C_t a_t(w)d\mathbf{s}. \tag{4}$$

The contact forces can be determined by integrating these three equations subject to the initial conditions $N = \mathbf{T} = 0$ at $w = 0$, yielding

$$N = C_n A_n(w), \quad \mathbf{T} = C_t \int_{\text{path}} a_t(\xi)d\mathbf{s} \tag{5}$$

where A_n is a path-independent quantity having the dimension of area:

$$A_n(w) = \int_0^w a_n(\xi)d\xi. \tag{6}$$

The precise form of $\mathbf{T}$ therefore depends upon the path $\mathbf{s}(w)$. For example, consider a linear relationship,

$$\frac{d\mathbf{s}}{dw} = \text{constant}, \tag{7}$$

and the constant can vary from contact to contact. Equations (5) become

$$N = C_n A_n(w), \quad \mathbf{T} = C_t a_t^{(1)}(w)\mathbf{s}, \tag{8}$$

where $a_t^{(1)}$ also has the dimension of a length

$$a_t^{(1)}(w) = \frac{1}{w}\int_0^w a_t(\xi)d\xi. \tag{9}$$

We emphasize that w and $\mathbf{s}$ are *not* independent variables in Eq. (8). The constraint (7) implies that the spheres approach one another along a constantly directed line.

Alternatively, one could assume that the line of action of the force at each contact remains constant. That is,

$$\frac{d\mathbf{T}}{dN} = \text{constant}, \tag{10}$$

and the constant can differ from contact to contact. The two constraints (7) and (10) are equivalent only if the ratio D_t/D_n is constant along the loading path. This is the case for the path-dependent models Ib, IIb, and IIIb, but not for IV. We will use

Downloaded 04 May 2010 to 171.66.16.34. Redistribution subject to ASME license or copyright; see http://www.asme.org/terms/Terms_Use.cfm

Table 1 The lengths a_n and a_t for different contact conditions. Models I, II, and III have two subcases, corresponding to (a) smooth contact with reversible slip; and (b) rough contact with no subsequent slip. See the Appendix for further details and definitions.

Contact model	Description	$a_n(w)$	$a_t(w)$ (a)	$a_t(w)$ (b)
I	Hertzian contact	$(Rw)^{\frac{1}{2}}$	0	a_n
II	initial contact radius b (Digby)	$[R^2w^2+\frac{b^4}{4})^{\frac{1}{2}}+\frac{b^2}{2}]^{\frac{1}{2}}$	b	a_n
III	ogival/spherical contact $d = R\alpha\frac{\pi}{2}$ (Spence/Goddard)	$(Rw+d^2)^{\frac{1}{2}}-d$	0	a_n
IV	frictional sliding (special loading) (Mindlin and Deresiewicz)	$(Rw)^{\frac{1}{2}}$	$(\frac{\theta}{a_n}+\frac{1-\theta}{c})^{-1}$	

(7) later for specific examples, but emphasize that the subsequent analysis applies to arbitrary self-repeating paths $\mathbf{s} = \mathbf{s}(w)$.

The path-independent smooth models (Ia, IIa, and IIIa), do not require an assumption of the form $\mathbf{s} = \mathbf{s}(w)$, and can be integrated directly to give forces with the same functional form as in Eq. (8). Furthermore,

$$a_t^{(1)} = a_t = \begin{cases} 0 \text{ for Ia and IIIa,} \\ b \text{ for IIa.} \end{cases} \tag{11}$$

3 Finite Energy, Strain and Stress

3.1 A Single Contact. Let $\mathbf{F}$ be the total force exerted by a sphere at a single contact, and let $\mathbf{u}$ be the total displacement of the center of the sphere from its original position. The sphere then moves a further distance $d\mathbf{u}$. The work done by the sphere associated with that contact, assuming it does not rotate, is

$$dW = \mathbf{F}\cdot d\mathbf{u} = Ndw + \mathbf{T}\cdot d\mathbf{s}. \tag{12}$$

Alternatively, the potential energy for a single contact is $2dW$, when viewed in terms of the two spheres each contributing dW. We speak of a "potential energy" function for the path-dependent models with the understanding that we are restricting our discussion to motion on one specific path. The work done along that path is a conserved quantity; going down the path is the reverse of going up.

For either the path-independent models, or assuming (7) for the path-dependent ones, the explicit nature of N and T in (8) and (12) implies that

$$W = C_nV_n(w) + \tfrac{1}{2}C_ta_t^{(2)}(w)s^2, \tag{13}$$

where V_n is a volume and $a_t^{(2)}$ a length,

$$V_n(w) = \int_0^w d\zeta \int_0^\zeta a_n(\xi)d\xi,$$

$$a_t^{(2)}(w) = \frac{2}{w^2}\int_0^w d\zeta \int_0^\zeta a_t(\xi)d\xi. \tag{14}$$

We have set $W = 0$ at the initial point, with no loss in generality. Thus, W is one half of the energy stored in a single contact. The result (13) is valid for all contact models, with the understanding that w and $s = |\mathbf{s}|$ are related for the path-dependent models. For the others, we have the simplification that

$$a_t^{(2)} = a_t = \begin{cases} 0 & \text{for Ia and IIIa,} \\ b & \text{for IIa.} \end{cases} \tag{15}$$

The length a_n, area A_n, and volume V_n are fundamental quantities, as is the dimensionless quantity $a_n'(w)$ which occurs later. Explicit formulae for $a_n'(w)$, A_n, and V_n are given in Table 2 for models I, II and III, (a) or (b).

3.2 The Ensemble of Spheres. We now turn to the random packing of spheres, and make the standard kinematic assumption relating the displacement of sphere m to the macroscopic deformation gradient f_{ij} (Digby, 1981; Walton, 1987; Jenkins, 1991). The displacement of the center of a given sphere is

$$u_i = f_{ij}X_j, \quad \text{or} \quad \mathbf{u} = \mathbf{f}\cdot\mathbf{X}, \tag{16}$$

where $\mathbf{X}$ is the position of the center of the sphere. Let $\hat{\mathbf{n}}$ be the unit vector joining the centers of two contacting spheres, at $\mathbf{X}$ and $\mathbf{X} + 2R\hat{\mathbf{n}}$. The associated displacements are $\mathbf{f}\cdot\mathbf{X}$ and $\mathbf{f}\cdot\mathbf{X} + 2R\,\mathbf{f}\cdot\hat{\mathbf{n}}$, and so the components of the relative displacement are

$$w = -\hat{\mathbf{n}}\cdot\mathbf{f}\cdot\hat{\mathbf{n}}R, \quad \mathbf{s} = \mathbf{P}\cdot\mathbf{f}\cdot\hat{\mathbf{n}}R, \tag{17}$$

where $\hat{\mathbf{n}}\cdot\mathbf{f}\cdot\hat{\mathbf{n}} = n_if_{ij}n_j$, and $\mathbf{P}$ projects onto the tangent plane,

$$P_{ij} \equiv \delta_{ij} - n_in_j. \tag{18}$$

The total strain energy density per unit volume is

$$U = \frac{1}{V}\sum_{\text{contacts}} W = \frac{1}{V}\sum_{\text{contacts}}\int \mathbf{F}\cdot d\mathbf{u}, \tag{19}$$

where the sum is over all contacts on each sphere (each contact is counted twice since W is only half the contact energy), and V is the total volume of the sample. The effective medium approximation we employ for this article is that statistically all grains are "the same" and each may be replaced by its ensemble average: $\Sigma_{\text{contacts}}W(w_i, s_i) \approx Nn\langle W[w(\hat{\mathbf{n}}), s(\hat{\mathbf{n}})]\rangle$ where N is the number of grains in the volume V, n is the number of

Table 2 The quantities a_n', A_n, and V_n for the three contact models I, II, and III; see Table 1.

Model	$a_n'(w)$	$A_n(w)$	$V_n(w)$
I	$\frac{R}{2a_n} = \frac{1}{2}R^{1/2}w^{-1/2}$	$\frac{2}{3}wa_n = \frac{2}{3}R^{1/2}w^{3/2}$	$\frac{4}{15}w^2a_n = \frac{4}{15}R^{1/2}w^{5/2}$
II	$\frac{R(a_n^2-b^2)^{1/2}}{2a_n^2-b^2}$	$\frac{2}{3}w\left(a_n+\frac{b^2}{2a_n}\right)$	$\frac{4}{15}w^2\left(a_n+\frac{b^2}{a_n}\right) - \frac{(a_n-b)b^4}{15R^2}$
III	$\frac{R}{2(a_n+d)}$	$\frac{2}{3}a_nw - \frac{a_n^2d}{3R}$	$\frac{2}{5}\frac{A_n}{R}(a_n+d)^2 - \frac{w^2d}{10}$

Downloaded 04 May 2010 to 171.66.16.34. Redistribution subject to ASME license or copyright; see http://www.asme.org/terms/Terms_Use.cfm

contacts per grain, and $\langle \ldots \rangle$ denotes average over the distribution of directions $\hat{\mathbf{n}}$. Therefore,

$$U = \frac{n(1-\phi)}{V_0} \langle W[w(\hat{\mathbf{n}}), s(\hat{\mathbf{n}})] \rangle$$
$$= \frac{n(1-\phi)}{V_0} \left\langle \int \mathbf{F} \cdot d\mathbf{u} \right\rangle, \quad (20)$$

where ϕ is the porosity of the sample and V_0 is the volume of a single grain. In this article we explore the consequences of assuming an isotropic distribution $P(\hat{\mathbf{n}}) = 1/4\pi$ although there is some evidence that this is not necessarily the case (Jenkins et al., 1989).

Before we compute U we must address the issue of whether or not each sphere rotates under the action of the applied strain (Schwartz et al., 1984). If the neighbors of a given sphere rotate, then there will be an energy cost unless that sphere rotates, too. We now show that, within the context of our effective medium approach, each sphere will not rotate if the deformation gradient is symmetric $f_{ij} = f_{ji}$. First, let us consider a rigid rotation of the system about an axis $\hat{\boldsymbol{\theta}}$ by an amount θ. In terms of the rotation matrix $\mathbf{R}$ each coordinate moves to a new position $\mathbf{r}' = \mathbf{R} \cdot \mathbf{r}$ and the displacement is $\mathbf{u} = \mathbf{r}' - \mathbf{r}$. It is straightforward to show that

$$\nabla \times \mathbf{u} = 2 \sin \theta \hat{\boldsymbol{\theta}}. \quad (21)$$

Such a rigid-body rotation is an example of Eq. (16) which gives

$$\nabla \times \mathbf{u} = (f_{32} - f_{23}, f_{13} - f_{31}, f_{21} - f_{12}). \quad (22)$$

Therefore it is clear that if the macroscopic deformation gradient is symmetric, there is no macroscopic rigid-body rotation. Under such a deformation we may assume that each sphere *does not* rotate so as to match the positions of its neighbors. The deformation gradient is then equal to the strain tensor. In order to make explicit this assumption we rewrite (17) as

$$w = -\hat{\mathbf{n}} \cdot \mathbf{e} \cdot \hat{\mathbf{n}} R, \quad \mathbf{s} = \mathbf{Pe}\hat{\mathbf{n}} R, \quad (23)$$

where $\mathbf{e}$ is the symmetric part of the macroscopic strain,

$$\mathbf{e} \equiv \tfrac{1}{2}(\mathbf{f} + \mathbf{f}^T), \quad (24)$$

and we shall write $\mathbf{Pe}\hat{\mathbf{n}}$ as a shorthand for the vector $\mathbf{P} \cdot \mathbf{e} \cdot \hat{\mathbf{n}}$ (w is unaffected). In summary, within the mean field approximation adopted here only the symmetric part of the macroscopic deformation gradient influences the internal strain energy and so we need consider only symmetric deformations.

We are now ready to calculate the deformation energy from Eq. (20). We assume there are N spheres with an average of n contacts per sphere. First, consider the case where each contact follows the linear path defined by Eq. (7), so that

$$\mathbf{F} = -C_n A_n(-\hat{\mathbf{n}} \cdot \mathbf{e} \cdot \hat{\mathbf{n}} R)\hat{\mathbf{n}} + C_t a_t^{(1)}(-\hat{\mathbf{n}} \cdot \mathbf{e} \cdot \hat{\mathbf{n}} R) R \mathbf{Pe}\hat{\mathbf{n}},$$
$$d\mathbf{u} = R(d\mathbf{e}) \cdot \hat{\mathbf{n}}. \quad (25)$$

The energy can now be obtained by substitution into Eq. (20) followed by integration, yielding

$$U = (1-\phi)\frac{n}{V_0}\{C_n \langle V_n(-\hat{\mathbf{n}} \cdot \mathbf{e} \cdot \hat{\mathbf{n}} R)\rangle$$
$$+ \tfrac{1}{2} C_t R^2 \langle a_t^{(2)}(-\hat{\mathbf{n}} \cdot \mathbf{e} \cdot \hat{\mathbf{n}} R)|\mathbf{Pe}\hat{\mathbf{n}}|^2 \rangle\}, \quad (26)$$

where $\langle \cdot \rangle$ denotes the average over all directions $\hat{\mathbf{n}}$, V_0 is the volume of a single sphere, and ϕ is the porosity of the sample,

$$V_0 = \tfrac{4}{3}\pi R^3, \quad 1 - \phi = \frac{NV_0}{V}. \quad (27)$$

Strictly speaking, Eqs. (27) do not apply to the Digby model II because of the missing spherical caps, nor to the Spence/Goddard model III because the ogive volume is not the same as the sphere's. We note that the same formula for U in (26) may also be obtained more directly using Eqs. (13) and (23).

We may generalize (25) and (26) to the case of an arbitrary path in $w - \mathbf{s}$ space. Let the path be parameterized by $w = \xi$, $\mathbf{s} = \mathbf{s}(\xi)$. The path may differ from contact to contact and is subject only to the constraints that it is self-repeating and the end points are given by Eq. (23). Then, using Eq. (5),

$$\mathbf{F} = -C_n A_n(-\hat{\mathbf{n}} \cdot \mathbf{e} \cdot \hat{\mathbf{n}} R)\hat{\mathbf{n}} + C_t \int_{\text{path}} a_t(\xi) d\mathbf{s}(\xi),$$
$$d\mathbf{u} = R(d\mathbf{e}) \cdot \hat{\mathbf{n}}, \quad (28)$$

and the energy U follows accordingly. In summary, the energy U is defined for arbitrary strain $\mathbf{e}$ for the models with constant tangential stiffness. However, for the path-dependent models U is acquired under the specific loading path chosen.

3.3 Elasticity for the Energy Models. The energy can also be defined by

$$U = \int_0^{\mathbf{e}} \sigma_{ij} de_{ij}, \quad (29)$$

where $\sigma_{ij} = \sigma_{ij}(\mathbf{e})$ is the effective stress, which can be calculated separately by considering an average stress over many spheres. This is the approach taken by Walton (see Eq. (3.15) of Walton, 1987). We note at this stage that σ_{ij} cannot be obtained by simply differentiating U with respect to $\mathbf{e}$, because the energy is path specific in general. However, it is important to note that

$$\sigma_{ij} = \frac{\partial U}{\partial e_{ij}} \text{ for models Ia, IIa, and IIIa,} \quad (30)$$

and hence the strain energy function $U(\mathbf{e})$ of (26) is all that is required in order to determine the macroscopic stress for these models. Thus, from Eqs. (15), (26), and (30),

$$\sigma_{ij} = (1-\phi)\frac{nR}{V_0}\{C_t a_t R \langle \tfrac{1}{2}(n_i P_{jk} + n_j P_{ik}) e_{kl} n_l \rangle$$
$$- C_n \langle A_n(-\hat{\mathbf{n}} \cdot \mathbf{e} \cdot \hat{\mathbf{n}} R) n_i n_j \rangle\}. \quad (31)$$

This gives the finite stress at any strain $\mathbf{e}$ for models Ia, IIa, and IIIa.

If a further small strain, $\boldsymbol{\epsilon}_{ij}$, is superimposed upon $\mathbf{e}$ then the resulting stress can be found by simply substituting $e_{ij} + \epsilon_{ij}$ for e_{ij} in (31). Let the total stress be $\sigma_{ij} + \tau_{ij}$, then τ_{ij} is a nonlinear function of $\boldsymbol{\epsilon}_{ij}$, which can be expanded in a Taylor series about $\boldsymbol{\epsilon}_{ij} = 0$. The linear coefficients are, by definition, the coefficients of linear elasticity at the finite strain $\mathbf{e}$. These can be obtained directly by inspection from the strain energy expansion. Thus,

$$U(\mathbf{e} + \boldsymbol{\epsilon}) = U(\mathbf{e}) + \sigma_{ij}\epsilon_{ij} + \tfrac{1}{2} C^*_{ijkl}\epsilon_{ij}\epsilon_{kl}$$
$$+ \tfrac{1}{6} C^*_{ijklmn}\epsilon_{ij}\epsilon_{kl}\epsilon_{mn} + \ldots, \quad (32)$$

where C^*_{ijkl} and C^*_{ijklmn} are the second and third order elastic moduli, respectively. They satisfy the usual symmetries associated with a material possessing a strain energy:

$$C^*_{ijkl} = C^*_{jikl}, \quad C^*_{ijkl} = C^*_{klij}, \quad (33)$$

$$C^*_{ijklmn} = C^*_{jiklmn}, \quad C^*_{ijklmn} = C^*_{klijmn} = C^*_{mnklij}. \quad (34)$$

The first identity is a statement of the symmetry of the stress.

Explicit expansion of the strain energy, using Eqs. (15), (26), (30), and (32) yields

$$C^*_{ijkl} = (1-\phi)\frac{nR^2}{V_0}\{\langle [C_n a_n(-\hat{\mathbf{n}} \cdot \mathbf{e} \cdot \hat{\mathbf{n}} R) - C_t a_t] n_i n_j n_k n_l \rangle$$
$$+ C_t a_t \langle Q_{ijkl}(\hat{\mathbf{n}}) \rangle\}, \quad (35)$$

Downloaded 04 May 2010 to 171.66.16.34. Redistribution subject to ASME license or copyright; see http://www.asme.org/terms/Terms_Use.cfm

where

$$Q_{ijkl}(\hat{\mathbf{n}}) \equiv \tfrac{1}{4}(\delta_{ik}n_jn_l + \delta_{il}n_jn_k + \delta_{jl}n_in_k + \delta_{jk}n_in_l). \quad (36)$$

Note that the part of the moduli C^*_{ijkl} attributable to the constant tangential stiffness $D_t = C_t a_t$ is isotropic, i.e.,

$$C^*_{ijkl} = (1 - \phi)\frac{nR^2}{V_0}\left\{C_n\langle a_n(-\hat{\mathbf{n}}\cdot\mathbf{e}\cdot\hat{\mathbf{n}}R)n_in_jn_kn_l\rangle + \frac{C_ta_t}{15}(3I_{ijkl} - \delta_{ij}\delta_{kl})\right\}, \quad (37)$$

where $I_{ijkl} = (\delta_{ik}\delta_{jl} + \delta_{il}\delta_{jk})/2$ is the identity tensor. Similarly, the third-order constants are given by

$$C^*_{ijklmn} = -(1-\phi)\frac{3n}{4\pi}C_n\langle a_n'(-\hat{\mathbf{n}}\cdot\mathbf{e}\cdot\hat{\mathbf{n}}R)n_in_jn_kn_ln_mn_n\rangle. \quad (38)$$

The tangential stiffness does not contribute to the third-order moduli because it has been assumed to be a Hookean spring.

3.4 Finite Elasticity and Finite Strain. Here we make explicit our earlier remark that we neglect the change in sample dimensions as being a smaller effect compared to that due to the change(s) in stiffness(es). Consider the sample subject to a strain of order $\epsilon \ll 1$. The change in the sample dimension is $\Delta V/V = O(\epsilon)$, whereas the relative change in the stiffness of the system is of order $\epsilon C^*_{ijklmn}/C^*_{pqrs}$. The relative magnitude of the second and third-order moduli follows from Eqs. (37) and (38) and Tables 1 and 2:

$$\frac{\text{Second-order moduli}}{\text{Third-order moduli}} = O\left(\frac{a_n(w)}{Ra_n'(w)}\right) = O\left(\frac{a_n^2}{R^2}\right) \ll 1. \quad (39)$$

Hence, the relative stiffness change far exceeds the relative volume change. This is a fundamental characteristic of granular media with Hertzian contact forces. It is manifested in the relatively large change of elastic wave speeds as a function of confining stress, which we discuss in detail in Section 5.

We have so far omitted any mention of the finite strain tensor, defined as $\mathbf{E} = \mathbf{e} + \frac{1}{2}\mathbf{f}^T\mathbf{f}$. This is normally the fundamental quantity of finite elasticity, in particular, a hyperelastic material is a function of $\mathbf{E}$. The strain energy is assumed to have a power series expansion of symbolic form $U = U_0 + C_2EE + C_3EEE + \ldots$, where C_2, C_3 represent second and third-order moduli. Alternatively, expanding in terms of $\mathbf{f}$, we have

$$U = U_0 + C_2eee + C_3eee + O(C_2eff, C_3eeff). \quad (40)$$

The scaling of the moduli in (39) indicates that the correction term, C_2eff, is negligible in comparison with C_3eee, and hence it is entirely consistent to take the energy as $U = U_0 + C_2ee + C_3eee$, correct to third order in the finite strain. Consequently, there is no necessity to distinguish the finite strain $\mathbf{E}$ from the linear strain $\mathbf{e}$, even for the purpose of discussing nonlinear elastic effects (up to the order considered here).

4 Energy and Elasticity for Path-Dependent Models

The previous results for the effective moduli are not immediately applicable to the path-dependent models because there is no analog of Eq. (30) for determining σ_{ij}. This difficulty can be resolved by considering small departures from the path-dependent loading, which is physically reasonable for small wave motion or incremental deformation superimposed upon the finite deformation $\mathbf{e}$. The central difficulty is present at the level of the individual contacts, so it makes sense to start there before considering the aggregate.

4.1 A Single Contact. The path-dependent strain energy for a single contact, W of (13), is not a function of w and $\mathbf{s}$, and hence cannot be differentiated arbitrarily. It is, however, possible to consider variations in W for arbitrary unconstrained changes in w and $\mathbf{s}$ about their equilibrium values, w_0 and $\mathbf{s}_0$. Let $w = w_0 + w_1$ and $\mathbf{s} = \mathbf{s}_0 + \mathbf{s}_1$, where $|w_1| \ll |w_0|$ and $|\mathbf{s}_1| \ll |\mathbf{s}_0|$, and the extra displacements w_1 and $\mathbf{s}_1$ are, in general, unrelated to one another. We first note that

$$dW = N(w, \mathbf{s})dw + \mathbf{T}(w, \mathbf{s})\cdot d\mathbf{s} \quad (41)$$

and hence

$$W = W_0(w_0, \mathbf{s}_0) + N_0(w_0, \mathbf{s}_0)w_1 + \mathbf{T}_0(w_0, \mathbf{s}_0)\cdot\mathbf{s}_1 + \int_0^{w_1} N_1 dw_1 + \int_0^{s_1}\mathbf{T}_1\cdot d\mathbf{s}_1, \quad (42)$$

where $N = N_0 + N_1$ and $\mathbf{T} = \mathbf{T}_0 + \mathbf{T}_1$. The values of W_0, $\mathbf{T}_0$, N_0 may depend on the loading history $\mathbf{s}(w)$ to that point. The incremental force equations are, from (4),

$$dN_1 = C_na_n(w_0 + w_1)dw_1,, \quad d\mathbf{T}_1 = C_ta_t(w_0 + w_1)d\mathbf{s}_1. \quad (43)$$

Expanding and integrating gives

$$N_1(w_0, \mathbf{s}_0; w_1, \mathbf{s}_1) = C_n[a_n(w_0)w_1 + \tfrac{1}{2}a_n'(w_0)w_1^2 + \ldots], \quad (44)$$

$$\mathbf{T}_1(w_0, \mathbf{s}_0; w_1, \mathbf{s}_1) = C_t[a_t(w_0)\mathbf{s}_1 + a_t'(w_0)\int_0^{s_1} w_1 d\mathbf{s} + \ldots]. \quad (45)$$

The form of N_1 is unambiguous because of the fact that N is always a function of w. On the contrary, the integral in $\mathbf{T}_1$ depends upon the loading path, or equivalently, upon the functional relationship between w_1 and $\mathbf{s}_1$, if any. This integral is second order in the additional displacements; the first-order term $C_ta_t(w_0)\mathbf{s}_1$ does not depend on the loading history of $(w_1, \mathbf{s}_1)$. Substituting for N_1 and $\mathbf{T}_1$ into (42) we see that the incremental strain energy is defined only up to second order in the incremental displacements, but not to third or higher order, i.e.,

$$W(w_0 + w_1, \mathbf{s}_0 + \mathbf{s}_1) = W_0(w_0, \mathbf{s}_0) + C_nA_n(w_0)w_1 + C_ta_t^{(1)}(w_0)\mathbf{s}_0\cdot\mathbf{s}_1 + \tfrac{1}{2}C_na_n(w_0)w_1^2 + \tfrac{1}{2}C_ta_t(w_0)s_1^2 + \text{path-dependent third-order terms in } (w_1, \mathbf{s}_1). \quad (46)$$

The third-order terms depend upon the path taken from (0, 0) to $(w_1, \mathbf{s}_1)$. This distinguishes the path-dependent models Ib, IIb, IIIb, and IV from the others which possess well-defined strain energy functions. The concept of second-order elasticity is valid for path-dependent models but we cannot use or define third-order elasticity. We will now see how this functional restriction translates into the macroscopic strain energy, and also the effective moduli for the granular medium.

4.2 The Granular Medium. We now consider a departure from the stress/strain state $(\boldsymbol{\sigma}, \mathbf{e})$, such that the total strain and stress are $\mathbf{e} + \boldsymbol{\epsilon}$ and $\boldsymbol{\sigma} + \boldsymbol{\tau}$, respectively, where $|\boldsymbol{\epsilon}| \ll |\mathbf{e}|$ and $|\boldsymbol{\tau}| \ll |\boldsymbol{\sigma}|$. The force at a contact becomes $\mathbf{F} + \mathbf{G}$, where $|\mathbf{G}| \ll |\mathbf{F}|$, and the associated incremental displacement $2\mathbf{v}$ of the pair of spheres relative to one another is given by

$$\mathbf{v} = R\boldsymbol{\epsilon}\cdot\hat{\mathbf{n}}. \quad (47)$$

Downloaded 04 May 2010 to 171.66.16.34. Redistribution subject to ASME license or copyright; see http://www.asme.org/terms/Terms_Use.cfm

The increment in energy for a single contact, along a specific but arbitrary path, is therefore $dW = (\mathbf{F} + \mathbf{G})\cdot d\mathbf{v}$, implying that

$$W = W_0 + \mathbf{F}\cdot\mathbf{v} + \int \mathbf{G}\cdot d\mathbf{v}, \tag{48}$$

where W_0 is the (in general, path-dependent) energy for $\boldsymbol{\epsilon} = 0$, as given by Eqs. (13) and (17), for example. The total energy density of the aggregate is

$$U = U_0 + \frac{R}{V}\sum_{\text{contacts}} \mathbf{F}\cdot\boldsymbol{\epsilon}\cdot\hat{\mathbf{n}} + \frac{R}{V}\sum_{\text{contacts}}\int \mathbf{G}\cdot(d\boldsymbol{\epsilon})\cdot\hat{\mathbf{n}}, \tag{49}$$

where U_0 is the strain energy at $\boldsymbol{\epsilon} = 0$, given by (26).

We can now take advantage of the arbitrariness in ϵ_{ij} to express the total stress as

$$\sigma_{ij} + \tau_{ij} = \frac{\partial U}{\partial \epsilon_{ij}}. \tag{50}$$

The effective stress at strain $\mathbf{e}$ is therefore

$$\sigma_{ij} = \left.\frac{\partial U}{\partial \epsilon_{ij}}\right|_{\boldsymbol{\epsilon}=0}, \tag{51}$$

and the total energy density may be rewritten, from Eqs. (49) and (51),

$$U = U_0 + \sigma_{ij}\epsilon_{ij} + U_1, \tag{52}$$

where U_1 is defined as the ultimate term in (49). Finally, the incremental stress is

$$\tau_{ij} = \frac{\partial U_1}{\partial \epsilon_{ij}}. \tag{53}$$

The macroscopic stress follows from Eqs. (49) and (51) as

$$\sigma_{ij} = \frac{R}{2V}\sum_{\text{contacts}} (F_i n_j + F_j n_i). \tag{54}$$

This is an exact relation for point contacts, and it is commonly used to derive the stress (Digby, 1981; Walton, 1987; Jenkins, 1991). The main point of note here is that the same formula drops out quite naturally from the strain energy. Combining Eq. (54) with Eq. $(28)_1$ for $\mathbf{F}$ gives

$$\sigma_{ij} = (1-\phi)\frac{nR}{V_0}\left\{\frac{C_t}{2}\left\langle\int_{\text{path}} a_t(\xi)(n_i\,ds_j + n_j\,ds_i)\right\rangle - C_n\langle A_n(-\hat{\mathbf{n}}\cdot\mathbf{e}\cdot\hat{\mathbf{n}}R)n_i n_j\rangle\right\}, \tag{55}$$

which is valid for arbitrary deformation paths, with the end condition $(23)_2$ for $\mathbf{s}$. As a specific example, we consider the linear $\mathbf{s}$ trajectory of Eq. (7), for which (55) reduces to

$$\sigma_{ij} = (1-\phi)\frac{nR}{V_0}\times\left\{C_t R\left\langle a_t^{(1)}(-\hat{\mathbf{n}}\cdot\mathbf{e}\cdot\hat{\mathbf{n}}R)\frac{1}{2}(n_i P_{jk} + n_j P_{ik})e_{kl}n_l\right\rangle - C_n\langle A_n(-\hat{\mathbf{n}}\cdot\mathbf{e}\cdot\hat{\mathbf{n}}R)n_i n_j\rangle\right\}. \tag{56}$$

When the length $a_t^{(1)}$ and the area A_n for the contact models Ia and Ib of Table 1 are used, Eq. (56) gives precisely the results derived separately by Walton (1987) for Hertzian contact with either smooth or infinitely rough contacts. Schwartz et al. (1994) have based their theory of stress-induced anisotropy upon this model. We also note that the stress σ_{ij} for the energy models, Eq. (31), is clearly a special case of (56), and follows from the latter by simply replacing the variable length $a_t^{(1)}$ by its constant value appropriate to the energy models, see Eq. (11). Finally, by substituting (56) into (29) and integrating, it can be checked that the energy agrees with (26).

The incremental behavior depends upon the additional strain and stress in excess of $\mathbf{e}$ and $\boldsymbol{\sigma}$, the crucial quantity being the extra contact force $\mathbf{G}$. It follows from the preceding analysis for the single contact that $\mathbf{G}$ is only path independent to first order in the incremental strain. The associated linear form is

$$\mathbf{G} = -RC_n a_n(-\hat{\mathbf{n}}\cdot\mathbf{e}\cdot\hat{\mathbf{n}}R)(-\hat{\mathbf{n}}\cdot\boldsymbol{\epsilon}\cdot\hat{\mathbf{n}})\hat{\mathbf{n}} + RC_t a_t(-\hat{\mathbf{n}}\cdot\mathbf{e}\cdot\hat{\mathbf{n}}R)\mathbf{P}\boldsymbol{\epsilon}\hat{\mathbf{n}}. \tag{57}$$

The integral in (49) can now be evaluated, yielding

$$U_1 = (1-\phi)\frac{nR^2}{2V_0}\{C_n\langle a_n(-\hat{\mathbf{n}}\cdot\mathbf{e}\cdot\hat{\mathbf{n}}R)(\hat{\mathbf{n}}\cdot\boldsymbol{\epsilon}\cdot\hat{\mathbf{n}})^2\rangle + C_t\langle a_t(-\hat{\mathbf{n}}\cdot\mathbf{e}\cdot\hat{\mathbf{n}}R)|\mathbf{P}\boldsymbol{\epsilon}\hat{\mathbf{n}}|^2\rangle\}, \tag{58}$$

or

$$U_1 = \tfrac{1}{2}C^*_{ijkl}\epsilon_{ij}\epsilon_{kl}, \tag{59}$$

where

$$C^*_{ijkl}(\mathbf{e}) = (1-\phi)\frac{nR^2}{V_0}\times\{\langle[C_n a_n(-\hat{\mathbf{n}}\cdot\mathbf{e}\cdot\hat{\mathbf{n}}R) - C_t a_t(-\hat{\mathbf{n}}\cdot\mathbf{e}\cdot\hat{\mathbf{n}}R)]n_i n_j n_k n_l\rangle + \langle C_t a_t(-\hat{\mathbf{n}}\cdot\mathbf{e}\cdot\hat{\mathbf{n}}R)Q_{ijkl}(\hat{\mathbf{n}})\rangle\}. \tag{60}$$

We wish to emphasize that Eq. (60) is always a well-defined path-independent function of the macroscopic strain, $\mathbf{e}$, even for the path-dependent models. Of course, the stress $\boldsymbol{\sigma}$ corresponding to that strain $\mathbf{e}$ may well be path dependent. In the special case of Hertz-Mindlin contacts, for which $a_n(w) \equiv a_t(w) = (Rw)^{1/2}$, Eq. (60) reduces exactly to Eq. (4.6) of (Walton, 1987) but without the necessity of invoking his assumption that $\mathbf{s}/w$ = constant.

The incremental stress follows from Eqs. (53) and (59),

$$\tau_{ij} = C^*_{ijkl}\epsilon_{kl}. \tag{61}$$

Note that the moduli possess the usual symmetries associated with an elastic material, (33). The linear stress-strain relation for τ_{ij} may also be found without using the concept of strain energy, e.g. Walton (1987), but rather from a force balance on the macroscopic scale. This results in an identity which has the same form as (54) but with σ_{ij}, F_i replaced by τ_{ij}, G_i. It can be easily checked that this yields the same stress as (61).

5 Sensitivity of Wave Speeds to Confining Strain and Stress

The wave speeds for small motion superimposed upon the large strain $\mathbf{e}$ are defined by the effective moduli C^*_{ijkl} and the effective density, $\rho^* = (1-\phi)\rho$, where ρ is the granular density. If the wave or phase normal is $\mathbf{m}$, $|\mathbf{m}| = 1$, and the polarization direction is $\mathbf{p}$, $|\mathbf{p}| = 1$, then the wave speed v satisfies

$$\rho^* v^2 = C^*_{ijkl}(\mathbf{e})m_j m_l p_i p_k. \tag{62}$$

Note that $\mathbf{m}$ and $\mathbf{p}$ are not independent, but must satisfy the eigenvector relation $C^*_{ijkl}(\mathbf{e})m_j m_l p_k = \rho^* v^2 p_i$. We are interested in the incremental change in speed, Δv, when the strain is changed to $\mathbf{e} + \Delta\mathbf{e}$. The additional strain arises from a static deformation, and need not be proportional to the original, finite strain $\mathbf{e}$.

Downloaded 04 May 2010 to 171.66.16.34. Redistribution subject to ASME license or copyright; see http://www.asme.org/terms/Terms_Use.cfm

For the models with energy potentials we can use the standard theory of acoustoelasticity (Toupin and Bernstein, 1961),

$$\rho^*\Delta v^2 = C^*_{ijklmn}m_j m_l p_i p_k \Delta f_{mn} + (C^*_{ikqr}\Delta f_{qr}\delta_{jl} + C^*_{qjkl}\Delta f_{iq} + C^*_{iqkl}\Delta f_{jq} + C^*_{ijkl}\Delta f_{kq} + C^*_{ijkq}\Delta f_{lq})p_i p_l m_j m_k, \quad (63)$$

where $\Delta\mathbf{f}$ is the incremental deformation gradient and $C^*_{ijklmn}(\mathbf{e})$ are the third-order moduli. Based on Eq. (39) we can safely and consistently ignore the terms in (63) involving the second-order moduli as being of a smaller order than the third-order moduli terms for the granular medium. Furthermore, using the symmetries of C^*_{ijklmn} in (38) implies

$$\rho^*\Delta v^2 = C^*_{ijklmn}(\mathbf{e})m_j m_l p_i p_k \Delta e_{mn}, \quad (64)$$

that is, the change in speed depends only upon the symmetric strain increment defined in accordance with Eq. (24).

The analogous result for the path-dependent models can be obtained by returning to the fundamental relation for the incremental strain energy of a single contact, (46). At issue is how the coefficients of w_1^2 and s_1^2 are altered as we change w_0 to $w_0 + \Delta w_0$, and $\mathbf{s}_0$ to $\mathbf{s}_0 + \Delta\mathbf{s}_0$. The change in the terms W_0 and $a^{(1)}(w_0)$ in (46) are path dependent, and require that the increment in $\mathbf{s}_0$ be related to that for w_0. However, this path dependence does not effect the terms of interest, i.e., we simply replace the arguments of a_n and a_t with $w_0 + \Delta w_0$ in the quadratic terms. The increment in W involving the quadratic small strain is therefore

$$\Delta W = \ldots + \tfrac{1}{2}(C_n a_n'(w_0)w_1^2 + C_t a_t'(w_0)s_1^2)\Delta w_0. \quad (65)$$

When we translate this result to the aggregate, it is clear that the change in the wave speed is of the form

$$\rho^*\Delta v^2 = B^*_{ijklmn}(\mathbf{e})m_j m_l p_i p_k \Delta e_{mn}, \quad (66)$$

where B^*_{ijklmn} are simply the derivatives of $C^*_{ijkl}(\mathbf{e})$, given by Eq. (60),

$$B^*_{ijklmn}(\mathbf{e}) = \frac{\partial C^*_{ijkl}(\mathbf{e})}{\partial e_{mn}}. \quad (67)$$

The explicit form follows from Eqs. (60) and (67),

$$B^*_{ijklmn} = -(1-\phi)\frac{3n}{4\pi} \times \{\langle[C_n a_n'(-\hat{\mathbf{n}}\cdot\mathbf{e}\cdot\hat{\mathbf{n}}R) - C_t a_t'(-\hat{\mathbf{n}}\cdot\mathbf{e}\cdot\hat{\mathbf{n}}R)]n_i n_j n_k n_l n_m n_n\rangle + C_t\langle a_t'(-\hat{\mathbf{n}}\cdot\mathbf{e}\cdot\hat{\mathbf{n}}R)Q_{ijkl}n_m n_n\rangle\}. \quad (68)$$

Comparing Eqs. (38) and (68) we see that

$$B^*_{ijklmn} = C^*_{ijklmn} \text{ if and only if } a_t \text{ is constant.} \quad (69)$$

In general, the third-order tensor B^*_{ijklmn} does not have all the symmetries of the third-order elastic moduli C^*_{ijklmn} in (33). Thus,

$$B^*_{jiklmn} = B^*_{ijklmn}, \quad B^*_{klijmn} = B^*_{ijklmn}, \quad B^*_{ijklnm} = B^*_{ijklmn}. \quad (70)$$

6 Example: Hydrostatic Confining Pressure

Consider a hydrostatic strain, $e_{ij} = e\delta_{ij}$, $e < 0$. The macroscopic stress $\boldsymbol{\sigma}$ of (56) is hydrostatic, $\sigma_{ij} = -p\delta_{ij}$, and the confining pressure is

$$p = (1-\phi)\frac{nR}{3V_0}C_n A_n(-eR). \quad (71)$$

This is true for both the energy models and the path-dependent models, because it is independent of the tangential stiffness. The effective moduli are isotropic with two second-order and (when applicable) three third-order moduli. The Lamé moduli, for all models considered in this paper, are

$$\left.\begin{matrix}\lambda^*\\ \mu^*\\ K^*\end{matrix}\right\} = (1-\phi)\frac{n}{20\pi R} \times \begin{cases} C_n a_n(-eR) - C_t a_t(-eR), \\ C_n a_n(-eR) + \frac{3}{2}C_t a_t(-eR) \\ \frac{5}{3}C_n a_n(-eR). \end{cases} \quad (72)$$

If the model possesses a unique potential energy then the third order moduli are

$$\left.\begin{matrix}C^*_{111}\\ C^*_{112}\\ C^*_{123}\end{matrix}\right\} = \frac{-(1-\phi)n}{140\pi}C_n a_n'(-eR) \times \begin{cases}15,\\ 3,\\ 1.\end{cases} \quad (73)$$

Note that these are all negative and

$$C^*_{111}:C^*_{112}:C^*_{123} = 15:3:1. \quad (74)$$

All other nonzero elastic constants are simply related to these three (Green, 1973). There are many alternative systems of notation for the third-order moduli, and Eqs. (73) and (74) can be converted accordingly. Green (1973) has provided a very useful table for converting from one system of notation to another. For example, Eq. (74) implies that the moduli of Toupin and Bernstein (1961) are identical, i.e., $\nu_1 = \nu_2 = \nu_3$, while those of Landau and Lifshitz (1986) satisfy $A:B:C = 8:2:1$, *viz.*

$$\left.\begin{matrix}A\\ B\\ C\end{matrix}\right\} = \frac{-(1-\phi)n}{140\pi}C_n a_n'(-eR) \times \begin{cases}4,\\ 1,\\ 1/2.\end{cases} \quad (75)$$

Departures from linear elasticity for the path-dependent models requires the moduli B^*_{ijklmn}, which are of the form

$$B^*_{ijklmn} = B_{ijklmn} + \tilde{B}I_{ijkl}\delta_{mn}. \quad (76)$$

Here, B_{ijklmn} satisfy all the symmetries of third-order elastic moduli, *viz.* Eq. (33), and

$$\left.\begin{matrix}B_{111}\\ B_{112}\\ B_{123}\\ \tilde{B}\end{matrix}\right\} = \frac{-(1-\phi)n}{140\pi} \times \begin{cases}15C_n a_n'(-eR) - C_t a_t'(-eR), \\ 3C_n a_n'(-eR) - 3C_t a_t'(-eR), \\ C_n a_n'(-eR) - C_t a_t'(-eR), \\ 7C_t a_t'(-eR).\end{cases} \quad (77)$$

We can now test the general expression (66) for the change in wave speeds. We consider the change in the speed of longitudinal and transverse waves, v_c, and v_s, for which $\mathbf{p}$ is parallel to $\mathbf{m}$ and $\mathbf{p}$ is perpendicular to $\mathbf{m}$, respectively. Noting that $dp/de = -3K^*$, where $K^* \equiv \lambda^* + 2\mu^*/3$ is the effective bulk modulus, it follows from Eq. (66) that

$$\rho^*\frac{dv_c^2}{dp} = -\frac{(B^*_{111} + 2B^*_{112})}{3K^*}, \qquad \rho^*\frac{dv_s^2}{dp} = -\frac{(B^*_{441} + 2B^*_{442})}{3K^*}, \quad (78)$$

where (Green, 1973) $B^*_{441} = (B_{112} - B_{123} + \tilde{B})/2$, $B^*_{442} = (B_{111} - B_{112} + 2\tilde{B})/4$. The results for the elastic models simplify because $a_t' \equiv 0$: We have $B^*_{111} + 2B^*_{112} = 21B$ and $B^*_{441} + 2B^*_{442} = 7B$.

Downloaded 04 May 2010 to 171.66.16.34. Redistribution subject to ASME license or copyright; see http://www.asme.org/terms/Terms_Use.cfm

The speeds of propagation of small-amplitude compressional and shear waves are

$$v_c = \left(\frac{\lambda^* + 2\mu^*}{\rho^*}\right)^{1/2}, \quad v_s = \left(\frac{\mu^*}{\rho^*}\right)^{1/2}, \tag{79}$$

respectively. The derivatives of the speeds with respect to pressure can then be worked out directly from the definitions of the effective moduli in Eq. (72). It is then simply a matter of some algebra to check that these do in fact agree with the expressions in Eq. (78).

Note that $C_n a_n'(-eR)$ is the modulus determining all the third-order moduli in (73) and (75). The additional modulus $C_t a_t'(-eR)$ is required when the length a_t governing shear deformation at the granular level is not constant, but depends upon the loading. In the path-dependent models Ib, IIb, and IIIb, this parameter is the same as a_n. The behavior of a_n' is quite different for each of models I, II, and III. Thus, as the applied strain e tends to zero, we have $C_n a_n'(-eR)$ tending to ∞, 0, and the finite value $(2/\alpha\pi)C_n$, respectively, for models I, II, and III.

7 Numerical Examples and Experimental Data

In this section we present numerical calculations of the speeds and the moduli as a function of confining pressure. For the sake of specificity we limit our analysis to the Digby model, IIa. We note that there is a scale invariance which guarantees that the moduli, considered as functions of pressure, depend only on the ratio of b/R. We consider glass beads for which we assume the elastic constants and the density to be those measured by Johnson and Plona (1982). We take $n = 9$ as deduced by Bernal and Mason (1960). The calculated speeds are presented in Fig. 2. This figure is essentially the same as that of Fig 5 of Digby (1981). We note that when $b = 0$ the sound speeds are proportional to $p^{1/6}$ as discussed by Digby and others.

Also shown in Fig. 2 are the speeds of sound which Domenico (1977) has measured in glass beads under confining pressure. We have converted his values to more conventional units. Although it is not perfect, we see that the Digby model with $b \equiv 0$ provides a reasonable description of the sound speeds, with no adjustable parameters. Winkler (1983) has pointed out that, in the context of contact models treated via the present effective medium theory, the Hertz-Mindlin model with $0 < a_t < a_n$ would provide a better description. Goddard (1990) has further critiqued the pressure dependence of the speeds. He has argued that in a disordered packing there is a variation in the number density of Hertzian contacts, which can lead to a sound speed which varies more rapidly than $p^{1/3}$, especially at lower pressures. Experimental and numerical data of Jenkins et al. (1989) and Cundall et al. (1989) at much lower confining pressures (<140 kPa) than those considered here gave values for the shear modulus of about one third that predicted by Digby's model. They also found many redundant grains, with an average coordination number closer to five. The present model is not appropriate to this type of "loose" packing, where shear banding is common, and the mean field assumption needs to be reexamined. Thus, Jenkins et al. (1989) considered anisotropic orientation distribution functions for the contacts, and they also permitted the grains to rotate individually.

For the purposes of the present article, we consider the model to give a reasonable semi-quantitative description of the acoustic properties of granular media. In Fig. 3(*a*) we plot the pressure dependence of the second-order elastic constant $C_{11} = \lambda + 2\mu$ (the *P*-wave modulus) from Eq. (72). In Fig. 3(*b*), we plot the corresponding pressure dependence for the third-order constant, $-B$, using Eq. (75). The dimensionless rate of change of *P*-wave speed, $\rho^*(dV_p^2/dp)$ from Eq. (78), is plotted in Fig. 3(*c*). The following points emerge from these figures:

(a) When $b = 0$ the second-order elastic constants vanish, and the third-order constants diverge, in the limit $p \to 0$.

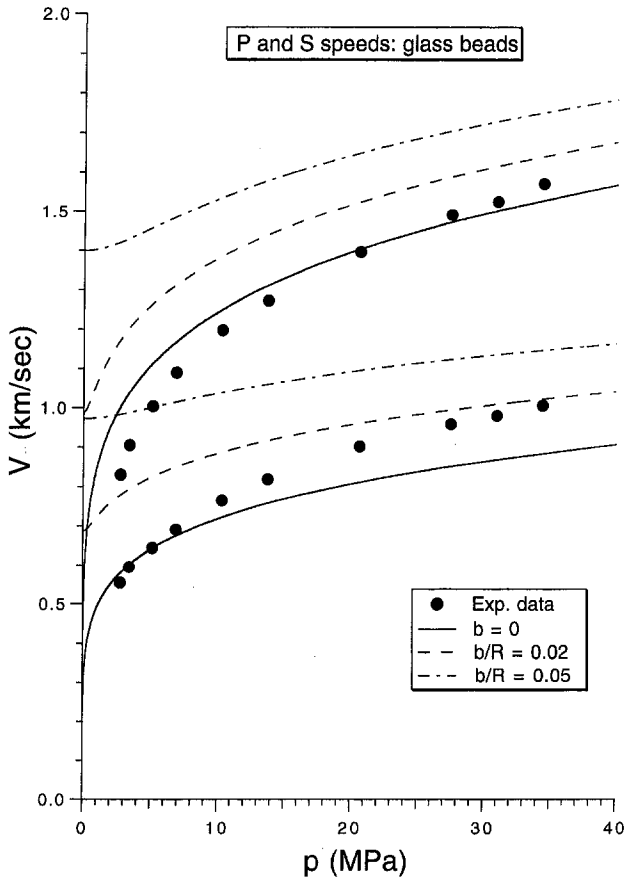


Fig. 2 Compressional and shear speeds in unsintered glass beads as a function of confining pressure. The continuous lines are calculated results based upon the Digby model of grain-grain contacts. We have used the values $n = 9$, $\mu = 49.9$ GPa, $\nu = 0.277$, and $\rho_s = 2.48$ gm · cm^{-3}. The symbols represent the experimental data of Domenico (1977) which should be compared against the $b = 0$ curves.

(b) When $b \neq 0$ the second-order elastic constants tend to a finite value and the third-order constants tend to zero, in the limit $p \to 0$. This is obvious from Eq. (13) and Table 2: V_n is an even function of w for the Digby model and so there is no third-order term in an expansion around $w = 0$.

(c) In the range of pressure over which there is experimental data, the third-order elastic coefficients are much larger than the second, thus justifying our neglect in the change of sample size as the pressure is increased. This approximation is also valid for small nonzero values of b/R.

(d) Typical values of $\rho^*(dV_p^2/dp)$ in Fig. 3(*c*) are much larger than the corresponding values for nongranular solids which are in the range 5–10. (See, for example, Johnson et al., (1994) and references therein.) They are, however, much less than values which have been seen in consolidated sedimentary rocks (Johnson et al., 1994). This may be due to the fact that the asperities in grain-grain contacts are much smaller than the average grain diameters and/or the ogival contact model is the more appropriate one.

8 Conclusion

We have developed a simple theory of macroscopic elasticity of granular systems based upon various models of the grain-grain contact forces which have appeared in the literature. For all models considered, the second-order elastic constants are well defined at any given static state of stress. Thus the speeds of sound are well defined at a given state of stress. The same cannot be said of third or higher-order elastic constants; in general, the change in sound speeds due to an incremental

Downloaded 04 May 2010 to 171.66.16.34. Redistribution subject to ASME license or copyright; see http://www.asme.org/terms/Terms_Use.cfm

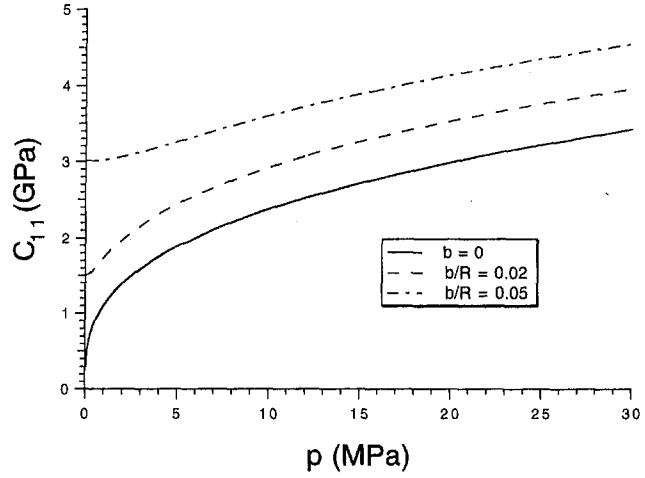


Fig. 3(*a*)

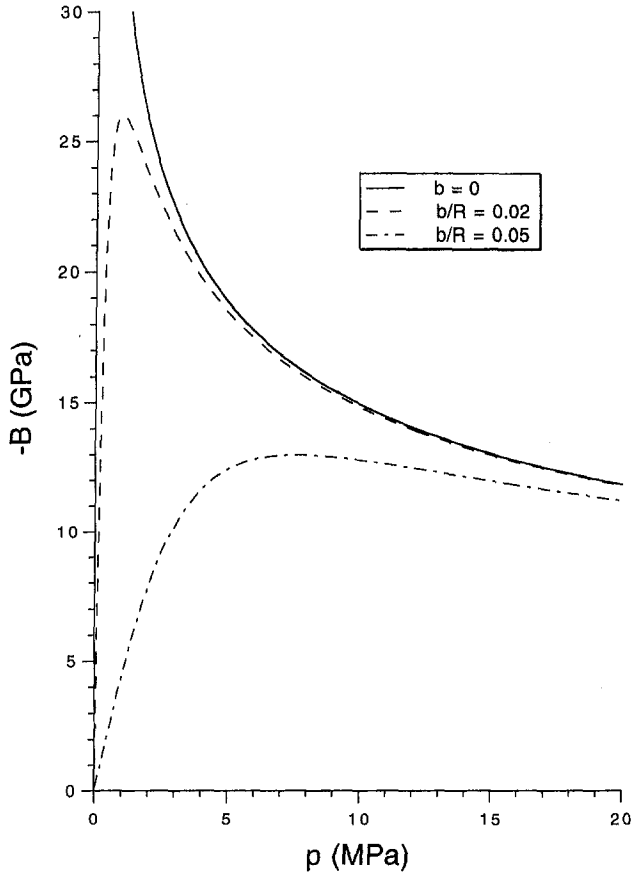


Fig. 3(*b*)

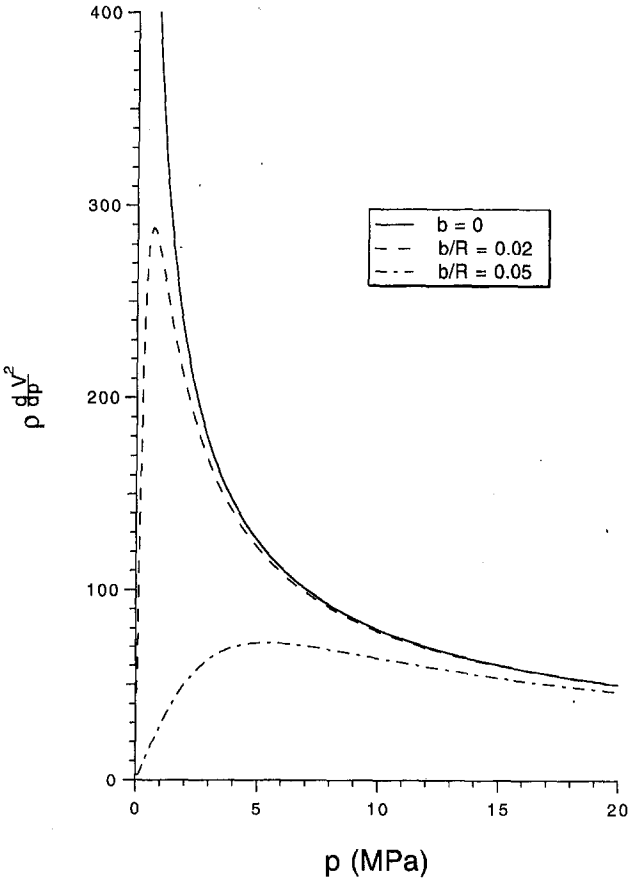


Fig. 3(*c*)

Fig. 3 Calculated elastic properties of granular media within the context of the Digby model. Same values of input parameters as in Fig. 2 with $\phi = 0.38$. (*a*) Second-order elastic constant C_{11} as a function of pressure. (*b*) Third-order elastic constant, B, as a function of confining pressure. (*c*) $\rho^*(dV_p^2/dp)$ as a function of confining pressure. Note the differing scales.

change in state of stress is dependent on the history in which that change is applied. The exceptions occur for models of grain-grain contact forces which are derivable from a potential energy function, which guarantees that the solid is hyperelastic. Here, the third-order elastic constants are well defined, as are all higher order constants, independent of the path of the deformation.

We have illustrated our results with some calculations relevant to glass beads under confining pressure. The calculated speeds of sound are in semi-quantitative agreement with the existing data of Domenico (1977), as has been noted before by others. For such a system we believe this lends credence to the approximate validity of our calculations of the third-order constants. This theory can be extended to other states of stress, as well as to other models of the contact forces.

Acknowledgments

We are grateful to J. G. Berryman and L. M. Schwartz for stimulating our interest in this problem and for several useful discussions along the way. We are grateful to B. Sinha for several insightful clarifications and to K. Winkler and D. Elata for help with the exposition of the manuscript.

References

Bernal, J. D., and Mason, J., 1960, "Coordination of Randomly Packed Spheres," *Nature*, Vol. 188, pp. 910–911.

Christensen, N. I., and Wang, H. F., 1985, "The influence of pore pressure and confining pressure on dynamic elastic properties of Berea sandstone," *Geophysics*, Vol. 50, pp. 207–213.

Cundall, P. A., Jenkins, J. T., and Ishibashi, I., 1989 "Evolution of elastic moduli in a deforming granular assembly," *Powders and Grains*, J. Biarez and R. Gourves, eds., Balkema, Rotterdam, pp. 319–322.

Deresiewicz, H., 1958a, "Stress-Strain Relations for a Simple Model of a Granular Medium," ASME JOURNAL OF APPLIED MECHANICS, Vol. 25, pp. 402–406.

Deresiewicz, H., 1958b, "Mechanics of granular media," *Adv. Appl. Mech.*, Vol. 5, pp. 233–306.

Digby, P. J., 1981, "The effective elastic moduli of porous granular rock," ASME JOURNAL OF APPLIED MECHANICS, Vol. 48, pp. 803–808.

Domenico, S. N., 1977, "Elastic properties of unconsolidated porous sand reservoirs," *Geophysics*, Vol. 42, pp. 1339–1368.

Downloaded 04 May 2010 to 171.66.16.34. Redistribution subject to ASME license or copyright; see http://www.asme.org/terms/Terms_Use.cfm

Duffy, J., and Mindlin, R. D., 1957, "Stress-Strain Relations and Vibrations of a Granular Medium," ASME JOURNAL OF APPLIED MECHANICS, Vol. 24, pp. 585–593.

Goddard, J. D., 1990, "Nonlinear elasticity and pressure-dependent wave speeds in granular media," *Proc. R. Soc. Lond.*, Vol. A430, pp. 105–131.

Green, R. E., 1973, *Ultrasonic Investigation of Mechanical Properties*, (Treatise on Materials Science and Technology, Vol. 3), Academic Press, New York.

Jenkins, J. T., 1991, "Anisotropic elasticity for random arrays of identical spheres," *Modern Theory of Anisotropic Elasticity and Applications*, J. Wu, T. C. T. Ting, and D. M. Barnett, eds., SIAM, Philadelphia, PA, pp. 368–377.

Jenkins, J. T., Cundall, P. A., and Ishibashi, I., 1989 "Micromechanical modeling of granular materials with the assistance of experiments and numerical simulations," *Powders and Grains*, J. Biarez and R. Gourves, eds., pp. 257–264. Balkema, Rotterdam.

Johnson, D. L., Kostek, S., and Norris, A. N., 1994, "Nonlinear Tube Waves," *J. Acoust. Soc. Am.*, Vol. 96, pp. 1829–1843.

Johnson, D. L., and Norris, A. N., 1995, "Rough elastic spheres in contact," *J. Mech. Phys. Solids*, to be published.

Johnson, D. L., and Plona, T. J., 1982, "Acoustic Slow Waves and the Consolidation Transition," *J. Acoust. Soc. Am.*, Vol. 72, pp. 556–565.

Landau, L. D., and Lifshitz, E. M., 1986, *Theory of Elasticity*, 3rd ed., Pergamon Press, Oxford, pp. 106–107.

Mindlin, R. D., 1949, "Compliance of Elastic Bodies in Contact," ASME JOURNAL OF APPLIED MECHANICS, Vol. 71, pp. 259–268.

Mindlin, R. D., and Deresiewicz, H., 1953, "Elastic Spheres in Contact Under Varying Oblique Forces," ASME JOURNAL OF APPLIED MECHANICS, Vol. 75, pp. 327–344.

Schwartz, L. M., Johnson, D. L., and Feng, S., 1984, "Vibrational Modes in Granular Materials," *Phys. Rev. Lett.* Vol. 52, pp. 831–834.

Schwartz, L. M., Murphy, W. F., III, and Berryman, J. G., 1994, "Stress-induced transverse isotropy in rocks," *Proceedings of the Society of Exploration Geophysicists*, Annual Meeting, Los Angeles, CA, Oct. 23–27, 1081–1085.

Spence, D. A., 1968, "Self similar solutions to adhesive contact problems with incremental load," *Proc. R. Soc. Lond.*, Vol. A305, pp. 55–80.

Toupin, R. A., and Bernstein, B., 1961, "Sound waves in deformed perfectly elastic materials. Acoustoelastic effect," *J. Acoust. Soc. Am.*, Vol. 33, pp. 216–225.

Truesdell, C., and Noll, W., 1965, "The nonlinear field theories of mechanics," *Handbuch der Physik III/3*, S. Flugge, ed., Springer, New York.

Walton, K., 1987, "The effective elastic moduli of a random packing of spheres," *J. Mech. Phys. Solids*, Vol. 35, pp. 213–226.

Winkler, K. W., 1983, "Contact stiffness in granular porous materials: Comparison between theory and experiment," *Geophys. Res. Lett.*, Vol. 10, pp. 1073–1076.

APPENDIX

Alternative Theories for Intergranular Forces

Oblique Loading on a Pair of Spheres. In a series of papers Mindlin and Deresiewicz (Mindlin, 1949; Mindlin and Deresiewicz, 1953; Deresiewicz, 1958) provided an exhaustive analysis of the mcchanics near the contact region of two elastic spheres. This work extended the classical analysis of Hertz (who verified his contact theory by experiment) to account for tangential forces and oblique loading. Mindlin and Deresiewicz (1953) showed that the relation between the tangential force and the tangential displacement depends upon the loading history.

Consider two spheres forced together under a load N. This results in a circular contact zone of radius a and a normal displacement w,

$$a = \left(\frac{3RN}{2C_n}\right)^{1/3}, \quad w = a^2/R. \tag{A1}$$

That is, the spheres approach twice the distance achieved by slicing off caps of radius a on each. Equations (A1) imply that

$$N = \tfrac{2}{3}C_n R^{1/2} w^{3/2}. \tag{A2}$$

Let a_0 be the initial contact radius for applied force N_0. An oblique compressive force is now applied, resulting in a tangential force $\mathbf{T}$ and total normal force N. The *additional* force is applied incrementally in such a manner that its line of action is constant, and it lies outside the friction cone, that is

$$\frac{dT}{dN} = \beta > f, \tag{A3}$$

where β is constant and f is the coefficient of friction between the surfaces. The contact zone then grows to

$$a = (N/N_0)^{1/3} a_0 = (1 + \theta L)^{1/3} a_0, \tag{A4}$$

where

$$\theta = \frac{f}{\beta}, \quad L = \frac{T}{fN_0}. \tag{A5}$$

Note that $0 \le \theta \le 1$, and the upper limit corresponds to infinite roughness at the contact, and hence no slip. As the contact zone grows a slip zone in the shape of a circular annulus also grows inward, so that the adhered region is of radius c where

$$c = (1 - T/fN)^{1/3} a = [1 - (1 - \theta)L]^{1/3} a_0. \tag{A6}$$

Thus, $c \le a_0$, as expected, with equality only for infinitely rough surfaces.

The incremental change in the relative tangential displacement between the two spheres, $2s$, is related to the applied load by the differential relation (Eq. (82) of Mindlin and Deresiewicz (1953))

$$\frac{dT}{ds} = C_t \left(\frac{\theta}{a} + \frac{1 - \theta}{c}\right)^{-1}. \tag{A7}$$

There are three limits of this general relation that are of interest.

(i) First, if the surfaces are frictionless, then $c \equiv 0$ identically (there is no adhered region) and case Ia of Table 1 is obtained.

(ii) Second, if the friction is infinite, or $\theta = 1$, then $\mathbf{T}$ satisfies $(1)_2$ with $a_n = a_0$. If we integrate this relation with the initial condition that $N_0 = 0$ (which only makes sense for infinite roughness), we recover Walton's result (Eq. $(2.5)_1$ of Walton (1987))

$$\mathbf{T} = \tfrac{2}{3}C_t a \mathbf{s}. \tag{A8}$$

Thus, Walton's model corresponds to homothetic loading from zero confining stress. This is model Ib in Table 1. The more general relation in Eq. (A7) allows us to consider different load paths and finite friction. However, we will use Walton's formula in practice.

(iii) Alternatively, if the normal load is kept fixed as the tangential force is applied, then $\theta = 0$, and we have instead

$$d\mathbf{T} = C_t c \, d\mathbf{s}. \tag{A9}$$

This is the case considered by Mindlin in Eq. (103) of Mindlin (1949), and is model IV in Table 1.

Normal Loading of a Pair of Spheres in Contact. The models of the previous subsection can be generalized to account for initial contact. Digby (1981) considered the case of a circular zone of radius b of initial contact between the spheres at zero confining force. He showed that the contact zone for a compressive normal force N is a circular region of radius a given by the formula

$$a(a^2 - b^2)^{1/2} = Rw. \tag{A10}$$

This gives the formula for $a_n = a$ in Table 1, for model II.

Downloaded 04 May 2010 to 171.66.16.34. Redistribution subject to ASME license or copyright; see http://www.asme.org/terms/Terms_Use.cfm

The Spence/Goddard Contact Model. An *ogival* indenter, composed of a sphere with a conical tip of interior angle $\pi - 2\alpha$, $0 \leq \alpha \ll 1$, is pressed into a sphere of the same radius. This type of contact geometry was discussed by Goddard (1990), and is based on a class of solutions generated by Spence (1968) for frictionless indentation of self-similar shapes on planar surfaces. Thus, the normal force required to press the ogival body a distance w against a planar surface of the same material is

$$N = C_n \frac{a^2}{2}\left(B_0 - \frac{\pi}{4}B_1 - \frac{2}{3}B_2\right), \qquad \text{(A11)}$$

where a is the contact radius, $w = B_0 a$, $B_0 = (\pi/2)B_1 + 2B_2$, and $B_1 = \alpha$, $B_2 = a/2R$. These follow from Appendix D of Spence (1968). The analogous force for the ogive/sphere contact is obtained simply by the replacement $B_2 = a/R$, which combined with (A11) leads to the incremental form of the force equation, $(1)_I$ and $(2)_I$, where a_n is given in Table 1 under model III.

Downloaded 04 May 2010 to 171.66.16.34. Redistribution subject to ASME license or copyright; see http://www.asme.org/terms/Terms_Use.cfm

Seismic Waves in a Laterally Inhomogeneous Layered Medium, Part I: Theory

Ruichong Zhang
Research Assistant Professor,
Department of Civil Engineering,
University of Southern California,
University Park,
Los Angeles, 90089-2531
Assoc. Mem. ASME.

Liyang Zhang
Structural Engineer,
Weidlinger Associates, Inc.,
New York, NY 10001

Masanobu Shinozuka
Fred Champion Chair in Civil Engineering,
Department of Civil Engineering,
University of Southern California,
Los Angeles, CA 90089-2531
Fellow ASME.

Seismic waves in a layered half-space with lateral inhomogeneities, generated by a buried seismic dislocation source, are investigated in these two consecutive papers. In the first paper, the problem is formulated and a corresponding approach to solve the problem is provided. Specifically, the elastic parameters in the laterally inhomogeneous layer, such as P and S wave speeds and density, are separated by the mean and the deviation parts. The mean part is constant while the deviation part, which is much smaller compared to the mean part, is a function of lateral coordinates. Using the first-order perturbation approach, it is shown that the total wave field may be obtained as a superposition of the mean wave field and the scattered wave field. The mean wave field is obtainable as a response solution for a perfectly layered half-space (without lateral inhomogeneities) subjected to a buried seismic dislocation source. The scattered wave field is obtained as a response solution for the same layered half-space as used in the mean wave field, but is subjected to the equivalent fictitious distributed body forces that mathematically replace the lateral inhomogeneities. These fictitious body forces have the same effects as the existence of lateral inhomogeneities and can be evaluated as a function of the inhomogeneity parameters and the mean wave field. The explicit expressions for the responses in both the mean and the scattered wave fields are derived with the aid of the integral transform approach and wave propagation analysis.

1 Introduction

In modeling earthquake ground motion, the earth medium is usually assumed as piece-wise homogeneous in the vertical direction, i.e., a layered half-space. With a properly assumed seismic source mechanism such as a dislocation source, the simulated ground motion in such a modeled layered half-space may reasonably explain most of what has been observed in the actual earthquake records, e.g., various body waves and surface waves. However, in reality, there exists lateral variation of up to ten percent in elastic parameters of the earth medium (Aki and Richards, 1980; Kennett, 1972). The variation is even higher for the earth medium near the ground surface. Most earthquake records and associated research (see, e.g., Kennett, 1972; Aki, 1975; Askar and Cakmak, 1988) indicate that the existence of the lateral inhomogeneities of the earth medium results in wave scattering which affects seismogram envelops and power spectra, generates coda waves, etc. Therefore, it is fundamentally important for both engineers and seismologists to know the effects of the lateral inhomogeneities of the earth medium on the ground or underground earthquake motion.

For the earth medium with slight lateral inhomogeneities, wave scattering may be easily described with the aid of the first-order perturbation technique or Born-type approximation approach (see, e.g., Chow, 1972, 1975; Aki and Richards, 1980). Kennett (1972) first used the integral equation formulation and Born-type expansion in the wave number domain to solve the two-dimensional wave scattering problem in the earth medium with both lateral and vertical inhomogeneities. The Born approximation approach was also applied by Sato (1984, 1989) to deal with a three-dimensional wave scattering problem in a full-space with a randomly inhomogeneous lithosphere. Associated developments on the subject were also carried out by Chu et al. (1981), Wu (1982), Weaver (1984), Wu and Aki (1985), Farra and Madariaga (1987), Bataille and Flatte (1988), among others. However, their analyses are restricted in either two-dimensional wave scattering in such modeled earth medium as a layered half-space or three-dimensional wave scattering in the earth medium with inhomogeneities existing in a finite area. In practice, the earth medium is probably best described by a layered half-space with the top layer or layers (close to the ground surface) being of slight lateral inhomogeneities (see Askar and Cakmak, 1988). Stauber (1985) investigated a three-dimensional wave scattering problem in a layered half-space with laterally inhomogeneous layers. However, only acoustic waves are involved in his analysis, which may not be directly applied to seismic waves. In particular, when seismic waves such as *P* and *S* waves hit the laterally inhomogeneous medium, coupling between different kind of waves such as *P-SV* and *SH* waves occurs (Zhang, 1994), which can be found neither for seismic waves in a two-dimensional inhomogeneous medium nor for the acoustic waves in a three-dimensional inhomogeneous medium.

In this study, seismic waves in a layered half-space with lateral inhomogeneities, generated by a buried seismic dislocation source, are investigated. In this paper, the problem is formulated and a corresponding approach is provided. The explicit expressions for responses are derived using the integral transform approach and wave propagation analysis, in which *P-SV* and *SH* waves are decoupled and analyzed separately.

2 Outline of Problem and Its Approach

As shown in Fig. 1, the earth is modeled as a layered half-space. Each layer is assumed to be perfectly homogeneous, isotropic, and linearly elastic, except layer j, which is slightly laterally inhomogeneous. A seismic dislocation source is buried

Contributed by the Applied Mechanics Division of THE AMERICAN SOCIETY OF MECHANICAL ENGINEERS for publication in the ASME JOURNAL OF APPLIED MECHANICS.

Discussion on the paper should be addressed to the Technical Editor, Professor Lewis T. Wheeler, Department of Mechanical Engineering, University of Houston, Houston, TX 77204-4792, and will be accepted until four months after final publication of the paper itself in the ASME JOURNAL OF APPLIED MECHANICS.

Manuscript received by the ASME Applied Mechanics Division, June 27, 1995; final revision, Oct. 11, 1996. Associate Technical Editor: L. T. Wheeler.

Copyright © 1997 by ASME

Downloaded 04 May 2010 to 171.66.16.34. Redistribution subject to ASME license or copyright; see http://www.asme.org/terms/Terms_Use.cfm

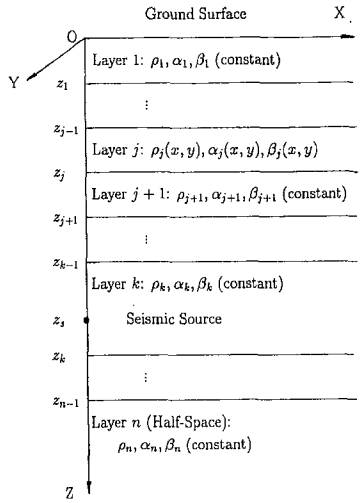


Fig. 1 Schematic of layered medium with one laterally inhomogeneous layer subjected to seismic dislocation source

in layer k. The seismic fault orientation (see Fig. 2) is defined by the strike direction ϕ_s [0, 2π) and dip δ [0, $\pi/2$], which are measured clockwise from north and down from the horizontal, respectively. The slip direction is described by the rake λ [0, 2π), measured counterclockwise from strike direction within the fault plane. A pure strike-slip corresponds to $\lambda = 0$ or π, while a pure dip-slip to $\lambda = -\pi/2$ or $\pi/2$. Therefore, a shear slip of arbitrary orientation can always be decomposed into a pure strike-slip and a pure dip-slip component.

Without loss of generality, the coordinate system is selected so that (x, y)-plane coincides with the horizontal ground surface, the x-direction coincides with the strike direction, and the z-direction with the depth direction (see Fig. 1). When the distance between observation site and the seismic dislocation at a discretized subfault is much larger than the dimension of the subfault, the corresponding dislocation (the shear slip on the subfault) can be idealized as an effective point source associated with a double couple of body forces. Therefore, the seismic waves are generated by a series of double couples, which are distributed over the entire seismic fault and triggered at different time instants. Mathematically, they can be obtained by solving the following governing equation:

$$\mathcal{L}\{\mathbf{u}(x, y, z, t)\} = \mathbf{p}^m(x, y, z, t) \tag{1}$$

in conjunction with pertinent conditions that are continuity conditions at each layer-to-layer interface and boundary conditions at both free ground surface and infinite depth (radiation condition). In Eq. (1), $\mathbf{u} = \{u_x, u_y, u_z\}^T$ denotes the displacement field; $\mathcal{L}$ is a linear operator, characterizing the modeled earth medium with lateral inhomogeneities and being a function of the elastic parameters (such as P and S wave speeds, etc.) and the structure of earth medium (such as the depths of interfaces); and $\mathbf{p}^m = \{p_x^m, p_y^m, p_z^m\}^T$ is the double couple of body forces, equivalent to the seismic dislocation $\Delta\mathbf{u}(x, y, z, t)$ in the fault area, and can be mathematically represented on the basis of $\Delta\mathbf{u}$ through the known operator $\mathcal{F}$, i.e.,

$$\mathbf{p}^m(x,y,z,t) = \begin{cases} \mathcal{F}\{\Delta\mathbf{u}(x,y,z,t)\}; \\ \qquad (x,y,z) \in \text{seismic fault area} \\ 0; \quad (x,y,z) \ni \text{seismic fault area.} \end{cases} \tag{2}$$

The lateral inhomogeneities in layer j means that P and S wave speeds (α_j and β_j) and density (ρ_j) are a function of lateralcoordinates (x, y) and may be decomposed into two parts as follows:

$$\zeta_j(x, y) = \zeta_j^m + \epsilon\zeta_j^s(x, y); \quad \zeta = \alpha, \beta \text{ or } \rho \tag{3}$$

where the first part is the average value, taken to be independent of lateral coordinates (x, y), and the second part is the deviation from the average value, assumed to be of order of smallness ϵ. Correspondingly, the displacement field may also be decomposed into two parts, i.e.,

$$\mathbf{u}(x, y, z, t) = \mathbf{u}^m(x, y, z, t) + \epsilon\mathbf{u}^s(x, y, z, t) \tag{4}$$

where superscript m denotes corresponding average value (called the mean wave field), obtainable as the response solution for the layered half-space without the lateral inhomogeneities subjected to a series of double couples of body forces, and superscript s denotes the corresponding perturbation due to the lateral inhomogeneities (called the scattered wave field). The convention for the superscripts m and s will be used in what follows without further indication. Since the linear operator $\mathcal{L}$ is a function of the elastic parameters of the laterally inhomogeneous layer, it may also be expanded as a Taylor series with respect to the corresponding mean elastic parameters, i.e.,

$$\mathcal{L} = \mathcal{L}^m + \epsilon\mathcal{L}^s + O(\epsilon^2) \tag{5}$$

where $\mathcal{L}^m$ denotes the mean linear operator, characterizing the layered half-space without the lateral inhomogeneities; $\epsilon\mathcal{L}^s$ stands for the first-order scattered linear operator due to the lateral inhomogeneities; and $O(\epsilon^2)$ denotes the order of ϵ^2 and may be neglected in the study, since the first-order perturbation approach (Born approximation) is considered adequate to reveal the fundamental characteristics of the seismic waves in the earth medium with slight lateral inhomogeneities.

Substituting Eqs. (3)–(5) into Eq. (1) and neglecting the second and higher order of smallness ϵ, the following two sets of equations instead of one for the original problem (i.e., Eq. (1)) can be found as

$$\mathcal{L}^m\{\mathbf{u}^m(x, y, z, t)\} = \mathbf{p}^m(x, y, z, t) \tag{6}$$

and

$$\mathcal{L}^m\{\mathbf{u}^s(x, y, z, t)\} = \mathbf{p}^s(x, y, z, t) \tag{7}$$

in which

$$\mathbf{p}^s(x, y, z, t) = \begin{cases} -\mathcal{L}^s\{\mathbf{u}^m(x, y, z, t)\}; & z_{j-1} \le z \le z_j \\ 0; \quad z_{j-1} < z \quad \text{or} \quad z > z_j. \end{cases} \tag{8}$$

The physical meanings of Eqs. (6) and (7) are quite apparent and can be explained as follows. Both the mean ($\mathbf{u}^m$) and the scattered ($\mathbf{u}^s$) wave fields share the same linear operator $\mathcal{L}^m$, which indicates they should be computed on the basis of the same layered half-space without the lateral inhomogeneities. The mean wave field ($\mathbf{u}^m$) is obtained first from Eq. (6) with a series of double couples of body forces $\mathbf{p}^m$ distributed on the seismic fault in source layer k, which are equivalent to the seismic dislocation $\Delta\mathbf{u}$ (cf. Eq. (2)). The scattered wave field ($\mathbf{u}^s$) can then be found from Eq. (7) with distributed fictitious body forces $\mathbf{p}^s$ in the layer that is originally laterally inhomogeneous, which are computed in terms of the mean wave field $\mathbf{u}^m$ and the quantities of the lateral inhomogeneities involved in the operator $\mathcal{L}^s$ (cf. Eq. (8)) and have equivalent effects of the lateral inhomogeneities. The total wave field in a layered half-

Downloaded 04 May 2010 to 171.66.16.34. Redistribution subject to ASME license or copyright; see http://www.asme.org/terms/Terms_Use.cfm

space with laterally inhomogeneities may finally be obtained as a superposition of these two fields from Eq. (4).

3 Equivalent Body Forces for Both Wave Fields

With a proper mathematical manipulation, one can find the equivalent body forces for both mean and scattered wave fields as follows.

3.1 Mean Wave Field. The mean wave field is generated by the seismic dislocation source in the layered half-space in which no lateral inhomogeneities exist. The equivalent body forces $\mathbf{p}^m$ can be represented by the seismic moment components, which are related to the seismic dislocation quantities. In particular, for a point seismic source equivalent to a dislocation $\Delta\mathbf{u}$ on the subfault area centered at location (x_s, y_s, z_s) and activated at time t_s, the double couple of body forces can be found as (Aki and Richards, 1980)

$$p_x^m(x, y, z, t) = \sum_{\zeta=x,y,z} \frac{\partial[M_{x\zeta}(t - t_s)\delta(x - x_s)\delta(y - y_s)\delta(z - z_s)]}{\partial\zeta} \quad (9)$$

$$p_y^m(x, y, z, t) = \sum_{\zeta=x,y,z} \frac{\partial[M_{y\zeta}(t - t_s)\delta(x - x_s)\delta(y - y_s)\delta(z - z_s)]}{\partial\zeta} \quad (10)$$

$$p_z^m(x, y, z, t) = \sum_{\zeta=x,y,z} \frac{\partial[M_{z\zeta}(t - t_s)\delta(x - x_s)\delta(y - y_s)\delta(z - z_s)]}{\partial\zeta} \quad (11)$$

where $M_{\zeta_1,\zeta_2}(\zeta_1, \zeta_2 = x, y, z)$ are the seismic moment components and can be found in terms of the dislocation quantities in Appendix A.

3.2 Scattered Wave Field. The scattered wave field is generated by the fictitious body forces in layer j in the layered half-space in which no lateral inhomogeneities exist. The double couple of body forces $\mathbf{p}^m$, which are equivalent to the seismic dislocation source, no longer exists in layer k since it has been accounted for in determining the mean wave field. However, fictitious body forces $\mathbf{p}^s$ for the scattered wave field, which are equivalent to the effects of the existence of lateral inhomogeneities in layer j, can be found as

$$\begin{aligned} p_x^s = {} & \lambda_{j,x}^s(u_{x,x}^m + u_{y,y}^m + u_{z,z}^m) + 2\mu_{j,x}^s u_{x,x}^m \\ & + \lambda_j^s(u_{x,xx}^m + u_{y,xy}^m + u_{z,xz}^m) + 2\mu_j^s u_{x,xx}^m + \mu_{j,y}^s(u_{x,y}^m + u_{y,x}^m) \\ & + \mu_j^s(u_{x,yy}^m + u_{y,xy}^m) + \mu_j^s(u_{x,zz}^m + u_{z,xz}^m) - \rho_j^s u_{x,tt}^m \end{aligned} \quad (12)$$

$$\begin{aligned} p_y^s = {} & \lambda_{j,y}^s(u_{x,x}^m + u_{y,y}^m + u_{z,z}^m) + 2\mu_{j,y}^s u_{y,y}^m \\ & + \lambda_j^s(u_{x,xy}^m + u_{y,yy}^m + u_{z,yz}^m) + 2\mu_j^s u_{y,yy}^m + \mu_{j,x}^s(u_{x,y}^m + u_{y,x}^m) \\ & + \mu_j^s(u_{x,xy}^m + u_{y,xx}^m) + \mu_j^s(u_{y,zz}^m + u_{z,yz}^m) - \rho_j^s u_{y,tt}^m \end{aligned} \quad (13)$$

$$\begin{aligned} p_z^s = {} & \lambda_j^s(u_{x,xz}^m + u_{y,yz}^m + u_{z,zz}^m) + 2\mu_j^s u_{z,zz}^m \\ & + \mu_{j,x}^s(u_{x,z}^m + u_{z,x}^m) + \mu_j^s(u_{x,xz}^m + u_{z,xx}^m) + \mu_{j,y}^s(u_{y,z}^m + u_{z,y}^m) \\ & + \mu_j^s(u_{y,yz}^m + u_{z,yy}^m) - \rho_j^s u_{z,tt}^m \end{aligned} \quad (14)$$

where λ and μ are two Lame constants which are related to parameters α, β and ρ, $u_{x,y}$ stands for $\partial u_x/\partial y$, etc., for the other similar symbols. It can be seen from Eqs. (12)–(14) that the equivalent body forces are dependent upon the quantities of lateral inhomogeneities such as deviations of elastic parameters and their derivatives (such as λ_j^s and $\lambda_{j,x}^s$) and upon the responses in the mean wave field (such as $u_{x,x}^m$).

4 Solution for the Total Wave Field

The response solution for the total wave field can be found if the responses in both the mean and the scattered wave fields are obtained. The latter can be solved with the aid of the well-developed integral transform approach and wave propagation technique. Typical associated work in the last decade may be mentioned of Bouchon (1981, 1987), Apsel and Luco (1983), Luco and Apsel (1983), Olson et al. (1984), Luco and Wong (1987), Korn (1987), Deodatis et al. (1990a, b), and Zhang et al. (1991a, b), among others. In this section, following Dunkins (1967), Bouchon (1987), Chouet (1987), and Deodatis et al. (1990), the explicit expressions for the responses in both the mean and the scattered wave fields at any level z, especially at ground surface $z = z_0$, are derived.

4.1 Decomposition of Total Wave Field. The d-direction displacement field ($d = x, y, z$) may have the following integral representation

$$u_d(x, y, z, t) = \int_{-\infty}^{\infty}\int_{-\infty}^{\infty}\int_{-\infty}^{\infty} \tilde{u}_d(\kappa_x, \kappa_y, z, \omega) \times \exp[-i\kappa_x x - i\kappa_y y + i\omega t]d\kappa_x d\kappa_y d\omega \quad (15)$$

where κ_x and κ_y are the wave numbers in the x and y-directions, respectively. Revoking equation (4), one may find $\tilde{u}_d = \tilde{u}_d^m + \epsilon\tilde{u}_d^s$. The displacements in the frequency wave number domain in the coordinate system (x, y, z) may be further transformed to those in a new coordinate system (x', y', z') as follows:

$$\tilde{u}_x^\eta = \frac{\kappa_x}{\kappa}\tilde{u}_{x'}^\eta - \frac{\kappa_y}{\kappa}\tilde{u}_{y'}^\eta; \quad \tilde{u}_y^\eta = \frac{\kappa_y}{\kappa}\tilde{u}_{x'}^\eta + \frac{\kappa_x}{\kappa}\tilde{u}_{y'}^\eta; \quad \tilde{u}_z^\eta = \tilde{u}_{z'}^\eta \quad (16)$$

where $\eta = m$ or s and $\kappa = \sqrt{\kappa_x^2 + \kappa_y^2}$. The transformation of the coordinates such as Eq. (16) is nothing but for simplifying the analysis of wave propagation in a layered half-space. It can be shown (e.g., Aki and Richards, 1980; Bouchon, 1987) that $\tilde{u}_{x'}^\eta$ and $\tilde{u}_{z'}^\eta$ are related to the *P-SV* wave motion and $\tilde{u}_{y'}^\eta$ to the *SH* wave motion in the mean ($\eta = m$) or in the scattered ($\eta = s$) wave field. Both *P-SV* and *SH* wave propagation in the layered half-space can be separately analyzed in the following two sections.

4.2 Response in the Mean Wave Field. Introducing state vector $\mathbf{S}$ as

$$\mathbf{S}_{i;P\text{-}SV}^m(z) \equiv \begin{Bmatrix} \mathbf{u}_{i;P\text{-}SV}^m(z) \\ \mathbf{s}_{i;P\text{-}SV}^m(z) \end{Bmatrix} = \{\tilde{u}_{x'}^m(z) \quad \tilde{u}_{z'}^m(z) \quad \tilde{\sigma}_{z'z'}^m(z) \quad \tilde{\sigma}_{z'x'}^m(z)\}^T \quad (17)$$

$$\mathbf{S}_{i;SH}^m(z) \equiv \begin{Bmatrix} \mathbf{u}_{i;SH}^m(z) \\ \mathbf{s}_{i;SH}^m(z) \end{Bmatrix} = \{\tilde{u}_{y'}^m(z) \quad \tilde{\sigma}_{z'y'}^m(z)\}^T \quad (18)$$

and wave vector $\mathbf{\Phi}$ as

$$\mathbf{\Phi}_{i;P\text{-}SV}^m(z) \equiv \begin{Bmatrix} \mathbf{w}_{i;P\text{-}SV;+}^m(z) \\ \mathbf{w}_{i;P\text{-}SV;-}^m(z) \end{Bmatrix} = \{\phi_{i;P;+}^m(z) \quad \psi_{i;SV;+}^m(z) \quad \phi_{i;P;-}^m(z) \quad \psi_{i;SV;-}^m(z)\}^T \quad (19)$$

Downloaded 04 May 2010 to 171.66.16.34. Redistribution subject to ASME license or copyright; see http://www.asme.org/terms/Terms_Use.cfm

$$\mathbf{\Phi}^m_{i;SH}(z) \equiv \begin{Bmatrix} \mathbf{w}^m_{i;SH;+}(z) \\ \mathbf{w}^m_{i;SH;-}(z) \end{Bmatrix} = \{\psi^m_{i;SH;+}(z) \quad \psi^m_{i;SH;-}(z)\}^T \quad (20)$$

In Eq. (17)–(20), symbol $\equiv$ denotes "by definition"; subscript i denotes layer number, indicating the state or wave vector at level z is in layer i; subscripts P, SV, P-SV and SH denote the quantities associated with P, SV, P-SV and SH wave motion, respectively; subscripts + and − denotes the up-going and down-going waves, respectively; and ϕ and ψ denote, respectively, P and S wave potentials.

4.2.1 Wave Motion in the Layer Without Source and Pertinent Conditions. The governing equation of motion in layer i without the existence of body forces can be solved in the frequency wave number domain $(\kappa_x, \kappa_y, \omega)$, leading to

$$\mathbf{\Phi}^m_{i;\zeta}(z) = \mathbf{E}_{i;\zeta}(z - z_{i-1})\mathbf{\Phi}^m_{i;\zeta}(z_{i-1}) \quad (21)$$

where the state and the wave vectors are related by

$$\mathbf{S}^m_{i;\zeta}(z) = \mathbf{T}_{i;\zeta}\mathbf{\Phi}^m_{i;\zeta}(z); \quad \mathbf{\Phi}^m_{i;\zeta}(z) = \mathbf{T}^{-1}_{i;\zeta}\mathbf{S}^m_{i;\zeta}(z) \quad (22)$$

In Eqs. (21) and (22), subscript ζ stands for either P-SV or SH, and the expressions for matrices $\mathbf{E}_{i;\zeta}$, $\mathbf{T}_{i;\zeta}$ and $\mathbf{T}^{-1}_{i;\zeta}$ are provided in Appendix B. The relation between two state vectors in the same layer can thus be obtained with the use of Eqs. (21) and (22), i.e.,

$$\mathbf{S}^m_{i;\zeta}(z) = \mathbf{G}_{i;\zeta}(z - z_{i-1})\mathbf{S}^m_{i;\zeta}(z_{i-1}) \equiv \mathbf{T}_{i;\zeta}\mathbf{E}_{i;\zeta}(z - z_{i-1})\mathbf{T}^{-1}_{i;\zeta}\mathbf{S}^m_{i;\zeta}(z_{i-1}) \quad (23)$$

The pertinent conditions are continuity condition at each layer-to-layer interface which is

$$\mathbf{S}^m_{i;\zeta}(z_i) = \mathbf{S}^m_{i+1;\zeta}(z_i); \quad i = 1, 2, \ldots, n-1 \quad (24)$$

the boundary condition at ground surface ($z = z_0$) which is no traction, i.e.,

$$\mathbf{S}^m_{1;\zeta}(z_0) = \{\mathbf{u}^m_{1;\zeta}(z_0) \quad \mathbf{s}^m_{1;\zeta}(z_0) = \mathbf{0}\}^T \quad (25)$$

and the boundary condition at infinite depth which implies no up-going waves from the infinite depth, i.e.,

$$\mathbf{\Phi}^m_{n;\zeta}(z) = \{\mathbf{w}^m_{n;\zeta;+}(z) = \mathbf{0} \quad w^m_{n;\zeta;-}(z)\}^T; \quad z > \max(z^*_s, z_{n-1}) \quad (26)$$

where z^*_s is the deepest depth of the seismic source.

4.2.2 Full Space Solution $\hat{\mathbf{S}}^m_{k;\zeta}$ of Response to Source Only. A seismic dislocation source buried in layer k can always be decomposed into a series of double couples of body forces, each of which acts at the lth subfault centered at (x^l_s, y^l_s, z^l_s) and activated at t^l_s, $l = 1, 2, \ldots, L$. Then following Deodatis et al. (1990) and Bouchon (1987), one may find

$$\{\hat{\mathbf{S}}^m_{k;\zeta}(z)\} = \begin{Bmatrix} \mathbf{T}^{11}_{k;\zeta} \\ \mathbf{T}^{21}_{k;\zeta} \end{Bmatrix} \sum_{l=1}^{L} [E^{11}_{k;\zeta}(z - z^l_s)\hat{\mathbf{w}}^m_{k;\zeta;+}(z^l_s)]; \quad z < \min(z^1_s, \ldots, z^L_s) \quad (27)$$

$$\{\hat{\mathbf{S}}^m_{k;\zeta}(z)\} = \begin{Bmatrix} \mathbf{T}^{12}_{k;\zeta} \\ \mathbf{T}^{22}_{k;\zeta} \end{Bmatrix} \sum_{l=1}^{L} [E^{22}_{k;\zeta}(z - z^l_s)\hat{\mathbf{w}}^m_{k;\zeta;-}(z^l_s)]; \quad z > \max(z^1_s, \ldots, z^L_s) \quad (28)$$

where

$$\begin{Bmatrix} \hat{\mathbf{w}}^m_{k;P\text{-}SV;+}(z^l_s) \\ \cdots\cdots\cdots \\ \hat{\mathbf{w}}^m_{k;SH;+}(z^l_s) \end{Bmatrix} \equiv \begin{Bmatrix} \hat{\phi}^m_{k;P;+}(z^l_s) \\ \hat{\psi}^m_{k;SV;+}(z^l_s) \\ \cdots\cdots\cdots \\ \hat{\psi}^m_{k;SH;+}(z^l_s) \end{Bmatrix} = \frac{1}{8\pi^3}\frac{i}{2\rho_k\omega^2}\exp[i\kappa_x x^l_s + i\kappa_y y^l_s]$$

$$\times \begin{bmatrix} \frac{2\kappa_x\kappa_y}{\nu_k} & -2\kappa_x & \vdots & \frac{\kappa_y^2}{\nu_k} & \nu_k & -2\kappa_y \\ \frac{2\kappa_x\kappa_y}{\kappa} & \frac{\kappa_x(\kappa^2-\gamma_k^2)}{\kappa\gamma_k} & \vdots & \frac{\kappa_y^2}{\kappa} & -\kappa & \frac{\kappa_y(\kappa^2-\gamma_k^2)}{\kappa\gamma_k} \\ \cdots\cdots & \cdots\cdots & \cdots & \cdots\cdots & \cdots & \cdots\cdots \\ \frac{i(\kappa^2+\gamma_k^2)(\kappa_y^2-\kappa_x^2)}{\kappa\gamma_k} & -\frac{i\kappa_y(\kappa^2+\gamma_k^2)}{\kappa} & \vdots & -\frac{i\kappa_x\kappa_y(\kappa^2+\gamma_k^2)}{\kappa\gamma_k} & 0 & \frac{i\kappa_x(\kappa^2+\gamma_k^2)}{\kappa} \end{bmatrix} \begin{Bmatrix} \tilde{M}^l_{xy} \\ \tilde{M}^l_{xz} \\ \cdots \\ \tilde{M}^l_{yy} \\ \tilde{M}^l_{zz} \\ \tilde{M}^l_{yz} \end{Bmatrix} \quad (29)$$

$$\begin{Bmatrix} \hat{\mathbf{w}}^m_{k;P\text{-}SV;-}(z^l_s) \\ \cdots\cdots\cdots \\ \hat{\mathbf{w}}^m_{k;SH;-}(z^l_s) \end{Bmatrix} \equiv \begin{Bmatrix} \hat{\phi}^m_{k;P;-}(z^l_s) \\ \hat{\psi}^m_{k;SV;-}(z^l_s) \\ \cdots\cdots\cdots \\ \hat{\psi}^m_{k;SH;-}(z^l_s) \end{Bmatrix} = \frac{1}{8\pi^3}\frac{i}{2\rho_k\omega^2}\exp[i\kappa_x x^l_s + i\kappa_y y^l_s]$$

$$\times \begin{bmatrix} \frac{2\kappa_x\kappa_y}{\nu_k} & 2\kappa_x & \vdots & \frac{\kappa_y^2}{\nu_k} & \nu_k & 2\kappa_y \\ -\frac{2\kappa_x\kappa_y}{\kappa} & \frac{\kappa_x(\kappa^2-\gamma_k^2)}{\kappa\gamma_k} & \vdots & -\frac{\kappa_y^2}{\kappa} & \kappa & \frac{\kappa_y(\kappa^2-\gamma_k^2)}{\kappa\gamma_k} \\ \cdots\cdots & \cdots\cdots & \cdots & \cdots\cdots & \cdots & \cdots\cdots \\ \frac{i(\kappa^2+\gamma_k^2)(\kappa_y^2-\kappa_x^2)}{\kappa\gamma_k} & \frac{i\kappa_y(\kappa^2+\gamma_k^2)}{\kappa} & \vdots & -\frac{i\kappa_x\kappa_y(\kappa^2+\gamma_k^2)}{\kappa\gamma_k} & 0 & -\frac{i\kappa_x(\kappa^2+\gamma_k^2)}{\kappa} \end{bmatrix} \begin{Bmatrix} \tilde{M}^l_{xy} \\ \tilde{M}^l_{xz} \\ \cdots \\ \tilde{M}^l_{yy} \\ \tilde{M}^l_{zz} \\ \tilde{M}^l_{yz} \end{Bmatrix}. \quad (30)$$

Downloaded 04 May 2010 to 171.66.16.34. Redistribution subject to ASME license or copyright; see http://www.asme.org/terms/Terms_Use.cfm

In Eqs. (27)–(30), $\mathbf{T}^{ij}_{k;\zeta}$ and $\mathbf{E}^{ij}_{k;\zeta}$ $(i, j = 1, 2)$ are the submatrices of $\mathbf{T}_{k;\zeta}$ and $\mathbf{E}_{k;\zeta}$, as shown in Appendix B, and all the quantities associated with a hat, such as $\hat{\phi}$, denote the corresponding quantities generated by the source only in the associated full space. The physical meanings of Eqs. (27)–(30) can be explained as follows. For example, $\hat{\phi}^m_{k;P+}(z^l_s)$ and $\hat{\psi}^m_{k;SV;+}(z^l_s)$ are the magnitudes of up-going P and SV waves at level z^l_s, generated by the lth seismic moment vector through Eq. (29). The lth seismic moment vector is related to the seismic source at the lth subfault area (see Appendix A). The product of $\mathbf{E}_{k;P\text{-}SV}(z - z^l_s)$ and $\hat{\mathbf{w}}^m_{k;\text{P-SV}}(z^l_s)$ in Eq. (27) or (28) indicates that those generated up or down-going P-SV waves propagate from level z^l_s to z. Summation in Eq. (27) or (28) is used to take into account all the contribution of a series of double couples of body forces (or seismic moment vectors) to the up or down-going waves at level z. Finally, submatrix of $\mathbf{T}_{k;\zeta}$ in Eq. (27) or (28) is used to transform the wave vector into the state vector.

4.2.3 Response in a Layered Half-Space to the Source. In source layer k, Eq. (21) no longer holds since there exists source (equivalent body forces). However, after subtracting the source effects from the original state vector, Eq. (21) can still hold. In particular, Eq. (21) holds only if Eq. (22) is replaced by

$$\mathbf{\Phi}^m_{k;\zeta}(z) = \mathbf{T}^{-1}_{k;\zeta}[\mathbf{S}^m_{k;\zeta}(z) - \hat{\mathbf{S}}^m_{k;\zeta}(z)]; \quad z_{k-1} \le z \le z_k. \quad (31)$$

Substituting Eq. (31) into both sides of Eq. (21) and repeatedly using Eqs. (23) and (24), one may obtain

$$\begin{aligned}\mathbf{T}^{-1}_{k;\zeta}&[[\mathbf{G}_{n-1;\zeta}(h_{n-1}) \ldots \mathbf{G}_{k+1;\zeta}(h_{k+1})]^{-1} \\ &\times \mathbf{T}_{n;\zeta}\mathbf{\Phi}^m_{n;\zeta}(z_{n-1}) - \hat{\mathbf{S}}^m_{s;\zeta}(z_k)] \\ &= \mathbf{E}_{k;\zeta}(h_k)\mathbf{T}^{-1}_{k;\zeta}[\mathbf{G}_{k-1;\zeta}(h_{k-1}) \ldots \\ &\qquad \mathbf{G}_{1;\zeta}(h_1)\mathbf{S}_{1;\zeta}(z_0) - \hat{\mathbf{S}}^m_{k;\zeta}(z_{k-1})] \quad (32)\end{aligned}$$

With the aid of the boundary conditions in Eqs. (25) and (26), the displacement response $\mathbf{u}_{1;\zeta}$ at ground surface z_0 can then be found from the above equation as

$$\begin{aligned}\mathbf{u}^m_{1;\zeta}(z_0) = \mathbf{R}^{-1}_{11;\zeta}&[\mathbf{P}_{11;\zeta} \quad \mathbf{P}_{12;\zeta}](\hat{\mathbf{S}}^m_{k;\zeta}(z_{k-1}) \\ &- \mathbf{G}^{-1}_{k;\zeta}(h_k)\hat{\mathbf{S}}^m_{k;\zeta}(z_k)) \quad (33)\end{aligned}$$

where

$$[\mathbf{P}_\zeta] \equiv \begin{bmatrix}\mathbf{P}_{11;\zeta} & \mathbf{P}_{12;\zeta} \\ \mathbf{P}_{21;\zeta} & \mathbf{P}_{22;\zeta}\end{bmatrix} = \mathbf{T}^{-1}_{n;\zeta}\mathbf{G}_{n-1;\zeta}(h_{n-1}) \ldots \mathbf{G}_{k;\zeta}(h_k) \quad (34)$$

$$[\mathbf{R}_\zeta] \equiv \begin{bmatrix}\mathbf{R}_{11;\zeta} & \mathbf{R}_{12;\zeta} \\ \mathbf{R}_{21;\zeta} & \mathbf{R}_{22;\zeta}\end{bmatrix} = \mathbf{T}^{-1}_{n;\zeta}\mathbf{G}_{n-1;\zeta}(h_{n-1}) \ldots \mathbf{G}_{1;\zeta}(h_1). \quad (35)$$

As a special case, consider the source is in the half-space ($k = n$). Substituting Eq. (31) into the right-hand side of Eq. (21) and repeatedly using Eqs. (23) and (24), one may obtain the following equation instead of Eq. (32):

$$\begin{aligned}\mathbf{\Phi}^m_{n;\zeta}(z) = \mathbf{E}_{n;\zeta}&(z - z_{n-1})\mathbf{T}^{-1}_{n;\zeta}[\mathbf{G}_{n-1;\zeta}(h_{n-1}) \ldots \\ &\mathbf{G}_{1;\zeta}(h_1)\mathbf{S}^m_{1;\zeta}(z_0) - \hat{\mathbf{S}}^m_{n;\zeta}(z_{n-1})] \quad (36)\end{aligned}$$

where $z > \max(z^1_s, z^2_s, \ldots, z^L_s)$. The corresponding response at the ground surface can then be found from the above equation, which can be cast in the same form as Eq. (33) with $\hat{\mathbf{S}}^m_{k;\zeta}(z_k) = \mathbf{0}$ and $\mathbf{P}_\zeta$ is degenerated to $\mathbf{T}^{-1}_{n;\zeta}$.

It is noted that Dunkin's technique has to be applied in evaluating $\mathbf{R}^{-1}_{11;P\text{-}SV}$ in Eq. (33). Otherwise, numerical problems will arise.

As long as the ground motion $\mathbf{S}^m_{1;\zeta}(z_0) = \{\mathbf{u}^m_{1;\zeta}(z_0) \; \mathbf{s}^m_{1;\zeta}(z_0) = \mathbf{0}\}^T$ is obtained, the response at any level z can be obtained by repeatedly using Eq. (23). Finally, the mean wave response in both frequency wave number domain and time-space domain, i.e., $\tilde{u}_d$ and u_d, can be found with the use of Eqs. (16) and (15).

4.3 Response in the Scattered Wave Fields. As shown in Section 3, the only difference between the mean and the scattered wave fields is the source term. The former is a series of double couples of body forces buried in layer k, while the latter is fictitious body forces distributed in layer j. Therefore, the analytical expression and formulae presented in the last subsection can totally be used in the analysis of wave propagation and response in the scattered wave field with the superscript m and subscript k replaced by s and j, respectively, except the full space solution of response to source, which is discussed below.

Using the integral transform and Eqs. (15)–(18), one may find the fictitious body forces in the frequency wave number domain as

$$\begin{aligned}\begin{Bmatrix}\tilde{p}^s_x(\kappa_x, \kappa_y, z, \omega) \\ \tilde{p}^s_y(\kappa_x, \kappa_y, z, \omega) \\ \tilde{p}^s_z(\kappa_x, \kappa_y, z, \omega)\end{Bmatrix} &= \int_{-\infty}^{\infty}\int_{-\infty}^{\infty}[\tilde{\mathbf{A}}(\tilde{\zeta}^s_j)] \\ &\times \begin{Bmatrix}\mathbf{S}^m_{j;P\text{-}SV}(\kappa_x - \kappa'_x, \kappa_y - \kappa'_y, z, \omega) \\ \cdots\cdots\cdots\cdots \\ \mathbf{S}^m_{j;SH}(\kappa_x - \kappa'_x, \kappa_y - \kappa'_y, z, \omega)\end{Bmatrix} d\kappa'_x d\kappa'_y \quad (37)\end{aligned}$$

where $\tilde{\zeta}^s_j$ ($\zeta = \alpha, \beta$ or ρ) are the corresponding form of ζ^s_j in the wave number domain, i.e.,

$$\begin{aligned}\zeta^s_j(x, y) = \int_{-\infty}^{\infty}\int_{-\infty}^{\infty}&\tilde{\zeta}^s_j(\kappa'_x, \kappa'_y) \\ &\times \exp[-i\kappa'_x x - i\kappa'_y y]d\kappa'_x d\kappa'_y. \quad (38)\end{aligned}$$

With the aid of some mathematical manipulations and the fundamental solution to the sinusoidal body force derived by Deodatis et al. (1990), the response solution in full space due to the fictitious body forces in the frequency wave number domain (Eq. (37)) can then be found as follows:

$$\{\hat{\mathbf{S}}^s_{j;\zeta}(z_{j-1})\} = \begin{Bmatrix}\mathbf{T}^{11}_{j;\zeta} \\ \mathbf{T}^{21}_{j;\zeta}\end{Bmatrix}\int_{z_{j-1}}^{z_j}[\mathbf{E}^{11}_{k;\zeta}(z_{j-1} - z)\hat{\mathbf{w}}^s_{j;\zeta;+}(z)]dz \quad (39)$$

$$\{\hat{\mathbf{S}}^s_{j;\zeta}(z_j)\} = \begin{Bmatrix}\mathbf{T}^{12}_{j;\zeta} \\ \mathbf{T}^{22}_{j;\zeta}\end{Bmatrix}\int_{z_{j-1}}^{z_j}[\mathbf{E}^{22}_{j;\zeta}(z_j - z)\hat{\mathbf{w}}^m_{j;\zeta;-}(z)]dz \quad (40)$$

where

$$\begin{aligned}\begin{Bmatrix}\hat{\mathbf{w}}^s_{j;P\text{-}SV;\pm}(\kappa_x, \kappa_y, z, \omega) \\ \cdots\cdots\cdots\cdots \\ \hat{\mathbf{w}}^s_{j;SH;\pm}(\kappa_x, \kappa_y, z, \omega)\end{Bmatrix} &\equiv \begin{Bmatrix}\hat{\phi}^s_{j;P;\pm}(z) \\ \hat{\psi}^s_{j;SV;\pm}(z) \\ \cdots\cdots \\ \hat{\psi}^s_{j;SH;\pm}(z)\end{Bmatrix} \\ = \int_{-\infty}^{\infty}\int_{-\infty}^{\infty}&\begin{bmatrix}\mathbf{C}^{\pm}_{11} & \vdots & \mathbf{C}^{\pm}_{12} \\ \cdots & \cdots & \cdots \\ \mathbf{C}^{\pm}_{21} & \vdots & \mathbf{C}^{\pm}_{22}\end{bmatrix} \\ &\times \begin{Bmatrix}\mathbf{S}^m_{j;P\text{-}SV}(\kappa_x - \kappa'_x, \kappa_y - \kappa'_y, z, \omega) \\ \cdots\cdots\cdots\cdots \\ \mathbf{S}^m_{j;SH}(\kappa_x - \kappa'_x, \kappa_y - \kappa'_y, z, \omega)\end{Bmatrix} d\kappa'_x d\kappa'_y \quad (41)\end{aligned}$$

Downloaded 04 May 2010 to 171.66.16.34. Redistribution subject to ASME license or copyright; see http://www.asme.org/terms/Terms_Use.cfm

and

$$[\mathbf{C}^{\pm}(\kappa_x, \kappa_y, \kappa_x', \kappa_y', \omega)] \equiv \begin{bmatrix} \mathbf{C}_{11}^{\pm} & \vdots & \mathbf{C}_{12}^{\pm} \\ \cdots & \cdots & \cdots \\ \mathbf{C}_{21}^{\pm} & \vdots & \mathbf{C}_{22}^{\pm} \end{bmatrix}$$

$$\equiv \begin{bmatrix} c_{11}^{\pm} & c_{12}^{\pm} & c_{13}^{\pm} & c_{14}^{\pm} & \vdots & c_{15}^{\pm} & c_{16}^{\pm} \\ c_{21}^{\pm} & c_{22}^{\pm} & c_{23}^{\pm} & c_{24}^{\pm} & \vdots & c_{25}^{\pm} & c_{26}^{\pm} \\ \cdots & \cdots & \cdots & \cdots & \cdots & \cdots & \cdots \\ c_{31}^{\pm} & c_{32}^{\pm} & c_{33}^{\pm} & c_{34}^{\pm} & \vdots & c_{35}^{\pm} & c_{36}^{\pm} \end{bmatrix}. \quad (42)$$

In Eq. (42), coefficients $c_{ij}^{\pm}$ are given in Appendix C. As seen in Eq. (41), the up or down-going scattered *P-SV* waves at level $z(\hat{\mathbf{w}}_{j;P\text{-}SV;\pm}^{s})$ are generated by both the mean *P-SV* wave field ($\mathbf{S}_{j;P\text{-}SV}^{m}$) and the mean *SH* wave field ($\mathbf{S}_{j;SH}^{m}$). So are the scattered *SH* waves ($\hat{\mathbf{w}}_{j;SH;\pm}^{s}$). Consequently, the state vector of the scattered wave motion $\hat{\mathbf{S}}_{j;P\text{-}SV}^{s}(\hat{\mathbf{S}}_{j;SH}^{s})$ is related to both the mean *P-SV* and *SH* wave motion. Thus, the existence of an inhomogeneous layer causes the coupling between the total *P-SV* wave field and the *SH* wave field unless all the cross coupling terms can be neglected, i.e., all the elements in $[\mathbf{C}_{12}^{\pm}]$ and $[\mathbf{C}_{21}^{\pm}]$ are much smaller than those in $[\mathbf{C}_{11}^{\pm}]$ and $[\mathbf{C}_{22}^{\pm}]$. Equation (41) also reveals that, for the lateral inhomogeneities with given wave number pair (κ_x', κ_y'), the spectral level of the scattered wave at the wave number pair (κ_x, κ_y) is related to the spectral level of the mean wave at the wave number pair $(\kappa_x - \kappa_x', \kappa_y - \kappa_y')$. Therefore, the lateral inhomogeneities give rise to the shifting effects from the mean wave field to the scattered wave field in the wave number domain. These two properties will be further investigated in the companion paper (Zhang et al., 1997).

With the use of Equation (23), i.e.,

$$\mathbf{S}_{j;\zeta}^{m}(z) = \mathbf{G}_{j;\zeta}\mathbf{S}_{j;\zeta}^{m}(z_{j-1}) \equiv \mathbf{T}_{j;\zeta}\mathbf{E}_{j;\zeta}(z - z_{j-1})\mathbf{T}_{j;\zeta}^{-1}\mathbf{S}_{j;\zeta}^{m}(z_{j-1}) \quad (43)$$

Eqs. (39)–(42) can be further simplified to

$$\{\hat{\mathbf{S}}_{j;\zeta}^{s}(z_{j-1})\} = \begin{Bmatrix} \mathbf{T}_{j;\zeta}^{11} \\ \mathbf{T}_{j;\zeta}^{21} \end{Bmatrix}\hat{\mathbf{v}}_{\zeta;+}; \quad \{\hat{\mathbf{S}}_{j;\zeta}^{s}(z_j)\} = \begin{Bmatrix} \mathbf{T}_{j;\zeta}^{12} \\ \mathbf{T}_{j;\zeta}^{22} \end{Bmatrix}\hat{\mathbf{v}}_{\zeta;-} \quad (44)$$

where

$$\begin{Bmatrix} \hat{\mathbf{v}}_{P\text{-}SV;\pm} \\ \cdots\cdots \\ \hat{\mathbf{v}}_{SH;\pm} \end{Bmatrix} = \int_{-\infty}^{\infty}\int_{-\infty}^{\infty} \begin{bmatrix} \mathbf{B}_{11}^{\pm} & \vdots & \mathbf{B}_{12}^{\pm} \\ \cdots & \cdots & \cdots \\ \mathbf{B}_{21}^{\pm} & \vdots & \mathbf{B}_{22}^{\pm} \end{bmatrix} \times \begin{Bmatrix} \mathbf{S}_{j;P\text{-}SV}^{m}(\kappa_x - \kappa_x', \kappa_y - \kappa_y', z_{j-1}, \omega) \\ \cdots\cdots\cdots\cdots\cdots\cdots \\ \mathbf{S}_{j;SH}^{m}(\kappa_x - \kappa_x', \kappa_y - \kappa_y', z_{j-1}, \omega) \end{Bmatrix} d\kappa_x' d\kappa_y' \quad (45)$$

which shows the relationship between the state vectors in the mean and the scattered wave fields. Coefficients of matrices $\mathbf{B}_{ij}^{\pm}$ in Eq. (45) are given in Appendix D.

After obtaining the solution of $\hat{\mathbf{S}}_{j;\zeta}^{s}$ at both z_{j-1} and z_j, the responses in the scattered wave field at any level z is straightforward, as shown in the mean wave field (cf. Section 4.2.1). Mathematically, the response in the scattered wave field can be simply represented by

$$\epsilon\tilde{u}_d^{s}(\kappa_x, \kappa_y, z, \omega) = \int_{-\infty}^{\infty}\int_{-\infty}^{\infty} \tilde{H}_d^{s}(\kappa_x, \kappa_y, z, \omega; \kappa_x', \kappa_y')d\kappa_x' d\kappa_y' \quad (46)$$

where $\tilde{H}_d^{s}$ is the d-direction response solution of the scattered wave field in the frequency wave number domain corresponding to the sinusoidal lateral inhomogeneities described by the form of Eq. (38) without a twofold integral.

On the basis of the present analysis for the response of the scattered wave field, three basic properties for $\tilde{H}_d^{s}$ can thus be obtained.

1 $\tilde{H}_d^{s}$ has the same basic properties as the response of the mean wave field $\tilde{u}_d^{m}$ because both the mean and the scattered wave fields are computed in the same layered half-space.

2 Wave number shifting effects are found between the mean and the scattered wave fields. In particular, $\tilde{H}_d^{s}(\kappa_x, \kappa_y, z, \omega; \kappa_x', \kappa_y')$ is related to, or more strictly speaking, proportional to the frequency wave number response of the mean wave field, i.e., $\tilde{u}_d^{m}(\kappa_x - \kappa_x', \kappa_y - \kappa_y', z, \omega)$.

3 Both the mean *P-SV* wave response and the mean *SH* wave response contribute toward the *P-SV* scattered wave response, as well as *SH* scattered wave response. Consequently, the *P-SV* waves in a layered half-space with the lateral inhomogeneities are coupled with the *SH* waves, which is reflected in the scattered wave response $\tilde{H}_d^{s}$.

The first two of the above characteristics can also be found by use of a two-dimensional lateral inhomogeneity model. However, the third characteristic can be reached only with the theoretical model of three-dimensional lateral inhomogeneities, which also makes the three-dimensional wave scattering problem fundamentally different from the two-dimensional wave scattering problem. These properties will be discussed in detail in Zhang et al. (1997), which is fundamentally important to estimating quantitatively and qualitatively the effects of the scattered wave response on the corresponding mean wave response, or directly speaking, the effects of the lateral inhomogeneities on the earthquake ground (or underground) motion.

5 Concluding Remarks

A model of three-dimensional wave scattering, generated by a seismic dislocation source in a layered half-space with lateral inhomogeneities, is proposed. The corresponding response is obtained as a superposition of the responses in both the mean and the scattered wave fields with the use of a first-order perturbation approach. It is shown theoretically that the lateral inhomogeneities cause the coupling between *P-SV* and *SH* waves in the total wave field. In particular, both the *P-SV* and *SH* mean waves give the contribution to the *P-SV* or *SH* scattered waves. The effects of the lateral inhomogeneities on the seismic wave motion will be presented in the companion paper (Zhang et al. 1997).

Acknowledgments

This work was supported by the National Center for Earthquake Engineering Research under Grant NCEER 94-3302A. The opinions, findings, and conclusions expressed herein are those of the writers and do not necessarily reflect the views of ther sponsors.

References

Aki, K., 1975, "Original of coda waves: source, attenuation, and scattering effects," *Journal of Geophysical Research,* Vol. 80, pp. 3322–3342.

Aki, K., and Richards, P. G., 1980, *Quantitative Seismology—Theory and Methods,* W. H. Freeman, San Francisco, CA.

Apsel, R. J., and Luco, J. E., 1983, "On the Green's function for a layered half-space, Part II," *Bulletin of the Seismological Society of America,* Vol. 73, No. 4, pp. 931–951.

Askar, A., and Cakmak, A. S., 1988, "Seismic waves in random media," *Probabilistic Engineering Mechanics,* Vol. 3, pp. 124–129.

Bataille, K., and Flatte, S. M., 1988, "Inhomogeneities near the core-mantle boundary inferred from short-period scattered PKP waves recorded at the global digital seismograph network," *Journal of Geoelastic Research,* Vol. 93, No. B12, pp. 15,057–15,064.

Bouchon, M., 1981, "A simple method to calculate Green's functions for elastic layered media," *Bulletin of the Seismological Society of America,* Vol. 71, No. 4, pp. 959–971.

Bouchon, M., 1987, "Discrete wave number representation of elastic wave fields in three-space dimensions," *Journal of Geophysical Research,* Vol. 84, No. B7, pp. 3609–3614.

Downloaded 04 May 2010 to 171.66.16.34. Redistribution subject to ASME license or copyright; see http://www.asme.org/terms/Terms_Use.cfm

Chouet, B., 1987, "Representation of an extented seismic source in a propagator-based formalism," *Bulletin of the Seismological Society of America,* Vol. 77, No. 1, pp. 14–27.

Chow, P. L., 1972, "Applications of function space integral to problems in wave propagation in random media," *J. Math. Phys.,* Vol. 13, No. 8, pp. 1224–1236.

Chow, P. L., 1975, "Perturbation methods in stochastic wave propagation," *SIAM Review,* Vol. 17, No. 1, pp. 57–81.

Chu, L., Askar, A., and Cakmak, S., 1981, "Earthquake waves in a random medium," *International Journal for Numerical and Analytical Methods in Geomechanics,* Vol. 5, pp. 79–96.

Deodatis, G., Shinozuka, M., and Papageorgiou, A. P., 1990a, "Stochastic wave representation of seismic ground motion. I: F-K spectra," *J. Engineering Mechanics,* Vol. 116, No. 11, pp. 2363–2379.

Deodatis, G., Shinozuka, M., and Papageorgiou, A. P., 1990b, "Stochastic wave representation of seismic ground motion. II: Simulation," *J. Engineering Mechanics,* Vol. 116, No. 11, pp. 2381–2399.

Dunkin, J. W., 1965, "Computation of modal solutions in layered, elastic media at high frequencies," *Bulletin of the Seismological Society of America,* Vol. 55, No. 2, pp. 335–358.

Farra, V., and Madariaga, R., 1987, "Seismic waveform modeling in heterogeneous media by ray perturbation theory," *Journal of Geoelastic Research,* Vol. 92, No. B3, pp. 2697–2712.

Kennett, B. L. N., 1972, "Seismic waves in laterally inhomogeneous media," *Geophys. J. R. astr. Soc.,* Vol. 27, pp. 301–325.

Kennett, B. L. N., 1983, *Seismic Wave Propagation in Stratified Media,* Cambridge University Press, Cambridge, U.K.

Korn, M., 1987, "Computation of wave fields in vertically inhomogeneous media by a frequency domain finite-difference method and application to wave propagation in earth models with random velocity and density perturbations," *Geophys. J. R. Astr. Soc.,* Vol. 88, No. 2, pp. 345–377.

Luco, J. E., and Apsel, R. J., 1983, "On the Green's function for a layered half-space, Part I," *Bulletin of the Seismological Society of America,* Vol. 73, No. 4, pp. 909–929.

Luco, J. E., and Wong, H. L., 1987, "Seismic response of foundations embedded in a layered half-space," *Earthquake Engineering and Structural Dynamics,* Vol. 15, pp. 233–247.

Olson, A. H., Orcutt, J. A., and Frazier, G. A., 1984, "The discrete wave number/finite element method for synthetic seismograms," *Geophys. J. R. Astr. Soc.,* Vol. 77, No. 2, pp. 421–460.

Sato, H., 1984, "Attenuation and envelope formation of three-component seismograms of small local earthquakes in randomly inhomogeneous lithosphere," *Journal of Geophysical Research,* Vol. 89, No. B2, pp. 1221–1241.

Sato, H., 1989, "Broadening of seismogram envelopes in the randomly inhomogeneous lithosphere based on the parabolic approximation: southeastern Honshu, Japan," *Journal of Geophysical Research,* Vol. 94, No. B12, pp. 17,735–17,747.

Stauber, D. A., 1985, "Linear inversion of transmitted acoustic wave fields for three-dimensional modulus and density perturbations using a bore-type approximation," *Bulletin of the Seismological Society of America,* Vol. 75, No. 1, pp. 93–114.

Su, F., 1992, "Study of earthquake source, propagation medium attenuation and recording site amplification using coda waves," Ph.D. Dissertation, University of Southern California, Los Angeles, CA.

Weaver, R., 1984, "Waves in random media," *Int. J. Engrg. Sci.,* Vol. 22, No. 8–10, pp. 1149–1157.

Wu, R. S., 1982, "Mean field attenuation and amplitude attenuation due to wave scattering," *Wave Motion,* No. 4, pp. 305–316.

Wu, R. S., and Aki, K., 1985, "Elastic wave scattering by a random medium and the small-scale inhomogeneities in the lithosphere," *Journal of Geoelastic Research,* Vol. 90, No. B12, pp. 10,261–10,273.

Zhang, R., 1992, "Stochastic earthquake ground motion modeling," Ph.D. Dissertation, Florida Atlantic University, Boca Raton, FL.

Zhang, R., 1994, "Stochastic seismic ground motion modeling with imperfectly stratified earth medium," *Journal of Sound and Vibration,* Vol. 176, No. 1, pp. 69–92.

Zhang, R., Yong, Y., and Lin, Y. K., 1991a, "Earthquake ground motion modeling. I: Deterministic point source," *J. Engineering Mechanics,* Vol. 117, No. 9, pp. 2114–2132.

Zhang, R., Yong, Y., and Lin, Y. K., 1991b, "Earthquake ground motion modeling. II: Stochastic line source," *J. Engineering Mechanics,* Vol. 117, No. 9, pp. 2133–2148.

Zhang, R., Zhang, L., and Shinozuka, M., 1997, "Seismic Waves in a Laterally Inhomogeneous Layered Medium, Part II: Analysis," Vol. 64, pp. 59–65.

APPENDIX A

Relation Between Seismic Moment and Discontinuities

With knowledge of the seismic dislocation $\Delta\mathbf{u}$ in the discretized subfault area Σ^l centered at location (x_s^l, y_s^l, z_s^l) and activated at time t_s^l, the corresponding seismic moment components can be found by

$$M_{xy}^l(t - t_s^l) = M_0^l \sin(\delta)\cos(\lambda^l)F(t - t_s^l) \quad (47)$$

$$M_{xz}^l(t - t_s^l) = -M_0^l \cos(\delta)\cos(\lambda^l)F(t - t_s^l) \quad (48)$$

$$M_{yy}^l(t - t_s^l) = -M_0^l \sin(2\delta)\sin(\lambda^l)F(t - t_s^l) \quad (49)$$

$$M_{yz}^l(t - t_s^l) = M_0^l \cos(2\delta)\sin(\lambda^l)F(t - t_s^l) \quad (50)$$

$$M_{zz}^l(t - t_s^l) = M_0^l \sin(2\delta)\sin(\lambda^l)F(t - t_s^l) \quad (51)$$

in which F is the slip function with a unit final slip and the magnitude of the seismic moment M_0^l is

$$M_0^l = \mu_k \Sigma^l \overline{\Delta u_F^l} \quad (52)$$

where dip δ and rake λ^l are defined in Fig. 2 for the discretized fault Σ^l, μ_k is the rigidity of layer k, and Δu_F^l is the average final slip on the discretized fault. Correspondingly, one may easily obtain the Fourier transform of the seismic moment components $\tilde{M}_{ij}$.

APPENDIX B

Matrices $E_{i;\zeta}$, $T_{i;\zeta}$ and $T_{i;\zeta}^{-1}$

Matrices $\mathbf{E}_{i;\zeta}$, $\mathbf{T}_{i;\zeta}$, and $\mathbf{T}_{i;\zeta}^{-1}$ may be partitioned as follows:

$$[\mathbf{X}_{i;\zeta}] \equiv \begin{bmatrix} \mathbf{X}_{i;\zeta}^{11} & \mathbf{X}_{i;\zeta}^{12} \\ \mathbf{X}_{i;\zeta}^{21} & \mathbf{X}_{i;\zeta}^{2} \end{bmatrix}; \quad \mathbf{X} = \mathbf{E}, \mathbf{T} \quad \text{or} \quad \mathbf{T}^{-1}. \quad (53)$$

Specifically

$$\mathbf{E}_{i;P\text{-}SV}(z - z_{i-1}) = \begin{bmatrix} e^{i\nu_i(z-z_{i-1})} & 0 & 0 & 0 \\ 0 & e^{i\gamma_i(z-z_{i-1})} & 0 & 0 \\ 0 & 0 & e^{-i\nu_i(z-z_{i-1})} & 0 \\ 0 & 0 & 0 & e^{-i\gamma_i(z-z_{i-1})} \end{bmatrix} \quad (54)$$

$$\mathbf{E}_{i;SH}(z - z_{i-1}) = \begin{bmatrix} e^{i\gamma_i(z-z_{i-1})} & 0 \\ 0 & e^{-i\gamma_i(z-z_{i-1})} \end{bmatrix} \quad (55)$$

$$\mathbf{T}_{i;P\text{-}SV} = \begin{bmatrix} -i\kappa & -i\gamma_i & -i\kappa & i\gamma_i \\ i\nu_i & -i\kappa & -i\nu_i & -i\kappa \\ \mu_i l_i & 2\mu_i\gamma_i\kappa & \mu_i l_i & -2\mu_i\gamma_i\kappa \\ 2\mu_i\nu_i\kappa & -\mu_i l_i & -2\mu_i\nu_i\kappa & -\mu_i l_i \end{bmatrix} \quad (56)$$

$$\mathbf{T}_{i;SH} = \begin{bmatrix} 1 & 1 \\ i\mu_i\gamma_i & -i\mu_i\gamma_i \end{bmatrix} \quad (57)$$

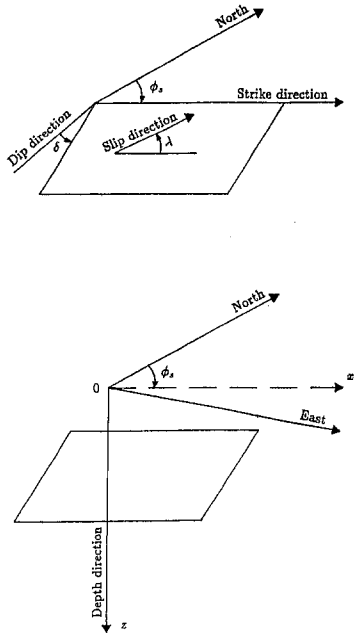


Fig. 2 Fault orientation and related terminology

Downloaded 04 May 2010 to 171.66.16.34. Redistribution subject to ASME license or copyright; see http://www.asme.org/terms/Terms_Use.cfm

$$\mathbf{T}^{-1}_{i;P\text{-}SV} = \frac{\beta_i^2}{2\mu_i\nu_i\gamma_i\omega^2}\begin{bmatrix} 2i\mu_i\nu_i\gamma_i\kappa & i\mu_i\gamma_i l_i & -\nu_i\gamma_i & \gamma_i\kappa \\ -i\mu_i\nu_i l_i & 2i\mu_i\nu_i\gamma_i\kappa & \nu_i\kappa & \nu_i\gamma_i \\ 2i\mu_i\nu_i\gamma_i\kappa & -i\mu_i\gamma_i l_i & -\nu_i\gamma_i & -\gamma_i\kappa \\ i\mu_i\nu_i l_i & 2i\mu_i\nu_i\gamma_i\kappa & -\nu_i\kappa & \nu_i\gamma_i \end{bmatrix} \tag{58}$$

$$\mathbf{T}^{-1}_{i;SH} = \frac{1}{2i\mu_i\gamma_i}\begin{bmatrix} i\mu_i\gamma_i & 1 \\ i\mu_i\gamma_i & -1 \end{bmatrix}. \tag{59}$$

In the above equations

$$\nu_i = \left[\frac{\omega^2}{\alpha_i^2} - \kappa^2\right]^{1/2}; \quad \gamma_i = \left[\frac{\omega^2}{\beta_i^2} - \kappa^2\right]^{1/2}; \quad l_i = 2\kappa^2 - \frac{\omega^2}{\beta_i^2} \tag{60}$$

where $\mathrm{Im}(\nu_i) \le 0$ and $\mathrm{Im}(\gamma_i) \le 0$ and

$$\alpha_i = c_{p;i}\left(1 + i\frac{1}{2Q_{p;i}}\right); \quad \beta_i = c_{s;i}\left(1 + i\frac{1}{2Q_{s;i}}\right) \tag{61}$$

where $c_{p;i}$ and $c_{s;i}$ are the P and S wave speeds in layer i and $Q_{p;i}$ and $Q_{s;i}$ are corresponding attenuation factors summarizing the gross effect of internal friction.

APPENDIX C

Matrices $C^{\pm}$

For simplicity in notation, the superscript m associated with the elastic parameters in layer j, such as α_j^m, is dropped in this appendix.

$$c_{11}^{+} = \frac{1}{2\rho_j\omega^2}\left[-\frac{2\kappa^2\kappa''\beta_j^2}{\nu_j\alpha_j^2}\tilde{\lambda}_j^s + \frac{\kappa_{xyp}(-2\kappa_{xyp}\beta_j^2 + 4\kappa''^2\upsilon_1\beta_j^2 - \omega^2)}{\nu_j\kappa''\beta_j^2}\tilde{\mu}_j^s + \frac{\omega^2\kappa_{xyp}}{\nu_j\kappa''}\tilde{p}_j^s\right] \tag{62}$$

$$c_{12}^{+} = \frac{1}{2\rho_j\omega^2}\left[\frac{\omega^2 - 2\beta_j^2\kappa''^2}{\alpha_j^2}\tilde{\lambda}_j^s + \frac{2(\kappa''^2\alpha_j^2 - 2\kappa''^2\beta_j^2 + \omega^2)}{\alpha_j^2}\tilde{\mu}_j^s - \omega^2\tilde{p}_j^s\right] \tag{63}$$

$$c_{13}^{+} = \frac{1}{2\rho_j\omega^2}\left[-\frac{i\kappa^2}{\nu_j\rho_j\alpha_j^2}\tilde{\lambda}_j^s + \frac{i\kappa_{xyp}\upsilon_2}{\mu_j\nu_j}\tilde{\mu}_j^s\right] \tag{64}$$

$$c_{14}^{+} = \frac{1}{2\rho_j\omega^2}\left[\frac{i\kappa''}{\rho_j\alpha_j^2}\tilde{\lambda}_j^s + \left(\frac{i\kappa_{xyp} - 2i\kappa''^2\upsilon_1}{\mu_j\kappa''}\right)\tilde{\mu}_j^s\right] \tag{65}$$

$$c_{15}^{+} = \frac{1}{2\rho_j\omega^2}\left[\left(\frac{2\kappa_x''\kappa_y''\kappa_{xy2} - 2\kappa_x\kappa_y\kappa_{xy2}'' + \gamma_j^2\kappa_{xym}}{\nu_j\kappa''}\right)\tilde{\mu}_j^s - \frac{\omega^2\kappa_{xym}}{\nu_j\kappa''}\tilde{p}_j^s\right] \tag{66}$$

$$c_{16}^{+} = -\frac{1}{2\rho_j\omega^2}\frac{i\kappa_{xym}}{\kappa''\mu_j}\tilde{\mu}_j^s \tag{67}$$

$$c_{21}^{+} = \frac{1}{2\rho_j\omega^2}\left[-\frac{2\kappa\kappa''\beta_j^2}{\alpha_j^2}\tilde{\lambda}_j^s + \frac{\kappa_{xyp}(-2\kappa_{xyp}\beta_j^2 + 4\kappa''^2\upsilon_1\beta_j^2 - \omega^2)}{\kappa\kappa''\beta_j^2}\tilde{\mu}_j^s + \frac{\omega^2\kappa_{xyp}}{\kappa\kappa''}\tilde{p}_j^s\right] \tag{68}$$

$$c_{22}^{+} = \frac{1}{2\rho_j\omega^2}\left[\frac{\kappa(2\kappa''^2\beta_j^2 - \omega^2)}{\gamma_j\alpha_j^2}\tilde{\lambda}_j^s - \frac{2\kappa(\kappa''^2\upsilon_2\alpha_j^2 + \omega^2)}{\gamma_j\alpha_j^2}\tilde{\mu}_j^s + \frac{\omega^2\kappa}{\gamma_j}\tilde{p}_j^s\right] \tag{69}$$

$$c_{23}^{+} = \frac{1}{2\rho_j\omega^2}\left[-\frac{i\kappa}{\rho_j\alpha_j^2}\tilde{\lambda}_j^s + \frac{i\kappa_{xyp}\upsilon_2}{\kappa\mu_j}\tilde{\mu}_j^s\right] \tag{70}$$

$$c_{24}^{+} = \frac{1}{2\rho_j\omega^2}\left[-\frac{i\kappa\kappa''}{\gamma_j\rho_j\alpha_j^2}\tilde{\lambda}_j^s + \frac{i\kappa(2\kappa''^2\upsilon_1 - \kappa_{xyp})}{\gamma_j\mu_j\kappa''}\tilde{\mu}_j^s\right] \tag{71}$$

$$c_{25}^{+} = \frac{1}{2\rho_j\omega^2}\left[\frac{2\kappa_x''\kappa_y''\kappa_{xy2} - 2\kappa_x\kappa_y\kappa_{xy2}'' + \gamma_j^2\kappa_{xym}}{\kappa\kappa''}\tilde{\mu}_j^s - \frac{\omega^2\kappa_{xym}}{\kappa\kappa''}\tilde{p}_j^s\right] \tag{72}$$

$$c_{26}^{+} = \frac{1}{2\rho_j\omega^2}\frac{i\kappa\kappa_{xym}}{\kappa''\mu_j\gamma_j}\tilde{\mu}_j^s \tag{73}$$

$$c_{31}^{+} = \frac{i\kappa_{gp}}{2\rho_j\omega^2}\left[\frac{\kappa_{xym}(2\kappa_{xyp}\beta_j^2 - 4\kappa''^2\upsilon_1\beta_j^2 + \omega^2)}{\beta_j^2\kappa''}\tilde{\mu}_j^s - \frac{\omega^2\kappa_{xym}}{\kappa''}\tilde{p}_j^s\right] \tag{74}$$

$$c_{33}^{+} = -\frac{i\kappa_{gp}}{2\rho_j\omega^2}\frac{i\kappa_{xym}\upsilon_2}{\mu_j}\tilde{\mu}_j^s \tag{75}$$

$$c_{35}^{+} = \frac{i\kappa_{gp}}{2\rho_j\omega^2}\left[\frac{4\kappa_x\kappa_y\kappa_x''\kappa_y'' + \kappa_{xy2}\kappa_{xy2}'' + \gamma_j^2\kappa_{xyp}}{\kappa''}\tilde{\mu}_j^s - \frac{\omega^2\kappa_{xyp}}{\kappa''}\tilde{p}_j^s\right] \tag{76}$$

$$c_{32}^{+} = c_{34}^{+} = c_{36}^{+} = 0 \tag{77}$$

$$c_{ij}^{-} = c_{ij}^{+}; \quad i + j = \text{even}, \quad i = 1, 2, \quad j = 1, \ldots, 6 \tag{78}$$

$$c_{ij}^{-} = -c_{ij}^{+}; \quad i + j = \text{odd}, \quad i = 1, 2, \quad j = 1, \ldots, 6 \tag{79}$$

$$c_{31}^{-} = -\frac{i\kappa_{gp}}{2\rho_j\omega^2}\left[\frac{\kappa_{xym}(-2\kappa_{xyp}\beta_j^2 + 4\kappa''^2\upsilon_1\beta_j^2 - \omega^2)}{\beta_j^2\kappa''}\tilde{\mu}_j^s + \frac{\omega^2\kappa_{xym}}{\kappa''}\tilde{p}_j^s\right] \tag{80}$$

$$c_{33}^{-} = -\frac{i\kappa_{gp}}{2\rho_j\omega^2}\frac{i\kappa_{xym}\upsilon_2}{\mu_j}\tilde{\mu}_j^s \tag{81}$$

Downloaded 04 May 2010 to 171.66.16.34. Redistribution subject to ASME license or copyright; see http://www.asme.org/terms/Terms_Use.cfm

$$c_{35}^{-} = -\frac{i\kappa_{gp}}{2\rho_j\omega^2}\left[\frac{-4\kappa_x\kappa_y\kappa_x''\kappa_y'' - \kappa_{xy2}\kappa_{xy2}'' - \gamma_j^2\kappa_{xyp}}{\kappa''}\tilde{\mu}_j^s + \frac{\omega^2\kappa_{xyp}}{\kappa''}\tilde{p}_j^s\right] \quad (82)$$

$$c_{32}^{-} = c_{34}^{-} = c_{36}^{-} = 0 \quad (83)$$

where

$$\kappa_\zeta'' = \kappa_\zeta - \kappa_\zeta'; \quad \zeta = x, y \quad (84)$$

$$\tilde{\mu}_j^s = 2\rho_j\beta_j\tilde{\beta}_j^s + \tilde{p}_j^s\beta_j^2,$$

$$\tilde{\lambda}_j^s = 2\rho_j(\alpha_j\tilde{\alpha}_j^s - 2\beta_j\tilde{\beta}_j^s) + \tilde{p}_j^s(\alpha_j^2 - 2\beta_j^2) \quad (85)$$

$$\kappa_{xyp} = \kappa_x\kappa_x'' + \kappa_y\kappa_y''; \quad \kappa_{xym} = \kappa_x\kappa_y'' - \kappa_x''\kappa_y \quad (86)$$

$$\kappa_{xy2} = \kappa_x^2 - \kappa_y^2; \quad \kappa_{xy2}'' = \kappa_x''^2 - \kappa_y''^2 \quad (87)$$

$$\kappa_{gp} = \frac{\kappa^2 + \gamma_j^2}{\kappa\gamma_j}; \quad v_1 = 1 - \frac{\beta_j^2}{\alpha_j^2}; \quad v_2 = 1 - \frac{2\beta_j^2}{\alpha_j^2} \quad (88)$$

APPENDIX D

Matrices $B^{\pm}$

In this appendix, all the matrices $\mathbf{T}_{j;\zeta}$ and $\mathbf{T}_{j;\zeta}^{-1}$ are evaluated at the wave number pair $(\kappa_x - \kappa_x', \kappa_y - \kappa_y')$.

$$\begin{bmatrix} \mathbf{B}_{11}^{\pm} & \vdots & \mathbf{B}_{12}^{\pm} \\ \cdots & \cdots & \cdots \\ \mathbf{B}_{21}^{\pm} & \vdots & \mathbf{B}_{22}^{\pm} \end{bmatrix} = \begin{bmatrix} \mathbf{Y}_{11}^{\pm}\mathbf{T}_{j;P\text{-}SV}^{-1} & \vdots & \mathbf{Y}_{12}^{\pm}\mathbf{T}_{j;SH}^{-1} \\ \cdots & \cdots & \cdots \\ \mathbf{Y}_{21}^{\pm}\mathbf{T}_{j;P\text{-}SV}^{-1} & \vdots & \mathbf{Y}_{22}^{\pm}\mathbf{T}_{j;SH}^{-1} \end{bmatrix} \quad (89)$$

where

$$y_{ij}^{\pm} = x_{ij}a_{ij}^{\pm}; \quad i = 1, 2, 3; \quad j = 1, \ldots, 6 \quad (90)$$

Matrix $\mathbf{X}$ is

$$\begin{bmatrix} \mathbf{X}_{11}^{\pm} & \vdots & \mathbf{X}_{12}^{\pm} \\ \cdots & \cdots & \cdots \\ \mathbf{X}_{21}^{\pm} & \vdots & \mathbf{X}_{22}^{\pm} \end{bmatrix} = \begin{bmatrix} \mathbf{C}_{11}^{\pm}\mathbf{T}_{j;P\text{-}SV} & \vdots & \mathbf{C}_{12}^{\pm}\mathbf{T}_{j;SH} \\ \cdots & \cdots & \cdots \\ \mathbf{C}_{21}^{\pm}\mathbf{T}_{j;P\text{-}SV} & \vdots & \mathbf{C}_{22}^{\pm}\mathbf{T}_{j;SH} \end{bmatrix}. \quad (91)$$

Coefficients of $a_{ij}^{\pm}$ are

$$a_{11}^{+} = \frac{1}{i(\nu_j'' - \nu_j)}[e^{i(\nu_j^* - \nu_j)h_j} - 1] \quad (92)$$

$$a_{12}^{+} = a_{15}^{+} = \frac{1}{i(\gamma_j'' - \nu_j)}[e^{i(\gamma_j^* - \nu_j)h_j} - 1] \quad (93)$$

$$a_{13}^{+} = \frac{1}{i(\nu_j + \nu_j'')}[1 - e^{-i(\nu_j + \nu_j^*)h_j}] \quad (94)$$

$$a_{14}^{+} = a_{16}^{+} = \frac{1}{i(\gamma_j'' + \nu_j)}[1 - e^{-i(\gamma_j^* + \nu_j)h_j}] \quad (95)$$

$$a_{21}^{+} = a_{31}^{+} = \frac{1}{i(\nu_j'' - \gamma_j)}[e^{i(\nu_j^* - \gamma_j)h_j} - 1] \quad (96)$$

$$a_{22}^{+} = a_{25}^{+} = a_{32}^{+} = a_{35}^{+} = \frac{1}{i(\gamma_j'' - \gamma_j)}[e^{i(\gamma_j^* - \gamma_j)h_j} - 1] \quad (97)$$

$$a_{23}^{+} = a_{33}^{+} = \frac{1}{i(\nu_j'' + \gamma_j)}[1 - e^{-i(\nu_j^* + \gamma_j)h_j}] \quad (98)$$

$$a_{24}^{+} = a_{26}^{+} = a_{34}^{+} = a_{36}^{+} = \frac{1}{i(\gamma_j'' + \gamma_j)}[1 - e^{-i(\gamma_j^* + \gamma_j)h_j}] \quad (99)$$

$$a_{11}^{-} = \frac{1}{i(\nu_j + \nu_j'')}[e^{i\nu_j^* h_j} - e^{-i\nu_j h_j}] \quad (100)$$

$$a_{12}^{-} = a_{15}^{-} = \frac{1}{i(\gamma_j'' + \nu_j)}[e^{i\gamma_j^* h_j} - e^{-i\nu_j h_j}] \quad (101)$$

$$a_{13}^{-} = \frac{1}{i(\nu_j - \nu_j'')}[e^{-i\nu_j^* h_j} - e^{-i\nu_j h_j}] \quad (102)$$

$$a_{14}^{-} = a_{16}^{-} = \frac{1}{i(\nu_j - \gamma_j'')}[e^{-i\gamma_j^* h_j} - e^{-i\nu_j h_j}] \quad (103)$$

$$a_{21}^{-} = a_{31}^{-} = \frac{1}{i(\gamma_j + \nu_j'')}[e^{i\nu_j^* h_j} - e^{-i\gamma_j h_j}] \quad (104)$$

$$a_{22}^{-} = a_{25}^{-} = a_{32}^{-} = a_{35}^{-} = \frac{1}{i(\gamma_j'' + \gamma_j)}[e^{i\gamma_j^* h_j} - e^{-i\gamma_j h_j}] \quad (105)$$

$$a_{23}^{-} = a_{33}^{-} = \frac{1}{i(\gamma_j - \nu_j'')}[e^{-i\nu_j^* h_j} - e^{-i\gamma_j h_j}] \quad (106)$$

$$a_{24}^{-} = a_{26}^{-} = a_{34}^{-} = a_{36}^{-} = \frac{1}{i(\gamma_j - \gamma_j'')}[e^{-i\gamma_j^* h_j} - e^{-i\gamma_j h_j}] \quad (107)$$

where

$$\nu_j'' = \left[\frac{\omega^2}{\alpha_j^2} - \kappa''^2\right]^{1/2}; \quad \gamma_j'' = \left[\frac{\omega^2}{\beta_j^2} - \kappa''^2\right]^{1/2} \quad (108)$$

Downloaded 04 May 2010 to 171.66.16.34. Redistribution subject to ASME license or copyright; see http://www.asme.org/terms/Terms_Use.cfm

Seismic Waves in a Laterally Inhomogeneous Layered Medium, Part II: Analysis

Ruichong Zhang
Research Assistant Professor,
Department of Civil Engineering,
University of Southern California,
University Park,
Los Angeles, CA 90089-2531
Assoc. Mem. ASME

Liyang Zhang
Structural Engineer,
Widlinger Associates, Inc.,
New York, NY 10001

Masanobu Shinozuka
Fred Champion Chair in Civil Engineering,
Department of Civil Engineering,
University of Southern California,
Los Angeles, CA 90089-2531
Fellow ASME

Seismic wave scattering representation for the layered half-space with lateral inhomogeneities subjected to a seismic dislocation source has been formulated in the companion paper with the use of first-order perturbation (Born-type approximation) technique. The total wave field is obtained as a superposition of the mean and the scattered wave fields, which are generated, respectively, by a series of double couples of body forces equivalent to the seismic dislocation source and by fictitious body forces equivalent to the existence of the lateral inhomogeneities in the layered half-space. The responses in both the mean and the scattered wave fields are found with the aid of an integral transform technique and wave propagation analysis. The characteristics of the scattered waves and their effects on the mean waves or corresponding induced ground and/or underground mean responses are investigated in this paper. In particular, coupling phenomena between P-SV and SH waves and wave number shifting effects between the mean and the scattered wave responses are presented in detail. With the lateral inhomogeneities being assumed as a homogeneous random field, a qualitative analysis is provided for estimating the effects of the lateral inhomogeneities on the ground motion, which is related to a fundamental issue: whether a real earth medium can or cannot be approximately considered as a laterally homogeneous layer. The effects of the lateral inhomogeneities on the ground motion time history are also presented as a quantitative analysis. Finally, a numerical example is carried out for illustration purposes.

1 Introduction

Wave scattering phenomena in a laterally inhomogeneous medium subjected to incident seismic plane waves have been attracting the concerns of seismologists and engineers for the last two decades, since the induced wave scattering explains the generation of coda waves (Aki, 1975) and affects the seismogram envelops and power spectra (Sato, 1984, 1989) that are obtained without taking into account the lateral inhomogeneities, etc. Wave scattering may be efficiently characterized by the scattered wave field besides the mean wave field, as shown in Zhang et al. (1997) with the aid of the first-order perturbation technique. Therefore, the properties of the scattered wave field and its effects on the mean waves or its correspondingly induced ground and/or underground mean responses become important, which is the primary concern of this paper.

As is known in a two-dimensional wave scattering problem, the *P-SV* and *SH* waves can be separately analyzed. This is due to the fact that the incident *P-SV* (*SH*) waves generate only the scattered *P-SV* (*SH*) waves (see, e.g., Kennett, 1972). However, it is no longer valid in three-dimensional wave scattering, which was observed in Zhang (1994) among others that coupling phenomena are found between *P-SV* and *SH* waves for a layered half-space with irregular interfaces. Similar phenomena are also found in a layered half-space with lateral inhomogeneities (Zhang et al., 1997). Whether the coupling phenomena are important or not to the seismology and/or its engineering applications is investigated in this paper.

In reality, the earth medium can never be of perfect lateral homogeneities and is always of stochastic lateral inhomogeneities to a certain extent. It is apparent that not all of these lateral inhomogeneities are necessarily concerned in the present model from the engineering point of view. This is thus related to a fundamental issue: whether or not an earth medium can be approximated as laterally homogeneous on the basis of its real inhomogeneities and the seismic waves under consideration (see, e.g., Ishimaru, 1978; Caviglia and Morro, 1992). Therefore, a corresponding qualitative analysis is presented in this paper.

Finally, a numerical example is carried out in which the effects of the lateral inhomogeneities on the ground motion time history are quantitatively analyzed.

2 Wave Scattering With Reduction of Independent Elastic Parameters

As shown in Zhang et al. (1997), seismic waves in a layered half-space with lateral inhomogeneities, generated by a buried seismic dislocation source, may be constructed as the superposition of a mean and a scattered wave fields, i.e.,

$$\mathbf{u}(x, y, z, t) = \mathbf{u}^m(x, y, z, t) + \epsilon\mathbf{u}^s(x, y, z, t) \quad (1)$$

where $\mathbf{u}^m$ is obtained as the response solution for a perfectly layered half-space (without the lateral inhomogeneities) subjected to a seismic dislocation source buried in layer k that is replaced by a series of double couples of equivalent body forces, and $\mathbf{u}^s$ is obtained as the response solution for the same layered half-space as used in the mean wave field subjected to the fictitious distributed body forces in layer j which are equivalent to the effects of the lateral inhomogeneities. Mathematically, the total wave response may be expressed as

$$u_d(x, y, z, t) = \int_{-\infty}^{\infty}\int_{-\infty}^{\infty}\int_{-\infty}^{\infty} \tilde{u}_d(\kappa_x, \kappa_y, z, \omega) \times \exp[-i\kappa_x x - i\kappa_y y + i\omega t]d\kappa_x d\kappa_y d\omega \quad (2)$$

Contributed by the Applied Mechanics Division of THE AMERICAN SOCIETY OF MECHANICAL ENGINEERS for publication in the ASME JOURNAL OF APPLIED MECHANICS.

Discussion on the paper should be addressed to the Technical Editor, Professor Lewis T. Wheeler, Department of Mechanical Engineering, University of Houston, Houston, TX 77204-4792, and will be accepted until four months after final publication of the paper itself in the ASME JOURNAL OF APPLIED MECHANICS.

Manuscript received by the ASME Applied Mechanics Division, June 27, 1995; final revision, Oct. 11, 1996. Associate Technical Editor: L. T. Wheeler.

Copyright © 1997 by ASME

Downloaded 04 May 2010 to 171.66.16.34. Redistribution subject to ASME license or copyright; see http://www.asme.org/terms/Terms_Use.cfm

where κ_x and κ_y are the wave numbers in the x and y-directions, respectively, $d = x$, y or z, and

$$\tilde{u}_d(\kappa_x, \kappa_y, z, \omega) = \tilde{u}_d^m(\kappa_x, \kappa_y, z, \omega) + \epsilon\tilde{u}_d^s(\kappa_x, \kappa_y, z, \omega). \quad (3)$$

With the lateral inhomogeneities described by

$$\zeta_j(x, y) = \zeta_j^m + \epsilon\zeta_j^s(x, y) \quad (4)$$

where $\zeta = \alpha$ (S wave speed), β (P wave speed), or ρ (density) and

$$\epsilon\zeta_j^s(x, y) = \int_{-\infty}^{\infty}\int_{-\infty}^{\infty} \epsilon\tilde{\zeta}_j^s(\kappa_x', \kappa_y') \exp[-i\kappa_x' x - i\kappa_y' y]d\kappa_x' d\kappa_y' \quad (5)$$

the response of the scattered wave field $\epsilon\tilde{u}_d^s$ can be found as

$$\epsilon\tilde{u}_d^s(\kappa_x, \kappa_y, z, \omega) = \int_{-\infty}^{\infty}\int_{-\infty}^{\infty} \tilde{H}_d^s(\kappa_x, \kappa_y, z, \omega; \kappa_x', \kappa_y')d\kappa_x' d\kappa_y' \quad (6)$$

where $\tilde{H}_d^s$ is the response solution for the scattered wave field corresponding to the sinusoidal lateral inhomogeneities described by the form of Eq. (5) without a twofold integral, and its expression can be found in Zhang et al. (1997).

In theory, three independent elastic parameters, as shown in Eq. (4) or (5), are used to describe the lateral inhomogeneities. However, in practice, they can approximately be reduced to one for ease in analyzing. As advocated by Sato (1984), the following relations may be applied:

$$\epsilon\zeta^s(x, y) = \epsilon\zeta_j^m a(x, y) = \epsilon\zeta_j^m \int_{-\infty}^{\infty}\int_{-\infty}^{\infty} \tilde{a}(\kappa_x', \kappa_y') \times \exp[-i\kappa_x' x - i\kappa_y' y]d\kappa_x' d\kappa_y' \quad (7)$$

$$\epsilon\rho_j^s(x, y) = \epsilon\gamma_j\rho_j^m a(x, y) = \epsilon\gamma_j\rho_j^m \int_{-\infty}^{\infty}\int_{-\infty}^{\infty} \tilde{a}(\kappa_x', \kappa_y') \times \exp[-i\kappa_x' x - i\kappa_y' y]d\kappa_x' d\kappa_y' \quad (8)$$

where $\zeta = \alpha$ or β, $a(x, y)$ is a normalized common factor and

$$\gamma_j = \frac{\alpha_j^m}{\alpha_j^m - c} \quad \text{or} \quad \gamma_j = \frac{\beta_j^m}{\beta_j^m - c'} \quad (9)$$

in which c and c' are constants. Therefore, the response of the scattered wave field represented by Eq. (6) may be rewritten as

$$\epsilon\tilde{u}_d^s(\kappa_x, \kappa_y, z, \omega) = \int_{-\infty}^{\infty}\int_{-\infty}^{\infty} \tilde{\mathcal{H}}_d^s(\kappa_x, \kappa_y, z, \omega; \kappa_x', \kappa_y') \times \tilde{a}(\kappa_x', \kappa_y')d\kappa_x' d\kappa_y' \quad (10)$$

where $\tilde{\mathcal{H}}_d^s$ is the response of the scattered wave field in the frequency wave number domain to the sinusoidal lateral inhomogeneities, described by the form of Eqs. (7) and (8) without a twofold integral and common factor $\tilde{a}(\kappa_x', \kappa_y')$, which can actually be obtained from the expression of $\tilde{H}_d^s$ with parameters $\tilde{\alpha}^s$, $\tilde{\beta}^s$ and $\tilde{\rho}^s$ replaced by α^m, β^m and $\gamma_j\rho^m$, respectively. Since $\tilde{u}_d^s$ is constituted of $\tilde{\mathcal{H}}_d^s$ with $\tilde{a}$ as a weight function (cf. Eq. (10)), $\tilde{\mathcal{H}}_d^s$ is thus referred to as a frequency wave number response function of the scattered wave field or simply a fundamental solution of the scattered wave field in the following text.

In summary, the seismic wave motion in a layered half-space with lateral inhomogeneities is obtained as a superposition of the mean and the scattered wave fields; i.e., u_d^m and ϵu_d^s. They can be effectively described by the complex Fourier amplitudes $\tilde{u}_d^m$ and $\epsilon\tilde{u}_d^s$. The latter is further related to the fundamental solution $\tilde{\mathcal{H}}_d^s$ and the common factor of the lateral inhomogeneities $\tilde{a}$. Therefore, knowledge of the properties of fundamental solution $\tilde{\mathcal{H}}_d^s$ is substantial to the analysis of the effects of lateral inhomogeneities on seismic wave motion.

Table 1 Properties of layered half-space

Layer no.	Density (kg/m^3)	P wave speed (m/sec)	S wave speed (m/sec)	Attenuation factor	Depth of layer (km)
1	1670	3100	1790	50	0–0.5
2	2280	5000	2887	100	0.5–20
3	2580	6000	3464	200	20–∞

3 Properties of Fundamental Solution $\tilde{\mathcal{H}}_d^s$

As presented in the last section, fundamental solution $\tilde{\mathcal{H}}_d^s$ is obtained as the response of the scattered wave field in a layered half-space subjected to fictitious body forces in layer j which are equivalent to the effects of the sinusoidal lateral inhomogeneities. It can be actually obtained from the expression of $\tilde{H}_d^s$ with some parameters properly replaced (e.g., $\tilde{\alpha}^s$, $\tilde{\beta}^s$, and $\tilde{\rho}^s$ replaced by α^m, β^m, and $\gamma_j\rho^m$, respectively). Therefore, $\tilde{\mathcal{H}}_d^s$ has the same three properties as $\tilde{H}_d^s$, as shown in Zhang et al. (1997). Specifically,

(1) the fundamental solution $\tilde{\mathcal{H}}_d^s$ has the same basic properties as the response of the mean wave field $\tilde{u}_d^m$ because both the mean and the scattered wave fields computed in the same layered half-space.

(2) the wave number shifting effects are found between the mean and the scattered wave fields. In particular, the fundamental solution $\tilde{\mathcal{H}}_d^s(\kappa_x, \kappa_y, z, \omega; \kappa_x', \kappa_y')$ is related to, or more strictly speaking, proportional to the frequency wave number response of the mean wave field $\tilde{u}_d^m(\kappa_x - \kappa_x', \kappa_y - \kappa_y', z, \omega)$.

(3) both the mean P-SV wave response and the mean SH wave response contribute toward the P-SV scattered wave response, as well as SH scattered wave response. Consequently, the P-SV waves in a layered half-space with the lateral inhomogeneities are coupled with the SH waves.

These properties may be verified in the following numerical example. Consider a three-layer medium subjected to a pure strike-slip source with dip $\delta = 0$ deg. The pure strike-slip source is idealized as one double couple of equivalent body forces with seismic moment $M_0 = 1.9 \times 10^{19}$ N·m acting at $x_s = y_s = 0$ and $z_s = 10$ km. The dislocation function is assumed as a ramp function with rise time being 0.628 sec. The elastic parameters of three layers are listed in Table 1. The first layer is assumed to be laterally inhomogeneous with $\epsilon = 0.1$, $\gamma_1 = 1$, $\kappa_x' = 0.8$ km^{-1} and $\kappa_y' = 0.4$ km^{-1}.

The Fourier amplitude of the x-direction (coincident with the strike-direction) ground displacement associated with mean wave field ($|\tilde{u}_x^m|$) and its corresponding fundamental solution of the scattered wave field ($|\tilde{\mathcal{H}}_d^s|$) with $\omega = 4$ rad/sec are plotted in Fig. 1 (a, b). The wave number shifting effects are apparently observed from the whole figuration shifting by comparing two figures in Fig. 1, in which more shifting occurs for the fundamental solution $|\tilde{\mathcal{H}}_d^s|$ in the κ_x-direction than in the κ_y-direction, due to the fact that κ_x' is selected to be larger than κ_y' in this numerical example. Coupling between P-SV and SH waves may not be seen directly from in Fig. 1, although it is indeed reflected in the figures.

To see the coupling phenomena clearly, the ground displacement associated with the mean wave field and the fundamental solution of the scattered wave field are further decomposed into a P-SV and an SH wave components. Specifically, they may be symbolically represented by

$$\tilde{u}_x^m = \tilde{u}_{x;P\text{-}SV}^m + \tilde{u}_{x;SH}^m \quad (11)$$

$$\tilde{\mathcal{H}}_x^s = \tilde{\mathcal{H}}_{x;P\text{-}SV}^s + \tilde{\mathcal{H}}_{x;SH}^s = [\tilde{\mathcal{H}}_{x;P\text{-}SV;\overline{P\text{-}SV}}^s + \tilde{\mathcal{H}}_{x;P\text{-}SV;\overline{SH}}^s] + [\tilde{\mathcal{H}}_{x;SH;\overline{P\text{-}SV}}^s + \tilde{\mathcal{H}}_{x;SH;\overline{SH}}^s] \quad (12)$$

Downloaded 04 May 2010 to 171.66.16.34. Redistribution subject to ASME license or copyright; see http://www.asme.org/terms/Terms_Use.cfm

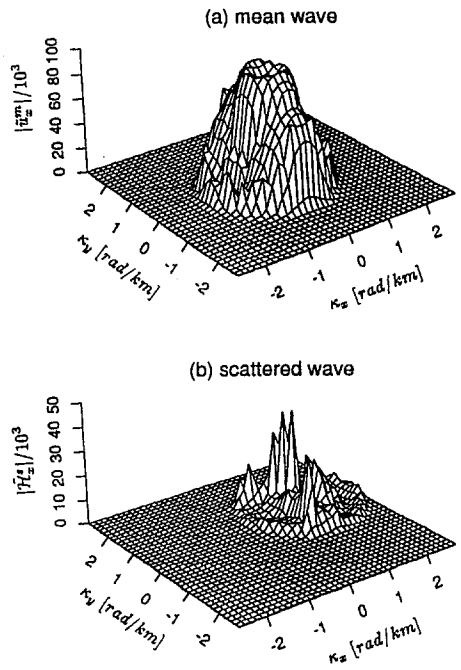


Fig. 1 Fourier amplitudes of ground displacements associated with (*a*) the mean waves and (*b*) the scattered waves

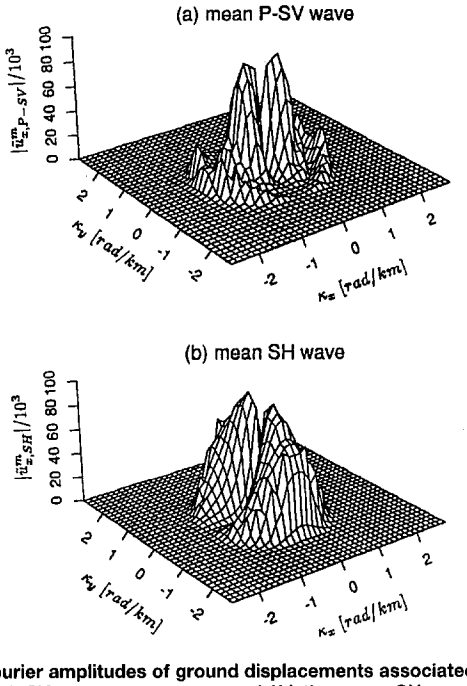


Fig. 2 Fourier amplitudes of ground displacements associated with (*a*) the mean *P-SV* wave components and (*b*) the mean *SH* wave components

where the corresponding first subscript stands for the direction of the response component; the second subscript stands for the wave component of the mean or the scattered wave field; and the third subscript stands for the wave component of the mean wave field. Equations (11) and the first equality in Eq. (12) are obtained on the basis of Eq. (16) in Zhang et al. (1997), while the second equality in Eq. (12) is obtained via the following fact: the fictitious body forces for the scattered wave field, which are equivalent to the effects of lateral inhomogeneities, are generated by two kinds of mean wave responses: one is the mean *P-SV* waves and the other is the mean *SH* waves, as shown in Eqs. (37)–(45) in Zhang et al. (1997). The two parts on the right-hand side of the second equality in Eq. (12) corresponds to two terms on the right-hand side of the first equality, respectively, which indicates that the fundamental solution in the scattered wave motion associated with each wave component (*P-SV* or *SH*) consists of two parts: one is caused by the mean *P-SV* wave motion and the other by the mean *SH* wave motion. The *y* and *z*-direction fundamental solution of the scattered wave field have a similar interpretation.

Figure 2(a, b) presents Fourier amplitudes of the x-direction ground displacements associated with the mean *P-SV* and *SH* wave motion, while Fig. 3(a, b) presents the corresponding fundamental solution associated with the scattered *P-SV* and *SH* wave motion. As can be seen from these figures, the fundamental solution of the scattered *P-SV* (*SH*) wave motion, $\tilde{\mathcal{H}}^s_{x;P\text{-}SV}(\tilde{\mathcal{H}}^s_{x;SH})$, is not simply proportional to the mean *P-SV* (*SH*) wave response, $\tilde{u}^m_{x;P\text{-}SV}(\tilde{u}^m_{x;SH})$, implying the existence of the coupling between *P-SV* and *SH* waves. The contribution of the mean *P-SV* and *SH* waves to the scattered *P-SV* waves, as well as *SH* waves, is depicted in Fig. 4(a–d), which reflects the extent of the coupling between *P-SV* and *SH* waves. These numerical results show that the contribution of the mean *P-SV* (*SH*) waves to the scattered *P-SV* (*SH*) waves is comparable to the contribution of the mean *SH* (*P-SV*) waves to the scattered *P-SV* (*SH*) waves, indicating that the coupling effects are substantial in formulating the scattered wave field, at least in this numerical example.

In addition, the fundamental solution of the scattered wave field associated with only one of three elastic parameters (*P* and *S* wave speeds and density) being function of lateral coordinates (x, y) is also investigated here. In Fig. 5(a–c) is shown the x-direction fundamental solution of the scattered wave field with the lateral inhomogeneity described by either $\alpha^s_1(\beta^s_1 = \rho^s_1 = 0)$, or $\beta^s_1(\alpha^s_1 = \rho^s_1 = 0)$, or $\rho^s_1(\alpha^s_1 = \beta^s_1 = 0)$. It can be seen that the wave speed variation is more sensitive to the fundamental solution of the scattered wave field than the density variation and that the *S* wave speed variation is more sensitive than the *P* wave speed variation. This may be explained as follows from the energy point of view since the energy primarily controls the response amplitude. The more weight a factor has

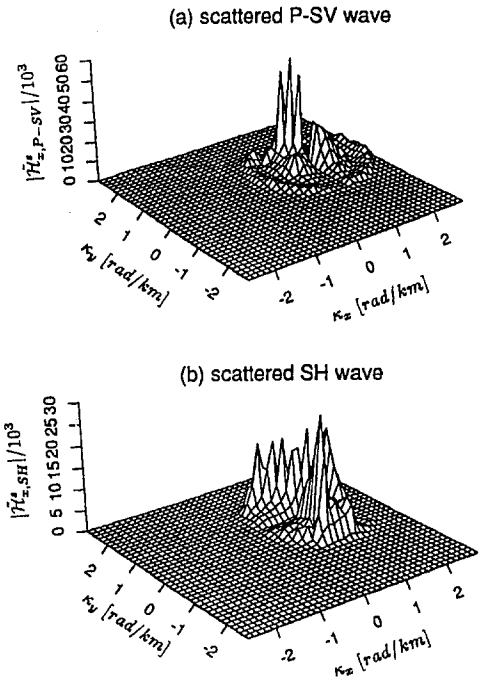


Fig. 3 Fourier amplitudes of ground displacements (fundamental solution) associated with (*a*) the scattered *P-SV* wave components and (*b*) the mean *SH* wave components

Downloaded 04 May 2010 to 171.66.16.34. Redistribution subject to ASME license or copyright; see http://www.asme.org/terms/Terms_Use.cfm

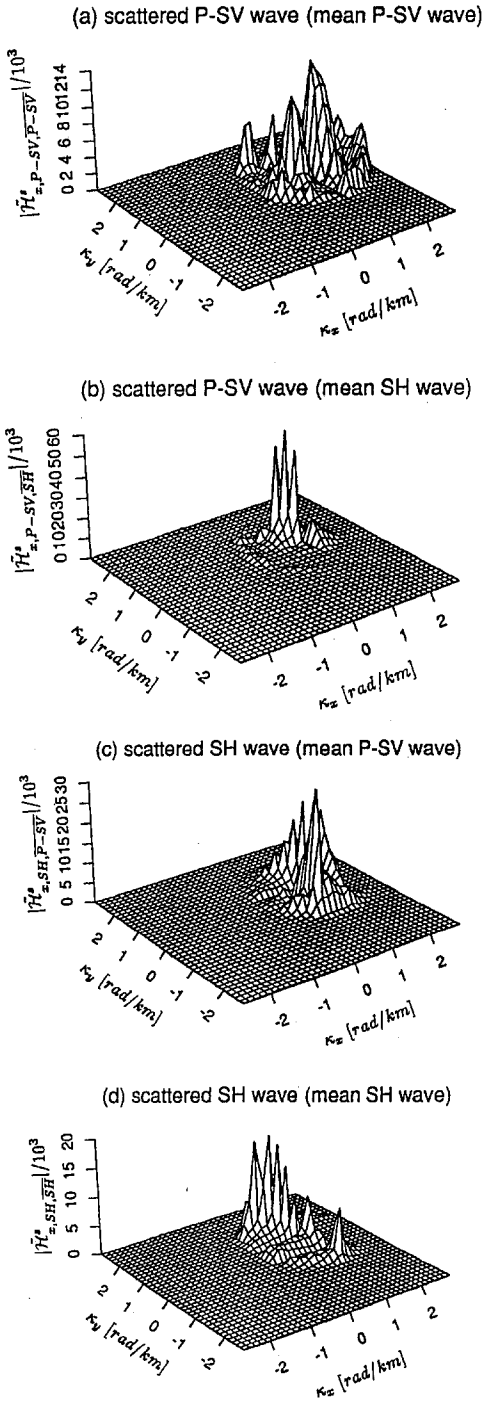


Fig. 4 Fourier amplitudes of ground displacements (fundamental solution) associated with (*a*) the scattered *P-SV* wave components due to the mean *P-SV* waves, (*b*) the scattered *P-SV* wave components due to the mean *SH* waves, (*c*) the scattered *SH* wave components due to the mean *P-SV* waves, and (*d*) the scattered *SH* wave components due to the mean *SH* waves

in an energy representation, the more sensitive the factor variation is to the response. Since the energy density is proportional to the product of density and square wave speed, it becomes apparent that the wave speed variation is more sensitive to the scattered wave response, specifically the fundamental solution of the scattered wave field, than the density variation. It is well known that S waves carry most of the seismic energy compared with the P waves. Therefore, at the same variation extent, the variation of the S wave speed generates a larger scattered wave response than that of the P wave speed.

4 Qualitative Estimate of Effects of Lateral Inhomogeneities

As mentioned in the Introduction, the real earth medium is always stochastically laterally inhomogeneous to a certain extent. It is neither necessary nor possible to take into account all of these lateral inhomogeneities in the present model from the engineering point of view. A question is thus raised: In what conditions may or may not the effects of the lateral inhomogeneities be neglected? In other words, with what kind of seismic waves (or corresponding responses such as displacement and acceleration) under consideration, what kind of lateral inhomogeneities can or cannot be approximately considered as lateral homogeneities? To see it clearly, a layered half-space, with only one laterally inhomogeneous layer, is considered in the following study. The response in both the mean and the scattered wave fields are qualitatively analyzed. Since the earthquake ground motion is mostly concerned in structural and other related engineering, the following analysis will be focused on its effects on the ground motion.

4.1 Statistical Response in the Scattered Wave Field. Assume that the elastic parameters of the laterally inhomogeneous layer, such as P and S wave speeds and density which are functions of lateral coordinates (x, y), are a homogeneous stochastic field. On the basis of their representations in Eqs. (4), (7), and (8), the normalized common factor $a(x, y)$ is a

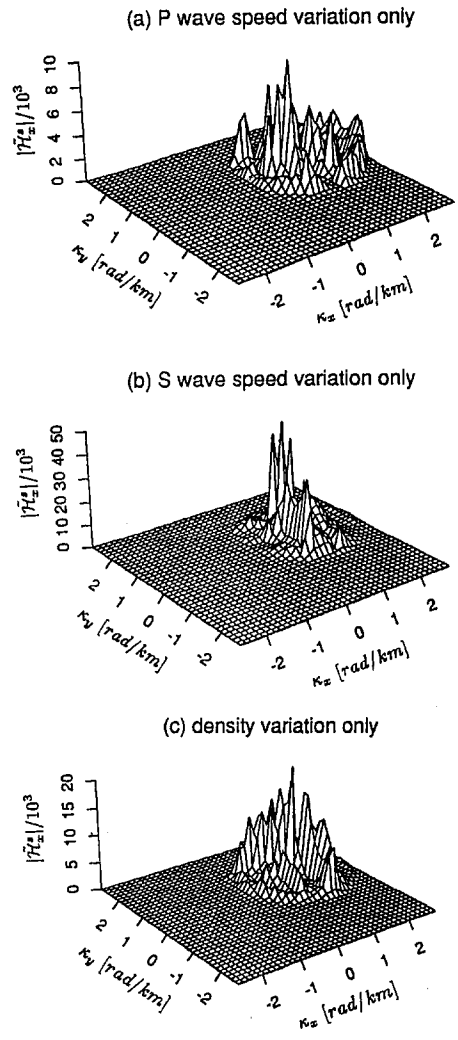


Fig. 5 Fourier amplitudes of the ground displacements associated with the lateral inhomogeneities being (*a*) *P* wave speed variation only, (*b*) *S* wave speed variation only, and (*c*) density variation only

Downloaded 04 May 2010 to 171.66.16.34. Redistribution subject to ASME license or copyright; see http://www.asme.org/terms/Terms_Use.cfm

homogeneous stochastic field with zero-mean and its statistics may be efficiently described by the wave number spectrum, i.e.,

$$E\{\tilde{a}(\kappa_x', \kappa_y')\} = 0 \tag{13}$$

$$E\{\tilde{a}(\kappa_x', \kappa_y')\tilde{a}^*(\kappa_x'', \kappa_y'')\}d\kappa_x'd\kappa_y' = \begin{cases} \Phi_a(\kappa_x', \kappa_y'), & \kappa_x' = \kappa_x'' \text{ and } \kappa_y' = \kappa_y'' \\ 0, & \kappa_x' \neq \kappa_x'' \text{ or } \kappa_y' \neq \kappa_y'' \end{cases} \tag{14}$$

where an asterisk denotes a complex conjugate, E denotes an ensemble average, and Φ_a is the wave number spectrum of $a(x, y)$. With the aid of Eq. (10), the mean ($\tilde{u}_d^s$) and standard deviation ($\tilde{\sigma}_d^s$) of the scattered wave response in the frequency wave number domain are found to be

$$\tilde{\mu}_d^s(\kappa_x, \kappa_y, z, \omega) = E\{\epsilon\tilde{u}_d^s(\kappa_x, \kappa_y, z, \omega)\} = 0 \tag{15}$$

and

$$\tilde{\sigma}_d^s(\kappa_x, \kappa_y, z, \omega) = \sqrt{E[|\epsilon\tilde{u}_d^s(\kappa_x, \kappa_y, z, \omega)|^2]} = \sqrt{\int_{-\infty}^{\infty}\int_{-\infty}^{\infty} |\tilde{\mathcal{H}}_d^s(\kappa_x, \kappa_y, z, \omega; \kappa_x', \kappa_y')|^2\Phi_a(\kappa_x', \kappa_y')d\kappa_x'd\kappa_y'}. \tag{16}$$

Since the time-space response (e.g., $u_d^s(x, y, z, t)$) is directly related to the frequency wave number response (e.g., $\tilde{u}_d^s(\kappa_x, \kappa_y, z, \omega)$) through a threefold Fourier transform (cf. Eq. (2)), a comparison of the statistics of the scattered wave response given in Eqs. (15) – (16) and the mean frequency-wave number response $\tilde{u}_d^m(\kappa_x, \kappa_y, z, \omega)$ may provide a qualitative estimate of the effects of the scattered wave response on the the corresponding mean wave response, or directly speaking, the effects of lateral inhomogeneities on the seismic wave motion. In particular, with $|\tilde{u}_d^m|$ as a reference, the larger the magnitude of $\tilde{\sigma}_d^s$ is, the larger the effects of the scattered wave response on the mean wave response and thus the larger the effects of the lateral inhomogeneities on the ground motion. Such an analysis will be presented in the next two subsections.

The quantitative estimates of the statistical effects of the lateral inhomogeneities on the time-space ground motion are very time consuming, since the scattered wave response $u_d^s(x, y, z = 0, t)$ is neither a homogeneous stochastic field nor a stationary stochastic process. This is due to the fact that the scattered wave response is dependent upon both the response of the mean wave field and the lateral inhomogeneities and the former is neither homogeneous nor stationary in statistics. However, they may still be evaluated at relatively less computational time if the scattered ground motion is assumed to be both homogeneous and stationary statistically in a specific time-space window that is very small compared with the whole time-space domain (Zhang, 1996). Because of limited space, this will be presented in another paper.

4.2 Qualitative Analysis of a Mean Wave Response. Since $\tilde{u}_d^m$ is used as a reference in investigating the effects of scattered wave response on the mean wave response, a qualitative analysis of the mean response has to be provided first, which is also useful in the later qualitative analysis of a scattered frequency wave number response. To do that, the following concepts are first introduced. For a given frequency ω, the waves at a certain wave number pair (κ_x, κ_y) are called propagating waves if they can propagate in the earth medium with only a proper phase change (no damping is considered in the earth medium). Otherwise, the waves are called evanescent waves, which decay exponentially while increasing the depth the waves travel (Kennett, 1983). The physical meanings for such a classification is that the propagating waves can carry the energy flux in the z-direction while the evanescent waves can not. Correspondingly, the wave number domain can be classified as a propagating regime and an evanescent regime for the waves at a given frequency. Specifically, the propagating regimes for P and S waves in layer i are

$$\kappa = \sqrt{\kappa_x^2 + \kappa_y^2} \leq \frac{\omega}{\alpha_i} \quad \text{for } P \text{ waves;}$$

$$\kappa = \sqrt{\kappa_x^2 + \kappa_y^2} \leq \frac{\omega}{\beta_i} \quad \text{for } S \text{ waves} \tag{17}$$

where κ is the wave number in the radial direction, α_i and β_i are, respectively, P and S wave speeds in layer i, $i = 1, 2, \ldots, n$. Revoking the seismic waves that are generated by a seismic dislocation source buried in layer k and noticing that the propagating regime for P waves is a subpropagating regime for S waves for a given layer, the propagating regime for the propagating seismic waves (including P and S waves and their combinations) in a layered half-space is thus governed by the propagating regime for S waves in layer k. In other words, only part of the seismic wave energy generated by the seismic source in layer k can be propagated out of the depth level of the seismic source, implying that the waves at the wave number pair within the propagating regime gives a significant contribution to the response at the level far away from the source level. It is noted that the above analysis is based on the fact that the earth medium has no damping. With consideration of the existence of damping, the seismic waves at the wave number within the wave number regime defined by

$$\kappa = \sqrt{\kappa_x^2 + \kappa_y^2} \leq a_f^m \frac{\omega}{\beta_k} \equiv \kappa_k(\omega) \tag{18}$$

will give the primary contribution to the response at the level far away from the source level, compared with those outside the wave number regime. In Eq. (18), a_f^m is a factor and chosen as larger than 1.0, dependent upon the frequency and relative depth of observation site to source. Basically, the larger the frequency and/or the relative depth of observation site to the source are, the closer to unity the factor a_f^m is. On the basis of the previous analysis, $|\tilde{u}_d^m(\kappa_x, \kappa_y, z = 0, \omega)|$ is much larger and thus dominant within the wave number regime given in Eq. (18) compared with those outside the regime. This can be confirmed from Fig. 1(*a*) in which the large magnitude of $\tilde{u}_d^m$ is restricted in the wave number regime given by $\kappa \leq \kappa_k$ (ω = 4 rad/sec) = 1.66 rad/km ($a_f^m = 1.2$).

4.3 Qualitative Analysis of a Scattered Wave Response. The effects of the scattered wave response on the mean wave field may be clearly seen by comparing the mean wave response $\tilde{u}_d^m$ and the corresponding standard deviation of the scattered wave response $\tilde{\sigma}_d^s$. The latter is dependent on two factors: one is $\tilde{\mathcal{H}}_d^s$ and the other is wave number spectrum Φ_a (cf. Eq. (16)). $\tilde{\mathcal{H}}_d^s$ is obtained as a response solution in the perfectly layered half-space subjected to the fictitious body forces distributed in layer j. Since the fictitious body forces are distributed in layer j and the fundamental solution has the same basic properties as the mean frequency wave number response as stated in Section 3, $|\tilde{\mathcal{H}}_d^s(\kappa_x, \kappa_y, z = 0; \kappa_x', \kappa_y')|$ will be large or dominant only within the wave number regime

$$\kappa = \sqrt{\kappa_x^2 + \kappa_y^2} \leq a_f^s \frac{\omega}{\beta_j} \equiv \kappa_j(\omega) \tag{19}$$

which is obtained using the same reason as in the mean wave field described in the last subsection.

As also mentioned in Section 3, $\tilde{\mathcal{H}}_d^s(\kappa_x, \kappa_y, z; \kappa_x', \kappa_y')$ is proportional to $\tilde{u}_d^m(\kappa_x - \kappa_x', \kappa_y - \kappa_y', z, \omega)$. Therefore, $\tilde{\mathcal{H}}_d^s$ will be large in magnitude only when the amplitude of $\tilde{u}_d^m(\kappa_x - \kappa_x', \kappa_y - \kappa_y', z, \omega)$ is large, which requires the basis of the results drawn from the last subsection (cf. Eq. (18))

Downloaded 04 May 2010 to 171.66.16.34. Redistribution subject to ASME license or copyright; see http://www.asme.org/terms/Terms_Use.cfm

$$|\kappa - \kappa'| \leq \sqrt{(\kappa_x - \kappa_x')^2 + (\kappa_y - \kappa_y')^2}$$

$$\leq a_f^m \frac{\omega}{\beta_k} \equiv \kappa_k(\omega) \quad (20)$$

where the first inequality is obtained with the aid of simple mathematical treatment. In short, the large magnitude of $\tilde{\mathcal{H}}_d^s$ is subjected to two conditions expressed in equations (19) and (20). With proper mathematical manipulation, these two conditions may be rewritten as

$$\max \{\kappa' - \kappa_k(\omega), 0\}$$

$$\leq \kappa \leq \min \{\kappa' + \kappa_k(\omega), \kappa_j(\omega)\}. \quad (21)$$

and

$$\max \{\kappa - \kappa_k(\omega), 0\}$$

$$\leq \kappa' \leq \kappa_k(\omega) + \kappa \leq \kappa_k(\omega) + \kappa_j(\omega) \equiv \kappa_c(\omega). \quad (22)$$

Recalling the integral representation of the standard deviation of the scattered wave response in Eq. (16) and noticing that the scattered wave response is of order ϵ compared with the mean wave response, one may easily find that, for a given frequency ω, $\tilde{\sigma}_d^s$ is large and comparable to $|\tilde{u}_d^m|$ only if the wave number spectrum Φ_a is large within the wave number regime given by Eq. (22). Otherwise, $\tilde{\sigma}_d^s$ is much small and may thus be neglected, compared with $|\tilde{u}_d^m|$. In other words, the effects of lateral inhomogeneities on the ground motion for that specific frequency may be neglected if Φ_a has a dominant intensity outside the wave number regime given by Eq. (22).

Noting that $\kappa_c(\omega_1) < \kappa_c(\omega_2)$ if $\omega_1 < \omega_2$, a conclusion may be withdrawn that the effects of lateral inhomogeneities on the ground motion with $\omega \leq \omega_c$ may be neglected if the lateral inhomogeneities have no or very small intensity of Φ_s at $\kappa' < \kappa_c(\omega_c)$, or equivalently, if the lateral inhomogeneities have a dominant intensity of Φ_a at $\kappa' \geq \kappa_c(\omega_c)$.

As an example, consider again a three-layer medium with the first layer being laterally inhomogeneous subjected to a pure strike-slip dislocation source buried in the second layer. All the pertinent parameters are the same as used in the last section. Selecting $\omega_c = 3$ rad/sec, then the lateral inhomogeneities with dominant intensity at $\kappa' > \kappa_c(\omega_c) = 3.53$ rad/km ($a_f^m = a_f^s = 1.3$) will have almost no effect on the ground motion with $\omega < \omega_c = 3$ rad/sec.

If the dominant frequency of the ground displacement is assumed to be less than ω_c (this is actually not the assumption for most of cases), the above conclusion may be alternatively stated as follows: the lateral inhomogeneities with the dominant wave length less than 1.78 km ($2\pi/\kappa_c(\omega_c)$) will have almost no effect on the ground displacement response. Consequently, the lateral inhomogeneities with the dominant wavelength less than 1.78 km may be approximated as a homogeneous layer as long as only the ground displacement response is concerned. On the other hand, the above conclusion also implies that the lateral inhomogeneities with the dominant wave length less than 1.78 km will affect the ground acceleration response, since the dominant acceleration frequency is usually larger than 3 rad/sec. Therefore, one may roughly say on the basis of the analysis that the lateral inhomogeneities with longer wave length affect the ground displacement response, while those with shorter wavelengths affect the ground acceleration response, which is consistent with Caviglia and Morro (1992).

5 Numerical Example

The three-layer half-space subjected to a pure strike-slip dislocation source, used in the last two sections, is considered again in the numerical example. The wave number spectrum Φ_a is assumed as the following form:

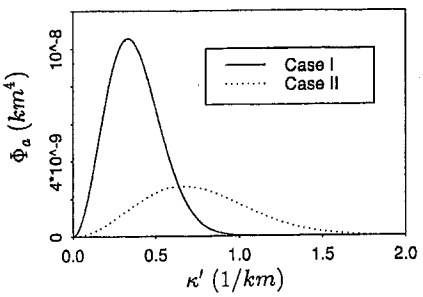


Fig. 6 Wave number spepctra Φ_a with $s = 1$

$$\Phi_a(\kappa_x', \kappa_y') = \frac{s^2}{16\pi} l^4(\kappa_x'^2 + \kappa_y'^2) \exp\left[-\frac{l^2}{4}(\kappa_x'^2 + \kappa_y'^2)\right] \quad (23)$$

where s is the standard deviation of $a(x, y)$ and l is the constant which is kind of measure of the "mean" or "dominant" wavelength of $a(x, y)$. Figure 6 presents two wave number spectra Φ_a with I: $s = 1$ and $l = 6$ km and II: $s = 1$ and $l = 3$ km. The corresponding sample realizations of the common factor $a(x, y)$, characterizing the lateral inhomogeneities, are simulated in Fig. 7 using the spectral representation method (Shinozuka and Deodatis, 1991) as follows:

$$a(x, y) = \sqrt{2} \sum_{i=1}^{N_1} \sum_{j=1}^{N_2} \sqrt{2\Phi_a(i\Delta\kappa_x', j\Delta\kappa_y')\Delta\kappa_x'\Delta\kappa_y'}$$

$$\times [\cos(i\Delta\kappa_x' x + j\Delta\kappa_y' y + \phi_{ij}) + \cos(i\Delta\kappa_x' x - j\Delta\kappa_y' y + \phi_{ij}')] \quad (24)$$

where ϕ_{ij} and ϕ_{ij}' are the random phase angles, independent each other and uniformly distributed between 0 and 2π, and the intervals, $\Delta\kappa_x'$ and $\Delta\kappa_y'$, are taken, respectively, as κ_{xu}'/N_1 and κ_{yu}'/N_2 in which κ_{xu}' and κ_{yu}' are, respectively, cut-off wave numbers in both the x and y-directions.

The z-direction ground accelerations at selected observation sites with and without the presented lateral inhomogeneities are depicted in Fig. 7, respectively, from which the effects of lateral inhomogeneities on the ground acceleration responses can be estimated. Specifically, the variation of peak acceleration due to "smooth" lateral inhomogeneities is relatively large compared with that due to "rough" lateral inhomogeneities, while the broadening of the seismogram envelopes is vice versa. This may be explained as follows. The "rougher" the lateral inhomogeneities are, the stronger the extent of the wave scattering is, and vice versa. Therefore, the arrival time of the scattered waves due to the smooth lateral inhomogeneities will be later than that of mean waves and earlier than that due to the rough lateral inhomogeneities. Consequently, the effects of smooth lateral inhomogeneities on the ground responses are primarily on the variation of peak acceleration if the difference of the arrival time between mean and scattered waves is small, while the effects of rough lateral inhomogeneities on the ground responses are primarily on the broadening of the seismogram envelopes. These phenomena are consistent with Aki (1975) and Sato (1984).

6 Concluding Remarks

Effects of lateral inhomogeneities on the seismic waves and their induced responses are qualitatively and quantitatively investigated using the first-order perturbation approach. The properties of the scattered wave response, especially those of the fundamental solution, are analyzed in detail. It has been shown that the effects of lateral inhomogeneities are strongly depen-

Downloaded 04 May 2010 to 171.66.16.34. Redistribution subject to ASME license or copyright; see http://www.asme.org/terms/Terms_Use.cfm

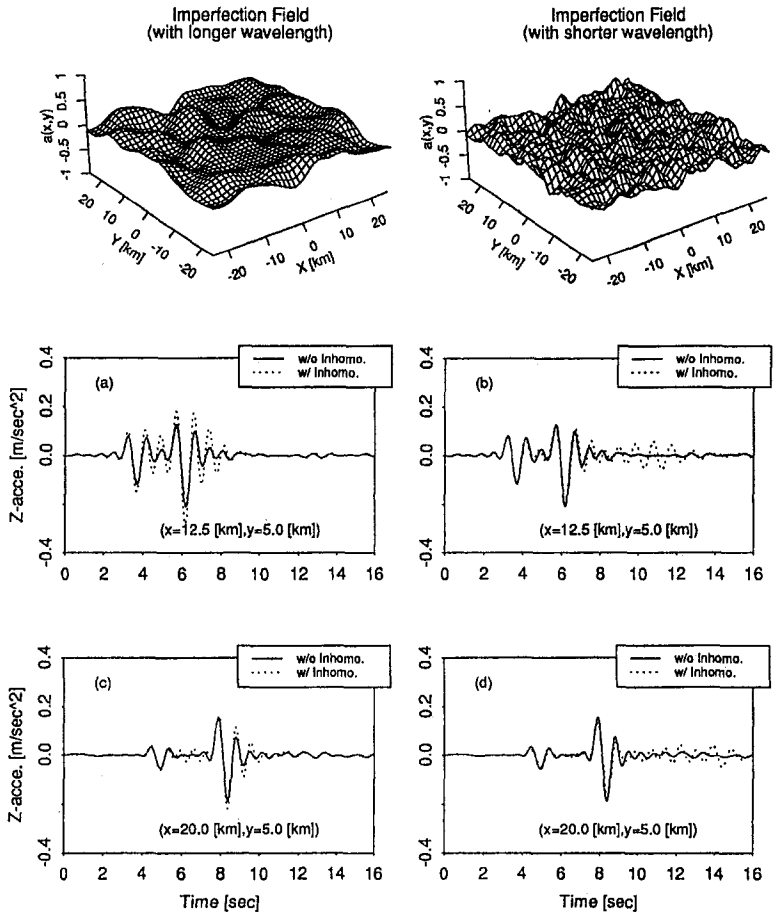


Fig. 7 Simulated common factor $a(x, y)$ and z-direction ground acceleration time history with and without lateral inhomogeneities

dent upon the relation of the wave number spectrum of the lateral inhomogeneities and the seismic waves under consideration, or more specifically, upon the relation of the wave number contents between the wave number spectrum of the lateral inhomogeneities and the seismic waves. Knowledge of such a relation determines whether or not the laterally inhomogeneous medium can be approximately considered as a laterally homogeneous medium, or equivalently, whether or not the effects have to be concerned in the present model.

Based on the observation of the numerical example, the effects of lateral inhomogeneities on the ground motion time history are non-negligible for some cases. The peak acceleration with lateral inhomogeneities may be changed up to ten percent or even higher, compared with that without lateral inhomogeneities, which is primarily dependent on the dominant wave length of the lateral inhomogeneities. Extended numerical examples will be compiled in another paper, which includes the use of an actual earthquake model such as the 1989 Loma Prieta earthquake and compares the ground motion obtained by the present approach with the corresponding earthquake records.

Acknowledgments

This work was supported by the National Center for Earthquake Engineering Research under Grant NCEER 94-3302A. The opinions, findings, and conclusions expressed herein are those of the writers and do not necessarily reflect the views of the sponsors.

References

Aki, K., 1975, "Original of coda waves: Source, attenuation, and scattering effects," *Journal of Geophysical Research,* Vol. 80, pp. 3322–3342.

Caviglia, G., and Morro, A., 1992, *Inhomogeneous waves in solids and fluids,* World Scientific, Singapore.

Ishimaru, A., 1978, *Wave Propagation and Scattering in Random Media,* Vols. 1 and 2, Academic Press, New York.

Kennett, B. L. N., 1972, "Seismic waves in laterally inhomogeneous media," *Geophys. J. R. astr. Soc.,* Vol. 27, pp. 301–325.

Kennett, B. L. N., 1983, *Seismic Wave Propagation in Stratified Media,* Cambridge University Press, Cambridge, UK.

Sato, H., 1984, "Attenuation and envelope formation of three-component seismograms of small local earthquakes in randomly inhomogeneous lithosphere," *Journal of Geophysical Research,* Vol. 89, No. B2, pp. 1221–1241.

Sato, H., 1989, "Broadening of seismogram envelopes in the randomly inhomogeneous lithosphere based on the parabolic approximation: southeastern Honshu, Japan," *Journal of Geophysical Research,* Vol. 94, No. B12, pp. 17,735–17,747.

Shinozuka, M., and Deodatis, G., 1991, "Stochastic wave models for stationary and homogeneous seismic ground motion," *Structural Safety,* Vol. 10, Nos. 1–3, pp. 235–246.

Zhang, R., 1994, "Stochastic seismic ground motion modeling with imperfectly stratified earth medium," *Journal of Sound and Vibration,* Vol. 176, No. 1, pp. 69–92.

Zhang, R., 1996, "Statistical Estimation of Strong Earthquake Ground Motion," Proceedings of the 11th World Conference on Earthquake Engineering, Acapulco, Mexico, submitted to *Journal of Engineering Mechanics.*

Zhang, R., Zhang, L., and Shinozuka, M., 1997, "Seismic Waves in a Laterally Inhomogeneous Layered Medium. I: Theory," ASME JOURNAL OF APPLIED MECHANICS, Vol. 64, pp. 50–58.

Downloaded 04 May 2010 to 171.66.16.34. Redistribution subject to ASME license or copyright; see http://www.asme.org/terms/Terms_Use.cfm

Dynamic Crack Propagation in a Layered Medium Under Antiplane Shear

Chien-Ching Ma
Professor.

Yi-Shyong Ing
Graduate Student

Department of Mechanical Engineering,
National Taiwan University,
Taipei, Taiwan 10617
Republic of China

In this study, the transient analysis of dynamic antiplane crack propagation with a constant velocity in a layered medium is investigated. The individual layers are isotropic and homogeneous. Infinite numbers of reflected cylindrical waves, which are generated from the interface of the layered medium, will interact with the propagating crack and make the problem extremely difficult to analyze. A useful fundamental solution is proposed in this study, and the solution can be determined by superposition of the fundamental solution in the Laplace transform domain. The proposed fundamental problem is the problem of applying exponentially distributed traction (in the Laplace transform domain) on the propagating crack faces. The Cagniard's method for Laplace inversion is used to obtain the transient solution in time domain. The exact closed-form transient solutions of dynamic stress intensity factors are expressed in compact formulations. These solutions are valid for an infinite length of time and have accounted for contributions from all the incident and reflected waves interaction with the moving crack tip. Numerical results of dynamic stress intensity factors for the propagation crack in layered medium are evaluated and discussed in detail.

1 Introduction

Most of the analyses done regarding cracked bodies are quasi-static. There are numerous situations that the material inertia becomes significant and must be taken into account in the analyses. The question of whether or not inertial effects are significant depends on the loading conditions and the geometrical configuration of the body. Inertial effects can arise either from applying dynamic loading on a cracked solid or from rapid crack propagation. The inherent time dependence of a dynamic fracture process results in mathematical models that are more complex than equivalent quasi-static models. However, there is substantial interest in the dynamic fracture problem due to its importance in many engineering applications. The relevant applications are NDE of layered media, rupture due to earthquakes in earth's crust, plate tectonics, composite materials, and functionally graded materials.

The main purpose in solving problems concerned with dynamic crack propagation is to determine the dependence of the crack-tip field characterizing parameters on the applied loading and on the configuration of the body. The investigation of a propagation crack in a brittle solid began with the pioneering analysis of Yoffe (1951). She considered a steady-state crack growth problem of a crack of fixed length propagating in an infinite elastic body subjected to a uniform remote tensile loading normal to the crack line. Although this is a physically unrealistic problem, it did at least provide an indication of the influence of crack speed on the stress state of a rapidly propagating crack. Craggs (1960) considered a semi-infinite crack extending at constant speed, with the crack face loading moving with the same speed as the crack tip in such a way that the entire deformation field is constant as seen by an observer moving with the crack tip. The self-similar dynamic crack propagation problem was contributed by Broberg (1960) who was among the first to present detailed analyses of crack propagation as a transient process. He solved the dynamic problem of a crack that suddenly grows from zero length at a constant speed. Baker (1962) subsequently generalized Broberg's solution to include a finite initial crack. Although the above mentioned artificial solutions have no direct application, they also have provided useful insights and continue to be used today for the assessment of dynamic numerical analyses.

In a series of papers, Freund (1972a, 1972b, 1973, 1974) developed important analytical methods for evaluation of the transient stress field of a propagating crack in a two-dimensional geometric configuration under quite general dynamic loading situation. These particular cases analyzed by Freund are also self-similar, but they are solved by means of integral transform methods rather than by direct application to similarity arguments. An indirect analytical approach proposed by Freund based on superposition over a fundamental solution, which opens a way for analysis of certain problems of crack propagation at nonuniform speed. Based on the superposition method proposed by Freund, a series of problems for nonplanar crack propagation in an infinite domain was solved by Ma and Burgers (1986, 1987, 1988) and Ma (1988, 1990). The structure of the near-tip field of crack propagation at nonuniform speeds was discussed in detail by Freund and Rosakis (1992). A representation of the crack-tip field was obtained in the form of an expansion about the crack tip in powers of radial coordinate, with the coefficients depending on the time rates of change of crack-tip speed and stress intensity factor. This representation was used to interpret some experimental observations and some estimates were made of the practical limits of using a stress intensity factor field alone to characterize the local fields. A thorough summary of the application of the main direct methods of analysis for transient problem in dynamic fracture has been given by Freund (1990).

Most of the solved dynamic fracture problems are regarded as a crack subjected to applying a uniformly distributed dynamic loading on the crack faces or subjected to incident plane waves. For the above-mentioned problems, either the direct application

Contributed by the Applied Mechanics Division of THE AMERICAN SOCIETY OF MECHANICAL ENGINEERS for publication in the ASME JOURNAL OF APPLIED MECHANICS.

Discussion on this paper should be addressed to the Technical Editor, Professor Lewis T. Wheeler, Department of Mechanical Engineering, University of Houston, Houston, TX 77204-4792, and will be accepted until four months after final publication of the paper itself in the ASME JOURNAL OF APPLIED MECHANICS.

Manuscript received by the ASME Applied Mechanics Division, July 10, 1995; final revision, Aug. 26, 1996. Associate Technical Editor: J. W. Ju.

Copyright © 1997 by ASME

Downloaded 04 May 2010 to 171.66.16.34. Redistribution subject to ASME license or copyright; see http://www.asme.org/terms/Terms_Use.cfm

of the well-known Wiener-Hopf technique is used or the superposition method proposed by Freund is performed to solve the problems. However, if a crack is subjected to incident nonplanar waves, none of the known methods can be used to obtain the transient solutions. Recently Tsai and Ma (1992) proposed a new fundamental solution to overcome these difficulties. The fundamental problem they considered is an exponentially distributed traction applied on crack faces and the solution is constructed by superposition of the fundamental solution in the Laplace transform domain. Tsai and Ma (1992) used this new fundamental solution to obtain the transient solution for a stationary semi-infinite crack subjected to a suddenly applied dynamic inplane body force in an unbounded medium. This alternative fundamental solution is also successfully applied towards solving more complicated transient problems (Tsai and Ma, 1993a, 1993b; Ma and Chen, 1994) for a subsurface stationary inclined crack subjected to dynamic loadings.

Determination of the dependence of the dynamic stress intensity factor on body configuration and applied loading during rapid crack propagation is a principal objective in dynamic fracture. Analytical results for configurations with boundaries other than the crack faces are rare. It was noted that after the stress waves reflected from the boundaries arrived at the crack tip, the nature of crack propagation changed. The interaction of stress waves with propagating cracks provides a way of altering the crack-tip stress field, and thus provide the basis for the crack branching phenomenon. Dynamic analysis of a mode III crack in a strip was discussed in a paper by Nilsson (1973) and Ma and Ing (1995). They considered the problem of a semi-infinite crack in a strip of finite width subjected to a uniformly distributed static load and propagating with a constant velocity, only the stress intensity factor and its time-dependence was determined.

The mechanical behavior of many newly developed multiphase materials are mainly controlled by the response of the interfaces. Many researchers have devoted to investigating the field of dynamic debonding along a bimaterial interface recently. Yang et al. (1991) examined singular fields around a running crack along the interface between two anisotropic substrates. The stress singularities and the angular stress distributions near a propagating interface crack in different transonic regimes for both antiplane and in-plane cases are determined by Yu and Yang (1994, 1995). Yang and Shih (1994) characterized the transition of the elastic moduli across the bimaterial interface by introducing a nonhomogeneous interlayer. The interlayer model provides some important concepts of interface fracture mechanics.

Since the interaction of stress waves with a propagating crack is an important event in dynamic fracture research, we shall investigate it in greater detail in the following. In this study, we will extend the methodology that was used successfully in solving dynamic stationary crack problem to construct the transient solution for crack propagation in the configuration of a layered medium. The problem considered in this study is a horizontal semi-infinite crack propagating with constant velocity in an infinitely long strip with finite width for a layered medium as shown in Fig. 1. In analyzing the above-mentioned problems, the interface boundaries and propagating crack are considered into the analysis. The interaction of infinitely many reflected waves generated from the interface boundaries and the propagating crack must be taken into account which will make the analysis extremely difficult. A useful fundamental solution is proposed to overcome these difficulties. This proposed fundamental solution is successfully applied towards solving the problem and is demonstrated as an efficient methodology to solve similar problems. Since the stress intensity factor is the key parameter in characterizing dynamic crack grows, we will focus our attention mainly on the determination of the dynamic stress intensity factor.

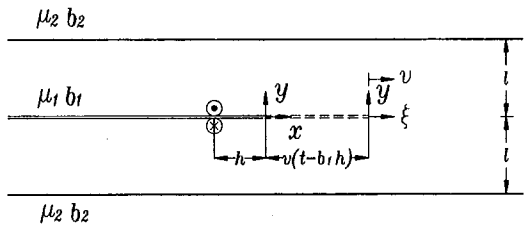


Fig. 1 Configuration and coordinate systems of a propagating crack in a layered medium

2 Required Fundamental Solutions

As usual in problems of the type considered here, superposition of solutions plays a significant role. The solutions of the problem considered in this study can be determined by superposition of the following problems. Problem A treats a dynamic concentrated loading acting on semi-infinite crack faces in an unbounded medium at time $t = 0$, at $t = t_f$, a new crack propagates out of the original semi-infinite crack with constant velocity, which induces incident cylindrical waves propagating toward the plane that will eventually define the interface boundary. In problem B, an interface in an unbounded medium is considered in which the interface is subjected to incident waves which are equal to the corresponding waves generated from the crack tip in problem A. Problem C considers an infinite body containing a propagating semi-infinite crack in which the crack is subjected to the reflected waves which are generated by the interface boundary in problem B. The three fundamental problems A, B, and C which are superimposed to obtain the solution for propagating crack in a layered medium interaction with stress waves. The reflected waves induced from the interface boundary as indicated in problem B, can be obtained by constructing the solution for incident cylindrical waves interaction with a interface in a layered medium. While problem A is a well-known problem for a semi-infinite crack propagating in an unbounded medium and many efforts have been devoted to analyze this problem.

Problem C in the above mentioned three fundamental problems is the only one which needs careful analysis. The problem we will deal with is the interaction of the propagating crack with cylindrical reflected waves, which causes the only difficulty in this investigation. For most of the dynamic problems, the propagating waves can be represented in an exponential functional form in the Laplace transform domain of time. The reflected and diffracted waves generated by the half-plane boundary and by the crack can be constructed by the proposed superposition method if the responses toward an applied exponentially distributed traction on boundaries in the Laplace transform domain can be obtained preliminarily. The superposition scheme proposed in this study, unlike usual superposition methods which are performed in the time domain, is performed in the Laplace transform domain.

Consider the fundamental problem for a propagating semi-infinite crack with constant velocity in an unbounded medium. The solution for an exponentially distributed loading applied at the crack faces in the Laplace transform domain will be referred to as the fundamental solution. The problem can be viewed as a half-plane problem with the material occupying the region $y \geq 0$, and subjected to the following mixed boundary conditions in the Laplace transform domain:

$$\bar{\tau}_{yz}(\xi, 0, s) = e^{s\eta\xi} \quad -\infty < \xi < 0, \tag{2.1}$$

$$\bar{w}(\xi, 0, s) = 0 \quad 0 < \xi < \infty, \tag{2.2}$$

where s is the Laplace transform parameter and η is a constant. The coordinate ξ is fixed with respect to the moving crack tip, that is $\xi = x - vt$. The overbar symbol is used for denoting the

Downloaded 04 May 2010 to 171.66.16.34. Redistribution subject to ASME license or copyright; see http://www.asme.org/terms/Terms_Use.cfm

transform on time t. The one-sided Laplace transform with respect to time and the two-sided Laplace transform with respect to ξ are defined by

$$\bar{w}(\xi, y, s) = \int_0^\infty w(\xi, y, t)e^{-st}dt,$$

$$\tilde{w}(\lambda, y, s) = \int_{-\infty}^\infty \bar{w}(\xi, y, s)e^{-s\lambda\xi}d\xi.$$

This fundamental problem can be solved by using the standard transform method and the Wiener-Hopf technique. The governing equation can be represented by the two-dimensional wave equation

$$\frac{\partial^2 w}{\partial x^2} + \frac{\partial^2 w}{\partial y^2} = b^2 \frac{\partial^2 w}{\partial t^2}, \tag{2.3}$$

where b is the slowness of the shear wave and is given by

$$b = 1/v_s = \sqrt{\rho/\mu},$$

in which $w(x, y, t)$ is the displacement normal to the xy-plane; v_s is the shear wave speed, μ and ρ are the respective shear modulus and the mass density of the material. The nonvanishing shear stresses are

$$\tau_{yz} = \mu \frac{\partial w}{\partial y}, \quad \tau_{xz} = \mu \frac{\partial w}{\partial x}. \tag{2.4}$$

In analyzing this problem, it is convenient to express the governing equation in the moving coordinates $\xi - y$ as follows:

$$(1 - b^2v^2) \frac{\partial^2 w}{\partial \xi^2} + \frac{\partial^2 w}{\partial y^2} + 2(b^2v) \frac{\partial^2 w}{\partial \xi \partial t} - b^2 \frac{\partial^2 w}{\partial t^2} = 0.$$

This fundamental problem can be solved by the application of integral transforms. Applying the one-sided Laplace transform over time, the two-sided Laplace transform over ξ under the restriction of $\mathrm{Re}(\eta) > \mathrm{Re}(\lambda)$, finally the Wiener-Hopf technique is implemented. The solutions of stresses and displacement in the transform domain for the boundary conditions (2.1) and (2.2) are

$$\bar{\tau}_{yz}(\xi, y, s) = \frac{1}{2\pi i} \int_{\Gamma_\lambda} \frac{\alpha^+_+(\lambda)e^{-s(\alpha^* y - \lambda\xi)}}{\alpha^+_+(\eta)(\eta - \lambda)} d\lambda, \tag{2.5}$$

$$\bar{\tau}_{xz}(\xi, y, s) = -\frac{1}{2\pi i} \int_{\Gamma_\lambda} \frac{\lambda e^{-s(\alpha^* y - \lambda\xi)}}{\alpha^+_+(\eta)(\eta - \lambda)\alpha^+_-(\lambda)} d\lambda, \tag{2.6}$$

$$\bar{w}(\xi, y, s) = -\frac{1}{2\pi i} \int_{\Gamma_\lambda} \frac{e^{-s(\alpha^* y - \lambda\xi)}}{\mu s \alpha^+_+(\eta)(\eta - \lambda)\alpha^+_-(\lambda)} d\lambda, \tag{2.7}$$

where

$$\alpha^*(\lambda) = \sqrt{b + \lambda(1 - bv)}\sqrt{b - \lambda(1 + bv)} = \alpha^+_+(\lambda)\alpha^+_-(\lambda).$$

The corresponding result of the dynamic stress intensity factor in the Laplace transform domain is

$$\bar{K}(s) = \lim_{\xi \to 0} \sqrt{2\pi\xi}\bar{\tau}_{yz}(\xi, 0, s) = -\frac{\sqrt{2}\sqrt{1 - bv}}{\sqrt{s}\alpha^+_+(\eta)}. \tag{2.8}$$

3 Transient Analysis for Propagating Crack in a Layered Media

Consider the problem of a semi-infinite crack in an infinitely long strip with finite width $2l$ of a layered medium as shown in Fig. 1. At time $t = 0$, a pair of equal and opposite concentrated antiplane dynamic loadings with magnitude p are applied at the crack faces with a distance h from the crack tip, the crack starts to propagate with constant velocity v at a delay time that the wave reach the crack tip (i.e., $t_f = b_1 h$) in the x-direction along the symmetry line $y = 0$ of the strip. The time dependence of the loading is represented by the Heaviside step function $H(t)$. In this problem, the cylindrical wave induced from the dynamic concentrated loading and the diffracted waves generated from the propagating crack tip will be reflected from horizontal interface boundaries, these waves will interact with the propagating crack at some later time. The major difficulty in analyzing this problem will be the one that deals with the interaction of reflected waves with the propagating crack and the superposition technique of the fundamental solutions in the Laplace transform domain will be used in the analysis. The transient solutions are composed of incident field, reflected field and diffracted field, which will be denoted by superscripts of i, r, and d, respectively. Before the time that the i and d waves reflected from the interface boundaries of the strip, the problem can be considered as a semi-infinite crack propagating in an unbounded medium. In the following analysis, the solution is valid for the case that crack starts to propagating before the waves (i.e., i wave and d wave) generated from the stationary crack returns to the stationary crack (i.e., $t_f < 2bl$) and $b_1 < b_2$.

The incident field of the cylindrical wave generated by the concentrated loading expressed in the Laplace transform domain can be obtained as follows:

$$\bar{\tau}_{yz}(x, 0, s) = \frac{1}{2\pi i} \int_{\Gamma_\lambda} -pe^{s\lambda(x+h)}d\lambda. \tag{3.1}$$

The applied traction on the crack face as indicated in (3.1), has a functional form $e^{s\lambda x}$. Since the solutions of applying traction $e^{s\eta x}$ on crack faces in the Laplace transform domain have been solved in Section 2 by setting $v = 0$, the diffracted field generated from the stationary semi-infinite crack can be constructed by superimposing the incident wave traction that is equal to (3.1). When we combine (2.5) (by setting $v = 0$) and (3.1), the solution of diffracted wave in the Laplace transform domain can be expressed as follows:

$$\bar{\tau}^s_{yz}(x, y, s) = \frac{1}{2\pi i} \int_{\Gamma_\lambda} -p \left\{ \frac{1}{2\pi i} \int_{\Gamma_{\eta_2}} \frac{(b_1 + \eta_2)^{1/2}}{(\lambda - \eta_2)(b_1 + \lambda)^{1/2}} \times e^{s\lambda h}e^{-s(\alpha_1 y - \eta_2 x)}d\eta_2 \right\} d\lambda. \tag{3.2}$$

By using the Cagniard-de Hoop method of Laplace inversion, the incident and diffracted stress fields in time domain for the stationary crack are obtained as follows:

$$\tau^i_{yz}(x, y, t) = \frac{-pt \sin\theta}{\pi r(t^2 - b_1^2 r^2)^{1/2}} H(t - b_1 r), \tag{3.3}$$

$$\tau^d_{yz}(x, y, t) = \frac{p}{2\pi^2} \int_{b_1 h}^{t - b_1 r_2} \mathrm{Re}\left[H(\eta_1^+, \eta_2^+) \frac{\partial \eta_1^+}{\partial t_1} \frac{\partial \eta_2^+}{\partial t_2} - H(\eta_1^-, \eta_2^+) \frac{\partial \eta_1^-}{\partial t_1} \frac{\partial \eta_2^+}{\partial t_2} \right] dt_1, \tag{3.4}$$

where

$$\eta_1^\pm = -\frac{t_1}{h} \pm i\varepsilon,$$

$$\eta_2^\pm = -\frac{t_2}{r_2}\cos\theta_2 \pm i\left(\frac{t_2^2}{r_2^2} - b_1^2\right)^{1/2} \sin\theta_2,$$

$$r = [(x + h)^2 + y^2]^{1/2}, \quad \theta = \cos^{-1}[(x + h)/r],$$

$$r_2 = (x^2 + y^2)^{1/2}, \quad \theta_2 = \cos^{-1}(x/r_2),$$

Downloaded 04 May 2010 to 171.66.16.34. Redistribution subject to ASME license or copyright; see http://www.asme.org/terms/Terms_Use.cfm

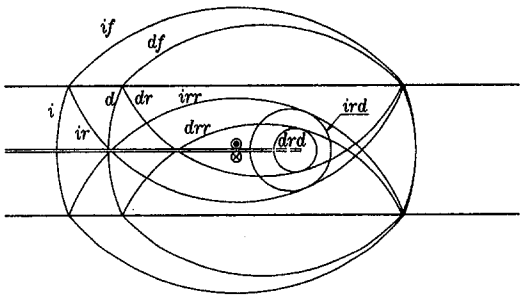


Fig. 2 Configuration of wave fronts in the layered medium after the crack propagates with constant velocity

$$H(\eta_1, \eta_2) = \frac{(b_1 + \eta_2)^{1/2}}{(\eta_1 - \eta_2)(b_1 + \eta_1)^{1/2}},$$

$$t = t_1 + t_2.$$

The corresponding dynamic stress intensity factor induced by diffracted wave will be

$$K^s(t) = p\sqrt{\frac{2}{\pi h}}\, H(t - b_1 h). \tag{3.5}$$

The dynamic stress intensity factor shown in (3.5) jumps from zero at the instant that the cylindrical wave generated by the concentrated loading reaches the crack tip. At time $t = t_f = b_1 h$, the dynamic stress intensity factor reaches its critical value and the crack starts to propagate with constant velocity v along the line $y = 0$. The transient full-field analysis for a propagating crack just mentioned above has also been solved by Ma and Chen (1992) by using the method proposed by Freund (1972b). In their investigations, the transient solution for constant-speed crack propagation is obtained by determining a fundamental solution for a concentrated force appearing through the moving crack tip, and then building up the general solution by superposition. In this study, a more direct and simple methodology will be used to solve this problem. We consider the transient problem of a semi-infinite crack propagates at $t = t_f = b_1 h$ with symmetric concentrated loading applied only on the original crack faces $-\infty < x < 0$. The applied symmetric concentrated loading p on the original crack faces written in the Laplace transform domain for the moving coordinate system will have the following form:

$$\bar{\tau}_{yz}(\xi, 0, s) = \frac{1}{2\pi i}\int_{\Gamma_\lambda} \frac{pd}{(\lambda - d)}\, e^{sh(1-b_1 v)\lambda + s\lambda\xi} d\lambda, \tag{3.6}$$

in which $d = 1/v$ is the slowness of the crack velocity and $\xi = x - vt$. The applied traction on crack faces as expressed in (3.6), has the functional form $e^{s\lambda\xi}$. Since the Laplace transform solutions of applying traction $e^{s\eta\xi}$ on crack faces have been solved in the previous section, the diffracted field generated from the propagating crack tip can be constructed by superimposing the fundamental solution and the stress distribution in (3.6). The result of shear stress expressed in the Laplace transform domain will be

$$\bar{\tau}^d_{yz}(\xi, y, s) = \frac{1}{2\pi i}\int_{\Gamma_{\eta_1}} \frac{pd}{(\eta_1 - d)}\, e^{sh(1-b_1 v)\eta_1}$$

$$\times \left\{\frac{1}{2\pi i}\int_{\Gamma_{\eta_2}} \frac{\alpha^*_{1+}(\eta_2)}{(\eta_1 - \eta_2)\alpha^*_{1+}(\eta_1)}\, e^{-s[\alpha^*_1 y - \eta_2 \xi]} d\eta_2\right\} d\eta_1, \tag{3.7}$$

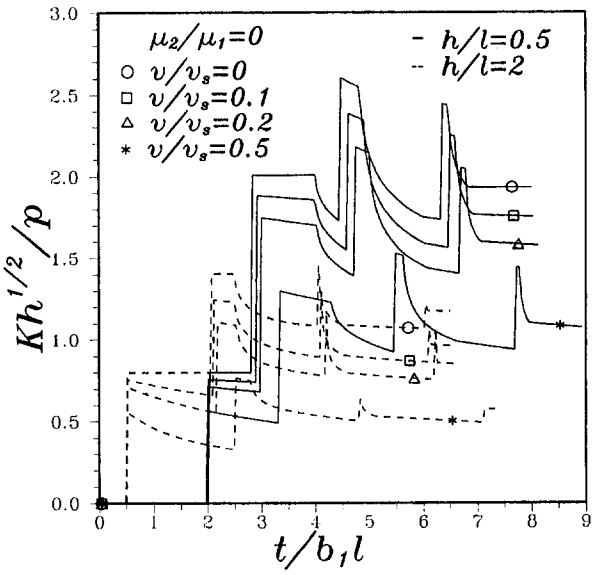


Fig. 3 Transient response of the dynamic stress intensity factor for various crack propagating speed

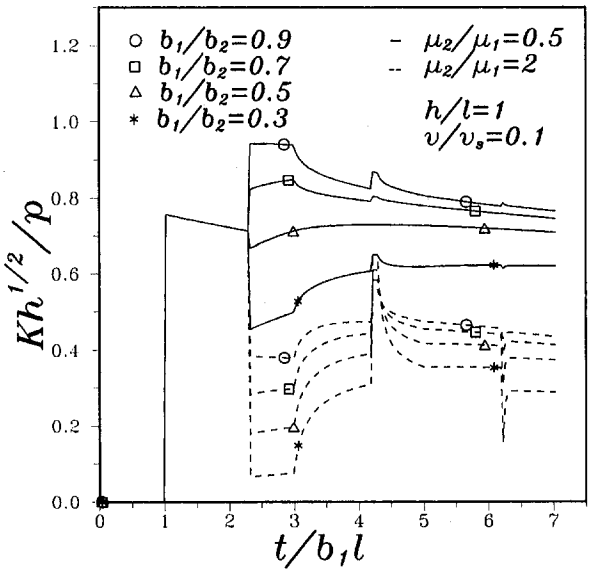


Fig. 4 Transient response of the dynamic stress intensity factor for different ratio of shear wave speed

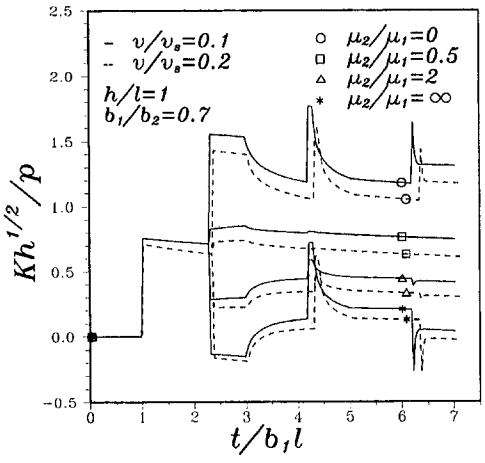


Fig. 5 Transient response of the dynamic stress intensity factor for different ratio of shear modulus of the layered medium

Downloaded 04 May 2010 to 171.66.16.34. Redistribution subject to ASME license or copyright; see http://www.asme.org/terms/Terms_Use.cfm

The exact transient solutions for a propagating crack in an unbounded medium in time domain can be obtained by inverting the Laplace transform domain of (3.7). The result is

$$\tau^d_{yz}(\xi, y, t) = \frac{-1}{2\pi^2}\int_{b_1 h}^{t-t_d} \mathrm{Re}\left[G(\eta_1^+, \eta_2^+)\frac{\partial \eta_1^+}{\partial t_1}\frac{\partial \eta_2^+}{\partial t_2} - G(\eta_1^-, \eta_2^+)\frac{\partial \eta_1^-}{\partial t_1}\frac{\partial \eta_2^+}{\partial t_2}\right] dt_1, \quad (3.8)$$

where

$$G(\eta_1, \eta_2) = \frac{pd\alpha^*_{1+}(\eta_2)}{(\eta_1 - d)\alpha^*_{1+}(\eta_1)(\eta_1 - \eta_2)},$$

$$\eta_1^{\pm} = \frac{-t_1}{h(1 - b_1 v)} \pm i\varepsilon,$$

$$\eta_2^{\pm} = \frac{-(\xi t_2 + b_1^2 v y^2) \pm iy\sqrt{t_2^2 - b_1^2[y^2 + (\xi + vt_2)^2)]}}{\xi^2 + (1 - b_1^2 v^2)y^2},$$

$$\frac{\partial \eta_2^+}{\partial t_2} = \frac{-\xi + iy\{t_2^2 - b_1^2[y^2 + (\xi + vt_2)^2]\}^{-1/2}[t_2(1 - b_1^2 v^2) - b_1^2 v\xi]}{\xi^2 + (1 - b_1^2 v^2)y^2},$$

$$t_d = \frac{b_1\{b_1 v\xi + [\xi^2 + (1 - b_1^2 v^2)y^2]^{1/2}\}}{1 - b_1^2 v^2},$$

$$t_1 + t_2 = t.$$

The dynamic stress intensity factor for a propagating crack at an infinite medium can also be constructed by a similar manner. The result in the Laplace transform domain can be obtained from (2.8) and (3.6) and is expressed as follows:

$$K^d(s) = \frac{1}{2\pi i}\int_{\Gamma_\lambda} \frac{pd}{(\lambda - d)} e^{sh(1 - b_1 v)\lambda} \times \left\{\frac{-\sqrt{2}\sqrt{1 - b_1 v}}{\sqrt{s}\alpha^*_{1+}(\lambda)}\right\} d\lambda. \quad (3.9)$$

The inversion Laplace transform of (3.9) will have the following form:

$$K^d(t) = p\sqrt{\frac{2}{\pi[v(t - b_1 h) + h]}} \times (1 - b_1 v)^{1/2} H(t - b_1 h). \quad (3.10)$$

The expression for $K^d(t)$ in (3.10) has the interesting form of the product of a function of the crack velocity $(1 - b_1 v)^{1/2}$ and the corresponding stationary crack solution $K^s(t)$ in (3.5) with a distance $v(t - b_1 h) + h$ from the crack tip. The value $(1 - b_1 v)^{1/2}$ is an universal function which depends only on crack speed and material properties. After some later time, the incident wave (i wave) generated from the dynamic concentrated loading and the diffracted wave (d wave) radiated out from the propagating crack will be reflected from the interface which will be indicated as the ir and dr wave, respectively. The solutions for reflected waves generated from the interface expressed in the Laplace transform domain can be obtained as follows:

$$\bar{\tau}^{ir+dr}_{yz}(\xi, y, s) = \frac{1}{4\pi^2}\iint \frac{\gamma^*_{1/2}(\eta_2)pd\alpha^*_{1+}(\eta_2)}{(\eta_1 - d)(\eta_1 - \eta_2)\alpha^*_{1+}(\eta_1)} \times e^{sh(1 - b_1 v)\eta_1} e^{s\alpha_1^*(y - 2l) + s\eta_2\xi} d\eta_2 d\eta_1, \quad (3.11)$$

where

$$\gamma^*_{1/2} = \frac{\mu_1\alpha_1^* - \mu_2\alpha_2^*}{\mu_1\alpha_1^* + \mu_2\alpha_2^*}.$$

The induced dynamic stress intensity factor by reflected ir and dr waves can be obtained by setting $y = 0$ in (3.11) and the fundamental solution expressed in (2.8). The result for the stress intensity factor expressed in the Laplace transform domain will have the following form:

$$\bar{K}^{ird+drd}(s) = \frac{1}{4\pi^2}\iint \frac{pd\sqrt{2}\sqrt{1 - b_1 v}\gamma^*_{1/2}(\eta_2)}{\sqrt{s}(\eta_1 - d)(\eta_1 - \eta_2)\alpha^*_{1+}(\eta_1)} \times e^{sh(1 - b_1 v)\eta_1 - 2s\alpha_1^*(\eta_2)l} d\eta_2 d\eta_1. \quad (3.12)$$

The dynamic stress intensity factor expressed in time domain will be

$$K^{ird}(t) = \frac{-\sqrt{2}pd\sqrt{1 - b_1 v}}{\pi^{3/2}}\int_{t_{ird}}^{t} \frac{1}{\sqrt{t - \tau}} \times \mathrm{Im}\left\{\frac{\gamma^*_{1/2}(\lambda^+)\dfrac{\partial \lambda^+}{\partial t}}{(\lambda^+ - d)\alpha^*_{\ddagger}(\lambda^+)}\right\}_{t=\tau} d\tau, \quad (3.13)$$

where

$$\lambda^{\pm} = \frac{-h(1 - b_1 v)t - 4b_1^2 vl^2 \pm i2l\sqrt{t^2 - b_1^2\{[vt + h(1 - b_1 v)]^2 + 4l^2\}}}{h^2(1 - b_1 v)^2 + 4l^2(1 - b_1^2 v^2)},$$

$$t_{ird} = \frac{b_1^2 vh(1 - b_1 v) + b_1\sqrt{h^2(1 - b_1 v)^2 + 4l^2(1 - b_1^2 v^2)}}{1 - b_1^2 v^2},$$

and

$$K^{drd}(t) = \frac{1}{2\pi^2}\int_{b_1 h + t'_{drd}}^{t}\int_{b_1 h}^{\tau - t'_{drd}} \frac{\sqrt{2(1 - b_1 v)}}{\sqrt{\pi(t - \tau)}} \times \mathrm{Re}\left[\frac{\gamma^*_{1/2}(\eta_2^+)G(\eta_1^+, \eta_2^+)}{\alpha^*_{1+}(\eta_2^+)}\frac{\partial \eta_1^+}{\partial t_1}\frac{\alpha\eta_2^+}{\partial t_2} - \frac{\gamma^*_{1/2}(\eta_2^+)G(\eta_1^-, \eta_2^+)}{\alpha^*_{1+}(\eta_2^+)}\frac{\partial \eta_1^-}{\partial t_1}\frac{\alpha\eta_2^+}{\partial t_2}\right]_{t=\tau} dt_1 d\tau, \quad (3.14)$$

where

$$\eta_1^{\pm} = \frac{-t_1}{h(1 - b_1 v)} \pm i\varepsilon,$$

$$\eta_2^{\pm} = \frac{-2b_1^2 vl \pm i\sqrt{(1 - b_1^2 v^2)t_2^2 - 4l^2 b_1^2}}{2l(1 - b_1^2 v^2)},$$

$$t'_{drd} = \frac{-2lb_1}{\sqrt{(1 - b_1^2 v^2)}},$$

$$t_1 + t_2 = t.$$

Finally, the complete transient solutions of dynamic stress intensity factor that account for the contributions of all the reflected and diffracted waves are obtained explicitly. The solutions can be simplified into a very compact form as follows:

$$K(t) = K^0(t) + \sum_{m=1}^{\infty} 2K^m(t) + \sum_{n=1}^{\infty} 2^n K^{0,n}(t) + \sum_{m=1}^{\infty}\sum_{n=1}^{\infty} 2^{n+1} K^{m,n}(t), \quad (3.15)$$

where

$$K^0(t) = p\sqrt{\frac{2}{\pi[v(t - b_1 h) + h]}} \times (1 - b_1 v)^{1/2} H(t - b_1 h), \quad (3.16)$$

Downloaded 04 May 2010 to 171.66.16.34. Redistribution subject to ASME license or copyright; see http://www.asme.org/terms/Terms_Use.cfm

$$K^m(t) = \frac{p\sqrt{2(1-b_1 v)}}{\pi^{3/2}} \int_{t_{v,m}}^{t} \frac{1}{\sqrt{t-\tau}} \times \mathrm{Im}\left\{ \frac{[\gamma^*_{1/2}(\eta^+_{1,m})]^m}{(1-\eta^+_{1,m} v)\alpha^*_{1+}(\eta^+_{1,m})} \frac{\partial \eta^+_{1,m}}{\partial t_1} \right\}_{t_1=\tau} d\tau, \quad (3.17)$$

$$K^{m,n}(t) = \frac{2p\sqrt{2(1-b_1 v)}\, i^q}{\sqrt{\pi}(2\pi i)^{n+1}} \int_{t_{v,m}+nt_{rr}}^{t} \int_{t_{v,m}}^{a_1} \int_{t_{rr}}^{a_2} \int_{t_{rr}}^{a_3} \cdots \int_{t_{rr}}^{a_n} \frac{1}{\sqrt{t-\tau}} \mathrm{SIFV}_{m,n} dt_n dt_{n-1} \cdots dt_1 d\tau, \quad (3.18)$$

in which

$$a_1 = \tau - nt_{rr},$$

$$a_j = \tau - t_1 - t_2 - \ldots - t_{j-1} - (n-j+1)t_{rr}, \qquad j = 2, 3, \ldots, n$$

$$q = 0 \quad \text{when} \quad n = 1, 3, 5, \ldots;$$

$$q = 1 \quad \text{when} \quad n = 2, 4, 6, \ldots$$

$$\mathrm{SIFV}_{m,n} = \mathrm{Re}\left[\frac{[\gamma^*_{1/2}(\eta^\pm_{1,m})]^m \gamma^*_{1/2}(\eta^\pm_2)\gamma^*_{1/2}(\eta^\pm_3)\cdots\gamma^*_{1/2}(\eta^\pm_{n+1}) \left(\pm\frac{\partial \eta^\pm_{1,m}}{\partial t_1}\right)\cdots\left(\pm\frac{\partial \eta^\pm_n}{\partial t_n}\right)\left(\pm\frac{\partial \eta^+_{n+1}}{\partial t_{n+1}}\right)}{(1-\eta^\pm_{1,m} v)\alpha^*_{1+}(\eta^\pm_{1,m})(\eta^\pm_{1,m}-\eta^\pm_2)(\eta^\pm_2-\eta^\pm_3)\cdots(\eta^\pm_{n-1}-\eta^\pm_n)(\eta^\pm_n-\eta^+_{n+1})} \right]_{t=\tau} \quad \text{for } n = 1, 3, 5, \ldots$$

$$\mathrm{SIFV}_{m,n} = \mathrm{Im}\left[\frac{[\gamma^*_{1/2}(\eta^\pm_{1,m})]^m \gamma^*_{1/2}(\eta^\pm_2)\gamma^*_{1/2}(\eta^\pm_3)\cdots\gamma^*_{1/2}(\eta^\pm_{n+1}) \left(\pm\frac{\partial \eta^\pm_{1,m}}{\partial t_1}\right)\cdots\left(\pm\frac{\partial \eta^\pm_n}{\partial t_n}\right)\left(\pm\frac{\partial \eta^+_{n+1}}{\partial t_{n+1}}\right)}{(1-\eta^\pm_{1,m} v)\alpha^*_{1+}(\eta^\pm_{1,m})(\eta^\pm_{1,m}-\eta^\pm_2)(\eta^\pm_2-\eta^\pm_3)\cdots(\eta^\pm_{n-1}-\eta^\pm_n)(\eta^\pm_n-\eta^+_{n+1})} \right]_{t=\tau} \quad \text{for } n = 2, 4, 6, \ldots$$

$$\eta^\pm_{1,m} = \frac{-h(1-b_1 v)t_1 - (2ml)^2 b_1^2 v \pm i2ml\sqrt{t_1^2 - b_1^2\{[vt_1 + h(1-b_1 v)]^2 + (2ml)^2\}}}{h^2(1-b_1 v)^2 + (2ml)^2(1-b_1^2 v^2)},$$

$$\eta^\pm_j = \frac{-b_1^2 vl \pm i\sqrt{(1-b_1^2 v^2)t_j^2 - 4l^2 b_1^2}}{2l(1-b_1^2 v^2)}, \quad j = 2, 3, 4, \ldots$$

$$t_{v,m} = \frac{b_1^2 vh(1-b_1 v) + b_1\sqrt{h^2(1-b_1 v)^2 + (2ml)^2(1-b_1^2 v^2)}}{1-b_1^2 v^2},$$

$$t_j = t - t_1 - t_2 - \ldots - t_{j-1}, \quad j = 2, 3, 4, \ldots$$

$$\gamma^*_{1/2}(\eta) = \frac{\mu_1\alpha^*_1(\eta) - \mu_2\alpha^*_2(\eta)}{\mu_1\alpha^*_1(\eta) + \mu_2\alpha^*_2(\eta)},$$

$$\alpha^*_1(\eta) = \alpha^*_{1+}(\eta)\alpha^*_{1-}(\eta) = \sqrt{b_1 + \eta(1-b_1 v)}\sqrt{b_1 - \eta(1+b_1 v)},$$

$$\alpha^*_2(\eta) = \sqrt{b_2 + \eta(1-b_2 v)}\sqrt{b_2 - \eta(1+b_2 v)},$$

$$t_{rr} = \frac{2lb_1}{\sqrt{1-b_1^2 v^2}}.$$

For the numerical calculation of the transient stress intensity factor, we consider a semi-infinite crack in a layered medium and subjected to a symmetric dynamic concentrated loading on a stationary crack faces at time $t = 0$. At nondimensional delay time $t/b_1 h = 1$, the crack starts to propagate with a constant speed v from the semi-infinite crack, the reflected and diffracted waves generated in the layered medium are shown in Fig. 2. The dynamic stress intensity factors of propagating crack for various situations are shown in Figs. 3–5. Figure 3 shows the dynamic stress intensity factor of a single strip for various crack propagating speed. We can see that the stress intensity factor is large when the propagating speed is low. Figure 4 shows the dynamic stress intensity factor for different ratio of shear wave speed. It indicates that the stress intensity factor is small when the magnitude of the ratio b_1/b_2 is low. Figure 5 shows the transient dynamic stress intensity factor for different ratio of shear modulus of the layered medium, in which $\mu_2/\mu_1 = 0$ corresponds to the traction-free boundary condition and $\mu_2/\mu_1 = \infty$ corresponds to the rigid boundary condition. Figure 5 indicates that the traction-free boundary condition will cause the largest value of stress intensity factor in the transient analysis.

4 Conclusions

The phenomena of crack propagation, arrest, and branching are important subjects in the areas of dynamic fracture analysis. The interaction of reflected waves generated from boundaries with the moving crack had only been discussed in experimental works. Experimental results indicated that the reflected waves dominate the stability of crack propagation. It is very important to have the analytical results to investigate this important event. But it seems difficult to obtain the analytical solutions by using the well-known conventional method.

We have proposed a powerful superposition methodology and a useful fundamental solution is constructed in this study to solve the problem of a propagating crack in a layered medium. The fundamental solution is the problem of applying an exponentially distributed traction on the propagating crack face and the solution is determined by superposition of the fundamental solution in the Laplace transform domain. The dynamic crack propagation with constant velocity in a configuration of layered medium with a strip is investigated. An explicit and complete result of the dynamic stress intensity factor is obtained in closed form and numerical results are evaluated in detail. The numerical results show that the stress intensity factors induced by reflected waves from the interface are significant.

There still have many unanswered questions in dynamic fracture and this work may provide a useful technique for further investigation in more complicated dynamic fracture problems especially on the crack propagation event. The proposed method in this study has already been extended to solve more difficult in-plane problem of crack propagation with boundary effect, the results will be shown in a future paper.

Acknowledgments

The authors gratefully acknowledge the financial support of this research by the National Science Council (Republic of China) under Grant NSC 83-0401-E-002-115. Some portions of the manuscript appeared at the 1995 ASME PVP meeting.

References

Baker, B. R., 1962, "Dynamic Stresses Created by a Moving Crack," ASME JOURNAL OF APPLIED MECHANICS, Vol. 29, pp. 449–458.

Downloaded 04 May 2010 to 171.66.16.34. Redistribution subject to ASME license or copyright; see http://www.asme.org/terms/Terms_Use.cfm

Broberg, K. B., 1960, "The Propagation of a Brittle Crack," *Arkiv for Fysik,* Vol. 18, pp. 159–192.

Craggs, J. W., 1960, "On the Propagation of a Crack in an Elastic-Brittle Solid," *Journal of the Mechanics and Physics of Solids,* Vol. 8, pp. 66–75.

Freund, L. B., 1972a, "Crack Propagation in an Elastic Solid Subjected to General Loading—I. Constant Rate of Extension," *Journal of the Mechanics and Physics of Solids,* Vol. 20, pp. 129–140.

Freund, L. B., 1972b, "Crack Propagation in an Elastic Solid Subjected to General Loading—II. Non-uniform Rate of Extension," *Journal of the Mechanics and Physics of Solids,* Vol. 20, pp. 141–152.

Freund, L. B., 1973, "Crack Propagation in an Elastic Solid Subjected to General Loading—III. Stress Wave Loading," *Journal of the Mechanics and Physics of Solids,* Vol. 21, pp. 47–61.

Freund, L. B., 1974, "Crack Propagation in an Elastic Solid Subjected to General Loading—IV. Obliquely Incident Stress Pulse," *Journal of the Mechanics and Physics of Solids,* Vol. 22, pp. 137–146.

Freund, L. B., 1990, *Dynamic Fracture Mechanics,* Cambridge University Press, Cambridge, U.K.

Freund, L. B., and Rosakis, A. J., 1992, "The Structure of the Near-tip Field during Transient Elastodynamic Crack Growth," *Journal of the Mechanics and Physics of Solids,* Vol. 40, pp. 699–719.

Ma, C. C., and Burgers, P., 1986, "Mode III Crack Kinking with Delay Time: An Analytical Approximation," *International Journal of Solids and Structures,* Vol. 22, pp. 883–899.

Ma, C. C., and Burgers, P., 1987, "Dynamic Mode I and Mode II Crack Kinking Including Delay Time Effects," *International Journal of Solids and Structures,* Vol. 23, pp. 897–918.

Ma, C. C., and Burgers, P., 1988, "Initiation, Propagation, and Kinking of an Antiplane Crack," ASME JOURNAL OF APPLIED MECHANICS, Vol. 55, pp. 111–119.

Ma, C. C., 1988, "Initiation, Propagation, and Kinking of an In-plane Crack," ASME JOURNAL OF APPLIED MECHANICS, Vol. 55, pp. 587–595.

Ma, C. C., 1990, "Dynamic Mixed Mode I-II Crack Kinking under Oblique Stress Wave Loading in Brittle Solids," ASME JOURNAL OF APPLIED MECHANICS, Vol. 57, pp. 117–127.

Ma, C. C., and Chen, S. K., 1994, "Exact Transient Full Field Analysis of an Antiplane Subsurface Crack Subjected to Dynamic Impact Loading," ASME JOURNAL OF APPLIED MECHANICS, Vol. 61, pp. 649–655.

Ma, C. C., and Ing, Y. S., 1995, "Transient Analysis of Dynamic Crack Propagation with Boundary Effect," ASME JOURNAL OF APPLIED MECHANICS, in press.

Nilsson, F., 1973, "A Transient Crack Problem for an Infinite Strip under Antiplane Shear," *Dynamic Crack Propagation,* G. C. Sih, ed., Nordhoff, Dordrecht, The Netherlands, pp. 543–551.

Tsai, C. H., and Ma, C. C., 1992, "Transient Analysis of a Semi-infinite Crack Subjected to Dynamic Concentrated Forces," ASME JOURNAL OF APPLIED MECHANICS, Vol. 59, pp. 804–811.

Tsai, C. H., and Ma, C. C., 1993a, "The Transient Analysis of a Subsurface Inclined Crack Subjected to a Buried Dynamic Dilatational Source," *International Journal of Solids and Structures,* Vol. 30, pp. 399–412.

Tsai, C. H., and Ma, C. C., 1993b, "The Stress Intensity Factor of a Subsurface Inclined Crack Subjected to a Dynamic Impact Loading," *International Journal of Solids and Structures,* Vol. 30, pp. 2163–2175.

Yang, W., Suo, Z., and Shih, C. F., 1991, "Mechanics of Dynamic Debonding," *Proc. R. Soc. Lond.,* Vol. A433, pp. 679–697.

Yang, W., and Shih, C. F., 1994, "Fracture along an Interlayer," *International Journal of Solids and Structures,* Vol. 31, pp. 985–1002.

Yoffe, E. H., 1951, "The Moving Griffith Crack," *Philosophical Magazine,* Vol. 42, pp. 739–750.

Yu, H., and Yang, W., 1994, "Mechanics of Transonic Debonding of a Bimaterial Interface: The Anti-plane Shear Case," *Journal of the Mechanics and Physics of Solids,* Vol. 42, pp. 1789–1802.

Yu, H., and Yang, W., 1995, "Mechanics of Transonic Debonding of a Bimaterial Interface: The In-plane Case," *Journal of the Mechanics and Physics of Solids,* Vol. 43, pp. 207–232.

Downloaded 04 May 2010 to 171.66.16.34. Redistribution subject to ASME license or copyright; see http://www.asme.org/terms/Terms_Use.cfm

Circular Rigid Punch With One Smooth and Another Sharp Ends on a Half-Plane With Edge Crack

Norio Hasebe

Jun Qian

Department of Civil Engineering,
Nagoya Institute of Technology,
Gokiso-cho, Showa-ku, Nagoya 466
Japan

A circular rigid punch with friction is assumed to contact with a half-plane with one end sliding on the half-plane and another end with a sharp corner. The contact length is determined by satisfying the finite stress condition at the sliding end of the punch. The crack is initiated near the end with a sharp corner where infinite stresses exist. Coulomb's frictional force is supposed to act on the contact region. The cracked half-plane is mapped into a unit circle by using a rational mapping function, and the problem is transformed into a standard Riemann-Hilbert problem, which is solved by introducing a Plemelj function. The contact length, the stress intensity factors of the crack, and the resultant moment about the origin of the coordinates on the contact region are calculated for different frictional coefficients, Poisson's ratios of the half-plane, crack lengths, and distances from the crack to the punch, respectively. The stress distributions on the contact region are also shown.

Introduction

In civil and mechanical engineering, load is often transferred between components by contact, such as in bolted joints, bearings, gear teeth, etc. A knowledge of the stresses and deformations developed through the contact of those components, especially in the presence of crack on the contact region, is an important consideration. Though some fundamental problems have been solved (Galin, 1953; Muskhelishvili, 1963; De Pater and Kalker, 1975; Gladwell, 1980), there still exist many problems that have not been considered or are difficult to be solved in an analytical way.

The concept of a rigid punch on an elastic half-plane was presented many years ago (Muskhelisvili, 1963; England, 1971). It was pointed that there generally exist two types of contact for a punch with curve shape; one is called complete contact, in which the length of the contact region is given, and there exist two sharp corners for the punch to come into the half-plane; the other type of contact is called incomplete contact, in which one or both ends of the punch slide on the surface of the half-plane, and the length of the contact region is undetermined.

In practice, a punch problem is often connected with a fracture problem since infinite tensile stress occurs at the sharp corners of the punch to initiate a crack in the half-plane or a pre-existing crack in the matrix is developed by the action of the punch. In a fretting problem, crack initiated by a punch is the main consideration. When a punch on a half-plane with a crack is concerned, some difficulties are met in computation. Though the problem is possible to be dealt with by some numerical methods (Hill, 1994), the modeling of the contact interface and the semi-infinite property of the half-plane as well as the singularity of the crack often result in some inconveniences. In order to analyze the problem precisely, it is necessary to present an analytical or semi-analytical method to solve the problem so that the inherent properties of the problem can be revealed in precision without much computation.

Contributed by the Applied Mechanics Division of THE AMERICAN SOCIETY OF MECHANICAL ENGINEERS for publication in the ASME JOURNAL OF APPLIED MECHANICS.

Discussion on this paper should be addressed to the Technical Editor, Professor Lewis T. Wheeler, Department of Mechanical Engineering, University of Houston, Houston, TX 77204-4792, and will be accepted until four months after final publication of the paper itself in the ASME JOURNAL OF APPLIED MECHANICS.

Manuscript received by the ASME Applied Mechanics Division, Oct. 10, 1995; final revision, Sept. 3, 1996. Associate Technical Editor: J. W. Ju.

A circular rigid punch problem with corners coming into contact with a cracked half-plane has been analyzed recently (Hasebe and Qian, 1995), in which the length of the contact region is given beforehand, and infinite stresses exist at both ends of the punch due to the corners. In the present paper, a circular punch with one end sliding on a half-plane and the other end with a corner coming into the half-plane with a vertical edge crack is considered. Since there is no corner at the sliding end, stresses are no longer infinite. This can be used as a restraining condition of the problem, and at the other end of the punch, infinite stresses exist and may initiate a crack in the surrounding area. In order to solve the problem analytically, the cracked half-plane is first mapped into a unit circle by a rational mapping function (Hasebe and Inohara, 1980; Hasebe et al., 1989). By a complex stress function method (Muskhelishvili, 1963), the problem is transformed into the Riemann-Hilbert problem, and is solved by introducing a Plemelj function (Hasebe et al., 1989). Owing to the use of the rational mapping function, the complex stress function can be derived analytically. The problem is solved under the condition that the punch does not incline. Therefore the position of the vertical force on the punch differs for different material constants, crack lengths, and radius of curvature of the punch, to keep the punch vertical. The position of the vertical force on the punch is determined by the resultant moment due to the stresses on the contact region about the origin. To satisfy the finite stress condition at the sliding end, the coefficient of the singular term of stress components at the sliding end must be zero, then the restraining condition is obtained. The length of the contact region is determined by solving the restraining equation. With the result of the contact length, the corresponding stress distributions on the contact region are presented. The stress intensity factors of the crack and resultant moment on the contact region about the origin are calculated under different circumstances.

Complex Stress Functions

Figure 1 shows a circular rigid punch with the left end sliding on a half-plane and the right end with a sharp corner in the half-plane. A vertical crack is initiated near the right end of the punch. The distance from the punch to the crack is c. R is the radius of curvature of the punch, b is the crack length, a' represents the length of the contact region, and a is the double length between the bottom (origin of the coordinate) and the right end of the punch. The position of the left end of the contact region

Copyright © 1997 by ASME

Downloaded 04 May 2010 to 171.66.16.34. Redistribution subject to ASME license or copyright; see http://www.asme.org/terms/Terms_Use.cfm

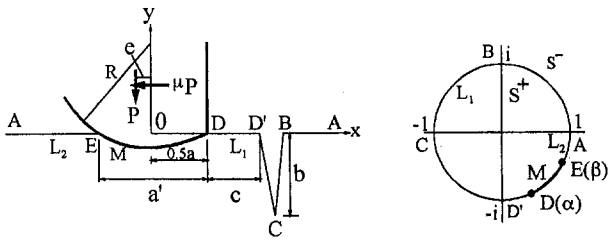


Fig. 1 Circular rigid punch and the unit circle

is changed with the conditions of the problem, while the right end is contacted, and is supposed to be $0.5a$ from the origin of the coordinate.

The cracked half-plane can be mapped into a unit circle on the ζ-plane by the following rational mapping function (Hasebe and Inohara, 1980):

$$z = \frac{E_0}{1-\zeta} + \sum_{k=1}^{N} \frac{E_k}{\zeta_k - \zeta} + E_c \equiv \omega(\zeta). \tag{1}$$

The coefficients of the above equation are shown in Hasebe et al. (1994) and $N = 24$ is selected with enough precision to reflect the sharpness at the crack tip (Hasebe et al., 1980) in the present paper.

The points α and β on the unit circle correspond to points D and E in the z-plane which represent the right and left ends of the contact region, respectively.

The resultant forces and displacements on the boundary $\zeta = \sigma$ can be expressed by the complex stress function $\phi(\zeta)$, which is regular inside the unit circle, as follows (Hasebe et al., 1989):

$$\phi^+(\sigma) - \phi^-(\sigma) = i \int (p_x + ip_y) ds \tag{2a}$$

$$\kappa\phi^+(\sigma) + \phi^-(\sigma) = 2G(u + iv) \tag{2b}$$

where p_x and p_y are x and y components of external force on the boundary, and u and v are components of displacement. κ equals to $3 - 4\nu$ for plane-strain state and $(3 - \nu)/(1 + \nu)$ for generalized plane stress state, and ν and G are the Poisson's ratio and shear modulus of the half-plane, respectively. $\phi^+(\sigma)$ denotes a value of $\phi(\zeta)$ on the unit circle approaching from the inside region S^+ and $\phi^-(\sigma)$ from the outside region S^- (see Fig. 1).

Since there exists a part of traction-free boundary, another complex stress function $\psi(\zeta)$ can be obtained by analytic continuation (Muskhelishvili, 1963),

$$\psi(\zeta) = -\bar{\phi}\left(\frac{1}{\zeta}\right) - \frac{\bar{\omega}\left(\frac{1}{\zeta}\right)}{\omega'(\zeta)} \phi'(\zeta). \tag{3}$$

The boundary conditions of the problem are expressed as follows:

On the free boundary

$$p_x = p_y = 0 \quad \text{on} \quad L_1 \text{ and } L_2. \tag{4a}$$

On the contact region M, by the law of Coulomb's friction

$$p_x = \mu p_y \quad \text{on} \quad M \tag{4b}$$

$$\int_D^E p_y ds = P \quad \text{on} \quad M \tag{4c}$$

$$V = \frac{x^2}{2R} \quad \text{on} \quad M. \tag{4d}$$

The resultant force on M equals to P and the displacement is in circular shape, $L_1 = ABCD'D$, $L_2 = EA$, $M = DE$, and μ is the Coulomb's frictional coefficient on the contact region.

Using (2), the following boundary equations are obtained (Hasebe et al., 1989):

$$\phi^+(\sigma) + \frac{1}{g}\phi^-(\sigma) = f_M(\sigma) \quad \text{on} \quad M \tag{5a}$$

$$\phi^+(\sigma) - \phi^-(\sigma) = f_L(\sigma) \quad \text{on} \quad L = L_1 + L_2 \tag{5b}$$

where

$$\frac{1}{g} = \frac{(\kappa+1) + i\mu(\kappa-1)}{(\kappa+1) - i\mu(\kappa-1)} \tag{5c}$$

$$f_M(\sigma) = \frac{4(1-i\mu)GiV + (1+i\mu)(1+\kappa)S(\sigma)}{(\kappa+1) - i\mu(\kappa-1)} \tag{5d}$$

$$f_L(\sigma) = \begin{cases} 0 & \text{on} \quad L_1 \\ P(1-i\mu) & \text{on} \quad L_2. \end{cases} \tag{5e}$$

$S(\sigma)$ is a rational function to be determined.

Equations (5a, b) denote a standard Riemann-Hilbert problem which can be solved by introducing the following Plemelj function:

$$\chi(\zeta) = (\zeta - \alpha)^m (\zeta - \beta)^{1-m} \tag{6a}$$

$$m = 0.5 - i \ln(g)/(2\pi) \tag{6b}$$

where the absolute value of g is one and thus m is a real number.

The general solution of (5a, b) is expressed as

$$\phi(\zeta) = H_A(\zeta) + H_B(\zeta) + \frac{1+i\mu}{2} J(\zeta) + Q(\zeta)\chi(\zeta) \tag{7a}$$

where

$$H_A(\zeta) = \frac{\chi(\zeta)}{2\pi i} \int_L \frac{f_L(\sigma)}{\chi(\sigma)(\sigma - \zeta)} d\sigma$$

$$P = \frac{(1-i\mu)\chi(\zeta)}{2\pi i} \int_\beta^1 \frac{d\sigma}{\chi(\sigma)(\sigma - \zeta)} \tag{7b}$$

$$H_B(\zeta) = \frac{4Gi(1-i\mu)}{(\kappa+1) - i\mu(\kappa-1)} \cdot \frac{\chi(\zeta)}{2\pi i} \int_M \frac{V}{\chi(\sigma)(\sigma - \zeta)} d\sigma$$

$$Gi = \frac{(1-i\mu)}{R(\kappa+1)} \frac{\chi(\zeta)}{2\pi i} \oint_M \frac{\{\omega(\sigma)\}^2}{\chi(\sigma)(\sigma - \zeta)} d\sigma \tag{7c}$$

$$J(\zeta) = \frac{(\kappa+1)(1+i\mu)}{(\kappa+1) - i\mu(\kappa-1)} \frac{\chi(\zeta)}{2\pi i} \int_M \frac{S(\sigma)}{\chi(\sigma)(\sigma - \zeta)} d\sigma$$

$$= \frac{\chi(\zeta)}{2\pi i} \oint_M \frac{S(\sigma)}{\chi(\sigma)(\sigma - \zeta)} d\sigma. \tag{7d}$$

The integral of $H_B(\zeta)$ can be transformed into a line integral around the contour M and can be carried out explicitly. $S(\zeta)$, $J(\zeta)$ and $Q(\zeta)\chi(\zeta)$ have been derived in detail in the previous paper (Hasebe et al., 1989). Owing to the limited length of the paper, they are omitted here.

The stress function $\phi(\zeta)$ is finally expressed as follows:

$$\phi(\zeta) = \frac{P(1-i\mu)}{2\pi i} \chi(\zeta) \int_\beta^1 \frac{d\sigma}{\chi(\sigma)(\sigma - \zeta)}$$

$$+ \frac{Gi(1-i\mu)}{R(\kappa+1)} \left[\{\omega(\zeta)\}^2 - \frac{\chi(\zeta)}{\chi(1)} \right.$$

$$\left. \times \left\{ \frac{E_0^2}{1-\zeta} \left[\frac{m}{1-\alpha} + \frac{1-m}{1-\beta} \right] + \frac{2E_0E_c}{1-\zeta} + \frac{E_0^2}{(1-\zeta)^2} \right\} \right.$$

Downloaded 04 May 2010 to 171.66.16.34. Redistribution subject to ASME license or copyright; see http://www.asme.org/terms/Terms_Use.cfm

$$- \sum_{k=1}^{N} \frac{2E_0E_k}{\zeta_k - 1}\left\{\frac{\chi(\zeta)}{\chi(1)(1-\zeta)} - \frac{\chi(\zeta)}{\chi(\zeta_k)(\zeta_k-\zeta)}\right\}$$

$$- \sum_{k\neq l}^{N} \frac{E_kE_l}{\zeta_k - \zeta_l}\left\{\frac{\chi(\zeta)}{\chi(\zeta_l)(\zeta_l-\zeta)} - \frac{\chi(\zeta)}{\chi(\zeta_k)(\zeta_k-\zeta)}\right\}$$

$$- \sum_{k=1}^{N} \frac{\chi(\zeta)}{\chi(\zeta_k)}\left\{\frac{E_k^2}{\zeta_k-\zeta}\left[\frac{m}{\zeta_k-\alpha} + \frac{1-m}{\zeta_k-\beta}\right]\right.$$

$$\left. + \frac{2E_kE_c}{\zeta_k-\zeta} + \frac{E_k^2}{(\zeta_k-\zeta)^2}\right\}\Bigg] - \frac{1+i\mu}{2}\sum_{k=1}^{N}\frac{\bar{A}_kB_k}{\zeta_k-\zeta}$$

$$+ \frac{1-i\mu}{2}\sum_{k=1}^{N}\frac{A_k\bar{B}_k\zeta_k'^2}{\zeta_k'-\zeta} - \frac{1-i\mu}{2}$$

$$\times\left(\sum_{k=1}^{N}\frac{\bar{A}_kB_k\chi(\zeta)}{\chi(\zeta_k)(\zeta_k-\zeta)} + \sum_{k=1}^{N}\frac{A_k\bar{B}_k\zeta_k'^2\chi(\zeta)}{\chi(\zeta_k')(\zeta_k'-\zeta)}\right) \quad (8a)$$

where

$$A_k \equiv \phi'(\zeta_k) \quad (k = 1, 2, \ldots, N) \quad (8b)$$

$$\bar{B}_k \equiv \frac{\bar{E}_k}{\omega'(\zeta_k')} \quad (k = 1, 2, \ldots, N) \quad (8c)$$

$$\zeta_k' \equiv \frac{1}{\bar{\zeta}_k} \quad (k = 1, 2, \ldots, N). \quad (8d)$$

The first integral of the right-hand side of (8a) is difficult to be carried out, but the first derivative of the integral can be obtained without integral form (see (12)). Therefore the first derivative of $\phi(\zeta)$ can be obtained without integral term and thus it is easy to determine A_k and calculate the stress components. A_k can be determined by solving $2N = 48$ simultaneous linear equations of real and imaginary parts of (8b).

The stress function for a half-plane without crack can be obtained by taking $E_k = 0$ and thus $B_k = 0$ ($k = 1, 2, \ldots, N$). When $R = \infty$, i.e., $H_B(\zeta) = 0$, the stress function becomes one for a flat-ended punch (Hasebe et al., 1989). When $P = 0$, i.e., $H_A(\zeta) = 0$, the stress function becomes one with the term $H_B(\zeta)$ which holds the punch vertical, and the resultant horizontal frictional force on the contact region is zero in this special case.

Restraining Condition and Contact Length

Because there is no corner at the sliding end of the punch, the stresses at this end must be finite, which can be used as the restraining condition of the present problem. Therefore the expression of stress components at the sliding end of the punch is derived beforehand. The stress components in the curvilinear coordinates represented by the mapping function can be expressed by $\phi(\zeta)$ and $\psi(\zeta)$ as (Muskhelishvili, 1963)

$$\sigma_\theta + \sigma_r = 2\left[\frac{\phi'(\zeta)}{\omega'(\zeta)} + \overline{\frac{\phi'(\zeta)}{\omega'(\zeta)}}\right] \quad (9a)$$

$$\sigma_\theta - \sigma_r + 2i\tau_{r\theta} = \frac{2\zeta^2}{|\zeta|^2\overline{\omega'(\zeta)}}\left[\overline{\omega(\zeta)}\left(\frac{\phi'(\zeta)}{\omega'(\zeta)}\right)' + \psi'(\zeta)\right]. \quad (9b)$$

Substituting (3) into (9), and let $\zeta \to \sigma$, the stress components on the boundary of the unit circle can then be expressed as

$$\sigma_\theta + \sigma_r = 2\left[\frac{\phi'^+(\sigma)}{\omega'(\sigma)} + \overline{\frac{\phi'^+(\sigma)}{\omega'(\sigma)}}\right] \quad (10a)$$

$$\sigma_\theta - \sigma_r + 2i\tau_{r\theta} = 2\left[\overline{\frac{\phi'^-(\sigma)}{\omega'(\sigma)}} + \frac{\phi'^+(\sigma)}{\omega'(\sigma)}\right]. \quad (10b)$$

From (10) it is found that

$$\sigma_r + i\tau_{r\theta} = \frac{1}{\omega'(\sigma)}\{\phi'^+(\sigma) - \phi'^-(\sigma)\}. \quad (11)$$

$\phi'(\zeta)$ can be derived from (8a) as follows:

$$\phi'(\zeta) = \frac{i(1-i\mu)P}{2\pi}\frac{\chi(\zeta)(1-\alpha)(1-\beta)}{\chi(1)(1-\zeta)(\zeta-\alpha)(\zeta-\beta)} + \frac{G}{R}\frac{i(1-i\mu)}{\kappa+1}F(\zeta) + G(\zeta) \quad (12)$$

where $F(\zeta)$ and $G(\zeta)$ are expressed in Appendix A, and the first term of the above equation is the first derivative of $H_A(\zeta)$ (Hasebe et al., 1989).

Substituting (12) into (11), it is given that

$$\sigma_r + i\tau_{r\theta} = \frac{1}{\omega'(\sigma)} \times\left\{\frac{i(1-i\mu)P}{2\pi}\frac{(1-\alpha)(1-\beta)}{\chi(1)(1-\sigma)(\sigma-\alpha)(\sigma-\beta)} + \frac{mf(\sigma)}{\sigma-\alpha} + \frac{(1-m)f(\sigma)}{\sigma-\beta} + g(\sigma)\right\} \times [\chi^+(\sigma) - \chi^-(\sigma)] \quad (13)$$

where $f(\sigma)$ and $g(\sigma)$ are expressed in Appendix B.

It is found from (13) that the stress components become infinite when σ tends to α or β. In order to satisfy the finite stress condition at the sliding end ($\sigma = \beta$), the coefficient of $1/(\sigma - \beta)$ in (13) must be vanished. Therefore the restraining condition is established as follows:

$$\frac{i(1-i\mu)(1-\alpha)}{2\pi\chi(1)(\beta-\alpha)}P + (1-m)f(\beta) = 0. \quad (14)$$

If the value of $Ga^2/(PR)$ and α which gives the location of the right end of the punch are given, β satisfying (14) can be determined by iterative calculation. After β is found, the contact length is then calculated by

$$a' = \omega(\alpha) - \omega(\beta) \quad (15)$$

$Ga^2/(PR)$ is a parameter that gives a relation among shear modulus G, punch width (see Fig. 1), radius of the circular punch and vertical force P. R is supposed to be sufficiently larger than the length of the contact region, and $Ga^2/(PR) = 1$ is taken for numerical calculation in this paper.

Figure 2 shows a'/a with different κ, μ and b/a, c/a is typically taken as zero, which means the crack exists at the end

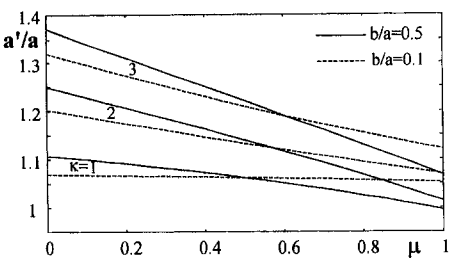


Fig. 2 The length of the contact region with different μ and κ under b/a = 0.5 and 0.1 and c/a = 0.0, solid lines for b/a = 0.5 and dashed lines for b/a = 0.1

Downloaded 04 May 2010 to 171.66.16.34. Redistribution subject to ASME license or copyright; see http://www.asme.org/terms/Terms_Use.cfm

of the punch. It is shown that the contact length decreases with the increase of the frictional coefficient, which represents that the frictional force on the contact region shortens the length of the contact region in order to satisfy the finite stress condition at the sliding end of the punch. It is also shown that the length of the contact region decreases with the decrease of the value of κ, and for each value of κ, when μ is relatively small, the length of the contact region for short crack is shorter than that for long crack; while μ is relatively large, it is on the contrary. The conclusion is on the condition that the crack is at the end of the right corner of the punch. Owing to the limited length of the paper, the results for the crack at other positions of the punch are omitted here.

Stress Distributions

With the known expression of $\phi'(\zeta)$ in (12) and (3) it is not difficult to calculate the stress components by (9) or (10) on the boundary. Figure 3 shows the normal stress σ_y on the contact region with different frictional coefficients. It is shown that the stress becomes infinite at the right sharp end, while at the left smoothly sliding end, the stress tends to zero. It is also shown that the contact length decreases with the increase of the frictional coefficient. The degree of the singularity at the right end increases with the increase of the frictional coefficient, while in the region except the sharp end, the stress decreases with the increase of the frictional coefficient.

Stress Intensity Factors

The stress intensity factors of the crack are calculated by

$$K_I - iK_{II} = 2\sqrt{\pi}\exp\left(-\frac{\delta}{2}i\right)\frac{\phi'(\sigma)}{\sqrt{\omega''(\sigma)}} \qquad (16)$$

where $\delta = -\pi/2$ and $\sigma = -1$ in this paper (Hasebe and Inohara, 1980).

The corresponding nondimensional stress intensity factors are defined as follows:

$$F_I + iF_{II} = \frac{K_I + iK_{II}}{P\sqrt{\pi}}\sqrt{a} \qquad (17)$$

Figure 4 shows F_I and F_{II} with different μ and κ, $b/a = 0.5$ and $c/a = 0$. The relation between F_I or F_{II} and μ is approximately in linear state, and the slope of each line is always positive. Therefore the larger frictional coefficient always results in greater singularity of the crack. When $\mu > 0.5$, F_I becomes positive, which is important in engineering viewpoint. On the other hand, the Poisson's ratio has little influence on F_I, which generally increases with the decrease of κ. Figure 5 shows

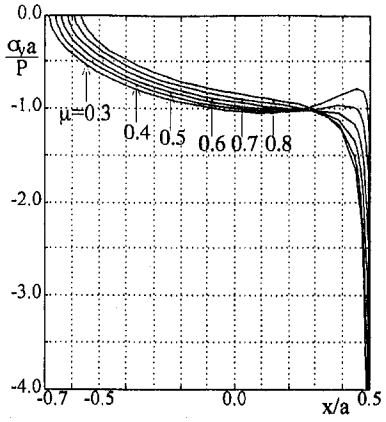


Fig. 3 The normal stress on the contact region with different μ, b/a = 0.5, c/a = 0.0, and κ = 2

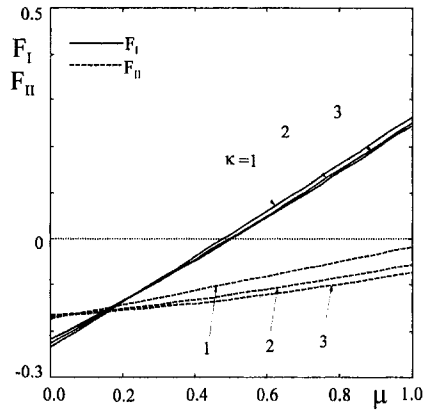


Fig. 4 The nondimensional stress intensity factors of the crack with different μ and κ, b/a = 0.5 and c/a = 0.0, solid lines for F_I, dashed lines for F_{II}

the relation among the stress intensity factors of the crack, b/a and μ. F_I and F_{II} usually decrease with the increase of the crack length. For larger μ, F_I is always positive, and for small μ, F_I is always negative, while for middle μ, there exists a critical value of b/a for F_I to change from positive to negative so that the development of the crack stops. The critical value of b/a increases with the increase of the frictional coefficient. F_{II} is always negative for all b/a and μ in Fig. 5. As for the influence of the distance from the crack to the punch on the stress intensity factors, as shown in Fig. 6, with the increase of c/a, the stress intensity factors increase at the beginning and then gradually decrease to zero for each μ and $b/a = 0.5$. For large μ, F_I is positive for all c/a, and for small μ, F_I is negative for all c/a, while for middle μ, there exists a critical value of c/a for F_I to change from negative to positive. The larger the frictional coefficient becomes, the smaller the critical value of c/a. For each μ and b/a, the critical position of the crack exists, which means the stress intensity factors change from negative to positive. F_{II} usually changes from negative to positive and finally tends to zero for each μ with the increase of c/a, which is owing to the phenomenon that the influence of the vertical force on the punch to the crack becomes less and less with the increase of c/a. On the other hand, since the frictional force on the contact region becomes the main factor to the value of F_I when the crack is far from the punch, F_I approaches zero slowly for each μ. When there does not exist any frictional force on the contact region, i.e., $\mu = 0$, F_I tends to zero more quickly as estimated.

Resultant Moment

In this paper, the problem is analyzed under the condition that the punch does not incline. Therefore the resultant moment

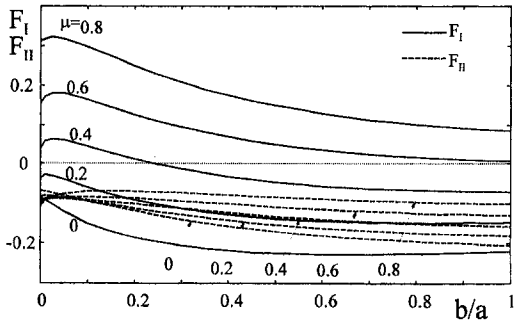


Fig. 5 The nondimensional stress intensity factors of the crack with different μ and b/a, c/a = 0.0 and κ = 2, solid lines for F_I, dashed lines for F_{II}

Downloaded 04 May 2010 to 171.66.16.34. Redistribution subject to ASME license or copyright; see http://www.asme.org/terms/Terms_Use.cfm

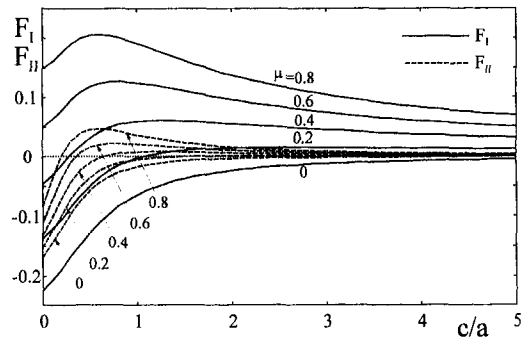


Fig. 6 The nondimensional stress intensity factors of the crack with different μ and c/a, $b/a = 0.5$ and $\kappa = 2$, solid lines for F_I, dashed lines for F_{II}

M_R about the origin of the coordinates can be used to determine the location of the vertical force P which applies at the location with a distance e from the y-axis to satisfy that $Pe = M_R$ (see Fig. 1).

The nondimensional resultant moment on the contact region is defined as

$$M_r = \frac{M_R}{Pa} \tag{18}$$

where M_R is calculated by (Muskhelishvili, 1963)

$$M_R = \mathrm{Re}\left[\int_\alpha^\beta \psi(\sigma)\omega'(\sigma)d\sigma\right] - \mathrm{Re}\left[\omega(\sigma)\overline{\omega(\sigma)}\,\frac{\phi'(\sigma)}{\omega'(\sigma)}\right]_\alpha^\beta - \mathrm{Re}[\omega(\sigma)\psi(\sigma)]_\alpha^\beta = -\mathrm{Re}\left[\int_\alpha^\beta \omega(\sigma)\overline{\phi'}\left(\frac{1}{\sigma}\right)\frac{d\sigma}{\sigma^2} + \int_\alpha^\beta \overline{\omega}\left(\frac{1}{\sigma}\right)\phi'(\sigma)d\sigma\right]. \tag{19}$$

The positive value of the moment denotes the counterclockwise direction.

Figure 7 shows the moment with various μ, κ and b/a. It is shown that the moment changes from positive to negative value with the increase of μ, which represents that the resultant force P on the contact region moves from the left side to the right side of the origin with the increase of the frictional coefficient for the punch not to incline. For small μ, the value of M_r for a long crack is usually larger than that of a short crack, and there usually exists a critical value of μ that makes M_r become zero for each case, which corresponds to the situation that the load P on the punch is just at the position of the origin of the

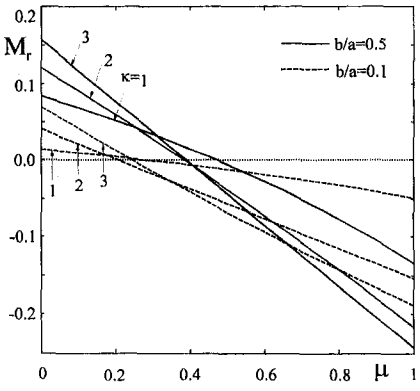


Fig. 7 The nondimensional resultant moment with different μ and κ, $b/a = 0.5$ and 0.1 and $c/a = 0.0$, solid lines for $b/a = 0.5$ and dashed lines for $b/a = 0.1$

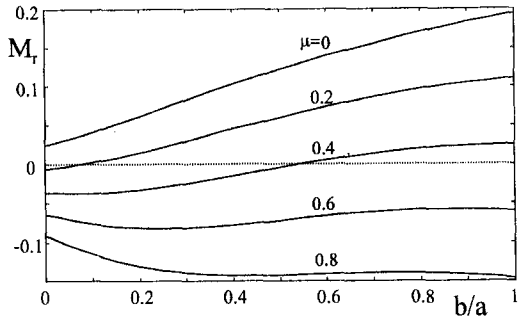


Fig. 8 The nondimensional resultant moment with different μ and b/a, $c/a = 0.0$ and $\kappa = 2$

coordinates, i.e., the point with a distance of $a/2$ from the right end of the punch. Figure 8 shows M_r with various μ and b/a. For small μ, M_r is always positive, and increases with the increase of b/a. And for large μ, M_r is always negative, and decreases with the increase of b/a; while for middle μ, M_r increases from negative to positive with the increase of b/a, and there exists a critical value of b/a for M_r to change sign. The larger the frictional coefficient becomes, the longer the critical crack length becomes. To analyze the influence of the position of the crack on the resultant moment on the contact region, Fig. 9 shows M_r with various μ and c/a. When $c/a < 0.5$, the moment is greatly influenced by c/a. When $c/a > 1$, it is shown that the moment becomes almost unchanged for each μ, which reflects that the influence of the crack on M_r becomes smaller and smaller with the increase of c/a, and can almost be neglected when $c/a > 1$.

Conclusion

The problem of the circular rigid punch with one end sliding on a half-plane and another end with a sharp corner coming into the half-plane with a crack was analyzed. The solution is given by (8a) and its first derivative by (12), under the restraining condition (14). If a crack initiates at the location away from the end of the punch, the crack first must be initiated from the boundary vertically since the maximum stress is along the boundary. For the case of an oblique edge crack, the mapping function in the reference (Hasebe and Inohara, 1980) can be used. The solution for a half-plane without any edge crack can be obtained by simply taking $E_k = 0$ ($k = 1, 2, \ldots, N$) in (8a). When $R = \infty$, the solution of the flat-ended punch with one smooth and another sharp end is obtained.

The contact length is found by solving the restraining equation to satisfy the condition that the stresses at the sliding end are finite. $Ga^2/(PR)$ is a parameter which gives the relation among G, a, R, and P. The length of the contact region decreases with the increase of the frictional coefficient. After obtaining the contact length, the corresponding stress components

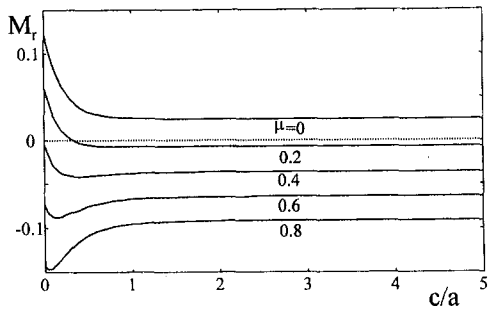


Fig. 9 The nondimensional resultant moment with different μ and c/a, $b/a = 0.5$ and $\kappa = 2$

Downloaded 04 May 2010 to 171.66.16.34. Redistribution subject to ASME license or copyright; see http://www.asme.org/terms/Terms_Use.cfm

are calculated. It is found that the singularity at the end with a sharp corner increases with the increase of μ, and the stress decreases with the increase of μ in the region except the sharp end (see Fig. 5). The stress intensity factors of the crack increases with the increase of the frictional coefficient, and decreases with the increase of the crack length. The position of the crack has certain influence on the stress intensity factors of the crack. The resultant moment on the contact region is calculated, which decides the location of the force P for the punch not to incline. Along with the increase of the frictional coefficient, the location of the force P on the contact region moves from the left side to the right side of the origin. If the vertical force P is applied at the origin, the punch is usually inclined for an angle. The corresponding solution can be obtained by the superposition of the inclined flat punch problem to the present solution (Hasebe et al., 1989; Okumura et al., 1990; Hasebe and Qian, 1995).

References

Bakirtas, I., 1980, "The problem of a rigid punch on a non-homogeneous elastic half space," *Int. J. Engrg. Sci.*, Vol. 18, pp. 597–610.

De Pater, A. D., and Kalker, J. J., eds., 1974, *The mechanics of the contact between deformable bodies*, Delft University Press, The Netherlands.

England, A. H., 1971, *Complex variable methods in elasticity*, John Wiley and Sons, London.

Galin, L. A., 1953, *Contact problems in the theory of elasticity*, Gastekhizdat, Moscow, U.S.S.R. (in Russian).

Gladwell, G. M., 1980, *Contact problems in the classical theory of elasticity*, Sijthoff and Noordhoff, The Netherlands.

Hasebe, N., and Iida, J., 1980, "A crack originating from a triangular notch on a rim of a semi-infinite plate," *Engrg. Fracture Mech.*, Vol. 10, pp. 773–782.

Hasebe, N., and Inohara, S., 1980, "Stress analysis of a semi-infinite plate with an oblique edge crack," *Ingenieur Archiv*, Vol. 49, pp. 51–62.

Hasebe, N., 1981, "An edge crack in a semi-infinite plate welded to a rigid stiffener," *Proc. of Japan Soc. of Civ. Engrs.*, Vol. 314, pp. 149–157.

Hasebe, N., Okumura, M., and Nakamura, T., 1989, "Frictional punch and crack in plane elasticity," *J. Engrg. Mech.*, Vol. 115, No. 6, pp. 1137–1147.

Hasebe, N., Nakamura, T., and Ito, Y., 1994, "Analysis of the Second Mixed Boundary Value Problem for a Thin Plate," ASME JOURNAL OF APPLIED MECHANICS, Vol. 61, pp. 555–559.

Hasebe, N., and Qian, J., 1995, "Circular inclined punch problem with two corners to contact with a half plane with a surface crack," *Contact Mechanics II*, M. H. Aliabadi and C. Alessandri, eds., Computational Mechanics Publications, Southampton, U.K., pp. 159–166.

Hills, D. A., and Nowell, D., 1994, *Mechanics of fretting fatigue*, Kluwer Academic Publishers, The Netherlands.

Muskhelishvili, N. I., 1963, *Some basic problems of mathematical theory of elasticity*, 4th ed., Noordhoff, The Netherlands.

Okumura, M., Hasebe, N., and Nakamura, T., 1990, "Crack due to wedge-shaped punch with friction," *J. Engrg. Mech*, Vol. 119, No. 10, pp. 2173–2185.

APPENDIX A

$F(\zeta)$ and $G(\zeta)$ in Eq. (12)

$$F(\zeta) = 2\omega(\zeta)\omega'(\zeta) - \left\{E_0^2\left(\frac{m}{1-\alpha}+\frac{1-m}{1-\beta}\right)+2E_0E_c\right\}$$

$$\times\left(\frac{\chi'(\zeta)(1-\zeta)+\chi(\zeta)}{\chi(1)(1-\zeta)^2}\right)$$

$$-\frac{E_0^2}{\chi(1)}\frac{\chi'(\zeta)(1-\zeta)+2\chi(\zeta)}{(1-\zeta)^3}$$

$$-\sum_{k=1}^{N}\frac{2E_0E_k}{\zeta_k-1}\left\{\frac{\chi'(\zeta)(1-\zeta)+\chi(\zeta)}{\chi(1)(1-\zeta)^2}\right.$$

$$\left.-\frac{\chi'(\zeta)(\zeta_k-\zeta)+\chi(\zeta)}{\chi(\zeta_k)(\zeta_k-\zeta)^2}\right\}$$

$$-\sum_{k\neq l}^{N}\frac{E_kE_l}{\zeta_k-\zeta_l}\left\{\frac{\chi'(\zeta)(\zeta_l-\zeta)+\chi(\zeta)}{\chi(\zeta_l)(\zeta_l-\zeta)^2}\right.$$

$$\left.-\frac{\chi'(\zeta)(\zeta_k-\zeta)+\chi(\zeta)}{\chi(\zeta_k)(\zeta_k-\zeta)^2}\right\}$$

$$-\sum_{k=1}^{N}\left\{E_k^2\left(\frac{m}{\zeta_k-\alpha}+\frac{1-m}{\zeta_k-\beta}\right)+2E_kE_c\right\}$$

$$\times\frac{\chi'(\zeta)(\zeta_k-\zeta)+\chi(\zeta)}{\chi(\zeta_k)(\zeta_k-\zeta)^2}$$

$$-\sum_{k=1}^{N}\frac{E_k^2}{\chi(\zeta_k)}\frac{\chi'(\zeta)(\zeta_k-\zeta)+2\chi(\zeta)}{(\zeta_k-\zeta)^3}$$

$$G(\zeta) = -\frac{1-i\mu}{2}\sum_{k=1}^{N}\frac{\overline{A}_kB_k}{\chi(\zeta_k)(\zeta_k-\zeta)^2}$$

$$\times\{\chi(\zeta)+\chi'(\zeta)(\zeta_k-\zeta)\}$$

$$-\frac{1+i\mu}{2}\sum_{k=1}^{N}\frac{\overline{A}_kB_k}{(\zeta_k-\zeta)^2}+\frac{1-i\mu}{2}\sum_{k=1}^{N}\frac{A_k\overline{B}_k\zeta_k'^2}{(\zeta_k'-\zeta)^2}$$

$$-\frac{1-i\mu}{2}\sum_{k=1}^{N}\frac{A_k\overline{B}_k\zeta_k'^2}{\chi(\zeta_k')(\zeta_k'-\zeta)^2}\{\chi(\zeta)+\chi'(\zeta)(\zeta_k'-\zeta)\}$$

where

$$\chi'(\zeta) = \left(\frac{m}{\zeta-\alpha}+\frac{1-m}{\zeta-\beta}\right)\chi(\zeta).$$

APPENDIX B

$f(\sigma)$ and $g(\sigma)$ in Eq. (13)

$$f(\sigma) = -\frac{G}{R}\frac{(1-i\mu)}{\kappa+1}$$

$$\times\left[\left\{E_0^2\left(\frac{m}{1-\alpha}+\frac{1-m}{1-\beta}\right)+2E_0E_c\right\}\frac{1}{\chi(1)(1-\sigma)}\right.$$

$$+\frac{E_0^2}{\chi(1)(1-\sigma)^2}+\sum_{k=1}^{N}\frac{2E_0E_k}{\zeta_k-1}$$

$$\times\left\{\frac{1}{\chi(1)(1-\sigma)}-\frac{1}{\chi(\zeta_k)(\zeta_k-\sigma)}\right\}$$

$$+\sum_{k\neq l}^{N}\frac{E_kE_l}{\zeta_k-\zeta_l}\left\{\frac{1}{\chi(\zeta)(\zeta_l-\sigma)}-\frac{1}{\chi(\zeta_k)(\zeta_k-\sigma)}\right\}$$

$$+\sum_{k=1}^{N}\left\{E_k^2\left(\frac{m}{\zeta_k-\alpha}+\frac{1-m}{\zeta_k-\beta}\right)+2E_kE_c\right\}$$

$$\left.\times\frac{1}{\chi(\zeta_k)(\zeta_k-\sigma)}+\sum_{k=1}^{N}\frac{E_k^2}{\chi(\zeta_k)(\zeta_k-\sigma)^2}\right]$$

$$-\frac{1-i\mu}{2}\left(\sum_{k=1}^{N}\frac{\overline{A}_kB_k}{\chi(\zeta_k)(\zeta_k-\sigma)}+\sum_{k=1}^{N}\frac{A_k\overline{B}_k\zeta_k'^2}{\chi(\zeta_k')(\zeta_k'-\sigma)}\right)$$

Downloaded 04 May 2010 to 171.66.16.34. Redistribution subject to ASME license or copyright; see http://www.asme.org/terms/Terms_Use.cfm

$$g(\sigma) = -\frac{G}{R}\frac{i(1-i\mu)}{\kappa+1}$$

$$\times\left[\left\{E_0^2\left(\frac{m}{1-\alpha}+\frac{1-m}{1-\beta}\right)+2E_0E_c\right\}\frac{1}{\chi(1)(1-\sigma)^2}\right.$$

$$+\frac{2E_0^2}{\chi(1)(1-\sigma)^3}+\sum_{k=1}^{N}\frac{2E_0E_k}{\zeta_k-1}$$

$$\times\left\{\frac{1}{\chi(1)(1-\sigma)^2}-\frac{1}{\chi(\zeta_k)(\zeta_k-\sigma)^2}\right\}$$

$$+\sum_{k\neq l}^{N}\frac{E_kE_l}{\zeta_k-\zeta_l}\left\{\frac{1}{\chi(\zeta_l)(\zeta_l-\sigma)^2}-\frac{1}{\chi(\zeta_k)(\zeta_k-\sigma)^2}\right\}$$

$$+\sum_{k=1}^{N}\left\{E_k^2\left(\frac{m}{\zeta_k-\alpha}+\frac{1-m}{\zeta_k-\beta}\right)+2E_kE_c\right\}$$

$$\times\left.\frac{1}{\chi(\zeta_k)(\zeta_k-\sigma)^2}+\sum_{k=1}^{N}\frac{2E_k^2}{\chi(\zeta_k)(\zeta_k-\sigma)^3}\right]$$

$$-\frac{1-i\mu}{2}\left(\sum_{k=1}^{N}\frac{\overline{A_k}B_k}{\chi(\zeta_k)(\zeta_k-\sigma)^2}+\sum_{k=1}^{N}\frac{A_k\overline{B_k}\zeta_k'^2}{\chi(\zeta_k')(\zeta_k'-\sigma)^2}\right)$$

Downloaded 04 May 2010 to 171.66.16.34. Redistribution subject to ASME license or copyright; see http://www.asme.org/terms/Terms_Use.cfm

Linear Complementary Formulations Involving Frictional Contact for Elasto-Plastic Deformable Bodies

Maocheng Li[1]
Graduate Research Assistant.

Desong Sha[2]
Visiting Scholar.

K. K. Tamma[3]
Professor.
Mem. ASME.

Department of Mechanical Engineering,
University of Minnesota,
111 Church Street, SE,
Minnesota, MN 55455

In the present study, an incremental variational inequality is described for frictional contact problems with material non linear behavior assumed to be elasto-plastic for the contacting bodies. On the contacting boundaries, the constraint conditions include noninterpenetration along the normal direction of the contact boundary and Coulomb friction law in the sliding direction. After numerical discretization using the finite element method, an effective linear complementary formulation is then established with two unknown variables and two complementary variables for each contact nodal pair. The proposed developments permit a reduced number of unknown variables which are chosen as the gap function for the normal direction and the norm of the incremental sliding displacements for the tangential direction; and the complementary variables are taken as the normal contact forces and slack variables in the tangential directions. The resulting linear complementary equations are then solved employing an explicit Conjugate Gradient Based Projection (CGBP) method in conjunction with a generalized Newton-Raphson iteration procedure to account for the material nonlinear behavior. The methodology is valid for three-dimensional frictional contact representations; however, for purposes of illustration of the proposed approaches, attention is confined to applications involving two-dimensional static elasto-plastic problems under small deformation. Numerical examples are presented which clearly show that the developments satisfy the problem physics and contact conditions with features to include high accuracy and reduced computational costs.

1 Introduction

For the problems of two or more solid bodies in contact with friction at the interface, the unknowns include the contact area, the normal and shear forces at the interface, the relative sliding distance of the bodies, and the stress and strain fields for each. Such frictional contact problems are boundary nonlinear problems, that is, the boundary conditions on the contact interface must satisfy noninterpenetration along the normal direction and a friction law (such as Coulomb's law of friction) along the tangential direction. They need to be satisfied simultaneously when a contact problem is solved. These two constraints are described by nonlinear inequalities in addition to the equilibrium equations. In the finite element analysis, a constraint problem, such as the frictional contact problem, may be described by a single variational inequality or by variational equality with the corresponding constraint conditions (for the discretization using finite elements). However, a key issue is to impose the constraint conditions accurately and efficiently when one solves the problem.

In some FEM developments for contact problems, solution algorithms often impose the contact constraints by trial-error iterative methods, that is, the constraint conditions are treated as convergence checking conditions for each step of the iteration. A typical iterative procedure was given by Bathe and Chaudhary (1985) which employed a Newton-Raphsion type iteration in conjunction with a constraint method similar to the Lagrangian multiplier method. In their analysis, the application is for a two-dimensional or axisymmetric contact problems involving sticking, frictional sliding, and separation with the material undergoing a large deformation. Also, the exact Coulomb law of friction was applied in their analysis. Because of the presence of an overlap at the contact interface to enable calculation of the contact forces, the approach requires small load increments as discussed by Bohm (1987). It was reported that the algorithm had been developed for solving three-dimensional problems and implemented in the ADINA software for metal forming simulations (Chaudhary and Bathe, 1986; Walczak and Bathe, 1990).

Currently, new mathematical theories and better optimization techniques as identified by Bohm (1987) suggest the application of variational inequalities, which are a generalization of the principle of virtual work and include complicated constraint conditions as natural conditions. In the literature, much of the attention has been focused upon solution methods to the variational inequality problems. To deal with the variational inequality, mathematical programming has been considered as an effective tool as indicated by Panagiotopoulos (1985) and Stavroulakis et al. (1991). Several approaches based on reduced variational inequality have been discussed by Panagiotopoulos (1985), and by Kikuchi and Oden (1988).

One important aspect in mathematical programming is to transfer the problem described by variational inequality into a free constraint problem or reduced constraints. For this purpose, the penalty function method described in Kikuchi and Song (1988), Hallquist (1983), Belytschko and Lin (1987), and Belytschko and Neal (1991) and the Lagrangian multiplier

[1] Currently, Senior R&D Engineer, Applied Materials, Inc., San Jose, CA.
[2] Permanent address: Dalian University of Technology, P. R. China.
[3] To whom all correspondence should be addressed.

Contributed by the Applied Mechanics Division of THE AMERICAN SOCIETY OF MECHANICAL ENGINEERS for publication in the ASME JOURNAL OF APPLIED MECHANICS.

Discussion on this paper should be addressed to the Technical Editor, Professor Lewis T. Wheeler, Department of Mechancial Engineering, University of Houston, Houston, TX 77204-4792, and will be accepted until four months after final publication of the paper itself in the ASME JOURNAL OF APPLIED MECHANICS.

Manuscript received by the ASME Applied Mechanics Division, Mar. 17, 1994; final revision, May 22, 1995. Associate Technical Editor: W. K. Liu.

Copyright © 1997 by ASME

Downloaded 04 May 2010 to 171.66.16.34. Redistribution subject to ASME license or copyright; see http://www.asme.org/terms/Terms_Use.cfm

method described in Belytschko and Neal (1991), Irons and Draper (1965), Katona (1983), and Zhong (1993) are the two most commonly used approaches to impose the constraint conditions for contact problems. Besides, there also exists the augmented Lagrangian method as described by Simo and Laursen (1992) and the perturbed Lagrangian method in Simo et al. (1985) to improve the performance of the Lagrangian multiplier method. However, a viable alternative is to transform the variational inequality into a linear complementary formulation as presented in Panagiotopoulos (1985) and Stavroulakis et al. (1991), Sha et al. (1992), and Tamma et al. (1994).

According to mathematical programming theory, the penalty method, the Lagrangian multiplier method, and linear complementary formulation are three different approaches to solve constraint minimization problems as illustrated by Bohm (1987). For the frictional contact problem with material and geometric nonlinearities, the analysis belongs to the class of problem in nonlinear programming.

The penalty method approaches the solution in the nonfeasible region, i.e., violating the contact constraints more or less is taken as a basis of this method. As the interpenetration at the contact interface and the violation of the friction law are introduced by penalty parameters, the solution accuracy depends on these user-defied parameters: The larger the penalty parameter is, the more accurate are the results, and the more difficult it is to obtain a converged solution. Besides, it also changes the profile and skyline of the global tangent stiffness matrix, which in turn affects the solution time in a strong way (Zhong and Mackerle, 1992). Although the penalty method does not introduce any additional unknowns and is easy to implement in existing FEM programs, the requirement of user-defined parameters by experience may make the trial-and-error effort to be time-consuming.

The Lagrangian multiplier method transforms a constraint minimization problem into a saddle point problem while the contact problem is frictionless and linear elastic. If friction is involved, such as the highly nonlinear friction model: exact Coulomb law, the approach to the solution is mathematically and numerically difficult. In the Lagrangian multiplier method, the contact forces are taken as additional unknowns. Hence, the size of the resulting global stiffness matrix and the half bandwidth for the contact problem are increased, thus requiring more storage and CPU time. Another weakness of the Lagrangian multiplier method is that some of diagonal terms in the global matrix are zero. This will cause slow convergence in the solution procedure for solving the resulting system of equations. Despite the fact that the nonpenetration condition is enforced exactly in the Lagrangian multiplier method, the introduction of additional variables and some zero diagonal terms in the stiffness matrix slow down the computation. In practice, it is commonly recognized by finite element analysis that the penalty method results in improved computational performance than the Lagrangian multiplier methods.

Linear complementary based formulations approach the solution by transforming a constraint minimization problem into a linear complementary problem. In frictional contact analysis, it is a new and very impressive alternative. By using the natural properties of the contact constraint conditions, it casts the constraints into the so-called Linear Complementary Equations (LCE) with the complementary conditions. Thus, when the system of LCE is solved by using modern mathematical programming solvers, such as Lemke's method, gradient projection method, quasi-Newton method (Panagiotopoulos, 1985; Bazaraa and Shetty, 1993) or the conjugate gradient projection method (Tamma et al., 1994) the computation can quickly converge to the solution and the constraint conditions are exactly satisfied. This approach does not use user-defined parameters nor additional variables, though it is somewhat difficult to implement in existing FEM codes than the penalty method or the Lagrangian multiplier method due to the involved changes in the source code structure. As an approach for frictional contact problems with linear elastic materials, a form of LCE was described by Stavroulakis et al. (1991) who used three unknown variables and three complementary variables (3×3) for each contact nodal pair in a typical two-dimensional analysis.

Recently, an effective finite element methodology employing a new form of LCE with a reduced number of variables (2×2) is given by Sha et al. (1992) for solving two-dimensional contact problems involving Coulomb's friction for linear elastic bodies. The Lemke's algorithm, which implicitly solves the LCE was chosen as the solver for the solution procedure. Subsequently, Tamma et al. (1994) described a new explicit solution approach for the LCE termed as the Conjugate Gradient Based Projection (CGBP) method, which yields the same efficiency as the Lemke's method and is also suitable for future efforts in parallel computations.

In this paper, the Coulomb slack variable (see Sha et al., 1992) which represents the exact Coulomb friction, is employed in the proposed approach to solve frictional contact problems. A new type of incremental variational inequality is described for frictional contact problems with the consideration that the contacting bodies are elasto-plastic deformable. On the contacting boundaries, the constraint conditions are described as nonpenetration along the normal direction of the contact boundary and the Coulomb friction law in the sliding direction. After numerical discretization using the finite element method, the corresponding LCE is then established with two unknown variables and two complementary variables (2×2) for each contact nodal pair. The unknown variables are chosen as (1) the gap function for the normal direction, and (2) the norm of the incremental sliding displacements for the tangential direction. The complementary variables are taken as (1) the normal contact forces, and (2) the Coulomb slack variables in the tangential directions. For handling material nonlinear situations, a generalized Newton-Raphson iteration procedure is developed in conjunction with the Conjugate Gradient Based Projection (CGBP) method to obtain the displacement and stress fields for two-dimensional contact problems.

The present computational methodology possesses high accuracy and also involves features for reduced computational cost. Although the theoretical developments are valid for three-dimensional frictional contact, for expository purposes, attention is confined to validations for two-dimensional frictional contact problems with elasto-plastic material behavior. Numerical examples are presented to demonstrate the proposed developments.

2 Governing Equations and Incremental Variational Inequality

Of interest are contact problems with Coulomb friction between two deformation bodies and the constitutive material behavior is assumed to be elasto-plastic. It is assumed that deformation bodies ${}^k\Omega \in R^N$ ($k = 1, 2$; and $N = 2$ or 3 for number of dimensions) are bounded by surfaces ${}^k\Gamma$, which consist of a mutually disjoint open manifold, ${}^k\Gamma_d$, ${}^k\Gamma_f$ and Γ_c, such that

$$ {}^k\Gamma = {}^k\Gamma_d \cup {}^k\Gamma_f \cup \Gamma_c \quad k = 1, 2. $$

The boundary Γ_c includes the true contact surface between two bodies ${}^k\Omega$ which are given displacements along ${}^k\Gamma_d$, and surface traction ${}^k\mathbf{p}$ ($k = 1, 2$) applied on boundaries ${}^k\Gamma_f$.

Introducing the local Cartesian coordinate system on the contact surfaces, the displacements ${}^k\mathbf{u} = \{{}^ku_i\} \in R^N$ and contact forces ${}^k\mathbf{s} = \{{}^ks_i\} \in R^N$ ($k = 1, 2$; and $N = 2$ or 3) on contact surfaces can be decomposed as

$$ {}^k\mathbf{u} = {}^ku_n{}^k\mathbf{n} + {}^k\mathbf{u}_t \quad k = 1, 2 $$

$$ {}^k\mathbf{s} = {}^ks_n{}^k\mathbf{n} + {}^k\mathbf{s}_t \quad k = 1, 2 $$

Downloaded 04 May 2010 to 171.66.16.34. Redistribution subject to ASME license or copyright; see http://www.asme.org/terms/Terms_Use.cfm

where ${}^k\mathbf{n}$ are the outward unit normal vectors to the contact surface, ${}^k u_n$ and ${}^k s_n$ are the normal components of ${}^k\mathbf{u}$ and ${}^k\mathbf{s}$, ${}^k\mathbf{u}_t$ and ${}^k\mathbf{s}_t$ are tangent components of ${}^k\mathbf{u}$ and ${}^k\mathbf{s}$, respectively.

We next consider frictional contact with an initial gap between deformation bodies. Incremental forms are adopted since frictional contact is a highly nonlinear problem. Denoting the gap at the last state loaded be the function $g(\mathbf{u}_0)$, the contact condition at the present state is described following Panagiotopoulos (1985):

$$g(\mathbf{u}) = g(\mathbf{u}_0) - \Delta u_n \geq 0 \tag{1a}$$

$$g(\mathbf{u})\sigma_n = 0 \tag{1b}$$

$$\sigma_n \leq 0 \tag{1c}$$

where $\mathbf{u}_0$ is the displacement at the last loaded state, σ_n is normal contact force density, and Δu_n is the normal incremental relative displacement on the boundary Γ_c, which are determined by

$$\Delta u_n = \Delta^1 u_n + \Delta^2 u_n \quad \text{on } \Gamma_c$$

$$\sigma_n = \sigma_{ij} n_i n_j \quad \text{on } \Gamma_c$$

where the condition $(1a)$ describes a noninterpenetrating condition, $(1b)$ describes the complimentary condition, and $(1c)$ implies a single side contact; i.e., it is not possible to have a tensile force on surface Γ_c.

Let the factor μ be the Coulomb frictional coefficient which is isotropic on the contact boundary, the Coulomb frictional law is expressed by

$$\|\boldsymbol{\sigma}_t\| + \mu\sigma_n \leq 0 \tag{2a}$$

$$\lambda \geq 0 \tag{2b}$$

$$\lambda(\|\boldsymbol{\sigma}_t\| + \mu\sigma_n) = 0 \tag{2c}$$

$$\Delta\mathbf{u}_t = -\lambda \frac{\boldsymbol{\sigma}_t}{\|\boldsymbol{\sigma}_t\|} \tag{2d}$$

where

$$\sigma_{ti} = \sigma_{ij} n_j - \sigma_n n_i$$

$$\Delta\mathbf{u}_t = \Delta^1\mathbf{u}_t + \Delta^2\mathbf{u}_t$$

and $\|\boldsymbol{\sigma}_t\|$ is defined as

$$\|\boldsymbol{\sigma}_t\| = \sqrt{\sigma_{ti}\sigma_{ti}}. \tag{3}$$

In condition $(2d)$, $\boldsymbol{\sigma}_t/\|\boldsymbol{\sigma}_t\|$ gives a sliding direction which is a unit vector and thus

$$\lambda = \|\Delta\mathbf{u}_t\|. \tag{4}$$

Since an elasto-plastic constitutive model is considered which is representative of nonlinear material property of the contact bodies, a yield criterion must be chosen for each deformation body and is generally expressed as a yield function represented as

$${}^kF(\boldsymbol{\sigma}, \kappa) \leq 0, \quad k = 1, 2 \tag{5}$$

where κ is hardening parameter (see Owen and Hinton, 1980). The corresponding incremental stress-strain relations are taken as

$$\Delta\boldsymbol{\sigma} = \mathbf{D}(\Delta\boldsymbol{\epsilon} - \Delta\boldsymbol{\epsilon}^p) \tag{6a}$$

$$\Delta\boldsymbol{\epsilon} = \Delta\boldsymbol{\epsilon}^e + \Delta\boldsymbol{\epsilon}^p \tag{6b}$$

$$\Delta\boldsymbol{\epsilon}^p = \lambda^p \frac{\partial F(\boldsymbol{\sigma}, \kappa)}{\partial\boldsymbol{\sigma}} \tag{6c}$$

where $\boldsymbol{\sigma}$ and $\boldsymbol{\epsilon}$ are the stress and strain vectors, respectively, $\mathbf{D}$ is the matrix of elastic constants for an isotropic material, and λ^p is a proportionality constant termed as plastic multiplier. The superscripts, e and p, denote elastic and plastic terms, respectively. From Eqs. $(6a-c)$, we can derive

$$\Delta\boldsymbol{\sigma} = \mathbf{D}_{ep}\Delta\boldsymbol{\epsilon} \tag{6d}$$

where

$$\mathbf{D}_{ep} = \mathbf{D} - \rho\frac{\mathbf{Da}\{\mathbf{Da}\}^T}{H' - \mathbf{a}^T\mathbf{Da}} \quad \rho = \begin{cases} 0 & \text{if } F < 0 \\ 1 & \text{if } F = 0 \end{cases} \tag{6e}$$

and

$$\mathbf{a}^T = \frac{\partial F(\boldsymbol{\sigma}, \kappa)}{\partial\boldsymbol{\sigma}} \quad \text{for } {}^kF(\boldsymbol{\sigma}, \kappa) \leq 0 \tag{6f}$$

here H' is the hardening function, and $\mathbf{a}$ the plastic flow vector.

Hence, the contact problem with Coulomb friction for the elasto-plastic body deformation can be described employing the weak form as follows:

Define a space of the admissible displacement field as

$$\Re = \{\boldsymbol{\nu} | \boldsymbol{\nu} = \{{}^1\boldsymbol{\nu}, {}^2\boldsymbol{\nu}\}, \quad {}^k\boldsymbol{\nu} \in [\mathbf{H}^1({}^k\Omega)]^N,$$

$${}^k\boldsymbol{\nu} = \Delta^k\mathbf{u}_d \quad \text{on } {}^k\Gamma_d, \quad g_n(\boldsymbol{\nu}) \geq 0, \quad \boldsymbol{\nu}_t = -\alpha\frac{\boldsymbol{\sigma}_t}{\|\boldsymbol{\sigma}_t\|},$$

$$\alpha \geq 0 \quad \text{on } \Gamma_c\} \quad (k = 1, 2; \text{ and } N = 2 \text{ or } 3).$$

Find a function $\Delta\mathbf{u} \in \Re$ such that

$$\sum_{k=1}^{2}\left(\int_{{}^k\Omega}\{\boldsymbol{\epsilon}(\boldsymbol{\nu} - \Delta\mathbf{u}^{n+1})\}^T\Delta\boldsymbol{\sigma}^{n+1}d\Omega\right.$$

$$+\int_{{}^k\Omega}\{\boldsymbol{\epsilon}(\boldsymbol{\nu} - \Delta\mathbf{u}^{n+1})\}^T\boldsymbol{\sigma}^n d\Omega$$

$$\left.-\int_{{}^k\Gamma_f}\{\boldsymbol{\nu} - \Delta\mathbf{u}^{n+1}\}^T\mathbf{p}^{n+1}d\Gamma\right)$$

$$-\mu\int_{\Gamma_c}(\|\boldsymbol{\nu}_t\| - \|\Delta\mathbf{u}_t^{n+1}\|)^T\boldsymbol{\sigma}_n^{n+1}d\Gamma \geq 0 \quad \forall\boldsymbol{\nu} \in \Re \tag{7}$$

where Taylor's expansion is taken at σ^n, and Eq. (7) is an incremental form from the step n to $n+1$, i.e.,

$$\sigma^{n+1} = \sigma^n + \Delta\sigma^{n+1}. \tag{8}$$

Here σ^{n+1} must satisfy ${}^kF(\boldsymbol{\sigma}, \kappa) \leq 0$ and the stress-strain relation is determined by Eqs. $(6a-f)$.

3 Finite Element Discretization

The variational inequality (7) is next approximated by the finite element technique. Let ${}^kn$ $(k = 1, 2)$ be the number of nodal degrees of freedom in domains ${}^k\Omega$, and n_c be the number of nodal degrees of freedom on the frictional contact boundary Γ_c, respectively. Let ${}^k\Delta\mathbf{U}$ be the nodal incremental displacement vector, $\mathbf{V}$ the virtual field, $\mathbf{S}$ the nodal frictional contact force vector on Γ_c, $\mathbf{f}_{in}$ the internal force vector, and $\mathbf{f}_{ex}$ the external load vector. The admissible displacement set is defined as

$$\Re_{ad} = \{\Delta\mathbf{U} | \Delta\mathbf{U} = \{\Delta^1\mathbf{U}, \Delta^2\mathbf{U}\}; \quad {}^k\Delta\mathbf{U} \in R^{{}^kn};$$

$${}^kF(\sigma, \kappa) \leq 0 \quad \text{in} \quad R^{{}^kn}$$

$${}^k\Delta\mathbf{U} = {}^k\Delta\mathbf{U}_d \quad \text{on nodes of } {}^k\Gamma_d;$$

$$\mathbf{g}_n(\mathbf{U}) \geq 0, \quad \text{and} \quad \Delta\mathbf{U}_t = -\lambda\frac{\mathbf{S}_t}{\|\mathbf{S}_t\|},$$

$$\lambda \geq 0 \quad \text{on nodes of } \Gamma_c\} \quad k = 1, 2. \tag{9}$$

The finite element approximation of the variational inequality (7) is next obtained as follows:

Downloaded 04 May 2010 to 171.66.16.34. Redistribution subject to ASME license or copyright; see http://www.asme.org/terms/Terms_Use.cfm

Find an incremental displacement $\Delta \mathbf{U} \in \Re_{ad}$ such that

$$\sum_{k=1}^{2} \{\mathbf{V} - {}^k\Delta\mathbf{U}^{n+1}\}^T\{{}^k\mathbf{K}({\mathbf{U}}^n){}^k\Delta\mathbf{U}^{n+1} + {}^k\mathbf{f}_{in}^n - {}^k\mathbf{f}_{ex}^{n+1}\}$$

$$- \mu\{\|\mathbf{V}\|_\nu - \|\Delta\mathbf{U}_t^{n+1}\|_\nu\}^T\mathbf{S}_n^{n+1} \geq 0 \quad \forall \mathbf{V} \in \Re_{ad} \quad (10a)$$

where vector $\mathbf{S}_n$ is the normal contact forces on nodal pairs, and $\|\cdot\|_\nu$ denotes a vector consisting of the norm of "$\cdot$" at the contact nodal pairs, i.e.,

$$\|\Delta\mathbf{U}_t\|_\nu = \{\|\Delta\mathbf{u}_{t1}\|, \|\Delta\mathbf{u}_{t2}\|, \ldots, \|\Delta\mathbf{u}_{tM}\|\}^T$$

M = number of nodal pairs.

Since material nonlinearities are involved in the analysis, the tangential stiffness matrix ${}^k\mathbf{K}$ depends on the current stress state which is a function of the displacement field, $\mathbf{U}^n$. Similarly the internal force field is also a function of $\mathbf{U}^n$. In summary,

$${}^k\mathbf{K}^n = {}^k\mathbf{K}(\mathbf{U}^n) \quad k = 1, 2$$

$${}^k\mathbf{f}_{in}^n = {}^k\mathbf{f}_{in}(\mathbf{U}^n) \quad k = 1, 2.$$

For each load incremental step n to $n + 1$, an iteration procedure, which is represented here as the generalized Newton-Raphson procedure (discussed in a later part of this paper), has to be employed so as to obtain converged solution for the elasto-plastic deformation model. Thus we have

$$\sum_{k=1}^{2} \{\mathbf{V} - {}^k\Delta\mathbf{U}_{m+1}^n\}^T\{{}^k\mathbf{K}(\mathbf{U}_m^n){}^k\Delta\mathbf{U}_{m+1}^n + {}^k\mathbf{f}_{in}(\mathbf{U}_m^n) - {}^k\mathbf{f}_{ex}^{n+1}\}$$

$$- \mu\{\|\mathbf{V}\|_\nu - \|(\Delta\mathbf{U}_t)_{m+1}^n\|_\nu\}^T \times (\mathbf{S}_n)_{m+1}^n \geq 0 \quad \forall \mathbf{V} \in \Re_{ad} \quad (10b)$$

and

$${}^k\mathbf{U}_{m+1}^n = {}^k\mathbf{U}_m^n + {}^k\Delta\mathbf{U}_{m+1}^n \quad k = 1, 2 \quad (10c)$$

where m denotes the number of iterations.

In the inequality (10a), the internal force vectors are calculated by

$${}^k\mathbf{f}_{in}(\mathbf{U}_m^n) = \sum_{e \in k} \int_{e_\Omega} \mathbf{B}^T\boldsymbol{\sigma}(\mathbf{U}_m^n)d\Omega \quad k = 1, 2 \quad (10d)$$

where $\boldsymbol{\sigma}(\mathbf{U}_m^n)$ satisfies the yielding condition

$${}^kF(\sigma, \kappa) \leq 0 \quad \text{in} \quad R^{k_n} \quad k = 1, 2.$$

Considering elasto-plastic material nonlinearity,

$${}^k\mathbf{K}_m(\mathbf{U}_m^n) = \sum_{e \in k} \int_{e_\Omega} \mathbf{B}^T\mathbf{D}_{ep}(\mathbf{U}_m^n)\mathbf{B}d\Omega \quad k = 1, 2. \quad (10e)$$

For each contact body, the iteration under an incremental loading will exit to the next loading step when

$$|{}^k\mathbf{f}_{ex}^{n+1} - {}^k\mathbf{f}_{in}(\mathbf{U}_m^n)| \leq \epsilon \quad k = 1, 2 \quad (10f)$$

are satisfied. In Eq. (10f), ϵ is a given convergence tolerance.

The issue now involves the solution of the finite element approximation of the variational inequality in the incremental form, Eq. (10b). We describe a special technique to transform the resulting FEM variational inequality, Eq. (10b), into a linear complementary formulation. The first step towards the solution is to condense the unknowns onto the contact boundary. After some algebraic manipulation, the inequality given by Eq. (10b) is finally transformed into a system of linear complementary equations (LCE). This transform includes normal restraint-unilateral contact, and tangential restraint-Coulomb friction as complementary conditions. Solving the LCE yields the solution of the unknown variables on the contact boundaries. They are the normal and shear forces on the contacting nodes, the magnitude of the gap between nodal pairs, and relative sliding distance of nodal pairs. Once the above solution variables are obtained, the stress and strain fields of each deforming body can be calculated accordingly.

4 Condense Unknowns Upon Contact Boundary

The problem now has been reduced to the solution of the variational inequality, Eq. (10a). As the first step, the stiffness ${}^k\mathbf{K}$ is written in block form as

$${}^k\mathbf{K} = \begin{bmatrix} {}^k\mathbf{K}_{ii} & {}^k\mathbf{K}_{ic} \\ {}^k\mathbf{K}_{ci} & {}^k\mathbf{K}_{cc} \end{bmatrix} \quad k = 1, 2 \quad (11a)$$

where the subscript c denotes the nodal degree-of-freedom on the boundary Γ_c, and i denotes the other nodes of the body.

Taking any vector $\forall \mathbf{V} \in \Re_{ad}$ satisfying $\mathbf{V} = {}^k\Delta\mathbf{U}_c^{n+1}$ on the Γ_c, the variational inequality (10a) yields

$${}^k\mathbf{K}_{ii}{}^k\Delta\mathbf{U}_i^{n+1} + {}^k\mathbf{K}_{ic}{}^k\Delta\mathbf{U}_c^{n+1} = {}^k\Delta\mathbf{P}^{n+1} \quad k = 1, 2 \quad (11b)$$

where

$${}^k\Delta\mathbf{P}^{n+1} = {}^k\mathbf{f}_{ex}^{n+1} - {}^k\mathbf{f}_{in}^n \quad k = 1, 2 \quad (11c)$$

is a residual force vector for each body, and Eq. (10a) becomes

$$\sum_{k=1}^{2} \{\mathbf{V} - {}^k\Delta\mathbf{U}_c^{n+1}\}^T\{{}^k\mathbf{K}_{ci}^n{}^k\Delta\mathbf{U}_i^{n+1} + {}^k\mathbf{K}_{cc}^n{}^k\Delta\mathbf{U}_c^{n+1} - {}^k\Delta\mathbf{P}^{n+1}\}$$

$$- \mu\{\|\mathbf{V}\|_\nu - \|\Delta\mathbf{U}_t^n\|_\nu\}^T\mathbf{S}_n^{n+1} \geq 0. \quad (11d)$$

Substituting Eq. (11b) into the variational inequality (11d) gives

$$\begin{Bmatrix} \mathbf{V} - {}^1\Delta\mathbf{U}_c \\ \mathbf{V} - {}^2\Delta\mathbf{U}_c \end{Bmatrix}^T \left\{ \begin{bmatrix} {}^1\bar{\mathbf{K}}_{cc} & 0 \\ 0 & {}^2\bar{\mathbf{K}}_{cc} \end{bmatrix} \begin{Bmatrix} {}^1\Delta\mathbf{U}_c \\ {}^2\Delta\mathbf{U}_c \end{Bmatrix} - \begin{Bmatrix} {}^1\Delta\bar{\mathbf{P}} \\ {}^2\Delta\bar{\mathbf{P}} \end{Bmatrix} \right\}$$

$$- \mu\{\|\mathbf{V}\|_\nu - \|\Delta\mathbf{U}_t\|_\nu\}^T\mathbf{S}_n \geq 0 \quad (12a)$$

where

$${}^k\bar{\mathbf{K}}_{cc} = {}^k\mathbf{K}_{cc} - {}^k\mathbf{K}_{ci}[{}^k\mathbf{K}_{ii}]^{-1}{}^k\mathbf{K}_{ic} \quad k = 1, 2 \quad (12b)$$

$${}^k\Delta\bar{\mathbf{P}} = {}^k\Delta\mathbf{P} - {}^k\mathbf{K}_{ci}[{}^k\mathbf{K}_{ii}]^{-1}{}^k\Delta\mathbf{P} \quad k = 1, 2. \quad (12c)$$

Introducing the transformation from based on $\Delta\mathbf{U}_c = {}^1\Delta\mathbf{U}_c + {}^2\Delta\mathbf{U}_c$ by

$$\begin{Bmatrix} {}^1\Delta\mathbf{U}_c \\ {}^2\Delta\mathbf{U}_c \end{Bmatrix} = \begin{bmatrix} \mathbf{I} & 0 \\ -\mathbf{I} & \mathbf{I} \end{bmatrix} \begin{Bmatrix} {}^1\Delta\mathbf{U}_c \\ \Delta\mathbf{U}_c \end{Bmatrix} \quad (13a)$$

and substituting it into the variational inequality Eq. (12a) yields

$$\begin{Bmatrix} \mathbf{V} - {}^1\Delta\mathbf{U}_c \\ \mathbf{V} - {}^2\Delta\mathbf{U}_c \end{Bmatrix}^T \left\{ \begin{bmatrix} {}^1\bar{\mathbf{K}}_{cc} + {}^2\bar{\mathbf{K}}_{cc} & -{}^2\bar{\mathbf{K}}_{cc} \\ -{}^2\bar{\mathbf{K}}_{cc} & {}^2\bar{\mathbf{K}}_{cc} \end{bmatrix} \begin{Bmatrix} {}^1\Delta\mathbf{U}_c \\ {}^2\Delta\mathbf{U}_c \end{Bmatrix} \right.$$

$$\left. - \begin{Bmatrix} {}^1\Delta\bar{\mathbf{P}} - {}^2\Delta\bar{\mathbf{P}} \\ {}^2\Delta\bar{\mathbf{P}} \end{Bmatrix} \right\} - \mu\{\|\mathbf{V}\|_\nu - \|\Delta\mathbf{U}_t\|_\nu\}^T\mathbf{S}_n \geq 0. \quad (14)$$

Introducing a further transform

$${}^1\Delta\mathbf{U}_c = [{}^1\bar{\mathbf{K}}_{cc} + {}^2\bar{\mathbf{K}}_{cc}]^{-1}\{{}^2\bar{\mathbf{K}}_{cc}\Delta\mathbf{U}_c + {}^1\Delta\bar{\mathbf{P}} - {}^2\Delta\bar{\mathbf{P}}\} \quad (13b)$$

the inequality (14) becomes

$$\{\mathbf{V} - \Delta\mathbf{U}_c\}^T\{\tilde{\mathbf{K}}\Delta\mathbf{U}_c - \tilde{\mathbf{P}}\}$$

$$- \mu\{\|\mathbf{V}\|_\nu - \|\Delta\mathbf{U}_t\|_\nu\}^T\mathbf{S}_n \geq 0 \quad (15)$$

where

$$\tilde{\mathbf{K}} = {}^2\bar{\mathbf{K}}_{cc} - {}^2\bar{\mathbf{K}}_{cc}[{}^1\bar{\mathbf{K}}_{cc} + {}^2\bar{\mathbf{K}}_{cc}]^{-1/2}\bar{\mathbf{K}}_{cc} \quad (16a)$$

$$\tilde{\mathbf{P}} = {}^2\Delta\bar{\mathbf{P}} - {}^2\bar{\mathbf{K}}_{cc}[{}^1\bar{\mathbf{K}}_{cc} + {}^2\bar{\mathbf{K}}_{cc}]^{-1}\{{}^1\Delta\bar{\mathbf{P}} - {}^2\Delta\bar{\mathbf{P}}\}. \quad (16b)$$

Downloaded 04 May 2010 to 171.66.16.34. Redistribution subject to ASME license or copyright; see http://www.asme.org/terms/Terms_Use.cfm

Equation (15) describes a variational inequality on the frictional contact boundary. A complementary linear equation is then set up according to Eq. (15), which is discussed in the section to follow.

5 Linear Complementary Formulation

Attention is next focused on the solution methodology for the variational inequality Eq. (15). For frictionless contact, i.e., $\mu = 0$, a linear complementary equation can be simply set up, which is actually equivalent to a quadratic programming. But for frictional contact, providing a general method to transfer it into the standard complementary representation is much more difficult, especially for the three-dimensional problems. In the proposed new variational formulation for general frictional contact, it can be seen that

$$\mathbf{S} = \tilde{\mathbf{K}}\Delta\mathbf{U}_c - \hat{\mathbf{P}}. \tag{17a}$$

So that the variational inequality becomes

$$\{\mathbf{V} - \Delta\mathbf{U}_c\}^T\mathbf{S} - \mu\{\|\mathbf{V}\|_\nu - \|\Delta\mathbf{U}_t\|_\nu\}^T\mathbf{S}_n \geq 0. \tag{17b}$$

For generalized three-dimensional frictional contact, introducing the matrix of sliding direction

$$\mathbf{d} = \text{diag.}\left[\frac{\mathbf{S}_t}{\|\mathbf{S}_t\|}\right],$$

and considering frictional slide rule at the boundary Γ_c

$$\Delta\mathbf{U}_t = -\mathbf{d}\boldsymbol{\lambda},$$

the noninterpenetrating condition for each iteration step can be written as

$$\mathbf{g}(\mathbf{U}^n_{m+1}) = \mathbf{g}(\mathbf{U}^n_m) - \Delta\mathbf{U}_n \geq 0.$$

Denoting

$$\mathbf{g} = \mathbf{g}(\mathbf{U}^n_{m+1})$$

$$\mathbf{g}^0 = \mathbf{g}(\mathbf{U}^n_m)$$

we have the following representation with the variables

$$\Delta\mathbf{U}_c = \begin{Bmatrix}\Delta\mathbf{U}_n\\ \Delta\mathbf{U}_t\end{Bmatrix} = \begin{bmatrix}\mathbf{I} & 0\\ 0 & -\mathbf{d}\end{bmatrix}\begin{Bmatrix}\Delta\mathbf{U}_n\\ \boldsymbol{\lambda}\end{Bmatrix}$$

or

$$\Delta\mathbf{U}_c = \begin{Bmatrix}\mathbf{g}^0\\ 0\end{Bmatrix} - \begin{bmatrix}\mathbf{I} & 0\\ 0 & \mathbf{d}\end{bmatrix}\begin{Bmatrix}\mathbf{g}\\ \boldsymbol{\lambda}\end{Bmatrix}. \tag{18}$$

Substituting the above expression into Eqs. (17a, b) and noting that

$$\boldsymbol{\lambda} = \|\Delta\mathbf{U}_t\|_\nu,$$

we have

$$\begin{Bmatrix}\mathbf{g}^* - \mathbf{g}\\ \boldsymbol{\lambda}^* - \boldsymbol{\lambda}\end{Bmatrix}^T\left\{\begin{bmatrix}-\mathbf{I} & 0\\ 0 & -\mathbf{d}^T\end{bmatrix}\begin{Bmatrix}\mathbf{S}_n\\ \mathbf{S}_t\end{Bmatrix} - \begin{Bmatrix}0\\ \mu\mathbf{S}_n\end{Bmatrix}\right\} \geq 0$$

$$\forall\mathbf{g}^*, \boldsymbol{\lambda}^* \in R^{n_c} \quad \text{and} \quad \mathbf{g}^* \geq 0, \quad \boldsymbol{\lambda}^* \geq 0 \tag{19a}$$

and

$$\begin{Bmatrix}\mathbf{S}_n\\ \mathbf{S}_t\end{Bmatrix} = \tilde{\mathbf{K}}\left\{\begin{Bmatrix}\mathbf{g}^0\\ 0\end{Bmatrix} - \begin{bmatrix}\mathbf{I} & 0\\ 0 & \mathbf{d}\end{bmatrix}\begin{Bmatrix}\mathbf{g}\\ \boldsymbol{\lambda}\end{Bmatrix}\right\} - \hat{\mathbf{P}}. \tag{19b}$$

Let

$$\begin{Bmatrix}\boldsymbol{\alpha}\\ \boldsymbol{\beta}\end{Bmatrix} = \begin{bmatrix}-\mathbf{I} & 0\\ 0 & -\mathbf{d}^T\end{bmatrix}\begin{Bmatrix}\mathbf{S}_n\\ \mathbf{S}_t\end{Bmatrix} - \begin{Bmatrix}0\\ \mu\mathbf{S}_n\end{Bmatrix}. \tag{20a}$$

It can be readily shown that

$$\begin{Bmatrix}\mathbf{g}^* - \mathbf{g}\\ \boldsymbol{\lambda}^* - \boldsymbol{\lambda}\end{Bmatrix}^T\begin{Bmatrix}\boldsymbol{\alpha}\\ \boldsymbol{\beta}\end{Bmatrix} \geq 0$$

$$\forall\mathbf{g}^*, \boldsymbol{\lambda}^* \in R^{n_c} \quad \text{and} \quad \mathbf{g}^* \geq 0, \boldsymbol{\lambda}^* \geq 0. \tag{20b}$$

Equation (20b) is equivalent to

$$\mathbf{Y} - \mathbf{M}\mathbf{X} = \mathbf{F}$$

where matrix $\mathbf{M}$ and vectors $\mathbf{X}$, $\mathbf{Y}$, $\mathbf{F}$ are as follows:

$$\mathbf{M} = \begin{bmatrix}\mathbf{I} & 0\\ \mu\mathbf{I} & \mathbf{d}^T\end{bmatrix}\tilde{\mathbf{K}}\begin{bmatrix}\mathbf{I} & 0\\ 0 & \mathbf{d}\end{bmatrix} \tag{21a}$$

$$\mathbf{F} = -\begin{bmatrix}\mathbf{I} & 0\\ \mu\mathbf{I} & \mathbf{d}^T\end{bmatrix}\left\{\tilde{\mathbf{K}}\begin{Bmatrix}\mathbf{g}^0\\ 0\end{Bmatrix} - \hat{\mathbf{P}}\right\} \tag{21b}$$

$$\mathbf{X} = \begin{Bmatrix}\mathbf{g}\\ \boldsymbol{\lambda}\end{Bmatrix} \tag{21c}$$

$$\mathbf{Y} = \begin{Bmatrix}\boldsymbol{\alpha}\\ \boldsymbol{\beta}\end{Bmatrix}. \tag{21d}$$

From the variational inequality (20b), it can be seen that the unknown variables $\mathbf{X}$ and complemenatary unknown variables $\mathbf{Y}$ satisfy the conditions

$$\mathbf{X}^T\mathbf{Y} = 0$$

$$\mathbf{X} \geq 0$$

$$\mathbf{Y} \geq 0$$

where the unknown variables, $\mathbf{X}$, are chosen as (1) the gap function for the normal direction, $\mathbf{g} = \mathbf{g}(\Delta\mathbf{U}_c) \geq 0$, and (2) the norm of the incremental sliding displacements for the tangential direction, $\lambda = \|\Delta\mathbf{U}_t\|_\nu \geq 0$. The complementary variables, $\mathbf{Y}$, are taken as (1) the normal contact forces, $\boldsymbol{\alpha} = -\mathbf{S}_n \geq 0$, and (2) the Coulomb slack variables in the tangential directions, $\boldsymbol{\beta} = -\mu\mathbf{S}_n - \mathbf{d}^T\mathbf{S}_t \geq 0$. There are two unknown variables and two complementary variables (2×2) for each contact nodal pair. The contact problem with Coulomb's friction is finally described as follows:

Find $\mathbf{X}, \mathbf{Y} \in R^{2n_c}$ satisfy the linear complementary equations

$$\mathbf{Y} - \mathbf{M}\mathbf{X} = \mathbf{F} \tag{22a}$$

where

$$\mathbf{X}^T\mathbf{Y} = 0 \tag{22b}$$

$$\mathbf{X} \geq 0, \quad \mathbf{Y} \geq 0. \tag{22c}$$

There are a several methods to solve the resulting formulations described by Eqs. (22a–c). For the solution of the incremental displacement fields on the contact boundary with/without frictional contact, either an implicit solution method such as the Lemke's algorithm (Panagiotopoulos, 1985; Stavroulakis et al., 1991; Sha et al., 1992) or an explicit solution strategy employing a Conjugate Gradient Based Projection (CGBP) method (Appendix) as suggested in this study can be utilized. We propose to use the new explicit strategy not only because of the high accuracy and good efficiency of the method, but also because of our future efforts to provide effective techniques

Downloaded 04 May 2010 to 171.66.16.34. Redistribution subject to ASME license or copyright; see http://www.asme.org/terms/Terms_Use.cfm

suitable for parallel computing environments. Gauss-Seidel type explicit iteration techniques do exist but their slow convergence limits their application. The proposed CGBP method inherits superior convergence characteristics from the conjugate gradient method, and in conjunction with projection procedures, the explicit nature of the methodology can be used to solve the linear complementary equations efficiently.

After $\mathbf{X}$ and $\mathbf{Y}$ are obtained, the contact forces $\mathbf{S}_n$ and the frictional forces $\mathbf{S}_t$ on the nodes of the contact boundary can be computed by Eq. (20a); the incremental displacements ${}^k\Delta\mathbf{U}_c$ $k = 1, 2$ on nodes of contact boundary can be obtained by Eqs. (18), (13b) and (13a); and consequently the incremental displacement fields ${}^k\Delta\mathbf{U}$ ($k = 1, 2$) in the each bodies are finally obtained employing Eqs. (11a), from which the stress field can be computed.

6 Generalized Newton-Raphson Procedure in Conjunction With CGBP Method: Approach for Solving Nonlinear System of LCE

Our aim now is to solve the variational inequality Eq. (10a) in a finite element presentation. By condensing the unknowns onto the contact boundaries and performing the necessary transformation, the presentation of the problem becomes a linear complementary equation, Eq. (22a), with the conditions given by Eqs. (22b, c). For a contact problem between elastic bodies within an incremental step, all the solution of unknown variables can be obtained by solving the LCE only once. However, if material nonlinearity is considered in the LCE,

$$\mathbf{Y} - \mathbf{MX} = \mathbf{F},$$

the matrix $\mathbf{M}$ is also a function of $\mathbf{X}$ and $\mathbf{Y}$. In the numerical treatment, to handle the material nonlinearity, such as elasto-plastic behavior, we have to apply a special iteration procedure to obtain converged results for each incremental step. Analogous to the Newton-Raphson method for the solution of nonlinear system of equations, in this paper we describe a solution procedure termed as the generalized Newton-Raphson procedure to handle general nonlinear problems modeled by LCE. It is a Newton-Raphson type iteration, since the $\mathbf{M}$ matrix is condensed from the tangential stiffness matrix ${}^k\mathbf{K}$, which is symmetric and positive definite; and also, the incremental displacement fields ${}^k\Delta\mathbf{U}^{n+1}$ in each step of the iteration is obtained by updating the residual force vector ${}^k\Delta\mathbf{P}^{n+1}$. In conjunction with the Conjugate Gradient Based Projection method, we implemented this special iteration procedure to solve frictional contact problems with material and/or geometric nonlinearities. The algorithm is described as follows.

For each load increment n to $n + 1$, set iteration number $m = 0$:

Step 1: Assemble stiffness matrix for each contact body (see Eq. (10e)):

$${}^k\mathbf{K}_m(\mathbf{U}_m^n) = \sum_{e \in k} \int_{e_\Omega} \mathbf{B}^T\mathbf{D}_{ep}(\mathbf{U}_m^n)\mathbf{B}\,d\Omega \quad k = 1, 2$$

where

$$\mathbf{D}_{ep} = \mathbf{D} - \rho\frac{\mathbf{Da}\{\mathbf{Da}\}^T}{H' - \mathbf{a}^T\mathbf{Da}} \quad \rho = \begin{cases} 0 & \text{if} \quad F < 0 \\ 1 & \text{if} \quad F = 0 \end{cases}$$

$$\mathbf{a}^T = \frac{\partial F(\boldsymbol{\sigma}, \kappa)}{\partial \boldsymbol{\sigma}} \quad \text{for} \quad {}^kF(\boldsymbol{\sigma}, \kappa) \le 0, \quad k = 1, 2.$$

Step 2: Condense the stiffness matrices and load vectors onto the contact boundary in the description of local coordinates which is determined by contact nodal pairs (see Eqs. (16a, b)):

$$\tilde{\mathbf{K}} = {}^2\bar{\mathbf{K}}_{cc} - {}^2\bar{\mathbf{K}}_{cc}[{}^1\bar{\mathbf{K}}_{cc} + {}^2\bar{\mathbf{K}}_{cc}]^{-1}\,{}^2\bar{\mathbf{K}}_{cc}$$

$$\tilde{\mathbf{P}} = {}^2\Delta\bar{\mathbf{P}} - {}^2\bar{\mathbf{K}}_{cc}[{}^1\bar{\mathbf{K}}_{cc} + {}^2\bar{\mathbf{K}}_{cc}]^{-1}\{{}^1\Delta\bar{\mathbf{P}} - {}^2\Delta\bar{\mathbf{P}}\}$$

where (see Eqs. (11c), (12b, c))

$${}^k\Delta\mathbf{P}^{n+1} = {}^k\mathbf{f}_{ex}^{n+1} - {}^k\mathbf{f}_{in}^n \quad k = 1, 2$$

$${}^k\bar{\mathbf{K}}_{cc} = {}^k\mathbf{K}_{cc} - {}^k\mathbf{K}_{ci}[{}^k\mathbf{K}_{ii}]^{-1}\,{}^k\mathbf{K}_{ic} \quad k = 1, 2$$

$${}^k\Delta\bar{\mathbf{P}} = {}^k\Delta\mathbf{P} - {}^k\mathbf{K}_{ci}[{}^k\mathbf{K}_{ii}]^{-1}\,{}^k\Delta\mathbf{P}. \quad k = 1, 2.$$

Step 3: Calculate $\mathbf{M}$ and $\mathbf{F}$ (see Eqs. (21a, b)

$$\mathbf{M} = \begin{bmatrix} \mathbf{I} & 0 \\ \mu\mathbf{I} & \mathbf{d}^T \end{bmatrix}\tilde{\mathbf{K}}\begin{bmatrix} \mathbf{I} & 0 \\ 0 & \mathbf{d} \end{bmatrix}$$

$$\mathbf{F} = -\begin{bmatrix} \mathbf{I} & 0 \\ \mu\mathbf{I} & \mathbf{d}^T \end{bmatrix}\left\{\tilde{\mathbf{K}}\begin{Bmatrix} \mathbf{g}^0 \\ 0 \end{Bmatrix} - \tilde{\mathbf{P}}\right\}$$

and solve the following linear complementary equation employing the conjugate gradient based projection method (Appendix). Thus,

$$\mathbf{Y} - \mathbf{MX} = \mathbf{F}$$

$$\mathbf{X}^T\mathbf{Y} = 0 \quad \mathbf{X} \ge 0 \quad \mathbf{Y} \ge 0$$

where (see Eqs. (20a), (21c))

$$\mathbf{Y} = \begin{Bmatrix} \boldsymbol{\alpha} \\ \boldsymbol{\beta} \end{Bmatrix} = \begin{bmatrix} -\mathbf{I} & 0 \\ 0 & -\mathbf{d}^T \end{bmatrix}\begin{Bmatrix} \mathbf{S}_n \\ \mathbf{S}_t \end{Bmatrix} - \begin{Bmatrix} 0 \\ \mu\mathbf{S}_n \end{Bmatrix}$$

$$\mathbf{X} = \begin{Bmatrix} \mathbf{g} \\ \boldsymbol{\lambda} \end{Bmatrix} = \begin{Bmatrix} \mathbf{g}^0 - \Delta\mathbf{U}_n \\ \|\Delta\mathbf{U}_t\|_\nu \end{Bmatrix}.$$

The solution variables include $\Delta\mathbf{U}_c$, $\mathbf{S}_n$, $\mathbf{S}_t$ and $\mathbf{g}$ on the contact boundary.

Step 4: Calculate ${}^k\Delta\mathbf{U}_c$, $k = 1, 2$ for each contact body (see Eq. (13a–b)):

$${}^1\Delta\mathbf{U}_c = [{}^1\bar{\mathbf{K}}_{cc} + {}^2\bar{\mathbf{K}}_{cc}]^{-1}\{{}^2\bar{\mathbf{K}}_{cc}\Delta\mathbf{U}_c + {}^1\Delta\bar{\mathbf{P}} - {}^2\Delta\bar{\mathbf{P}}\}$$

$${}^2\Delta\mathbf{U}_c = \Delta\mathbf{U}_c - {}^1\Delta\mathbf{U}_c$$

where $[{}^1\bar{\mathbf{K}}_{cc} + {}^2\bar{\mathbf{K}}_{cc}]^{-1}$ is obtained during the calculation of Eq. (16a) in Step 2, and stored for this step. Then, transfer ${}^k\Delta\mathbf{U}_c$ into the representation of global coordinates.

Step 5: Calculate the incremental deformation fields for each body (see Eq. (11a):

$${}^k\Delta\mathbf{U}_i = [{}^k\mathbf{K}_{ii}]^{-1}\{{}^k\Delta\mathbf{P} - {}^k\mathbf{K}_{ic}\,{}^k\Delta\mathbf{U}_c\} \quad k = 1, 2$$

which is rewritten from

$${}^k\mathbf{K}_{ii}\,{}^k\Delta\mathbf{U}_i + {}^k\mathbf{K}_{ic}\,{}^k\Delta\mathbf{U}_c = {}^k\Delta\mathbf{P} \quad k = 1, 2$$

where $[{}^k\mathbf{K}_{ii}]^{-1}$ is obtained during the calculation of Eq. (12a) in Step 2, and stored for this step.

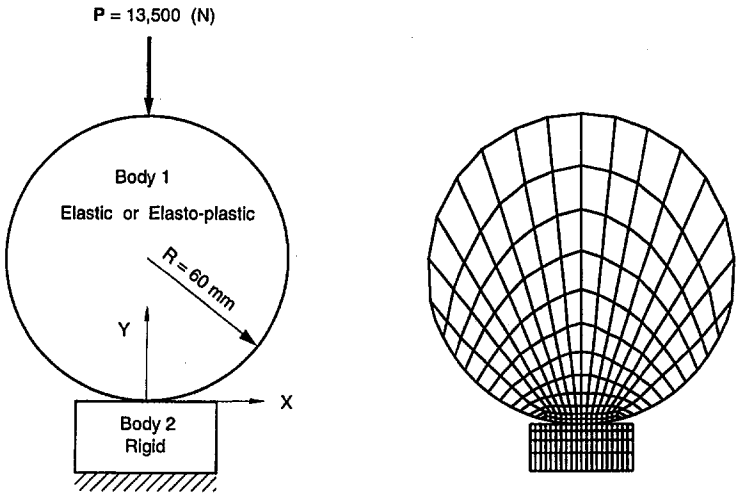
Step 6: Calculate the total displacement vectors for each contact body (see Eq. (10c)):

$${}^k\mathbf{U}_{m+1}^n = {}^k\mathbf{U}_m^n + {}^k\Delta\mathbf{U}_{m+1}^n \quad k = 1, 2.$$

Step 7: Set: $m = m + 1$, and evaluate the new internal force vectors (see Eq. (10d)):

$${}^k\mathbf{f}_{in}(\mathbf{U}_m^n) = \sum_{e \in k} \int_{e_\Omega} \mathbf{B}^T\boldsymbol{\sigma}(\mathbf{U}_m^n)\,d\Omega \quad k = 1, 2.$$

Downloaded 04 May 2010 to 171.66.16.34. Redistribution subject to ASME license or copyright; see http://www.asme.org/terms/Terms_Use.cfm



(a) (b)

Fig. 1(*a*) A cylinder is pressed on to a rigid body under the loading of P, E = 6897 MPa, υ = 0.3. σ_y = 300 MPa, and H' = 68.97 MPa for the case of elasto-plastic deformation. (*b*) The finite element model for the problem.

Step 8: Check the residual forces for the following convergence (see Eq. $(10f)$):

$$|{}^k\mathbf{f}_{ex}^{n+1} - {}^k\mathbf{f}_{in}(\mathbf{U}_m^n)| \leq \epsilon \quad k = 1, 2.$$

If Yes, set $n = n + 1$ for next loading increment.
If No, update residual force vector by

$${}^k\Delta\mathbf{P}^{n+1} = {}^k\mathbf{f}_{ex}^{n+1} - {}^k\mathbf{f}_{ex}^{n} \quad k = 1, 2$$

and also set the current gap vector $\mathbf{g}^0 - \Delta\mathbf{U}_n$ to $\mathbf{g}^0$ as the initial gap for the next iteration. Go back to Step 1 until Eq. $(10f)$ is satisfied. This iteration loop is the generalized Newton-Raphson iteration procedure to handle the nonlinear LCE formulations for frictional contact problems involving small deformation and an elasto-plastic material model.

7 Numerical Examples

In order to test the effectiveness of the proposed methodology and developments, frictional contact problems with initial gap and without initial gap were examined. In the numerical examples to follow, the material nonlinearity for the contacting bodies was considered as elasto-plastic with plane strain, and the yield criterion was chosen as the Von Mises criterion.

Example 1. Figures 1–6 show a two-dimensional contact problem of a cylinder that is compressed onto a flat rigid body under the loading, P = 13,500 N. The cylinder with R = 60 mm is divided into 192 quadrilateral four-noded elements, and initially only one pair of nodes is in contact from a total of 15 candidate contact nodal pairs. The material property is chosen as E = 6897 MPa, ν = 0.3, σ_y = 300 MPa, and H' = E/100 (the linear hardening rate). For validation, we consider the elastic case only and μ = 0 at the contact interface; the result of the normal stress distribution via the proposed method is in excellent agreement with that of the Hertz solution, which is shown in Fig. 2. In Fig. 3, the two curves show the distribution of normal force, S_n, and tangential force, S_t, at the contact interface with μ = 0.35 for the case of elastic deformation. It is shown that in the sliding region $|S_t| = \mu|S_n|$, and in the sticking region $|S_t| < \mu|S_n|$. In this example, the result shows that $S_t \neq 0$ occurs at 80 percent of sticking nodes where the relative sliding distances are zero. If an ever-slipping friction model was used, a result such as this would not be obtained. To perform the analysis for the case of elasto-plastic deformation, the total load (P = 13,500 N) is applied in three loading steps with the factors 0.6, 0.2, and 0.2 consequently. Figure 4 shows the comparison of distribution of contact forces for both cases of elastic and elasto-plastic when μ = 0. The curve for elasto-plastic case is flat compared with the curve for the elastic case. This result represents a realistic physical phenomenon that contact pressure significantly changes when material yielding

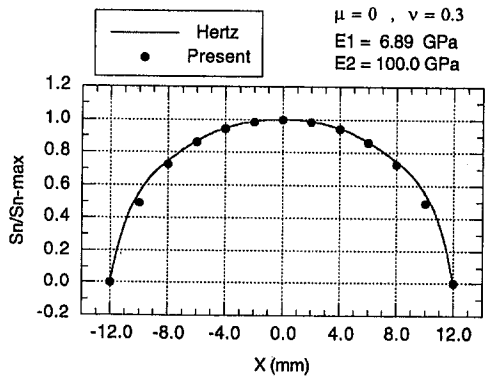


Fig. 2 The result of normal stress distribution on contact interface via the proposed method with comparison to the Hertz solution

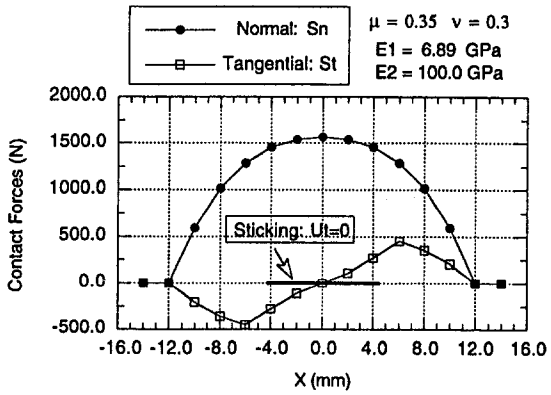


Fig. 3 Results of normal and tangential force distribution at the contact interface using present method for the elastic case

Downloaded 04 May 2010 to 171.66.16.34. Redistribution subject to ASME license or copyright; see http://www.asme.org/terms/Terms_Use.cfm

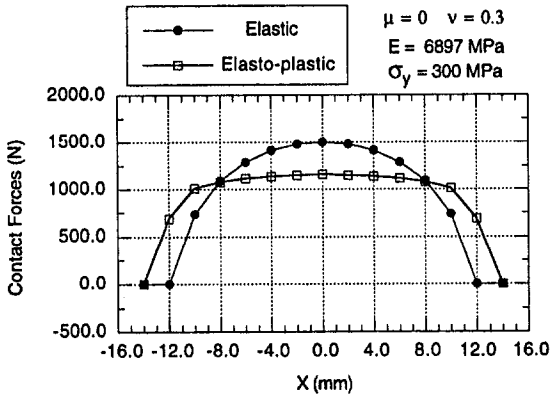


Fig. 4 The comparison of distribution of contact forces for elastic and elasto-plastic cases when $\mu = 0$

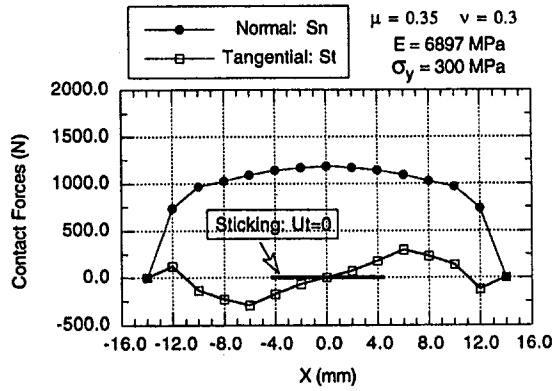


Fig. 5 Results of normal and tangential force distribution at the contact interface using present method for the elasto-plastic case

occurs. For the case of $\mu = 0.35$, the normal and the tangential force distributions at the interface is shown in Fig. 5, and the maximum principal stress distribution and stress derivative distribution for the entire cross section of the cylinder are shown in Fig. 6 and Fig. 7, respectively. These results serve quite well to validate the proposed numerical methodology.

Example 2. Figure 8 shows a typical frictional contact problem which simulates the upsetting of a rectangular workpiece in plane strain. It is assumed that an elasto-plastic block is deformed between rigid platens. 120 quadrilateral four-noded elements are used to discretize the compressed block, and 60

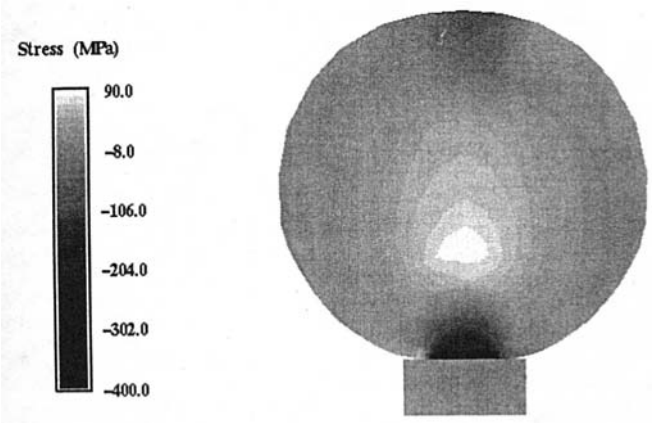


Fig. 6 Distribution of maximum principal stress in the cross section of the cylinder using present method for the elasto-plastic case

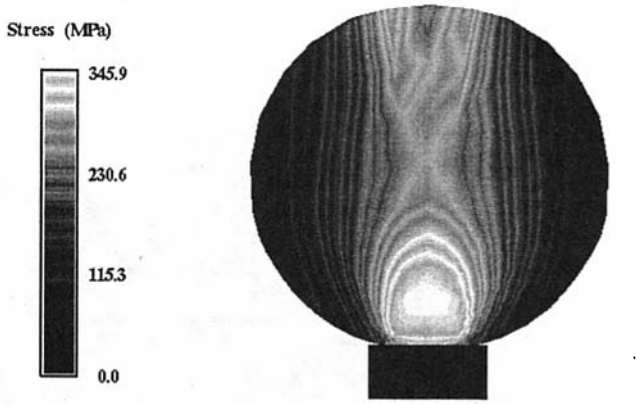


Fig. 7 Distribution of the effective stress in the cross section of the cylinder using present method for the elasto-plastic case

elements are used for the rigid platen, where 2×2 Gauss points are taken for each element. The initial gaps for all 21 candidate contacting nodal pairs are all zero. Figure 9 shows that when $\mu = 0$, the normal stress is uniformly distributed; and when $\mu = 0.5$, sticking occurs at the interface and a friction hill occurs for the normal stress distribution as expected. For the case when the whole block is at the onset of yielding, the total load (Fig. 3(*c*), **P** = 57,600 N) with friction is higher than that with no friction (Fig. 3(*b*), **P** = 48,000 N). This is to be expected because the work required to overcome friction must be supplied by the upsetting force.

8 Discussion and Concluding Remarks

A new incremental variational inequality formulation is described in this paper dealing with the material nonlinear behavior; i.e., the two contacting bodies with/without frictional effects are taken as an elasto-plastic model. The proposed approach employing finite elements for the discretization has been developed for solving frictional contact problems, in which the methodology and theoretical formulations are valid for general contact problems with Coulomb friction. The linear complementary equations were established by means of the variational

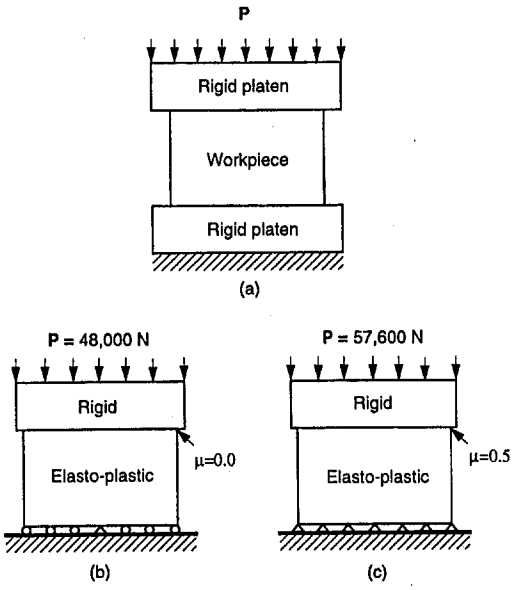


Fig. 8 (*a*) Upseting of a rectangular workpiece in plane strain. For the workpiece material, $E = 689$ GPa, $\nu = 0.3$, $\sigma_y = 0.48$ MPa, and $H' = 68.97$ MPa. (*b*) Problem simplified for $\mu = 0$. (*c*) Problem simplified for $\mu = 0.5$.

Downloaded 04 May 2010 to 171.66.16.34. Redistribution subject to ASME license or copyright; see http://www.asme.org/terms/Terms_Use.cfm

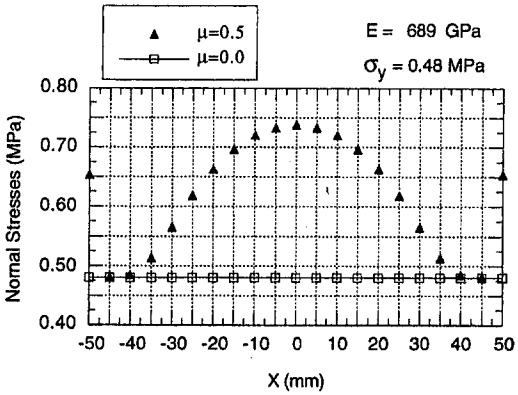


Fig. 9 Results of normal stress distribution at the interface for $\mu = 0$ and for $\mu = 0.5$ when the elasto-plastic workpiece is at onset of yielding.

inequality theory and the solver for the linear complementary equations was chosen as the explicit conjugate gradient based projection approach. In the solution procedure, a generalized Newton-Raphson iteration is described for the LCE to handle the material nonlinearity.

Currently, the penalty method and the Lagrangian multiplier method are the two most commonly used approaches to solve contact problems using the finite element method. The penalty method requires user-defined parameters by experience. The parameters chosen will directly influence the contact boundary penetration and the accuracy of the solution. It also changes the profile and the skyline of global tangent stiffness matrix which will affect the convergence and the CPU time in a strong way (Zhong and Mackerle, 1992). In the Lagrangian multiplier method, the contact forces are taken as the primary unknowns, hence the method introduces the additional variables. Another negative consequence of the Lagrangian multiplier method is that some of diagonal indices in the resulting global matrix are zeros. This causes slow convergence during equation solving; however, the proposed method does not have this drawback. In comparison with the Lagrangian multiplier method, the storage and the CPU time to solve the equations by the proposed method may be reduced to 50 percent, and this will further decrease if the problem is larger. On comparison with the penalty method, the present development does not need user-defined parameters, and the nonpenetration condition as well as Coulomb's law of friction are enforced exactly. Since contact problems are transformed into linear complementary equations in this study, the nonpenetration and Coulomb's law are directly cast as the complementary conditions for the LCE. These two constraints are satisfied automatically when we solve the LCE. As a consequence, the need to involve iterations for both nonpenetration and the Coulomb's law are eliminated in this method. Nevertheless, such iterations have to be imposed by the penalty method or by the Lagrangian multiplier method as convergence-check conditions.

In this paper, the linear complementary equations stated in Eqs. (22*a–c*)

$$\mathbf{Y} - \mathbf{MX} = \mathbf{F}$$

$$\mathbf{X}^T\mathbf{Y} = 0$$

$$\mathbf{X} \geq 0, \quad \mathbf{Y} \geq 0$$

were established with only two unknown variables and two complementary variables (2×2) for each contact nodal pair. The unknown variables, $\mathbf{x}$, are taken as (1) the normal contact forces, $\boldsymbol{\alpha} = -\mathbf{S}_n \geq 0$, and (2) slack variables in the tangential directions, $\boldsymbol{\beta} = -\mu\mathbf{S}_n - \mathbf{d}^T\mathbf{S}_t \geq 0$. On comparison, an existing formulation of the LCE (which is valid for two-dimensions and employed for elastic problem) employs three unknown variables and three complementary variables (3×3) for each nodal pair in two-dimensional contact analysis (Stavroulakis et al., 1991):

$$\mathbf{X} = \begin{Bmatrix} \mathbf{r} \\ \Delta\mathbf{u}^+ \\ \Delta\mathbf{u}^- \end{Bmatrix} \quad \mathbf{Y} = \begin{Bmatrix} \mathbf{y} \\ \mathbf{v}^+ \\ \mathbf{v}^- \end{Bmatrix} \quad \Delta\mathbf{u} = \Delta\mathbf{u}^+ + \Delta\mathbf{u}^-.$$

Hence, the proposed methodology has reduced storage and computational cost, and is also easier to implement into three-dimensional contact analysis.

The substructure technique was employed to improve computing speed for solving the linear complementary equations. The numerical computations showed that the cost for solving the linear complementary equations was only a small part of the total computing time and the solution results of the problems tested satisfy all of the nonlinear inequality constraints on the frictional contact boundary. The approach offers significant promise and potential to more complex problems, and currently research is underway to include large sliding, large deformation, and dynamic applications.

Acknowledgments

Acknowledgment is due to support, in part, from NASA Johnson Space Center, and due to computer grants furnished by the Minnesota Supercomputer Institute. Acknowledgement is also due to the Center for Advanced Manufacturing, Design and Control (CAMDAC), Department of Mechanical Engineering, University of Minnesota. More recent support, in part by the U.S. Army Research Office under grant number DAAH04-96-1-0172, is also gratefully acknowledged. Dr. Bruce Henriksen is the technical monitor. Special thanks are due to the ASHPCD and the Materials Directorate at the U.S. Army Research Laboratory, APG, Maryland, and the U.S. Waterways Experiment Station, Vicksburg, MS. Thanks are due to Messrs. A. Mark, W. Mermagen, Sr., C. Nietubicz, K. Kimsey, R. Namburu, and John Balsara.

References

Bathe, K. J., and Chaudhary, A. B., 1985, "A Solution Method for Planar and Axisymmetric Contact Problems," *International Journal for Numerical Methods in Engineering,* Vol. 21, pp. 65–88.

Bazaraa, M. S., and Shetty, C. M., 1993, *Nonlinear Programming Theory and Algorithm,* John Wiley and Sons, New York.

Belytschko, T., and Lin, J. I., 1987, "A Three-Dimensional Impact-Penetration Algorithm With Erosion," *Computers & Structures,* Vol. 25, No. 1, pp. 95–104.

Belytschko, T., and Neal, M. O., 1991, "Contact—Impact by Pinball Algorithm With Penalty and Lagrangian Methods," *International Journal for Numerical Methods in Engineering,* Vol. 31, pp. 547–572.

Bohm, J., 1987, "Comparison of Different Contact Algorithms With Applications," *Computers & Structures,* Vol. 26, No. 1-2, pp. 207–221.

Chaudhary, A. B., and Bathe, K. J., 1986, 1986, "A Solution Method for Static and Dynamic Analysis of Three-Dimensional Contact Problems with Friction," *Computers & Structures,* Vol. 24, No. 6, pp. 855–873.

Hallquist, J. P., 1983a, "NIKE2D—A Vectorized, Implicit, Finite Deformation Finite Element Code for Analyzing the Static and Dynamic Response of 2-D Solids," Lawrence Livermore National Laboratory Report, Livermore, CA.

Hallquist, J. O., 1983b, "Theoretical Manual for DYN-3D," Lawrence Livermore National Laboratory Report, Livermore, CA.

Irons, B. M., and Draper, K. J., 1985, "Lagrangian Multiplier Techniques in Structural Analysis," *AIAA Journal,* Vol. 3, No. 6, pp. 1172–1174.

Katona, M. G., 1983, "A Simple Contact—Friction Interface Element With Applications to Buried Culverts," *International Journal for Numerical and Analytical Methods in Geomechanics,* Vol. 7, pp. 371–384.

Kikuchi, N., and Oden, J. T., 1988, *Contact Problems in Elasticity: A Study of Variational Inequalities and Finite Element Methods,* SIAM Philadelphia.

Kikuchi, N., and Song, Y. J., 1981, "Penalty/Finite Element Approximations of a Class of Unilateral problems in Linear Elasticity," *Quarterly of Applied Mechanics,* Vol. 39, pp. 1–22.

Owen, D. R., and Hinton, E., 1980, *Finite Element in Plasticity: Theory and Practice,* Pineridge Press, Ltd., Swansea, UK.

Panagiotopoulos, P. D., 1985, *Inequality Problems in Mechanics and Applications,* Birkhauser.

Sha, D., Li, M., and Tamma, K., 1992, "An Effective Linear Complementary Model Involving General Contact With Colomb Friction," *Numerical Methods*

Downloaded 04 May 2010 to 171.66.16.34. Redistribution subject to ASME license or copyright; see http://www.asme.org/terms/Terms_Use.cfm

for Simulation of Industrial Metal Forming Processes, CED-Vol 5/AMD-Vol. 156, ASME, New York, pp. 27–36.

Simo, J. C., and Laursen, T. A., 1992, "An Augmented Lagrangian Treatment of Contact Problems Involving Friction," *Computers & Structures,* Vol. 42, No. 1, pp. 97–116.

Simo, J. C., Wriggers, P., and Taylor, R. L., 1985, "A Perturbed Lagrangian Formulation for the Finite Element Solution of Contact Problems," *Computer Methods in Applied Mechanics and Engineering,* Vol. 50, pp. 163–180.

Stavroulakis, G. E., Panagiotopoulos, P. D., and Al-Fahed, A. M., 1991, "On the Rigid Body Displacement and Rotations in Unilateral Contact Problems and Applications," *Computers & Structures,* Vol. 40, No. 3, pp. 599–614.

Tamma, K. K., Li, M., and Sha, D., 1992, "Conjugate Gradient Based Projection: A New Explicit Methodology for Frictional Contact," *Communications in Numerical Methods in Engineering,* Vol. 10, pp. 633–648.

Walczak, J., and Bathe, K. J., 1990, "Finite Element Analysis of Metal Forming Problems," *Proceedings of First U.S. National Congress on Computational Mechanics.*

Zhong, Z., 1993, *Finite Element Procedures for Contact-Impact Problems,* Oxford University Press, New York.

Zhong, Z., and Mackerle, J., 1992, "Static Contact Problems—A Review," *Engineering Computations,* Vol. 9, pp. 3–37.

APPENDIX

Conjugate Gradient Based Projection: A New Explicit Strategy for Solving Linear Complementary Equations

This is an explicit methodology for solving linear complementary equations, Tamma et al. (1994). The method is herein referred as the "conjugate gradient based projection" (CGBP) approach. Comparing this with the commonly employed Gauss-Seidel iteration, the proposed new method possesses improved efficiency, and convergence characteristics, and is also well suited to capitalize upon parallel computing environments.

The discussion to follow will focus on the solution of the linear complementary equations given by

$$\mathbf{Y} - \mathbf{MX} = \mathbf{F}$$

$$\mathbf{X}^T\mathbf{Y} = 0$$

$$\mathbf{X} \geq 0$$

$$\mathbf{Y} \geq 0.$$

For convenience we introduce a set of subscript $\mathbf{I}(\mathbf{X}^{(k)})$ as

$$\mathbf{I}(\mathbf{X}_i^{(k)}) = \{ i | \mathbf{X}_i^{(k)} = 0 \}.$$

Assuming $\mathbf{I}(\mathbf{X}^{(k)}) = 1, 2, \ldots, q$, the q planes

$$\mathbf{X}_i^{(k)} = 0.$$

A projection operator $\mathbf{P}_d(\mathbf{X})$ is defined as

$$\mathbf{P}_d(\mathbf{X}): s_i = \begin{cases} 0 & \text{for} \quad s_i < 0, \quad i \in \mathbf{I}(\mathbf{X}) \\ s_i & \text{otherwise} \end{cases}.$$

Since the conjugate gradient method has advantages of saving storage and a fast rate of convergence, applying the projection to the standard Fletcher-Reeves conjugate gradient method, the conjugate gradient based projection method is developed as follows:

Step 1. Set $k = 0$. Assume $\mathbf{M}^* = \text{diag. } [\mathbf{M}]$, and an initial value $\mathbf{X}^{(0)}$ is determined by

$$\mathbf{X}^{(0)} = \max\ (-\mathbf{M}^{*-1}\mathbf{F}, 0).$$

If $\mathbf{X}^{(0)} = 0$ then the solution $\mathbf{X}^* = \mathbf{X}^{(0)}$ and stop iteration, otherwise go to Step 2.

Step 2. Calculate projective gradient $\mathbf{g}^{(k)}$ and projective conjugate direction $\mathbf{s}^{(k)}$

$$\mathbf{Y}^{(k)} = \mathbf{MX}^{(k)} + \mathbf{F}$$

$$\mathbf{g}^{(k)} = -\mathbf{P}_d(\mathbf{X}^{(k)})\{-\mathbf{Y}^{(k)}\}$$

$$\mathbf{s}^{(k)} = -\mathbf{g}^{(k)}$$

then, go to Step 4.

Step 3. Calculate the gradient $\mathbf{Y}^{(k)}$, projective gradient $\mathbf{g}^{(k)}$, conjugate direction $\bar{\mathbf{s}}^{(k)}$ and projective conjugate direction $\mathbf{s}^{(k)}$

$$\mathbf{Y}^{(k)} = \mathbf{MX}^{(k)} + \mathbf{F}$$

$$\mathbf{g}^{(k)} = -\mathbf{P}_d(\mathbf{X}^{(k)})\{-\mathbf{Y}^{(k)}\}$$

$$\bar{\mathbf{s}}^{(k)} = -\mathbf{g}^{(k)} + \gamma^{(k-1)}\mathbf{s}^{(k-1)}$$

$$\gamma^{(k-1)} = \frac{\|\mathbf{g}^{(k)}\|^2}{\|\mathbf{g}^{(k-1)}\|^2}$$

$$\mathbf{s}^{(k)} = \mathbf{P}_d(\mathbf{X}^{(k)})\bar{\mathbf{s}}^{(k)}.$$

Step 4. Calculate maximum step size $\alpha_{\max}$ and actual step size α by

$$\alpha_{\max} = \min\left\{ -\frac{x_i^{(k)}}{s_i^{(k)}} | s_i^{(k)} < 0, \quad i \notin \mathbf{I}(\mathbf{X}^{(k)}) \right\}$$

$$\tilde{\alpha} = -\frac{\{\mathbf{s}^{(k)}\}^T\mathbf{Y}^{(k)}}{\{\mathbf{s}^{(k)}\}^T\mathbf{Ms}^{(k)}}$$

$$\alpha = \min\ \{\tilde{\alpha}, \alpha_{\max}\}.$$

Step 5. Update the matrix $\mathbf{X}^{(k+1)}$ as

$$\mathbf{X}^{(k+1)} = \mathbf{X}^{(k)} + \alpha\mathbf{s}^{(k)}.$$

Step 6. Calculate the norm of the increment $\Delta\mathbf{X}^{(k+1)} = \mathbf{X}^{(k+1)} - \mathbf{X}^{(k)}$ as $\|\Delta\mathbf{X}^{(k+1)}\|$. If $\|\Delta\mathbf{X}^{(k+1)}\| \leq \epsilon$ then the solution is $\mathbf{X}^* = \mathbf{X}^{(k+1)}$ and stop iterative procedure, else set $k = k + 1$ and if $\alpha = \alpha_{\max}$ or $\mathbf{s}^{(k)} \neq \bar{\mathbf{s}}^{(k)}$ then go to Step 2, else go to Step 3, until the converged solution is obtained.

Downloaded 04 May 2010 to 171.66.16.34. Redistribution subject to ASME license or copyright; see http://www.asme.org/terms/Terms_Use.cfm

Minimum Weight Design of Symmetric Angle-Ply Laminates With Incomplete Information on Initial Imperfections

S. Adali
Professor,
Mem. ASME.

A. Richter
Research Associate.

V. E. Verijenko
Professor,
Mem. ASME.

Department of Mechanical Engineering,
University of Natal,
Durban 4001, South Africa

An angle-ply laminated plate is optimized with the objective of minimizing its weight subject to maximum deflection and buckling constraints. The plate has an initial deflection the shape of which is not known a priori, i.e., the initial deflection is not specified in a "deterministic" manner and as such it is "uncertain." The weight is proportional to the laminate thickness which is minimized taking the ply angles as design variables and under the least favorable conditions of initial imperfections. The convex modeling approach is employed to analyze the uncertain initial deflection with the uncertain quantities allowed to vary arbitrarily around their average values subject to the requirement that these variations are bounded in L_2 norm. The results are given for both single load and multiple load cases and the effect of uncertainty on the optimal design is investigated. It is shown that the minimum weight increases with increasing level of uncertainty and the optimal ply angles also depend on the level of uncertainty.

1 Introduction

Initial deflection of a structural component may occur as a result of manufacturing imperfections and/or long-term environmental effects such as creep and material aging. Quite often the exact shape of an initial deflection is not known a priori and this lack of information usually leads to adopting an approach in which an approximate shape for the initial deflection is assumed based on available data and the problem is solved in a deterministic setting. Although this procedure may produce an acceptable estimate of the final deflection in an analysis situation, such an approach becomes unacceptable in an optimal design situation especially in the presence of compressive in-plane loads which affect the transverse deflection adversely. This is due to the fact that a design subject to a maximum deflection constraint is likely to violate this constraint unless the design is based on a worst case of imperfections. In the context of a deflection constrained design, the worst case of imperfections is defined as that initial shape of the deflection which will produce the least favorable final deflection, i.e., the maximum possible deflection.

An approach based on statistical distributions or probabilistic functions is usually not practical as information for these quantities may not be available for initial deflections. In the present study an approach based on a recently developed technique for modeling uncertainties, namely, the convex analysis (Ben-Haim and Elishakoff, 1990), is adopted to analyze the initial imperfections and to determine the least favorable deflection. The only information needed to solve the analysis problem is an upper bound on the L_2 norm of the initial deflection. The method of solution incorporates uncertainty analysis with optimization techniques to produce a minimum weight angle-ply laminate subject to deflection and buckling constraints with the ply angles determined optimally. Optimal designs are obtained under single as well as multiple transverse loads in view of the fact that, in practice, structural components are often subjected to multiple loads during their service life.

The convex modelling was applied to a number of structural analysis problems with various kinds of uncertainties. Geometrical imperfections of shells were investigated by Ben-Haim and Elishakoff (1989) and Elishakoff and Ben-Haim (1990), initial imperfection of a column by Elishakoff et al. (1994), vibrations of beams and composite plates under uncertain excitations by Elishakoff and Colombi (1993) and Sadek et al. (1993), scatter in material properties in Elishakoff et al. (1994), and the failure of a beam with uncertain initial deflection by Ben-Haim (1993).

Application of convex modeling approach to the optimal design of structures with incomplete information was initiated by Adali (1992). Designs of a sandwich plate and of a symmetric angle-ply laminate subject to a single uncertain load and with initial deflections were given by Adali et al. (1995) and Adali et al. (1994), respectively.

In the present study optimization and convex analysis are employed to design a symmetric angle-ply laminate under single and multiple loads and in the presence of initial imperfections the precise form of which is not known a priori. The uncertain initial deflection producing the least favorable response of the laminate is computed by convex modeling. The minimum weight of the laminate is determined such that the maximum deflection does not exceed a given upper bound under worst case of imperfections. The design problem involves determining the optimal ply angle subject to a buckling constraint and provides an angle-ply laminate designed against the worst case of uncertainty.

The effect of uncertainties in the initial deflection are investigated numerically. Optimal designs for various aspect ratios are presented for laminates under in-plane loading.

2 Plate With Initial Imperfections

Consider a simply supported angle-ply laminate of length a, width b and thickness $\bar{h}$ in the $\bar{x}$, $\bar{y}$, and $\bar{z}$-directions, respectively. The plate is symmetrically laminated and balanced with

Contributed by the Applied Mechanics Division of THE AMERICAN SOCIETY OF MECHANICAL ENGINEERS for publication in the ASME JOURNAL OF APPLIED MECHANICS.

Discussion on this paper should be addressed to the Technical Editor, Professor Lewis T. Wheeler, Department of Mechanical Engineering, University of Houston, Houston, TX 77204-4792, and will be accepted until four months after final publication of the paper itself in the ASME JOURNAL OF APPLIED MECHANICS.

Manuscript received by the ASME Applied Mechanics Division, June 17, 1994; final revision, Apr. 27, 1995. Associate Technical Editor: W. K. Liu.

Copyright © 1997 by ASME

Downloaded 04 May 2010 to 171.66.16.34. Redistribution subject to ASME license or copyright; see http://www.asme.org/terms/Terms_Use.cfm

equal number of layers with positive and negative ply angles. It consists of n layers so that the distance from the midplane, $\bar{z} = 0$, to the upper surface of the kth lamina ($\bar{z} \geq 0$) is equal to $\bar{t}_k = k\bar{h}/n$. The ply angle is denoted by θ, and the stiffnesses $\bar{Q}_{ij}$ are functions of θ and $\bar{h}$. The stacking sequence for a symmetric and balanced laminate is of the form $((+\theta/-\theta)_j)_{\text{sym}}$ where $j = n/4$ is the number of $+\theta$ and $-\theta$ combinations.

The total deflection $\bar{w}(x, y)$ of the plate consists of the initial deflection, $\bar{w}^0(x, y)$, and the deflection induced by loading, $\bar{w}^l(x, y)$. The loads applied on the plate are in-plane loads $N_x^{(i)}$ and $N_y^{(i)}$ in the x and y-directions, respectively, and transverse loads $\bar{q}_i$ where the load index i changes from 1 to $\Im$ with $\Im$ denoting the number of multiple loads. The multiple loads act at different times during the service life of the laminate.

Hereafter dimensionless quantities are employed in the analysis by introducing the quantities

$$x = \bar{x}/a, \quad y = \bar{y}/b, \quad t_k = \bar{t}_k/\bar{h}, \quad w = \bar{w}/b,$$
$$h = \bar{h}/bq_i = \bar{q}_i/E_T, P_i = N_x^{(i)}/(E_T b), \quad \lambda_i = N_y^{(i)}/N_x^{(i)},$$
$$\hat{Q}_{ij} = \bar{Q}_{ij}/E_T, \quad W = \bar{W}/(\rho ab^2) = h \tag{1}$$

where E_T is the transverse Young's modulus, ρ is the density, and $\bar{W}$ the weight of the plate given by $\bar{W} = \rho ab\bar{h}$. It is noted that the nondimensional weight W is equal to h which is the nondimensional laminate thickness.

The bending of the plate is governed by the equation

$$D_{11}r^{-4}w^l_{,xxxx} + 2(D_{12} + 2D_{66})r^{-2}w^l_{,xxyy} + D_{22}w^l_{,yyyy} = q - r^{-2}P(w^l + w^0)_{,xx} - \lambda P(w^l + w^0)_{,yy} \tag{2}$$

where $D_{ij} = (2/3)\sum_{k=1}^{n/2} \hat{Q}_{ij}(t_k^3 - t_{k-1}^3)$, $i, j = 1, 2, 6$, are flexural stiffnesses, $r = a/b$ is the aspect ratio of the plate, $w^l = \bar{w}^l/b$ and $w^0 = \bar{w}^0/b$ according to (1). The number of layers, n, is chosen large enough to ensure that the contributions of flexural stiffnesses D_{16} and D_{26} are negligible as estimated by Nemeth (1986).

The boundary conditions for the simply supported plate are

$$w = 0, \quad D_{11}w^l_{,xx} + r^2D_{12}w^l_{,yy} = 0 \quad \text{at} \quad x = 0, 1 \tag{3}$$
$$w = 0, \quad D_{12}w^l_{,xx} + r^2D_{22}w^l_{,yy} = 0 \quad \text{at} \quad y = 0, 1 \tag{4}$$

3 Problem Formulation

Design Analysis Problem. The initial deflection containing deterministic and uncertain parts can be expressed as

$$w_i^0(x, y) = w_0^0(x, y) + \tilde{w}_i^0(x, y), \quad i = 1, 2, \ldots, \Im \tag{5}$$

where the subscript "$_0$" denotes the deterministic part and the symbol "$\tilde{\ }$" the uncertain part. The deterministic part of initial deflection $w_0^0(x, y)$ does not depend on the loading. The uncertain part $\tilde{w}_i^0$ depends on the in-plane loads which could be different for different loadings. The uncertain components $\tilde{w}_i^0$ are arbitrary functions of x and y but are bounded in L_2 norm so that

$$\|\tilde{w}_i^0\|_2^2 \leq \epsilon_i^2, \quad i = 1, 2, \ldots, \Im \tag{6}$$

where ϵ_i is the prescribed level of uncertainty in the initial deflection, and L_2 norm of a function $f(x, y)$ is defined as

$$\|f\|_2^2 = \int_0^1 \int_0^1 |f(x, y)|^2 dxdy. \tag{7}$$

The design analysis problem for the plate with initial imperfections involves the determination of the least favorable deflection $w_i^l(x, y; \tilde{w}^0)$ of the laminate at a given point (x_0, y_0) and the corresponding expression for uncertain initial deflection $\tilde{w}_i^0$. In the present context, the least favorable deflection at (x_0, y_0) corresponds to the maximum possible deflection at that point for the given level of uncertainty. Thus, the analysis problem can be stated as follows:

Determine the least favorable deflection under the ith loading such that

$$w_i^l(x_0, y_0; \epsilon_i) = \max_{\tilde{w}_i^0} w_i^l(x_0, y_0; \tilde{w}_i^0), \; i = 1, 2, \ldots, \Im \tag{8}$$

where $w_i^l(x_0, u_0; \epsilon_i)$ denotes the deflection at (x_0, y_0) under the ith loading with the uncertain initial imperfection $\tilde{w}_i^0$ being determined from the solution of the problem (8) for a given value of the uncertainty bound ϵ_i.

Optimal Design Problem. The optimal design problem involves the computation of the minimum weight of the laminate such that the maximum deflection of the plate does not exceed a given upper bound δ. Moreover, the laminate is optimized with respect to ply angle θ. The resulting design is required not to fail by buckling. In terms of the nondimensional quantities $W = h$ as given by Eq. (1) where W and h refer to the weight and the thickness of the plate, respectively. In view of this relation, the laminate thickness h is used as the design objective in the rest of the paper. Let $w_i(x, y; \epsilon_i)$ denote the least favorable total deflection of the plate at (x, y) subject to the uncertainty level of ϵ_i in the initial deflection. The total deflection $w_i(x, y; \epsilon_i)$ is given by

$$w_i = w_i^l(x, y; \epsilon_i) + w_i^0(x, y; \epsilon_i). \tag{9}$$

The design problem can be stated as follows:

Determine the minimum thickness h_{min} and the optimal angle θ_{opt} such that

$$\max_{i=1,2,\ldots,\Im} \max_{x_0,y_0} w(x_0, y_0; \epsilon_i) \leq \delta \tag{10}$$

$$P_i < P_{cr}, \quad i = 1, 2, \ldots, \Im \tag{11}$$

where P_i is the in-plane load for the ith loading case and P_{cr} is the buckling load.

4 Method of Solution

For a simply supported rectangular plate, the deflection induced by the ith load may be expressed as

$$w_i^l(x, y; \epsilon_i) = \sum_{m=1}^{\infty}\sum_{n=1}^{\infty} C_{mn}^{(i)} \sin(m\pi x) \sin(n\pi y) \tag{12}$$

which satisfies the boundary conditions (3), (4).

The transverse load $q^{(i)}$ can also be expressed in terms of the eigenfunctions and is given by

$$q_i(x, y) = \sum_{m=1}^{\infty}\sum_{n=1}^{\infty} A_{mn}^{(i)} \sin(m\pi x) \sin(n\pi y) \tag{13}$$

where the coefficients $A_{mn}^{(i)}$ define a particular load distribution and can be most generally expressed as

$$A_{mn}^{(i)} = 4\int_0^1 \int_0^1 q_i(x, y) \sin(m\pi x) \sin(n\pi y) dxdy \tag{14}$$

The initial deflection w_i^0 can be expressed in terms of the eigenfunctions as well and is given by

$$w_i^0(x, y) = \sum_{m=1}^{\infty}\sum_{n=1}^{\infty} B_{mn}^{(i)} \sin(m\pi x) \sin(n\pi y) \tag{15}$$

where the coefficients $B_{mn}^{(i)}$ define the initial deflection and consists of deterministic and uncertain parts so that

$$B_{mn}^{(i)} = \mathfrak{B}_{mn} + \tilde{B}_{mn}^{(i)} \tag{16}$$

where $\mathfrak{B}_{mn}$ refers to the deterministic initial deflection and $\tilde{B}_{mn}^{(i)}$ to the uncertain initial deflection under ith loading.

Downloaded 04 May 2010 to 171.66.16.34. Redistribution subject to ASME license or copyright; see http://www.asme.org/terms/Terms_Use.cfm

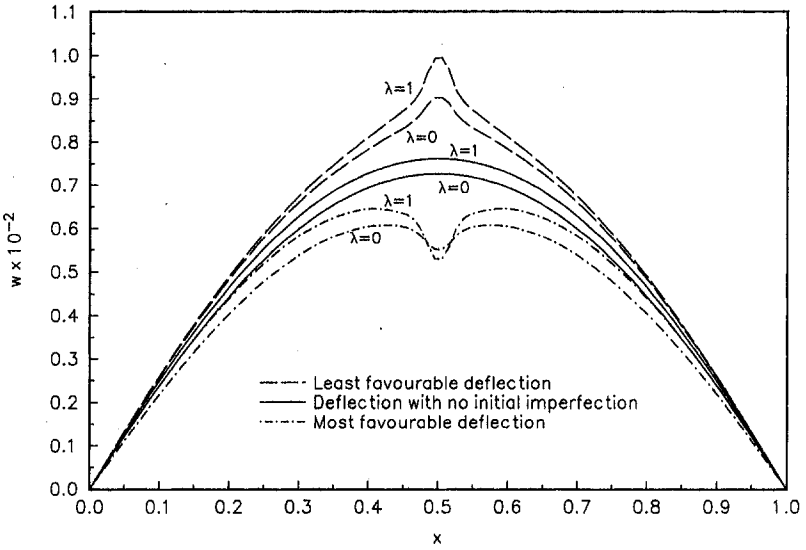


Fig. 1 Deflection w $(x, 0.5; 0.1)$ of a square plate with $x_0 = y_0 = 0.5$

The uncertain components of the initial deflection is subject to the inequality (6). Moreover, it is required that the uncertain parts can be represented by a finite number of eigenmodes, i.e., $\tilde{B}_{mn}^{(i)} \neq 0$ for $m = 1, \ldots, M$ and $n = 1, \ldots, N$, and $\tilde{B}_{mn}^{(i)} = 0$ for $m > M, n > N$. By substituting Eq. (15) and (6), we obtain

$$\sum_{m=1}^{M} \sum_{n=1}^{N} (\tilde{B}_{mn}^{(i)})^2 \leq 4\epsilon_i^2, \quad i = 1, 2, \ldots, \Im. \tag{17}$$

The coefficients $C_{mn}^{(i)}$ in Eq. (12) are obtained by substituting equations (12), (15), and (16) into the differential Eq. (2). This computation gives

$$C_{mn}^{(i)} = \frac{A_{mn}^{(i)} + P_i \pi^2 (m^2 r^{-2} + \lambda_i n^2)(\mathfrak{B}_{mn} + \tilde{B}_{mn}^{(i)})}{F_i(m, n)} \tag{18}$$

where $\lambda_i = N_x^{(i)}/N_y^{(i)}$ and

$$F_i(m, n) = \pi^4 [D_{11}(m/r)^4 + 2(d_{12} + D_{66})(mn/r)^2 + D_{22} n^4] - P_i \pi^2 (m^2/r^2 + \lambda_i n^2). \tag{19}$$

It is now possible to compute the least favorable deflection at any point using Eqs. (12), (16), and (18) provided the uncertainty coefficients $\tilde{B}_{mn}^{(i)}$ producing the least favorable response are known. These coefficients are evaluated in the next section by using the method of convex analysis.

5 Uncertainty Analysis

The values of the coefficients $\tilde{B}_{mn}^{(i)}$ have to be determined such that they yield the least favorable deflection at a given point (x_0, y_0). The convex modeling approach is employed to solve this problem.

The coefficients $\tilde{B}_{mn}^{(i)}$ form a convex set defined by

$$\mathfrak{G}_i = \{(\tilde{B}_{mn}^{(i)}) \mid \sum_{m=1}^{M} \sum_{n=1}^{N} (\tilde{B}_{mn}^{(i)})^2 \leq 4\epsilon_i^2\}, \quad i = 1, 2, \ldots, \Im \tag{20}$$

in the coordinates $(\tilde{B}_{mn}^{(i)})$. It follows from a theorem by Kelly and Weiss (1979) involving convex sets that the deflection function $w_i^l(x, y; \epsilon_i)$ takes on its maximum value at an extreme point on the boundary of the convex set $\mathfrak{G}_i$. Since $\mathfrak{G}_i$'s are

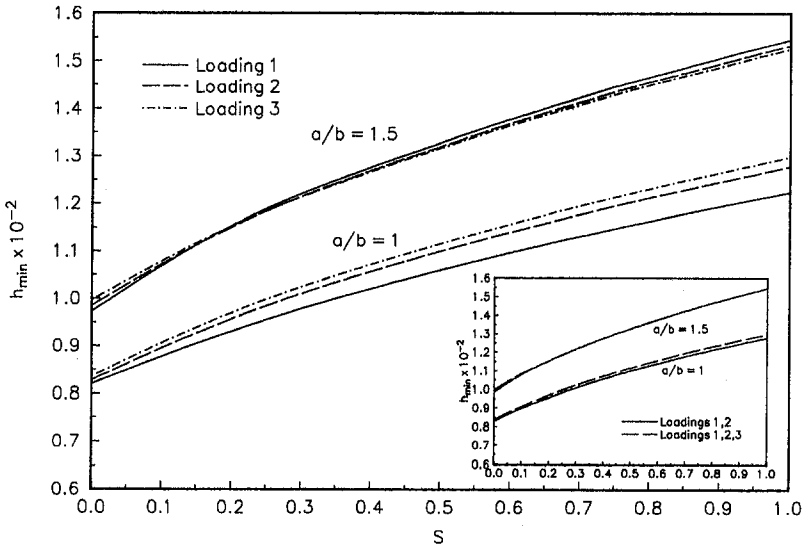


Fig. 2 Minimum thickness versus the uncertainty parameter for single load cases, and the insert for multiple load cases

Downloaded 04 May 2010 to 171.66.16.34. Redistribution subject to ASME license or copyright; see http://www.asme.org/terms/Terms_Use.cfm

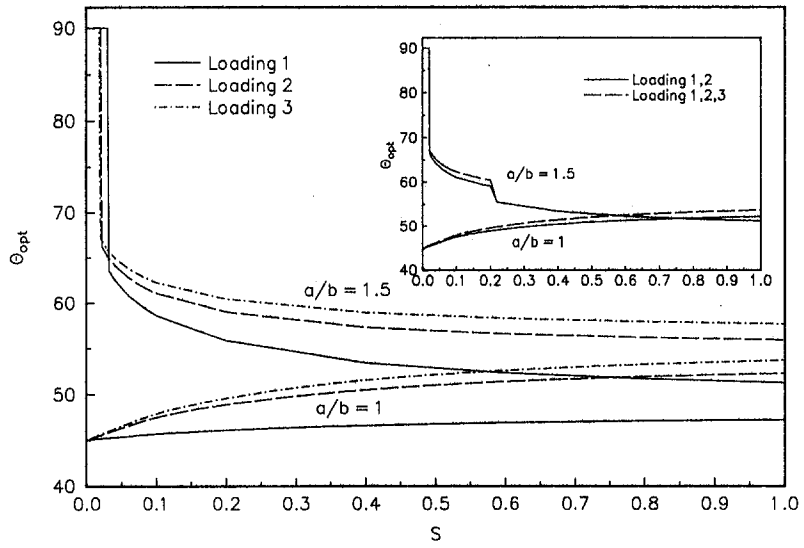


Fig. 3 Optimal ply angle versus the uncertainty parameter for single load cases, and the insert for multiple load cases

elliptic cylinders, the set of all extreme points lies on the set $\partial\mathfrak{G}_i$ as shown by Sadek et al. (1993) where ∂ denotes the boundary of the domain. Consequently equality must hold for the constraints (17), viz.

$$\sum_{m=1}^{M}\sum_{n=1}^{N}(\tilde{B}_{mn}^{(i)})^2 = 4\epsilon_i^2, \quad i = 1, 2, \ldots, \Im \tag{21}$$

for the initial imperfection producing the least favourable deflection in each loading case.

To obtain the least favorable deflection at a point (x_0, y_0), it is necessary to maximize the function $w_i^l(x_0, y_0; \epsilon_i)$ over the uncertainty coefficients subject to the equality constraint (21). The method of Lagrange multipliers is employed to solve this optimization problem. The Lagrangian for the ith loading condition has the form

$$\mathfrak{L}_i(\tilde{B}_{mn}^{(i)}) = w_i^l(x_0, y_0; \epsilon_i) + \mu_i\Big(\sum_{m=1}^{M}\sum_{n=1}^{N}(\tilde{B}_{mn}^{(i)})^2 - 4\epsilon_i^2\Big) \tag{22}$$

where μ_i is the Lagrange multiplier.

The extremum conditions for the Lagrangian (22) are given by

$$\frac{\partial\Im_i}{\partial\mu_i} = 0, \quad \frac{\partial\Im_i}{\partial\tilde{B}_{mn}^{(i)}} = 0, \quad m = 1 \ldots M, \quad n = 1 \ldots N. \tag{23}$$

By substituting the deflection $w_i^l(x, y; \delta_i)$ given by (12) into (22), and using the extremum conditions (23), the optimal values of $\tilde{B}_{mn}^{(i)}$ are computed as

$$\tilde{B}_{mn}^{(i)} = -\frac{2}{\mu_i}\cdot V_{mn}^{(i)}(x_0, y_0) \tag{24}$$

where

$$V_{mn}^{(i)}(x_0, y_0) = \frac{P_i\pi^2(m^2/r^2 + \lambda_i n^2)}{F_i(m, n)}\sin(m\pi x_0)\sin(n\pi y_0). \tag{25}$$

The values of the Lagrange multipliers are determined from

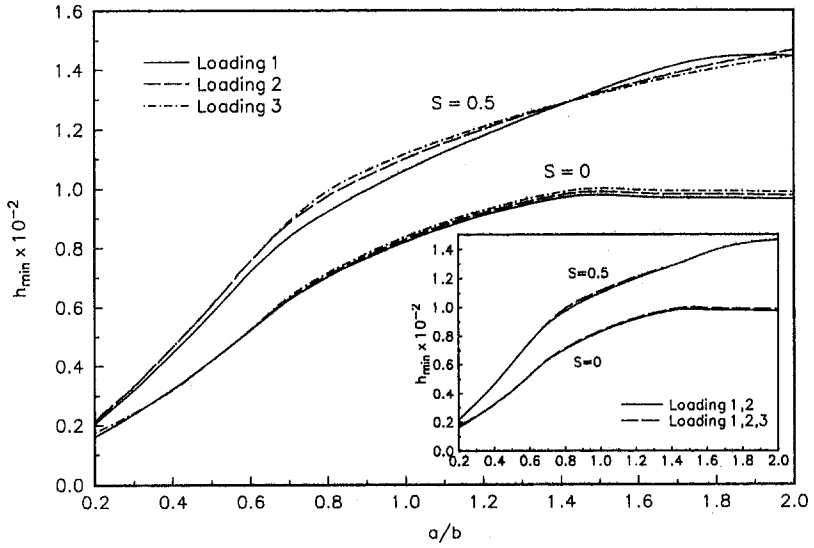


Fig. 4 Minimum thickness versus the aspect ratio for single load cases, and the insert for multiple load cases

Downloaded 04 May 2010 to 171.66.16.34. Redistribution subject to ASME license or copyright; see http://www.asme.org/terms/Terms_Use.cfm

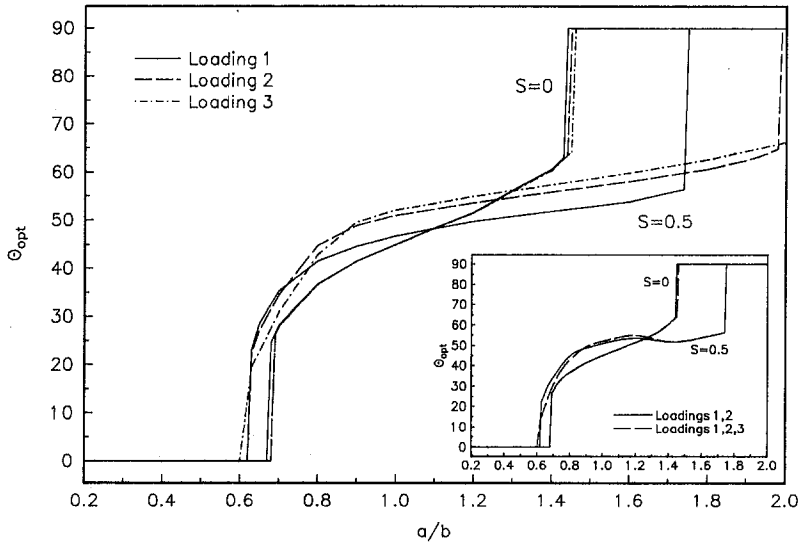


Fig. 5 Optimal ply angle versus the aspect ratio for single load cases, and the insert for multiple load cases

the constraints (21) with the values of $\tilde{B}_{mn}^{(i)}$ given by (24). This computation yields

$$\mu_i = \mp \frac{1}{\epsilon_i} \left[\sum_{m=1}^{M} \sum_{n=1}^{N} [V_{mn}^{(i)}(x_0, y_0)]^2 \right]^{1/2} \tag{26}$$

where $V_{mn}^{(i)}$ is given by Eq. (25). The sign of the expression for μ_i is chosen so as to yield the least favorable response.

To be able to compare the relative magnitudes of the deterministic and uncertain deflections, the norm of the uncertain initial deflection is related to the deterministic deflection by

$$\|\tilde{w}_i^0\|_2^2 = \epsilon_i^2 = S_i^2 \|w_i^l(x, y; 0)\|_2^2 \tag{27}$$

where $w_i^l(x, y; 0)$ denotes the deterministic deflection of the plate under the ith loading and S_i is a constant which specifies the level of uncertainty relative to the L_2 norm of the deterministic deflection.

6 Optimization Algorithm

An optimization algorithm is developed to determine the minimum thickness $h_{\min}$ and the optimal ply angle θ_{opt}. Due to the presence of in-plane loads it is not possible to express the thickness h explicitly in terms of the ply angle θ and subsequently minimize it with respect to θ. To overcome this difficulty an iterative solution procedure is devised to minimize h and to determine θ_{opt} such that the design constraints (10) and (11) are satisfied.

An initial design involving the estimates of h and θ is specified within the feasible region and the deterministic deflection is calculated which is to be used in Eq. (27). Then a minimum thickness satisfying the deflection and buckling constraints (10), (11) is calculated without changing the ply angle. The next step involves the minimization of the least favorable deflection by obtaining an optimal ply angle for the value of h computed in the previous step. Thus one iteration of the solution procedure consists of the following computations:

$$\min_{h^{(i)}} \left| \max_{x_0, y_0} w_i(x_0, y_0; \epsilon_i) - \delta \right| \tag{28}$$

$$\min_{\theta} \left(\max_{i} \left| \max_{x_0, y_0} w_i(x_0, y_0; \epsilon_i) \right| \right) \tag{29}$$

subject to the constraint (11).

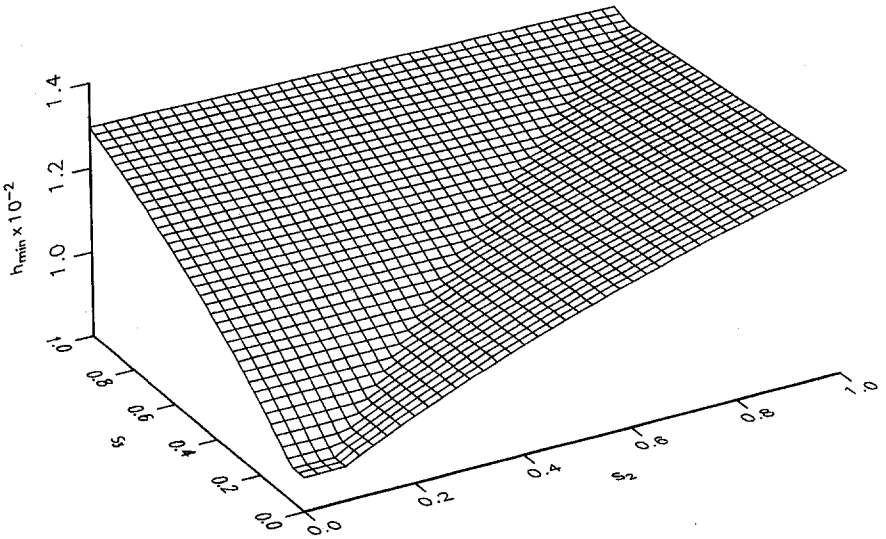


Fig. 6 Minimum thickness under loads 1, 2, and 3 plotted against S_2 and S_3 with $S_1 = 0.1$ and $a/b = 1.0$

Downloaded 04 May 2010 to 171.66.16.34. Redistribution subject to ASME license or copyright; see http://www.asme.org/terms/Terms_Use.cfm

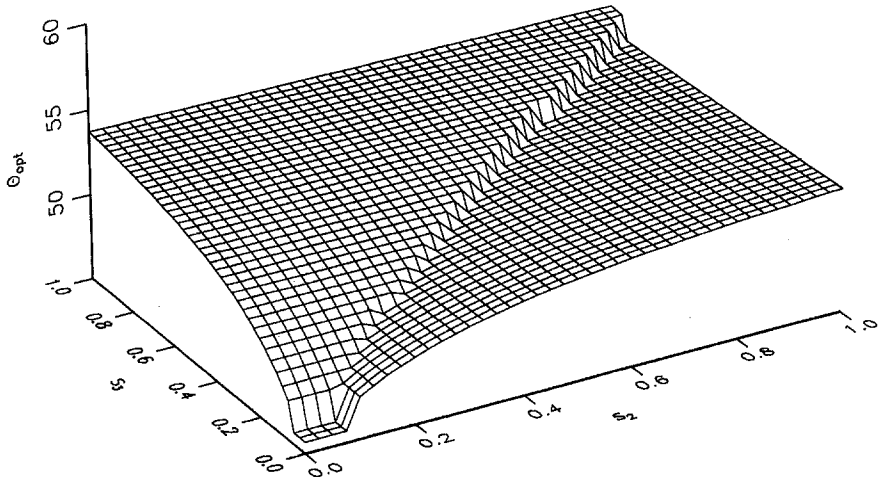


Fig. 7 Optimal ply angle under loads 1, 2, and 3 plotted against S_2 and S_3 with $S_1 = 0.1$ and $a/b = 1.0$

The process is a convergent one producing the laminate with the minimum thickness $h_{\min}^{(i)}$ and optimal ply angle θ_{opt} which are determined using the Golden Section method (Press, Teukolsky, Vetterling, and Flannery 1992). The minimum thickness $h_{\min}$ of the laminate satisfying the constraints (10) and (11) for every loading is obtained from

$$h_{\min} = \max_{i=1,2,\ldots,3} h_{\min}^{(i)}. \tag{30}$$

Optimal ply angle θ_{opt} follows from the optimization step (29). The convergence criterion is defined as the relative change in the objective function of the optimization problem, viz.

$$\left| \frac{h_{\min}^{(s)} - h_{\min}^{(s-1)}}{h_{\min}^{(s-1)}} \right| \leq \Delta \tag{31}$$

where s is the iteration number, and Δ is the required accuracy. The iterative procedure is repeated until the desired accuracy Δ is achieved for $h_{\min}$.

7 Numerical Results

Numerical results are given for a laminate with a stacking sequence $((+\theta/-\theta)_j)_{\text{sym}}$, where j is chosen large enough such that the stiffnesses D_{16} and D_{26} become negligibly small. It is noted that D_{11}, D_{12}, D_{22}, and D_{66} do not depend on the value of j. Results are given for a graphite/epoxy material for which $E_L = 181$ GPa, $E_T = 10.3$ GPa, $G_{LT} = 7.17$ GPa, $\nu_{LT} = 0.28$, where indices L and T refer to the longitudinal and transverse directions, respectively.

In the numerical example, the multiple loads consist of a uniformly distributed transverse load q_i and in-plane loads with different load ratios λ_i. The coefficients $A_{mn}^{(i)}$ are obtained from (14) as

$$A_{mn}^{(i)} = \frac{16 q_i}{\pi^2 mn} \sin(m\pi/2) \sin(n\pi/2) \times \sin(m\pi/2) \sin(n\pi/2). \tag{32}$$

Three cases of multiple loads are considered. These are specified as

(i) Loading 1: $q_1 = 10^{-6}$, $P = 10^{-6}$ and $\lambda = 0.0$,
(ii) Loading 2: $q_2 = 10^{-6}$, $P = 10^{-6}$ and $\lambda = 0.5$,
(iii) Loading 3: $q_3 = 10^{-6}$, $P = 10^{-6}$ and $\lambda = 1.0$.

The deterministic initial deflection is taken to be zero. The least and most favorable deflections of a square plate are shown in Fig. 1 for loading cases 1 and 3 with x_0 and y_0 in (8) specified as $x_0 = y_0 = 0.5$. The deflections of the plate with no initial imperfections are also shown. It is observed that the gap between the maximum and minimum possible deflections is quite large. Moreover, it is clear that a design neglecting the effect of initial imperfections or not based on the worst case of imperfections will violate the deflection constraint if the least favourable conditions occur.

Designs Under Single Loads. First, the effect of uncertain initial imperfections on the optimal design is studied for plates under single loads. The dependence of an optimal design on the level of uncertainty is investigated in Fig. 2 which shows the minimum thickness of the plate versus the uncertainty level $S = S_1 = S_2 = S_3$ for each loading case. The minimum thickness increases as the uncertainty level increases. However, Fig. 2 shows that the rate of the increase varies for different loading cases. For example, the plate with the aspect ratio $a/b = 1.5$ under the loading condition 1 requires a smaller minimum thickness $h_{\min}$ as compared to the loading cases 2 and 3 for the deterministic case ($S = 0$) but a larger $h_{\min}$ for the uncertainty level $S \geq 0.22$. Figure 3 shows the optimal ply angles corresponding to the minimum thicknesses shown in Fig. 2. It is observed that neglecting the effect of initial imperfections will lead to substantial design errors.

The optimal designs as functions of the aspect ratio are investigated in Figs. 4 and 5. Figure 4 shows the curves of minimum thickness versus the aspect ratio for no imperfections ($S = 0$) and uncertain imperfections ($S = 0.5$), while Fig. 5 shows the corresponding optimal ply angles. Figure 4 shows that the gap between the deterministic and the uncertain solutions increases as the aspect ratio increases.

Designs Under Multiple Loads. Designs for multiple load cases 1 and 2 as well as for 1, 2, and 3 are shown in the inserts of Figs. 2 and 3 for minimum thickness and optimal ply angle, respectively. It is observed that the loading case 3 is the critical one for any level of uncertainty for a square plate ($a/b = 1$). For a rectangular plate ($a/b = 1.5$) the critical loading case is case 3 for $S < 0.22$, and case 1 for $S \geq 0.22$. This effect results in the abrupt change in the optimal ply angle at $S = 0.22$ as shown in the insert in Fig. 3.

The inserts in Figs. 4 and 5 gives the multiple load designs as a function of the aspect ratio. For the deterministic case ($S = 0$) the loading case 3 is critical for $a/b < 0.32$ and $a/b \geq 0.5$, while the loading case 1 becomes critical in the range of aspect ratios $0.32 \leq a/b < 0.5$. For the uncertain conditions ($S = 0.5$) the critical thickness is determined by loading 3 for $0 \leq a/b < 1.4$, by loading 1 for $1.4 \leq a/b < 1.92$, and by

Downloaded 04 May 2010 to 171.66.16.34. Redistribution subject to ASME license or copyright; see http://www.asme.org/terms/Terms_Use.cfm

loading 2 for $a/b \geq 1.92$. It is interesting to note that the optimum fiber orientation is heavily influenced by uncertainty in imperfections.

The minimum thicknesses and optimal ply angles of a square plate under the loads 1, 2, and 3 are plotted against the uncertainty parameters S_2 and S_3 in Figs. 6 and 7, respectively, in which the value of S_1 is taken as 0.1. As expected the thickness increases as S_2 and/or S_3 increases.

Conclusions

Optimal designs of symmetric angle-ply laminates under single and multiple transverse and in-plane loads are determined with incomplete data on the initial imperfections. The design involves determining the minimum thickness of the laminate and the optimal fibre orientation subject to maximum deflection and buckling constraints for a given level of uncertainty in data. Minimum weight designs are obtained for the worst case of imperfections producing the maximum possible deflection. It is observed that the minimum thickness and optimal ply angle depend on the level of uncertainty and the thickness increases with increasing uncertainty.

The solution technique makes use of convex modelling of the uncertain data which is bounded in L_2 norm, but can vary arbitrarily around an average value. The least favorable response of the laminate at a point is defined as the maximum possible deflection at that point. The initial deflection producing the least favorable response are determined in the course of the solution. An iterative optimization algorithm is developed to obtain the minimum thickness and the corresponding optimal ply angles.

References

Adali, S., 1992, "Convex and fuzzy modellings of uncertainties in the optimal design of composite structures," Optimal Design with Advanced Materials, P. Pedersen, ed., Elsevier, Amsterdam, The Nederlands.

Adali, S., Richter, A., and Verijenko, V. E., 1994, "Optimal design of symmetric angle-ply laminates subject to uncertain loads and initial imperfections," *Proceedings of the Fourth International Conference on Computer Aided Design in Composite Materials Technology* (CADCOMP-94), W. R. Blair and W. P. de Wilde, eds., June 29–July 1, Southampton, England, pp. 39–48.

Adali, S., Richter, A., and Verijenko, V., 1995, "Non-probabilistic modelling and design of sandwich plates subject to uncertain loads and initial deflections," *International Journal of Engineering Sciences,* Vol. 33, pp. 855–866.

Ben-Haim, Y., 1993, "Failure of an axially compressed beam with uncertain initial deflection of bounded strain energy," *International Journal of Engineering Science,* Vol. 31, pp. 989–1001.

Ben-Haim, Y., and Elishakoff, I., 1989, "Non-probabilistic Models of Uncertainty in the Nonlinear Buckling of Shells With General Imperfections: Theoretical Estimates of the Knockdown Factor," ASME JOURNAL OF APPLIED MECHANICS, Vol. 56, pp. 403–410.

Ben-Haim, Y., and Elishakoff, I., 1990, *Convex Models of Uncertainty in Applied Mechanics,* Elsevier, Amsterdam, The Nederlands.

Elishakoff, I., and Ben-Haim, Y., 1990, "Dynamics of a thin cylindrical shell under impact with limited deterministic information on its initial imperfections," *Journal of Structural Safety,* Vol. 8, pp. 103–112.

Elishakoff, I., Cai, G. Q., and Starnes, J. H., 1994, "Non-linear buckling of a column with initial imperfection via stochastic and non-stochastic convex models," *International Journal of Non-Linear Mechanics,* Vol. 29, pp. 71–82.

Elishakoff, I., and Colombi, P., 1993, "Combination of probabilistic and convex models of uncertainty when scarce knowledge is present on acoustic excitation parameters," *Computer Methods in Applied Mechanics and Engineering,* Vol. 104, pp. 187–209.

Elishakoff, I., Li, Y. W., and Starnes, J. H., 1994, "A deterministic method to predict the effect of unknown-but-bounded elastic moduli on the buckling of composite structures," *Computer Methods in Applied Mechanics and Engineering,* Vol. 111, pp. 155–167.

Kelly, P. J., and Weiss, M. L., 1979, *Geometry and Convexity: A Study in Mathematical Methods.* John Wiley and Sons, New York.

Nemeth, M. P., 1986, "Importance of anisotropy on buckling of compression-loaded symmetric composite plates," *AIAA Journal,* Vol. 24, pp. 1831–1835.

Press, W. H., Teukolsky, S. A., Vetterling, W. T., and Flannery, B. P., 1992, *Numerical Recipes in C: The Art of Scientific Computing,* 2nd ed., Cambridge University Press, Cambridge, U.K.

Sadek, I. S., Sloss, J. M., Adali, S., and Bruch, J. C., Jr., 1993, "Nonprobabilistic modelling of dynamically loaded beams under uncertain excitations," *Mathematical and Computer Modelling,* Vol. 18, pp. 59–67.

Downloaded 04 May 2010 to 171.66.16.34. Redistribution subject to ASME license or copyright; see http://www.asme.org/terms/Terms_Use.cfm

Left Eigenvectors: Extraction From Measurements and Physical Interpretation

I. Bucher

S. G. Braun
Mem. ASME.

Faculty of Mechanical Engineering,
Technion-Israel Institute of Technology,
Technion City, Haifa 32000,
Israel

In this paper the extraction of left eigenvectors from measured frequency response functions is presented and discussed. It is shown that contrary to the extraction of right eigenvectors from measured response data, the extraction of left eigenvectors is inherently ill-posed when the same measured information is being used. The ill-posedness can result in a spatially oscillating additive component (short wavelength) appearing in the identified left eigenvectors, a property which is not described in existing literature on structural dynamics. Some well-known regularization methods are hence used to reduce the inaccuracies appearing in the extracted left eigenvectors. It is also shown that a further improvement in the accuracy of the solution can be achieved by making use of an approximation of the mass distribution combined with regularization. Throughout this paper, an attempt is made to provide a physical insight to the various aspects related to the left eigenvectors and their extraction. This includes (a) the interpretation of left eigenvectors as internal force distributions; (b) the inherent reason for the ill-conditioning, and (c) the spatial filtering of short wavelength achieved by regularization, yielding an improved estimate of the left eigenvectors.

1 Introduction and Background

Modal decomposition is one of the main tools used in vibration engineering. Experimental modal analysis attempts to extract modal parameters from measured data to provide a physically meaningful model. Specifically, eigenvectors and eigenvalues can be obtained through an identification process using excitation and response measurements.

Many procedures use information in the form of frequency response functions (FRFs). These exhibit an inherent limitation of any experimental measurement: a finite frequency bandwidth of the acquired data. Engineering structures, being continuous, have an infinite number of vibrating modes, but the experimental identification can only extract a finite subset of these. The result of this effect is usually addressed as "modal truncation" (Inman, 1989; Ewins, 1984).

Left eigenvectors, which can be extracted from measured frequency response functions (FRF) of structures and systems, convey important information on their dynamic behavior (Meirovitch, 1985). Some important engineering applications make use of this information in order to better control or modify the vibratory behavior of engineering structures (Meirovitch, 1985; Bucher and Braun, 1993; Zhang et al., 1990). Unfortunately, the extraction of left eigenvectors from measured data appear to pose some difficulties that cannot be overlooked.

The unavoidable modal truncation can have significant effects on engineering applications of modal analysis. One such area is that of structural modifications, where changes in the dynamic characteristics are obtained by modifying the structure. The modal truncation makes an exact prediction of the effect of modifications impossible (Ram et al., 1990; Bucher and Braun, 1993). Another area is that of model updating, where an analytical model is tuned to agree with experimentally obtained model (Lallement et al., 1991). The control of flexible structures is yet another area where out of the measured frequency-range modes may result in instability (Meirovitch, 1985).

There exist a set of dual vectors, the left eigenvectors, which also characterize some aspects of the dynamic behavior. It will be shown, that a physical interpretation of such left eigenvectors is one of forces. Using the left eigenvectors, most errors caused by the modal truncation, can be reduced or eliminated in engineering applications. This can be done even when truncation of left eigenvectors occurs whenever those are identified experimentally.

Forces proportional to the left eigenvectors, outside the measured frequency band, will have a small effect on the responses in the measured band, but those forces do exist (Bucher and Braun, 1993). Using the information residing in the left eigenvectors, the effect of such out-of-band forces can be eliminated, thus preventing unmodeled frequency ranges from influencing the combined response. In a prior work (Bucher and Braun, 1993, 1994) it was shown how to constrain the forces generated by the modifications to reside within the subspace of identified left eigenvectors. This constraint could then help to overcome the unpredictability of the effect of the structural modification. The use of left eigenvectors is the key for achieving this constraint using only measured quantities.

To use the left eigenvectors in practice, they have to be extracted from experimental data. In this paper the extraction of left eigenvectors from measured frequency response functions (FRFs) will be discussed and it will be shown that a set of ill-posed linear equations has to be solved. Some regularization methods (Glasko, 1988; Hansen, 1987; Lawson and Hanson, 1974), combined with knowledge about the nature of the problem being solved, are applied, in order to reduce the effect of ill-conditioning. This reduction in the error of the left eigenvector estimate, relies on the physical interpretation of the left eigenvectors. One of the main contributions of this paper will be the physical interpretation of the left eigenvectors, the error mechanism and its mathematical and geometrical interpretation. This interpretation motivates the regularization and the mathematical procedure for improving the estimates of the left eigenvectors from measured data.

Contributed by the Applied Mechanics Division of THE AMERICAN SOCIETY OF MECHANICAL ENGINEERS for publication in the ASME JOURNAL OF APPLIED MECHANICS.

Discussion on this paper should be addressed to the Technical Editor, Professor Lewis T. Wheeler, Department of Mechanical Engineering, University of Houston, Houston, TX 77204-4792, and will be accepted until four months after final publication of the paper itself in the ASME JOURNAL OF APPLIED MECHANICS.

Manuscript received by the ASME Applied Mechanics Division, Feb. 25, 1995; final revision, Feb. 2, 1996. Associate Technical Editor: M. Ortiz.

Copyright © 1997 by ASME

Downloaded 04 May 2010 to 171.66.16.34. Redistribution subject to ASME license or copyright; see http://www.asme.org/terms/Terms_Use.cfm

In previous works (Zhang et al., 1990; Shelley and Allemang, 1992), the use and the extraction of left eigenvectors was discussed. The fact that the problem is inherently ill-posed was not mentioned and the minimum-length solution, which is demonstrated here to perform badly, was recommended.

The paper is organized as follows: Section 2 provides the basic definitions of left eigenvectors and their interpretation. Section 3 compares the identification of right and left eigenvectors from measured frequency response functions. Section 4 applies some methods of regularization, including one practical and effective method utilizing the mass distribution. A physical interpretation of the improvement achieved by the regularization is given. In Section 5, two simulated examples comparing standard and the suggested methods are presented and discussed.

2 Definitions and Background

In this section we present the basic equations enabling us to define the right and left eigenvectors for a vibrating structures. We then discuss the physical interpretation of the right and left eigenvectors and briefly mention some engineering applications using left eigenvectors especially in the field of structural modification.

The simple model of a conservative (undamped) structure is used in this paper. This allows the introduction of the main ideas using simple and short expressions. In practice, a structure is bound to include some damping, but this complicates the formulation. We thus analyze an undamped vibrating system, obeying the following equation of motion:

$$\mathbf{M}\ddot{\mathbf{x}}(t) + \mathbf{K}\mathbf{x}(t) = \mathbf{f}(t) \quad \mathbf{x}(t),\ \mathbf{f}(t) \in \Re^{nx1}. \tag{1}$$

Here, $\mathbf{M}$, $\mathbf{K}$ are the constant mass and stiffness matrices, $\mathbf{x}(t)$ is the response vector, and $\mathbf{f}(t)$ is the external excitation. The unforced ($\mathbf{f}(t) = 0$) harmonic response $\mathbf{x}(t) = \phi_k e^{i\omega_k t}$ substituted in Eq. (1) (Meirovitch, 1980; Inman, 1989) yields, after multiplication by $\mathbf{M}^{-1}$,

$$(\mathbf{M}^{-1}\mathbf{K})\phi_k = \omega_k^2\phi_k \quad k = 1 \ldots n. \tag{2}$$

Here ϕ_k is the kth (right) eigenvector and ω_k^2 (kth squared natural frequency) is an eigenvalue.

The left eigenvectors, appear in a similar construct (Meirovitch, 1980; Inman, 1989; Lancaster, 1969), only this time multiplying the system matrix ($\mathbf{M}^{-1}\mathbf{K}$) to the left,

$$\mathbf{l}_k^T(\mathbf{M}^{-1}\mathbf{K}) = \omega_k^2\mathbf{l}_k^T. \tag{3}$$

The right and left eigenvectors are related by the following relations (Lancaster, 1969; Bucher and Braun, 1993):

$$\mathbf{l}_k = \mathbf{M}\phi_k. \tag{4a}$$

It can also be shown that the right and left eigenvectors are related by

$$\mathbf{L}^T = \mathbf{\Phi}^{-1} \tag{4b}$$

where

$$\mathbf{L} = [\mathbf{l}_1 \quad \mathbf{l}_2 \quad \ldots \quad \mathbf{l}_n], \quad \mathbf{\Phi} = [\phi_1 \quad \phi_2 \quad \ldots \quad \phi_n].$$

Equation (4b) can be used to show that the right and left eigenvectors are orthogonal with respect to each other and can be scaled to become orthonormal, i.e., $\mathbf{L}^T\mathbf{\Phi} = \mathbf{I}$. This orthonormality relationship can be written as

$$\mathbf{l}_k^T\boldsymbol{\phi}_j = \delta_{k,j} = \begin{cases} 1 & k = j \\ 0 & k \neq j. \end{cases} \tag{4c}$$

By substitution of Eq. (4a) in Eq. (4c), the well-known biorthonormality relation is obtained,

$$\phi_k^T\mathbf{M}\phi_j = \delta_{k,j}. \tag{4d}$$

The Physical Interpretation of Left Eigenvectors. The jth left eigenvector is proportional to the inertia force, $\mathbf{f}_j(t)$, which is related to the jth mode of vibration, i.e.,

$$\mathbf{f}_j(t) = \mathbf{M}\ddot{\mathbf{x}}(t) = -\omega_j^2\mathbf{M}\phi_j \sin \omega_j t = -\omega_j^2\mathbf{l}_j \sin \omega_j t. \tag{5}$$

Multiplying Eq. (2) by $\mathbf{M}$, we obtain the eigenvalues problem in a more familiar form (Meirovitch, 1980),

$$\mathbf{K}\phi_j = \omega_j^2\mathbf{M}\phi_j. \tag{5a}$$

This form of the eigenvalue equation shows that the inertia forces, related to the jth right eigenvectors, are proportional to the potential (spring) forces.

Substitution of Eq. (5a) in Eq. (5) yields

$$\mathbf{f}_j(t) = -\mathbf{K}\phi_j \sin \omega_j t = -\omega_j^2\mathbf{l}_j \sin \omega_j t. \tag{5b}$$

It was thus shown that the left eigenvector is proportional to both the inertia and potential forces for a particular natural frequency and hence represents force.

A somewhat intuitive interpretation can be attached to orthogonality relations in Eqs. (4c, d): Inertia and potential forces, related to the kth mode, do not perform any mechanical work on other modes (i.e., on the jth mode, where $k \neq j$). This point is of paramount importance in several areas: structural modifications, model updating, (Lallement et al., 1991) and control of flexible structures (Meirovitch, 1985; Zhang et al., 1990).

2.1 The Importance of Left Eigenvectors in Some Applications. Using the orthonormality relations in Eq. (4c), the solution for Eq. (1) can be expressed using a modal expansion:

$$\mathbf{x}(t) = \sum_{k=1}^{n} \left(\phi_k\phi_k^T \frac{1}{\omega_k} \int_0^t \mathbf{f}(t-\tau) \sin \omega_k\tau d\tau \right). \tag{6}$$

The interpretation of the left eigenvectors as modal forces is used to show that each right eigenvector (e.g., response) can be selectively controlled by the matching left eigenvectors. In particular, influencing a specific mode is achieved by selecting the force vector to be parallel to that left eigenvectors, i.e.,

$$\mathbf{f}(t) = \alpha(t)\mathbf{l}_j. \tag{7}$$

Using Eq. (4c), it is clear that only the response due to ϕ_j is influenced by the force in Eq. (7). Substitution of Eq. (7) in Eq. (6) yields

$$\mathbf{x}(t) = \phi_j \left(\frac{1}{\omega_j} \int_0^t \alpha(t-\tau) \sin \omega_j\tau d\tau \right). \tag{8}$$

This fact can be used to control only a selected set of modes in a desired frequency range. This approach is known in control applications as modal control (Meirovitch, 1985).

We now extend this idea to structural modifications. In such applications, mass and stiffness modification are introduced in order to obtain more desirable dynamic properties.

We may rewrite the unforced equation of motion after applying mass and stiffness modifications. It is assumed that the structural modifications are in form of incremental matrices $\Delta\mathbf{M}$, $\Delta\mathbf{K}$. The modified structure obeys:

$$(\mathbf{M} + \Delta\mathbf{M})\ddot{\mathbf{x}}(t) + (\mathbf{K} + \Delta\mathbf{K})\mathbf{x}(t) = 0. \tag{9}$$

Defining

$$\mathbf{f}(t) = -(\Delta\mathbf{M}\ddot{\mathbf{x}}(t) + \Delta\mathbf{K}\mathbf{x}(t)), \tag{10}$$

it is apparent that Eq. (9) is equivalent to Eq. (1), and the structural modification can be treated in a similar manner to external excitation. In this case the forces acting on the structure are the potential and inertia forces of the added mass and stiffness.

Downloaded 04 May 2010 to 171.66.16.34. Redistribution subject to ASME license or copyright; see http://www.asme.org/terms/Terms_Use.cfm

Forcing $\mathbf{f}(t)$ (and hence introducing a constraint on $\Delta\mathbf{M}$, $\Delta\mathbf{K}$ (see Eq. (11)) to reside in a subspace spanned by selected left eigenvectors yields modification of only pre-selected modes, other modes, unchanged (Bucher and Braun, 1993).

A major obstacle in using experimentally obtained data is the unavoidable finite frequency range. Only a subset of the eigenproperties (natural frequencies and mode shapes) can be extracted. An immediate result is that the mass $\mathbf{M}$ and stiffness $\mathbf{K}$ cannot be retrieved from the experimental data (Ram, 1989; Ewins, 1984). We overcome this limitation by replacing the products $\mathbf{M}\ddot{\mathbf{x}}(t)$ and $\mathbf{K}\mathbf{x}(t)$ according to Eq. (5*b*) with a linear combination of the left eigenvectors residing in the measured range.

In structural modifications it is desired to control selectively some of the right eigenvectors and the natural frequencies. It can be shown (Bucher and Braun, 1993) that a specific right-eigenvector, ϕ_j and its accompanied natural frequency ω_j, can be selectively modified by requiring

$$(\Delta\mathbf{M}\ddot{\mathbf{x}}(t) + \Delta\mathbf{K}\mathbf{x}(t)) \subset \text{span } \mathbf{l}_j. \tag{11}$$

Equation (11) can be generalized to control a set of modes by demanding that the inertia and stiffness forces (exerted by the modification) reside in a subspace spanned by the corresponding set of left eigenvectors (Bucher and Braun, 1993).

The constraint equation is simplified when the response $\mathbf{x}(t)$ is a linear combination of m measured modes. In this case the result of the experimental modal testing can be used to replace Eq. (11) by

$$(-\omega_j^2\Delta\mathbf{M} + \Delta\mathbf{K})\phi_j \subset \text{span } \mathbf{l}_j. \tag{12}$$

Equation (12) can also be generalized to the modification of several right eigenvectors (Bucher and Braun, 1993) and can be interpreted as follows: We constrain the additional inertia and potential forces to affect specified modes only, leaving all other modes unaffected.

Recalling the fact that higher modes are unknown, the benefit in using the left eigenvectors is obvious: It allows one to eliminate any influence of the out-of-range forces and thus to provide the desired control or exact modification without the side effects of the unmodeled, high-frequency related dynamics. This can be achieved by using experimentally obtained models.

3 The Extraction of Right and Left Eigenvectors From Measured Data

The frequency response matrix (FRM) of a vibrating structure can be expanded in an eigenvector series (Lancaster, 1969).

$$[\mathbf{H}_1 \quad \mathbf{H}_2 \quad \dots \quad \mathbf{H}_n] = \sum_{k=1}^{n} \frac{1}{\omega_k^2 - \omega^2}\phi_k\phi_k^T \tag{13}$$

One column, $\mathbf{H}_p$, of the FRM (frequency response matrix) can be experimentally identified by using a single excitation (applied at the pth location). This FRM column can be expressed as

$$\mathbf{H}_p = \sum_{k=1}^{n} \frac{\phi_k[p]}{\omega_k^2 - \omega^2}\phi_k = \sum_{k=1}^{n} \frac{1}{\omega_k^2 - \omega^2}\psi_k \tag{14}$$

where we use the definition $\psi_k = \phi_k[p]\phi_k$ and $\phi_k[p]$ is the pth element of ϕ_k.

In Eq. (14), the vector $\mathbf{H}_p$ is a linear combination of the modal vectors ϕ_k. The coefficients for this linear combination are $\phi_k[p]/(\omega_k^2 - \omega^2)$ (which are frequency dependent).

Normally, some natural frequencies reside well above the measured range, i.e., $\omega_k^2 \gg \omega^2$ (for $k = m + 1, \dots, n$). The coefficients related to these modes are negligible, i.e., $\phi_k[p]/(\omega_k^2 - \omega^2) \approx 0\ \forall k > m$. The FRM column in Eq. (14) will then be a linear combination of only m modes. We thus express Eq. (14) as a combination of the m modes (where $m < n$) within the measured range

$$\mathbf{H}_p \approx \sum_{k=1}^{m} \frac{\phi_k[p]}{\omega_k^2 - \omega^2}\phi_k = \sum_{k=1}^{m} \frac{1}{\omega_k^2 - \omega^2}\psi_k. \tag{15}$$

The next step is to develop a set of linear equations relating eigenvectors to the measured frequency-response-function (FRF).

3.1 Extraction of Right Eigenvectors From Measured FRF. The frequency response matrix's column can be decomposed into

$$\mathbf{H}_p = [\psi_1 \quad \psi_2 \quad \dots] \begin{pmatrix} \frac{1}{\omega_1^2 - \omega^2} \\ \frac{1}{\omega_2^2 - \omega^2} \\ \vdots \end{pmatrix}. \tag{16}$$

It is assumed that the natural frequencies, ω_k, can be identified with high accuracy by well-established methods (Ewins, 1984; Inman, 1989).

The frequency response matrix (FRM) is measured at a number of frequencies, $\omega = \Omega_1, \Omega_2, \dots$. Augmenting all FRM columns (Eq. (16) transposed) we obtain

$$\begin{bmatrix} H_{1p}(\Omega_1) & H_{2p}(\Omega_1) & \cdots \\ H_{1p}(\Omega_2) & H_{2p}(\Omega_2) & \cdots \\ \vdots & \vdots \end{bmatrix}$$

$$= \begin{bmatrix} \frac{1}{\omega_1^2 - \Omega_1^2} & \frac{1}{\omega_2^2 - \Omega_1^2} & \cdots \\ \frac{1}{\omega_1^2 - \Omega_2^2} & \frac{1}{\omega_2^2 - \Omega_2^2} & \cdots \\ \vdots & \vdots \end{bmatrix} \begin{pmatrix} \psi_1^T \\ \psi_2^T \\ \vdots \end{pmatrix}. \tag{17}$$

Provided that the FRM is measured with sufficient frequency resolution (hence a sufficient number of frequencies (Ω_k) is available), the coefficients matrix in Eq. (17) will be of rank m. Since the coefficients matrix is composed of the natural frequencies and the known frequencies of excitation, Eq. (17) can be solved directly for the m right eigenvectors within the measured range (Ewins, 1984).

3.2 Extraction of the Left Eigenvectors From Measured FRF. The extraction of the left eigenvectors is more problematic due to the rank deficiency of the coefficients matrix. In physical terms this rank deficiency is due to the difficulty in obtaining the applied force given the measured response. The formulation leading to a set of equations, from which the left eigenvectors are extracted, is developed here.

Multiplying the pth column of the frequency response matrix $\mathbf{l}_j^T$, we may write

$$\mathbf{l}_j^T\mathbf{H}_p = \sum_{k=1}^{m} \frac{\phi_k[p]}{\omega_k^2 - \omega^2}\mathbf{l}_j^T\phi_k. \tag{18}$$

Substituting Eq. (4*c*) in Eq. (18), the former equation is simplified into

$$\mathbf{l}_j^T\mathbf{H}_p = \frac{\phi_j[p]}{\omega_j^2 - \omega^2} \tag{19}$$

or, assuming no particular normalization for the left eigenvector,

$$\tilde{\mathbf{l}}_j^T\mathbf{H}_p = \frac{1}{\omega_j^2 - \omega^2}. \tag{20}$$

Downloaded 04 May 2010 to 171.66.16.34. Redistribution subject to ASME license or copyright; see http://www.asme.org/terms/Terms_Use.cfm

It should be mentioned that the left eigenvector could be normalized by using the related right eigenvector to retain the orthonomality relation in Eq. (4c). This is done by multiplying the left eigenvector by performing

$$\mathbf{l}_j^T = \left(\frac{1}{\tilde{\mathbf{l}}_j^T \phi_j}\right) \tilde{\mathbf{l}}_j^T. \tag{20a}$$

As before, Eq. (20) can be evaluated at different frequencies, $\omega = \Omega_1, \Omega_2, \ldots$ (e.g., choosing the appropriate entries from the experimentally obtained FRF).

Repeating Eq. (20) for the m left eigenvectors in the measured range, i.e., for $j = 1, 2, \ldots m$, we obtain

$$\begin{bmatrix} H_{1p}(\Omega_1) & H_{2p}(\Omega_1) & \cdots \\ H_{1p}(\Omega_2) & H_{2p}(\Omega_2) & \cdots \\ \vdots & \vdots & \end{bmatrix} [\hat{\mathbf{l}}_1 \quad \hat{\mathbf{l}}_2 \quad \ldots]$$

$$= \begin{bmatrix} \dfrac{1}{\omega_1^2 - \Omega_1^2} & \dfrac{1}{\omega_2^2 - \Omega_1^2} & \cdots \\ \dfrac{1}{\omega_1^2 - \Omega_2^2} & \dfrac{1}{\omega_2^2 - \Omega_2^2} & \cdots \\ \vdots & \vdots & \end{bmatrix} \tag{21}$$

where $\hat{\mathbf{l}}_1$ is the estimate of $\mathbf{l}_1$.

The same equation can be written for each column of the FRM, i.e., for $p = 1 \ldots n$. When a multi-exciter experiment is performed, several columns of the FRM are measured and the extra information can be used to enhance the accuracy of the estimate. When using several columns, the scaling factors $\phi_k[p]$ should be retained.

We then write Eq. (21) in matrix form for a single left eigenvector as

$$\mathbf{A}\hat{\mathbf{l}}_k = \mathbf{B}_k \tag{22}$$

where $\mathbf{A}$ is the coefficients matrix and $\mathbf{B}_k$ is the kth column of the right-hand side matrix in Eq. (21).

We note that the coefficients and the right-hand side matrices, used in the extraction of the right eigenvectors Eq. (17), were interchanged. It is important to note that the coefficients matrix in Eq. (21), (22) has at most rank m. This can be deduced from the fact that each row in this matrix is a combination of only m (right) modes (Bucher and Braun, 1993). The set of equations in Eq. (21), (22) does not posses a unique solution and hence is ill-conditioned. This will be discussed further in Section 3.3

The solution for Eq. (22), $\hat{\mathbf{l}}_k$, is thus not unique and can be expressed generally as a general family of solutions (Ben-Israel and Greville, 1974), all maintaining Eq. (22). The physical explanation for this nonuniqueness is the fact that all forces related to unmeasured modes cannot be measured in the low-frequency range. This leads to the arbitrariness in components of the left eigenvectors residing in the subspace spanned by these forces. The general solution for the kth left eigenvectors, can be expressed as

$$\hat{\mathbf{l}}_k = \mathbf{l}_k + \mathbf{v} \tag{23}$$

where $\mathbf{v}$ is any vector from the null space of the coefficients matrix in Eq. (22). The vector $\mathbf{v}$ can be expressed, using $(n - m)$ arbitrary constants, as the following sum:

$$\mathbf{v} = \sum_{k=m+1}^{n} \alpha_k \mathbf{l}_k. \tag{24}$$

Mathematically $\mathbf{v}$ can be defined: $\mathbf{v} \subset \text{span}\,[\mathbf{l}_{m+1} \quad \ldots \quad \mathbf{l}_n]$.

The fact that an arbitrary vector from the null space of $\mathbf{A}$ can be added to the solution vector may result in an arbitrarily large erroneous solution, unless treated properly.

The extraction of left eigenvectors from Eq. (22) consists actually of solving an inverse problem: Given the measured response (we actually measure a force normalized response in the form of a frequency band limited frequency response function), we strive to deduce forces (the left eigenvectors) yielding this measured response. The fact that these forces are not unique, as shown in Eq. (23), is due to the fact that out of range forces (namely $\mathbf{v}$) do not influence the response in the measured range.

3.3 Presentation of the Ill-Conditioning for a Simple Case. The following example gives a simple geometrical explanation for the ill-conditioning of the left eigenvectors extraction. This occurs when a truncated (frequency band limited) model is used. Given a two-degree-of-freedom (having two modes) model of a vibrating structure, the nonuniqueness of the extracted left eigenvector is demonstrated. Assuming that the second natural frequency is much greater than the first one, and that the measured range, $\{0 \le \omega \le \omega_{\max}\}$, includes only the first natural frequency, i.e., $0 \le \omega_1 \le \omega_{\max}$ and $\omega_{\max} \ll \omega_2$. The Fourier transformed measured response is

$$\mathbf{X}(\omega) = \frac{\phi_1^T \mathbf{F}(\omega)}{\omega_1^2 - \omega^2} \phi_1 + \frac{\phi_2^T \mathbf{F}(\omega)}{\omega_2^2 - \omega^2} \phi_2 \tag{25}$$

where $\mathbf{X}(\omega)$ represents the forced response and $\mathbf{F}(\omega)$ represents the excitation.

The assumption that the second mode is far beyond the measured range leads to the assumption that the second term is negligible, i.e.,

$$\frac{|\omega_2^2 - \omega^2|}{|\omega_1^2 - \omega^2|} \gg 1 \quad \forall\, \omega \in [0, \omega_{\max}]. \tag{26}$$

We thus conclude that the response is dominated by the first mode and can be approximated as

$$\mathbf{X}(\omega) \approx \frac{\phi_1^T \mathbf{F}(\omega)}{\omega_1^2 - \omega^2} \phi_1. \tag{27}$$

Expanding the force vector in terms of the left eigenvectors (this is possible since those span $\Re^2$), yields

$$\mathbf{F}(\omega) = \beta_1(\omega)\mathbf{l}_1 + \beta_2(\omega)\mathbf{l}_2. \tag{28}$$

Substitution of Eq. (18) in Eq. (15) provides

$$\mathbf{X}(\omega) = \frac{\beta_1(\omega)}{\omega_1^2 - \omega^2} \phi_1 + \frac{\beta_2(\omega)}{\omega_2^2 - \omega^2} \phi_2 \approx \frac{\beta_1(\omega)}{\omega_1^2 - \omega^2} \phi_1. \tag{29}$$

Since we already established that the second term in Eq. (29) is negligible with respect to the first one, we conclude that the projection of the force in the direction of $\mathbf{l}_2$ does not contribute to the response in the mentioned frequency range. This makes the contribution of $\mathbf{l}_2$ invisible in the response. The problem of extracting $\mathbf{l}_2$ is thus necessarily ill-conditioned.

The purpose of this section is to demonstrate via a simple example why the influence of $\mathbf{l}_2$ cannot be deduced from measurements in a band-limited frequency range. Other considerations will be used in Section 4 to reduce this uncertainty.

3.4 The Ill-Conditioning Aspect: Summary. A basic and simple physical reasoning can be given for the ill-conditioning of the equations. Our knowledge is based on the system's *frequency band-limited response,* what is attempted is the extraction of information about exciting internal forces a wider band than the measured frequency range. Hence, we address an inverse problem (Glasko, 1988; Gladwell, 1986). Such a problem is encountered, for example, when attempting to extract the excitation from a response measurements, i.e., by deconvolving (inverting) the band-limited frequency response function with the response.

Downloaded 04 May 2010 to 171.66.16.34. Redistribution subject to ASME license or copyright; see http://www.asme.org/terms/Terms_Use.cfm

It is thus clear that the ill-conditioning in extracting left eigenvectors should not be ignored. Previous investigators using left eigenvectors did not address these aspects fully and hence did not suggest a solution for it (Zhang et al., 1990; Shelley and Allemang, 1992).

4 Procedures for Reducing the Effect of Ill-Conditioning in the Extraction of Left-Eigenvectors

There exist a multitude of methods geared to deal with various aspects of ill-conditioning (Glasko, 1988; Hansen, 1987).

We make no attempt at a comprehensive investigation of existing methods. Instead of this, we will use one candidate method for regularization. The one used by us has the advantage of simplicity and also of providing a physical insight into the improvement and interpretation of the results. We also show that knowledge about the mass distribution can be used to obtain an *exact solution* for a subset of left eigenvectors and thus we use and approximation of the mass distribution to further improve the estimate of the left eigenvectors.

4.1 Standard Approach Using the Pseudo Inverse. The standard approach for solving an overdetermined set of equation (similar to Eq. (22)), is customarily approached by direct or indirect computation of the pseudo inverse (Ben-Israel and Greville, 1974; Lawson and Hanson, 1974). For the solution of Eq. (22), where the rank of $\mathbf{A}$ is not full, the shortest solution vector (in the Euclidean sense) is chosen from the infinite number of available solutions. This approach is strictly mathematical and does not involve any physical insight about the problem being solved.

All methods presented in this section make use of an SVD of $\mathbf{A}$ (from Eq. (22)). (Lawson and Hanson, 1974):

$$\begin{bmatrix} H_{1p}(\Omega_1) & H_{2p}(\Omega_1) & \cdots \\ H_{1p}(\Omega_2) & H_{2p}(\Omega_2) & \cdots \\ \vdots & \vdots & \end{bmatrix} \triangleq \mathbf{A}$$

$$= \sum_{q=1}^{n} \sigma_q \mathbf{u}_q \mathbf{v}_q \approx \sum_{q=1}^{m_0} \sigma_q \mathbf{u}_q \mathbf{v}_q \quad (30)$$

Here m_0 is the estimated rank of $\mathbf{A}$.

Using the SVD, the minimal length solution (pseudo inverse) of Eq. (22), is approximated by the first summation term in Eq. (31) (Lawson and Hanson, 1974)

$$\hat{\mathbf{l}}_j = \sum_{k=1}^{m_0} \frac{\mathbf{u}_k^T \mathbf{B}_j}{\sigma_k} \mathbf{v}_k + \sum_{k=m_0+1}^{n} \alpha_k \mathbf{v}_k. \quad (31)$$

This solution includes two summation terms. The first summation term, consists of a linear combination of m_0 vectors belonging to the range space of $\mathbf{A}$ (in physical terms the range space describes the internal forces yielding the measured response). The second term includes the $(n - m_0)$ vectors in the null space of $\mathbf{A}$ and is a function of all the left eigenvectors beyond the measured frequency range (or in spatial terms: representing short wavelength having negligible effect in the measured frequency range). Actually, any arbitrary set of the linear combination coefficients, α_k, maintains Eq. (22) without affecting (theoretically) the residual norm, $\|\mathbf{A}\hat{\mathbf{l}}_j - \mathbf{B}_j\|$ (Lawson and Hanson, 1974; Ben-Israel and Greville, 1974), thus components having influence only beyond the measured range can alter the solution considerably.

The number of terms in the solution, m_0, (which is an estimate of the true rank of $\mathbf{A}$) is chosen such that $\sigma_{m_0}/\sigma_1 < \epsilon$. The constant ϵ represents a threshhold related to the numerical precision used, and is machine and problem-size dependent. This approach which is taken in several works (Zhang et al., 1990; Shelley and Allemang, 1992) might be inaccurate. The unavoidable measurement noise and imperfections, that always exist in actual experiments, lead to an over estimation of the rank (m_0). It will be demonstrated below that an over estimation of m_0 may cause large errors in the estimate.

It is well known that singular vectors related to the smaller singular values are very oscillatory (Hansen, 1987; Gladwell, 1986) and are related to the high-frequency range. These represent short wavelengths and thus highly oscillatory (spatially) vectors. Using only the singular values as a criterion and ignoring this important spatial interpretation in this case, yields large errors. This problem can be partially cured by using the truncated SVD (TSVD) (Hansen, 1987) as shown below.

4.2 Truncated SVD-Based Regularized Solution (TSVD). The fact that the singular vectors tend to become more spatially oscillating (hence including shorter and shorter wavelengths) for smaller singular values (the same phenomenon is observed for the mode-shapes of vibrating systems) (Hansen, 1987; Gladwell, 1986), allows the application of a spatial filtering scheme. This is simply done, in this work, by truncating the SVD series which results in rejection of short wavelength related errors. The "correct" number of terms in the SVD series (m_0, in Eq. (31)) is chosen by the L-curve method (Lawson and Hanson, 1974; Hansen, 1987), which is briefly referred to in Section 5 and in the Appendix.

Rejection of high-frequency out-of-band terms, or more important, rejection of short wavelength related components, is achieved by choosing fewer terms for Eq. (31). The rejection of spatially high-frequency terms (short wavelength) has a clear physical meaning, in this case justifying the use of truncated SVD (TSVD).

The actual selection of m_0 is done by a choosing a compromise between the decrease in the residual norm, $\|\mathbf{A}\hat{\mathbf{l}}_j - \mathbf{B}_j\|$ and an increase in the solution norm, $\|\hat{\mathbf{l}}_j\|$ (Lawson and Hanson, 1974).

The obtained left eigenvectors are not mathematically exact (not even theoretically) since the left eigenvectors do not form an orthogonal basis. The TSVD approach yields an exact solution only when the right (and hence the left) eigenvectors form an orthogonal basis, which prevents the inclusion of other modes.

An orthogonalization stage, yielding theoretically an exact solution, is introduced below. The method makes use of the mass distribution.

A more sophisticated approach for regularization, that includes explicitly a penalty term for short wavelength, may be used in more demanding applications (for example, Thikhonov's method) (Glasko, 1988). This is beyond the scope of this paper where we are merely trying to provide the physical significance through a basic approach.

4.3 Mass Weighted Truncated SVD Solution. In this section we make use of the approximate mass distribution in the structure to form an (approximately) orthogonal basis. It is clear that the knowledge the mass matrix provides the left eigenvectors from the right eigenvectors via Eq. (4*a*). On the other hand, an approximation of the mass matrix used directly leads to erroneous results. We thus suggest to combine the estimation of the mass matrix with the regularization process

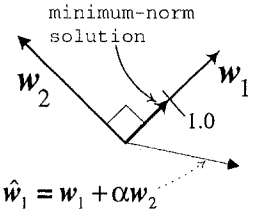


Fig. 1 The uniqueness of the orthogonalized (mass-weighted TSVD) extraction of left eigenvectors

Downloaded 04 May 2010 to 171.66.16.34. Redistribution subject to ASME license or copyright; see http://www.asme.org/terms/Terms_Use.cfm

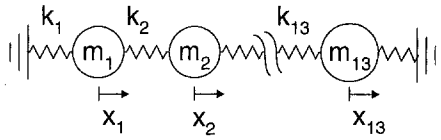


Fig. 2 Series of masses and springs

and show in an example that an improvement is achieved. It is important to mention that this is not a general result since it depends very much of the measured data and the quality of the mass matrix estimate. Still, a combined approach using the approximate mass distribution and the regularization seems to provide an improvement over using each approach separately. It is shown that using mass weighting can improve the obtained TSVD solution significantly while computing directly $\mathbf{M}\phi$ yields large deviations.

Assuming that we have some approximation of the structural mass matrix, $\mathbf{M}$, we can define a Cholesky factor $\mathbf{U}$ (Meirovitch, 1980),

$$\mathbf{M} = \mathbf{U}\mathbf{U}^T. \tag{32}$$

The right eigenvectors can be transformed to obtain an orthogonal basis $\mathbf{W}$

$$\mathbf{W} = \mathbf{U}^T\mathbf{\Phi} \quad \mathbf{w}_k = \mathbf{U}^T\phi_k \tag{33}$$

(i.e., $\mathbf{w}_k^T\mathbf{w}_j = \delta_{k,j}$).

This yields a transformed equation. Instead of solving Eq. (22), we solve

$$\tilde{\mathbf{A}}\mathbf{w}_k = \mathbf{B}_k \tag{34}$$

where $\tilde{\mathbf{A}} = \mathbf{A}\mathbf{U}$.

After solving Eq. (34) for $\mathbf{w}_k$, the left-eigenvector is computed by

$$\mathbf{l}_k = \mathbf{U}\mathbf{w}_k. \tag{35}$$

If the estimate of the mass matrix is exact, the obtained solution will be exact as well, even when the measured data is truncated (a proof is provided in the Appendix).

The orthogonalization stage can be demonstrated by means of the previously described two-degree-of-freedom system (see Fig. 1). Substitution of Eq. (35) in Eq. (18), yields

$$\mathbf{l}_j^T\mathbf{H}_p = \mathbf{w}_j^T\mathbf{U}^T\mathbf{H}_p = \mathbf{w}_j^T\left(\sum_{k=1}^{n}\frac{\phi_k[p]}{\omega_k^2 - \omega^2}\mathbf{U}^T\phi_k\right)$$

$$= \mathbf{w}_j^T\left(\sum_{k=1}^{n}\frac{\phi_k[p]}{\omega_k^2 - \omega^2}\mathbf{w}_k\right). \tag{36}$$

The transformation in Eq. (35) gives rise to a new equation, Eq. (36), which describes a transformed system. The transformed right and the left eigenvectors are identical and are represented by $\mathbf{w}_k$; $k = 1 \ldots n$ which form an orthogonal basis. The transformed problem is depicted in the Fig. 1.

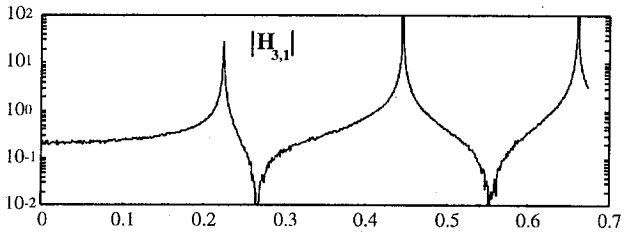


Fig. 3 Typical frequency response used in the numerical experiment

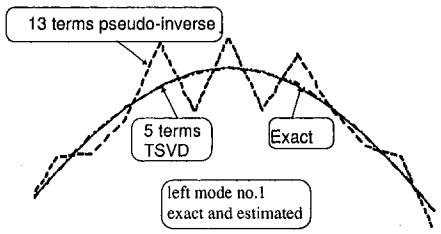


Fig. 4 The true and estimated first left eigenvector l_1

4.3.1 Graphical Description of the Mass-Weighted Equation. Figure 1 shows the graphical description of the right and left eigenvectors for the special case of a two-sensor measurement system.

Figure 1 shows that the minimal-length solution (the one obtained for the selection of $\alpha = 0$) coincides with the true solution, $\mathbf{w}_1$. This can obviously be obtained without the knowledge of ϕ_2 (and hence $\mathbf{w}_2$), i.e., by means of a truncated model.

5 Examples for the Extraction of Left Eigenvectors

In this section, two examples demonstrating the use and the importance of the regularization for the extraction of left-eigenvectors. Three methods are used: the standard minimal-length pseudo-inverse approach (Shelley and Allemang; Lawson and Hanson, 1974), the truncated SVD (TSVD) (Hansen, 1987) and the mass-weighted TSVD. A comparison is also made between the mass-weighted TSVD and a direct estimate $\mathbf{M}\phi$ (using the definition in Eq. (4*a*)) making use of an approximation of $\mathbf{M}$.

5.1 Example Using a Discrete Spring Mass System. The following example demonstrates the inherent ill-conditioning by comparing the standard minimum-length approach and the TSVD. The methods supply a unique solution from the infinity of possible ones, each according to a specific criterion.

Consider a series of masses and springs representing a discrete system having 13 degrees-of-freedom. (See Fig. 2.)

The measured frequency range contains only 3 modes, but the effect of some of the out-of band modes is reflected in the rank of the measured FRM which is larger than 3.

A single FRF from the 13 measured is shown in Figure 3, As can be observed from this Figure, the calculated FRF was deliberately contaminated with random noise (in this case Gaussian with $\sigma = 5 \cdot 10^{-3}\sqrt{\|H\|_F}$). The added noise, as expected, causes some numerical difficulties and gives rise to a wrong estimate of the FRF matrix's rank. The pseudo inverse included 13 terms, as determined by standard routines (using MATLAB). The minimum norm solution using the pseudo-inverse of the FRF matrix, includes more terms than should be included due to the actual number of modes participating in the measured FRF.

The results of the application of the pseudo-inverse and the TSVD are shown graphically in figures 4 and 5.

The over-estimation of the FRF-matrix's rank yields an erroneous estimation by the pseudo-inverse giving rise to a bad estimate of the true left-eigenvectors. The appearance of short

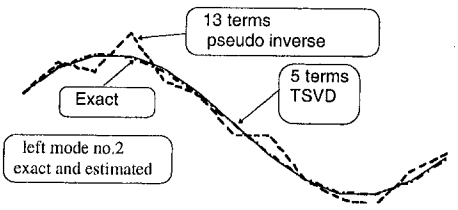


Fig. 5 The true and estimated first left eigenvector l_2

Downloaded 04 May 2010 to 171.66.16.34. Redistribution subject to ASME license or copyright; see http://www.asme.org/terms/Terms_Use.cfm

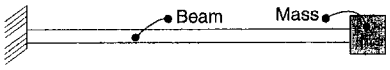


Fig. 6 15 elements model of a beam with a tip point mass

wavelengths is apparent in this case which agrees with what was described before. The regularization method which determines (truncates) the number of terms in the SVD series, the TSVD solution, rejected the short wavelength related terms and thus gives rise to a smoother estimation. The nature of low-frequency-related modes is much less oscillatory than the high-frequency related ones, hence the truncation of high frequency (short wavelength) terms yields a much better estimation.

4.2 Example Using a Finite Element Model With Discontinuous Mass. In cases where the structural mass (or stiffness) are not distributed in a uniform manner, the modes are not smooth due to the large inertia (or spring) forces concentrated in small areas. In such cases, the TSVD method yields a too smooth estimation which fails to estimate the discontinuity in the internal forces and, as a result, fails to estimate of the left eigenvector closely. Using an approximation of the mass matrix (only diagonal elements of the true mass matrix are used and an intentional 5 percent error is introduced), the transformed equation was obtained by the procedure described in Section 3. This improved the estimation greatly, even for the approximate mass matrix used.

In this example, a finite element model (using 15 elements) of a cantilever-lever beam was constructed. A large mass was placed at the beam's tip. The model is depicted in Fig. 6.

Three methods, namely the standard SVD-based pseudo-inverse, the truncated SVD and the mass-weighted SVD were applied to a truncated model of a simulated measured FRF containing two modes. A typical measured FRF is depicted in Fig. 7.

Once the first two right eigenvectors (out of 28) have been identified, we are able to estimate the first two left eigenvectors. The results obtained by applying the various methods are presented for the second left eigenvector. This is depicted in Fig. 8, which shows that the mass-weighted TSVD estimates the left eigenvector very closely. The TSVD (without weighting) gives a too smooth estimate and fails to "follow" the steep change near the tip caused by the concentrated mass. The pseudo inverse obviously failed to estimate the correct number of modes participating in the measured response. (The numerical rank estimated by MATLAB was 30 hence 30 terms were used. The TSVD methods used only five terms). The extra terms give rise to a too oscillatory left eigenvector, as shown by the dashed line.

The L-curve method (Hansen, 1987; Lawson and Hanson, 1974), used to estimate the desired number of terms is depicted in Fig. 9.

The desired number of terms is selected as the corner point of this curve. This selection reflects the most drastic decrease in the residual norm while avoiding a too spatially oscillatory solution. The left eigenvectors (as well as the right ones) become more oscillatory for the higher natural frequencies. Thus, our of choice of the number of terms included in the solution implies that the influence of high-frequency related modes is rejected. This demonstrates the validity of the interpretation for the refinement obtained by the suggested solution refinement.

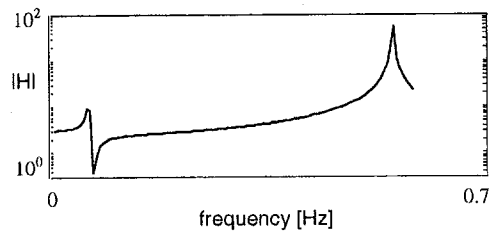


Fig. 7 A typical "measured" FRF used in the extraction of the first two left eigenvectors

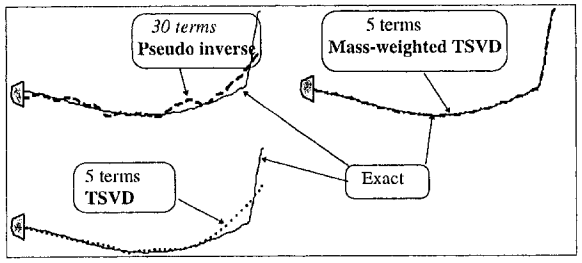


Fig. 8 The second left eigenvectors. Exact versus estimated by the three methods.

The mass-weighted TSVD was compared with a direct application of the definition, i.e., $\mathbf{l} = \mathbf{M}\phi$. The results are depicted in Fig. 10, which shows clearly that the combined approach of using an estimate of the mass matrix (in fact a very crude estimate using only the diagonal elements with 5 percent of additive noise) is superior to using the definition in Eq. (4*a*), $\mathbf{M}\phi$. The fact that the general shape of $\mathbf{M}\phi$ resembles the true left eigenvector is because, in this case the right and left eigenvectors have the same general shape (this can be seen in Fig. 10). Unfortunately the improvement obtained when using the approximate-mass weighting, is not guaranteed as it depends heavily on the quality of the mass matrix estimate, on the nature of the structure and on the quality of the measurements. Still, the physical meaning of the left eigenvectors combined with the understanding of the meaning of orthogonality in vibrating systems helped us in improving the estimate of the left eigenvectors considerably.

5 Conclusions

This paper briefly introduces the concept of left eigenvectors for vibrating structures as well as some engineering application using those.

We have addressed the problem of extracting right and left eigenvectors from experimentally derived FRFs. This necessitates the solution of a linear set of equations in which, for the left eigenvectors, rank deficiency is introduced as a result of the finite frequency range in the measured FRFs.

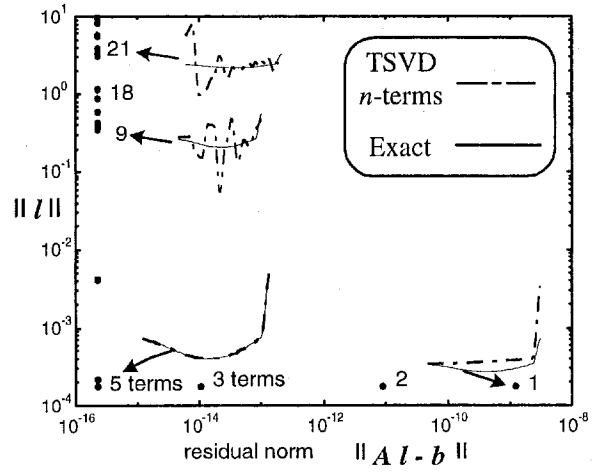


Fig. 9 L-curve for the extraction of the first left eigenvectors using the mass-weighted TSVD.

Downloaded 04 May 2010 to 171.66.16.34. Redistribution subject to ASME license or copyright; see http://www.asme.org/terms/Terms_Use.cfm

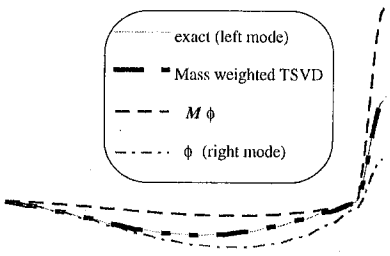


Fig. 10 The second left eigenvector compared with the right eigenvector and with a direct estimate using Eq. (4*a*) ($\mathbf{l} = \mathbf{M}\phi$)

We showed how the problem of solving for right eigenvectors was well posed, whereas the one for the left eigenvectors was ill posed. Hence special procedures are necessary in order to identify these later ones. All procedures made use of the SVD decomposition of the FRF matrix.

It was demonstrated that one commonly used approach, the pseudo-inverse solution, could result in significant errors. Two improved procedures were presented: one based on estimating the number of participating vectors by means of the L-curve, and a second one utilizing, in addition, mass weighing. The use of even an approximate mass distribution, as would be available in practice, was shown to be potentially beneficial. Examples demonstrating the improvements are given.

Throughout the paper, an attempt is made to provides a physical interpretation of the left eigenvectors. The left eigenvectors, which have the meaning of force, are indirectly extracted from measurements of the response. The procedure for extracting the left eigenvectors is trying to estimate the forces giving rise to the measured spatial distribution of the response. This measured response is band limited, hence the forces which could result in this response are not unique. In order to obtain a better estimate, additional knowledge in the form of the spatial smoothness of the eigenvectors must be incorporated in the extraction procedure. This knowledge is enforced on the solution by the application of regularization. Further improvement in the accuracy of the solution is achieved by incorporating an estimate of the mass distribution of the vibrating structure. The importance of the relation between the frequency of the response and the spatial wavelength of both the response and the internal forces was demonstrated. This point is of great significance for the control and structural updating of applications.

References

Ben-Israel, A., and Greville, T. N. E., 1974, *Generalized Inverses: Theory and Applications,* John Wiley and Sons, New York.

Bucher, I., and Braun, S. G., 1993, "The Structural Modification Inverse Problem: an Exact Solution," *Mechanical Systems and Signal Processing,* Vol. 7, pp. 217–238.

Bucher, I., and Braun, S. G., 1994, "Structural Response Optimization for Minimizing Vibratory Response via Redesign or Modification, Part I: Theory," *Journal of Sound and Vibration,* Vol. 175, pp. 433–454.

Ewins, D. J., 1984, *Modal Testing,* Reseach Studies Press.

Gladwell, G. M. L., 1986, *Inverse Problems in Vibration,* Martinus Nijhoff.

Glasko, V. B., 1988, *Inverse Problems of Mathematical Physics,* American Institute of Physics, New York.

Hansen, P. C., 1987, "The Truncated SVD as a Method for Regularization," *B.I.T.,* Vol. 28, pp. 543–553.

Inman, D. J., 1989, *Vibration: With Control, Measurement, and Stability,* Prentice-Hall, Englewood Cliffis, NJ.

Lallement, G., Link, M., and Cesar, B., 1991, "Procedures for Updating Dynamic Mathematical Models," European Space Agency Contract Report, No. BE5463.

Lancaster, P., 1969, *Theory of Matrices,* Academic Press, New York.

Lawson, C. L., and Hanson, D. J., 1974, *Solving Least Squares Problems,* Prentice-Hall, Englewood Cliffs, NJ.

Meirovitch, L., 1980, *Computational Methods in Structural Dynamics,* Sijhoff and Noordhoff.

Meirovitch, L., 1985, "The Implementation of Modal Filters for Control of Structures," *Journal of Guidance Control and Dynamics,* Vol. 8, No. 6, pp. 707–716.

Ram, 1989, "Modal Analysis in Truncates Systems," Ph.D. Thesis, Technion Israel Institure of Technology. Haifa, Israel.

Ram, Y. M., and Braun, S. G., 1990, "Structural Dynamic Modifications Using Truncated Data: Bounds for the Eigenvalues," *Mechanical Systems and Signal Processing,* Vol. 4, No. 1, pp. 39–52.

Shelley, S. J., and Allemange, R. J., 1992, "Calculation of Discrete Modal Filters Using the Modified Reciprocal Vector Method," *Proceedings of the International Modal Analysis Conference,* San Diego, CA.

Zhang, Q., Allemange, R. J., and Brown, D. L., 1992, "Calculation of Discrete Modal filters Using the Modified Reciprocal Modal Vector Method," *Proceedings of the International Modal Analysis Conference,* San Diego, CA.

APPENDIX A

Development of the Mass-Weighted TSVD

The rank deficiency of Eq. (22) gives rise to an infinite number of solutions, all expressed as

$$\hat{\mathbf{l}}_j = \mathbf{l}_j + \sum_{k=m_2+1}^{n} \alpha_k \mathbf{l}_k = \mathbf{l}_j + [\mathbf{l}_{m_2+1} \quad \dots \quad \mathbf{l}_n]\boldsymbol{\alpha} \qquad \text{(A1)}$$

where $[\mathbf{l}_{m_2+1} \quad \dots \quad \mathbf{l}_n]$ span the null space of $\mathbf{A}$ and $\boldsymbol{\alpha}$ are arbitrary coefficients.

Any selection of $\boldsymbol{\alpha}$ gives a solution which satisfies Eq. (22). Since we use the truncated SVD solution, we would like to have this solution coincide with the minimum norm solution which takes into account only vectors in the range of the coefficients matrix. It will be shown here that the transformation in Eq. (33), gives rise to an orthogonal set of (transformed) vectors. The obtained equation is developed and the fact that this yields an exact solution is proved.

Using the definition in Eq. (33) it can be shown that

$$\mathbf{w}_k^T \mathbf{w}_j = \phi_k^T \mathbf{U}\mathbf{U}^T \phi_j = \phi_k^T \mathbf{M} \phi_j = \delta_{k,j}. \qquad \text{(A2)}$$

The left-hand side of Eq. (22) becomes

$$\mathbf{A}\mathbf{l}_j = \mathbf{A}\mathbf{M}\phi_j = (\mathbf{A}\mathbf{U})\mathbf{U}^T\phi_j = (\mathbf{A}\mathbf{U})\mathbf{w}_j \qquad \text{(A3)}$$

or in short

$$\tilde{\mathbf{A}}\mathbf{w}_j = \mathbf{B}_j \qquad \text{(A4)}$$

where, $\tilde{\mathbf{A}} = \mathbf{A}\mathbf{U}$.

After solving for $\mathbf{w}_j$ we can calculate the requested left eigenvector by

$$\mathbf{l}_j = \mathbf{M}\phi_j = \mathbf{U}(\mathbf{U}^T\phi_j) = \mathbf{U}\mathbf{w}_j. \qquad \text{(A5)}$$

The minimum norm solution is calculated by derivation of Eq. (A1),

$$\frac{\partial \|\hat{\mathbf{l}}_j\|^2}{\partial \boldsymbol{\alpha}} = 2[\mathbf{l}_{m_2+1} \quad \dots \quad \mathbf{l}_n]^T \hat{\mathbf{l}}_j + 2[\mathbf{l}_{m_2+1} \quad \dots \quad \mathbf{l}_n]^T [\mathbf{l}_{m_2+1} \quad \dots \quad \mathbf{l}_n]\boldsymbol{\alpha} = 0$$

$$\boldsymbol{\alpha} = -([\mathbf{l}_{m_2+1} \quad \dots \quad \mathbf{l}_n]^T [\mathbf{l}_{m_2+1} \quad \dots \quad \mathbf{l}_n])^{-1} \times [\mathbf{l}_{m_2+1} \quad \dots \quad \mathbf{l}_n]^T \hat{\mathbf{l}}_j. \qquad \text{(A6)}$$

An exact solution is obtained if $\boldsymbol{\alpha} = 0$, hence $[\mathbf{l}_{m_2+1} \dots \mathbf{l}_n]^T \hat{\mathbf{l}}_j = 0$. In other words $\hat{\mathbf{l}}_j$ is orthogonal with respect to all vectors in the null space of $\mathbf{A}$, which is exactly what the transformation achieves.

APPENDIX B

Selection of the Number of Terms in the SVD Using the L-Curve

The desired number of terms to include in the TSVD solution is found by plotting the residual norm versus the obtained length of the solution vector in log scale. It was observed by others

Downloaded 04 May 2010 to 171.66.16.34. Redistribution subject to ASME license or copyright; see http://www.asme.org/terms/Terms_Use.cfm

(Lawson and Hanson, 1974; Hansen, 1987) that for rank-deficient equations, this curve resembles the shape of the letter L. The desired number of terms is selected as the corner point of this curve. A typical L-curve is depicted in Fig. 9.

The number of terms is chosen to give the most drastic decrease in the residual norm while not allowing the solution to be too oscillatory (spatially), i.e., not allowing for a too large norm for the solution vector. Since the left eigenvectors (as well as the right ones) become more oscillatory with increased natural frequency (Hansen, 1887; Gladwell, 1986), this means that we reject the influence of high-frequency related modes.

Downloaded 04 May 2010 to 171.66.16.34. Redistribution subject to ASME license or copyright; see http://www.asme.org/terms/Terms_Use.cfm

Anisotropic Damage Effect Tensors for the Symmetrization of the Effective Stress Tensor

G. Z. Voyiadjis
Boyd Professor, Mem. ASME.

T. Park
Research Associate.

Department of Civil and Environmental Engineering, Louisiana State University, Baton Rouge, LA 70803

Based on the concept of the effective stress and on the description of anisotropic damage deformation within the framework of continuum damage mechanics, a fourth order damage effective tensor is properly defined. For a general state of deformation and damage, it is seen that the effective stress tensor is usually asymmetric. Its symmetrization is necessary for a continuum theory to be valid in the classical sense. In order to transform the current stress tensor to a symmetric effective stress tensor, a fourth order damage effect tensor should be defined such that it follows the rules of tensor algebra and maintains a physical description of damage. Moreover, an explicit expression of the damage effect tensor is of particular importance in order to obtain the constitutive relation in the damaged material. The damage effect tensor in this work is explicitly characterized in terms of a kinematic measure of damage through a second-order damage tensor. In this work, tensorial forms are used for the derivation of such a linear transformation tensor which is then converted to a matrix form.

Introduction

In 1958, Kachanov (Kachanov, 1958) introduced the concept of effective stress in damaged materials. This pioneering work started the subject that is now known as continuum damage mechanics. Research in this area has steadily grown and reached a stage that warrants its use in today's engineering applications. Continuum damage mechanics is now widely used in different areas including brittle (Krajcinovic, 1983; Krajcinovic and Foneska, 1981) and ductile failure (Lemaitre, 1985, 1986). In this theory, a continuous damage variable is defined and used to represent degradation of the material which reflects various types of damage at the microscale level like nucleation and growth of voids, cavities, microcrack, and other microscopic defects.

In continuum damage mechanics, the effective stress tensor is usually not symmetric. This leads to a complicated theory of damage mechanics involving micropolar media and the Cosserat continuum. Therefore, to avoid such a theory, symmetrization of the effective stress tensor is used to formulate a continuum damage theory in the classical sense. Several methods used in order to symmetrize the effective stress tensor are proposed by Lee et al. (1986) and Sidoroff (1979). A linear transformation tensor, defined as a fourth-order damage effect tensor, is proposed by Sidoroff (1979); however, no explicit form of this tensor is given. Moreover, damage tensor of higher order than two may fail to convey the physical meaning of damage. In addition, the works of Lee et al. (1986) and Sidoroff (1979) are confined to two-dimensional problems. Furthermore, no explicit expressions are derived for the fourth-order linear transformation tensors for the general anisotropic damage behavior of three-dimensional problems.

In this work, continuum damage mechanics will be reviewed based on the concept of effective stress. The effective stress is defined as the stress acting on a hypothetical undamaged configuration that produces the same elastic strain or elastic strain energy as the actual state of stress acting on the current damaged configuration based on the equivalence hypothesis. This equivalence statement is known as the hypothesis of elastic strain equivalence or the hypothesis of elastic energy equivalence. Using the definition of the effective stress and the hypothesis of elastic energy equivalence, one can solve for variable in the hypothetical undamaged configuration, such as the effective strain. However, strain in the hypothetical undamaged configuration is equal to that in the current damaged configuration under the hypothesis of elastic strain equivalence. For a detailed review of the principles of continuum damage mechanics as used in this work, the reader is referred to the works of Kachanov (1958), Lemaitre (1985, 1986), Krajcinovic (1985), Chaboche (1981, 1988a, b), Murakami (1988), Sidoroff (1979, 1980), and Voyiadjis and Kattan (1992).

In a general state of deformation and damage, the effective stress tensor $\bar{\boldsymbol{\sigma}}$ is related to the stress tensor $\boldsymbol{\sigma}$ by the following linear transformation:

$$\bar{\sigma}_{ij} = M_{ijkl}\sigma_{kl} \tag{1}$$

where $\boldsymbol{\sigma}$ is the Cauchy stress tensor and $\mathbf{M}$ is a fourth-order linear transformation operator called the damage effect tensor. Depending on the form used for $\mathbf{M}$, it is very clear from Eq. (1) that the effective stress tensor $\bar{\boldsymbol{\sigma}}$ is generally not symmetric. Using a nonsymmetric effective stress tensor as given by Eq. (1) to formulate a constitutive model will result in the introduction of the Cosserat and micropolar continua. However, the use of such complicated mechanics can be easily avoided if the proper fourth-order linear transformation tensor is formulated in order to symmetrize the effective stress tensor. Such a linear transformation tensor called the damage effect tensor is obtained in the literature (Lee et al., 1986; Sidoroff, 1979) using symmetrization methods. However, it lacks a systematic and consistent approach. It is the aim of this work to provide a solid basis for such transformation of the second-order stress tensor and its justification for the symmetrization. Three different formulations for symmetrization of the effective stress tensors proposed by Lee et al. (1986) and Sidoroff (1979) are described below. The effective stress tensor is symmetrized using the following laws:

Contributed by the Applied Mechanics Division of THE AMERICAN SOCIETY OF MECHANICAL ENGINEERS for publication in the ASME JOURNAL OF APPLIED MECHANICS.

Discussion on this paper should be addressed to the Technical Editor, Professor Lewis T. Wheeler, Department of Mechanical Engineering, University of Houston, Houston, TX 77204-4792, and will be accepted until four months after final publication of the paper itself in the ASME JOURNAL OF APPLIED MECHANICS.

Manuscript received by the ASME Applied Mechanics Division, Aug. 31, 1995; final revision, May 24, 1996. Associate Technical Editor: J. W. Ju.

Copyright © 1997 by ASME

Downloaded 04 May 2010 to 171.66.16.34. Redistribution subject to ASME license or copyright; see http://www.asme.org/terms/Terms_Use.cfm

$$\bar{\sigma}_{ij} = (\delta_{ik} - \phi_{ik})^{-1/2}\sigma_{kl}(\delta_{jl} - \phi_{jl})^{-1/2} \quad (2)$$

$$\bar{\sigma}_{ij} = \tfrac{1}{2}[\sigma_{ik}(\delta_{kj} - \phi_{kj})^{-1} + (\delta_{jk} - \phi_{jk})^{-1}\sigma_{ki}] \quad (3)$$

$$\sigma_{ij} = \tfrac{1}{2}[\bar{\sigma}_{ik}(\delta_{kj} - \phi_{kj}) + (\delta_{jk} - \phi_{jk})\bar{\sigma}_{ki}]. \quad (4)$$

Other forms for symmetrization are defined by many researchers through the fourth-order damage effect tensor such as that by Cordebois and Sidoroff (1982)

$$M_{ikjl} = (\delta_{ik} - \phi_{ik})^{-1/2}(\delta_{jl} - \phi_{jl})^{-1/2}, \quad (5)$$

by Murakami and Ohno (1980)

$$M_{ikjl} = \tfrac{1}{4}[\delta_{ij}(\delta_{kl} - \phi_{kl})^{-1} + \delta_{il}(\delta_{kj} - \phi_{kj})^{-1} + (\delta_{ij} - \phi_{ij})^{-1}\delta_{kl} + (\delta_{il} - \phi_{il})^{-1}\delta_{kj}], \quad (6)$$

by Betten (1983)

$$M_{ikjl} = \tfrac{1}{2}[(\delta_{ij} - \phi_{ij})^{-1}(\delta_{kl} - \phi_{kl})^{-1} + (\delta_{il} - \phi_{il})^{-1}(\delta_{kj} - \phi_{kj})^{-1})], \quad (7)$$

and by Lu and Chow (1990)

$$M_{ikjl} = \tfrac{1}{2}[\exp(\phi_{ij}/2)\exp(\phi_{kl}/2) + \exp(\phi_{il}/2)\exp(\phi_{kj}/2)]. \quad (8)$$

$\boldsymbol{\phi}$ in the above equations is a damage tensor characterized by a second-order symmetric tensor and is given by (Murakami, 1983)

$$\phi_{ij} = \sum_{k=1}^{3} \hat{\phi}_k \hat{n}_i^k \hat{n}_j^k \text{ (no sum in } k) \quad (9)$$

where $\hat{\mathbf{n}}^k$ is an eigenvector corresponding to the eigenvalue, $\hat{\phi}_k$, of the damage tensor, $\boldsymbol{\phi}$. Voyiadjis and Venson (1995) quantified the physical values of the eigenvalues $\hat{\phi}_k$ ($k = 1, 2, 3$) and the second-order damage tensor $\boldsymbol{\phi}$ for the unidirectional fibrous composite by measuring the crack density with the assumption that one of the eigendirections of damage tensor coincides with the fiber direction. This introduces a distinct kinematic measure of damage which is complimentary to the deformation kinematic measure of strain. A thermodynamically consistent evolution equation for damage tensor $\boldsymbol{\phi}$ together with a generalized thermodynamic force conjugate, $\mathbf{Y}$, to the damage tensor is presented in the paper by Voyiadjis and Park (1995).

Numerous fourth-order damage effect tensors are defined by using the symmetrization laws indicated above. However, only the one by Cordebois and Sidoroff (1982) may be obtained from the symmetrization procedure given by Eq. (2). One cannot deduce explicitly the fourth-order damage effect tensor $\mathbf{M}$ from the remaining proposed procedures. In the case of Cordebois and Sidoroff (1982) it is impossible to get the explicit form of the square root of the second-order tensor in Eq. (5). Alternatively, the damage effect tensor using the fourth-order damage tensor $\boldsymbol{\psi}$ is defined by Chaboche (1979) as follows:

$$M_{ikjl} = (I_{ikjl} - \psi_{ikjl})^{-1} \quad (10)$$

where I_{ikjl} is a fourth-order identity tensor and is given by

$$I_{ikjl} = \tfrac{1}{2}(\delta_{ij}\delta_{kl} + \delta_{il}\delta_{kj}). \quad (11)$$

However, it is not easy to characterize physically the fourth-order damage tensor ψ_{ijkl} rather than the second-order damage tensor ϕ_{ij}. For the case of isotropic damage, the fourth-order damage tensor is defined by Ju (1990) as follows:

$$\psi_{ikjl} = d_1\delta_{ik}\delta_{jl} + d_2 I_{ikjl} \quad (12)$$

where d_1 and d_2 are scalar (dependent or independent) damage variables. Using the second-order anisotropic damage tensor ϕ_{ij} in the damage effect tensors given by Eqs. (5), (6), (7), and (8) one may lose the physical view of the net stress tensor due to the presence of the off diagonal elements of the damage tensor ϕ_{ij}. In order to avoid this problem, the principal damage tensor rather than the second-order damage tensor is used in conjunction the damage effect tensor. However, the eigendirections of the damage tensor do not coincide with the stress tensor or eigendirection of the stress tensor. Since the damage tensor $\boldsymbol{\phi}$ always has three orthogonal principal directions $\hat{\mathbf{n}}^k$($k = 1, 2, 3$) and the three corresponding principal values $\hat{\phi}_k$($k = 1, 2, 3$), Eqs. (2), (3), and (4) can be expressed as follows in the coordinates that coincide with the three orthogonal principal directions of the damage tensor:

$$\hat{\bar{\sigma}}_{mn} = (\delta_{mp} - \hat{\phi}_{mp})^{-1/2}\hat{\sigma}_{pq}(\delta_{nq} - \hat{\phi}_{nq})^{-1/2} \quad (13)$$

$$\hat{\bar{\sigma}}_{mn} = \tfrac{1}{2}[\hat{\sigma}_{mr}(\delta_{rn} - \hat{\phi}_{rn})^{-1} + (\delta_{nr} - \hat{\phi}_{nr})^{-1}\hat{\sigma}_{rm}] \quad (14)$$

$$\hat{\sigma}_{mn} = \tfrac{1}{2}[\hat{\bar{\sigma}}_{mr}(\delta_{rn} - \hat{\phi}_{rn}) + (\delta_{nr} - \hat{\phi}_{nr})\hat{\bar{\sigma}}_{rm}] \quad (15)$$

where $\hat{\boldsymbol{\phi}}$ is a principle damage tensor that is given by

$$\hat{\phi}_{ij} = b_{ik}b_{jl}\phi_{kl} = \begin{bmatrix} \hat{\phi}_1 & 0 & 0 \\ 0 & \hat{\phi}_2 & 0 \\ 0 & 0 & \hat{\phi}_3 \end{bmatrix} \quad (16)$$

and the second-order transformation tensor $\mathbf{b}$ is given by

$$b_{ik} = \begin{bmatrix} n_1^1 & n_2^1 & n_3^1 \\ n_1^2 & n_2^2 & n_3^2 \\ n_1^3 & n_2^3 & n_3^3 \end{bmatrix}. \quad (17)$$

This transformation tensor called the proper orthogonal tensor requires that

$$b_{ij}b_{kj} = \delta_{ik}. \quad (18)$$

The effective stress tensor in the principal damage direction coordinates system is given by

$$\hat{\bar{\sigma}}_{mn} = b_{mi}b_{nj}\bar{\sigma}_{ij}. \quad (19)$$

Similarly, the stress tensor in the principal damage direction coordinates system is given by

$$\hat{\sigma}_{pq} = b_{pk}b_{ql}\sigma_{kl}. \quad (20)$$

Using the principle damage direction coordinate system, Eq. (1) is given by

$$\hat{\bar{\sigma}}_{mn} = \hat{M}_{mpnq}\hat{\sigma}_{pq} \quad (21)$$

The fourth-order damage effect tensors given by Eqs. (5), (6), (7), and (8) should be now expressed as follows:

$$\hat{M}_{mpnq} = (\delta_{mp} - \hat{\phi}_{mp})^{-1/2}(\delta_{nq} - \hat{\phi}_{nq})^{-1/2} \quad (22)$$

$$\hat{M}_{mpnq} = \tfrac{1}{4}[\delta_{mn}(\delta_{pq} - \hat{\phi}_{pq})^{-1} + \delta_{mq}(\delta_{pn} - \hat{\phi}_{pn})^{-1} + (\delta_{mn} - \hat{\phi}_{mn})^{-1}\delta_{pq} + (\delta_{mq} - \hat{\phi}_{mq})^{-1}\delta_{pn}] \quad (23)$$

$$\hat{M}_{mpnq} = \tfrac{1}{2}[(\delta_{mn} - \hat{\phi}_{mn})^{-1}(\delta_{pq} - \hat{\phi}_{pq})^{-1} + (\delta_{mq} - \hat{\phi}_{mq})^{-1}(\delta_{pn} - \hat{\phi}_{pn})^{-1})] \quad (24)$$

$$\hat{M}_{mpnq} = \tfrac{1}{2}[\exp(\hat{\phi}_{mn}/2)\exp(\hat{\phi}_{pq}/2) + \exp(\hat{\phi}_{mq}/2)\exp(\hat{\phi}_{pn}/2)], \quad (25)$$

respectively. These tensors are termed the principal damage effect tensors.

Downloaded 04 May 2010 to 171.66.16.34. Redistribution subject to ASME license or copyright; see http://www.asme.org/terms/Terms_Use.cfm

Fourth-Order Anisotropic Damage Effect Tensor

The explicit representation of the fourth-order damage effect tensor $\mathbf{M}$ using the second-order damage tensor $\boldsymbol{\phi}$ is of particular importance in the constitutive modeling of damage mechanics. However, it is impossible to use the damage tensor $\boldsymbol{\phi}$ rather than the principal damage tensor $\hat{\boldsymbol{\phi}}$ directly in the formulation. Therefore the damage effect tensor $\mathbf{M}$ in Eq. (1) should be obtained from Eq. (21) using coordinate transformation.

Substituting Eqs. (19) and (20) into Eq. (21), one obtains the following relation:

$$\bar{\sigma}_{ij} = b_{mi}b_{nj}b_{pk}b_{ql}\hat{M}_{mpnq}\sigma_{kl}. \tag{26}$$

Therefore the fourth-order tensor $\mathbf{M}$ in Eq. (1) is given as follows:

$$M_{ikjl} = b_{mi}b_{nj}b_{pk}b_{ql}\hat{M}_{mnpq}. \tag{27}$$

It is clear that the fourth-order damage effect tensors presented by Eqs. (5), (6), (7), and (8) differ from the damage effect tensor obtained by Eq. (27). Therefore the fourth-order damage effect tensor presented by the Eqs. (5), (6), (7), and (8) should be expressed in the princpal damage direction coordinate system using the principal damage tensor $\hat{\boldsymbol{\phi}}$.

One of the explicit expression for the fourth-order damage effect tensors using the principal damage effect tensor given by Eq. (22) is presented here. The principal damage effect tensor given by Eq. (22) can be written as follows:

$$\hat{M}_{mpnq} = \hat{a}_{mp}\hat{a}_{nq} \tag{28}$$

where the second-order tensor $\hat{\mathbf{a}}$ is given by

$$\hat{a}_{mp} = \begin{bmatrix} \dfrac{1}{\sqrt{1-\hat{\phi}_1}} & 0 & 0 \\ 0 & \dfrac{1}{\sqrt{1-\hat{\phi}_2}} & 0 \\ 0 & 0 & \dfrac{1}{\sqrt{1-\hat{\phi}_2}} \end{bmatrix}. \tag{29}$$

Substituting Eq. (28) into Eq. (27), one obtains the following relation:

$$\begin{aligned} M_{ikjl} &= b_{mi}b_{nj}b_{pk}b_{ql}\hat{a}_{mp}\hat{a}_{nq} \\ &= a_{ik}a_{jl}. \end{aligned} \tag{30}$$

Using Eq. (30), a second-order tensor $\mathbf{a}$ is defined as follows:

$$a_{ik} = b_{mi}b_{pk}\hat{a}_{mp}. \tag{31}$$

The matrix form of Eq. (31) is as follows:

$$[a] = [b]^T[\hat{a}][b]$$

$$= \begin{bmatrix} \dfrac{b_{11}b_{11}}{\sqrt{1-\hat{\phi}_1}} + \dfrac{b_{21}b_{21}}{\sqrt{1-\hat{\phi}_2}} + \dfrac{b_{31}b_{31}}{\sqrt{1-\hat{\phi}_3}} & \dfrac{b_{11}b_{12}}{\sqrt{1-\hat{\phi}_1}} + \dfrac{b_{21}b_{22}}{\sqrt{1-\hat{\phi}_2}} + \dfrac{b_{31}b_{32}}{\sqrt{1-\hat{\phi}_3}} & \dfrac{b_{11}b_{13}}{\sqrt{1-\hat{\phi}_1}} + \dfrac{b_{21}b_{23}}{\sqrt{1-\hat{\phi}_2}} + \dfrac{b_{31}b_{33}}{\sqrt{1-\hat{\phi}_3}} \\ \dfrac{b_{12}b_{11}}{\sqrt{1-\hat{\phi}_1}} + \dfrac{b_{22}b_{21}}{\sqrt{1-\hat{\phi}_2}} + \dfrac{b_{32}b_{31}}{\sqrt{1-\hat{\phi}_3}} & \dfrac{b_{12}b_{12}}{\sqrt{1-\hat{\phi}_1}} + \dfrac{b_{22}b_{22}}{\sqrt{1-\hat{\phi}_2}} + \dfrac{b_{32}b_{32}}{\sqrt{1-\hat{\phi}_3}} & \dfrac{b_{12}b_{13}}{\sqrt{1-\hat{\phi}_1}} + \dfrac{b_{22}b_{23}}{\sqrt{1-\hat{\phi}_2}} + \dfrac{b_{32}b_{33}}{\sqrt{1-\hat{\phi}_3}} \\ \dfrac{b_{13}b_{11}}{\sqrt{1-\hat{\phi}_1}} + \dfrac{b_{23}b_{21}}{\sqrt{1-\hat{\phi}_2}} + \dfrac{b_{33}b_{31}}{\sqrt{1-\hat{\phi}_3}} & \dfrac{b_{13}b_{12}}{\sqrt{1-\hat{\phi}_1}} + \dfrac{b_{23}b_{22}}{\sqrt{1-\hat{\phi}_2}} + \dfrac{b_{33}b_{32}}{\sqrt{1-\hat{\phi}_3}} & \dfrac{b_{13}b_{13}}{\sqrt{1-\hat{\phi}_1}} + \dfrac{b_{23}b_{23}}{\sqrt{1-\hat{\phi}_2}} + \dfrac{b_{33}b_{33}}{\sqrt{1-\hat{\phi}_3}} \end{bmatrix} \tag{32}$$

In order to obtain the matrix form of the damage effect tensor, the stress tensors σ_{ij} and $\bar{\sigma}_{kl}$ in Eq. (1) are converted into vector form as follows:

$$\{\sigma\} = \{\sigma_{11}\ \sigma_{22}\ \sigma_{33}\ \sigma_{12}\ \sigma_{23}\ \sigma_{13}\}^T \tag{33}$$

$$\{\bar{\sigma}\} = \{\bar{\sigma}_{11}\ \bar{\sigma}_{22}\ \bar{\sigma}_{33}\ \bar{\sigma}_{12}\ \bar{\sigma}_{23}\ \bar{\sigma}_{13}\}^T. \tag{34}$$

Using the notation of Eqs. (33) and (34), Eq. (1) is now represented in matrix notation as follows:

$$\{\bar{\sigma}\} = [M]\{\sigma\} \tag{35}$$

where $[M]$ is the 6×6 matrix representation of the fourth-order tensor $\mathbf{M}$. The explicit form of the matrix $[M]$ is given as follows:

$$[M] = \begin{bmatrix} a_{11}a_{11} & a_{12}a_{12} & a_{13}a_{13} & 2a_{11}a_{12} & 2a_{12}a_{13} & 2a_{11}a_{13} \\ a_{21}a_{21} & a_{22}a_{22} & a_{23}a_{23} & 2a_{21}a_{22} & 2a_{22}a_{23} & 2a_{21}a_{23} \\ a_{31}a_{31} & a_{32}a_{32} & a_{33}a_{33} & 2a_{31}a_{32} & 2a_{32}a_{33} & 2a_{31}a_{33} \\ a_{11}a_{21} & a_{12}a_{22} & a_{23}a_{23} & (a_{11}a_{22} + a_{12}a_{21}) & (a_{12}a_{23} + a_{13}a_{22}) & (a_{11}a_{23} + a_{13}a_{21}) \\ a_{21}a_{31} & a_{22}a_{32} & a_{23}a_{33} & (a_{21}a_{32} + a_{23}a_{31}) & (a_{22}a_{33} + a_{23}a_{32}) & (a_{21}a_{33} + a_{23}a_{31}) \\ a_{11}a_{31} & a_{12}a_{32} & a_{13}a_{33} & (a_{11}a_{32} + a_{13}a_{31}) & (a_{12}a_{33} + a_{13}a_{31}) & (a_{11}a_{33} + a_{13}a_{31}) \end{bmatrix}. \tag{36}$$

It is clear that the various explicit representation forms of the fourth-order damage effect tensors given by Eqs. (5), (6), (7), and (8) using the second damage tensor $\boldsymbol{\phi}$ are violated by the tensor transformation law.

Matrix Forms of the Damage Effect Tensors for Two-Dimensional Problems

The explicit matrix forms of the damage effect tensors for two-dimensional problems are presented in this section. For the shake of simplicity, a plane state of damage, $\hat{\phi}_3 = 0$ or $\phi_{33} = \phi_{23} = \phi_{32} = \phi_{13} = \phi_{31} = 0$, is assumed for both plane stress and plane strain problems. Similar stress vector of Eqs. (33) and (34), for the two-dimensional problems are given by

$$\{\hat{\sigma}\} = \{\hat{\sigma}_{11}\ \hat{\sigma}_{22}\ \hat{\sigma}_{12}\}^T \tag{37}$$

$$\{\hat{\bar{\sigma}}\} = \{\hat{\bar{\sigma}}_{11}\ \hat{\bar{\sigma}}_{22}\ \hat{\bar{\sigma}}_{12}\}^T. \tag{38}$$

Using the notation of Eqs. (37) and (38), one obtains Eq. (21) represented in matrix notation as follows:

$$\{\hat{\bar{\sigma}}\} = [\hat{M}]\{\hat{\sigma}\} \tag{39}$$

where the 3×3 matrix, $[\hat{M}]$, termed principal damage effect matrix is given by

$$[\hat{M}] = \begin{bmatrix} \hat{M}_{1111} & \hat{M}_{1212} & \hat{M}_{1112} + \hat{M}_{1211} \\ \hat{M}_{2121} & \hat{M}_{2222} & \hat{M}_{2122} + \hat{M}_{2221} \\ \hat{M}_{1121} & \hat{M}_{1222} & \hat{M}_{1122} + \hat{M}_{1221} \end{bmatrix}. \tag{40}$$

The principal damage effect matrices corresponding to Eqs. (22), (23), (24), and (25) are as follows, respectively,

Downloaded 04 May 2010 to 171.66.16.34. Redistribution subject to ASME license or copyright; see http://www.asme.org/terms/Terms_Use.cfm

$$[\hat{M}] = \begin{bmatrix} \frac{1}{1-\hat{\phi}_1} & 0 & 0 \\ 0 & \frac{1}{1-\hat{\phi}_2} & 0 \\ 0 & 0 & \frac{1}{\sqrt{(1-\hat{\phi}_1)(1-\hat{\phi}_2)}} \end{bmatrix} \quad (41)$$

where the principal damage values, $\hat{\phi}_1$ and $\hat{\phi}_2$, are given by

$$\hat{\phi}_1 = \frac{\phi_{11}+\phi_{22}}{2} + \sqrt{\left(\frac{\phi_{11}+\phi_{22}}{2}\right)^2 + \phi_{12}^2} \quad (45)$$

$$\hat{\phi}_2 = \frac{\phi_{11}+\phi_{22}}{2} - \sqrt{\left(\frac{\phi_{11}+\phi_{22}}{2}\right)^2 + \phi_{12}^2}, \quad (46)$$

respectively. Finally, the damage effect matrix can be obtained by coordinate transformation. The complete set of transformation equations for stresses in the principal damage direction coordinate system is given by

$$\{\hat{\sigma}\} = [T]\{\sigma\}. \quad (47)$$

Similarly, the effective stress vector in the principal damage direction coordinate system is given by

$$\{\hat{\bar{\sigma}}\} = [T]\{\bar{\sigma}\} \quad (48)$$

where the transformation matrix, $[T]$, and its inverse matrix, $[T]^{-1}$ are given by

$$[T] = \begin{bmatrix} \cos^2\theta & \sin^2\theta & -2\cos\theta\sin\theta \\ \sin^2\theta & \cos^2\theta & 2\cos\theta\sin\theta \\ \cos\theta\sin\theta & -\cos\theta\sin\theta & \cos^2\theta-\sin^2\theta \end{bmatrix} \quad (49)$$

$$[\hat{M}] = \begin{bmatrix} \frac{1}{1-\hat{\phi}_1} & \frac{1}{4}\left(\frac{1}{1-\hat{\phi}_1}+\frac{1}{1-\hat{\phi}_2}\right) & 0 \\ \frac{1}{4}\left(\frac{1}{1-\hat{\phi}_1}+\frac{1}{1-\hat{\phi}_2}\right) & \frac{1}{1-\hat{\phi}_2} & 0 \\ 0 & 0 & \frac{1}{4}\left(\frac{1}{1-\hat{\phi}_1}+\frac{1}{1-\hat{\phi}_2}\right) \end{bmatrix} \quad (42)$$

$$[\hat{M}] = \begin{bmatrix} \frac{1}{(1-\hat{\phi}_1)^2} & \frac{1}{2(1-\hat{\phi}_1)(1-\hat{\phi}_2)} & 0 \\ \frac{1}{2(1-\hat{\phi}_1)(1-\hat{\phi}_2)} & \frac{1}{(1-\hat{\phi}_1)^2} & 0 \\ 0 & 0 & \frac{1}{2(1-\hat{\phi}_1)(1-\hat{\phi}_2)} \end{bmatrix} \quad (43)$$

$$[\hat{M}] = \begin{bmatrix} \exp(\hat{\phi}_1/2)\exp(\hat{\phi}_1/2) & \frac{1}{2}(\exp(\hat{\phi}_1/2)\exp(\hat{\phi}_1/2)+1) & 2\exp(\hat{\phi}_1/2) \\ \frac{1}{2}(\exp(\hat{\phi}_1/2)\exp(\hat{\phi}_1/2)+1) & \exp(\hat{\phi}_2/2)\exp(\hat{\phi}_2/2) & 2\exp(\hat{\phi}_2/2) \\ \exp(\hat{\phi}_1/2) & \exp(\hat{\phi}_2/2) & 2 \end{bmatrix} \quad (44)$$

$$[T]^{-1} = \begin{bmatrix} \cos^2\theta & \sin^2\theta & 2\cos\theta\sin\theta \\ \sin^2\theta & \cos^2\theta & -2\cos\theta\sin\theta \\ -\cos\theta\sin\theta & \cos\theta\sin\theta & \cos^2\theta-\sin^2\theta \end{bmatrix} \quad (50)$$

where θ is given by

$$\theta = \frac{1}{2}\tan^{-1}\left(\frac{2\phi_{12}}{\phi_{11}-\phi_{22}}\right). \quad (51)$$

Substituting Eqs. (47) and (48) into Eq. (39), one obtains the following relation:

$$\{\bar{\sigma}\} = [T]^{-1}[\hat{M}][T]\{\sigma\} = [M]\{\sigma\}. \quad (52)$$

The damage effect matrix $[M]$ is defined as follows:

$$[M] = [T]^{-1}[\hat{M}][T]. \quad (53)$$

Using the principal damage effect matrix given by Eq. (41), the damage effect matrix $[M]$ is given by

$$[M] = \begin{bmatrix} \frac{c^4}{1-\hat{\phi}_1}+\frac{s^4}{1-\hat{\phi}_2}+\frac{2c^2s^2}{\sqrt{(1-\hat{\phi}_1)(1-\hat{\phi}_2)}} & \frac{c^2s^2}{1-\hat{\phi}_1}+\frac{c^2s^2}{1-\hat{\phi}_2}+\frac{-2c^2s^2}{\sqrt{(1-\hat{\phi}_1)(1-\hat{\phi}_2)}} & \frac{-2c^3s}{1-\hat{\phi}_1}+\frac{2cs^3}{1-\hat{\phi}_2}+\frac{2(c^3s-cs^3)}{\sqrt{(1-\hat{\phi}_1)(1-\hat{\phi}_2)}} \\ \frac{c^2s^2}{1-\hat{\phi}_1}+\frac{c^2s^2}{1-\hat{\phi}_2}+\frac{-2c^3s}{\sqrt{(1-\hat{\phi}_1)(1-\hat{\phi}_2)}} & \frac{s^4}{1-\hat{\phi}_1}+\frac{c^4}{1-\hat{\phi}_2}+\frac{2c^2s^2}{\sqrt{(1-\hat{\phi}_1)(1-\hat{\phi}_2)}} & \frac{-2cs^3}{1-\hat{\phi}_1}+\frac{2c^3s}{1-\hat{\phi}_2}+\frac{-2(c^3s-cs^3)}{\sqrt{(1-\hat{\phi}_1)(1-\hat{\phi}_2)}} \\ \frac{-2c^3s}{1-\hat{\phi}_1}+\frac{2cs^3}{1-\hat{\phi}_2}+\frac{2(c^3s-cs^3)}{\sqrt{(1-\hat{\phi}_1)(1-\hat{\phi}_2)}} & \frac{-2cs^3}{1-\hat{\phi}_1}+\frac{2c^3s}{1-\hat{\phi}_2}+\frac{-2(c^3s-cs^3)}{\sqrt{(1-\hat{\phi}_1)(1-\hat{\phi}_2)}} & \frac{2c^2s^2}{1-\hat{\phi}_1}+\frac{2c^2s^2}{1-\hat{\phi}_2}+\frac{(c^2-s^2)^2}{\sqrt{(1-\hat{\phi}_1)(1-\hat{\phi}_2)}} \end{bmatrix} \quad (54)$$

Downloaded 04 May 2010 to 171.66.16.34. Redistribution subject to ASME license or copyright; see http://www.asme.org/terms/Terms_Use.cfm

where $c = \cos\theta$ and $s = \sin\theta$.

Conclusions

The fourth-order anisotropic damage effect tensor, $\mathbf{M}$, using the kinematic measure for damage, expressed through the second-order damage tensor $\boldsymbol{\phi}$, is reviewed here in reference to the symmetrization of the effective stress tensor. This introduces for a distinct kinematic measure of damage which is complimentary to the deformation kinematic measure of strain. A thermodynamically consistent evolution equation for the damage tensor, $\boldsymbol{\phi}$ together with a generalized thermodynamic force conjugate, $\mathbf{Y}$, to the damage tensor is presented in the paper by Voyiadjis and Park (1995). It is pointed out that the principal damage tensor, $\hat{\boldsymbol{\phi}}$, should be used in the formulation of the anisotropic damage effect tensor. Voyiadjis and Venson (1995) quantified the physical values of the eigenvalues, $\hat{\phi}_k (k = 1, 2, 3)$, and the second-order damage tensor, $\boldsymbol{\phi}$, for the unidirectional fibrous composite by measuring the crack density with the assumption that one of the eigendirections of damage tensor coincides with the fiber direction.

The fourth-order anisotropic damage effect tensor in the principal damage direction coordinate system is termed the principal damage effect tensor. By coordinate transformation, the fourth-order anisotropic damage effect tensor is obtained. This fourth-order anisotropic damage effect tensor has both physical significance and explicit form. It is therefore not a mere implicit mathematical expression to transform the current stress tensor to a symmetric effective stress tensor. Moreover, an explicit expression of the damage effect tensor is of particular importance in order to obtain the constitutive relation in the damaged material.

In this work, tensorial forms are used for the derivation of such a linear transformation tensor which is then converted to a matrix form. The explicit matrix expressions of the damage effect tensor are derived for both three-dimensional and two-dimensional problems. Especially the damage effect matrix of two-dimensional problems can be expressed by the damage variables, ϕ_{11}, ϕ_{22} and ϕ_{12}.

References

Betten, J., 1983, "Damage Tensors in Continuum Mechanics," *Journal of Mécanique Théorique et Appliquée,* Vol. 2, No. 1, pp. 13–32.

Chaboche, J. L., 1979, "Le concept de contrainte effective appliqué à l'élasticité et à la viscoplasticité en présence d'un endommagement anisotrope," *Colooque Euromech 115,* Villard de Lans, June.

Chaboche, J. L., 1981, "Continuum Damage Mechanics—A Tool to Describe Phenomena Before Crack Initiation," *Nuclear Engineering and Design,* Vol. 64, pp. 233–247.

Chaboche, J. L., 1988a, "Continuum Damage Mechanics: Part I—General Concepts," ASME JOURNAL OF APPLIED MECHANICS, Vol. 55, pp. 59–64.

Chaboche, J. L., 1988b, "Continuum Damage Mechanics: Part II—Damage Growth, Crack Initiation, and Crack Growth," ASME JOURNAL OF APPLIED MECHANICS, Vol. 55, pp. 65–72.

Cordebois, J. P., and Sidoroff, F., 1982, "Anisotropic Damage in Elasticity and Plasticity," *Journal de Mécanique Théorique et Appliquée,* Numéro Spécial, pp. 45–60.

Ju, J. W., 1990, "Isotropic and Anisotropic Damage Variables in Continuum Damage Mechanics," *Journal of Engineering Mechanics,* Vol. 116, No. 12, pp. 2764–2770.

Kachanov, L. M., 1958, "On the Creep Fracture Time," *Izv. Adad. Nauk. USSR Otd. Tekh.,* Vol. 8, pp. 26–31.

Krajcinovic, D., 1983, "Constitutive Equations for Damaging Materials," ASME JOURNAL OF APPLIED MECHANICS, Vol. 50, pp. 335–360.

Krajcinovic, D., 1985, "Continuous Damage Mechanics Revisited: Basic Concepts and Definitions," ASME JOURNAL OF APPLIED MECHANICS, Vol. 52, pp. 829–834.

Krajcinovic, D., and Foneska, G. U., 1981, "The Continuum Damage Theory for Brittle Materials," ASME JOURNAL OF APPLIED MECHANICS, Vol. 48, pp. 809–834.

Lee, H., Li, G., and Lee, S., 1986, "The Influence of Anisotropic Damage on the Elastic Behavior of Materials," *International Seminar on Local Approach of Fracture,* Moret-sur-Loing, France, June, pp. 79–90.

Lemaitre, J., 1985, "A Continuous Damage Mechaics Model of Ductile Fracture," ASME *Journal of Engineering Materials and Technology,* Vol. 107, No. 42, pp. 83–89.

Lemaitre, J., 1986, "Local Approach of Fracture," *Engineering Fracture Mechanics,* Vol. 25, No. 5–6, pp. 523–537.

Lu, T. J., and Chow, C. L., 1990, "On Constitutive Equations of Inelastic Solids With Anisotropic Damage," *Theoretical and Applied Fracture Mechanics,* Vol. 14, pp. 187–218.

Murakami, S., 1983, "Notion of Continuum Damage Mechanics and Its Application to Anisotropic Creep Damage Theory," *Journal of Engineering Materials and Technology,* Vol. 105, pp. 99–105.

Murakami, S., 1988, "Mechanical Modeling of Material Damage," ASME JOURNAL OF APPLIED MECHANICS, Vol. 55, pp. 280–286.

Murakami, S., and Ohno, N., 1980, "A Continuum Theory of Creep and Creep Damage," *Creep in Structures,* A. R. S. Ponter and D. R. Hayhurst, eds., IUTAM 3rd Symposium, Leichester, U.K., Sept. 8–12, Springer-Verlag, New York, pp. 422–443.

Sidoroff, F., 1979, "Description of Anisotropic Damage Application to Elasticity," *Mechanical Behavior of Anisotropic Solids* (No. 295 Comportement Mechanique Des Solides Anisotropes), J.-P. Boehler, ed., Martinus Nijhoff, Dordrecht, The Netherlands.

Sidoroff, F., 1980, "Description of Anisotropic Damage Application to Elasticity," *Physical Non-Linearities in Structural Analysis* (IUTAM Series), J. Hult and J. Lemaitre, eds., Springer-Verlag, New York, pp. 237–244.

Voyiadjis, G. Z., and Kattan, P. I., 1992, "A Plasticity-Damage Theory for Large Deformation of Solids, Part I: Theoretical Formulation," *International Journal of Engineering Science,* Vol. 30, No. 9, pp. 1089–1108.

Voyiadjis, G. Z., and Park, T., 1995, "Local and Interfacial Damage Analysis of Metal Matrix Composites," *International Journal of Engineering Science,* Vol. 33, No. 11, pp. 1595–1621.

Voyiadjis, G. Z., and Venson, A. R., 1995, "Experimental Damage Investigation of a SiC–Ti Aluminide Metal Matrix Composite," *International Journal of Damage Mechanics,* Vol. 4. No. 4, Oct., pp. 338–361.

Downloaded 04 May 2010 to 171.66.16.34. Redistribution subject to ASME license or copyright; see http://www.asme.org/terms/Terms_Use.cfm

Elastothermodynamic Damping in Particulate Composites: Hollow Spherical Inclusions

V. K. Kinra
General Dynamics Professor,
Fellow ASME.

J. E. Bishop
Center for Mechanics of Composites,
Department of Aerospace Engineering,
Texas A&M University,
College Station, TX 77843-3141

When a composite material is subjected to a time-harmonic stress field (homogeneous or inhomogeneous), different phases undergo different temperature fluctuations due to the well-known thermoelastic effect. As a result irreversible heat conduction occurs within each phase and between phases, and entropy is produced. This entropy production is the genesis of elastothermodynamic damping and, as a consequence of the second law of thermodynamics, manifests itself as a conversion of work into heat. This paper is concerned with the calculation of elastothermodynamic damping in a matrix reinforced with hollow spheres. Numerical results are presented for an alumina/aluminum composite sphere subjected to a uniform radial stress at the outer boundary. When the cavity occupies more than 75 percent volume fraction of the alumina inclusion, the total damping becomes vanishingly small.

Introduction

Whenever a material is stressed in a reversible adiabatic (i.e., isentropic) process, there is always a change in its temperature, however small. This phenomenon is known as the thermoelastic effect and can be deduced from the Maxwell's relations (Zemansky and Dittman, 1981); for an isotropic material

$$\left(\frac{\partial T}{\partial \sigma_{kk}}\right)_s = -T\frac{\alpha}{C} \tag{1}$$

where T is the absolute temperature, σ_{kk} is the hydrostatic stress, α is the linear coefficient of thermal expansion, C is the specific heat *per unit volume,* and the subscript S denotes an isentropic process. Since the temperature and stress fields are coupled, inhomogeneities in stress and/or material properties result in inhomogeneities in temperature. Heat conducts from the high-temperature regions to the low-temperature regions and, as a consequence of the second law of thermodynamics, entropy is produced which is manifested as a conversion of useful mechanical energy into heat; we define this process as elastothermodynamic damping (the entropic description). An alternative yet equivalent view of this phenomenon is as follows. The fluctuating temperature produces a thermal strain field that is out of phase with the applied stress field. This phase difference may be used to calculate the conversion of useful mechanical energy into heat; we define this as the mechanical description of elastothermodynamic damping. Recently, Bishop and Kinra (1996b) have proven the equivalence of the two descriptions for a general composite material with anisotropic (or triclinic) phases and with thermally perfect or imperfect interfaces between the constituent phases.

A theory for calculating elastothermodynamic damping was presented by Kinra and Milligan (1994) and Bishop and Kinra (1996b). Using this theory, elastothermodynamic damping has been reported for a number of problems of practical interest, for example, fiber-reinforced composites (Milligan and Kinra, 1995a, b), particle-reinforced composites (Bishop and Kinra, 1996a), laminated composites (Bishop and Kinra, 1993, 1994, 1996c), and a Griffith crack (Kinra and Bishop, 1995). The objective of the present work is to extend this analysis to the case of a matrix reinforced with hollow spheres. The motivation for performing this calculation comes from the fact that such materials (for example, an aluminum, magnesium, or a titanium matrix reinforced with hollow alumina spheres) are under active development for use in applications where weight is a critical consideration, e.g., space structures, submarine hulls, armored tank walls, etc. As a first step towards estimating the damping of a particulate composite, we analyze a three-phase composite sphere, with a cavity as the innermost phase, subjected to a uniform radial stress at the outer boundary. Results are presented for temperature, entropy produced, work lost and total damping; the interface between the matrix and the inclusion may be thermally perfect or imperfect. When the cavity occupies more the 75 percent volume fraction of the inclusion, the total damping becomes vanishingly small.

Theory

For conciseness we will merely reproduce the governing field equations. For an explanation of the underlying physics, a derivation of these equations, and an extensive reference to the published literature, the reader is referred to the references cited above.

Consider a matrix reinforced by hollow spheres. As a first step towards estimating the damping in the composite under a hydrostatic loading at infinity we consider a three-phase composite sphere shown in Fig. 1. Let V_f be the volume fraction of the matrix occupied by the spheres in the particulate composite; we choose $(a/b)^3 = V_f$. Let V_h be the volume fraction of the spheres occupied by the holes in the particulate composite; we choose $(h/a)^3 = V_h$. We introduce a spherical coordinate system (r, θ, ϕ) at the center of the composite sphere. The outer boundary, $r = b$, is subjected to a time-harmonic uniform radial stress $\sigma_{rr} = \sigma e^{i\omega t}$, $\sigma_{r\theta} = \sigma_{r\phi} = 0$. The heat conduction occurs only in the radial direction. Let T_0 be the equilibrium temperature of the composite sphere. Let $Ve^{i\omega t}$ be the fluctuations of temperature about T_0. In general V is complex valued and is governed by the linearized one-way-coupled heat-conduction equation (Nowinski, 1978)

Contributed by the Applied Mechanics Division of THE AMERICAN SOCIETY OF MECHANICAL ENGINEERS for publication in the ASME JOURNAL OF APPLIED MECHANICS.

Discussion on this paper should be addressed to the Technical Editor, Professor Lewis T. Wheeler, Department of Mechanical Engineering, University of Houston, Houston, TX 77204-4792, and will be accepted until four months after final publication of the paper itself in the ASME JOURNAL OF APPLIED MECHANICS.

Manuscript received by the ASME Applied Mechanics Division, Aug. 31, 1995; final revision, June 10, 1996. Associate Technical Editor: J. T. Jenkins.

Copyright © 1997 by ASME

Downloaded 04 May 2010 to 171.66.16.34. Redistribution subject to ASME license or copyright; see http://www.asme.org/terms/Terms_Use.cfm

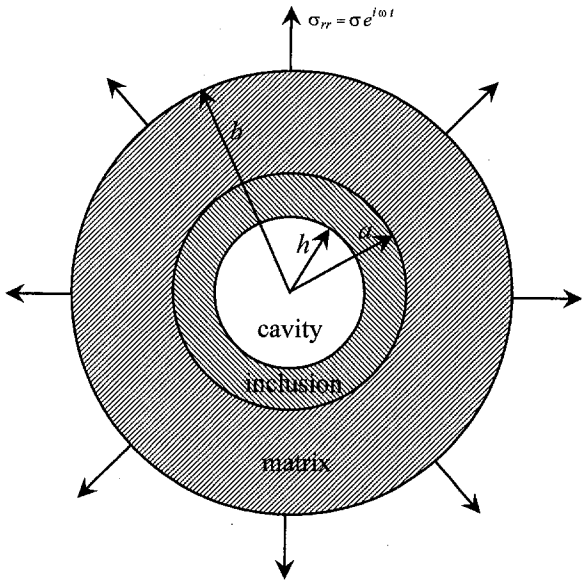


Fig. 1 A three-phase composite sphere. The innermost phase is a cavity. The subscripts ( )$_1$ and ( )$_2$ refer to the inclusion and matrix, respectively.

$$C\frac{\partial V}{\partial t} = k\frac{1}{r^2}\frac{\partial}{\partial r}\left(r^2\frac{\partial V}{\partial r}\right) - \alpha T_0\frac{\partial \sigma_{kk}}{\partial t} \tag{2}$$

where k is the thermal conductivity, and σ_{kk} is the hydrostatic stress. Let Δs be the entropy produced per unit volume per cycle due to irreversible heat conduction, then

$$\Delta s(r) = \frac{k}{T_0^2}\frac{\pi}{\omega}\,\mathrm{Re}(\nabla V\cdot\overline{\nabla V}) \tag{3}$$

where the symbol $\cdot$ denotes the dot product of two vectors, and the overbar $\overline{\ }$ denotes the complex conjugate. If the interface between the matrix and the inclusion is thermally imperfect, the temperature becomes discontinuous at the interface, and an additional amount of entropy, $\Delta S^{\text{interface}}$, is produced (Bishop and Kinra, 1996b). For the special case of one-dimensional radial heat conduction under consideration, the *total* entropy produced at the interface, $r = a$, per cycle is given by

$$\Delta S^{\text{interface}} = (4\pi a^2)\left(\frac{-\pi}{\omega T_0^2}\right)\left[k_1\,\mathrm{Re}\left(\frac{dV_1}{dr}\,\overline{V}_1\right)_{r=a^-} - k_2\,\mathrm{Re}\left(\frac{dV_2}{dr}\,\overline{V}_2\right)_{r=a^+}\right] \tag{4}$$

where, unless stated otherwise, the subscripts ( )$_1$ and ( )$_2$ refer to the inclusion and matrix, respectively. The entropy produced per cycle over the entire composite sphere occupying a region R is given by

$$\Delta S(\omega) = \int_R \Delta s\,dR + \Delta S^{\text{interface}}. \tag{5}$$

Let Δw be the work lost per unit volume per cycle, then

$$\Delta w(r,\omega) = -\pi\alpha\sigma_{kk}(r)\,\mathrm{Im}\,V(r,\omega). \tag{6}$$

The *total* work lost throughout the composite sphere is given by

$$\Delta W(\omega) = \int_R \Delta w\,dR. \tag{7}$$

Recently, we have shown that whereas $\Delta W = T_0\Delta S$, $\Delta w \neq T_0\Delta s$ pointwise (Bishop and Kinra, 1996b).

Solution

It is assumed that the frequency is sufficiently small so that the dynamic stress field may be approximated by the static stress field. Then σ_{kk} in (2) is the solution to the isothermal elastostatic problem shown in Fig. 1. The boundary conditions for the elasticity problem are taken to be as follows: I at $r = b$, $\sigma_{r\theta} = \sigma_{r\phi} = 0$, $\sigma_{rr} = \sigma$; II at $r = a$, continuity of displacements and tractions; and III at $r = h$, the cavity surface is traction free. The problem was solved using standard elasticity methods. The nonzero stresses in the inclusion are

$$(\sigma_{rr})_1 = 3K_1D_1 - 4\mu_1D_3(a/r)^3 \tag{8}$$

$$(\sigma_{\theta\theta})_1 = (\sigma_{\phi\phi})_1 = 3K_1D_1 + 2\mu_1D_3(a/r)^3 \tag{9}$$

and in the matrix are

$$(\sigma_{rr})_2 = 3K_2D_2 - 4\mu_2D_4(a/r)^3 \tag{10}$$

$$(\sigma_{\theta\theta})_2 = (\sigma_{\phi\phi})_2 = 3K_2D_2 + 2\mu_2D_4(a/r)^3 \tag{11}$$

so that

$$(\sigma_{kk})_j = 9K_jD_j \quad j = 1, 2 \tag{12}$$

where

$$D_1 = \frac{4\mu_1}{3K_1}\frac{D_3}{V_h}, \quad D_2 = \frac{1}{3K_2}(4\mu_2V_fD_4 + \sigma)$$

$$D_3 = \frac{\sigma}{\det}\left(1 + \frac{4\mu_2}{3K_2}\right),$$

$$D_4 = \frac{\sigma}{\det}\left[1 + \frac{4\mu_1}{3K_1}\frac{1}{V_h} + \frac{4\mu_1}{3K_2}(1 - 1/V_h)\right]$$

$$\det = -\left[1 + \frac{4\mu_1}{3K_1}\frac{1}{V_h}\right]4\mu_2(V_f - 1) - \left[1 + \frac{4\mu_2}{3K_2}V_f\right]4\mu_1(1 - 1/V_h)$$

and K_j and μ_j are the bulk and shear moduli, respectively. As an interesting aside, we note that even though σ_{rr}, $\sigma_{\theta\theta} = \sigma_{\phi\phi}$ are functions of r, fortuitously, σ_{kk} is independent of r in both the matrix and the inclusion. Let w be the elastic strain energy density, $w = \frac{1}{2}\sigma_{ij}\epsilon_{ij}$, then the *total* strain energy stored in the composite sphere is given by

$$W = \int_R w\,dR = \frac{4\pi b^3}{3}\left[\begin{array}{l}(\frac{9}{2}K_1D_1^2 + 6\mu_1D_3^2V_h)(1 - V_h)V_f \\ \quad + (\frac{9}{2}K_2D_2^2 + 6\mu_2D_4^2V_f)(1 - V_f)\end{array}\right]. \tag{13}$$

Next, we substitute σ_{kk} into (2). The boundary conditions for the thermal problem are: I the surfaces $r = h$ and $r = b$ are adiabatic; and II at $r = a$, the condition of *imperfect* thermal contact, $-k_1\partial T_1/\partial r = f(T_1 - T_2)$, where f is the thermal contact conductance. For a thermally perfect interface, $f \to \infty$, and we recover the familiar continuity of temperature, $T_1 = T_2$ at $r = a$; III at $r = a$ the continuity of heat flux, $-k_1\partial T_1/\partial r = -k_2\partial T_2/\partial r$. For a thermally imperfect interface, the solution is

$$V_j(r) = -T_0(\alpha\sigma_{kk}/C)_1\sum_{n=0}^{\infty}\frac{\Omega_1^2 + i\Omega_1\gamma_n^2}{\Omega_1^2 + \gamma_n^4}R_n[b\phi_{jn}(r)] \quad j = 1, 2 \tag{14}$$

Downloaded 04 May 2010 to 171.66.16.34. Redistribution subject to ASME license or copyright; see http://www.asme.org/terms/Terms_Use.cfm

where we have introduced a normalized frequency of vibration as $\Omega_1 = \omega C_1 a^2/k_1$. The ϕ_{jn} are given by

$$\phi_{1n} = (1/x)\sin(\gamma_n x/a) + B_{1n}(1/x)\cos(\gamma_n x/a) \quad (15)$$

$$\phi_{2n} = A_{2n}(1/x)\sin(\eta_n x/b) + B_{2n}(1/x)\cos(\eta_n x/b) \quad (16)$$

where the constants B_{1n}, A_{2n}, B_{2n} are given by

$$B_{1n} = \frac{-a_{11}}{a_{12}}, \quad A_{2n} = \frac{-1}{\Delta}\, a_{44}(a_{12}a_{21} - a_{22}a_{11}),$$

$$B_{2n} = \frac{a_{43}}{\Delta}(a_{12}a_{21} - a_{22}a_{11})$$

where $\Delta = a_{12}(a_{23}a_{44} - a_{43}a_{24})$, $\eta_n = \gamma_n(b/a\sqrt{C_2k_1/C_1k_2})$, and the γ_n are the roots of the following transcendental equation

$$\begin{vmatrix} a_{11} & a_{12} & 0 & 0 \\ a_{21} & a_{22} & a_{23} & a_{24} \\ a_{31} & a_{32} & a_{33} & a_{34} \\ 0 & 0 & a_{43} & a_{44} \end{vmatrix} = 0 \quad (17)$$

where the constants a_{ij}, $i, j \in \{1, 2, 3, 4\}$ are given by

$$a_{11} = (\gamma_n h/a)\cos(\gamma_n h/a) - \sin(\gamma_n h/a),$$

$$a_{12} = -(\gamma_n h/a)\sin(\gamma_n h/a) - \cos(\gamma_n h/a)$$

$$a_{21} = (k_1/k_2)(\gamma_n \cos\gamma_n - \sin\gamma_n),$$

$$a_{22} = -(k_1/k_2)(\gamma_n \sin\gamma_n + \cos\gamma_n)$$

$$a_{23} = -(\eta_n a/b)\cos(\eta_n a/b) + \sin(\eta_n a/b)$$

$$a_{24} = (\eta_n a/b)\sin(\eta_n a/b) + \cos(\eta_n a/b)$$

$$a_{31} = (k_1/k_2)(-\gamma_n \cos\gamma_n + \sin\gamma_n) - (fa/k_2)\sin\gamma_n$$

$$a_{32} = (k_1/k_2)(\gamma_n \sin\gamma_n + \cos\gamma_n) - (fa/k_2)\cos\gamma_n$$

$$a_{33} = (fa/k_2)\sin(\eta_n a/b), \quad a_{34} = (fa/k_2)\cos(\eta_n a/b)$$

$$a_{43} = \eta_n \cos(\eta_n) - \sin(\eta_n), \quad a_{44} = -\eta_n \sin(\eta_n) - \cos(\eta_n).$$

The R_n are given by

$$R_n = \left[(a/b)^2 I_1 + \frac{\alpha_2}{\alpha_1}\frac{(\sigma_{kk})_2}{(\sigma_{kk})_1} I_2\right] \Big/ \left[\frac{a}{b} I_3 + \frac{C_2}{C_1} I_4\right] \quad (18)$$

with

$$I_1 = \frac{1}{\gamma_n}\left\{\left[\frac{1}{\gamma_n}(\sin(\gamma_n) - \sin(\gamma_n h/a)) - \cos(\gamma_n) + \frac{h}{a}\cos(\gamma_n h/a)\right] + B_{1n}\left[\frac{1}{\gamma_n}(\cos(\gamma_n) - \cos(\gamma_n h/a)) + \sin(\gamma_n) - \frac{h}{a}\sin(\gamma_n h/a)\right]\right\}$$

$$I_2 = \frac{1}{\eta_n}\left\{A_{2n}\left[\frac{1}{\eta_n}(\sin(\eta_n) - \sin(\eta_n a/b)) - \cos(\eta_n) + \frac{a}{b}\cos(\eta_n a/b)\right] + B_{2n}\left[\frac{1}{\eta_n}(\cos(\eta_n) - \cos(\eta_n a/b)) + \sin(\eta_n) - \frac{a}{b}\sin(\eta_n a/b)\right]\right\}$$

$$I_3 = \frac{1}{2}\left(1 - \frac{h}{a}\right)(1 + B_{1n}^2) + \frac{1}{4\gamma_n}(B_{1n}^2 - 1)[\sin(2\gamma_n) - \sin(2\gamma_n h/a)] - \frac{1}{2\gamma_n} B_{1n}[\cos(2\gamma_n) - \cos(2\gamma_n h/a)]$$

$$I_4 = \frac{1}{2}\left(1 - \frac{a}{b}\right)(A_{2n}^2 + B_{2n}^2) + \frac{1}{4\eta_n}(B_{2n}^2 - A_{2n}^2)[\sin(2\eta_n) - \sin(2\eta_n a/b)] - \frac{1}{2\eta_n} A_{2n}B_{2n}[\cos(2\eta_n) - \cos(2\eta_n a/b)].$$

The entropy produced per cycle per unit volume is given by

$$\Delta s_j(r) = \pi k_j \tau_1 (\alpha\sigma_{kk}/C)_1^2 \sum_{n=0}^{\infty}\sum_{m=0}^{\infty} \frac{\Omega_1(\Omega_1^2 + \gamma_n^2\gamma_m^2)}{(\Omega_1^2 + \gamma_n^4)(\Omega_1^2 + \gamma_m^4)} \times R_n R_m \frac{d}{dr}(b\phi_{jn})\frac{d}{dr}(b\phi_{jm}) \quad j = 1, 2. \quad (19)$$

Next we introduce a normalized measure of the entropy produced, $\chi = T_0\Delta s/\bar{w}$, where $\bar{w} = W/(4\pi b^3/3)$ is the average strain energy density. The work lost per cycle per unit volume is given by

$$\Delta w_1(r) = \pi T_0(\alpha^2\sigma_{kk}^2/C)_1 \sum_{n=0}^{\infty} \frac{\Omega_1\gamma_n^2}{\Omega_1^2 + \gamma_n^4} R_n[b\phi_{jn}(r)] \quad (20)$$

$$\Delta w_2(r) = \pi T_0(\alpha\sigma_{kk}/C)_1(\alpha\sigma_{kk})_2 \sum_{n=0}^{\infty} \frac{\Omega_1\gamma_n^2}{\Omega_1^2 + \gamma_n^4} R_n[b\phi_{jn}(r)]. \quad (21)$$

Next, we introduce a normalized measure of the work lost, $\psi = \Delta w/\bar{w}$. Finally, the specific damping capacity of the composite sphere is defined as $\Psi = \Delta W/W$, then

$$\Psi = \frac{\Psi_{B1}\sum_{n=1}^{\infty}\frac{\Omega_1\gamma_n^2}{\Omega_1^2 + \gamma_n^4} Q_n}{\frac{1}{27}\left[\frac{1}{2}V_f(1 - V_h) + \frac{2}{3}\frac{\mu_1}{K_1}(D_3/D_1)^2 V_f V_h(1 - V_h) + \frac{K_2}{2K_1}(D_2/D_1)^2(1 - V_f) + \frac{2\mu_2}{3K_1}(D_4/D_1)^2 V_f(1 - V_f)\right]} \quad (22)$$

where we have defined a modulus of elastothermodynamic damping as $\Psi_B = \pi T_0 K\alpha^2/C$, and

$$Q_n = \left[(a/b)^2 I_1 + \frac{\alpha_2}{\alpha_1}\frac{(\sigma_{kk})_2}{(\sigma_{kk})_1} I_2\right]^2 \Big/ \left[\frac{a}{b} I_3 + \frac{C_2}{C_1} I_4\right].$$

Numerical Results

We present numerical results for the case of alumina microballoons in an aluminum matrix with a thermally perfect interface; the thermomechanical properties of the two phases are

Downloaded 04 May 2010 to 171.66.16.34. Redistribution subject to ASME license or copyright; see http://www.asme.org/terms/Terms_Use.cfm

Table 1 Thermoelastic constants (nominal values)

	K	μ	k	α	C	Ψ_s
	GPa	GPa	$(J/sm\,K)$	$(10^{-6}\,K^{-1})$	$(10^6\,J/m^3\,K)$	
Al_2O_3	349	131	29	9	3.19	0.0084
Al	70	26	220	24	2.4	0.0151

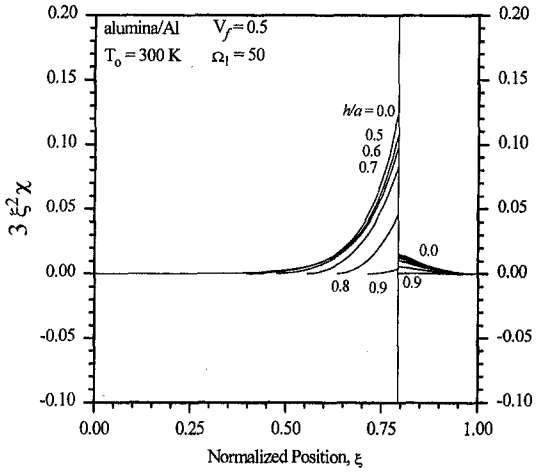


Fig. 2 Modified entropy produced versus a normalized radial coordinate $\xi = r/b$. Most of the entropy is produced in the inclusion.

listed in Table 1. Let $\xi \equiv r/b$. We introduce a *modified* work lost $\psi_M = 3\xi^2\psi$ for the following reasons. In a spherical coordinate system the contribution to the *total damping* from a spherical shell of thickness dr at r is $(4\pi r^2 dr)\psi(r)$. Moreover, for the purpose of visualization we require that the area under the curve, ψ_M versus ξ, $0 \le \xi \le 1$, should equal the *total damping*, Ψ; this naturally led to $\psi_M = 3\xi^2\psi$. For precisely the same reasons we introduce a modified entropy $\chi_M = 3\xi^2\chi$.

In Fig. 2, χ_M is plotted versus ξ with (h/a) as the parameter, and $T_0 = 300$ K, $V_f = 0.5$, and $\Omega_1 = 50$. Most of the entropy is produced in the inclusion. As the cavity radius increases from 0 to 0.5, it has no noticeable effect on χ; thereafter, χ_M decreases monotonically with (h/a). The influence of the cavity size on the modified work lost, $3\xi^2\psi$, is shown in Fig. 3. Most of the work lost is in the matrix. Consistent with the results of Bishop and Kinra (1996b), pointwise, $\psi \neq \chi$; i.e., $\Delta w \neq T_0 \Delta s$. More

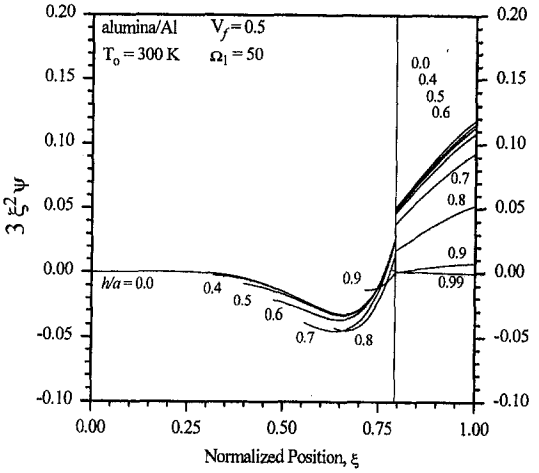


Fig. 3 Modified work lost versus a normalized radial coordinate $\xi = r/b$. Most of the work is lost in the matrix.

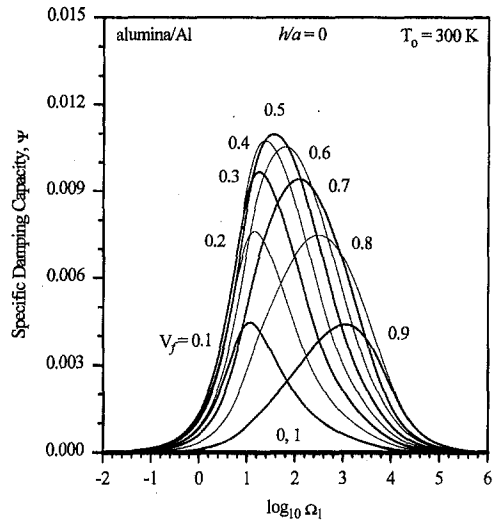


Fig. 4 Specific damping capacity versus normalized frequency for a solid spherical inclusion. The frequency at which the highest damping occurs increases monotonically with the volume fraction.

importantly, the damping is generally *negative* in the inclusion. At first sight this may appear quite disturbing for it implies that work is being produced rather than dissipated. However, the only constraint imposed by the second law of thermodynamics is that the *total* entropy produced throughout the composite sphere (a closed thermodynamic system which does not exchange heat with its surroundings) during one cycle of loading is either zero or positive, i.e., $\Delta S \ge 0$. It follows that $T_0 \Delta S \equiv \Delta W \ge 0$, i.e., the *total* work lost throughout the composite sphere during one cycle must be zero or positive. It then follows that $\Psi \ge 0$. For any (h/a) in Fig. 3, it is clear that the total area under the curve (Ψ) is positive. Looking ahead, $\Psi \ge 0$ for all frequencies in Fig. 4 (solid spheres) and for all (h/a) and all frequencies in Fig. 5 (hollow spheres). Thus the constraint

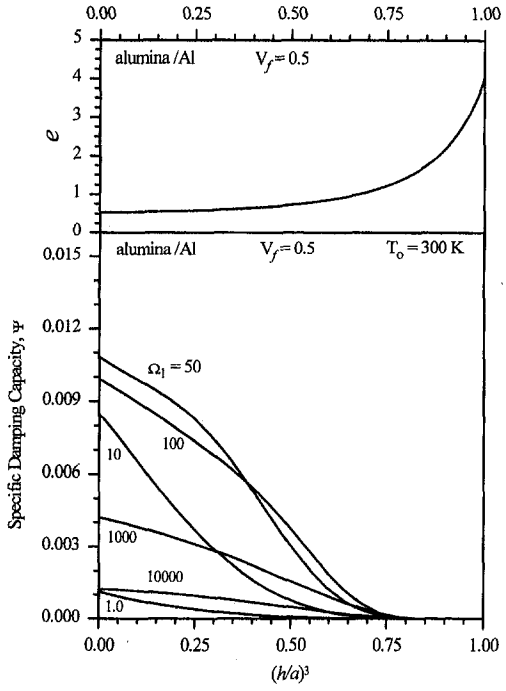


Fig. 5 Specific damping capacity of the three-phase composite sphere versus cavity volume fraction. For $(h/a)^3 \ge 0.75$, $\Psi \approx 0$. Inset: the normalized average strain energy density e increases dramatically for $(h/a)^3 \ge 0.67$.

Downloaded 04 May 2010 to 171.66.16.34. Redistribution subject to ASME license or copyright; see http://www.asme.org/terms/Terms_Use.cfm

imposed by the second law of thermodynamics is indeed satisfied. (We note in passing that Δs is proportional to the *square* of the temperature gradient, therefore $\Delta s \geq 0$ everywhere; see Kinra and Milligan (1994)). Through a comparison of Figs. 2 and 3 we make an interesting observation that whereas the entropy is produced mainly in the inclusion, work is dissipated mainly in the matrix. Finally, recall that $\chi = T_0 \Delta s / \bar{w}$ and $\psi = \Delta w / \bar{w}$. Figures 2 and 3 have been plotted on identical scales. Therefore, the areas under two corresponding curves in Figs. 2 and 3 are equal to each other, and equal to Ψ.

For a *solid* sphere ($h/a = 0$), we have plotted Ψ versus Ω_1 in Fig. 4. When $V_f = 0$ (all matrix) or $V_f = 1$ (all inclusion), the composite sphere reduces to a single phase. In the absence of a second phase with which to exchange heat, there is no damping, i.e., $\Psi = 0$. For any V_f, as $\Omega_1 \to 0$, essentially isothermal conditions are obtained and $\Psi \to 0$; as $\Omega_1 \to \infty$, essentially adiabatic conditions are obtained (with the exception of the immediate vicinity of the interface where there is always some heat conduction no matter how high the frequency) and, once again, $\Psi \to 0$. The maximum damping is about one percent and occurs at approximately $V_f = 0.5$ and $\Omega_1 = 50$. The frequency at which the highest damping occurs increases monotonically with V_f from about 10 for $V_f = 0.1$ to about 1000 for $V_f = 0.9$.

In Fig. 5 we study the influence of the cavity volume fraction, $(h/a)^3$, on Ψ for a fixed $V_f = 0.5$. From a practical engineering consideration, we make an important observation that Ψ vanishes for $(h/a)^3 > 0.75$. For $(h/a)^3 < 0.75$, Ψ decreases almost linearly with $(h/a)^3$. In order to understand this peculiar behavior we first recall that $\Psi = \Delta W/W$, $\bar{w} = W/(4\pi b^3/3)$, and then introduce a *normalized* average elastic strain energy density, $e = \bar{w}/w_0$, where $w_0 = \sigma^2/2K_2$; e is plotted in the inset of Fig. 5. For $(h/a)^3 < 0.67$, e is rather small; at $(h/a)^3 = 0.67$, $e = 1$; for $(h/a)^3 > 0.67$ or $(h/a = 0.87)$ it increases dramatically with $(h/a)^3$, i.e., as the shell becomes thin, the composite sphere becomes extremely compliant. This increase is partly responsible for the peculiar observation made above. Figure 5 serves as a *design curve:* it gives cost (in terms of lost damping) versus benefit (in terms of weight reduction).

Finally, to guard against fortuitous results, calculations were also carried out for a different candidate for inclusion material, namely, SiC in an aluminum matrix; essentially similar results were obtained.

Conclusions

Analytical expressions for the temperature, entropy produced, work lost, and the elastothermodynamic specific damping capacity (Ψ) for a three-phase composite sphere with a cavity as the innermost phase, subjected to a uniform radial stress at the outer boundary have been obtained; the matrix-inclusion interface may be thermally perfect or imperfect. Numerical results are presented for the case of alumina microballoons in an aluminum matrix with a thermally perfect interface. Whereas most of the entropy is produced in the inclusion, most of the work is converted into heat in the matrix. Damping was studied as a function of frequency and the volume fraction of the inclusion occupied by the cavity, V_h; for $V_h > 0.75$, Ψ becomes vanishingly small.

Acknowledgments

This research is supported by the Office of Naval Research through Grant Number N 00014-90-J-1130 to Texas A&M University, College Station, TX. The continued and keen interest taken by the program manager, Dr. Lawrence T. Kabacoff, in the evolution of this work is gratefully acknowledged.

References

Bishop, J., and Kinra, V., 1993, "Thermoelastic Damping of a Laminated Beam in Flexure and Extension," *Journal of Reinforced Plastics and Composites,* Vol. 12, pp. 210–226.

Bishop, J., and Kinra, V., 1994, "Elastothermodynamic Damping in Composite Materials," *Mechanics of Composite Materials and Structures,* Vol. 1, pp. 75–93.

Bishop, J., and Kinra, V., 1996a, "Elastothermodynamic Damping in Particle-Reinforced Metal-Matrix Composites," *Metallurgical and Materials Transactions,* Vol. 26A, No. 11, pp. 2773–2783.

Bishop, J., and Kinra, V., 1996b, "Equivalence of the Mechanical and Entropic Descriptions of Elastothermodynamic Damping in Composite Materials," *Mechanics of Composite Materials and Structures,* Vol. 3, No. 2, pp. 83–95.

Bishop, J., and Kinra, V., 1997, "Elastothermodynamic Damping in Laminated Composites," *The International Journal of Solids and Structures,* Vol. 34, No. 9, pp. 1093–1104.

Kinra, V., and Bishop, J., 1996, "Elastothermodynamic Analysis of a Griffith Crack," *Journal of the Mechanics and Physics of Solids,* Vol. 44, No. 8, pp. 1305–1336.

Kinra, V., and Milligan, K., 1994, "A Second Law Analysis of Thermoelastic Damping," ASME JOURNAL OF APPLIED MECHANICS, Vol. 61, pp. 71–76.

Milligan, K., and Kinra, V., 1995a, "Elastothermodynamic Damping of Fiber-Reinforced Metal-Matrix Composites," ASME JOURNAL OF APPLIED MECHANICS, Vol. 62, pp. 441–449.

Milligan, K., and Kinra, V., 1995b, "A Numerical Investigation of the Elastothermodynamic Damping of Fiber-Reinforced Metal-Matrix Composites," ASME JOURNAL OF APPLIED MECHANICS, Vol. 62, pp. 816–818.

Nowinski, J., 1978, *Theory of Thermoelasticity with Applications,* Sijthoff and Noordhoff, Alphen Aan Den Rijn, The Netherlands, Chapter 6.1.

Zemansky, M., and Dittman, R., 1981, *Heat and Thermodynamics,* 6th ed., McGraw-Hill, New York, pp. 199–206.

Downloaded 04 May 2010 to 171.66.16.34. Redistribution subject to ASME license or copyright; see http://www.asme.org/terms/Terms_Use.cfm

Investigation of a New Formulation of the Lagrange Method for Constrained Dynamic Systems

A. Rosen

E. Edelstein

Faculty of Aerospace Engineering,
Technion-Israel Institute of Technology,
Haifa 32000, Israel

Lagrange multipliers are often used in order to model constrained dynamic systems. This method results in problems of constraints violations and therefore various methods of constraints stabilization have been presented in the past. The purpose of the present paper is to present a new formulation of the method that stabilizes the constraints, but unlike other stabilization methods it is also consistent within the framework of variational methods. The new formulation can be applied to holonomic or nonholonomic constraints. After the presentation of the new formulation, its application to constrained rigid rod systems is presented. The results of the new method are compared with other stabilization techniques.

1 Introduction

Consider a dynamic system that is modeled by n generalized coordinates: $q_1, q_2, \ldots q_n$. The vector of generalized coordinates, $\mathbf{q}$, becomes

$$\mathbf{q} = [q_1, q_2, \ldots q_n]^T. \tag{1}$$

The system Lagrangian is defined as

$$L(\dot{\mathbf{q}}, \mathbf{q}) = T - V \tag{2}$$

where $T(\dot{\mathbf{q}}, \mathbf{q})$ and $V(\mathbf{q})$ are the kinetic and potential energies of the system, respectively. If the system is unconstrained, then the system Lagrangian equations of motion become (Lanczos, 1949)

$$\frac{d}{dt}\left(\frac{\partial L}{\partial \dot{q}_i}\right) - \frac{\partial L}{\partial q_i} = Q_i \quad i = 1 \ldots n \tag{3}$$

where d/dt indicates differentiation with respect to time and $\dot{q}_i$ is a generalized velocity. Q_i is the generalized applied force associated with the generalized coordinate q_i.

In many of the practical cases the elements of $\mathbf{q}$ are not independent. The relations between the generalized coordinates are defined by the constraint equations. Let us assume that there are m independent holonomic constraint equations:

$$\Phi_k(\mathbf{q}, t) = 0 \quad 1 \le k \le m. \tag{4}$$

It is convenient to define a constraint vector $\boldsymbol{\Phi}$:

$$\boldsymbol{\Phi} = [\Phi_1, \ldots \Phi_m]^T. \tag{5}$$

In the case of a constrained system the Lagrangian of Eq. (2) is replaced by a modified Lagrangian, L_c (Lanczos, 1949)

$$L_c(\dot{\mathbf{q}}, \mathbf{q}) = L - \boldsymbol{\Phi}^T\boldsymbol{\lambda} \tag{6}$$

where $\boldsymbol{\lambda}$ is a vector of Lagrange multipliers

$$\boldsymbol{\lambda} = [\lambda_1 \ldots \lambda_m]^T. \tag{7}$$

Then the system is treated as an unconstrained one by replacing L in Eq. (3) by L_c. The resulting equations are

$$\frac{d}{dt}\left(\frac{\partial L}{\partial \dot{q}_i}\right) - \frac{\partial L}{\partial q_i} = Q_i - \sum_{k=1}^{m} \lambda_k \frac{\partial \Phi_k}{\partial q_i} \quad 1 \le i \le n. \tag{8}$$

Equation (8) together with Eq. (4) form a system of $(n + m)$ equations in the $(n + m)$ elements of the two unknown vectors $\mathbf{q}$ and $\boldsymbol{\lambda}$. The system of $(n + m)$ equations represents in fact a mixed set of algebraic and differential equations. This system of equations can in principal be solved if a proper set of initial conditions is defined:

$$\mathbf{q}(0) = \mathbf{q}_0\,; \quad \dot{\mathbf{q}}(0) = \dot{\mathbf{q}}_0. \tag{9}$$

The initial conditions must satisfy Eqs. (4) and (8).

Except for a few simple cases, exact closed-form solutions of the equations do not exist. Therefore, numerical methods must be employed. Unfortunately, numerical solutions of mixed systems of differential and algebraic equations, that are generally nonlinear, are still difficult and problematic.

Basically there are two conceptual approaches of solving the equations of motion of a constrained system (see, for example, Garcia de Jalon and Bayo, 1993):

(a) A set of $(n - m)$ independent generalized coordinates is defined. Only independent state equations are integrated using a direct numerical integration approach. Solution of the remaining m dependent generalized coordinates from the constraint equations ensures nonviolation of the constraints. The choice of the set of independent generalized coordinates presents a crucial problem. These coordinates often change as the system undergoes large motions. An inappropriate selection of independent coordinates may result in ill-conditioned matrices. This approach has been investigated by many researchers (Wehage, 1982; Mani et al., 1985; Kim and Vanderploeg, 1986; Garcia de Jalon et al., 1987; Agrawal, 1987) who presented various methods of choosing the independent coordinates.

(b) The second approach includes a simultaneous solution of the n equations of motion together with the m constraint equations, to find the vectors $\mathbf{q}$ and $\boldsymbol{\lambda}$ at any moment.

Contributed by the Applied Mechanics Division of THE AMERICAN SOCIETY OF MECHANICAL ENGINEERS for publication in the ASME JOURNAL OF APPLIED MECHANICS.

Discussion on this paper should be addressed to the Technical Editor, Professor Lewis T. Wheeler, Department of Mechanical Engineering, University of Houston, Houston, TX 77204-4792, and will be accepted until four months after final publication of the paper itself in the ASME JOURNAL OF APPLIED MECHANICS.

Manuscript received by the ASME Applied Mechanics Division, Aug. 19, 1994; final revision, Aug. 17, 1996. Associate Technical Editor: E. J. Haug, Jr.

Copyright © 1997 by ASME

Downloaded 04 May 2010 to 171.66.16.34. Redistribution subject to ASME license or copyright; see http://www.asme.org/terms/Terms_Use.cfm

Since the subject matter of the present paper belongs to the second approach, it will be discussed in more detail.

A solution of a system of differential/algebraic equations was investigated by various researchers who suggested different methods (Gear, 1984; Petzold, 1982). One of the more attractive approaches is to change the equations such that it will be possible to apply well-known efficient methods of direct integration of ordinary differential equations.

In order to be able to directly integrate the constraint equations (Eq. (4)), they are differentiated twice with respect to time, to yield

$$\ddot{\Phi} = \Phi_q \ddot{\mathbf{q}} - \mathbf{c} = 0 \tag{10a}$$

$$\mathbf{c} = -(\Phi_q \dot{\mathbf{q}})_q \dot{\mathbf{q}} - 2\Phi_{qt}\dot{\mathbf{q}} - \Phi_{tt}. \tag{10b}$$

$\Phi_q \equiv \partial\Phi/\partial\mathbf{q}$ is the constraint Jacobian matrix.

The combined system of $(n + m)$ Eqs. (8), (10a) can now be described as follows:

$$\begin{bmatrix} \mathbf{M} & \Phi_q^T \\ \Phi_q & 0 \end{bmatrix} \begin{bmatrix} \ddot{\mathbf{q}} \\ \boldsymbol{\lambda} \end{bmatrix} = \begin{bmatrix} \mathbf{g} \\ \mathbf{c} \end{bmatrix}. \tag{11}$$

The matrix $\mathbf{M}$ is the generalized mass matrix. $\mathbf{g}$ is the vector of modified generalized forces that include Coriolis and centrifugal contributions. $\mathbf{M}$ and Φ_q are in general functions of $\mathbf{q}$, while $\mathbf{g}$ and $\mathbf{c}$ are functions of $\mathbf{q}$ and $\dot{\mathbf{q}}$.

If $\mathbf{q}$ and $\dot{\mathbf{q}}$ are known at a certain moment, then Eq. (11) can be solved for $\ddot{\mathbf{q}}$ and $\boldsymbol{\lambda}$. A numerical integration algorithm is used to find $\dot{\mathbf{q}}$ and $\mathbf{q}$ after a certain time step, and this procedure is repeated as long as necessary. Since numerical integration provides only an approximate solution, it is clear that one can expect violations of the constraints that grow with time.

Various methods of constraint violation stabilization were presented. A penalty form of the constraints equations was used to achieve stabilization (Park and Chiou, 1988). One of the most successful, easy to apply and reliable methods was presented by Baumgarte (1972). This method can be looked upon as an extension of feedback control theory. The principle of the method is to damp out the acceleration constraint violations of Eq. (10a) by feeding back the violations of the constraints (Eq. (4)) and velocity constraints ($\dot{\Phi}_k$). Thus Eq. (10a) is replaced by

$$\Phi_a = \alpha\ddot{\Phi} + \beta\dot{\Phi} + \gamma\Phi = 0 \quad \alpha > 0; \quad \beta, \gamma \geq 0. \tag{12}$$

$\ddot{\Phi}$ is defined by Eqs. (10a, b) while $\dot{\Phi}$ is given by

$$\dot{\Phi} = \Phi_q \dot{\mathbf{q}} + \Phi_t. \tag{13}$$

Equation (11) is now replaced by (choosing $\alpha = 1$)

$$\begin{bmatrix} \mathbf{M} & \Phi_q^T \\ \Phi_q & 0 \end{bmatrix} \begin{bmatrix} \ddot{\mathbf{q}} \\ \boldsymbol{\lambda} \end{bmatrix} = \begin{bmatrix} \mathbf{g} \\ \mathbf{d} \end{bmatrix} \tag{14}$$

where

$$\mathbf{d} = \mathbf{c} - \beta\dot{\Phi} - \gamma\Phi. \tag{15}$$

In a later paper Baumgarte (1983) recommended a modified integro-differential form of Eq. (12) for holonomic constraints. Bayo et al. (1988) present a modified Lagrangian formulation that is based on Hamilton's Principle. Constraint equations are taken into account using the penalty approach. The form of these constraint equations is similar to the form proposed by Baumgarte's Stabilization Method (1972).

One of the problems associated with Baumgarte's method involves the determination of the values of β and γ. This problem is especially crucial in the case of employing variable step-size/order integration algorithms. Chang and Nikravesh (1985) presented an adaptive mechanism for determining the parameters.

The discussion above was confined, for the sake of simplicity, to the case of holonomic constraints. Nevertheless, usually the above described methods are also applicable, with certain variations (see above references), to nonholonomic constraints.

The purpose of the present paper is to present and investigate a new formulation of the Lagrange method for constrained dynamic systems. This formulation is based on replacing the actual constraints, Eq. (4), by the modified acceleration constraints as presented by Eq. (12). Unlike Baumgarte's approach, the modified constraints are substituted into the Lagrangian, Eq. (6). The new Lagrangian equations of motion are ordinary differential equations in contrast to the differential/algebraic Eqs. (4), (8). Well-established methods of solving ordinary differential equations are directly applied to the solution of these equations. A few examples of using the new formulation will be presented. This formulation can be applied to both, holonomic and nonholonomic constraints.

2 Description of the Method

2.1 Holonomic Constraints. Consider the system that was described in the previous section. This system is modeled by n generalized coordinates (Eq. (1)) and there exist m holonomic constraints (Eq. (4)) between the coordinates.

Let us replace the vector of constraints Φ by its modified form Φ_a, as defined by Eq. (12). It is clear that if the initial conditions, Eq. (9), are feasible and an exact integration is assumed, then the replacement of Eq. (4) by Eq. (12) does not alter the solution.

Now the Lagrangian of the constrained system is defined:

$$L_d(\ddot{\mathbf{q}}, \dot{\mathbf{q}}, \mathbf{q}) = T - V - \Phi_a^T \boldsymbol{\lambda}_d. \tag{16}$$

Application of the variational principles in this case (see Appendix or Gelfand, 1963) imply

$$-\frac{d^2}{dt^2}\left(\frac{\partial L_d}{\partial \ddot{q}_i}\right) + \frac{d}{dt}\left(\frac{\partial L_d}{\partial \dot{q}_i}\right) - \frac{\partial L_d}{\partial q_i} = Q_i \quad i = 1, \ldots n. \tag{17}$$

Substitution of Eq. (16) into Eq. (17) results in a system of n equations, that together with the m constraints form the following $(n + m)$ coupled equations (see also Eqs. (10a, b), (13)):

$$\begin{bmatrix} \mathbf{M} & \alpha\Phi_q^T \\ \alpha\Phi_q & 0 \end{bmatrix} \begin{bmatrix} \ddot{\mathbf{q}} \\ \ddot{\boldsymbol{\lambda}}_d \end{bmatrix} = \begin{bmatrix} \mathbf{h} \\ \mathbf{d} \end{bmatrix} \tag{18}$$

where

$$\mathbf{h} = \mathbf{g} + \Phi_q^T(\beta\dot{\boldsymbol{\lambda}}_d - \gamma\boldsymbol{\lambda}_d). \tag{19}$$

Equation (18) is totally different from Eq. (14). While there are certain differences between the right side of both equations, the important differences appear on the left side. While Eq. (14) represents a system of ordinary differential equations (ODE) coupled with algebraic equations, Eq. (18) represents a system of ODE alone.

The system of Eq. (18) can be integrated directly by using any algorithm suitable for a system of ordinary differential equations. In addition to the initial conditions of Eq. (9), it is necessary to add conditions on $\boldsymbol{\lambda}_d$ and $\dot{\boldsymbol{\lambda}}_d$. The initial conditions of $\boldsymbol{\lambda}_d$ depend on the nature of the problem. In most of the cases where the initial condition involves a certain equilibrium, $\boldsymbol{\lambda}_d$ and $\dot{\boldsymbol{\lambda}}_d$ are obtained after solving this equilibrium (see examples in the next section).

2.2 Nonholonomic Constraints. It is assumed that the system is subjected to l nonholonomic constraints of the form

$$\psi_k(\dot{\mathbf{q}}, \mathbf{q}, t) = 0 \quad 1 \leq k \leq l. \tag{20}$$

Downloaded 04 May 2010 to 171.66.16.34. Redistribution subject to ASME license or copyright; see http://www.asme.org/terms/Terms_Use.cfm

The constraint vector $\boldsymbol{\psi}$ is defined as

$$\boldsymbol{\psi} = [\psi_1, \ldots \psi_l]^T. \tag{21}$$

The modified constraint vector in this case is (compare to Eq. (12))

$$\boldsymbol{\psi}_a = \delta\dot{\boldsymbol{\psi}} + \epsilon\boldsymbol{\psi} \tag{22}$$

where

$$\dot{\boldsymbol{\psi}} = \boldsymbol{\psi}_q\ddot{\mathbf{q}} + \boldsymbol{\psi}_q\dot{\mathbf{q}} + \boldsymbol{\psi}_t. \tag{23}$$

$\boldsymbol{\psi}_{\dot{q}}$ is analogous to $\boldsymbol{\psi}_q$, $\boldsymbol{\psi}_{\dot{q}} \equiv \partial\boldsymbol{\psi}/\partial\dot{\mathbf{q}}$. δ and ϵ are coefficients similar to α, β, γ in Eq. (12).

The Lagrangian of the constrained system is now

$$L_e = T - V - \boldsymbol{\psi}_a^T\boldsymbol{\lambda}_e. \tag{24}$$

Replacing L_d in Eq. (17) by L_e, and performing the differentiation, imply

$$\begin{bmatrix} \mathbf{M}_e & \delta\boldsymbol{\psi}_q^T \\ \delta\boldsymbol{\psi}_{\dot{q}} & 0 \end{bmatrix} \begin{Bmatrix} \ddot{\mathbf{q}} \\ \ddot{\boldsymbol{\lambda}}_e \end{Bmatrix} = \begin{Bmatrix} \mathbf{h}_e \\ \mathbf{d}_e \end{Bmatrix} \tag{25}$$

where

$$\mathbf{M}_e = \mathbf{M} + \sum_{k=1}^{l} (\delta\dot{\lambda}_k - \epsilon\lambda_k)\boldsymbol{\psi}_{k,\dot{q}\dot{q}} \tag{26a}$$

$$\mathbf{h}_e = \mathbf{g} - \sum_{k=1}^{l} (\delta\dot{\lambda}_k - \epsilon\lambda_k)\boldsymbol{\psi}_{k,\dot{q}q}\dot{\mathbf{q}} - (\boldsymbol{\psi}_{\dot{q}t}^T - \boldsymbol{\psi}_q^T)(\delta\dot{\boldsymbol{\lambda}}_e - \epsilon\boldsymbol{\lambda}_e) + \epsilon\boldsymbol{\psi}_{\dot{q}}^T\dot{\boldsymbol{\lambda}}_e \tag{26b}$$

$$\mathbf{d}_e = -\delta\boldsymbol{\psi}_q\dot{\mathbf{q}} - \delta\boldsymbol{\psi}_t - \epsilon\boldsymbol{\psi} \tag{26c}$$

and

$$\boldsymbol{\psi}_{k,\dot{q}\dot{q}} = \begin{bmatrix} \dfrac{\partial\psi_k}{\partial\dot{q}_1\partial\dot{q}_1} & \cdots & \dfrac{\partial\psi_k}{\partial\dot{q}_1\partial\dot{q}_n} \\ \vdots & & \\ \dfrac{\partial\psi_k}{\partial\dot{q}_n\partial\dot{q}_1} & \cdots & \dfrac{\partial\psi_k}{\partial\dot{q}_n\partial\dot{q}_n} \end{bmatrix} \tag{27a}$$

$$\psi_{k,\dot{q}q} = \begin{bmatrix} \dfrac{\partial\psi_k}{\partial\dot{q}_1\partial q_1} & \cdots & \dfrac{\partial\psi_k}{\partial\dot{q}_1\partial q_n} \\ \vdots & & \\ \dfrac{\partial\psi_k}{\partial\dot{q}_n\partial q_1} & \cdots & \dfrac{\partial\psi_k}{\partial\dot{q}_n\partial q_n} \end{bmatrix}. \tag{27b}$$

2.3 The Constraints Forces. The constraints can be replaced by equivalent constraints forces. If Q_{ci} is the equivalent generalized constraints force associated with the generalized coordinate q_i, then the Lagrangian equations of motion of the system become (see Eq. (3)):

$$\frac{d}{dt}\left(\frac{\partial L}{\partial\dot{q}_i}\right) - \frac{\partial L}{\partial q_i} = Q_i + Q_{ci}. \tag{28}$$

If Eq. (28) is compared with Eq. (17) for the case of holonomic constraints, it is clear that

$$Q_{ci} = \frac{d^2}{dt^2}\left(\frac{\partial L_a'}{\partial\ddot{q}_i}\right) - \frac{d}{dt}\left(\frac{\partial L_a'}{\partial\dot{q}_i}\right) + \frac{\partial L_a'}{\partial q_i} \tag{29}$$

where

$$L_a' = -\boldsymbol{\Phi}_a^T\boldsymbol{\lambda}_d. \tag{30}$$

Substitution of Eq. (12) into Eq. (30) and then into Eq. (29) results in

$$\mathbf{Q}_c = -\boldsymbol{\Phi}_q^T(\alpha\ddot{\boldsymbol{\lambda}}_d - \beta\dot{\boldsymbol{\lambda}}_d + \gamma\boldsymbol{\lambda}_d) \tag{31}$$

where $\mathbf{Q}_c$ is the vector of constraint forces

$$\{\mathbf{Q}_c\}^T = [\mathbf{Q}_{c1}, Q_{c2}, \ldots, Q_{cm}]. \tag{32}$$

It is interesting to note that the constraint forces are not only functions of $\boldsymbol{\lambda}_d$, but also of its first and second derivatives with respect to time. This is different from the case of using L_c (Eq. (6)) where

$$\mathbf{Q}_c = -\boldsymbol{\Phi}_q^T\boldsymbol{\lambda}. \tag{33}$$

Furthermore, based on Eq. (31) and in light of Eq. (33), one can define

$$\boldsymbol{\lambda}_b = \alpha\ddot{\boldsymbol{\lambda}}_d - \beta\dot{\boldsymbol{\lambda}}_d + \gamma\boldsymbol{\lambda}_d. \tag{34}$$

Based on the last definition, Eq. (18) can be written as follows:

$$\begin{bmatrix} \mathbf{M} & \boldsymbol{\Phi}_q^T \\ \boldsymbol{\Phi}_q & 0 \end{bmatrix} \begin{bmatrix} \ddot{\mathbf{q}} \\ \boldsymbol{\lambda}_b \end{bmatrix} = \begin{bmatrix} \mathbf{g} \\ \mathbf{d} \end{bmatrix}. \tag{35}$$

Equation (35) is identical to Eq. (14) and represents the Baumgarte approach.

In the case of nonholonomic constraints, L_a in Eq. (29) is replaced by L_b where

$$L_b' = -\boldsymbol{\psi}_a^T\boldsymbol{\lambda}_e. \tag{36}$$

$\boldsymbol{\psi}_a$ is defined by Eq. (22). This replacement results in the following expression for the vector of constraint forces:

$$\mathbf{Q}_c = -\boldsymbol{\psi}_{\dot{q}}^T(\delta\ddot{\boldsymbol{\lambda}}_e - \epsilon\dot{\boldsymbol{\lambda}}_e) - (\boldsymbol{\psi}_{\dot{q}t}^T - \boldsymbol{\psi}_q^T)(\delta\dot{\boldsymbol{\lambda}}_e - \epsilon\boldsymbol{\lambda}_e) - \sum_{k=1}^{l} (\boldsymbol{\psi}_{k,\dot{q}\dot{q}}\ddot{\mathbf{q}} + \boldsymbol{\psi}_{k,\dot{q}q}\dot{\mathbf{q}})(\delta\dot{\lambda}_k - \epsilon\lambda_k). \tag{37}$$

3 Examples

3.1 General Description of the Examples. The examples that will be considered include a "chain" of rigid rods that are connected tip to root. In Fig. 1 two consequent rods are presented: rod $(j-1)$ and rod (j). A rod coordinate system (x^j, y^j, z^j) is attached to the root of each rod. x^j coincides with the rod axis. X, Y, Z form an inertial system of coordinates. Finite rotations are allowed between the tip and root of consequent rods. These rotations are restrained by three linear torsional springs about the axes x^j, y^j, and z^j.

The spatial kinematics of each rod is described by seven generalized coordinates: three translational components and four Euler parameters that describe finite rotations (see Shepperd, 1978).

The relative rotation between the tip of the rod $(j-1)$ and the root of the rod j represents the elasticity of the system. These rotations will be described in the present case by three Euler angles: $\theta_x^{j,j-1}$, $\theta_y^{j,j-1}$, $\theta_z^{j,j-1}$.

The constraints of the system describe the nature of the connections between the tip and the root of consequent rods. Three

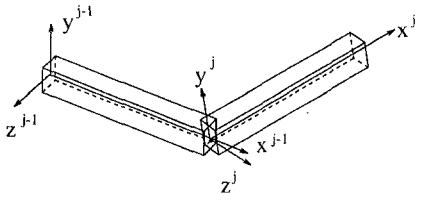


Fig. 1 Description of two consequent rods: rod $(j-1)$ and rod (j)

Downloaded 04 May 2010 to 171.66.16.34. Redistribution subject to ASME license or copyright; see http://www.asme.org/terms/Terms_Use.cfm

translational and four rotational constraint equations can be written for each connection $(j-1, j)$.

A detailed description of the above-mentioned rods system (equations of motion, constraint equations) can be found in Rosen and Edelstein (1995).

3.2 The Case of a Single Rod. In this case $j = 1$. Thus the vector of generalized coordinates includes ten elements (three translational coordinates, four Euler parameters and three Euler angles). Since there are seven constraints the system has three degrees-of-freedom. It is convenient to refer to $\theta_x^{1,0}$, $\theta_y^{1,0}$, and $\theta_z^{1,0}$ as those three degrees-of-freedom.

The rod is uniform and its length is $l^1 = 0.508$ m. The mass per unit length is 0.113 kg/m. The cross-sectional moments of inertia are

$$I_{yy} = 1521 \cdot 10^{-9}\ \text{kg}\cdot\text{m} \quad I_{zz} = 95.1 \cdot 10^{-9}\ \text{kg}\cdot\text{m}.$$

The stiffnesses of the torsional springs at the root are

$$k_y^1 = k_z^1 = 20\text{N}\cdot\text{m}; \quad k_x^1 = 2 \cdot 10^{-3}\ \text{N}\cdot\text{m}.$$

The initial conditions are

$$\theta_x^{1,0} = \theta_y^{1,0} = \theta_z^{1,0} = 0.$$

An axial compressive concentrated force, $P_x^1(t)$, is applied at the tip of the rod (see Fig. 2):

$$P_x^1(t) = \begin{cases} -P \sin \dfrac{\pi}{0.8} t, & t \le 0.4 \text{ sec} \\ -P, & t \ge 0.4 \text{ sec} \end{cases}$$

$$P_y^1 - P_z^1 = 0.$$

If the applied force P_x^1 is less than the value of the critical buckling force (in the present case $(P_{cr} = (k_y/l))$, the dynamic response of the system is zero. If $|P_x^1| \ge P_{cr}$ and a very small component of force in the z-direction is applied, the exact response of the rod includes only the angle $\theta_y^{1,0}$. The influence of the disturbance force (in the z-direction) on the phenomenon is negligible.

The (exact) equation of motion in this case becomes

$$\frac{m(l^1)^2}{3} \ddot{\theta}_y^{1,0} + k_y^1 \theta_y^{1,0} = -P_x^1(t) \cdot l^1 \cdot \sin \theta_y^{1,0}. \quad (38)$$

The exact expression for the lateral component of the constraint force at the rod root (in the Z-direction, see Fig. 2), F_c^z, is

$$F_c^z = \frac{m(l^1)^2}{2} [(\dot{\theta}_y^{1,0})^2 \cdot \sin \theta_y^{1,0} - \ddot{\theta}_y^{1,0} \cdot \cos \theta_y^{1,0}]. \quad (39)$$

The system response ($\theta_y^{1,0}$ and F_c^z) will be calculated using three different methods:

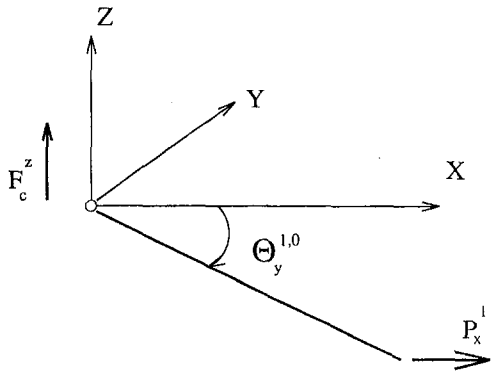


Fig. 2 A single-rod system

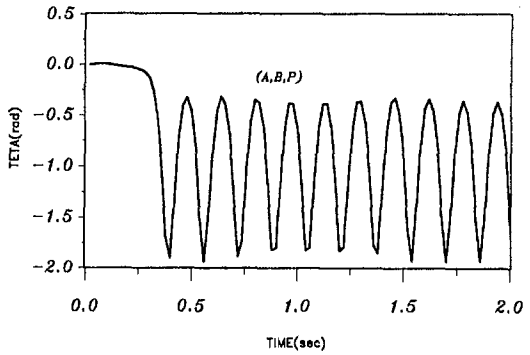


Fig. 3 A single rod system—the rotation $\theta_y^{1,0}$ as a function of time: *A*—"Accurate," *B*—Baumgarte, *P*—Present method

(a) Direct integration of Eq. (38) and substitution into Eq. (39) in order to calculate F_c^z. This solution will be referred to as "accurate" and will be used to assess the accuracy of the other methods.

(b) Baumgarte (stabilization) method—The 17 equations of the system, Eqs. (14), are used to calculate $\ddot{\mathbf{q}}$ and $\boldsymbol{\lambda}$, then direct integration of $\mathbf{q}$ is carried out. The reaction force F_c^z is calculated using Eq. (33).

(c) The present formulation—Direct integration of Eq. (18). The reaction force is calculated by using Eq. (31). When the present formulation is used initial conditions on $\boldsymbol{\lambda}$ and $\dot{\boldsymbol{\lambda}}$ are also required. Since the system is initially at rest (for $t <$ 0 sec) it is clear that $\dot{\boldsymbol{\lambda}}$ is initially zero. $\boldsymbol{\lambda}$ itself is obtained by solving the static equilibrium equations (Eq. (18) when $\dot{\mathbf{q}} = \ddot{\mathbf{q}} = \dot{\boldsymbol{\lambda}} = \ddot{\boldsymbol{\lambda}} = 0$).

For comparison purposes an identical integration scheme will be used in all the examples that will be presented. It will be an Adam's integration scheme (NAG FORTRAN Library, 1991). For all examples α, β, γ parameters have been chosen as (they are fixed through the entire analysis)

$$\alpha = 1, \quad \beta = 0, \quad \gamma = 10{,}000.$$

Results of an investigation of various numerical aspects of the new formulation (influences of values of α, β, γ, comparison of the CPU time required for integration and the development of the errors) can be found in Rosen and Edelstein, (1994).

It is clear from the constraint equations (Eq. (12)) that increasing γ leads to a higher accuracy of the constraints ($\boldsymbol{\Phi} = 0$). On the other hand, an increase of γ stiffens the equations of motion and thus may cause difficulties in the numerical integration of the equations (increasing the integration time, convergence problems; see, for example, Ascher and Petzold, 1993).

Numerical experiments that were performed by the authors (Rosen and Edelstein, 1994) show that if the parameter $\omega_\gamma = \sqrt{\gamma/\alpha}$ is chosen close to the first frequencies of the investigated system, it gives good accuracy in the system constraints and does not cause stiffness problems. The first natural frequency of the rod systems investigated in this paper is about $60 \div 70$ rad/sec. It has been shown (see Rosen and Edelstein, 1994) that choosing a nonzero value of β, results in only small improvements in the constraint accuracy, but increases CPU time.

The angular response of the system ($\theta_y^{1,0}$) when the axial load amplitude is $P = 55$N (post-buckling behavior), as calculated by the three methods, is shown in Fig. 3. Practically the results of all three methods coincide.

The lateral component of the reaction force at the root joint, F_c^z, as a function of time, that is obtained by using the three methods, is investigated next. The results of the three methods during the first half-second ($0 \le t \le 0.5$ sec) are practically identical. Then deviations between the three methods appear and increase with time. For $0.5 \le t \le 1.0$ the deviations are

Downloaded 04 May 2010 to 171.66.16.34. Redistribution subject to ASME license or copyright; see http://www.asme.org/terms/Terms_Use.cfm

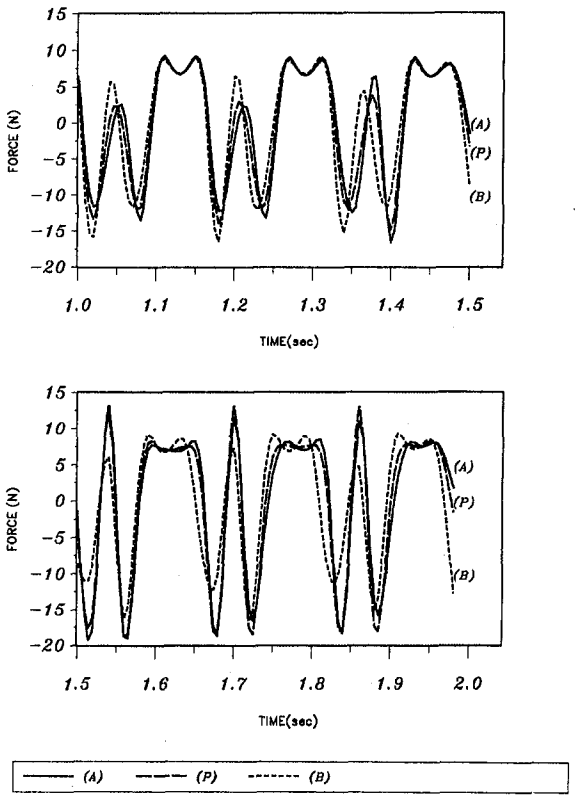


Fig. 4 A single rod system—the lateral component of the reaction force at the root joint, F_c^z, as a function of time: *A*—"Accurate," *B*—Baumgarte, *P*—Present method

still relatively small and thus are not shown here. Results for $1.0 \leq t < 1.5$ sec and $1.5 \leq t < 2.0$ sec are shown in Fig. 4. During the next second of response ($1 \text{ sec} < t \leq 2$ sec) the Baumgarte method exhibits significant deviations from the exact results, concerning amplitude and phase, while the results of the present method exhibit close agreement with the accurate results.

Thus it can be concluded that while the Baumgarte method and the present method practically give the identical accurate results for the angular response of the single-rod system, increasing deviations appear in the calculation of the constraint force. The results of the present method exhibit clear superiority over the results of the Baumgarte method.

3.3 The Case of Two Rods. In this case two identical rods (see Fig. 5) are connected such that in the unloaded case their axes lie along a straight line. This system is described by 20 generalized coordinates and 14 constraints. Thus there are

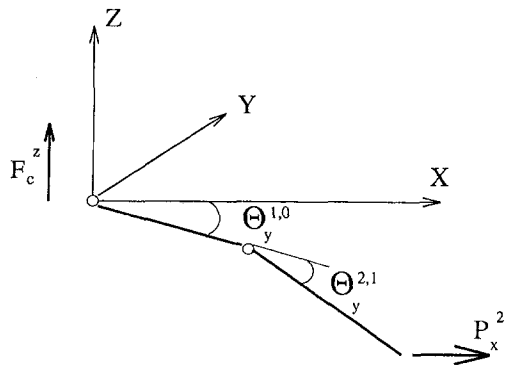


Fig. 5 Two-rods system

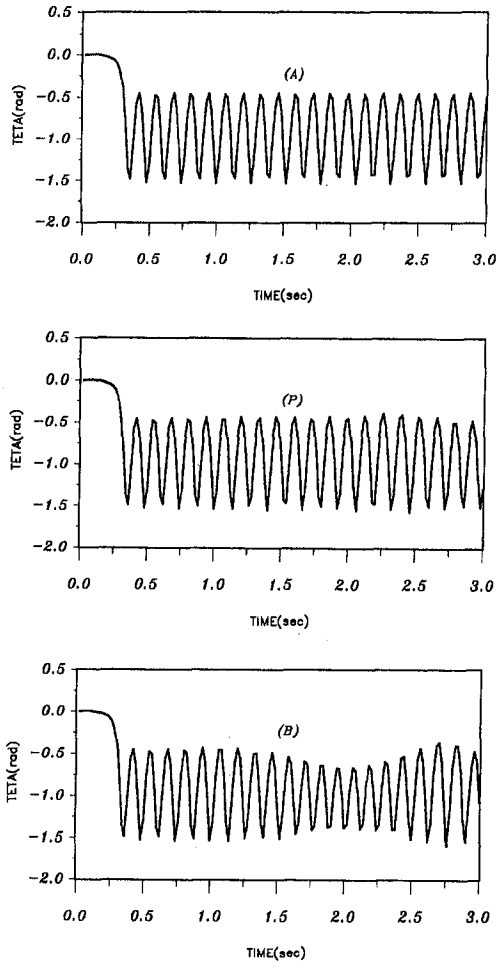


Fig. 6 Two-rods system—the rotation $\theta_y^{1,0}$ as a function of time: *A*—"Accurate," *B*—Baumgarte, *P*—Present method

six degrees-of-freedom. The components of the cross-sectional moments of inertia of the rods are uniform and identical to those of the single rod of subsection 3.2. The mass per unit length of each rod is 0.113 kg, while its length is 0.254 m. The flexibility in the joints—about the x, y, and z-axes—is identical to the appropriate flexibility in the example of a single rod in Subsection 3.2.

The system is loaded again by a compressive axial concentrated force $P_x^2(t)$ (see Fig. 5) at the tip of the second rod, in the same manner as in the single rod example. Similar to the single rod case, a very small lateral disturbance force, in the z-direction, is also applied. Its influence is negligible.

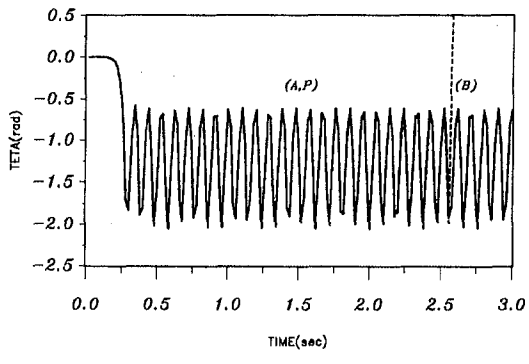


Fig. 7 Two-rods system—the rotation $\theta_y^{1,0}$ as a function of time: *A*—"Accurate," *B*—Baumgarte, *P*—Present method

Downloaded 04 May 2010 to 171.66.16.34. Redistribution subject to ASME license or copyright; see http://www.asme.org/terms/Terms_Use.cfm

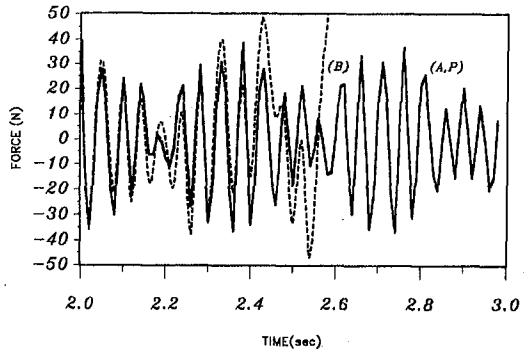


Fig. 8 Two-rods system—F_c^z as a function of time: *A*—"Accurate," *B*—Baumgarte, *P*—Present method

The exact response of the system includes two degrees-of-freedom—θ_y^1 and θ_y^2. Again three methods are used: accurate approach where two exact equations are integrated numerically and exact expression for the constraint force is used, the Baumgarte method and the present method. In Fig. 6 the angle θ_y^1 is presented, as a function of time, in the case of an axial load amplitude $P = 45$N (post-buckling behavior). Results of the three methods are compared. The present method exhibits very good agreement with the accurate method while the Baumgarte method has stability problems and as a result exhibits significant changes in the amplitude of $\theta_y^{1.0}$ during the time.

Figure 7 represents results of $\theta_y^{1.0}$ as a function of time in the case of an axial load amplitude of $P = 60$N. During the first two seconds, both methods (Baumgarte an the present method) exhibit results that are practically identical to the accurate solution. When $t = 2.56$ sec Baumgarte integration fails, while the present method continues to give results that are identical to the accurate results. The constraint force component F_c^z at the root joint, as a function of time, is shown in Fig. 8 ($P = 60$N). During the first two seconds (that are not presented in the figure) all three methods exhibit identical results. For $t > 2$ sec there appear increasing deviations between the Baumgarte method and the "accurate" results, while the results of the present method coincide with the "accurate" results. The failure of the Baumgarte method is clearly seen at $t = 2.56$ sec.

The superiority of the present method, as compared to the Baumgarte method, is shown again.

4 Conclusions

The method of Lagrange multipliers is very useful in the solution of dynamic problems of constrained dynamic systems. This method results in a system of differential/algebraic equations. In order to solve these equations it is common to differentiate the constraint equations. This differentiation leads to a system that can be solved by well-established methods of integration of ordinary differential equations.

Since numerical integration results in integration errors, violations of the constraints accompany the calculations. In order to cope with these violations, methods of constraint stabilization have been developed and applied during the years. These methods, that in many cases originates from modern control theory, can be considered as "artificial" correction and do not emerge from a formal consistent variational approach, as is the classical approach of Lagrange multipliers.

The present paper presents a new formulation of the Lagrange approach of solving the dynamic behavior of constrained systems. This formulation, that is consistent from a variational point of view, results in a system of ordinary differential equations that also include second derivatives of the Lagrange multipliers. This formulation can be applied to holonomic or nonholonomic constraints.

Comparisons of the performance of the present formulation with Baumgarte's method, that is one of the most successful and popular stabilization methods, show that for the examples shown the present method exhibits better efficiency and stability than Baumgarte's methods. It should be pointed out that in other cases that were investigated and are not reported here, the present formulation gave identical results to Baumgarte's method. It seems that the advantages of the present formulation are especially important in cases where the applied forces cause sharp nonlinear changes in velocities and accelerations of the system, as in the case of sudden buckling.

The present paper concentrated on presenting the new formulation and exhibit its basic capabilities. Yet further investigation is required in order to study the characteristics of this new formulation (in comparison to other methods) and the benefits of a consistent variational formulation.

References

Agrawal, O. P., 1987, "Dynamic Analysis of Multi-body Systems Using Tangent Coordinates," *Proc. 7th World Congress on the Theory of Machines and Mechanisms,* Vol. 1, pp. 533–536.

Ascher, U., and Petzold, L., 1993, "Stability of Computational Methods for Constrained Dynamic Systems," *SIAM J. SISC,* Vol. 14, pp. 95–120.

Baumgarte, J., 1972, "Stabilization of Constraints and Integrals of Motion in Dynamical Systems," *Computer Methods in Applied Mechanics and Engineering,* Vol. 1, pp. 1–16.

Baumgarte, J. W., 1983, "A New Method of Stabilization for Holonomic Constraints," ASME JOURNAL OF APPLIED MECHANICS, Vol. 50, pp. 869–870.

Bayo, E., Garcia de Jalon, J., and Serna, M. A., 1988, "A Modified Lagrangian Formulation for the Dynamic Analysis of Constrained Mechanical Systems," *Computer Methods in Applied Mechanics and Engineering,* Vol. 17, pp. 183–195.

Chang, C. O., and Nikravesh, P. E., 1985, "An Adaptive Constraint Violation Stabilization Method for Dynamic Analysis of Mechanical Systems," ASME *Journal of Mechanisms, Transmissions and Automation in Design,* Vol. 107, pp. 488–492.

Garcia de Jalon, J., Avello, A., and Jimenez, J. M., 1987, "Basis for the Null Space for the Jacobian Matrix of Constrained Multibody System," *Proc. 7th World Congress on the Theory of Machines and Mechanisms,* Vol. 1, pp. 501–504.

Garcia de Jalon, J., and Bayo, E., 1993, *Kinematic and Dynamic Simulation of Multibody Systems,* Springer-Verlag, New York.

Gear, C. W., 1984, "Differential-Algebraic Equations," *Computer Aided Analysis and Optimization of Mechanical System Dynamics,* E. J. Haug, ed., Springer-Verlag, Berlin, pp. 323–334.

Gelfand, I. M., and Fomin, S. V., 1963, *Calculus of Variations,* Prentice-Hall, Englewood Cliffs, NJ.

Kim, S. S., and Vanderploeg, M. J., 1986, "QR Decomposition for State Space Representation of Constrained Mechanical Dynamic Systems," ASME *Journal of Mechanisms, Transmissions, and Automation in Design,* Vol. 108, pp. 183–187.

Lanczos, C., 1949, *The Variational Principles of Mechanics,* University of Toronto Press, Toronto, Canada.

Mani, N. K., Haug, E. J., and Atkinson, K. E., 1985, "Application of Singular Value Decomposition for Analysis of Mechanical System Dynamics," ASME *Journal of Mechanisms, Transmissions, and Automation in Design,* Vol. 107, pp. 82–87.

NAG FORTRAN Library, 1991, Mark 15 Chapter DO2—Ordinary Differential Equations.

Park, K. C., and Chiou, J. C., 1988, "Stabilization of Computational Procedures for Constrained Dynamical Systems," *AIAA J. of Guidance and Control,* Vol. 11, pp. 365–370.

Petzold, L., 1982, "Differential/Algebraic Equations are not ODEs," *SIAM J. of Scientific Statistical Computation,* Vol. 13, pp. 367–384.

Rosen, A., and Edelstein, E., 1994, "Investigation of a New Formulation of the Lagrange Method for Constrained Dynamic Systems," *Proceedings 34th Israel Annual Conference on Aerospace Sciences,* Feb. 16–17, 1994, Israel, pp. 31–41.

Rosen, E., and Edelstein, E., 1995, "A New Formulation of the Lagrange Method for Constrained Dynamic Systems," TAE Report No. 755, Faculty of Aerospace Engineering, Technion, Haifa, Israel.

Shepperd, S. W., 1978, "Quaternion from Rotation Matrix," *AIAA J. of Guidance and Control,* Vol. 1, No. 3, pp. 223–224.

Wehage, R. A., and Haug, E. J., 1982, "Generalized Coordinate Partitioning for Dimension Reduction in Analysis of Constrained Dynamic Systems," ASME *Journal of Mechanical Design,* Vol. 104, pp. 247–255.

Appendix

Hamilton's Principle is presented in the next equation:

$$A = \int_{t_1}^{t_2} L dt + \int_{t_1}^{t_2} W_{nc} dt. \qquad (A1)$$

L is the system Lagrangian. W_{nc} is the work done by nonconservative forces.

Downloaded 04 May 2010 to 171.66.16.34. Redistribution subject to ASME license or copyright; see http://www.asme.org/terms/Terms_Use.cfm

For constrained dynamic systems Hamilton's Principle can be generalized by means of the Lagrange multipliers method (see, for example, Garcia de Jalon and Bayo, 1993). Accordingly, the action A is augmented with the additional term

$$A = \int_{t_1}^{t_2} L dt + \int_{t_1}^{t_2} W_{nc} dt - \int_{t_1}^{t_2} \Phi_a^T \boldsymbol{\lambda} dt \qquad \text{(A2)}$$

where

$\boldsymbol{\lambda}$–vector of Lagrange multipliers

Φ_a–vector of constraints.

The variation of the action vanishes, thus

$$\delta A = \int_{t_1}^{t_2} \delta L dt + \int_{t_1}^{t_2} \delta W_{nc} dt - \int_{t_1}^{t_2} \delta \Phi_a^T \boldsymbol{\lambda} dt = 0. \qquad \text{(A3)}$$

The constraint vector of the system is chosen to be

$$\Phi_a = \alpha \ddot{\Phi} + \beta \dot{\Phi} + \gamma \Phi \qquad \text{(A4)}$$

where Φ is the vector of holonomic constraints. In general $\Phi_a = \Phi_a(\ddot{q}, \dot{q}, q, t)$.

For simplicity the following derivation will be confined to the case of scleronomic constraints, $\Phi_a = \Phi_a(\ddot{q}, \dot{q}, q)$. Similar derivations can be applied to the reonomic constraints.

The variation of the vector Φ_a becomes

$$\delta \Phi_a = \delta \ddot{\mathbf{q}}^T \frac{\partial \Phi_a}{\partial \ddot{q}} + \delta \dot{\mathbf{q}}^T \frac{\partial \Phi_a}{\partial \dot{\mathbf{q}}} + \delta \mathbf{q}^T \frac{\partial \Phi_a}{\partial \mathbf{q}} \qquad \text{(A5)}$$

while the variation of the system Lagrangian is

$$\delta L = \delta T - \delta V \qquad \text{(A6)}$$

where

$$\delta T = \delta \dot{\mathbf{q}}^T \frac{\partial T}{\partial \dot{\mathbf{q}}} + \delta \mathbf{q}^T \frac{\partial T}{\partial \mathbf{q}} \qquad \text{(A7)}$$

$$\delta V = \delta \mathbf{q}^T \frac{\partial V}{\partial \mathbf{q}} \qquad \text{(A8)}$$

$$\delta W_{nc} = \delta \mathbf{q}^T \mathbf{Q}_{\text{ext}}. \qquad \text{(A9)}$$

$\mathbf{Q}_{\text{ext}}$ represents the external nonconservative forces.

The application of Hamilton's Principle defined by Eq. (A3), leads to the following expression:

$$\int_{t_1}^{t_2} \left\{ \delta \mathbf{q}^T \left[\frac{\partial T}{\partial \mathbf{q}} - \frac{\partial V}{\partial \mathbf{q}} + \mathbf{Q}_{\text{ext}} - \left(\frac{\partial \Phi_a}{\partial \mathbf{q}} \right)^T \boldsymbol{\lambda} \right] + \delta \dot{\mathbf{q}}^T \left[\frac{\partial T}{\partial \dot{\mathbf{q}}} - \left(\frac{\partial \Phi_a}{\partial \dot{\mathbf{q}}} \right)^T \boldsymbol{\lambda} \right] - \delta \ddot{\mathbf{q}}^T \left(\frac{\partial \Phi_a}{\partial \ddot{\mathbf{q}}} \right)^T \boldsymbol{\lambda} \right\} = 0. \qquad \text{(A10)}$$

The last two terms can be integrated by parts to yield

$$\int_{t_1}^{t_2} \left\{ \delta \dot{\mathbf{q}}^T \left[\frac{\partial T}{\partial \dot{\mathbf{q}}} - \left(\frac{\partial \Phi_a}{\partial \mathbf{q}} \right)^T \boldsymbol{\lambda} \right] = \delta \mathbf{q}^T \left[\frac{\partial T}{\partial \dot{\mathbf{q}}} - \left(\frac{\partial \Phi_a}{\partial \dot{\mathbf{q}}} \right)^T \boldsymbol{\lambda} \right]_{t_1}^{t_2} - \int_{t_1}^{t_2} \delta \mathbf{q}^T \frac{d}{dt} \left[\frac{\partial T}{\partial \dot{\mathbf{q}}} - \left(\frac{\partial \Phi_a}{\partial \mathbf{q}} \right)^T \boldsymbol{\lambda} \right]. \qquad \text{(A11)}$$

The first two terms on the RHS vanishes because the motion is specified at the two ends, t_1 and t_2, therefore the variations there are zero: $\delta \mathbf{q}(t_1) = \delta \mathbf{q}(t_2) = 0$.

$$\int_{t_1}^{t_2} \delta \ddot{\mathbf{q}}^T \left(\frac{\partial \Phi_a}{\partial \ddot{\mathbf{q}}} \right)^T \boldsymbol{\lambda} dt$$

$$= \left[\delta \dot{\mathbf{q}}^T \left(\frac{\partial \Phi_a}{\partial \ddot{\mathbf{q}}} \right)^T \boldsymbol{\lambda} \right] \Big|_{t_1}^{t_2} - \int_{t_1}^{t_2} \delta \dot{\mathbf{q}}^T \frac{d}{dt} \left[\left(\frac{\partial \Phi_a}{\partial \ddot{\mathbf{q}}} \right) \cdot \boldsymbol{\lambda} \right] dt$$

$$= \left[\delta \dot{\mathbf{q}}^T \left(\frac{\partial \Phi_a}{\partial \ddot{\mathbf{q}}} \right)^T \boldsymbol{\lambda} \right] \Big|_{t_1}^{t_2} - \left[\delta \mathbf{q}^T \cdot \frac{d}{dt} \left(\left(\frac{\partial \Phi_a}{\partial \ddot{\mathbf{q}}} \right)^T \boldsymbol{\lambda} \right) \right] \Big|_{t_1}^{t_2} + \int_{t_1}^{t_2} \delta \mathbf{q}^T \frac{d^2}{dt^2} \left[\left(\frac{\partial \Phi_a}{\partial \ddot{\mathbf{q}}} \right)^T \boldsymbol{\lambda} \right] dt. \qquad \text{(A12)}$$

Since $\delta \dot{\mathbf{q}}(t_1) = \delta \dot{\mathbf{q}}(t_2) = 0$, Eq. (A10) can be written in the following form:

$$\int_{t_1}^{t_2} \delta \mathbf{q}^T \left\{ \frac{\partial T}{\partial \mathbf{q}} - \frac{\partial V}{\partial \mathbf{q}} + \mathbf{Q}_{\text{ext}} - \left(\frac{\partial \Phi_a}{\partial \mathbf{q}} \right)^T \boldsymbol{\lambda} - \frac{d}{dt} \left[\frac{\partial T}{\partial \dot{\mathbf{q}}} - \left(\frac{\partial \Phi_a}{\partial \dot{\mathbf{q}}} \right)^T \boldsymbol{\lambda} \right] - \frac{d^2}{dt^2} \left[\left(\frac{\partial \Phi_a}{\partial \ddot{\mathbf{q}}} \right) \boldsymbol{\lambda} \right]^T \right\} = 0. \qquad \text{(A13)}$$

The equation of motion becomes

$$\frac{d^2}{dt^2} \left[\left(\frac{\partial \Phi_a}{\partial \ddot{\mathbf{q}}} \right)^T \boldsymbol{\lambda} \right] + \frac{d}{dt} \left[\frac{\partial T}{\partial \dot{\mathbf{q}}} - \left(\frac{\partial \Phi_a}{\partial \dot{\mathbf{q}}} \right)^T \boldsymbol{\lambda} \right] - \frac{\partial T}{\partial \mathbf{q}} + \frac{\partial V}{\partial \mathbf{q}} + \left(\frac{\partial \Phi_a}{\partial \dot{\mathbf{q}}} \right)^T \boldsymbol{\lambda} = \mathbf{Q}_{\text{ext}}. \qquad \text{(A14)}$$

The last equation can be written in the form

$$-\frac{d^2}{dt^2} \left(\frac{\partial L_d}{\partial \ddot{\mathbf{q}}} \right) + \frac{d}{dt} \left(\frac{\partial L_d}{\partial \dot{\mathbf{q}}} \right) - \frac{\partial L_d}{\partial \mathbf{q}} = \mathbf{Q}_{\text{ext}} \qquad \text{(A15)}$$

where

$$L_d \triangleq T - V - \Phi_a^T \lambda. \qquad \text{(A16)}$$

Equation (A15) is identical to Eq. (17) in the text.

Downloaded 04 May 2010 to 171.66.16.34. Redistribution subject to ASME license or copyright; see http://www.asme.org/terms/Terms_Use.cfm

A Variable Sensitivity Displacement Interferometer With Application to Wave Propagation Experiments

H. D. Espinosa
Assistant Professor,
School of Aeronautics and Astronautics,
Purdue University,
West Lafayette, IN 47907-1282
Assoc. Mem. ASME

M. Mello
Research Engineer,
Division of Engineering,
Brown University,
Providence, RI 02912

Y. Xu
Research Associate,
School of Aeronautics and Astronautics,
Purdue University,
West Lafayette, IN 47907

The present paper introduces a variable sensitivity displacement interferometer (VSDI) used to monitor both normal and in-plane particle displacements in wave propagation experiments. The general system consists of two interferometers working in tandem. Normally reflected light is interfered with each of two symmetrically diffracted light beams generated by the specimen rear surface. In cases where the surface motion simultaneously exhibits both in-plane and normal displacements, the fringes represent a linear combination of the longitudinal and transverse components of motion. Decoupling of the normal and in-plane displacement histories may be achieved through a linear combination of the two VSDI records. Alternatively, it is always possible to decouple the components of motion by combining a VSDI record with an independent measurement of either component. Moreover, it is shown that in the case of pure normal motion, the VSDI system functions as a desensitized normal displacement interferometer (DNDI). Similarly, in situations involving purely in-plane motion, the VSDI is shown to function as a desensitized transverse displacement interferometer (DTDI). The DNDI and DTDI fringe sensitivities are in general shown to depend on the angle θ or equivalently, the frequency σ of a grating manufactured at the observation point and the order n *of the diffracted beams. The variable sensitivity feature of the VSDI greatly desensitizes normal displacement measurements and is particularly well suited for wave propagation studies in which normal particle velocities in excess of 100 m/s are generated. Experimental results are presented which demonstrate the application of this technique to monitoring particle motion histories in plate impact* recovery *experiments.*

1 Introduction

Laser interferometry has proven to be a highly reliable and accurate means for measuring particle motion in wave propagation experiments. Particle velocity histories were initially monitored in wave propagation experiments by means of a Normal Velocity Interferometer (NVI) developed by Barker and Hollenbach in 1965. In this technique, normally reflected laser light is collected and split into two separate beams which are subsequently interfered after traveling through different path lengths. The interferometer's sensitivity is a function of the delay time τ between the interfering beams, and the resulting fringe signal is related directly to changes in normal particle velocity.

In 1972 Barker and Hollenbach introduced a significantly improved NVI system termed VISAR (velocity interferometer for any reflecting surface). The VISAR was developed by using the wide angle Michelson interferometer (WAM) concept, resulting in an interferometer capable of velocity measurements from either a spectrally or diffusely reflecting specimen surface. Another improvement incorporated into the VISAR was the simultaneous monitoring of two fringe signals 90 deg out-of-phase. Quadrature coding is obtained by adding an eight-wave retardation plate and two polarizing beam splitters. It eliminates ambiguity in the sign of the acceleration and improves accuracy when data reduction is performed using the high resolution regions of the traces. In most VISAR systems, three signals are recorded, the two quadrature optical signals obtained from horizontally and vertically polarized components of light that differ in phase because of the retardation plate, plus the intensity monitoring signal used in data reduction. However, higher signal-to-noise ratios can be obtained by substructing the two s-polarized beams and the two p-polarized beams, both pairs 180 deg out-of-phase (Hemsing, 1978). This feature known as push-pull significantly reduces the noise introduced by incoherent light entering the interferometer. The VISAR has been successfully used to monitor normal particle velocity histories in shock wave experiments for over two decades and remains a principal tool of the field.

Another laser interferometer to emerge in that decade was the LDV or (Laser Doppler Velocimeter) developed by Sullivan et al., in 1974. The LDV can be used to monitor in-plane motion but does not lend itself to the simultaneous monitoring of normal motion. The need to measure both normal and in-plane displacements prompted the development of the TDI (transverse displacement interferometer) by Kim et al. in 1977. The TDI takes advantage of diffracted laser beams generated by a grating deposited or etched onto the specimen rear surface. In this technique, the 0th-order reflected beam is used to monitor longitudinal motion in a conventional way by means of an NVI, or NDI (normal displacement interferometer) while any pair of nth-order symmetrically diffracted beams may be interfered to obtain a direct measure of the transverse particle displacement history. The sensitivity of the TDI is given by $1/2\sigma n$ [mm/fringe] where σ is the grating frequency and n represents the order of the interfering diffracted beams.

Contributed by the Applied Mechanics Division of THE AMERICAN SOCIETY OF MECHANICAL ENGINEERS for publication in the ASME JOURNAL OF APPLIED MECHANICS.

Discussion on this paper should be addressed to the Technical Editor, Professor Lewis T. Wheeler, Department of Mechanical Engineering, University of Houston, Houston, TX 77204-4792, and will be accepted until four months after final publication of the paper itself in the ASME JOURNAL OF APPLIED MECHANICS.

Manuscript received by the ASME Applied Mechanics Division, May 11, 1995; final revision, April 22, 1996. Associate Technical Editor: W. N. Sharpe, Jr.

Copyright © 1997 by ASME

Downloaded 04 May 2010 to 171.66.16.34. Redistribution subject to ASME license or copyright; see http://www.asme.org/terms/Terms_Use.cfm

In 1979, Chhabildas et al. presented an alternative interferometric technique particularly suited for monitoring in-plane particle velocities in shock wave experiments. The technique employs two VISARs which monitor specific diffracted laser beams from a target surface. Since one or both of the resulting signals contains a linear combination of the normal and in-plane components of surface motion, it is always possible to decouple the transverse velocity from the normal velocity through a linear combination of the two fringe records.

Both techniques, the two VISAR and the NDI-TDI, have advantages and disadvantages. The combined NDI-TDI system has a much better resolution at low velocities, but requires the deposition of grids on the free surface of the target plate. On the other hand, the two VISAR technique provides velocity profiles directly without the need to differentiate displacement profiles. Although the two VISAR technique is simpler to use when optical windows are needed, it was shown by Espinosa (1996) that a combined NVI-TDI with window interferometer is feasible. In contrast to the embedded electromagnetic gauge technique to measure velocity histories, both of these interferometers can be applied to a wide variety of materials, metallic or nonmetallic. Moreover, the noncontact feature of the measurement system makes these techniques ideal for high-temperature studies of materials.

A common feature of all interferometers discussed in this section is that successful signal acquisition requires good fringe contrast during the time of the experiment. Contrast losses arise from two main causes, interferometer imperfections and target motion (displacement and tilt). These losses can be in general time varying. For instance, a beamsplitter that does not split light equally will produce a constant loss of contrast, while unevenly curved surfaces will produce a variable contrast change as a function of the light path in the interferometer. Target rotations that change the light path can be very detrimental to most interferometers. In this respect, interferometers that use scatter light from the target and fiber optics to transfer the laser light will minimize the loss in fringe contrast because the light path in the interferometer is fixed. Furthermore, even target rotations of a few milliradians will not result in signal loss in such systems. By contrast, standard interferometer set ups, without fiber optics, require tilts smaller than 1 milliradian to avoid a change in the light path that can offset the beam from the optical components of the interferometer. This feature is particularly relevant in Two-Dimensional and Three-Dimensional wave propagation problems, e.g., penetration experiments, in which significant surface rotations are expected at diagnostic points. Recently, Barker developed a VISAR with these features (Valyn VISAR User's Handbook, 1995).

2 Motivation

Need for a Desensitized Normal Displacement Interferometer. The development of the normal velocity interferometer (NVI) was motivated by the relatively small range of velocities that can be measured by the normal displacement interferometer (NDI). The latter interferometer is a derivative of the original Michelson interferometer in which a light beam reflected from a moving target is interfered at a beamsplitter with a stationary reference beam. The sensitivity of the NDI is given by $\lambda/2$ [mm/fringe] where λ represents the laser light wavelength. Multibeam NDI systems (Mello et al., 1991) have been successfully employed in the recording of normal displacements in impact soft-recovery experiments performed on ceramic composites (Espinosa and Clifton, 1991). The experimental configuration and the stress-time history at the specimen-momentum trap interface are given in Espinosa and Clifton (1991). The important feature to be noted in their stress histories is that the displacement interferometer can resolve slow changes in velocity with very high accuracy and hence provide very valuable information for damage identification. Nonetheless, the extreme sensitivity of this interferometer severely limits its application in wave propagation experiments due to the inordinately high signal frequencies which may be generated.

The "velocity limit" for such an interferometer may be approximated by $V^{\max} = \lambda/2 f^{\max}$ where f represents the frequency cutoff of the light detection system. The velocity limitation is best illustrated by considering a fast light-detection system (photodetector, amplifier, shielded BNC cables, and a 2 Gs/s digital storage oscilloscope) possessing a system 3 dB analog frequency response of 400 MHz. Such a system is reasonable to consider in light of recent advances in the electronics industry and is representative of present day systems having large storage capacity. Next, consider an interferometer signal having a 400 MHz frequency component generated by a particle velocity of 0.103 mm/μsec at the target surface. It is clear that a 400 MHz signal falls well within the bounds established by the Nyquist sampling theorem and that such a signal sampled at 2 Gs/s is deemed fully reconstructible. Observe, however, that a 400 MHz fringe when sampled at 2 Gs/s will at most be represented by only five bits of data. In light of system noise and undesirable amplitude fluctuations, it would be difficult to extract displacement information beyond this frequency even after applying filters and correcting for amplitude variations. It, therefore, seems reasonable to regard a particle velocity of 0.1 mm/μsec as an upper bound for the NDI in wave propagation experiments. Studies of damage and inelasticity in materials may at times require much higher particle velocities making quite impractical the use of normal displacement interferometers having such a high fixed level of sensitivity.

A normal velocity interferometer (NVI) or a VISAR on the other hand, has a variable sensitivity given by $\lambda/(2\tau(1+\delta))$ [mm/μs/fringe] whereby τ represents a time delay between the interfering light beams introduced by an air delay leg or etalon in the interferometer. The factor $(1+\delta)$ is a correction term to account for the refractive index of the etalon. A quite appealing feature of this interferometer is that the fringe record is a direct measure of particle velocity, thereby alleviating the need for differentiation of the reduced signal. Moreover, signal frequencies generated by an NVI are proportional to particle acceleration and are therefore lower than equivalent signal frequencies generated by an NDI. However, during an initial time period τ, an NVI is functioning as an NDI since the delayed light arriving at the detector from the delay leg or etalon is reflected from a stationary target (Clifton, 1970). Ironically, it is the interpretation of the NVI in the interval where it operates as an NDI that limits the usefulness of the NVI in the low-velocity range (0.1–0.25 mm/μsec). In this velocity range, values of τ in the neighborhood of 5 nsec or more are required in order to obtain records with at least three or four fringes. This in turn leads to a greater averaging of the velocity measurements. Furthermore, elastic precursors causing velocity jumps of more than 0.1 mm/μsec in a time less than τ cannot be detected because the early time NDI signal frequency may exceed the frequency response of the light detection system. This feature is described as lost fringes in the Valyn VISAR User's Handbook (1995).

Clearly, the NDI and VISAR principles described here indicate that there is a velocity range between 0.1–0.25 mm/μsec over which particle velocities may not be measured with the desired accuracy. Barker and Hollenbach (1972), have investigated the accuracy of the VISAR experimentally. They found that measurements with two percent accuracy can be obtained when a delay time of approximately 1 nsec corresponding to a velocity per fringe constant equal to 0.2 mm/μsec is used. Certainly, velocities below 0.2 mm/μsec can be measured, but the uncertainty of the measurement increases because only a fraction of a fringe is recorded. In this case, signals in quadrature have to be recorded immediately before the experiment and assume the amplitude remains the same during the experiment (Valyn VISAR Data Reduction Program, 1995). It should be

Downloaded 04 May 2010 to 171.66.16.34. Redistribution subject to ASME license or copyright; see http://www.asme.org/terms/Terms_Use.cfm

pointed that the VISAR data reduction is very sensitive to the position and shape of the Lissajous, Valyn VISAR Data Reduction Program (1995). In both interferometers it might appear that sophisticated light detection systems having several GHz of bandwidth are required. Such systems, although currently attainable, remain for the most part prohibitively expensive.

The particle velocity limitation is particularly relevant in the case of soft recovery experiments (Kumar and Clifton, 1979; Espinosa, 1992, 1996) in which impact velocities below 0.2 mm/μsec are utilized. In these experiments, damage (microcracking, interfacial failure) and inelasticity (plasticity, phase transformations) are identified based on the recorded velocity histories and on microscopy studies of the recovered samples. It is clear that information about the early stages of inelasticity is contained in the first few nanoseconds of the velocity signal. Furthermore, velocity jumps occurring within a few nanoseconds may result from inelastic and failure events. Therefore, if the information is not captured, the experiment is only partially successful.

The variable sensitivity displacement interferometer (VSDI) presented here has been designed to overcome the inherent high-frequency requirement of the NDI and VISAR within the noted velocity range of interest. Furthermore, it does not require the utilization of very expensive optical components and oscilloscopes. The sensitivity of such an interferometer is fully variable; thus, it can be adjusted to operate over a wide range of particle velocities without exceeding the frequency response of the light detection system.

3 VSDI Theory

To derive the governing equation for a variable sensitivity displacement interferometer, consider Fig. 1 in which a normally incident laser beam impinges on the rear free surface of a target plate. Diffracted beams are generated by a diffraction grating either written into a layer of photoresist or directly etched into a metallic coating. High-quality photoresists are now available which make it quite feasible to write holographic phase gratings of 600–1600 lines/mm with high diffraction efficiencies. Furthermore, "lithographic techniques" may also be applied to photoresist gratings which yield etched gratings on metallic coatings (Espinosa, 1992). Such gratings, although more difficult to produce, are more durable than photoresist gratings and can be used in severe environments such as elevated temperatures. Alternatively, the specimen rear surface may be preferentially roughened in which case light will be scattered back in all directions. In the latter case, light may be collected by a fiber optic probe whose optic axis makes an angle θ with the normal to the specimen surface.

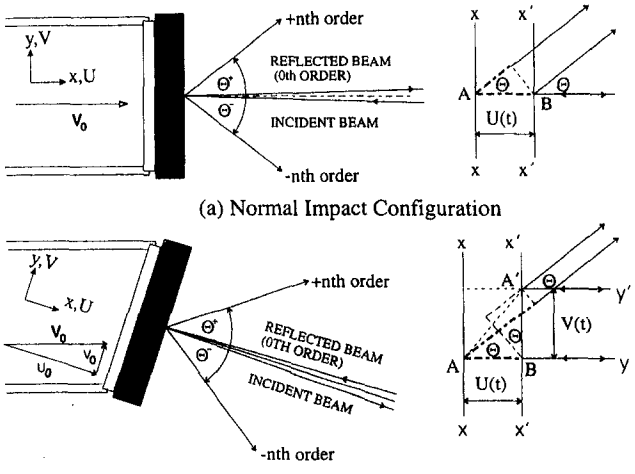


Fig. 1 Optical path for incident, reflected, and diffracted beams

In all cases the generated diffracted beams satisfy the Bragg equation

$$d \sin \theta = n\lambda \quad n = \pm 1, 2, 3, \ldots \tag{1}$$

where d is the grating period, n is the beam order, and λ is the wavelength of the laser source.

The target free surface may undergo only normal motion as depicted in Fig. 1(a), or it may have combined normal and in-plane motion as in Fig. 1(b). Far from the target surface, e.g., at the photodetector, the reflected and diffracted beams can be represented as plane waves, i.e.,

$$\begin{aligned}
\mathbf{E}^0(\mathbf{r}, t) &= \mathbf{A}^0 \exp\{i[kl^0 - \omega t - \Phi^0(t)]\} \\
\mathbf{E}^{\theta^+}(\mathbf{r}, t) &= \mathbf{A}^+ \exp\{i[kl^+ - \omega t - \Phi^+(t)]\} \\
\mathbf{E}^{\theta^-}(\mathbf{r}, t) &= \mathbf{A}^- \exp\{i[kl^- - \omega t - \Phi^-(t)]\}
\end{aligned} \tag{2}$$

where $k = 2\pi/\lambda$ is the wave number, ω is the angular frequency, and l^+, l^-, and l^0 represent the fixed initial path lengths traversed from target to detector by the $\theta^\pm$ diffracted beams and the normally reflected beam, respectively; $\mathbf{A}^\pm$ and $\mathbf{A}^0$ are vector quantities which characterize the amplitude and polarization of the diffracted and reflected light beams, respectively. The functions Φ^0, Φ^+, Φ^-, are the phase terms which are related to the target free surface motion by

$$\Phi^0(t) = 2kU\left(t - \frac{l^0}{c}\right) + \phi^0$$

$$\Phi^+(t) = k\left[U\left(t - \frac{l^+}{c}\right)(1 + \cos\theta^+) + V\left(t - \frac{l^+}{c}\right)\sin\theta^+\right] + \phi^+$$

$$\Phi^-(t) = k\left[U\left(t - \frac{l^-}{c}\right)(1 + \cos\theta^-) - V\left(t - \frac{l^-}{c}\right)\sin\theta^-\right] + \phi^- \tag{3}$$

where $U(t)$ and $V(t)$ represent the normal and in-plane displacements of the point of observation from its position at time $t = 0$, and where ϕ^0, ϕ^+, ϕ^- represent constant arbitrary phase terms.

Next, consider the effect of interfering the normally reflected beam with a beam diffracted at an angle $\theta^\pm$ with respect to the specimen normal as shown in Fig. 2. The normally reflected beam is split at beamsplitter BS1. Each half of the normal beam is then made to interfere with one of the diffracted beams via beamsplitters BS2 and BS3. The resulting signals generated by each interfering beam pair are monitored by photodetectors. The combined field for either pair of interfering plane waves is

$$\mathbf{E}^\pm(\mathbf{r}, t) = \mathbf{E}^0(\mathbf{r}, t) + \mathbf{E}^{\theta^\pm}(\mathbf{r}, t) \tag{4}$$

from which the time-averaged intensity relation

$$I(t) \propto \mathbf{E}^\pm(\mathbf{r}, t)\mathbf{E}^{\pm *}(\mathbf{r}, t) \tag{5}$$

leads directly to a classical interference expression of the form

$$I(t) \propto I^0 + I^\pm + 2\sqrt{(I^0 I^\pm)}\cos(\beta)\cos\Psi^\pm(t). \tag{6}$$

Here, I^0 and $I^\pm$ represent the time-averaged intensities of the respective contributing light fields, and β is the angle between their respective polarization vectors. Normal and transverse par-

Downloaded 04 May 2010 to 171.66.16.34. Redistribution subject to ASME license or copyright; see http://www.asme.org/terms/Terms_Use.cfm

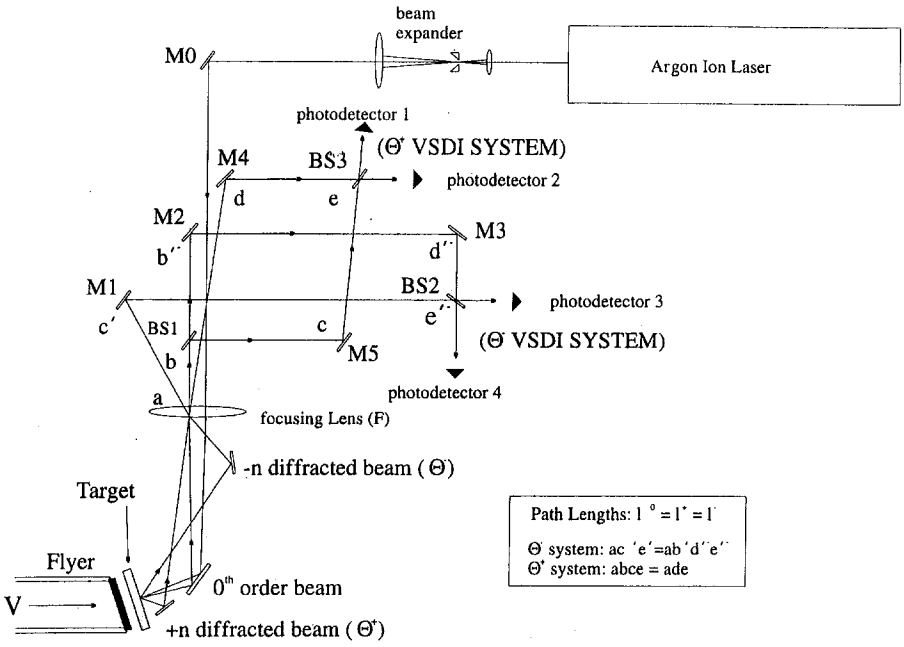


Fig. 2 Optical layout of VSDI system. The $\Theta^{\pm}$ VSDI system is obtained by combining a normally reflected beam and a diffracted beam at an angle $\theta^{\pm}$.

ticle motion introduce frequency modulation through the time-varying phase term

$$\Psi^{\pm}(t) = \frac{2\pi}{\lambda}\left[2U\left(t - \frac{l^0}{c}\right) - U\left(t - \frac{l^{\pm}}{c}\right)(1 + \cos\theta^{\pm}) \mp V\left(t - \frac{l^{\pm}}{c}\right)\sin\theta^{\pm} + (l^0 - l^{\pm})\right] + \phi^0 - \phi^{\pm}. \quad (7)$$

Observe that the transverse motion phase term is subtracted for the case where the θ^+ beam is employed and otherwise added when interfering with the θ^- beam. Next, setting $l^0 = l^+ = l^-$ and $\theta^+ = \theta^- = \theta$ leads to a more simplified and useful form, i.e.,

$$\Psi^{\pm}(t) = \frac{2\pi}{\lambda}\left[U\left(t - \frac{l}{c}\right)(1 - \cos\theta) \mp V\left(t - \frac{l}{c}\right)\sin\theta\right] + \phi^0 - \phi^{\pm}. \quad (8)$$

Equation (8) shows that each VSDI system will generate a different signal frequency when used to monitor the same given combined state of motion. This effect is confirmed in pressure shear experiments at the time corresponding to the arrival of the shear wave at the target rear surface. Initially, each VSDI system functions as a desensitized normal displacement interferometer (DNDI) having a fringe sensitivity $\lambda/(1 - \cos\theta)$, see derivation of Eq. (10) below. With the delayed arrival of the shear wave, the signal now represents a linear combination of the two motion components. Consequently, the signal frequency is altered as indicated by Eq. (8) and each VSDI system exhibits a sudden increase or decrease depending upon whether the θ^+ or θ^- beam is being interfered.

Case of Purely Normal Motion: (DNDI). For $V(t) = 0$, a full fringe shift associated with a normal displacement δU satisfies

$$\Delta\Psi(t) = \frac{2\pi}{\lambda}[\delta U(t - l/c)](1 - \cos\theta)] = 2\pi. \quad (9)$$

Rearrangement of this expression and use of Eq. (1) gives the fringe constant relation

$$\frac{\text{normal displacement}}{\text{fringe}} = \frac{\lambda}{1 - \cos\theta} = \frac{\lambda}{1 - \sqrt{1 - (n\lambda\sigma)^2}} \quad (10)$$

where $\sigma = 1/d$ represents the frequency of the diffraction grating and θ is used for $\theta^{\pm}$ since both the Θ^+ and Θ^- VSDI systems will function as identical desensitized normal displacement interferometers. The effect of θ (or equivalently the grating frequency σ) on the interferometer's sensitivity is summarized in Fig. 3. The fringe constant varies from infinity at $\theta = 0$ deg to λ [mm/fringe] at $\theta = 90$ deg. As an example, using the second-order beam from a diffraction grating with $\sigma = 600$ lines/mm, the DNDI is found to have a fringe constant of 4.697λ; for light of wavelength $\lambda = 514.5$ nm the fringe constant is 2.4 μm/fringe, which is nearly an order of magnitude less sensitive than that of a conventional NDI which has a fringe

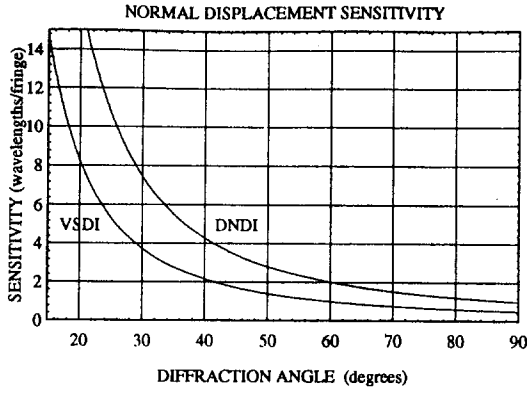


Fig. 3 DNDI and VSDI sensitivities as a function of diffraction angle

Downloaded 04 May 2010 to 171.66.16.34. Redistribution subject to ASME license or copyright; see http://www.asme.org/terms/Terms_Use.cfm

constant of 0.2572 μm/fringe. Frequencies will likewise be reduced by an order of magnitude, thereby extending the applicability of the normal displacement interferometer to wave propagation experiments in which particle velocities in excess of 0.1 mm/μs are generated.

Case of Purely In-Plane Motion: (DTDI). Referring to Eq. (8), we may consider the case where $U(t) = 0$, i.e., the case of pure in-plane motion. In this case, the variable phase is

$$\Psi(t)^{\pm} = \frac{2\pi}{\lambda}\left[\mp V\left(t - \frac{l}{c}\right)\sin\theta^{\pm}\right] + \phi^{0} - \phi^{+} \quad (11)$$

and the Θ^+ and Θ^- VSDI systems now act as identical transverse displacement interferometers. A full fringe shift associated with a transverse displacement δV corresponds to

$$\delta\Psi(t) = \frac{2\pi}{\lambda}\left[\delta V\left(t - \frac{l}{c}\right)\sin\theta\right] = 2\pi \quad (12)$$

which may be rearranged and combined with Eq. (1) to give the fringe constant relation

$$\frac{\text{transverse displacement}}{\text{fringe}} = \frac{\lambda}{\sin\theta} = \frac{1}{\sigma n}. \quad (13)$$

The DTDI sensitivity ranges from a complete loss of sensitivity at $\theta = 0$ deg to a theoretical sensitivity limit of λ [mm/fringe] at $\theta = 90$ deg (see Fig. 4). The interferometer is "desensitized" in the sense that, for the same diffraction orders, it exhibits one-half the sensitivity of the transverse displacement interferometer (TDI).

Case of Combined Normal and In-Plane Motions (VSDI System). When the material point exhibits both normal and in-plane components of displacement, for instance, in pressure-shear experiments or in normal impact experiments of anisotropic crystals, frequency modulation results through a linear combination of both motion components as dictated by Eq. (8). Decoupling of the normal motion component $U(t)$ from the in-plane component $V(t)$ is obtained through one of two possible schemes. Both schemes involve the simultaneous application of two interferometers and the use of Eq. (8) to decouple the two components of motion. In the first option, two VSDI systems are employed. The normally reflected beam is split into two beams, one of which interferes with the θ^+ beam to form the Θ^+ VSDI system and a second one which is made to interfere with the θ^- beam to form the Θ^- VSDI system. The two resulting signals may then be linearly combined through use of Eq. (8) to solve for the longitudinal motion $U(t)$ and the transverse motion $V(t)$, respectively. Addition of the phase terms of the Θ^+ and Θ^- VSDI signals provides an expression for a new phase term associated solely with a normal displacement U given by

$$\Psi(t)^{+} + \Psi(t)^{-} = \frac{4\pi}{\lambda}U\left(t - \frac{l}{c}\right)(1 - \cos\theta) + 2\phi_0 - \phi^{-} - \phi^{+}. \quad (14)$$

Hence, the fringe constant relation of this new signal is

$$\left[\frac{\text{normal displacement}}{\text{fringe}}\right] = \frac{\lambda}{2(1 - \cos\theta)}. \quad (15)$$

It should be noted that this sensitivity is twice the sensitivity obtained by a single VSDI system for the case of pure normal motion, basically, because the signal obtained by addition of two VSDI systems exhibits a double recording of the normal displacement.

By subtracting the phase terms of the Θ^+ and Θ^- VSDI signals, an expression for a phase term associated solely with an in-plane motion V is obtained, viz.,

$$\Psi(t)^{-} - \Psi(t)^{+} = \frac{4\pi}{\lambda}V\left(t - \frac{l}{c}\right)\sin\theta - \phi^{-} + \phi^{+}. \quad (16)$$

The fringe constant of this new signal is given by

$$\left[\frac{\text{transverse displacement}}{\text{fringe}}\right] = \frac{\lambda}{2\sin\theta}. \quad (17)$$

This sensitivity is the same as the one exhibit by the transverse displacement interferometer (TDI, Kim et al., 1977). This result is not surprising since the signal obtained by subtracting the two VSDI systems eliminates the effect of the normally reflected beam. We can conclude that this resulting signal is nothing other than a TDI signal.

It is conceivable, however, that in some cases frequency limitations may render this option impractical. This might be the case if the "combined motion" signal frequency associated with the Θ^- VSDI system suddenly exceeds the frequency response of the light detection system. Yet another possibility might involve the "combined signal" frequency associated with the Θ^+ VSDI system, suddenly decreasing to the point where too few fringes are counted thereby rendering the measurement too insensitive. Clearly then, the decision to employ the dual VSDI arrangement in a pressure-shear experiment should be based upon some a priori knowledge of the frequency range that will be spanned.

In cases where the dual VSDI arrangement is ruled out due to frequency considerations, it is always possible to independently monitor one of the motion components through the simultaneous implementation of an alternative technique. For example, the corresponding transverse displacement history $V(t)$ may be obtained through the employment of a transverse displacement interferometer (TDI). In this technique, the transverse displacement history is obtained by interfering two symmetrically diffracted laser beams. It was shown by Kim et al., 1977, that if the path lengths l^+ and l^- of the diffracted beams are kept equal, then the resulting fringe record remains unaffected by the presence of normal motion and is solely a measure of the in-plane displacement. The transverse displacement history $V(t)$ determined in this way can be combined with a VSDI record to decouple the normal displacement $U(t)$ through the use of Eq. (8). For instance, by subtracting the time-varying phases of a Θ^- VSDI system and a TDI system we obtain an expression

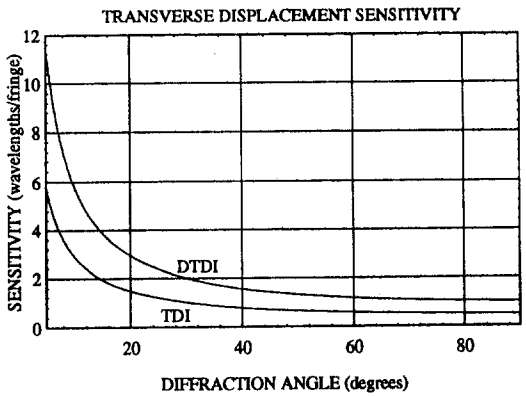


Fig. 4 DTDI and TDI sensitivities as a function of diffraction angle

Downloaded 04 May 2010 to 171.66.16.34. Redistribution subject to ASME license or copyright; see http://www.asme.org/terms/Terms_Use.cfm

for a phase term associated solely with the normal displacement $U(t)$, namely,

$$2\Psi(t)_{\Theta-\mathrm{VSDI}} - \Psi(t)_{\mathrm{TDI}} = \frac{4\pi}{\lambda} U\left(t - \frac{l}{c}\right)(1 - \cos\theta) + \phi_0 - \phi_{\mathrm{TDI}} - \phi_{\Theta-\mathrm{VSDI}}. \quad (18)$$

This equation shows once more that the normal motion can be recorded with the sensitivity given by Eq. (15). The in-plane motion V can be directly obtained from the TDI signal.

4 VSDI Applied to Pressure-Shear Recovery Experiments

In this section we examine the applicability of the VSDI system to pressure-shear soft-recovery experiments (Espinosa, 1992, 1996; Yadav et al., 1993). This experiment is particularly suitable to investigate the usefulness of the variable sensitivity displacement interferometer (VSDI) because it requires the measurement of both normal and in-plane motions. The configuration is shown in Fig. 5(*a*). Compression-shear loading is accomplished by inclining the flyer and target plates with respect to the axis of the projectile. By varying the angle of inclination a variety of loading states can be obtained.

Pressure-shear recovery experiments offer several advantages over other experimental techniques in the study of damage and inelasticity in metals, ceramics, and composite materials. The stress amplitudes and deformation rates obtained in these experiments allow the identification of microcracking and shear localization. Furthermore, the information obtained from these experiments is substantially increased by correlation of real-time velocity profiles and microstructural features associated with the mechanisms of inelasticity and damage.

The principal difficulties of the pressure-shear recovery experiment are thought to be (1) simultaneous trapping of the longitudinal and shear momentum by a back plate, and (2) satisfactory mitigation of radial release waves at the stress levels and pulse durations required in these experimental studies. Such mitigation can be accomplished by means of a star-shaped flyer design (Espinosa et al., 1992). A design that meets the first requirement is obtained by means of a multiplate flyer. Such a flyer consists of a thin film made of material with very low shear flow stress, e.g., a polymer, sandwiched between two thicker hard plates. The selection of given materials for the flyer plates is a function of the application. As in the case of the normal soft-recovery experiment, and for the same reasons, the flyer plate is backed by a low impedance material and the projectile is stopped by an anvil.

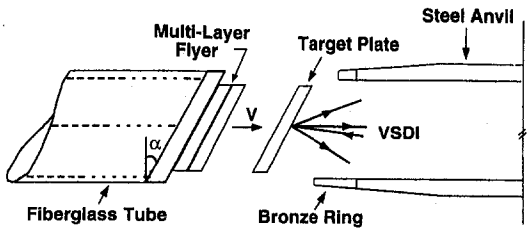


Fig. 5(*a*)

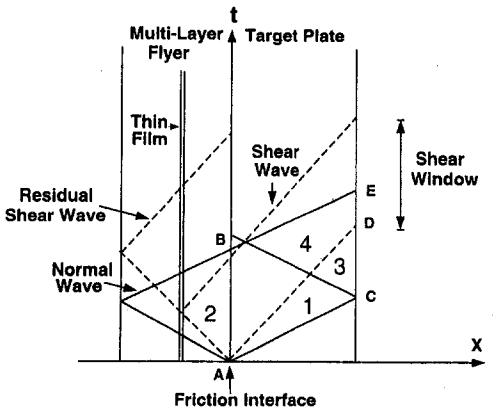


Fig. 5(*b*)

Fig. 5 (*a*) Pressure-shear soft-recovery experimental configuration, (*b*) Lagrangian *X-t* diagram of pressure-shear friction experiment

The elastic wave fronts for a plane wave analysis of a pressure-shear recovery friction experiment are given in a Lagrangian *X-t* diagram in Fig. 5(*b*). At impact, plane compression waves and shear waves are produced in both the impactor and the target. Since the shear wave velocity is approximately half the longitudinal wave velocity, a thin film with very low shear resistance needs to be added to the flyer plate such that the arrival of the unloading shear wave to the impact surface precedes the arrival of the unloading longitudinal wave generated at the back surface of the second flyer plate. Certainly, the thickness of the target plate must be selected so that the arrival of longitudinal unloading to the impact surface, from the target back surface, does not prevent the transfer of the main shear pulse to the target plate. It should be noted that a residual shear wave remains trapped into the flyer plate for two reasons: (i) the small but finite shear resistance of the thin film, and (ii) the possibility of interfacial sliding in the case of friction experiments.

Due to mismatch in impedances between the thin film and the bounding plates, a few reverberations within the polymer film are required for the achievement of the normal stress imposed at the impact face. This feature imposes another requirement in the design and manufacturing of the thin polymer film. The thickness of the thin film needs to be minimized such that the time required to achieve a homogeneous state is only a small fraction of a microsecond. We have manufactured such a multiplate flyer by bonding two hard plates with a uniform 1 μm-thick polymer layer (photoresist AZ 1350J-HOECHST CELANESE). We have observed that the uniformity of the thin film prevents tilt between the flyer plates which would otherwise perturb the interferometric measurements.

A pressure-shear recovery friction experiment was performed in a 3.0-in. gas gun at Purdue University to test the new interferometer. A combined Θ^- VSDI-TDI system was utilized to monitor the normal and transverse velocities at the target free surface. The target rear surface was polished and then a thin layer of photoresist was deposited using a spinning machine. A holographic phase grating was constructed by interference of two laser beams. The angle between the beams was selected such that a sinusoidal profile with 600 lines/mm was obtained. The zero-order reflected beam was combined with the negative first-order diffracted beam to produce a Θ^- VSDI. A TDI interferometer was obtained by mixing the two first-order diffracted beams.

The multiplate impactor and target plates were made of 4340 steel. The plate surfaces were mirror-polished to examine friction and wear in the recovered samples. The impactor was glued to the front end of a fiber glass tube with the impact plane skewed from the axis of the tube at an angle of 18 deg. An aluminum back with two rubber O-rings was mounted in the rear end of the tube to seal the wrap-around breech. A key was mounted on the middle of the fiber glass tube to prevent rotation of the projectile. The projectile velocity was measured, just before impact, by recording the times of contact of four wire pins placed in the path of the projectile.

Plates 2.25 inches in diameter were chosen to maximize the arrival time of the first unloading wave, from the plate periphery to the displacement recording point. The two steel plates used as multiplate impactor were 2.68 and 3.25 mm thick, respec-

Downloaded 04 May 2010 to 171.66.16.34. Redistribution subject to ASME license or copyright; see http://www.asme.org/terms/Terms_Use.cfm

tively. The target plate was 6.99 mm thick. The plates were lapped flat using a lapping machine and 15 μm alumina powder. A flatness better than three rings was measured by means of a Newton interferometer.

After the target plate was mounted in a holder ring, it was aligned to the impactor surface within 0.5 milliradians using an optical technique developed by Kumar and Clifton (1977). In order to check the angle of misalignment at impact, the times of contact at four voltage-biased pins were recorded. Through a logical circuit, contact of the four pins gave four voltage steps, in the ratio of 1:2:4:8, which were recorded in an oscilloscope. A tilt of 1.7×10^{-3} radians was measured in the experiment.

The signals produced by the combined Θ^- VSDI-TDI system, recorded in a Tektronix DSA 602A oscilloscope, are plotted in Figs. 6(a) and 6(b). Upon arrival of the normal wave, fringes are produced in the Θ^- VSDI channel. A significant frequency increase is observed after arrival of the shear wave in accordance with Eq. (8). The TDI trace (see Fig. 6(b)) shows an initially strong fringe contrast. A contrast reduction follows probably due to a change in intensity in the diffracted beams caused by the grating motion and/or target tilt. Decoupling between the normal and in-plane motions was accomplished by first obtaining the in-plane motion, V, directly from the TDI signal and then the normal motion, U, from Eq. (18). To eliminate electronic noise, the interference fringes were filtered using a Fast-Fourier Transform method and a cut-off frequency higher than the maximum fringe frequency. Furthermore, since the signal amplitude does not contain displacement information, it is customary to scale the signal to a constant amplitude prior to the displacement calculation. Hence, the filtered fringes were then scaled to obtain uniform fringe amplitude. Based on the displacement interferometer principles, one can assume that the interferometer signal consists of fringes in a sine-like function of voltage versus time, e.g., $y(t) = a(t) \sin(f(t)) + b(t)$, where $a(t)$ is the amplitude, $b(t)$ is the zero offset, and $f(t)$ is the phase function. In general, $a(t)$ and $b(t)$ are not constant. They can be evaluated by finding the envelopes, $h(t)$ and $l(t)$, formed by peaks and valleys, respectively. These functions are given by $a(t) = 0.5(h(t) - l(t))$ and $b(t) = 0.5(h(t) + l(t))$ (Tong, 1991). The amplitude corrected signal, $y_0(t)$, is then determined by $y_0(t) = (y(t) - b(t))/a(t)$. The signal phase function can be obtained from $f(t) = \arcsin(y_0(t))$. Then the displacement can be computed from $d(t) = d_0 f(t)/2\pi$. The constant d_0 is a function of the interferometer and is defined by Eqs. (15) and (17) for the VSDI and TDI systems, respectively. Velocities were obtained by differentiating the displacement histories numerically. All the calculations were automatically performed with MATLAB. The functions MENU, GINPUT, INPUT, and STRCMP were used to input the data files. The functions FIR1 and FFTFILT were used to perform the fast Fourier transform filtering. The function INTERP1 was employed to fit the peaks and valleys with cubic splines. The function GRADIENT was utilized to perform the numerical differentiation.

In Fig. 7, the normal free surface velocity history is plotted together with the Θ^- VSDI amplitude corrected signal. Upon arrival of the longitudinal wave to the the target free surface, the normal velocity exhibits an increase in velocity to a level

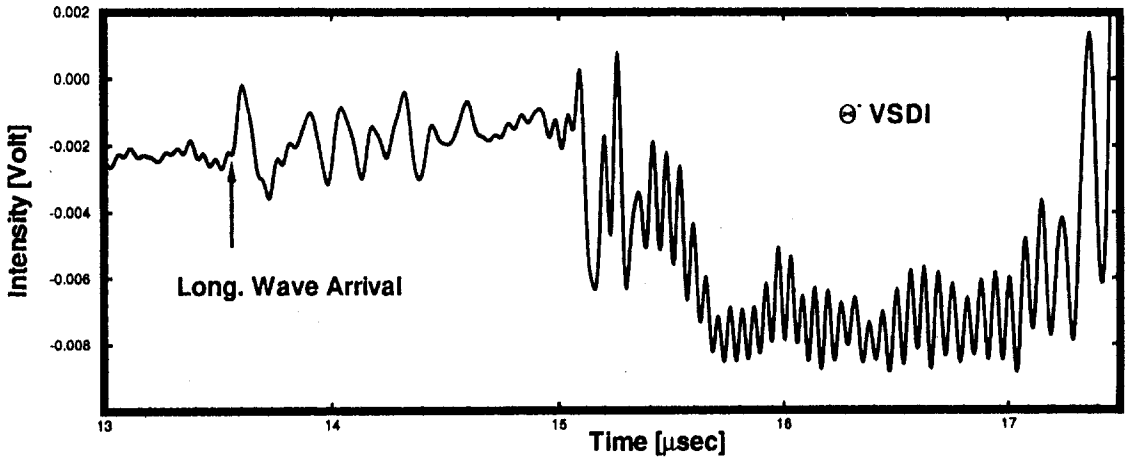


Fig. 6(a)

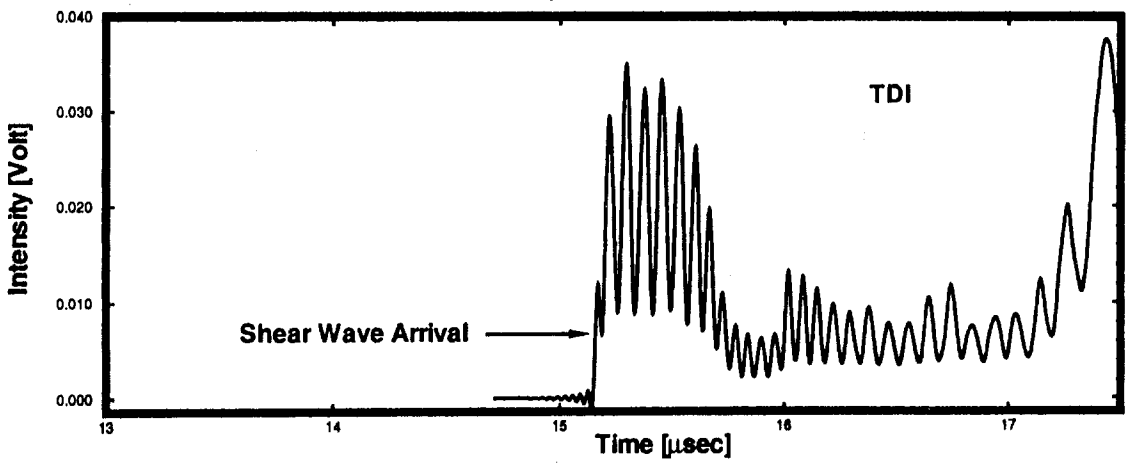


Fig. 6(b)

Fig. 6 (a) Tektronix digital signal from Θ^- VSDI, (b) Tektronix digital signal from TDI

Downloaded 04 May 2010 to 171.66.16.34. Redistribution subject to ASME license or copyright; see http://www.asme.org/terms/Terms_Use.cfm

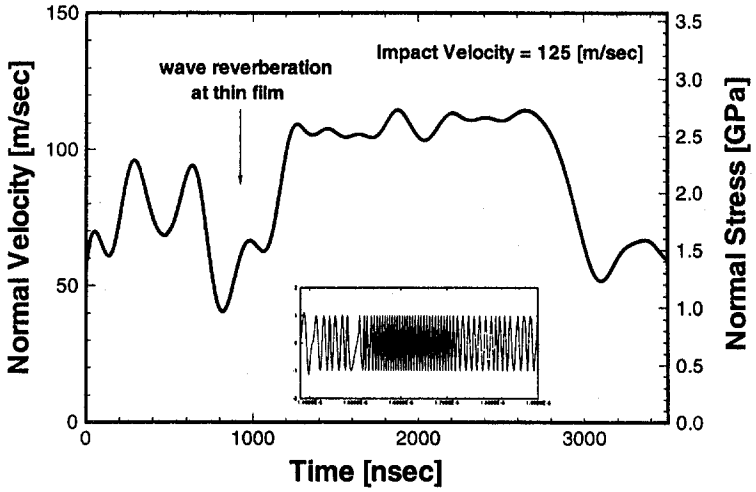


Fig. 7 Normal particle velocity-time profile. The inside box shows the Θ^- VSDI trace after amplitude correction.

of approximately 80 m/sec followed by a reduction and increase in velocity due to wave reverberations in the thin polymer layer used in the multiplate flyer. A few bumps are observed in the first 900 nanoseconds of the normal velocity history. These variations in normal velocity are likely the result of the low signal to noise ratio in the early part of the record (see Fig. 6(a)). They are also in part due to errors in data reduction arising from the insensitivity of the displacement interferometer at the peaks and valleys of the trace (Espinosa and Clifton, 1991). Experience suggests that signals with higher frequency are less sensitive to errors caused by signal noise. The noise level can be observed in the part of the record preceding the longitudinal wave arrival. In later experiments we have increased the angle θ used in the Θ^- VSDI with good results. An approximately constant velocity of 115 m/sec is monitored in the next 1.8 μsec which is in agreement with the elastic prediction. It should be noted that this normal velocity would lead to a frequency of 450 MHz in an NDI, while in the VSDI system a much smaller frequency is recorded.

In Fig. 8 the transverse velocity history and the TDI amplitude corrected signal are shown. A transverse velocity well below the impact shear velocity is measured indicating interface sliding. Small fluctuations in the transverse velocity are due in part to errors in data reduction arising from the insensitivity of the TDI at the peaks and valleys of the trace (Espinosa and Clifton, 1991). An in-plane wave release is observed at approximately two microseconds. This wave release is in agreement with the wave release predicted by one-dimensional elastic wave theory. It should be noted that the reduction in in-plane motion is progressive. A residual transverse velocity of 5 m/sec is recorded likely due to the shear resistance of the thin polymer film used in the multiplate flyer. Modeling of the experiment including the frictional behavior of the steel interface, and the nonlinear behavior of the polymer thin film is required to fully interpret the transverse velocity history. Further evidence on the shear wave duration can be observed in Fig. 9 in which an optical micrograph shows sliding marks, approximately 50 μm in length. From the transverse velocity history, an average sliding velocity of 26 m/sec is computed. This velocity during 2 μsec leads to a sliding length of 52 μm, which correlates very well with the sliding marks observed on the micrographs.

5 Concluding Remarks

We have presented a novel variable sensitivity displacement interferometer obtained by interfering a normally reflected beam with a beam diffracted at an angle θ with respect to the specimen

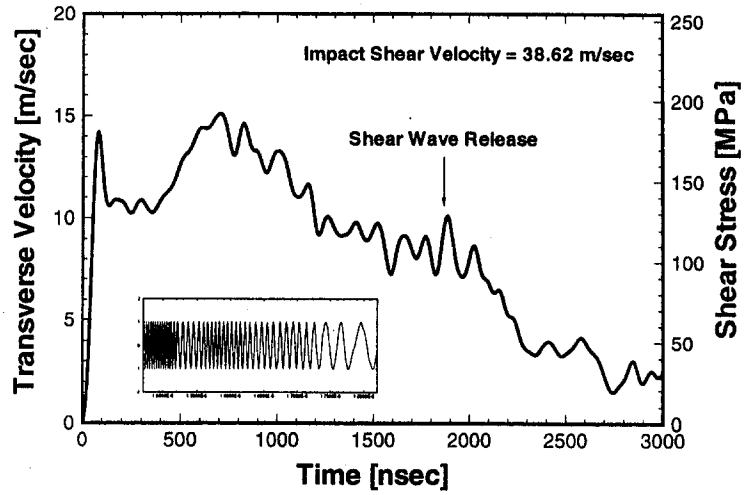


Fig. 8 Transverse particle velocity-time profile. The inside box shows the TDI trace after amplitude correction.

Downloaded 04 May 2010 to 171.66.16.34. Redistribution subject to ASME license or copyright; see http://www.asme.org/terms/Terms_Use.cfm

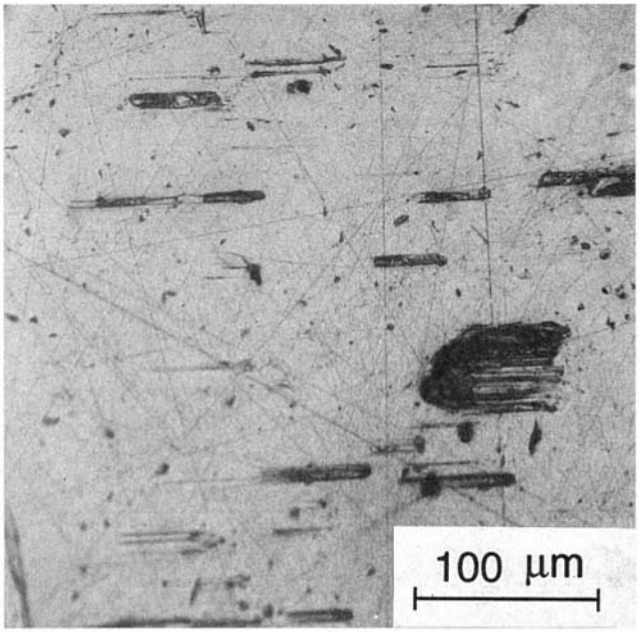


Fig. 9 Optical micrograph from the recovered flyer impact surface. Sliding marks approximately 50 μm in length are observed.

normal. A wide range of sensitivities can be obtained by changing the angle between the two beams. In principle, the VSDI interferometer presented here can be used in wave propagation experiments conducted on metallic and nonmetallic materials in a variety of impact configurations including those in which an optical window is employed (Espinosa and Clifton, 1991). Moreover, it should be possible to extend the technique to the case where scattered light from a preferentially roughened surface is collected by three fiber optic probes: a central one for illuminating the specimen and collecting normally reflected light, and two side probes for collecting diffracted light at $\theta^{\pm}$. In this case, the light is transported to the interferometer through optical fibers, thereby increasing the versatility of the system. Observe that in normal impact experiments the DNDI can be combined with other interferometers, for instance a VISAR, to produce optimal velocity histories. For example, the sensitivity of the DNDI can be adjusted so that a high resolution of the elastic precursor is obtained while the measurement of very high velocities is accomplished with the VISAR system. A similar result can be obtained if two DNDI's at different diffracted angles are utilized. Hence, it appears that the VSDI exhibits promise as a new tool for monitoring particle displacements in wave propagation experiments, particularly within the previously noted problematic velocity gap spanning 0.1–0.2 mm/μsec.

Acknowledgments

This research was supported by the National Science Foundation through Grants Nos. MSS-9309006 and MSS-9311289. The first author wishes to thank L. Barker for providing very valuable insight about the VISAR concept, and to R. J. Clifton and D. Dandekar for facilitating blue prints and other materials during the development of the impact facility employed in the experimental work reported here. The assistance of B. Sanders, D. Bower, J. Le, D. Reagan, W. Bader, M. Chadwell, and J. Zachary, in the manufacturing of the light gas gun at Purdue is gratefully acknowledged.

References

Barker, L. M., and Hollenbach, R. E., 1965, "Interferometer Technique for Measuring the Dynamic Mechanical Properties of Materials," *Rev. Sci. Instru.,* Vol. 36, No. 11, pp. 1617–1620.

Barker, L. M., and Hollenbach, R. E., 1972, "Laser Interferometry for Measuring High Velocities of Any Reflecting Surface," *J. Appl. Physics,* Vol. 43, No. 11, pp. 4669–4675.

Chhabildas, L. C., Sutherland, H. J., and Asay, J. R., 1979, "A Velocity Interferometer Technique to Determine Shear-Wave Particle Velocity in Shock-Loaded Solids," *J. Appl. Phys.,* Vol. 50, No. 8, pp. 5196–5201.

Clifton, R. J., 1970, "Analysis of the Laser Velocity Interferometer," *J. Appl. Phys.,* Vol. 41, No. 13, pp. 5335–5337.

Espinosa, H. D., and Clifton, R. J., 1991, "An Experimental Investigation of Inelasticity in Shock Loaded AlN/Al Composites," *Symposium on Experiments in Micromechanics of Fracture-Resistant Materials,* ASME Winter Annual Meeting, K. S. Kim, ed., Atlanta, GA, pp. 37–56.

Espinosa, H. D., 1992, "Micromechanics of the Dynamic Response of Ceramics and Ceramic Composites," Ph.D. Thesis, Brown University, Providence, RI.

Espinosa, H. D., Raiser, G., Clifton, R. J., and Ortiz, M., 1992, "Performance of the Star-Shaped Flyer in the Study of Brittle Materials: Three Dimensional Computer Simulations and Experimental Observations," *J. Appl. Phys.,* Vol. 72, No. 8, pp. 3451–3457.

Espinosa, H. D., 1996, "Dynamic Compression-Shear Loading with In-Material Interferometric Measurements," *Rev. Sci. Inst.,* Vol. 67, No. 11, pp. 3931–3939.

Hemsing, W. F., 1979, "Velocity Sensing Interferometer (VISAR) Modification," *Rev. Sci. Instrum.,* Vol. 50, No. 1, pp. 73–78.

Kim, K. S., Clifton, R. J., and Kumar, P., 1977, "A Combined Normal and Transverse Displacement Interferometer with an Application to Impact of Y-Cut Quartz," *J. Appl. Phys.,* Vol. 48, No. 10, pp. 4132–4139.

Kumar, P., and Clifton, R. J., 1977, "Optical Alignment of Impact Faces for Plate Impact Experiments," *J. Appl. Physics,* Vol. 48, No. 3, pp. 1366–1367.

Kumar, P., and Clifton, R. J., 1979, "Dislocation Motion and Generation in LiF Single Crystals Subjected to Plate-Impact," *J. Appl. Physics,* Vol. 50, No. 7, pp. 4747–4762.

Mello, M. C., Prakash, V., and Clifton, R. J., 1991, "Multi-Point Interferometer for Monitoring Two Dimensional Wave Motion," *Proceedings of 1991 APS Topical Conference on Shock Compression of Condensed Matter,* S. C. Schmidt, R. D. Dick, J. W. Forbes, and D. G. Tasker, eds., Williamsburg, VA, pp. 763–766.

Sullivan, J. P., and Ezekiel, S., 1974, "A Two-Component Laser Doppler Velocimeter for Periodic Flow Fields," *J. Phys.* Vol. E7, pp. 272–274.

Tong, W., 1991, "Pressure-Shear Impact Investigation of Strain-Rate History Effects in OFHC Copper," PhD Thesis, Brown University, Providence, RI.

VALYN VISAR, 1995, *User's Handbook,* Valyn International, Alburquerque, NM.

VALYN VISAR DATA REDUCTION PROGRAM, 1995, *User's Handbook,* Valyn International, Alburquerque, NM.

Yadav, S., Davis, J. A., and Ramesh, K. T., 1993, "Damage and Recovery Experiments Using Pressure-Shear Plate Impact," *Experimental Techniques in the Dynamics of Deformable Solids,* ASME AMD-Vol. 165, pp. 71–78.

Downloaded 04 May 2010 to 171.66.16.34. Redistribution subject to ASME license or copyright; see http://www.asme.org/terms/Terms_Use.cfm

Damping Characteristics of Laminated Thick Plates

T. W. Taylor[1]
Assoc. Mem. ASME.

A. H. Nayfeh

Department of Aerospace Engineering
and Engineering Mechanics,
University of Cincinnati,
Cincinnati, OH 45221

We develop the analysis for the exact three-dimensional viscoelastic solution for simply supported, thick multilayered composite plate strips. Each layer is assumed to possess monoclinic or higher material symmetry and to be perfectly bonded to adjacent layers. The damping capacity, or loss factor, of the composite plate is derived using energy principles, allowing analysis of arbitrary through-the-thickness geometry for the composite plate. The damping characteristics of the composite plate, as well as its natural modes of vibration, are obtained with the aid of the matrix transfer technique. The matrix transfer method simplifies the requisite analytical developments as well as speeding the numerical calculations. While our analysis treats general material anisotropy and arbitrary through-the-thickness geometry, we examine, as special cases of our analysis, constrained layer damping treatments and sandwich plates. We compare our solution with previous well-known solutions that rely on complex bending modulus formulations and isotropic materials in simple layered treatments. The modal damping capacity of the composite plate is investigated as a function of both frequency of vibration and as a function of material damping modulus.

Introduction

Damping of structures has historically been of great importance in nearly all branches of engineering endeavors. Mechanical and structural systems rely on various damping mechanisms to dissipate energy during undesirable vibratory motions. Viscous damping treatments rely on the damping properties of a wide range of viscoelastic materials. Viscoelastic materials are, typically, easily integrated with structural and mechanical systems, which makes viscoelastic material damping treatments popular.

Viscoelastic materials used for damping of vibrations are, however, typically much less stiff than the materials of the load carrying structures to which they are intended to provide damping. Damping materials usually add little load carrying capability to a structural or mechanical system. Consequently, many theoretical investigations have been carried out analyzing the relative effectiveness of damping treatments, with the intent of predicting optimum amounts of the damping material needed to provide the required damping, but yet not greatly impact the load carrying ability of the overall mechanism or structure.

Early analytical investigations of the damping of flexural motions in thin bars by layers of damping materials were based on complex flexural stiffness derivations. In a classical study, Kerwin (1959) analyzed constrained layer damping treatments that damp flexural vibrations of a plate by the application of a layer of damping material that is in turn constrained by a stiff backing layer or foil. Kerwin's analysis showed the damping factor depends on the wavelength of the bending waves in the composite plate (and thus the frequency of vibration), and on the thickness and elastic moduli of the base plate, the damping layer, and the constraining layer. A complex shear modulus was assigned to the damping layer, where all of the energy dissipation was assumed to take place.

Ross, Ungar, and Kerwin (1959), extended Kerwin's analysis to practical damping treatments including homogeneous layers, damping tape, multiple damping tapes, spaced damping treatments, and sandwich plates with dissipative cores. In this work, the authors estimated the maximum amount of damping that can be achieved as a function of the relative dimensions of the treatment, and presented some relationships for the design of optimum treatments.

Ungar (1962) subsequently showed that the results of Ross et al. apply to more general geometry in the case of flexural structural members. Ungar and Kerwin (1962) then reformulated the loss factor of a dissipative system in terms of energy concepts. This reformulation provides the basis for more recent analyses of viscoelastic structural systems. Energy concepts allow the consideration of much more general forms of material symmetry and plate thickness geometry than the isotropic materials and thin plate geometry of the earlier studies based on complex bending stiffnesses.

The extensional stiffness of the dissipative core layer was added to the Kerwin formulation by DiTaranto and Blasingame (1966) in their study of sandwich plate systems. However, their work showed that, for typical dissipative core materials, the extensional stiffness had negligible effect on the response of the damped system. They compared damping characteristics of three and five-layer systems in which structural layers were alternated with dissipative layers. DiTaranto (1965) and DiTaranto and McGraw (1969) subsequently extended the alternating layer analysis to plate systems with more general boundary conditions.

A limiting feature for all of the previously cited literature is that each one relies on thin plate theory. The results of these analyses are limited to plates and beams that are relatively much longer (approximately ten times or more) than the total composite thickness dimension (or for infinite plates, thin relative to the wavelength). This assumption restricts the accuracy of the previous works with thick or moderately thick beams and plates. Siu and Bert (1974) considered laminated anisotropic rectangular plates with material damping in which they included thickness-shear flexibility and rotary and coupling inertia. Their solution was obtained by the Rayleigh-Ritz method, extended to include the energy dissipated and the work done by a forcing

[1] Current address: Ford Motor Company, M/D 3039, Building No. 3, Room 3061, Dearborn, MI 48121.

Contributed by the Applied Mechanics Division of THE AMERICAN SOCIETY OF MECHANICAL ENGINEERS for publication in the ASME JOURNAL OF APPLIED MECHANICS.

Discussion on this paper should be addressed to the Technical Editor, Professor Lewis T. Wheeler, Department of Mechanical Engineering, University of Houston, Houston, TX 77204-4792, and will be accepted until four months after final publication of the paper itself in the ASME JOURNAL OF APPLIED MECHANICS.

Manuscript received by the ASME Applied Mechanics Division, Feb. 21, 1995; final revision, Sept. 3, 1996. Associate Technical Editor: J. N. Reddy.

Copyright © 1997 by ASME

Downloaded 04 May 2010 to 171.66.16.34. Redistribution subject to ASME license or copyright; see http://www.asme.org/terms/Terms_Use.cfm

function. Their analysis, while not a thick plate theory, went beyond simple thin plate theory in the analysis of material damping in plates.

Several approximate thick plate theories have been developed to characterize damping in viscoelastic plates. Lin, Ni, and Adams (1984) analyzed the damping characteristics of thin plates using the finite element method. They defined the plate's specific damping capacity using energy concepts for free-free carbon and glass fiber-reinforced plastics plates. Dubbelday (1986) extended the Kerwin constrained-layer damping model and the resulting extended model is further improved by a hybrid model that uses exact elasticity theory to describe the base plate. Saravanos and Chamis (1990, 1990) performed an approximate two-dimensional analysis of damping in fiber composite laminates in which they included thermal and hygral (moisture) effects and effects of friction from broken fibers in the laminae.

Dubbelday (1993) and Dubbelday and Fausett (1994) recently developed two-dimensional exact solution for infinite plates which they compared with an approximate hybrid constrained layer model based on the Kerwin model. Their results showed the exact formulation superior to the hybrid model and also superior to a thin plate theory for constrained layer treatments. Saravanos (1994) recently developed a semi-analytical approach to damping characteristics of rectangular plates using three-dimensional elasticity but assuming constant through-the-thickness displacements within the layers.

Recent research investigates the use of constrained layer damping in active damping systems, as in Shen (1994), for example. Active constrained layer damping systems rely on accurate predictions of the displacements and strains in the laminae. Therefore, exact solutions for viscoelastic constrained layer damping systems are desirable for efficient active, as well as passive, damping systems. Our motivation for this paper is to provide the exact solution for three-dimensional viscoelastic systems using methods that lend themselves to fast, efficient numerical calculations. We are also motivated by the desire to investigate the inherent error in the available solutions based on thin plate theory.

In this paper we develop the analysis for the exact three-dimensional viscoelastic solution for simply supported, thick multilayered composite plate strips, following our previous analysis of the vibration characteristics of thick elastic multilayered laminates (Taylor and Nayfeh, 1994a, b; Taylor, Nayfeh, and Wade, 1994). We place no restrictions on through-the-thickness displacements, and solve the three-dimensional elasticity field equations exactly. These solutions are either trigonometric or hyperbolic, depending on material properties and frequency. The damping capacity of the composite plate system is derived using energy principles, allowing analysis of arbitrary material symmetry in each of the layers and arbitrary through-the-thickness geometry for the composite plate.

Each layer of the composite plate is assumed to possess monoclinic or higher material symmetry and to be perfectly bonded to adjacent layers. Interlaminar shear is accounted for in the three-dimensional elasticity theory, as is the location of the neutral bending axis for flexural vibrations. Consequently, in contrast to thin plate theories, no assumptions on interlaminar shear or on the location of the neutral axis need be made. The general nature of our solution allows our model to be applied to any layered damping treatment whose lamina possess monoclinic or higher material symmetry.

Even though our solution is developed for general material anisotropy and for arbitrary through-the-thickness geometry, we easily accommodate isotropic material symmetry and historically popular, and useful, simple layered damping treatments. Consequently, our analysis reproduces, as special cases, all previous analyses for beams and plate strip damping treatments. In particular, as special cases of our analysis, we examine constrained layer damping treatments and sandwich plates, as both of these systems are popular damping treatments used throughout the aerospace, automotive, and electronics industries. Our general analysis has a great variety of applications for composite laminates, a field of material research currently experiencing widespread growth.

While our analysis is for general material anisotropy and for arbitrary through-the-thickness geometry, we concentrate our numerical investigations on simple damping treatments and isotropic materials. We choose to investigate these damping treatments since the original classical work was limited to simple geometry and isotropic materials. This approach both verifies our results and provides insight into the relative errors inherent in the solutions.

The damping capacity of the composite plate is investigated as a function of both frequency of vibration and damping modulus. The damping characteristics of the composite plate, as well as the natural modes of vibration, are obtained with the aid of the matrix transfer technique. The use of the matrix transfer method simplifies the requisite analytical developments as well as speeding the numerical calculations (Taylor and Nayfeh, 1994a). The matrix transfer method has been used in a variety of applications including ultrasonics and wave propagation, (Nayfeh and Taylor, 1988, 1990; Nayfeh and Chimenti, 1988, 1989), the calculation of internal displacements and stresses of thick anisotropic layered plates (Taylor and Nayfeh, 1992), and in the analysis of vibrational characteristics of thick anisotropic laminates (Taylor and Nayfeh, 1994a, b).

Formulation of the Problem

We consider a thick multilayered plate strip consisting of an arbitrary number N of anisotropic layers, each layer with unique thickness $d^{(k)}$ and common width L. We assume each layer exhibits monoclinic or higher material symmetry and to be stacked normal to the x_3-axis of a global orthogonal Cartesian coordinate system $x_i = (x_1, x_2, x_3)$ as shown in Fig. 1. Hence, the plane of each layer is parallel to the x_1-x_2 plane, which is also chosen to coincide with a lateral surface of the layered plate.

To describe the lamina relative ply orientations of the layers, we assign an index k for each layer, $k = 1, 2, \ldots, N$, as depicted in Fig. 2(a), and a reference ply angle ϕ_k measured relative to the global x_1-axis as shown in Fig. 2(b). Here the reference ply angle does not imply measurement from axes of material symmetry but is merely a convenience to express the monoclinic material constants in terms of a set of reference material constants.

We carry forth our analysis assuming that the constitutive relations matrix for a monoclinic viscoelastic material is fully populated for each layer, that is, 13 independent nonzero material constants in both the elastic properties matrix and 13 independent nonzero constants in the viscous properties matrix. This assumption implies that we conduct our analysis with the global coordinate system axes formed by normals to the plate boundaries rather than by material symmetry axes. We do, however, define a local coordinate $x_3^{(k)}$ for each layer k to conveniently specify arbitrary locations within the layers.

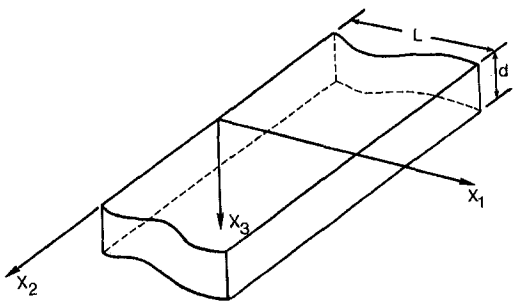


Fig. 1 Layered plate strip with global coordinate system

Downloaded 04 May 2010 to 171.66.16.34. Redistribution subject to ASME license or copyright; see http://www.asme.org/terms/Terms_Use.cfm

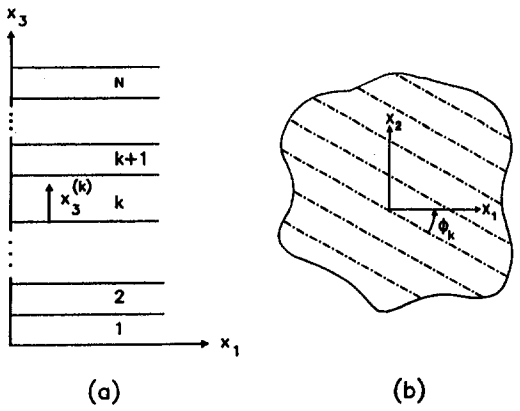


Fig. 2 The laminated plate model with (*a*) layer numbering scheme and representative local coordinate system and (*b*) a plan view of a representative layer k showing the transformation angle ϕ_k with the reference material ply direction represented by the dashed lines and the global x_1 and x_2 directions superposed

The momentum equations and strain-displacement relations, expressed in our global coordinate system, are

$$\frac{\partial \sigma_{ij}}{\partial x_j} = \rho \frac{\partial^2 u_i}{\partial t^2} \tag{1a}$$

$$\epsilon_{ij} = \frac{1}{2}\left(\frac{\partial u_i}{\partial x_j} + \frac{\partial u_j}{\partial x_i}\right). \tag{1b}$$

These field equations must be satisfied for each layer of our composite plate, and thus each layer's material properties must be explicitly characterized. We describe each layer's viscoelastic material properties with the monoclinic constitutive relations relative to $\phi_k = 0$ deg. The viscoelastic constitutive relations for each layer are then given by

$$\underline{\sigma}^{(k)} = [\mathbf{B}^{(k)}]\underline{\epsilon}^{(k)}, \tag{2}$$

where

$$[\mathbf{B}^{(k)}] = [\mathbf{C}^{(k)}] + \mathbf{i}[\mathbf{H}^{(k)}] \tag{3a}$$

$$\underline{\sigma}^{(k)} = [\sigma_{11}^{(k)} \quad \sigma_{22}^{(k)} \quad \sigma_{33}^{(k)} \quad \sigma_{23}^{(k)} \quad \sigma_{13}^{(k)} \quad \sigma_{12}^{(k)}]^T \tag{3b}$$

$$\underline{\epsilon}^{(k)} = [\epsilon_{11}^{(k)} \quad \epsilon_{22}^{(k)} \quad \epsilon_{33}^{(k)} \quad \gamma_{23}^{(k)} \quad \gamma_{13}^{(k)} \quad \gamma_{12}^{(k)}]^T \tag{3c}$$

$$[\mathbf{C}^{(k)}] = \begin{bmatrix} C_{11} & C_{12} & C_{13} & 0 & 0 & C_{16} \\ C_{12} & C_{22} & C_{23} & 0 & 0 & C_{26} \\ C_{13} & C_{23} & C_{33} & 0 & 0 & C_{36} \\ 0 & 0 & 0 & C_{44} & C_{45} & 0 \\ 0 & 0 & 0 & C_{45} & C_{55} & 0 \\ C_{16} & C_{26} & C_{36} & 0 & 0 & C_{66} \end{bmatrix}^{(k)}, \tag{3d}$$

where $i = \sqrt{-1}$, σ_{ij} are the stresses and ϵ_{ij} and γ_{ij} are the engineering strains. We assume the viscosity matrix $[\mathbf{H}^{(k)}]$ to be frequency independent and to have the same form as the elastic matrix $[\mathbf{C}^{(k)}]$, (Auld, 1990)

$$[\mathbf{H}^{(k)}] = \begin{bmatrix} \eta_{11} & \eta_{12} & \eta_{13} & 0 & 0 & \eta_{16} \\ \eta_{12} & \eta_{22} & \eta_{23} & 0 & 0 & \eta_{26} \\ \eta_{13} & \eta_{23} & \eta_{33} & 0 & 0 & \eta_{36} \\ 0 & 0 & 0 & \eta_{44} & \eta_{45} & 0 \\ 0 & 0 & 0 & \eta_{45} & \eta_{55} & 0 \\ \eta_{16} & \eta_{26} & \eta_{36} & 0 & 0 & \eta_{66} \end{bmatrix}^{(k)}. \tag{3e}$$

The viscoelastic material properties matrix of Eq. (2) transforms, under in-plane rotation ϕ_k, according to the relation

$$[\mathbf{B}^{(k)}] = [\mathbf{R}^{(k)}]^T[\mathbf{B}_0^{(k)}][\mathbf{R}^{(k)}], \tag{4a}$$

where $[\mathbf{B}_0^{(k)}]$ is the matrix of reference material constants for $\phi_k = 0$ deg,

$$[\mathbf{R}^{(k)}] = \begin{bmatrix} c^2 & s^2 & 0 & sc & 0 & 0 \\ s^2 & c^2 & 0 & -sc & 0 & 0 \\ 0 & 0 & 1 & 0 & 0 & 0 \\ -2sc & 2sc & 0 & (c^2 - s^2) & 0 & 0 \\ 0 & 0 & 0 & 0 & c & -s \\ 0 & 0 & 0 & 0 & s & c \end{bmatrix}^{(k)}, \tag{4b}$$

and $c = \cos \phi_k$ and $s = \sin \phi_k$. Combining Eqs. (1), (2), and (3) for each layer k, yields N systems of three partial differential equations

$$[\mathbf{L}]\underline{\mathbf{u}}^{(k)} = \rho \frac{\partial^2 \underline{\mathbf{u}}^{(k)}}{\partial^2 t}, \tag{5}$$

where the entries of the second-order operator $[\mathbf{L}]$ are given in the Appendix.

We present relevant results from our previous works required for the formal solutions of Eq. (5) for each layer of the composite plate. These solutions satisfy in-plane, simply supported boundary conditions ($w = \sigma_{11} = \sigma_{12} = 0$ at $x_1 = 0, L$) for plate strips from which we obtain appropriate expressions for the displacements within each layer (Taylor and Nayfeh, 1994a, b; Taylor et al., 1994; Jones, 1970, 1971; Pagano, 1970; Srinivas and Rao, 1970),

$$\underline{\mathbf{u}}^{(k)}(x_1, x_3^{(k)}, t) = \sum_{n=1}^{\infty} [\mathbf{S}(x_1)][\mathbf{D}^{(k)}][\mathbf{E}^{(k)}(x_3^{(k)})]\underline{\mathbf{U}}^{(k)} e^{i\omega t}, \tag{6a}$$

where Eq. (6*a*) explicitly shows the solution's independence of the x_2-coordinate which is a consequence of the assumed infinite dimension in the x_2-direction, and where

$$\underline{\mathbf{u}}^{(k)}(x_1, x_3^{(k)}, t) = [u^{(k)} \quad v^{(k)} \quad w^{(k)}]^T \tag{6b}$$

$$[\mathbf{S}(x_1)] = \text{diag} \quad [\cos(p_n x_1) \cos(p_n x_1) \sin(p_n x_1)] \tag{6c}$$

$$[\mathbf{D}^{(k)}] = \begin{bmatrix} 1 & 1 & 1 & 1 & 1 & 1 \\ V_1 & V_2 & V_3 & V_4 & V_5 & V_6 \\ W_1 & W_2 & W_3 & W_4 & W_5 & W_6 \end{bmatrix}^{(k)} \tag{6d}$$

$$[\mathbf{E}^{(k)}(x_3^{(k)})] = \text{diag}\,[e^{\lambda_q^{(k)} x_3^{(k)}}], \quad q = 1, \ldots, 6 \tag{6e}$$

$$\underline{\mathbf{U}}^{(k)} = [U_1^{(k)} \quad U_2^{(k)} \quad U_3^{(k)} \quad U_4^{(k)} \quad U_5^{(k)} \quad U_6^{(k)}]^T \tag{6f}$$

$$p_n = \frac{n\pi}{L}. \tag{6g}$$

Here $U_q^{(k)}$ are the modal amplitudes, ω is the circular frequency and $\lambda^{(k)}$ is the x_3-direction mode number to be determined later.

In subsequent analysis, we suppress the modal subscript n to avoid notational complexity, but with the understanding that U_q, ($q = 1, \ldots, 6$) p, λ, and ω stand for U_{qn}, p_n, λ_n, and ω_n, respectively. Similarly, hereafter we suppress the superscript k designating quantities associated with layer k, unless needed to avoid ambiguity. In the above relations λ satisfies the characteristic equation

$$\lambda^6 + A_1\lambda^4 + A_2\lambda^2 + A_3 = 0, \tag{7}$$

which relates λ to ω for each layer k and whose coefficients A_1, A_2, and A_3 are listed in the Appendix. Similarly, for each layer the displacement ratios V_q and W_q of Eq. (6*d*) are given in the Appendix.

Downloaded 04 May 2010 to 171.66.16.34. Redistribution subject to ASME license or copyright; see http://www.asme.org/terms/Terms_Use.cfm

Matrix Formulation

We define a "response" vector containing the field quantities that are continuous across the layer interfaces,

$$\underline{\Phi}^{(k)} = \begin{bmatrix} \underline{u}^{(k)} \\ \underline{\tau}^{(k)} \end{bmatrix}, \tag{8a}$$

where

$$\underline{\tau}^{(k)} = [\sigma_{33}^{(k)} \quad \sigma_{13}^{(k)} \quad \sigma_{23}^{(k)}]^T. \tag{8b}$$

Our motivation for this definition is our subsequent implementation of the matrix transfer technique which relates the displacements $\underline{u}^{(k)}$ of Eq. (6*b*) and stresses $\underline{\tau}^{(k)}$ of one face to those of the other of layer k. Using Eqs. (6*b*) and (2), the response vector is explicitly given by

$$\underline{\Phi}^{(k)} = [\mathbf{T}(x_1)][\mathbf{X}^{(k)}][\mathbf{E}^{(k)}(x_3^{(k)})]\underline{\mathbf{U}}^{(k)} e^{i\omega t}, \tag{9}$$

where

$$[\mathbf{T}(x_1)] = \text{diag}\,[c_n \quad c_n \quad s_n \quad s_n \quad c_n \quad c_n] \tag{10a}$$

$$[\mathbf{X}^{(k)}] = [\underline{\mathbf{1}} \quad \underline{\mathbf{V}} \quad \underline{\mathbf{W}} \quad \underline{\mathbf{D}}_1 \quad \underline{\mathbf{D}}_2 \quad \underline{\mathbf{D}}_3]^{\mathbf{T}} \tag{10b}$$

$$\underline{\mathbf{D}}_1 = [-B_{13}p\underline{\mathbf{1}} + B_{33}(\underline{\mathbf{W}}\underline{\lambda}) - B_{36}p\underline{\mathbf{V}}] \tag{10c}$$

$$\underline{\mathbf{D}}_2 = [B_{45}(\underline{\mathbf{V}}\underline{\lambda}) + B_{55}(\underline{\lambda} + p\underline{\mathbf{W}})] \tag{10d}$$

$$\underline{\mathbf{D}}_3 = [B_{44}(\underline{\mathbf{V}}\underline{\lambda}) + B_{45}(\underline{\lambda} + p\underline{\mathbf{W}})]. \tag{10e}$$

$c_n = \cos(p_n x_1)$, $s_n = \sin(p_n x_1)$, and no summation is implied by repeated indices.

We relate the displacements and stresses at one face of layer k, $x_3^{(k)} = d^{(k)}$, in terms of those at the other face of layer k, $x_3^{(k)} = 0$, by specializing Eq. (9) to the two locations and eliminating the common amplitude vector $\underline{\mathbf{U}}^{(k)}$

$$\underline{\Phi}^{(k)}(d^{(k)}) = [\mathbf{a}^{(k)}]\underline{\Phi}^{(k)}(0^{(k)}). \tag{11}$$

Here, $[\mathbf{a}^{(k)}]$ is the local transfer matrix for layer k and

$$[\mathbf{a}^{(k)}] = [\mathbf{X}^{(k)}][\mathbf{E}^{(k)}(d^{(k)})][\mathbf{X}^{(k)}]^{-1}. \tag{12}$$

Matrix Transfer Technique

We relate the composite plate's lateral boundary responses to one another by exploitation of the matrix transfer technique. The perfect interfacial bonding assumption is conveniently summarized at the interface between layers k and $k+1$ by

$$\underline{\Phi}^{(k+1)}(0^{(k+1)}) = \underline{\Phi}^{(k)}(d^{(k)}). \tag{13}$$

The matrix transfer technique then yields, through repeated application of the interfacial continuity conditions (13) with (11), the response vector at $x_3 = d$ in terms of the response vector at $x_3 = 0$

$$\underline{\Phi}^{(N)}(d) = [\mathbf{A}]\underline{\Phi}^{(1)}(0), \tag{14}$$

where $[\mathbf{A}]$ is the global transfer matrix for the composite plate, whose properties are discussed by Nayfeh (1991), and

$$[\mathbf{A}] = [\mathbf{a}^{(N)}][\mathbf{a}^{(N-1)}]\cdots[\mathbf{a}^{(1)}]. \tag{15}$$

Damping Capacity

We define the damping capacity, or loss factor, of the composite plate as the ratio of the dissipated energy to the stored elastic energy (Lazan, 1968). Each vibration mode has the characteristic damping capacity (Ungar and Kerwin, 1962)

$$\eta_c = \frac{U_d}{U_e}, \tag{16}$$

where

$$U_d = \int_V \underline{\epsilon}^T[\mathbf{H}]\underline{\epsilon}^* dV, \tag{17a}$$

is the dissipated energy and

$$U_e = \int_V \underline{\epsilon}^T[\mathbf{C}]\underline{\epsilon}^* dV, \tag{17b}$$

is the stored elastic energy, η_c is the composite plate's damping capacity, the asterisk denotes the complex conjugate, and the integration is over the volume of the plate. Using the matrix transfer method the strain vector in Eqs. (17*a*, *b*) is

$$\underline{\epsilon}^{(\mathbf{k})} = [\mathbf{Q}(\mathbf{x}_1)][\mathbf{F}^{(\mathbf{k})}][\mathbf{E}^{(\mathbf{k})}(x_3^{(\mathbf{k})})][\mathbf{X}^{(\mathbf{k})}]^{-1}[\mathbf{A}_{\mathbf{k-1}}]\underline{\Phi}_0, \tag{18a}$$

where,

$$[\mathbf{Q}] = \text{diag}\,[s_n \quad 0 \quad s_n \quad c_n \quad c_n \quad s_n] \tag{18b}$$

$$[\mathbf{F}] = [-p\underline{\mathbf{1}} \quad \underline{\mathbf{0}} \quad (\underline{\lambda}\underline{\mathbf{W}}) \quad (\underline{\lambda}\underline{\mathbf{V}}) \quad (\underline{\lambda} + \mathrm{p}\underline{\mathbf{W}}) \quad -\mathrm{p}\underline{\mathbf{V}}]^T \tag{18c}$$

$$[\mathbf{A}^{(k-1)}] = [\mathbf{a}^{(k-1)}][\mathbf{a}^{(k-2)}]\cdots[\mathbf{a}^{(1)}] \tag{18d}$$

$$\underline{\Phi}_0 = \underline{\Phi}^{(1)}(0). \tag{18e}$$

Integration over x_1 in Eqs. (17*a*, *b*) leads to a common factor of $L/2$ in both the numerator and denominator of Eq. (16) as all terms in scalars U_e and U_d have x_1 dependency of the form $\cos^2(px_1)$ or $\sin^2(px_1)$. However, integration over x_3 results in terms of the form

$$R_{ij}^{(k)} = \frac{P_{ij}^{(k)}}{(\lambda_i + \lambda_j^*)}[e^{(\lambda_i+\lambda_j^*)d^{(k)}} - 1], \quad \lambda_i \neq -\lambda_j^* \tag{19a}$$

$$R_{ij}^{(k)} = P_{ij}^{(k)} d^{(k)}, \quad \lambda_i = -\lambda_j^*, \tag{19b}$$

where

$$[\mathbf{P}^{(k)}] = [\mathbf{F}^{(k)}]^T[\mathbf{C}^{(k)}][\mathbf{F}^{(k)}]^*, \tag{19c}$$

for U_e, and $[\mathbf{C}]$ is replaced by $[\mathbf{H}]$ for U_d.

Modal Frequencies

The modal frequencies ω and bottom boundary mode shapes $\underline{\mathbf{u}}_0$ for the free vibration modes of the plate strip are obtained from our previous analysis (Taylor and Nayfeh, 1994). The characteristic equation for free vibration of the plate with its layers all perfectly bonded is

$$[\mathbf{M}]\underline{\mathbf{u}}_0 = \underline{\mathbf{0}}, \tag{20a}$$

where the entries of $[\mathbf{M}]$ are

$$M_{ij} = A_{(i+3)j}, \quad i, j = 1, 2, 3, \tag{20b}$$

and,

$$\underline{\mathbf{u}}_0 = \underline{\mathbf{u}}^{(1)}(0). \tag{20c}$$

Results and Discussion

Our analysis of the damping capacity (loss factor) of plate strips (and beams) is an "exact" analysis, consistent with the assumptions of linear viscoelasticity. Consequently, our formulation relies on no assumptions of the relative thickness of the individual layers of the composite plate. We also need not deter-

Downloaded 04 May 2010 to 171.66.16.34. Redistribution subject to ASME license or copyright; see http://www.asme.org/terms/Terms_Use.cfm

mine the neutral axis of bending a priori, as in earlier analyses of damped beams and plates. Finally, we need not make any assumption on interlaminar shear as required by many recent analyses of both viscoelastic and purely elastic layered plate systems. In fact, the power of our exact solution is especially apparent when used to analyze constrained layer damping systems, whose analysis has historically been limited by the use of thin plate theory requiring assumptions on both relative thickness and stiffness of the composite plate's layers.

We simplify our presentation of results by using a single ratio, β, for the damping modulus matrix $[\mathbf{H}]$ relative to the elastic modulus matrix $[\mathbf{C}]$. Therefore, all of our results have constitutive relationships of the form

$$[\mathbf{B}] = (1 + i\beta)[\mathbf{C}] \tag{21}$$

where now the damping modulus matrix is $[\mathbf{H}] = \beta[\mathbf{C}]$. So that we may compare our analysis with thin plate theories we choose length $L = 100$ cm and plate thickness, d, as approximately 1 cm, assuring thin plate behavior from our model. We further restrict our material selection by specializing the elastic material properties matrix $[\mathbf{C}]$ to the case of isotropy so that we may compare our general analysis with previous analyses. These restrictions on geometry and material symmetry are easily accommodated by our analysis as all material symmetry classes, as well as all through-the-thickness geometry arrangements, are implicitly contained in our solution. The material properties for our example laminae are listed in the Appendix.

Constrained Layer Damping

We examine a constrained layer damping treatment to show the utility and relative ease of use of our model. A constrained layer damping treatment consists of a base plate that is subjected to transverse excitations which result in undesirable flexural vibrations. A dissipative material, relatively compliant in extension compared to the base plate, is then perfectly bonded to the base plate. A third layer, the constraining layer, relatively thin compared to the base plate is, in turn, perfectly bonded to the dissipative layer. During flexural vibrations the dissipative layer is subjected to relatively large shear strains, through the constraint provided by the thin, stiff top layer, which is the mechanism of damping for the composite plate.

Momentarily departing from our thin plate simulation, Fig. 3 presents a typical constrained layer damping treatment with a steel base plate, an epoxy dissipative layer, and a relatively thin steel constraining layer, with thicknesses 0.4 cm, 0.5 cm, and 0.1 cm, respectively, and width 7 cm. Figures 3(b) and 3(c) show the composite plate undergoing its first two characteristic fundamental modes of vibration. For our comparison of constrained layer damping systems we limit our results to the first thickness mode of vibration since the thin plate theory of previous analyses are limited to predicting only the first thickness mode. Figures 3(b) and 3(c) are drawn from our exact solutions, using the matrix transfer method, where

$$\underline{\mathbf{u}}^{(k)} = [\mathbf{S}(x_1)][\mathbf{F}^{(k)}][\mathbf{E}^{(k)}(x_3^{(k)})][\mathbf{X}^{(k)}]^{-1}[\mathbf{A}^{(k-1)}]\underline{\Phi}_0. \tag{22}$$

Figures 3(b) and 3(c) reveal the constraining action of the top layer on the top surface of the dissipative layer. This action restrains the dissipative layer from bending with the base plate, resulting in the characteristic shearing strain of the dissipative layer. In our analysis, the physics of the damping mechanism is embodied in the exact viscoelasticity theory, through Eq. (22), requiring no special assumptions on the formulation for the plate's damping characteristics. We emphasize that the constraining action and characteristic displaced shape of the constrained layer damping treatment of Fig. 3 is a "by-product" of our analysis. Earlier thin plate analyses, as in Kerwin (1959), are founded on, and developed from this assumed shape, as given by the illustration in Figs. 2 and 6 of Ross, Ungar, and Kerwin (1959).

In Fig. 4 we return to our thin plate simulation and present the damping capacity for a constrained layer damping treatment with a .3175-cm-thick steel baseplate, a relatively compliant .00635-cm-thick dissipative layer and a .0508-cm-thick steel constraining layer. The damping capacity is presented as a function of the modified shear parameter $g(1 + k_3)$, as adopted by previous authors (Ross, Ungar, and Kerwin, 1959), where

$$g = \frac{\beta G_2}{K_3 d^{(2)} p^2} \tag{23}$$

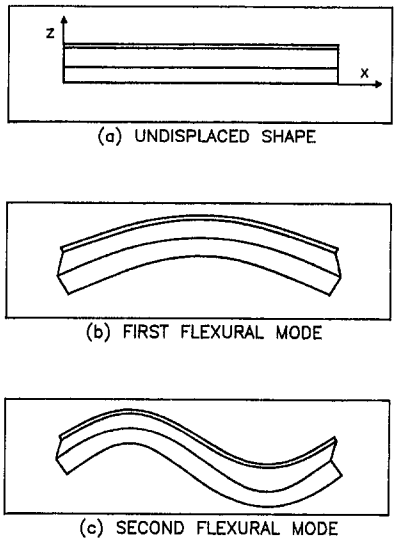


Fig. 3 A typical constrained layer damping treatment (a) undisplaced shape, (b) first flexural mode and (c) second flexural mode

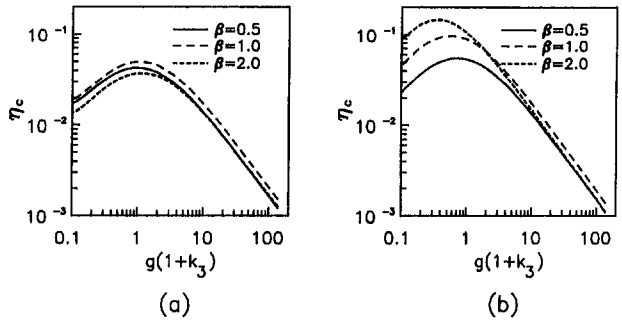


Fig. 4 Damping capacity for a constrained layer treatment as a function of the modified shear parameter using (a) the exact solution and (b) the approximate solution

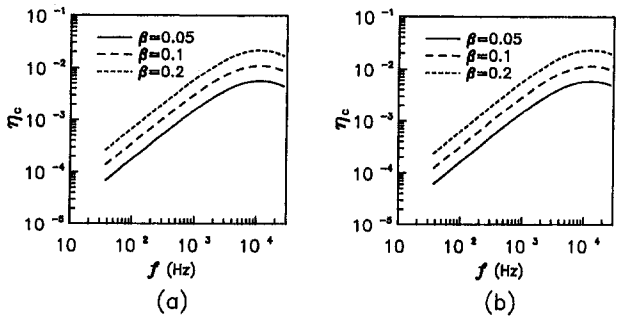


Fig. 5 Damping capacity of the plate of Fig. 4 as a function of frequency for small values of β using (a) the exact solution and (b) the approximate solution

Downloaded 04 May 2010 to 171.66.16.34. Redistribution subject to ASME license or copyright; see http://www.asme.org/terms/Terms_Use.cfm

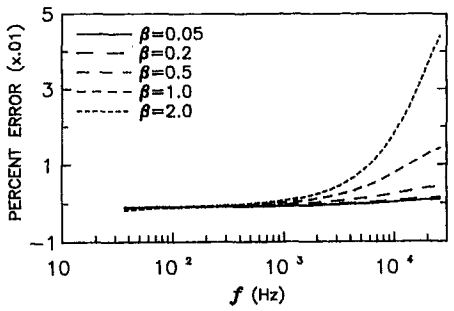


Fig. 6 Relative error between the approximate and exact solutions of the constrained layer treatment as a function of frequency and as a function β, the ratio of the loss modulus with the elastic modulus

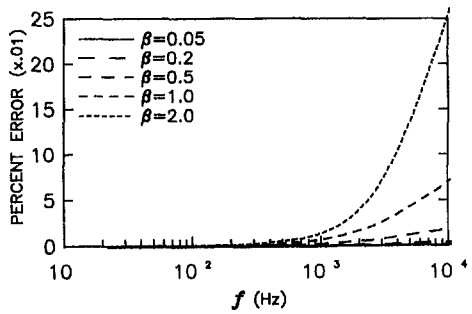


Fig. 8 Relative error between the approximate and exact solutions of the sandwich plate as a function of natural frequency and as a function β, the ratio of the loss modulus with the elastic modulus

with $K_3 = d^{(3)}E_3$, $k_3 = K_3/(E_1 d^{(1)})$, E_3 is the Young's modulus of layer 3, G_2 is the elastic shear modulus of the dissipative layer, β is the ratio of the damping modulus to the elastic modulus of the dissipative layer, and p is the mode number of the vibration. We compare the variation in the plate's damping capacity with the results of classical approximate analyses (Fig. 13 of Ross, Ungar, and Kerwin (1959)) to both validate our model and to show the effects of the assumptions inherent in the classical analyses.

Curves calculated using our exact analysis, Fig. 4(a), and the classical Kerwin analysis, Fig. 4(b), are presented for comparison. At high values of the modified shear parameter, $g(1 + k_3)$ (below $f = 200$ Hz), the damping capacity predicted by both analyses are identical. However, at low values of the modified shear parameter (above $f = 200$ Hz) our exact solution predicts a lower damping capacity than the approximate solution. The disparity between the solutions increases as the dissipative material's damping coefficient β increases. In addition, our exact solution predicts that the maximum values of damping capacity, for high β, occur at lower frequencies than those predicted by the approximate solution.

Figure 5 presents the damping capacity as a function of frequency for this plate at relatively low values of β for the exact solution, Fig. (5a), and Kerwin's approximate solution, Fig. (5b). Here, no error is apparent between the exact and approximate solutions in the displayed frequency range. The error between our exact analysis and the approximate solution, relative to the exact solution, is presented in Fig. 6 as a function of frequency and β. Little error is apparent below 200 Hz, but above 200 Hz the error increases dramatically with frequency for relatively large values of β. Figure 6 implies that, for even moderate frequencies (200–2000 Hz) and moderate values of β (.2–.5), the approximate solution yields considerable error with increasing frequency.

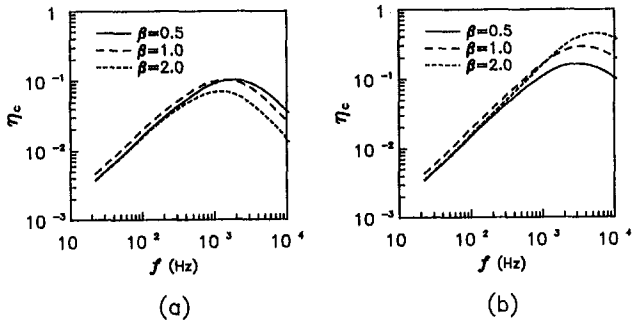


Fig. 7 The damping capacity of a sandwich plate as a function of frequency for large values of β using (a) the exact solution and (b) the approximate solution

Sandwich Plates

Plates composed of two equal thickness elastic structural layers, separated by a thin dissipative bonding layer are commonly referred to as sandwich plates. Figure 7 presents the damping capacity for a sandwich plate with steel layers each .43942 cm thick and a viscoelastic bonding layer .01778 cm thick. We compare the damping capacity from the exact solution in Fig. 7(a) with the approximate solution of DiTaranto and Blasingame (1966) in Fig. 7(b). Again, high values of the damping modulus ratio, β, yield considerable disparity in the predicted damping capacity of the two solutions with increasing frequency.

As with the constrained layer treatment example, the maximum damping is predicted to occur at lower frequencies by our exact solution compared to those predicted by DiTaranto and Blasingame's approximate solution. The error between the damping capacity calculated using the exact and approximate solutions, relative to the exact solution, is presented in Fig. 8 as a function of frequency and as a function of β. Again, the disparity between solutions increases with frequency as β is increased.

Summary and Conclusions

We have developed a computationally efficient exact solution for calculating the damping capacity of thick laminated plate strips. Our exact solution relies only on assumptions consistent with three-dimensional linear viscoelasticity. Our exact solution may be applied to plates of arbitrary thickness, arbitrary number of layers, and layers with anisotropic material symmetry as low as monoclinic. Results show that earlier available approximate solutions for the damping capacity of plates and beams, using thin plate theory, agree with the exact theory for relatively low values of frequency and loss moduli. As the loss moduli are increased, relative to the elastic moduli, the solutions diverge with increasing frequency. Our exact solution predicts the maximum value of the composite plate's damping capacity to occur at lower frequency than that predicted by the available approximate theories for all but very small values of material damping.

References

Auld, B. A., 1990, *Acoustic Fields and Waves in Solids*, 2nd ed., Robert E. Kreiger, Malabar, FL.

DiTaranto, R. A., 1965, "Theory of Vibratory Bending for Elastic and Viscoelastic Layered Finite-Length Beams," ASME JOURNAL OF APPLIED MECHANICS, Vol. 87, Series E, pp. 881–886.

DiTaranto, R. A., and Blasingame, W., 1966, "Composite Loss Factors of Selected Laminated Beams," *Journal of the Acoustical Society of America*, Vol. 40, No. 1, pp. 187–194.

DiTaranto, R. A., and McGraw, J. R., Jr., 1969, "Vibratory Bending of Damped Laminated Plates," ASME *Journal of Engineering for Industry*, Vol. 91, pp. 1081–1090.

Dubbelday, P. S., 1986, "Constrained-Layer Model Investigation Based on Exact Elasticity Theory," *Journal of the Acoustical Society of America*, Vol. 80, No. 4, pp. 1097–1102.

Downloaded 04 May 2010 to 171.66.16.34. Redistribution subject to ASME license or copyright; see http://www.asme.org/terms/Terms_Use.cfm

Dubbelday, P. S., 1993, "Constrained-Layer Damping Analysis for Extensional Waves in Infinite, Fluid-Loaded Plates," *Journal of the Acoustical Society of America,* Vol. 93, No. 4, pp. 1927–1935.

Dubbelday, P. S., and Fausett, L. V., 1994, "Constrained-Layer Damping Analysis for Flexural Waves in Infinite Fluid-Loaded Plates," *Journal of the Acoustical Society of America,* Vol. 90, No. 3, pp. 1475–1487.

Jones, A. T., 1970, "Exact Natural Frequencies for Cross-Ply Laminates," *Journal of Composite Materials,* Vol. 4, pp. 476–491.

Jones, A. T., 1971, "Exact Natural Frequencies and Modal Functions for a Thick Off-Axis Lamina," *Journal of Composite Materials,* Vol. 5, pp. 504–520.

Kerwin, E. M., Jr., 1959, "Damping of Flexural Waves by a Constrained Viscoelastic Layer," *Journal of the Acoustical Society of America,* Vol. 31, No. 7, pp. 952–962.

Lazan, B. J., 1968, *Damping of Materials and Members in Structural Mechanics,* 1st ed., Pergamon Press, Oxford, U.K.

Lin, D. X., Ni, R. G., and Adams, R. D., 1984, "Prediction and Measurement of the Vibrational Damping Parameters of Carbon and Glass Fibre-Reinforced Plastics Plates," *Journal of Composite Materials,* Vol. 18, pp. 132–152.

Nayfeh A. H., 1991, "The General Problem of Elastic Wave Propagation in Multilayered Anisotropic Media," *Journal of the Acoustical Society of America,* Vol. 89, No. 4, Pt. 1, pp. 1521–1531.

Nayfeh A. H., and Chimenti, D. E., 1988, "Ultrasonic Wave Reflection From Liquid-Coupled Orthotropic Plates With Application to Fibrous Composites," ASME JOURNAL OF APPLIED MECHANICS, Vol. 55, pp. 863–870.

Nayfeh A. H., and Chimenti, D. E., 1989, "Free Wave Propagation in Plates of General Anisotropic Media," ASME JOURNAL OF APPLIED MECHANICS, Vol. 56, pp. 881–886.

Nayfeh A. H., and Chimenti, D. E., 1991, "Elastic Wave Propagation in Fluid-Loaded Multi Axial Anisotropic Media," *Journal of the Acoustical Society of America,* Vol. 89, pp. 542–549.

Nayfeh A. H., and Taylor, T. W., 1988, "Surface Wave Characteristics of Fluid-Loaded Multilayered Media," *Journal of the Acoustical Society of America,* Vol. 84, No. 6, pp. 2187–2191.

Nayfeh, A. H., and Taylor, T. W., 1990, "Dynamic Distribution of Displacement and Stress Considerations in the Ultrasonic Immersion Nondestructive Evaluation of Multilayered Plates," ASME *Journal of Engineering Materials and Technology,* Vol. 112, pp. 260–265.

Pagano, N. J., 1970, "Exact Solutions for Rectangular Bidirectional Composites and Sandwich Plates," *Journal of Composite Materials,* Vol. 4, pp. 20–34.

Ross, D., Ungar, E. E., and Kerwin, E. M. Jr., 1959, *Structural Damping,* ASME, New York.

Saravanos, D. A., 1994, "Integrated Damping Mechanics for Thick Composite Laminates and Plates," ASME JOURNAL OF APPLIED MECHANICS, Vol. 61, pp. 375–383.

Saravanos, D. A., and Chamis, C. C., 1990a, "Unified Micromechanics of Damping for Unidirectional and Off-Axis Fiber Composites," *Journal of Composites Technology and Research,* Vol. 12, No. 1, pp. 31–40.

Saravanos, D. A., and Chamis, C. C., 1990b, "Mechanics of Damping for Fiber Composite Laminates Including Hygrothermal Effects," *AIAA Journal,* Vol. 28, No. 10, pp. 1813–1819.

Shen, I. Y., 1994, "Hybrid Damping Through Intelligent Constrained Layer Treatments," ASME *Journal of Vibration and Acoustics,* Vol. 116, pp. 341–349.

Siu, C. C., and Bert, C. W., 1974, "Sinusoidal Response of Composite-Material Plates With Material Damping," ASME *Journal of Engineering for Industry,* Vol. 96, Series B, pp. 603–610.

Srinivas, S., and Rao, A. K., 1970, "Bending, Vibration and Buckling of Simply Supported Thick Orthotropic Rectangular Plates and Laminates," *International Journal of Solids and Structures,* Vol. 6, pp. 1463–1481.

Taylor, T. W., and Nayfeh A. H., 1992, "Dynamic Internal Response of Fluid-Loaded Multilayered Anisotropic Media," *Journal of the Acoustical Society of America,* Vol. 91, No. 5, pp. 2519–2528.

Taylor, T. W., and Nayfeh A. H., 1994a, "Natural Frequencies of Thick Anisotropic Composite Plates," *Composites Engineering,* Vol. 4, No. 10, pp. 1011–1021.

Taylor, T. W., and Nayfeh A. H., 1994b, "The Vibration Characteristics of Thick Rectangular Multilayered Plates," submitted to *Composites Engineering.*

Taylor, T. W., Nayfeh A. H. and Wade, J. E., 1994, "Dynamic Response of Thick Anisotropic Composite Plates," *Composites Engineering,* Vol. 4, No. 5, pp. 475–486.

Ungar, E. E., 1962, "Loss Factors of Viscoelastically Damped Beam Structures," *Journal of the Acoustical Society of America,* Vol. 34, No. 8, pp. 1082–1089.

Ungar, E. E., and Kerwin, E. M., Jr., 1962, "Loss Factors of Viscoelastic Systems in Terms of Energy Concepts," *Journal of the Acoustical Society of America,* Vol. 34, No. 7, pp. 954–957.

APPENDIX

The entries of the second-order operator matrix [**L**] of Eq. (5) are

$$L_{11} = B_{11}\frac{\partial^2}{\partial x_1^2} + B_{55}\frac{\partial^2}{\partial x_3^2}, \quad L_{11} = B_{16}\frac{\partial^2}{\partial x_1^2} + B_{45}\frac{\partial^2}{\partial x_3^2} \tag{A1}$$

$$L_{13} = (B_{13} + B_{55})\frac{\partial^2}{\partial x_1 \partial x_3}, \quad L_{22} = B_{66}\frac{\partial^2}{\partial x_1^2} + B_{44}\frac{\partial^2}{\partial x_3^2} \tag{A2}$$

$$L_{23} = (B_{36} + B_{45})\frac{\partial^2}{\partial x_1 \partial x_3}, \quad L_{33} = B_{55}\frac{\partial^2}{\partial x_1^2} + B_{33}\frac{\partial^2}{\partial x_3^2}. \tag{A3}$$

The coefficients of the characteristic equation (Eq. (7)) are

$$\begin{aligned} A_1 = [&B_{11}B_{33}B_{44} - B_{13}^2B_{44} + 2B_{13}B_{36}B_{45} - 2B_{13}B_{44}B_{55} \\ &+ B_{13}B_{45}^2 - 2B_{16}B_{33}B_{45} + B_{33}B_{55}B_{66} - B_{36}^2B_{55} \\ &- (B_{33}B_{44} + B_{33}B_{55} + B_{44}B_{55} - B_{45}^2)\rho c^2]/\Delta \end{aligned} \tag{A4}$$

$$\begin{aligned} A_2 = [&B_{11}B_{33}B_{66} - B_{11}B_{36}^2 - 2B_{11}B_{36}B_{45} + B_{11}B_{44}B_{55} \\ &- B_{11}B_{45}^2 + B_{45}^2B_{66} + 2B_{13}B_{16}B_{36} + 2B_{13}B_{16}B_{45} \\ &- 2B_{13}B_{55}B_{66} - B_{16}^2B_{33} + 2B_{16}B_{36}B_{55} \\ &- (B_{11}B_{33} + B_{11}B_{44} - B_{13}^2 - 2B_{13}B_{55} - 2B_{16}B_{45} \\ &+ B_{33}B_{66} - B_{36}^2 - 2B_{36}B_{45} + B_{44}B_{55} - B_{45}^2 + B_{55}B_{66}) \\ &\times \rho c^2 + (B_{33} + B_{44} + B_{55})\rho^2 c^4]/\Delta \end{aligned} \tag{A5}$$

$$\begin{aligned} A_3 = [&B_{11}B_{55}B_{66} - B_{16}^2B_{55} \\ &- (B_{11}B_{55} + B_{11}B_{66} + B_{16}^2 + B_{55}B_{66})\rho c^2 \\ &+ (B_{11} + B_{55} + B_{66})\rho^2 c^4 - \rho^3 c^6]/\Delta \end{aligned} \tag{A6}$$

$$\Delta = B_{33}B_{44}B_{55} - B_{33}B_{45}^2 \tag{A7}$$

where

$$c = \frac{\omega}{\rho}. \tag{A8}$$

The displacement ratios Vq and Wq of Eq. (6c) are

$$V_q = \frac{K_{11}K_{23} - K_{13}K_{12}}{K_{13}K_{22} - K_{12}K_{23}} \tag{A9}$$

$$W_q = \frac{K_{11}K_{23} - K_{12}K_{13}}{K_{12}K_{33} - K_{23}K_{13}} \tag{A10}$$

where

$$K_{11} = B_{55}\lambda^2 - B_{11}p^2 + \rho\omega^2, \quad K_{12} = B_{45}\lambda^2 - B_{16}p^2 \tag{A11}$$

$$K_{13} = (B_{13} + B_{55})\lambda p, \quad K_{22} = B_{44}\lambda^2 - B_{66}p^2 + \rho\omega^2 \tag{A12}$$

$$K_{23} = (B_{36} + B_{45})\lambda p,$$

$$K_{33} = -B_{33}\lambda^2 + B_{55}p^2 - \rho\omega^2. \tag{A13}$$

The elastic properties of our example materials are, for the structural layers (steel)

$$E = 206.7 \text{ GPa}, \quad G = 80.12 \text{ GPa}, \quad \rho = 7.84 \text{ g/cm},$$

for the dissipative epoxy layer material of Fig. 3

$$E = 3.085 \text{ GPa},$$

$$G = 1.28 \text{ GPa}, \rho = 1.25 \text{ g/cm and } \beta = 0.01,$$

and for the dissipative layer material of Figs. 4 through 8

$$E = 0.77744 \text{ GPa}, \quad G = 0.0689 \text{ GPa},$$

$$\rho = 2.0 \text{ g/cm and } \beta \text{ as given in the text.}$$

Downloaded 04 May 2010 to 171.66.16.34. Redistribution subject to ASME license or copyright; see http://www.asme.org/terms/Terms_Use.cfm

Parametric Resonance of a Spinning Disk Under Space-Fixed Pulsating Edge Loads

Jen-San Chen
Associate Professor,
Department of Mechanical Engineering,
National Taiwan University,
Taipei, Taiwan 107

The parametric resonance of a spinning disk under a space-fixed pulsating edge load is investigated analytically. We assume that the radial edge load can be expanded in a Fourier series. With use of the orthogonality properties among the eigenfunctions of a gyroscopic system, the partial differential equation of motion is discretized into a system of generalized Hill's equations in the first-order form. The method of multiple scale is employed to determine the conditions for single mode as well as combination resonances to occur. For any two modes, with s and υ nodal diameters, respectively, combination resonance occurs only when there exists a specific Fourier component cos kθ in the edge load, where s + υ = ±k. Sum type resonance occurs when both modes are reflected or both modes are nonreflected. On the other hand, difference type resonance occurs when one mode is reflected and the other is nonreflected. In applying this rule, the number of nodal diameters of a forward and a reflected wave is considered as negative. Several typical loadings are discussed, including uniform and concentrated edge loads.

Introduction

The vibration analysis of a spinning disk under a space-fixed edge load attracts attention because of its possible application in such fields as circular saw cutting and grind wheel operation. Carlin and his co-workers' investigation (1975) appears to be the first paper attempting to calculate the natural frequencies of a spinning disk under a concentrated radial edge load. Radcliffe and Mote (1977) extended the work of Carlin et al. by considering a general concentrated edge load with both radial and tangential components. The formulations in these two papers did not take into account the effects of relative motion between the spinning disk and the space-fixed edge load. Recently Chen (1994) reformulated the problem with emphasis on the effects of relative motion between the disk and the edge load on the stability and natural frequencies of the loaded disk. He reported that both divergence and flutter instabilities are induced by the space-fixed edge load when the disk is spinning at or beyond the first critical speed.

The edge loads in these aforementioned works are assumed to be independent of time. In the case when the edge loads are periodically varying, parametric resonance may be induced. Tani and Nakamura (1978, 1980) studied the dynamic instability of an annular disk under periodically varying in-plane edge traction. The disk considered in their papers is clamped on both the inner and outer radii, and the edge traction is uniform in the circumferential direction. Zajaczkowski (1983) investigated the parametric resonance of a clamped-free disk under both uniform and concentrated pulsating torques. In these papers both the annular disk and the periodic loading are fixed in space.

A natural extension of these previous analyses is to study the dynamic instability of a spinning annular disk under periodically varying edge load which is fixed in space. This investigation may find application in the wood cutting industry as it represents a more general model for the cutting process by a circular saw. In the present paper, we first write the equation of motion for a spinning disk under a periodically varying in-plane load with arbitrary distribution on the outer rim. We assume that the edge load can be expressed as a Fourier series expansion. The resulted equation of motion is gyroscopic, and can be discretized with use of the orthogonality properties among the eigenfunctions of the unloaded disk. A system of generalized Hill's equations in the first-order form is obtained. The method of multiple scale is then employed to determine the conditions for parametric resonance to occur. Several typical forms of radial edge loads are considered, including uniform and concentrated loading.

Equation of Motion

Figure 1 shows a circular disk, which is clamped at the inner radius $r = a$ and subjected to a periodic radial traction at the outer radius $r = b$. We assume that the edge in-plane traction can be expanded in a Fourier series $\epsilon \cos \gamma t \sum_{k=0}^{\infty} f_k \cos k\theta$. ϵ has a dimension of stress, and γ is the excitation frequency of the edge load. f_k is a dimensionless scalar representing the weighting of each Fourier component. The disk is rotating with constant speed Ω, while the edge load is fixed in space. The direction of the edge load remains the same when the disk vibrates laterally. The equation of motion of the system, in terms of the transverse displacement w and with respect to the stationary coordinate system (r, θ), is

$$\rho h\left(\frac{\partial^2 w}{\partial t^2} + 2\Omega \frac{\partial^2 w}{\partial t \partial \theta} + \Omega^2 \frac{\partial^2 w}{\partial \theta^2}\right) + D\nabla^4 w + Lw + \epsilon \cos \gamma t \sum_{k=0}^{\infty} f_k \hat{L}_k w = 0 \quad (1)$$

where

$$D = \frac{Eh^3}{12(1 - \nu^2)}.$$

The parameters ρ, h, E, and ν are the mass density, thickness, Young's modulus, and Poisson ratio of the disk, respectively. L is the membrane operator associated with the axisymmetrical

Contributed by the Applied Mechanics Division of THE AMERICAN SOCIETY OF MECHANICAL ENGINEERS for publication in the ASME JOURNAL OF APPLIED MECHANICS.

Discussion on this paper should be addressed to the Technical Editor, Professor Lewis T. Wheeler, Department of Mechanical Engineering, University of Houston, Houston, TX 77204-4792, and will be accepted until four months after final publication of the paper itself in the ASME JOURNAL OF APPLIED MECHANICS.

Manuscript received by the ASME Applied Mechanics Division, Jan. 23, 1995; final revision, May 1, 1996. Associate Technical Editor: S. W. Shaw.

Copyright © 1997 by ASME

Downloaded 04 May 2010 to 171.66.16.34. Redistribution subject to ASME license or copyright; see http://www.asme.org/terms/Terms_Use.cfm

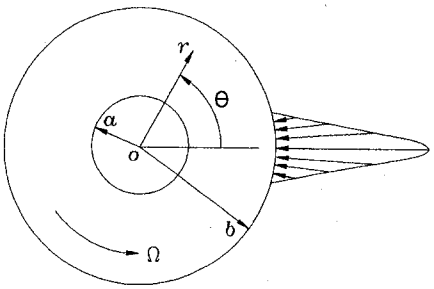


Fig. 1 A spinning disk subjected to a space-fixed pulsating edge load

stress field due to the centrifugal force, and $\hat{L}_k$ is the membrane operator associated with the stress field due to the Fourier component cos $k\theta$ of the edge traction,

$$L \equiv -\frac{h}{r}\left[\frac{\partial}{\partial r}\left(r\sigma_r\frac{\partial}{\partial r}\right)+\frac{\partial}{\partial\theta}\left(\frac{1}{r}\sigma_\theta\frac{\partial}{\partial\theta}\right)\right]$$

$$\hat{L}_k \equiv -\frac{h}{r}\left[\frac{\partial}{\partial r}\left(r\hat{\sigma}_{rk}\frac{\partial}{\partial r}+\hat{\sigma}_{r\theta k}\frac{\partial}{\partial\theta}\right)+\frac{\partial}{\partial\theta}\left(\hat{\sigma}_{r\theta k}\frac{\partial}{\partial r}+\frac{1}{r}\hat{\sigma}_{\theta k}\frac{\partial}{\partial\theta}\right)\right].$$

Stress fields σ_r and σ_θ are due to the centrifugal force and are proportional to Ω^2. On the other hand, $\hat{\sigma}_{rk}$, $\hat{\sigma}_{r\theta k}$, and $\hat{\sigma}_{\theta k}$ are the dimensionless stress fields induced by the radial edge traction cos $k\theta$ and can be expressed as

$$\hat{\sigma}_{rk}(r,\theta)=\tilde{\sigma}_{rk}(r)\cos k\theta$$

$$\hat{\sigma}_{\theta k}(r,\theta)=\tilde{\sigma}_{\theta k}(r)\cos k\theta \qquad k=0,1,2,\ldots.$$

$$\hat{\sigma}_{r\theta k}(r,\theta)=\tilde{\sigma}_{r\theta k}(r)\sin k\theta$$

$\tilde{\sigma}_{rk}$, $\tilde{\sigma}_{\theta k}$, and $\tilde{\sigma}_{r\theta k}$ are functions of radial coordinate r only, and can be found readily in Coker and Filon (1957). It is noted that $\tilde{\sigma}_r(b)=1$ and $\tilde{\sigma}_{r\theta}(b)=0$ due to the in-plane traction boundary conditions on the outer rim.

The associated boundary conditions for Eq. (1) are

$$w = w_{,r} = 0 \quad \text{at} \quad r=a \tag{2a}$$

$$B_1 w + \epsilon\cos\gamma t\sum_{k=0}^{\infty} f_k\hat{B}_{1k}w = B_2 w = 0 \quad \text{at} \quad r=b \tag{2b}$$

where the boundary operators are defined as

$$B_1 \equiv \frac{\partial}{\partial r}\left(\frac{\partial^2}{\partial r^2}+\frac{\partial}{r\partial r}+\frac{\partial^2}{r^2\partial\theta^2}\right)+\frac{1-\nu}{r^2}\left(\frac{\partial^3}{\partial r\partial\theta^2}-\frac{\partial^2}{r\partial\theta^2}\right)$$

$$\hat{B}_{1k} \equiv \frac{h\cos(k\theta)}{D}\frac{\partial}{\partial r}, \quad B_2 \equiv \frac{\partial^2}{\partial r^2}+\frac{\nu}{r}\left(\frac{\partial}{\partial r}+\frac{\partial^2}{r\partial\theta^2}\right).$$

The transverse component of the edge traction can also be included in Eq. (1), and excluded from boundary condition (2b). The equivalent boundary value problem becomes

$$\rho h\left(\frac{\partial^2 w}{\partial t^2}+2\Omega\frac{\partial^2 w}{\partial t\partial\theta}+\Omega^2\frac{\partial^2 w}{\partial\theta^2}\right)+D\nabla^4 w+Lw$$

$$+\epsilon\cos\gamma t\sum_{k=0}^{\infty} f_k\left[\hat{L}_k w+h\delta(r-b)\cos k\theta\frac{\partial w}{\partial r}\right]=0 \tag{3}$$

and

$$w = w_{,r} = 0 \quad \text{at} \quad r=a \tag{4a}$$

$$B_1 w = B_2 w = 0 \quad \text{at} \quad r=b. \tag{4b}$$

$\delta(\cdot)$ is the Dirac delta function.

It is convenient to introduce dimensionless variables (denoted with an asterisk),

$$w^* = \frac{w}{h}, \quad r^* = \frac{r}{b}, \quad \eta^* = \frac{a}{b}, \quad \delta^*(\cdot) = b\delta(\cdot), \tag{5}$$

$$\gamma^* = \gamma b^2\sqrt{\frac{\rho h}{D}}, \quad t^* = \frac{t}{b^2}\sqrt{\frac{D}{\rho h}}, \quad \Omega^* = \Omega b^2\sqrt{\frac{\rho h}{D}}, \tag{6}$$

$$\sigma_r^* = \frac{hb^2}{D}\sigma_r, \quad \sigma_r^* = \frac{hb^2}{D}\sigma_r, \quad \epsilon^* = \frac{hb^2}{D}\epsilon \tag{7}$$

and operators

$$L^* \equiv -\left[\frac{\partial}{\partial r^*}\left(r^*\sigma_r^*\frac{\partial}{\partial r^*}\right)+\frac{\partial}{\partial\theta}\left(\frac{1}{r^*}\sigma_\theta^*\frac{\partial}{\partial\theta}\right)\right] \tag{8}$$

$$\hat{L}_k^* \equiv -\left[\frac{\partial}{\partial r^*}\left(r^*\hat{\sigma}_{rk}\frac{\partial}{\partial r^*}+\hat{\sigma}_{r\theta k}\frac{\partial}{\partial\theta}\right)+\frac{\partial}{\partial\theta}\left(\hat{\sigma}_{r\theta k}\frac{\partial}{\partial r^*}+\frac{1}{r^*}\hat{\sigma}_{\theta k}\frac{\partial}{\partial\theta}\right)\right]. \tag{9}$$

After substituting Eqs. (5)–(9) into Eqs. (3) and (4), and dropping the asterisks in what follows for brevity, Eq. (3) can be rewritten in the dimensionless operator form

$$M\frac{\partial^2 w}{\partial t^2}+G\frac{\partial w}{\partial t}+(K+\hat{K})w=0 \tag{10}$$

where

$$M \equiv 1, \quad G \equiv 2\Omega\frac{\partial}{\partial\theta}, \quad K \equiv \Omega^2\frac{\partial^2}{\partial\theta^2}+\nabla^4+L,$$

$$\hat{K} \equiv \epsilon\cos\gamma t\sum_{k=0}^{\infty} f_k\left[\hat{L}_k+\delta(r-1)\cos k\theta\frac{\partial}{\partial r}\right].$$

Equation (10) can also be cast in the first-order operator form

$$(\mathbf{A}+\hat{\mathbf{A}})\frac{\partial\mathbf{x}}{\partial t}-(\mathbf{B}+\hat{\mathbf{B}})\mathbf{x}=0 \tag{11}$$

by defining the state vector

$$\mathbf{x} \equiv \begin{Bmatrix}\dfrac{\partial w}{\partial t}\\ w\end{Bmatrix}$$

and the matrix differential operators

$$\mathbf{A} \equiv \begin{bmatrix}M & 0\\ 0 & K\end{bmatrix}, \quad \hat{\mathbf{A}} \equiv \begin{bmatrix}0 & 0\\ 0 & \hat{K}\end{bmatrix},$$

$$\mathbf{B} \equiv \begin{bmatrix}-G & -K\\ K & 0\end{bmatrix}, \quad \hat{\mathbf{B}} \equiv \begin{bmatrix}0 & -\hat{K}\\ \hat{K} & 0\end{bmatrix}.$$

Downloaded 04 May 2010 to 171.66.16.34. Redistribution subject to ASME license or copyright; see http://www.asme.org/terms/Terms_Use.cfm

For a freely spinning disk (i.e., in the absence of the edge load), Eq. (10) can be reduced to

$$M\frac{\partial^2 w}{\partial t^2} + G\frac{\partial w}{\partial t} + Kw = 0 \tag{12}$$

Since M and K are symmetric and G is skew, Eq. (12) is a standard gyroscopic equation. The eigenvalues of the $e^{\lambda t}$ time-reduced form of Eq. (12), together with the associated homogeneous boundary conditions, are purely imaginary and occur in complex conjugate pairs, i.e., $\lambda_{mn} = i\omega_{mn}$, where ω_{mn} is real. The eigenfunction corresponding to λ_{mn} is in general complex and assumes the form

$$w_{mn} = R_{mn}(r)e^{in\theta}. \tag{13}$$

R_{mn} is a real-valued function of r. The natural frequency corresponding to eigenfunction $\bar{w}_{mn}$ is $\bar{\lambda}_{mn}$, where overbar means complex conjugate. It is noted that $\bar{w}_{mn} = w_{m,-n}$. If we consider only positive natural frequency, then w_{mn} in Eq. (13) with positive n is a backward traveling wave with n nodal diameters and m nodal circles, which is also denoted by $(m, n)_b$. Similarly, w_{mn} with negative n is a forward traveling wave $(m, -n)_f$. The critical speed Ω_c for the mode (m, n) is defined as the rotation speed at which ω_{mn} of the backward traveling wave $(m, n)_b$ becomes zero. For Ω greater than Ω_c, this mode is a forward traveling wave, and is called a "reflected wave," denoted by $(m, -n)_r$. Figure 2 shows the dimensionless natural frequencies ω_{mn} of a freely spinning disk as functions of dimensionless rotation speed Ω. For simplicity, only the modes with less than four nodal diameters are shown here. The material properties of the disk used in the calculation are: $\rho = 7.84 \times 10^3$ kg/m^3, $E = 203 \times 10^9$ N/m^2, $\nu = 0.27$, $h = 1.02$ mm (0.04 in.), $a =$ 101.6 mm (4 in.), and $b = 203.2$ mm (8 in.). The natural frequencies of the modes with nodal circle(s) are beyond the range of Fig. 2.

Discretization

It has been shown in Chen and Bogy (1992) that for a freely spinning disk, the orthogonality relations among the eigenfunctions can be written as follows:

$$\langle \mathbf{x}_{mn}, \mathbf{A}\mathbf{x}_{pq}\rangle = 0, \quad \langle \mathbf{x}_{mn}, \mathbf{B}\mathbf{x}_{pq}\rangle = 0 \quad \text{if} \quad \lambda_{mn} \neq \lambda_{pq} \tag{14}$$

where the inner product between two vectors $\mathbf{x}_{mn}$ and $\mathbf{x}_{pq}$ is defined as

$$\langle \mathbf{x}_{mn}, \mathbf{x}_{pq}\rangle = \int_0^{2\pi}\int_\eta^1 \bar{\mathbf{x}}_{mn}^T \mathbf{x}_{pq} r dr d\theta. \tag{15}$$

$\mathbf{x}_{mn}^T$ is the transpose of the state vector $\mathbf{x}_{mn}$. Although Chen and Bogy (1992) only showed orthogonality properties among eigenfunctions with distinct eigenvalues for general gyroscopic systems, orthogonal relations still exist when the eigenmodes happen to be degenerate in the case of a freely spinning disk. It is noted that while eigenfunctions w_{mn} and $\bar{w}_{mn}$ represent the same mode of vibration physically, $\mathbf{x}_{mn}$ and $\bar{\mathbf{x}}_{mn}$ are two orthogonal state vectors in the inner product space defined by Eq. (15).

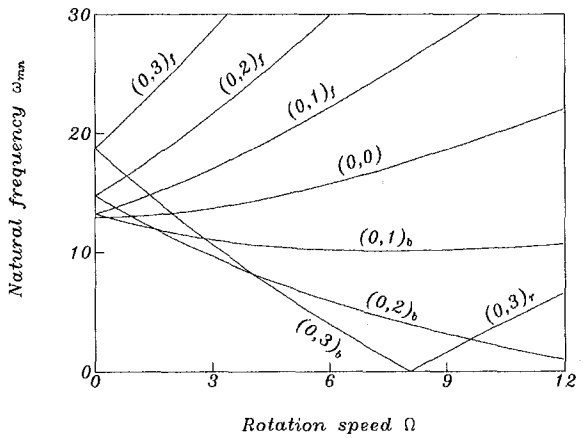


Fig. 2 Dimensionless natural frequency ω_{mn} versus dimensionless rotation speed Ω for a freely spinning disk

Since a closed-form solution for Eq. (11) does not exist in general, we use an expansion in terms of finite number of eigenfunctions of the freely spinning disk to approximate the true solution of Eq. (11),

$$\mathbf{x}(r, \theta; t) \approx \sum_{p=0}^{N_1}\sum_{q=-N_2}^{N_2} c_{pq}(t)\mathbf{x}_{pq}(r, \theta). \tag{16}$$

N_1 and N_2 are the maximum numbers of nodal circles and nodal diameters, respectively, of the modes used in the expansion. Scalar amplitude function $c_{pq}(t)$ is in general complex. It is noted that the right-hand side of Eq. (16) involves both modes $\mathbf{x}_{pq}$ and $\bar{\mathbf{x}}_{pq}$. The validity of expansion (16) has been confirmed in Chen (1996), in which the eigenvalues of a spinning disk under time-invariant space-fixed edge loads are calculated and compared both by expansion (16) and an independent finite element scheme. Substituting Eq. (16) into (11) and taking the inner product between $\mathbf{x}_{mn}$ and both sides of Eq. (11), with use of the orthogonality properties (14), we obtain a system of generalized Hill's equations in the first order form,

$$\frac{dc_{mn}}{dt} - i\omega_{mn}c_{mn} + \epsilon\cos\gamma t \times \sum_{k=0}^{\infty}\sum_{p=0}^{N_1}\sum_{q=-N_2}^{N_2}\left[\frac{\hat{A}_{pq(k)}^{mn}}{A_{mn}^{mn}}\frac{dc_{pq}}{dt} - \frac{\hat{B}_{pq(k)}^{mn}}{A_{mn}^{mn}}c_{pq}\right] = 0 \tag{17}$$

where

$$A_{mn}^{mn} = 4\pi\omega_{mn}(\omega_{mn} + n\Omega)\int_\eta^1 R_{mn}^2(r) r dr. \tag{18}$$

The physical meaning of the above discretization procedure is to force the error function of the approximation (16) to be orthogonal to all eigenfunctions $\mathbf{x}_{pq}(r, \theta)$ used in the expansion. Therefore, the above discretization technique falls into the category of the so-called Galerkin's method. It can be shown that constant A_{mn}^{mn} is a positive real number when the mode (m, n) is a nonreflected wave, and it is negative when (m, n) is a reflected wave (Chen and Bogy, 1992). When $n - q \neq \pm k$, $\hat{A}_{pq(k)}^{mn} = \hat{B}_{pq(k)}^{mn} = 0$. On the other hand, when $n - q = \pm k$, we obtain

$$\hat{A}_{pq(k)}^{mn} = \hat{A}_{mn(k)}^{pq} = \alpha_k\int_\eta^1\left[r\tilde{\sigma}_{rk}\frac{dR_{mn}}{dr}\frac{dR_{pq}}{dr} + q\left(n\frac{\tilde{\sigma}_{\theta k}}{r} - \frac{d\tilde{\sigma}_{r\theta k}}{dr}\right)R_{mn}R_{pq} - (n+q)\tilde{\sigma}_{r\theta k}R_{mn}\frac{dR_{pq}}{dr}\right]dr \tag{19}$$

$$\hat{B}_{pq(k)}^{mn} = i(\omega_{mn} + \omega_{pq})\hat{A}_{pq(k)}^{mn} \tag{20}$$

where $\alpha_0 = 2\pi f_0$, and $\alpha_k = \pi f_k$ when $k \neq 0$. In summary, the coefficients $\hat{A}_{pq(k)}^{mn}$ and $\hat{B}_{pq(k)}^{mn}$ are determined by the eigenfunctions w_{mn} and w_{pq}, and are affected only by the specific Fourier component $\cos k\theta$ of the edge loads with $n - q = \pm k$.

It is in general difficult to find the closed-form expression for the real-valued function $R_{mn}(r)$ when the disk is spinning. However, it is possible to obtain the values of this function at discrete radial points by a finite element method (Ono and Maeno, 1987). The matrices A_{mn}^{mn}, $\hat{A}_{pq}^{mn}$, and $\hat{B}_{pq}^{mn}$ in Eqs. (18)–(20) can then be obtained through numerical integration.

Downloaded 04 May 2010 to 171.66.16.34. Redistribution subject to ASME license or copyright; see http://www.asme.org/terms/Terms_Use.cfm

Perturbation Technique

In this section we apply the method of multiple scale to determine the conditions for parametric resonance to occur. The methodology of this perturbation technique has been described and applied by Nayfeh and Mook (1977) to a system of second-order nongyroscopic equations. In this section we extend this methodology to solve a system of gyroscopic equations in the first-order form.

The method of multiple scale assumes an expansion of the form

$$c_{mn}(t) = c_{mn}^{(0)}(t, T_1) + \epsilon c_{mn}^{(1)}(t, T_1) + O(\epsilon^2) \tag{21}$$

where $T_1 \equiv \epsilon t$. In Eq. (21) the amplitude parameter ϵ is assumed to be smaller than 1. Substituting (21) into (17) and equating coefficients of like powers of ϵ yield

$$\epsilon^0: \quad D_0 c_{mn}^{(0)} - i\omega_{mn} c_{mn}^{(0)} = 0 \tag{22}$$

$$\epsilon^1: \quad D_0 c_{mn}^{(1)} - i\omega_{mn} c_{mn}^{(1)} = -D_1 c_{mn}^{(0)} - \cos \gamma t \sum_{k=0}^{\infty} \sum_{p=0}^{N_1} \sum_{q=-N_2}^{N_2} \frac{\hat{A}_{pq(k)}^{mn}}{A_{mn}^{mn}} D_0 c_{pq}^{(0)} - \frac{\hat{B}_{pq(k)}^{mn}}{A_{mn}^{mn}} c_{pq}^{(0)} \tag{23}$$

where $D_0 \equiv (\partial/\partial t)$, and $D_1 \equiv (\partial/\partial T_1)$. The general solution of Eq. (22) can be written in the form

$$c_{mn}^{(0)} = H_{mn}(T_1) e^{i\omega_{mn} T_0}. \tag{24}$$

Substituting (24) into (23) yields

$$D_0 c_{mn}^{(1)} - i\omega_{mn} c_{mn}^{(1)} = -D_1 H_{mn} e^{i\omega_{mn} T_0} + \frac{\omega_{mn}}{2} \sum_{k=0}^{\infty} \sum_{p=0}^{N_1} \sum_{q=-N_2}^{N_2} \frac{\hat{A}_{pq(k)}^{mn}}{A_{mn}^{mn}} H_{pq} [e^{i(\omega_{pq}+\gamma)T_0} + e^{i(\omega_{pq}-\gamma)T_0}] \tag{25}$$

Combination Resonance at $\gamma = \omega_{rs} + \omega_{uv} + \epsilon\zeta$. In the case when γ is near $\omega_{rs} + \omega_{uv}$, we assume that $\gamma = \omega_{rs} + \omega_{uv} + \epsilon\zeta$, where ζ is a detuning parameter. The secular terms in Eq. (25) are eliminated if

$$D_1 H_{rs} - i\omega_{rs} \frac{\sum_{k=0}^{\infty} \hat{A}_{u,-v(k)}^{rs}}{2A_{rs}^{rs}} \bar{H}_{uv} e^{i\zeta T_1} = 0 \tag{26}$$

and

$$D_1 H_{uv} - i\omega_{uv} \frac{\sum_{k=0}^{\infty} \hat{A}_{r,-s(k)}^{uv}}{2A_{uv}^{uv}} \bar{H}_{rs} e^{i\zeta T_1} = 0 \tag{27}$$

Equations (26) and (27) admit nontrivial solutions having the form

$$H_{rs} = h_{rs} e^{-i\lambda T_1} \quad \text{and} \quad H_{uv} = h_{uv} e^{i(\bar{\lambda}+\zeta)T_1} \tag{28}$$

where h_{rs} and h_{uv} are complex constants, and

$$\lambda = \frac{-\zeta \pm \sqrt{\zeta^2 - \Lambda_{uv}^{rs}}}{2} \tag{29}$$

where

$$\Lambda_{uv}^{rs} = \frac{\omega_{rs}\omega_{uv} \left[\sum_{k=0}^{\infty} \hat{A}_{u,-v(k)}^{rs}\right]^2}{A_{rs}^{rs} A_{uv}^{uv}}. \tag{30}$$

It follows from Eq. (29) that the solution of Eq. (17) is bounded if and only if

$$\zeta^2 \geq \Lambda_{uv}^{rs} \tag{31}$$

On the other hand, combination resonance may occur when $\zeta^2 < \Lambda_{uv}^{rs}$. Frequency $\omega_{rs} + \omega_{uv}$ is called the center frequency and $\sqrt{\Lambda_{uv}^{rs}}$ is called the width parameter of the parametric resonance.

Single-Mode Resonance at $\gamma = 2\omega_{rs} + \epsilon\zeta$. In this case the secular term in Eq. (25) is eliminated if

$$D_1 H_{rs} - i\omega_{rs} \frac{\sum_{k=0}^{\infty} \hat{A}_{r,-s(k)}^{rs}}{2A_{rs}^{rs}} \bar{H}_{rs} e^{i\zeta T_1} = 0 \tag{32}$$

Equation (32) admits nontrivial solution having the form

$$H_{rs} = [\alpha(T_1) + i\beta(T_1)] e^{(i/2)\zeta T_1}. \tag{33}$$

Substituting Eq. (33) into (32), equating the real and imaginary parts to zero, and evoking the condition for $\alpha(T_1)$ and $\beta(T_1)$ to be bounded result in the condition

$$\zeta^2 \geq \Lambda_{rs}^{rs} \tag{34}$$

where

$$\Lambda_{rs}^{rs} = \left[\frac{\omega_{rs} \sum_{k=0}^{\infty} \hat{A}_{r,-s(k)}^{rs}}{A_{rs}^{rs}}\right]^2 \geq 0. \tag{35}$$

Consequently, single-mode parametric resonance may occur if the summation $\sum_{k=0}^{\infty} \hat{A}_{r,-s(k)}^{rs}$ does not vanish. It is noted that Eq. (35) can also be obtained by substituting (u, v) by (r, s) directly in Eq. (30).

Typical Edge Loading

Concentrated Edge Load. We first consider the case when the spinning disk is subjected to a space-fixed concentrated edge load. In this case the Fourier decomposition of the edge load would include all the harmonics of cos $k\theta$, and the summation $\sum_{k=0}^{\infty} \hat{A}_{u,-v(k)}^{rs}$ in Eq. (30) reduces to a single nonzero term $\hat{A}_{u,-v(k)}^{rs}$, where $s + v = \pm k$. In other words, for any two modes (r, s) and (u, v), there always exists a specific Fourier component which renders the summation $\sum_{k=0}^{\infty} \hat{A}_{u,-v(k)}^{rs}$ nonzero. Bearing the relation $\omega_{mn} = -\omega_{m,-n}$ in mind and speaking of only positive natural frequencies, we can conclude that combination resonance of the sum type occurs when both modes are nonreflected or both modes are reflected. On the other hand, combination resonance of the difference type can occur only when one mode is reflected and the other is nonreflected. Single mode parametric resonance can occur for any mode, reflected or nonreflected.

The center frequency and the width parameter of a spinning disk under a pulsating concentrated edge load are shown in Fig. 3. Solid lines represent the single-mode parametric resonance, while dashed lines and dotted lines represent the cases of combination resonance of the sum type and difference type, respectively. In the frequency range of Fig. 3 only the modes with zero nodal circle contribute to the parametric resonance. The mode labels in Fig. 3 are simplified by neglecting the number of nodal circle. For instance, $0 + 2_f$ represents the combination resonance of the sum type involving modes (0, 0) and $(0, 2)_f$, and $2_b - 3_r$ represents the combination resonance of the difference type involving modes $(0, 2)_b$ and $(0, 3)_r$. It can be seen from Fig. 3 that the rotation speed tends to squeeze the width of parametric resonance region.

In the special case when the excitation frequency γ approaches zero, which corresponds to the case of constant con-

Downloaded 04 May 2010 to 171.66.16.34. Redistribution subject to ASME license or copyright; see http://www.asme.org/terms/Terms_Use.cfm

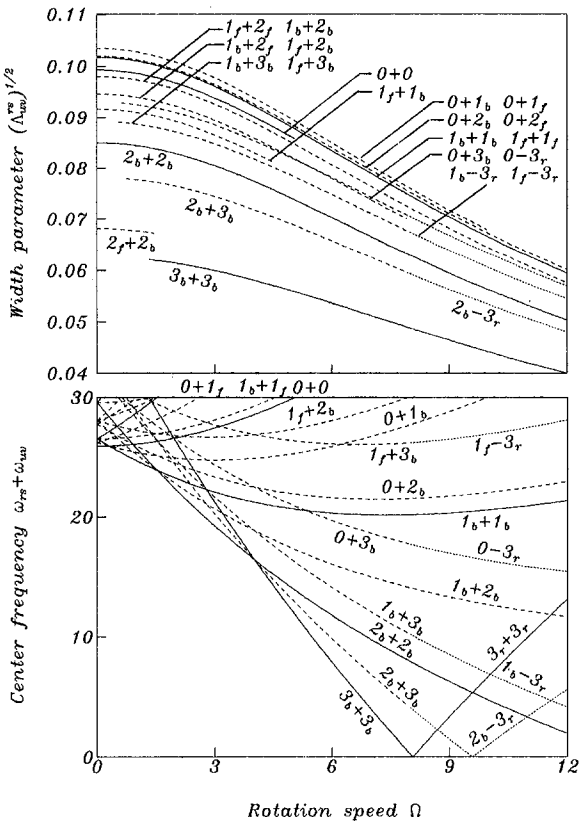


Fig. 3 Center frequencies and width parameters of a spinning disk under a space-fixed pulsating concentrated edge load. Solid lines represent the single mode parametric resonance. Dashed and dotted lines represent the combination resonance of the sum type and the difference type, respectively.

centrated edge load, we can see from Fig. 3 that there exist two rotation speeds at which parametric resonance can occur. The rotation speed at which the solid line labeled $3_b + 3_b$ intersects the horizontal line $\omega_{rs} + \omega_{uv} = 0$ corresponds to the first critical speed. Therefore, the divergence instability reported by Chen (1994) can be considered as a limit case of single mode parametric resonance. On the other hand, the rotation speed at which the dotted line labeled $2_b - 3_r$ intersects the line $\omega_{rs} + \omega_{uv} = 0$ is a speed at which the backward wave $(0, 2)_b$ and reflected wave $(0, 3)_r$ become degenerate. Therefore, the flutter instability reported by Chen (1994) can be considered as a limit case of combination resonance of the difference type.

Uniform Edge Load. In this case the summation $\sum_{k=0}^{\infty} \hat{A}^{rs}_{u,-\nu(k)}$ in Eq. (30) reduces to $\hat{A}^{rs}_{u,-\nu(0)}$, and is equal to zero unless $s = -\nu$. Consequently, we can conclude that combination resonance of the sum type occurs only when both modes have the same number of nodal diameters, and one of them is a forward wave while the other is a backward wave. On the other hand, combination resonance of the difference type occurs when both modes have the same number of nodal diameters, and one mode is a backward wave while the other is a reflected wave. From Eq. (35) we can see that single-mode parametric resonance is possible only for zero-nodal diameter modes. Therefore, the center frequency and width parameter graphs for a spinning disk under uniform edge load can be obtained by retaining only the dashed curve $1_f + 1_b$ and solid curve $0 + 0$ in Fig. 3.

Another way to look at the above problem is to fix the coordinate system onto the spinning disk. Since the loading is uniform circumferentially, it appears no difference to both the stationary and the spinning coordinate systems. To an observer spinning along with the disk, there is only one natural frequency for the (0, 1) mode, which is the average of the natural frequencies of modes $(0, 1)_f$ and $(0, 1)_b$ as observed by another observer in the stationary coordinate system. Therefore, the curves $1_f + 1_b$ and $0 + 0$ in Fig. 3 represent the single mode parametric resonance involving modes (0, 1) and (0, 0), respectively, as observed by a spinning observer.

As the rotation speed Ω approaches zero, the natural frequency of the forward wave $(r, s)_f$ and the backward wave $(r, s)_b$ coincide. Consequently, single mode parametric resonance occurs for each mode when a stationary disk is under uniform loading. Furthermore, combination resonance of the sum type can occur whenever two modes have the same number of nodal diameters.

Conclusions

Dynamic stability of a spinning annular disk under periodically varying in-plane loading on the outer rim is studied analytically. The equation of motion is gyroscopic due to relative motion between the spinning disk and the space-fixed edge loading. The differential equation of motion is first discretized into a system of generalized Hill's equations of the first-order form. Conventional method of multiple scale is extended to treat the system of gyroscopic equations. The results show that combination resonance is possible only when there exists a specific Fourier component $\cos k\theta$ in the edge load, where k equals the sum of the number of nodal diameters of these two modes. Sum type resonance occurs when both modes are nonreflected or both modes are reflected. On the other hand, difference type resonance occurs when one mode is reflected and the other is nonreflected.

References

Carlin, J. F., Appl, F. C., Bridwell, H. C., and Dubois, R. P., 1975, "Effects of Tensioning on Buckling and Vibration of Circular Saw Blades," ASME *Journal of Engineering for Industry,* Vol. 2, pp. 37–48.

Chen, J.-S., 1994, "Stability Analysis of a Spinning Elastic Disk Under a Stationary Concentrated Edge Load," ASME JOURNAL OF APPLIED MECHANICS, Vol. 61, pp. 788–792.

Chen, J.-S., 1996, "Vibration and Stability of a Spinning Disk Under Stationary Distributed Edge Loads," ASME JOURNAL OF APPLIED MECHANICS, Vol. 63, pp. 439–444.

Chen, J.-S., and Bogy, D. B., 1992, "Effects of Load Parameters on the Natural Frequencies and Stability of a Flexible Spinning Disk With a Stationary Load System," ASME JOURNAL OF APPLIED MECHANICS, Vol. 59, pp. S230–S235.

Coker, E. G., and Filon, L. N. G., 1957, *A Treatise on Photo-Elasticity,* Cambridge University Press, London, U.K.

Nayfeh, A. H., and Mook, D. T., 1977, "Parametric Excitations of Linear Systems Having Many Degrees of Freedom," *Journal of Acoustical Society of America,* Vol. 62, pp. 375–381.

Ono, K., and Maeno, T., 1987, "Theoretical and Experimental Investigation on Dynamic Characteristics of a 3.5-Inch Flexible Disk Due to a Point Contact Head," *Tribology and Mechanics of Magnetic Storage Systems,* Vol. 3, SP.21 (STLE), pp. 144–151.

Radcliffe, C. J., and Mote, C. D., Jr., 1977, "Stability of Stationary and Rotating Discs Under Edge Load," *International Journal of Mechanical Sciences,* Vol. 19, pp. 567–574.

Tani, J., and Nakamura, T., 1978, "Dynamic Stability of Annular Plates Under Periodic Radial Loads," *Journal of Acoustical Society of America,* Vol. 64, pp. 827–831.

Tani, J., and Nakamura, T., 1980, "Dynamic Stability of Annular Plates Under Pulsating Torsion," ASME JOURNAL OF APPLIED MECHANICS, Vol. 47, pp. 595–600.

Zajaczkowski, J., 1983, "Stability of Transverse Vibration of a Circular Plate Subjected to a Periodically Varying Torque," *Journal of Sound and Vibration,* Vol. 89, pp. 273–286.

Downloaded 04 May 2010 to 171.66.16.34. Redistribution subject to ASME license or copyright; see http://www.asme.org/terms/Terms_Use.cfm

J. F. Cuttino
Department of Mechanical Engineering,
Box 870276,
The University of Alabama,
Tuscaloosa, AL 35487
Assoc. Mem. ASME

T. A. Dow
Precision Engineering Center,
Box 7918,
North Carolina State University,
Raleigh, NC 27695-7918
Fellow ASME

Contact Between Elastic Bodies With an Elliptic Contact Interface in Torsion

When two elastic three-dimensional bodies of specified radii come into contact, Hertzian forces at the interface result in the formation of an elliptical contact area. The rotation of one body relative to the other about an axis normal to the contact induces a nonlinear torque due to the progression of sliding in the contact interface. Using finite element analysis, a relationship describing torsional compliance with slip is presented for two elastic bodies with an elliptic contact interface under pure twist. The effect of changing material and geometric parameters is studied, and the relationships between torque generation and angle are defined with respect to these nondimensionalized parameters.

Background

Mindlin (1949) and Cattaneo (1938) both independently developed models for the interaction between two elastic bodies in contact under various loading conditions. Of particular interest is Mindlin's analysis of two elastic bodies in contact subjected to a variety of loading conditions. Using the potential functions of Boussinesq and Cerruti, Mindlin derives the closed-form solutions for traction and compliance between, among others, two bodies subjected to tangential loads including the presence of slip and two bodies subjected to a twisting couple assuming no slip. Unfortunately, a closed-form solution has not been developed for the general case of two bodies with an elliptic contact region that are subjected to a couple that results in relative slip. Mindlin offers a solution for the torsional compliance of two bodies with no slip, which represents a *boundary* for the case of gradual slipping of the contact patch as rotation of a ball in a race is induced. The results are given as

$$\frac{\beta}{M_z} = \frac{3}{16b^3G}\frac{8\{BD - \nu CE\}}{\pi\{E - 4\nu(1 - k^2)C\}} \tag{1}$$

where β is the angle of rotation of the contact surface with respect to a distance point in the body above the plane of contact, M_z is the applied moment, G is the shear modulus, ν is Poisson's ratio, and a and b are the major and minor semi-axes of the elliptical contact patch. The parameter k is defined as

$$k = \sqrt{1 - a^2/b^2}. \tag{2}$$

The functions B, C, D, and E are defined by Jahnke and Emde (1943) to be

$$B = \frac{\pi}{4}\left[1 + \left(\frac{k^2}{8}\right) + 3\left(\frac{k^2}{8}\right)^2 + \frac{25}{2}\left(\frac{k^2}{8}\right)^3 + \frac{245}{4}\left(\frac{k^2}{8}\right)^4 + \ldots\right] \tag{3}$$

$$C = \frac{\pi}{16}\left[1 + 6\left(\frac{k^2}{8}\right) + \frac{75}{2}\left(\frac{k^2}{8}\right)^2 + 245\left(\frac{k^2}{8}\right)^3 + \frac{6615}{4}\left(\frac{k^2}{8}\right)^4 + \ldots\right] \tag{4}$$

$$D = \frac{\pi}{4}\left[1 + 3\left(\frac{k^2}{8}\right) + 15\left(\frac{k^2}{8}\right)^2 + \frac{175}{2}\left(\frac{k^2}{8}\right)^3 + \frac{2205}{4}\left(\frac{k^2}{8}\right)^4 + \ldots\right] \tag{5}$$

$$E = \frac{\pi}{2}\left[1 - 2\left(\frac{k^2}{8}\right) - 3\left(\frac{k^2}{8}\right)^2 - 10\left(\frac{k^2}{8}\right)^3 - \frac{175}{4}\left(\frac{k^2}{8}\right)^4 - \ldots\right]. \tag{6}$$

Similar studies concerning the formation of contact zones of ball bearings have been conducted by Harris (1971) and Jones (1959) for thrust loaded, angular contact bearings. Harris also presents the derivation of total moment in an elliptic contact patch for steady-state sliding (Harris, 1991). For pure rotation, this is defined as

$$M_s = \frac{3\mu N}{2\pi ab}\int_{-a}^{a}\int_{-b\sqrt{1-(x/a)^2}}^{b\sqrt{1-(x/a)^2}} (x^2 + y^2)^{0.5} \times \left(1 - \left(\frac{x}{a}\right)^2 - \left(\frac{y}{b}\right)^2\right)^{0.5} dydx \tag{7}$$

where μ is the friction coefficient, N is the normal load applied over the contact ellipse, and a and b are as defined previously. This defines the maximum torque that can be obtained in the contact patch.

Johnson provides a good review of the works conducted concerning contact between elastic bodies in his book *Contact Mechanics* (Johnson, 1985). Specifically, he points out the works of Lubkin (1951) and Deresiewicz (1954) dealing with elastic spheres in contact subjected to torsion. Lubkin expands the work done by Mindlin by developing a relationship between torsional traction and relative rotation for like spheres in contact subjected to a twisting moment starting from a state of no

Contributed by the Applied Mechanics Division of THE AMERICAN SOCIETY OF MECHANICAL ENGINEERS for publication in the ASME JOURNAL OF APPLIED MECHANICS.

Discussion on this paper should be addressed to the Technical Editor, Professor Lewis T. Wheeler, Department of Mechancial Engineering, University of Houston, Houston, TX 77204-4792, and will be accepted until four months after final publication of the paper itself in the ASME JOURNAL OF APPLIED MECHANICS.

Manuscript received by the ASME Applied Mechanics Division, May 10, 1995; final revision, May 5, 1996. Associate Technical Editor: J. T. Jenkins.

Copyright © 1997 by ASME

Downloaded 04 May 2010 to 171.66.16.34. Redistribution subject to ASME license or copyright; see http://www.asme.org/terms/Terms_Use.cfm

residual torsional stresses. This relationship links the case of no slip to that of steady-state slip and is shown in Fig. 1. The vertical axis is $M_z/\mu Na$, where M_z is the applied moment, μ is the coefficient of friction, N is the normal load, and a is the contact radius. The horizontal axis is $\beta a^2 G/\mu N$, where β is the angle of rotation between the contact and a distant point in the body and G is the shear modulus.

Since Lubkin's solution deals only with the onset of rotation from an unstressed state, another solution is necessary for the prestressed state. Deresiewicz attempts to advance the solution of Lubkin to include reversal of the torsional moment, resulting in the prediction of hysteretic losses in the contact area. This problem is significant since many mechanisms rely on repetitive tasks which include reversal of direction. Unfortunately, Deresiewicz's solution is valid only for modest moments where the slip region remains very small.

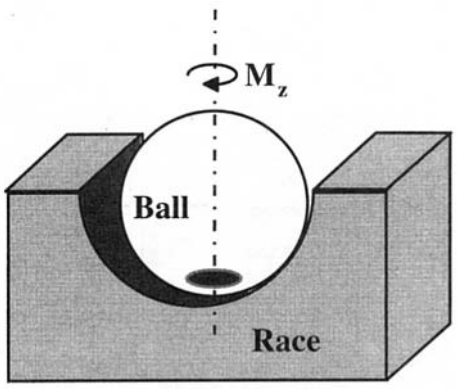


Fig. 2 Geometry of bodies in finite element study

Description of Finite Element Model

A finite element model of the contact between two elastic bodies was conducted using ANSYS/ED Version 5.0 software on a 486DX2 PC. In order to control ellipse parameters, one body was given a spherical geometry and the other a cylindrical geometry as shown in Fig. 2. Since this arrangement closely represents a ball rolling in a cylindrical race, the two bodies will be referred to as such. By changing the radius of the race, the aspect ratio of the contact ellipse can be controlled.

The geometry of the finite element model is shown in Fig. 3. The model considers only the material in the immediate vicinity of the contact to reduce the problem size. There are two distinct regions of interest, an inner region encompassing the contact area, and an outer region representing the mass of the ball and race immediately surrounding the contact region. The outer region was selected to be sufficiently wide such that edge effects near the contact region would diminish before reaching the boundary conditions applied to the outer surface. The dimensions of the inner region were chosen to encompass the elliptical Hertzian contact region with major and minor axis dimensions of a and b, respectively (half-widths). The vertical dimension was also chosen to be large (2.5 times larger than the major axis dimension of the contact region) to prevent local effects of applying uniform normal displacements on the top of the ball.

The interface relationships were calculated from the Hertzian contact described by Timoshenko and Goodier (1970). Three-dimensional isoparametric elements defined by eight nodes and having translational degrees-of-freedom in the r, θ, and z directions are used for the solids. Prior to solution, these elements are used to construct two superelements, one for the ball and one for the race, which replace the isoparametric elements and greatly reduce the computation time. Three-dimensional interface elements are used to construct the friction interface between the two components. These elements can maintain or break physical contact and allow slip between the two surfaces. They support only compression forces in the normal direction and shear forces due to Coulomb friction in the tangential direction. Slip occurs when the shear loads exceed the maximum frictional force of an element.

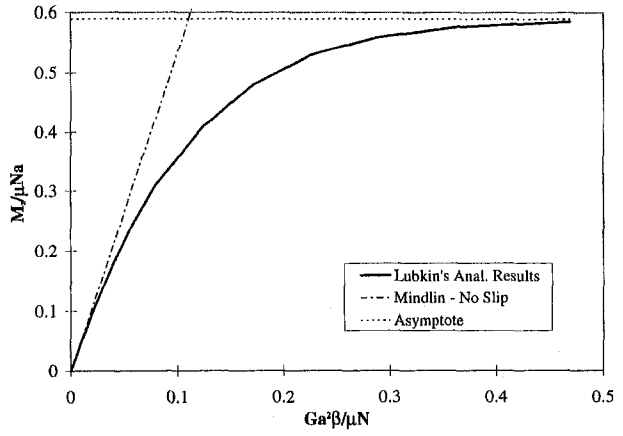


Fig. 1 Relationship of twisting moment and angle for a circular contact

Model Loading Conditions. The loading of the model is executed in three steps, normal loading, prestress rotation, and reversal rotation. In the first step, the top portion of the model (representing the ball) is first displaced in the z-direction until it contacts the race and begins to deform under Hertzian contact. This displacement is achieved via specified displacement boundary conditions applied to the top surface in the z-direction. The normal deformation is then iterated until the normal loads summed at the top surface of the ball model equal the desired preload. The race is held stationary throughout the analysis by zero displacement boundary conditions applied at the bottom surface in r, θ, and z directions. The circumferential surfaces of the ball and race are both restrained in the radial directions via zero displacement boundary conditions in the r direction.

The second load step involves rotating the ball to induce a prestressed state prior to reversal. This step represents the transition between a state of zero rotational stresses to one of maximum rotational stresses that is achieved when the entire contact surface surrounding the center has reached a state of sliding. To achieve this prestressed state, the normal displacement is kept constant, but the top surface of the ball model is incrementally rotated using displacement boundary conditions in the θ direction until nominal overall slip occurs. This load step is very time consuming due to the nonlinearity of the contact elements. The solution is iterative because the program must first converge to a solution, and then check each interface element to see if it is still in contact and if it has slipped. If the status of contact changes, the program automatically reiterates the solution based on the new contact states. If the iteration fails to converge, the increment size is automatically decreased and the process is repeated.

Upon completion of the prestress step, the ball is rotated in the counterclockwise direction until overall slip is obtained once again. This load step represents rotation of the ball *after residual stresses have been introduced by previous rotation and reversal has taken place.* This final loading requires the largest amount of time due to the nonlinearity of the analysis and the larger rotation angle.

In each load step, the reaction torque is obtained from the finite element post processor and is plotted against the rotation angle of the ball. The hysteresis loop is closed by rotating the curve 180 deg.

Downloaded 04 May 2010 to 171.66.16.34. Redistribution subject to ASME license or copyright; see http://www.asme.org/terms/Terms_Use.cfm

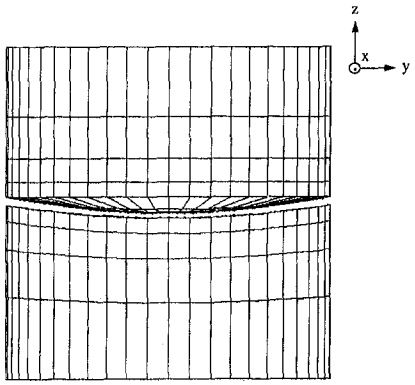


Fig. 3(a)

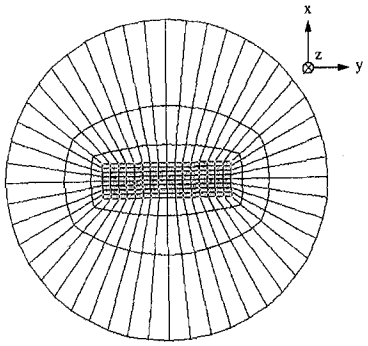


Fig. 3(b)

Fig. 3 Geometry of the finite element model; (*a*) side view, (*b*) bottom view

Parametric Study and Results

Each of the major model parameters was modified to determine its effect on the torque/angle relationship. These parameters include the ratio of the major and minor ellipse dimensions, a/b, the normal load, N, shear modulus, G, and the friction coefficient, μ. The use of the ellipse ratio a/b, where a is the major axis length and b the minor, removed the dependence on radii of the bodies so that the only geometric parameters that must be known are a and b. This independence was verified by generating a model whose geometric dimensions were increased but whose relative ratio between the ellipse dimensions was kept constant.

The model parameters are shown in Table 1. The basic geometries are broken into three categories, a round contact analysis (denoted *Rnd*), an elliptical contact analysis of ratio 3.17:1 (denoted *Mid*), and an elliptical contact with ratio 5:1 (denoted *Thin*). The dimensions chosen for the study come from a study of ball screw mechanisms and represent pertinent applications for such an analysis (Cuttino and Dow, 1991, 1992). The two

Table 1 Parameter variations for FEA test cases

	Rball	Rrace	N	μ	G	a	b	a/b	ρ	J
Rnd CP	1.588	∞	14.14	0.1270	7.96E+4	0.0524	0.0526	1.00	0.0525	1.52E-5
Rnd Low G	1.588	∞	2.40	0.1270	7.96E+4	0.0407	0.0409	1.00	0.0408	5.53E-6
Mid CP	1.588	1.925	14.14	0.1270	7.96E+4	0.1210	0.0381	3.17	0.0795	7.42E-5
Low Fric	1.588	1.925	14.14	0.0625	7.96E+4	0.1210	0.0381	3.17	0.0795	7.42E-5
Hi Fric	1.588	1.925	14.14	0.2500	7.96E+4	0.1210	0.0381	3.17	0.0795	7.42E-5
Hi Norm	1.588	1.925	41.10	0.1270	7.96E+4	0.1727	0.0544	3.17	0.1136	3.08E-4
Low Mod	1.588	1.925	13.42	0.1270	7.96E+4	0.1668	0.0525	3.17	0.1097	2.68E-4
Lg Geom	3.176	3.850	14.14	0.1270	7.96E+4	0.1524	0.0480	3.17	0.1002	1.87E-4
Thin CP	1.588	1.734	14.14	0.1270	7.96E+4	0.1664	0.0333	5.00	0.0998	1.59E-4

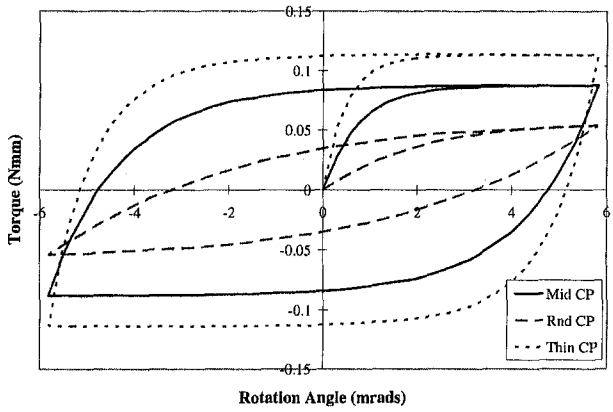


Fig. 4 Results of changing ellipse aspect ratios

round contact analyses (differing only in normal load and shear modulus) were conducted for comparison with Lubkin's results (Lubkin, 1951). The *Mid* contact analyses represent the ball screw study mentioned above and also contain the most parameter changes. This geometry was chosen for the majority of the parameter studies because of its elliptic contact (no solutions are available for elliptic contacts in twist). *Low Fric* and *Hi Fric* refer to low and high friction coefficients, respectively, and *Hi Norm* refers to an increased normal load. *Low Mod* contains a lowered shear modulus, and *Lg Geom* has increased dimensions to assure the solution's independence on body size as opposed to contact area dimensions.

The parameters a, b, and a/b are calculated using Hertzian contact theory described by Timoshenko and Goodier (1970). These parameters may introduce some error due to the approximation of the ellipse dimensions using the tables specified by Timoshenko and Goodier. This is shown in the values calculated for the round contact patch of $a = 0.0524$ and $b = 0.0526$ (the values should be equal). Two new parameters are also included in Table 1. First, ρ is defined as the average of the ellipse dimensions a and b. Second, J is related to the polar moment of inertia about the center of contact, a parameter of great importance in problems involving torsion of shafts. These two variables are defined as follows:

$$\rho = 0.5(a + b) \tag{8}$$

$$J = \frac{ab}{2}(a^2 + b^2). \tag{9}$$

Figures 4 through 7 show the relationships of parameter changes to the torsional compliance of the system. Figure 4 compares the results of test cases *Rnd CP*, *Mid CP*, and *Thin*

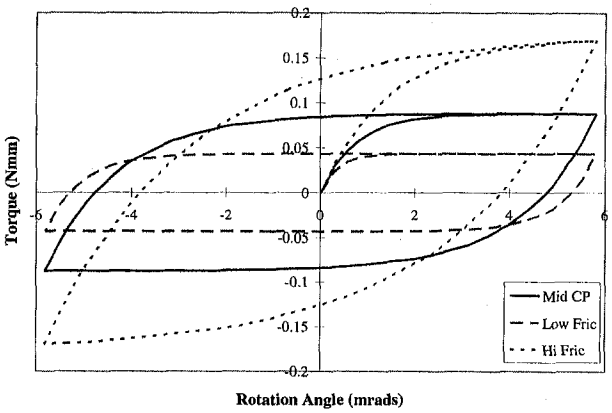


Fig. 5 Results of changing the friction coefficient

Downloaded 04 May 2010 to 171.66.16.34. Redistribution subject to ASME license or copyright; see http://www.asme.org/terms/Terms_Use.cfm

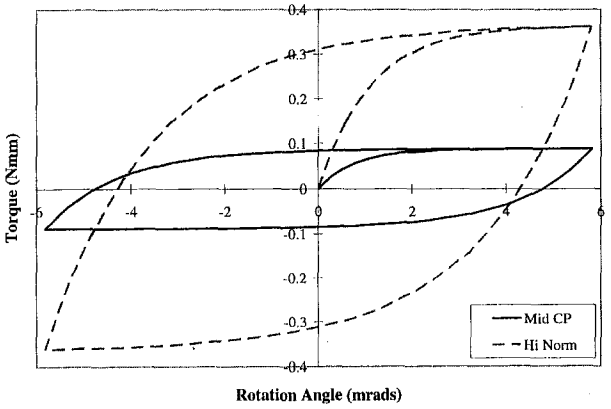


Fig. 6 Results of changing normal load

CP and shows the effect of differing ellipse ratio on the torsional compliance. As shown in the figure, increasing the aspect ratio increases the maximum torque as well as the angle that must be traversed before the maximum torque is reached. For instance, the angle at which the maximum torque is nominally reached progresses from 8 mrads for the *Thin CP* case to more than 12 mrads for the *Rnd CP* case. Using *Mid CP* as a benchmark, the value of ρ for *Rnd CP* is 0.66 times that of *Mid CP*, and that of *Thin* is 1.255 times greater. Noting that the maximum values of torque are 0.61 and 1.29 times that of *Mid*, respectively, it appears that the maximum torque is proportional to the parameter ρ. The errors in this relationship are 7.36 percent and 3.17 percent, which are reasonable due to discretization of the models.

Figure 5 shows the relationship to friction coefficient by comparing the cases *Mid CP*, *Low Fric*, and *Hi Fric*. Theses three cases have similar geometric properties and differ only by friction coefficient, being 0.127, 0.0625, and 0.250, respectively. As expected, increasing friction coefficient increases maximum torque. Similarly to the parameter ρ, it can be shown that the maximum torque is proportional to the friction coefficient. It is also apparent that increasing μ increases the angle necessary to achieve maximum torque.

Figures 6 and 7 show the effects of changing normal load and shear modulus. Changing normal load has similar effects to changing μ, where higher load results in increased torque and larger angle to achieve maximum torque. The torque is increased not only due to the higher frictional forces, but due to the larger contact area as well. The normal loads for the *Mid CP* case and the *Hi Norm* case were $14.14N$ and $41.1N$, respectively. Like the friction coefficient, torque is proportional to the normal load as is the angle of rotation necessary for full sliding.

As shown in Fig. 7, decreasing the shear modulus resulted in increased torque and required a greater rotation to reach complete sliding. However, the lowered modulus also results in a larger contact area and subsequently a larger value of ρ. Removing the effect of ρ from the torque as described earlier results in similar maximum values of T/ρ. It can be deduced that changing shear modulus alone does not effect torque but increasing ρ does.

Normalization of Parameters

The results presented above were assembled and nondimensionalized into a form similar to Fig. 1. This was done in two steps, one for the case of initial windup with no prestress, and another for the case after residual stresses have been introduced into the system.

The first case is shown in Fig. 8. The horizontal axis is nondimensionalized using the relationship $\alpha J^{0.5}G/\mu N$. This nondimensionalization is very similar to Lubkin's in Fig. 1 with the exception that the term a^2 is replaced by $J^{0.5}$. The use of this term related to the moment of inertia is justified by its common use in problems involving torsion of shafts. Note that as the contact surface becomes round, $J^{0.5}$ approaches the term a^2.

The vertical axis is normalized by the term $M_z/\mu N\rho$, which is also similar to that of Lubkin. In this term, Lubkin's parameter a is replaced by $\rho = 0.5(a + b)$, which also reduces to a as the contact surface becomes circular.

The curves of each of the test cases follow the analytical solution of Lubkin well. The round contact patch cases follow with the least error, and that of the thin contact surface has the worst error. The errors may be due to the coarseness of the finite element models or due to the Hertzian approximation of the ellipse dimensions, which ultimately effect the value of ρ. The general shape of the curve is preserved, however, and the results hold within 7 percent error. Using the curve from the *Mid CP* case, a curve fit was used to identify the relationship between all of the parameters for the case of no prestress in the contact patch. The resulting expression is

$$\frac{M_z}{\mu N\rho} = 0.62[1 - e^{-10(\alpha J^{0.5}G/\mu N)}]. \tag{10}$$

The cases of residual stresses are shown in Fig. 9. The factors for nondimensionalizing the problem are the same as for the cases where no residual stresses existed. Each of the curves was shifted to make zero the minimum value on the horizontal axis. Using this normalization, the curves each follow that of the *Mid CP* case closely on the upper side of the hysteresis curve. The portion of the curves on the lower side of the curve was included to show the hysteretic

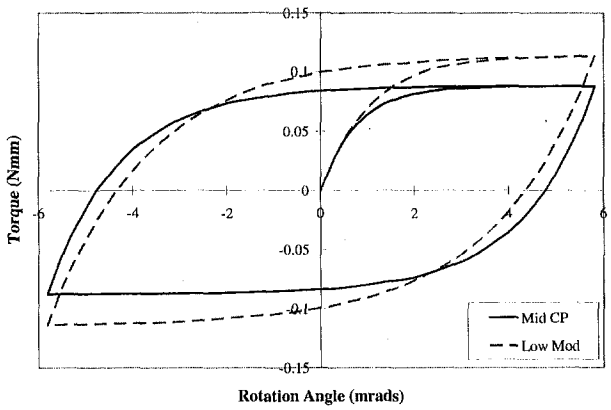


Fig. 7 Results of changing shear modulus

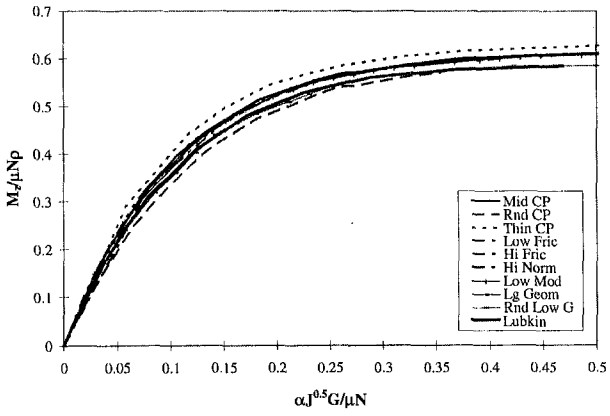


Fig. 8 Normalized parameters for case of no prestress

Downloaded 04 May 2010 to 171.66.16.34. Redistribution subject to ASME license or copyright; see http://www.asme.org/terms/Terms_Use.cfm

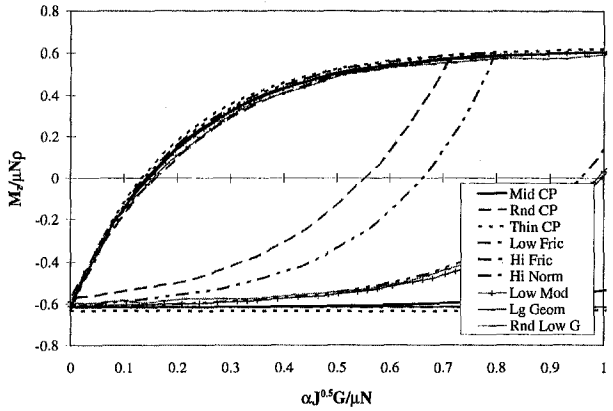


Fig. 9 Normalized parameters for case of residual stresses

relationships. The area within the hysteresis curves, however, is also a function of the parameters in the study and therefore prevent the lower portions of the curves from overlaying.

Using the *Mid CP* case as a reference, a curve was also fit to this case and is represented by the equation

$$\frac{M_z}{\mu N\rho} = -0.62 + 1.24[1 - e^{-5(\alpha J^{0.5}G/\mu N)}]. \qquad (11)$$

Using Eqs. (10) and (11), the torque versus angle relationship for two bodies in pure twist can be predicted based on the state of prestress.

Conclusion

The relationship between torque and angle of twist for two bodies of elliptical contact has been determined for the state of no previous stresses as well as the state of residual stresses using finite element analysis. These relationships are important when studying the mechanics of nonlinear torque in applications such as ball bearings. The study confirms and extends the works of Mindlin (1949), Lubkin (1951), and Deresiewicz (1954). It accounts for the parameters normal load, friction coefficient, shear modulus, and contact ellipse dimensions.

References

Cattaneao, C., 1938, "Sul Contatto di Due Corpi Elastici", *Accademia dei Lincei, Rendiconti,* Series 6, Vol. 27.

Cuttino, J. F., and T. A. Dow, 1991, "The Preloaded Ball Screw as a Nanometer Actuator," *Proceedings of the American Society for Precision Engineering,* pp. 181–184.

Cuttino, J. F., and T. A. Dow, 1992, "Ball Screw Nonlinearity and Dynamic Slideway Performance," *Proceedings of the American Society for Precision Engineering,* pp. 367–371.

Deresiewicz, H., 1954, "Contact of Elastic Spheres Under an Oscillating Torsional Couple," ASME JOURNAL OF APPLIED MECHANICS, Vol. 21, pp. 52–56.

Harris, T. A., 1971, "Ball Motion in Thrust-Loaded, Angular Contact Bearings with Coulomb Friction," ASME *Journal of Lubrication Technology,* V. Series F, Vol. 93.

Harris, T. A., 1991, *Rolling Bearing Analysis,* 3rd ed., John Wiley and Sons, New York, pp. 458–472.

Jahnke, E., and Emde, F., 1943, *Tables of Functions,* Dover, New York, pp. 82–83.

Johnson, K. L., 1985, *Contact Mechanics,* Cambridge University Press, Cambridge, U.K., pp. 231–233.

Jones, A. B., 1959, "Ball Motion and Sliding Friction in Ball Bearings," *Journal of Basic Engineering,* Vol. 81, No. 1, pp. 1–12.

Lubkin, J. L., 1951, "The Torsion of Elastic Spheres in Contact," ASME JOURNAL OF APPLIED MECHANICS, Vol. 18, No. 1, pp. 183–187.

Mindlin, R. D., 1949, "Compliance of Elastic Bodies in Contact," ASME JOURNAL OF APPLIED MECHANICS, Vol. 71, pp. 259–268.

Timoshenko, S. P., and Goodier, J. N., 1970, *Theory of Elasticity,* 3rd ed., McGraw-Hill, New York, pp. 409–420.

Downloaded 04 May 2010 to 171.66.16.34. Redistribution subject to ASME license or copyright; see http://www.asme.org/terms/Terms_Use.cfm

Stability of the Unison Response for a Rotating System With Multiple Tautochronic Pendulum Vibration Absorbers

Chang-Po Chao
Graduate Student.

S. W. Shaw
Professor,
Fellow ASME.

Cheng-Tang Lee
Research Associate,
Assoc. Mem. ASME.

Department of Mechanical Engineering,
Michigan State University,
East Lansing, MI 48824

Due to spatial and balancing considerations, the implementation of centrifugal pendulum absorbers (CPVA's) invariably requires that the total absorber inertia be divided into several absorber masses and stationed about the center of rotation. To achieve the designed-for performance, the CPVA's are expected to move in exact unison, since the selection of the total absorber mass is made by assuming an equivalent single absorber mass. In this paper, we determine the conditions under which the unison motion of a system of several identical CPVA's is dynamically stable. This is done for the special case of tautochronic absorbers subjected to a purely harmonic torque. The stability criterion is obtained by an asymptotic method that exploits certain symmetries in the equations of motion and is based on the assumption that total moment of inertia of the absorbers is much smaller than that of the entire rotating system—an assumption that is almost always satisfied in practice. It is expressed in terms of a critical torque level that is proportional to the square root of the equivalent viscous damping of the individual absorbers. The result is verified by numerical simulations of the system near the critical parameter conditions. A future paper will consider the post-critical response of the system.

1 Introduction

In the cylinders of a reciprocating internal combustion engine, combustion generates torques and forces which cause undesirable oscillatory torques acting on the crankshaft, and these result in torsional oscillations of the crankshaft which produce roughness and fatigue difficulties. A similar situation is encountered in helicopter rotors wherein the loads are induced by aerodynamic effects. A centrifugal pendulum vibration absorber (CPVA) is a device used for reducing these torsional oscillations. CPVA's were invented as early as 1929 for use in internal combustion engines (Carter, 1929). They have been successfully employed to suppress noise and vibration caused by torsional oscillations in light aircraft engines (Ker Wilson, 1968) and helicopter rotors (Wachs, 1973).

The CPVA is a mass restricted to move freely along a prescribed path relative to the base rotating system. The absorber is driven by the centrifugal field generated by rotation. The motion of this CPVA provides a restoring torque which, when properly designed, reduces torsional oscillations. In most applications, the input torque for the rotating system can be considered as a nominal constant torque, which keeps the rotating system at a nominally constant speed, plus a periodic fluctuating part whose base frequency is n times that of rotating system rotation. Such a torque is referred to as a *torque of order n*, and this torque is typically considered in terms of its low-order harmonic components. Early designs of CPVA's were based on linear theory which tunes an absorber (that is, designs the path) such that its oscillatory frequency of *small amplitude motion* matches that of the disturbing torque in the neighborhood of its operating point. However, such design may fail for moderate amplitude motions (Newland, 1964; Sharif-Bakhtiar and Shaw, 1992).

To solve this problem, one needs to consider nonlinear aspects of the system dynamics, and in particular the fact that the pendulum frequency decreases as its amplitude is increased, due to the circular nature of the path of the absorber's center of mass. This mistuning gives rise to a jump in the system response curve that can have disastrous consequences (Newland, 1964). Knowledge of this fact, first pointed out by Den-Hartog (1938), lead to the suggestion that the paths be slightly intentionally mistuned so that their small amplitude performance is not optimal, but the absorbers will survive over a larger torque range. This approach is still used in practice. Later, a different solution was proposed wherein one allows the absorber to move on noncircular paths, such as the cycloidal path proposed by Madden (Madden, 1980). This cycloid does improve performance, but is not optimal in avoiding the mistuning problem (Shaw and Lee, 1995). Denman (1985) proposed an epicycloidal path which totally avoids the mistuning. This path, known as the *tautochrone,* is such that the absorber has a constant oscillatory frequency regardless of its amplitude of oscillation. Tuned to have the same frequency as the disturbing torque of order n, the absorber, said to be *of order n*, provides a periodic torque which counteracts most of the disturbing torque while the rotating system is in rotation, thereby reducing torsional oscillations. However, Shaw and Lee (1995) showed that due to nonlinear effects, the motion of this absorber also generates higher-order harmonic torques which generally deteriorate performance of the CPVA. To tackle this problem, two methods are suggested. First, in addition to the CPVA's tuned of order n, one can use additional CPVA's tuned to the troublesome higher-order torques, say at order $2n$, $3n$, ... This idea was used by Borowski et al. (1991). Also, one can employ the subharmonic absorber system developed by Lee et al. (1994), which consists of a pair of absorbers tuned to order $n/2$, such

Contributed by the Applied Mechanics Division of THE AMERICAN SOCIETY OF MECHANICAL ENGINEERS for publication in the ASME JOURNAL OF APPLIED MECHANICS.

Discussion on this paper should be addressed to the Technical Editor, Professor Lewis T. Wheeler, Department of Mechanical Engineering, University of Houston, Houston, TX 77204-4792, and will be accepted until four months after final publication of the paper itself in the ASME JOURNAL OF APPLIED MECHANICS.

Manuscript received by the ASME Applied Mechanics Division, Nov. 25, 1995; final revision, Sept. 3, 1996. Associate Technical Editor: L. T. Wheeler.

Copyright © 1997 by ASME

Downloaded 04 May 2010 to 171.66.16.34. Redistribution subject to ASME license or copyright; see http://www.asme.org/terms/Terms_Use.cfm

that this system can produce a pure harmonic torque of order n without generating higher-order torques. (It must be said that this type of absorber system has not been experimentally tested.)

In addition to designing the paths of the CPVA's, one needs to choose the total absorber inertia to be sufficiently large such that the absorbers do not hit motion-limiting stops, or snubbers, under severe operating conditions. This is typically accomplished by stationing several absorber masses along and around the axis of rotation. In many cases these absorbers have identical mass and tuning, and this paper is concerned with the condition under which such sets of absorbers are moving in unison.

This study provides a method for deriving a criterion which is used to predict the stability bound of the unison motions. While limited to a set of N identical tautochronic absorbers, the analysis presented herein can be generalized to different arrangements of absorbers with different paths, although the analysis will be more involved. To obtain the desired criterion, we derive a mathematical model for describing the system behavior by formulating the total system kinetic energy and applying Lagrange's method. Then, by assuming that the ratio of the total moment of inertia of all absorbers to that of the base rotating system is small, say $\mathcal{O}(\epsilon)$, and doing some rearranging, we are able to derive a set of weakly coupled, one-degree-of-freedom equations of motion, one for each absorber. These equations have the nice property that the zeroth and first-order terms in ϵ are uncoupled from the dynamics of the rotor. Transforming these equations of motion into the standard periodic form and performing first-order averaging over one excitation period, we obtain the corresponding averaged system. A bifurcation criterion in terms of the disturbing torque for predicting instability of the unison motion is found based on the Jacobian of the averaged system evaluated on the unison motion. This criterion shows that the critical torque level at the bifurcation point is proportional to the square root of the effective damping coefficient for each absorber and to the square root of N.

This paper is organized as follows. In Section 2, the dynamic model is formulated. In Section 3, this model is transformed into periodic standard form and integrated over one period of the excitation to obtain the averaged equations. In Section 4, the stability criterion is derived and verified by numerical simulations. In Section 5, some conclusions and suggestions for future work are presented.

2 Mathematical Model

A general mathematical model used to describe the dynamics of a simple rotating inertia with CPVA's was derived by Shaw and Lee (1994). The system is shown schematically by the cross-section view of the rotor in Fig. 1. This dynamical system consists of a rotor with a moment of inertia, I_d, with respect to the rotating center of rotation, denoted by O, and N absorbers moving freely on the prescribed paths relative to the rotor. Each individual absorber, denoted by a subscript i for the ith absorber, is considered to be a point mass with mass m_i. The path for each absorber is specified by the function $R_i = R_i(S_i)$, where R_i is the distance from the C. G. of the absorber to point O and S_i is an arc variable along the path defined relative to the rotating frame of reference, with its origin at the point where R_i reaches its maximum, $R_{i0} = R_i(0)$. Thus, the nominal moment of inertia with respect to O for each absorber is defined by $I_i = m_i R_{i0}^2$. In our designs, the path is designed to be symmetric with respect to $S_i = 0$; i.e., $R_i(S_i) = R_i(-S_i)$. The applied torque is assumed to be a nominal constant torque T_0 plus a disturbing torque $T_\theta(\theta)$ which is periodic in θ. The nominal steady-state rotational speed of the rotor, Ω, is the speed at which the constant torque T_0 balances the mean component of the torque which arises from the damping between the rotor and its bearings; thus,

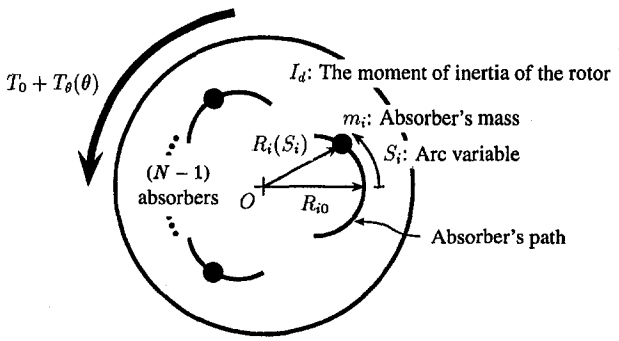


Fig. 1 Schematic diagram for the CPVA's and the rotor from the cross-section view

$$\Omega = \frac{T_0}{c_0}. \tag{1}$$

With the above assumptions, the kinetic energy is given by

$$\text{K.E.} = \tfrac{1}{2}\{I_d\dot\theta^2 + \sum_{i=1}^{N} m_i[X_i(S_i)\dot\theta^2 + \dot S_i^2 + 2G_i(S_i)\dot\theta\dot S_i]\} \tag{2}$$

where $(\dot{\ })$ denotes $d(\cdot)/dt$, t is time, and

$X_i(S_i) = R_i^2(S_i)$ and

$$G_i(S_i) = \sqrt{X_i(S_i) - \frac{1}{4}\left(\frac{dX_i}{dS_i}(S_i)\right)^2}. \tag{3}$$

In the expression for the kinetic energy (2), $\frac{1}{2} I_d\dot\theta^2$ is the rotational energy of the rotor, $\frac{1}{2} m_i[X_i(S_i)\dot\theta^2 + \dot S_i^2]$ is sum of the rotational energy relative the fixed frame and translational energy relative to the rotating frame for the ith absorber, and the term $2G_i(S_i)\dot\theta\dot S_i$ arises from the Coriolis effects.

Assuming that gravitational effects are small and the corresponding potential energy is negligible, the governing equations of motion are determined as follows by applying Lagrange's method to the kinetic energy:

$$m_i\left[\ddot S + G_i(S_i)\ddot\theta - \frac{1}{2}\frac{dX_i}{dS_i}(S_i)\dot\theta^2\right] = -c_{ai}\dot S_i, \quad 1 \le i \le N \tag{4}$$

$$I_d\ddot\theta + \sum_{i=1}^{N} m_i\left[\frac{dX_i}{dS_i}(S_i)\dot S_i\dot\theta + X_i(S_i)\ddot\theta + G_i(S_i)\ddot S_i + \frac{dG_i}{dS_i}(S_i)\dot S_i^2\right] = \sum_{i=1}^{N} c_{ai}G_i(S_i)\dot S_i - c_0\dot\theta + T_0 + T_\theta(\theta), \tag{5}$$

where c_0 and c_{ai} are damping coefficients for the rotor and the ith absorber, respectively. Note that Eq. (4) describes the dynamics of the ith absorber, which are coupled to the dynamics of the rotor through the terms $\ddot\theta$ and $\dot\theta^2$. Equation (5) results from the balance among the applied torques $T_0 + T_\theta(\theta)$, the rotor damping $c_0\dot\theta$, the damping and resistive torques caused by the motions of all absorbers—as described in the two summation terms, respectively—and the inertial resistance of the rotor $I_d\ddot\theta$.

Note that the equations of motion are autonomous and that the periodic forcing term $T_\theta(\theta)$ is the only term that depends on θ. In order to put the system in a form that is more amenable to asymptotic analysis, we transform the equations into a set of periodically forced, nonautonomous equations. To this end, we first introduce a new nondimensionalized dependent variable y as

$$y \equiv \frac{\dot\theta}{\Omega}. \tag{6}$$

Downloaded 04 May 2010 to 171.66.16.34. Redistribution subject to ASME license or copyright; see http://www.asme.org/terms/Terms_Use.cfm

Assuming that θ is a smooth and invertible function of t, applying the chain rule and using (6), one can obtain the following relationships between derivatives with respect to t and θ:

$$\ddot{\theta} = \Omega^2 yy', \quad (\dot{\cdot}) = \Omega y(\cdot)' \quad \text{and}$$

$$(\ddot{\cdot}) = \Omega^2 yy'(\cdot)' + \Omega^2 y^2(\cdot)'', \quad (7)$$

where $(\cdot)'$ denotes $d(\cdot)/d\theta$. With the relationships (6) and (7), each term in Eqs. (4) and (5) can be rewritten in a form such that θ is now the independent variable, replacing t. After this transformation and nondimensionalization, Eqs. (4) and (5) become

$$ys_i'' + [s_i' + g_i(s_i)]y' - \frac{1}{2}\frac{dx_i}{ds_i}(s_i)y = -\hat{\mu}_{ai}s_i', \quad 1 \le i \le N, \quad (8)$$

$$\sum_{i=1}^{N} b_i\left[\frac{dx_i}{ds_i}s_i'y^2 + x_i(s_i)yy' + g_i(s_i)s_i'yy' + g_i(s_i)s_i''y^2 + \frac{dg_i(s_i)}{ds_i}s_i'^2y^2\right] + yy' = \sum_{i=1}^{N} b_i\hat{\mu}_{ai}g_i(s_i)s_i'y - \hat{\mu}_0 y + \Gamma_0 + \Gamma_\theta(\theta) \quad (9)$$

where

$$s_i = \frac{S_i}{R_{i0}}, \quad x_i(s_i) = \frac{X_i(S_i)}{R_{i0}^2}, \quad g_i(s_i) = \frac{G_i(S_i)}{R_{i0}},$$

$$I_i = m_i R_{i0}^2, \quad b_i = \frac{I_i}{I_d}, \quad \hat{\mu}_{ai} = \frac{c_{ai}}{m_i\Omega}, \quad \hat{\mu}_0 = \frac{c_0}{I_d\Omega},$$

$$\Gamma_0 = \frac{T_0}{I_d\Omega^2}, \quad \Gamma_\theta(\theta) = \frac{T_\theta(\theta)}{I_d\Omega^2},$$

and

$$x_i(s_i) = r_i^2(s_i), \quad \text{and}$$

$$g_i(s_i) = \sqrt{x_i(s_i) - \frac{1}{4}\left(\frac{dx_i}{ds_i}(s_i)\right)^2} \quad (10)$$

with $r_i(s_i) = (R_i(s_i))/(R_{i0})$. Note that in terms of these definitions and that of Ω, it follows that $\hat{\mu}_0 = \Gamma_0$ (this simply implies that the nondimensional value of the nominal rotating speed is unity).

To set the stage for the multiple-absorber system, we consider the limiting behavior of a single tautochronic CPVA with mass m_0 riding on an epicycloid path tuned to order n; i.e., $x(s) = 1 - n^2s^2$. From Eq. (10), one can notice that at a certain amplitude of motion, the absorber will hit a singularity in the path; this occurs at the cusp of the epicycloid. In order to accommodate as large motion of the absorber as possible, we choose an absorber mass large enough so that it just reaches the cusp when subjected to the peak nondimensional torque level (typically at high-torque low-speed operating conditions). At the cusp point, $g(s) = 0$. Therefore, during regular steady operation of the system it is required that

$$s(\theta)^2 \le \frac{1}{(n^2 + n^4)} \ \forall\ \theta \quad (11)$$

so that $g(s)$ remains real.

In practice, an absorber system of total mass m_0 is often divided into N absorbers, each of which has mass $m_i = (1/N)m_0$, the damping coefficient $\hat{\mu}_a = \hat{\mu}_{ai}$ for each i and the same path, which we take to be specified by $x_i(s_i) = 1 - n^2s_i^2$ with $R_{i0} = R_0$ for each i.

The disturbance torque is assumed to be harmonic and of order n; i.e., $\Gamma_\theta(\theta) = \hat{\Gamma}_\theta \sin(n\theta)$. With these assumptions Eqs. (8) and (9) become

$$ys_i'' + [s_i' + g_i(s_i)]y' + n^2s_iy = -\hat{\mu}_a s_i', \quad 1 \le i \le N, \quad (12)$$

$$\frac{b_0}{N}\sum_{i=1}^{N}\left[-2n^2s_is_i'y^2 + (1 - n^2s_i^2)yy' + g_i(s_i)s_i'yy' + g_i(s_i)s_i''y^2 + \frac{dg_i(s_i)}{ds_i}s_i'^2y^2\right] + yy' = \frac{b_0}{N}\sum_{i=1}^{N}\hat{\mu}_a g_i(s_i)s_i'y - \hat{\mu}_0 y + \Gamma_0 + \hat{\Gamma}_\theta \sin(n\theta) \quad (13)$$

where

$$I_0 = m_0R_0^2, \quad b_0 = \frac{I_0}{I_d}, \quad g_i(s_i) = \sqrt{1 - (n^2 + n^4)s_i^2}$$

$$\text{and} \quad \frac{dg_i(s_i)}{ds_i} = \frac{-(n^2 + n^4)s_i}{\sqrt{1 - (n^2 + n^4)s_i^2}}. \quad (14)$$

Some discussion of the damping in the system is pertinent at this point. The damping on the main rotor system and the mean torque set the nominal speed and play no other vital role in the the system dynamics. However, the damping in the absorbers plays a central role in the performance of the system, and this is a notoriously difficult thing to get a handle on. First, the source of the damping is complicated and depends on the specifics of how the absorbers are implemented. Second, even if one knows the basic damping mechanisms, the physical constants are difficult to measure and vary with operating conditions (such as temperature). We have assumed a form of equivalent viscous damping in our equations, and will consider two different types of damping—viscous and hysteretic. Note that if the damping is viscous, the associated coefficient c_a (herein $c_{ai} = c_i$ for each i since we assume $\hat{\mu}_a = \hat{\mu}_{ai}$) in equation (4) is assumed to be independent of the mass of the absorber, as in the linear case, then

$$\hat{\mu}_a = \frac{Nc_a}{m_0\Omega} \quad (15)$$

which shows that the nondimensional "effective" damping coefficient $\hat{\mu}_a$ is proportional to the number of absorbers. However, an experimental result given by (Cronin, 1992) indicates that there exists a hysteretic damping factor that is independent of the absorber mass, implying that c_a is proportional to mass of the absorber. Therefore, c_a/m_i is a constant in this case. According to this result, introducing the quantity c_{a0} as the coefficient for a single absorber, we can express $\hat{\mu}_a$ as

$$\hat{\mu}_a = \frac{c_{a0}}{m_0\Omega}. \quad (16)$$

In our results we will consider these two types of damping.

3 Averaged Equations

In this section we proceed with an asymptotic analysis that is based on the fact that in most applications the ratio of the total nominal moment of inertia of all absorbers to that of the rotor is generally much smaller than one. This motivates the definition of the small parameter, $\epsilon \equiv b_0$. We further assume that the nondimensional damping and excitation parameters, $\hat{\mu}_a$, $\hat{\mu}_0$, $\hat{\Gamma}_0$, and $\hat{\Gamma}_\theta$, are also small as the same order of b_0 such that we can scale them as follows:

$$\hat{\mu}_a = \epsilon\tilde{\mu}_a, \quad \hat{\mu}_0 = \epsilon\tilde{\mu}_0, \quad \Gamma_0 = \epsilon\tilde{\Gamma}_0, \quad \text{and} \quad \hat{\Gamma}_\theta = \epsilon\tilde{\Gamma}_\theta. \quad (17)$$

Downloaded 04 May 2010 to 171.66.16.34. Redistribution subject to ASME license or copyright; see http://www.asme.org/terms/Terms_Use.cfm

The analysis will proceed by first uncoupling to first order the dynamics of the rotor from those of the absorbers. This results in a simplified set of equations to which averaging is applied.

By the definitions of Ω in Eq. (1), y in Eq. (6) and with the constant torque balanced by the rotor damping; i.e., $\Gamma_0 = \hat{\mu}_0$, the global steady-state solution of the unperturbed equation (13) with $\epsilon = 0$, is simply a constant rotor speed, $y = 1$, and harmonic motion of the absorbers with frequency n. (The unperturbed system can be imagined as the case with an enormous flywheel attached to the rotor and frictionless absorber motions.) Note that due to the absorber paths used, this motion is valid even for large amplitudes, up to the cusps on the epicycloid paths. By the smoothness of y in ϵ, we can expand y as follows:

$$y(\theta) = 1 + \epsilon y_1(\theta) + \mathcal{O}(\epsilon^2) \tag{18}$$

where y_1 captures fluctuations in speed that are induced by the net interaction of the applied torques, the damping, and the torques induced by the motion of the absorbers. Since $\epsilon \ll 1$, $y(\theta)$ oscillates about unity and is never zero. Therefore, we can divide Eq. (12) through by y and obtain an expression for s_i'' in terms of s_i, s_i', and y. Substitution of this expression into Eq. (13) and utilization of Eq. (14) gives an exact expression for the nondimensionalized angular acceleration of the rotor; i.e., yy' $(= \ddot{\theta}/\Omega)$. Then utilizing the definition $\epsilon \equiv b_0$, the scalings in (17), the expansion in (18), and the fact $\Gamma_0 = \hat{\mu}_0$, we are able to obtain a series approximation for yy' in terms of ϵ as follows:

$$yy'(\theta) = -\epsilon\left\{\frac{1}{N}\sum_{j=1}^{N}\left(-2n^2 s_j s_j' - n^2 g(s_j)s_j + \frac{dg(s_j)}{ds_j}s_j'^2\right) - \tilde{\Gamma}_\theta \sin(n\theta)\right\} + \mathcal{O}(\epsilon^2). \tag{19}$$

The above equation shows that the nondimensionalized angular acceleration is of order ϵ, a result consistent with physical intuition for the limiting case (as $\epsilon \to 0$). Also, one can show that y'/y has the same leading ϵ-order term as yy' based on the expansion of $y(\theta)$ stated in Eq. (18).

To obtain the equations in the correct form for the application of averaging, Eq. (12) is divided through by y, yielding a modified equation describing the absorbers' dynamics in terms of y'/y. Substituting the ϵ-series approximation of y'/y into this modified version of Eq. (12), and expanding it in terms of ϵ, a set of weakly coupled, weakly nonlinear oscillators are obtained for the absorber dynamics. These oscillators, in which the dynamics of the rotor has been eliminated to first order, are as follows:

$$s_i'' + n^2 s_i = \epsilon f_i(s_1, \ldots, s_N, s_1', \ldots, s_N', \theta) + \mathcal{O}(\epsilon^2), \quad 1 \le i \le N \tag{20}$$

where

$$f_i(s_1, \ldots, s_N, s_1', \ldots, s_N', \theta) = -\tilde{\mu}_a s_i' + [s_i' + g_i(s_i)]\left[\frac{1}{N}\sum_{j=1}^{N} \times \left(-2n^2 s_j s_j' + g_j(s_j)s_j'' + \frac{dg_j(s_j)}{ds_j}s_j'^2\right) - \tilde{\Gamma}_\theta \sin(n\theta)\right].$$

Note that these equations are not only weakly coupled, they are also weakly nonlinear, even though the amplitudes of motion of the absorbers are not assumed to be small. This comes about due to the tautochronic nature of the absorber dynamics, which renders their large-amplitude dynamics as linear in the unperturbed system, for all amplitudes that satisfy condition (11). For other absorber paths, say circles, these equations would have the same general structure but would be perturbations of conservative, nonlinear oscillators for the absorber dynamics.

To perform averaging, the following transformation to amplitude and phase variables is introduced:

$$s_i = a_i \cos(\phi_i - n\theta) \quad \text{and} \quad s_i' = n a_i \sin(\phi_i - n\theta) \quad 1 \le i \le N$$

in order to obtain the standard periodic form, as follows:

$$\frac{da_i}{d\theta} = \frac{\epsilon}{n} f_i(a_1 \cos(\phi_1 - n\theta), \ldots, a_N \cos(\phi_N - n\theta), n a_1 \sin(\phi_1 - n\theta), \ldots, n a_N \sin(\phi_N - n\theta)) \sin(\phi_i - n\theta) + \mathcal{O}(\epsilon^2)$$

$$\frac{d\phi_i}{d\theta} = \frac{\epsilon}{n a_i} f_i(a_1 \cos(\phi_1 - n\theta), \ldots, a_N \cos(\phi_N - n\theta), n a_1 \sin(\phi_1 - n\theta), \ldots, n a_N \sin(\phi_N - n\theta)) \cos(\phi_i - n\theta) + \mathcal{O}(\epsilon^2). \tag{21}$$

We now average the first-order terms in the R. H. S. above over one period of the excitation, $2\pi/n$. The resulting averaged equations are expressed in terms of the new variables r_i and φ_i, (that is, the first-order averaged quantities of a_i and ϕ_i, respectively), as follows:

$$\frac{dr_i}{d\theta} = \epsilon\left\{\frac{-1}{2}\tilde{\mu}_a r_i + \frac{\tilde{\Gamma}_\theta}{n}\cos\varphi_i F_1(r_i) + \frac{1}{N}\sum_{j\neq i}\left[\frac{1}{4}n^3 r_i r_j^2 \sin(2\alpha_{ji}) - n r_j G_1(r_i, r_j, \alpha_{ji}) - n(n^2 + n^4) r_j^3 H_1(r_i, r_j, \alpha_{ji})\right]\right\} + \mathcal{O}(\epsilon^2)$$

$$\frac{d\varphi_i}{d\theta} = \epsilon\left\{\frac{-\tilde{\Gamma}_\theta}{n r_i}\sin\varphi_i F_2(r_i) + \frac{1}{N}\left(\frac{1}{4}n^5 r_i^2 - \frac{1}{2}n\right) + \frac{1}{N}\sum_{j\neq i}\left[\frac{-1}{4}n^3 r_j^2 \cos(2\alpha_{ji}) - \frac{n r_j}{r_i}G_2(r_i, r_j, \alpha_{ji}) - n(n^2 + n^4)\frac{r_j^3}{r_i}H_2(r_i, r_j, \alpha_{ji})\right]\right\} + \mathcal{O}(\epsilon^2) \tag{22}$$

where

$$\alpha_{ji} = \varphi_j - \varphi_i,$$

$$F_1(r_i) = \frac{1}{2\pi}\int_0^{2\pi} \sin^2 x[1 - (n^2 + n^4)r_i^2 \cos^2 x]^{1/2} dx,$$

$$F_2(r_i) = \frac{1}{2\pi}\int_0^{2\pi} \cos^2 x[1 - (n^2 + n^4)r_i^2 \cos^2 x]^{1/2} dx,$$

$$G_1(r_i, r_j, \alpha_{ji}) = \frac{1}{2\pi}\int_0^{2\pi} \cos(x)\sin(x - \alpha_{ji}) \times [1 - (n^2 + n^4)r_j^2 \cos^2 x]^{1/2} \times [1 - (n^2 + n^4)r_i^2 \cos^2(x - \alpha_{ji})]^{1/2} dx,$$

$$G_2(r_i, r_j, \alpha_{ji}) = \frac{1}{2\pi}\int_0^{2\pi} \cos(x)\cos(x - \alpha_{ji}) \times [1 - (n^2 + n^4)r_j^2 \cos^2 x]^{1/2} \times [1 - (n^2 + n^4)r_i^2 \cos^2(x - \alpha_{ji})]^{1/2} dx,$$

Downloaded 04 May 2010 to 171.66.16.34. Redistribution subject to ASME license or copyright; see http://www.asme.org/terms/Terms_Use.cfm

$$H_1(r_i, r_j, \alpha_{ji}) = \frac{1}{2\pi}\int_0^{2\pi} \cos(x)\sin^2(x)\sin(x-\alpha_{ji}) \times \left[\frac{1-(n^2+n^4)r_i^2\cos^2(x-\alpha_{ji})}{1-(n^2+n^4)r_j^2\cos^2 x}\right]^{1/2} dx,$$

$$H_2(r_i, r_j, \alpha_{ji}) = \frac{1}{2\pi}\int_0^{2\pi} \cos(x)\sin^2(x)\cos(x-\alpha_{ji}) \times \left[\frac{1-(n^2+n^4)r_i^2\cos^2(x-\alpha_{ji})}{1-(n^2+n^4)r_j^2\cos^2 x}\right]^{1/2} dx.$$

These equations govern the first-order slow-time dynamics of the absorber motions, from which the first-order rotor dynamics can be obtained from (19). While these equations cover quite general motion, the present interest is in the existence and stability of the important unison motion of the absorbers, to which we now turn.

4 Stability Criterion

In order to express the unison steady-state solution for the averaged Eqs. (22), we introduce new variables r and φ as the steady-state amplitude and phase of unison oscillation, respectively. When the system undergoes unison motions,

$$r_i = r, \quad \varphi_i = \varphi \quad \text{and} \quad \alpha_{ji} = 0 \quad \text{for } 1 \le i, j \le N. \tag{23}$$

Based on Eqs. (22), it can be shown that r and φ must satisfy the following:

$$\tilde{\Gamma}_\theta = nr\sqrt{\left(\frac{\tilde{\mu}_a}{2F_1(r)}\right)^2 + \left(\frac{n^5r^2-2n}{4F_2(r)}\right)^2} \tag{24}$$

$$\tan\varphi = \left(\frac{n^5r^2-2n}{2\tilde{\mu}_a}\right)\left(\frac{F_1(r)}{F_2(r)}\right) \tag{25}$$

where r can be numerically solved using Eq. (24) and then φ can be easily calculated by Eq. (25). To determine the stability of this response, the Jacobian matrix of averaged equations (22) is evaluated at the unison steady-state solution. Due to the symmetry of this motion, this value of the Jacobian C has the particular form

$$C_{2N\times 2N} = \begin{bmatrix} A_{2\times2} & B_{2\times2} & \cdot & B_{2\times2} \\ B_{2\times2} & A_{2\times2} & \cdot & B_{2\times2} \\ \cdot & \cdot & \cdot & B_{2\times2} \\ B_{2\times2} & B_{2\times2} & B_{2\times2} & A_{2\times2} \end{bmatrix} \tag{26}$$

where entries of A and B are given by

$$A_{11} = \frac{-1}{2}\tilde{\mu}_a + \frac{1}{2}\tilde{\mu}_a r F_1(r)^{-1}\frac{\partial F_1(r)}{\partial r}$$

$$A_{12} = F_1(r)F_2(r)^{-1}r\left(\frac{1}{2}n - \frac{1}{4}n^5r^2\right) + \frac{N-1}{N} \times \left(\frac{-1}{2}nr - \frac{1}{4}n^3r^3 + \frac{1}{4}n^5r^3 - nr^3(n^2+n^4)\left.\frac{\partial H_1}{\partial\varphi_i}\right|_{s.s.}\right)$$

$$A_{21} = \left(F_2(r)^{-1}\frac{\partial F_2(r)}{\partial r} - \frac{1}{r}\right)\left(\frac{1}{2}n - \frac{1}{4}n^5r^2\right) + \frac{1}{2N}n^5r + \frac{N-1}{N}\left(\frac{n}{2r} + \frac{1}{8}n^3r + \frac{1}{8}n^5r - nr^2(n^2+n^4)\left.\frac{\partial H_2}{\partial r_i}\right|_{s.s.}\right)$$

$$A_{22} = \frac{-1}{2}\tilde{\mu}_a F_1(r)^{-1}F_2(r)$$

$$B_{11} = 0$$

$$B_{12} = \frac{1}{N}\left(\frac{1}{2}nr + \frac{1}{4}n^3r^3 - \frac{1}{4}n^5r^3 - nr^3(n^2+n^4)\left.\frac{\partial H_1}{\partial\varphi_j}\right|_{s.s.}\right)$$

$$B_{21} = \frac{1}{N}\left(\frac{-n}{2r} - \frac{1}{8}n^3r + \frac{3}{8}n^5r - nr^2(n^2+n^4)\left.\frac{\partial H_2}{\partial r_j}\right|_{s.s.}\right)$$

$$B_{22} = 0$$

where $(\cdot)|_{s.s.}$ indicates that the quantity is evaluated at the unison steady-state solution. Expressions for $(\partial H_1)/(\partial\varphi_i)|_{s.s.}$, $(\partial H_2)/(\partial r_i)|_{s.s.}$, $(\partial H_1)/(\partial\varphi_j)|_{s.s.}$, and $(\partial H_2)/(\partial r_j)|_{s.s.}$ are given in Appendix A.

It can be proved that an eigenvalue of $[A-B]$ is an $(N-1)$ times repeated eigenvalue of C and an eigenvalue of $[A+(N-1)B]$ is also an eigenvalue of C (this is a standard result from bifurcations with symmetry; refer to Section XVIII.4 of (Golubitsky et al., 1988)). Under the assumption that the absorber does not hit the cusp during the unison motion, all eigenvalues of $[A+(N-1)B]$ have negative real parts (see Appendix B). Thus, the stability of the unison motion is dictated by the eigenvalues of $[A-B]$.

For a 2×2 matrix such as $[A-B]$, both eigenvalues have negative real parts if and only if the trace of matrix is negative and the determinant is positive. It can be shown (see Appendix C) that

$$\text{Trace}[A-B] = -\tilde{\mu}_a \tag{27}$$

so that the trace is always negative. Therefore, $[A-B]$ will have an eigenvalue with positive real part only when its determinant becomes negative. In addition, condition (27) indicates that only those bifurcations corresponding to a zero eigenvalue can occur, i.e., Hopf bifurcations cannot occur.

From Eq. (26) one can obtain the determinant of $[A-B]$. We proceed to solve the condition for the loss of stability in two ways: The first is an "exact" form, using numerical determination of the determinant in terms of the functions F_i and H_i. The second way uses an expansion that is based on the observation that when $\tilde{\mu}_a \to 0$, the amplitude at which the instability occurs, r^*, also approaches zero. By assuming $\tilde{\mu}_a \ll 1$, an expansion in r^{*2} in terms of $\tilde{\mu}_a$ is carried out for the condition $\det[A-B]=0$, which yields

$$r^{*2} = \frac{2}{n^3}\tilde{\mu}_a - \frac{(1+n^2)(14n^2+6n^4)}{8n^6}\tilde{\mu}_a^2 + \mathcal{O}(\tilde{\mu}_a^3). \tag{28}$$

Note that based on the computational results shown in Eq. (28), r^* is not an explicit function of N although it may depend on N through $\tilde{\mu}_a$ if the linear viscous damping described in Eq. (15) is assumed.

The first-order approximation in Eq. (28) gives the simple result

$$r^* \simeq \left(\frac{2\tilde{\mu}_a}{n^3 b_0}\right)^{1/2}. \tag{29}$$

When r exceeds r^* the determinant of $[A-B]$ becomes negative such that $[A-B]$ has one real eigenvalue with positive real part, and therefore C has $(N-1)$ such eigenvalues.

Recall that condition (11) must be satisfied for the absorbers to not reach their maximum amplitude during the unison motion; i.e.,

$$r \le r_{\max} = \frac{1}{n\sqrt{n^2+1}}. \tag{30}$$

Downloaded 04 May 2010 to 171.66.16.34. Redistribution subject to ASME license or copyright; see http://www.asme.org/terms/Terms_Use.cfm

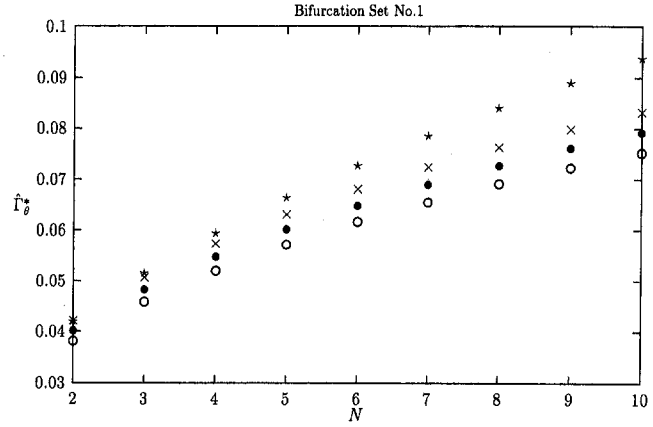


Fig. 2 The critical torque level, $\hat{\Gamma}_\theta^*$, versus the number of absorbers, N with $c_a/m_0\Omega \simeq 0.0013$. "●" represents the bifurcation point derived from "Det $[A - B] = 0$". "★" represents the bifurcation point derived from the simplified criterion (33). "×" represents a nonunison motion from numerical simulations. "○" represents an unison motion from numerical simulations.

This indicates that r will necessarily be small for $n > 1$. The results regarding the instability and the limiting absorber amplitude, Eqs. (29) and (30), respectively, can be used to obtain a condition on the system parameters which will insure that the unison motion will be stable over the entire feasible operating range. This holds if $r^* > r_{\max}$, and provides the following condition on the level of damping that will ensure the stability of the unison motion for all amplitudes up to $r_{\max}$:

$$\hat{\mu}_a \geq \frac{nb_0}{2(1+n^2)}. \tag{31}$$

In terms of the dimensional damping coefficients, this yields the following conditions for the cases of viscous and hysteretic damping, respectively:

$$\begin{cases} c_a \geq \dfrac{m_0^2 R_{0\omega}^2 \Omega n}{2I_d N(1+n^2)}, & \text{if (15) is assumed} \\ c_{a0} \geq \dfrac{m_0^2 R_0^2 \Omega n}{2I_d(1+n^2)}, & \text{if (16) is assumed.} \end{cases} \tag{32}$$

It is observed that the only difference in these results is that the damping level required for the viscous model to remain in unison motion decreases as the number of absorbers is increased (while holding the total absorber mass fixed), while for the hysteretic model the damping level required is independent of the number of absorbers. (It should be noted that in any case, desirable absorber performance requires that the absorber damping be as small as possible.)

If condition (31) does not hold, then there will exist a critical torque level at which the absorbers, moving in unison, will reach an amplitude of r^*, and the instability will occur. In order to determine this critical torque we use the relationship between $\tilde{\Gamma}_\theta$ and r given in Eq. (24), expanded for $r \ll 1$ and $\tilde{\mu}_a \ll n$, which yields $\tilde{\Gamma}_\theta \simeq n^2 r$ (the undamped, linear response relationship, which is a sufficient approximation for motions with amplitudes nearly up to $r_{\max}$). With this result, Eq. (29) can be re-expressed in term of the critical level of the disturbing torque as[1]

$$\hat{\Gamma}_\theta^* \simeq \sqrt{2b_0 n\hat{\mu}_a}. \tag{33}$$

The corresponding dimensional forms of the critical torque for the cases of viscous and hysteretic damping are, respectively,

$$\hat{T}_\theta^* \simeq \begin{cases} \sqrt{2nNc_a I_d \Omega^3 R_0^2}, & \text{if (15) is assumed} \\ \sqrt{2nc_{a0} I_d \Omega^3 R_0^2}, & \text{if (16) is assumed.} \end{cases} \tag{34}$$

This result indicates that the critical torque level for the viscous damping case depends on the number of absorbers N, and is raised by splitting a given total absorber mass into more absorbers. In contrast, for hysteretic damping, the critical torque level is independent of the number of absorbers used. (Recall that this result is valid only if the instability occurs before the absorbers reach the maximum amplitude of the unison motion.)

For the case of linear viscous damping, the effective damping $\hat{\mu}_a$ in (15) is proportional to the the number of absorbers and the quantity $c_a/m_0\Omega = \hat{\mu}_a/N$ is a fixed physical quantity. Based on this assumption, Fig. 2 shows the critical disturbing torques levels $\hat{\Gamma}_\theta^*$'s for different numbers of absorbers, N. The specific numerical values used for parameters are: $b_0 = 0.1662$, $n = 2$ (values taken from the 2.5 liter, in-line four-stroke four-cylinder engine considered by Denman (1992)), and $\hat{\mu}_a/N = \tilde{\mu}_a/N \times b_0 = 0.008 \times b_0 \simeq 0.0013$. The notation "●" in Fig. 2 denotes the critical torque levels determined by numerically solving Det $[A - B] = 0$ for the critical r value and using (24), while "★" denotes the results derived from the simplified small-amplitude criterion (33). In this figure, we also show simulation results obtained using $\hat{\mu}_0 = 0.005$ at selected "check points." Points marked by "×" denote the upper check points, which lie at torque levels five percent above the critical values—here the system undergoes nonunison motions after bifurcation—more on this below. The symbols "○" denote the lower check points, which lie at torque levels five percent below the critical values—here the system undergoes unison motion. The responses near the check points converge to their respective steady-states very slowly since they are close to the instability.

One can see that the predicted critical torque levels derived from "Det $[A - B] = 0$" are within the range bounded by the corresponding upper and lower check points, while the simplified criterion diverges away from the more accurate result as N increases.

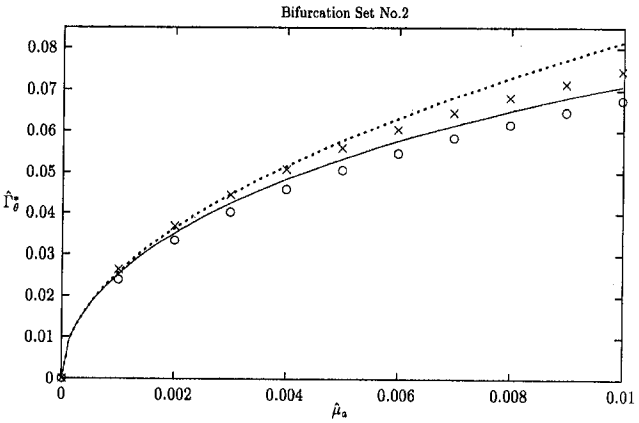


Fig. 3 The critical torque level, $\hat{\Gamma}_\theta^*$, versus various absorber damping $\hat{\mu}_a$. The solid line represents bifurcation points derived from "Det $[A - B] = 0$". The dashed line represents bifurcation points derived from the simplified criterion (33). "×" represents a nonunison motion from numerical simulations. "○" represents an unison motion from numerical simulations.

[1] See the work by Lee et al. (1996) for an alternate derivation of the critical torque level in which a pair of absorbers is considered and one assumes from the outset that the amplitude, r, is small, but allows for arbitrary values of the mass ratio b_0. In this case, the critical torque level contains a correction term involving b_0^2—a correction that can be captured in the present analysis only by carrying out second-order averaging, a nontrivial task for this system.

Downloaded 04 May 2010 to 171.66.16.34. Redistribution subject to ASME license or copyright; see http://www.asme.org/terms/Terms_Use.cfm

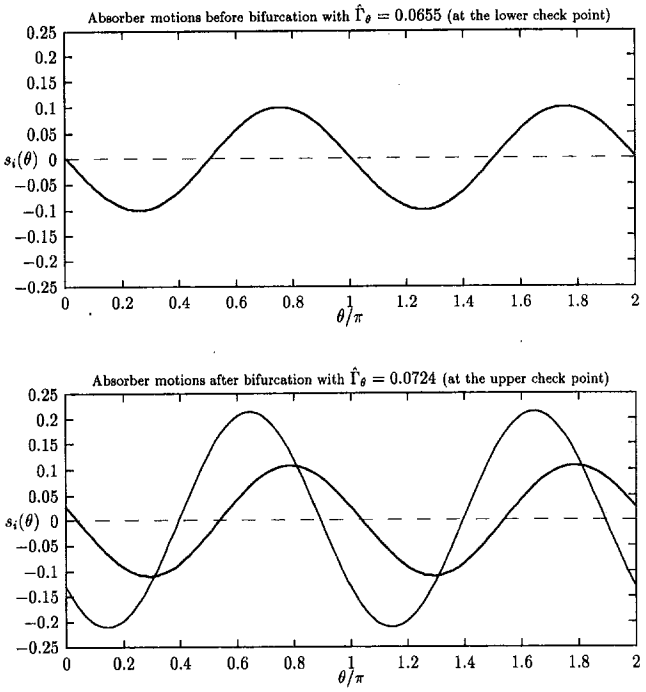


Fig. 4 Absorber motions before and after the bifurcation point for $N = 7$

Figure 3 shows the approximations for the critical disturbing torque level $\hat{\Gamma}_\theta^*$ versus absorber damping $\hat{\mu}_a$, as given by the simplified criterion (33) and by "Det $[A - B] = 0$". Note that by the results obtained from using Eq. (28), the curves in this figure are independent of the number of absorbers N. The remaining system parameters used are the same as those in Fig. 2. The upper bound of $\hat{\mu}_a$ ($= 0.01$) is chosen to prevent any absorber from hitting a cusp after bifurcation for $N \leq 10$, based on simulations. This figure also shows simulation results at check points "×" and "○", which indicate that utilizing "Det $[A - B] = 0$" gives a very accurate prediction of the bifurcation.

Figure 4 shows the absorber responses for $N = 7$ at the two check points. The unison motion is obvious. It is interesting to note that the post-critical nonunison motion involves six absorbers moving together while the seventh has a different motion with a larger amplitude. This supercritical bifurcation was the only type observed in many simulations involving different values of system parameters, different N, and different initial conditions. Note that there will be N such responses possible that are virtually identical, since the symmetry of the problem allows any one of the absorbers to be the one that is "out of step." The determination of this response and its effect on the performance of the absorber system is the topic of another paper (Chao et al., 1996).

5 Conclusion and Future Work

This study investigated the stability of unison motions for multiple identical tautochronic vibration absorbers (CPVA's). This problem has practical importance, as systems of CPVA's are typically divided into N identical masses due to spatial restrictions and in order to balance the rotating system. However, the selection of the total absorber mass is always done based on the assumption of unison motion. Using the method of averaging, a stability criterion for unison motions was derived in terms of the disturbance torque level and the system parameters. The results indicate that the number of absorbers has an effect on the system stability if the absorber damping is viscous. If the absorber damping is hysteretic, however, the number of absorbers does not affect the instability. In practice, this damping, while critical for good operation, is extremely difficult to determine, either in type or magnitude.

Designers with the aim of improving performance by lowering absorber damping should keep this instability in mind, as it is more likely to occur with smaller damping. The net result of lowering the damping is that the system will have improved performance, but over a smaller operating range, since the post-critical motion of the absorbers will reach amplitude limits at a smaller torque level than the unison motion.

This work only investigates the case in which each absorber path is epicycloid and tuned to order n, that is, the same order as the applied torque. In future works, we will apply the same methodology to different cases, including pairs of subharmonic absorbers (Lee et al., 1994), absorbers with (possibly mistuned) circular paths, and sets of nonidentical absorbers. In addition, the influence of large, but finite rotor flexibility will be considered. In addition, we will investigate the post-critical system response. We have taken some steps in this direction, and have shown that for $N = 2$ the instability/bifurcation can actually provide some improvement in torsional vibration reduction (Lee and Shaw, 1996). This requires a more systematic treatment, however, and the determination of the post-critical responses involves an analysis of bifurcations with symmetry.

References

Borowski, V. J., Denman, H. H., Cronin, D. L., Shaw, S. W., Hanisko, J. P., Brooks, L. T., Milulec, D. A., Crum, W. B., and Anderson, M. P., 1991, "Reducing vibration of reciprocating engines with crankshaft pendumlum vibration absorbers," The Engineering Society for Advanced Mobility Land, Sea, Air and space, SAE Technical Paper Series 911876.

Carter, B. C., 1929, *British Patent,* No. 337, p. 446.

Chao C.-P., Shaw, S. W., and Lee, C.-T., 1996, "Non-unison dynamics of multiple centrifugal pendenlum vibration absorbers," Deptment of Mechanical Engineering, Michigan State University, preprint.

Cronin, D. L., 1992, "Shake reduction in an automobile engine by means of crankshaft-mounted pendulums," *Mechanism and Machine Theory,* Vol. 27, No. 5, pp. 517–533.

Den Hartog, J. P., 1938, "Tuned pendulums as tosional vibration eliminators," *Stephen Timoshenko 60th Anniversary,* Vol. 17–26, Macmillan, New York.

Denman, H. H., 1985, "Remarks on brachistochrone-tautochrone problems," *American Journal of Physics,* Vol. 53, pp. 781–782.

Denman, H. H., 1992, "Tautochronic bifilar pendulum torsion absorbers for reciprocating engines," *Journal of Sound and Vibration,* Vol. 159, pp. 251–277.

Golubitsky, M., Stewart, I., and Schaeffer, D. G., 1988, *Singularities and Groups in Bifurcation Theory,* Vol. II, Springer-Verlag, New York.

Ker Wilson, W., 1968, "Practical Solution of Torsional Vibration Problems," Vol IV, 3rd ed., Chapman and Hall, London, Chapter 30.

Lee, C-T., and Shaw, S. W., 1996, "Nonlinear dynamic response of paired centrifugal pendunlum vibration absorb," *Journal of Sound and Vibration,* to appear.

Lee, C-T., Shaw, S. W., and Coppola, V. T., 1997, "A Subharmonic Vibration Absorber for Rotating Machinery," ASME *Journal of Vibration and Acoustics,* in press.

Madden, J. F., 1980, "Constant frequency bifilar vibration absorber," *United States Patent,* No. 4218187.

Newland, D. E., 1964, "Nonlinear Aspects of the Performance of Centrifugal Pendunlum Vibration Absorbers," ASME *Journal of Engineering for Industry,* Vol. 86, pp. 257–263.

Sharif-Bakhtiar, M., and Shaw, S. W., 1992, "Effects of Nonlinearities and Damping on the Dynamics Response of a Centrifugal Pendulum Absorber," ASME *Journal of Vibration and Acoustics,* Vol. 114, pp. 305–311.

Shaw, S. W., and Lee, C-T., 1995, "On the nonlinear dynamics of centrifugal pendulum vibration absorbers," *Smart Structure, Nonlinear Vibration, and Control,* A. Guran, and D. J. Inman, eds., Prentice Hall, Englewood Cliffs, NJ, Chapter 7, pp. 247–309.

Wachs, M. A., 1973, "The main rotor bifilar absorber and its effect on helicopter reliability/maintainability," SAE Technical Paper Series 739874.

APPENDIX A

The terms $(\partial H_1)/(\partial \varphi_i)|_{s.s.}$, $(\partial H_2)/(\partial r_i)|_{s.s.}$, $(\partial H_1)/(\partial \varphi_j)|_{s.s.}$ and $(\partial H_2)/(\partial r_j)|_{s.s.}$ in (26) are given by

$$\left.\frac{\partial H_1}{\partial \varphi_i}\right|_{s.s.} = \frac{1}{8} + \frac{1}{(n^2+n^4)^2 r^4}\left[(1-(n^2+n^4)r^2)^{3/2} - \frac{1}{8}(3(n^2+n^4)^2 r^4 - 12(n^2+n^4)r^2 + 8)\right]$$

Downloaded 04 May 2010 to 171.66.16.34. Redistribution subject to ASME license or copyright; see http://www.asme.org/terms/Terms_Use.cfm

$$\left.\frac{\partial H_1}{\partial \varphi_j}\right|_{s.s.} = -\left.\frac{\partial H_1}{\partial \varphi_i}\right|_{s.s.}$$

$$\left.\frac{\partial H_2}{\partial r_i}\right|_{s.s.} = \frac{1}{8(n^2+n^4)^2 r^5}\left[(n^2+n^4)^2 r^4 + 4(n^2+n^4)r^2 - 8 + 8\sqrt{1-(n^2+n^4)r^2}\right]$$

$$\left.\frac{\partial H_2}{\partial r_j}\right|_{s.s.} = -\left.\frac{\partial H_2}{\partial r_i}\right|_{s.s.}.$$

The above results were obtained using contour integrals and the residue theorem.

APPENDIX B

In Section 4 we claim that all the real parts of the eigenvalues of $[A + (N-1)B]$ are negative. To show this is equivalent to prove that its trace is negative and its determinant is positive. From (26), they can be determined in series form as follows:

$$\text{Trace}\,[A + (N-1)B] = -\tilde{\mu}_a$$

$$\text{Det}\,[A + (N-1)B] = \frac{n^2+\tilde{\mu}_a^2}{4} + \left(\frac{n^4}{4} - \frac{n^6}{4}\right) r^2 + \left[15n^2 + 10n^4 + 7n^6 - \tilde{\mu}_a^2(1+n^2)^2\right]\frac{n^4 r^4}{64} + \left[(1+n^2)(40n^2+10n^4 - 6n^6 - 3\tilde{\mu}_a^2(1+n^2)^2)\right]\frac{n^6 r^6}{256} + \mathcal{O}(r^7).$$

Obviously the trace is negative. (Since $B_{11} = B_{22} = 0$, this trace is the same as the trace of $[A - B]$. See Appendix D for the proof of (iii).) The general proof that Det $[A + (N-1)B]$ is positive appears to be quite difficult, so we satisfy ourselves here by proving that the sum of the first two terms in the series is positive. Since the function $g_i(s_i)$ in (14) is required to be real, r must satisfy $r \le (1/n\sqrt{n^2+1})$. Under this condition, we can derive that the sum of the first two terms in Det $[A + (N-1)B]$ is positive if

$$\frac{1}{n^2+n^4} < \frac{n^2+\tilde{\mu}_a^2}{n^6-n^4}.$$

This inequality can be proved by the fact

$$\frac{n^6-n^4}{n^2+n^4} - n^2 = \frac{-2n^4}{n^2+n^4} < 0 < \tilde{\mu}_a^2, \quad \text{for} \quad n = 1, 2, 3, \ldots.$$

Thus, for sufficiently small r, it follows that Det $[A + (N-1)B]$ is positive.

APPENDIX C

In Section 4 we claim that

$$\text{Trace}\,[A - B] = -\tilde{\mu}_a.$$

To prove this, we first show

$$F_2(r) - F_1(r) = \frac{1}{2\pi}\int_0^{2\pi} \cos 2x \times [1-(n^2+n^4)r^2\cos^2 x]^{1/2} dx = \frac{1}{4\pi}\int_0^{2\pi} [1-(n^2+n^4) \times r^2\cos^2 x]^{1/2} d(\sin 2x) = \frac{-(n^2+n^4)}{2\pi}\int_0^{2\pi} [r\cos(x)\sin(x)]^2 \times [1-(n^2+n^4)r^2\cos^2 x]^{-1/2} dx = r\frac{\partial F_1}{\partial r}.$$

Note that the third step is completed using integration by parts. With the expressions for A_{11} and A_{22} from Eq. (26) and the above result, we can show that

$$\text{Trace}\,[A - B] = A_{11} + A_{22} = -\tilde{\mu}_a.$$

Downloaded 04 May 2010 to 171.66.16.34. Redistribution subject to ASME license or copyright; see http://www.asme.org/terms/Terms_Use.cfm

Stochastic Averaging of Quasi-Nonintegrable-Hamiltonian Systems

W. Q. Zhu
Professor.

Y. Q. Yang
Graduate Student.

Department of Mechanics,
Zhejiang University,
Hangzhou, 310027, P. R. China

A stochastic averaging method is proposed to predict approximately the response of multi-degree-of-freedom quasi-nonintegrable-Hamiltonian systems (nonintegrable Hamiltonian systems with lightly linear and (or) nonlinear dampings and subject to weakly external and (or) parametric excitations of Gaussian white noises). According to the present method, a one-dimensional approximate Fokker-Planck-Kolmogorov equation for the transition probability density of the Hamiltonian can be constructed and the probability density and statistics of the stationary response of the system can be readily obtained. The method is compared with the equivalent nonlinear system method for stochastically excited and dissipated nonintegrable Hamiltonian systems and extended to a more general class of systems. An example is given to illustrate the application and validity of the present method and the consistency of the present method and the equivalent nonlinear system method.

Introduction

The stochastic averaging method is an effectively approximate method for prediction of the response, decision of the stability, and estimation of the reliability of nonlinear systems with lightly linear and (or) nonlinear dampings and subject to weakly external (additive) and (or) parametric (multiplicative) excitations of wide band random processes. It has been extensively used in theoretical investigation and engineering applications of nonlinear random vibration (Roberts and Spanos, 1986; Zhu, 1988, 1996). The method was developed initially by Stratonovich (1963) and justified rigorously by Khasminskii (1966). In the case of single-degree-of-freedom (SDOF) systems, there are basically two versions of the stochastic averaging method: stochastic averaging of the amplitude and stochastic averaging of the energy envelope. For systems with linear restoring force the two versions are equivalent. In the case of strongly nonlinear restoring force, however, only the second version, namely stochastic averaging of the energy envelope, leads to accurate results.

The stochastic averaging of the energy envelope, or the so-called quasi-conservative stochastic averaging, was first proposed by Landa and Stratonovich (1962) for stochastically excited Duffing oscillaor and by Khasminskii (1964) for two-dimensional quasi-Hamiltonian systems, respectively. Later, an alternative heuristic derivation of the Fokker-Planck-Kolmogorov (FPK) equation for the averaged energy envelope of Duffing oscillator subject to wide band exciation was given by Roberts (1978) based on an energy balance principle. The result was the same as that obtained by Stratonovich (1963). Subsequently, Zhu (1983) and Zhu and Lin (1991) developed a more rigorous formulation for this method based on a theorem due to Khasminskii (1968) and applied it to generally quasi-conservative nonlinear oscillators of SDOF subject to external and (or) parametric excitations of correlated Gaussion white noises. The method of stochastic averaging of energy envelope has been applied successfully to a variety of problems, including ship rolling in irregular seas (Roberts, 1982), hysteretic systems under wide band random excitations (Roberts, 1988; Zhu and Lei, 1988; Zhu and Lin, 1991), stability of nonlinear stochastic systems (Zhu 1983), and the first-passage time over a threshold of randomly excited nonlinear systems (Cai and Lin, 1994; Roberts, 1976; Zhu and Lei, 1989).

The method of stochastic averaging of energy envelope has been developed so far only for stochastically excited SDOF quasi-conservative nonlinear systems. The method of standard (or Stratonovich) stochastic averaging, on the other hand, is applicable only to the systems with linear or quasi-linear restoring forces although the systems may be of multi-degree-of-freedom (MDOF). Thus, it has been a desire for years to develop a stochastic averaging method for MDOF strongly nonlinear stochastic systems.

In the present paper, a stochastic averaging method is developed for MDOF quasi-nonintegable-Hamiltonian systems. For such a system, the Hamiltonian is the only slowly varying process and, based on a theorem due to Khasminskii (1968), it converges in probability to an one-dimensional diffusion process. A one-dimensional approximate FPK equation for the transition probability density of the Hamiltonian can be constructed by averaging with respect to rapidly varying processes in the system. The solution of the FPK equation subject to certain initial and boundary conditions would yield the statistics of the stochastic response of the system. Especially, the statistics of stationary response of the system can be obtained readily. The stochastic averaging method for quasi-nonintegrable-Hamilitonian systems is compared with the equivalent nonlinear system method for stochastically excited and dissipated nonintegrable Hamiltonian systems (Zhu, Soong, and Lei, 1994) and extended to a more general class of systems. To illustrate the application and validity of the present method, the method is applied to two linearly and nonlinearly coupled van der Pol oscillators subject to parametric excitations of two independent Gaussian white noises. The results are then compared with those obtained by using the equivalent nonlinear system method (Zhu, Soong, and Lei, 1994) and those from digital simulation. The good agreement of the three results justifies both the present method and the equivalent nonlinear system method.

The Stochastic Averaging Method

Consider an n DOF stochastically excited and dissipated Hamiltonian system governed by the following n pairs of equations of motion:

Contributed by the Applied Mechanics Division of THE AMERICAN SOCIETY OF MECHANICAL ENGINEERS for publication in the ASME JOURNAL OF APPLIED MECHANICS.

Discussion on this paper should be addressed to the Technical Editor, Professor Lewis T. Wheeler, Department of Mechanical Engineering, University of Houston, Houston, TX 77204-4792, and will be accepted until four months after final publication of the paper itself in the ASME JOURNAL OF APPLIED MECHANICS.

Manuscript received by the ASME Applied Mechanics Division, Dec. 1, 1994; final revision, Sept. 17, 1996. Associate Technical Editor: M. Shinozuka.

Copyright © 1997 by ASME

Downloaded 04 May 2010 to 171.66.16.34. Redistribution subject to ASME license or copyright; see http://www.asme.org/terms/Terms_Use.cfm

$$\dot{Q}_i = \frac{\partial H'}{\partial P_i} \tag{1a}$$

$$\dot{P}_i = -\frac{\partial H'}{\partial Q_i} - \epsilon C_{ij}\frac{\partial H'}{\partial P_j} + \epsilon^{1/2} f_{ik} W_k(t) \tag{1b}$$

$$i, j = 1, 2, \ldots, n; \quad k = 1, 2, \ldots, m$$

where Q_i and P_i are generalized displacements and generalized momenta, respectively; $H' = H'(\mathbf{Q}, \mathbf{P})$ is a Hamiltonian with continuous second-order derivatives; $C_{ij} = C_{ij}(\mathbf{Q}, \mathbf{P})$ are differentiable functions; $f_{ik} = f_{ik}(\mathbf{Q}, \mathbf{P})$ are twice-differentiable functions; ϵ is a small parameter; $W_k(t)$ are Gaussian white noises in the sense of Stratonovich with correlation functions

$$E[W_k(t)W_l(t+\tau)] = 2D_{kl}\delta(\tau). \tag{2}$$

The system governed by Eqs. (1a) and (1b) is termed a quasi-Hamiltonian one and it is generally nonlinear. The first summation terms on the right-hand side of Eq. (1b) may represent a set of linear and (or) nonlinear damping mechanisms, while the second summation terms may include external and (or) parametric excitations of Gaussion white noises.

Equations (1a) and (1b) are equivalent to the following set of Itô stochastic differential equations:

$$dQ_i = \frac{\partial H'}{\partial P_i}\,dt \tag{3a}$$

$$dP_i = \left(-\frac{\partial H'}{\partial Q_i} - \epsilon C_{ij}\frac{\partial H'}{\partial P_j} + \epsilon D_{kl} f_{jl}\frac{\partial f_{ik}}{\partial P_j}\right)dt + \epsilon^{1/2} f_{ik}\,dB_k(t) \tag{3b}$$

$$i, j = 1, 2, \ldots, n; \quad k, l = 1, 2, \ldots, m,$$

where $B_k(t)$ are the Weiner processes. The double summation terms on the right-hand side of Eq. (3b) are known as the Wong-Zakai correct terms (Wong and Zakai, 1965). These terms can usually be split into two parts: one has the effect of modifying the conservative forces and another modifying the damping forces. The first part can be combined with $-\partial H'/\partial Q_i$ to form overall effective conservative forces $-\partial H/\partial Q_i$ with modified Hamiltonian $H = H(\mathbf{Q}, \mathbf{P})$ and with $\partial H/\partial P_i = \partial H'/\partial P_i$. The second part may be combined with $-\epsilon C_{ij}\partial H'/\partial P_j$ to constitute effective damping forces $-\epsilon m_{ij}\partial H/\partial P_j$ with $m_{ij} = m_{ij}(\mathbf{Q}, \mathbf{P})$. With these accomplished, Eqs. (3a) and (3b) can be rewritten as follows:

$$dQ_i = \frac{\partial H}{\partial P_i}\,dt \tag{4a}$$

$$dP_i = -\left(\frac{\partial H}{\partial Q_i} + \epsilon m_{ij}\frac{\partial H}{\partial P_j}\right)dt + \epsilon^{1/2} f_{ik}\,dB_k(t) \tag{4b}$$

$$i, j = 1, 2, \ldots, n; \quad k = 1, 2, \ldots, m$$

Without dampings and Gaussian white noise excitations, Eqs. (4a) and (4b) become

$$\dot{q}_i = \frac{\partial H}{\partial p_i} \tag{5a}$$

$$\dot{p}_i = -\frac{\partial H}{\partial q_i} \tag{5b}$$

$$i = 1, 2, \ldots, n$$

which represent an n-DOF Hamiltonian system with modified Hamiltonian H. It is well known (Tabor, 1989) that a Hamiltonian system may be integrable or nonintegrable. An n-DOF Hamiltonian system is said to be integrable or completely integrable if there exist n independent integrals of the motion which are in involution. This last term means that the Poisson bracket of any two of these integrals vanishes. For a nonintegrable or completely nonintegrable Hamiltonian system, there is only one independent integral of the motion, i.e., the Hamiltonian H. Completely integrable Hamiltonian systems are exceptional. Siegel and Morser (1971) have shown that, in certain classes of Hamiltonian systems, the nonintegrable ones form a dense set. In view of this fact, in the present paper, the Hamiltonian system governed by Eqs. (5a) and (5b) is assumed to be nonintegrable.

Since H is a function of Q_i and P_i, an Itô stochastic differential equation for H can be derived from Eqs. (4a) and (4b) by using Itô differential rule (Itô, 1951) as follows:

$$dH = \epsilon\left(-m_{ij}\frac{\partial H}{\partial P_i}\frac{\partial H}{\partial P_j} + D_{kl} f_{ik} f_{jl}\frac{\partial^2 H}{\partial P_i \partial P_j}\right)dt + \epsilon^{1/2}\frac{\partial H}{\partial P_i} f_{ik}\,dB_k(t) \tag{6}$$

Now introduce new variable H

$$H = H(Q_1, \ldots, Q_n, P_1, \ldots, P_n) \tag{7}$$

to replace P_1. Since the Hamiltonian system is nonintegrable and the dampings are light and Gaussian white noise excitations are weak, the Hamiltonian H is a slowly varying process while the generalized displacements $Q_1, Q_2, \ldots, Q_n$ and generalized momenta $P_2, P_3, \ldots P_n$ are rapidly varying processes. According to a theorem due to Khasminskii (1968), the H process converges in probability to a one-dimensional diffusion process as $\epsilon \to 0$, in a time interval $0 \leq t \leq T$, where $T \sim 0(\epsilon^{-1})$. In other words, the H process may be replaced in the first approximation by a diffusion process for small ϵ. For simplicity, the same symbol H will be used to denote this diffusion process, although it is only an approximation, not the original Hamiltonian process.

The Itô equation for this diffusion process is obtained by applying time averaging to Eq. (6). Making use the first (or ith) equation of Eq. (4a), the time averaging can be replaced by a space averaging with respect to Q_1 (or Q_i) under the condition that H is kept constant. To eliminate $Q_2, \ldots, Q_n, P_2, \ldots P_n$ in the averaged Itô equation, the resulting equation is further averaged with respect to $Q_2, \ldots, Q_n, P_2, \ldots P_n$. The last step involves an ergodic hypothesis which may be stated as follows: The evolution of a completely nonintegrable Hamiltonian system takes it, with equal probability, through all stated which are accessible from the starting point subject to the constraint of energy conservation (Binney, et al., 1992). The averaged Itô equation for the Hamiltonian H is thus given by

$$dH = \epsilon U(H)dt + \epsilon^{1/2} V(H)dB(t) \tag{8}$$

where

$$U(H) = \frac{1}{T(H)V_{\Omega_1}}\int_\Omega \left[\left(-m_{ij}\frac{\partial H}{\partial p_i}\frac{\partial H}{\partial p_j} + D_{kl} f_{ik} f_{jl}\frac{\partial^2 H}{\partial p_i \partial p_j}\right)\Big/\frac{\partial H}{\partial p_1}\right] dq_1 \ldots dq_n dp_2 \ldots dp_n \tag{9a}$$

$$V^2(H) = \frac{1}{T(H)V_{\Omega_1}}\int_\Omega \left[2D_{kl} f_{ik} f_{jl}\frac{\partial H}{\partial p_i}\frac{\partial H}{\partial p_j}\Big/\frac{\partial H}{\partial p_1}\right] \times dq_1 \ldots dq_n dp_2 \ldots dp_n \tag{9b}$$

$$T(H) = \frac{1}{V_{\Omega_1}}\int_\Omega \left(1\Big/\frac{\partial H}{\partial p_1}\right) dq_1 \ldots dq_n dp_2 \ldots dp_n \tag{9c}$$

$$V_{\Omega 1} = \int_{\Omega 1} dq_2 \ldots dq_n dp_2 \ldots dp_n \tag{10}$$

Downloaded 04 May 2010 to 171.66.16.34. Redistribution subject to ASME license or copyright; see http://www.asme.org/terms/Terms_Use.cfm

in which domain Ω of the $(2n-1)$-fold integrals in Eqs. $(9a)$–$(9c)$ and domain Ω_1 of the $(2n-1)$-fold integral in Eq. (10) are defined as follows:

$$\Omega = \{(q_1, \ldots, q_n, p_2, \ldots, p_n) | H(q_1, \ldots, q_n, 0, p_2, \ldots, p_n) \leq H\} \quad (11)$$

$$\Omega_1 = \{q_2, \ldots, q_n, p_2, \ldots, p_n) | H(0, q_2, \ldots, q_n, 0, p_2, \ldots, p_n) \leq H\}. \quad (12)$$

The FPK equation associated with Itô Eq. (8) is

$$\frac{\partial p}{\partial t} = \epsilon\left\{-\frac{\partial}{\partial H}[U(H)p] + \frac{1}{2}\frac{\partial^2}{\partial H^2}[V^2(H)p]\right\} \quad (13)$$

where $p = p(H, t|H_0)$ is the transition probability density of Hamiltonian H with initial condition

$$p(H, 0|H_0) = \delta(H - H_0) \quad (14)$$

or $p = p(H, t)$ is the probability density of Hamiltonian H with initial condition

$$p(H, 0) = p(H_0) \quad (15)$$

depending on whether an initial state or an initial probability density is specified. The FPK equation is usually subjected to the following boundary conditions:

$$p, dp/dH \to 0, H \to \infty \quad (16)$$

One-dimensional FPK Eq. (13) usually can only be solved numerically (Roberts, 1986; Zhu and Lei, 1989). However, the stationary solution, i.e., the solution of FPK Eq. (13) without a time derivative term, can always be obtained analytically. Considering non-negativeness of probability density and the boundary conditions in Eq. (16), the stationary solution is assumed of the form

$$p(H) = C\exp[-\varphi(H)]. \quad (17)$$

Substituting Eq. (17) into Eq. (13) without a time derivative term, one can obtain

$$\varphi(H) = \int_0^H \left\{\left[\frac{dV^2(x)}{dx} - 2U(x)\right] \Big/ V^2(x)\right\} dx. \quad (18)$$

The normalization constant C is determined by

$$C^{-1} = \int_0^\infty \exp[-\varphi(H)]dH. \quad (19)$$

The statistics of stationary Hamiltonian H can then be obtained from Eq. (17).

The solution of FPK Eq. (13) is a first approximation for the (transition) probability density of the modified Hamiltonian of the original system governed by Eqs. $(1a)$ and $(1b)$. The first approximation for the corresponding joint probability density of the generalized displacements and generalized momenta can be obtained as follows:

$$p(\mathbf{q}, \mathbf{p}) = p(q_1, \ldots, q_n, p_2, \ldots, p_n|H)p(H)\left|\frac{\partial H}{\partial p_1}\right|.$$

The derivation leading to Eqs. $(9a)$ and $(9b)$ implies that $p(q_1, \ldots, q_n, p_2, \ldots, p_n|H) = C/|\partial H/\partial p_1|$. Normalizing it and further averaging with respect to $q_2, \ldots, q_n, p_2, \ldots, p_n$, one can obtain

$$p(\mathbf{q}, \mathbf{p}) = \frac{p(H)}{T(H)}\bigg|_{H=H(\mathbf{q},\mathbf{p})}. \quad (20)$$

It is noted that for SDOF systems the stochastic averaging method developed in this section is reduced to the method of stochastic averaging of energy envelope.

Comparison With The Equivalent Nonlinear System Method

An approximate method, which may be applicable to quasi-nonintegrable-Hamiltonian systems, is the equivalent nonlinear system method proposed by Zhu, Soong, and Lei (1994). In their paper the method was developed for a less general class of systems. For comparison with the present stochastic averaging method here the equivalent nonlinear system method is developed for stochastically excited and dissipated nonintegrable Hamiltonian systems, which are of the same form as those in Eqs. $(1a)$ and $(1b)$, but without assumptions of light dampings and weak excitations. We start our derivation from Itô Eqs. $(4a)$ and $(4b)$ without ϵ, i.e.,

$$dQ_i = \frac{\partial H}{\partial P_i}dt \quad (21a)$$

$$dP_i = -\left(\frac{\partial H}{\partial Q_i} + m_{ij}\frac{\partial H}{\partial P_j}\right)dt + f_{ik}dB_k(t) \quad (21b)$$

$$i, j = 1, 2, \ldots, n; \quad k = 1, 2, \ldots, m$$

where the Hamiltonian system with Hamiltonian H is assumed to be nonintegrable. The exact stationary solution of the system governed by $(21a)$ and $(21b)$, if it exists, is of the form (Zhu and Yang, 1996)

$$p(\mathbf{q}, \mathbf{p}) = C\exp\left[-\int_0^H \lambda(u)du\right]\bigg|_{H=H(\mathbf{q},\mathbf{p})} \quad (22)$$

where C is a normalization constant and $\lambda(H)$ is the solution of the following n equations:

$$\lambda(H) = \left(2m_{ij}\frac{\partial H}{\partial p_j} + \frac{\partial b_{ij}}{\partial p_j}\right) \Big/ \left(b_{ij}\frac{\partial H}{\partial p_j}\right) \quad (23)$$

$$i, j = 1, 2, \ldots, n$$

in which $b_{ij} = 2D_{kl}f_{ik}f_{jl}$ are the diffusion coefficients of the FPK equation associated with Itô Eqs. $(21a)$ and $(21b)$.

Now suppose that Eq. (23) is not satisfied and the system governed by Itô Eqs. $(21a)$ and $(21b)$ has no exact stationary solution. Our aim is to find an equivalent nonlinear system which has the exact stationary solution of the form in Eq. (22) and whose behavior is closest to the given one. Then the exact stationary solution of the equivalent system is taken as the approximate stationary solution of the given system. The differences of the two systems are in dampings and can be expressed by

$$\epsilon_i = [2m_{ij} - \lambda(H)b_{ij}]\frac{\partial H}{\partial P_j} + \frac{\partial b_{ij}}{\partial P_j} \quad (24)$$

$$i, j = 1, 2, \ldots, n.$$

Once $\lambda(H)$ is found based on some criterion and substituted into Eq. (22), we obtain the approximate stationary solution for the given system.

Three criteria have been proposed for this purpose (Zhu, Soong, and Lei, 1994). The first one is to minimize the mean-squared ϵ with respect to $\lambda(H)$. It means that if $\lambda(H)$ is replaced by $\lambda(H) + \mu\eta(H)$ where μ is a constant and $\eta(H)$ is a function of H similar to $\lambda(H)$, then $E[\epsilon_i\epsilon_i]$, as function of μ, is minimized by letting $\mu = 0$, i.e.,

Downloaded 04 May 2010 to 171.66.16.34. Redistribution subject to ASME license or copyright; see http://www.asme.org/terms/Terms_Use.cfm

$$\frac{\partial}{\partial \mu} E[\epsilon_i \epsilon_i]|_{\mu=0} = 0. \quad (25)$$

Equation (25) is equivalent to $\delta E[\epsilon_i \epsilon_i]/\delta \lambda = 0$, i.e.,

$$\int \left\{ [2m_{ij} - \lambda(H) b_{ij}] \frac{\partial H}{\partial p_j} + \frac{\partial b_{ij}}{\partial p_j} \right\} \left(-b_{ij} \frac{\partial H}{\partial p_j} \right) p(\mathbf{q}, \mathbf{p}) d\mathbf{q} d\mathbf{p} = 0. \quad (26)$$

The $2n$-fold integral in Eq. (26) can be simplified by replacing p_1 with H according to Eq. (7), i.e.,

$$\int_0^\infty p(H) dH \int_\Omega \left\{ [2m_{ij} - \lambda(H) b_{ij}] \frac{\partial H}{\partial p_j} + \frac{\partial b_{ij}}{\partial p_j} \right\} \times \left[\left(-b_{ij} \frac{\partial H}{\partial p_j} \right) \Big/ \frac{\partial H}{\partial p_1} \right] dq_1 \ldots dq_n dp_2 \ldots dp_n \quad (27)$$

where Ω is defined in Eq. (11). Since $p(H)$ is still unknown, to proceed further, Eq. (27) is replaced by a more restrictive sufficient condition requiring that the integration on $q_1, \ldots, q_n, p_2, \ldots, p_n$ vanishes for every H (Cai and Lin, 1988). This condition leads to the following expression for $\lambda(H)$:

$$\lambda(H) = \frac{\int_\Omega \left[\left(2m_{ij} \frac{\partial H}{\partial p_j} + \frac{\partial b_{ij}}{\partial p_j} \right) \left(b_{ij} \frac{\partial H}{\partial p_j} \right) \Big/ \frac{\partial H}{\partial p_1} \right] dq_1 \ldots dq_n dp_2 \ldots dp_n}{\int_\Omega \left[\left(b_{ij} \frac{\partial H}{\partial p_j} \right) \left(b_{ij} \frac{\partial H}{\partial p_j} \right) \Big/ \frac{\partial H}{\partial p_1} \right] dq_1 \ldots dq_n dp_2 \ldots dp_n}. \quad (28)$$

The second criterion to find $\lambda(H)$ is to make the difference in the dissipated energies in the given system and in the equivalent one vanish. A similar derivation leads to

$$\lambda(H) = \frac{\int_\Omega \left[\frac{\partial H}{\partial p_i} \left(2m_{ij} \frac{\partial H}{\partial p_j} + \frac{\partial b_{ij}}{\partial p_j} \right) \Big/ \frac{\partial H}{\partial p_1} \right] dq_1 \ldots dq_n dp_2 \ldots dp_n}{\int_\Omega \left[\frac{\partial H}{\partial p_i} \left(b_{ij} \frac{\partial H}{\partial p_j} \right) \Big/ \frac{\partial H}{\partial p_1} \right] dq_1 \ldots dq_n dp_2 \ldots dp_n}. \quad (29)$$

The third criterion to find $\lambda(H)$ is to minimize the mean-squared difference in the dissipated energies in the given and equivalent systems. A similar derivation leads to

$$\lambda(H) = \frac{\int_\Omega \left[\frac{\partial H}{\partial p_i} \left(2m_{ij} \frac{\partial H}{\partial p_j} + \frac{\partial b_{ij}}{\partial p_j} \right) \left(\frac{\partial H}{\partial p_i} b_{ij} \frac{\partial H}{\partial p_j} \right) \Big/ \frac{\partial H}{\partial p_1} \right] dq_1 \ldots dq_n dp_2 \ldots dp_n}{\int_\Omega \left[\left(\frac{\partial H}{\partial p_i} b_{ij} \frac{\partial H}{\partial p_j} \right) \left(\frac{\partial H}{\partial p_i} b_{ij} \frac{\partial H}{\partial p_j} \right) \Big/ \frac{\partial H}{\partial p_1} \right] dq_1 \ldots dq_n dp_2 \ldots dp_n}. \quad (30)$$

To compare the two stationary probability densities of the generalized displacements and generalized momenta obtained by using the stochastic averaging method and the equivalent nonlinear system method, we rewrite Eq. (20) in the following form:

$$p(\mathbf{q}, \mathbf{p}) = C \exp\left[-\int_0^H \psi(u) du \right]\Big|_{H=H(\mathbf{q},\mathbf{p})} \quad (31)$$

which is similar to Eq. (22). $\psi(H)$ in Eq. (31) can be obtained from Eqs. (17)–(20) as follows:

$$\psi(H) = \frac{\frac{d}{dH} V^2(H) - 2U(H)}{V^2(H)} \frac{dT(H)}{dH} + \frac{dT(H)}{T(H)}. \quad (32)$$

Substituting Eqs. (9a)–(10) into Eq. (32), we obtain

$$\psi(H) = \left[\int_\Omega \left\{ \left[\frac{\partial H}{\partial p_i} \left(2m_{ij} \frac{\partial H}{\partial p_j} + \frac{\partial b_{ij}}{\partial p_1} \frac{\partial H}{\partial p_j} \Big/ \frac{\partial H}{\partial p_1} \right) - b_{ij} \frac{\partial^2 H}{\partial p_i \partial p_j} + 2b_{ij} \frac{\partial^2 H}{\partial p_i \partial p_1} \frac{\partial H}{\partial p_j} \Big/ \frac{\partial H}{\partial p_1} - b_{ij} \frac{\partial^2 H}{\partial p_1^2} \frac{\partial H}{\partial p_i} \frac{\partial H}{\partial p_j} \Big/ \left(\frac{\partial H}{\partial p_1} \right)^2 \right] \Big/ \frac{\partial H}{\partial p_1} \right\} dq_1 \ldots dq_n dp_2 \ldots dp_n + \left(b_{ij} \frac{\partial H}{\partial p_i} \frac{\partial H}{\partial p_j} \right) \Big/ \frac{\partial H}{\partial p_1} \Big|_{\partial\Omega} \frac{d}{dH} \partial\Omega \Big] \Big/ \int_\Omega \left[\frac{\partial H}{\partial p_i} \left(b_{ij} \frac{\partial H}{\partial p_j} \right) \Big/ \frac{\partial H}{\partial p_1} \right] dq_1 \ldots dq_n dp_2 \ldots dp_n \quad (33)$$

where $\partial\Omega$ is the boundary of domain Ω. For SDOF quasi-Hamiltonian system, Eq. (33) is reduced to

$$\psi(H) = \frac{\int_\Omega \left(2m \frac{\partial H}{\partial p} + \frac{\partial b}{\partial p} \right) dq}{\int_\Omega b \frac{\partial H}{\partial p} dq}, \quad (34)$$

which is the same as Eq. (29) for SDOF systems. It means that for SDOF quasi-Hamiltonian systems the stochastic averaging method and the equivalent nonlinear system method based on the criterion of dissipation energy balancing yield the same stationary solution. This conclusion is consistent with that (Zhu and Lin, 1991) the method of stochastic averaging of energy envelope and the dissipation energy balancing technique (Cai and Lin, 1988) yield the same stationary joint probability density of the displacement and velocity. For MDOF quasi-nonintegrable-Hamiltonian systems, it seems that the two methods generally yield different stationary solutions. However, the numerical results obtained by using the two methods for the same example indicate that the two methods may yield very close results.

Extension

The stochastic averaging method developed for quasi-nonintegrable-Hamiltonian system governed by Itô Eqs. (4a) and

Downloaded 04 May 2010 to 171.66.16.34. Redistribution subject to ASME license or copyright; see http://www.asme.org/terms/Terms_Use.cfm

(4*b*) can be further extended to a more general class of systems, which include the quasi-nonintegrable-Hamiltonian systems as special cases. Consider a system governed by the following Itô equations:

$$dQ_i = \left[D \frac{\partial H}{\partial P_i} + \epsilon G_i \right] dt + \epsilon^{1/2} F_{ik} dB_k(t) \qquad (35a)$$

$$dP_i = -\left[D \frac{\partial H}{\partial Q_i} + \epsilon g_i \right] dt + \epsilon^{1/2} f_{ik} dB_k(t) \qquad (35b)$$

where $D = D(\mathbf{Q})$, $G_i = G_i(\mathbf{Q}, \mathbf{P})$, $g_i = g_i(\mathbf{Q}, \mathbf{P})$, $F_{ik} = F_{ik}(\mathbf{Q}, \mathbf{P})$, $f_{ik} = f_{ik}(\mathbf{Q}, \mathbf{P})$. The system governed by Eqs. (4*a*) and (4*b*) is a special case with $D(\mathbf{Q}) = 1$, $G_i = F_{ik} = 0$ and $g_i = m_{ij}\partial H/\partial P_j$. Assume that the Hamiltonian system with Hamiltonian H is nonintegrable. A similar derivation as that leading to Eqs. (8)–(10) yields the following one-dimensional averaged FPK equation:

$$\frac{\partial p^*}{\partial t} = \epsilon \left[-\frac{\partial}{\partial H}(ap^*) + \frac{1}{2}\frac{\partial^2}{\partial H^2}(bp^*) \right] \qquad (36)$$

where

$$a = a(H) = \frac{1}{T^*(H)V_{\Omega_1}} \int_\Omega \left[\left(G_i \frac{\partial H}{\partial q_i} - g_i \frac{\partial H}{\partial p_i} + D_{kl}F_{ik}F_{jl}\frac{\partial^2 H}{\partial q_i \partial q_j} + 2D_{kl}F_{ik}f_{jl}\frac{\partial^2 H}{\partial q_i \partial p_j} + D_{kl}f_{ik}f_{jl}\frac{\partial^2 H}{\partial p_i \partial p_j} \right) \Big/ D\frac{\partial H}{\partial p_1} \right] dq_1 \ldots dq_n dp_2 \ldots dp_n \qquad (37a)$$

$$b = b(H) = \frac{1}{T^*(H)V_{\Omega_1}} \int_\Omega \left[\left(2D_{kl}F_{ik}F_{jl}\frac{\partial H}{\partial q_i}\frac{\partial H}{\partial q_j} + 4D_{kl}F_{ik}f_{jl}\frac{\partial H}{\partial q_i}\frac{\partial H}{\partial p_j} + 2D_{kl}f_{ik}f_{jl}\frac{\partial H}{\partial p_i}\frac{\partial H}{\partial p_j} \right) \Big/ D\frac{\partial H}{\partial p_1} \right] \times dq_1 \ldots dq_n dp_2 \ldots dp_n \qquad (37b)$$

$$T^*(H) = \frac{1}{V_{\Omega_1}} \int_\Omega \left(1/D\frac{\partial H}{\partial p_1} \right) dq_1 \ldots dq_n dp_2 \ldots dp_n. \qquad (37c)$$

Ω and V_{Ω_1} are the same as those in Eqs. (11) and (10), respectively. Obviously, the stationary solution of averaged FPK Eq. (36) is of the same form as that in Eq. (17) with U and V^2 in Eq. (18) replaced by a and b, respectively, and Eq. (20) still applies provided that $p(\mathbf{q}, \mathbf{p})$, $p(H)$, and $T(H)$ are replaced by $p^*(\mathbf{q}, \mathbf{p})$, $\mathbf{p}^*(H)$ and $T^*(H)$, respectively.

Example

The stochastic averaging method developed in the present paper is applicable to MDOF quasi-nonintegrable-Hamiltonian systems whose Itô equations are of the form in Eqs. (4*a*) and (4*b*), or more generally, to MDOF quasi-conservative systems whose Itô equations are of the form in Eqs. (35*a*) and (35*b*). The main limitations in applying the method to engineering problems are as follows: the Hamiltonian system modified by Wong-Zakai correct terms is nonintegrable, i.e., the Hamiltonian is the only independent integral of the motion; the dampings can be linear and (or) nonlinear but should be light; the excitations can be external and (or) parametric but should be weak and modeled as Gaussian white noises.

As an example of the application of the stochastic averaging method, consider two linearly and nonlinearly coupled van der Pol oscillators subject to parametric excitations of two uncorrelated Gaussian white noises. The equation of motion of the system is of the form

$$\ddot{X} - \lambda_1\dot{X} + \alpha_1 X^2\dot{X} + \omega_1^2 X + aY + b(X - Y)^3 = c_1 X W_1(t)$$

$$\ddot{Y} - (\lambda_1 - \lambda_2)\dot{Y} + \alpha_2 Y^2\dot{Y} + \omega_2^2 Y + aX + b(Y - X)^3 = c_2 Y W_2(t) \qquad (38)$$

where λ_1, λ_2, α_1, α_2, ω_1, ω_2, a, b, c_1 and c_2 are constants; $W_1(t)$ and $W_2(t)$ are uncorrelated Gaussian white noises with spectral densities S_1 and S_2, respectively. The Hamiltonian system governed by Eq. (38) without dampings (λ_1, λ_2, α_1 and α_2 vanish) and without random excitations (c_1 and c_2 vanish) is generally nonintegrable since the potential energy of the system is nonseparable when $b \neq 0$. This system has been studied by To and Lin (1989) using the standard (or Stratonovich) stochastic averaging method for the case of light dampings, weak couplings, and small excitations. The results obtained by them are those for the two uncoupled van der Pol oscillators subject to parametric excitations of two uncorrelated Gaussian white noises since the coupling terms vanish during the averaging. In fact, the same results can be obtained by using the method of stochastic averaging of energy envelope (Zhu, 1983; Zhu and Lin, 1991) for SDOF nonlinear stochastic systems. The system has also been studied recently by Zhu, Soong, and Lei (1994) using the equivalent nonlinear system method for stochastically excited Hamiltonian systems. The results are in very good agreement with those from digital simulation for wide ranges of values of the system parameters and excitation strength. Especially, the equivalent nonlinear system method yields better results for stronger nonlinear coupling between the two van der Pol oscillators. The reasons for this fact are that the equivalent nonlinear systems method proposed by Zhu, Soong, and Lei (1994) is applicable to stochastically excited and dissipated nonintegrable Hamiltonian systems and that the stronger is the nonlinear coupling (larger b), the stronger is the nonintegrability of the Hamiltonian system governed by Eq. (38) without dampings and random excitations.

The Hamiltonian of system (38) is the total energy

$$H = \dot{X}^2/2 + \dot{Y}^2/2 + \bar{U}(X, Y) \qquad (39)$$

where

$$\bar{U}(X, Y) = \omega_1^2 X^2/2 + \omega_2^2 Y^2/2 + aXY + b(X - Y)^4/4 \qquad (40)$$

is the potential energy of the two coupled oscillators. Note that for this example the Wong-Zakai correct terms vanish and the modified Hamiltonian is the same as the original one.

The drift coefficient and diffusion coefficient of the averaged FPK equation for this example are

$$U(H) = \frac{1}{T(H)V_{\Omega_1}} \int_\Omega \{ [(\lambda_1 - \alpha_1 x^2)\dot{x}^2 + (\lambda_1 - \lambda_2 - \alpha_2 y^2)\dot{y}^2 + \pi S_1 c_1^2 x^2 + \pi S_2 c_2^2 y^2]/\dot{x} \} dx dy d\dot{y} \qquad (41a)$$

$$V^2(H) = \frac{1}{T(H)V_{\Omega_1}} \int_\Omega [2\pi(c_1^2 S_1 x^2\dot{x}^2 + c_2^2 S_2 y^2\dot{y}^2)/\dot{x}] dx dy d\dot{y} \qquad (41b)$$

where

$$T(H) = \frac{1}{V_{\Omega_1}} \int_\Omega (1/\dot{x}) dx dy d\dot{y} \qquad (42)$$

$$V_{\Omega_1} = \int_{\Omega_1} dy d\dot{y} \qquad (43)$$

Downloaded 04 May 2010 to 171.66.16.34. Redistribution subject to ASME license or copyright; see http://www.asme.org/terms/Terms_Use.cfm

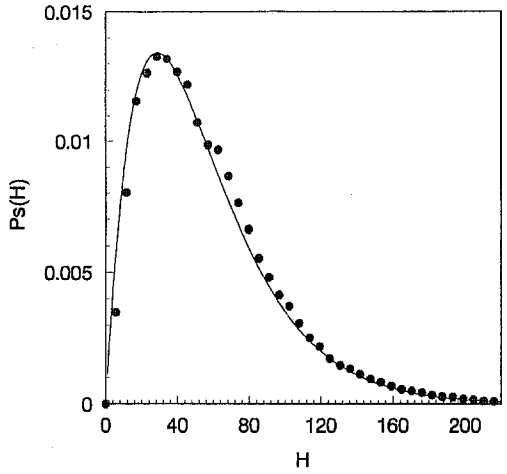


Fig. 1 Stationary probability density of the tolal energy of system (38) with $\lambda_1 = \lambda_2 = 0.01$, $\alpha_1 = 0.01$, $\alpha_2 = 0.02$, $\omega_1 = 1.0$, $\omega_2 = 2.0$, $a = 0.01$, $b = 1.0$, $c_1 = c_2 = 0.2$, $S_1 = S_2 = S_0 = 3.0$. —— The present stochastic averaging method; • digital simulation.

and

$$\Omega = \{(x, y, \dot{y}) | H(x, y, 0, \dot{y}) \leq H\} \tag{44}$$

$$\Omega_1 = \{(y, \dot{y}) | H(0, y, 0, \dot{y}) \leq H\}. \tag{45}$$

Completing the integration in Eqs. (41*a*) – (43) (see Appendix) and substituting the resultant $U(H)$ and $V^2(H)$ into Eq. (18) and then substituting the resultant $\varphi(H)$ into Eqs. (17) and (19), one obtains the approximate stationary probability density $p(H)$ of the Hamiltonian. The approximate stationary probability density $p(x, y, \dot{x}, \dot{y})$ for the displacements and velocities of original system (38) is obtained by substituting the $p(H)$ and $T(H)$ (from Eq. (42)) into Eq. (20). Other stationary statistics are then obtained from this $p(x, y, \dot{x}, \dot{y})$. For example, the stationary mean-square value of displacement X may be computed as follows:

$$E[X^2] = C \int x^2 p(x, y, \dot{x}, \dot{y}) dx dy d\dot{x} d\dot{y} \tag{46}$$

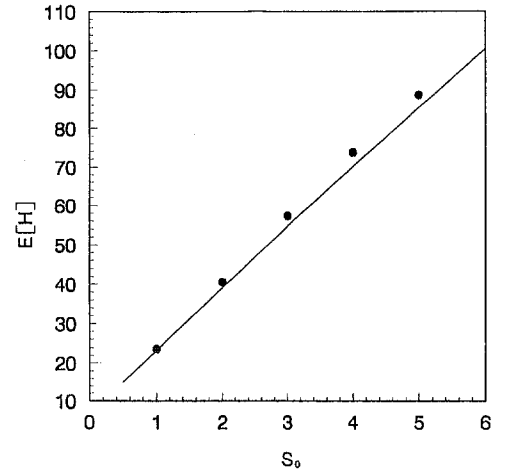


Fig. 2 Stationary mean value of the total energy of system (38). The parameters and the symbols are the same as in Fig. 1 except $S_1 = S_2 = S_0$.

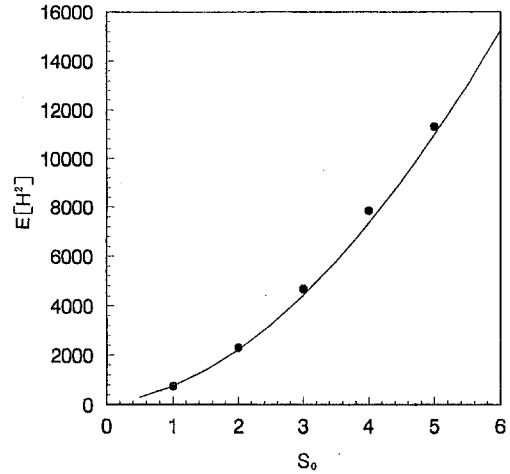


Fig. 3 Stationary mean-square value of the total energy of system (38). The parameters and the symbols are the same as in Fig. 1 except $S_1 = S_2 = S_0$.

which can be transformed into

$$E[X^2] = C \int_0^\infty [p(H)/T(H)] dH \times \int_\Omega \left(\pm \frac{x^2}{\sqrt{2H - \dot{y}^2 - 2\bar{U}(x, y)}} \right) dx dy d\dot{y}$$

$$= 2\pi C \int_0^\infty [p(H)/T(H)] dH \int_{\Omega_2} x^2 dx dy \tag{47}$$

where the normalization constant C is determined by the following equation

$$2\pi C \int_0^\infty [p(H)/T(H)] dH \int_{\Omega_2} dx dy = 1 \tag{48}$$

and integration domain Ω_2 in Eqs. (47) and (48) is

$$\Omega_2 = \{(x, y) | \bar{U}(x, y) \leq H\}. \tag{49}$$

Some numerical results for the stationary probability density, the stationary first and second moments of Hamiltonian H of system (38) computed by using the stochastic averaging method are shown in Figs. 1–3 by solid lines. To assess the accuracy

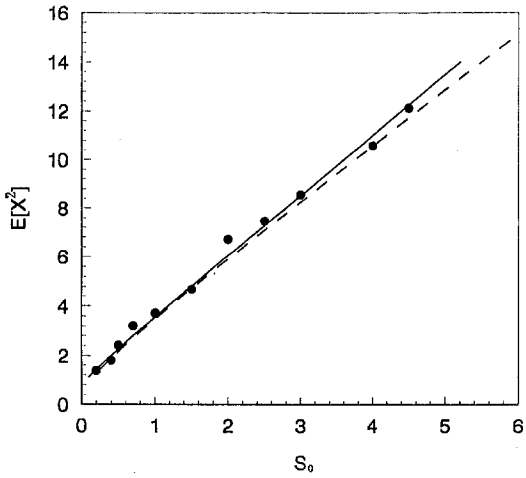


Fig. 4 Stationary variance of displacement X of system (38). The parameters are the same as in Fig. 1 except $S_1 = S_2 = S_0$. The symbols —— and • are the same as in Fig. 1. – – – The equivalent nonlinear system method based on criterion of least mean-squared difference in damping forces.

Downloaded 04 May 2010 to 171.66.16.34. Redistribution subject to ASME license or copyright; see http://www.asme.org/terms/Terms_Use.cfm

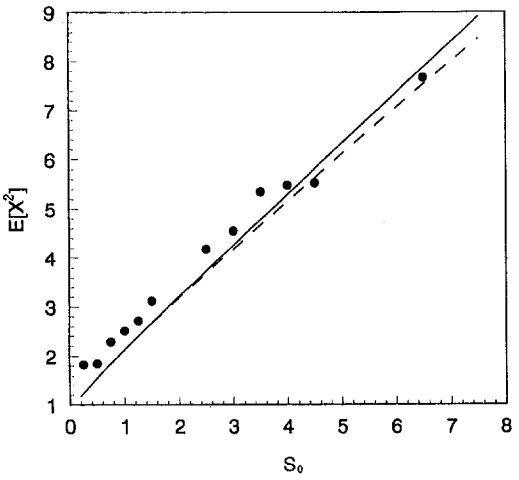


Fig. 5 Stationary variance of displacement X of system (38). The parameters are the same as in Fig. 1 except $\lambda_1 = \lambda_2 = 0.03$, $\alpha_1 = 0.03$, $\alpha_2 = 0.04$, and $S_1 = S_2 = S_0$. The symbols —— and • are the same as in Fig. 1. – – – The equivalent nonlinear system method based on criterion of dissipation energy balancing.

of the analytical results, digital simulations were carried out and the results are represented by dots in the same figures. It is seen from these figures that the analytical results agree very well with the corresponding results from digital simulation.

The numerical results for the stationary variance of displacement X of system (38) obtained by using the stochastic averaging method, by using the equivalent nonlinear system method and from digital simulation are shown in Figs. 4 and 5 by solid lines, dashed lines, and dots, respectively. For light linear and nonlinear dampings, the stochastic averaging method and the equivalent nonlinear system method based on criterion of least mean-squared difference in damping forces yield very close results and both the two results agree very well with those from digital simulation. For relatively heavier linear and nonlinear dampings, the stochastic averaging method and the equivalent nonlinear system method based on the criterion of dissipation energy balancing yield very close results and both the two results agree quite well with those from digital simulation.

Concluding Remarks

In the present paper a stochastic averaging method is developed to predict approximately the response of MDOF quasi-nonintegrable-Hamiltonian systems based on a theorem due to Khasminskii. The method can be regarded as a generalization of the method of stochastic averaging of energy envelope for stochastically excited quasi-conservative systems of SDOF. The outstanding advantages of the present method are that for any n-DOF quasi-nonintegrable-Hamiltonian system a one-dimensional averaged FPK equation for the probability density of the Hamiltonian can be constructed and that at least the probability density of the stationary response of the system can be obtained readily. Numerical integration is usually required but the computation is simple and straightforward. The comparisons of the results given by the present method with those from digital simulation for two linearly and nonlinearly coupled van der Pol oscillators subject to parametric excitations of two uncorrelated Gaussian white noises indicate that the present method is a feasible procedure for solving random vibration problems involving strongly coupled MDOF nonlinear systems (including those exhibiting intrinsically nonlinear phenomena) under external and (or) parametric excitations of Gaussian white noises. Although the example is given to illustrate only the application of the present method to the prediction of stochastic response, the method has the potential of applications to the decision of stochastic stability and the estimation of reliability.

Both the present stochastic averaging method and the equivalent nonlinear system method have been developed to predict the response of stochastically excited and dissipated nonintegrable Hamiltonian systems. For SDOF systems the two methods yield the same stationary solution. For MDOF systems, although no analytical relationship between the two methods can be established, the excellent agreement of the two results obtained by using the two methods for the same example indicates that the two methods are consistent. Since the present method is derived on a rigorously mathematical basis, the consistency of the two methods justifies indirectly the equivalent nonlinear system method in the case of light dampings and weak excitations.

Acknowledgment

The support from National Natural Science Foundation of China is gratefully acknowledged.

References

Binney, J. J., et al., 1992, *The Theory of Critical Phenomena, An Introduction to the Renormalization Group,* Clarendon Press, Oxford, U.K.

Cai, G. Q., and Lin, Y. K., 1988, "A New Approximate Solution Technique for Randomly Excited Nonlinear Oscillators," *Int. J. Non-Linear Mech.*, Vol. 23, pp. 409–420.

Cai, G. Q., and Lin, Y. K., 1994, "On Statistics of First-Passage Failure," ASME JOURNAL OF APPLIED MECHANICS, Vol. 61, pp. 93–99.

Itô, K., 1951, "On Stochastic Differential Equations," *Mem. Amer. Math. Soc.*, Vol. 4, pp. 289–302.

Khasminskii, R. Z., 1964, "On the Behavior of a Conservative System With Friction and Small Random Noise," *Prikladnaya Matematika i Mechanica* (Applied Mathematics and Mechanics), Vol. 28, pp. 1126–1130 (in Russian).

Khasminskii, R. Z., 1966, "A Limit Theorem for Solutions of Differential Equations With Random Right Hand Sides," *Theory of Probability and Applications,* Vol. 11, pp. 390–405.

Khasminskii, R. Z., 1968, "On the Averaging Principle for Stochastic Differential Itô Equation," *Kibernetika,* Vol. 4, pp. 260–279 (in Russian).

Landa, P. S., and Stratonovich, R. L., 1962. "Theory of Stochastic Transitions of Various Systems Between Different States," *Vestnik MGU* (Proc. of Moscow University), Series III, No. 1, pp. 33–45, (in Russian).

Lin, Y. K., and Cai, G. Q., 1994, "Stochastic Stability of Nonlinear Systems," *Int. J. Non-Linear Mech.*, Vol. 29, pp. 539–553.

Roberts, J. B., 1978, "The Energy Envelope of a Randomly Excited Nonlinear Oscillator," *Journal of Sound and Vibration,* Vol. 60, pp. 177–185.

Roberts, J. B., 1982, "A Stochastic Theory for Nonlinear Ship Rolling in Irregular Seas," *Journal of Ship Research,* Vol. 26, pp. 229–245.

Roberts, J. B., 1986, "First-Passage Time for Randomly Excited Nonlinear Oscillators," *Journal of Sound and Vibration,* Vol. 109, pp. 33–50.

Roberts, J. B., 1988, "Application of Averaging Method to Randomly Excited Hysteretic Systems," *Nonlinear Stochastic Dynamic Engineering Systems,* Proc. IUTAM Symposium, F. Ziegler and G. I. Schuëller, eds., Springer-Verlag, Berlin, pp. 361–379.

Roberts, J. B., and Spanos, P. D., 1986, "Stochastic Averaging: An Approximate Method of Solving Random Vibration Problems," *Int. J. Non-Linear Mech.*, Vol. 21, pp. 111–134.

Siegel, C. L., and Morser, J. K., 1971, *Lecture on Celestical Mechanics,* Springer-Verlag, New York.

Stratonovich, R. L., 1963, *Topics in the Theory of Random Noise,* Vol. 1, Gordon and Breach, New York.

Tabor, M., 1989, *Chaos and Integrability in Nonlinear Dynamics,* John Wiley and Sons, New York.

To, C. W. S., and Lin, R., 1989, "Bifurcation in a Stochastically Disturbed Nonlinear Two-Degree-of-Freedom Systems," *Structural Safety,* Vol. 6, pp. 223–231.

Wong, E., and Zakai, M., 1965, "On the Relation Between Ordinary and Stochastic Equations," *Int. J. Engineering Science,* Vol. 3, pp. 213–229.

Zhu, W. Q., 1983, "Stochastic Averaging of The Energy Envelope of Nearly Lyapunov Systems," *Random Vibrations and Reliability,* Proc. IUTAM Symposium, K. Hennig, ed., Akademie-Verlag, Berlin, pp. 347–357.

Zhu, W. Q., 1988, "Stochastic Averaging Methods in Random Vibration," ASME *Applied Mechanics Reviews,* Vol. 41, No. 5, pp. 189–199.

Zhu, W. Q., 1996, "Recent Developments and Applications of the Stochastic Averaging Method in Random Vibration," ASME *Applied Mechanics Reviews,* Vol. 49, No. 10, Part 2, pp. 572–580.

Zhu, W. Q., and Lei, Y., 1988, "Stochastic Averaging of Energy Envelope of Bilinear Hysteretic Systems," *Nonlinear Stochastic Dynamic Engineering Systems,* Proc. IUTAM Symposium, F. Ziegler and G. I. Schuëller, eds., Springer-Verlag, Berlin, pp. 381–391.

Zhu, W. Q., and Lei, Y., 1989, "First Passage Time for State Transition of Randomly Excited Systems," *Bulletin of the International Statistical Institute,* Proc. 47th Session, Paris, LIV, Book 3 (invited papers), pp. 517–531.

Downloaded 04 May 2010 to 171.66.16.34. Redistribution subject to ASME license or copyright; see http://www.asme.org/terms/Terms_Use.cfm

Zhu, W. Q., and Lin, Y. K., 1991, "Stochastic Averaging of Energy Envelope," ASCE *Journal of Engineering Mechanics,* Vol. 117, pp. 1890–1905.

Zhu, W. Q., Soong, T. T., and Lei, Y., 1994, "Equivalent Nonlinear System Method for Stochastically Excited Hamiltonian Systems," ASME JOURNAL OF APPLIED MECHANICS, Vol. 61, pp. 618–623.

Zhu, W. Q., and Yang, Y. Q., 1996, "Exact Stationary Solutions of Stochastically Excited and Dissipated Integrable Hamiltonian Systems," ASME JOURNAL OF APPLIED MECHANICS, Vol. 63, pp. 493–500.

APPENDIX

Introducing polar coordinates

$$x = r\cos\theta \quad y = r\sin\theta \tag{A1}$$

and completing partial integration, the threefold integrals in Eqs. (41*a*), (41*b*), and (42) and the twofold integral in Eq. (43) can be reduced to the following single-fold integrals:

$$U(H) = \frac{2\pi}{T(H)V_{\Omega_1}}\int_0^{\pi}[(2\lambda_1 - \lambda_2)A(H,\theta) - (\alpha_1\cos^2\theta + \alpha_2\sin^2\theta)B(H,\theta) + \pi R^4(H,\theta)(S_1c_1^2\cos^2\theta + S_2c_2^2\sin^2\theta)/2]d\theta \tag{A2}$$

$$V^2(H) = \frac{4\pi^2}{T(H)V_{\Omega_1}}\int_0^{\pi}(S_1c_1^2\cos^2\theta + S_2c_2^2\sin^2\theta)B(H,\theta)d\theta \tag{A3}$$

$$T(H) = 2\pi\int_0^{\pi}R^2(H,\theta)d\theta/V_{\Omega_1} \tag{A4}$$

$$V_{\Omega_1} = \int_0^{\pi}r^2(H,\theta)d\theta \tag{A5}$$

where

$$A(H,\theta) = HR^2 - \frac{R^4}{4}(\omega_1^2\cos^2\theta + \omega_2^2\sin^2\theta + a\sin 2\theta) - \frac{b}{12}R^4(\cos\theta - \sin\theta)^4 \tag{A6}$$

$$B(H,\theta) = \frac{HR^2}{2} - \frac{R^6}{6}(\omega_1^2\cos^2\theta + \omega_2^2\sin^2\theta + a\sin 2\theta) - \frac{b}{16}R^8(\cos\theta - \sin\theta)^4 \tag{A7}$$

and $R^2 = R^2(H,\theta)$ and $r^2(H,\theta)$ are the solutions of the following two equations:

$$H - \frac{R^2}{2}(\omega_1^2\cos^2\theta + \omega_2^2\sin^2\theta + a\sin 2\theta) - \frac{b}{4}R^4(\cos\theta - \sin\theta)^4 = 0 \tag{A8}$$

$$H - \frac{r^2}{2}\cos^2\theta - \frac{r^2}{2}\omega_1^2\cos^2\theta - \frac{b}{4}r^4\cos^4\theta = 0, \tag{A9}$$

respectively.

Downloaded 04 May 2010 to 171.66.16.34. Redistribution subject to ASME license or copyright; see http://www.asme.org/terms/Terms_Use.cfm

A Nonclassical Vibration Analysis of a Multiple Rotating Disk and Spindle Assembly[1]

I. Y. Shen
Associate Professor,
Department of Mechanical Engineering,
University of Washington,
Seattle, WA 98195-2600
Mem. ASME

C.-P. R. Ku
Senior Staff Engineer,
Seagate Technology,
Mem. ASME.

This paper studies natural frequencies and mode shapes of a spinning disk/spindle assembly consisting of multiple elastic circular plates mounted on a rigid spindle that undergoes infinitesimal rigid-body translation and rotation. Through use of Lagrangian mechanics, linearized equations of motion are derived in terms of Euler angles, rigid-body translation, and elastic vibration modes of each disk. Compared with a single rotating disk whose spindle is fixed in space, the free vibration of multiple disks with rigid-body motion is significantly different in the following ways. First of all, lateral translation of the spindle, rigid-body rotation (or rocking) of the spindle, and one-nodal diameter modes of each disk are coupled together. When all the disks (say N *disks) are identical, the coupled disk/spindle vibration splits into* N − 1 *groups of "balanced modes" and a group of "unbalanced modes." For each group of the balanced modes, two adjacent disks vibrate entirely out of phase, while other disks undergo no deformation. Because the out-of-phase vibration does not change the angular momentum, the natural frequencies of the balanced modes are identical to those of the one-nodal-diameter modes of each disk. For the group of the unbalanced modes, all disks undergo the same out-of-plane vibration resulting in a change of angular momentum and a steady precession of the spindle. As a result, the frequencies of the unbalanced modes are significantly lower than those of one-nodal-diameter modes of each disk. Secondly, axial translation of the spindle and the axisymmetric modes of each disk are couple together. Similarly, the coupled motion split into* N − 1 *groups of "balanced modes" and one group of "unbalanced modes," where the frequencies of the balanced and unbalanced modes are identical to and smaller than those of the axisymmetric modes of each disk, respectively. Thirdly, the rigid-body motion of the spindle does not affect disk vibration modes with two or more nodal diameters. Response of those modes can be determined through the classical vibration analysis of rotating disks. Moreover, vibration response of the disk/spindle assembly from a ground-based observer is derived. Finally, a calibrated experiment is conducted to validate the theoretical predictions.*

1 Introduction

In the past several years, advances of manufacturing and electronic technologies have substantially increased the capacity of computer disk drives by enhancing the data storage density (e.g., 6000 tracks per inch) and by stacking more disks (e.g., ten disks) into modern disk drives. In the meantime, the computer industry continues to reduce the size and weight of disk drives by using smaller and thinner disks mounted on spindles with shorter bearing spans. As a result of these design trends, researchers have observed repeatedly in experiments significant vibration resonances below 500 Hz, which has long been a specification for vibration testing in the disk drive industry. These vibration resonances are extremely detrimental, because the vibration takes place in the disk plane (i.e., lateral direction of the spindle). When the in-plane vibration exceeds the allowable track misregistration (about 0.6 μm), the disk drive servo system may not be able to position the recording heads back to the data track and read/write errors may occur. Unfortunately, these vibration resonances can neither be explained nor predicted by existing mathematical models developed for rotating disks.

As a concrete example, experimental results of a disk drive with four identical disks are presented as follows. The experimental setup is shown in Fig. 1. Four identical disks were clamped to a motor spindle (the hub), which was in turn supported by two antifriction bearings at both ends to the stationary shaft. The read/write heads were temporarily removed during the experiment. In these experiments, the disks were rotating at constant speed ω_3, and a small disturbance was applied to the first disk through an impact hammer. The transient transverse vibration of the first disk was measured, and its frequency spectrum was obtained through a spectrum analyzer. The system has no external excitations except the motor noise, the windage, and the unbalance of the disk/spindle system. Figure 2 shows the waterfall plot of the frequency spectrum at various rotational speed. The experimental results were fairly repetitive and the variations of the measurements were within ± 1.25 Hz.

The first attempt to explain the resonances in Fig. 2 was to use existing mathematical models of rotating disks. Since Lamb and Southwell (1921) published the first paper on rotating disk vibration, classical vibration analysis of rotating disks assumes a single elastic disk clamped to a rigid spindle rotating at constant angular speed ω_3. Moreover, the orientation of the disk/spindle system is fixed in space, and the disk/spindle system does not wobble. For a disk/spindle system containing multiple disks, the classical vibration analysis predicts that each disk vibrates

[1] The research was done when the second author worked at Conner Peripherals.

Contributed by the Applied Mechanics Division of THE AMERICAN SOCIETY OF MECHANICAL ENGINEERS for publication in the ASME JOURNAL OF APPLIED MECHANICS.

Discussion on this paper should be addressed to the Technical Editor, Professor Lewis T. Wheeler, Department of Mechanical Engineering, University of Houston, Houston, TX 77204-4792, and will be accepted until four months after final publication of the paper itself in the ASME JOURNAL OF APPLIED MECHANICS.

Manuscript received by the ASME Applied Mechanics Division, June 9, 1995; final revision, Feb. 6, 1996. Associate Technical Editor: S. W. Shaw.

Copyright © 1997 by ASME

Downloaded 04 May 2010 to 171.66.16.34. Redistribution subject to ASME license or copyright; see http://www.asme.org/terms/Terms_Use.cfm

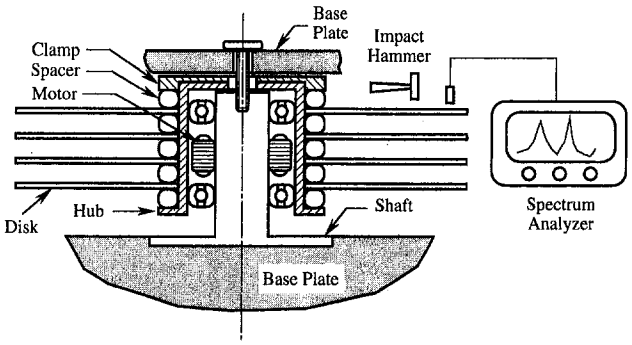


Fig. 1 Experimental setup for a disk drive with four identical disks

independently. Moreover, a pair of (m, n) vibration modes, which have m nodal circles and n nodal diameters ($n > 0$) with repeated natural frequencies ω_{mn} when $\omega_3 = 0$, will split into two modes with different frequencies $\omega_{mn} \pm n\omega_3$ for a ground-based observer. The mode splitting phenomenon and its theories can be found in the papers by Mote (1970) or Iwan and Moeller (1976).

If the classical vibration analysis is used to explain the experimental data shown in Fig. 2, it can quickly be identified that branches (2A,2B) are (0,1) modes split by the rotational speed ω_3, branch (3) is the (0,0) axisymmetric mode, and branches (4A,4B) are (0,2) modes split by the rotational speed ω_3. Branches (1A,1B), however, cannot be explained by the classical vibration analysis. Moreover, Low and Shen (1996) have shown through experimental modal analysis that the vibration associated with branch 1A involves strong rocking motion of the spindle. The rocking motion will lead to a significant vibration component in the disk plane preventing the recording head servo from reading or writing the data correctly and repeatedly. Also note that the large amplitude vibrations in the upper left corner of Fig. 2 are repeatable runouts, which occur at integer harmonics of the rotational speed and can be corrected easily by disk drive servo systems.

The purpose of this paper is to present a new mathematical model to explain and to predict the nontraditional vibration resonance branches (1A,1B) encountered in modern disk drives containing multiple disks. Only natural frequencies and mode shapes of the disk/spindle system will be studied in this paper. Because the needs for such a new mathematical model are fairly recent, appropriate literature on this topic is very limited. Nevertheless, there are three closely related areas that need to be addressed in great detail to avoid possible confusion.

The first area is rotordynamics. Much effort has been devoted to studying how disk flexibility affects rotor whirling and vibration; see Dopkin and Shoup (1974), Chivens and Nelson (1975), Wu and Flowers (1992), and Flowers and Ryan (1993). In their analyses, both the rotors and the disks are flexible with infinitesimal deflection. Therefore, it is natural to question the necessity of a new mathematical model. Why couldn't one use the existing rotordynamics models to explain the behavior of branches 1A and 1B? Moreover, why hasn't this phenomenon been observed in steam and gas turbines?

To answer the first question, the existing rotordynamics models are by all means elaborate. Nevertheless, they become too complicated to reveal analytical insights for disk drive applications, because disk drives usually have very short and fairly rigid spindles. According to finite element analyses by Frees (1995) and by Ku and Shen (1996), the spindle (the hub) experiences almost no elastic deformation at all in disk drive applications. Therefore, employing the existing rotor dynamics models will introduce superfluous field variables (e.g., spindle deflections between disks), which are not only insignificant in disk drive applications but also make the analysis exceptionally unwieldy. Not until very recently did Shen and Ku (1995) and Flowers (1996) develop new rotor models that assumed a single flexible disk mounted on a rigid spindle supported by elastic bearings. Nevertheless, Shen and Ku (1995) have demonstrated that rotor models involving a single disk cannot explain the resonance branches (1A, 1B) in Fig. 2.

As far as the second question is concerned, this phenomenon hasn't been observed in turbine applications because the disks in turbines are in general much stiffer than the rotors. As a result, major vibration resonances observed in turbine applications result mostly from rotor or bearing deformation. In contrast, the nontraditional resonance phenomenon (1A, 1B) results from disk deformation and rigid-body rocking of the spindle, because the spindle is much stiffer than the disks in disk drive applications.

The second area worth addressing is free tilting and floating disks with constant rotational speed subjected to a stationary lateral load system. In this area, Mote (1976) studied the response of a rotating flexible disk that was free to translate axially and was subjected to lateral loads. Recently, Yang (1993) studied the response of a rotating flexible disk that was free to tilt and free to translate axially. In addition, the disk was subjected to a stationary load system consisting of a linear and an angular spring-mass-dashpot system. The papers by Yang (1993) and Chen and Bogy (1993) modeled the rigid-body rocking of the spindle, and concluded that the rigid-body rocking will not affect disk vibration modes with two or more nodal diameters. Nevertheless, both papers assumed a single disk and did not discuss how bearing stiffness would affect vibration resonances of the disk/spindle system.

The third area is vibration of coupled multiple disks. Orgun and Tongue (1994a, b) studied mode localization of multiple disks coupled by weak springs. The disks they considered, however, did not undergo rigid-body motion.

The new model to be developed in this paper consists of a rigid spindle (the hub) and N elastic disks clamped to the spindle. The spindle, rotating at constant speed ω_3, is simply supported by two elastic antifriction bearings. Therefore, the spindle can undergo infinitesimal rigid-body rotation (rocking) and translation. The bearings are modeled as concentrated linear springs. The damping of the bearings are neglected because of the following two reasons. First, ball bearings have small damp-

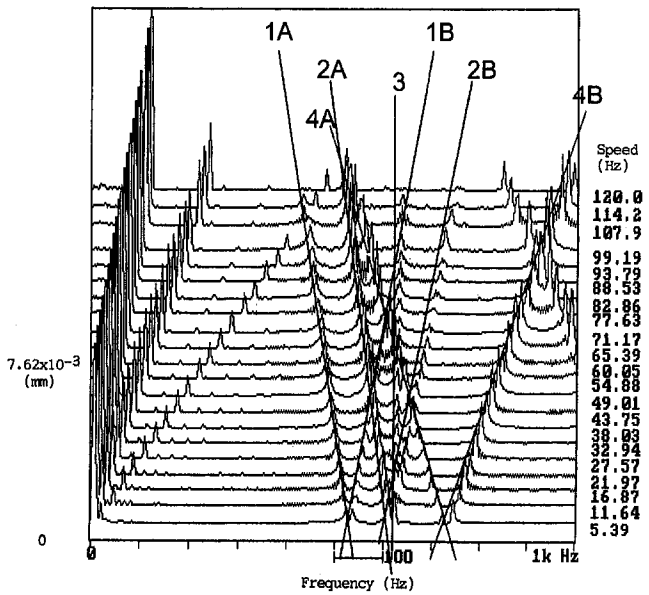


Fig. 2 Waterfall plot of the four-disk experiment. Branches 1A and 1B cannot be identified using classical analysis. The distance on the left axis from 0 to 7.62 × 10^{-3} amounts to a vibration amplitude of 7.62 × 10^{-3} mm (3 × 10^{-4} in.).

Downloaded 04 May 2010 to 171.66.16.34. Redistribution subject to ASME license or copyright; see http://www.asme.org/terms/Terms_Use.cfm

ing. (Otherwise, this resonance phenomenon will not be significant.) Secondly, neglecting the small damping does not significantly affect the prediction of natural frequencies and mode shapes. (Damping could not be neglected if the forced response was studied.) Also, this new model uses the linearized classical plate theory to approximate the elastic disks, because the vibration amplitude is tiny in disk drive applications (about 10 μm). Equations of motion are derived through use of Lagrangian mechanics. The vibration modes are classified as "balanced modes" and "unbalanced modes." Finally, an experiment is conducted to validate the theoretical predictions.

2 Formulation

Consider a disk/spindle system E that consists of N elastic circular disks and a rigid spindle (the hub) shown in Fig. 3. Let $\mathbf{R}_G$ be the position vector from a fixed reference point O to the center of mass[2] G of the disk/spindle system, let $\mathbf{R}_i$ be the position vector from G to the center C_i of the ith disk, and let $\mathbf{r}_i$ be the position vector from C_i to a mass point A_i, which undergoes transverse elastic deformation $\mathbf{u}_i$. Therefore, the position vector $\mathbf{R}_i^{(d)}$ and velocity $\dot{\mathbf{R}}_i^{(d)}$ of the mass point A_i are

$$\mathbf{R}_i^{(d)} = \mathbf{R}_G + \mathbf{R}_i + \mathbf{r}_i + \mathbf{u}_i \tag{1}$$

and

$$\dot{\mathbf{R}}_i^{(d)} = \dot{\mathbf{R}}_G + \dot{\mathbf{R}}_i + \boldsymbol{\omega} \times \mathbf{r}_i + \dot{\mathbf{u}}_i \tag{2}$$

where $\boldsymbol{\omega}$ is the angular velocity of the disk/spindle system E. In addition, let $\mathbf{R}_s$ be the position vector from O to the center of mass S of the spindle. Therefore, the kinetic energy of E is

$$T = \sum_{i=1}^{N} \frac{1}{2} \int \dot{\mathbf{R}}_i^{(d)} \cdot \dot{\mathbf{R}}_i^{(d)} dm_i + \frac{m_s}{2} \dot{\mathbf{R}}_s \cdot \dot{\mathbf{R}}_s + \frac{1}{2} \omega \cdot \mathbf{I}_s \cdot \omega \tag{3}$$

where m_s and $\mathbf{I}_s$ are the mass and the mass moment of inertia tensor of the spindle with respect to the center of mass S of the spindle, respectively.

Consider the ith disk of the disk/spindle system. In the following, a subscript i or a superscript (i) will refer to quantities of the ith disk. The subscript i will sometimes be dropped to simplify the notation. Let the ith disk have inner radius a_i, outer radius b_i, thickness h_i, density ρ_i, flexural rigidity D_i, and Poisson ratio ν_i. In addition, the disk is free at the outer rim and is rigidly fixed to the spindle at the inner rim[3] through the center C_i, which is z_i away from the center of mass G of the disk/spindle system. The rigid spindle is rotating with a constant angular speed ω_3 and is simply supported by two bearings A and B. The bearing A, which is distance z_a from the center of mass G, has transverse stiffnesses k_{ax}, k_{ay} and axial stiffness k_{az}. The bearing B can be described in the same manner with the subscript a replaced by b.

Figure 4 shows the Euler angles θ_x, θ_y, and ψ together with a set of rocking coordinates xyz with unit vectors $\mathbf{i}$, $\mathbf{j}$, and $\mathbf{k}$. The rocking coordinate system xyz is related to the inertia frame XYZ through the coordinate transformation

$$\begin{pmatrix} \mathbf{i} \\ \mathbf{j} \\ \mathbf{k} \end{pmatrix} = \begin{bmatrix} \cos\theta_y & \sin\theta_x \sin\theta_y & -\cos\theta_x \sin\theta_y \\ 0 & \cos\theta_x & \sin\theta_x \\ \sin\theta_y & -\sin\theta_x \cos\theta_y & \cos\theta_x \cos\theta_y \end{bmatrix} \begin{pmatrix} \mathbf{I} \\ \mathbf{J} \\ \mathbf{K} \end{pmatrix} \tag{4}$$

where $\mathbf{I}$, $\mathbf{J}$, and $\mathbf{K}$ are unit vectors of the inertia frame XYZ. In addition, the third set of coordinate system $x''y''z''$ is fixed to the rotating disk.

[2] The center of mass is defined when no elastic deformation is present in E.

[3] In fact, the method developed in this paper can be applied to any self-adjoint boundary conditions; see Section 3.

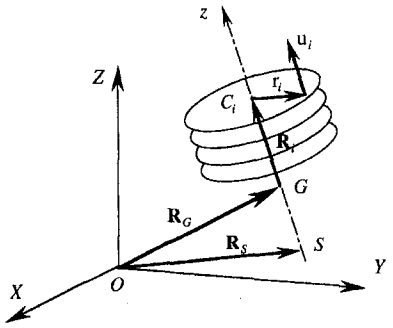


Fig. 3 A disk/spindle system with *N* flexible disks and a rigid spindle

Under these coordinate systems,

$$\mathbf{R}_G = R_x\mathbf{I} + R_y\mathbf{J} + R_z\mathbf{K} \tag{5}$$

$$\mathbf{R}_i = z_i\mathbf{k} \tag{6}$$

$$\mathbf{R}_s = \mathbf{R}_G + z_s\mathbf{k} \tag{7}$$

where z_s characterizes the relative position of the center of mass S of the spindle with respect to the center of mass G of the disk/spindle assembly. In addition, the deformation of the bearings A and B are

$$\Delta\mathbf{R}_j = \mathbf{R}_G + z_j(\mathbf{k} - \mathbf{K}), j = a, b. \tag{8}$$

Moreover, the angular velocity $\boldsymbol{\omega}_a$ of the rocking coordinate xyz is

$$\boldsymbol{\omega}_a = \dot{\theta}_x \cos\theta_y\mathbf{i} + \dot{\theta}_y\mathbf{j} + \dot{\theta}_x \sin\theta_y\mathbf{k} \tag{9}$$

and the angular velocity $\boldsymbol{\omega}$ of the disk/spindle system is

$$\boldsymbol{\omega} = \boldsymbol{\omega}_a + \dot{\psi}\mathbf{k} = \dot{\theta}_x \cos\theta_y\mathbf{i} + \dot{\theta}_y\mathbf{j} + (\dot{\psi} + \dot{\theta}_x \sin\theta_y)\mathbf{k}. \tag{10}$$

For the ith disk, the location of A_i is characterized by the radial distance r from the center C_i and the fixed angular position α from the body-fixed axes $x''y''z''$. Also notice that the position of A_i can be characterized by radial distance r and the angular position β from the rocking coordinates xyz, where

$$\beta = \alpha + \psi(t). \tag{11}$$

Therefore, the position vector of A_i is

$$\mathbf{r}_i = r\cos\beta\mathbf{i} + r\sin\beta\mathbf{j}. \tag{12}$$

In addition, the elastic deformation of the ith disk is

$$\mathbf{u}_i = \hat{w}_i(r, \alpha, t)\mathbf{k} = w_i(r, \beta, t)\mathbf{k}. \tag{13}$$

Notice that $\hat{w}_i(r, \alpha, t)$ is the deflection of the plate measured from a plate-base observer and $w_i(r, \beta, t)$ is the deflection of the plate measured from an observer rocking with xyz. Therefore, the velocity of the elastic deformation is

$$\dot{\mathbf{u}}_i = \frac{dw_i}{dt}\mathbf{k} + w_i\frac{d\mathbf{k}}{dt} \tag{14}$$

where dw_i/dt is the material derivative given by

$$\frac{dw_i}{dt} = \dot{w}_i(r, \beta, t) + \dot{\psi}\frac{\partial w_i(r, \beta, t)}{\partial\beta} \tag{15}$$

and

$$\frac{d\mathbf{k}}{dt} = \boldsymbol{\omega}_a \times \mathbf{k} = \dot{\theta}_y\mathbf{i} - \dot{\theta}_x \cos\theta_y\mathbf{j}. \tag{16}$$

Downloaded 04 May 2010 to 171.66.16.34. Redistribution subject to ASME license or copyright; see http://www.asme.org/terms/Terms_Use.cfm

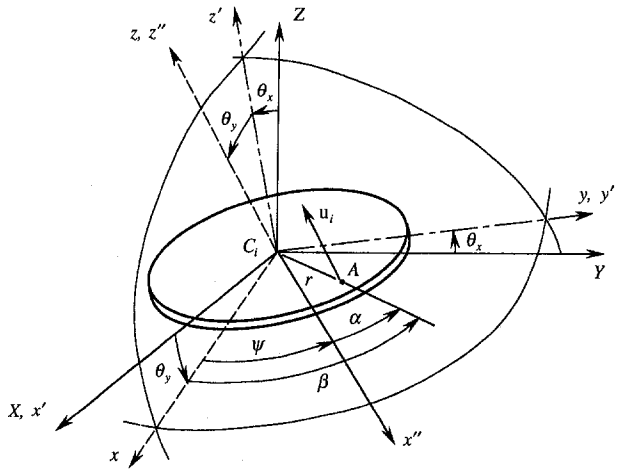


Fig. 4 Euler angles of the spinning elastic disk

In (15) and (16), ($\dot{}$) is a partial derivative with respect to time. Substitute (15) and (16) into (14) to obtain

$$\dot{\mathbf{u}}_i = w_i(\dot{\theta}_y\mathbf{i} - \dot{\theta}_x \cos\theta_y \mathbf{j}) + \left(\dot{w}_i + \dot{\psi}\frac{\partial w_i}{\partial \beta}\right)\mathbf{k}. \quad (17)$$

To obtain the kinetic energy of the system, substitution of (5), (6), (7), (10), (12), and (17) into (3) results in

$$\begin{aligned} T = {} & \frac{M}{2}(\dot{R}_x^2 + \dot{R}_y^2 + \dot{R}_z^2) + \frac{1}{2}\boldsymbol{\omega}\cdot(\bar{\mathbf{I}} + \mathbf{I}')\cdot\boldsymbol{\omega} \\ & + \frac{1}{2}\sum_{i=1}^{N}\int\left(\dot{w}_i + \dot{\psi}\frac{\partial w_i}{\partial\beta}\right)^2 dm_i \\ & + \dot{\theta}_x\cos\theta_y\sum_{i=1}^{N}\int\left(\dot{w}_i + \dot{\psi}\frac{\partial w_i}{\partial\beta}\right) r\sin\beta dm_i \\ & - \dot{\theta}_y\sum_{i=1}^{N}\int\left(\dot{w}_i + \dot{\psi}\frac{\partial w_i}{\partial\beta}\right) r\cos\beta dm_i \\ & + (\dot{R}_x\mathbf{I} + \dot{R}_y\mathbf{J} + \dot{R}_z\mathbf{K})\cdot\mathbf{k}\sum_{i=1}^{N}\int\left(\dot{w}_i + \dot{\psi}\frac{\partial w_i}{\partial\beta}\right) dm_i \quad (18) \end{aligned}$$

where

$$\bar{\mathbf{I}} = \bar{I}_1\mathbf{ii} + \bar{I}_1\mathbf{jj} + \bar{I}_3\mathbf{kk} \quad (19)$$

is the mass moment of inertia tensor of the disk/spindle system with respect to the center of mass G of the system in the dyadic form, and

$$\begin{aligned} \mathbf{I}' = {} & \left(\sum_{i=1}^{N}\int w_i^2 dm + \sum_{i=1}^{N} z_i\int w_i dm\right)(\mathbf{ii} + \mathbf{jj}) \\ & - \left(\sum_{i=1}^{N}\int w_i r\cos\beta dm\right)(\mathbf{ik} + \mathbf{ki}) \\ & - \left(\sum_{i=1}^{N}\int w_i r\sin\beta dm\right)(\mathbf{jk} + \mathbf{kj}) \quad (20) \end{aligned}$$

is the mass moment of inertia tensor resulting from the deformation of the disks.

The potential energy of the disk/spindle system is

$$V = \sum_{i=1}^{N}\tfrac{1}{2}V_i(w_i, w_i) + V_b \quad (21)$$

where V_i is the potential energy associated with the ith disk, which consists of the strain energy of the disk and the potential energy associated with the axisymmetric membrane stresses of the disk from rotation. The explicit quadratic expression of $V_i(u, v)$ is

$$\begin{aligned} V_i(u, v) = {} & D_i\int_{A_i}\left\{\nabla^2 u\nabla^2 v - (1-\nu_i)\left[u_{,rr}\left(\frac{v_{,r}}{r} + \frac{v_{,\beta\beta}}{r^2}\right)\right.\right. \\ & \left. + v_{,rr}\left(\frac{u_{,r}}{r} + \frac{u_{,\beta\beta}}{r^2}\right) - 2\left(\frac{u_{,\beta}}{r}\right)_{,r}\left(\frac{v_{,\beta}}{r}\right)_{,r}\right]\Bigg\} dA_i \\ & + h_i\int_{A_i}\left(\sigma_r^{(i)}u_{,r}v_{,r} + \frac{\sigma_\beta^{(i)}}{r^2}u_{,\beta}v_{,\beta}\right) dA_i. \quad (22) \end{aligned}$$

In (22), the commas represent partial spatial derivatives, and $\sigma_r^{(i)}$ and $\sigma_\beta^{(i)}$ are axisymmetric membrane stresses in the ith disk resulting from rotation (Chen and Bogy, 1992)

$$\begin{aligned} \sigma_r^{(i)} &= \rho_i\omega_3^2\left(C_1^{(i)} + \frac{C_2^{(i)}}{r^2} + C_3^{(i)}r^2\right), \\ \sigma_\beta^{(i)} &= \rho_i\omega_3^2\left(C_1^{(i)} - \frac{C_2^{(i)}}{r^2} + C_4^{(i)}r^2\right) \end{aligned} \quad (23)$$

with

$$C_1^{(i)} = \frac{1+\nu_i}{8}\frac{(\nu_i-1)a_i^4 - (3+\nu_i)b_i^4}{(\nu_i-1)a_i^2 - (1+\nu_i)b_i^2} \quad (24)$$

$$C_2^{(i)} = \frac{1-\nu_i}{8}a_i^2b_i^2\frac{(\nu_i+1)a_i^2 - (3+\nu_i)b_i^2}{(\nu_i-1)a_i^2 - (1+\nu_i)b_i^2} \quad (25)$$

$$C_3^{(i)} = -\frac{3+\nu_i}{8}, \quad C_4^{(i)} = -\frac{1+3\nu_i}{8}. \quad (26)$$

In (21), V_b is the potential energy of the bearings given by

$$V_b = \sum_{j=a,b}\tfrac{1}{2}\Delta\mathbf{R}_j\cdot(k_{jx}\mathbf{II} + k_{jy}\mathbf{JJ} + k_{jz}\mathbf{KK})\cdot\Delta\mathbf{R}_j \quad (27)$$

where the sum is over both bearings A and B.

Because only free vibration is studied in this paper, all external forces are not considered. In addition, damping of the bearings is ignored.

3 Discretization

There are two fundamentally different ways to obtain approximate solutions of the disk/spindle system. The first way is to derive the equations of motion and the boundary conditions either through a Newtonian approach or through the Hamilton's principle with T and V given in (18) and (21). Then the resulting partial differential equations and their boundary conditions will be discretized into ordinary differential equations for approximate solutions. This discretization scheme largely depends on the explicit form of the boundary conditions, and will become very tedious when the boundary conditions are not simple. For example, disk drives usually have disks clamped by small spacers, which serve more like an elastic foundation than a fixed end; see Fig. 1. In this case, the exact boundary conditions will be difficult to identify and the discretization will be difficult to implement.

An alternative way to obtain approximate solutions is to discretize T and V at the beginning in terms of generalized coordi-

Downloaded 04 May 2010 to 171.66.16.34. Redistribution subject to ASME license or copyright; see http://www.asme.org/terms/Terms_Use.cfm

nates. Then the equations of motion are derived through use of Lagrange's equations. The resulting equations are ordinary differential equations, and finite equations are retained to approximate the solutions. Compared with the first approach, this discretization scheme approximates the stationarity of the action integral instead of the equations of motion with boundary conditions. With this approach, the disk deflection w_i is discretized through an eigenfunction expansion

$$w_i(r, \beta, t) = \sum_{m=0}^{\infty} \sum_{n=-\infty}^{\infty} w_{mn}^{(i)}(r, \beta) q_{mn}^{(i)}(t) \tag{28}$$

where $w_{mn}^{(i)}(r, \beta)$ is the mode shapes (or eigenfunctions) of the ith elastic disk subjected to the axisymmetric membrane stresses from rotation. Also notice that $w_{mn}^{(i)}(r, \beta)$ satisfy fixed-end boundary conditions at the inner rim and free-end boundary conditions at the outer rims. Therefore,

$$w_{mn}^{(i)}(r, \beta) = \begin{cases} R_{mn}^{(i)}(r) \cos n\beta, & n \geq 0 \\ R_{m|n|}^{(i)}(r) \sin |n|\beta, & n < 0 \end{cases} \tag{29}$$

In addition, the mode shapes are normalized so that

$$\int w_{mn}^{(i)} w_{pq}^{(i)} dm_i = I_1^{(i)} \delta_{mp} \delta_{nq} \tag{30}$$

and

$$V_i(w_{mn}^{(i)}, w_{pq}^{(i)}) = I_1^{(i)} [\omega_{mn}^{(i)}]^2 \delta_{mp} \delta_{nq} \tag{31}$$

where $I_1^{(i)}$ is the mass moment of inertia of the ith disk about its diameter, $\omega_{mn}^{(i)}$ is the natural frequency of the ith disk subjected to the rotational axisymmetric membrane stresses observed from a plate-based observer, and δ_{mp} is the Kronecker delta. Notice that $\omega_{mn}^{(i)}$ and $R_{mn}^{(i)}$ are functions of the rotational speed ω_3, because the membrane stresses result from the disk rotation. An easy way to approximate $\omega_{mn}^{(i)}$ and $R_{mn}^{(i)}$ is the sensitivity analysis developed by Chen and Bogy (1992).

Substitute (28), (29), and (30) into (18) and recall (4), (10), and (19) to obtain

$$\begin{aligned} T = {} & \tfrac{1}{2} M(\dot{R}_x^2 + \dot{R}_y^2 + \dot{R}_z^2) + \tfrac{1}{2} \bar{I}_3 (\dot{\psi} + \dot{\theta}_x \sin \theta_y)^2 \\ & + \tfrac{1}{2} \{ \bar{I}_1 + \sum_{i=1}^{N} I_1^{(i)} [\sum_{m=0}^{\infty} \sum_{n=-\infty}^{\infty} (q_{mn}^{(i)})^2] \\ & + \sum_{i=1}^{N} z_i I_1^{(i)} [\sum_{m=0}^{\infty} b_m^{(i)} q_{m0}^{(i)}] \} (\dot{\theta}_x^2 \cos^2 \theta_y + \dot{\theta}_y^2) \\ & - (\dot{\psi} + \dot{\theta}_x \sin \theta_y) \{ \dot{\theta}_x \cos \theta_y \sum_{i=1}^{N} I_1^{(i)} [\sum_{m=0}^{\infty} a_m^{(i)} q_{m1}^{(i)}] \\ & + \dot{\theta}_y \sum_{i=1}^{N} I_1^{(i)} [\sum_{m=0}^{\infty} a_m^{(i)} q_{m,-1}^{(i)}] \} \\ & + \tfrac{1}{2} \sum_{i=1}^{N} I_1^{(i)} [\sum_{m=0}^{\infty} \sum_{n=-\infty}^{\infty} (\dot{q}_{mn}^{(i)} + n\dot{\psi} q_{m,-n}^{(i)})^2] \\ & + \dot{\theta}_x \cos \theta_y \sum_{i=1}^{N} I_1^{(i)} [\sum_{m=0}^{\infty} a_m^{(i)} (\dot{q}_{m,-1}^{(i)} - \dot{\psi} q_{m1}^{(i)})] \\ & - \dot{\theta}_y \sum_{i=1}^{N} I_1^{(i)} [\sum_{m=0}^{\infty} a_m^{(i)} (\dot{q}_{m1}^{(i)} + \dot{\psi} q_{m,-1}^{(i)})] \\ & + (\dot{R}_x \sin \theta_y - \dot{R}_y \sin \theta_x \cos \theta_y + \dot{R}_z \cos \theta_x \cos \theta_y) \\ & \times \sum_{i=1}^{N} I_1^{(i)} [\sum_{m=0}^{\infty} b_m^{(i)} \dot{q}_{m0}^{(i)}] \end{aligned} \tag{32}$$

where

$$a_m^{(i)} = \frac{\pi \rho_i h_i}{I_1^{(i)}} \int_{a_i}^{b_i} R_{m1}^{(i)}(r) r^2 dr \tag{33}$$

and

$$b_m^{(i)} = \frac{2\pi \rho_i h_i}{I_1^{(i)}} \int_{a_i}^{b_i} R_{m0}^{(i)}(r) r dr. \tag{34}$$

Similarly, substitute (28) and (31) into (21) and substitute (4) and (8) into (27) to obtain

$$\begin{aligned} V = {} & \tfrac{1}{2} \sum_{i=1}^{N} I_1^{(i)} \sum_{m=0}^{\infty} \sum_{n=-\infty}^{\infty} [\omega_{mn}^{(i)} q_{mn}^{(i)}]^2 + \sum_{j=a,b} [\tfrac{1}{2} k_{jx} (R_x + z_j \sin \theta_y)^2 \\ & + \tfrac{1}{2} k_{jy} (R_y - z_j \sin \theta_x \cos \theta_y)^2 \\ & + \tfrac{1}{2} k_{jz} (R_z + z_j \cos \theta_x \cos \theta_y - z_j)^2] \end{aligned} \tag{35}$$

Two remarks are made here regarding this discretization scheme. First, this discretization scheme and their results (32) and (35) are valid for any self-adjoint systems for which the orthonormality conditions (30) and (31) hold. For example, when disks are clamped by small elastic spacers in disk drives, (32) and (35) remain valid as long as corresponding $\omega_{mn}^{(i)}$ and $R_{mn}^{(i)}$ are used. Secondly, this discretization scheme does not ignore the boundary conditions, although they do not appear explicitly. Instead, the boundary conditions are embedded implicitly in the natural frequencies $\omega_{mn}^{(i)}$ and the mode shapes $R_{mn}^{(i)}$. Systems with different boundary conditions will result in different $\omega_{mn}^{(i)}$ and $R_{mn}^{(i)}$.

4 Equations of Motion

The equations of motion are derived through use of Lagrange's equation followed by a linearization assuming constant $\dot{\psi} = \omega_3$, $\theta_x \ll 1$, and $\theta_y \ll 1$. The θ_x equation is

$$\begin{aligned} & \bar{I}_1 \ddot{\theta}_x + \bar{I}_3 \omega_3 \dot{\theta}_y + \sum_{i=1}^{N} I_1^{(i)} [\sum_{m=0}^{\infty} a_m^{(i)} (\ddot{q}_{m,-1}^{(i)} - 2\omega_3 \dot{q}_{m1}^{(i)})] \\ & + z_a k_{ay} (z_a \theta_x - R_y) + z_b k_{by} (z_b \theta_x - R_y) = 0. \end{aligned} \tag{36}$$

Similarly, the θ_y equation is

$$\begin{aligned} & \bar{I}_1 \ddot{\theta}_y - \bar{I}_3 \omega_3 \dot{\theta}_x - \sum_{i=1}^{N} I_1^{(i)} [\sum_{m=0}^{\infty} a_m^{(i)} (\ddot{q}_{m1}^{(i)} + 2\omega_3 \dot{q}_{m,-1}^{(i)})] \\ & + z_a k_{ax} (z_a \theta_y + R_x) + z_b k_{bx} (z_b \theta_y + R_x) = 0. \end{aligned} \tag{37}$$

The R_x equation is

$$M\ddot{R}_x + k_{ax}(R_x + z_a \theta_y) + k_{bx}(R_x + z_b \theta_y) = 0. \tag{38}$$

The R_y equation is

$$M\ddot{R}_y + k_{ay}(R_y - z_a \theta_x) + k_{by}(R_y - z_b \theta_x) = 0. \tag{39}$$

The R_z equation is

$$M\ddot{R}_z + \sum_{i=1}^{N} I_1^{(i)} [\sum_{m=0}^{\infty} b_m^{(i)} \ddot{q}_{m0}^{(i)}] + (k_{az} + k_{bz}) R_z = 0. \tag{40}$$

The $q_{mn}^{(i)}$ equation is

$$\begin{aligned} & I_1^{(i)} \{ \ddot{q}_{mn}^{(i)} + 2n\omega_3 \dot{q}_{m,-n}^{(i)} + \{ [\omega_{mn}^{(i)}]^2 - n^2 \omega_3^2 \} q_{mn}^{(i)} + \ddot{R}_z b_m^{(i)} \delta_{n0} \\ & + a_m^{(i)} \delta_{n,-1} (\ddot{\theta}_x + 2\omega_3 \dot{\theta}_y) - a_m^{(i)} \delta_{n1} (\ddot{\theta}_y - 2\omega_3 \dot{\theta}_x) \} = 0 \\ & m = 0, 1, 2, \ldots, \quad n = 0, \pm 1, \pm 2, \ldots. \end{aligned} \tag{41}$$

Downloaded 04 May 2010 to 171.66.16.34. Redistribution subject to ASME license or copyright; see http://www.asme.org/terms/Terms_Use.cfm

5 Balanced and Unbalanced Modes

When the bearing stiffnesses are isotropic, i.e., $k_{ax} = k_{ay} = k_a$ and $k_{bx} = k_{by} = k_b$, the complex representations

$$\theta \equiv \theta_x + j\theta_y, \quad R \equiv R_x + jR_y, \quad Q_{mn}^{(i)} \equiv q_{m,-n}^{(i)} - jq_{mn}^{(i)} \tag{42}$$

where $j = \sqrt{-1}$, substantially simplify the equations of motion (36) to (41). Consider a special case when all N disks are identical and when the rigid-body translation R and the rigid-body rocking θ are decoupled.[4] In this case, the vibration modes of the disk/spindle system can be found analytically in terms of balanced and unbalanced modes. A general case for which R and θ are coupled will be discussed later.

To reveal the existence of balanced and unbalanced modes, only $\theta, Q_{01}^{(1)}, Q_{01}^{(2)}, \ldots, Q_{01}^{(N)}$ are retained. Then (36), (37), and (41) result in

$$\begin{bmatrix} \eta_1 & a_0 & a_0 & \cdots & a_0 \\ a_0 & 1 & 0 & \cdots & 0 \\ a_0 & 0 & 1 & \cdots & 0 \\ \vdots & \vdots & \vdots & \ddots & \vdots \\ a_0 & 0 & 0 & \cdots & 1 \end{bmatrix} \begin{pmatrix} \ddot{\theta} \\ \ddot{Q}_{01}^{(1)} \\ \ddot{Q}_{01}^{(2)} \\ \vdots \\ \ddot{Q}_{01}^{(N)} \end{pmatrix} - j\omega_3 \begin{bmatrix} \eta_3 & 2a_0 & 2a_0 & \cdots & 2a_0 \\ 2a_0 & 2 & 0 & \cdots & 0 \\ 2a_0 & 0 & 2 & \cdots & 0 \\ \vdots & \vdots & \vdots & \ddots & \vdots \\ 2a_0 & 0 & 0 & \cdots & 2 \end{bmatrix} \begin{pmatrix} \dot{\theta} \\ \dot{Q}_{01}^{(1)} \\ \dot{Q}_{01}^{(2)} \\ \vdots \\ \dot{Q}_{01}^{(N)} \end{pmatrix} + \begin{bmatrix} \omega_b^2 & 0 & 0 & \cdots & 0 \\ 0 & \omega_r^2 & 0 & \cdots & 0 \\ 0 & 0 & \omega_r^2 & \cdots & 0 \\ \vdots & \vdots & \vdots & \ddots & \vdots \\ 0 & 0 & 0 & \cdots & \omega_r^2 \end{bmatrix} \begin{pmatrix} \theta \\ Q_{01}^{(1)} \\ Q_{01}^{(2)} \\ \vdots \\ Q_{01}^{(N)} \end{pmatrix} = \mathbf{0} \tag{43}$$

where

$$\eta_1 = \frac{\bar{I}_1}{I_1^{(i)}}, \quad \eta_3 = \frac{\bar{I}_3}{I_1^{(i)}}, \quad \omega_b = \sqrt{\frac{k_a z_a^2 + k_b z_b^2}{I_1^{(i)}}}, \quad \omega_r^2 = \omega_{01}^2 - \omega_3^2. \tag{44}$$

To determine free vibration modes, let

$$(\theta, Q_{01}^{(1)}, Q_{01}^{(2)}, \ldots, Q_{01}^{(N)})^T = \mathbf{x}e^{j\omega t} \tag{45}$$

which assumes that the rigid spindle has a steady precession about the Z-axis with angular speed ω and all disks vibration with the same frequency ω at the same time. Substitution of (45) into (43) and the existence of nontrivial $\mathbf{x}$ result in the following $(N + 1) \times (N + 1)$ determinant

$$\begin{vmatrix} A_1 & B_1 & B_1 & \cdots & B_1 \\ B_1 & E_1 & 0 & \cdots & 0 \\ B_1 & 0 & E_1 & \cdots & 0 \\ \vdots & \vdots & \vdots & \ddots & \vdots \\ B_1 & 0 & 0 & \cdots & E_1 \end{vmatrix} = (A_1E_1 - NB_1^2)E_1^{N-1} = 0 \tag{46}$$

where

$$A_1 = -\eta_1\omega^2 + \eta_3\omega_3\omega + \omega_b^2 \tag{47}$$

$$B_1 = -a_0\omega(\omega - 2\omega_3) \tag{48}$$

$$E_1 = -\omega^2 + 2\omega_3\omega + \omega_{01}^2 - \omega_3^2. \tag{49}$$

[4] The decoupling between the translation and the rocking, characterized by $k_a z_a + k_b z_b = 0$, occurs when the bearings A and B are identical and when the center of mass G is at the center of the bearing span for example.

Since $N + 1$ complex modes are retained in this approximation, (46) provides $2(N + 1)$ natural frequencies and real modes. When $A_1E_1 - NB_1^2 = 0$, ω satisfies

$$D_1\omega^4 + D_2\omega^3 + D_3\omega^2 + D_4\omega + D_5 = 0 \tag{50}$$

where

$$D_1 = \eta_1 - Na_0^2, \quad D_2 = -\omega_3[\eta_3 + 2(\eta_1 - 2Na_0^2)] \tag{51}$$

$$D_3 = \omega_3^2(\eta_1 - 4Na_0^2 + 2\eta_3) - \omega_b^2 - \eta_1\omega_{01}^2 \tag{52}$$

$$D_4 = \omega_3[2\omega_b^2 + \eta_3(\omega_{01}^2 - \omega_3^2)], \quad D_5 = \omega_b^2(\omega_{01}^2 - \omega_3^2). \tag{53}$$

In addition, the corresponding mode shapes are

$$\left(-\frac{E_1}{B_1}, 1, \ldots, 1\right)^T. \tag{54}$$

For this mode, all disks have the same deflection as shown in Fig. 5. The inertia forces associated with the disk deformation result in an unbalanced moment about the center of mass. Because the disk/spindle assembly is spinning with an angular momentum in the z direction, the presence of the unbalanced moment causes steady precession of the spindle. In the following, these modes will be termed *unbalanced* (0,1) *modes.*

When $E_1 = 0$, (46) and (49) imply $(N - 1)$-fold repeated frequency pairs

$$\omega = \omega_3 \pm \omega_{01}. \tag{55}$$

The mode shapes correspond to the $(N - 1)$ frequency pairs are

$$\begin{pmatrix} 0 \\ 1 \\ -1 \\ 0 \\ \vdots \\ 0 \end{pmatrix}, \begin{pmatrix} 0 \\ 0 \\ 1 \\ -1 \\ \vdots \\ 0 \end{pmatrix}, \ldots, \begin{pmatrix} 0 \\ 0 \\ \vdots \\ 0 \\ 1 \\ -1 \end{pmatrix}. \tag{56}$$

For each mode in (56), only two adjacent disks have out-of-phase motion and the remaining disks are undeformed; see Fig. 6. In addition, the two deformed disks both have one-nodal-diameter forward and backward traveling waves as described by the frequency pair (55). For each mode in (56), the inertia forces of the two deformed disks are balanced resulting in no net moment with respect to the center of mass; therefore, the spindle does not undergo a steady precession as can be seen by the zero θ component of the mode shapes in (56). In the following, these modes will be termed *balanced* (0,1) *modes.* Notice that any linear combination of the balanced modes in (56) is also of a balanced mode corresponding to the same natural

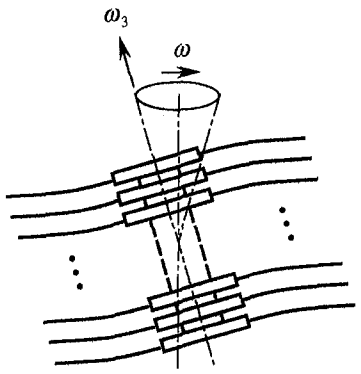


Fig. 5 Unbalanced (0,1) mode

Downloaded 04 May 2010 to 171.66.16.34. Redistribution subject to ASME license or copyright; see http://www.asme.org/terms/Terms_Use.cfm

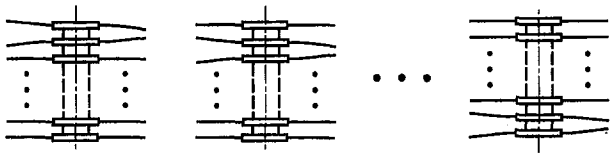


Fig. 6 $(N-1)$ balanced (0,1) mode

frequencies (55). For example, $(0, 2, -1, 0, \ldots, 0, -1)^T$ is also a balanced mode, because

$$\begin{pmatrix} 0 \\ 2 \\ -1 \\ 0 \\ \vdots \\ 0 \\ -1 \end{pmatrix} = 2\begin{pmatrix} 0 \\ 1 \\ -1 \\ 0 \\ \vdots \\ 0 \end{pmatrix} + \begin{pmatrix} 0 \\ 0 \\ 1 \\ -1 \\ \vdots \\ 0 \end{pmatrix} + \ldots + \begin{pmatrix} 0 \\ 0 \\ \vdots \\ 0 \\ 1 \\ -1 \end{pmatrix}. \quad (57)$$

There are two cases that need additional attention: single disk and translation/rotation coupling. When only a single disk is present, $N = 1$ and (46) shows that $A_1E_1 - B_1^2 = 0$. Therefore, only the unbalanced modes exist. This is the case discussed by Shen and Ku (1995). When the translation R and the rocking θ are coupled, i.e., $k_az_a + k_bz_b \neq 0$, a similar (but more complicated) derivation shows that the balanced modes remain unchanged and the unbalanced modes are governed by

$$D_1\omega^6 + D_2\omega^5 + (D_3 - \omega_t^2 D_1)\omega^4 + (D_4 - \omega_t^2 D_2)\omega^3 + (D_5 - \omega_t^2 D_3 - \omega_c^2)\omega^2 + (2\omega_3\omega_c^2 - \omega_t^2 D_4)\omega + [\omega_c^2(\omega_{01}^2 - \omega_3^2) - \omega_t^2 D_5] = 0 \quad (58)$$

where

$$\omega_t = \sqrt{\frac{k_a + k_b}{M}}, \quad \omega_c = \sqrt{\frac{(z_ak_a + z_bk_b)^2}{MI_1^{(i)}}} \quad (59)$$

and D_1 to D_5 are given in (51), (52), and (53).

Balanced and unbalanced modes also occur in the axial rigid-body motion coupled with axisymmetric modes in a slightly different manner. If only R_z, $q_{00}^{(1)}$, $q_{00}^{(2)}$, $\ldots$, $q_{00}^{(N)}$ are retained in (40) and (41), then

$$\begin{bmatrix} \frac{M}{I_1^{(i)}} & b_0 & b_0 & \cdots & b_0 \\ b_0 & 1 & 0 & \cdots & 0 \\ b_0 & 0 & 1 & \cdots & 0 \\ \vdots & \vdots & \vdots & \ddots & \vdots \\ b_0 & 0 & 0 & \cdots & 1 \end{bmatrix} \begin{pmatrix} \ddot{R}_z \\ \ddot{q}_{00}^{(1)} \\ \ddot{q}_{00}^{(2)} \\ \vdots \\ \ddot{q}_{00}^{(N)} \end{pmatrix} + \begin{bmatrix} \frac{M}{I_1^{(i)}}\omega_z^2 & 0 & 0 & \cdots & 0 \\ 0 & \omega_{00}^2 & 0 & \cdots & 0 \\ 0 & 0 & \omega_{00}^2 & \cdots & 0 \\ \vdots & \vdots & \vdots & \ddots & \vdots \\ 0 & 0 & 0 & \cdots & \omega_{00}^2 \end{bmatrix} \begin{pmatrix} R_z \\ q_{00}^{(1)} \\ q_{00}^{(2)} \\ \vdots \\ q_{00}^{(N)} \end{pmatrix} = \mathbf{0} \quad (60)$$

where

$$\omega_z = \sqrt{\frac{k_{az} + k_{bz}}{M}}. \quad (61)$$

To determine free vibration modes, assume that $(R_z, q_{00}^{(1)}, q_{00}^{(2)}, \ldots, q_{00}^{(N)})^T = \mathbf{x}e^{j\omega t}$ and nontrivial solutions of (60) require

$$\begin{vmatrix} A_0 & B_0 & B_0 & \cdots & B_0 \\ B_0 & C_0 & 0 & \cdots & 0 \\ B_0 & 0 & C_0 & \cdots & 0 \\ \vdots & \vdots & \vdots & \ddots & \vdots \\ B_0 & 0 & 0 & \cdots & C_0 \end{vmatrix} = (A_0C_0 - NB_0^2)C_0^{N-1} = 0 \quad (62)$$

where

$$A_0 = \frac{M}{I_1^{(i)}}(\omega_z^2 - \omega^2) \quad (63)$$

$$B_0 = -b_0\omega^2 \quad (64)$$

$$C_0 = \omega_{00}^2 - \omega^2. \quad (65)$$

The frequencies of unbalanced modes satisfy $(A_0C_0 - NB_0^2) = 0$, resulting in

$$\omega^2 = \frac{\omega_{00}^2 + \omega_z^2 \pm \sqrt{(\omega_{00}^2 - \omega_z^2)^2 + 4\eta_2\omega_{00}^2\omega_z^2}}{2(1 - \eta_2)} \quad (66)$$

where

$$\eta_2 = \frac{Nb_0^2 I_1^{(i)}}{M}. \quad (67)$$

The mode shape of the unbalanced modes is

$$\left(-\frac{C_0}{B_0}, 1, \ldots, 1\right)^T \quad (68)$$

which shows that all disks undergo the same axisymmetric deformation resulting in an unbalanced inertia force that has to be compensated for by the axial motion of the disk/spindle assembly. Similarly, the frequencies of balanced modes satisfy $C_0 = 0$ resulting in $(N-1)$-fold frequencies

$$\omega = \omega_{00} \quad (69)$$

with corresponding mode shapes in (56).

As far as disk vibration modes with two or more nodal diameters, (41) implies that

$$\ddot{q}_{mn}^{(i)} + 2n\omega_3\dot{q}_{m,-n}^{(i)} + \{[\omega_{mn}^{(i)}]^2 - n^2\omega_3^2\}q_{mn}^{(i)} = 0, \quad (70)$$

which is the standard gyroscopic equation of motion encountered in rotating disk vibration and the vibration response is

$$q_{mn}^{(i)}(t) = A_1 \cos[(\omega_{mn}^{(i)} + n\omega_3)t + B_1] + A_2 \sin[(\omega_{mn}^{(i)} - n\omega_3)t + B_2] \quad (71)$$

and

$$q_{m,-n}^{(i)}(t) = A_1 \sin[(\omega_{mn}^{(i)} + n\omega_3)t + B_1] + A_2 \cos[(\omega_{mn}^{(i)} - n\omega_3)t + B_2], \quad (72)$$

where A_1, A_2, B_1, and B_2 are arbitrary constants. This result is identical to that found by Yang (1993) and Chen and Bogy (1993) for a single free tilting disk.

6 Response From a Ground-Based Observer

By substituting (5), (6), (12), and (13) into (1) and applying the coordinate transformation (4), the response of the ith disk from a ground-based observer is

$$\mathbf{R}_i^{(d)} = [R_x + r\cos\beta\cos\theta_y + (w_i + z_i)\sin\theta_y]\mathbf{I} + [R_y + r\cos\beta\sin\theta_x\sin\theta_y + r\sin\beta\cos\theta_x - (w_i + z_i)\sin\theta_x\cos\theta_y]\mathbf{J} + [R_z - r\cos\beta\cos\theta_x\sin\theta_y + r\sin\beta\sin\theta_x + (w_i + z_i)\cos\theta_x\cos\theta_y]\mathbf{K}. \quad (73)$$

Downloaded 04 May 2010 to 171.66.16.34. Redistribution subject to ASME license or copyright; see http://www.asme.org/terms/Terms_Use.cfm

For a point very close to the x-axis (i.e., $\beta \ll 1$) and a disk/spindle system undergoing small oscillations, (73) becomes

$$\mathbf{R}_i^{(d)} = (R_x + r + z_i\theta_y)\mathbf{I} + (R_y + r\beta - z_i\theta_x)\mathbf{J} + (R_z - r\theta_y + w_i + z_i)\mathbf{K} + O(2). \quad (74)$$

Therefore, for a ground-based observer located at $X_0\mathbf{I}$, the observer is looking at a point (r, β) such that

$$r = X_0 - R_x - z_i\theta_y, \quad \beta = \frac{1}{r}(z_i\theta_x - R_y). \quad (75)$$

Substitute (75) into (74) and neglect the second-order terms to obtain the transverse vibration seen by the ground-based observer

$$\mathbf{R}_i^{(d)} \approx X_0\mathbf{I} + (R_z - X_0\theta_y + w_i + z_i)\mathbf{K}. \quad (76)$$

7 An Example

In this section, the theoretical predictions developed above will be compared with the experimental results in Fig. 2. The experimental results were obtained through the setup in Fig. 1, which has been explained in detail in the Introduction section. Table 1 shows additional properties of the disk/spindle system. The bearing stiffnesses k_a, k_b, k_{az}, and k_{bz} are calculated based on the bearing model of Jones and McGrew (1978) assuming zero tolerance in the bearings. According to (76), the displacement measured in Fig. 2 is $(R_z - X_0\theta_y + w_i)\mathbf{K}$.

Balanced Modes. According to the theory developed above, (0,2) modes, balanced (0,1) modes, and balanced (0,0) mode can be predicted by the classical vibration analysis of rotating disks. In this paper, the sensitivity approach developed by Chen and Bogy (1992) is used to predict these classical vibration modes. After split by the rotational speed, the low frequency of (m, n) modes is given by the backward traveling wave

$$\omega_{mn}^{(l)} \approx \omega_{mn}^{(0)} - n\omega_3 + \frac{\omega_3^2 A_{mn}}{2\omega_{mn}^{(0)}} \quad (77)$$

and the high frequency of (m, n) modes is given by the forward traveling wave

$$\omega_{mn}^{(h)} \approx \omega_{mn}^{(0)} + n\omega_3 + \frac{\omega_3^2 A_{mn}}{2\omega_{mn}^{(0)}} \quad (78)$$

where $\omega_{mn}^{(0)}$ is the natural frequency of (m, n) modes when the disk is nonrotating and

$$A_{mn} = \frac{\int_a^b (C_1 + C_2 r^{-2} + C_3 r^2)[dR_{mn}^{(0)}/dr]^2 r dr + \int_a^b (C_1 - C_2 r^{-2} + C_4 r^2)[nR_{mn}^{(0)}/r]^2 r dr}{\int_a^b [R_{mn}^{(0)}(r)]^2 r dr} \quad (79)$$

with $R_{mn}^{(0)}(r)$ being the radial distribution of the mode shape when the disk is nonrotating. Also in (79), C_1 to C_4 are coefficients for axisymmetric membrane stresses from rotation; see (24) to (26).

A rigorous way to obtain $\omega_{mn}^{(0)}$ and $R_{mn}(r)$ is to go through the standard eigenvalue problem of a circular plate with fixed-free boundary conditions. This approach, however, becomes impractical for the current experimental setup, because the spacers holding the disks behave more like an elastic foundation instead of a fixed end. (The thickness ratio and clamping ratio of the spacers to the disk were about 1.79 and 0.116, respectively.) This makes theoretical predictions of $\omega_{mn}^{(0)}$ and $R_{mn}^{(0)}(r)$ from the standard eigenvalue problem very difficult, because the exact effective stiffness of the spacers is unknown. To demonstrate the effect of the spacers, the authors estimated $\omega_{mn}^{(0)}$ through a three-term Rayleigh-Ritz approximation assuming fixed-free boundary conditions. As a test for accuracy, the three-term approximation resulted in one percent error for a fixed-free circular plate with clamping ratio of 0.5 (Mote, 1970). When the three-term approximation was applied to the 4-platter disk drive, the calculated $\omega_{mn}^{(0)}$ were 40 Hz off the experimental measurements. Obviously, a more practical way is needed to replace the standard eigenvalue problem in estimating $\omega_{mn}^{(0)}$ and $R_{mn}(r)$.

Fortunately, the algorithm developed in this paper remains valid for disks supported by elastic foundations, as long as the corresponding natural frequencies and mode shapes are used. To facilitate theoretical predictions, two approximations were made. First, $\omega_{00}^{(0)}$, $\omega_{01}^{(0)}$, and $\omega_{02}^{(0)}$ were measured experimentally for the same stationary disk (without the bearing) from a separate experiment. The measured frequencies were $\omega_{00}^{(0)} = 632.5$ Hz, $\omega_{01}^{(0)} = 618.75$ Hz, and $\omega_{02}^{(0)} = 732.5$ Hz, and they were used subsequently in (77) and (78). Secondly, $R_{01}(r)$ and $R_{02}(r)$ in (79) are approximated by

$$R_{01}(r), R_{02}(r) \approx \sqrt{\frac{15(b^4 - a^4)}{2(b-a)^5(5b+a)}}(r-a)^2 \quad (80)$$

and $R_{00}(r)$ is approximated by

$$R_{00}(r) \approx \sqrt{\frac{15(b^4 - a^4)}{4(b-a)^5(5b+a)}}(r-a)^2. \quad (81)$$

Notice that $R_{01}(r)$ and $R_{02}(r)$ in (80) and $R_{00}(r)$ in (81) are chosen so that they satisfy the orthonormality condition (30).

Unbalanced Modes. According to the theoretical analysis presented in this paper, the natural frequencies of unbalanced (0,1) modes are predicted through (58). In the calculation, a_0 defined in (33) is approximated using $R_{01}(r)$ given by (80). In addition, ω_{01} is approximated by $(\omega_{01}^{(l)} + \omega_{01}^{(h)})/2$ from the sensitivity analysis. The natural frequency of the unbalanced (0,0) mode is predicted through (66). In the calculation, b_0 defined in (34) is approximated using $R_{00}(r)$ given by (81). In addition, ω_{00} is approximated by either $\omega_{00}^{(l)}$ or $\omega_{00}^{(h)}$ from the sensitivity analysis.

Comparison. Figure 7 shows the comparison of the theoretical predictions above (solid lines) and the experimental results (circles). The subscripts "U" and "B" represent the unbalanced and balanced modes, respectively. Notice that the unbalanced (0,1) and the balanced (0,0) modes cannot be predicted by existing analysis. Both the unbalanced (0,0) mode, balanced (0,1) modes, and (0,2) modes have very good agreement with experimental results. The balanced (0,0) mode, however, was not observed in the experiments. As far as unbalanced (0,1) modes, the predicted frequencies are about 20 Hz higher than those measured in the experiment. Because the frequency of the unbalanced (0,1) modes ranges from 400 to 600 Hz, the 20 Hz difference amounts to an error less than five percent. Possible causes leading to these discrepancies are discussed as follows.

Theoretically, the hammer will excite the balanced (0,0) mode. In reality, the presence of (0,0) mode resonance may or may not be noticeable depending on the disk geometry. For example, (0,0) mode resonance appears as a tiny and almost

Downloaded 04 May 2010 to 171.66.16.34. Redistribution subject to ASME license or copyright; see http://www.asme.org/terms/Terms_Use.cfm

Table 1 Properties of the disk/spindle system used in experiments and numerical simulations. The bearing stiffnesses k_a, k_b, k_{az}, and k_{bz} are calculated based on the bearing model of Jones and McGrew (1978) assuming zero tolerance in the bearings.

Disk				Shaft		Bearings	
b	47.50 mm	z_1	- 3.712 mm	I_1^s	3.941 kg-mm^2	k_a, k_b	2.021×10^4 N/mm
a	16.51 mm	z_2	- 0.9747 mm	I_3^s	4.739 kg-mm^2	k_{az}, k_{bz}	8.666×10^3 N/mm
$I_1^{(i)}$	8.827 kg-mm^2	z_3	1.762 mm	m_s	3.189×10^{-2} kg	z_a	- 8.077 mm
$I_3^{(i)}$	17.65 kg-mm^2	z_4	4.601 mm			z_b	5.131 mm
m	1.371×10^{-2} kg						

unnoticeable bump in the spectrum shown in Figs. 5 to 7 of Yu and Mote (1987). To make sure that the disks in the current experiment also present an unnoticeable (0,0) mode resonance, the authors did conduct several experiments employing disks with a thick wide flange at the outer rim. In those experiments, the authors observed a significant (0,0) mode resonance, because the large inertia force associated with the flange makes (0,0) mode resonance more noticeable. By reducing the size of the flange, the authors were able to conclude that the (0,0) mode resonance was weak and unnoticeable for the disks in the current experiment.

The exact causes of the 20 Hz error of unbalanced (0,1) modes remain open, but the discrepancy may result from several sources. First of all, estimating exact bearing stiffnesses such as those in Table 1 is not trivial. Different bearing models predict different bearing stiffnesses; see Fig. 2 of the paper by Kraus et al. (1987). Unfortunately, the frequencies of unbalanced (0,1) modes depend substantially on the bearing stiffness and the bearing span. Secondly, the bearing stiffnesses listed in Table 1 was based on the assumption of zero tolerance of the bearings. In reality, the bearings will have tolerances in the preload, inner and outer race curvatures, radial internal clearance, and so on. Therefore, the range of exact bearing stiffnesses becomes extremely difficult to estimate accurately given the many sources of possible tolerances. Thirdly, the bearing span is so short (13.22 mm) that modeling the bearings as springs perpendicular to the spindle may no longer be adequate. For example, maybe the bearings should be modeled as elastic foundations. Maybe the bearings should be modeled as springs along the contact angles of the bearings. Also, estimating a_0 by $R_{mn}(r)$ in (80) could be a very rough approximation. Notice that the exact form of $R_{mn}(r)$ cannot be determined or approximated accurately, because the exact boundary condition at the inner rim is unknown. Finally, only (0,1) modes are retained in deriving (58). Maybe (1,1) modes should also be retained to improve the accuracy. Given that there are many possible sources contributing to the 20 Hz difference, the authors consider the theoretical predictions with less than five percent error as reasonable preliminary results.

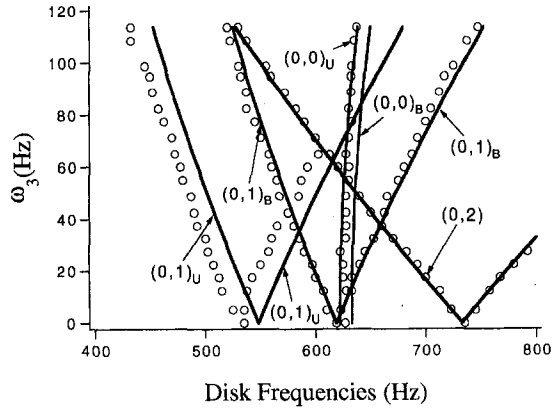


Fig. 7 Comparison of the theoretical predictions and experimental measurements. $(0,1)_U$ and $(0,0)_U$ cannot be predicted by existing analysis.

8 Conclusions

1 Lateral translation of the spindle, rigid-body rotation (or rocking) of the spindle, and one-nodal diameter modes of each disk are coupled together. When all the disks (say N disks) are identical, the coupled disk/spindle vibration splits into $N - 1$ groups of "balanced modes" and a group of "unbalanced modes." For each group of the balanced modes, two adjacent disks vibrate entirely out of phase, while other disks undergo no deformation. The natural frequencies of the balanced modes are identical to that of the one-nodal-diameter modes of each disk. In addition, each group of the balanced modes consist of two modes, i.e., the forward and backward traveling waves. For the group of the unbalanced modes, all disks undergo the same out-of-plane vibration resulting in a steady precession of the rigid spindle. The frequencies of the unbalanced modes are significantly lower than those of one-nodal-diameter modes of each disk.

2 Axial translation of the spindle and the axisymmetric modes of each disks are coupled together. The coupled motion also splits into $N - 1$ groups of "balanced modes" and one group of "unbalanced modes." The frequencies of the balanced and unbalanced modes are identical to and smaller than those of the axisymmetric modes of each disk.

3 The rigid-body motion of the spindle does not affect disk vibration modes with two or more nodal diameters. Response of those modes can be determined through the classical vibration analysis of rotating disks. This result is identical to that found earlier by Yang (1993) and Chen and Bogy (1993) for a single disk.

4 Experimental results and theoretical predictions agree very well for all vibration modes, except that unbalanced (0,1) modes have 20 Hz difference (<5 percent error). The theory and the experiment confirm the existence of balanced and unbalanced modes.

Acknowledgment

This paper is based on the work supported by Conner Peripherals through a research grant to the University of Washington. The first author also thanks the National Science Foundation for supporting this research through the grant CMS-9634557. Both authors thank the reviewers for their invaluable comments and suggestions.

References

Chen, J.-S., and Bogy, D. B., 1992, "Effects of Load Parameters on the Natural Frequencies and Stability of a Flexible Spinning Disk with a Stationary Load System," ASME JOURNAL OF APPLIED MECHANICS, Vol. 59, pp. S230–S235.

Chen, J.-S., and Bogy, D. B., 1993, "Natural Frequencies and Stability of a Flexible Spinning Disk-Stationary Load System with Rigid-Body Tilting," ASME JOURNAL OF APPLIED MECHANICS, Vol. 60, pp. 470–477.

Chivens, D. R., and Nelson, H. D., 1975, "The Natural Frequencies and Critical Speeds of a Rotating, Flexible Shaft-Disk System," ASME *Journal of Engineering for Industry*, pp. 881–886.

Downloaded 04 May 2010 to 171.66.16.34. Redistribution subject to ASME license or copyright; see http://www.asme.org/terms/Terms_Use.cfm

Dopkin, J. A., and Shoup, T. E., 1974, "Rotor Resonant Speed Reduction Caused by Flexibility of Disks," ASME *Journal of Engineering for Industry,* pp. 1328–1333.

Flowers, G. T., 1996, "Modelling of an Elastic Disk with Finite Hub Motions and Small Elastic Vibrations with Application to Rotordynamics," ASME *Journal of Vibration and Acoustics,* Vol. 118, pp. 10–15.

Flowers, G. T., and Ryan, S. G., 1993, "Development of a Set of Equations for Incorporating Disk Flexibility Effects in Rotordynamic Analyses," ASME *Journal of Engineering for Gas Turbines and Power,* Vol. 115, pp. 227–233.

Frees, Gregory M., 1995, "Disk Drive Spindle Dynamics—Analysis and Measurement," ASME *Advanced Information Storage Systems,* Vol. 6, pp. 237–261.

Iwan, W. D., and Moeller, T. L., 1976, "The Stability of a Spinning Elastic Disk with a Transverse Load System," ASME JOURNAL OF APPLIED MECHANICS, Vol. 43, pp. 485–490.

Jones, A. B., and McGrew, J. M., Jr., 1978, "Rotor-Bearing Dynamics Technology Design Guide—Part II: Ball Bearing," Wright Patterson Air Force Aero Propulsion Lab., WPAFB, OH, Report No. AFAPL-TR-78-6.

Kraus, J., Blech, J. J., and Braun, S. G., 1987, "In Situ Determination of Rolling Bearing Stiffness and Damping by Modal Analysis," ASME *Journal of Vibration, Acoustics, Stress, and Reliability in Design,* Vol. 109, pp. 235–240.

Ku, C.-P. Roger, and Shen, I. Y., 1996, "Effect of Disk Flexibility on Natural Frequencies of a Multiple-Disk Spindle Motor in Data Storage Information Systems," STLE *Tribology Transactions,* Vol. 39, No. 3, pp. 579–586.

Lamb, H., and Southwell, R. V., 1921, "The Vibration of a Spinning Elastic Disk," *Proceedings of the Royal Society,* Vol. 99, pp. 272–280.

Low, M., and Shen, I. Y., 1996, "Experimental Modal Analysis of a Hard Disk Drive Spindle Carrying Multiple Disks," *The Six International Symposium on Transport Phenomena and Dynamics of Rotating Machinery,* Vol. 1, pp. 187–194.

Mote, C. D., Jr., 1970, "Stability of Circular Plates Subjected to Moving Loads," *Journal of the Franklin Institute,* Vol. 290, No. 4, pp. 329–344.

Mote, C. D., Jr., 1976, "Moving-load Stability of a Circular Plate on a Floating Central Collar," *Journal of the Acoustical Society of America,* Vol. 61, pp. 439–447.

Orgun, C. O., and Tongue, B. H., 1994a, "Mode Localization in Coupled Circular Plates," ASME *Journal of Vibration and Acoustics,* Vol. 116, pp. 286–294.

Orgun, C. O., and Tongue, B. H., 1994b, "On Localization in Coupled, Spinning, Circular Plates," ASME *Journal of Vibration and Acoustics,* Vol. 116, pp. 555–561.

Shen, I. Y., and Ku, C.-P. Roger, 1995, "On the Rocking Motion of a Rotating Flexible-Disk/Rigid-Shaft Systems," *Advances in Information Storage and Processing Systems,* ASME, ISPS-Vol. 1, pp. 271–282.

Wu, F., and Flowers, G. T., 1992, "A Transfer Matrix Technique for Evaluating the Natural Frequencies and Critical Speeds of a Rotor with Multiple Flexible Disks," ASME *Journal of Vibration and Acoustics,* Vol. 114, pp. 242–248.

Yang, S. M., 1993, "Vibration of a Spinning Annular Disk With Coupled Rigid-Body Motion," ASME *Journal of Vibration and Acoustics,* Vol. 115, pp. 159–164.

Yu, R. C., and Mote, C. D., Jr., 1987, "Vibration and Parametric Excitation in Asymmetric Circular Plates Under Moving Loads," *Journal of Sound and Vibration,* Vol. 119, No. 3, pp. 409–427.

Downloaded 04 May 2010 to 171.66.16.34. Redistribution subject to ASME license or copyright; see http://www.asme.org/terms/Terms_Use.cfm

Slaving the In-Plane Motions of a Nonlinear Plate to Its Flexural Motions: An Invariant Manifold Approach

I. T. Georgiou
Assoc. Mem. ASME

I. B. Schwartz

Special Project for Nonlinear Science,
Code 6700.3,
Naval Research Laboratory,
Washington, DC 20375

We show that the in-plane motions of a nonlinear isotropic plate can be decoupled from its transverse motions. We demonstrate this decoupling by showing analytically and numerically the existence of a global nonlinear invariant manifold in the phase space of three nonlinearly coupled fundamental oscillators describing the amplitudes of the coupled fundamental modes. The invariant manifold carries a continuum of slow periodic motions. In particular, for any motion on the slow invariant manifold, the transverse oscillator executes a periodic motion and it slaves the in-plane oscillators into periodic motions of half its period. Furthermore, as the energy level of a motion on the slow manifold increases, the frequency of the largest harmonic of the in-plane motion approaches the in-plane natural frequencies.

1 Introduction

Large transverse motions of an elastic plate are coupled nonlinearly to the in-plane motions, the nonlinearity stemming from the stretching of the middle plane (Chu and Herrmann, 1956; Bolotin, 1964). It is customary to uncouple these motions by neglecting the in-plane inertia forces in comparison to the in-plane resultant stresses (Chu and Herrmann, 1956; Bolotin, 1964; Yang and Sethna, 1991). This assumption reduces the in-plane equations of motion to static partial differential equations. Thus, it is degenerate since the dynamics of the in-plane motions are neglected: *all motions evolving in a time scale set by the in-plane fundamental frequencies are completely ignored.* The following questions rise naturally: Under what conditions is this degenerate decoupling a good approximation to the coupled motions of the plate? It is usually assumed that it is valid for motions in a sufficiently small neighborhood of the equilibrium state of the plate. How do the transverse motions interact with the in-plane motions outside this small neighborhood of decoupling? How does the size of this neighborhood change as the aspect ratio, and the thickness of the plate change?

To address the above questions, we analyze the dynamic von Karman equations in terms of two dimensionless parameters: the aspect ratio of the plate, and the square root of the ratio of thickness to one of the dimensions of the plate. Using the Galerkin projection method, we approximate the scaled nonlinear dynamic von Karman equations with three nonlinearly coupled fundamental oscillators. One of the oscillators describes the amplitude dynamics of the transverse fundamental vibration mode, while the other two oscillators describe the amplitude dynamics of the two in-plane fundamental vibration modes. We transform the amplitude equations for the fundamental oscillators into a set of singularly perturbed first-order differential equations, and thus analyze their dynamics from the point of view of invariant manifolds of motion. The singular perturbation technique combined with the theory of invariant manifolds of motion (Fenichel, 1979; Knobloch and Aullback, 1984) constitutes a useful way to analyze globally the dynamics of mechanical and structural dynamical systems (Georgiou, 1993; Georgiou et al., 1994; Georgiou and Schwartz, 1996).

2 Coupled Fundamental Oscillations of a Nonlinear Isotropic Plate

Consider a rectangular isotropic plate of thickness h and edge lengths a and b. We refer the plate to a Cartesian coordinate system $Oxyz$, with Oxy in the middle plane of the plate and the origin at a corner of the plate. The motion of the plate can be approximated by von Karman-type equations such as the following (Chu and Herrmann, 1956):

$$\frac{h^2}{12}(w_{xxxx} + 2w_{xxyy} + w_{yyyy}) - u_x w_{xx} - \frac{1}{2}w_x^2 w_{xx} - \nu\left(v_y w_{xx} + \frac{1}{2}w_x^2 w_{xx}\right) - v_y w_{yy} - \frac{1}{2}w_y^2 w_{yy} - \nu\left(u_x w_{yy} + \frac{1}{2}w_x^2 w_{yy}\right) - (1-\nu) \times (u_y w_{xy} + v_x w_{xy} + w_x w_y w_{xy}) = \frac{1}{c_p^2}(\ddot{u}w_x + \ddot{v}w_y - \ddot{w})$$

$$u_{xx} + w_x w_{xx} + \nu(v_{xy} + w_y w_{xy}) + \frac{1-\nu}{2}(u_{yy} + v_{xy} + w_y w_{xy} + w_x w_{yy}) = \frac{1}{c_p^2}\ddot{u},$$

$$v_{xx} + w_y w_{yy} + \nu(u_{xy} + w_x w_{xy}) + \frac{1-\nu}{2}(v_{xx} + u_{xy} + w_x w_{xy} + w_y w_{xx}) = \frac{1}{c_p^2}\ddot{v} \quad (1)$$

where u and v are the displacements of a particle in the middle plane of the plate in the x and y directions, respectively, w is the displacement of the particle normal to the mid-plane, ν is the Poisson ratio, $c_p = \{E/[\rho(1-\nu^2)]\}^{1/2}$, where E and ρ are, respectively, Young's modulus and the density of the plate

Contributed by the Applied Mechanics Division of THE AMERICAN SOCIETY OF MECHANICAL ENGINEERS for publication in the ASME JOURNAL OF APPLIED MECHANICS.

Discussion on this paper should be addressed to the Technical Editor, Professor Lewis T. Wheeler, Department of Mechanical Engineering, University of Houston, Houston, TX 77204-4792, and will be accepted until four months after final publication of the paper itself in the ASME JOURNAL OF APPLIED MECHANICS.

Manuscript received by the ASME Applied Mechanics Division, June 8, 1995; final revision, June 28, 1996. Associate Technical Editor: M. Shinozuka.

Copyright © 1997 by ASME

Downloaded 04 May 2010 to 171.66.16.34. Redistribution subject to ASME license or copyright; see http://www.asme.org/terms/Terms_Use.cfm

material. Dots indicate differentiation with respect to time t_1 and the subscripts x and y denote spatial derivatives.

Equations (1) describe moderately large vibrations (of magnitude in the order of the thickness) of the plate, neglecting the effects of rotatory inertia, transverse shearing, and nonlinear curvatures. The nonlinear coupling stems from finite stretching of the middle plane.

To nondimensionalize the equations of motion, introduce geometric parameters,

$$\epsilon = \frac{h}{a}, \quad \lambda = \frac{a}{b}, \tag{2}$$

the independent variables,

$$\xi = \frac{x}{a}, \quad \eta = \frac{y}{b}, \quad t = \frac{\epsilon}{\sqrt{12}} \frac{c_p}{a} t_1, \tag{3}$$

and the dependent variables,

$$\hat{U} = \frac{u}{a}, \quad \hat{V} = \frac{v}{a}, \quad \hat{W} = \frac{w}{\epsilon a}. \tag{4}$$

The nondimensional equations of motion can been written as follows:

$$\frac{\epsilon^2}{12}[\hat{W}_{\xi\xi\xi\xi} + 2\lambda^2\hat{W}_{\xi\xi\eta\eta} + \lambda^4\hat{W}_{\eta\eta\eta\eta}] = [\hat{U}_\xi\hat{W}_{\xi\xi} + \tfrac{1}{2}\epsilon^2\hat{W}_\xi^2\hat{W}_{\xi\xi}]$$
$$+ \nu[\lambda\hat{V}_\eta\hat{W}_{\xi\xi} + \tfrac{1}{2}\epsilon^2\lambda^2\hat{W}_\eta\hat{W}_{\xi\xi}] + [\lambda^3\hat{V}_\eta\hat{W}_{\eta\eta} + \tfrac{1}{2}\epsilon^2\lambda^4\hat{W}_\eta^2\hat{W}_{\eta\eta}]$$
$$+ \nu[\hat{U}_\xi\hat{W}_{\xi\xi} + \tfrac{1}{2}\epsilon^2\lambda^2\hat{W}_\xi^2\hat{W}_{\eta\eta}]$$
$$+ (1-\nu)[\lambda^2\hat{U}_\eta\hat{W}_{\xi\eta} + \lambda\hat{V}_\xi\hat{W}_{\xi\eta} + \epsilon^2\lambda^2\hat{W}_\xi\hat{W}_\eta\hat{W}_{\xi\eta}]$$
$$+ \frac{\epsilon^2}{12}[\hat{U}''\hat{W}_\xi + \lambda\hat{V}''\hat{W}_\eta - \hat{W}''],$$

$$\hat{U}_{\xi\xi} + \epsilon^2\hat{W}_\xi\hat{W}_{\xi\xi} + \nu[\lambda\hat{V}_{\xi\eta} + \epsilon^2\lambda^2\hat{W}_\eta\hat{W}_{\eta\xi}] + \frac{1-\nu}{2}$$
$$\times [\lambda^2\hat{U}_{\eta\eta} + \lambda\hat{V}_{\eta\xi} + \epsilon^2\lambda^2\hat{W}_\eta\hat{W}_{\eta\xi} + \epsilon^2\lambda^2\hat{W}_\xi\hat{W}_{\eta\eta}] = \frac{\epsilon^2}{12}\hat{U}'',$$

$$\lambda^2\hat{V}_{\eta\eta} + \epsilon^2\lambda^3\hat{W}_\eta\hat{W}_{\eta\eta} + \nu[\lambda\hat{U}_{\xi\eta} + \epsilon^2\lambda\hat{W}_\xi\hat{W}_{\eta\xi}] + \frac{1-\nu}{2}$$
$$\times [\hat{V}_{\xi\xi} + \lambda\hat{U}_{\eta\xi} + \epsilon^2\lambda\hat{W}_\xi\hat{W}_{\eta\xi} + \epsilon^2\lambda\hat{W}_\eta\hat{W}_{\xi\xi}] = \frac{\epsilon^2}{12}\hat{V}'' \tag{5}$$

where $(')$ denotes differentiation with respect to time t. We are interested in the nonlinear free vibrations of a plate with all its edges hinged. All boundary conditions are satisfied if we assume the following spectral representation for the displacements:

$$\hat{W}(\xi, \eta, t) = \sum W_{mn}(t)\phi_{mn}^{(1)}(\xi, \eta),$$
$$\hat{U}(\xi, \eta, t) = \sum U_{mn}(t)\phi_{mn}^{(2)}(\xi, \eta),$$
$$\hat{V}(\xi, \eta, t) = \sum V_{mn}(t)\phi_{mn}^{(3)}(\xi, \eta), \quad m, n = 1, \ldots, \infty \tag{6}$$

where

$$\phi_{mn}^{(1)}(\xi, \eta) = \sin(m\pi\xi)\sin(n\pi\eta),$$
$$\phi_{mn}^{(2)}(\xi, \eta) = \sin(2m\pi\xi)\sin(m\pi\eta),$$
$$\phi_{mn}^{(3)}(\xi, \eta) = \sin(m\pi\xi)\sin(2n\pi\eta), \quad m, n = 1, \ldots, \infty \tag{7}$$

are the spatial modes of the linearized equations. To explore the nature of the interaction between the in-plane motions and the transverse motions, we retain only the fundamental mode of vibration in each of the displacements components, Eq. (6). In particular, let W, U, V denote the amplitudes of the fundamental modes $\phi_{11}^{(1)}$, $\phi_{11}^{(2)}$, $\phi_{11}^{(3)}$. First substituting the expressions for the fundamental modes into the equations of motion, then projecting them onto the independent linear spaces spanned by the modes $\phi_{11}^{(1)}$, $\phi_{11}^{(2)}$, $\phi_{11}^{(3)}$, we obtain three coupled fundamental oscillators whose uncoupled natural frequencies are given, respectively, by

$$\omega_W^2 = \pi^4(1+\lambda^2)^2, \quad \omega_U^2 = \frac{6\pi^2(8+\lambda^2(1-\nu))}{\epsilon^2},$$
$$\omega_V^2 = \frac{6\pi^2(1-\nu+8\lambda^2)}{\epsilon^2}. \tag{8}$$

Now the amplitude equations for the three coupled fundamental oscillators, in the dimensionless time scale $\tau = \omega_W t$, are

$$\ddot{W} = -W - \frac{\hat{N}_3}{\epsilon^2}UW - \frac{\hat{N}_4}{\epsilon^2}VW - \hat{N}_5W_1^3,$$
$$\ddot{U} = -\frac{\hat{A}_{11}}{\epsilon^2}U - \frac{\hat{A}_{12}}{\epsilon^2}V - \hat{N}_1W_1^2,$$
$$\ddot{V} = -\frac{\hat{A}_{21}}{\epsilon^2}U - \frac{\hat{A}_{22}}{\epsilon^2}V - \hat{N}_2W_1^2. \tag{9}$$

The coefficients $\hat{A}_{ij}$, $i, j = 1, 2$, and $\hat{N}_n$, $n = 1, 2, 3, 4, 5$, are positive functions of the variable (λ, ν); they are given in the Appendix. The corresponding normalized uncoupled linear frequencies are $\hat{\omega}_W^2 = 1$, $\hat{\omega}_U^2 = \hat{A}_{11}/\epsilon^2$, $\hat{\omega}_V^2 = \hat{A}_{22}/\epsilon^2$. We call the first oscillator in Eq. (9) the transverse oscillator. Note the second and third oscillators are coupled nonlinearly to the transverse oscillator. We call them the x-in-plane and the y-in-plane oscillators, respectively.

3 Singular Perturbation Analysis

We analyze the dynamics of a thin plate (the three coupled fundamental oscillators) using the methodology of singular perturbations and invariant manifolds of motion. For a thin plate, the parameter ϵ, the normalized thickness, is small. The singular perturbation-invariant manifold approach is a natural choice since Eq. (8) shows that the in-plane fundamental frequencies $\hat{\omega}_U$ and $\hat{\omega}_V$ are larger than the transverse fundamental frequency $\hat{\omega}_W$, normalized to 1, for small ϵ. Towards this end, we define the following frequency ratios:

$$\mu \equiv \frac{1}{\hat{\omega}_U} = \frac{\epsilon}{\sqrt{\hat{A}_{11}}} = \frac{\sqrt{6}\pi\epsilon(\lambda^2+1)}{6\sqrt{\lambda^2+8-\lambda^2\nu}},$$
$$\kappa \equiv \frac{\hat{\omega}_U}{\hat{\omega}_V} = \sqrt{\frac{\hat{A}_{11}}{\hat{A}_{22}}} = \frac{\sqrt{\lambda^2+8-\lambda^2\nu}}{\sqrt{1+8\lambda^2-\nu}}. \tag{10}$$

The following linear transformation

$$W = W_1, \quad \dot{W} = W_2,$$
$$U = \mu^2U_1, \quad \dot{U} = \mu U_2,$$
$$V = \mu^2\kappa^2V_1, \quad \dot{V} = \mu\kappa V_2 \tag{11}$$

transforms the second-order Eqs. (9) into the following set of singularly perturbed first-order equations:

$$\dot{W}_1 = W_2,$$
$$\dot{W}_2 = -W_1 - N_3U_1W_1 - N_4V_1W_1 - N_5W_1^3,$$
$$\mu\dot{U}_1 = U_2,$$
$$\mu\dot{U}_2 = -U_1 - A_{12}V_1 - N_1W_1^2,$$
$$\mu\kappa\dot{V}_1 = V_2,$$
$$\mu\kappa\dot{V}_2 = -A_{21}U_1 - V_1 - N_2W_1^2 \tag{12}$$

Downloaded 04 May 2010 to 171.66.16.34. Redistribution subject to ASME license or copyright; see http://www.asme.org/terms/Terms_Use.cfm

where

$$N_1 = \hat{N}_1, \quad N_2 = \hat{N}_2, \quad N_3 = \frac{\hat{N}_3}{\hat{A}_{11}}, \quad N_4 = \frac{\hat{N}_4}{\hat{A}_{22}}, \quad N_5 = \hat{N}_5,$$

$$A_{12} = \frac{\hat{A}_{12}}{\hat{A}_{22}}, \quad A_{21} = \frac{\hat{A}_{21}}{\hat{A}_{11}}. \tag{13}$$

The singular parameter μ, which is of order ϵ, measures the strength of coupling between the transverse oscillator and the in-plane oscillators. It turns out that for relatively thick plates the singular parameter μ is relatively small since Eq. (10) shows that $\mu/\epsilon < 1$ for $0 < \lambda \leq 1$ and admissible ν. The parameter κ measures the strength of coupling between the x-in-plane oscillator and the y-in-plane oscillator. Note that by definition $0 < \kappa \leq 1$ for $0 < \lambda \leq 1$ and admissible ν.

4 Slow Invariant Manifold of Motion

A generic motion of the three coupled oscillators, Eq. (12), will consist of slow (low-frequency) and fast (high-frequency) components whenever μ is small. We seek a nonlinear, two-dimensional, invariant manifold carrying only slow motions. In other words, the slow invariant manifold is an equilibrium manifold for fast motions. For convenience, we rewrite Eq. (12) in the following compact form:

$$\dot{W} = \mathbf{A}W + \mathbf{B}_1(Z)W + \mathbf{B}_2(W),$$
$$\mu\dot{Z} = \mathbf{C}Z + \mathbf{F}(W) \tag{14}$$

where

$$W = (W_1, W_2), \quad Z = (U_1, U_2, V_1, V_2), \tag{15}$$

and

$$\mathbf{A} = \begin{bmatrix} 0 & 1 \\ -1 & 0 \end{bmatrix}, \quad \mathbf{C} = \begin{bmatrix} 0 & 1 & 0 & 0 \\ -1 & 0 & -A_{12} & 0 \\ 0 & 0 & 0 & 1/\kappa \\ -A_{21}/\kappa & 0 & -1/\kappa & 0 \end{bmatrix}. \tag{16}$$

$$\mathbf{B}_1(Z) = \begin{bmatrix} 0 & 0 \\ -N_3Z_1 - N_4Z_3 & 0 \end{bmatrix},$$

$$\mathbf{F}(W) = \begin{bmatrix} 0 \\ -N_1W_1^3 \\ 0 \\ -N_2/\kappa W_1^3 \end{bmatrix}, \quad \mathbf{B}_2 = \begin{bmatrix} 0 \\ -N_5W_1^3 \end{bmatrix}. \tag{17}$$

Vector-valued functions of the independent variables W, U, V are denoted by boldface letters. Linearizing Eq. (14) about the center equilibrium state $(W, Z) = (0, 0)$ reveals that the linearized transverse motions are decoupled from the in-plane linearized motions. Figure 1 shows the dependence of $\epsilon\omega_U$ and $\epsilon\omega_V$ on the aspect ratio λ. Note that, for a square plate, the in-plane frequencies become of the same order.

Now the nonlinearities in Eq. (14) and their first-order derivatives vanish at the origin. Furthermore, the eigenvalues of the matrix C/μ are not integer multiples, for admissible (λ, ν), of the eigenvalues of the matrix A, being $\pm i$. Then Lyapunov's Center Manifold Theorem (Kelly, 1967; Schmidt, 1978) guarantees the existence of a locally unique, two-dimensional, center invariant manifold. This local manifold consists of one-parameter ($E \geq 0$, E denotes total energy) periodic motions, and as $E \to 0$ the corresponding orbit goes to the origin, its period going to 2π.

We assume that, for small μ, there exists a global, nonlinear two-dimensional, invariant manifold $\mathcal{W}_\mu$ described by the graph of the vector-valued function

$$Z = \mathbf{H}_\mu(W). \tag{18}$$

The property of invariance is equivalent to requiring that the equation of motion for the two in-plane oscillators becomes an indentity for all motions on the invariant manifold $\mathcal{W}_\mu$, i.e.,

$$\mathbf{C}\mathbf{H}_\mu(W) + \mathbf{F}(W) - \mu\dot{\mathbf{H}}_\mu(W) = 0. \tag{19}$$

In view of the first equation in (14), Eq. (19) becomes

$$\mathbf{C}\mathbf{H}_\mu(W) + \mathbf{F}(W) - \mu D_W\mathbf{H}_\mu(W)[\mathbf{A}W + \mathbf{B}_2(W)]$$
$$- \mu D_W\mathbf{H}_\mu(W)\mathbf{B}_1\mathbf{H}_\mu(W)W = 0, \tag{20}$$

where D_W denotes the first-order derivative of $\mathbf{H}_\mu$ with respect to the variable W. Equation (20), called the *slow manifold condition,* is a nonlinear partial differential equation. It could have multiple solutions $\mathbf{H}_\mu$. However, only a unique solution (nonresonance case) passes through the origin. We now assume a series representation for $\mathbf{H}_\mu$:

$$\mathbf{H}_\mu(W) = \mathbf{H}_0(W) + \sum_{m=1}^{\infty} \mu^m\mathbf{H}_m(W). \tag{21}$$

Substituting Eq. (21) into Eq. (20) yields the following recursive relations for $\mathbf{H}_j$:

$$\mathbf{C}\mathbf{H}_0(W) = -F(W), \tag{22}$$

$$\mathbf{C}\mathbf{H}_1(W) = D_W\mathbf{H}_0(W)[\mathbf{A}W + \mathbf{B}_2(W)]$$
$$+ D_W\mathbf{H}_0(W)\mathbf{B}_1\mathbf{H}_0W, \tag{23}$$

$$\mathbf{C}\mathbf{H}_{m+1}(W) = D_W\mathbf{H}_m(W)[\mathbf{A}W + \mathbf{B}_2(W)]$$
$$+ \sum_{0\leq i\leq m} D_W\mathbf{H}_i(W)\mathbf{B}_1\mathbf{H}_{m-i}(W)W, \quad m = 1, 2, \ldots. \tag{24}$$

It should be clear that the graph of $\mathbf{H}_0$ describes the exact slow invariant manifold $\mathcal{W}_0$ of system (14) (equivalently system (12)) at $\mu = 0$. Since this manifold is global, it is logical to assume the existence, under certain conditions, of a global invariant manifold for sufficiently small μ.

For the particular problem we study, the function $\mathbf{H}_\mu$ has four components. The components $H_{1\mu}$ and $H_{3\mu}$ give the positions of the in-plane oscillators whenever the motion is on the slow manifold. Therefore, we call the components $\mathcal{W}_{1\mu}$ and $\mathcal{W}_{3\mu}$ of the slow manifold $\mathcal{W}_\mu$ *configuration* manifolds. Similarly, we call $\mathcal{W}_{2\mu}$ and $\mathcal{W}_{4\mu}$ the *momentum* manifolds since $H_{2\mu}$ and $H_{4\mu}$ give the velocities of the in-plane oscillators.

The recursive relations, up to $O(\mu^8)$, where solved using the symbolic algebra computer package MAPLE V. Here we give $\mathbf{H}_j$, $(j = 0, 1, 2, 3)$, where H_{kj}, $(k = 1, 2, 3, 4)$, denotes the kth component of $\mathbf{H}_j$.

Zeroth-Order Approximation Term $\mathbf{H}_0$:

$$H_{10}(W) = -C_{101}W_1^2, \quad H_{20}(W) = 0,$$
$$H_{30}(W) = -C_{301}W_1^2, \quad H_{40}(W) = 0. \tag{25}$$

First-Order Correction Term $\mathbf{H}_1$:

$$H_{11}(W) = 0, \quad H_{21}(W) = -2C_{101}W_1W_2,$$
$$H_{31}(W) = 0, \quad H_{41}(W) = -2\kappa C_{301}W_1W_2. \tag{26}$$

Second-Order Correction Term $\mathbf{H}_2$:

$$H_{12}(W) = -C_{121}W_1^2 + C_{121}W_2^2 - C_{123}W_1^4, \quad H_{22}(W) = 0,$$
$$H_{32}(W) = -C_{321}W_1^2 + C_{321}W_2^2 - C_{323}W_1^4,$$
$$H_{42}(W) = 0. \tag{27}$$

Third-Order Correction Term $\mathbf{H}_3$:

$$H_{13}(W) = 0, \quad H_{23}(W) = -C_{231}W_1W_2 - C_{232}W_1^3W_2,$$
$$H_{33}(W) = 0, \quad H_{43}(W) = -C_{431}W_1W_2 - C_{432}W_1^3W_2. \tag{28}$$

Downloaded 04 May 2010 to 171.66.16.34. Redistribution subject to ASME license or copyright; see http://www.asme.org/terms/Terms_Use.cfm

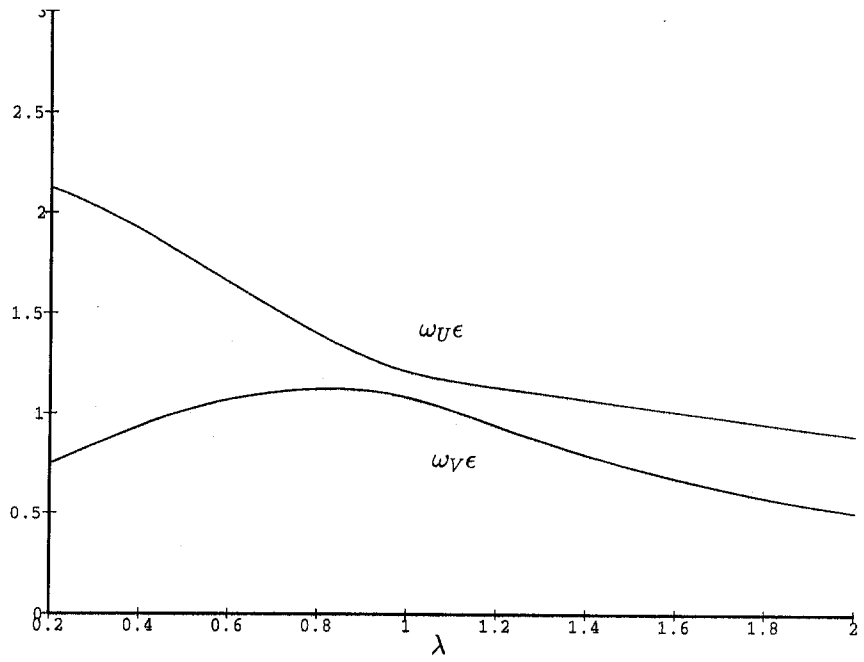


Fig. 1 Behavior of the in-plane coupled natural frequencies, $\nu = 0.318$

The coefficients in the above expressions are positive functions of (λ, ν); they are given in the Appendix.

The approximate solution reveals the following properties for the components of each $\mathbf{H}_j$:

$$H_{2m} = H_{4m} = 0, \quad \text{for} \quad m = 0, \quad \text{even},$$
$$H_{1m} = H_{3m} = 0, \quad \text{for} \quad m = 1, \quad \text{odd}. \qquad (29)$$

Equation (25) and Eq. (26) in connection with Eq. (11) indicate that both the displacements and velocities of the in-plane oscillators are of $O(\mu^2)$ for any motion on $\mathcal{W}_\mu$. Equation (27) indicates that the displacements of the in-plane oscillators do not vanish whenever the displacement of the transverse oscillator vanishes. This is a nonlinear phenomenon without a counterpart in linear oscillatory systems. Furthermore, note that $\mathbf{H}_j$ maps periodic functions of t of period T onto periodic functions of period $T/2$. *Therefore, for all motions on the slow invariant manifold, the in-plane oscillations have period exactly half of the period of the transverse oscillations.* Georgiou and Schwartz (1996) have shown that the above conclusion holds true for the oscillatory motions on the slow invariant manifold of a pendulum-oscillator system.

The approximate solution reveals the following symmetry property for $\mathbf{H}_j$:

$$\mathbf{H}_j(-W_1, -W_2) = \mathbf{H}_j(W_1, W_2), \quad j = 0, 1, \ldots, \infty. \qquad (30)$$

The point reflective symmetry (30) reveals that the slow flow, the restriction of the vector field of Eq. (12) on $\mathcal{W}_\mu$, does not possess a reflexive symmetry about the origin. In other words, if a point (W, Z) belongs to the slow manifold $\mathcal{W}_\mu$, the point $(-W, -Z)$ does not belong to it.

We identify the nth approximation to the slow manifold $\mathcal{W}_\mu$ with the graph of the nth approximation to $\mathbf{H}_\mu$ given by

$$\mathbf{H}_\mu^n(W) = \mathbf{H}_0(W) + \sum_{m=1}^{n} \mu^m \mathbf{H}_m(W). \qquad (31)$$

Equation (31) approximates the state of the in-plane oscillators for all motions on the slow invariant manifold.

We give numerical results for a square plate, i.e., $\lambda = 1$, with a normalized thickness $\epsilon = 0.05$ and made of isotropic material with Poisson's ratio $\nu = 0.318$. The value of the singular parameter μ is 0.044. The values of the coupled natural frequencies are $1/2\pi$ for the transverse oscillator, 3.852 for the x-in-plane oscillator, and 3.451 for the y-in-plane oscillator. Figure 2 depicts the $O(\mu^2)$ approximation to the configuration invariant manifold $\mathcal{W}_{1\mu}$. Note that the manifold possesses a point reflective symmetry induced by the symmetry property (30) of $H_{1\mu}$, the first component of $\mathbf{H}_\mu$.

5 Numerical Construction of the Slow Flow

In this section, using the approximations to the function describing the slow manifold, we construct numerically the slow flow, i.e., the phase portrait of the restriction of the dynamics of the three coupled oscillators on the slow manifold. Let $\hat{\mathbf{H}}_\mu$ denote the restriction of the function $\mathbf{H}_\mu$ on the W_1 space. The graph of $\hat{\mathbf{H}}_\mu$ defines a one-dimensional noninvariant submanifold on the slow manifold. We call it the stagnation submanifold since it is characterized by zero momentum, i.e., $W_2 = U_2 = V_2 \equiv 0$. Because of conservation of energy a motion on the slow manifold intersects the stagnation manifold at two points, located symmetrically about $W_1 = 0$. We have searched the neighborhood around the computed analytic approximations to the stagnation submanifold and have located a continuum of periodic motions symmetric about the displacement W_1. For small μ, we identify this continuum of slow periodic motions with the invariant manifold whose analytical approximations we have computed in the previous section. Figure 3(*a*) shows the projection of a set of nine slow periodic motions, their energies ranging from a low to a high level, onto the phase space W of the transverse nonlinear oscillator. Note that all motions trace closed curves with reflective symmetry about the origin of the W plane. This point reflective symmetry indicates that the manifold of slow motions possesses a point reflective symmetry. Figure 3(*b*) shows the projection of the above set of slow motions onto the configuration plane $W_1 - U_1$. All motions project onto open, non-self-intersecting symmetric curves about $W_1 = 0$, in agreement with the analysis. When a motion reaches the end of the curve it traces, it intersects the stagnation submanifold. In fact, the end points of the curves define the stagnation submanifold.

Figure 4(*a*) shows a typical time history of the displacement W_1 of the transverse oscillator and the displacement U_1

Downloaded 04 May 2010 to 171.66.16.34. Redistribution subject to ASME license or copyright; see http://www.asme.org/terms/Terms_Use.cfm

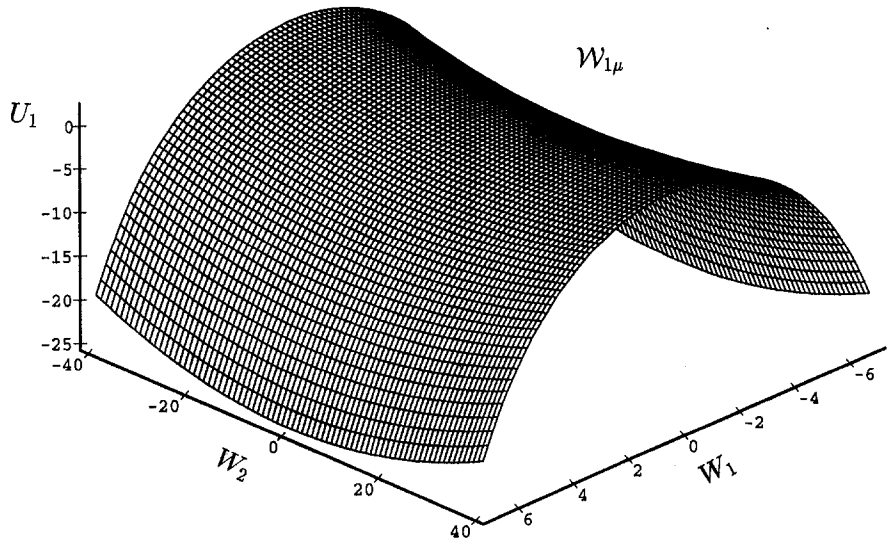


Fig. 2 $O(\mu^2)$ **approximation to the slow configuration invariant manifold** $\mathcal{W}_{1\mu}$

of the x-in-plane oscillator for a motion of low energy level on the slow invariant manifold. In agreement with the analysis, the in-plane motions evolve at a period half of that of the transverse motions. Over half of the period, the in-plane oscillators are in-phase with the transverse oscillator, and over the other half of the period they are out-of-phase with the transverse oscillator. The spectrum of $W_1(t)$ is dominated by a single harmonic while those of $U_1(t)$ and $V_1(t)$ are dominated by two discrete harmonics with frequencies that are respectively twice and quadruple than that of the dominant harmonic of $W_1(t)$. As the energy level increases, the basic harmonic shifts to the right. This is in agreement with the result of Rao and Pillai (1992) who studied the effect of large-amplitude vibrations on the frequency of transverse motions with the effects of in-plane inertias included. At some energy level, the frequency of the high harmonic of U_1 and V_1 coincides with the smallest of the natural in-plane frequencies. Thus, the in-plane oscillators undergo an internal parametric resonance which in turn precipitates a local oscillation about the maximum displacement of the in-plane oscillators as shown in Fig. 4(b). Figure 5(a) shows the spectrum of the displacement U_1. As the energy level increases, the difference in the amplitudes of the harmonics of the in-plane oscillations approaches zero. When the difference in the amplitudes is zero, see Fig. 5(b), the high harmonic of the in-plane oscillations coincides with the other in-plane natural frequency. It seems that the internal parametric resonance constitutes a mechanism transferring energy from the low to the high harmonic of the in-plane slow oscillations.

6 Slow Normal Mode-Slow Transverse Oscillator

We identify the two-dimensional slow invariant manifold with a slow nonlinear normal mode although the motions carried by it do not satisfy all properties of vibrations in unison (Rosenberg 1964). The natural projection, induced by the function $\mathbf{H}_\mu$, of the slow system, all orbits on the slow invariant manifold, onto the space W yields the following nonlinear system:

$$\dot{W} = \mathbf{A}W + \mathbf{B}_1\mathbf{H}_\mu(W)W + \mathbf{B}_2(W). \tag{32}$$

Slow system (32) is well defined only over a region of space W where $\mathbf{H}_\mu$ is a single-valued function. The explicit form of the slow system for the system of the three coupled oscillators we study is

$$\dot{W}_1 = W_2,$$

$$\dot{W}_2 = -W_1 - N_3H_{1\mu}(W_1, W_2)W_1 - N_4H_{3\mu}(W_1, W_2)W_1 - N_5W_1^3, \tag{33}$$

or

$$\dot{W} + [1 + N_3H_{1\mu}(W, \dot{W}) + N_4H_{3\mu}(W, \dot{W})]W + N_5W^3 = 0 \tag{34}$$

in the form of a second-order differential equation. Equation (33) is called the *slow* transverse oscillator; it describes the state of the transverse oscillator for all motions on the slow invariant manifold. Notice that the point reflective symmetry of $\mathbf{H}_\mu$, Eq. (30), renders the vector field of the slow oscillator symmetric about the origin.

The state of motion of the x-in-plane oscillator is given by

$$U(t) = \mu^2H_{1\mu}(W_1(t), W_2(t)),$$

$$\dot{U}(t) = \mu H_{2\mu}(W_1(t), W_2(t)) \tag{35}$$

and that of the y-in-plane oscillator by

$$V(t) = \mu^2H_{2\mu}(W_1(t), W_2(t)),$$

$$\dot{V}(t) = \mu H_{4\mu}(W_1(t), W_2(t)). \tag{36}$$

It is clear that the point reflective symmetry of the slow invariant manifold renders the phase portraits of the in-plane oscillators nonsymmetric about the origins of the planes $U - \dot{U}$ and $V - \dot{V}$. In the terminology of the master-slave principle, we say that the in-plane oscillators are slaved to the master *slow* transverse oscillator.

Next we consider the zeroth and second-order approximations to the slow transverse oscillator. Substituting Eq. (25) into Eq. (33), it yields the zeroth-order slow oscillator:

$$\dot{W}_1 = W_2,$$

$$\dot{W}_2 = -W_1 - K_3W_1^3 \tag{37}$$

Downloaded 04 May 2010 to 171.66.16.34. Redistribution subject to ASME license or copyright; see http://www.asme.org/terms/Terms_Use.cfm

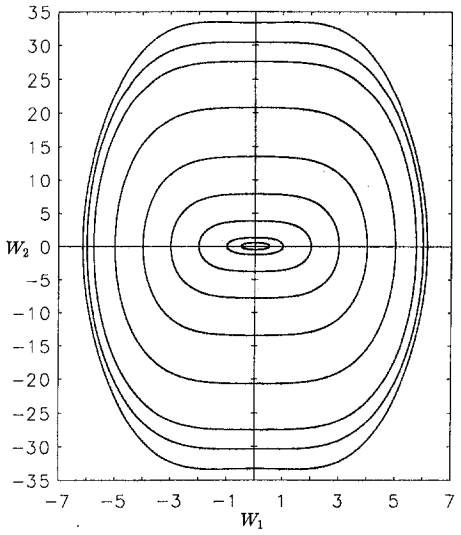


Fig. 3(*a*)

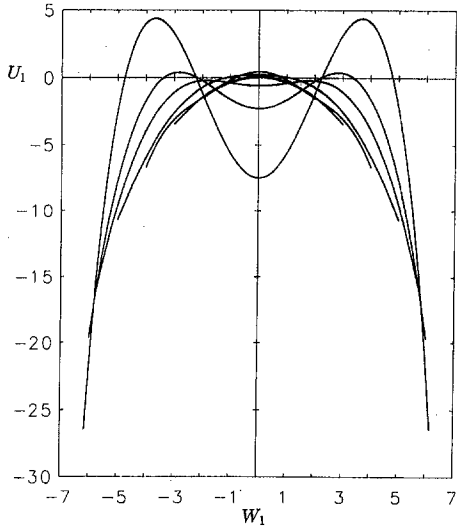


Fig. 3(*b*)

Fig. 3 Projection of motions on the slow manifold $\mathcal{W}_\mu$ onto (*a*) the phase space of the transverse oscillator, (*b*) the configuration plane $W_1 - U_1$

where

$$K_3 \equiv N_5 + \frac{(N_1 - A_{12}A_{21})N_3 + (N_2 - A_{21}A_{12})N_4}{A_{12}A_{21} - 1} \tag{38}$$

and where $A_{12}A_{21} - 1 \neq 0$ for all admissible (λ, ν).

The difference $K_3 - N_5$ measures the static effect of the in-plane motions on the transverse motion. The zeroth-order slow transverse oscillator gives the one-mode approximation of large-amplitude transverse vibrations of a plate with the static effects of the in-plane motions included (Chu and Herrmann, 1956; Bolotin, 1964; Yang and Sethna, 1991).

Substituting Eq. (25) and Eq. (27) into (33) yields the second-order slow oscillator:

$$\dot{W}_1 = W_2,$$

$$\dot{W}_2 = -W_1 - K_3 W_1^3 + \mu^2 F(W_1, W_2) \tag{39}$$

where

$$F(W_1, W_2) = -S_1 W_1 W_2^2 + S_1 W_1^3 + S_5 W_1^5. \tag{40}$$

S_1 and S_5 are positive functions of (λ, ν). Nonlinear term $\mu^2 F(W_1, W_2)$ measures the dynamic effect of the in-plane motions on the transverse motions. This effect appears explicitly in the nonlinear frequency of the slow oscillator: The second-order slow oscillator can be thought of as a regular perturbation of the zeroth-order oscillator; and, thus, terms $-\mu^2 S_1 W_2^2$ and $\mu^2(S_1 W_1^3 + S_5 W_1^5)$ cause a dynamic stiffening and softening, respectively, of the zeroth-order slow transverse oscillator. Numerical experiments show that the zeroth-order slow oscillator and the zeroth-order approximation to $\mathbf{H}_\mu$ approximate exceptionally well slow motions of low energy level for given μ (equivalently ϵ). For high energy levels, the second-order slow oscillator and the second-order approximation to $\mathbf{H}_\mu$ result in a better approximation to the slow motions that the zeroth-order slow oscillator and $\mathbf{H}_0$ do as Fig. 6(*a*) and Fig. 6(*b*) show.

Although the motions carried by the slow manifold do not satisfy all properties of vibrations in unison, as defined by Rosenberg (1964), we identify it with a global, nonlinear slow normal mode. Shaw and Pierre (1993) have identified a local, two-dimensional, invariant manifold carrying vibrations in unison with a local normal mode. Georgiou et al. (1994) have generalized the properties of vibrations in unison and thus have

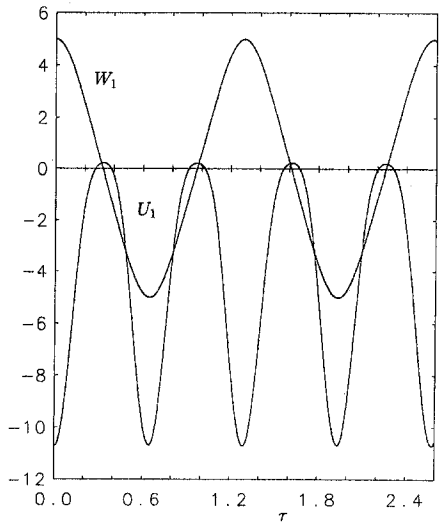


Fig. 4(*a*)

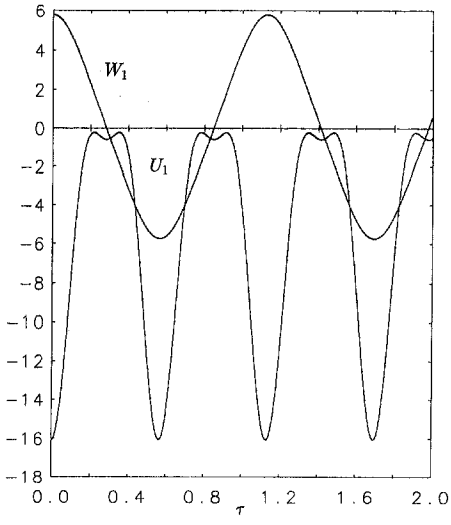


Fig. 4(*b*)

Fig. 4 Time history of motions on the slow invariant manifold $\mathcal{W}_\mu$: (*a*) orbit of low energy level, (*b*) orbit of moderately high energy level (first internal resonance)

Downloaded 04 May 2010 to 171.66.16.34. Redistribution subject to ASME license or copyright; see http://www.asme.org/terms/Terms_Use.cfm

identified a global, two-dimensional, invariant manifold carrying one or more static equilibria with a global nonlinear normal mode.

7 Conclusions and Discussion

To study the effect of the in-plane motions to the transverse motions and vice versa of an isotropic plate with hinged edges, we approximated the nonlinearly coupled equations of motion with three coupled oscillators, each oscillator describing the amplitude dynamics of a fundamental mode of vibration. We approximated analytically a two-dimensional smooth manifold described by the graph of a function of the state to the transverse nonlinear oscillator. Using successive approximations of this manifold, we have detected numerically a continuum of slow, periodic symmetric motions. We identify this continuum with a slow invariant manifold of motion, or a slow nonlinear normal mode of oscillation. On this invariant manifold, the slow transverse oscillator slaves the in-plane oscillators into periodic motions of half its period. Furthermore, the slow transverse oscillator resonates the in-plane oscillators at some critical energy level. For energy levels above the critical energy level, the in-plane oscillators develop a local oscillation at the peaks and they oscillate initially in pure compression. As the energy level of motions on the slow manifold increases, the amplitude of the local oscillation grows.

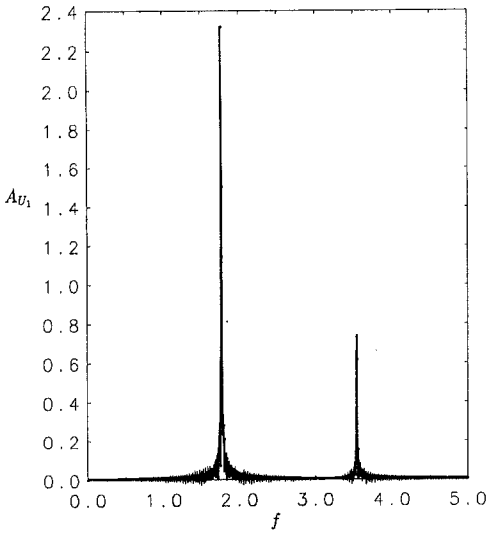


Fig. 5(*a*)

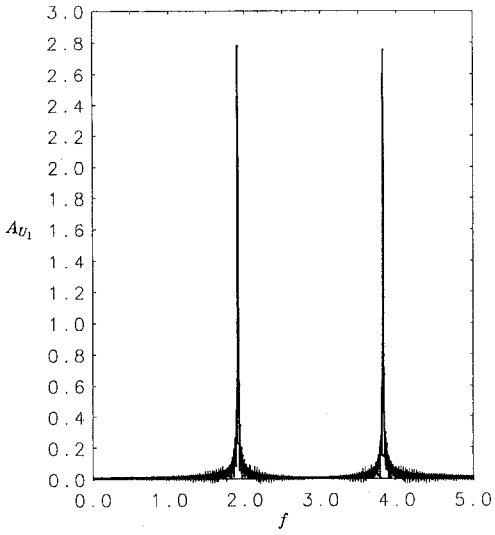


Fig. 5(*b*)

Fig. 5 Spectrum density A_{U_1} of a displacement U_1 on the slow invariant manifold $\mathcal{W}_\mu$: (*a*) motion close to the first internal resonance, (*b*) motion close to the second internal resonance

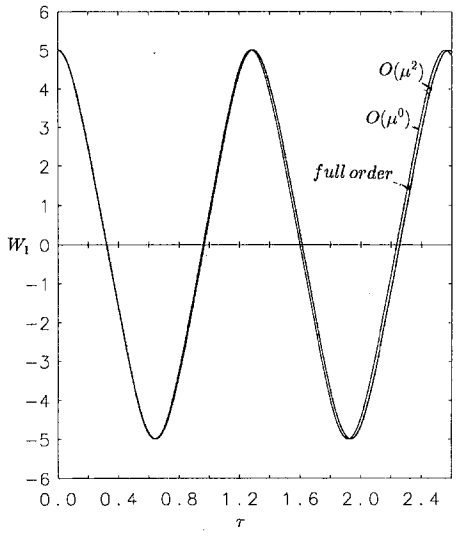


Fig. 6(*a*)

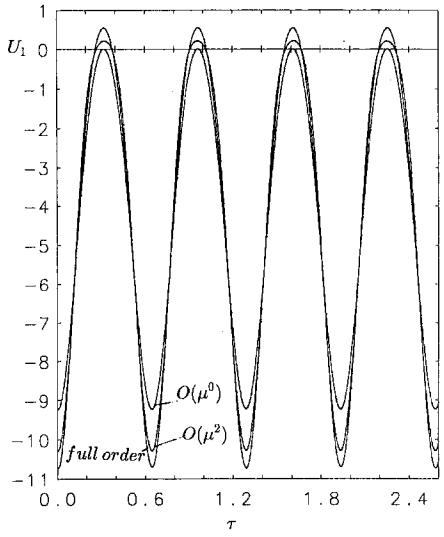


Fig. 6(*b*)

Fig. 6 Comparison of a motion on the slow manifold $\mathcal{W}_\mu$ to a motion predicted by the approximate slow system: (*a*) displacement of slow oscillator, (*b*) displacement of *x*-in-plane oscillator

Here we mention that we have detected other families of symmetric and unsymmetric periodic motions besides the symmetric periodic motions locally guaranteed by Lyapunov's Center Manifold Theorem. Issues remaining are the stability of the slow invariant manifold and the nature of bifurcations giving rise to the nonsymmetric family of periodic motions, which manifold of periodic motions is excited in the parametrically forced dissipative system, and whether one can control the transverse motions of a plate via in-plane parametric forcing by inferring small changes to the in-plane modulus of elasticity. Furthermore, it will be interesting to see if there is a connection between the internal resonance we have detected and a secondary resonance Bolotin (1964) has detected in his study of dynamic stability of a parametrically forced plate. He was able to detect this secondary resonance because he considered the effect of in-plane inertial forces.

Downloaded 04 May 2010 to 171.66.16.34. Redistribution subject to ASME license or copyright; see http://www.asme.org/terms/Terms_Use.cfm

Finally, the results predicted by the singular perturbation analysis of the three fundamental coupled oscillators will hold true for the partial differential equation model of the plate since the equations of motion of the plate can be formulated as a singular perturbation of the transverse equation of motion of a beam, that is, a plate of small aspect ratio (the thickness and the aspect ratio provide two singular parameters). Determining the nature of generic bifurcations of a motion on the slow invariant manifold will be fundamental since it will provide the nonlinear mechanisms governing the transition of the nonlinear vibrations of a plate of small thickness and small aspect ratio, essentially a beam, to the nonlinear vibrations of a thick square plate.

Acknowledgment

The first author gratefully acknowledges the support of the National Research Council. IBS acknowledges support from the Office of Naval Research. We thank the reviewers for their critical and constructive comments.

References

Bolotin, V. V., 1964, *The Dynamic Stability of Elastic Systems,* Holden-Day, San Francisco, CA pp. 398–416.

Chu, H.-N., and Herrmann, G., 1956, "Influence ol Large Amplitudes on Free Flexural Vibrations of Rectangular Elastic Plates," ASME JOURNAL OF APPLIED MECHANICS, Vol. 23, pp. 532–540.

Fenichel, N., 1979, "Geometric Singular Perturbation Theory for Ordinary Differential Equations," *Journal of Differential Equations,* Vol. 31, pp. 53–98.

Georgiou, I. T., 1993, "Nonlinear Dynamics and Chaotic Motions of a Singularly Perturbed Nonlinear Viscoelastic Beam," Ph.D. Thesis, Purdue University, West Lafayette, IN.

Georgiou, I. T., and Schwartz, I. B., 1996, "The Slow Invariant Manifold of a Conservative Pendulum-Oscillator System," *International Journal of Bifurcation and Chaos,* Vol. 6, No. 4, pp. 673–692.

Georgiou, I. T., Bajaj, A. K., and Corless, M., 1994, "Slow Normal Modes in a Singularly Perturbed Nonlinear Oscillator with Applications to Structural Dynamics," *Nonlinear and Stochastic Dynamics: Proceedings of the International Mechanical Engineering Congress and Exposition,* A. K. Bajaj, N. S. Namachchivaya, and A. R. Ibrahim, eds., ASME AMD-Vol. 192, DE-Vol. 78, pp. 17–30.

Kelly, A., 1967, "On the Lyapunov Subcenter Manifold," *J. Math. Anal. Appl.,* Vol. 18, pp. 472–478.

Knobloch, H. W., and Aullback, B., 1984, "Singular Perturbations and Integral Manifolds," *Journal of Mathematical and Physical Sciences,* Vol. 18, No. 5, pp. 415–423.

Shaw, S. W., and Pierre, C., 1993, "Normal Modes for Nonlinear Vibratory Systems," *Journal of Sound and Vibration,* Vol. 164, pp. 85–124.

Rao, N. B., and Pillai, S. R. R., 1992, "Non-Linear Vibrations of a Simply Supported Rectangular Antisymmetric Cross-Ply Plate with Immovable Edges," *Journal of Sound and Vibration,* Vol. 152, pp. 568–572.

Rosenberg, R. M., 1964, "On the Existence of Normal Mode Vibrations of Nonlinear Systems With Two Degrees of Freedom," *Quarterly of Applied Mathematics,* Vol. 22, No. 3, 217–234.

Yang, L. X., and Sethna, P. R., 1991, "Local and Global Bifurcations in Parametrically Excited Vibrations of Nearly Square Plates," *Int. J. Non-Linear Mechanics,* Vol. 26, No. 2, pp. 199–220.

APPENDIX

The coefficients in Eq. (9) are given by

$$\hat{A}_{11} = \frac{(6-6\nu)\lambda^2+48}{\pi^2(\lambda^2+1)^2}, \quad \hat{A}_{12} = \frac{128\lambda(\nu+1)}{3\pi^4(\lambda^2+1)^2}$$

$$\hat{A}_{21} = \frac{128\lambda(\nu+1)}{3\pi^4(\lambda^2+1)^2}, \quad \hat{A}_{22} = \frac{-6\nu+48\lambda^2+6}{\pi^2(\lambda^2+1)^2},$$

$$\hat{N}_1 = \frac{(4-12\nu)\lambda^2+16}{\pi^2(\lambda^2+1)^2}, \quad \hat{N}_2 = \frac{16\lambda^3+(4-12\nu)\lambda}{\pi^2(\lambda^2+1)^2},$$

$$\hat{N}_3 = -\frac{32((9\pi^2-16)\nu-16)\lambda^2-288\pi^2}{9\pi^4(\lambda^2+1)^2},$$

$$\hat{N}_4 = \frac{32\lambda(9\lambda^2\pi^2-(-9\pi^2+16)\nu+16)}{9\pi^4(\lambda^2+1)^2},$$

$$\hat{N}_5 = \frac{(27\pi^2+512)\lambda^4+((72\pi^2-768)\nu-18\pi^2+256)\lambda^2+27\pi^2+512}{24\pi^2(\lambda^2+1)^2}.$$

The coefficients in Eqs. (25)–(28) are given by

$$C_{101} = \frac{N_1-A_{12}N_2}{-1+A_{21}A_{12}}, \quad C_{301} = \frac{N_2-A_{12}N_1}{-1+A_{21}A_{12}},$$

$$C_{121} = 2\frac{-(1+\kappa^2A_{12}A_{21})N_1+A_{12}(1+\kappa^2)N_2}{(-1+A_{21}A_{12})^2},$$

$$C_{123} = -2\beta\frac{(N_1-A_{12}A_{21})+(N_2-A_{21}N_1)+N_5}{(-1+A_{21}A_{12})^3},$$

$$\beta = N_1-A_{12}N_2-\kappa^2(N_2-A_{21}N_1)A_{12},$$

$$C_{321} = 2\frac{(A_{21}+\kappa^2A_{12}N_1)N_1-(A_{12}A_{21}+\kappa^2)N_2}{(-1+A_{21}A_{12})^2},$$

$$C_{323} = 2\beta_1\frac{(N_1-A_{12}A_{21})N_3+(N_2-A_{21}N_1)N_4+N_5}{(-1+A_{21}A_{12})^3},$$

$$\beta_1 = \kappa^2(N_2-A_{21}N_1)+(N_1-A_{12}N_2)A_{21},$$

$$C_{231} = -8\frac{(1+\kappa^2A_{12}A_{21})N_1-(1+\kappa^2A_{12}A_{21})N_2}{(-1+A_{21}A_{12})^2},$$

$$C_{232} = -12\beta\frac{(N_1-A_{12}N_2)N_3+(N_2-A_{21}N_1)N_4+N_5}{(-1+A_{21}A_{12})^2},$$

$$C_{431} = 8\frac{\kappa(1+\kappa^2)A_{21}N_1-\kappa(\kappa^2+A_{21}A_{12})N_2}{(-1+A_{21}A_{12})^2},$$

$$C_{432} = 12\beta_1\kappa\frac{(N_1-A_{12}N_2)N_3+(N_2-A_{21}N_1)N_4-(1-A_{12}A_{21})N_5}{(-1+A_{21}A_{12})^3}.$$

The coefficients in Eq. (40) are given by

$$S_1 = -2\frac{\beta N_3+\beta_1N_4}{(-1+A_{21}A_{12})^2},$$

$$S_5 = 2\frac{(N_1-A_{12}N_2)\beta N_3^2+(\beta(N_2-A_{21}N_1)N_4-\beta_1(N_1-A_{12}N_2)N_4)N_3}{(-1+A_{21}A_{12})^3}$$

$$+2\frac{-\beta_1(N_2-A_{21}N_1)N_4^2+(\beta N_3-\beta_1N_4)N_5(-1+A_{12}A_{21})}{(-1+A_{21}A_{12})^3}.$$

Downloaded 04 May 2010 to 171.66.16.34. Redistribution subject to ASME license or copyright; see http://www.asme.org/terms/Terms_Use.cfm

Gwolong Lai
Associate Professor,
Department of Construction Engineering,
National Yunlin Institute of Technology,
Yunlin, Taiwan 640, R.O.C.

A. R. Robinson
Professor Emeritus,
Department of Civil Engineering,
University of Illinois at Urbana-Champaign,
Urbana, IL 61801

Exact Solutions of Some Shear Dislocation Problems Involving a Stopping Effect[1]

An analytical approach is developed for dealing with the sudden stopping of a shear dislocation that acts over an expanding circular or elliptical region. The analysis begins with the case of circular region. Despite the fact that this problem is not self-similar, it has been possible to express the solution as a superposition of several self-similar problems that have different degrees of homogeneity. The use of a new rotational superposition technique that includes a stretching effect developed by the authors allows the extension to elliptical shear dislocation problems.

1 Introduction

Dislocation theory has been widely adopted by seismologists as an effective model for evaluating the strong ground motions induced by a shallow-focus earthquake (Trifunac and Udwadia, 1974). As asserted by Reid's elastic rebound theory, which is supported by seismological evidence, the processes of occurrence of shallow earthquakes are connected with ruptures which occur as a result of sudden shift of Earth material on a fault plane (Reid, 1911). It has been shown that the dislocation theory gives results in good agreement with field geodetic measurements (Chinnery, 1961; Wyss and Brune, 1967).

Many studies using dislocation theory have been carried out since the 1960s. Most of the analytical ones use a double-couple point source (Burridge and Knopoff, 1964; Kennett, 1974). In a quite different approach, Seyyedian-Choobi and Robinson (1975) developed a two-dimensional analytical seismic source model using a finite propagating dislocation instead of a point source. With the aid of a simple idea of superposition of sources starting at different time and locations, Seyyedian-Choobi and Robinson (1975) showed that the induced motions change character considerably if the front of the propagating fault in the dislocation model is suddenly stopped.

In the present paper, the studies of Seyyedian-Choobi and Robinson are extended to include three-dimensional effects. A very different approach is needed to solve the analytical problem of the sudden stopping of an expanding circular shear dislocation in an infinite elastic medium. It is shown that four self-similar problems not all having the same degree of homogeneity can be combined to give the required solution. Recent work by the authors (Lai and Robinson, 1996) is then applied to extend the solution technique to the case of sudden stopping of an expanding dislocation with an elliptical boundary.

The stopping of the expansion of a dislocation with either a circular or elliptical boundary might seem to have no physical significance. At first sight, it would seem to imply either the presence of a stronger material at just the right locations in a solid or the existence of a stopping signal that propagates at infinite speed. However, for an ellipse of high eccentricity, what happens near one end of the major axis when the entire expansion is stopped should not differ greatly from the interesting case of a localized stopping of the dislocation.

2 Method of Self-Similar Potentials

The method of self-similar potentials is an effective method, first developed by V. I. Smirnov and S. L. Sobolev in the 1930s, for solving two-dimensional wave propagation problems in an elastic half-space (Thompson and Robinson, 1969; Eringen and Suhubi, 1975). This approach is directly applicable to self-similar problems, where the boundary and initial conditions are homogeneous functions of the spatial variables and time. It can sometimes be applied to non-self-similar problems as well.

For self-similar plane-strain problems in which the displacement field $(u_x, u_y, 0)$ is a homogeneous function of x, y, and t, it is not difficult to show that the motion of body can be described by a pair of functions of complex variables $\Phi(\theta_1)$ and $\Psi(\theta_2)$ that serve as potentials and satisfy the two-dimensional wave equations.

$$\left(\frac{\partial}{\partial x^2}+\frac{\partial}{\partial y^2}-\frac{1}{a^2}\frac{\partial^2}{\partial t^2}\right)\Phi=0$$

$$\left(\frac{\partial}{\partial x^2}+\frac{\partial}{\partial y^2}-\frac{1}{b^2}\frac{\partial^2}{\partial t^2}\right)\Psi=0 \tag{1}$$

where a and b stand for the speeds of the P and S waves, and θ_1, θ_2 are complex variables defined implicitly by

$$t-\theta_1 x-y\sqrt{a^{-2}-\theta_1^2}=0$$
$$t-\theta_2 x-y\sqrt{b^{-2}-\theta_2^2}=0. \tag{2}$$

Depending on the degree of homogeneity, the displacements of the plane-strain field can be expressed in terms of the potentials as

$$\frac{\partial^n u_x}{\partial t^n}=\mathrm{Re}\,\frac{\partial^n u_x^*}{\partial t^n}=\mathrm{Re}\left(\frac{\partial\Phi(\theta_1)}{\partial x}+\frac{\partial\Psi(\theta_2)}{\partial y}\right)$$

$$\frac{\partial^n u_y}{\partial t^n}=\mathrm{Re}\,\frac{\partial^n u_y^*}{\partial t^n}=\mathrm{Re}\left(\frac{\partial\Phi(\theta_1)}{\partial y}-\frac{\partial\Psi(\theta_2)}{\partial x}\right) \tag{3}$$

where u_x^* and u_y^* are the complex-valued displacements corresponding to u_x and u_y. The value of n is taken such that the left-hand side of each equation is a homogeneous function of

[1] This paper contains a portion of the dissertation submitted by the first author to the Graduate College of the University of Illinois Urbana-Champaign in partial fulfillment of the requirements for the degree of Doctor of Philosophy.

Contributed by the Applied Mechanics Division of THE AMERICAN SOCIETY OF MECHANICAL ENGINEERS for publication in the ASME JOURNAL OF APPLIED MECHANICS.

Discussion on this paper should be addressed to the Technical Editor, Professor Lewis T. Wheeler, Department of Mechancial Engineering, University of Houston, Houston, TX 77204-4792, and will be accepted until four months after final publication of the paper itself in the ASME JOURNAL OF APPLIED MECHANICS.

Manuscript received by the ASME Applied Mechanics Division, July 24, 1995; final revision, Mar. 21, 1996. Associate Technical Editor: X. Markenscoff.

Copyright © 1997 by ASME

Downloaded 04 May 2010 to 171.66.16.34. Redistribution subject to ASME license or copyright; see http://www.asme.org/terms/Terms_Use.cfm

degree -1.[2] For problems in which the boundary tractions at $y = 0$ are homogeneous of degree zero, the expressions for the complex plane-strain fields are found to be

$$u_x^* = -\int_0^t \left[\int_0^{\theta_1} \theta\Phi'(\theta)d\theta + \int_0^{\theta_2} \sqrt{b^{-2} - \theta^2}\, \Psi'(\theta)d\theta \right] d\tau$$

$$u_y^* = -\int_0^t \left[\int_0^{\theta_1} \sqrt{a^{-2} - \theta^2}\, \Phi'(\theta)d\theta - \int_0^{\theta_2} \theta\Psi'(\theta)d\theta \right] d\tau$$

$$\frac{\sigma_x^*}{\mu} = \int_0^{\theta_1} (b^{-2} + 2\theta^2 - 2a^{-2})\Phi'(\theta)d\theta + \int_0^{\theta_2} 2\theta\sqrt{b^{-2} - \theta^2}\, \Psi'(\theta)d\theta$$

$$\frac{\sigma_y^*}{\mu} = \int_0^{\theta_1} (b^{-2} - 2\theta^2)\Phi'(\theta)d\theta - \int_0^{\theta_2} 2\theta\sqrt{b^{-2} - \theta^2}\, \Psi'(\theta)d\theta$$

$$\frac{\tau_{xy}^*}{\mu} = \int_0^{\theta_1} 2\theta\sqrt{a^{-2} - \theta^2}\, \Phi'(\theta)d\theta + \int_0^{\theta_2} (b^{-2} - 2\theta^2)\Psi'(\theta)d\theta \quad (4)$$

where μ is shear modulus, $\Phi' = d\Phi/d\theta_1$, and $\Psi' = d\Psi/d\theta_2$.

An essential feature of the method of self-similar potentials is the form of Eqs. (2) in which the values of θ_1 and θ_2 are the same for the same x and t on the boundary plane $y = 0$. If y is set equal to zero in Eqs. (4), boundary conditions on displacement or traction on $y = 0$ lead to equations that permit solution for the complex potentials. The plane-strain field is then completely determined by substituting the potentials into Eqs. (4) and taking the real parts.

Antiplane problems in which the displacement field (0, 0, u_z) is a homogeneous function of x, y, and t can be solved in a similar manner as plane-strain problems. The only difference is that the solution is found in terms of a single complex-valued displacement function of θ_2 which itself serves as a potential function. The displacement function $W(\theta_2)$ satisfies the wave equation, as does the nonzero displacement component u_z.

$$\left(\frac{\partial}{\partial x^2} + \frac{\partial}{\partial y^2} - \frac{1}{b^2}\frac{\partial^2}{\partial t^2}\right)W = 0. \quad (5)$$

In a manner analogous to that for plane-strain problems, the displacement and stresses for antiplane problems with homogeneous tractions of degree zero on $y = 0$ are found to be

$$u_z = \mathrm{Re}\, u_z^* = \mathrm{Re} \int_0^t \left\{ \int_0^{\theta_2} W'(\theta)d\theta \right\} d\tau$$

$$\frac{\tau_{zx}^*}{\mu} = -\int_0^{\theta_2} \theta W'(\theta)d\theta$$

$$\frac{\tau_{zy}^*}{\mu} = -\int_0^{\theta_2} \sqrt{b^{-2} - \theta^2}\, W'(\theta)d\theta \quad (6)$$

3 The Rotational Superposition Technique for Circular Shear Dislocation Problems

Consider the dynamic problem of an expanding circular shear dislocation nucleated from the origin on the $y = 0$ plane in an unbounded medium as shown in Fig. 1. The boundary conditions on the dislocation plane are given by the following equations:

$$u_\varrho(\varrho, \omega, t)|_{y=0^+} = -u_\varrho(\varrho, \omega, t)|_{y=0^-} = u_x(\varrho, t)\cos\omega$$

$$u_\omega(\varrho, \omega, t)|_{y=0^+} = -u_\omega(\varrho, \omega, t)|_{y=0^-} = -u_x(\varrho, t)\sin\omega$$

$$\sigma_y = 0 \quad \text{for} \quad y = 0 \quad (7)$$

where $u_x(\varrho, t)$ is the distribution function of the tangential relative displacements in the x direction. Here (ϱ, ω, y) are cylindrical coordinates corresponding to the Cartesian coordinates (x, z, y).

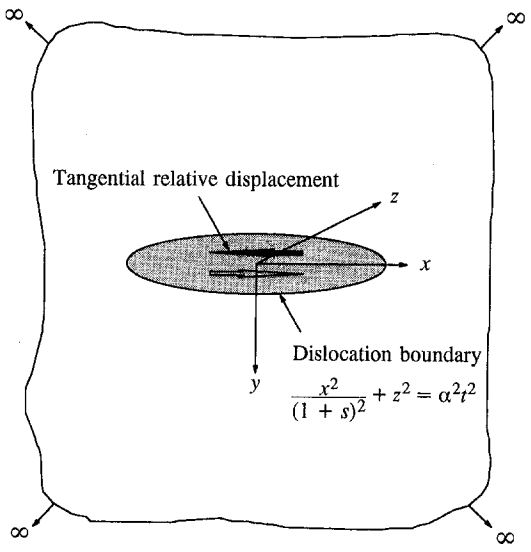
The Smirnov-Sobolev method can treat plane-strain and antiplane problems directly by calculating the results from boundary conditions on $y = 0$. The method of rotational superposition can sometimes be used to express the three-dimensional field in terms of integrals of a single plane-strain problem and a single antiplane problem (Kostrov, 1964; Johnson and Robinson, 1972). In particular for the symmetries of the present problem

$$u_\varrho = \left\{ \int_0^\pi u_{x2}(\varrho\cos\eta, y, t)\cos^2\eta d\eta - \int_0^\pi u_{z2}(\varrho\cos\eta, y, t)\sin^2\eta d\eta \right\} \cos\omega$$

$$u_\omega = \left\{ -\int_0^\pi u_{x2}(\varrho\cos\eta, y, t)\sin^2\eta d\eta + \int_0^\pi u_{z2}(\varrho\cos\eta, y, t)\cos^2\eta d\eta \right\} \sin\omega$$

$$u_y = \left\{ \int_0^\pi u_{y2}(\varrho\cos\eta, y, t)\cos\eta d\eta \right\} \cos\omega \quad (8)$$

where u_{x2} and u_{y2} correspond to the plane-strain problem and u_{z2} to the antiplane problem. The corresponding expressions for the stresses can be found in Johnson and Robinson (1972).



$a = 5.6$ km/sec, $b = 3.2$ km/sec

$\alpha = \frac{1.92}{1+s}$ km/sec

Fig. 1 An expanding elliptical shear dislocation (circular when $s = 0$) on the $y = 0$ plane

[2] The derivatives for negative n's are merely interpreted as integrals.

Downloaded 04 May 2010 to 171.66.16.34. Redistribution subject to ASME license or copyright; see http://www.asme.org/terms/Terms_Use.cfm

The boundary conditions of Eqs. (7) then take the form of integral equations with u_{x2}, u_{y2} and u_{z2} under the integral sign and known functions on the right side. These integral equations are of Abel type (Hamel, 1949) and have a unique, closed-form solution, which gives the boundary values on $y_2 = 0^+$ for the plane-strain and antiplane problems as follows (Lai and Robinson, 1996):

1 The plane-strain problem,

$$u_{x2}(x_2, t) = \frac{1}{\pi}\frac{\partial}{\partial x_2}\left\{\int_0^{x_2} u_x(\xi, t)\frac{\xi}{\sqrt{x_2^2 - \xi^2}}\,d\xi\right\}$$

$$\sigma_{y2} = 0. \tag{9}$$

2 The antiplane problem,

$$u_{z2}(x_2, t) = -\frac{1}{\pi}\frac{\partial}{\partial x_2}\left\{\int_0^{x_2} u_x(\xi, t)\frac{\xi}{\sqrt{x_2^2 - \xi^2}}\,d\xi\right\}. \tag{10}$$

These are then known boundary conditions for the plane-strain and antiplane problems. The final result for the actual three-dimensional displacements are then determined directly from Eqs. (8) even off the surface $y = 0$.

To summarize the procedure of the method of rotational superposition:

1 determine the boundary values for the fictitious plane problems corresponding to the given three-dimensional problem by solving Abel integral equations;
2 solve the plane problems, here by the self-similar potential technique; and finally
3 superpose the plane fields rotationally to find the solution of the three-dimensional problem being considered.

4 A Spreading Circular Shear Dislocation in an Unbounded Medium

Consider a plane in an infinite elastic, homogeneous, and isotropic medium on which a relative slip, a dislocation, originates at some initial time. The two opposite sides of the fault experience a relative tangential displacement in a fixed direction which is a function of time and the distance to the starting point. This problem can be described as an expanding circular shear dislocation nucleated from the origin on the $y = 0$ plane at time $t = 0$, as in the previous section. In this study, the relative displacement function in Eqs. (7) is taken as

$$u_x(\varrho, t) = D\sqrt{\alpha^2 t^2 - \varrho^2} \quad \text{for} \quad \varrho \le \alpha t$$
$$= 0 \quad \text{for} \quad \varrho > \alpha t \tag{11}$$

where D is a dimensionless measure of the intensity of the dislocation and α is the speed of propagation of the edge of the dislocation. The above form for the relative displacement distribution on the fault plane is chosen because it is the solution form for the crack surface in self-similar problems of crack propagation in a medium subjected to a homogeneous shear (Kostrov, 1964). Therefore it should be a good approximation for the relative displacement distribution on the fault plane.

By the use of Eqs. (9) and (10) the corresponding plane problems can be readily determined. The boundary values of the plane problems for $y_2 = 0^+$ are as follows.

1 For the plane-strain problem,

$$u_{x2}(x_2, t) = \frac{D}{\pi}\left[\alpha t + \frac{|x_2|}{2}\log\left(\frac{\alpha t - |x_2|}{\alpha t + |x_2|}\right)\right] \quad \text{for} \quad |x_2| \le \alpha t$$
$$= \frac{D}{\pi}\left[\alpha t + \frac{|x_2|}{2}\log\left(\frac{|x_2| - \alpha t}{|x_2| + \alpha t}\right)\right] \quad \text{for} \quad |x_2| > \alpha t$$
$$\sigma_{y2} = 0. \tag{12}$$

2 For the antiplane problem,

$$u_{z2}(x_2, t) = -\frac{D}{\pi}\left[\alpha t + \frac{|x_2|}{2}\log\left(\frac{\alpha t - |x_2|}{\alpha t + |x_2|}\right)\right] \quad \text{for} \quad |x_2| \le \alpha t$$
$$= -\frac{D}{\pi}\left[\alpha t + \frac{|x_2|}{2}\log\left(\frac{|x_2| - \alpha t}{|x_2| + \alpha t}\right)\right] \quad \text{for} \quad |x_2| > \alpha t. \tag{13}$$

Since the tangential displacement for $y_2 = 0^+$ is a homogeneous function of degree 1, the plane-strain problem can be solved straightforwardly by the method of self-similar potentials. The complex potentials that describe the plane-strain field for $y_2 \ge 0^+$ are found to be

$$\Phi'(\theta_1) = \frac{4D\alpha^3 b^2}{\pi}\frac{\theta_1^2}{(1 - \alpha^2\theta_1^2)^2}$$
$$\Psi'(\theta_2) = \frac{2D\alpha^3 b^2}{\pi}\frac{\theta_2(b^{-2} - 2\theta_2^2)}{(1 - \alpha^2\theta_2^2)^2\sqrt{b^{-2} - \theta_2^2}}. \tag{14}$$

The displacement and stress fields are then determined by substituting the complex potentials Φ' and Ψ' into Eqs. (4).

The solution for the antiplane problem can also be found readily by using the self-similar potential technique, which gives the derivative of the complex displacement function as below:

$$W'(\theta_2) = \frac{2D\alpha^3}{\pi}\frac{\theta_2}{(1 - \alpha^2\theta_2^2)^2}. \tag{15}$$

Substituting the displacement potential W' into Eqs. (6) leads to the displacement and stress fields for the antiplane problem.

The three-dimensional displacement field for the shear dislocation problem being considered is then found by substituting the plane strain and antiplane fields obtained into Eqs. (8). It is noted that only the real parts of the results represent the physical disturbance in the medium due to an expanding circular shear dislocation on the $y = 0$ plane.

5 The Stopping of a Spreading Circular Shear Dislocation

It is generally agreed that the relative earthquake motion on the fault plane is an intermittent process. An initial failure occurs near the focus and then a series of cracks develop sequentially (Heck, 1936). Seyyedian-Choobi and Robinson (1975) developed a simple two-dimensional model to simulate this phenomenon. In the two-dimensional case, it is easy to stop a dislocation and yet solve only self-similar problems. If the dislocation is a uniform relative motion that grows in extent at a constant rate, all that must be done is to superpose a second self-similar motion that begins at the time of stopping, has an origin at the end that is being stopped, and is of intensity equal and opposite to that of the original relative motion. However,

Downloaded 04 May 2010 to 171.66.16.34. Redistribution subject to ASME license or copyright; see http://www.asme.org/terms/Terms_Use.cfm

a direct extension to three-dimensional cases fails since the second problem is no longer self-similar. A proper extension to three-dimensional problems, which will be termed a "stopping technique," is developed and discussed next.

Consider the situation that the spreading circular shear dislocation stops suddenly after propagating from its nucleation at time $t = 0$ to time $t = t_0$. For $t > t_0$, the relative displacements on the fault surface are assumed to remain unchanged. The boundary conditions on the $y = 0$ plane for $t \geq t_0$ are then given by the same expressions as the Eqs. (7) but with a relative displacement distribution that is now fixed at the value it had just before stopping, which is

$$\begin{aligned} u_x(\varrho, t) &= D\sqrt{R_0^2 - \varrho^2} \quad \text{for} \quad \varrho \leq R_0 \\ &= 0 \quad \text{for} \quad \varrho > R_0 \end{aligned} \tag{16}$$

where $R_0 = \alpha t_0$ is the radius of the stopped circular dislocation distribution. It should be noted that this would not be the solution for a crack that stops, for in this case some rebound of the already displaced crack surfaces would be expected.

One convenient approach for determining the response of the medium after the stopping occurs is to superpose a second three-dimensional dislocation problem starting at $t = t_0$. This second or "correcting" solution when added to the original propagating problem for $t \geq t_0$ gives the field satisfying the boundary conditions for the stopping problem, defined by Eqs. (7) and (16). The correcting shear dislocation problem can be formulated readily. The relative displacement distribution on the dislocation plane for the correcting problem is obtained by subtracting Eq. (11) from Eq. (16), which gives

$$\begin{aligned} u_x(\varrho, t) &= D(\sqrt{R_0^2 - \varrho^2} - \sqrt{\alpha^2 t^2 - \varrho^2}) \quad \text{for} \quad \varrho < R_0 \\ &= -D\sqrt{\alpha^2 t^2 - \varrho^2} \quad \text{for} \quad R_0 \leq \varrho \leq \alpha t \\ &= 0 \quad \text{for} \quad \varrho > \alpha t. \end{aligned} \tag{17}$$

The correcting problem is then determined by the boundary values on the $y = 0$ plane, given by Eqs. (7) and (17).

5.1 The Fictitious Plane Problems Corresponding to the Correcting Problem. The fictitious plane problems corresponding to the correcting shear dislocation problem originating at $t = t_0$ can be found from Eqs. (9) and (10) as in the expanding problem. It is not difficult to show that the corresponding boundary values for $y_2 = 0^+$ of the plane problems are given by the following equations:

1 The plane strain problem,

$$\begin{aligned} u_{x2}(x_2, t) &= u_c(x_2, t) - u_a(x_2, t) \quad \text{for} \quad |x_2| \leq R_0 \\ &= u_d(x_2, t) - u_a(x_2, t) \quad \text{for} \quad R_0 < |x_2| \leq \alpha t \\ &= u_d(x_2, t) - u_b(x_2, t) \quad \text{for} \quad |x_2| > \alpha t \\ \sigma_{y2} &= 0. \end{aligned} \tag{18}$$

2 The antiplane problem,

$$\begin{aligned} u_{z2}(x_2, t) &= u_a(x_2, t) - u_c(x_2, t) \quad \text{for} \quad |x_2| \leq R_0 \\ &= u_a(x_2, t) - u_d(x_2, t) \quad \text{for} \quad R_0 < |x_2| \leq \alpha t \\ &= u_b(x_2, t) - u_d(x_2, t) \quad \text{for} \quad |x_2| > \alpha t, \end{aligned} \tag{19}$$

where

$$u_a(x_2, t) = \frac{D}{\pi}\left[\alpha t + \frac{|x_2|}{2}\log\left(\frac{\alpha t - |x_2|}{\alpha t + |x_2|}\right)\right]$$

$$u_b(x_2, t) = \frac{D}{\pi}\left[\alpha t + \frac{|x_2|}{2}\log\left(\frac{|x_2| - \alpha t}{|x_2| + \alpha t}\right)\right]$$

$$u_c(x_2, t) = \frac{D}{\pi}\left[R_0 + \frac{|x_2|}{2}\log\left(\frac{R_0 - |x_2|}{R_0 + |x_2|}\right)\right]$$

$$u_d(x_2, t) = \frac{D}{\pi}\left[R_0 + \frac{|x_2|}{2}\log\left(\frac{|x_2| - R_0}{|x_2| + R_0}\right)\right].$$

5.2 Decomposition of the Fictitious Plane Problems Into Self-Similar Problems. It is apparent that the fictitious plane problems corresponding to the correcting problem are not self-similar and cannot be solved directly by the method of self-similar potentials. However, they can be decomposed into self-similar subproblems, each of which can be solved by the Smirnov-Sobolev technique. The solutions for the fictitious plane problems are then found by simply adding up the results for their corresponding self-similar subproblems. These subproblems turn out to have homogenous boundary conditions, but of different orders. This may explain why the decomposition does not seem to have been proposed before.

In order to express the fictitious plane problems in terms of self-similar subproblems, new coordinates, as defined below, are introduced to facilitate the decomposition:

$$t' = t - t_0 = t - \frac{R_0}{\alpha} \quad x_R = x_2 - R_0 \quad x_L = x_2 + R_0. \tag{20}$$

This decomposition can then be carried out by expressing the boundary values of the fictitious plane problems as self-similar components in terms of (x_L, t') or (x_R, t'). The decomposition for the $u_{x2}(x_2, t)$ in Eqs. (18) is performed in detail, as follows: For $0 < x_2 < R_0$,

$$\begin{aligned} u_{x2}(x_2, t) &= \frac{D}{\pi}\left[R_0 + \frac{x_2}{2}\log\left(\frac{R_0 - x_2}{R_0 + x_2}\right) - \alpha t - \frac{x_2}{2}\log\left(\frac{\alpha t - x_2}{\alpha t + x_2}\right)\right] \\ &= -\frac{D}{\pi}\left[\alpha t - R_0 + \frac{x_2}{2}\log\left(\frac{\alpha t - x_2}{\alpha t + x_2}\cdot\frac{R_0 + x_2}{R_0 - x_2}\right)\right] \\ &= -\frac{D}{\pi}\left[\alpha t - R_0 + \frac{x_2}{2}\log\left(\frac{\alpha t - x_2}{R_0 - x_2}\cdot\frac{R_0 + x_2}{\alpha t + x_2}\right)\right] \\ &= -\frac{D}{\pi}\left[\alpha t' + \frac{x_2}{2}\log\left(\frac{\alpha t' - x_R}{-x_R}\cdot\frac{x_L}{\alpha t' + x_L}\right)\right] \\ &= -\frac{D}{\pi}\left[\alpha t' + \frac{x_2}{2}\log\left(1 - \frac{\alpha t'}{x_R}\right) - \frac{x_2}{2}\log\left(1 + \frac{\alpha t'}{x_L}\right)\right] \\ &= -\frac{D}{\pi}\left[\alpha t' + \frac{x_R + R_0}{2}\log\left(1 - \frac{\alpha t'}{x_R}\right) - \frac{x_L - R_0}{2}\log\left(1 + \frac{\alpha t'}{x_L}\right)\right] \\ &= -\frac{D}{2\pi}\left[\alpha t' + x_R\log\left(1 - \frac{\alpha t'}{x_R}\right) + R_0\log\left(1 - \frac{\alpha t'}{x_R}\right) + \alpha t' - x_L\log\left(1 + \frac{\alpha t'}{x_L}\right) + R_0\log\left(1 + \frac{\alpha t'}{x_L}\right)\right]. \end{aligned}$$

Downloaded 04 May 2010 to 171.66.16.34. Redistribution subject to ASME license or copyright; see http://www.asme.org/terms/Terms_Use.cfm

Similarly, for $-R_0 < x_2 < 0$, $x_2 > \alpha t$, and $x_2 < -\alpha t$,

$$u_{x2}(x_2, t) = -\frac{D}{2\pi}\left[\alpha t' + x_R \log\left(1 - \frac{\alpha t'}{x_R}\right) + R_0 \log\left(1 - \frac{\alpha t'}{x_R}\right) + \alpha t' - x_L \log\left(1 + \frac{\alpha t'}{x_L}\right) + R_0 \log\left(1 + \frac{\alpha t'}{x_L}\right)\right].$$

For $R_0 < x_2 < \alpha t$,

$$u_{x2}(x_2, t) = -\frac{D}{2\pi}\left[\alpha t' + x_R \log\left(\frac{\alpha t'}{x_R} - 1\right) + R_0 \log\left(\frac{\alpha t'}{x_R} - 1\right) + \alpha t' - x_L \log\left(1 + \frac{\alpha t'}{x_L}\right) + R_0 \log\left(1 + \frac{\alpha t'}{x_L}\right)\right].$$

For $-\alpha t < x_2 < -R_0$,

$$u_{x2}(x_2, t) = -\frac{D}{2\pi}\left[\alpha t' + x_R \log\left(1 - \frac{\alpha t'}{x_R}\right) + R_0 \log\left(1 - \frac{\alpha t'}{x_R}\right) + \alpha t' - x_L \log\left(-1 - \frac{\alpha t'}{x_L}\right) + R_0 \log\left(-1 - \frac{\alpha t'}{x_L}\right)\right].$$

It can thus be seen that the distribution $u_{x2}(x_2, t)$ is expressible as the sum of the following four self-similar functions in terms of (x_L, t') or (x_R, t') with different degrees of homogeneity:

$$(1)\quad u_{x2}^{R1}(x_R, t') = -\frac{D}{2\pi}\left(\alpha t' + x_R \log\left|1 - \frac{\alpha t'}{x_R}\right|\right)$$

$$(2)\quad u_{x2}^{R2}(x_R, t') = -\frac{D}{2\pi}\cdot R_0 \cdot \log\left|1 - \frac{\alpha t'}{x_R}\right|$$

$$(3)\quad u_{x2}^{L1}(x_L, t') = -\frac{D}{2\pi}\left(\alpha t' - x_L \log\left|1 + \frac{\alpha t'}{x_L}\right|\right)$$

$$(4)\quad u_{x2}^{L2}(x_L, t') = -\frac{D}{2\pi}\cdot R_0 \cdot \log\left|1 + \frac{\alpha t'}{x_L}\right| \qquad (21)$$

The decomposition for $u_{z2}(x_2, t)$ is then obtained readily from the results for $u_{x2}(x_2, t)$. The four self-similar functions to compose $u_{z2}(x_2, t)$ are defined by

$$u_{z2}^{R1}(x_R, t') = -u_{x2}^{R1}(x_R, t') \quad u_{z2}^{R2}(x_R, t') = -u_{x2}^{R2}(x_R, t')$$
$$u_{z2}^{L1}(x_L, t') = -u_{x2}^{L1}(x_L, t') \quad u_{z2}^{L2}(x_L, t') = -u_{x2}^{L2}(x_L, t'). \qquad (22)$$

Both the fictitious plane-strain problem and the fictitious antiplane problem have thus been expressed as the sum of four self-similar plane subproblems. For the plane-strain contribution, we have

$$(1)\quad u_{x2}|_{y_2=0^+} = u_{x2}^{R1}(x_R, t'); \quad \sigma_{y2}|_{y_2=0} = 0 \quad \text{for} \quad t' \geq 0$$

$$(2)\quad u_{x2}|_{y_2=0^+} = u_{x2}^{R2}(x_R, t'); \quad \sigma_{y2}|_{y_2=0} = 0 \quad \text{for} \quad t' \geq 0$$

$$(3)\quad u_{x2}|_{y_2=0^+} = u_{x2}^{L1}(x_L, t'); \quad \sigma_{y2}|_{y_2=0} = 0 \quad \text{for} \quad t' \geq 0$$

$$(4)\quad u_{x2}|_{y_2=0^+} = u_{x2}^{L2}(x_L, t'); \quad \sigma_{y2}|_{y_2=0} = 0 \quad \text{for} \quad t' \geq 0 \qquad (23)$$

and for the antiplane contribution,

$$(1)\quad u_{z2}|_{y_2=0^+} = u_{z2}^{R1}(x_R, t') \quad \text{for} \quad t' \geq 0$$

$$(2)\quad u_{z2}|_{y_2=0^+} = u_{z2}^{R2}(x_R, t') \quad \text{for} \quad t' \geq 0$$

$$(3)\quad u_{z2}|_{y_2=0^+} = u_{z2}^{L1}(x_L, t') \quad \text{for} \quad t' \geq 0$$

$$(4)\quad u_{z2}|_{y_2=0^+} = u_{z2}^{L2}(x_L, t') \quad \text{for} \quad t' \geq 0 \qquad (24)$$

5.3 Solutions to the Self-Similar Plane Subproblems. As in Section 4, the four self-similar plane-strain subproblems that have just been found can be solved directly using the self-similar potential technique. The solutions are in terms of the complex variables θ_i^R or θ_i^L which are defined by substituting t' for t and x_R or x_L for x in Eqs. (2). The complex potentials for the plane strain subproblems are summarized as follows:

$$(1)\quad u_{x2}|_{y_2=0^+} = u_{x2}^{R1}(x_R, t'); \quad \sigma_{y2}|_{y_2=0} = 0 \quad \text{for} \quad t' \geq 0$$

$$\Phi'(\theta_1^R) = -\frac{D\alpha^2 b^2}{\pi}\frac{\theta_1^R}{(1 - \alpha\theta_1^R)^2}$$

$$\Psi'(\theta_2^R) = -\frac{D\alpha^2 b^2}{2\pi}\frac{b^{-2} - 2\theta_2^{R^2}}{(1 - \alpha\theta_2^R)^2\sqrt{b^{-2} - \theta_2^{R^2}}} \qquad (25)$$

$$(2)\quad u_{x2}|_{y_2=0^+} = u_{x2}^{R2}(x_R, t'); \quad \sigma_{y2}|_{y_2=0} = 0 \quad \text{for} \quad t' \geq 0$$

$$\Phi'(\theta_1^R) = -\frac{DR_0\alpha b^2}{\pi}\frac{\theta_1^R}{1 - \alpha\theta_1^R}$$

$$\Psi'(\theta_2^R) = -\frac{DR_0\alpha b^2}{2\pi}\frac{b^{-2} - 2\theta_2^{R^2}}{(1 - \alpha\theta_2^R)\sqrt{b^{-2} - \theta_2^{R^2}}} \qquad (26)$$

$$(3)\quad u_{x2}|_{y_2=0^+} = u_{x2}^{L1}(x_L, t'); \quad \sigma_{y2}|_{y_2=0} = 0 \quad \text{for} \quad t' \geq 0$$

$$\Phi'(\theta_1^L) = \frac{D\alpha^2 b^2}{\pi}\frac{\theta_1^L}{(1 + \alpha\theta_1^L)^2}$$

$$\Psi'(\theta_2^L) = \frac{D\alpha^2 b^2}{2\pi}\frac{b^{-2} - 2\theta_2^{L^2}}{(1 + \alpha\theta_2^L)^2\sqrt{b^{-2} - \theta_2^{L^2}}} \qquad (27)$$

$$(4)\quad u_{x2}|_{y_2=0^+} = u_{x2}^{L2}(x_L, t'); \quad \sigma_{y2}|_{y_2=0} = 0 \quad \text{for} \quad t' \geq 0$$

$$\Phi'(\theta_1^L) = \frac{DR_0\alpha b^2}{\pi}\frac{\theta_1^L}{1 + \alpha\theta_1^L}$$

$$\Psi'(\theta_2^L) = \frac{DR_0\alpha b^2}{2\pi}\frac{b^{-2} - 2\theta_2^{L^2}}{(1 + \alpha\theta_2^L)\sqrt{b^{-2} - \theta_2^{L^2}}}. \qquad (28)$$

Likewise, the solutions for the self-similar antiplane subproblems can also be found straightforwardly by the Smirnov-Sobolev technique. The results may be summarized as

$$(1)\quad u_{z2}|_{y_2=0^+} = u_{z2}^{R1}(x_R, t') \quad \text{for} \quad t' \geq 0$$

$$W'(\theta_2^R) = -\frac{D\alpha^2}{2\pi}\frac{1}{(1 - \alpha\theta_2^R)^2} \qquad (29)$$

$$(2)\quad u_{z2}|_{y_2=0^+} = u_{z2}^{R2}(x_R, t') \quad \text{for} \quad t' \geq 0$$

$$W'(\theta_2^R) = -\frac{DR_0\alpha}{2\pi}\frac{1}{1 - \alpha\theta_2^R} \qquad (30)$$

$$(3)\quad u_{z2}|_{y_2=0^+} = u_{z2}^{L1}(x_L, t') \quad \text{for} \quad t' \geq 0$$

$$W'(\theta_2^L) = \frac{D\alpha^2}{2\pi}\frac{1}{(1 + \alpha\theta_2^L)^2} \qquad (31)$$

Downloaded 04 May 2010 to 171.66.16.34. Redistribution subject to ASME license or copyright; see http://www.asme.org/terms/Terms_Use.cfm

(4) $u_{z2}|_{y_2=0^+} = u_{z2}^{L2}(x_L, t')$ for $t' \geq 0$

$$W'(\theta_2^L) = \frac{DR_0\alpha}{2\pi} \frac{1}{1 + \alpha\theta_2^L}. \tag{32}$$

From the above potentials, the displacement fields $(u_{x2}^{R1*}, u_{y2}^{R1*})$, $(u_{x2}^{R2*}, u_{y2}^{R2*})$, $(u_{x2}^{L1*}, u_{y2}^{L1*})$, $(u_{x2}^{L2*}, u_{y2}^{L2*})$ for the four plane-strain subproblems can be obtained just as for the plane problems in Section 4. The displacement fields u_{z2}^{R1*}, u_{z2}^{R2*}, u_{z2}^{L1*}, u_{z2}^{L2*} of the four antiplane subproblems are calculated in the same way.

5.4 Three-Dimensional Displacement Field for the Correcting Problem. The three-dimensional displacement field for the correcting problem is found by summing up the solutions for the plane-strain and antiplane subproblems, respectively, and then substituting the results into Eqs. (8), which performs the rotational superposition. This gives

$$u_\varrho^{c*} = \left\{ \int_0^\pi (u_{x2}^{R1*} + u_{x2}^{R2*} + u_{x2}^{L1*} + u_{x2}^{L2*}) \cos^2 \eta d\eta - \int_0^\pi (u_{z2}^{R1*} + u_{z2}^{R2*} + u_{z2}^{L1*} + u_{z2}^{L2*}) \sin^2 \eta d\eta \right\} \cos \omega$$

$$u_\omega^{c*} = \left\{ -\int_0^\pi (u_{x2}^{R1*} + u_{x2}^{R2*} + u_{x2}^{L1*} + u_{x2}^{L2*}) \sin^2 \eta d\eta + \int_0^\pi (u_{z2}^{R1*} + u_{z2}^{R2*} + u_{z2}^{L1*} + u_{z2}^{L2*}) \cos^2 \eta d\eta \right\} \sin \omega$$

$$u_y^{c*} = \left\{ \int_0^\pi (u_{y2}^{R1*} + u_{y2}^{R2*} + u_{y2}^{L1*} + u_{y2}^{L2*}) \cos \eta d\eta \right\} \cos \omega. \tag{33}$$

The solutions of the plane subproblems that are superposed in Eqs. (33) are finally expressed in terms of the original coordinates ϱ, η, and y.

$$x_R = x_2 - R_0 = \varrho \cos \eta - R_0$$

$$x_L = x_2 + R_0 = \varrho \cos \eta + R_0$$

and, since the superposition is about the y-axis,

$$y_2 = y. \tag{34}$$

5.5 Three-Dimensional Displacement Field for the Stopping Problem. Before the shear dislocation stops spreading, the three-dimensional displacement field $(u_\varrho^*, u_\omega^*, u_y^*)$ found in Section 4 describes the response of the medium. Once the stopping occurs at time $t = t_0$, the solution to the stopping problem for $t \geq t_0$ is then given by simply adding those of the expanding and the correcting problems, i.e.,

$$u_\varrho = \mathrm{Re}(u_\varrho^* + u_\varrho^{c*})$$

$$u_\omega = \mathrm{Re}(u_\omega^* + u_\omega^{c*})$$

$$u_y = \mathrm{Re}(u_y^* + u_y^{c*}). \tag{35}$$

Since the above displacement field satisfies the boundary conditions on the $y = 0$ plane for the stopping problem, Eqs. (35) are the solution for $t \geq t_0$ which describes the response of the body after the circular shear dislocation stops expanding.

Seyyedian-Choobi and Robinson (1975) showed how the two-dimensional stopping problem can be generalized to the case of a layered half space. It is shown in Lai (1994) that this generalization is straightforward only for cases where the boundary planes between layers and the boundary of the half-space are all parallel to the plane of the dislocation. The stopping problem for the circular expanding dislocation is also solvable for this special case of a layered half space.

6 The Rotational Superposition Method for Elliptical Shear Dislocation Problems

In addition to the usual rotational superposition method as in Section 3, Lai and Robinson (1996) have developed a different rotational superposition technique that can be applied to problems with boundary values given over an elliptical region. The application of this method to the elliptical shear dislocation problem is described in this section.

Consider the problem of an expanding elliptical shear dislocation nucleated from the origin on the $y = 0$ plane at time $t = 0$ in an unbounded medium, as shown in Fig. 1. The boundary conditions on the surface $y = 0$ are taken as follows:

$$u_\varrho(x, z, t)|_{y=0^+} = -u_\varrho(x, z, t)|_{y=0^-} = u_x(\varrho_b, t) \cos \omega$$

$$u_\omega(x, z, t)|_{y=0^+} = -u_\omega(x, z, t)|_{y=0^-} = -u_x(\varrho_b, t) \sin \omega$$

$$\sigma_y = 0 \quad \text{for} \quad y = 0 \tag{36}$$

where

$$\varrho_b(x, z) = \sqrt{\frac{x^2}{(1 + s)^2} + z^2} \tag{37}$$

and $1 + s$ is the aspect ratio of the ellipse.

Lai and Robinson (1996) showed that if a circular distribution of boundary values on the surface $y = 0$ is "stretched" by the ratio $1 + s$ in the x direction, the fictitious two-dimensional problems for the circular case give the solution for the elliptical case provided that the superposition is modified in the following way:

1 An additional weighting function is introduced in terms of the dummy variable β_1 for the superposition.

$$w_e(\beta_1) = \frac{1 + s}{(1 + s)^2 \cos^2 \beta_1 + \sin^2 \beta_1} \tag{38}$$

2 The boundary values of the plane-strain and antiplane problems for the circular case are also stretched as functions of β_1 as follows: for $y_2 = 0^+$,

(i) the plane strain problem is determined by

$$u_{x2}^e(x_{e2}, t, \beta_1) = u_{x2}\left(\frac{x_{e2}}{p(\beta_1)}, t\right) = U\left(\frac{x_{e2}}{p(\beta_1)}, t\right)$$

$$\sigma_{y2}^e = 0; \tag{39}$$

(ii) the antiplane problem is determined by

$$u_{z2}^e(x_{e2}, t, \beta_1) = u_{z2}\left(\frac{x_{e2}}{p(\beta_1)}, t\right) = -U\left(\frac{x_{e2}}{p(\beta_1)}, t\right) \tag{40}$$

where

$$p(\beta_1) = \sqrt{(1 + s)^2 \cos^2 \beta_1 + \sin^2 \beta_1} \tag{41}$$

and

$$U(x_2, t) = \frac{1}{\pi} \frac{\partial}{\partial x_2} \left\{ \int_0^{x_2} u_x(\xi, t) \frac{\xi}{\sqrt{x_2^2 - \xi^2}} d\xi \right\}; \tag{42}$$

3 the final superposition is in the form

Downloaded 04 May 2010 to 171.66.16.34. Redistribution subject to ASME license or copyright; see http://www.asme.org/terms/Terms_Use.cfm

$$u_\varrho = \int_0^\pi u^e_{x2}(\varrho \cos(\beta_1 - \omega), y, t, \beta_1) \times \cos(\beta_1 - \omega) \cos\beta_1 w_e(\beta_1) d\beta_1 - \int_0^\pi u^e_{z2}(\varrho \cos(\beta_1 - \omega), y, t, \beta_1) \times \sin(\beta_1 - \omega) \sin\beta_1 w_e(\beta_1) d\beta_1$$

$$u_\omega = \int_0^\pi u^e_{x2}(\varrho \cos(\beta_1 - \omega), y, t, \beta_1) \times \sin(\beta_1 - \omega)\cos\beta_1 w_e(\beta_1) d\beta_1 + \int_0^\pi u^e_{z2}(\varrho \cos(\beta_1 - \omega), y, t, \beta_1) \times \cos(\beta_1 - \omega) \sin\beta_1 w_e(\beta_1) d\beta_1$$

$$u_y = \int_0^\pi u^e_{y2}(\varrho \cos(\beta_1 - \omega), y, t, \beta_1) \times \cos\beta_1 w_e(\beta_1) d\beta_1. \quad (43)$$

In Lai and Robinson (1996), it has been verified that these "stretched" plane problems rotationally superposed as in Eqs. (43) indeed give rise to the elliptical shear dislocation problem determined by Eqs. (36).

7 An Expanding Elliptical Shear Dislocation in an Infinite Medium

A specific problem of an expanding elliptical shear dislocation in an infinite medium is treated in this section. The relative displacement distribution on the dislocation plane is assumed to be a stretch in the x direction of the distribution Eqs. (7) and (11) for the circular dislocation problem in Section 4. Therefore the relative displacement function $u_x(\varrho_b, t)$ that, together with Eqs. (36), define the boundary conditions on the $y = 0$ plane takes the following form:

$$u_x(\varrho_b, t) = D\sqrt{\alpha^2 t^2 - \varrho_b^2} \quad \text{for} \quad \varrho_b \le \alpha t$$
$$= 0 \quad \text{for} \quad \varrho_b > \alpha t \quad (44)$$

where D is a dimensionless constant and the parameter $\varrho_b(x, z)$ is as in Eqs. (37). It is thus no accident that Eq. (44) is the solution form for the crack surface in self-similar problems of an elliptical shear crack propagating in an isotropic medium subjected to a homogeneous shear (Burridge and Willis, 1969). However, when the elliptical dislocation stops spreading, it will no longer correspond to a crack problem, as noted after Eq. (16) for the circular case.

Since the plane problems corresponding to the circular dislocation problem have been found in Section 4, the corresponding plane problems for the expanding elliptical shear dislocation problem can be straightforwardly obtained by stretching. Their boundary values for $y_2 = 0^+$ are then determined by using Eqs. (39) and (40), which gives

1 the plane strain problem,

$$u^e_{x2}(x_{e2}, t, \beta_1) = \frac{D}{\pi p(\beta_1)}\left[\alpha_{\beta_1} t + \frac{|x_{e2}|}{2}\log\left(\frac{\alpha_{\beta_1} t - |x_{e2}|}{\alpha_{\beta_1} t + |x_{e2}|}\right)\right] \quad \text{for} \quad |x_{e2}| \le \alpha_{\beta_1} t$$

$$= \frac{D}{\pi p(\beta_1)}\left[\alpha_{\beta_1} t + \frac{|x_{e2}|}{2}\log\left(\frac{|x_{e2}| - \alpha_{\beta_1} t}{|x_{e2}| + \alpha_{\beta_1} t}\right)\right] \quad \text{for} \quad |x_{e2}| > \alpha_{\beta_1} t$$

$$\sigma^e_{y2}(x_{e2}, t, \beta_1) = 0; \quad (45)$$

2 the antiplane problem,

$$u^e_{z2}(x_{e2}, t, \beta_1) = -\frac{D}{\pi p(\beta_1)}\left[\alpha_{\beta_1} t + \frac{|x_{e2}|}{2}\log\left(\frac{\alpha_{\beta_1} t - |x_{e2}|}{\alpha_{\beta_1} t + |x_{e2}|}\right)\right] \quad \text{for} \quad |x_{e2}| \le \alpha_{\beta_1} t$$

$$= -\frac{D}{\pi p(\beta_1)}\left[\alpha_{\beta_1} t + \frac{|x_{e2}|}{2}\log\left(\frac{|x_{e2}| - \alpha_{\beta_1} t}{|x_{e2}| + \alpha_{\beta_1} t}\right)\right] \quad \text{for} \quad |x_{e2}| > \alpha_{\beta_1} t \quad (46)$$

where

$$\alpha_{\beta_1} = p(\beta_1)\cdot\alpha = \sqrt{(1+s)^2\cos^2\beta_1 + \sin^2\beta_1}\cdot\alpha. \quad (47)$$

As in the circular case, the above plane-strain problem can be solved by the self-similar potential technique. The complex potentials for the stretched plane-strain problem are found to be

$$\Phi'(\theta_1, \beta_1) = \frac{4D\alpha^3_{\beta_1} b^2}{\pi p(\beta_1)}\frac{\theta_1^2}{(1 - \alpha^2_{\beta_1}\theta_1^2)^2}$$

$$\Psi'(\theta_2, \beta_1) = \frac{2D\alpha^3_{\beta_1} b^2}{\pi p(\beta_1)}\frac{\theta_2(b^{-2} - 2\theta_2^2)}{(1 - \alpha^2_{\beta_1}\theta_2^2)^2\sqrt{b^{-2} - \theta_2^2}}. \quad (48)$$

The displacement and stress fields for the stretched plane-strain problem can then be determined by substituting the complex potentials Φ' and Ψ' into Eqs. (4).

Similarly, the solution for the antiplane problem determined by Eq. (46) can be found directly using the Smirnov-Sobolev method. The derivative of the complex displacement potential for the stretched antiplane problem is

$$W'(\theta_2, \beta_1) = \frac{2D\alpha^3_{\beta_1}}{\pi p(\beta_1)}\frac{\theta_2}{(1 - \alpha^2_{\beta_1}\theta_2^2)^2}. \quad (49)$$

Substituting the displacement potential W' into Eqs. (6) leads to the displacement and stress fields for the stretched antiplane problem.

Once the stretched plane problems have been solved, the three-dimensional displacement field for the expanding elliptical shear dislocation problem is completely determined by superposing the two-dimensional fields for the stretched plane problems in accordance with Eqs. (43).

8 The Stopping of an Expanding Elliptical Shear Dislocation

The approach to the stopping of a spreading elliptical shear dislocation is the same as that used for the stopping of a circular shear dislocation in Section 5. The expanding elliptical shear dislocation in Section 7 propagates from its nucleation at time $t = 0$ to time $t = t_0$ and is then assumed to stop suddenly. The relative displacement function in the first two boundary conditions of Eqs. (36) is now taken the following form that

Downloaded 04 May 2010 to 171.66.16.34. Redistribution subject to ASME license or copyright; see http://www.asme.org/terms/Terms_Use.cfm

expresses the constancy of the relative displacement distribution on the dislocation plane for $t \geq t_0$:

$$u_x(\varrho_b, t) = D\sqrt{R_0^2 - \varrho_b^2} \quad \text{for} \quad \varrho_b \leq R_0$$
$$= 0 \quad \text{for} \quad \varrho_b > R_0 \tag{50}$$

where

$$R_0 = \alpha t_0 \quad \text{and} \quad \varrho_b(x, z) = \sqrt{\frac{x^2}{(1+s)^2} + z^2}.$$

As in Section 5, the correcting problem starting at $t = t_0$ is developed which, when added to the expanding problem in Section 7, results in the stopping problem for $t \geq t_0$. The boundary conditions on the $y = 0$ plane for the correcting problem are then given by the Eqs. (36) together with the relative displacement function which is the difference of Eqs. (50) and (44):

$$u_x(\varrho_b, t) = D(\sqrt{R_0^2 - \varrho_b^2} - \sqrt{\alpha^2 t^2 - \varrho_b^2}) \quad \text{for} \quad \varrho_b < R_0$$
$$= -D\sqrt{\alpha^2 t^2 - \varrho_b^2} \quad \text{for} \quad R_0 \leq \varrho_b \leq \alpha t$$
$$= 0 \quad \text{for} \quad \varrho_b > \alpha t. \tag{51}$$

The fictitious plane problems corresponding to the correcting problem are determined simply by stretching the results Eqs. (18) and (19) for the circular case. That is, the boundary values for $y_2 = 0^+$ are

1 the plane-strain problem,

$$u_{x2}^e(x_{e2}, t, \beta_1)$$
$$= u_c^e(x_{e2}, t, \beta_1) - u_a^e(x_{e2}, t, \beta_1) \quad \text{for} \quad |x_{e2}| \leq R_{\beta_1}$$
$$= u_d^e(x_{e2}, t, \beta_1) - u_a^e(x_{e2}, t, \beta_1)$$
$$\text{for} \quad R_{\beta_1} < |x_{e2}| \leq \alpha_{\beta_1} t$$
$$= u_d^e(x_{e2}, t, \beta_1) - u_b^e(x_{e2}, t, \beta_1) \quad \text{for} \quad |x_{e2}| > \alpha_{\beta_1} t$$
$$\sigma_{y2}^e(x_{e2}, t, \beta_1) = 0; \tag{52}$$

2 the antiplane problem

$$u_{z2}^e(x_{e2}, t, \beta_1) = -u_{x2}^e(x_{e2}, t, \beta_1) \tag{53}$$

where

$$R_{\beta_1} = R_0 p(\beta_1) = \alpha t_0 p(\beta_1) = \alpha_{\beta_1} t_0 \tag{54}$$

and

$$u_a^e(x_{e2}, t, \beta_1) = \frac{D}{\pi p(\beta_1)} \times \left[\alpha_{\beta_1} t + \frac{|x_{e2}|}{2} \log\left(\frac{\alpha_{\beta_1} t - |x_{e2}|}{\alpha_{\beta_1} t + |x_{e2}|}\right)\right]$$

$$u_b^e(x_{e2}, t, \beta_1) = \frac{D}{\pi p(\beta_1)} \times \left[\alpha_{\beta_1} t + \frac{|x_{e2}|}{2} \log\left(\frac{|x_{e2}| - \alpha_{\beta_1} t}{|x_{e2}| + \alpha_{\beta_1} t}\right)\right]$$

$$u_c^e(x_{e2}, t, \beta_1) = \frac{D}{\pi p(\beta_1)} \times \left[R_{\beta_1} + \frac{|x_{e2}|}{2} \log\left(\frac{R_{\beta_1} - |x_{e2}|}{R_{\beta_1} + |x_{e2}|}\right)\right]$$

$$u_d^e(x_{e2}, t, \beta_1) = \frac{D}{\pi p(\beta_1)} \times \left[R_{\beta_1} + \frac{|x_{e2}|}{2} \log\left(\frac{|x_{e2}| - R_{\beta_1}}{|x_{e2}| + R_{\beta_1}}\right)\right].$$

In a similar manner as in Section 5, the above stretched plane problems corresponding to the correcting problem can also be decomposed into self-similar subproblems with boundary values for $y_2 = 0^+$ in terms of $(x_{L\beta_1}, t')$ or $(x_{R\beta_1}, t')$, where

$$t' = t - t_0 = t - \frac{R_{\beta_1}}{\alpha_{\beta_1}} \quad x_{R\beta_1} = x_{e2} - R_{\beta_1}$$
$$x_{L\beta_1} = x_{e2} + R_{\beta_1} \tag{55}$$

It is not difficult to show that the boundary value distribution $u_{x2}^e(x_{e2}, t, \beta_1)$ in Eqs. (52) for the plane-strain problem can be written as the sum of the following four self-similar distributions:

(P1) $u_{x2}^{eR1}(x_{R\beta_1}, t', \beta_1)$

$$= -\frac{D}{2\pi p(\beta_1)}\left(\alpha_{\beta_1} t' + x_{R\beta_1} \log\left|1 - \frac{\alpha_{\beta_1} t'}{x_{R\beta_1}}\right|\right)$$

(P2) $u_{x2}^{eR2}(x_{R\beta_1}, t', \beta_1) = -\frac{D}{2\pi p(\beta_1)} \cdot R_{\beta_1} \cdot \log\left|1 - \frac{\alpha_{\beta_1} t'}{x_{R\beta_1}}\right|$

(P3) $u_{x2}^{eL1}(x_{L\beta_1}, t', \beta_1)$

$$= -\frac{D}{2\pi p(\beta_1)}\left(\alpha_{\beta_1} t' - x_{L\beta_1} \log\left|1 + \frac{\alpha_{\beta_1} t'}{x_{L\beta_1}}\right|\right)$$

(P4) $u_{x2}^{eL2}(x_{L\beta_1}, t', \beta_1)$

$$= -\frac{D}{2\pi p(\beta_1)} \cdot R_{\beta_1} \cdot \log\left|1 + \frac{\alpha_{\beta_1} t'}{x_{L\beta_1}}\right| \tag{56}$$

Similarly, the distribution $u_{z2}^e(x_{e2}, t, \beta_1)$ in Eq. (53) for the antiplane problem can also be decomposed into four self-similar distributions as below:

(A1) $u_{z2}^{eR1}(x_{R\beta_1}, t', \beta_1) = -u_{x2}^{eR1}(x_{R\beta_1}, t', \beta_1)$

(A2) $u_{z2}^{eR2}(x_{R\beta_1}, t', \beta_1) = -u_{x2}^{eR2}(x_{R\beta_1}, t', \beta_1)$

(A3) $u_{z2}^{eL1}(x_{L\beta_1}, t', \beta_1) = -u_{x2}^{eL1}(x_{L\beta_1}, t', \beta_1)$

(A4) $u_{z2}^{eL2}(x_{L\beta_1}, t', \beta_1) = -u_{x2}^{eL2}(x_{L\beta_1}, t', \beta_1)$ (57)

Each of above self-similar distributions then corresponds to a self-similar subproblem that can be solved by the Smirnov-Sobolev technique as was done for the circular case in Section 5.3, and the results can be summed directly. The solutions are in terms of the complex variables $\theta_i^{R\beta_1}$ or $\theta_i^{L\beta_1}$, which are defined by substituting t' for t and $x_{R\beta_1}$ or $x_{L\beta_1}$ for x in Eqs. (2). Part of the results are given as follows:

(P1) $u_{x2}^e|_{y_2=0^+} = u_{x2}^{eR1}(x_{R\beta_1}, t', \beta_1)$;

$$\sigma_{y2}^e|_{y_2=0} = 0 \quad \text{for} \quad t' \geq 0$$

$$\Phi'(\theta_1^{R\beta_1}, \beta_1) = -\frac{D\alpha_{\beta_1}^2 b^2}{\pi p(\beta_1)} \frac{\theta_1^{R\beta_1}}{(1 - \alpha_{\beta_1}\theta_1^{R\beta_1})^2}$$

$$\Psi'(\theta_2^{R\beta_1}, \beta_1)$$
$$= -\frac{D\alpha_{\beta_1}^2 b^2}{2\pi p(\beta_1)} \frac{b^{-2} - 2\theta_2^{R\beta_1 2}}{(1 - \alpha_{\beta_1}\theta_2^{R\beta_1})^2\sqrt{b^{-2} - \theta_2^{R\beta_1 2}}} \tag{58}$$

Downloaded 04 May 2010 to 171.66.16.34. Redistribution subject to ASME license or copyright; see http://www.asme.org/terms/Terms_Use.cfm

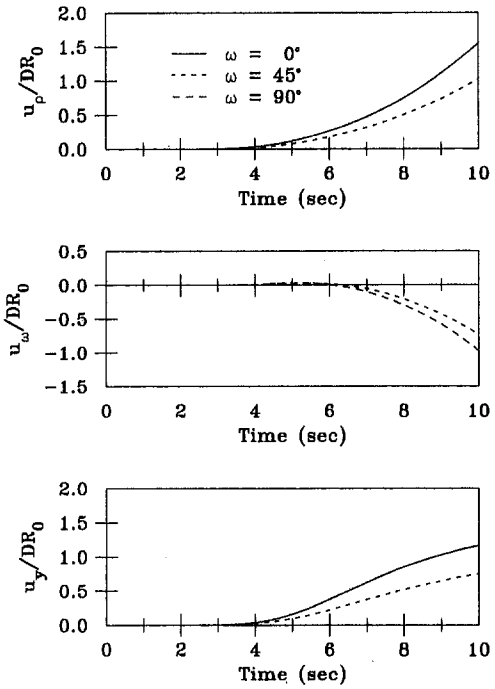


Fig. 2 Response at (ϱ = 10 km, ω, y = 10 km) due to an expanding elliptical shear dislocation (s = 0.5)

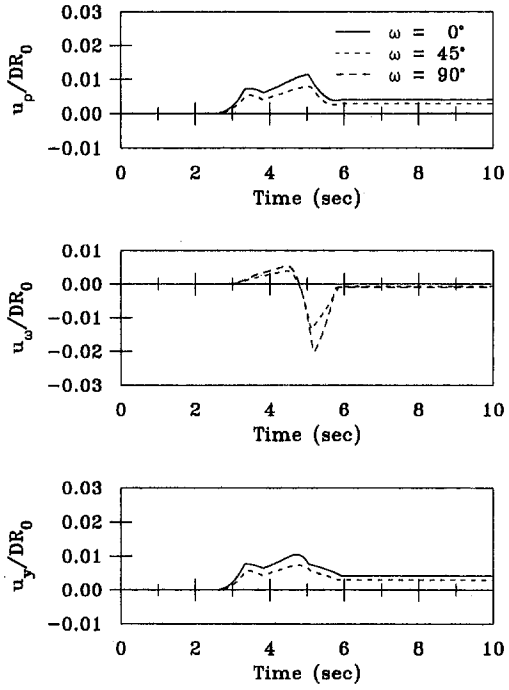


Fig. 3 Response at (ϱ = 10 km, ω, y = 10 km) due to an expanding elliptical shear dislocation (s = 0.5) that stops suddenly at t = 1.04 sec

$$\text{(A1)}\quad u^e_{z2}|_{y_2=0^+} = u^{eR1}_{z2}(x_{R\beta_1}, t', \beta_1) \quad \text{for} \quad t' \geq 0$$

$$W'(\theta_2^{R\beta_1}, \beta_1) = -\frac{D\alpha^2_{\beta_1}}{2\pi p(\beta_1)} \frac{1}{(1 - \alpha_{\beta_1}\theta_2^{R\beta_1})^2}. \quad (59)$$

The remaining calculations to find the solution for the correcting problem are quite straightforward and almost the same as those for the circular case in Section 5.4 except that the rotational superposition is now performed in accordance with Eqs. (43). The solution for the stopping problem that describes the response of the medium for $t \geq t_0$ is simply the sum of those of the expanding problem in Section 7 and of the correcting problem here. The generalization to a layered half-space can be carried out under the restriction noted at the end of Section 5.

9 Numerical Examples

Numerical results for the problem of an elliptical shear dislocation in Fig. 1 (in an infinite homogeneous medium) have been calculated and are discussed in this section. The elliptical dislocation is assumed to expand in the y = 0 plane from a point of nucleation at time t = 0 and then suddenly stops at time t = 1.04 sec. The dynamic responses for two elliptical dislocation sources with different aspect ratios have been computed. In the two cases, the major axes of the ellipses have been kept the same. Figure 3 exhibits the time history of the displacements at some points for the first case (s = 0.5). For the purpose of comparison, the motion due to the same source that does not stop spreading is also shown in Fig. 2. Figure 4 illustrates the response at the same points for the other case (s = 4.0). Because of symmetry, in all cases the radial and vertical displacements are zero when ω = 90 deg, and the circumferential displacement is zero when ω = 0 deg.

From the results, we can easily see that if stopping does not occur, all motions in the three directions are very smooth curves. By contrast, the inclusion of stopping changes the response significantly and involves slope discontinuities. In addition, it can be observed that the effects of the arrivals of P and S waves due to stopping are fairly apparent in Figs. 3 and 4. After all wave fronts pass the point at which the response is calculated, only a static deformation is left in each direction. Regarding the influence of the aspect ratio of the elliptical sources, the results in Figs. 3 and 4 are similar although the magnitudes of the motion are different. The response becomes smaller when the aspect ratio 1 + s is larger because the area on which the dislocation acts then becomes smaller. The effect of a bounding plane is discussed in Lai (1994).

10 Conclusion

A method of solution is presented for three-dimensional problems of circular and elliptical shear dislocations that spread in

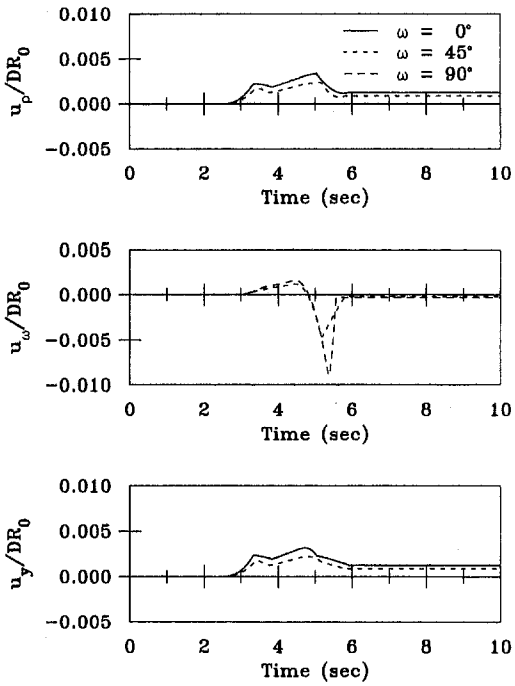


Fig. 4 Response at (ϱ = 10 km, ω, y = 10 km) due to an expanding elliptical shear dislocation (s = 4.0) that suddenly stops at t = 1.04 sec

Downloaded 04 May 2010 to 171.66.16.34. Redistribution subject to ASME license or copyright; see http://www.asme.org/terms/Terms_Use.cfm

an infinite elastic medium and then stop suddenly. This permits solution for a half-space and a layered half-space where all planes of discontinuity are parallel to the plane of the dislocation. Numerical results are given for two cases of elliptical dislocations that spread and then stop abruptly in an unbounded elastic medium.

As expected, the sudden stopping of a spreading dislocation changes the character of the induced motions considerably compared with the case of the same source that keeps expanding. The results suggest that any dynamic faulting process is a very important factor in the development of a seismic source model. In addition to the application to the dislocation problems, the "stopping" approach developed in this study could prove useful in dealing with a number of other problems. In particular, the idea of mixing self-similar solutions having different degrees of homogeneity may point to other applications where there is no apparent self-similarity.

References

Burridge, R., and Knopoff, L., 1964, "Body Force Equivalents for Seismic Dislocations," *Bulletin of the Seismological Society of America,* Vol. 54, pp. 1875–1888.

Burridge, R., and Willis, J. R., 1969, "The Self-Similar Problem of the Expanding Elliptical Crack in an Anisotropic Solid," *Proceedings of the Cambridge Philosophical Society,* Vol. 66, pp. 443–468.

Chinnery, M. A., 1961, "The Deformation of the Ground Around Surface Faults," *Bulletin of the Seismological Society of America,* Vol. 51, pp. 355–372.

Eringen, A. C., and Suhubi, E. S., 1975, *Elastodynamics, Volume II, Linear Theory,* Academic Press, New York.

Hamel, G., 1949, *Integralgleichungen,* Springer-Verlag, Berlin.

Heck, N. H., 1936, *Earthquake,* Princeton University Press, Princeton, NJ.

Johnson, J. J., and Robinson, A. R., 1972, "Wave Propagation in a Half Space Due to an Interior Point Load Parallel to the Surface," Civil Engineering Studies, SRS 388, University of Illinois, Urbana, IL.

Kennett, B. L. N., 1974, "Reflections, Rays, and Reverberations," *Bulletin of the Seismological Society of America,* Vol. 64, pp. 1685–1696.

Kostrov, B. V., 1964, "Self-Similar Problems of Propagation of Shear Cracks," *Journal of Applied Mathematics and Mechanics* (English translation), Vol. 28, pp. 1077–1087.

Lai, G., 1994, "Dynamic Propagation of Shear Dislocations Applied to Seismic Models," Ph.D. dissertation, Department of Civil Engineering, University of Illinois, Urbana, IL.

Lai, G., and Robinson, A. R., 1996, "A Generalized Method of Rotational Superposition for Problems with Elliptical Distribution of Boundary Values," ASME JOURNAL OF APPLIED MECHANICS, Vol. 63, pp. 911–918.

Reid, H. F., 1911, "The Elastic Rebound Theory of Earthquakes," *Bulletin of the Department of Geology, University of California,* Vol. 6, pp. 413–444.

Seyyedian-Choobi, M., and Robinson, A. R., 1975, "Motion on the Surface of a Layered Elastic Half Space Produced by a Buried Dislocation Pulse," Civil Engineering Studies, SRS 421, University of Illinois, Urbana, IL.

Smirnov, V. I., and Sobolev, S. L., 1933, "On the Application of a New Method of Investigation of the Elastic Vibrations in a Space with Axial Symmetry," (in Russian) *Trudy Instituta Seismologii, Akademiya Nauk SSSR,* No. 29.

Thompson, J. C., and Robinson, A. R., 1969, "Exact Solutions of Some Dynamic Problems of Indentation and Transient Loadings of an Elastic Half Space," Civil Engineering Studies, SRS 350, University of Illinois, Urbana, IL.

Trifunac, M. D., and Udwadia, F. E., 1974, "Parkfield, California, Earthquake of June 27, 1966: A Three-Dimensional Moving Dislocation," *Bulletin of the Seismological Society of America,* Vol. 64, pp. 511–533.

Wyss, M., and Brune, J. N., 1967, "The Alaska Earthquake of 28 March 1964: A Complex Multiple Rupture," *Bulletin of the Seismological Society of America,* Vol. 57, pp. 1017–1023.

Downloaded 04 May 2010 to 171.66.16.34. Redistribution subject to ASME license or copyright; see http://www.asme.org/terms/Terms_Use.cfm

Strain-Rate Effects in the Dynamic Buckling of a Simple Elastic-Plastic Model

D. Karagiozova
Bulgarian Academy of Sciences,
Institute of Mechanics,
Acad. G. Bonchev Str., Bl. 4,
1113 Sofia, Bulgaria

N. Jones
Impact Research Centre,
Department of Mechanical Engineering,
The University of Liverpool,
Liverpool L69 3GH, U.K.
Fellow ASME

The phenomenon of dynamic buckling is examined when the influence of material strain-rate sensitivity is retained in the basic equations for a simple elastic-plastic model with linear strain hardening when subjected to an impact by a mass. Two approaches are proposed for taking into account the material strain-rate effects and both use the Cowper-Symonds constitutive equation. The critical impact velocities depend on the impact mass and are determined for a wholly elastic material, a strain-rate insensitive elastic-plastic material and an elastic-plastic material with a dynamic yield force together with linear or nonlinear hardening due to the strain-rate effects. The results obtained show that both strain-rate sensitive models predict impact velocities which are higher than those predicted by the strain-rate insensitive idealization and that the influence of any initial imperfections is important for the three material models considered.

1 Introduction

Dynamic elastic-plastic buckling is a complex phenomenon involving various factors such as inertia forces and material strain-rate sensitivity which play important roles in the response of structures under large dynamic loads. It was observed by Symonds (1967), Jones (1989), and others that the influence of material strain-rate sensitivity exercised a significant effect on the response of structures and should be taken into account for strain-rate sensitive materials. Material strain-rate sensitivity enhances the flow stresses of many materials which increases the decelerations and thereby leads to the generation of large dynamic forces in structures or an unacceptable environment from a human injury perspective.

A simple model is used herein in order to estimate the importance of the strain-rate effects on the dynamic buckling of imperfection sensitive elastic-plastic structures. Such models have been used by many authors to provide insight into the buckling phenomenon. A Shanley-type model for studying static plastic buckling was proposed by Hutchinson (1972) who modified the model presented by Hutchinson and Budiansky (1966) by using bilinear springs to cater for the influence of material plasticity. A further extension of the simple imperfection-sensitive model was undertaken by Jones and dos Reis (1980). This model is a two-degrees-of-freedom system and is illustrated in Fig. 1. It is similar to that employed by Danielson (1969) except that the influence of material plasticity is retained in a manner similar to Hutchinson (1972). The model in Fig. 1 was subjected to a step loading and it was observed that dynamic elastic-plastic buckling was governed by two distinct types of response, which are known as direct and indirect buckling (see Jones and dos Reis, 1980). The influence of the pulse shape and the pulse duration on the critical pulse amplitude was studied by Karagiozova and Jones (1992a, b) using the same model and assuming that plastic reloading was possible. This idealized model takes into account the influence of axial inertia on the characteristics of dynamic buckling.

Simple models of one and two degrees-of-freedom systems for modeling the dynamic buckling of viscoelastic structural elements under a step loading were also studied by Kounadis et al. (1991a, b).

The Cowper-Symonds relation (Symonds, 1965) together with Perrone's simplification (Perrone, 1965) for an elastic-plastic material with linear strain hardening are used herein to study the behavior of the simple model in Fig. 1 when it is struck by a mass M traveling with an initial velocity v_0. This particular case idealizes the practical problem of an object dropped onto a structure, for example. It is observed that retaining the influence of material strain-rate sensitivity in the equations of motion can change significantly the model behavior and, therefore, by implication the response of practical engineering structures.

2 Basic Equations

2.1 Impact by a Mass M Having an Initial Velocity v_0. The imperfection sensitivity of structures which buckle in the plastic range is due to the interaction of geometric and material nonlinearities. Thus, the simple imperfection sensitive elastic-plastic model in Fig. 1, which was proposed by Jones and dos Reis (1980), is used in the present study to examine the influence of material rate-dependent properties. The model in Fig. 1 is subjected to an impact at H by a mass M traveling with an initial velocity v_0. The various members in Fig. 1(a) are rigid and weightless, $m_0 = 0$ and the only mass m_1 is concentrated at A and represents the transverse inertia of an actual structure. The unloaded model has a stress-free initial imperfection $\bar{\xi}$, while the member FHG is constrained to remain horizontal. The spring at A is introduced to bring in a strong nonlinearity in the sense suggested by von Karman et al. (1940) for the elastic buckling of imperfection sensitive structures. The behavior of this nonlinear spring is governed by the quadratic relation $F = \beta\xi^2$, where β is a constant which models the structural softening or hardening for β positive or negative, respectively, and $\xi + \bar{\xi}$ is the total horizontal displacement of A, as indicated in Fig. 1(b). The material behavior is simulated by springs 1 and 2 with the load characteristics shown in Fig. 2, and it is assumed that the springs have identical elastic-plastic characteristics for a strain-rate insensitive material. These springs provide an ideal-

Contributed by the Applied Mechanics Division of THE AMERICAN SOCIETY OF MECHANICAL ENGINEERS for publication in the ASME JOURNAL OF APPLIED MECHANICS.

Discussion on this paper should be addressed to the Technical Editor, Professor Lewis T. Wheeler, Department of Mechanical Engineering, University of Houston, Houston, TX 77204-4792, and will be accepted until four months after final publication of the paper itself in the ASME JOURNAL OF APPLIED MECHANICS.

Manuscript received by the ASME Applied Mechanics Division, Aug. 14, 1995; final revision, Oct. 31, 1995. Associate Technical Editor: S. Kyriakides.

Copyright © 1997 by ASME

Downloaded 04 May 2010 to 171.66.16.34. Redistribution subject to ASME license or copyright; see http://www.asme.org/terms/Terms_Use.cfm

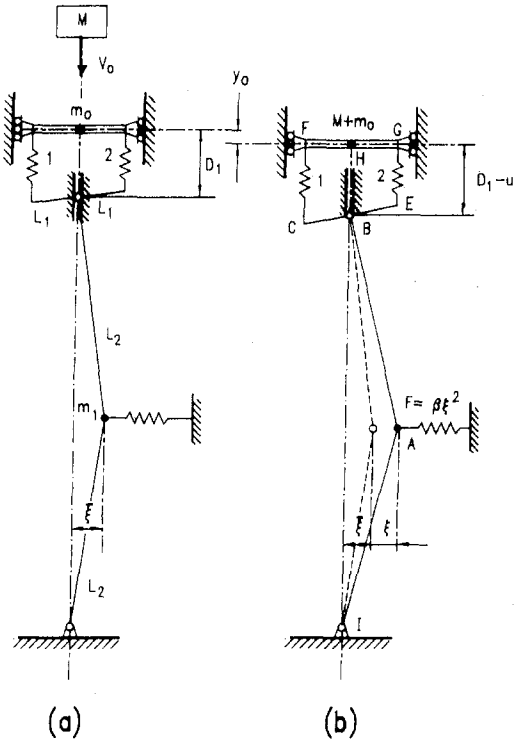


Fig. 1 Simple model, (*a*) initial position, (*b*) deformed position

ization of the axial membrane force and bending moment in an actual structure.

After impact, the mass M remains attached to H so that the model is now the same as that examined by Jones and dos Reis (1980) and Karagiozova and Jones (1992a).

The displacements u_1 and u_2 in springs 1 and 2, respectively, are

$$u_1 = u - r\xi, \quad u_2 = u + r\xi \quad \text{and} \qquad (1a\text{-}c)$$
$$u = y_0 - \xi(\xi + 2\bar{\xi})/L_2$$

provided $(\xi + \bar{\xi})/L_2 \ll 1$ for moderate changes in geometry. In Eqs. (1) y_0 and ξ are the respective vertical and horizontal displacements in Fig. 1, while the dimensionless displacements in springs 1 and 2 are

$$x_\alpha = u_\alpha/L_2, \quad \alpha = 1, 2. \qquad (2)$$

The equations of motion may be written in the dimensionless forms

$$\delta y'' + r^2(Q_1 + Q_2)/2 = 0$$

and

$$z'' - (z + \bar{z})(Q_1 + Q_2) - r(Q_1 - Q_2)/2 - az^2 = 0, \quad (3a, b)$$

where

$$y = y_0/L_2, \quad z = \xi/L_2, \quad \bar{z} = \bar{\xi}/L_2, \quad r = L_1/L_2,$$
$$\omega^2 = 2K/M, \quad \omega_1^2 = 2Kr^2/m_1, \quad \delta = \omega_1^2/\omega^2,$$
$$a = L_2\beta/2Kr^2, \quad P_C = KrL_1, \quad Q_1 = F_1/P_C, \quad Q_2 = F_2/P_C,$$
$$\tau = \omega_1 t \quad \text{and} \quad (\ )' = \partial(\ )/\partial\tau. \qquad (4a\text{-}m)$$

In Eqs. (4), F_1 and F_2 are the corresponding forces in springs 1 and 2, which are taken as positive for compressive loads, P_C is the Euler buckling load, β is a softening parameter for the spring at A (Fig. 1), m_1 is the mass of the model, M is the striking mass, K is the elastic characteristic of the springs in Fig. 2, and t is time. The initial conditions are

$$z(0) = z'(0) = 0 \quad \text{and} \quad y(0) = 0, \quad y'(0) = V_0, \quad (5a\text{-}c)$$

where $V_0 = v_0/L_2\omega_1$.

The dimensionless spring forces Q_α satisfy the relation

$$Q_\alpha = Q_\alpha^0 + \psi_\alpha(x_\alpha - x_\alpha^0)/r^2, \quad \alpha = 1, 2, \qquad (6)$$

where ψ_α is constant during each phase of elastic or plastic spring deformation for a strain-rate insensitive material. Q_α^0 and x_α^0 are the dimensionless forces and deformations at the beginning of each elastic or plastic phase of spring deformation and they remain constant during the associated phase. At $\tau = 0$, $Q_\alpha^0 = 0$ and $x_\alpha^0 = 0$. $\psi_\alpha = 1$, when $Q_\alpha^{\min} \le Q_\alpha \le Q_\alpha^{\max}$, where $Q_\alpha^{\max}$ is the largest dimensionless force in the previous plastic loading of spring α, or the dimensionless yield load $(\Delta_Y L_2/L_1^2)$ when no plastic flow has occurred. $Q_\alpha^{\min}$ is the smallest dimensionless yield load $(-\Delta_Y L_2/L_1^2)$ in tension when no plastic reloading has occurred and $Q_\alpha^{\min} = Q_\alpha^{\max} - 2\Delta_Y L_2/L_1^2$. $\psi_\alpha = \lambda$, when $Q_\alpha \ge Q_\alpha^{\max}$ and $Q_\alpha' > 0$ or when $Q_\alpha < Q_\alpha^{\min}$ and $Q_\alpha' < 0$. The displacement at initial yield in springs 1 and 2 is Δ_Y and the strain hardening parameter λ is K_t/K. Substituting Eqs. (1) and (6) into Eqs. (3), the governing equations of motion become

$$y'' + a_1 y + b_1 z + c_1 z^2 + d_1 = 0$$

and

$$z'' + a_2 y + b_2 z + c_2 z^2 + d_2 yz + e_2 z^3 + f_2 = 0, \quad (7a, b)$$

with the initial conditions from Eqs. (5) and where

$$a_1 = (\psi_1 + \psi_2)/(2\delta),$$
$$b_1 = -[(\psi_1 + \psi_2)\bar{z} + (\psi_1 - \psi_2)r/2]/\delta,$$
$$c_1 = -a_1, \quad d_1 = [(Q_1^0 + Q_2^0)r^2 - (\psi_1 x_1^0 + \psi_2 x_2^0)]/(2\delta),$$
$$a_2 = -(\psi_1 + \psi_2)\bar{z}/r^2 - (\psi_1 - \psi_2)/(2r),$$
$$b_2 = -[Q_1^0 + Q_2^0 - (\psi_1 x_1^0 + \psi_2 x_2^0)/r^2 - 2(\psi_1 + \psi_2)\bar{z}^2/r^2 - 2(\psi_1 - \psi_2)\bar{z}/r - (\psi_1 + \psi_2)/2],$$
$$c_2 = 3(\psi_1 + \psi_2)\bar{z}/r^2 + 3(\psi_1 - \psi_2)/(2r) - a,$$
$$d_2 = (\psi_1 + \psi_2)/r^2, \quad e_2 = -d_2 \quad \text{and}$$
$$f_2 = -[Q_1^0 + Q_2^0 - (\psi_1 x_1^0 + \psi_2 x_2^0)/r^2]\bar{z} - r(Q_1^0 - Q_2^0)/2 + (\psi_1 x_1^0 - \psi_2 x_2^0)/(2r). \quad (8a\text{-}j)$$

These equations are solved by Gear's stiff method (Gear, 1971) using a backward difference formula.

2.2 Influence of Material Strain-Rate Sensitivity. The widely used Cowper-Symonds constitutive equation for a rigid plastic material (Symonds, 1965) is used herein together with Perrone's approximation (Perrone, 1965) for a material with strain hardening. Two approaches are used to take into account the influence of material strain-rate sensitivity. The first method caters for the influence of strain rate on the initial yield force and assumes that the plastic deformations develop during a particular phase of motion with a constant hardening modulus.

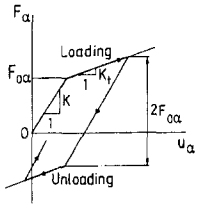


Fig. 2 Elastic-plastic characteristics of springs 1 and 2 for a strain-rate insensitive material

Downloaded 04 May 2010 to 171.66.16.34. Redistribution subject to ASME license or copyright; see http://www.asme.org/terms/Terms_Use.cfm

The second approach takes into account the actual variation of strain rate and, therefore, the flow stress during the whole process of plastic deformation.

2.2.1 Influence of Strain-Rate Sensitivity on the Initial Yield Force for Each Phase of Motion. Perrone's approximation is used to examine the influence of material strain-rate sensitivity on the dynamic response of the model in Fig. 1. Thus, material strain hardening and strain-rate sensitivity effects are uncoupled and the corresponding constitutive equation is expressed in the product form (Jones, 1989)

$$\frac{\sigma_0^d}{\sigma_0} = f(\dot{\epsilon})g(\epsilon), \tag{9}$$

where $\dot{\epsilon}$ is strain rate, $g(\epsilon)$ is a strain-hardening function, σ_0^d is the dynamic yield stress, and

$$f(\dot{\epsilon}) = 1 + \left(\frac{\dot{\epsilon}}{D}\right)^{1/q}, \tag{10}$$

where D and q are empirical parameters[1] in the Cowper-Symonds constitutive equation and $(\dot{\ }) = \partial(\ )/\partial t$.

In the model under consideration, the ratio σ_0^d/σ_0 may be related to the ratio of the dimensionless dynamic yield force $Q_{0\alpha}^d$ and the dimensionless static yield force $Q_{0\alpha}$ in springs 1 and 2. Thus,

$$\frac{Q_{0\alpha}^d}{Q_{0\alpha}} = \left[1 + \left(\frac{\dot{\epsilon}_\alpha}{D}\right)^{1/q}\right] g(\epsilon_\alpha), \tag{11}$$

where $g(\epsilon_\alpha)$ caters for strain hardening.

Now the stable response of the model under an impact by a mass M with an initial velocity v_0 is characterized by alternating phases of elastic and plastic deformations until the model shakes down to a wholly elastic behavior. Let spring α commence to load at $\tau = 0$. The elastic deformation of the model in Fig. 1 is described by Eqs. (7) with $g(\epsilon) = \psi_\alpha = 1$. Plastic deformation begins at $\tau = \tau_1$ when the spring force Q_α reaches the value of the dynamic yield force $Q_{0\alpha}^d$ given by Eq. (11), as shown in Fig. 3.

It is assumed that ψ_α does not depend on time during a phase of plastic deformation. Thus, the spring characteristics are linear but not identical because of the different values of Q_{01}^d and Q_{02}^d. During plastic deformations, the spring force Q_α is governed by the equation

$$Q_\alpha(\tau) = Q_{0\alpha}^d + \frac{\psi_\alpha}{r^2}\left[x_\alpha(\tau) - x_\alpha(\tau_1)\right]. \tag{12}$$

Following Perrone's approximation, the dynamic strength throughout the current phase of motion should correspond to the strain rate at $\tau = \tau_1$. Thus, using Eq. (10)

$$\psi_\alpha = \lambda\left\{1 + \left[\frac{\dot{\epsilon}_\alpha(\tau_1)}{D}\right]^{1/q}\right\}, \tag{13}$$

which means that ψ_α is equal to the static strain-hardening ratio λ when $\dot{\epsilon}_\alpha = 0$.

The model behavior remains plastic while $Q'_\alpha > 0$, and elastic unloading begins at $Q'_\alpha = 0$. If the spring loading is severe enough, then a process of plastic reloading is possible for $\tau \geq \tau_2$ when the reversed yield point is reached at $\tau = \tau_2$

$$Q_\alpha^{\min} = Q_\alpha^{\max} - 2Q_{0\alpha}^d(\tau_2), \tag{14a}$$

where

$$Q_{0\alpha}^d(\tau_2) = \left\{1 + \left[\frac{\dot{\epsilon}_\alpha(\tau_2)}{D}\right]^{1/q}\right\}\frac{\Delta_Y L_2}{L_1^2}.$$

This phase of motion continues while $Q'_\alpha \leq 0$ and a new elastic deformation phase begins when $Q'_\alpha = 0$. If another phase of plastic loading is possible, then the new yield condition is determined from the current value of $\dot{\epsilon}$ at $\tau = \tau_3$ as

$$Q_\alpha^{\max} = Q_\alpha^{\min} + 2Q_{0\alpha}^d(\tau_3), \tag{14b}$$

where

$$Q_{0\alpha}^d(\tau_3) = \left\{1 + \left[\frac{\dot{\epsilon}_\alpha(\tau_3)}{D}\right]^{1/q}\right\}\frac{\Delta_Y L_2}{L_1^2}$$

and τ_3 is the time when the plastic spring deformation phase begins. The current value of the strain rate is used at the beginning of every phase of plastic spring loading (Fig. 3). Thus, the yield conditions for each spring are different and depend on the magnitude of the strain rate. The model response is governed by Eqs. (7) with $\psi_\alpha = 1$ or ψ_α according to Eq. (13).

2.2.2 Influence of Strain-Rate Sensitivity Which is Allowed to Vary During Each Phase of Motion. In this section, the behavior of the model in Fig. 1, which is subjected to an impact by a mass M with an initial velocity v_0, is examined when the dimensionless spring forces Q_α depend on the current value of the strain rate throughout each phase of plastic deformation.

The spring forces Q_α during the elastic loading and unloading phases are

$$Q_\alpha(\tau) = Q_\alpha(\tau^*) + \frac{\psi_\alpha}{r^2}\left[x_\alpha(\tau) - x_\alpha(\tau^*)\right], \tag{15}$$

where $\psi_\alpha = 1$ and τ^* is the time when the spring deformation changes from plastic to elastic. The motion of the model is described by Eq. (7) and the yield forces are determined from Eq. (11).

The spring forces Q_α during the plastic deformation phase depend on the strain, as well as the strain rate. Assume, for a sufficiently small time integration step, that $Q_\alpha(x_\alpha)$ may be approximated linearly

$$Q_\alpha(\tau_{m+1}) = Q_\alpha(\tau_m) + \frac{\psi_\alpha(\tau_m)}{r^2}\left[x_\alpha(\tau_{m+1}) - x_\alpha(\tau_m)\right], \tag{16}$$

where τ_m is the current value of τ at the beginning of each time step and $\tau_{m+1} = \tau_m + \Delta\tau$. Thus, the deformation of the idealized model in Fig. 1 is governed by Eq. (7) but with ψ_α during the plastic deformation phase given as

$$\psi_\alpha(\tau) = f(\dot{\epsilon}_\alpha)g(\epsilon_\alpha) = \left\{1 + \left[\frac{\dot{\epsilon}_\alpha(\tau)}{D}\right]^{1/q}\right\}\lambda, \tag{17}$$

which is not constant and where $\dot{\epsilon}_\alpha = \dot{u}_\alpha/D_1 = \omega_1 x'_\alpha/r$, when $D_1 = L_1$. Thus, using Eqs. (1),

[1] The coefficients D and q have been determined for Mild steel $D = 40.4s^{-1}$, $q = 5$ (Cowper and Symonds, 1957), Aluminium alloy $D = 6500s^{-1}$, $q = 4$ (Bodner and Symonds, 1962), Ti 50A $D = 120s^{-1}$, $q = 9$ (Symonds and Chon, 1974), Stainless steel 304 $D = 100s^{-1}$, $q = 10$ (Forrestal and Sagartz, 1978).

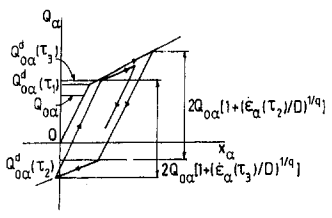


Fig. 3 Elastic-plastic characteristics of spring α for a strain-rate sensitive material (Section 2.2.1)

Downloaded 04 May 2010 to 171.66.16.34. Redistribution subject to ASME license or copyright; see http://www.asme.org/terms/Terms_Use.cfm

$$\psi_1(\tau_m) = \lambda + \lambda\left\{\frac{\omega_1}{rD}[y'_m - (2z_m + 2\bar{z} - r)z'_m]\right\}^{1/q}$$

and

$$\psi_2(\tau_m) = \lambda + \lambda\left\{\frac{\omega_1}{rD}[y'_m - (2z_m + 2\bar{z} + r)z'_m]\right\}^{1/q}. \quad (18a, b)$$

It is evident, when using Eqs. (16) and (18a, b), that the spring characteristics are nonlinear, but they could be linearized at each integration step within the plastic deformation phase (Fig. 4). Thus, the spring characteristics are not identical and depend on the strain-rate magnitude.

Plastic deformations are possible if $Q_\alpha > Q_\alpha^{\max}$ and $Q'_\alpha > 0$ or $Q_\alpha < Q_\alpha^{\min}$ and $Q'_\alpha < 0$, where

$$Q_\alpha^{\max} - Q_\alpha^{\min} = \frac{2\Delta_Y L_2}{L_1^2}\left\{1 + \left[\frac{\dot{\epsilon}_\alpha(\tau^{**})}{D}\right]^{1/q}\right\} \quad (19)$$

and τ^{**} is the time when the deformation changes from elastic to plastic (loading and reloading).

3 Types of Buckling and Stability of the Elastic-Plastic Model

It was observed by Jones and dos Reis (1980) that two types of dynamic buckling of the simple model in Fig. 1 can develop under a step loading when changing the parameter ω_1/ω. The first is called "direct" buckling when the transverse displacements (ξ) of the model at the transition load between a stable and an unstable behavior increase more or less monotonically. The second type is known as an "indirect" buckling since the behavior of the model at the transition load is characterized by small period vibrations modulated by vibrations having a large period and dynamic buckling develops after many cycles. For $r = 1$, a direct buckling of the model is observed for $\omega_1/\omega < 0.5$, while for $\omega_1/\omega > 0.5$ an indirect buckling occurs. This phenomenon can be explained by the fact that the linear terms in the governing equations for the wholly elastic model under a step loading are precisely those that appear in the Mathieu equation and the absence of the nonlinear terms would lead to an instability of the Mathieu type for certain values of ω_1/ω (Budiansky, 1966).

In the case of an impact by a mass M traveling with an initial velocity v_0, the linear parts of Eqs. (7) for $r = 1$ become

$$y'' + y/\delta = 0 \quad \text{and} \quad z'' + z - 2yz = 0 \quad (20a, b)$$

with the initial conditions

$$y(0) = 0, \quad y'(0) = V_0 \quad \text{and}$$
$$z(0) = 0, \quad z'(0) = 0. \quad (21a\text{-}d)$$

This gives a form of Mathieu's equation

$$\frac{d^2z}{d\theta^2} + 4\delta(1 - 2V_0\sqrt{\delta}\cos(2\theta)) = 0, \quad (22)$$

when using $\theta = \pi/4 - \tau/(2\sqrt{\delta})$ and $(d^2z/d\theta^2) = 4\delta z''$. A Mathieu type of instability is often associated with many cycles of oscillations and in this case the damping effects of the nonlinear terms, which are related to the plastic properties of the model, may be expected to alleviate the resonant response.

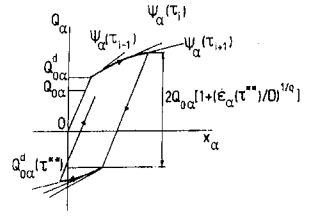


Fig. 4 Elastic-plastic characteristics of spring α for a strain-rate sensitive material (Section 2.2.2)

Because of the axial inertia effect, the response of the elastic-plastic model subjected to a dynamic load, which is less than the critical one, is characterized by a number of alternating elastic and plastic deformations in each of the springs until the model shakes down to a wholly elastic response (Karagiozova and Jones, 1992a) when the dimensionless displacements y and z then remain bounded. The response of the model to higher dynamic loads is characterized by an unbounded increase of the vertical and horizontal displacements during the elastic-plastic spring deformation phases.

A criterion of stability for the model in Fig. 1 with a linear strain-hardening material was suggested by Karagiozova and Jones (1992a). It is based on the intuitive criterion of a shakedown analysis that if the structure is going to shake down then the total amount of plastic energy dissipated over any possible load path must be finite (Konig, 1987). The plastic strain increments at each of the springs change sign during an elastic-plastic cycle tending to cancel each other out and thus providing a finite plastic deformation for a stable model behavior. However, for sufficiently large loads, the strain increments increase during each plastic loading or reloading phase causing unbounded plastic deformations and a loss of stability of the model.

The criterion for the boundedness of the maximum plastic strains of the model may be written as

$$\max_\alpha \lim_{t\to\infty} |\epsilon_\alpha^p| < \infty, \quad \alpha = 1, 2, \quad (23a)$$

or

$$\max_\alpha \lim_{t\to\infty} |\dot{\epsilon}_\alpha^p| \Rightarrow 0, \quad \alpha = 1, 2. \quad (23b)$$

For linear strain-hardening materials, the criterion (23b) is replaced by the increments of the spring forces accumulated during each plastic deformation phase as

$$\max_\alpha \lim_{t\to\infty} (|\Delta Q_\alpha^{\max}|/\Delta\tau_\alpha) \Rightarrow 0, \quad \alpha = 1, 2 \quad (24a)$$

and

$$\max_\alpha \lim_{t\to\infty} (|\Delta Q_\alpha^{\min}|/\Delta\tau_\alpha) \Rightarrow 0, \quad \alpha = 1, 2, \quad (24b)$$

where $\Delta Q_\alpha^{\max}$ and $\Delta Q_\alpha^{\min}$ are the force increments accumulated during the plastic loading and plastic reloading phases, respectively, and $\Delta\tau_\alpha$ are the corresponding time increments. This means that $\Delta Q_\alpha^{\max}$ and $\Delta Q_\alpha^{\min}$ tend to constant values with increase in time and the spring forces will lie between $\Delta Q_\alpha^{\min}$ and $\Delta Q_\alpha^{\max}$, which provides boundedness of the spring deformations $x_\alpha \in [x_\alpha^{\min}, x_\alpha^{\max}]$. This condition ensures that the vertical y and horizontal z displacements are also bounded when using Eqs. (1), (2), and (6). The criteria (24a, b) were used for all the cases considered herein including the nonlinear plastic spring behavior in Section 2.2.

4 Results and Discussion

The behavior of the simple elastic-plastic model in Fig. 1, which is impacted by a mass M travelling with an initial velocity v_0, is presented in Figs. 5 to 11 for strain-rate sensitive and insensitive materials.

In order to compare the model response under a pulse load with the response of the model when it is struck by a mass having an initial velocity, the model parameters suggested by Hutchinson (1972), Jones and dos Reis (1980), and Karagiozova and Jones (1992a) are considered again. The behavior of a model which is made from a strain-rate insensitive material

Downloaded 04 May 2010 to 171.66.16.34. Redistribution subject to ASME license or copyright; see http://www.asme.org/terms/Terms_Use.cfm

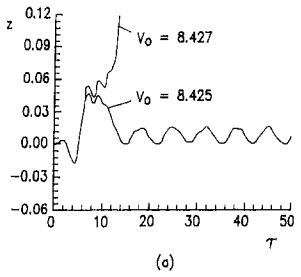


Fig. 5(*a*) Direct buckling, $\omega_1/\omega = 0.3$

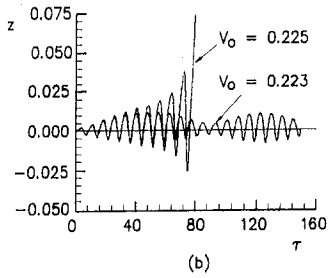


Fig. 5(*b*) Indirect buckling, $\omega_1/\omega = 1.8$

Fig. 5 Model behavior for a strain-rate insensitive material with $\lambda = 0.5$, $\bar{z} = 0.001$, $r = 1$, $a = 10$, $\Delta_Y L_2/L_1^2 = 0.268$, $\Delta\tau = 0.005$

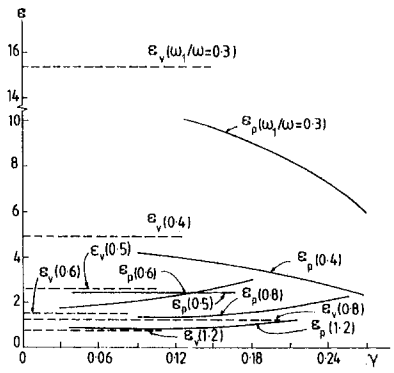


Fig. 6 Comparison between the critical values of the dimensionless energy of buckling for rectangular pressure pulses $\mathfrak{E}_P$ and the dimensionless energy $\mathfrak{E}_V$ of an impact by a mass for different values of ratio ω_1/ω; $\lambda = 0.75$, $\bar{z} = 0.001$, $r = 1$, $a = 10$ and $\Delta_Y L_2/L_1^2 = 0.268$. $\mathfrak{E}_V$ and $\mathfrak{E}_P$ are defined by Eqs. (25*a*, *b*).

is presented in Fig. 5 for the two frequency ratios $\omega_1/\omega = 0.3$ and $\omega_1/\omega = 1.8$. The results in Figs. 5(*a*) and 5(*b*) show two different types of buckling which are known as direct and

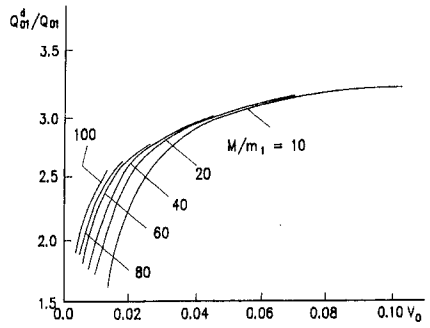


Fig. 7 Variation of the dimensionless initial dynamic yield force Q_{01}^d/Q_{01} with the dimensionless impact velocity V_0 for different mass ratios M/m_1; $\bar{z} = 0.004$, $r = 0.1$, $a = 5$, $\lambda = 0.005$, $\Delta_Y L_2/L_1^2 = 0.28$, $D = 40.4\ \text{sec}^{-1}$, $q = 5$, and $\Delta\tau = 0.002$

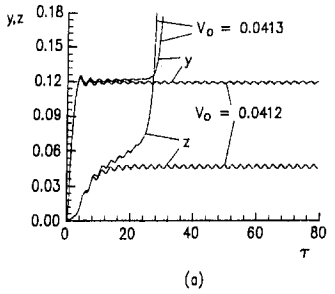


Fig. 8(*a*) Dimensionless displacement-time histories for a strain-rate insensitive material

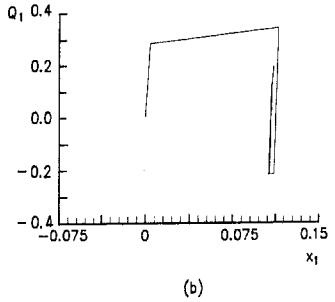


Fig. 8(*b*) Dimensionless force-displacement characteristic of spring 1 for a strain-rate insensitive material when $V_0 = 0.0412$

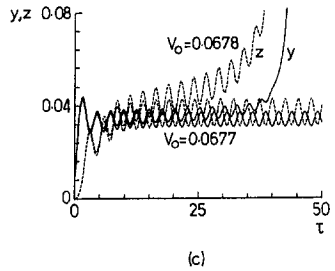


Fig. 8(*c*) Dimensionless displacement-time histories for a strain-rate sensitive material (Eq. (13))

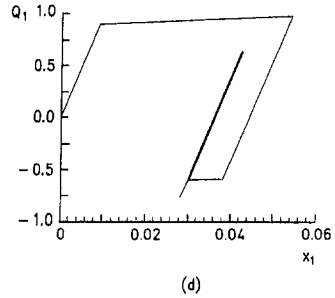


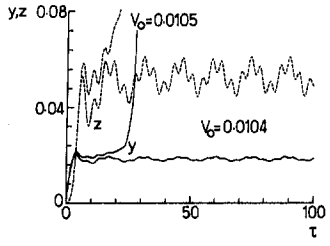
Fig. 8(*d*) Dimensionless force-displacement characteristic of spring 1 for a strain-rate sensitive material (Eq. (13)) when $V_0 = 0.06773$

Fig. 8 Dynamic buckling characteristics for an impact with $M/m_1 = 20$, $\bar{z} = 0.004$, $r = 0.1$, $a = 5$, $\lambda = 0.005$, $\Delta_Y L_2/L_1^2 = 0.28$, $D = 40.4\ \text{sec}^{-1}$, $q = 5$, and $\Delta\tau = 0.002$

indirect buckling, respectively. A similar behavior is observed when the model was subjected to a step loading and $m_0 \neq 0$ (see Jones and dos Reis, 1980).

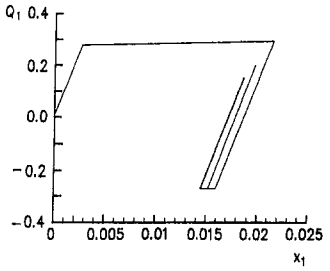
A comparison between the critical values of the dimensionless energy required to cause dynamic buckling ($\mathfrak{E}_V$) of the model in Fig. 1 by a mass M travelling with an initial velocity v_0 and the dimensionless buckling energy for a rectangular pressure pulse ($\mathfrak{E}_P$) having an amplitude P and short duration t_0 is shown in Fig. 6. The dimensionless energies are defined as

Downloaded 04 May 2010 to 171.66.16.34. Redistribution subject to ASME license or copyright; see http://www.asme.org/terms/Terms_Use.cfm



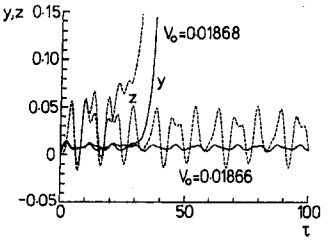
(a)

Fig. 9(*a*) Dimensionless displacement-time histories for a strain-rate insensitive material



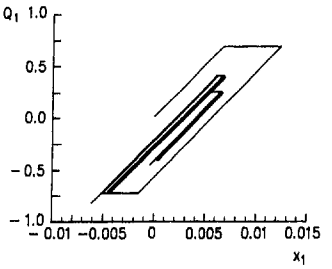
(b)

Fig. 9(*b*) Dimensionless force-displacement characteristic of spring 1 for a strain-rate insensitive material when V_0 = 0.0104



(c)

Fig. 9(*c*) Dimensionless displacement-time histories for a strain-rate sensitive material (Eq. (13))



(d)

Fig. 9(*d*) Dimensionless force-displacement characteristic of spring 1 for a strain-rate sensitive material (Eq. (13)) when V_0 = 0.01866

Fig. 9 Dynamic buckling characteristics for an impact with M/m_1 = 100, $\bar{z}$ = 0.004, r = 0.1, a = 5, λ = 0.005, $\Delta_Y L_2/L_1^2$ = 0.28, D = 40.4 sec^{-1}, q = 5, and $\Delta\tau$ = 0.002

$$\mathcal{E}_V = (Mv_0^2/2)/(m_1 L_2^2 \omega_1^2/2) = V_0^2 \delta / r^2$$

and

$$\mathcal{E}_P = \frac{2}{m_1 L_2^2 \omega_1^2} \int_0^{t_0} P \frac{dy_0}{dt}\, dt$$

$$= \bar{P} \int_0^{\tau_0} y' d\tau,\ \bar{P} = P/KrL_1, \qquad (25a, b)$$

which is obtained from the results presented by Karagiozova and Jones (1992a). The parameter γ in Fig. 6 is the ratio of

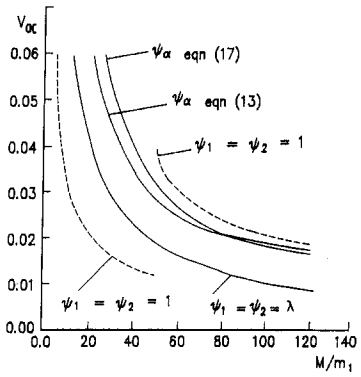


Fig. 10 Variation of the dimensionless critical impact velocity, V_{0c}, with the mass ratio M/m_1; $\bar{z}$ = 0.004, r = 0.1, a = 5, λ = 0.005, $\Delta_Y L_2/L_1^2$ = 0.28, D = 40.4 sec^{-1}, q = 5

the pulse duration to the natural period of the horizontal elastic vibrations of the model. It is evident that as γ decreases for short pulse durations the dimensionless energy $\mathcal{E}_P$ tends towards $\mathcal{E}_V$. However, this tendency is different for the two types of buckling. In the case of a direct buckling ($\omega_1/\omega < 0.5$) the dimensionless pulse energy ($\mathcal{E}_P$) increases as γ decreases, while $\mathcal{E}_P$ decreases for an indirect buckling which occurs when $\omega_1/\omega > 0.5$.

This phenomenon is related to the different histories of the spring deformations for the two kinds of buckling (see Karagiozova and Jones, 1992a). Indirect buckling is characterized by a large number of elastic-plastic cycles in each of the springs before instability occurs so that a large amount of energy can be absorbed for longer pulses. A small number of elastic-plastic cycles occurs, by way of contrast, in the case of direct buckling.

The results presented in Figs. 7–11 show the behavior of the simple imperfection sensitive elastic-plastic model when subjected to an axial impact. The various results are presented for a short mild steel column having E = 200 GPa, σ_y = 280 MPa, r = 0.1, $\bar{z}$ = 0.004 and λ = 0.005. The hardening parameter λ is determined as a ratio between the tangent modulus, E_t, and Young's modulus, E, from the equation

$$\sigma_u = \sigma_y + \lambda E \epsilon_u, \qquad (26)$$

where σ_y is the uniaxial yield stress and σ_u and ϵ_u are the stress and strain at the ultimate stress in an axial tensile test, respectively, and in this particular case are taken as σ_u = 480 MPa and ϵ_u = 0.2.

If it is assumed that the vibration frequency of the model, ω_1, is equal to the first vibration frequency of an elastic column having a rectangular cross section, then the dimensional initial velocity v_0 may be expressed as $v_0 = V_0 L_2 \omega_1 = \pi^2 r c V_0/(4\sqrt{3})$, where c is the elastic wave propagation speed.

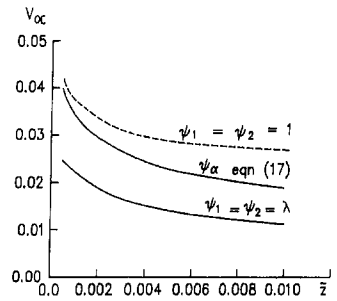


Fig. 11 Variation of the dimensionless critical impact velocity, V_{0c}, with the initial imperfections, $\bar{z}$, for different material models; M/m_1 = 60, r = 0.1, a = 5, λ = 0.005, $\Delta_Y L_2/L_1^2$ = 0.28, D = 40.4 sec^{-1}, q = 5

Downloaded 04 May 2010 to 171.66.16.34. Redistribution subject to ASME license or copyright; see http://www.asme.org/terms/Terms_Use.cfm

The increase of the initial dimensionless dynamic yield force in spring 1, Q_{01}^d, with the dimensionless initial impact velocity, V_0, for different mass ratios is presented in Fig. 7. It is evident that the yield force Q_{01}^d is sensitive to the velocity for small initial velocities when the larger impact masses cause higher yield forces for a given value of V_0. For higher impact velocities the dimensionless dynamic yield forces tend to a curve which is almost independent of the impact mass.

Figures 8(a–d) show the dynamic buckling characteristics of the simple model when it is subjected to an impact by a relatively small impact mass ($M/m_1 = 20$). The time-displacement histories in Fig. 8(a) for a strain-rate insensitive material show that at the dimensionless transition velocity $V_0 = 0.0412$ the stable model behavior is characterized by larger dimensionless displacements (y) than the dimensionless horizontal ones (z). A significant amount of energy is absorbed during the first phase of plastic loading of the springs (see Fig. 8(b) when they are compressed to the maximum dimensionless displacements; e.g., $x_1 = 0.1153$ in spring 1. After that only two additional reloading phases of plastic deformation are observed. The dynamic buckling of the model for a strain-rate sensitive material is presented in Fig. 8(c) where the values of D and q are selected for a hot rolled mild steel (Symonds, 1967; Jones, 1989). In this case, the dimensionless vertical and horizontal displacements are comparable at the larger transition dimensionless impact velocity of $V_0 = 0.06773$. The first plastic phase of the spring deformation is responsible for the absorption of a large amount of energy, but the maximum value of the dimensionless spring deformation, $x_1 = 0.054$ in Fig. 8(d) is less than one-half that for the strain-rate insensitive case in Fig. 8(b). The elastic unloading of the spring in Fig. 8(d) is followed by a significant plastic deformation upon reloading. After the completion of this phase a number of elastic-plastic cycles with very short phases of plastic loading and reloading occur until the model shakes down to a wholly elastic response when the force in spring 1 remains between $Q_1 = -0.32$ and $Q_1 = 0.24$.

The dynamic buckling characteristics of the same model in Fig. 8(a–d), but impacted by a larger mass ($M/m_1 = 100$) are presented in Fig. 9(a–d). The response of the strain-rate insensitive model at the dimensionless transition impact velocity of $V_0 = 0.0104$ (Fig. 9(a)) is different from the model response to the smaller impact mass in Fig. 8(a). Now the dimensionless horizontal displacements (z) are much larger than the dimensionless axial ones (y) because of the larger inertia of the impact mass. Thus, the dynamic buckling of the model when impacted by a small mass is accompanied by large axial compressive plastic deformations, while the plastic deformations of the model subjected to an impact by a large mass are due mainly to the buckling phenomenon producing large transverse deformations. The same phenomenon is observed when comparing the results for the strain-rate sensitive materials in Figs. 8(c) and 9(c), although the difference is not so marked because the material strain-rate sensitivity effect produces an enhanced dynamic yield force which allows the model to respond with large elastic displacements during the initial elastic spring deformation phase. A considerable difference between the behavior of the model for strain-rate insensitive and sensitive materials is observed in Figs. 9(b) and 9(d), which present the spring deformation histories at the corresponding transition velocities until the model shakes down to a wholly elastic response. For the strain-rate insensitive material (Fig. 9(b)), the energy is absorbed largely during the first phase of the plastic spring loading after which only a few elastic-plastic cycles occur. The process of spring deformation for the strain-rate sensitive material is characterized by a large number of elastic-plastic cycles and energy is absorbed during both the plastic loading and reloading phases.

The results presented in Figs. 8 and 9 also show that the critical dimensionless buckling energy decreases more rapidly for a strain-rate insensitive material than for a sensitive one. The critical energy for $M/m_1 = 20$ and a strain-rate insensitive material is $\mathcal{E}_V = 0.01697$, while for $M/m_1 = 100$ it is only 31.87 percent as large, or $\mathcal{E}_V = 0.005408$. The dimensionless buckling energies for a strain-rate sensitive material at the corresponding mass ratios are $\mathcal{E}_V = 0.04624$ and $\mathcal{E}_V = 0.0162$, respectively. The reduction in this case is 35 percent, approximately.

The variation of the dimensionless critical impact velocity with the mass ratio, M/m_1, is presented in Fig. 10 for several material idealizations: wholly elastic material, elastic-plastic strain-rate insensitive material, and linear and nonlinear material models catering for the strain-rate effects. The discontinuity in the elastic stability boundary arises from a Mathieu-type instability but the damping due to the plastic properties of the material causes considerable changes in the stability boundaries (Karagiozova and Jones, 1995a). Both of the strain-rate sensitive models predict impact velocities which are higher than those predicted by the strain-rate insensitive idealization and the nonlinear approximation of the stress-strain plastic relation gives the highest velocities for $M/m_1 < 75$, approximately. For higher mass ratios the behavior of the model at the transition velocity is characterized by a large number of elastic-plastic deformation cycles of the springs but having short phases of plastic loading and reloading. During the plastic deformation phases the strain rates $\dot{\epsilon}_\alpha$ do not change significantly between the beginning and the end of the corresponding phases, so for $M/m_1 > 70$, both strain-rate sensitive models predict similar critical impact velocities. The strain-rate effect, therefore, essentially only increases the dynamic yield force.

The variation of the dimensionless critical impact velocity, V_0, with the dimensionless initial imperfections, $\bar{z}$, is presented in Fig. 11. It is evident that the influence of the initial imperfections is important for the three material models.

Results are presented in Fig. 12 for hypothetical materials having $\sigma_y = 280$ MPa and different hardening moduli in order to examine the sensitivity of the critical velocity, V_{0c}, to the strain rate model. ΔV_{0c}^p is the difference between the critical velocity obtained using the nonlinear elastic-plastic model (Eq. (17)) and the critical velocity corresponding to the linear one (Eq. (13)), where V_{0c}^e is the critical elastic velocity. It is evident that the nonlinear effects during the plastic deformation phases are more significant for hardening ratios λ which lie between 0.005 and 0.1.

The proposed model has been used to predict the dynamic elastic-plastic behavior and energy absorbing properties of a simple plate structure when subjected to low velocity impacts up to 6 m/s (Karagiozova and Jones, 1995b). Good agreement was achieved between the experimental results (Tam and Calladine, 1991) and the theoretical predictions for specimens made of a rate sensitive material (mild steel) as well as specimens made from a strain-rate insensitive material (Al HP–30). Some further discussion on the relevance of the model in Fig. 1 for actual engineering problems is given by Karagiozova and

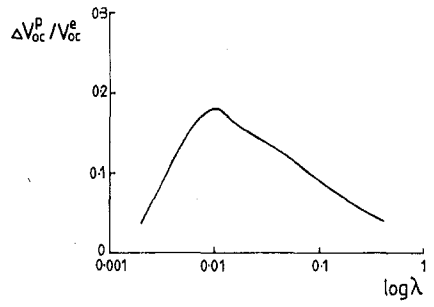


Fig. 12 Sensitivity of the critical impact velocity, V_{0c}, to the strain-hardening parameters; $M/m_1 = 64$, $\bar{z} = 0.004$, $r = 0.1$, $a = 5$, $\Delta_V L_2/L_1^2 = 0.28$, $D = 40.4\ \text{sec}^{-1}$, $q = 5$

Downloaded 04 May 2010 to 171.66.16.34. Redistribution subject to ASME license or copyright; see http://www.asme.org/terms/Terms_Use.cfm

Jones (1995a), where various relationships were developed between the parameters for the model and actual engineering structures. The two-degrees-of-freedom model in Fig. 1 is only expected to be suitable for idealizing low-velocity impacts since higher buckling modes would be developed in actual structures subjected to high impact velocities (Lindberg and Florence, 1987; Jones, 1989). Recently, a multi-degree-of-freedom model was proposed in order to explore some important features of the dynamic buckling phenomenon when higher buckling modes develop in elastic-plastic structures (Karagiozova and Jones, 1996).

5 Conclusions

The imperfection-sensitive two-degrees-of-freedom model in Fig. 1, which has elastic-plastic springs to cater for the material properties, is subjected to an axial impact by a mass traveling with an initial velocity.

The influence of material strain-rate sensitivity on the dynamic buckling of a simple model is studied using the Cowper-Symonds constitutive equation together with Perrone's simplification for an elastic-plastic material with linear strain hardening. The numerical results show that the dynamic yield force depends mainly on the impact velocity and is sensitive to the impact mass only for large ratios of M/m_1. The decrease of the strain-rate magnitudes in an idealized model during plastic deformations causes nonlinear material hardening, while static hardening would be linear. Nevertheless, the linear dynamic hardening model, which takes into account only the strain rate at the initial stage of plasticity, provides a good estimate of the influence of material strain-rate sensitivity, at least for the parameters examined in this paper.

The influence of material strain-rate sensitivity plays an important role on the magnitude of the critical impact velocity which is larger than that for the strain-rate insensitive case.

The imperfection sensitivity is somewhat similar for all of the material models examined in this paper.

Acknowledgments

The authors wish to express their gratitude to the British Council and to the Bulgarian National Research Fund (Project MM–77/92) for their support of the collaboration between the Impact Research Centre in the Department of Mechanical Engineering at the University of Liverpool and the Institute of Mechanics of the Bulgarian Academy of Sciences in Sofia. The authors are indebted to Mr. F. J. Cummins and Mr. H. Parker for their preparation of the drawings.

References

Bodner, S. R., and Symonds, P. S., 1962, "Experimental and Theoretical Investigation of the Plastic Deformation of Cantilever Beams subjected to Impulsive Loading," ASME JOURNAL OF APPLIED MECHANICS, Vol. 29, pp. 719–728.

Budiansky, B., 1966, "Dynamic Buckling of Elastic Structures: Criteria and Estimates," *Dynamic Stability of Structures,* Pergamon Press, New York, pp. 83–106.

Cowper, G. R., and Symonds, P. S., 1957, "Strain Hardening and Strain-Rate Effects in the Impact Loading of Cantilever Beams," Brown University Division of Applied Mathematics Report No. 28, Sept., 1957.

Danielson, D. A., 1969, "Dynamic Buckling Loads of Imperfection-Sensitive Structures from Perturbation Procedures," *AIAA Journal,* Vol. 7, No. 8, pp. 1506–1510.

Forrestal, M. J., and Sagartz, M. J., 1978, "Elastic-Plastic Response of 305 Stainless Steel Beams to Impulsive Loads," ASME JOURNAL OF APPLIED MECHANICS, Vol. 45, pp. 685–687.

Gear, C. W., 1971, *Numerical Initial Value Problem in Ordinary Differential Equations,* Prentice-Hall, Englewood Cliffs, NJ.

Hutchinson, J. W., 1972, "On the Post-Buckling Behaviour of Imperfection-Sensitive Structures in the Plastic Range," ASME JOURNAL OF APPLIED MECHANICS, Vol. 39, pp. 155–162.

Hutchinson, J. W., and Budiansky, B., 1966, "Dynamic Buckling Estimates," *AIAA Journal,* Vol. 4, No. 3, pp. 525–530.

Jones, N., 1989, *Structural Impact,* Cambridge University Press, Cambridge, UK.

Jones, N., and dos Reis, H. L. M., 1980, "On the Dynamic Buckling of a Simple Elastic-Plastic Model," *Int. J. Solid Struct.,* Vol. 16, pp. 969–989.

Karagiozova, D., and Jones, N., 1992a, "Dynamic Pulse Buckling of a Simple Elastic-Plastic Model Including Axial Inertia," *Int. J. Solid Struct.,* Vol. 29, No. 10, pp. 1255–1272.

Karagiozova, D., and Jones, N., 1992b, "Dynamic Buckling of a Simple Elastic-Plastic Model under Pulse Loading," *Int. J. Non-Linear Mechs.,* Vol. 27, No. 6, pp. 981–1005.

Karagiozova, D., and Jones, N., 1995a, "Some Observations on the Dynamic Elastic-Plastic Buckling of a Structural Model," *Int. J. Impact Engng.,* Vol. 16, No. 4, pp. 621–635.

Karagiozova, D., and Jones, N., 1995b, "A Note on the Inertia and Strain-Rate Effects in the Tam and Calladine Model," *Int. J. Impact Engng.,* Vol. 16, No. 4, pp. 637–649.

Karagiozova, D., and Jones, N., 1996, "Multi-degrees of Freedom Model for Dynamic Buckling of an Elastic-Plastic Structure," *Int. J. Solid Struct.,* Vol. 33, No. 23, pp. 3377–3398.

Kounadis, A. N., Malles, J., and Raftoyiannis, J., 1991a, "Dynamic Buckling Estimates of Discrete Systems under Step Loading," *ZAMM,* Vol. 71, No. 10, pp. 391–402.

Kounadis, A. N., 1991b, "Nonlinear Dynamic Buckling of Discrete Dissipative or Nondissipative Systems under Step Load," *AIAA Journal,* Vol. 29, No. 2, pp. 280–289.

Konig, J. A., 1987, *Shakedown of Elastic-Plastic Structures,* Elsevier, New York.

Lindberg, H. E., and Florence, A. L., 1987, *Dynamic Pulse Buckling,* Martinus Nijhoff, Norwell, MA.

Perrone, N., 1965, "On the Simplified Method for Solving Impulsively Loaded Structures of Rate-Sensitive Materials," ASME JOURNAL OF APPLIED MECHANICS, Vol. 32, pp. 489–492.

Symonds, P. S., 1965, "Viscoplastic Behaviour in Response of Structures to Dynamic Loading," *Behaviour of Materials Under Dynamic Loading,* N. J. Huffington, ed., ASME, New York, pp. 106–124.

Symonds, P. S., 1967, "Survey of Methods of Analysis for Plastic Deformation of Structures under Dynamic Loading," Brown University., Division of Engineering, Report BU/NSRDC/1-67.

Symonds, P. S., and Chon, C. T., 1974, "Approximation Techniques for Impulsive Loading of Structures of Time-Dependent Plastic Behaviour with Finite Deflections," *Mechanical Properties of Materials at High Strain Rates,* Institute of Physics Conference Series, No. 21, pp. 299–316.

Tam, L. L., and Calladine, C. R., 1991, "Inertia and Strain-Rate Effects in a Simple Plate Structure under Impact Loading," *Int. J. Impact Engng.,* Vol. 11, pp. 349–377.

von Karman, T., Dunn, L. G., and Tsien, H.-S., 1940, "The Influence of Curvature on the Buckling Characteristics of Structures," *J. Aeronaut. Sci.,* Vol. 7, pp. 276–289.

Downloaded 04 May 2010 to 171.66.16.34. Redistribution subject to ASME license or copyright; see http://www.asme.org/terms/Terms_Use.cfm

W. R. Qualls
Research Associate,
Lecturer,
Mem. ASME.

J. K. Good
Professor,
Noble Research Fellow,
Mem. ASME.

Department of Mechanical and
Aerospace Engineering,
Oklahoma State University,
Stillwater, OK 74078

An Orthotropic Viscoelastic Winding Model Including a Nonlinear Radial Stiffness

A realistic and adaptive viscoelastic model for prediction of transient wound roll stress distributions is presented. The web material is taken to be orthotropic with a nonlinear radial stiffness dependent upon interlayer pressure. Viscoelastic behavior is represented by a generalized Maxwell model for creep written as a convolution integral. Numerical solutions to the resulting integral boundary value problem give both initial and transient stress distributions within the wound roll. The model is successfully compared to the analytical solution for a simple case of isotropy as well as to published works on this topic. In contrasting the solutions, the advantages and adaptability of this formulation will be readily seen.

Introduction

Wound structures, termed rolls, built by winding thin webs with little or no resistance to bending, such as paper, polymeric films, or magnetic tape, onto a compliant core develop both radial and circumferential stress distributions along their radii. Due to the viscoelastic nature of most polymers and many paper products, the stress distributions within many rolls are dependent upon both storage environment and time. Rolls wound from viscoelastic material are prone to decreasing stress profiles and if stored for prolonged periods of time, may experience significant reduction in resident stresses. If the interlayer stresses are substantially reduced, the roll structure is subject to damage during transportation or subsequent rewind operations. Foreknowledge of transient stress distributions allow operating parameters or rewind schedules to be devised such that structural integrity of the wound roll can be maintained. This paper provides a simulation technique which may be used to predict transient wound roll stress distributions where optimum winding parameters and roll geometry may be chosen.

Detailed analysis of initial wound roll stresses began with the work of Gutterman (1959). Altmann (1968) followed and presented an analytical solution to the winding problem by assuming homogeneous and anisotropic elastic web properties constant throughout the roll. Yogada (1980) was the first to accurately treat the inner boundary condition, which accounted for core deformation. Pfeiffer (1966) included a nonlinear radial stiffness, written as an exponential, and provided an approximate solution to the elastic case using an energy balance formulation which neglected core flexibility. Prediction of initial wound roll stresses was modernized by Hakiel (1987) who presented a numerical method employing a pressure-dependent radial stiffness. Hakiel solved the resulting nonlinear second-order differential equation using finite difference techniques by employing two boundary conditions including (1) that the deformation of the first layer be equal to the deformation of the core and (2) that the webline tension be equal to the wound-on-tension in the current outer layer of the winding roll. These boundary conditions are suitable for the condition of centerwinding, and Hakiel verified his method for that condition. In centerwinding, the roll is wound through the provision of torque applied to the core with no driven or undriven rolls impinged on the outer surface of the winding roll.

Transient analysis of wound roll stresses was first considered by Tramposch (1965, 1967) who modeled viscoelastic web behavior with a Maxwell-Kelvin constitutive law. Tramposch's first work assumed roll isotropy; however, he later allowed for the circumferential and radial modulus to differ by a multiplicative constant. Lin and Westmann (1989) expanded the work in viscoelastic winding mechanics by accounting for winding time in the analysis. Lin and Westmann assumed roll isotropy and chose a generalized Maxwell model to describe the roll's viscoelastic behavior. Still, no author has coupled the nonlinear orthotropic attributes of a wound roll with a complex viscoelastic constitutive relation.

In this paper, a realistic orthotropic viscoelastic model for centerwound rolls is presented. Viscoelastic behavior of the wound structure is characterized by a generalized Maxwell model with allowance for pressure dependent radial behavior. Choice of a generalized Maxwell model enables accurate portrayal of most any material behavior since the number of retardation times is limited only by computational resources. Results are compared to an analytical solution developed herein for a simplified isotropic case with one time constant. In addition, this work is successfully compared to the published works of Tramposch and to that of Lin and Westmann.

Governing Equations

The process of winding has historically been viewed as the addition of pretensioned concentric hoops of web material onto a compliant core. The process is then one of accretion in which the stresses in the roll are incrementally changed as each layer is added. Assuming the wound roll is axisymmetric dictates the stresses, strains, and displacements are functions only of roll radius. The governing equations in polar coordinates are the following:

Equilibrium Equation

$$r\frac{\partial \sigma_r}{\partial r} + \sigma_r - \sigma_\theta = 0; \tag{1}$$

Strain Compatibility Equation

$$r\frac{\partial \epsilon_\theta}{\partial r} + \epsilon_\theta - \epsilon_r = 0; \tag{2}$$

Contributed by the Applied Mechanics Division of THE AMERICAN SOCIETY OF MECHANICAL ENGINEERS for publication in the ASME JOURNAL OF APPLIED MECHANICS.

Discussion on this paper should be addressed to the Technical Editor, Professor Lewis T. Wheeler, Department of Mechanical Engineering, University of Houston, Houston, TX 77204-4792, and will be accepted until four months after final publication of the paper itself in the ASME JOURNAL OF APPLIED MECHANICS.

Manuscript received by the ASME Applied Mechanics Division, Sept. 11, 1995; final revision, Mar. 23, 1996. Associate Technical Editor: W. J. Drugan.

Copyright © 1997 by ASME

Downloaded 04 May 2010 to 171.66.16.34. Redistribution subject to ASME license or copyright; see http://www.asme.org/terms/Terms_Use.cfm

Strain-Displacement Relation

$$\epsilon_r = \frac{\partial u}{\partial r} \quad \epsilon_\theta = \frac{u}{r}; \tag{3}$$

Viscoelastic Constitutive Equations

$$\epsilon_r = \int_0^t \left[J_r(t-t') \frac{\partial \sigma_r}{\partial t'} + J_{r\theta}(t-t') \frac{\partial \sigma_\theta}{\partial t'} \right] dt'; \tag{4}$$

$$\epsilon_\theta = \int_0^t \left[J_\theta(t-t') \frac{\partial \sigma_\theta}{\partial t'} + J_{\theta r}(t-t') \frac{\partial \sigma_r}{\partial t'} \right] dt'; \tag{5}$$

where $J_r(t)$ and $J_\theta(t)$ are the radial and circumferential creep functions, respectively, and $J_{r\theta}(t)$ and $J_{\theta r}(t)$ are Poisson creep functions that are analogous to the elastic ratios $-\nu_{r\theta}/E_\theta$ and $-\nu_{\theta r}/E_r$, respectively. Specifically, $J_{r\theta}(t)$ characterizes the amount of radial strain caused by an applied circumferential stress, and $J_{\theta r}(t)$ relates the amount of circumferential strain caused by an applied radial stress. Both $J_{r\theta}(t)$ and $J_{\theta r}(t)$ are defined independently based upon the findings of Willett and Poesch (1988), who showed the value of the radial elastic Poisson's ratio, $\nu_{\theta r}$, differed from that calculated by assuming the compliance matrix is symmetric. As no experimental measures of the radial viscoelastic Poisson's ratio appear in open literature, the governing equations presented in this text are written in terms of four independent creep functions such that the general case may be well represented. These equations are easily simplified for specific application in the event symmetry of the compliance matrix is perceived or experimentally verified. Also note that u, ϵ_r, ϵ_θ, σ_r, and σ_θ are implied functions of time and that t' is integrated over as a variable of integration. Model development continues by eliminating the circumferential stress, σ_θ, by solving (1) for σ_θ and substituting the result into (4) and (5). This yields two equations, one for the radial strain and the other for the circumferential strain. These equations describing the radial strain, ϵ_r, and circumferential strain, ϵ_θ, are substituted into the compatibility Eq. (2). This treatment leads to the following integral boundary value problem written as a second order partial differential equation in terms of radial stress, σ_r, the radius, r, and time, t.

$$\int_0^t \left[J_\theta(t-t') \frac{\partial}{\partial t'} \left(r^2 \frac{\partial^2 \sigma_r}{\partial r^2} \right) + \left\{ 3J_\theta(t-t') + J_{\theta r}(t-t') - J_{r\theta}(t-t') + r \frac{\partial}{\partial r} J_\theta(t-t') \right\} \frac{\partial}{\partial t'} \left(r \frac{\partial \sigma_r}{\partial r} \right) + \left\{ r \frac{\partial}{\partial r} (J_\theta(t-t') + J_{\theta r}(t-t')) + J_\theta(t-t') + J_{\theta r}(t-t') - J_r(t-t') - J_{r\theta}(t-t') \right\} \frac{\partial \sigma_r}{\partial t'} \right] dt' = 0 \tag{6}$$

Solution Method

The method of solution consists of first choosing the generalized Maxwell model to represent the viscoelastic behavior. With this choice, the creep compliance takes the following form:

$$J(t-t') = J_o + \sum_{i=1}^{N} J_i e^{-(t-t')/\tau_i} \tag{7}$$

The generalized Maxwell model provides for instantaneous deformation followed by time-dependent deformation, termed creep, when subjected to a step change in stress. For an orthotropic material, the creep compliance in the radial and circumferential directions must be defined independently. Pfeiffer (1966) and Hakiel (1987) have shown the instantaneous radial stiffness to be a function of interlayer pressure. As a result, J_0 of the radial creep function must be a function of the radial stress. At this point, special treatment of the nonlinear behavior is not required but will be handled during the accretion process. Each integral in the boundary value problem can now be analyzed separately. All terms in Eq. (6) can be segregated into the two distinct forms defined in Eqs. (8) and (9).

$$I = \int_0^t J(t-t') \frac{\partial f}{\partial t'} dt' \tag{8}$$

$$II = \int_0^t r \frac{\partial}{\partial r} [J(t-t')] \frac{\partial f}{\partial t'} dt' \tag{9}$$

First, integral I is discretized over time in either constant or in some cases variable intervals by replacing the continuous function, f, with a step function. The integral I can then be written at some time $t = t_j$ as follows:

$$I_j = J(t_j - t_{j-1})(\partial f/\partial t)_j \Delta t + J(t_j - t_{j-2})(\partial f/\partial t)_{j-1} \Delta t + \ldots + J(t_j - 0)(\partial f/\partial t)_1 \Delta t. \tag{10}$$

Substitution of the finite difference approximation

$$\left(\frac{\partial f}{\partial t} \right)_j = \Delta f_j / \Delta t \tag{11}$$

where

$$\Delta f_{t=j} = f_{t=j} - f_{t=j-1} \tag{12}$$

enables Eq. (10) to be rewritten as

$$I_j = J(t_j - t_{j-1}) \Delta f_j + \sum_{n=1}^{n=j-1} J(t_j - t_{n-1}) \Delta f_n. \tag{13}$$

Replacing the general form of the creep compliance with the chosen Maxwell model permits the above integral to be further simplified as follows:

$$I_j = (J_o + \sum_{i=1}^{N} J_i e^{-(t_j - t_{j-1})/\tau_i}) \Delta f_j + J_o f_{j-1} + \sum_{i=1}^{N} J_i \alpha_{i,j} \tag{14}$$

where

$$f_{j-1} = \sum_{k=1}^{j-1} \Delta f_k \tag{15}$$

and

$$\alpha_{i,j} = e^{-2\Delta t/\tau_i} \Delta f_{j-1} + e^{-\Delta t/\tau_i} \alpha_{i,j-1}. \tag{16}$$

Equation (16) is a recursive formula which allows the current value of $\alpha_{i,j}$ to be calculated from only the previous value. Applying a similar treatment to the integral in (9) yields another recursion parameter defined as $\beta_{i,j}$. As shown in (6), the partial derivative with respect to the radius operates on the creep functions J_θ and $J_{\theta r}$. It is then appropriate to question whether J_θ and $J_{\theta r}$ are functions of roll radius.

Nonlinear behavior in the radial direction has been attributed to factors including entrapped air and the contact of asperities. There are no such mechanisms in the circumferential direction. This coupled with the fact that circumferential material properties presented in Gutterman (1959), Altmann (1968), Yagoda (1980), Pfeiffer (1966), Hakiel (1987), Tramposch (1965, 1967), Lin and Westman (1989), and Willet and Poesch (1988) are independent of radial pressure suggests that J_θ is also radially independent. The creep function $J_{\theta r}$ is analogous to the negative of the elastic radial Poisson's ratio divided by the radial stiffness, $-\nu_{\theta r}/E_r$. The radial Poisson's ratio, $\nu_{\theta r}$, was

Downloaded 04 May 2010 to 171.66.16.34. Redistribution subject to ASME license or copyright; see http://www.asme.org/terms/Terms_Use.cfm

measured by Willett and Poesch (1988) to be approximately 0.07 and was suggested by Hakiel (1987) to be on the order of 0.01. Note that $\nu_{\theta r}$ differs significantly from the in-plane Poisson' ratio, $\nu_{r\theta}$, which is typically on the order of 0.30. Although, the radial stiffness is known to vary with roll radius, the ratio, $\nu_{\theta r}/E_r$, is extremely small and any variation with roll radius is insignificant. Hence, the creep function $J_{\theta r}$ may be assumed radially independent by this analogy and derivatives with respect to roll radius, negligible. As a result of this discussion, the derivatives with respect to roll radius are considered insignificant and all recursion parameters, $\beta_{i,j}$, will be neglected. If thermal influences are to be accounted for and the thermal profile is radially dependent, these creep functions may vary with roll radius. Special attention must then be given to the differentials of the creep compliance. A detailed derivation of the recursion parameters occurring from the generalized Maxwell model was published by Zak (1968) in analyzing thermoviscoelastic stresses in solid rocket propellants.

As a direct result of this particular method of solution, the terms $\alpha_{i,j}$ and $\beta_{i,j}$ contain all history effects of the viscoelastic material. Since all history effects are held within the recursion formulas, significant storage space in the form of computer memory is saved. Once the integrals in Eq. (6) are replaced by the discretized form, the boundary value problem collectively reduces to the following:

$$\left[F_1(r)r^2\frac{\partial^2\Delta\sigma_r}{\partial^2 r} + F_2(r)r\frac{\partial\Delta\sigma_r}{\partial r} + F_3(r)\Delta\sigma_r + F_4(r)\right]_{t=t_j} = 0 \quad (17)$$

where in the above second-order differential equation, $\Delta\sigma_r$ is the change in radial stress from time $t = t_{j-1}$ to time $t = t_j$. An analytical solution is not possible since the coefficients are functions of the radius. As a result, a numerical solution technique is employed. The wound roll is discretized radially and the derivatives replaced by finite difference operators. Central difference approximations for the first and second derivatives of the radial stress are

$$\frac{\partial\sigma_r}{\partial r} \approx \frac{\Delta\sigma_{r(i+1)} - \Delta\sigma_{r(i-1)}}{2h} \quad (18a)$$

$$\frac{\partial^2\sigma_r}{\partial r^2} \approx \frac{\Delta\sigma_{r(i+1)} - 2\Delta\sigma_{r(i)} + \Delta\sigma_{r(i-1)}}{h^2}. \quad (18b)$$

Substituting these into Eq. (17) yields (19), which is written once for each internal layer within the roll. Writing Eq. (19) at each spatial location leads to a set of $N - 1$ simultaneous algebraic equations with $N + 1$ unknowns. When boundary conditions are applied, the tridiagonal system of equations is solved by Gaussian elimination for the change in radial stress at the current time step.

$$\left(F_1(r)\frac{r_i^2}{h^2} + F_2(r)\frac{r_i}{2h}\right)\Delta\sigma_{r(i+1)} + \left(F_3(r) - 2F_1(r)\frac{r_i^2}{h^2}\right)\Delta\sigma_{r(i)} + \left(F_1(r)\frac{r_i^2}{h^2} - F_2(r)\frac{r_i}{2h}\right)\Delta\sigma_{r(i-1)} + F_4(r) = 0 \quad (19)$$

Inner Boundary Condition

The inner boundary condition provides for continuity of displacement at the core. This condition is one which many researchers have implemented in previous winding algorithms. However, this specific application is more delicate in that it contains an integral subject to temporal discretization. Taking the deformation of the core and the first lap of wound material to be equivalent requires

$$\frac{(\sigma_r)_j}{E_c} = (\epsilon_\theta)_j \quad (20)$$

where r_{in} is the inner radius of the wound roll, E_c is the core stiffness defined as the radial pressure divided by the hoop strain at the outer diameter of the core, and the subscript, j, refers to the current time, $t = t_j$. This definition of core stiffness is convenient to use as the core stiffness is commonly determined by applying a known pressure to the outer perimeter of the core and measuring the resulting hoop strain, Gerhardt (1990). Replacing the circumferential strain by its integral form defined in (5) and substituting for the total stress, $(\sigma_r)_j$, the sum of the total stress at the previous time step, $(\sigma_r)_{j-1}$, and the change in stress from the previous to the current time step, $(\Delta\sigma_r)_j$, gives a form which can be discretized temporally and radially. The result of this operation is shown below.

$$\frac{(\sigma_r)_{j-1} + (\Delta\sigma_r)_j}{E_c} = \int_0^t \left[J_\theta(t-t')\frac{\partial}{\partial t'}\left(r\frac{\partial\sigma_r}{\partial r}\right) + J_\theta(t-t')\frac{\partial\sigma_r}{\partial t'} + J_{\theta r}(t-t')\frac{\partial\sigma_r}{\partial t'}\right]dt' \quad (21)$$

Once the right-hand side is discretized and the derivatives replaced by their corresponding finite difference operators, an equation is developed in terms of the unknown change in radial stress, $\Delta\sigma_{r=1}$ and $\Delta\sigma_{r=2}$, at the current time, $t = t_j$. This equation will become the first row in the tridiagonal system of equations.

Outer Boundary Condition

The outer boundary condition is developed by taking the strain in the outer layer to be constant and equal to the winding stress, T_w, multiplied by the circumferential creep function, J_θ evaluated at time, $t = 0$. In taking the strain in the outer layer as constant, it is assumed the deformation, u, at the outside radius caused by changes in stress of the underlying structure is negligible. In typical winding applications, the radial stiffness is sufficiently large so that moderate changes in stress are accompanied by only minute changes in strain. As a result, the total radial displacement or change in radius may be considered negligible. Hence, changes in the internal stress field do not influence the strain in the outermost layer. There are certainly cases were this assumption may not be accurate. For example, cases involving highly compressive materials which have been addressed in the elastic domain (Good et al., 1992). In such cases, this assumption should be reviewed.

The outer boundary condition becomes (22) when the circumferential strain is replaced with its definition in (5).

$$T_w J_\theta(0) = \int_0^t \left[J_\theta(t-t')\frac{\partial\sigma_\theta}{\partial t'} + J_{\theta r}(t-t')\frac{\partial\sigma_\theta}{\partial t'}\right]dt' \quad (22)$$

The right-hand side is discretized temporally using methods aforementioned. Equation (22) is then solved explicitly for the change in circumferential stress, $(\Delta\sigma_\theta)_j$. With the change in circumferential stress known, the corresponding change in radial stress beneath the outer layer can be determined by employing the hoop stress formula.

$$(\Delta\sigma_r)_j = \frac{(\Delta\sigma_\theta)_j h}{r_{\text{out}}} \quad (23)$$

where h is the thickness of the radial segment and r_{out} is the

Downloaded 04 May 2010 to 171.66.16.34. Redistribution subject to ASME license or copyright; see http://www.asme.org/terms/Terms_Use.cfm

current outer radius of the roll. This condition provides the final constraint needed to solve the simultaneous set of equations.

Accretion of the Wound Roll

Accretion of initial pressures within the wound roll is accomplished using a similar method to that employed by Hakiel (1987). The stress state within a roll wound of N layers is taken to be the superposition of stress states resulting from the addition of each layer from 1 to N. Thus, the roll is considered to be composed of N subrolls or substructures. The first subroll consists of only one layer, the second consists of two layers, etc. The Nth and final subroll contains N layers. The stress state of each subroll consists only of that resulting from the addition of that subroll's outermost layer. The total stress of a single layer in the actual wound roll is found by superimposing the stress state corresponding to that layer from all subrolls. Pressure-dependent material properties are evaluated at each spatial location from the total pressure existing in the wound roll at the time that material property is first needed.

Analytical Solution—Isotropic Linear Viscoelastic Case

An analytical solution was developed to provide a verification example for the orthotropic model which has been described. The solution developed is for the isotropic linear viscoelastic case and employs the viscoelastic correspondence principle (Lee, 1955), in which the viscoelastic problem is transformed by an integral operator to an associated elastic problem. Once the solution to the elastic problem is found, the expression is inverted back to time domain giving the solution to the viscoelastic problem. In this work the Laplace transform will be used exclusively with the frequency variable, s. For the viscoelastic problem both the radial and circumferential stress are functions of time. Let the Laplace transform of the radial stress be denoted $\bar{\sigma}_r$ and that of the circumferential stress be denoted $\bar{\sigma}_\theta$. The stress distribution for an axisymmetric hollow cylinder with homogeneous and isotropic material properties is given by Timoshenko and Goddier (1970). Taking the Laplace transform of these stress distributions yields

$$\bar{\sigma}_r = \frac{A}{r^2} + 2C \tag{24}$$

$$\bar{\sigma}_\theta = -\frac{A}{r^2} + 2C. \tag{25}$$

The parameters A and C are unknown and must be evaluated by applying appropriate boundary conditions sufficient to constrain the problem. Boundary conditions similar to those aforementioned will be used with some modification. When the strain is replaced by the transformed circumferential stress divided by the transformed modulus, the inner boundary condition can be given as

$$\frac{\bar{\sigma}_r}{E_c} = \frac{\bar{\sigma}_\theta}{\bar{E}} \quad \text{at} \quad r = r_{\text{in}} \tag{26}$$

where

$$\bar{E} = \frac{\bar{\sigma}}{\bar{\epsilon}} \tag{27}$$

and r_{in} is the inner radius of the winding roll. The outer boundary condition remains conceptually identical to that given in (22) and (23), but the form slightly differs. Equating the hoop stress formula, $\sigma_r = T_w h/r$, with the core displacement relation, then solving for the transformed radial stress in terms of the winding tension yields (28).

$$\bar{\sigma}_r = \frac{T_w \bar{E} h}{E_0 r_{\text{out}}} \quad \text{at} \quad r = r_{\text{out}} \tag{28}$$

where E_0 is the value of the modulus at time, $t = 0$. With these boundary conditions, the two unknown coefficients can be found algebraically.

To this point the constitutive law has remained arbitrary and represented only as $\bar{E}$. It is necessary to define this function so that it is consistent with the generalized Maxwell model. As shown in Fig. 1, a generalized Maxwell model with one-time constant consists of an elastic element connected in series with a parallel combination of a viscous and elastic element. This is equivalent to a series connection of an elastic element with a Kelvin model. As a result, the total strain can be written as the sum of the Kelvin and elastic components.

$$\bar{\epsilon} = \bar{\epsilon}_K + \bar{\epsilon}_E. \tag{29}$$

Replacing the Kelvin and elastic components of strain with their stress-modulus equivalents gives

$$\bar{\epsilon} = \frac{\bar{\sigma}}{E_1 + \eta_1 s} + \frac{\bar{\sigma}}{E_0}. \tag{30}$$

Using (27) allows the transformed modulus to be written in terms of specific material properties, E_0, E_1, and η_1 as shown in (31).

$$\bar{E} = \frac{E_1 + \eta_1 s}{1 + \dfrac{E_1}{E_0} + \dfrac{\eta_1 s}{E_0}} \tag{31}$$

As stated, each concentric layer is pretensioned at the winding stress when added to the roll structure. The layer is then assumed to have undergone a step change in stress. Making use of the Heaviside operator, the Laplace transform of the preload is found.

$$T_w H(t) \Rightarrow \frac{T_w}{s} \tag{32}$$

Making the substitution of T_w/s for the winding tension and performing the inverse transform gives the stress distribution throughout the roll as a function of time. Of primary interest is the radial stress, which simplifies to that shown below.

$$\sigma_r(r, t) = \frac{2E_c^2 E_0 T_w r_{\text{in}}^2 r_{\text{out}} h (r_{\text{out}}^2 - r^2)(r_{\text{in}}^2 + r_{\text{out}}^2)}{r^2 (r_{\text{in}}^2 - r_{\text{out}}^2) XY} e^{-tY/\eta_1 X} + \frac{E_0 T_w r_{\text{out}} h (r^2 - r_{\text{in}}^2)}{r^2 (r_{\text{in}}^2 - r_{\text{out}}^2)(E_0 + E_1)} e^{(-t(E_0+E_1))/\eta_1}$$
$$+ \frac{E_1 T_w r_{\text{out}} h \{E_1 [E_c (r_{\text{in}}^2 + r^2) + E_0 (r^2 - r_{\text{in}}^2)] + E_0 E_c (r_{\text{in}}^2 + r^2)\}}{r^2 (E_0 + E_1) Y} \tag{33}$$

where

$$X = E_c (r_{\text{in}}^2 + r_{\text{out}}^2) + E_0 (r_{\text{out}}^2 - r_{\text{in}}^2) \tag{34}$$

$$Y = E_1 X + E_1 E_0 r_{\text{in}} (r_{\text{in}}^2 + r_{\text{out}}^2). \tag{35}$$

These expressions give the radial stress in an isotropic hollow linear viscoelastic cylinder subjected to a time-dependent uni-

Downloaded 04 May 2010 to 171.66.16.34. Redistribution subject to ASME license or copyright; see http://www.asme.org/terms/Terms_Use.cfm

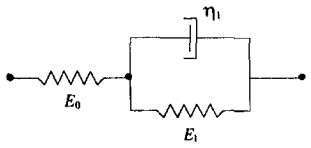


Fig. 1 Mechanical representation of the generalized Maxwell model with one-time constant

form external pressure and supported elastically at the inner surface. The wound roll stress distribution is found by superimposing stress states of all substructures.

Verification of the Orthotropic Viscoelastic Model

Numerical results are first compared to the analytical solution as just presented. Comparison serves to shown the numerical model degenerates to the analytical solution for an isotropic linear viscoelastic material with one retardation time. Values for creep parameters, J_0 and J_1, and the retardation time, τ_1, were taken from Lin and Westmann (1989) and are presented in Table 1(a). As both Fig. 1 and Eq. (27) imply, strains are not effected by out-of-plane stresses. Consequently, values for all Poisson terms will be selected as zero. This approach is supported by Altmann (1968) who suggests taking Poisson ratio to be nearly zero.

For comparison of solutions, a relation between coefficients of the creep compliance, $J(t)$, and the modulus, $\bar{E}(s)$, must be made. It can be shown that by applying the Laplace transform to the integral form of the constitutive equation, solving for the ratio of stress to strain and equating the result to the transformed modulus in (31), the parameters are related in the following manner.

$$E_0 = \frac{1}{J_0 - J_1} \quad E_1 = \frac{1}{J_1} \quad \eta_1 = \frac{\tau_1}{J_1} \tag{36}$$

Figure 2 presents the results for the normalized radial stress as a function of roll radius at various times steps. In this degenerate isotropic case, it is possible to plot the radial stress normalized by the winding stress. However, when nonlinear material properties are used, normalization is not possible as solutions are no longer linearly dependent upon the winding stress. In this illustration, the decaying stress profile can be observed. In all

Table 1 Isotropic material properties for the generalized Maxwell's model taken from Lin and Westmann (1989) used for verification of the orthotropic viscoelastic wound roll model

	$J_r = J_\theta$	$J_{r\theta} = J_{\theta r}$	
J_0	5.21697E−07	−1.56509E−07	(1/kPa)
J_1	−2.82132E−07	8.46396E−08	
τ_1	1.0E+4	1.0E+4	(sec)
	(a) $N = 1$		
J_0	5.20247E−07	−1.56074E−07	(1/kPa)
J_1	−1.31723E−10	3.95169E−11	
J_2	−2.45149E−09	7.35446E−10	
J_3	−1.52125E−08	4.56374E−09	
J_4	−2.50471E−08	7.51414E−09	
J_5	−5.66933E−08	1.70080E−08	
J_6	−9.05888E−08	2.71766E−08	
J_7	−9.35722E−08	2.80716E−08	
τ_1	1.0E−01	1.0E−01	(sec)
τ_2	1.0E+00	1.0E+00	
τ_3	1.0E+01	1.0E+01	
τ_4	1.0E+02	1.0E+02	
τ_5	1.0E+03	1.0E+03	
τ_6	1.0E+04	1.0E+04	
τ_7	1.0E+05	1.0E+05	
	(b) $N = 7$		

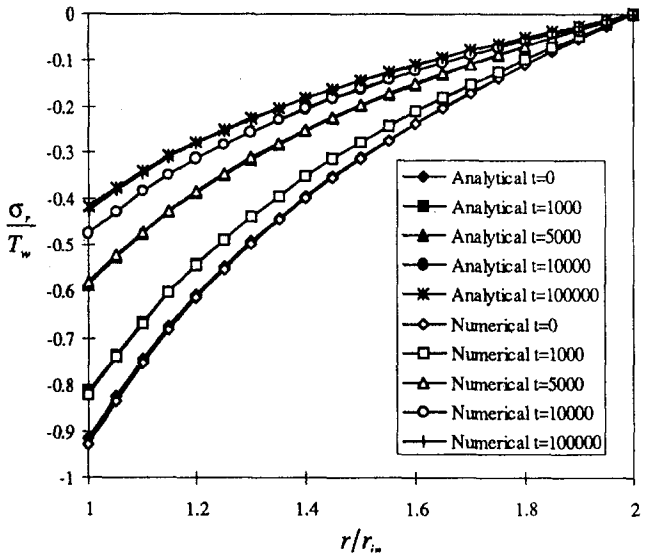


Fig. 2 Comparison of the interlayer stresses as predicted by the orthotropic viscoelastic model and the analytical solution at various times using the isotropic material properties given in Table 1(a), $E_c = \infty$, $h/r_{in} = 0.02$ and $\Delta t = t/10$ sec

cases shown, the numerical results agree very well with the analytical solution.

Comparison with the results of Lin and Westmann (1989) requires special consideration. Lin and Westmann require the circumferential stress at the outer boundary to be constant. As a result, the roll is viewed as a viscoelastic hollow cylinder subjected to an invariant external pressure and supported elastically at the inner surface. The response of the system just described should be clear. As the viscoelastic material becomes more fluid-like, the external pressure will be supported less by the roll structure and more by the elastic core. The circumferential stress in the outer layer of a wound roll is typically the maximum level of circumferential stress in the entire roll. Thus, the propensity for viscoelastic relaxation will be maximum at the outer layer. Although forcing the stress in the outer layer to remain constant is unrealistic for the case of a wound roll, the work of Lin and Westmann is an invaluable reference for comparison of results. A modification of the boundary condition presented in this work will be required to allow this comparison.

Once the task of altering the outer boundary condition is accomplished, comparison with Lin and Westmann's results is simple since they also chose the generalized Maxwell model. Again, the orthotropic viscoelastic model developed herein was reduced to the isotropic case as to make comparisons possible. Isotropic material properties shown in Table 1(b) and winding parameters used by Lin and Westmann are employed to construct this comparison. Using a total of seven retardation times and taking Poisson's ratio as a constant, the radial stress distribution was numerically obtained. Figures 3 and 4 present results which can be likened to Lin and Westmann's (1989) Figs. 6 and 7. The remarkable agreement of the numerical results to that of Lin and Westmann's is apparent. It can also be seen that by altering the outer boundary condition, the projected stress distribution now increases with time. Even so, this viscoelastic model has been proven to yield accurate results even when multiple retardation times are needed to model material behavior.

At first an accurate comparison of solutions to that of Tramposch (1965, 1967) seems unlikely since a Maxwell-Kelvin model was employed, whereas a generalized Maxwell model was utilized in this work. At this point, the adaptivity of the generalized Maxwell model will be shown. It was found the

Downloaded 04 May 2010 to 171.66.16.34. Redistribution subject to ASME license or copyright; see http://www.asme.org/terms/Terms_Use.cfm

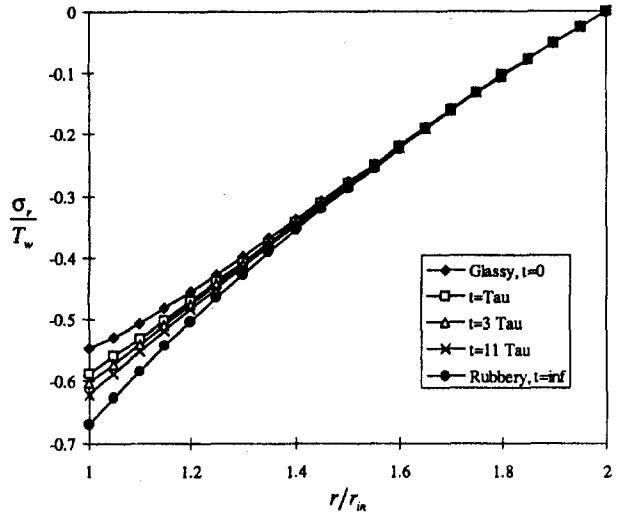


Fig. 3 Predicted radial stress distributions using the isotropic material properties for the generalized Maxwell's model shown in Table 1(*b*), E_c = 2.128 GPa, h/r_{in} = 0.02, and $\Delta t = t/10$ sec. For comparison with the results of Lin and Westmann (1989).

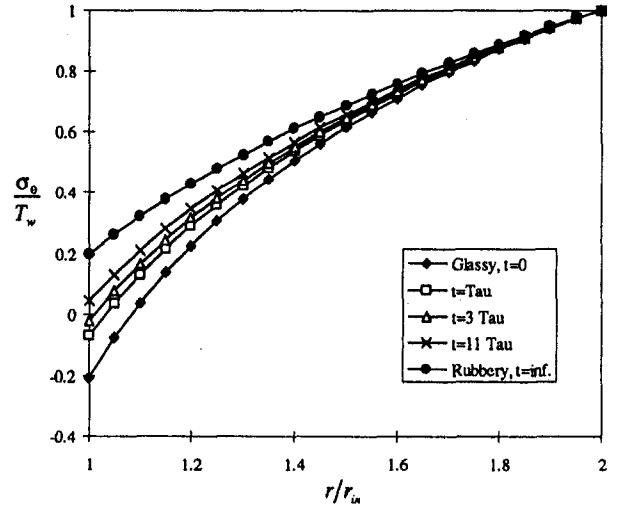


Fig. 4 Predicted circumferential stress distributions using the isotropic material properties for the generalized Maxwell's model given in Table 1(*b*), E_c = 2.128 GPa, h/r_{in} = 0.02 and $\Delta t = t/10$ sec. For comparison with the results of Lin and Westmann (1989).

Table 2 Isotropic mechanical properties for the generalized Maxwell's model used for a comparison of results with Tramposch (1965, 1967)

	$J_r = J_\theta$	$J_{r\theta} = J_{\theta r}$	
J_0	2.90065E−04	−1.10225E−04	(1/kPa)
J_1	−5.80131E−05	2.90065E−05	
J_2	−6.68644E−05	3.34322E−05	
J_3	4.73443E−03	−2.38896E−03	
J_4	−2.89276E−01	1.44638E−01	
J_5	2.84565E−01	−1.42282E−01	
τ_1	1.0E+00	1.0E+00	(sec)
τ_2	1.0E+03	1.0E+03	
τ_3	1.0E+04	1.0E+04	
τ_4	1.0E+05	1.0E+05	
τ_5	1.0E+06	1.0E+06	
	$N = 5$		

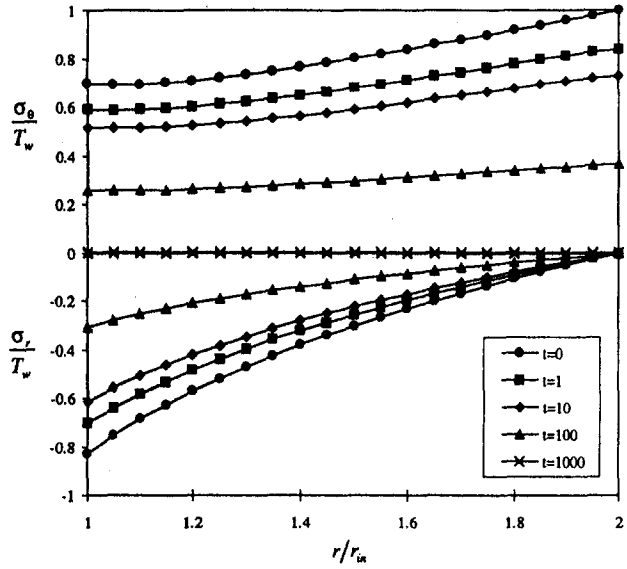


Fig. 5 Predicted radial and circumferential stress distributions using the isotropic material properties for the generalized Maxwell's model shown in Table 2, $E_c = \infty$, h/r_{in} = 0.02 and $\Delta t = t/10$. For comparison with Tramposch's isotropic results (Tramposch, 1965).

generalized Maxwell model can represent those material behaviors depicted by the Maxwell Kelvin model used by Tramposch. This requires converting the viscoelastic operators in Tramposch's Eqs. (20) and (21) to the equivalent creep functions as shown in (37) and (38).

$$J(t) = g_1 + g_2(1 - e^{-t}) + g_3 t \tag{37}$$

$$J_v(t) = \frac{7g_1}{20} + \frac{g_2}{2}(1 - e^{-t}) + \frac{g_3}{2} t \tag{38}$$

All terms, with the exception of the last, t, can be directly used in the generalized Maxwell model. Fitting a curve consisting of five exponentials to the linear term in time, over an interval

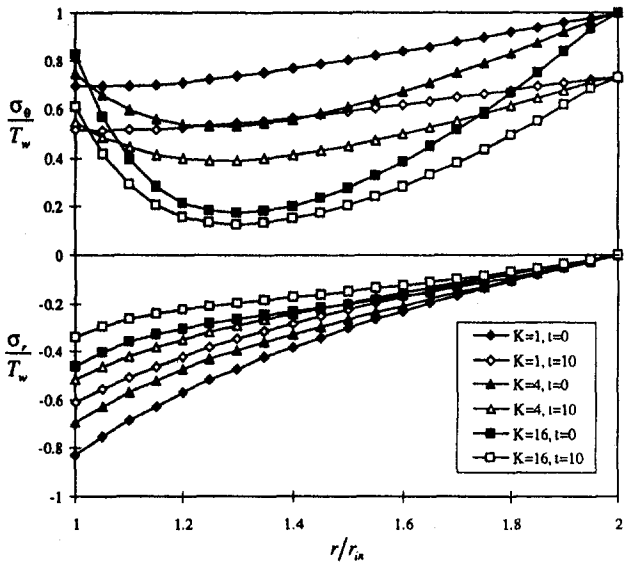


Fig. 6 Predicted radial and circumferential stress distributions using anisotropic material properties similar to those used by Tramposch (1967). Material coefficients for $J_\theta(t)$ are given in Table 2 and those for $J_r(t)$ are found by multiplying $J_\theta(t)$ by the proportionality factor, k. Numerical solutions were developed using $E_c = \infty$, h/r_{in} = 0.02 and $\Delta t = t/10$. These results were generated for comparison with Tramposch's anisotropic results (Tramposch, 1967).

Downloaded 04 May 2010 to 171.66.16.34. Redistribution subject to ASME license or copyright; see http://www.asme.org/terms/Terms_Use.cfm

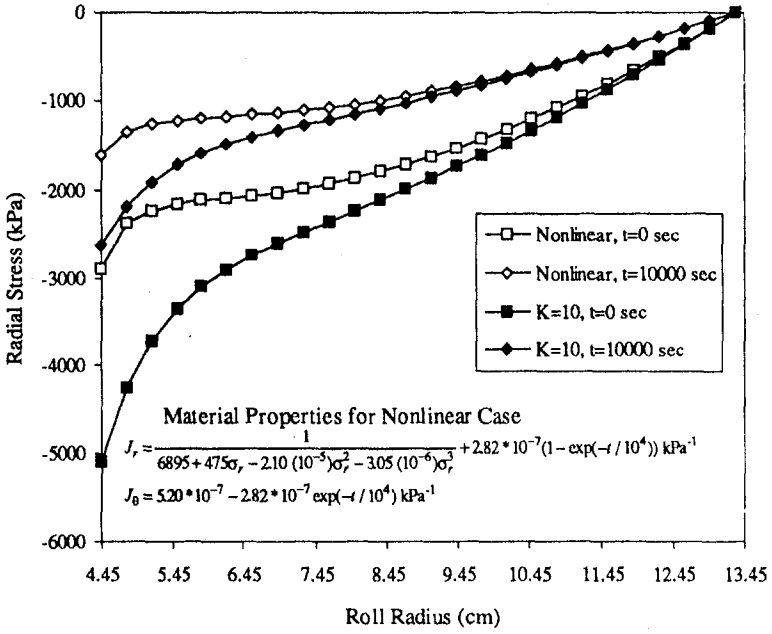


Fig. 7 Comparison of predicted radial stress distributions using (1) nonlinear material properties shown in the figure and (2) anisotropic material properties with constant coefficients. For the anisotropic case, material coefficients for $J_\theta(t)$ are given in Table 2 and those for $J_r(t)$ are found by multiplying $J_\theta(t)$ by the proportionality factor, k. Solutions were developed using $E_c = \infty$, $h/r_{in} = 0.02$ and $\Delta t = t/10$.

consistent with that used by Tramposch, gives a correlation coefficient of approximately one. Once these exponentials are united with Eqs. (37) and (38), the behavior of the Maxwell-Kelvin model was accurately represented by the generalized Maxwell model. Material properties resulting from the above procedure are presented in Table 2. Note that Tramposch's definition of the core flexibility, F, is inversely proportional to the core stiffness as defined in this work. For example a hub flexibility, $F = 0$, implies the core is perfectly rigid and has an infinite stiffness. Figure 5 presents results for the normalized radial stress in an isotropic wound roll at times, $t = 0$, 1, 10, 100, and 1000. As shown, the wound roll can approach a stress-free state when stored for a sufficiently long period of time. These results can be directly compared to those found in Tramposch's (1965) Fig. 3(a).

In Tramposch's second work (1967), allowance was made for the circumferential and radial moduli to differ. In doing so, Tramposch defined a proportionality factor, k, which was restricted to values greater or equal to unity. Interpretation of the proportionality factor is given as $k = E_\theta/E_r$. Extension of this factor to the creep compliances, $J_r(t)$ and $J_\theta(t)$, is simply made and is the ratio of the radial to circumferential creep compliance, $k = J_r(t)/J_\theta(t)$.

Parameter values used for this comparison are essentially the same as those shown in Table 2. The circumferential creep compliance will remain unchanged and the radial compliance will be equated to the circumferential compliance multiplied by the proportionality factor, k. Results of this comparison are given in Fig. 6, which displays the initial radial and circumferential stress profiles for various values of k at times, $t = 0$ and $t = 10$. These illustrations can be compared to Tramposch's (1967) Figs. (3a) and (3b). Both initial and transient stress distributions for various proportionality factors show excellent agreement with Tramposch's results. Here it is shown how the compressibility of the material in the radial direction directly affects the stress profiles. Larger values of k are shown to produce substantially higher stresses in the radial direction given all other winding parameters are held constant. This observation was also made by Pfeiffer (1966) and Hakiel (1987).

Importance of the Nonlinear Radial Stiffness

To illustrate the importance of the nonlinear creep function on the wound roll stress distribution, an example is presented in Fig. 7.The predicted radial stress distributions are shown for two cases (1) for anisotropic material properties with $J_r(t)/J_\theta(t) = 10$, constant coefficients, and $J_\theta(t)$ described in Table 1(a) and (2) for a nonlinear radial creep function with material properties described in Fig. 7. Pressure-dependent properties were chosen such that the ratio of $J_r(t)$ to $J_\theta(t)$ throughout the roll is approximately equal to ten. This figure shows the significance of the nonlinear term and its necessity for accurate prediction of interlayer stress distributions in wound rolls.

Conclusions

The model presented here can be used to predict transient stress profiles in wound rolls constructed of orthotropic viscoelastic material with nonlinear moduli. One limitation of this work is that thermal influences are not accounted for. As many viscoelastic creep functions are thermally dependent, a thermo-viscoelastic model would yield more accurate predictions of the stress state in wound rolls which are subjected to changing environments.

Numerical results presented have been shown to agree very well with the analytical solution, derived herein for the special case of linear viscoelasticity, and with published solutions. Model implementation must be preceded by determination of several material properties. We suggest measuring the instantaneous radial and tangential instantaneous moduli and creep functions separately and then combining the results. Also, it is suggested that all Poisson terms be taken as zero, based upon suggestions by Altmann (1968) and measured values provided by Willett and Poesch (1988) unless more accurate information is available.

References

Altmann, H. C., 1968, "Formulas for Computing the Stresses in Center-Wound Rolls," *TAPPI*, No. 51, No. 4, Apr., pp. 176–179.

Downloaded 04 May 2010 to 171.66.16.34. Redistribution subject to ASME license or copyright; see http://www.asme.org/terms/Terms_Use.cfm

Gerhardt, T. D., 1990, "External Pressure Loading of Spiral Paper Tubes: Theory and Experiment," ASME *Journal of Engineering Materials and Technology,* Vol. 112, Apr., pp. 144–150.

Good, J. K., Pfeiffer, J. D., and Giachetto, R. M., 1992, "Losses in Wound-on Tension in the Centerwinding of Wound Rolls," *Web Handling—1992,* J. K. Good, ed., ASME, New York, pp. 1–12.

Gutterman, R. P., 1959, "Theoretical and Practical Studies of Magnetic Tape Winding Tensions and of Environmental Roll Stability," Contract No. DA18-119-SC-42, General Kinetics, Arlington, VA.

Hakiel, Z., 1987, "Nonlinear Model for Wound Roll Stresses," *TAPPI,* May, pp. 113–117.

Lee, E. H., 1955, "Stress Analysis in Viscoelastic Bodies," *Quarterly of Applied Mechanics,* Vol. 13, No. 2, pp. 183–190.

Lin, J. Y., and Westmann, R. A., 1989, "Viscoelastic Winding Mechanics," ASME JOURNAL OF APPLIED MECHANICS, Vol. 56, pp. 821–827.

Pfeiffer, J. D., 1966, "Internal Pressures in a Wound Roll," *TAPPI,* No. 49, Aug., pp. 342–347.

Timoshenko, S. P., and Goddier, J. N., 1970, *Theory of Elasticity,* 3rd ed., McGraw-Hall, New York, pp. 69–71.

Tramposch, H., 1965, "Relaxation of Internal Forces in a Wound Reel of Magnetic Tape," ASME JOURNAL OF APPLIED MECHANICS, Vol. 34, pp. 865–873.

Tramposch, H., 1967, "Anisotropic Relaxation of Internal Forces in a Wound Reel of Magnetic Tape," ASME JOURNAL OF APPLIED MECHANICS, Vol. 34, pp. 888–894.

Willett, M. S., and Poesch, W. L., 1988, "Determining the Stress Distributions in Wound Reels of Magnetic Tape Using a Nonlinear Finite Difference Approach," ASME JOURNAL OF APPLIED MECHANICS, Vol. 55, pp. 365–371.

Yagoda, H. P., 1980, "Resolution of the Core Problem in Wound Rolls," ASME JOURNAL OF APPLIED MECHANICS, Vol. 47, pp. 847–854.

Zak, A. R., 1968, "Structural Analysis of Realistic Solid-Propellant Materials," *Journal of Spacecraft,* Vol. 5, No. 3, pp. 270–275.

Downloaded 04 May 2010 to 171.66.16.34. Redistribution subject to ASME license or copyright; see http://www.asme.org/terms/Terms_Use.cfm

Equivalent Nonlinear System Method for Stochastically Excited and Dissipated Integrable Hamiltonian Systems

W. Q. Zhu
Professor,
Department of Mechanics,
Zhejiang University,
Hangzhou 310027, P. R. China

Y. Lei
Lecturer,
Department of Architectural Engineering,
Shantou University,
Shantou 515063, Guangdong, P. R. China

An equivalent nonlinear system method is proposed to obtain the approximate probability density for the stationary response of multi-degree-of-freedom integrable Hamiltonian systems with linear and (or) nonlinear dampings and subject to external and (or) parametric excitations of Gaussian white noises. The equivalent nonlinear systems are obtained on the basis of one of the following three criteria: least mean-squared difference in damping forces, dissipation energy balancing, or least mean-squared difference in dissipation energies. Two examples are given to illustrate the application and validity of the method and the differences in the three equivalence criteria. The method is also extended to a more general class of systems which include the stochastically excited and dissipated integrable Hamiltonian systems as special cases.

Introduction

The equivalent nonlinear system method is becoming a powerful approximate approach to predicting the stochastic response of nonlinear systems. The basic idea of the method is to replace a given nonlinear stochastic system with another nonlinear stochastic system whose behavior is closest to the given one in some statistical sense and whose exact stationary solution is obtainable. The advantage of the method is that it yields the approximate probability density for the stationary response of nonlinear stochastic systems rather than just a few statistical moments and that it may be applicable to strongly nonlinear stochastic systems. A prerequisite for developing an equivalent nonlinear system technique is the availability of the exact stationary solutions for some class of nonlinear stochastic systems. Therefore, the method progresses as the exact stationary solutions for a more general class of nonlinear stochastic systems have been found.

The first equivalent nonlinear system technique was proposed by Lutes (1970). In his paper, a bilinear hysteretic system under external excitation of Gaussian white noise was replaced by an equivalent nonhysteretic nonlinear system subject to the same excitation for which the probability density of the stationary response was known. The criterion for selecting an equivalent system was devised specifically for hysteretic systems. Subsequently, Caughey (1986) published his method of equivalent nonlinear equation for a class of oscillators with linear stiffness and nonlinear damping subject to external excitation of Gaussian white noise. The criterion of equivalence was the least mean-squared difference in damping forces. Later, Caughey's technique was verified using digital simulation and generalized by Lin (1988) to include systems with both nonlinear damping and nonlinear stiffness, and further generalized by To and Li (1991) to include the case of stochastically parametric excitation.

Contributed by the Applied Mechanics Division of THE AMERICAN SOCIETY OF MECHANICAL ENGINEERS for publication in the ASME JOURNAL OF APPLIED MECHANICS.

Discussion on this paper should be addressed to the Technical Editor, Professor Lewis T. Wheeler, Department of Mechancial Engineering, University of Houston, Houston, TX 77204-4792, and will be accepted until four months after final publication of the paper itself in the ASME JOURNAL OF APPLIED MECHANICS.

Manuscript received by the ASME Applied Mechanics Division, Oct. 4, 1995; final revision, July 19, 1996. Associate Technical Editor: S. W. Shaw.

At the same time, an equivalent nonlinear system method for stochastically parametrically and (or) externally excited and dissipated nonlinear conservative systems was proposed by Zhu and Yu (1989) based on the equivalence of the drift and diffusion coefficients of the averaged total energies of the given and equivalent systems. Cai and Lin (1988b) developed a variation of equivalent nonlinear system method called the dissipation energy balancing technique, in which a given nonlinear system under external and (or) parametric excitations of Gaussian white noises is replaced by one belonging to the class of generalized stationary potential by using the criterion that the average dissipated energy remains the same. Later, Cai, Lin, and Elishakoff (1992) proposed the method of weighted residuals which includes the dissipation energy balancing as a special case. According to this method, a set of weighting functions is selected, and the replacement system is required to satisfy the constraint that each weighted residual be zero.

Various versions of the equivalent nonlinear system method mentioned previously are mainly applicable to single-degree-of-freedom nonlinear stochastic systems, although the method of weighted residuals was originally formulated for multi-degree-of-freedom (MDOF) nonlinear stochastic systems. Recently, an equivalent nonlinear system method for MDOF stochastically excited and dissipated nonintegrable Hamiltonian systems was proposed (Zhu, Soong, and Lei, 1994; Zhu and Yang, 1997) and three criteria of equivalence, i.e., least mean-squared difference in damping forces, dissipation energy balancing, and least mean-squared difference in dissipation energies, have been employed and compared.

In the present paper an equivalent nonlinear system method for MDOF stochastically excited and dissipated integrable Hamiltonian systems is developed based on the exact stationary solutions for a similar class of nonlinear stochastic systems (Zhu and Yang, 1996). The application and validity of the method are illustrated with two examples. It is pointed out that the method can be extended to a more geneal class of systems which includes the stochastically excited and dissipated integrable Hamiltonian systems as special cases.

Exact Stationary Solutions

Consider an n-DOF stochastically excited and dissipated Hamiltonian system governed by the following equations of motion:

Copyright © 1997 by ASME

Downloaded 04 May 2010 to 171.66.16.34. Redistribution subject to ASME license or copyright; see http://www.asme.org/terms/Terms_Use.cfm

$$\dot{Q}_i = \frac{\partial H'}{\partial P_i} \tag{1a}$$

$$\dot{P}_i = -\frac{\partial H'}{\partial Q_i} - C_{ij}\frac{\partial H'}{\partial P_j} + f_{ik}W_k(t)$$

$$i, j = 1, 2, \ldots, n; \quad k = 1, 2, \ldots, m \tag{1b}$$

where Q_i and P_i are generalized displacements and generalized momenta, respectively; $H' = H'(\mathbf{Q}, \mathbf{P})$ is twice differentiable Hamiltonian; $C_{ij} = C_{ij}(\mathbf{Q}, \mathbf{P})$ are differentiable functions; $f_{ik} = f_{ik}(\mathbf{Q}, \mathbf{P})$ are twice differentiable functions; and $W_k(t)$ are Gaussian white noises in the sense of Stratonovich with correlation functions

$$E[W_k(t)W_l(t+\tau)] = 2D_{kl}\delta(\tau) \quad k, l = 1, 2, \ldots, m. \tag{2}$$

The system governed by Eqs. (1a) and (1b) is generally nonlinear. The first summation terms on the right-hand side of Eq. (1b) may represent a set of linear and (or) nonlinear damping mechanisms, while the second summation terms may include external (additive) and (or) parametric (multiplicative) excitations of Gaussian white noises.

Equations (1a) and (1b) may be converted into its equivalent Itô stochastic differential equations by adding the Wong-Zakai correct terms to Eq. (1b). These added terms can be split into two parts: a conservative force part and a damping force part. After combining the two parts with $-\partial H'/\partial Q_i$ and $-C_{ij}\partial H'/\partial P_j$, respectively, one obtains the the following Itô equations:

$$dQ_i = \frac{\partial H}{\partial P_i}\,dt \tag{3a}$$

$$dP_i = -\left(\frac{\partial H}{\partial Q_i} + m_{ij}\frac{\partial H}{\partial P_j}\right)dt + f_{ik}dB_k(t)$$

$$i, j = 1, 2, \ldots, n; \quad k = 1, 2, \ldots, m \tag{3b}$$

where H is the modified Hamiltonian and $B_k(t)$ are the Wiener processes.

The reduced Fokker-Planck-Kolmogorov (FPK) equation associated with Itô Eqs. (3a) and (3b) can be written as (Zhu and Yang, 1996)

$$[p, H] + \frac{\partial}{\partial p_i}\left(m_{ij}\frac{\partial H}{\partial p_j}p\right) + \frac{\partial^2}{\partial p_i \partial p_j}(b_{ij}^{(i)}p) = 0 \tag{4}$$

where $p = p(\mathbf{q}, \mathbf{p})$ is the stationary probability density of generalized displacements and momenta; $[p, H]$ is the Poisson bracket of p and H (Tabor, 1989); $b_{ij} = 2D_{kl}f_{ik}f_{jl}$ and $b_{ij} = b_{ij}^{(i)} + b_{ji}^{(j)}$. b_{ij} are the diffusion coefficients of FPK Eq. (4) which are split into $b_{ij}^{(i)}$ and $b_{ji}^{(j)}$ to increase the flexibility of damping parameters (Cai and Lin, 1988a).

It has been shown that the structure and property of the exact solution of the reduced FPK Eq. (4) depend on the integrability and resonant property of the Hamiltonian system with Hamiltonian H (Zhu and Yang, 1996). Assume that the Hamiltonian system is integrable and nonresonant and has n independent integrals of the motion, $\mathbf{H} = [H_1, H_2, \ldots, H_n]^T$ with $H_\alpha = H_\alpha(\mathbf{q}, \mathbf{p})$, which are in involution. Then the exact solution of the reduced FPK Eq. (4) subject to the conditions of vanishing probability flow at boundaries is of the form

$$p(\mathbf{q}, \mathbf{p}) = C\exp[-\lambda(\mathbf{H})]|_{H_\alpha = H_\alpha(\mathbf{q},\mathbf{p})} \tag{5}$$

where C is a normalization constant, and λ is a functional of H_α satisfying the following set of n first-order linear partial differential equations:

$$m_{ij}\frac{\partial H}{\partial p_j} + \frac{\partial}{\partial p_j}b_{ij}^{(i)} - b_{ij}^{(i)}\frac{\partial H_\alpha}{\partial p_j}\frac{\partial \lambda}{\partial H_\alpha} = 0$$

$$i, j, \alpha = 1, 2, \ldots, n. \tag{6}$$

If $\partial\lambda/\partial H_\alpha$ can be obtained from Eq. (6) as functionals of H_β and satisfy the following compatibility conditions

$$\frac{\partial^2\lambda}{\partial H_\beta \partial H_\alpha} = \frac{\partial^2\lambda}{\partial H_\alpha \partial H_\beta} \quad \alpha, \beta = 1, 2, \ldots, n, \tag{7}$$

then the solution of Eq. (6) is

$$\lambda(\mathbf{H}) = \lambda_0 + \int_0^{\mathbf{H}}\frac{\partial\lambda}{\partial H_\alpha}\,dH_\alpha \tag{8}$$

where $\lambda_0 = \lambda(0)$, the second term on the right-hand side is a line integral and the integrand is a summation over $\alpha = 1, 2, \ldots, n$. The exact stationary solution of the system governed by Eqs. (1a) and (1b) is then obtained by substituting Eq. (8) into Eq. (5).

In principle, n action variables I_α and n angle variables θ_α can be found for an integrable Hamiltonian system of n-DOF via canonical transformation. If this is the case, then an exact stationary solution of the form in Eq. (5) with H_α replaced by I_α may be found for the system governed by Eqs. (1a) and (1b) (Zhu and Yang, 1996).

Note that in order to obtain an exact stationary solution of the form in Eq. (5) with $\lambda(\mathbf{H})$ defined by Eq. (8), usually $n(n+1)/2$ restrictions must be imposed on the parameters of the system and stochastic excitations (among them n restrictions for $\partial\lambda/\partial H_\alpha$ to be functionals of H_β and $n(n-1)/2$ restrictions for Eq. (7) to be satisfied). In some special cases, however, the number of the restrictions may be less than $n(n+1)/2$. For example, in the case of linear dampings, i.e., m_{ij} are constants, and external excitations, i.e., $b_{ij}^{(i)}$ are constants, $\partial\lambda/\partial H_\alpha$ may be also constants, and Eq. (7) is satisfied automatically.

Equivalent Nonlinear System Method

Suppose we are given an n-DOF stochastically excited and dissipated Hamiltonian system whose Itô equations are of the form

$$dQ_i = \frac{\partial H}{\partial P_i}\,dt \tag{9a}$$

$$dP_i = -\left(\frac{\partial H}{\partial Q_i} + M_{ij}\frac{\partial H}{\partial P_j}\right)dt + f_{ik}dB_K(t)$$

$$i, j = 1, 2, \ldots, n; \quad k = 1, 2, \ldots, m. \tag{9b}$$

Assume that the Hamiltonian system with Hamiltonian H is integrable and nonresonant and the given system governed by Eqs. (9a) and (9b) has no exact stationary solution. Our aim is to find an equivalent nonlinear system of the form in Eqs. (3a) and (3b). The given system and its equivalent one have the same Hamiltonian system and stochastic excitations. The only difference between the two systems is in damping coefficients, M_{ij} and m_{ij}. So, our task is to determine m_{ij} so that the equivalent system of the form in Eqs. (3a) and (3b) has an exact stationary solution and its behavior is closest to that of the given system in some statistical sense. Since the Hamiltonian system and the stochastic excitations of the equivalent system are given, the $n(n+1)/2$ restrictions to ensure the equivalent system having exact stationary solution of the form in Eq. (5) must be imposed on m_{ij}. Thus, the number of independent m_{ij} is $n(n-1)/2$. Let these independent m_{ij} be denoted by $\mathbf{s} = [\zeta_1, \zeta_2, \ldots, \zeta_{n(n-1)/2}]^T$. The difference between the given system and its equivalent one can be expressed by

$$\epsilon_i = [M_{ij} - m_{ij}(\mathbf{s})]\frac{\partial H}{\partial P_j} \quad i, j = 1, 2, \ldots, n. \tag{10}$$

Once $\mathbf{s}$ is determined based on some criterion, m_{ij} can be determined by the $n(n+1)/2$ restrictions. After that, $\partial\lambda/\partial H_\alpha$, $\lambda(\mathbf{H})$ and $p(\mathbf{q}, \mathbf{p})$ are obtained successively from Eqs. (6), (8), and

Downloaded 04 May 2010 to 171.66.16.34. Redistribution subject to ASME license or copyright; see http://www.asme.org/terms/Terms_Use.cfm

(5), and Eq. (5) is the approximate probability density of the stationary response of the given system governed by Eqs. (9*a*) and (9*b*).

Although a more general criterion such as that in the method of weighted residuals (Cai, Lin, and Elishakoff, 1992) can be devised mathematically, the three criteria employed by Zhu, Soong, and Lei (1994) are more meaningful physically and will be used in the following derivation. The first criterion to find $\mathbf{s}$ is to minimize the mean-squared difference in the damping forces of the two systems with respect to ζ_r. It means that if $\zeta_r(\mathbf{q}, \mathbf{p})$ in Eq. (10) are replaced by $\zeta_r(\mathbf{q}, \mathbf{p}) + \mu_r\eta_r(\mathbf{q}, \mathbf{p})$, where μ_r are constants and η_r are functions of $\mathbf{q}$, $\mathbf{p}$ similar to $\zeta_r(\mathbf{q}, \mathbf{p})$, then $E[\epsilon_i\epsilon_i]$, as functions of μ_r, is minimized by letting $\boldsymbol{\mu} = 0$, i.e.,

$$\frac{\partial}{\partial \mu_r} E[\epsilon_i\epsilon_i]|_{\mu=0} = 0$$

$$i = 1, 2, \ldots, n; \quad r = 1, 2, \ldots, n(n-1)/2. \quad (11)$$

Equation (11) is equivalent to $\delta E[\epsilon_i\epsilon_i]/\delta\zeta_r = 0$, i.e.,

$$\int \left[(M_{ij} - m_{ij}(\mathbf{s}))\frac{\partial H}{\partial p_j}\right]\left[\frac{\delta}{\delta\zeta_r} m_{ij}(\mathbf{s})\frac{\partial H}{\partial p_j}\right] p(\mathbf{q}, \mathbf{p}) d\mathbf{q}\, d\mathbf{p} = 0$$

$$i, j = 1, 2, \ldots, n; \quad r = 1, 2, \ldots, n(n-1)/2. \quad (12)$$

The $2n$-fold integrals in Eq. (12) can be simplified by the transformation from $\mathbf{q}$, $\mathbf{p}$ to $\mathbf{q}$, $\mathbf{H}$, i.e.,

$$\int_0^\infty p(\mathbf{H}) d\mathbf{H} \int_\Omega \left\{\left[(M_{ij} - m_{ij}(\mathbf{s}))\frac{\partial H}{\partial p_j}\right] \times \left[\frac{\delta}{\delta\zeta_r}(\mathbf{s})\frac{\partial H}{\partial p_j}\right] \Big/ \left|\frac{\partial \mathbf{H}}{\partial \mathbf{p}}\right|\right\} d\mathbf{q} = 0$$

$$i, j = 1, 2, \ldots, n; \quad r = 1, 2, \ldots, n(n-1)/2 \quad (13)$$

where $|\partial\mathbf{H}/\partial\mathbf{p}|$ is the absolute value of the Jacobian determinant of the transformation from $\mathbf{p}$ to $\mathbf{H}$, and the domain Ω of integration is defined by

$$\Omega = \{\mathbf{q} | \bigcap_{i=1}^{n} H_i(\mathbf{q}, 0) \le H_i\}. \quad (14)$$

Since $p(\mathbf{H})$ is still unknown, to proceed further, Eq. (13) is replaced by more restrictive sufficient conditions requiring that the integrations on $\mathbf{q}$ vanish for every $\mathbf{H}$ (Cai and Lin, 1988). These conditions lead to

$$\int_\Omega \left\{\left[(M_{ij} - m_{ij}(\mathbf{s}))\frac{\partial H}{\partial p_j}\right] \times \left[\frac{\delta}{\delta\zeta_r} m_{ij}(\mathbf{s})\frac{\partial H}{\partial p_j}\right] \Big/ \left|\frac{\partial \mathbf{H}}{\partial \mathbf{p}}\right|\right\} d\mathbf{q} = 0$$

$$i, j = 1, 2, \ldots, n; \quad r = 1, 2, \ldots, n(n-1)/2 \quad (15)$$

where $\mathbf{p}$ in the integrands should be replaced by $\mathbf{q}$ and $\mathbf{H}$.

The second criterion to find $\mathbf{s}$ is to make the difference in the dissipated energies in the given system and its equivalent one vanish, i.e.,

$$E\left[\frac{\partial H}{\partial P_i}\epsilon_i\right] = 0 \quad i = 1, 2, \ldots, n. \quad (16)$$

Then a similar derivation as that used in going from Eq. (12) to Eq. (15) leads to

$$\int_\Omega \left\{\frac{\partial H}{\partial p_i}[M_{ij} - m_{ij}(\mathbf{s})]\frac{\partial H}{\partial p_j} \Big/ \left|\frac{\partial \mathbf{H}}{\partial \mathbf{p}}\right|\right\} d\mathbf{q} = 0$$

$$i, j = 1, 2, \ldots, n. \quad (17)$$

Note that here there is only one equation for determining $\mathbf{s}$. So this criterion can be employed when there is only one independent unknown ζ.

The third criterion to find $\mathbf{s}$ is to minimize the mean-squared difference in the dissipation energies in the given system and its equivalent one, i.e.,

$$\delta E\left[\left(\frac{\partial H}{\partial P_i}\epsilon_i\right)^2\right] \Big/ \delta\zeta_r = 0$$

$$i = 1, 2, \ldots, n; \quad r = 1, 2, \ldots, n(n-1)/2. \quad (18)$$

A similar derivation leads to

$$\int_\Omega \left\{\left[\frac{\partial H}{\partial p_i}(M_{ij} - m_{ij}(\mathbf{s}))\frac{\partial H}{\partial p_j}\right] \times \left[\frac{\partial H}{\partial p_i}\frac{\delta}{\delta\zeta_r} m_{ij}(\mathbf{s})\frac{\partial H}{\partial p_j}\right] \Big/ \left|\frac{\partial \mathbf{H}}{\partial \mathbf{P}}\right|\right\} d\mathbf{q} = 0$$

$$i, j = 1, 2, \ldots, n; \quad r = 1, 2, \ldots, n(n-1)/2. \quad (19)$$

A few remarks about the proposed method should be made. To find an equivalent system for a given system, the function form of each m_{ij} needs to be determined in advance. The form depends upon the Hamiltonian system and stochastic excitations. However, so far no rule for the choice of the form is available. The choice of the form may affect the accuracy of the result. The three criteria proposed are applied to the system as a whole, not to individual degrees of freedom. Thus, the equivalent system found is optimal in some statistical sense for the whole system but may not be optimal for each degree-of-freedom. ζ_r determined by Eq. (15), (17), or (19) are usually functionals of $\mathbf{H}$ and so are m_{ij}. If, instead of n independent integrals of motion, n action variables can be found for the Hamiltonian system associated with Eqs. (9*a*) and (9*b*), then the exact stationary solution of the equivalent system is of the form of Eq. (5) with $\mathbf{H}$ replaced by $\mathbf{I}$, and the procedure to find the equivalent system is the same as stated above. The only difference is that in this case ζ_r and m_{ij} are functionals of $\mathbf{I}$ instead of $\mathbf{H}$.

As noted in the last section, the number of the restrictions imposed on m_{ij} for the equivalent system having exact stationary solution of the form in Eq. (5) may be less than $n(n+1)/2$. In this case, the number of the components of independent unknown vector $\mathbf{s}$ and the number of equations in Eq. (15) or (19) for determining $\mathbf{s}$ would be larger than $n(n-1)/2$. In any case, the sum of the number of the restrictions and the number of the equations in Eq. (15) or (19) would be equal to n^2.

Extension

The equivalent nonlinear system method developed in the last section can be further extended to a more general class of systems, which include the stochastically excited and dissipated Hamiltonian systems as special cases. Consider a system governed by the following Itô stochastic differential equations:

$$dQ_i = D(\mathbf{Q})\frac{\partial H}{\partial P_i} dt \quad (20a)$$

$$dP_i = -\left[D(\mathbf{Q})\frac{\partial H}{\partial Q_i} + M_{ij}\frac{\partial H}{\partial P_j}\right] dt + f_{ik} dB_k(t)$$

$$i, j = 1, 2, \ldots, n; \quad k = 1, 2, \ldots, m \quad (20b)$$

Downloaded 04 May 2010 to 171.66.16.34. Redistribution subject to ASME license or copyright; see http://www.asme.org/terms/Terms_Use.cfm

where $D(\mathbf{Q})$ is an arbitrary function of $\mathbf{Q}$. The system governed by Eqs. (9a) and (9b) is a special case with $D(\mathbf{Q}) = 1$.

Suppose that the Hamiltonian system with Hamiltonian H governed by Eqs. (20a) and (20b) with $D(\mathbf{Q}) = 1$ and $M_{ij} = f_{ik} = 0$ is integrable and nonresonant. It has been shown (Zhu and Yang, 1996) that if $M_{ij} = m_{ij}$ make the system governed by Eqs. (20a) and (20b) have exact stationary solution $p^*(\mathbf{q}, \mathbf{p})$, then

$$p^*(\mathbf{q}, \mathbf{p}) = \frac{C}{D(\mathbf{Q})} \exp[-\lambda(\mathbf{H})]|_{H_i = H_i(\mathbf{q},\mathbf{p})} \tag{21}$$

where $\lambda(\mathbf{H})$ is the solution of Eq. (6) and defined by Eq. (8) if Eq. (7) is satisfied.

Now suppose that the system governed by Eqs. (20a) and (20b) has no exact stationary solution. Then the procedures developed in the last section for finding the damping coefficients $m_{ij}(\mathbf{s})$ of the equivalent nonlinear system are still applicable provided that the equivalent system is of the form in Eqs. (20a) and (20b) with M_{ij} replaced by $m_{ij}(\mathbf{s})$, and that the exact stationary solution of the equivalent system is of the form in Eq. (21).

Examples

1 As first example of the application of the equivalent nonlinear system method for stochastically excited and dissipated integrable Hamiltonian systems developed in the last two sections, consider two linearly coupled van der Pol oscillators subject to parametric excitations of Gaussian white noises. The equations of motion of the system are of the form

$$\ddot{X} - \lambda_1\dot{X} + a_1X^2\dot{X} + k_{11}X + k_{12}Y = \sigma_1 X W_1(t)$$

$$\ddot{Y} - (\lambda_1 - \lambda_2)\dot{Y} + a_2Y^2\dot{Y} + k_{21}X + k_{22}Y = \sigma_2 Y W_2(t) \tag{1-1}$$

where λ_1, λ_2, a_1, a_2, k_{11}, $k_{12} = k_{21}$, k_{22}, σ_1 and σ_2 are constants; $W_1(t)$ and $W_2(t)$ are uncorrelated Gaussian white noises with intensities $2D_{11}$ and $2D_{22}$, respectively. This system is a special case of the system studied by Zhu and Yang (1996) as a first example.

Note that the Wong-Zakai correct terms vanish in this example. The Hamiltonian associated with the system is

$$H = \tfrac{1}{2}(\dot{x}^2 + \dot{y}^2 + k_{11}x^2 + k_{22}y^2 + 2k_{12}xy) \tag{1-2}$$

which is the total energy of the system, can be separated by using modal transformation, and expressed in terms of action variables I_1 and I_2 and frequencies ω_1 and ω_2 as

$$H = \omega_1 I_1 + \omega_2 I_2 \tag{1-3}$$

where

$$I_1 = \frac{1 + u_1^2}{2(u_1 - u_2)^2\omega_1}[(\dot{y} - u_2\dot{x})^2 + \omega_1^2(y - u_2x)^2]$$

$$I_2 = \frac{1 + u_2^2}{2(u_1 - u_2)^2\omega_2}[(u_1\dot{x} - \dot{y})^2 + \omega_2^2(u_1x - y)^2]$$

$$\omega_{1,2}^2 = \frac{k_{11} + k_{22}}{2} \mp \frac{1}{2}\sqrt{(k_{11} - k_{22})^2 + 4k_{12}^2}$$

$$u_1 = \frac{\omega_1^2 - k_{11}}{k_{12}}, \quad u_2 = \frac{\omega_2^2 - k_{11}}{k_{12}}. \tag{1-4}$$

Thus, the system governed by Eq. (1-1) is a stochastically excited and dissipated integrable Hamiltonian system. Assume that $\omega_1/\omega_2 \neq k_1/k_2$, where k_1 and k_2 are positive integers and the Hamiltonian system is nonresonant.

The equivalent nonlinear system for system (1-1) is of the form

$$\ddot{X} + c_{11}\dot{X} + k_{11}X + k_{12}Y = \sigma_1 X W_1(t)$$

$$\ddot{Y} + c_{22}\dot{Y} + k_{21}X + k_{22}Y = \sigma_2 Y W_2(t) \tag{1-5}$$

where k_{11}, k_{12}, k_{21}, k_{22}, σ_1 and σ_2 are the same as those in Eq. (1-1); c_{11} and c_{22} are unknown functionals of X, $\dot{X}$, Y, $\dot{Y}$ to be determined. In order that system (1-5) has the exact stationary solution, c_{11} and c_{22} should satisfy the following equation (Zhu and Yang, 1996):

$$c_{11}\sigma_2^2 D_{22}Y^2 = c_{22}\sigma_1^2 D_{11}X^2. \tag{1-6}$$

Let

$$c_{11} = \sigma_1^2 D_{11}X^2 d_{22}, \quad c_{22} = \sigma_2^2 D_{22}Y^2 d_{22} \tag{1-7}$$

where $d_{22} = d_{22}(I_1, I_2)$ is the independent unknown functional of I_1 and I_2 to be determined.

The differences of the given system and its equivalent one are in damping forces, i.e.,

$$\epsilon_1 = -\lambda_1\dot{X} + a_1X^2\dot{X} - \sigma_1^2 D_{11}X^2 d_{22}$$

$$\epsilon_2 = -(\lambda_1 - \lambda_2)\dot{Y} + a_2Y^2\dot{Y} - \sigma_2^2 D_{22}Y^2 d_{22}. \tag{1-8}$$

The criterion of the least mean-squared difference in damping forces, i.e., Eq. (15) yields

$$d_{22}\iint_\Omega [(\sigma_1^4 D_{11}^2 x^4\dot{x}^2 + \sigma_2^4 D_{22}^2 y^4\dot{y}^2)/|J|]dxdy$$

$$= \iint_\Omega \{[\sigma_1^2 D_{11}(-\lambda_1 + a_1x^2)x^2\dot{x}^2]$$

$$+ [\sigma_2^2 D_{22}(-\lambda_1 + \lambda_2 + a_2y^2)y^2\dot{y}^2]/|J|\}dxdy \tag{1-9}$$

where

$$J = \begin{vmatrix} \dfrac{\partial I_1}{\partial \dot{x}} & \dfrac{\partial I_1}{\partial \dot{y}} \\ \dfrac{\partial I_2}{\partial \dot{x}} & \dfrac{\partial I_2}{\partial \dot{y}} \end{vmatrix}$$

$$= -\frac{(1 + u_1^2)(1 + u_2^2)}{\omega_1^3\omega_2^3(u_1 - u_2)^3}(u_1\dot{x} - \dot{y})(\dot{y} - u_2\dot{x}) \tag{1-10}$$

and domain Ω of integration is determined by the following inequalities:

$$\omega_1(y - u_2x)^2 \leq \frac{2I_1(u_1 - u_2)^2}{1 + u_1^2}$$

$$\omega_2(u_1x - y)^2 \leq \frac{2I_2(u_1 - u_2)^2}{1 + u_2^2}. \tag{1-11}$$

Completing the integration in Eq. (1-9) (see Appendix A), we obtain $d_{22}(I_1, I_2)$ and then the exact stationary solution of the equivalent system (1-5) (Zhu and Yang, 1996) as follows:

$$p(x, \dot{x}, y, \dot{y}) = C\exp\left[-\frac{u_1(u_1 - u_2)\omega_1}{1 + u_1^2}\int_{I_{10}}^{I_1} d_{22}(I_1, I_{20})dI_1\right.$$

$$\left. - \frac{u_2(u_1 - u_2)\omega_2}{1 + u_2^2}\int_{I_{20}}^{I_2} d_{22}(I_1, I_2)dI_2\right]$$

$$= C\exp[-\lambda(I_1, I_2)] \tag{1-12}$$

where C is a normalization constant; I_1 and I_2 are defined by Eq. (1-4). Equation (1-12) is then the approximate probability density of the stationary response of the given system (1-1). The approximate statistics of the stationary response of system (1-1) can be obtained from Eq. (12), for example, the variance of displacement X is

Downloaded 04 May 2010 to 171.66.16.34. Redistribution subject to ASME license or copyright; see http://www.asme.org/terms/Terms_Use.cfm

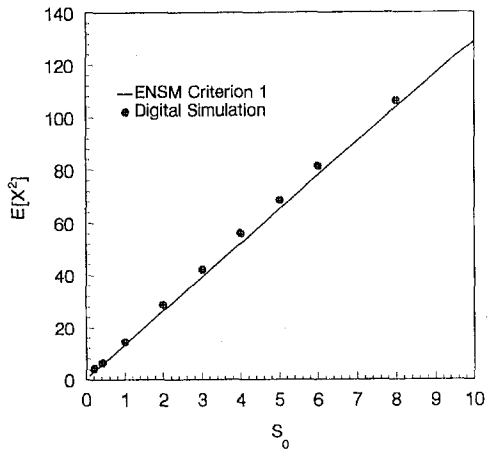


Fig. 1(*a*)

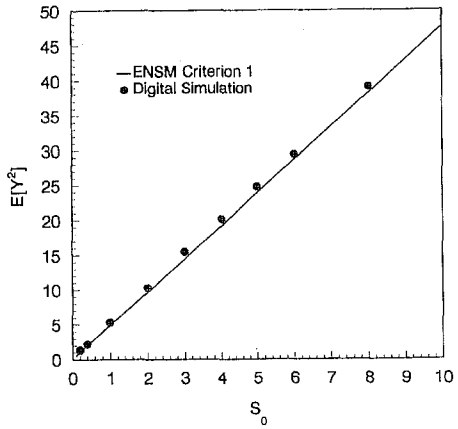


Fig. 1(*b*)

Fig. 1 Variance $E[X^2]$, (*a*), and $E[Y^2]$, (*b*), of stationary response of system (1-1) obtained by using the present method based on the criterion of the least mean-squared difference in damping forces (solid lines) and from digital simulation (dots). $\lambda_1 = \lambda_2 = 0.01$, $a_1 = 0.01$, $a_2 = 0.02$, $\sigma_1 = \sigma_2 = 0.2$, $k_{11} = 1.0$, $k_{22} = 2.0$, $k_{12} = k_{21} = 0.5$. $2D_{11} = 2\pi S_1$, $2D_{22} = 2\pi S_2$ and $S_1 = S_2 = S_0$.

$$E[X^2] = \int\int\int\int_{-\infty}^{\infty} x^2 p(x, \dot{x}, y, \dot{y})\,dx\,d\dot{x}\,dy\,d\dot{y}$$

$$= C \int\int_{0}^{\infty} \exp[-\lambda(I_1, I_2)]\,dI_1\,dI_2 \times \int\int_{\Omega} (x^2/|J|)\,dx\,dy. \quad (1\text{-}13)$$

Some numerical results for stationary variances $E[X^2]$ and $E[Y^2]$ of system (1-1) obtained by using the present method based on the criterion of the least mean-squared difference in damping forces are shown in Figs. 1 and 2. Results from digital simulation are also shown in these figures for comparison. It is seen from these figures that in the case of light damping, the present method yields excellent results, and for relatively larger damping the results obtained by using the present method are slightly less than the corresponding results from digital simulation.

2 As an example, having nonlinear restoring forces, consider two coupled quartic oscillators with nonlinear dampings subject to external excitations of Gaussian white nosies. The system is governed by the following equations of motion:

$$\ddot{X} + a_1 X^2 \dot{X} + AX + X^3 + 3XY^2 = \sigma_1 W_1(t)$$
$$\ddot{Y} + a_2 Y^2 \dot{Y} + AY + Y^3 + 3X^2 Y = \sigma_2 W_2(t) \quad (2\text{-}1)$$

where a_1, a_2, A, σ_1 and σ_2 are constants; $W_1(t)$ and $W_2(t)$ are uncorrelated Gaussian white noises with intensities $2D_{11}$ and $2D_{22}$, respectively. System (2-1) is a special case of the system studied by Zhu and Yang (1996) as Example 3.

The Hamiltonian of the system governed by Eq. (2-1) is

$$H = \tfrac{1}{2}(\dot{x}^2 + \dot{y}^2 + Ax^2 + Ay^2) + \tfrac{1}{4}(x^4 + y^4 + 6x^2y^2) \quad (2\text{-}2)$$

which can be separated as

$$H = H_1 + H_2 \quad (2\text{-}3)$$

with

$$H_1 = \tfrac{1}{8}[2(\dot{x} + \dot{y})^2 + 2A(x + y)^2 + (x + y)^4]$$

$$H_2 = \tfrac{1}{8}[2(\dot{x} - \dot{y})^2 + 2A(x - y)^2 + (x - y)^4]. \quad (2\text{-}4)$$

H_1 and H_2 are the two independent integrals of the motion in involution. Thus, the system governed by (2-1) is a stochastically excited and dissipated integrable Hamiltonian system. Note that the Hamiltonian system associated with Eq. (2-1) is nondegenerate (Tabor, 1989) and can be treated as a nonresonant one (Zhu and Yang, 1996).

The equivalent system for system (2-1) is of the form

$$\ddot{X} + c_{11}\dot{X} + AX + X^3 + 3XY^2 = \sigma_1 W_1(t)$$
$$\ddot{Y} + c_{22}\dot{Y} + AY + Y^3 + 3X^2 Y = \sigma_2 W_2(t) \quad (2\text{-}5)$$

where A, σ_1, and σ_2 are the same as those in Eq. (2-1); c_{11} and

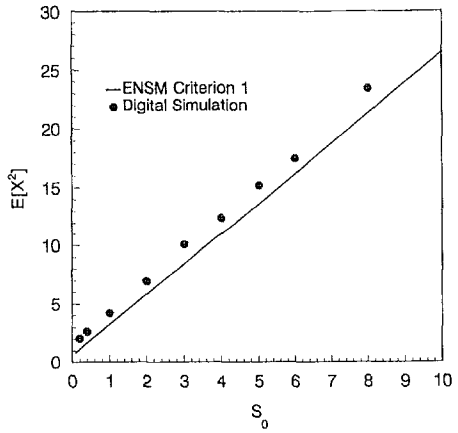


Fig. 2(*a*)

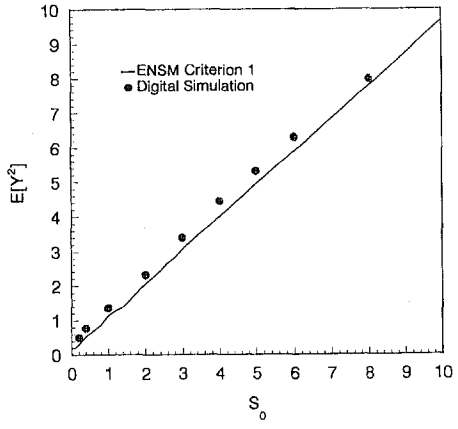


Fig. 2(*b*)

Fig. 2 Variance $E[X^2]$, (*a*), and $E[Y^2]$, (*b*), of stationary response of system (1-1). The symbols and parameters are the same as in Fig. 1 except $\lambda_1 = \lambda_2 = 0.05$, $a_1 = 0.1$, $a_2 = 0.2$.

Downloaded 04 May 2010 to 171.66.16.34. Redistribution subject to ASME license or copyright; see http://www.asme.org/terms/Terms_Use.cfm

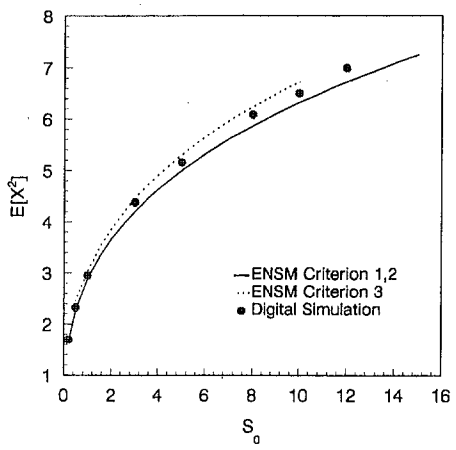


Fig. 3 Variance $E[X^2]$ of stationary response of system (2-1) obtained by using the present method based on criteria of the least mean-squared difference in damping forces and dissipation energy balancing (solid line), on criterion of the least mean-squared difference in djssipation energies (dashed line) and from digital simulation (dots). $A = \sigma_1 = \sigma_2 = 1.0$, $a_1 = 0.02$, $a_2 = 0.04$. $2D_{11} = 2\pi S_1$, $2D_{22} = 2\pi S_2$ and $S_1 = S_2 = S_0$.

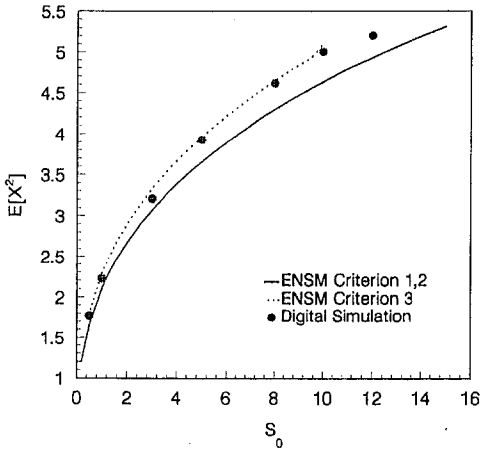


Fig. 4 Variance $E[X^2]$ of stationary response of system (2-1). The symbols and parameters are the same as in Fig. 3 except $a_1 = 0.05$ and $a_2 = 0.1$.

c_{22} are unknown functionals of X, $\dot{X}$, Y, and $\dot{Y}$ to be determined. In order that system (2-5) has the exact stationary solution, c_{11} and c_{22} should satisfy the following equation (Zhu and Yang, 1996):

$$c_{11}\sigma_2^2 D_{22} = c_{22}\sigma_1^2 D_{11}. \tag{2-6}$$

Let

$$\frac{c_{22}}{c_{11}} = \frac{\sigma_2^2 D_{22}}{\sigma_1^2 D_{11}} = r. \tag{2-7}$$

Then c_{11} is the only independent unknown damping coefficient to be determined as functional of H_1 and H_2.

The differences between the given system and its equivalent one are in damping forces, i.e.,

$$\epsilon_1 = a_1 X^2 \dot{X} - c_{11}\dot{X}$$

$$\epsilon_2 = a_2 Y^2 \dot{Y} - c_{22}\dot{Y} = a_2 Y^2 \dot{Y} - r c_{11}\dot{Y}. \tag{2-8}$$

The criterion of the least mean-squared difference in damping forces, i.e., Eq. (15) yields

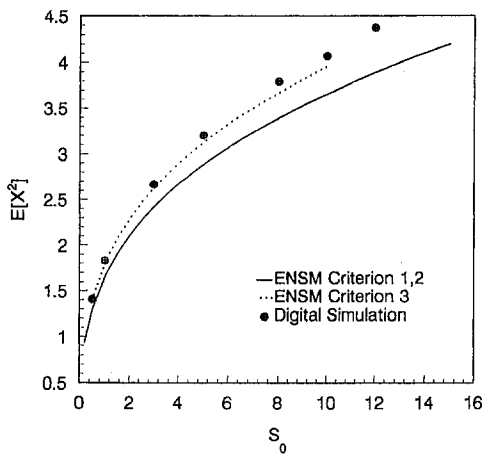


Fig. 5 Variance $E[X^2]$ of stationary response of system (2-1). The symbols and parameters are the same as in Fig. 3 except $a_1 = 0.1$ and $a_2 = 0.2$.

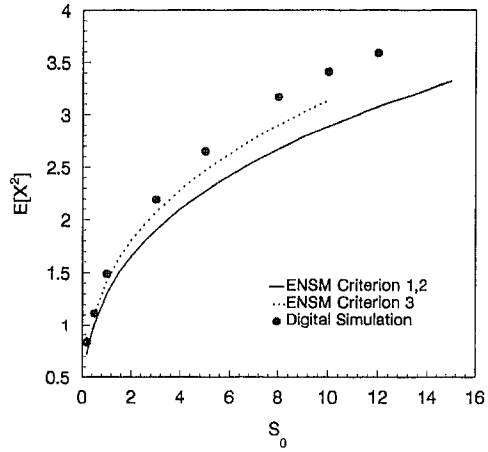


Fig. 6 Variance $E[X^2]$ of stationary response of system (2-1). The symbols and parameters are the same as in Fig. 3 except $a_1 = 0.2$ and $a_2 = 0.4$.

$$c_{11} = \frac{\iint_\Omega [(a_1 x^2 \dot{x}^2 + r a_2 y^2 \dot{y}^2)/|J|]\,dxdy}{\iint_\Omega [(\dot{x}^2 + r^2 \dot{y}^2)/|J|]\,dxdy} \tag{2-9}$$

where

$$J = \begin{vmatrix} \dfrac{\partial H_1}{\partial \dot{x}} & \dfrac{\partial H_1}{\partial \dot{y}} \\ \dfrac{\partial H_2}{\partial \dot{x}} & \dfrac{\partial H_2}{\partial \dot{y}} \end{vmatrix} = (\dot{y}^2 - \dot{x}^2)/4 \tag{2-10}$$

and domain Ω of integration is determined by the following inequalities:

$$2A(x + y)^2 + (x + y)^4 \le 8H_1$$
$$2A(x - y)^2 + (x - y)^4 \le 8H_2. \tag{2-11}$$

The criterion of dissipation energy balancing yields

$$c_{11} = \frac{\iint_\Omega [(a_1 x^2 \dot{x}^2 + a_2 y^2 \dot{y}^2)/|J|]\,dxdy}{\iint_\Omega [(\dot{x}^2 + r\dot{y}^2)/|J|]\,dxdy}. \tag{2-12}$$

The criterion of least mean-squared difference in dissipation energies yields

Downloaded 04 May 2010 to 171.66.16.34. Redistribution subject to ASME license or copyright; see http://www.asme.org/terms/Terms_Use.cfm

$$c_{11} = \frac{\iint_\Omega [(a_1 x^2 \dot{x}^2 + a_2 y^2 \dot{y}^2)(\dot{x}^2 + r\dot{y}^2)/|J|]dxdy}{\iint_\Omega [(\dot{x}^4 + 2r\dot{x}^2\dot{y}^2 + r^2\dot{y}^4)/|J|]dxdy}. \quad (2\text{-}13)$$

Completing the integration in Eqs. (2-9) (see Appendix B), (2-12), and (2-13), we obtain $c_{11}(H_1, H_2)$. The exact stationary solution of the equivalent system governed by Eq. (2-5) is then (Zhu and Yang, 1996)

$$p(x, \dot{x}, y, \dot{y}) = C \exp\left\{ -\frac{1}{\sigma_1^2 D_{11}} \left[\int_{H_{10}}^{H_1} c_{11}(H_1, H_{20}) dH_1 + \int_{H_{20}}^{H_2} c_{11}(H_1, H_2) dH_2 \right] \right\}$$

$$= C \exp[-\psi(H_1, H_2)] \quad (2\text{-}14)$$

where H_1 and H_2 are defined by Eq. (2-4). Equation (2-14) is also the approximate stationary probability density of the given system governed by Eq. (2-1). The approximate statistics of the stationary response of system (2-1) can be obtained from Eq. (2-14), for example, the variance of displacement X is

$$E[X^2] = \int_{-\infty}^{\infty}\int\int\int x^2 p(x, \dot{x}, y, \dot{y}) dxdy$$

$$= C \int_0^\infty\int \exp[-\psi(H_1, H_2)] dH_1 dH_2 \times \iint_\Omega (x^2/|J|)\, dxdy \quad (2\text{-}15)$$

Some numerical results for stationary variance $E[X^2]$ of system (2-1) obtained by using the present method based on the three criteria and from digital simulation are shown Figs. 3–6. Since $\sigma_1 = \sigma_2$ and $D_{11} = D_{22}$, $r = 1$ and the criterion of least mean-squared difference in damping forces and that of dissipation energy balancing yield the same c_{11} (see Eqs. (2–9) and (2–12)). It is seen from these figures that in the case of light damping the present method based on all the three criteria yields excellent results. For heavier damping, the results obtained by using the present method based on the criteria of least mean-squared difference in damping forces and dissipation energy balancing are less than the corresponding results from digital simulation while the present method based on the criterion of least mean-squared difference in dissipation energies still yields very good results.

Concluding Remarks

In the present paper an equivalent nonlinear system method for MDOF stochastically excited and dissipated integrable nonresonant Hamiltonian systems has been developed and three criteria of equivalence have been employed. The comparisons of the results obtained by using the present method with those from digital simulation for two examples indicate that in the case of light damping the present method based on all the three criteria of equivalence yields excellent results and that for heavier damping the present method based on criteria of least mean-squared difference in damping forces and dissipation energy balancing underestimates the mean-square response while the present method based on the criterion of least mean-squared difference in dissipation energies still yields very good results.

An integrable nonlinear Hamiltonian system is usually nondegenerate and it can be regarded as a nonresonant one. So, the present method is applicable to a MDOF stochastically excited and dissipated integrable nonlinear Hamiltonian system as well as a linear Hamiltonian system in a nonresonant case. The present method and the equivalent nonlinear system method for MDOF stochastically excited and dissipated nonintegrable Hamiltonian systems (Zhu, Soong and Lei, 1994; Zhu and Yang, 1995b) constitute an integrated method of an equivalent nonlinear system for MDOF stochastically excited and dissipated nonlinear Hamiltonian systems.

Acknowledgments

The support from the National Natural Science Foundation of China is gratefully acknowledged. The authors thank Dr. Z. G. Ying for printing the figures in the present paper.

References

Cai, G. Q., and Lin, Y. K., 1988a, "On Exact Stationary Solutions of Equivalent Non-Linear Stochastic Systems," *International Journal of Non-Linear Mechanics,* Vol. 23, pp. 315–325.

Cai, G. Q., and Lin, Y. K., 1988b, "A New Approximate Solution technique for Randomly Excited Nonlinear Oscillators," *International Journal of Non-Linear Mechanics,* Vol. 23, pp. 409–420.

Cai, G. Q., Lin, Y. K., and Elishakoff, I., 1992, "A New Approximate Solution Technique for Randomly Excited Nonlinear Oscillatiors," *International Journal of Non-Linear Mechanics,* Vol. 27, pp. 969–979.

Caughey, T. K., 1986, "On Response of Nonlinear Oscillators to Stochastic Excitation," *Probabilistic Engineering Mechanics,* Vol. 1, pp. 2–4.

Lin, A., 1988, "A Numerical Evaluation of the Method of Equivalent Nonlinearization," Ph.D. thesis, California Institute of Technology, Pasadena, CA.

Lutes, L. D., 1970, "Approximate Technique for Treating Random Vibration of Hysteretic Systems," *Journal of Acoustical Society of America,* Vol. 48, pp. 299–306.

Tabor, M., 1989, *Chaos and Integrability in Nonlinear Dynamics,* John Wiley and Sons, New York.

To, C. W. S., and Li, D. M., 1991. "Equivalent Nonlinearization of Nonlinear Systems to Random Excitations," *Probabilistic Engineering Mechanics,* Vol. 6, pp. 184–192.

Zhu, W. Q., Soong, T. T., and Lei, Y., 1994, "Equivalent Nonlinear System Method for Stochastically Excited Hamiltonian Systems," ASME JOURNAL OF APPLIED MECHANICS, Vol. 61, pp. 618–623.

Zhu, W. Q., and Yang, Y. Q., 1996, "Exact Stationary Solutions of sochastically Excited and Dissipated Integrable Hamiltonian Systems," ASME JOURNAL OF APPLIED MECHANICS, Vol. 63, pp. 493–500.

Zhu, W. Q., and Yang, Y. Q., 1997, "Stochastic Averaging of Quasi-Nonintegrable-Hamiltonian Systems," ASME JOURNAL OF APPLIED MECHANICS, Vol. 64, pp. 157–164.

Zhu, W. Q., and Yu, J. S., 1989, "The Equivalent Non-Linear System Method," *Journal of Sound and Vibration,* Vol. 129, pp. 385–395.

APPENDIX A

Let

$$\omega_1^2(y - u_2 x)^2 = z_1^2, \quad \omega_2^2(u_1 x - y)^2 = z_2^2$$

$$\frac{2I_1\omega_1(u_1 - u_2)^2}{1 + u_1^2} = A, \quad \frac{2I_2\omega_2(u_1 - u_2)^2}{1 + u_2^2} = B. \quad (A.1)$$

Then Eq. (1-9) becomes

$$d_{22}\left\{ \sigma_1^4 D_{11}^2 \int_{-\sqrt{A}}^{\sqrt{A}} \int_{-\sqrt{B}}^{\sqrt{B}} \frac{(z_1/\omega_1 + z_2/\omega_2)^4}{(u_1 + u_2)^6} \times \left[\frac{\sqrt{A - z_1^2}}{\sqrt{B - z_2^2}} + \frac{\sqrt{B - z_2^2}}{\sqrt{A - z_1^2}} \right] dz_1 dz_2 \right.$$

$$+ \sigma_2^4 D_{22}^2 \int_{-\sqrt{A}}^{\sqrt{A}} \int_{-\sqrt{B}}^{\sqrt{B}} \frac{(u_1 z_1/\omega_1 + u_2 z_2/\omega_2)^4}{(u_1 - u_2)^6} \times \left. \left[u_1^2 \frac{\sqrt{A - z_1^2}}{\sqrt{B - z_2^2}} + u_2^2 \frac{\sqrt{B - z_2^2}}{\sqrt{A - z_1^2}} \right] dz_1 dz_2 \right\}$$

$$= \sigma_1^2 D_{11} \int_{-\sqrt{A}}^{\sqrt{A}} \int_{-\sqrt{B}}^{\sqrt{B}} \left[-\lambda_1 \frac{(z_1/\omega_1 + z_2/\omega_2)^2}{(u_1 - u_2)^2} \right.$$

Downloaded 04 May 2010 to 171.66.16.34. Redistribution subject to ASME license or copyright; see http://www.asme.org/terms/Terms_Use.cfm

$$+ a_1 \frac{(z_1/\omega_1 + z_2/\omega_2)^4}{(u_1 - u_2)^4}\Bigg]\Bigg[\frac{\sqrt{A - z_1^2}}{\sqrt{B - z_2^2}} + \frac{\sqrt{B - z_2^2}}{\sqrt{A - z_1^2}}\Bigg]$$

$$\times \frac{dz_1 dz_2}{(u_1 - u_2)^2} + \sigma_2^2 D_{22} \int_{-\sqrt{A}}^{\sqrt{A}} \int_{-\sqrt{B}}^{\sqrt{B}} \frac{(-\lambda_1 + \lambda_2)}{(u_1 - u_2)^2}$$

$$\times \Bigg[\left(\frac{u_1 z_1}{\omega_1} + \frac{u_2 z_2}{\omega_2}\right)^2 + a_2 \frac{(u_1 z_1/\omega_1 + u_2 z_2/\omega_2)^4}{(u_1 - u_2)^4}\Bigg]$$

$$\times \Bigg[\frac{u_1^2\sqrt{A - z_1^2}}{\sqrt{B - z_2^2}} + \frac{u_2^2\sqrt{B - z_2^2}}{\sqrt{A - z_1^2}}\Bigg] \frac{dz_1 dz_2}{(u_1 - u_2)^2}. \quad \text{(A.2)}$$

Completing the integration in Eq. (A.2) yields d_{22} as a functional of I_1 and I_2 as follows:

$$d_{22}\{\sigma_1^4 D_{11}^2[\omega_2^4(a^3 + 3a^2 b) + \omega_1^4(b^3 + 3ab^2)$$
$$+ \omega_1^2\omega_2^2(6a^2 b + 6ab^2)] + \sigma_2^4 D_{22}^2[\omega_2^4(u_1^6 a^3 + 3u_1^2 a^2 b)$$
$$+ \omega_1^4(u_2^6 a^3 + 3u_2^2 ab^2) + \omega_1^2\omega_2^2(6u_1^2 a^2 b + 6u_2^2 ab^2)]\}$$
$$= -\sigma_1^2 D_{11}[2\lambda_1(\omega_1^2\omega_2^4(a^2 + 2ab) + \omega_1^4\omega_2^2(b^2 + 2ab)]$$
$$- a_1[\omega_2^4(a^3 + a^2 b) + \omega_1^4(b^3 + 3ab^2)$$
$$+ \omega_1^2\omega_2^2(6a^2 b + 6ab^2)] + \sigma_2^2 D_{22}\{-2(\lambda_1 - \lambda_2)$$
$$\times [\omega_1^2\omega_2^4(u_1^4 a^2 + 2ab) + \omega_1^4\omega_2^2(u_2^4 b^2 + 2ab)]$$
$$+ a_2[\omega_2^4(u_1^6 a^3 + 3u_1^2 a^2 b) + \omega_1^4(u_2^6 b^3 + 3u_2^2 ab^2)$$
$$+ \omega_1^2\omega_2^2(6u_1^2 a^2 b + 6u_2^2 ab^2)]\} \quad \text{(A.3)}$$

where

$$a = 2I_1\omega_1/(1 + u_1^2), \quad b = 2I_2\omega_2/(1 + u_2^2). \quad \text{(A.4)}$$

Introducing the transformations in Eqs. (A.4), Eq. (1-12) becomes

$$p(x, \dot{x}, y, \dot{y}) = C \exp\Bigg[-\frac{u_1(u_1 - u_2)}{2} \int_{a_0}^{a} d_{22}(a, b_0)da$$
$$- \frac{u_2(u_1 - u_2)}{2} \int_{b_0}^{b} d_{22}(a, b)db\Bigg]$$
$$= cf(a, b). \quad \text{(A.5)}$$

Introducing the transformations in Eqs. (A-1) and (A-4), Eq. (1-13) becomes

$$E[X^2] = \frac{4C\omega_1\omega_2}{(1 + u_1^2)(1 + u_2^2)} \iint_0^\infty \exp[-\lambda(I_1, I_2)]dI_1 dI_2$$
$$\times \int_{-\sqrt{A}}^{\sqrt{A}} \int_{-\sqrt{B}}^{\sqrt{B}} \left(\frac{z_1}{\omega_1} + \frac{z_2}{\omega_2}\right)^2 \times \frac{dz_1 dz_2}{\sqrt{A - z_1^2}\sqrt{B - z_2^2}}$$
$$= C \frac{(u_1 - u_2)^2 \pi^2 \omega_1\omega_2}{2}$$
$$\times \int_0^\infty \int_0^\infty f(a, b)\left(\frac{a}{\omega_1^2} + \frac{b}{\omega_1^2}\right)dadb. \quad \text{(A.6)}$$

APPENDIX B

Let

$$z_1 = x + y, \quad z_2 = x - y$$
$$a = -A + \sqrt{A^2 + 8H_1}, \quad b = -A + \sqrt{A^2 + 8H_2} \quad \text{(B.1)}$$

Eq. (2-9) becomes

$$4c_{11} \int_{-\sqrt{a}}^{\sqrt{a}} \int_{-\sqrt{b}}^{\sqrt{b}} \Bigg[(1 + r^2)\frac{\sqrt{H_1 - Az_1^2/4 - z_1^4/8}}{\sqrt{H_2 - Az_2^2/4 - z_2^4/8}}$$
$$+ (1 - r^2)\frac{\sqrt{H_2 - Az_2^2/4 - z_2^4/8}}{\sqrt{H_1 - Az_1^2/4 - z_1^4/8}}\Bigg]dz_1 dz_2$$
$$= (a_1 + ra_2) \int_{-\sqrt{a}}^{\sqrt{a}} \int_{-\sqrt{b}}^{\sqrt{b}} \Bigg[(z_1^2 + z_2^2)\frac{\sqrt{H_1 - Az_1^2/4 - z_1^4/8}}{\sqrt{H_2 - Az_2^2/4 - z_2^4/8}}$$
$$+ \frac{\sqrt{H_2 - Az_2^2/4 - z_2^4/8}}{\sqrt{H_1 - Az_1^2/4 - z_1^4/8}}\Bigg]dz_1 dz_2. \quad \text{(B.2)}$$

Completing the integration in Eq. (B-2) yields c_{11} as a functional of H_1 and H_2. Introducing the transformations in Eq. (B-1) and polar coordinates

$$H_1 = r\cos\theta, \quad H_2 = r\sin\theta, \quad 0 \le \theta \le \pi/2. \quad \text{(B.3)}$$

Equation (2-15) becomes

$$E[X^2] = \frac{C}{2} \int_0^\infty \int_0^{\pi/2} \exp[-\psi(r\cos\theta, r\sin\theta)]d\theta dr$$
$$\times \int_{-\sqrt{a}}^{\sqrt{a}} \int_{-\sqrt{b}}^{\sqrt{b}} \frac{(z_1^2 + z_2^2)dz_1 dz_2}{\sqrt{H_1 - Az_1^2/4 - z_1^4/8}\sqrt{H_2 - Az_2^2/4 - z_2^4/8}}. \quad \text{(B.4)}$$

Downloaded 04 May 2010 to 171.66.16.34. Redistribution subject to ASME license or copyright; see http://www.asme.org/terms/Terms_Use.cfm

Experiments on Nonlinear Dynamic Behavior of an Oscillator With Clearance and Periodically Time-Varying Parameters

A. Kahraman[1]

G. W. Blankenship
Mem. ASME.

General Motors Corporation,
Powertrain Division,
37350 Ecorse Road,
Romulus, MI 48174-1376

A number of experiments on a physical system with clearance having combined parametric and external forcing excitation are presented. The data demonstrate several nonlinear phenomena that exist in periodically excited oscillators subject to clearance at a contact interface. Jump discontinuities in forced response curves are shown to exist and subharmonic resonances which are formed by period-n (nT) motions with $n \geq 2$ are demonstrated. Long-period subharmonic motions with periods as long as nine times the excitation period are reported. Finally, several cases of measured chaotic motions are also illustrated through time-traces, phase portraits, Fourier spectra, and Poincare plots which form strange attractors.

1 Introduction

Certain classes of mechanical systems having clearances at a contact interface which transmits motion or force are also subject to periodically time-varying forcing and parametric excitations. This is especially common in rotating machinery. Such systems give rise to complex dynamic behavior exhibiting a rich spectrum of nonlinear phenomena. The single-degree-of-freedom mechanical oscillator shown in Fig. 1 can be considered as a generic model for such systems. The equation of motion for this oscillator is given in dimensionless form as

$$\frac{d^2x}{d\tau^2} + 2\zeta\frac{dx}{d\tau} + w(\tau)g[x(\tau)] = f(\tau) \qquad (1a)$$

where $x(\tau)$ is the displacement of the unit mass, ζ is the viscous damping ratio, and τ represents dimensionless time. The time-varying stiffness $w(\tau)$ and external excitation $f(\tau)$ functions are assumed to be periodic in τ and can therefore be expressed in terms of the Fourier series

$$w(\tau) = w_o + \sum_{r=1}^{\infty}[w_r \cos(r\Lambda\tau) + \tilde{w}_r \sin(r\Lambda\tau)], \quad (1b)$$

$$f(\tau) = f_o + \sum_{r=1}^{\infty}[f_r \cos(r\Lambda\tau) + \tilde{f}_r \sin(r\Lambda\tau)]. \quad (1c)$$

Both $w(\tau)$ and $f(\tau)$ are assumed to be commensurate with fundamental frequency Λ having respective Fourier coefficients w_r, $\tilde{w}_r$, f_r, and $\tilde{f}_r$ where r is a harmonic index. The mean component of $f(\tau)$ corresponds to a preload denoted by f_o and in general $w_o = 1$. All impacts are assumed to be purely elastic and a linear viscous damping term is assumed for clarity. The nonlinear displacement function $g[x(\tau)]$ can take on many forms depending upon the physical system. In this study, a symmetric backlash type function is considered without loss of generality:

$$g[x(\tau)] = \begin{cases} x(\tau) - 1; & x(\tau) > 1, \\ 0; & |x(\tau)| \leq 1, \\ x(\tau) + 1; & x(\tau) < -1. \end{cases} \qquad (1d)$$

Equation (1) is a nonlinear time-varying (NTV) equation due to the periodically time-varying stiffness $w(\tau)$ and the clearance $g[x(\tau)]$. There appear to be only a few published studies which consider the specific NTV formulation of Eq. (1). Kahraman and Singh (1991) and Sato et al. (1991) have solved forms of Eq. (1) numerically. A general analytical solution using a multiterm harmonic balance method approached was proposed by Blankenship and Kahraman (1995) and Kahraman and Blankenship (1996). In another recent study, a parametric continuation technique in conjunction with the harmonic balance method was utilized by Padmanabhan and Singh (1996) to solve Eq. (1).

Two limiting cases of Eq. (1) have been widely studied by several investigators; (i) linear systems with time-varying coefficients (LTV) having $g[x(\tau)] = x(\tau)$ and (ii) nonlinear systems with time-invariant coeficients (NTI) such that $w(\tau) = 1$ and having various discontinuous forms of $g[x(\tau)]$. Two pertinent LTV forms which are germane to this problem formulation are the well-studied forced Hill's equation (Hsu and Cheng, 1974) and the Meisner equation (Richards, 1983). Such systems exhibit parametric resonances at integer multiples of the harmonic excitation frequencies and also contain regions of instability. Several NTI systems having clearance-type nonlinearities have been studied by a large number of investigators. These NTI studies report a wide range of predicted nonlinear behavior. Discontinuities in the forced response curves formed by sudden *jumps* at or near the primary and subharmonic resonances, which arise as a result of multiple coexisting steady-state solutions, have been reported (Tomlinson and Lam, 1984; Natsiavas, 1989). The clearance-type function $g[x(\tau)]$ considered here has been shown to cause both single-sided impacts (SSI) and double-sided impacts (DSI) (Shaw, 1985; Comparin and Singh, 1989; Kahraman and Singh, 1990; Blankenship and

[1] To whom all correspondence should be addressed.

Contributed by the Applied Mechanics Division of THE AMERICAN SOCIETY OF MECHANICAL ENGINEERS for publication in the ASME JOURNAL OF APPLIED MECHANICS.

Discussion on this paper should be addressed to the Technical Editor, Professor Lewis T. Wheeler, Department of Mechancial Engineering, University of Houston, Houston, TX 77204-4792, and will be accepted until four months after final publication of the paper itself in the ASME JOURNAL OF APPLIED MECHANICS.

Manuscript received by the ASME Applied Mechanics Division, Nov. 11, 1995; final revision, June 3, 1996. Associate Technical Editor: S. W. Shaw.

Copyright © 1997 by ASME

Downloaded 04 May 2010 to 171.66.16.34. Redistribution subject to ASME license or copyright; see http://www.asme.org/terms/Terms_Use.cfm

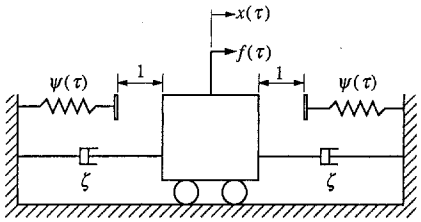


Fig. 1 A parametrically and externally excited mechanical oscillator subject to a clearance

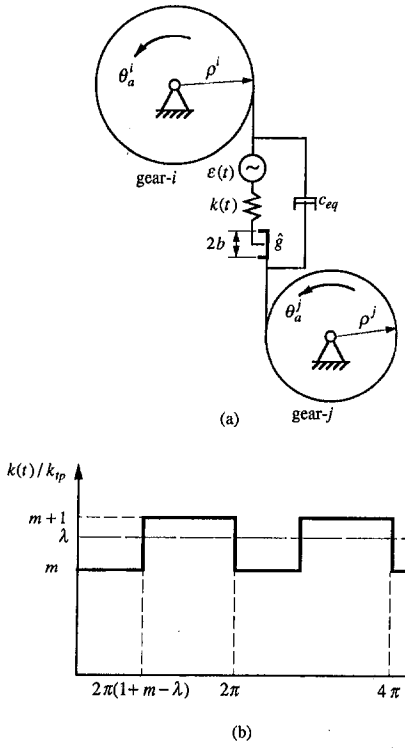


Fig. 2 (*a*) The dynamic model of a gear pair; (*b*) periodically time-varying stiffness function

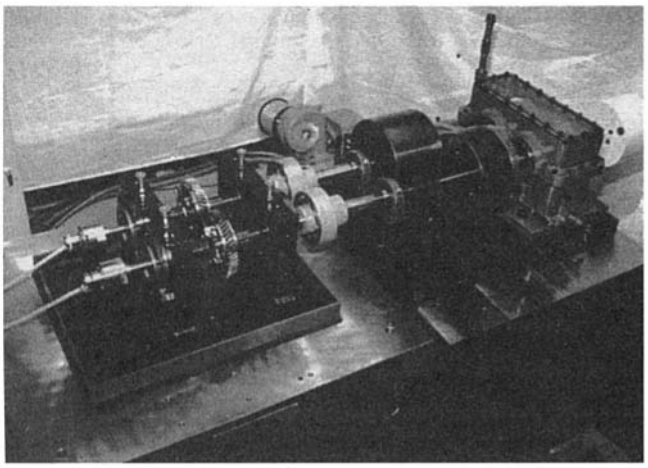


Fig. 3 The four-square gear dynamics test rig

Kahraman, 1996) and analytical criteria for the transitions from linear no-impact (NI) motions to nonlinear SSI and DSI motions were derived by using single-term harmonic balance formulations (Blankenship and Kahraman, 1996). Subharmonic

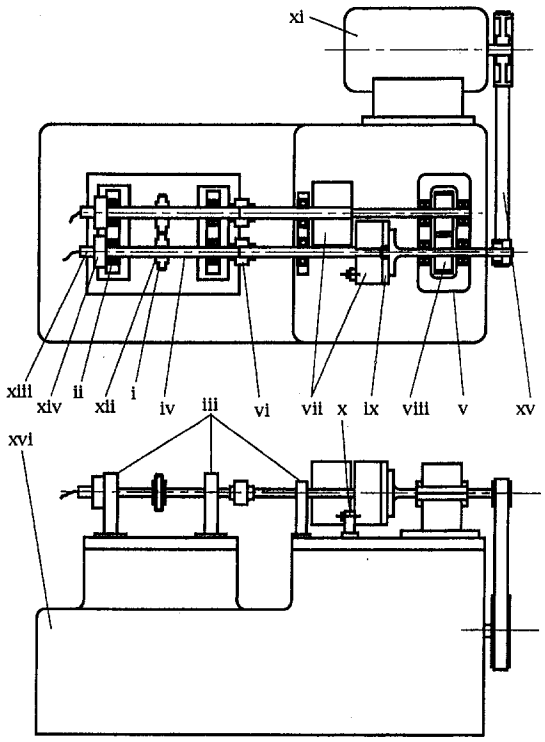


Fig. 4 Description of the components of the test rig. (i) precision test gear pair, (ii) precision spherical roller bearings, (iii) rigid bearing pedestals, (iv) test gear shafts, (v) slave gear box, (vi) compliant elastomer couplings, (vii) flywheels, (viii) precision helical slave gears, (ix) split hub coupling, (x) locking pin, (xi) DC motor, (xii) tangentially mounted piezoelectric accelerometers, (xiii) slip rings, (xiv) high-resolution optical encoders (18,000 lines) to control sampling rates, (xv) drive belt, and (xvi) polymer grenite base.

resonances have been predicted to occur near integer multiples of the primary resonance frequency (Shaw and Holmes, 1983; Thompson and Elvey, 1984; Choi and Noah, 1988, 1992; Natsiavas and Gonzalez, 1992; Kahraman and Blankenship, 1996; Padmanabhan and Singh, 1995). Numerical integration techniques were used to demonstrate the existence of other long-period subharmonic motions (Shaw and Holmes, 1983; Kahraman, 1992). Finally, several studies have reported cases of chaotic motions predicted numerically and proposed possible routes to chaos such as period-doubling cascades (Shaw and

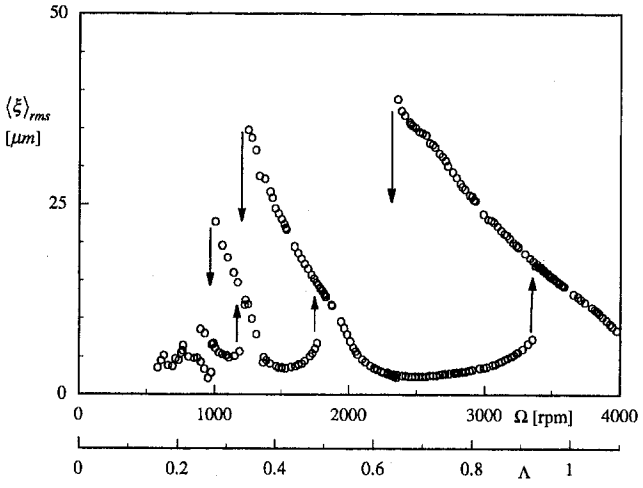


Fig. 5 Measured forced response of a gear pair with $\lambda = 1.75$ and $\epsilon(t) = 0$. Transmitted torque is 340 N-m.

Downloaded 04 May 2010 to 171.66.16.34. Redistribution subject to ASME license or copyright; see http://www.asme.org/terms/Terms_Use.cfm

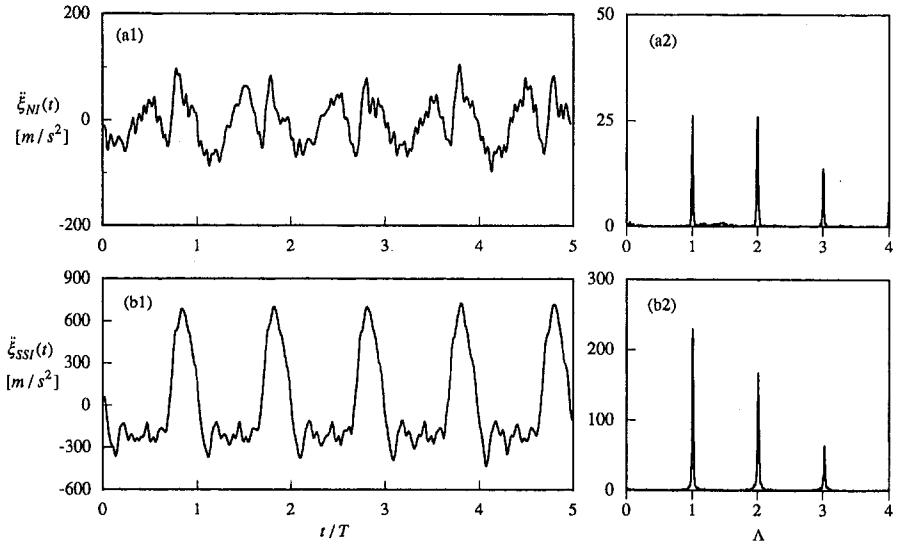


Fig. 6 Measured time traces $\ddot{\xi}(t)$ and the corresponding Fourier spectra of (*a*) lower branch NI motion and (*b*) upper branch SSI motion of Fig. 5 at $\Lambda = 0.76$

Holmes, 1983; Natsiavas, 1989; Sato et al., 1991; Kahraman, 1992; Mahfouz and Badrakhan, 1990; Kim and Noah, 1991; Karagiannis and Pfeiffer, 1991; Mevel and Guyader, 1993).

In contrast to the rich portfolio of theoretical work published on systems with clearances, only limited experiments have been reported in the literature that validate or, at least qualitatively, support the types of predicted nonlinear behavior mentioned above (Moon and Shaw, 1983; Shaw, 1985; Ehrich, 1992; Bayly and Virgin, 1993; Fang and Wickert, 1994; Blankenship and Kahraman, 1995; Kahraman and Blankenship, 1996). For instance, Shaw and Moon (1983) and Shaw (1985) used a beam subjected to a rigid stop to demonstrate the existence of subharmonic and chaotic motions in a low-frequency mechanical oscillator. The present authors (Blankenship and Kahraman, 1995; Kahraman and Blankenship, 1996) presented high-frequency rotating machinery vibration data which demonstrated the existence of jumps, multiple coexisting stable motions, and $2T$ subharmonic resonances. However, many nonlinear phenomena predicted to exist as a part of the overall dynamic behavior of oscillators with clearances and combined parametric and forcing excitation are yet to be demonstrated experimentally in the context of a commonplace mechanical system. Accordingly, the main objective of this study is to present a comprehensive set of experimental data that clearly demonstrates several of these phenomena. The intent here is not to mathematically describe the complex nature of the entire nonlinear system behavior, but to bring some relevance to the published theoretical work in this area.

2 Experiment

2.1 Physical System. The physical system considered in this experiment is a gear pair whose simplified mechanical model is shown in Fig. 2(*a*) (Blankenship and Kahraman, 1995). The rotation angle of each gear $\theta^i(t) = \Omega^i t + \theta^i_a(t)$ is written as the sum of a nominal rotation angle $\Omega^i t$ and a vibratory component $\theta^i_a(t)$ which arises due to the meshing action. Here superscripts i and j denote gear i and gear j, respectively; t represents real time and Ω^i is the mean rotational velocity of gear i. The Ω^i and Ω^j are related kinematically by $\rho^i\Omega^i = \rho^j\Omega^j$

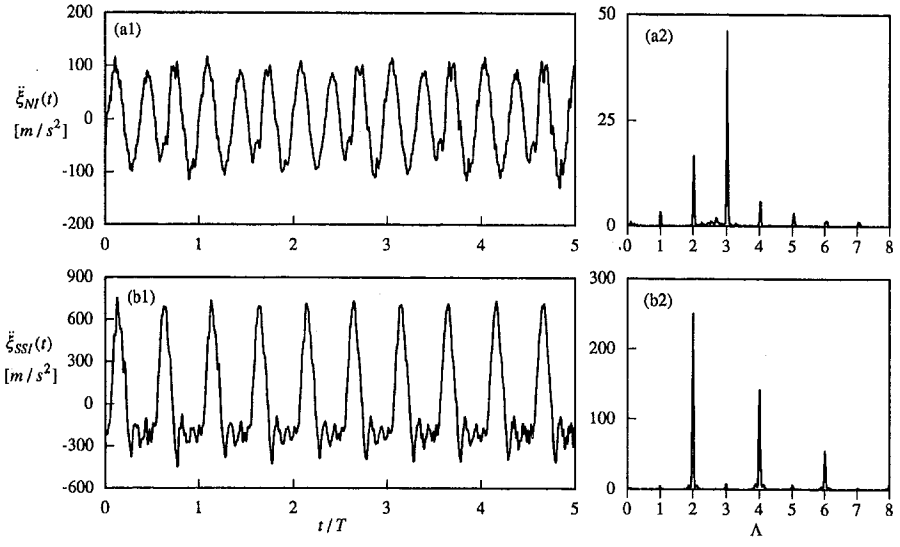


Fig. 7 Measured time traces $\ddot{\xi}(t)$ and the corresponding Fourier spectra of (*a*) lower branch NI motion and (*b*) upper branch SSI motion at $\Lambda = 0.39$ of Fig. 5

Downloaded 04 May 2010 to 171.66.16.34. Redistribution subject to ASME license or copyright; see http://www.asme.org/terms/Terms_Use.cfm

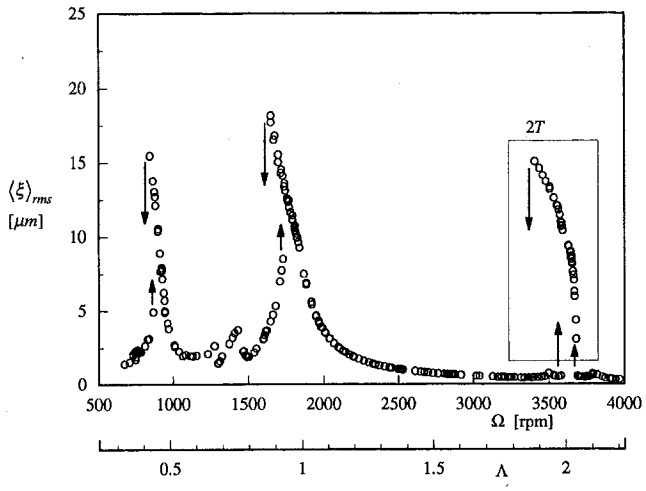


Fig. 8 Measured forced response of a gear pair with λ = 1.75 and $\epsilon(t)$ = 0. Transmitted torque is 130 N-m.

where ρ^i and ρ^j are the base radii. Since the system is semi-definite, the dynamic model may be reduced to a single degree-of-freedom in terms of the coordinate $\xi(t) = \rho^i\theta_a^i(t) + \rho^j\theta_a^j(t)$ which represents relative displacement across the mesh interface. The corresponding equation of motion is given by

$$m_{eq}\frac{d^2\xi}{dt^2} + c_{eq}\frac{d\xi}{dt} + k(t)\hat{g}\{\xi(t) - \epsilon(t)\} = F(t), \quad (2a)$$

$$\hat{g}\{\xi(t) - \epsilon(t)\} = \begin{cases} \xi(t) - \epsilon(t) - b; & \xi(t) - \epsilon(t) > b \\ 0; & |\xi(t) - \epsilon(t)| \le b \\ \xi(t) - \epsilon(t) + b; & \xi(t) - \epsilon(t) < -b \end{cases} \quad (2b)$$

where $m_{eq} = I^iI^j/[I^i(\rho^j)^2 + I^j(\rho^i)^2]$ is the system equivalent mass determined from the polar mass moment of inertia I^i of each gear, c_{eq} is an equivalent viscous damping coefficient, which can sufficiently describe frictional losses of the system (Blankenship and Kahraman, 1995), $F(t)$ is the periodically time-varying external excitation as a result of torque fluctuations, and $2b$ is the total backlash.

The term $\epsilon(t)$, *known as gear transmission error,* is an equivalent displacement excitation applied at the mesh interface which describes manufacturing errors and intentional modification of tooth profiles from perfect involute form. The instantaneous mesh stiffness $k(t)$ varies as the number of teeth in contact at any instant in time varies between m and $m + 1$. Here m is the minimum number of tooth pairs in contact at any instant assuming that no tooth separations occur. Both $\epsilon(t)$ and $k(t)$ are assumed to be periodic in t with fundamental meshing frequency $\Omega_{mesh} = N^i\Omega^i = N^j\Omega^j$ where N^i is the number of teeth on each gear i. Hence both $\epsilon(t)$ and $k(t)$ may be expressed in terms of the following Fourier series:

$$\epsilon(t) = \epsilon_o + \sum_{r=1}^{\infty}[\epsilon_r \cos(r\Omega_{mesh}t) + \tilde{\epsilon}_r \sin(r\Omega_{mesh}t)], \quad (3a)$$

$$k(t) = k_o + \sum_{r=1}^{\infty}[k_r \cos(r\Omega_{mesh}t) + \tilde{k}_r \sin(r\Omega_{mesh}t)]. \quad (3b)$$

In practice, the spectral content of $\epsilon(t)$ can be accurately controlled up to the $r = 2$ harmonic component by grinding topographical modifications on gear tooth flanks having amplitudes on the order of 1 to 10 μm. There is no mean component of $\epsilon(t)$; hence $\epsilon_o = 0$. For precision involute gear teeth having no tooth flank modifications, $\epsilon(t) \approx 0$. Similarly, the spectral content of $k(t)$ can be controlled in a spur gear pair by varying the so-called *involute contact ratio* λ, which corresponds to the average number of teeth in contact throughout a meshing cycle. The mesh stiffness function $k(t)$ can be approximated as a rectangular wave as shown in Fig. 2(*b*) which varies between mk_{tp} and $(m + 1)k_{tp}$ and has a mean value $k_o = \lambda k_{tp}$ where k_{tp} is the stiffness of a single tooth pair in contact. In general, $m \le \lambda \le m + 1$ where $m = \text{int}(\lambda)$. For integer values of λ, $\lambda = m$ and the alternating component of $k(t)$ is eliminated; i.e., $k(t) = mk_{tp} = k_o$.

Typically, λ can be varied by simply changing the addendum or outer diameter of each test gear while leaving all other gear design variables unchanged. Thus accurate control of the harmonic content of $k(t)$ up to $r = 3$ is possible.

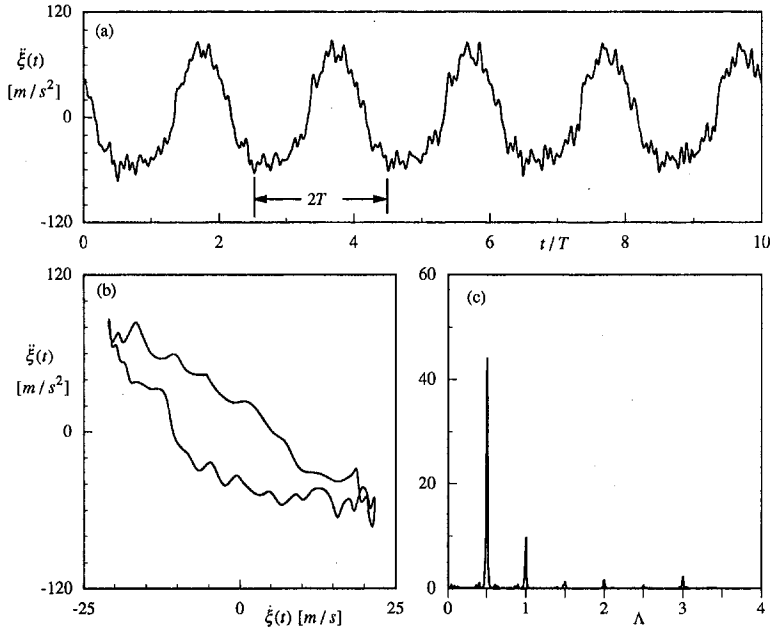


Fig. 9 Measured upper branch 2T motion of Fig. 8 at Λ = 1.9; (*a*) time trace $\ddot{\xi}(t)$, (*b*) phase plane plot $\ddot{\xi}(t)$ versus $\dot{\xi}(t)$, and (*c*) Fourier spectrum of $\ddot{\xi}(t)$

Downloaded 04 May 2010 to 171.66.16.34. Redistribution subject to ASME license or copyright; see http://www.asme.org/terms/Terms_Use.cfm

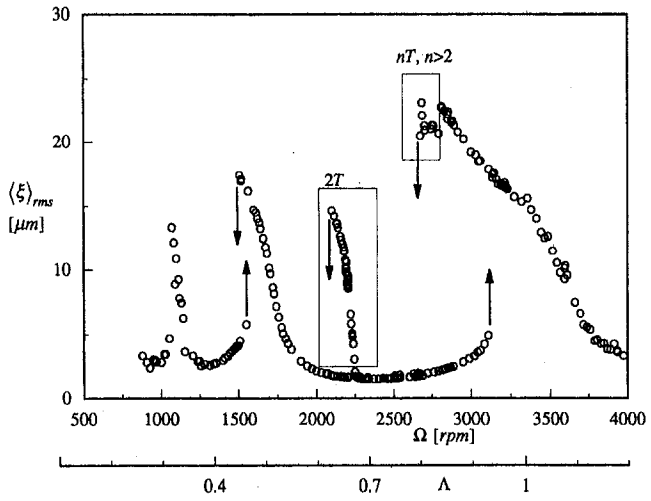


Fig. 10 Measured forced response of a gear pair with $\lambda = 1.1$ and $\epsilon(t) = 0$. Transmitted torque is 340 N-m.

Equation (2) can be reduced to the nondimensional form of Eq. (1) for the limiting case of $\epsilon(t) = 0$, by letting $\tau = \omega_n t$, $\omega_n = \sqrt{k_o/m_{eq}}$, $x(\tau) = \xi(\tau)/b$, $\zeta = c_{eq}/2\sqrt{m_{eq}k_o}$, $w(\tau) = k(\tau)/k_o$ and $f(\tau) = F(\tau)/k_o b$. The dimensionless excitation frequency is given by $\Lambda = \Omega_{mesh}/\omega_n$.

2.2 Test Rig. The four-square gear test rig shown in Fig. 3 was designed to measure $\xi(t)$ for a gear pair operating under a range of speed and load conditions with tightly controlled system parameters in order to generate nonlinear forced response curves having minimal scatter. A power recirculating gear box arrangement was employed for efficiency and to ensure precise torque regulation. No external torque fluctuations are possible with this arrangement so that $F(t) = F_o$. Several unique features are required in order to ensure that the behavior of the test rig is indeed described by Eq. (1); some of which are labeled in Fig. 4. Experimental investigations indicated that system damping is quite low $\zeta \approx 0.02$ and is dictated primarily by the bearings; thus the omission of a nonlinear damping term in Eq. (1) to account for a reduction in system damping when tooth separations occur is valid. The test gears are of a standard $N^i = N^j = 50$ tooth design and precision ground to control both $\epsilon(t)$ and $k(t)$. Readers are referred to Blankenship and Kahraman (1995) for further details of the test rig and hardware.

2.3 Instrumentation, Data Acquisition, and Signal Processing. The measurement of $\ddot{\xi}(t)$ was accomplished by mounting four piezoelectric accelerometers tangentially to the gear wheel. In order to cancel gravitational effects and any transverse vibrations, all four accelerometer signals are added vectorally. The resulting angular acceleration of each gear is then added in the time domain to obtain $\ddot{\xi}(t)$ and subsequently integrated to yield velocity $\dot{\xi}(t)$.

Analog signals representing $\ddot{\xi}(t)$ and $\dot{\xi}(t)$ are captured and analyzed in real time by using a high-speed multiple-channel spectrum analyzer. Synchronous time averaging was employed to average slight differences among individual teeth that might exist due to unavoidable manufacturing errors; the effects of which were otherwise neglected by the periodicity assumptions in Eqs. (3). The rth harmonic displacement amplitudes ξ_r of $\xi(t)$ are determined by double pseudo-integration of $\ddot{\xi}(t)$ in the orders domain according to

$$\xi_r = \frac{1}{(2\pi r\Omega_{mesh})^2}\left[\sum_{s^i=N^i-BW/2}^{N^i+BW/2} W_{\ddot{\xi}\ddot{\xi}}(rs^i)\right]^{1/2} \qquad (4a)$$

where $W_{\ddot{\xi}\ddot{\xi}}(s^i)$ is the one-sided discrete autopower spectrum of $\ddot{\xi}(t)$ corresponding to shaft order index s^i and BW is the analysis bandwidth in shaft orders. This method allows direct measurement of the ξ_r to an accuracy of 0.001 μm at 1000 Hz. A typical value of $BW = 4$ was chosen to account for certain errors inherent to experimental spectrum analysis.

2.4 Data Presentation. Five types of experimental plots are constructed using the measured $\ddot{\xi}(t)$ and $\dot{\xi}(t)$. Steady-state *time traces* were constructed by high-speed sampling of $\ddot{\xi}(t)$ and $\dot{\xi}(t)$ at a sampling period of $T/10$ where $T = 2\pi/$

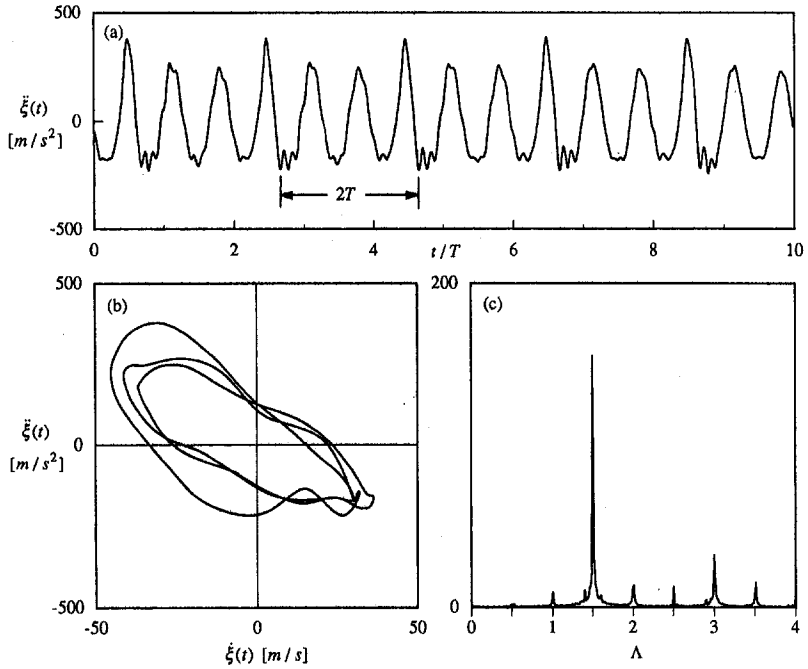


Fig. 11 Measured upper branch 2T motion of Fig. 10 at $\Lambda = 0.63$; (a) time trace $\ddot{\xi}(t)$, (b) phase plane plot $\ddot{\xi}(t)$ versus $\dot{\xi}(t)$, and (c) Fourier spectrum of $\ddot{\xi}(t)$

Downloaded 04 May 2010 to 171.66.16.34. Redistribution subject to ASME license or copyright; see http://www.asme.org/terms/Terms_Use.cfm

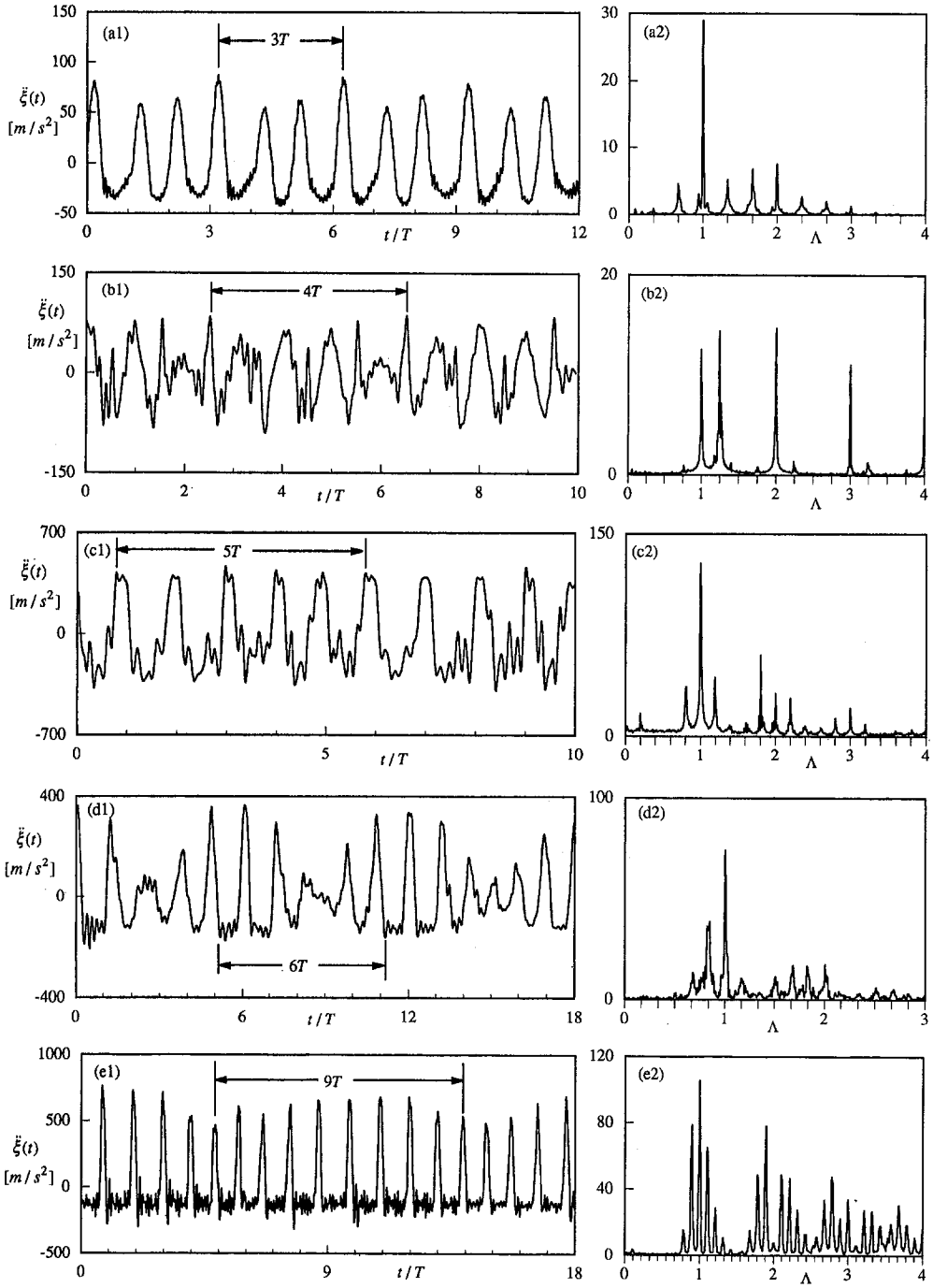


Fig. 12 Measured long-period subharmonic motions; (*a*) a 3*T* motion at $\Lambda = 0.89$ of a gear pair with $\lambda = 1.75$ and torque value of 42 N-m; (*b*, *c*) 4*T* and 5*T* motions of Fig. 10 at $\Lambda = 0.8$ and $\Lambda = 0.82$, respectively; (*d*) upper branch 6*T* motion of Fig. 13 at $\Lambda = 1.04$; and (*e*) upper branch 9*T* motion of Fig. 14 at $\Lambda = 0.56$

Ω_{mesh} is the tooth meshing period. Hence ten points per meshing cycle were collected at a maximum sampling frequency around 34,000 Hz. *Phase Portraits* were obtained by plotting discrete values of $\ddot{\xi}(t)$ versus $\dot{\xi}(t)$ over a period of $0 \le t/T \le N$ where N is the number of meshing cycles. Typically $N = 5$ mesh cycles were plotted to allow sufficient overlap of the trajectories to clearly demonstrate the periodicity and excellent repeatability of the system. *Fourier spectra* of $\ddot{\xi}(t)$ were obtained directly by Fast Fourier Transform of the analog signal using a spectrum analyzer. Autopower spectra were then used to compute ξ_r by using Eq. (4*a*). An equivalent root-mean-square (rms) amplitude ξ_{rms} of the alternating component of $\xi(t)$ is computed by using only the first three integer and half-mesh orders, i.e.,

$$\xi_{rms} = [\sum_{r=1}^{3} (\xi^2_{(2r-1)/2} + \xi^2_r)]^{1/2}. \quad (4b)$$

Forced response curves were then generated by plotting discrete values of ξ_{rms} versus shaft rotational speed Ω in rpm and dimensionless frequency Λ. Accordingly, the forced response functions shown in the subsequent sections represent only 1*T* and 2*T* motions completely. *Poincare plots* were generated by plotting discrete values of $\ddot{\xi}(nT)$ versus $\dot{\xi}(nT)$ over a period of $0 \le n \le 10{,}000$. Here both phase portraits and Poincare plots are generated from $\ddot{\xi}$ and $\dot{\xi}$ rather than $\dot{\xi}$ and ξ to minimize inaccuracies and misrepresentation of time traces due to the inherent filtering associated with the time-domain integration process.

Downloaded 04 May 2010 to 171.66.16.34. Redistribution subject to ASME license or copyright; see http://www.asme.org/terms/Terms_Use.cfm

3 Measured Nonlinear Phenomena

In this section, various types of nonlinear phenomena are demonstrated using the gear test rig by varying four operation and gear design parameters, namely, the gear involute contact ratio λ, gear transmission error $\epsilon(t)$, the mean torque transmitted F_o, and the gear rotational speed Ω_{mesh}.

3.1 Jump Discontinuities in Forced Response Curves. Figure 5 illustrates a typical measured forced response curve for a system having $\lambda = 1.75$ and $\epsilon(t) = 0$. Both Ω and $\Lambda = \Omega_{\text{mesh}}/\omega_n$ are displayed along the abscissa here since ω_n varies for each gear pair as a function of λ. Almost all motions represented are of $1T$ type and three sets of jumps are evident. Each is defined by a softening-type curve characterized by a *backbone* bent to the left and bounded by a *jump-up* as Λ is increased and a *jump-down* as Λ is reduced. In general, each jump is governed by a particular harmonic of the excitation having harmonic index r and takes place near the corresponding primary resonance frequency $\Lambda = 1/r$. For instance, the jump caused by the fundamental excitation harmonic ($r = 1$) is in the vicinity of $\Lambda \approx 1$ and bounded by jump-up and jump-down frequencies of $\Lambda = 0.92$ and $\Lambda = 0.63$, respectively. Softening-type nonlinear behavior of systems with clearances occurs due to loss of contact or separations which result in SSI motions. In the regimes bounded by jump-down and jump-up frequencies, two stable $1T$ motions coexist. This is illustrated in Figs. 6 and 7 which corresponds to motions at $\Lambda = 0.76$ and $\Lambda = 0.39$, respectively. The lower branch motions shown in Figs. 6(a) and 7(a) are linear NI motions which occur before separations take place. As Λ is increased, separations occur at a frequency soon after the lower branch SSI motion loses stability through a fold bifurcation and jumps up to the upper branch SSI motion as shown in Figs. 6(b) and 7(b). Here, multiple impacts occur during a given cycle which are characterized by the high-frequency fluctuations seen in the measured $\ddot{\xi}(t)$ time traces.

As a final note, the jumps illustrated in Fig. 5 are not exceptions. Such behavior has been commonly observed in the majority of over 100 tests conducted using systems having different λ and $\epsilon(t)$ operating under various speed and torque conditions. This is also evident in the many other frequency response curves presented in subsequent sections. As Λ is brought close to a resonant frequency, the amplitudes of $\xi(t)$ increase significantly since the system damping ratio is quite low. As a result of this, separations are initiated near resonance frequencies which gives rise to multiple coexisting stable motions and jumps. Finally, DSI motions could not be observed in these tests because the vibration amplitudes were small, $|\xi(t)| \leq 50$ μm, compared to the amount of clearance $2b \approx 100$ μm.

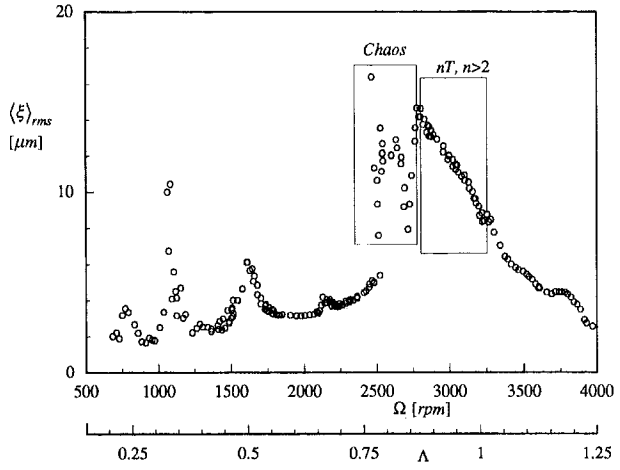


Fig. 13 Measured forced response of a gear pair with $\lambda = 1.4$, $\omega_n = 2665$ Hz (3200 rpm) and torque of 170 N-m. Gears have slight tooth flank modifications so that $\epsilon(t) \neq 0$.

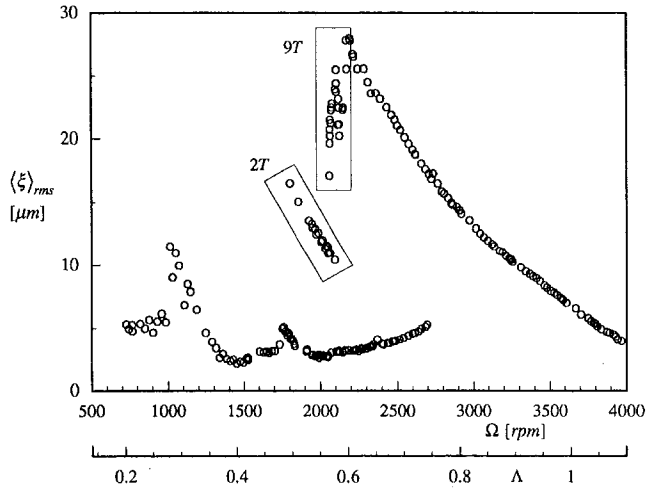


Fig. 14 Measured forced response of an unmodified gear pair with $\lambda = 1.4$ and $\epsilon(t) = 0$. The transmitted torque is 170 N-m.

3.2 Subharmonic Resonances. A typical forced response curve which exhibits both primary and subharmonic resonances is illustrated in Fig. 8. In addition to the primary resonances associated with the first two $r = 1$ and $r = 2$ harmonic components of the excitation near $\Lambda = 1$ and $\Lambda = \frac{1}{2}$, respectively, a third resonance peak with essentially the same type of jump characteristics exists at a frequency nearly twice that of the primary $r = 1$ resonance peak. This is a $\Lambda = 2r$ resonance due to the fundamental $r = 1$ component of the excitation, and occurs near $\Lambda = 2$. As Λ is increased, the $1T$ motion loses stability at $\Lambda = 1.98$ jumping up to another stable $2T$ motion. The spectral content of the $2T$ response at $\Lambda = 1.9$ shown in Fig. 9 is clearly dominated by the $\frac{1}{2}$ harmonic and the acceleration time trace has a period twice as long as the fundamental excitation period. Similarly, as Λ is reduced along the upper branch of $2T$ motions, the SSI type $2T$ subharmonic motion bifurcates to a NI type $1T$ motion resulting in a drastic jump down at $\Lambda = 1.86$. The overlap of upper and lower branches illustrates the coexistence of a stable nT subharmonic motion with a stable $1T$ motion.

The data shown in Fig. 8 undoubtedly demonstrates that the $r = 1$ harmonic of the excitation can cause subharmonic resonances formed by nT motions ($n > 1$) around $\Lambda \approx n$. Excitation harmonics with index other than $r = 1$ can also cause subharmonic resonances as shown in Fig. 10 for another system having $\lambda = 1.1$ and $\epsilon(t) = 0$. Here, the $r = 3$ harmonic component of the excitation, which produces a primary resonance near $\Lambda = 1/r = \frac{1}{3}$, also produces a $2T$ subharmonic resonance at $\Lambda = n/r = \frac{2}{3}$. The spectral content of this upper branch SSI response at $\Lambda = 0.65$ is characterized by a dominant $\frac{3}{2}$ harmonic component which results in a very well defined $2T$ acceleration time trace as shown in Fig. 11.

Similar to $2T$ subharmonic resonances, resonances of nT motions with $n > 2$ should also exist near their respective resonance frequencies $\Lambda = n/r$ (Kahraman and Blankenship, 1996). However, due to current speed limitations of the test rig, demonstration of such resonances beyond the ones governed by $2T$ motions are left to future work.

3.3 Long-Period Subharmonic Motions. In addition to $2T$ motions that are shown to exist at subharmonic resonance frequencies $\Lambda = 2/r$, other mostly long-period nT motions have also been recorded at frequencies away from $\Lambda = n/r$ during a series of experiments with λ values ranging from 1.4 to 2 and

Downloaded 04 May 2010 to 171.66.16.34. Redistribution subject to ASME license or copyright; see http://www.asme.org/terms/Terms_Use.cfm

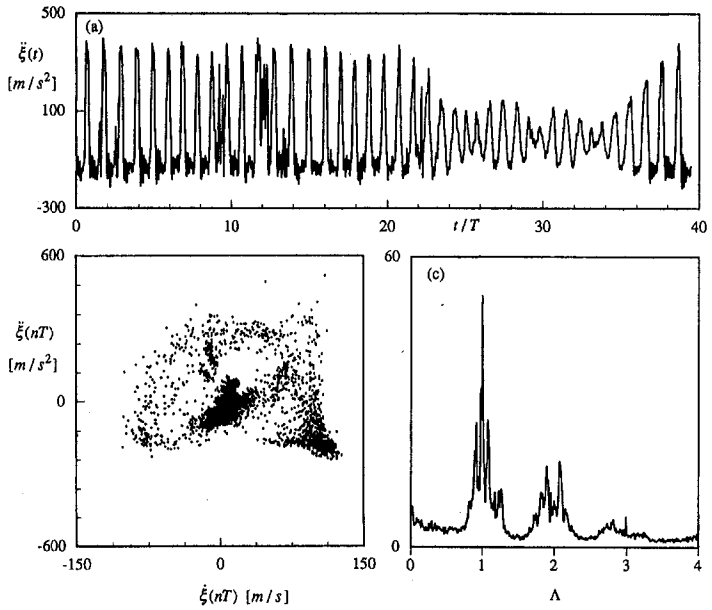


Fig. 15 Measured chaotic motion of Fig. 13 at $\Lambda = 0.8$; (*a*) time trace $\ddot{\xi}(t)$, (*b*) Poincare map $\ddot{\xi}(nT)$ versus $\dot{\xi}(nT)$ where n = 1 to 10,000, and (*c*) Fourier spectrum of $\ddot{\xi}(t)$

$\epsilon(t) \neq 0$. A representative set of such motions along with their corresponding acceleration time traces and Fourier spectra are shown in Fig. 12 including motions with $n = 3, 4, 5, 6$, and 9. Motions with $n = 7$ and 8 have also been observed. The majority of these nT motions are found on the upper branch of the $r = 1$ primary resonance during sweep-down. For instance, the $4T$ and $5T$ motions of Figs. 12(*b*) and (*c*) occur within the subharmonic regime identified in the frequency response curve of Fig. 10. Another regime of nT responses is specified in Fig. 13 from which the $6T$ motion illustrated in Fig. 12(*d*) is obtained. Similarly, the $9T$ motion of Fig. 12(*e*) is obtained using a different system whose forced response curve is shown in Fig. 14. This $9T$ motion was recorded immediately before the jump-down takes place and then bifurcates to either a SSI type $2T$ motion or a NI type $1T$ motion as Λ is decreased. This $2T$ motion is similar to the $2T$ motion of the system described by Figs. 10 and 11. As a noteworthy point, the $2T$ and $9T$ motions shown in Fig. 14 were obtained by first increasing Λ beyond the primary jump up frequency at $\Lambda = 0.75$ and then reducing Λ as the motions followed the upper branch. Otherwise such motions would be missed completely since the $1T$ motions of the lower branch are stable within this frequency range. Another significant observation from Fig. 14 is that two stable subharmonic motions of $2T$ and $9T$ coexist along with a $1T$ motion within a narrow range of frequency bounded by $\Lambda = 0.55$ and $\Lambda = 0.59$, emphasizing the importance of initial conditions in deciding which motion will be exhibited by the gear pair.

3.4 Chaotic Behavior. In addition to nT motions, motions with no apparent periodicity ($n \to \infty$) are also reported within the frequency range $0.75 < \Lambda < 0.85$ for the system described by Fig. 13. An example of such motions is shown in Fig. 15 for $\Lambda = 0.8$. Only a small portion of the time trace is shown and the phase portrait is replaced by a 10,000 point Poincare plot shown in Fig. 11(*b*). The *unrepeated* time trace, the *strange attractor* formed by the Poincare plot and the *broad-band* spectral content of the corresponding averaged Fourier spectrum all suggest that the motion is chaotic (Moon, 1992). The chaotic band of frequency occurs where the $r = 1$ primary resonance should exist. Within this frequency band, only chaotic motions were observed regardless of increasing or decreasing Λ. In some other cases, multiple frequency bands of chaos were observed. The forced response curve for such a case is shown in Fig. 16. This system exhibits chaotic behavior in the vicinity of both the $r = 1$ and $r = 2$ primary resonances between $0.65 < \Lambda < 0.85$ and $0.4 < \Lambda < 0.46$, respectively. Two time traces of chaotic motions corresponding to $\Lambda = 0.78$ and $\Lambda = 0.43$ are illustrated in Figs. 17 and 18, respectively. Again the time traces are unrepeated and the spectral content of the response goes far beyond the harmonic content of the excitation. In Fig. 18(*a*), a significantly longer segment of the acceleration time trace (400 periods) is shown to demonstrate that relatively regular motions are interrupted erratically by large-amplitude "chaotic bursts" which suggests that the motions illustrated in Figs. 15, 17, and 18 are cases of *intermittent chaos* (Moon, 1992).

Figure 13 and Figs. 15–18 conclusively demonstrate that chaotic behavior exists in mechanical systems with clearance type nonlinearities and time-varying parameters. Again, the chaotic behavior demonstrated here, much like the jump discontinuities and subharmonic resonances pointed out earlier, are not exceptions. Such behavior is commonly observed as the system

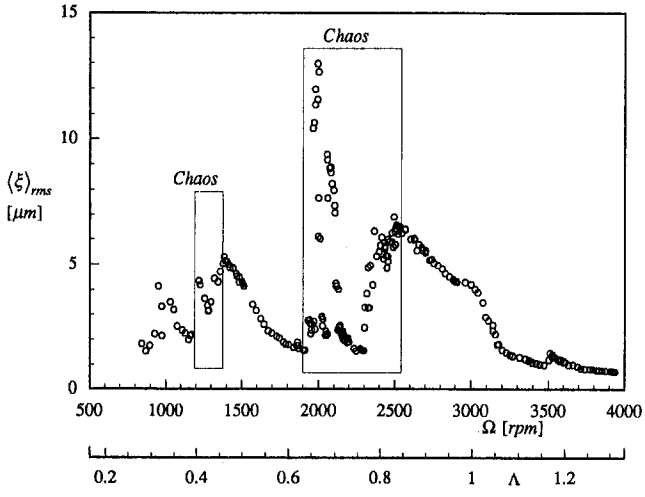


Fig. 16 Measured forced response of a gear pair with $\lambda = 1.5$ and $\epsilon(t) \neq 0$. The transmitted torque is 85 N-m.

Downloaded 04 May 2010 to 171.66.16.34. Redistribution subject to ASME license or copyright; see http://www.asme.org/terms/Terms_Use.cfm

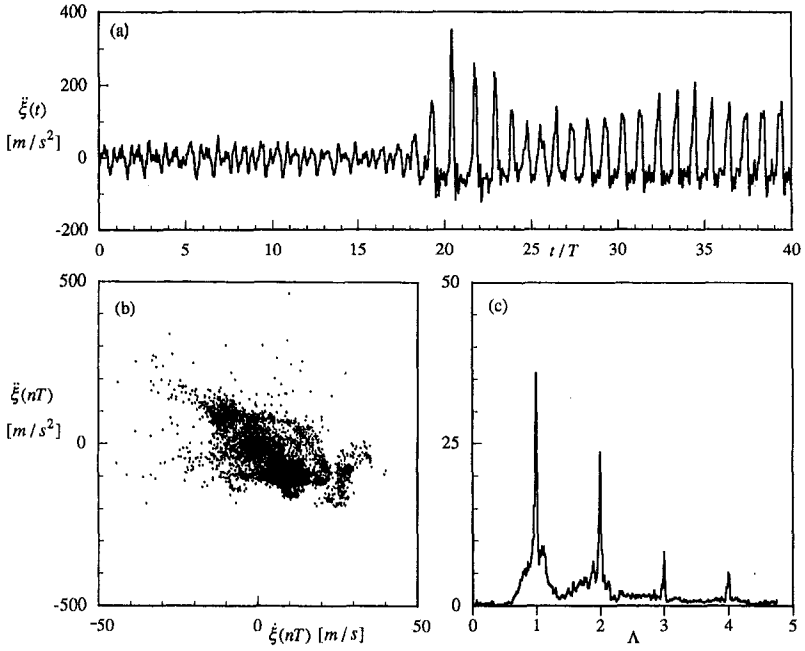


Fig. 17 Measured chaotic motion of Fig. 16 at $\Lambda = 0.78$; (*a*) time trace $\ddot{\xi}(t)$, (*b*) Poincare map $\ddot{\xi}(nT)$ versus $\dot{\xi}(nT)$ where $n = 1$ to 10,000, and (*c*) Fourier spectrum of $\ddot{\xi}(t)$

parameters are varied within realistic operational ranges of typical automotive and aerospace powertrain applications. Meanwhile further experimental investigation of chaotic motions including the mechanisms (routes) leading to them is necessary. The present authors intend to carry out such experimental investigations in the future.

4 Concluding Remarks

The existence of several predicted nonlinear dynamic behavior have been clearly demonstrated using a commonplace physical system. A rich spectrum of nonlinear phenomena including a softening-type backbone and jump discontinuities in forced response curves, multiple coexisting stable motions, sub and super harmonic resonances, fold bifurcations, long-period subharmonic motions, and chaotic motions have been shown to exist. The observed behavior is consistent with the previous theoretical predictions for a simple mechanical oscillators with clearance having combined parametric and forcing excitations. Accordingly, the model proposed here and in the previous two papers (Blankenship and Kahraman, 1995; Kahraman and Blankenship, 1996) is indeed capable of accurately describing the dynamic behavior of such systems both qualitatively and quantitatively. Other classes of physical systems with clearances should demonstrate similar nonlinear phenomena. The authors hope that this work will help bridge the gap between the aca-

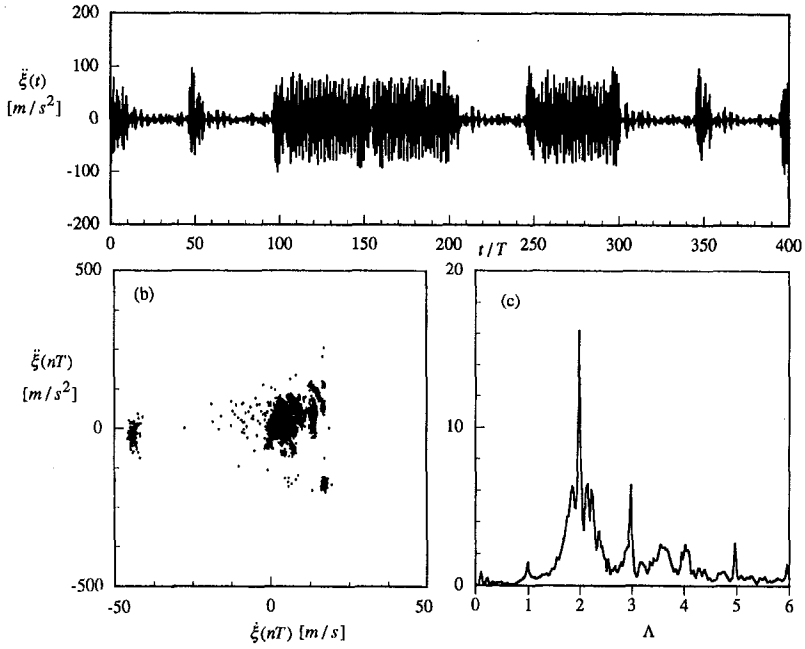


Fig. 18 Measured chaotic motion of Fig. 16 at $\Lambda = 0.43$; (*a*) time trace $\ddot{\xi}(t)$, (*b*) Poincare map $\ddot{\xi}(nT)$ versus $\dot{\xi}(nT)$ where $n = 1$ to 10,000, and (*c*) Fourier spectrum of $\ddot{\xi}(t)$

Downloaded 04 May 2010 to 171.66.16.34. Redistribution subject to ASME license or copyright; see http://www.asme.org/terms/Terms_Use.cfm

demic and engineering communities bringing more relevance to the emerging field of nonlinear dynamics.

Acknowledgments

The authors wish to gratefully acknowledge the invaluable contributions of Mr. T. Vogel for his assistance in conducting these experiments and Mr. S. Coan for grinding the test gears.

References

Bayly, P. V., and Virgin, L. N., 1993, "An Experimental Study of an Impacting Pendulum," *Journal of Sound and Vibration,* Vol. 164, pp. 364–374.

Blankenship, G. W., and Kahraman, A., 1995, "Steady State Forced Response of a Mechanical Oscillator With Combined Parametric Excitation and Clearance Type Nonlinearity," *Journal of Sound and Vibration,* Vol. 185, pp. 743–765.

Blankenship, G. W., and Singh, R., 1995, "Analytical Solutions for Modulation Sidebands Associated with a Class of Mechanical Oscillators," *Journal of Sound and Vibration,* Vol. 179, pp. 13–36.

Choi, Y. S., and Noah, S. T., "Forced Periodic Vibration of Unsymmetric Piecewise-Linear Systems," *Journal of Sound and Vibration,* Vol. 121, pp. 117–126.

Comparin, R. J., and Singh, R., 1989, "Nonlinear Frequency Response Characteristics of an Impact Pair," *Journal of Sound and Vibration,* Vol. 134, pp. 259–290.

Ehrich, F., 1992, "Observations of Subcritical Superharmonic and Chaotic Response in Rotordynamics," ASME *Journal of Vibration and Acoustics,* Vol. 114, pp. 93–100.

Fang, W., and Wickert, J. A., 1994, "Response of a Periodically Driven Impact Oscillator," *Journal of Sound and Vibration,* Vol. 170, pp. 397–409.

Hsu, C. S., and Cheng, W. -H., 1974, "Steady State Response of Dynamical System Under Combined Parametric and Forcing Excitations," ASME JOURNAL OF APPLIED MECHANICS, pp. 371–378.

Kahraman, A., and Singh, R., 1990, "Nonlinear Dynamics of a Spur Gear Pair," *Journal of Sound and Vibration,* Vol. 142, pp. 49–75.

Kahraman, A., and Singh, R., 1991, "Interactions Between Time-Varying Mesh Stiffness and Clearance Nonlinearity in a Gear System," *Journal of Sound and Vibration,* Vol. 146, pp. 135–156.

Kahraman, A., and Blankenship, G. W., 1996, "Interactions Between Commensurate Parametric and Forcing Excitations in a System with Clearance," *Journal of Sound and Vibration,* Vol. 194, pp. 317–336.

Kahraman, A., 1992, "On the Response of a Preloaded Mechanical Oscillator with a Clearance: Period Doubling and Chaos," *Nonlinear Dynamics,* Vol. 3, pp. 183–198.

Karagiannis, K., and Pfeiffer, F, 1991, "Theoretical and Experimental Investigation of Gear-Rattling," *Nonlinear Dynamics,* Vol. 2, pp. 367–387.

Kim, Y. B., and Noah, S. T., 1991, "Stability and Bifurcation Analysis of Oscillators with Piecewise-Linear Characteristics: A General Approach," ASME JOURNAL OF APPLIED MECHANICS, Vol. 58, pp. 545–553.

Lau, S. L., and Zhang, W. -S., 1992, "Nonlinear Vibrations of Piecewise Linear Systems by Incremental Harmonic Balance Method," ASME JOURNAL OF APPLIED MECHANICS, Vol. 59, pp. 153–160.

Mahfouz, I. A., and Badrakhan, F., 1990, "Chaotic Behavior of Some Piecewise-Linear Systems, Part II: Systems with Clearances," *Journal of Sound and Vibration,* Vol. 143, pp. 289–328.

Mevel, B. and Guyader, J. L., 1993, "Routes to Chaos in Ball Bearings," *Journal of Sound and Vibration,* Vol. 162, pp. 471–487.

Moon, F. C., 1992, *Chaotic and Fractal Dynamics,* Wiley-Interscience, New York.

Moon, F. C., and Shaw, S. W., 1983, "Chaotic Vibrations of a Beam with Nonlinear Boundary Conditions," *International Journal of Non-linear Mechanics,* Vol. 18, pp. 465–477.

Natsiavas, S., 1989, "Periodic Response and Stability of Oscillators with Symmetric Trilinear Restoring Force," *Journal of Sound and Vibration,* Vol. 134, pp. 315–331.

Natsiavas, S., and Gonzalez, H., 1992, "Vibration of Harmonically Excited Oscillators with Asymmetric Constraints," ASME JOURNAL OF APPLIED MECHANICS, Vol. 59, pp. S284–S290.

Padmanabhan, C., and Singh, R., 1995, "Dynamics of a Piecewise Nonlinear System Subject to Dual Harmonic Excitation Using Parametric Continuation," *Journal of Sound and Vibration,* Vol. 184, pp. 767–799.

Padmanabhan, C., and Singh, R., 1996, "Analysis of Periodically Forced Hill's Oscillator with Application to a Geared System," *Journal of Acoustical Society of America,* Vol. 99, pp. 324–334.

Richards, J. A., 1983, *Analysis of Periodically Time-Varying Systems,* Springer-Verlag, New York.

Sato, K., Yamamoto, S., and Kawakami, T., 1991, "Bifurcation Sets and Chaotic States of a Gear System Subjected to Harmonic Excitation," *Computational Mechanics,* Vol. 7, pp. 173–182.

Shaw, S. W., and Holmes, P. J., 1983, "A Periodically Forced Piecewise Linear Oscillator," *Journal of Sound and Vibration,* Vol. 90, pp. 129–155.

Shaw, S. W., 1985, "Forced Vibrations of a Beam with One-Sided Amplitude Constraint: Theory and Experiment," *Journal of Sound and Vibration,* Vol. 99, pp. 199–212.

Thompson, J. M. T, and Elvey, J. S. N., 1984, "Elimination of Sub-harmonic Resonances of Compliant Marine Structures," *Int. J. Mech. Sci.,* Vol. 26, pp. 419–426.

Tomlinson, G. R., and Lam, J., 1984, "Frequency Response Characteristics of Structures with Single and Multiple Clearance-Type Non-linearity," *Journal of Sound and Vibration,* Vol. 96, pp. 111–125.

Downloaded 04 May 2010 to 171.66.16.34. Redistribution subject to ASME license or copyright; see http://www.asme.org/terms/Terms_Use.cfm

Journal of Applied Mechanics

Brief Notes

A Brief Note is a short paper that presents a specific solution of technical interest in mechanics but which does not necessarily contain new general methods or results. A Brief Note should not exceed 1500 words *or equivalent* (a typical one-column figure or table is equivalent to 250 words; a one line equation to 30 words). Brief Notes will be subject to the usual review procedures prior to publication. After approval such Notes will be published as soon as possible. The Notes should be submitted to the Technical Editor of the JOURNAL OF APPLIED MECHANICS. Discussions on the Brief Notes should be addressed to the Editorial Department, ASME, United Engineering Center, 345 East 47th Street, New York, N. Y. 10017, or to the Technical Editor of the JOURNAL OF APPLIED MECHANICS. Discussions on Brief Notes appearing in this issue will be accepted until two months after publication. Readers who need more time to prepare a Discussion should request an extension of the deadline from the Editorial Department.

On the Motion of Lineal Bodies Subject to Linear Damping

M. F. Beatty[1]

Wilms (1995) has considered the plane motion of three lineal rigid bodies subject to linear damping over their length. He shows that these plane single-degree-of-freedom systems are governed by precisely the same fundamental differential equation. It is not unusual that several dynamical systems may be formally characterized by the same differential equation, but the universal differential equation for these systems is unusual because it is exactly the same equation for the three very different systems. It is shown here that these problems belong to a more general class of problems for which the differential equation is exactly the same for every lineal rigid body regardless of its geometry.

1 Introduction

A cable, rope, string, rubber band, wire, stick, a strand of hair, and a rod are familiar examples of thin-structured, essentially one-dimensional bodies that are commonly described by a straight or curved spatial line. Thus, any such one-dimensional material object of this kind is called a *lineal body.* Euler's famous *elastica,* an elastic curve model of a flexible, but inextensible lineal body commonly thought of as a slender, straight or curved rod, is well known. We recall that Euler's theory examines the shape of an arbitrary lineal, flexible and inextensible body subjected to a variety of end conditions and for which the bending moment at any section along its length is proportional to the curvature at that place. The vibratory motion of an arbitrary lineal, inextensible body having negligible bending stiffness and subjected to tensile loading is also familiar. The reader will recall other studies of the characteristics of lineal bodies subjected to various conditions. This paper examines the motion of an arbitrary, homogeneous lineal body subjected to a Stokes drag force acting over its length.

Beatty (1987) has shown that Euler's laws of motion for the momentum $\mathbf{p}^*$ of the center of mass G of a homogeneous, inextensible, lineal body l, and the moment of momentum $\mathbf{h}_G$ relative to G, have precisely the same form for the motion of every such body subjected to only a distributed linear, Stokes retarding force; namely,

$$\frac{d\mathbf{p}^*}{dt} = -\beta\mathbf{p}^*, \quad \frac{d\mathbf{h}_G}{dt} = -\beta\mathbf{h}_G, \tag{1}$$

in which the damping exponent β is a positive constant. Thus, the first integrals of these universal equations of motion are given by

$$\mathbf{p}^*(l, t) = \mathbf{p}_0 e^{-\beta t}, \quad \mathbf{h}_G(l, t) = \mathbf{h}_0 e^{-\beta t} \tag{2}$$

in which $\mathbf{p}_0 \equiv \mathbf{p}^*(l, 0)$ and $\mathbf{h}_0 \equiv \mathbf{h}_G(l, 0)$ are certain initial values. These solutions are consistent with our intuitively anticipated effects of linear viscous damping. It is evident that exactly the same equations hold universally when l is subjected to any additional system of forces that is equipollent to zero.

Wilms (1995) shows in three examples that the plane motions of distinct lineal bodies subject to a Stokes resistance and certain additional systems of forces are governed by exactly the same equation of motion. One of these examples consists of a homogeneous rigid rod spinning in the horizontal plane with angular velocity $\boldsymbol{\omega}(t)$ about an arbitrary fixed vertical axle. The same result is obtained if the rod turns in the vertical plane about its center of mass which is pinned to a smooth rigid support. It is not necessary that the rod be straight. In this case, the additional force system at the support is equipollent to zero; and, therefore, the motion of the rod is described by (2) in which $\mathbf{p}^* \equiv \mathbf{0}$ and $\mathbf{h}_G = I_G\boldsymbol{\omega}(t)$. Here I_G is the moment of inertia of the rod about its normal central axis. Then with $\boldsymbol{\omega}(0) \equiv \boldsymbol{\omega}_0$ initially, the damped motion is determined by $\boldsymbol{\omega}(t) = \boldsymbol{\omega}_0 \exp(-\beta t)$, as one might expect. We find the same result for the constrained horizontal motion. Notice, however, that the result is independent of the geometry of the rod; it is the same for every homogeneous lineal body subject to Stokes damping and to other forces that are equipollent to zero. In Wilm's other examples, however, the additional force systems are **not** equipollent to zero, so our previous universal equations (2) are not applicable. Nevertheless, Wilms still finds that these very different systems are governed by exactly the same universal rule for the spin $\boldsymbol{\omega}(t)$, independently of the geometry of the different rods. In this note I show that all of the problems described by Wilms (1995) and

[1] Department of Engineering Mechanics, University of Nebraska-Lincoln, Lincoln, NE 68588-0347. Fellow ASME.

Contributed by the Applied Mechanics Division of THE AMERICAN SOCIETY OF MECHANICAL ENGINEERS for publication in the ASME JOURNAL OF APPLIED MECHANICS. Manuscript received by the ASME Applied Mechanics Division, Aug. 28, 1995; final revision, Aug. 5, 1996. Associate Technical Editor: R. Abeyaratne.

Copyright © 1997 by ASME

Downloaded 04 May 2010 to 171.66.16.34. Redistribution subject to ASME license or copyright; see http://www.asme.org/terms/Terms_Use.cfm

Beatty (1987) belong to a more general class of problems for which the differential equation of motion is universal and whose solution is independent of the shape or length of the lineal body. The effect is due to the linear nature of Stokes damping.

2 Universal Motion Under Stokes Resistance

Consider a lineal rigid body l of arbitrary shape subject to a nonconservative force $\mathbf{F}_n$ per unit arc length s measured from one end of l. We shall suppose that all other forces, including any conservative forces, that act on l are workless. Therefore, in accordance with the general work-energy principle, the change ΔK in the total kinetic energy of the body is equal to the work W_n done by the nonconservative force: $\Delta K = W_n$. We recall that the mechanical power dissipated is defined by $P = \dot{W}_n$; therefore, we begin with

$$\dot{K} = P = \int_l \mathbf{F}_n \cdot \mathbf{v}_Q ds, \tag{3}$$

where $\mathbf{v}_Q(s)$ is the velocity of the material point Q on which the nonconservative force is acting at s along l. This principle is central to our discussion.

We now recall Stokes' law and consider the total power for a linear viscous Stokes force $\mathbf{F}_n = -\mu \mathbf{v}_Q(s)$ per unit elemental length ds of l. Then

$$P = -\mu \int_l \mathbf{v}_Q \cdot \mathbf{v}_Q ds, \tag{4}$$

where $\mu > 0$ denotes the constant coefficient of damping. Suppose further that the body is homogeneous with constant mass density ρ, per unit length. Then $m = \rho s$ is the total mass of a portion of l having length s. It thus follows that the power (4) may be written as

$$P = -\frac{2\mu}{\rho} K, \tag{5}$$

where K denotes the total kinetic energy of the lineal body:

$$K \equiv \int_l \tfrac{1}{2} \mathbf{v}_Q \cdot \mathbf{v}_Q dm. \tag{6}$$

Use of the result (5) in (3) yields *the universal differential equation characteristic of all dynamical systems in the class C of homogeneous lineal bodies subject a linear viscous damping force per unit length and for which all other forces acting on l are workless:*

$$\dot{K} + 2\beta K = 0, \quad \text{with} \quad \beta \equiv \frac{\mu}{\rho} > 0. \tag{7}$$

The general solution of (7) is

$$K(t) = K_0 e^{-2\beta t}, \tag{8}$$

in which $K_0 \equiv K(0)$ is the initial kinetic energy of the lineal body.

Notice that the damping exponent β is the ratio of the viscous damping constant μ to the constant mass density ρ per unit length of our arbitrary lineal body, but is independent of its shape or its length. The result (8) shows that the damped motion of every homogeneous lineal body having the same mass per unit length and for which all other forces are workless, regardless of its geometry, is exactly the same; therefore, it is said to be universal.

3 Universal Motion with Equipollent Forces

It is easily seen that for a lineal rigid body any system of additional forces $\mathbf{F}_Q$ equipollent to zero is workless. We first recall that a system of distributed forces $\mathbf{F}_Q$, per unit length s, is equipollent to zero if and only if

$$\int_l \mathbf{F}_Q ds = \mathbf{0}, \quad \int_l \mathbf{r} \times \mathbf{F}_Q ds = \mathbf{0}, \tag{9}$$

where $\mathbf{r}$ is the position vector of the point Q from any moment center at G, the center of mass say. Since the body is rigid, $\mathbf{v}_Q = \mathbf{v}_G + \boldsymbol{\omega} \times \mathbf{r}$; and hence the rate $\dot{W}_e$ at which work is done by the additional equipollent system (9) is

$$\dot{W}_e = \int_l \mathbf{F}_Q \cdot \mathbf{v}_Q ds = \mathbf{v}_G \cdot \int_l \mathbf{F}_Q ds + \boldsymbol{\omega} \cdot \int_l \mathbf{r} \times \mathbf{F}_Q ds = 0. \tag{10}$$

That is, the additional equipollent system of distributed forces is workless. Thus, the class of problems described by Beatty (1987) for which the motion is characterized by the universal equations (2) are among those in the class C characterized by the universal differential equation of motion (7), or more simply by (8).

4 Universal Motion of Rotating Rigid Bodies

Many dynamical problems in the class of interest, including the three studied by Wilms (1995) in which the additional systems of forces are workless, have the property that the total kinetic energy is proportional to the square of the angular speed ω of the body about a principal axis. For all such cases,

$$K = \kappa \omega^2, \tag{11}$$

wherein κ is a certain constant characteristic of the system. If ω_0 is the initial angular speed of l, $K_0 \equiv \kappa \omega_0^2$ and (8) becomes $\omega^2 = \omega_0^2 \exp(-2\beta t)$, or simply

$$\omega(t) = \omega_0 e^{-\beta t}. \tag{12}$$

Integration of (12) with $\omega \equiv d\theta/dt$ yields the angular placement of l:

$$\theta(t) = \theta_0 + \frac{\omega_0}{\beta}(1 - e^{-\beta t}), \tag{13}$$

in which $\theta_0 = \theta(0)$ is the initial placement. The reader will recall that we encountered the general result (12) in our earlier preliminary discussion.

Finally, we note that differentiation of (12) yields

$$\dot{\omega} + \beta \omega = 0, \tag{14}$$

or, in terms of θ,

$$\ddot{\theta} + \beta \dot{\theta} = 0. \tag{15}$$

This is Wilm's universal differential equation for each of the three mechanical systems investigated in his recent paper. Notice, however, that there is no need to mention any of the specific devices studied by Wilms (1995), each of which is a special example in the class C defined above. Moreover, notice again that *the equation of motion* (15) *is exactly the same for every homogeneous, lineal rigid body having the same mass per unit length, and it is independent of the shape and length of the body.*

5 General Motion With Additional Forces

Suppose that the body is subjected to an additional system of forces for which the total mechanical power is P_a, say. This may include additional conservative forces excluded in (3). In this case, it is seen that (7) is replaced by the differential equation

$$\dot{K} + 2\beta K = P_a, \tag{16}$$

which generally is not universal. Indeed, it is seen that the *universal equation* (7) *holds if and only if* $P_a = 0$, *that is, when and only when the additional system of forces is workless.* In

Downloaded 04 May 2010 to 171.66.16.34. Redistribution subject to ASME license or copyright; see http://www.asme.org/terms/Terms_Use.cfm

particular, the differential equation for the rotation in the vertical plane of a homogeneous, rigid rod about any point other than the center of mass is not in our universal class C. In this instance, the conservative gravitational force acting on our lineal body does work.

In the exceptional case for which the extra power may be proportional to the total kinetic energy of the body, so that $P_a = \gamma K$, where γ is a constant, the motion is characterized by the *similar* differential equation

$$\dot{K} + (2\beta - \gamma)K = 0, \tag{17}$$

with solution $K = K_0 e^{(\gamma - 2\beta)t}$. But this equation is *not exactly the same* as (7); and hence this exceptional case is not a member of the general universal class C for which β depends on only the viscosity of the medium and the mass density of the body, per unit length.

References

Beatty, M. F., 1987, "Motion of an Inextensible, Lineal Body Under Viscous Damping," *American Journal of Physics*, Vol. 55, p. 970.

Wilms, E. V., 1995, "Three Single Degree of Freedom Systems with Linear Damping," *Mechanics Research Communications*, Vol. 22, pp. 233–237.

On the Thermal Response of Antisymmetric Angle-Ply Laminated Plates

A. A. Khdeir[2]

Introduction

Thermal deformation and stress resultants in rectangular, antisymmetric cross-ply and angle-ply laminates were investigated by Wu and Tauchert (1980). Exact solutions were obtained for the response of simply supported plates to general three-dimensional temperature variations. For other types of boundary conditions, approximate methods such as the Rayleigh-Ritz and the finite element were used in Wu (1978) and Reddy and Hsu (1980), respectively. From the available results for the thermal deformation of antisymmetric angle-ply laminated plates, allow one to infer that exact solutions were developed mainly for the case of simply supported boundary conditions and approximate methods were used for other boundary conditions. In this paper, the state-space approach in conjunction with the Levy method is used to solve exactly the thermoelastic governing equations of the first-order shear deformation and the classical theories of antisymmetric angle-ply laminated plates under various boundary conditions.

Governing Equations

Consider a uniform rectangular plate of thickness h and planform dimensions a and b. The middle plane of the plate is assumed to coincide with the x-y plane ($0 < x < a$, $-b/2 < y < b/2$). The thermoelastic displacement equations of equilibrium of the first-order shear deformation theory (FSDT) of antisymmetric angle-ply laminated plates are

$$\begin{aligned}
&A_{11}u_{,xx} + A_{66}u_{,yy} + (A_{12} + A_{66})v_{,xy} \\
&\qquad + B_{16}(2\phi_{,xy} + \psi_{,xx}) + B_{26}\psi_{,yy} = N^T_{x,x} + N^T_{xy,y} \\
&(A_{12} + A_{66})u_{,xy} + A_{66}v_{,xx} + A_{22}v_{,yy} \\
&\qquad + B_{16}\phi_{,xx} + B_{26}(\phi_{,yy} + 2\psi_{,xy}) = N^T_{xy,x} + N^T_{y,y} \\
&A_{55}w_{,xx} + A_{44}w_{,yy} + A_{55}\phi_{,x} + A_{44}\psi_{,y} = 0 \\
&2B_{16}u_{,xy} + B_{16}v_{,xx} + B_{26}v_{,yy} - A_{55}(w_{,x} + \phi) + D_{11}\phi_{,xx} \\
&\qquad + D_{66}\phi_{,yy} + (D_{12} + D_{66})\psi_{,xy} = M^T_{x,x} + M^T_{xy,y} \\
&B_{16}u_{,xx} + B_{26}u_{,yy} + 2B_{26}v_{,xy} - A_{44}(w_{,y} + \psi) + (D_{12} \\
&\qquad + D_{66})\phi_{,xy} + D_{66}\psi_{,xx} + D_{22}\psi_{,yy} = M^T_{xy,x} + M^T_{y,y}.
\end{aligned} \tag{1}$$

A comma denotes partial differentiation with respect to the subscript. The thermal forces and moments are defined as

$$\begin{Bmatrix} N^T_x, M^T_x \\ N^T_y, M^T_y \\ N^T_{xy}, M^T_{xy} \end{Bmatrix} = \sum_{k=1}^{N} \int_{z_{k-1}}^{z_k} \begin{bmatrix} Q_{11} & Q_{12} & Q_{16} \\ Q_{12} & Q_{22} & Q_{26} \\ Q_{16} & Q_{26} & Q_{66} \end{bmatrix}_k \begin{Bmatrix} \alpha_x \\ \alpha_y \\ \alpha_{xy} \end{Bmatrix}_k (1, z)\Delta T dz \tag{2}$$

where $(Q_{ij})_k$ are the material coefficients of the kth lamina in the laminate coordinate system and $(\alpha_x, \alpha_y, \alpha_{xy})_k$ are the coefficients of linear thermal expansion for layer k in the laminate coordinates; ΔT denotes the temperature rise in the laminate.

Exact Solution

The generalized Levy-type solution in conjunction with the state variables technique is used to determine the thermal deformation of antisymmetric angle-ply laminated plates. The edges $x = 0, a$ will be considered simply supported while the remaining ones, $y = \pm b/2$ are subjected to arbitrary boundary conditions. In this approach, the displacement quantities will be represented so as to satisfy the simply supported boundary conditions at $x = 0, a$.

A sinusoidal distribution of the thermal loading, linearly varying through the thickness of the laminate, will be considered,

$$\Delta T = \bar{T}_1 z \cos \beta y \sin \alpha x, \tag{3}$$

where $\alpha = \pi/a$ and $\beta = \pi/b$. Accordingly, the unknown displacement functions will be expressed as

$$\begin{aligned}
u(x, y) &= U(y) \sin \alpha x \\
v(x, y) &= V(y) \cos \alpha x \\
w(x, y) &= W(y) \sin \alpha x \\
\phi(x, y) &= \Phi(y) \cos \alpha x \\
\psi(x, y) &= \Psi(y) \sin \alpha x.
\end{aligned} \tag{4}$$

Substitution of Eqs. (3) and (4) into (1) results in the following system of equations:

$$\begin{aligned}
U'' &= c_1 U + c_2 V' + c_3 W' + c_4 \Phi' + c_5 \Psi + g_1 \sin \beta y \\
V'' &= c_6 U' + c_7 V + c_8 W + c_9 \Phi + c_{10} \Psi' + g_2 \cos \beta y \\
W'' &= c_{11} W + c_{12} \Phi + c_{13} \Psi'
\end{aligned}$$

[2] Civil Engineering Department, Middle East Technical University, 06531 Ankara, Turkey.

Contributed by the Applied Mechanics Division of THE AMERICAN SOCIETY OF MECHANICAL ENGINEERS for publication in the ASME JOURNAL OF APPLIED MECHANICS. Manuscript received by the ASME Applied Mechanics Division, Dec. 10, 1993; final revision, Sept. 19, 1995. Associate Technical Editor: M. Taya.

Downloaded 04 May 2010 to 171.66.16.34. Redistribution subject to ASME license or copyright; see http://www.asme.org/terms/Terms_Use.cfm

particular, the differential equation for the rotation in the vertical plane of a homogeneous, rigid rod about any point other than the center of mass is not in our universal class C. In this instance, the conservative gravitational force acting on our lineal body does work.

In the exceptional case for which the extra power may be proportional to the total kinetic energy of the body, so that $P_a = \gamma K$, where γ is a constant, the motion is characterized by the *similar* differential equation

$$\dot{K} + (2\beta - \gamma)K = 0, \tag{17}$$

with solution $K = K_0 e^{(\gamma - 2\beta)t}$. But this equation is *not exactly the same* as (7); and hence this exceptional case is not a member of the general universal class C for which β depends on only the viscosity of the medium and the mass density of the body, per unit length.

References

Beatty, M. F., 1987, "Motion of an Inextensible, Lineal Body Under Viscous Damping," *American Journal of Physics*, Vol. 55, p. 970.

Wilms, E. V., 1995, "Three Single Degree of Freedom Systems with Linear Damping," *Mechanics Research Communications*, Vol. 22, pp. 233–237.

On the Thermal Response of Antisymmetric Angle-Ply Laminated Plates

A. A. Khdeir[2]

Introduction

Thermal deformation and stress resultants in rectangular, antisymmetric cross-ply and angle-ply laminates were investigated by Wu and Tauchert (1980). Exact solutions were obtained for the response of simply supported plates to general three-dimensional temperature variations. For other types of boundary conditions, approximate methods such as the Rayleigh-Ritz and the finite element were used in Wu (1978) and Reddy and Hsu (1980), respectively. From the available results for the thermal deformation of antisymmetric angle-ply laminated plates, allow one to infer that exact solutions were developed mainly for the case of simply supported boundary conditions and approximate methods were used for other boundary conditions. In this paper, the state-space approach in conjunction with the Levy method is used to solve exactly the thermoelastic governing equations of the first-order shear deformation and the classical theories of antisymmetric angle-ply laminated plates under various boundary conditions.

Governing Equations

Consider a uniform rectangular plate of thickness h and planform dimensions a and b. The middle plane of the plate is assumed to coincide with the x-y plane ($0 < x < a$, $-b/2 < y < b/2$). The thermoelastic displacement equations of equilibrium of the first-order shear deformation theory (FSDT) of antisymmetric angle-ply laminated plates are

$$\begin{aligned}
&A_{11}u_{,xx} + A_{66}u_{,yy} + (A_{12} + A_{66})v_{,xy} \\
&\qquad + B_{16}(2\phi_{,xy} + \psi_{,xx}) + B_{26}\psi_{,yy} = N^T_{x,x} + N^T_{xy,y} \\
&(A_{12} + A_{66})u_{,xy} + A_{66}v_{,xx} + A_{22}v_{,yy} \\
&\qquad + B_{16}\phi_{,xx} + B_{26}(\phi_{,yy} + 2\psi_{,xy}) = N^T_{xy,x} + N^T_{y,y} \\
&A_{55}w_{,xx} + A_{44}w_{,yy} + A_{55}\phi_{,x} + A_{44}\psi_{,y} = 0 \\
&2B_{16}u_{,xy} + B_{16}v_{,xx} + B_{26}v_{,yy} - A_{55}(w_{,x} + \phi) + D_{11}\phi_{,xx} \\
&\qquad + D_{66}\phi_{,yy} + (D_{12} + D_{66})\psi_{,xy} = M^T_{x,x} + M^T_{xy,y} \\
&B_{16}u_{,xx} + B_{26}u_{,yy} + 2B_{26}v_{,xy} - A_{44}(w_{,y} + \psi) + (D_{12} \\
&\qquad + D_{66})\phi_{,xy} + D_{66}\psi_{,xx} + D_{22}\psi_{,yy} = M^T_{xy,x} + M^T_{y,y}.
\end{aligned} \tag{1}$$

A comma denotes partial differentiation with respect to the subscript. The thermal forces and moments are defined as

$$\begin{Bmatrix} N^T_x, M^T_x \\ N^T_y, M^T_y \\ N^T_{xy}, M^T_{xy} \end{Bmatrix} = \sum_{k=1}^{N} \int_{z_{k-1}}^{z_k} \begin{bmatrix} Q_{11} & Q_{12} & Q_{16} \\ Q_{12} & Q_{22} & Q_{26} \\ Q_{16} & Q_{26} & Q_{66} \end{bmatrix}_k \begin{Bmatrix} \alpha_x \\ \alpha_y \\ \alpha_{xy} \end{Bmatrix}_k (1, z)\Delta T dz \tag{2}$$

where $(Q_{ij})_k$ are the material coefficients of the kth lamina in the laminate coordinate system and $(\alpha_x, \alpha_y, \alpha_{xy})_k$ are the coefficients of linear thermal expansion for layer k in the laminate coordinates; ΔT denotes the temperature rise in the laminate.

Exact Solution

The generalized Levy-type solution in conjunction with the state variables technique is used to determine the thermal deformation of antisymmetric angle-ply laminated plates. The edges $x = 0, a$ will be considered simply supported while the remaining ones, $y = \pm b/2$ are subjected to arbitrary boundary conditions. In this approach, the displacement quantities will be represented so as to satisfy the simply supported boundary conditions at $x = 0, a$.

A sinusoidal distribution of the thermal loading, linearly varying through the thickness of the laminate, will be considered,

$$\Delta T = \bar{T}_1 z \cos \beta y \sin \alpha x, \tag{3}$$

where $\alpha = \pi/a$ and $\beta = \pi/b$. Accordingly, the unknown displacement functions will be expressed as

$$\begin{aligned}
u(x, y) &= U(y) \sin \alpha x \\
v(x, y) &= V(y) \cos \alpha x \\
w(x, y) &= W(y) \sin \alpha x \\
\phi(x, y) &= \Phi(y) \cos \alpha x \\
\psi(x, y) &= \Psi(y) \sin \alpha x.
\end{aligned} \tag{4}$$

Substitution of Eqs. (3) and (4) into (1) results in the following system of equations:

$$\begin{aligned}
U'' &= c_1 U + c_2 V' + c_3 W' + c_4 \Phi' + c_5 \Psi + g_1 \sin \beta y \\
V'' &= c_6 U' + c_7 V + c_8 W + c_9 \Phi + c_{10} \Psi' + g_2 \cos \beta y \\
W'' &= c_{11} W + c_{12} \Phi + c_{13} \Psi'
\end{aligned}$$

[2] Civil Engineering Department, Middle East Technical University, 06531 Ankara, Turkey.

Contributed by the Applied Mechanics Division of THE AMERICAN SOCIETY OF MECHANICAL ENGINEERS for publication in the ASME JOURNAL OF APPLIED MECHANICS. Manuscript received by the ASME Applied Mechanics Division, Dec. 10, 1993; final revision, Sept. 19, 1995. Associate Technical Editor: M. Taya.

Copyright © 1997 by ASME

Downloaded 04 May 2010 to 171.66.16.34. Redistribution subject to ASME license or copyright; see http://www.asme.org/terms/Terms_Use.cfm

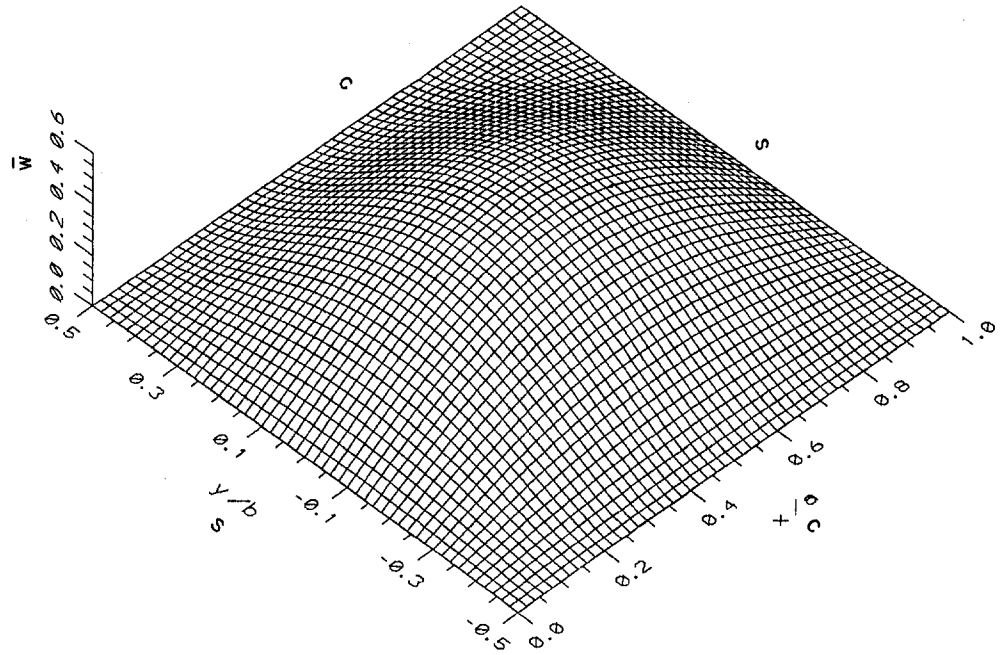


Fig. 1 Deflected shape of a square antisymmetric angle-ply (45/−45/45/−45) plate for SSCC boundary condition

$$\Phi'' = c_{15}U' + c_{16}V + c_{17}W + c_{18}\Phi + c_{19}\Psi' + g_4 \cos \beta y$$

$$\Psi'' = c_{20}U + c_{21}V' + c_{22}W' + c_{23}\Phi' + c_{24}\Psi + g_5 \sin \beta y \quad (5)$$

where a prime on a quantity denote differentiation with respect to y. g_i are defined as

$$g_1 = \beta \bar{T}_1 (B_{26}L_3 - D_{22}L_1)/(A_{66}D_{22} - B_{26}^2)$$

$$g_2 = \alpha \bar{T}_1 (D_{66}L_1 - B_{26}L_2)/(A_{22}D_{66} - B_{26}^2)$$

$$g_4 = \alpha \bar{T}_1 (A_{22}L_2 - B_{26}L_1)/(A_{22}D_{66} - B_{26}^2)$$

$$g_5 = \beta \bar{T}_1 (B_{26}L_1 - A_{66}L_3)/(A_{66}D_{22} - B_{26}^2)$$

where

$$L_1 = \sum_{k=1}^{N} \int_{z_{k-1}}^{z_k} (Q_{16}\alpha_x + Q_{26}\alpha_y + Q_{66}\alpha_{xy})_k z\, dz$$

$$L_2 = \sum_{k=1}^{N} \int_{z_{k-1}}^{z_k} (Q_{11}\alpha_x + Q_{12}\alpha_y + Q_{16}\alpha_{xy})_k z^2\, dz$$

$$L_3 = \sum_{k=1}^{N} \int_{z_{k-1}}^{z_k} (Q_{12}\alpha_x + Q_{22}\alpha_y + Q_{26}\alpha_{xy})_k z^2\, dz. \quad (6)$$

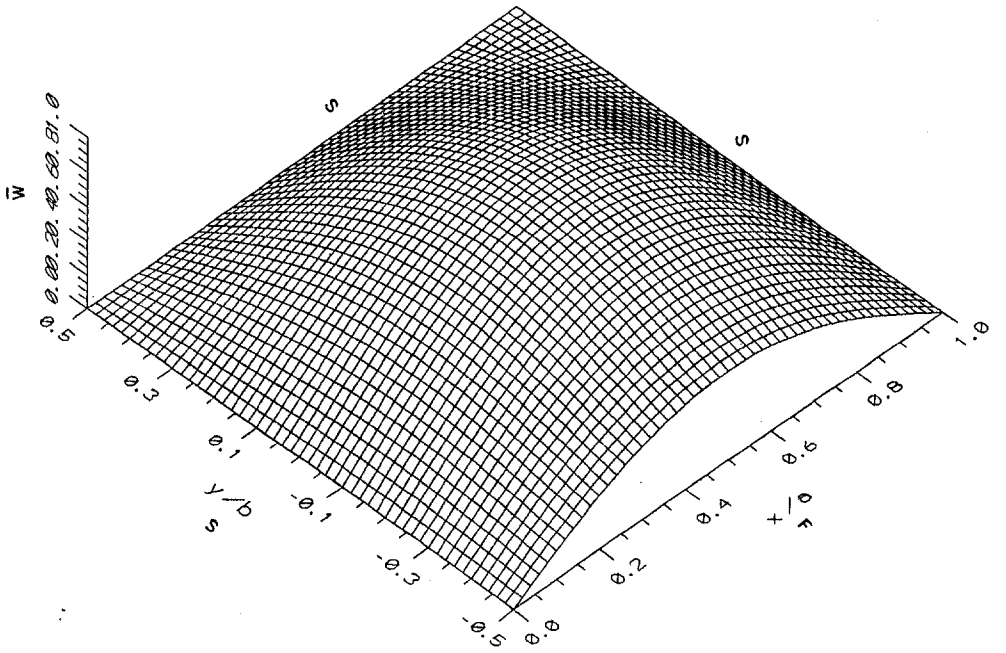


Fig. 2 Deflected shape of a square antisymmetric angle-ply (45/−45/45/−45) plate for SSFS boundary condition

Downloaded 04 May 2010 to 171.66.16.34. Redistribution subject to ASME license or copyright; see http://www.asme.org/terms/Terms_Use.cfm

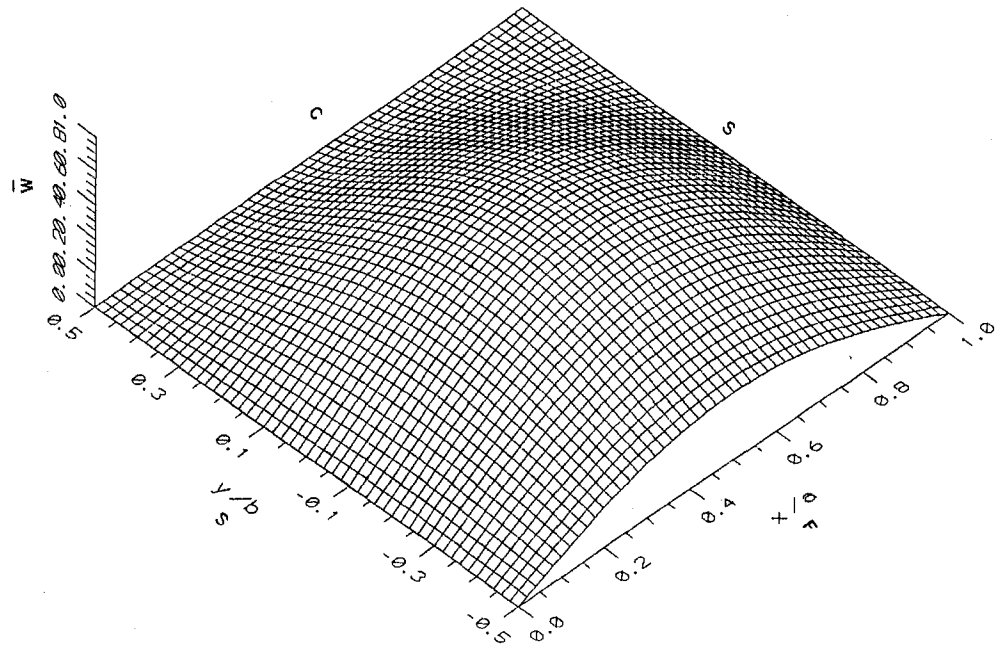


Fig. 3 Deflected shape of a square antisymmetric angle-ply (45/−45/45/−45) plate for SSFC boundary condition

The coefficients c_i in Eq. (5) are presented in Khdeir (1989).

In order to reduce the system of Eqs. (5) to a state form, the components of the state vector $\{\mathbf{Z}(y)\}$ will be defined as

$$Z_1 = U,\ Z_2 = U',\ Z_3 = V,\ Z_4 = V',\ Z_5 = W$$

$$Z_6 = W',\ Z_7 = \Phi,\ Z_8 = \Phi',\ Z_9 = \Psi,\ Z_{10} = \Psi'. \quad (7)$$

Using (7), the system of Eqs. (5) may be expressed in the form

$$\{\mathbf{Z}'\} = [\mathbf{A}]\{\mathbf{Z}\} + \{\mathbf{r}\} \quad (8)$$

where the matrix $[\mathbf{A}]$ is defined in Khdeir (1989), and the load vector $\{\mathbf{r}\}$ is given by

$$\{\mathbf{r}\}^T = \{0,\ g_1 \sin \beta y,\ 0,\ g_2 \cos \beta y,$$

$$0,\ 0,\ 0,\ g_4 \cos \beta y,\ 0,\ g_5 \sin \beta y\}. \quad (9)$$

The solution to Eq. (8) is given by

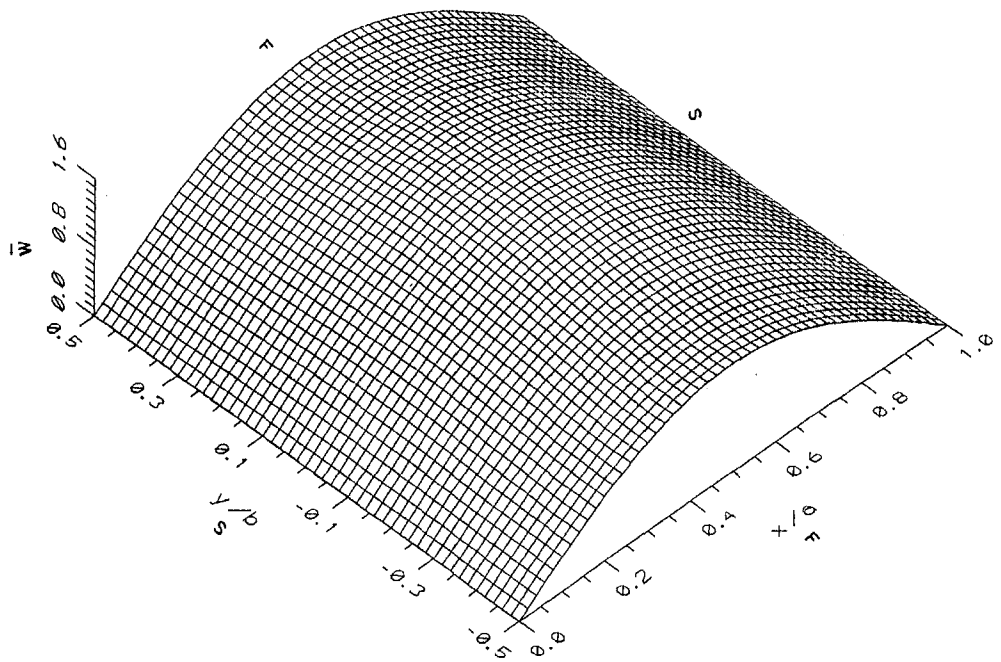


Fig. 4 Deflected shape of a square antisymmetric angle-ply (45/−45/45/−45) plate for SSFF boundary condition

Downloaded 04 May 2010 to 171.66.16.34. Redistribution subject to ASME license or copyright; see http://www.asme.org/terms/Terms_Use.cfm

Table 1 Nondimensional center deflection ($\bar{w}$) of antisymmetric angle-ply (30/−30) square plate for different side-to-thickness ratios

		$\bar{w}$					
a/h	Theory	SSSS	SSCS	SSCC	SSFF	SSFS	SSFC
10	FSDT	0.8627	0.7555	0.6591	1.1536	0.9722	0.8473
50	FSDT	0.8641	0.7343	0.6208	1.1550	0.9711	0.8144
100	FSDT	0.8641	0.7330	0.6185	1.1551	0.9711	0.8125
1000	FSDT	0.8641	0.7325	0.6177	1.1552	0.9710	0.8118
	CPT	0.8641	0.7325	0.6177	1.1552	0.9710	0.8118

$$\{\mathbf{Z}(y)\} = [\mathbf{D}]\begin{bmatrix} e^{\lambda_1 y} & & \mathbf{0} \\ & \ddots & \\ \mathbf{0} & & e^{\lambda_{10} y} \end{bmatrix}\{\mathbf{k}\} + \int [\mathbf{D}]\begin{bmatrix} e^{\lambda_1 (y-\eta)} & & \mathbf{0} \\ & \ddots & \\ \mathbf{0} & & e^{\lambda_{10}(y-\eta)} \end{bmatrix} \times [\mathbf{D}]^{-1}\{\mathbf{r}(\eta)\}d\eta \quad (10)$$

Here $\{\mathbf{k}\}$ is a constant column vector to be determined from the edge conditions at $y = \pm b/2$, where λ_i are the distinct eigenvalues of the matrix $[\mathbf{A}]$ while $[\mathbf{D}]$ denotes the matrix of eigenvectors of $[\mathbf{A}]$.

The same procedure has been carried to obtain the thermal response of antisymmetric angle-ply plates using the classical plate theory (CPT). For the sake of conciseness, it is not reported in this paper.

Numerical Results and Discussion

The numerical results, unless otherwise stated, are obtained for the case of a four-layered square plate (45/−45/45/−45). All the laminae are assumed to be of the same thickness and made of the same orthotropic material, having the following characteristics:

$$E_1 = 25E_2, \quad G_{12} = G_{13} = 0.5E_2, \quad G_{23} = 0.2E_2,$$
$$\nu_{12} = 0.25, \quad \alpha_2/\alpha_1 = 3.$$

The following nondimensional deflections have been used throughout the calculations:

$$\bar{w} = \frac{w(x, y, z)10}{\alpha_1 \bar{T}_1 b^2} \quad \text{for Figs. 1–4}$$

$$\bar{w} = \frac{w(a/2, 0, z)10}{\alpha_1 \bar{T}_1 b^2} \quad \text{for Fig. 5, Table 1.}$$

The notation SSFC, for example, means that the edges $x = 0$, a are simply supported, $y = -b/2$ is free, and $y = b/2$ is clamped. It was assumed that the transverse shear correction coefficients, $K_{44}^2 = K_{55}^2$ are equal to $\frac{5}{6}$. The nondimensionalized deflections have been displayed in Table 1 and Figs. 1–5 for various boundary conditions. In Figs. 1–4, $a = b = 10h$ and (FSDT) theory has been used to show the deflected shape of the plate. The effect of ply-angle and the number of layers on the thermal response is displayed in Fig. 5, where two, four, and ten-layer laminate cases are considered. For all B.C. the two-layer laminate gives higher deflection than four and ten-layer counterparts except for SSFF boundary condition in some range of ply-angle. In Table 1 the results are obtained for thick and very thin plates using (FSDT) and (CPT) theories to show that the solution procedure has no limitations and can be used for thick as well as thin plates.

Summary

Exact analytical solutions for the thermal deformations in antisymmetric angle-ply laminated plates are developed. A generalized Levy-type procedure in conjunction with the state variables technique is used to obtain these solutions for rectangular

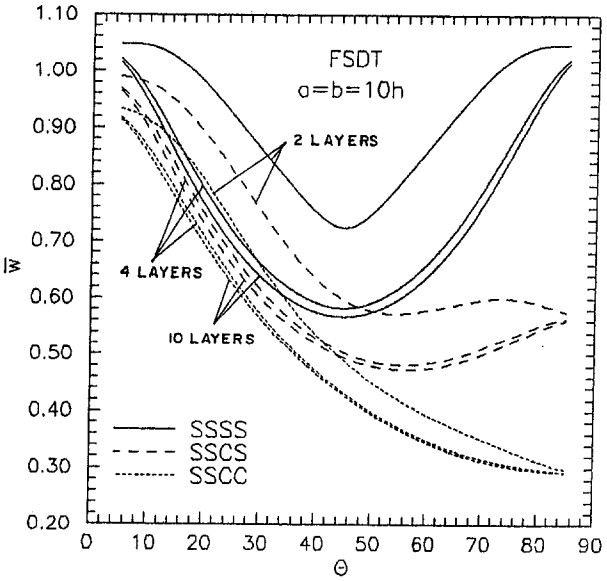


Fig. 5(*a*)

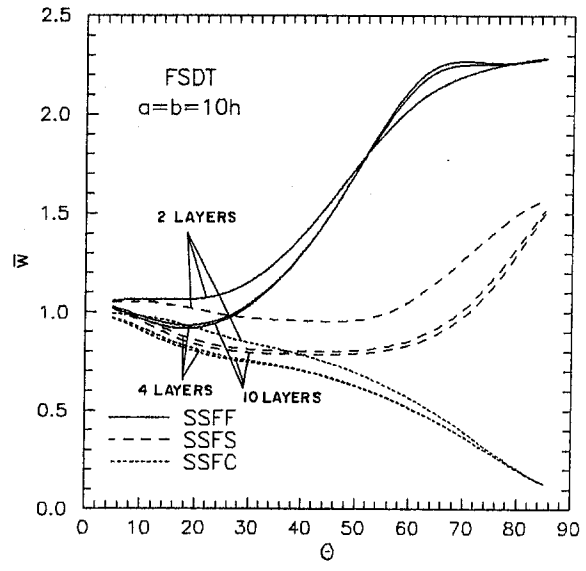


Fig. 5(*b*)

Fig. 5 Effect of ply-angle and number of layers on the thermal response for (*a*) SSSS, SSCS, SSCC (*b*) SSFF, SSFS, SSFC boundary conditions.

Downloaded 04 May 2010 to 171.66.16.34. Redistribution subject to ASME license or copyright; see http://www.asme.org/terms/Terms_Use.cfm

plates which are simply supported on two opposite edges and have arbitrary boundary conditions on the remaining ones. To illustrate the thermoelastic behavior, deflections are computed for laminates undergoing linearly varying temperature fields through the thickness while having sinusoidal distribution of thermal loading.

Acknowledgment

The author appreciate the help provided by Prof. Saleh Abdalla of the Civil Engineering Department of Middle East Technical University in plotting Figs. 1–4 in this paper.

References

Khdeir, A. A., 1989, "An Exact approach to the elastic state of stress of shear deformable antisymmetric angle-ply laminated plates," *Composite Structures*, Vol. 11, pp. 245–258.

Reddy, J. N., and Hsu, Y. S., 1980, "Effects of shear deformation and anisotropy on the thermal bending of layered composite plates," *Journal of Thermal Stresses*, Vol. 3, pp. 475–493.

Wu, C. H., 1978, "Thermal deformations and stresses in laminated plates," M. S. thesis, Univ. of Kentucky, Lexington, KY.

Wu, C. H., and Tauchert, T. R., 1980, "Thermoelastic analysis of laminated plates. 2: Antisymmetric cross-ply and angle-ply laminates," *Journal of Thermal Stresses*, Vol. 3, pp. 365–378.

Equilibrium of a Radially Symmetric Inhomogeneous Plate Under Tension and Load

A. R. Pineda[3,5] and R. G. Root[4,5]

This paper studies a mathematical model for small deflections of a radially symmetric strongly inhomogeneous elastic plate under a normal load and tension in the center plane. The type of inhomogeneity studied occurs in injection molded plastics. The model consists of a Dirichlet boundary value problem for a linear fourth-order ordinary differential equation. A general expression is derived for physically reasonable solutions under relatively broad restrictions on the inhomogeneity and load. The solutions are analyzed and interpreted in terms of their physical significance.

1 Introduction

Inhomogeneous elastic plates that support loads by several mechanisms appear in the modeling of composite materials. The types of radial inhomogeneities studied in this paper occur in circular injection molded plates due to differential cooling. Minor changes in the cooling time lead to major changes in crystal formation and mechanical properties including flexural rigidity (Rosato and Rosato, 1986). Our model approximates the situation when this inhomogeneity causes the flexural rigidity at the center of the plate to be of the same order as the thickness of the plate. Colloquially, we can visualize the plate as a soggy pizza. We look at the cases where the pizza is soggy in the middle but retains some stiffness at the crust.

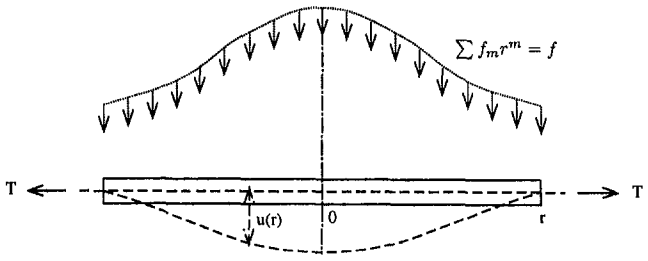


Fig. 1 Diagram of the plate in cross section

Relatively recently, many of the classical two-dimensional mathematical models of elastic plates have been rigorously derived from the general equations of three-dimensional elasticity by asymptotic analysis using the thickness of the plate as the asymptotic parameter. The classical linear model for an isotropic homogeneous plate was derived in this fashion by Duvaut and Lions (1972). The method became more popular after Ciarlet (1979) showed that the von Kármán model's solution is the zero-order term in an asymptotic expansion for the three-dimensional equations. It follows that large changes in constitutive parameters such as the flexural rigidity might be best modeled by allowing the smallest values to vanish entirely. Terms smaller than the leading terms by a factor of the same order as thickness of the plate ought to be ignored in order to be consistent with the asymptotic analysis. Root has applied this principle to the mathematical theory of anisotropic and inhomogeneous plates in both the linear (1991) and nonlinear (von Kármán) (1994) case. In this paper, we consider a concrete example of a radially symmetric plate that effectively loses stiffness at the center. We allow the flexural rigidity to vanish at the center with various rates of decay from the boundary where stiffness is preserved, and analyze the resulting model. The singularity at the origin determines the appropriate space of functions in which the problem has a unique solution.

In this paper we include the homogeneous plate and a plate which is perfectly rigid at its center. Even though this case is not justified through asymptotic analysis, we found our solutions to be physically reasonable.

2 Derivation of the Boundary Value Problem

The physical system modeled is shown in Fig. 1.

A classical plate supports the load f by bending; the amount of support is dependent on the magnitude of the rigidity (the modulus of flexural rigidity) and the curvature (the concavity is the usual linear approximation) of the displacement. A membrane supports the load by tension and the amount of support is dependent on the tensile force and the magnitude of the slope of the deflection. The inhomogeneous plate being studied supports the load both by bending and through in-plane tension.

The mathematical model for a plate with radially variable rigidity and for a membrane with constant tension are derived in many sources, the authors suggest Landau and Lifshitz (1959).

The Classical Linear Model for an Elastic Plate With Radial Inhomogeneity:

$$\Delta(D(r)\Delta u) = f, \tag{1}$$

where Δ is the Laplace operator, in the radially symmetric case $\Delta = (1/r)(d/dr)[r(d/dr)]$, and

u = vertical displacement
r = distance from the origin
D = flexural rigidity
f = vertical applied force density.

[3] Department of Chemical Engineering.
[4] Department of Mathematics.
[5] Lafayette College, Easton, PA 18042.

Contributed by the Applied Mechanics Division of THE AMERICAN SOCIETY OF MECHANICAL ENGINEERS for publication in the ASME JOURNAL OF APPLIED MECHANICS. Manuscript received by the ASME Applied Mechanics Division, July 21, 1995; final revision, Aug. 30, 1996. Associate Technical Editor: J. N. Reddy.

Downloaded 04 May 2010 to 171.66.16.34. Redistribution subject to ASME license or copyright; see http://www.asme.org/terms/Terms_Use.cfm

plates which are simply supported on two opposite edges and have arbitrary boundary conditions on the remaining ones. To illustrate the thermoelastic behavior, deflections are computed for laminates undergoing linearly varying temperature fields through the thickness while having sinusoidal distribution of thermal loading.

Acknowledgment

The author appreciate the help provided by Prof. Saleh Abdalla of the Civil Engineering Department of Middle East Technical University in plotting Figs. 1–4 in this paper.

References

Khdeir, A. A., 1989, "An Exact approach to the elastic state of stress of shear deformable antisymmetric angle-ply laminated plates," *Composite Structures*, Vol. 11, pp. 245–258.

Reddy, J. N., and Hsu, Y. S., 1980, "Effects of shear deformation and anisotropy on the thermal bending of layered composite plates," *Journal of Thermal Stresses*, Vol. 3, pp. 475–493.

Wu, C. H., 1978, "Thermal deformations and stresses in laminated plates," M. S. thesis, Univ. of Kentucky, Lexington, KY.

Wu, C. H., and Tauchert, T. R., 1980, "Thermoelastic analysis of laminated plates. 2: Antisymmetric cross-ply and angle-ply laminates," *Journal of Thermal Stresses*, Vol. 3, pp. 365–378.

Equilibrium of a Radially Symmetric Inhomogeneous Plate Under Tension and Load

A. R. Pineda[3,5] **and R. G. Root**[4,5]

This paper studies a mathematical model for small deflections of a radially symmetric strongly inhomogeneous elastic plate under a normal load and tension in the center plane. The type of inhomogeneity studied occurs in injection molded plastics. The model consists of a Dirichlet boundary value problem for a linear fourth-order ordinary differential equation. A general expression is derived for physically reasonable solutions under relatively broad restrictions on the inhomogeneity and load. The solutions are analyzed and interpreted in terms of their physical significance.

1 Introduction

Inhomogeneous elastic plates that support loads by several mechanisms appear in the modeling of composite materials. The types of radial inhomogeneities studied in this paper occur in circular injection molded plates due to differential cooling. Minor changes in the cooling time lead to major changes in crystal formation and mechanical properties including flexural rigidity (Rosato and Rosato, 1986). Our model approximates the situation when this inhomogeneity causes the flexural rigidity at the center of the plate to be of the same order as the thickness of the plate. Colloquially, we can visualize the plate as a soggy pizza. We look at the cases where the pizza is soggy in the middle but retains some stiffness at the crust.

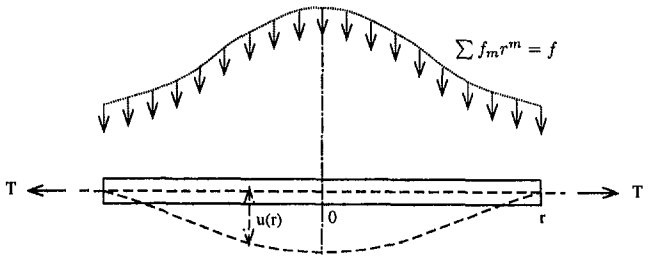


Fig. 1 Diagram of the plate in cross section

Relatively recently, many of the classical two-dimensional mathematical models of elastic plates have been rigorously derived from the general equations of three-dimensional elasticity by asymptotic analysis using the thickness of the plate as the asymptotic parameter. The classical linear model for an isotropic homogeneous plate was derived in this fashion by Duvaut and Lions (1972). The method became more popular after Ciarlet (1979) showed that the von Kármán model's solution is the zero-order term in an asymptotic expansion for the three-dimensional equations. It follows that large changes in constitutive parameters such as the flexural rigidity might be best modeled by allowing the smallest values to vanish entirely. Terms smaller than the leading terms by a factor of the same order as thickness of the plate ought to be ignored in order to be consistent with the asymptotic analysis. Root has applied this principle to the mathematical theory of anisotropic and inhomogeneous plates in both the linear (1991) and nonlinear (von Kármán) (1994) case. In this paper, we consider a concrete example of a radially symmetric plate that effectively loses stiffness at the center. We allow the flexural rigidity to vanish at the center with various rates of decay from the boundary where stiffness is preserved, and analyze the resulting model. The singularity at the origin determines the appropriate space of functions in which the problem has a unique solution.

In this paper we include the homogeneous plate and a plate which is perfectly rigid at its center. Even though this case is not justified through asymptotic analysis, we found our solutions to be physically reasonable.

2 Derivation of the Boundary Value Problem

The physical system modeled is shown in Fig. 1.

A classical plate supports the load f by bending; the amount of support is dependent on the magnitude of the rigidity (the modulus of flexural rigidity) and the curvature (the concavity is the usual linear approximation) of the displacement. A membrane supports the load by tension and the amount of support is dependent on the tensile force and the magnitude of the slope of the deflection. The inhomogeneous plate being studied supports the load both by bending and through in-plane tension.

The mathematical model for a plate with radially variable rigidity and for a membrane with constant tension are derived in many sources, the authors suggest Landau and Lifshitz (1959).

The Classical Linear Model for an Elastic Plate With Radial Inhomogeneity:

$$\Delta(D(r)\Delta u) = f, \tag{1}$$

where Δ is the Laplace operator, in the radially symmetric case $\Delta = (1/r)(d/dr)[r(d/dr)]$, and

u = vertical displacement
r = distance from the origin
D = flexural rigidity
f = vertical applied force density.

[3] Department of Chemical Engineering.
[4] Department of Mathematics.
[5] Lafayette College, Easton, PA 18042.

Contributed by the Applied Mechanics Division of THE AMERICAN SOCIETY OF MECHANICAL ENGINEERS for publication in the ASME JOURNAL OF APPLIED MECHANICS. Manuscript received by the ASME Applied Mechanics Division, July 21, 1995; final revision, Aug. 30, 1996. Associate Technical Editor: J. N. Reddy.

Copyright © 1997 by ASME

Downloaded 04 May 2010 to 171.66.16.34. Redistribution subject to ASME license or copyright; see http://www.asme.org/terms/Terms_Use.cfm

With a slight abuse of notation, we will assume the flexural rigidity has the form

$$D(r) = Dr^k,$$

where k is the parameter determining the nature of the degeneracy of the rigidity at the origin and D is now a constant determining the rate of increase of the rigidity. If $f = f(r)$ is radially symmetric then we can assume radial symmetry in the deflection, $u = u(r)$.

The Classical Linear Model for a Membrane Under Homogeneous Tension:

$$-\tau\Delta u = f, \tag{2}$$

where τ is the tensile force and f is the vertical load, as above.

Since the deflection of our degenerate plate supports the load through both of these mechanisms, the model sums the contributions:

$$D\Delta(r^k\Delta u) - \tau\Delta u = f. \tag{3}$$

Before solving the equation, we introduce a dimensionless variable ($R = r/\rho$ where ρ is the radius of the disk) and divide through by the flexural rigidity constant D. The resulting differential equation is

$$-\Delta(R^k\Delta u) + T\Delta u = -F \quad \text{in} \quad 0 \le R \le 1, \tag{4}$$

where

$$u = u(R), \quad T = \frac{\tau}{D}\rho^{k-2},$$

$$R = \frac{r}{\rho}, \quad F = \frac{f}{D}\rho^{k-4}.$$

We add the appropriate boundary conditions for a clamped plate to complete the boundary value problem:

$$u(1) = 0, \quad u'(1) = 0. \tag{5}$$

In Eq. (4), the parameter T denotes the relative contribution of in-plane tension (membrane-like behavior) to support the load.

3 General Procedure and Mathematical Results

We begin by identifying the function space where we find a unique solution to the boundary value problem. This is particularly important in problems with degeneracies, since inclusion in the space constitutes an implicit boundary condition on the solution to the problem. If u is a solution of the boundary value problem (4), (5), it follows from integration by parts that the L^2 inner product of an arbitrary function $v \in C^\infty[0, 1]$ satisfying the boundary conditions (5), and our load $F(\int_0^1 FvRdR)$ equals the inner product $(u, v)_{\mathcal{H}_k}$ of the solution space $\mathcal{H}_k$ for $T > 0$:

$$(u, v)_{\mathcal{H}_k} = \int_0^1 (R^k\Delta u\Delta v + T\nabla u\cdot\nabla v)RdR. \tag{6}$$

Here, the gradient is merely $\nabla = d/dr$ by virtue of the radial symmetry. The function space $\mathcal{H}_k$ is the completion of all $u \in C^\infty[0, 1]$ functions with $u(1) = u'(1) = 0$ under the norm $\|u\|_{\mathcal{H}_k} = \sqrt{(u, u)_{\mathcal{H}_k}}$. The Poincaré-Friedrichs inequality (see Ladyzhenskaya, 1985) guarantees that we in fact have a norm on the given functions, and that the resulting space has a continuous embedding into $L^2(0, 1)$. With this established, the Riesz Representation Theorem guarantees a unique weak solution in the Hilbert space $\mathcal{H}_k$. Readers interested in the mathematical details might refer to Hutson and Pym (1980).

Physically, the norm squared of our solution space can be interpreted as the potential energy (in dimensionless units) stored in a deflection satisfying the boundary conditions, thus we have proved that there exists only one deflection with finite potential energy that solves the given boundary value problem. The solution space also determines the expected smoothness of our solutions at the origin depending on the type of inhomogeneity.

Substituting the radially symmetric Laplace operator into Eq. (4) yields an ordinary differential equation of the form

$$L[u] = \phi_3(R, k)u^{(4)} + \phi_2(R, k)u^{(3)} + \phi_1(R, k, T)u'' + \phi_0(R, k, T)u' = -F, \tag{7}$$

where ϕ_n is a polynomial in R whose form depends on the value of the parameter k. The coefficients ϕ_0 and ϕ_1 depend on T. We can regard this as a third order equation in u' with the boundary condition $u'(1) = 0$ and define $u(x) = \int_1^x u'(t)dt$ to assure that the final solution satisfies the boundary condition $u(1) = 0$.

At this point we restrict our procedure to equations solvable through the method of Fröbenius, which requires a regular singularity at the origin. Physically, this limitation restricts how rapidly the rigidity can be lost and not cause the plate to rupture. For our model, we must require $k \le 2$ for this condition to be satisfied. The cases with $k > 2$ result in deflections with an essential singularity (in the sense of analytic functions) at the origin; this is not physically reasonable.

In every case, (that is, for every value of k considered), the Fröbenius method generates three linearly independent solutions u' to the homogeneous equation associated with the third-order equation in u' above, $L[u] = 0$. However, two of these solutions will have singularities at the origin that preclude the inclusion of the associated u in the solution space $\mathcal{H}_k$. A multiple of the remaining solution to the homogeneous equation is summed to a particular solution of the equation $L[u] = -F$ to arrive at a solution to the boundary value problem.

The $k = 2$ case generates a Cauchy-Euler equation. In this case alone, the indicial equation includes the parameter T. As a result, the validity and smoothness of the solution depends on the value of T. Using the properties of Cauchy-Euler equations (see, for example, Kreyszig, 1988), the solution for a polynomial load $F = \Sigma_m F_m R^m$ was found to be

$$u(R) = \sum_m \frac{-F_m R^{m+2}}{(m+2)^2(-4-4m-m^2+T)} + K + K'R^{\sqrt{T}}, \tag{8}$$

where, to satisfy the boundary conditions, the constants K and K' are given by

$$K' = \sum_m \frac{-F_m}{\sqrt{T}(m+2)(-4-4m-m^2+T)},$$

and

$$K = \sum_m \frac{-F_m}{(m+2)^2(-4-4m-m^2+T)} - K'.$$

For the cases where $k < 2$, the solution to the associated homogeneous equation with finite potential energy is

$$V = a\int_1^R \frac{d}{d\rho} I_0\left[\left(\frac{2\sqrt{T}}{2-k}\right)\rho^{2/(2-k)}\right]d\rho.$$

Here, I_0 is the modified Bessel function of the first kind with index 0. To find the particular solution also satisfying the first boundary condition, in the spirit of the method of undetermined coefficients we create a power series such that when the differential operator ($L[u]$) is applied to it, the result converges to the forcing function. The series expression for $F = \Sigma_m F_m R^m$ is

Downloaded 04 May 2010 to 171.66.16.34. Redistribution subject to ASME license or copyright; see http://www.asme.org/terms/Terms_Use.cfm

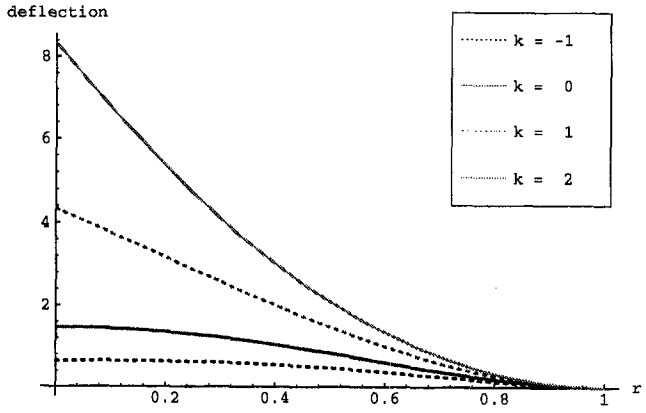


Fig. 2 Vertical deflection as a function of radius with tension parameter $T = 1$. The parameter k indicates the rate at which stiffness is lost in the center.

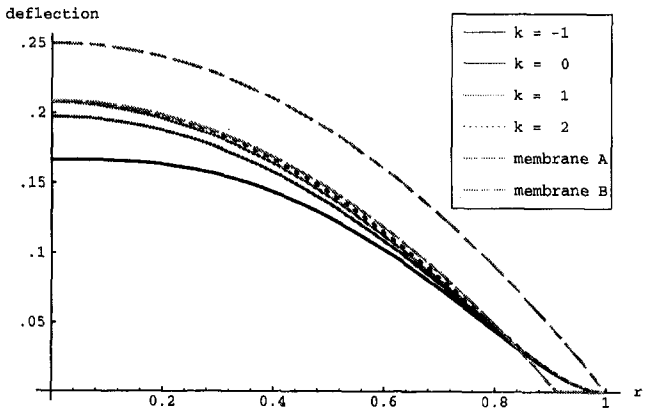


Fig. 4 Vertical deflection as a function of radius with tension parameter $T = 100$ (k as in Fig. 2)

$$W = \int_1^R \sum_m \frac{F_m}{\frac{(4 - k + m)(2 + m)^2}{2(4 - k)}} \times \sum_{j=0}^{\infty} \frac{T^j \rho^{3-k+m+j(2-k)}}{\prod_{i=0}^{j} (4 - k + i(m + 2 - k))(2 + i(m + 2 - k))} d\rho$$

The complete solution satisfying the entire boundary value problem is $u(R) = aV + W$, where $a = -W'(1)/V'(1)$.

4 Analysis of Results

The solution for the model was calculated for parameter $k \in \{-1, 0, 1, 2\}$ and a constant forcing function $F = 100$. Note that $k = 0$ corresponds to a homogeneous plate, and $k = -1$ to a plate that becomes perfectly rigid at its center. The following figures illustrate the relationship between the type of inhomogeneity and the magnitude of T. As the flexural rigidity degenerates more rapidly near the origin (that is, as k takes on larger values), greater displacement is necessary to generate sufficient tension to support the load. The expected smoothness of the solution at the origin also depends on the inhomogeneity of the plate. As the inhomogeneity decreases, the smoothness increases. In mathematical terms, the solution space places stronger restrictions on the solution at the origin as the inhomogeneity lessens. Figures displaying the solution u as a function of the variable R follow the text.

In Fig. 2, $T = 1$ models a plate that has the same relative magnitude of tension and bending forces near the boundary; note the graphs are consistent with the descriptions in the preceding paragraph. Figure 3 models a plate with little tension.

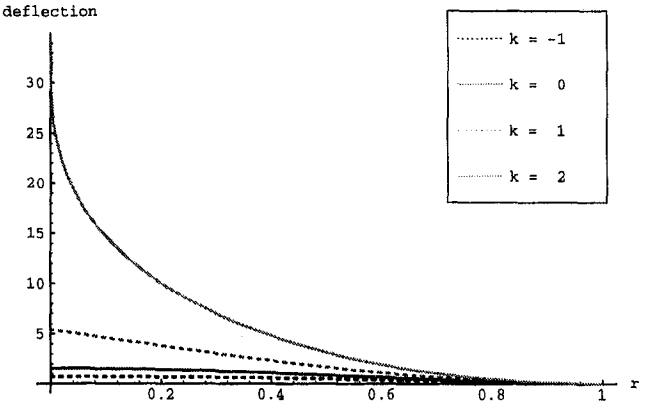


Fig. 3 Vertical deflection as a function of radius with tension parameter $T = 0.1$ (k as in Fig. 2)

Since the degeneracy of the rigidity is the dominant factor in this case, we see drastic differences in the deflections in each case since large slopes are necessary to obtain sufficient support for the load from the little available tension. These results ought not be duplicated experimentally, since the deformations are so large, they fall outside the linear regime used for this model. Figure 4 models a membrane with little rigidity. Since the membrane component of our model dominates with $T = 100$ for all k-values, the resulting deflections are similar for all k-values and approximate the behavior of a membrane. For comparison the figure contains the deflections of two membranes (modeled by the differential Eq. (2) with no fourth-order term). The largest membrane, labeled "membrane A" in the legend, has the same radius as the plates being modeled, and demonstrates the importance of the stiffness at the boundary in governing the deflection. The membrane with smaller deflection, labeled "membrane B," has a smaller radius, but identical maximum deflection under the specified tension and load. Notice that the plates that lose stiffness in the center (with $k = 1$ or 2) are both very well approximated by the membrane solution away from a boundary layer.

The final figure, Fig. 5, demonstrates the loss of smoothness of the deflection that accompanies loss of tension in the case of $k = 2$. This loss of smoothness is characteristic of this k-value; all others give smooth deflections no matter how little tension is applied. As this three-dimensional plot shows, the solution of this mode develops first a corner (seen when $T =$

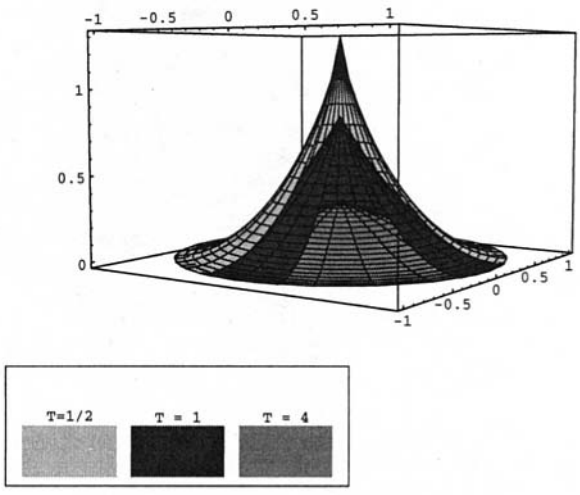


Fig. 5 Loss of smoothness of the deflection with loss of tension for $k = 2$

Downloaded 04 May 2010 to 171.66.16.34. Redistribution subject to ASME license or copyright; see http://www.asme.org/terms/Terms_Use.cfm

1) and eventually a cusp (seen at $T = 1/2$) as the tension supporting the load decreases. The plots shown all have a load of $F = 10$, but a uniform load of any magnitude will yield the same loss of smoothness.

Acknowledgment

The authors acknowledge the financial support from the EXCEL undergraduate research program at Lafayette College.

References

Ciarlet, P. G., 1980, "A Justification of the von Kármán Equations," *Archive for Rational Mechanics and Analysis,* Vol. 73, pp. 349–389.

Duvaut, G., and Lions, J. L., 1976, *Inequalities of Mechanics and Physics,* Springer-Verlag, New York.

Hutson, V., and Pym, J. S., 1980, *Applications of Functional Analysis and Operator Theory* (Mathematics in Science and Engineering, Vol. 146), Academic Press, New York.

Ladyzhenskaya, O. A., 1985, *The Boundary Value Problems of Mathematical Physics,* Springer-Verlag, New York.

Landau, L., and Lifshitz, E., 1959, *Theory of Elasticity,* Pergamon, Oxford, U.K.

Kreyszig, E., 1988, *Advanced Engineering Mathematics,* John Wiley and Sons, New York.

Root, R. G., 1991, "Existence Theory for Higher Order Elliptic-Parabolic Equations with an Application to Elasticity," *Journal of Mathematical Analysis and Applications,* Vol. 154, No. 1, pp. 255–272.

Root, R. G., 1994, "A Derivation of Degenerate von Kármán Equations for Strongly Anisotropic Plates," *Quarterly of Applied Mathematics,* to appear.

Rosato, D., and Rosato, D., 1986, *Injection Molding Handbook,* Van Nostrand Reinhold, New York.

On the Use of a Plane-Strain Model to Solve Generalized Plane-Strain Problems

Shoufeng Hu[6,7] and N. J. Pagano[7]

Many composite problems are generalized plane strain in nature. They are often solved using three-dimensional finite element analyses. We propose a technique to solve these problems with a plane-strain model, which is achieved by introducing some artificial out-of-plane thermal strains in a two-dimensional finite element analysis. These artificial thermal strains are chosen such that an identical stress field is obtained, while the actual strains and displacements can also be determined.

Introduction

Composite micromechanics deals with fibers and matrix each as distinct constituent materials. Each constituent phase is considered a homogeneous isotropic (or orthotropic) medium and has its own mechanical and thermal properties which may be significantly different from the others. Many composite micromechanics problems are plane problems in nature. A typical example is a composite under transverse loading (see Fig. 1), in which the stress field away from the free edge zone is two-dimensional since out-of-plane shear stresses vanish. This is a generalized plane-strain problem. The state of generalized plane strain is defined by the elastic field $u = u(x, y), v = v(x, y)$, and $w = \epsilon_0 z + C_1$; where u, v, w are the displacement components in the x, y and z directions, respectively, and ϵ_0 and C_1 are constants. When solving this problem using a finite element model, however, investigators often use a three-dimensional element model instead (Highsmith et al., 1990; Nimmer, 1990; Nimmer et al., 1991). The reason is that most commercial finite element packages do not support the application of generalized plane strain (Highsmith, 1990). Using their in-house finite element program, Chandra et al. (1994) have concluded that the generalized plane-strain model matches reasonably closely with the three-dimensional model. It is worth noting that a three-dimensional finite element analysis is much more costly than a two-dimensional one. The details of this will be discussed later.

In this note we propose a technique to solve generalized plane-strain problems using a plane-strain approach. The proposed technique leads to the achievement of a tremendous saving of computational resources without sacrificing accuracy. Since most commercial finite element packages support the use of orthotropic material properties, it is rather easy to introduce an artificial coefficient of thermal expansion in the out-of-plane direction for each material to assemble a generalized plane-strain model. The artificial thermal strains are chosen such that the created plane strain model provides an identical stress field to that of the generalized plane-strain problem.

Elasticity Analysis

Our purpose is to create an artificial plane-strain model in which the stresses are equivalent to those in the actual generalized plane-strain problem. To achieve this we keep all the stresses as well as the in-plane strains, displacements, and coefficients of thermal expansion for the generalized plane strain problem unchanged. The artificial out-of-plane (z-axis) thermal strain is determined such that the out-of-plane tractions for the plane strain and generalized plane-strain problems are identical.

For the generalized plane strain model,

$$\epsilon_{iz} + e_i = \epsilon_0 \tag{1}$$

where $\epsilon_{iz} = (1/E_i)(\sigma_{iz} - \nu_i(\sigma_{ix} + \sigma_{iy}))$ is the mechanical strain; $e_i = \Delta T \alpha_i$ is thermal strain; ΔT is the temperature difference; α_i is the actual coefficient of thermal expansion; ϵ_0 is the constant out-of-plane normal strain; i is the arbitrary material identifier.

For the plane-strain model:

$$\epsilon_{iz} + e_i^* = 0 \tag{2}$$

where $e_i^* = \Delta T \alpha_i^*$ is the artificial out-of-plane thermal strain and α_i^* is the artificial out-of-plane coefficient of thermal expansion. The artificial thermal strain which creates an equivalent plane-strain field is chosen such that ϵ_{iz} given by (1) and (2) are equivalent, i.e.,

$$e_i^* = e_i - \epsilon_0. \tag{3}$$

In the event that ϵ_0 is not known a priori, we conduct the following analysis. Consider the generalized plane-strain problem of a body composed of $N - 1$ cylindrical inclusions embedded in a cylindrical matrix $i = N$, and assume the interfacial boundary conditions are such that the tractions, but not necessarily the displacements, are all continuous. Integrating (1) over the material i cross-section area A_i leads to

$$E_i(\epsilon_0 - e_i)A_i = \int_{A_i} \sigma_{iz} dA - \nu_i \int_{A_i} (\sigma_{ix} + \sigma_{iy}) dA \tag{4}$$

Summation of (4) for all materials,

$$\sum_{i=1}^{N} E_i(\epsilon_0 - e_i)A_i = \sum_{i=1}^{N} \int_{A_i} \sigma_{iz} dA - \sum_{i=1}^{N} \nu_i \int_{A_i} (\sigma_{ix} + \sigma_{iy}) dA. \tag{5}$$

[6] Materials Directorate, Wright Laboratory, Wright-Patterson AFB, OH 45433.
[7] Currently with Hamilton Standard, United Technologies Corporation.

Contributed by the Applied Mechanics Division of THE AMERICAN SOCIETY OF MECHANICAL ENGINEERS for publication in the ASME JOURNAL OF APPLIED MECHANICS. Manuscript received by the ASME Applied Mechanics Division, Sept. 8, 1995; final revision, Aug. 8, 1996. Associate Technical Editor: J. W. Ju.

Downloaded 04 May 2010 to 171.66.16.34. Redistribution subject to ASME license or copyright; see http://www.asme.org/terms/Terms_Use.cfm

1) and eventually a cusp (seen at $T = 1/2$) as the tension supporting the load decreases. The plots shown all have a load of $F = 10$, but a uniform load of any magnitude will yield the same loss of smoothness.

Acknowledgment

The authors acknowledge the financial support from the EXCEL undergraduate research program at Lafayette College.

References

Ciarlet, P. G., 1980, "A Justification of the von Kármán Equations," *Archive for Rational Mechanics and Analysis,* Vol. 73, pp. 349–389.

Duvaut, G., and Lions, J. L., 1976, *Inequalities of Mechanics and Physics,* Springer-Verlag, New York.

Hutson, V., and Pym, J. S., 1980, *Applications of Functional Analysis and Operator Theory* (Mathematics in Science and Engineering, Vol. 146), Academic Press, New York.

Ladyzhenskaya, O. A., 1985, *The Boundary Value Problems of Mathematical Physics,* Springer-Verlag, New York.

Landau, L., and Lifshitz, E., 1959, *Theory of Elasticity,* Pergamon, Oxford, U.K.

Kreyszig, E., 1988, *Advanced Engineering Mathematics,* John Wiley and Sons, New York.

Root, R. G., 1991, "Existence Theory for Higher Order Elliptic-Parabolic Equations with an Application to Elasticity," *Journal of Mathematical Analysis and Applications,* Vol. 154, No. 1, pp. 255–272.

Root, R. G., 1994, "A Derivation of Degenerate von Kármán Equations for Strongly Anisotropic Plates," *Quarterly of Applied Mathematics,* to appear.

Rosato, D., and Rosato, D., 1986, *Injection Molding Handbook,* Van Nostrand Reinhold, New York.

On the Use of a Plane-Strain Model to Solve Generalized Plane-Strain Problems

Shoufeng Hu[6,7] and N. J. Pagano[7]

Many composite problems are generalized plane strain in nature. They are often solved using three-dimensional finite element analyses. We propose a technique to solve these problems with a plane-strain model, which is achieved by introducing some artificial out-of-plane thermal strains in a two-dimensional finite element analysis. These artificial thermal strains are chosen such that an identical stress field is obtained, while the actual strains and displacements can also be determined.

Introduction

Composite micromechanics deals with fibers and matrix each as distinct constituent materials. Each constituent phase is considered a homogeneous isotropic (or orthotropic) medium and has its own mechanical and thermal properties which may be significantly different from the others. Many composite micromechanics problems are plane problems in nature. A typical example is a composite under transverse loading (see Fig. 1), in which the stress field away from the free edge zone is two-dimensional since out-of-plane shear stresses vanish. This is a generalized plane-strain problem. The state of generalized plane strain is defined by the elastic field $u = u(x, y), v = v(x, y)$, and $w = \epsilon_0 z + C_1$; where u, v, w are the displacement components in the x, y and z directions, respectively, and ϵ_0 and C_1 are constants. When solving this problem using a finite element model, however, investigators often use a three-dimensional element model instead (Highsmith et al., 1990; Nimmer, 1990; Nimmer et al., 1991). The reason is that most commercial finite element packages do not support the application of generalized plane strain (Highsmith, 1990). Using their in-house finite element program, Chandra et al. (1994) have concluded that the generalized plane-strain model matches reasonably closely with the three-dimensional model. It is worth noting that a three-dimensional finite element analysis is much more costly than a two-dimensional one. The details of this will be discussed later.

In this note we propose a technique to solve generalized plane-strain problems using a plane-strain approach. The proposed technique leads to the achievement of a tremendous saving of computational resources without sacrificing accuracy. Since most commercial finite element packages support the use of orthotropic material properties, it is rather easy to introduce an artificial coefficient of thermal expansion in the out-of-plane direction for each material to assemble a generalized plane-strain model. The artificial thermal strains are chosen such that the created plane strain model provides an identical stress field to that of the generalized plane-strain problem.

Elasticity Analysis

Our purpose is to create an artificial plane-strain model in which the stresses are equivalent to those in the actual generalized plane-strain problem. To achieve this we keep all the stresses as well as the in-plane strains, displacements, and coefficients of thermal expansion for the generalized plane strain problem unchanged. The artificial out-of-plane (z-axis) thermal strain is determined such that the out-of-plane tractions for the plane strain and generalized plane-strain problems are identical.

For the generalized plane strain model,

$$\epsilon_{iz} + e_i = \epsilon_0 \tag{1}$$

where $\epsilon_{iz} = (1/E_i)(\sigma_{iz} - \nu_i(\sigma_{ix} + \sigma_{iy}))$ is the mechanical strain; $e_i = \Delta T \alpha_i$ is thermal strain; ΔT is the temperature difference; α_i is the actual coefficient of thermal expansion; ϵ_0 is the constant out-of-plane normal strain; i is the arbitrary material identifier.

For the plane-strain model:

$$\epsilon_{iz} + e_i^* = 0 \tag{2}$$

where $e_i^* = \Delta T \alpha_i^*$ is the artificial out-of-plane thermal strain and α_i^* is the artificial out-of-plane coefficient of thermal expansion. The artificial thermal strain which creates an equivalent plane-strain field is chosen such that ϵ_{iz} given by (1) and (2) are equivalent, i.e.,

$$e_i^* = e_i - \epsilon_0. \tag{3}$$

In the event that ϵ_0 is not known a priori, we conduct the following analysis. Consider the generalized plane-strain problem of a body composed of $N - 1$ cylindrical inclusions embedded in a cylindrical matrix $i = N$, and assume the interfacial boundary conditions are such that the tractions, but not necessarily the displacements, are all continuous. Integrating (1) over the material i cross-section area A_i leads to

$$E_i(\epsilon_0 - e_i)A_i = \int_{A_i} \sigma_{iz} dA - \nu_i \int_{A_i} (\sigma_{ix} + \sigma_{iy}) dA \tag{4}$$

Summation of (4) for all materials,

$$\sum_{i=1}^{N} E_i(\epsilon_0 - e_i)A_i = \sum_{i=1}^{N} \int_{A_i} \sigma_{iz} dA - \sum_{i=1}^{N} \nu_i \int_{A_i} (\sigma_{ix} + \sigma_{iy}) dA. \tag{5}$$

[6] Materials Directorate, Wright Laboratory, Wright-Patterson AFB, OH 45433.

[7] Currently with Hamilton Standard, United Technologies Corporation.

Contributed by the Applied Mechanics Division of THE AMERICAN SOCIETY OF MECHANICAL ENGINEERS for publication in the ASME JOURNAL OF APPLIED MECHANICS. Manuscript received by the ASME Applied Mechanics Division, Sept. 8, 1995; final revision, Aug. 8, 1996. Associate Technical Editor: J. W. Ju.

Copyright © 1997 by ASME

Downloaded 04 May 2010 to 171.66.16.34. Redistribution subject to ASME license or copyright; see http://www.asme.org/terms/Terms_Use.cfm

In the particular generalized plane-strain model of a composite under transverse loading, the strain ϵ_0 is computed from the force balance in the z-direction. Thus unlike the plane strain model in general, there is no external force in this direction and consequently[8]

$$\sum_{i=1}^{N} \int_{A_i} \sigma_{iz} dA = 0 \tag{6}$$

Now we focus on the last term in (5). For material i, Green's theorem leads to

$$\iint (\sigma_x + \sigma_y) dxdy = \oint (t_x x + t_y y) ds \tag{7}$$

where t_x and t_y are the boundary tractions; ds is the elemental arc length of the ith boundary (keeping the region on the left).

Note that the summation of the last term in (5) involves integrations along the interfaces and along the external boundary. Since the tractions across the interface between the adjacent materials j and N are continuous, the sum of the integrals along a particular interface between materials j and N is equal to

$$I_j = (\nu_j - \nu_N) \oint (t_x x + t_y y) ds \tag{8}$$

and this integration will not vanish unless the interfacial traction integral I_j is zero or the constituents j and N have an identical Poisson ratio.

If either of the conditions just mentioned is satisfied for each interface, the summation of the integrations along the interfaces will be zero and the only surviving term will be the integrals along the external boundary. Consequently,

$$\sum_{i=1}^{N} \nu_i \iint (\sigma_x + \sigma_y) dxdy = \nu_N \oint_s (t_x x + t_y y) ds \tag{9}$$

where ν_N is the Poisson ratio for the external (matrix) material and s is the external boundary. If only traction boundary conditions are prescribed on s, the integral will be known, i.e.,

$$\oint_s (t_x x + t_y y) ds = K. \tag{10}$$

However, if we have prescribed displacement or mixed boundary conditions, K will not be known a priori.

Substituting (9) and (10) into (5) leads to

$$\epsilon_0 = \frac{\sum_{i=1}^{N} E_i A_i e_i - \nu_N K}{\sum_{i=1}^{N} E_i A_i}, \tag{11}$$

which is the desired result.

For a composite of which the constituent materials have different Poisson ratios, or the interfacial traction integrals I_j are not zero, or the boundary conditions are mixed, we are not aware of any general analytical solution for ϵ_0. However, we can obtain the solution for this problem using a superposition technique according to the following procedure.

We superpose a generalized plane-strain problem and a plane-strain problem which are denoted as (A) and (B), respectively. For (A) we prescribe homogeneous boundary conditions of the same type as the imposed boundary conditions on s, zero thermal strains, and $\epsilon_0 = 1$. We solve this problem by use of the plane strain analogy. For (B) we prescribe the actual boundary condition on s and the actual thermal strains. The actual strain ϵ_0 will be obtained according to the condition (see the footnote for the case where resultant force is not zero)

[8] If the resultant force is not zero, a simple superposition leads to the correct result.

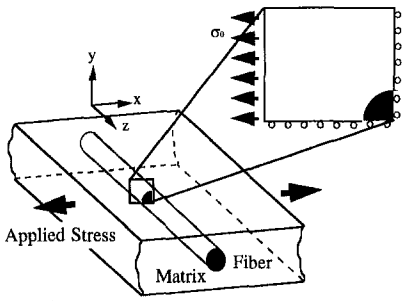


Fig. 1 A schematic illustration of a single fiber composite under transverse loading

$$\epsilon_0 \sum_{i=1}^{N} \int_{A_i} \sigma_{iz}^{\#} dA + \sum_{i=1}^{N} \int_{A_i} \sigma_{iz}^{\#\#} dA = 0 \tag{12}$$

where superscripts # and ## are of the components for problems (A) and (B), respectively. Finally, the solution for any dependent variable f is given by

$$f = \epsilon_0 f^{\#} + f^{\#\#}. \tag{13}$$

The actual displacement in z-direction can be expressed as follows, neglecting rigid-body motion

$$w = \epsilon_0 z = (e_i - e_i^*) z. \tag{14}$$

Finite Element Analysis

Consider an example of a single fiber composite of titanium matrix reinforced with a silicon carbide fiber under both thermal and mechanical loading. We performed several cases of analysis using the commercial finite element package ANSYS. In each case a three-dimensional model, which uses eight noded isoparametric elements and only one element in the z-direction, and the corresponding plane-strain model (using four-noded isoparametric elements) were performed and compared with each other. A quarter of the model was used owing to symmetry (see Fig. 1). For the three-dimensional model the generalized plane-strain condition was created by requiring the out-of-plane nodal displacements on the back face normal to the z-direction to be zero and that on the front-face to be constant, while the shear stresses on the end planes vanish. For the plane-strain model the boundary conditions on s, mesh, and material constants are the same except for the artificial out-of-plane coefficients of thermal expansion. The material and geometric constants are listed below:

Fiber:

$E_f = 414.0$ GPa $\alpha_f = 4.86\ 10^{-6}$/°C

Fiber diameter = 0.142 mm Fiber volume fraction = 0.1

Matrix:

$E_m = 113.7$ GPa $\alpha_m = 9.44\ 10^{-6}$/°C

Cross-section Dimensions = 0.4 mm by 0.4 mm

Loading conditions:

Constant temperature change ΔT and mechanical loading $\sigma_x = \sigma_0$

Results and Discussions

Three different loading cases are examined. For each case we individually discuss (a) the superposition solution obtained using (12) and (13), and (b) the analytical solution obtained using (11) which is an approximation for this case. For (b), we use a constant Poisson ratio which is the average of ν_f and ν_m. In the meantime, for each case we also consider two subcases for the effect of mismatch in the Poisson ratios using the following combinations of the Poisson ratios:

(1) $\nu_f = 0.1$ $\nu_m = 0.4$ (2) $\nu_f = 0.3$ $\nu_m = 0.32$

Downloaded 04 May 2010 to 171.66.16.34. Redistribution subject to ASME license or copyright; see http://www.asme.org/terms/Terms_Use.cfm

Case I: $\sigma_0 = 0$, $\Delta T = -500°C$
(a1) $\epsilon_0 = 8.2694\ 10^{-6}/°C$ (a2) $\epsilon_0 = 8.1438\ 10^{-6}/°C$
(b1) $\epsilon_0 = 8.1306\ 10^{-6}/°C$ (b2) $\epsilon_0 = 8.1306\ 10^{-6}/°C$

Case II: $\sigma_0 = 200$ MPa, $\Delta T = 0$
(a1) $\epsilon_0 = 1.0236\ 10^{-6}/°C$ (a2) $\epsilon_0 = 0.8860\ 10^{-6}/°C$
(b1) $\epsilon_0 = 0.6972\ 10^{-6}/°C$ (b2) $\epsilon_0 = 0.8646\ 10^{-6}/°C$

By comparing (a) and (b) for each case we can see that the differences are not large except for Case II (1). Furthermore, the differences for a smaller mismatch in the Poisson ratios (subcase 2) are even smaller. Thus, (11) may be a reasonable approximation for small mismatch in the Poisson ratios.

Without considering the prescribed displacement boundary conditions in the z-direction, the stiffness matrix of a three-dimensional model is three times as large as that of a two-dimensional model, even if only one element is used in the third direction. It is especially meaningful for finite element analyses involving iterations, such as contact problems, if a replacement of a three-dimensional analysis by a two-dimensional analysis is achieved. For these problems it is worthwhile even if we have to obtain the artificial out-of-plane thermal strains using a finite element model and superposition. In addition, a two-dimensional analysis can avoid the elements with large aspect ratios as may occur in a three-dimensional analysis, since only one element with a constant length in the z-direction is used in the latter case.

The savings of computer resources are illustrated in Table 1.

Table 1 Comparison of 2-D and 3-D finite element analyses

	db* file (byte)	No. of nodes (elements)	CP** time (sec)
2-D	1851392	793 (740)	22.704
3-D	3293184	1586 (740)	71.599

* db file is the solution file in ANSYS to be retrieved for post-processing.
** Computer processing time in a Sun SPARC Work Station. It may vary by a few percent for each run.

Acknowledgment

The first author gratefully acknowledges the support of National Research Council and Wright Laboratory. He also wants to express his appreciation to Mr. W. Scott Zemitis of EMI for some fruitful discussions about using ANSYS for this particular problem.

References

Chandra, N., Ananth, C. R., and Garmestani, H., 1994, "Micromechanical Modeling of Process-Induced Residual Stresses in Ti-24A1-11Nb/SCS-6 Composite," *Journal of Composites Technology and Research,* Vol. 16, pp. 37–46.

Highsmith, A. L., Shin, D., and Naik, R. A., 1990, "Local Stresses in Metal Matrix Composites Subjected to Thermal and Mechanical Loading," *Thermal and Mechanical Behavior of Metal Matrix and Ceramic Matrix Composites* (ASTM STP 1080), J. M. Kennedy, H. H. Moeller, and W. S. Johnson, eds., American Society for Testing and Materials, Philadelphia, PA, pp. 3–19.

Nimmer, R. P., 1990, "Fiber-Matrix Interface Effects in the Presence of Thermally Induced Residual Stresses," *Journal of Composites Technology and Research,* Vol. 12, pp. 65–75.

Nimmer, R. P., Bankert, R. J., Russel, E. S., Smith, G. A., and Wright, P. K., 1991, "Micromechanical Modeling of Fiber-Matrix Interface Effects in Transversely Loaded SiC/Ti–6–4 Metal Matrix Composites," *Journal of Composites Technology and Research,* Vol. 13, pp. 3–13.

Modal Decoupling of Systems Described by Three Linear Operators

A. A. Renshaw[9]

Introduction

This Brief Note demonstrates that the modal representation of the equation of motion of a forced dynamic system described by three linear operators always decouples whenever the system eigenfunctions are complete. No symmetry properties of the system operators are assumed, but it is assumed that all three operators have well-defined adjoints. This assumption, together with eigenfunction completeness, restrict the generality of the result since completeness of eigenfunctions for non-self-adjoint, continuous systems is difficult to verify. Equivalent and similar results have been described in numerous papers for discrete, symmetric systems (Foss, 1958; Caughey, 1960; Caughey and O'Kelly, 1965), continuous self-adjoint systems (Caughey and O'Kelly, 1965; Inman and Andry, 1982), discrete asymmetric systems (Lancaster, 1966; Meirovitch, 1975; Wahed and Bishop, 1976, Inman, 1983), and continuous non-self-adjoint systems (D'Eleuterio and Hughes, 1984; Inman and Olsen, 1988; Wickert and Mote, 1990). Consequently, the final result is not entirely new. However, the following derivation provides a concise and unified treatment of these diverse systems and, for those systems where completeness can be verified, establishes the effectiveness of a modal approach.

Orthogonalities and the Free Response

Consider the equation of motion

$$M\frac{\partial^2 u}{\partial t^2} + C\frac{\partial u}{\partial t} + Ku = f \tag{1}$$

where M, C, and K are linear, real, differential (or matrix) operators in the spatial domain Ω, $x \in \Omega$ is position, t is time, $u(x, t)$ is displacement, and $f(x, t)$ are external forces. Solutions of (1) satisfy boundary conditions $Bu = 0$ where B is a linear real differential operator defined on the boundary of Ω. We assume the existence of sufficiently differentiable domains of a Hilbert space on Ω with complex inner product $\langle , \rangle$ on which the three operators M, C, and K and their adjoint operators M^*, C^*, and K^* can be defined according to

$$\langle Mu, w\rangle = \langle u, M^*w\rangle \quad \langle Cu, w\rangle = \langle u, C^*w\rangle$$
$$\langle Ku, w\rangle = \langle u, K^*w\rangle \tag{2}$$

for u and w satisfying $Bu = 0$ and $B^*w = 0$, respectively, where B^* is the appropriate adjoint boundary operator.

The eigenvalue problem associated with (1) and $Bu = 0$ and the separable substitution $u(x, t) = e^{\lambda_n t}\psi_n(x)$ is

$$\lambda_n^2 M\psi_n + \lambda_n C\psi_n + K\psi_n = 0. \tag{3}$$

The eigensolutions $\{\lambda_n, \psi_n\}$ are generally complex and can be ordered such that $n = 1, 2, 3, \ldots$. If $\{\lambda_n, \psi_n\}$ is an eigensolution of (3), then $\{\bar{\lambda}_n, \psi_n^*\}$ is an eigensolution of the adjoint eigenvalue problem

$$\bar{\lambda}_n^2 M^*\psi_n^* + \bar{\lambda}_n C^*\psi_n^* + K^*\psi_n^* = 0 \tag{4}$$

where the overbar denotes complex conjugation.

There are three orthogonality relations associated with (3) and (4). Taking the inner product of (3) and $\bar{\lambda}_m\psi_m^*$ and subtracting the inner product of $\lambda_m\psi_m$ and (4) gives

[9] Department of Mechanical Engineering, Columbia University, 500 West 120th Street, Room 220, New York, NY 10027. Mem. ASME.

Contributed by the Applied Mechanics Division of THE AMERICAN SOCIETY OF MECHANICAL ENGINEERS for publication in the ASME JOURNAL OF APPLIED MECHANICS. Manuscript received by the ASME Applied Mechanics Division, Dec. 8, 1995; final revision, June 6, 1996. Associate Technical Editor: S. W. Shaw.

Downloaded 04 May 2010 to 171.66.16.34. Redistribution subject to ASME license or copyright; see http://www.asme.org/terms/Terms_Use.cfm

Case I: $\sigma_0 = 0$, $\Delta T = -500°C$
(a1) $\epsilon_0 = 8.2694\ 10^{-6}/°C$ (a2) $\epsilon_0 = 8.1438\ 10^{-6}/°C$
(b1) $\epsilon_0 = 8.1306\ 10^{-6}/°C$ (b2) $\epsilon_0 = 8.1306\ 10^{-6}/°C$

Case II: $\sigma_0 = 200$ MPa, $\Delta T = 0$
(a1) $\epsilon_0 = 1.0236\ 10^{-6}/°C$ (a2) $\epsilon_0 = 0.8860\ 10^{-6}/°C$
(b1) $\epsilon_0 = 0.6972\ 10^{-6}/°C$ (b2) $\epsilon_0 = 0.8646\ 10^{-6}/°C$

By comparing (a) and (b) for each case we can see that the differences are not large except for Case II (1). Furthermore, the differences for a smaller mismatch in the Poisson ratios (subcase 2) are even smaller. Thus, (11) may be a reasonable approximation for small mismatch in the Poisson ratios.

Without considering the prescribed displacement boundary conditions in the z-direction, the stiffness matrix of a three-dimensional model is three times as large as that of a two-dimensional model, even if only one element is used in the third direction. It is especially meaningful for finite element analyses involving iterations, such as contact problems, if a replacement of a three-dimensional analysis by a two-dimensional analysis is achieved. For these problems it is worthwhile even if we have to obtain the artificial out-of-plane thermal strains using a finite element model and superposition. In addition, a two-dimensional analysis can avoid the elements with large aspect ratios as may occur in a three-dimensional analysis, since only one element with a constant length in the z-direction is used in the latter case.

The savings of computer resources are illustrated in Table 1.

Table 1 Comparison of 2-D and 3-D finite element analyses

	db* file (byte)	No. of nodes (elements)	CP** time (sec)
2-D	1851392	793 (740)	22.704
3-D	3293184	1586 (740)	71.599

* db file is the solution file in ANSYS to be retrieved for post-processing.
** Computer processing time in a Sun SPARC Work Station. It may vary by a few percent for each run.

Acknowledgment

The first author gratefully acknowledges the support of National Research Council and Wright Laboratory. He also wants to express his appreciation to Mr. W. Scott Zemitis of EMI for some fruitful discussions about using ANSYS for this particular problem.

References

Chandra, N., Ananth, C. R., and Garmestani, H., 1994, "Micromechanical Modeling of Process-Induced Residual Stresses in Ti-24A1-11Nb/SCS-6 Composite," *Journal of Composites Technology and Research,* Vol. 16, pp. 37–46.

Highsmith, A. L., Shin, D., and Naik, R. A., 1990, "Local Stresses in Metal Matrix Composites Subjected to Thermal and Mechanical Loading," *Thermal and Mechanical Behavior of Metal Matrix and Ceramic Matrix Composites* (ASTM STP 1080), J. M. Kennedy, H. H. Moeller, and W. S. Johnson, eds., American Society for Testing and Materials, Philadelphia, PA, pp. 3–19.

Nimmer, R. P., 1990, "Fiber-Matrix Interface Effects in the Presence of Thermally Induced Residual Stresses," *Journal of Composites Technology and Research,* Vol. 12, pp. 65–75.

Nimmer, R. P., Bankert, R. J., Russel, E. S., Smith, G. A., and Wright, P. K., 1991, "Micromechanical Modeling of Fiber-Matrix Interface Effects in Transversely Loaded SiC/Ti–6–4 Metal Matrix Composites," *Journal of Composites Technology and Research,* Vol. 13, pp. 3–13.

Modal Decoupling of Systems Described by Three Linear Operators

A. A. Renshaw[9]

Introduction

This Brief Note demonstrates that the modal representation of the equation of motion of a forced dynamic system described by three linear operators always decouples whenever the system eigenfunctions are complete. No symmetry properties of the system operators are assumed, but it is assumed that all three operators have well-defined adjoints. This assumption, together with eigenfunction completeness, restrict the generality of the result since completeness of eigenfunctions for non-self-adjoint, continuous systems is difficult to verify. Equivalent and similar results have been described in numerous papers for discrete, symmetric systems (Foss, 1958; Caughey, 1960; Caughey and O'Kelly, 1965), continuous self-adjoint systems (Caughey and O'Kelly, 1965; Inman and Andry, 1982), discrete asymmetric systems (Lancaster, 1966; Meirovitch, 1975; Wahed and Bishop, 1976, Inman, 1983), and continuous non-self-adjoint systems (D'Eleuterio and Hughes, 1984; Inman and Olsen, 1988; Wickert and Mote, 1990). Consequently, the final result is not entirely new. However, the following derivation provides a concise and unified treatment of these diverse systems and, for those systems where completeness can be verified, establishes the effectiveness of a modal approach.

Orthogonalities and the Free Response

Consider the equation of motion

$$M\frac{\partial^2 u}{\partial t^2} + C\frac{\partial u}{\partial t} + Ku = f \tag{1}$$

where M, C, and K are linear, real, differential (or matrix) operators in the spatial domain Ω, $x \in \Omega$ is position, t is time, $u(x, t)$ is displacement, and $f(x, t)$ are external forces. Solutions of (1) satisfy boundary conditions $Bu = 0$ where B is a linear real differential operator defined on the boundary of Ω. We assume the existence of sufficiently differentiable domains of a Hilbert space on Ω with complex inner product $\langle , \rangle$ on which the three operators M, C, and K and their adjoint operators M^*, C^*, and K^* can be defined according to

$$\langle Mu, w\rangle = \langle u, M^*w\rangle \quad \langle Cu, w\rangle = \langle u, C^*w\rangle$$
$$\langle Ku, w\rangle = \langle u, K^*w\rangle \tag{2}$$

for u and w satisfying $Bu = 0$ and $B^*w = 0$, respectively, where B^* is the appropriate adjoint boundary operator.

The eigenvalue problem associated with (1) and $Bu = 0$ and the separable substitution $u(x, t) = e^{\lambda_n t}\psi_n(x)$ is

$$\lambda_n^2 M\psi_n + \lambda_n C\psi_n + K\psi_n = 0. \tag{3}$$

The eigensolutions $\{\lambda_n, \psi_n\}$ are generally complex and can be ordered such that $n = 1, 2, 3, \ldots$. If $\{\lambda_n, \psi_n\}$ is an eigensolution of (3), then $\{\bar{\lambda}_n, \psi_n^*\}$ is an eigensolution of the adjoint eigenvalue problem

$$\bar{\lambda}_n^2 M^*\psi_n^* + \bar{\lambda}_n C^*\psi_n^* + K^*\psi_n^* = 0 \tag{4}$$

where the overbar denotes complex conjugation.

There are three orthogonality relations associated with (3) and (4). Taking the inner product of (3) and $\bar{\lambda}_m\psi_m^*$ and subtracting the inner product of $\lambda_m\psi_m$ and (4) gives

[9] Department of Mechanical Engineering, Columbia University, 500 West 120th Street, Room 220, New York, NY 10027. Mem. ASME.

Contributed by the Applied Mechanics Division of THE AMERICAN SOCIETY OF MECHANICAL ENGINEERS for publication in the ASME JOURNAL OF APPLIED MECHANICS. Manuscript received by the ASME Applied Mechanics Division, Dec. 8, 1995; final revision, June 6, 1996. Associate Technical Editor: S. W. Shaw.

Copyright © 1997 by ASME

Downloaded 04 May 2010 to 171.66.16.34. Redistribution subject to ASME license or copyright; see http://www.asme.org/terms/Terms_Use.cfm

$$(\lambda_n - \lambda_m)[\lambda_n\lambda_m\langle M\psi_n, \psi_m^*\rangle - \langle K\psi_n, \psi_m^*\rangle] = 0 \quad (5)$$

which is an orthogonality relation for $\lambda_n \neq \lambda_m$. There is no guarantee that the second factor is nonzero when $\lambda_n = \lambda_m$, as happens, for instance, when $\lambda_n = 0$. However, we assume that this is not the case and normalize the eigenfunctions such that

$$\lambda_n\lambda_m\langle M\psi_n, \psi_m^*\rangle - \langle K\psi_n, \psi_m^*\rangle = \delta_{nm} \quad (6)$$

where δ_{nm} is the Kronecker delta. The normalization is not unique since it remains unchanged under the transformations $\psi_n \rightarrow a\psi_n$ and $\psi_n^* \rightarrow \psi_n^*/\bar{a}$ for any constant a. The other two orthogonality relations are obtained in a similar manner. These give

$$\lambda_n(\lambda_n + \lambda_m)\langle M\psi_n, \psi_m^*\rangle + \lambda_n\langle C\psi_n, \psi_m^*\rangle = \delta_{nm} \quad (7)$$

$$\lambda_n\lambda_m\langle C\psi_n, \psi_m^*\rangle + (\lambda_n + \lambda_m)\langle K\psi_n, \psi_m^*\rangle = -\lambda_n\delta_{nm}. \quad (8)$$

Equations (6), (7), and (8) are equivalent to orthogonalities given for specific kinds of systems by Foss (1958), Wahed and Bishop (1976), and Wickert and Mote (1990).

Although not always true, for many systems the eigenfunctions are complete in the sense that the free response solution for $f = 0$ with initial conditions

$$u|_{t=0} = u_o \qquad \left.\frac{\partial u}{\partial t}\right|_{t=0} = u_o' \quad (9)$$

is given by

$$u = \sum_{n=1}^{\infty} c_n e^{\lambda_n t}\psi_n(x) \quad (10)$$

where c_n are unique, complex constants. For example, when M, C, and K are self-adjoint and commutable operators and M is positive definite, the eigenfunctions are complete (Caughey and O'Kelly, 1965). In the following, we assume the eigenfunctions are complete. It follows immediately from (6) that

$$c_n = \langle Mu_o', \bar{\lambda}_n\psi_n^*\rangle - \langle Ku_o, \psi_n^*\rangle. \quad (11)$$

The Forced Response

Decoupling is achieved for $f \neq 0$ by using the orthogonalities (6), (7), and (8) and imposing a convenient constraint. Consider the generalized modal expansion

$$u = \sum_{n=1}^{\infty} d_n(t)\psi_n(x) \quad (12)$$

and the constraint

$$\frac{\partial u}{\partial t} = \sum_{n=1}^{\infty} \frac{\partial d_n}{\partial t}\psi_n = \sum_{n=1}^{\infty} \lambda_n d_n\psi_n. \quad (13)$$

Although the eigenfunctions are assumed complete, they are not linearly independent and (13) does not imply $\partial d_n/\partial t = \lambda_n d_n$. In the discrete case, for example, there are twice as many eigenfunctions as dimensions in the spatial domain. Consequently, the d_n are underdetermined, and we are free to impose an arbitrary constraint provided it can be subsequently verified. Substituting (12) and (13) into (1), taking the inner product with $\bar{\lambda}_m\psi_m^*$, and utilizing the orthogonalities, one immediately obtains

$$\frac{\partial d_n}{\partial t} - \lambda_n d_n = \langle f, \bar{\lambda}_n\psi_n^*\rangle \quad (14)$$

which has the solution

$$d_n = c_n e^{\lambda_n t} + \int_0^t \langle f(x, \tau), \bar{\lambda}_n\psi_n^*(x)\rangle e^{\lambda_n(t-\tau)}d\tau. \quad (15)$$

The solution (15) is only valid if the assumed constraint (13) is true. This requires

$$0 = \sum_{n=1}^{\infty}\left[\frac{\partial d_n}{\partial t} - \lambda_n d_n\right]\psi_n = \sum_{n=1}^{\infty}\langle f, \bar{\lambda}_n\psi_n^*\rangle\psi_n. \quad (16)$$

However, *the validity of* (16) *is implicit in the completeness of eigenfunctions.* Consider the initial conditions

$$u_o = 0 \quad u_o' = M^{-1}f(x, t_o) \quad (17)$$

where M^{-1} is the inverse of M and t_o is arbitrary. Direct substitution of (17) into (10) and (11) verifies (16). The solution for arbitrary initial conditions is the superposition of the solution defined by (17) and an additional, homogeneous solution of the form (10). This superposition also satisfies the constraint. Consequently, the modal equations decouple whenever the eigenfunctions are complete.

Modal analysis of systems of the form (1) is sometimes performed by first recasting (1) in a first-order state-space form involving two matrix operators and a composite inner product (Foss, 1958; Meirovitch, 1975; D'Eleuterio and Hughes, 1984; Wickert and Mote, 1990). In this formulation, a modal expansion is assumed using the first-order vector eigenfunctions

$$\begin{bmatrix}\frac{\partial u}{\partial t}\\ u\end{bmatrix} = \sum_{n=1}^{\infty} d_n(t)\begin{bmatrix}\lambda_n\psi_n(x)\\ \psi_n(x)\end{bmatrix} \quad (18)$$

which implies but does not verify (13). Thus, not surprisingly, first and second-order modal analysis are equivalent.

As a brief illustration, consider the two-dimensional problem posed by Wahed and Bishop (1976):

$$M = \begin{bmatrix}1 & 0\\ 0 & 1\end{bmatrix} \quad C = \begin{bmatrix}2 & 4\\ 1 & 2\end{bmatrix}$$

$$K = \begin{bmatrix}10 & 8\\ 0 & 1\end{bmatrix} \quad f = \begin{bmatrix}1\\ 0\end{bmatrix}e^{2it}. \quad (19)$$

The nonunique, orthonormal eigensolutions are

$$\lambda_1 = \bar{\lambda}_1^* = -1 + i \quad \psi_1 = [1 \quad -1 + i]^T$$

$$\psi_1^* = \frac{(1+i)}{12}[1 \quad 4 - 4i]^T$$

$$\lambda_2 = \bar{\lambda}_2^* = \bar{\lambda}_1 \quad \psi_2 = \bar{\psi}_1 \quad \psi_2^* = \bar{\psi}_1^*$$

$$\lambda_3 = \bar{\lambda}_3^* = -1 + 2i \quad \psi_3 = [4 \quad -1 + 2i]^T$$

$$\psi_3^* = \frac{(-2-i)}{60}[1 \quad 1 - 2i]^T$$

$$\lambda_4 = \bar{\lambda}_4^* = \bar{\lambda}_3 \quad \psi_4 = \bar{\psi}_3 \quad \psi_4^* = \bar{\psi}_3^*. \quad (20)$$

The modal coefficients that are independent of the free response are

$$d_1 = \frac{(1+i)}{12}e^{2it} \quad d_2 = \frac{(-3-i)}{60}e^{2it}$$

$$d_3 = \frac{-i}{12}e^{2it} \quad d_4 = \frac{(4+i)}{204}e^{2it} \quad (21)$$

for which

$$\frac{\partial d_1}{\partial t} - \lambda_1 d_1 = \frac{i}{6}e^{2it} \quad \frac{\partial d_2}{\partial t} - \lambda_2 d_2 = \frac{-i}{6}e^{2it}$$

Downloaded 04 May 2010 to 171.66.16.34. Redistribution subject to ASME license or copyright; see http://www.asme.org/terms/Terms_Use.cfm

$$\frac{\partial d_3}{\partial t} - \lambda_3 d_3 = \frac{-i}{12} e^{2it} \quad \frac{\partial d_4}{\partial t} - \lambda_4 d_4 = \frac{i}{12} e^{2it}. \qquad (22)$$

For these values, the constraint (13) is satisfied.

References

Caughey, T. K., 1960, "Classical Normal Modes in Damped Linear Dynamic Systems," ASME JOURNAL OF APPLIED MECHANICS, Vol. 27, pp. 269–271.

Caughey, T. K., and O'Kelly, M. E., 1965, "Classical Normal Modes in Damped Linear Dynamic Systems," ASME JOURNAL OF APPLIED MECHANICS, Vol. 32, pp. 583–588.

D'Eleuterio, G. M. T., and Hughes, P. C., 1984, "Dynamics of Gyroelastic Continua," ASME JOURNAL OF APPLIED MECHANICS, Vol. 51, pp. 415–422.

Foss, K. A., 1958, "Coordinates Which Uncouple the Equations of Motion of Damped Linear Dynamic Systems," ASME JOURNAL OF APPLIED MECHANICS, Vol. 25, pp. 361–364.

Inman, D. J., 1983, "Dynamics of Asymmetric Nonconservative Systems," ASME JOURNAL OF APPLIED MECHANICS, Vol. 50, pp. 199–203.

Inman, D. J., and Andry, Jr., A. N., 1982, "The Nature of the Temporal Solutions of Damped Distributed Systems with Classical Normal Modes," ASME JOURNAL OF APPLIED MECHANICS, Vol. 49, pp. 867–870.

Inman, D. J., and Olsen, C. L., 1988, "Dynamics of Symmetrizable Nonconservative Systems," ASME JOURNAL OF APPLIED MECHANICS, Vol. 55, pp. 206–212.

Lancaster, P., 1966, *Lambda-matrices and Vibrating Systems*, Pergamon Press, Oxford, UK.

Wahed, I. F. A., and Bishop, R. E. D., 1976, "On the Equations Governing the Free and Forced Vibrations of a General Non-Conservative System," *Journal of the Mechanical Engineering Sciences*, Vol. 18, No. 1, pp. 6–10.

Wickert, J. A., and Mote, Jr., C. D., 1990, "Classical Vibration Analysis of Axially Moving Continua," ASME JOURNAL OF APPLIED MECHANICS, Vol. 57, pp. 738–744.

Effect of Mass Transfer on a Similar Flow in the Magnetohydrodynamic Squeeze Film

R. Usha[10] and R. Sridharan[11]

An exact similarity solution has been obtained for the magnetohydrodynamic squeeze flow between two parallel disks with suction or injection at the porous disk. The disks, at time t^*, are spaced a distance $H(1 - \alpha t^*)^{1/2}$ apart and a magnetic field proportional to $B_0(1 - \alpha t^*)^{-1/2}$ is applied perpendicular to the disks. Approximate analytic solutions are given and a numerical solution to the resulting nonlinear ordinary differential equation is obtained. The effects of magnetic forces on the velocity profiles and on the normal forces which the fluid exerts on the disks with suction or injection on the stationary porous disk are studied. It has been found that the effect of injection is to increase the load carrying capacity and it is the reverse in the case of suction.

1 Introduction

The full unsteady Navier-Stokes equations with all the unsteady, nonlinear, and viscous terms are very difficult to solve and exact solutions are rare. The exact solutions obtained up to date are limited to (a) well-known parallel or concentric flows where the nonlinear terms vanish identically, or (b) flows without solid boundaries where the nonlinear terms partially cancel, or (c) similarity solutions where the velocity components vary as the inverse of time.

In this note we shall study an important problem of type (c) and obtain a similarity solution to the magnetohydrodynamic squeeze flow of an electrically conducting fluid between two parallel disks with surface injection or suction at the porous disk. The problem is of special interest in the theory of magnetohydrodynamics because of its importance in many industrial applications and its value in the study of other less tractable cases. The motivation for such investigations is due to the increased use of liquid metal lubricants in high temperature bearings. A number of theoretical and experimental investigations into magnetohydrodynamic effects in lubrication have been reported and they include Hughes and Elco (1962), Kuzma, Maki, and Donnelley (1964), Krieger, Day, and Hughes (1967), and Kamiyama (1969). In their theoretical analysis, they considered the electromagnetic force term but they neglected some or all the inertia terms in the Navier-Stokes equations. However, the study on the use of low viscosity lubricants to reduce energy losses has revealed the importance of inertial effects especially, in situations where the squeeze Reynolds number is not small. Hamza (1988, 1989) has included all the inertia terms and the combined effects of inertia, electromagnetic forces are studied in the magnetohydrodynamic squeeze film.

In what follows, we shall investigate the combined effect of inertia, electromagnetic forces, and surface suction or injection in a squeeze film between two parallel disks which at time t^*, are separated a distance $H(1 - \alpha t^*)^{1/2}$ apart and a magnetic field proportional to $B_0(1 - \alpha t^*)^{-1/2}$, where B_0 denotes a representative magnetic field, is applied perpendicular to the disks with surface suction or injection at the porous disk. The plates are made of nonconducting material. There is no applied electric field and the induced electric field is neglected. A similarity solution is obtained and is used to analyze the way in which the flow pattern and the load change with the squeeze Reynolds number S, Hartmann number M, and the suction or injection parameter A. The results obtained in this paper present a rare exact similarity solution of the unsteady Navier-Stokes equations in which the unsteady suction or injection velocity at the porous disk is prescribed by $w^* = -\alpha H(1 - \alpha t^*)^{-1/2} A$ and the nondimensional parameters S, M, and A govern the other fluid dynamic properties.

2 Mathematical Formulation

We consider axisymmetric incompressible flow between two parallel infinite disks, which at time t^*, are spaced a distance $H(1 - \alpha t^*)^{1/2}$ apart and a magnetic field proportional to $B_0(1 - \alpha t^*)^{-1/2}$ is applied perpendicular to the disks. The upper disk at $z = H(1 - \alpha t^*)^{1/2}$ is moving with velocity $-\alpha H(1 - \alpha t^*)^{-1/2}/2$ towards the stationary lower disk at $z = 0$. On the assumption that

$$u^* = \frac{\alpha r^*}{2(1 - \alpha t^*)} f'(\eta), \quad w^* = -\frac{\alpha H}{\sqrt{1 - \alpha t^*}} f(\eta),$$

$$B = \frac{B_0}{\sqrt{1 - \alpha t^*}}, \quad \eta = \frac{z^*}{H\sqrt{1 - \alpha t^*}}, \quad r = r^*, t = t^*, \qquad (1)$$

the equation of continuity is satisfied and the momentum equations reduce to

$$S[\eta f''' + 3f'' - 2ff'''] + M^2 f'' = f^{(iv)} \qquad (2)$$

where $(1/r)(\partial p^*/\partial r) = P_1(t)$ has been used, $S = \rho H^2/2\nu$ and $M = \sigma B_0^2/\mu$. (ρ denotes density, ν denotes kinematic viscosity

[10] Department of Mathematics, Indian Institute of Technology, Madras 600 036, India.

[11] Department of Mathematics, Stella Maris College, Madras 600 086, India.

Contributed by the Applied Mechanics Division of THE AMERICAN SOCIETY OF MECHANICAL ENGINEERS for publication in the ASME JOURNAL OF APPLIED MECHANICS. Manuscript received by the ASME Applied Mechanics Division, Aug. 29, 1994; final revision, June 3, 1996. Associate Technical Editor: S. A. Berger.

Downloaded 04 May 2010 to 171.66.16.34. Redistribution subject to ASME license or copyright; see http://www.asme.org/terms/Terms_Use.cfm

$$\frac{\partial d_3}{\partial t} - \lambda_3 d_3 = \frac{-i}{12} e^{2it} \quad \frac{\partial d_4}{\partial t} - \lambda_4 d_4 = \frac{i}{12} e^{2it}. \qquad (22)$$

For these values, the constraint (13) is satisfied.

References

Caughey, T. K., 1960, "Classical Normal Modes in Damped Linear Dynamic Systems," ASME JOURNAL OF APPLIED MECHANICS, Vol. 27, pp. 269–271.

Caughey, T. K., and O'Kelly, M. E., 1965, "Classical Normal Modes in Damped Linear Dynamic Systems," ASME JOURNAL OF APPLIED MECHANICS, Vol. 32, pp. 583–588.

D'Eleuterio, G. M. T., and Hughes, P. C., 1984, "Dynamics of Gyroelastic Continua," ASME JOURNAL OF APPLIED MECHANICS, Vol. 51, pp. 415–422.

Foss, K. A., 1958, "Coordinates Which Uncouple the Equations of Motion of Damped Linear Dynamic Systems," ASME JOURNAL OF APPLIED MECHANICS, Vol. 25, pp. 361–364.

Inman, D. J., 1983, "Dynamics of Asymmetric Nonconservative Systems," ASME JOURNAL OF APPLIED MECHANICS, Vol. 50, pp. 199–203.

Inman, D. J., and Andry, Jr., A. N., 1982, "The Nature of the Temporal Solutions of Damped Distributed Systems with Classical Normal Modes," ASME JOURNAL OF APPLIED MECHANICS, Vol. 49, pp. 867–870.

Inman, D. J., and Olsen, C. L., 1988, "Dynamics of Symmetrizable Nonconservative Systems," ASME JOURNAL OF APPLIED MECHANICS, Vol. 55, pp. 206–212.

Lancaster, P., 1966, *Lambda-matrices and Vibrating Systems*, Pergamon Press, Oxford, UK.

Wahed, I. F. A., and Bishop, R. E. D., 1976, "On the Equations Governing the Free and Forced Vibrations of a General Non-Conservative System," *Journal of the Mechanical Engineering Sciences*, Vol. 18, No. 1, pp. 6–10.

Wickert, J. A., and Mote, Jr., C. D., 1990, "Classical Vibration Analysis of Axially Moving Continua," ASME JOURNAL OF APPLIED MECHANICS, Vol. 57, pp. 738–744.

Effect of Mass Transfer on a Similar Flow in the Magnetohydrodynamic Squeeze Film

R. Usha[10] and R. Sridharan[11]

An exact similarity solution has been obtained for the magnetohydrodynamic squeeze flow between two parallel disks with suction or injection at the porous disk. The disks, at time t^*, are spaced a distance $H(1 - \alpha t^*)^{1/2}$ apart and a magnetic field proportional to $B_0(1 - \alpha t^*)^{-1/2}$ is applied perpendicular to the disks. Approximate analytic solutions are given and a numerical solution to the resulting nonlinear ordinary differential equation is obtained. The effects of magnetic forces on the velocity profiles and on the normal forces which the fluid exerts on the disks with suction or injection on the stationary porous disk are studied. It has been found that the effect of injection is to increase the load carrying capacity and it is the reverse in the case of suction.

1 Introduction

The full unsteady Navier-Stokes equations with all the unsteady, nonlinear, and viscous terms are very difficult to solve and exact solutions are rare. The exact solutions obtained up to date are limited to (*a*) well-known parallel or concentric flows where the nonlinear terms vanish identically, or (*b*) flows without solid boundaries where the nonlinear terms partially cancel, or (*c*) similarity solutions where the velocity components vary as the inverse of time.

In this note we shall study an important problem of type (*c*) and obtain a similarity solution to the magnetohydrodynamic squeeze flow of an electrically conducting fluid between two parallel disks with surface injection or suction at the porous disk. The problem is of special interest in the theory of magnetohydrodynamics because of its importance in many industrial applications and its value in the study of other less tractable cases. The motivation for such investigations is due to the increased use of liquid metal lubricants in high temperature bearings. A number of theoretical and experimental investigations into magnetohydrodynamic effects in lubrication have been reported and they include Hughes and Elco (1962), Kuzma, Maki, and Donnelley (1964), Krieger, Day, and Hughes (1967), and Kamiyama (1969). In their theoretical analysis, they considered the electromagnetic force term but they neglected some or all the inertia terms in the Navier-Stokes equations. However, the study on the use of low viscosity lubricants to reduce energy losses has revealed the importance of inertial effects especially, in situations where the squeeze Reynolds number is not small. Hamza (1988, 1989) has included all the inertia terms and the combined effects of inertia, electromagnetic forces are studied in the magnetohydrodynamic squeeze film.

In what follows, we shall investigate the combined effect of inertia, electromagnetic forces, and surface suction or injection in a squeeze film between two parallel disks which at time t^*, are separated a distance $H(1 - \alpha t^*)^{1/2}$ apart and a magnetic field proportional to $B_0(1 - \alpha t^*)^{-1/2}$, where B_0 denotes a representative magnetic field, is applied perpendicular to the disks with surface suction or injection at the porous disk. The plates are made of nonconducting material. There is no applied electric field and the induced electric field is neglected. A similarity solution is obtained and is used to analyze the way in which the flow pattern and the load change with the squeeze Reynolds number S, Hartmann number M, and the suction or injection parameter A. The results obtained in this paper present a rare exact similarity solution of the unsteady Navier-Stokes equations in which the unsteady suction or injection velocity at the porous disk is prescribed by $w^* = -\alpha H(1 - \alpha t^*)^{-1/2} A$ and the nondimensional parameters S, M, and A govern the other fluid dynamic properties.

2 Mathematical Formulation

We consider axisymmetric incompressible flow between two parallel infinite disks, which at time t^*, are spaced a distance $H(1 - \alpha t^*)^{1/2}$ apart and a magnetic field proportional to $B_0(1 - \alpha t^*)^{-1/2}$ is applied perpendicular to the disks. The upper disk at $z = H(1 - \alpha t^*)^{1/2}$ is moving with velocity $-\alpha H(1 - \alpha t^*)^{-1/2}/2$ towards the stationary lower disk at $z = 0$. On the assumption that

$$u^* = \frac{\alpha r^*}{2(1 - \alpha t^*)} f'(\eta), \quad w^* = -\frac{\alpha H}{\sqrt{1 - \alpha t^*}} f(\eta),$$

$$B = \frac{B_0}{\sqrt{1 - \alpha t^*}}, \quad \eta = \frac{z^*}{H\sqrt{1 - \alpha t^*}}, \quad r = r^*, t = t^*, \qquad (1)$$

the equation of continuity is satisfied and the momentum equations reduce to

$$S[\eta f''' + 3f'' - 2ff'''] + M^2 f'' = f^{(iv)} \qquad (2)$$

where $(1/r)(\partial p^*/\partial r) = P_1(t)$ has been used, $S = \rho H^2/2\nu$ and $M = \sigma B_0^2/\mu$. (ρ denotes density, ν denotes kinematic viscosity

[10] Department of Mathematics, Indian Institute of Technology, Madras 600 036, India.

[11] Department of Mathematics, Stella Maris College, Madras 600 086, India.

Contributed by the Applied Mechanics Division of THE AMERICAN SOCIETY OF MECHANICAL ENGINEERS for publication in the ASME JOURNAL OF APPLIED MECHANICS. Manuscript received by the ASME Applied Mechanics Division, Aug. 29, 1994; final revision, June 3, 1996. Associate Technical Editor: S. A. Berger.

Copyright © 1997 by ASME

Downloaded 04 May 2010 to 171.66.16.34. Redistribution subject to ASME license or copyright; see http://www.asme.org/terms/Terms_Use.cfm

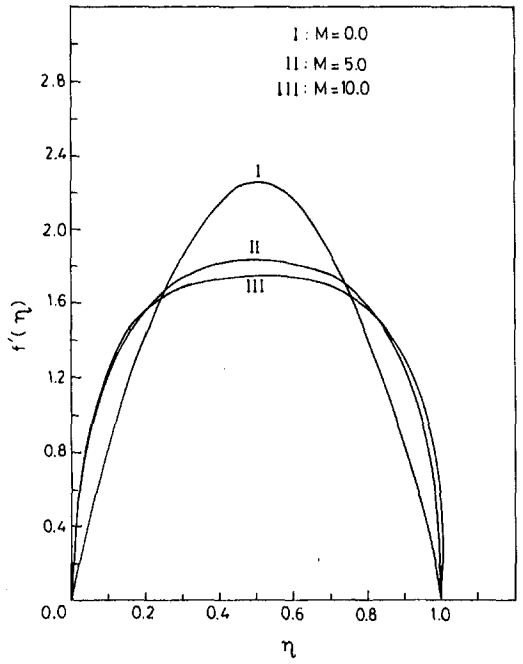


Fig. 1 Variation of dimensionless function f' with M when $S = 0.01$ and $A = -1.0$

and σ denotes fluid electrical conductivity). The boundary conditions are given by

$$f(0) = A, \quad f'(0) = 0, \quad f(1) = \tfrac{1}{2}, \quad f'(1) = 0 \tag{3}$$

where A is a constant parameter such that $A > 0$ corresponds to suction and $A < 0$ to injection.

If the disks are assumed to be of finite radius b and of negligible thickness, then the load W^* which the fluid exerts on the disks is given by

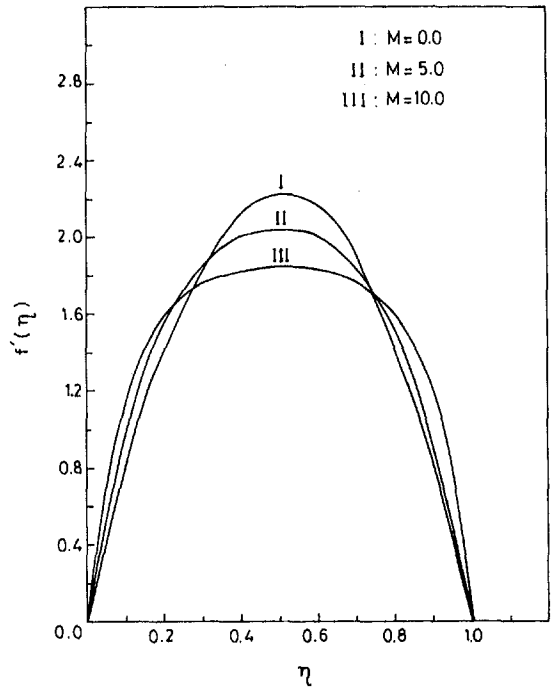


Fig. 2 Variation of dimensionless function f' with M when $R = 0.1$ and $A = -1.0$

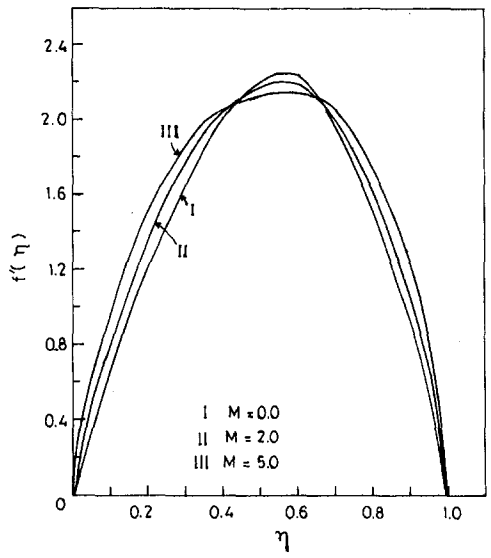


Fig. 3 Variation of dimensionless function f' with M when $S = 1.0$ and $A = -1.0$

$$W^* = 2\pi \int_0^b r[p(r, 1, t) - p(b, 1, t)]dr$$

$$= -\frac{\pi\rho\alpha^2 b^4}{16S(1 - \alpha t)^2}[f'''(0) + 2ASf''(0)] \tag{4}$$

or

$$W = -\frac{1}{6S}[f'''(0) + 2ASf''(0)] \tag{5}$$

where

$$W = \frac{8W^*(1 - \alpha t)^2}{3\rho\alpha^2\pi b^4}$$

3 Approximate Analytic Solutions

We describe the approximate analytic solutions of Eq. (2) subject to the boundary conditions (3) that can be obtained for $S = o(1)$ and $M = o(1)$. When $M = O(S^{1/2})$ and when $M = O(1)$, the unknown function $f(\eta)$ may be expanded for $S = o(1)$ in the form

$$f = f_0(\eta) + Sf_1(\eta) + O(S^2) \tag{6}$$

where, f_0, f_1 satisfy the conditions

$$f_0(0) = A, \quad f_0'(0) = 0, \quad f_0(1) = \tfrac{1}{2}, \quad f_0'(1) = 0,$$

$$f_1(0) = 0, \quad f_1'(0) = 0, \quad f_1(1) = 0, \quad f_1'(1) = 0. \tag{7}$$

Case (i). For $M = O(S^{1/2})$, $A = O(1)$, the functions f_0 and f_1 satisfy the equations

$$f_0'''' = 0$$

$$f_1'''' = \eta f_0''' + 3f_0'' - 2f_0f_0''' + \frac{M^2}{S}f_0'' \tag{8}$$

and the solutions satisfying the boundary conditions (7) are given by

$$f_0(\eta) = \tfrac{3}{2}\eta^2 - \eta^3 + A(2\eta^3 - 3\eta^2 + 1)$$

Downloaded 04 May 2010 to 171.66.16.34. Redistribution subject to ASME license or copyright; see http://www.asme.org/terms/Terms_Use.cfm

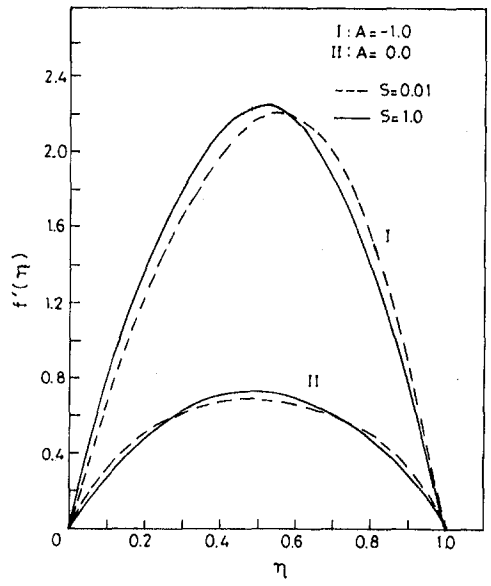


Fig. 4(*a*) Effect of injection on radial flow when $M = 0.0$

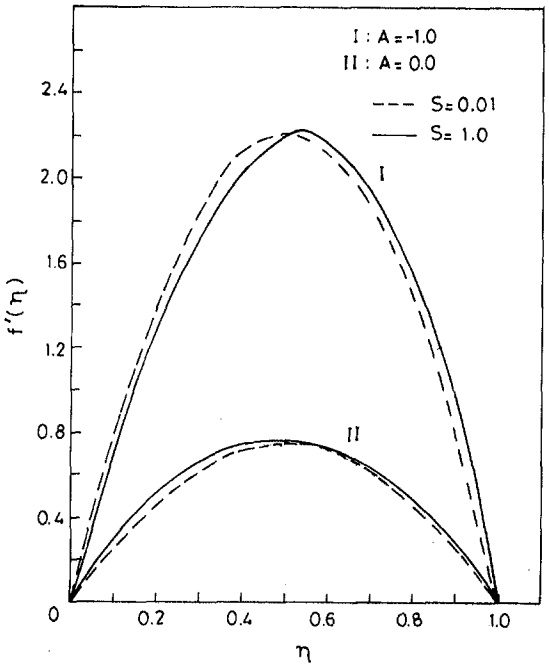


Fig. 4(*b*) Effect of injection on radial flow when $M = 2.0$

$$f_1(\eta) = \tfrac{1}{280}[19\eta^2 - 78\eta^3 + 105\eta^4 - 56\eta^5 + 14\eta^6 - 4\eta^7]$$

$$+ \frac{1}{40}\frac{M^2}{S}[\eta^2 - 4\eta^3 + 5\eta^4 - 2\eta^5]$$

$$+ \frac{A}{420}[75\eta^2 - 78\eta^3 - 105\eta^4 + 168\eta^5 - 84\eta^6 + 24\eta^7]$$

$$+ \frac{A}{20}\frac{M^2}{S}[-\eta^2 + 4\eta^3 - 5\eta^4 + 2\eta^5]$$

$$+ \frac{A^2}{420}[-264\eta^2 + 624\eta^3 - 420\eta^4 + 84\eta^6 - 24\eta^7] \quad (9)$$

and the load W is given by

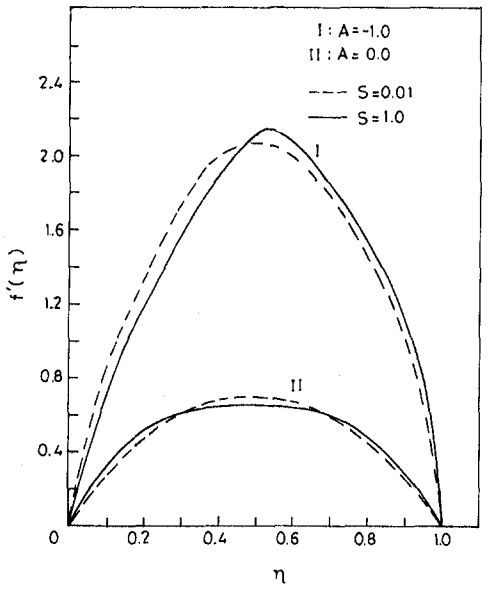


Fig. 4(*c*) Effect of injection on radial flow when $M = 5.0$

$$W = \frac{1}{S}\left[1 + \frac{S}{6}\left(\frac{117}{70} + \frac{3}{5}\frac{M^2}{S}\right)\right.$$

$$\left. + A\left\{-2 - \frac{S}{6}\left(\frac{171}{35} + \frac{6}{5}\frac{M^2}{S}\right) + \frac{108}{35}A\right\} + O(S^2)\right]. \quad (10)$$

Case (ii). For $M = O(1)$, $A = O(1)$, the equations satisfied by f_0, f_1 are

$$f_0'''' - M^2 f_0'' = 0$$

$$f_1'''' - M^2 f_1'' = \eta f_0''' + 3f_0'' - 2f_0 f_0'''. \quad (11)$$

We obtain

$$kf_0(\eta) = (1 - 2A)[g(\eta) + M\eta - \beta] + kA \quad (12)$$

where

$$g(\eta) = \beta \cosh M\eta - \sinh M\eta$$

$$k = 2M - 4\beta, \quad \beta = \tanh(M/2)$$

and the load W is given by

$$W = \frac{M}{18k^3 S}[3k^2M^2(1 - 2A)$$

$$+ S\{(57M^2 - 168\beta M + 34\beta^3 M - 27\beta^2 M^2 + 108\beta^2)$$

$$+ A(456\beta M - 100\beta^3 M + 90\beta^2 M^2 - 174M^2 - 216\beta^2)$$

$$+ A^2(120M^2 - 240\beta M + 64\beta^3 M - 72\beta^2 M^2)\}$$

$$+ O(S^2). \quad (13)$$

The solution $f_1(\eta)$ has been used in deriving the expression for load W.

4 Numerical Solution

The two-point boundary value problem given by Eqs. (2) and (3) has been integrated by applying a shooting and matching technique and the nature of the flow for values of S and M, which are not small has been obtained when $A = 1.0$ (suction) and $A = -1.0$ (injection). The initial estimates at $y = 0$ have been obtained for $S = o(1)$ and $M = o(1)$ from the regular perturbation results of the previous section and the solution for

Downloaded 04 May 2010 to 171.66.16.34. Redistribution subject to ASME license or copyright; see http://www.asme.org/terms/Terms_Use.cfm

larger values of S and M have been determined by progressively increasing S and M by small amounts and estimating the unknown boundary conditions from the available computed set of results. When $S = o(1)$ and $M = o(S)$, the dimensionless components of velocity in the axial and radial directions are

$$f = (1 - 2A)(3\eta^2 - 2\eta^3)/2 + A$$

$$f' = 3(1 - 2A)\eta(1 - \eta),$$

and the motion is well approximated by the solution relevant to squeezing with mass transfer with zero magnetic field and we obtain the usual parabolic distribution in the radial direction.

Figures 1 and 2 present the radial velocity profiles for the case of slight squeezing ($S = 0.01, 0.1$) with a large magnetic field and in Fig. 3, we present the case of slight squeezing ($S = 1.0$) with a slight and moderate magnetic field ($M = 0.0, 2.0$ and 5.0) when there is injection ($A = -1.0$) into the squeeze film. We observe a remarkable change in the radial flow for values of $M/S \gg 1$. Also, for a fixed value of S, an increase in M slightly increases the radial velocity in the region of the midplane $\eta = \frac{1}{2}$ and this change is more with more increase in M and the radial velocity profiles in the interior region become more flat.

For fixed values of M the magnitude of radial flow decreases with increase of S up to a region near the midplane $\eta = \frac{1}{2}$ whereas the magnitude of radial flow increases with increase of S beyond that (Figs. $4(a)$, (b), and (c)). Such a change in the radial velocity is due to the effect of injection since when the injection is absent (Hamza, 1989), the radial velocity decreases with increase of S for fixed values of M.

The load W exerted on the upper surface is large and positive when the magnetic field is absent and when there is injection ($A = -1.0$) and it decreases with increase of squeeze Reynolds number S and the same has been observed by Hamza (1989) in the absence of injection ($A = 0.0$). The presence of a magnetic field increases the load remarkably as observed by Hamza (1989) for the case $A = 0.0$ and the result of this study indicates that such an increase in load is further enhanced by injection ($A = -1.0$).

Figure 5 shows the variation of the load W with M for values of $S = 0.01, 0.1, 1.0, 5.0$ and 10.0 when $A = 0.0$ and $A = -1.0$. We observe that

(i) the load increases with increase of M,
(ii) for a fixed value of M, the load decreases with increase of S, for a fixed rate of injection,
(iii) for a fixed S, and for all values of M, there is a remarkable increase in the load on the upper disk when there is injection and this increase is more than that when there is no injection, and
(iv) for a fixed M, for all values of S, the load increases with the increase of the rate of injection in the squeeze film. The reverse effect is observed in the case of suction from the hydromagnetic squeeze film and hence is not presented here.

5 Conclusions

The similarity solutions to the governing equations of the motion of a thin film of fluid squeezed between two planes in the presence of magnetic field when there is mass transfer through the lower porous disk have been obtained and it has been observed that the effect of injection into the hydromagnetic squeeze film is to increase the load exerted on the upper disk and this increase in load is more than that observed in the absence of injection. The reverse effect is observed when there is suction. The increase of load-carrying capacity by injecting fluid into the hydromagnetic squeeze film is of significant interest in situations where it is not possible to avoid the use of liquid-metal lubricants in preference to the conventional lubricants. An improvement in the lubrication characteristics of liquid-metal lubricant can be achieved by injecting the lubricant into the hydromagnetic squeeze film.

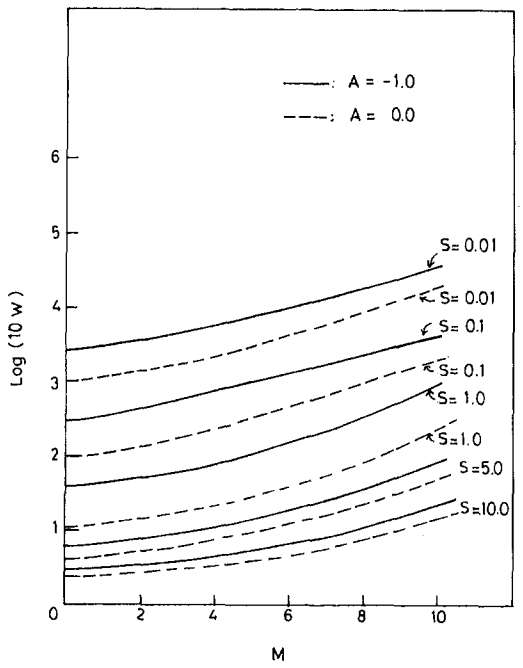


Fig. 5 Normal force or load variation with M when $A = -1.0$ and $A = 0.0$

Acknowledgment

We thank the referees for their very valuable suggestions and useful and encouraging comments.

References

Hamza, E. A., 1988, "The Magnetohydrodynamic Squeeze Film," ASME *Journal of Tribology,* Vol. 110, pp. 375–377.

Hamza, E. A., 1989, "A Similar Flow Between Two Disks in the Presence of a Magnetic Field," ASME JOURNAL OF APPLIED MECHANICS, Vol. 56, pp. 218–221.

Hughes, W. F., and Elco, R. A., 1962, "Magnetohydrodynamic Lubrication Flow Between Parallel Rotating Disks," *Journal of Fluid Mechanics,* Vol. 13, pp. 21–32.

Kamiyama, S., 1969, "Inertia Effects in MHD Hydrostatic Thrust Bearing," ASME *Journal of Lubrication Technology* Vol. 91, pp. 589–596.

Krieger, R. J., Day, H. J., and Hughes, W. F., 1967, "The MHD Hydrostatics Thrust Bearings—Theory and Experiments," ASME *Journal of Lubrication Technology,* Vol. 89, pp. 307–313.

Kuzma, D. C., Maki, E. R., and Donnelly, R. J., 1964, "The Magnetohydrodynamic Squeeze Film," *Journal of Fluid Mechanics,* Vol. 19, pp. 395–400.

Downloaded 04 May 2010 to 171.66.16.34. Redistribution subject to ASME license or copyright; see http://www.asme.org/terms/Terms_Use.cfm

Journal of Applied Mechanics

Discussion

A General Formulation of the Theory of Wire Ropes[1]

Steven A. Velinsky.[2] The author claims to have developed a simple and well-organized approach towards the formulation of wire strand and rope problems. He considers both the geometric nonlinear theory as well as the linearized theory, and while stating the ease in programming his theory, no numerical results are presented. The continued interest in wire strand and rope behavior exemplifies the importance of these elements. However, the author has missed a whole body of literature over the last ten years which has previously provided generalized theories for wire strands and ropes, and has done so in a much more usable form. In general, the theory of wire rope has been well developed by Costello and his associates, whose references are too numerous to mention, and they have examined a wide variety of problems from linear and nonlinear response of wire strands and ropes under static and dynamics loads to the response of viscoelastic ropes to the response of strands and ropes comprised of wires with various types of cross-sectional geometry. Typical of these works are the development of the basic theory and their use in the examination of specific wire rope problems. A few of the papers will be discussed to follow which have already accomplished far more than the paper under discussion.

First, as noted above, Jiang (1995) presents both the geometrically nonlinear and linear theories. Velinsky (1985) has already presented a general nonlinear theory for wire ropes and additionally, and of principal importance, through examination of a wide variety of complex configurations, he has shown that the geometrically nonlinear theory provides no value over the linear theory for the normal load range of wire ropes. This paper (Velinsky, 1985), thus further verified the linear theory. It might be added that the deviation from the linear theory is only of significance for strains that would be well beyond the linear elastic region for the rope material, and thus the material model would fail at loads far lower than that in which the linear geometric theory is no longer valid. As such, the first part of the Jiang paper provides no valuable contribution.

Costello and his associates use the wire rope axial and rotational strain to describe the deformation behavior of the total rope. Jiang in Eq. (18) of his paper also uses these parameters. One aspect should be noted, however, and that is that Jiang's rotational strain, ϕ, is not dimensionless.

Jiang states as one of his primary contributions is his showing that the strand structure can be characterized by seven stiffness and deformation constants. This is not a new idea. Velinsky (1988) stated, "We note that the global behavior of a strand can be completely described by the following strand quantities: the stiffness constants, S_1, S_2, S_3, and S_4, the effective strand radius, R^*, the strand effective Poisson's ratios, $\nu_{e\epsilon}$ and $\nu_{e\beta}$, and the strand bending stiffness, A^*." Velinsky has eight constants, and the reason is that the strand size is necessary which Jiang has omitted. It should also be noted that Jiang uses a different notation which is much less intuitive, but represents essentially the same parameters. It should also be stressed that these strand describing coefficients are all constants only for the linear theory (e.g., the stiffness varies with load for the nonlinear theory).

The Velinsky (1988) paper not only generalizes the analysis of strands of both Seale (close packed) and resting lay types, but also: examines the detailed geometry of these configurations, develops a design methodology for the configurations including methods for selecting the appropriate wire sizes, and examines the sensitivities of various strand properties to the design parameters. Velinsky's generalization recognizes that three independent variables, the wire axial strain, the change in helix radius and the change in helix angle, exist for each wire lay and requires the solution of three simultaneous linear equations for each lay. His formulation is performed in a dimensionless manner in order to quantify a class of strand configurations rather than a specific size and geometry. Furthermore, he examines parameters that describe global strand behavior which support the fact that optimal designs must exist.

Velinsky (1989) later extended the generalized approach of his 1988 paper to examine complex wire rope design. The Velinsky 1989 paper develops the general analysis for wire strand core, independent wire rope core, and fiber core types of wire ropes. The total rope analysis requires only the eight parameters for each strand, and a similar set of three linear equations are necessary for the deformations of each strand lay. Furthermore, as in the earlier paper, the theory is exercised in examining the sensitivities of various total rope properties to numerous strand and rope design parameters. In addition to total rope properties, Velinsky also examines the sensitivities of rope design parameters on individual wire stresses. The Velinsky formulation is easily programmed in a general manner (and has been), and is easily exercised as exhibited by the large amount of results that have been presented.

References

Velinsky, S. A., 1985, "General Nonlinear Theory for Complex Wire Rope," *International Journal of Mechanical Sciences,* Vol. 27, No. 7/8, pp. 497–507.

Velinsky, S. A., 1988, "Design and Mechanics of Multi-Lay Wire Strands," ASME *Journal of Mechanisms, Transmissions and Automation in Design,* Vol. 110, No. 2, pp. 152–160.

Velinsky, S. A., 1989, "On the Design of Wire Rope," ASME *Journal of Mechanisms, Transmissions and Automation in Design,* Vol. 111, No. 3, pp. 382–388.

Author's Closure[3]

Dr. Velinsky first criticizes that the paper presented "no numerical results" and "missed a whole body of literature over

[1] Jiang, W., 1995, "A General Formulation of the Theory of Wire Ropes," ASME JOURNAL OF APPLIED MECHANICS, Vol. 62, pp. 747–755.

[2] Professor, Department of Mechanical and Aeronautical Engineering, University of California-Davis, Davis, CA 95616.

[3] Department of Mechanical Engineering, College of Engineering and Design, Florida International University, University Park, Miami, FL 33199.

Copyright © 1997 by ASME

Downloaded 04 May 2010 to 171.66.16.34. Redistribution subject to ASME license or copyright; see http://www.asme.org/terms/Terms_Use.cfm

the last ten years.'' The original version of the paper did present considerable numerical examples and analyses, which, however, were dropped during the revision following reviewers' instructions that the paper was overlong. As a matter of fact, the published paper was still three pages over the limit, after considerable simplifications including the Introduction. As Dr. Velinsky points out, the relevant literatures are too numerous to mention. The author cannot see any reason to provide a complete publication list, in addition to those needed to be cited, especially in such an overlength situation. Dr. Velinsky then mentions a 1985 paper of his, and concludes that the ''nonlinear theory provides no value over the linear theory.'' The author disagrees with such a point of view. It is well known that almost all larger deformation problems encounter the possibility of plastic deformation. The elastic nonlinear theory, however, remains an important branch of mechanics. In general, Dr. Velinsky denies any contribution of the paper and only advocates his own accomplishment in this field. The author has no intention of making any comments on his claims, but believes that readers are professionals and have the best judgement.

Bifurcation of Orthotropic Solids[4]

A. Chattopadhyay[5,7] and H. Gu[6,7]. DeBotton and Schugasser (1996) recently presented an exact solution for bifurcation of orthotropic solids. In the paper, the following equilibrium equations were used.

$$\nabla \cdot [(\boldsymbol{\sigma} + \Sigma) \cdot \nabla(\mathbf{x} + \mathbf{u}) = \mathbf{0} \tag{1}$$

An assumption was made for plane-strain conditions that $\Sigma_{11} = -p$ is the only nonvanishing component of the initial stress in Eq. (1). Therefore, the remaining equilibrium equations can be derived by ignoring the product terms $\boldsymbol{\sigma} \cdot \nabla \mathbf{u}$ and their derivatives.

$$\frac{\partial \sigma_{11}}{\partial x_1} + \frac{\partial \sigma_{12}}{\partial x_2} - p \frac{\partial^2 u_1}{\partial x_1^2} = 0$$

$$\frac{\partial \sigma_{12}}{\partial x_1} + \frac{\partial \sigma_{22}}{\partial x_2} - p \frac{\partial^2 u_2}{\partial x_1^2} = 0 \tag{2}$$

However, it is our purpose to point out that their approach contains a fundamental error resulting from ignoring the primary prebuckling displacements, which normally provide the same order of contributions as prebuckling stresses at the buckling state. Of course, these prebuckling displacement contributions are not included in simplified plate-type theories for simplicity. For an exact elasticity solution, which is the motivation of DeBotton and Schugasser's work, these terms should be included to ensure a rigorous analysis procedure.

If the superscript $(\ )^0$ is used to denote the prebuckling terms, the primary prebuckling state of for an orthotropic half-space whose material axes are parallel to the geometric axes can be truly simulated by

$$\sigma_{11}^0 = -p, \quad \sigma_{22}^0 = \sigma_{12}^0 = 0. \tag{3}$$

Using the constitutive equation for this orthotropic half-space, the derivatives of prebuckling displacements are derived as follows:

$$\frac{\partial u_1^0}{\partial x_1} = -\frac{C_{22}}{C_{11}C_{22} - C_{12}^2} p, \quad \frac{\partial u_2^0}{\partial x_2} = \frac{C_{12}}{C_{11}C_{22} - C_{12}^2} p$$

$$\frac{\partial u_1^0}{\partial x_2} = \frac{\partial u_2^0}{\partial x_1} = 0. \tag{4}$$

Including these displacement contributions, the buckling equations can be finally stated as

$$\frac{\partial}{\partial x_1}\left[\sigma_{11}\left(1 + \frac{\partial u_1^0}{\partial x_1}\right)\right] + \frac{\partial}{\partial x_2}\left[\sigma_{12}\left(1 + \frac{\partial u_1^0}{\partial x_1}\right)\right] - p \frac{\partial^2 u_1}{\partial x_1^2} = 0$$

$$\frac{\partial}{\partial x_1}\left[\sigma_{12}\left(1 + \frac{\partial u_2^0}{\partial x_2}\right)\right] + \frac{\partial}{\partial x_2}\left[\sigma_{22}\left(1 + \frac{\partial u_2^0}{\partial x_2}\right)\right]$$

$$- p \frac{\partial^2 u_2}{\partial x_1^2} = 0 \tag{5}$$

and the buckling equation can also be expressed in terms of displacements as follows:

$$\left(1 - \frac{C_{22}}{C_{11}C_{22} - C_{12}^2} p\right)\left[C_{11} \frac{\partial^2 u_1}{\partial x_1^2} + C_{66} \frac{\partial^2 u_1}{\partial x_2^2} + (C_{12} + C_{66}) \frac{\partial^2 u_2}{\partial x_1 \partial x_2}\right] - p \frac{\partial^2 u_1}{\partial x_1^2} = 0$$

$$\left(1 + \frac{C_{12}}{C_{11}C_{22} - C_{12}^2} p\right)\left[(C_{12} + C_{66}) \frac{\partial^2 u_1}{\partial x_1 \partial x_2} + C_{66} \frac{\partial^2 u_2}{\partial x_1^2} + C_{22} \frac{\partial^2 u_2}{\partial x_2^2}\right] - p \frac{\partial^2 u_2}{\partial x_1^2} = 0. \tag{6}$$

The prebuckling displacement contributions in these two equations can be written as

$$\Delta_1 = -\frac{C_{22}}{C_{11}C_{22} - C_{12}^2} p\left[C_{11} \frac{\partial^2 u_1}{\partial x_1^2} + C_{66} \frac{\partial^2 u_1}{\partial x_2^2} + (C_{12} + C_{66}) \frac{\partial^2 u_2}{\partial x_1 \partial x_2}\right]$$

$$\Delta_2 = \frac{C_{12}}{C_{11}C_{22} - C_{12}^2} p\left[(C_{12} + C_{66}) \frac{\partial^2 u_1}{\partial x_1 \partial x_2} + C_{66} \frac{\partial^2 u_2}{\partial x_1^2} + C_{22} \frac{\partial^2 u_2}{\partial x_2^2}\right]. \tag{7}$$

Therefore, their effects in the buckling analysis can now be discussed.

Orthotropic Material With $C_{11} \gg C_{22}$

In this extreme case, the values of the material properties are assumed to be

$$C_{11} \gg C_{22}, \quad C_{12} \cong \frac{C_{22}}{3}, \quad C_{66} \cong \frac{C_{22}}{2}.$$

The prebuckling displacement contributions in the buckling equations are thus simplified as follows:

$$\Delta_1 \cong -p \frac{\partial^2 u_1}{\partial x_1^2} - \frac{C_{22}}{2C_{11}} p \frac{\partial^2 u_1}{\partial x_2^2} - \frac{C_{22}}{C_{11}} p \frac{\partial^2 u_2}{\partial x_1 \partial x_2} \cong -p \frac{\partial^2 u_1}{\partial x_1^2}$$

$$\Delta_2 \cong \frac{C_{22}}{3C_{11}} p \frac{\partial^2 u_1}{\partial x_1 \partial x_2} + \frac{C_{22}}{6C_{11}} p \frac{\partial^2 u_2}{\partial x_1^2} + \frac{C_{22}}{3C_{11}} p \frac{\partial^2 u_2}{\partial x_2^2} \cong 0. \tag{8}$$

[4] deBotton, G., and Schulgasser, K., 1996, ''Bifurcation of Orthotropic Solids,'' ASME JOURNAL OF APPLIED MECHANICS, Vol. 63, pp. 317–320.

[5] Associate Professor. Mem. ASME.

[6] Graduate Research Associate. Mem. ASME.

[7] Department of Mechanical and Aerospace Engineering, Arizona State University, Tempe, AZ 85287-6106.

 Copyright © 1997 by ASME

Downloaded 04 May 2010 to 171.66.16.34. Redistribution subject to ASME license or copyright; see http://www.asme.org/terms/Terms_Use.cfm

Compared to the prebuckling stress contributions, $-p(\partial^2 u_1/\partial x_1^2)$ and $-p(\partial^2 u_2/\partial x_1^2)$, in Eq. (6), it is clear that the prebuckling displacements in the first equation of Eq. (6) provide at least similar magnitudes of contributions as the prebuckling stress in this case.

Isotropic Material

The values of the material properties in an isotropic case are assumed to be

$$C_{11} = C_{22}, \quad C_{12} \cong \frac{C_{22}}{3}, \quad C_{66} \cong \frac{C_{22}}{2}.$$

The prebuckling displacement effects in the buckling equations are now written as follows:

$$\Delta_1 \cong -p\frac{\partial^2 u_1}{\partial x_1^2} - \frac{1}{2}p\frac{\partial^2 u_1}{\partial x_2^2} - p\frac{\partial^2 u_2}{\partial x_1 \partial x_2}$$

$$\Delta_2 \cong \frac{1}{3}p\frac{\partial^2 u_1}{\partial x_1 \partial x_2} + \frac{1}{6}p\frac{\partial^2 u_2}{\partial x_1^2} + \frac{1}{3}p\frac{\partial^2 u_2}{\partial x_2^2}. \qquad (9)$$

It can be concluded that, in this case, the prebuckling displacement contributions are at least the same as that due to the prebuckling stress in the first equation of Eq. (6) and are at least as much as one-sixth of that due to the prebuckling stress in the second equation of Eq. (6).

The contributions due to the prebuckling displacements, in cases other than the two cases discussed above, should be somewhere between these two extreme cases. Equations (6) were used by the authors (Chattopadhyay and Gu, 1996) in addressing the buckling of orthotropic plates and composite laminates. To our knowledge, excluding prebuckling displacement contributions will introduce as much as a ten percent error, depending upon the material properties and the length-to-thickness ratio of the plates.

Reference

Chattopadhyay, A., and Gu, H., 1996, "Exact Elasticity Solution for Buckling of Composite Laminates," *Composite Structures*, Vol. 34, pp. 291–299.

Authors' Closure[8]

A rigorous solution for the buckling of orthotropic solids was given in our paper. It was stated there explicitly that the equilibrium equation is expressed in terms of the second Piola-Kirchhoff stress which measures the tractions per unit area of the reference or undeformed configuration. Following Malvern (1969), in terms of the Piola-Kirchhoff stress $\tilde{\mathbf{T}}$, the equilibrium equation is

$$\nabla \cdot [\tilde{\mathbf{T}} \cdot \tilde{\mathbf{F}}^T] = \mathbf{0}, \qquad (1)$$

and it is clear that the deformation gradient $\mathbf{F}$ and hence the entire equation, will depend on the choice of the reference configuration. In some cases, such as the one considered by us, it is useful to let $\tilde{\mathbf{T}} = \boldsymbol{\sigma} + \boldsymbol{\Sigma}$, where $\boldsymbol{\Sigma}$ is a uniform stress field and $\boldsymbol{\sigma}$ is a stress increment beyond this pre-existing stress, and also to substitute $\mathbf{F} = \nabla(\mathbf{x} + \mathbf{u})$, where $\mathbf{x}$ is the position vector and $\mathbf{u}$ is the displacement vector which is measured from the reference configuration. If we further assume that the stress increment is small, Eq. (1) may be rewritten in the form

$$(\nabla \cdot \boldsymbol{\sigma}) \cdot (\mathbf{1} + \nabla \mathbf{u}) + \boldsymbol{\Sigma} : \nabla\nabla \mathbf{u} = \mathbf{0}. \qquad (2)$$

In our work the reference configuration for the Piola-Kirchhoff stress was specifically chosen as the prebuckled state, or, quoting from the paper: "Initially, the solid is in a state of homogeneous strain corresponding to compressive uniform stress p parallel to the free boundary along the x_1 direction". We note that, since the displacements are measured from the prebuckled state, the components of the displacement gradient which is proportional to $\boldsymbol{\sigma}$ are small. Obviously, in this case, the product term $(\nabla \cdot \boldsymbol{\sigma}) \cdot \nabla \mathbf{u}$ is small in comparison with other terms in the equation and may be neglected. If, on the other hand, another reference configuration is chosen and the displacements are measured from it, then, the term $(\nabla \cdot \boldsymbol{\sigma}) \cdot \nabla \mathbf{u}$ must be taken into account. As a result, terms that depend on the history of the deformation will appear explicitly in the equilibrium equation. Nonetheless, it should be realized that these terms appear solely due to the fact that Eqs. (1) and (2) are expressed in terms of the pseudo Piola-Kirchhoff stress and not in terms of the true Cauchy stress.

We note that, from a purely rigorous mathematical point of view, the choice of the reference configuration is immaterial. However, we also note that there exist good motivations in favor of choosing the reference configuration as the prebuckled configuration. First, this choice results in strictly simpler expressions because the term $(\nabla \cdot \boldsymbol{\sigma}) \cdot \nabla \mathbf{u}$ is neglected. Further, and even more important, is the fact that by adopting this approach the problem can be solved without the need to account for the entire history of the deformation up to the instant when the material buckles. Thus, as was used in our paper, the instantaneous stress-strain relation at the prebuckled configuration is all that is needed to obtain a rigorous solution for the problem, or in the words of our paper, "we assume a linear relationship between the stress increment and the *infinitesimal* strain increment". This feature enables utilizing the proposed solution to predict the buckling stress of nonlinearly deforming materials. In fact, while the instantaneous stress-strain relation at any point of the deformation history may be linearized, it is well known that when the deformation gradient is large, the overall or total stress-strain relationship is usually nonlinear. This, of course, provides an additional motivation for choosing the reference configuration as the prebuckled configuration. At the same time it renders the approach of Chattopadhyay and Gu tenuous at best.

It is possible that in some special cases a different reference configuration will be a more appropriate one. However, since in such cases the deformation history will be incorporated into the solution, it will be valid only to the particular class of materials that was considered. But, if such an approach is taken, it will generally not be adequate to utilize a linear stress-strain relationship and thus the analysis of Chattopadhyay and Gu is an unwarranted simplification. Finally, we note that in some cases, usually when the longitudinal Young's modulus is much larger than the other moduli, the critical buckling strain is small and the assumption of a linear stress-strain relationship is satisfactory. In these cases, since the strains are small, the choice of the reference configuration is unimportant and hence, for the sake of simplicity alone, the formulation that was proposed by us is an advantageous one.

Reference

Malvern, L. E., 1969, *Introduction to the Mechanics of a Continuous Medium*, Prentice-Hall, Englewood Cliffs, NJ.

[8] Department of Mechanical Engineering, Ben-Gurion University of the Negev, P.O. Box 653, Beer-Sheva 84105, Israel.

Downloaded 04 May 2010 to 171.66.16.34. Redistribution subject to ASME license or copyright; see http://www.asme.org/terms/Terms_Use.cfm

Compared to the prebuckling stress contributions, $-p(\partial^2 u_1/\partial x_1^2)$ and $-p(\partial^2 u_2/\partial x_1^2)$, in Eq. (6), it is clear that the prebuckling displacements in the first equation of Eq. (6) provide at least similar magnitudes of contributions as the prebuckling stress in this case.

Isotropic Material

The values of the material properties in an isotropic case are assumed to be

$$C_{11} = C_{22}, \quad C_{12} \cong \frac{C_{22}}{3}, \quad C_{66} \cong \frac{C_{22}}{2}.$$

The prebuckling displacement effects in the buckling equations are now written as follows:

$$\Delta_1 \cong -p\frac{\partial^2 u_1}{\partial x_1^2} - \frac{1}{2}p\frac{\partial^2 u_1}{\partial x_2^2} - p\frac{\partial^2 u_2}{\partial x_1 \partial x_2}$$

$$\Delta_2 \cong \frac{1}{3}p\frac{\partial^2 u_1}{\partial x_1 \partial x_2} + \frac{1}{6}p\frac{\partial^2 u_2}{\partial x_1^2} + \frac{1}{3}p\frac{\partial^2 u_2}{\partial x_2^2}. \qquad (9)$$

It can be concluded that, in this case, the prebuckling displacement contributions are at least the same as that due to the prebuckling stress in the first equation of Eq. (6) and are at least as much as one-sixth of that due to the prebuckling stress in the second equation of Eq. (6).

The contributions due to the prebuckling displacements, in cases other than the two cases discussed above, should be somewhere between these two extreme cases. Equations (6) were used by the authors (Chattopadhyay and Gu, 1996) in addressing the buckling of orthotropic plates and composite laminates. To our knowledge, excluding prebuckling displacement contributions will introduce as much as a ten percent error, depending upon the material properties and the length-to-thickness ratio of the plates.

Reference

Chattopadhyay, A., and Gu, H., 1996, "Exact Elasticity Solution for Buckling of Composite Laminates," *Composite Structures*, Vol. 34, pp. 291–299.

Authors' Closure[8]

A rigorous solution for the buckling of orthotropic solids was given in our paper. It was stated there explicitly that the equilibrium equation is expressed in terms of the second Piola-Kirchhoff stress which measures the tractions per unit area of the reference or undeformed configuration. Following Malvern (1969), in terms of the Piola-Kirchhoff stress $\tilde{\mathbf{T}}$, the equilibrium equation is

$$\nabla \cdot [\tilde{\mathbf{T}} \cdot \tilde{\mathbf{F}}^T] = \mathbf{0}, \qquad (1)$$

and it is clear that the deformation gradient $\mathbf{F}$ and hence the entire equation, will depend on the choice of the reference configuration. In some cases, such as the one considered by us, it is useful to let $\tilde{\mathbf{T}} = \boldsymbol{\sigma} + \boldsymbol{\Sigma}$, where $\boldsymbol{\Sigma}$ is a uniform stress field and $\boldsymbol{\sigma}$ is a stress increment beyond this pre-existing stress, and also to substitute $\mathbf{F} = \nabla(\mathbf{x} + \mathbf{u})$, where $\mathbf{x}$ is the position vector and $\mathbf{u}$ is the displacement vector which is measured from the reference configuration. If we further assume that the stress increment is small, Eq. (1) may be rewritten in the form

$$(\nabla \cdot \boldsymbol{\sigma}) \cdot (\mathbf{1} + \nabla \mathbf{u}) + \boldsymbol{\Sigma} : \nabla\nabla \mathbf{u} = \mathbf{0}. \qquad (2)$$

In our work the reference configuration for the Piola-Kirchhoff stress was specifically chosen as the prebuckled state, or, quoting from the paper: "Initially, the solid is in a state of homogeneous strain corresponding to compressive uniform stress p parallel to the free boundary along the x_1 direction". We note that, since the displacements are measured from the prebuckled state, the components of the displacement gradient which is proportional to $\boldsymbol{\sigma}$ are small. Obviously, in this case, the product term $(\nabla \cdot \boldsymbol{\sigma}) \cdot \nabla \mathbf{u}$ is small in comparison with other terms in the equation and may be neglected. If, on the other hand, another reference configuration is chosen and the displacements are measured from it, then, the term $(\nabla \cdot \boldsymbol{\sigma}) \cdot \nabla \mathbf{u}$ must be taken into account. As a result, terms that depend on the history of the deformation will appear explicitly in the equilibrium equation. Nonetheless, it should be realized that these terms appear solely due to the fact that Eqs. (1) and (2) are expressed in terms of the pseudo Piola-Kirchhoff stress and not in terms of the true Cauchy stress.

We note that, from a purely rigorous mathematical point of view, the choice of the reference configuration is immaterial. However, we also note that there exist good motivations in favor of choosing the reference configuration as the prebuckled configuration. First, this choice results in strictly simpler expressions because the term $(\nabla \cdot \boldsymbol{\sigma}) \cdot \nabla \mathbf{u}$ is neglected. Further, and even more important, is the fact that by adopting this approach the problem can be solved without the need to account for the entire history of the deformation up to the instant when the material buckles. Thus, as was used in our paper, the instantaneous stress-strain relation at the prebuckled configuration is all that is needed to obtain a rigorous solution for the problem, or in the words of our paper, "we assume a linear relationship between the stress increment and the *infinitesimal* strain increment". This feature enables utilizing the proposed solution to predict the buckling stress of nonlinearly deforming materials. In fact, while the instantaneous stress-strain relation at any point of the deformation history may be linearized, it is well known that when the deformation gradient is large, the overall or total stress-strain relationship is usually nonlinear. This, of course, provides an additional motivation for choosing the reference configuration as the prebuckled configuration. At the same time it renders the approach of Chattopadhyay and Gu tenuous at best.

It is possible that in some special cases a different reference configuration will be a more appropriate one. However, since in such cases the deformation history will be incorporated into the solution, it will be valid only to the particular class of materials that was considered. But, if such an approach is taken, it will generally not be adequate to utilize a linear stress-strain relationship and thus the analysis of Chattopadhyay and Gu is an unwarranted simplification. Finally, we note that in some cases, usually when the longitudinal Young's modulus is much larger than the other moduli, the critical buckling strain is small and the assumption of a linear stress-strain relationship is satisfactory. In these cases, since the strains are small, the choice of the reference configuration is unimportant and hence, for the sake of simplicity alone, the formulation that was proposed by us is an advantageous one.

Reference

Malvern, L. E., 1969, *Introduction to the Mechanics of a Continuous Medium*, Prentice-Hall, Englewood Cliffs, NJ.

[8] Department of Mechanical Engineering, Ben-Gurion University of the Negev, P.O. Box 653, Beer-Sheva 84105, Israel.

Copyright © 1997 by ASME

Downloaded 04 May 2010 to 171.66.16.34. Redistribution subject to ASME license or copyright; see http://www.asme.org/terms/Terms_Use.cfm

Stress and Strain Analysis in Molecular Dynamics Simulation of Solids[9]

O. R. Walton[10]. As the authors correctly point out, an expression for the stress due to a system of particles with forces acting between them can be obtained by discretizing the definition of stress in terms of integrals, so that they become summations over forces in an averaging volume. The relationship between stress and interparticle forces (noting that the momentum flux density tensor is equivalent to the stress tensor) is well established, and has been utilized in molecular dynamics calculations for decades. There are two components to the stress tensor, the *kinetic* contribution due to the motion of the atoms or particles (see Chapman and Cowling, 1952), and the *potential* contribution due to the forces of interaction between particles (Irving and Kirkwood, 1950). Evans (1979) pointed out that the stress tensor represented as a sum over particles and interparticle forces

$$\sigma = \frac{1}{V}\sum_i m_i(\mathbf{v}_i - \mathbf{u}_i)(\mathbf{v}_i - \mathbf{u}_i) + \frac{1}{V}\sum_{i>j}\mathbf{F}_{ij}\mathbf{R}_{ij}$$

(where m_i is the mass, $\mathbf{v}_i$ is the velocity of the atom due to microscopic vibrations, i.e., temperature, and $\mathbf{u}_i$ is the average velocity field at the location of particle i and $\mathbf{F}_{ij}$ is the force acting between particle i and j, and $\mathbf{R}_{ij}$ is the vector from the c.g. of particle i to the c.g. of particle j) need not be symmetric, if the forces are noncentral (as can happen for nonspherical molecules or for macroscopic particles interacting via elastic contact forces with friction). The first term in the above expression is the *kinetic* contribution and the second is the *potential* contribution to the stress. The second term is equivalent to what most engineers would consider to be the stress in a material at rest. Cundall and Strack (1983) derive an expression for the stress in a granular material which can easily be shown to be equivalent to the potential contribution to the stress in the above expression. The above summation has been used in the molecular dynamics community for the past three or four decades. Modern texts on molecular dynamics (e.g., Hoover (1986) or Rapaport (1995)) simply treat the above expression as the *definition* of the stress tensor (or pressure tensor).

References

Chapman, S., and Cowling, T. G., 1952, *The Mathematical Theory of Non-Uniform Gases,* Cambridge University Press, Cambridge, UK.

Cundall, P. A., and Strack, O. D. L., 1983, *Mechanics of Granular Materials: New Models and Constitutive Relations,* J. T. Jenkins and M. Satake, eds., Elsevier, New York, p. 137–149.

Evans, D., 1979, *J. Stat. Phys.,* **20,** No. 5, p. 547.

Irving, J. H., and Kirkwood, J. G., 1950, *J. Chem. Phys.,* Vol. 18, No. 6, p. 817.

Hoover, W. G., 1986, *Molecular Dynamics,* Springer-Verlag, New York.

Rapaport, D. C., 1995, *The Art of Molecular Dynamics Simulation,* Cambridge University Press, Cambridge, UK.

[9] Scagnetti, P. A., Nagem, R. J., Sandri, G. V. H., and Bifano, T. G., 1996, "Stress and Strain Analysis in Molecular Dynamics Simulation of Solids," ASME JOURNAL OF APPLIED MECHANICS, Vol. 63, pp. 450–452.

[10] Lawrence Livermore National Laboratory, University of California, P.O. Box 808, L-200, Livermore, CA 94550.

A Critical Study of the Applicability of Rigid-Body Collision Theory[11]

A. Chatterjee[12] **and A. Ruina**[13]. Stoianovici and Hurmuzlu (1996) present an interesting critique of rigid-body collision theory, based on experiments with, and simulations of, slender steel rods colliding with a massive steel object. However, the authors group certain ideas which we feel should be viewed as distinct. We feel their concluding dismissal of rigid-body collision theory is too harsh. In essence, we value the authors' experimental results, but disagree with some of their conclusions. This note is meant to be a partial defense of rigid-body collision theory, in the light of their study.

The authors study rods at various orientations, dropped vertically onto a massive anvil. High-speed photography is used to measure pre and post-collision velocities. It is found, experimentally and through simulations, that bending vibrations in the rod make the collisional interaction complicated. Their study is interesting both because experimental data for two-dimensional or three-dimensional collisions of objects other than spheres and disks is scarce, and because the fairly complicated experimental results are explained nicely with the help of a discrete dynamical model for the rods along with a spring/nonlinear dashpot contact model. Their observed coefficient of restitution varies strongly with orientation for a given slender rod, as well as for rods of different slenderness ratios at a fixed orientation. In their conclusions, the authors say:

> *"Is the coefficient of restitution relatively constant for highly rigid material and low-impact speeds?* The most important outcome is that the rigid-body theory (the invariance of the coefficient of restitution) has a very limited applicability even for highly rigid material and low-impact speeds."

In our opinion, it appears too restrictive to identify "rigid-body theory" with "invariance of the coefficient of restitution." The two (distinct) ideas each have their own strengths and weaknesses. While some pitfalls of special rigid-body collision models are revealed nicely by the authors' data, the most basic aspects of the rigid-body approach are preserved accurately in the system they study. While the dramatic variation they report in the coefficient of restitution is interesting, it is equally interesting to note the consistency of their data with general rigid-body collision modeling.

The system they studied clearly satisfies some of the standard fundamental assumptions of rigid body collision modeling: (i) the changes in the overall rigid-body velocities of the bodies, from just *before* to just *after* the collision, may be described by impulse-momentum relations for rigid bodies, i.e., an equation of the form

$$\mathbf{P} = \mathbf{M}\cdot\Delta\mathbf{V}, \tag{1}$$

where $\mathbf{P}$ is the impulse transmitted, $\mathbf{M}$ is a local inertia tensor, and $\mathbf{V}$ is the relative velocity at the contact point (see, e.g., Smith, 1991) (ii) collision contact forces and accelerations are very large, changes in velocities are bounded, and displacements are very small, (iii) the time of interaction is very small compared to the time scale of overall motions ($\sim$1 msec versus $\sim$100 msec), (iv) contact occurs over a small region that may be approximated as a point for purposes of impulse-momentum calculations, (v) a well-defined common tangent plane exists at the "point of contact," and (vi) kinetic energy is not created in a collision. These assumptions are in fact not very restrictive and are a reasonable model for a large variety of collisions that are of practical interest, including collisions of fairly stiff manipulators.

However, most rigid-body collision models are actually based on *far* more stringent, albeit often implicit, assumptions, about the rigidity of the bodies *during* the collision (e.g., see discussion in Chatterjee, 1997).

Examples of such models include that of Routh (1897), rediscovered recently by Keller (1986), based on infinite tangential stiffness and Coulomb friction, as well as Maw, Barber, and Fawcett's approach (1976), based on Mindlin and Deresie-

[11] Stoianovici, D. and Hurmuzlu, Y., 1996, "A Critical Study of the Applicability of Rigid-Body Collision Theory," ASME JOURNAL OF APPLIED MECHANICS, Vol. 63, pp. 307–316.

[12] Penn State University, 227 Hammond Building, University Park, PA 16801.

[13] Cornell University, 212 Kimball Hall, Ithaca, NY 14853.

Copyright © 1997 by ASME

Downloaded 04 May 2010 to 171.66.16.34. Redistribution subject to ASME license or copyright; see http://www.asme.org/terms/Terms_Use.cfm

Journal of Applied Mechanics

Book Review

Stability Problems in Fracture Mechanics (Wiley Series in Nonlinear Science), by Vladimir V. Bolotin. John Wiley and Sons, New York, 1996. 188 pages. Price: $59.95.

REVIEWED BY F. ZIEGLER[1]

This book combines stability theory of systems having a finite number of degrees-of-freedom with fracture mechanics by replacing the state variables by the crack parameters. Since fracture is accompanied by all kinds of dissipative processes, the author invites us to follow the approach he used in stability theory, an approach he has successfully employed in the past with his well-known books *Dynamic Stability of Elastic Systems* (1956) and *Nonconservative Problems of the Theory of Stability* (1961): Take the Dirichlet theorem on elastic stability, replace it by a sequence of equilibrium states, and find the bifurcation analysis. The main tools of the latter are the bifurcation diagrams. Take this idea into fracture mechanics and replace the Dirichlet theorem, on energy in linear mechanics, by the principle of virtual work when following the equilibrium states. Only an author with the long-term experience working on the forefront of research, in chronological order of stability theory, mechanics, of composites, stochastic mechanics, structural safety and reliability, and fracture, fatigue, and damage, can write such a book based solely on physical grounds.

In the 30-page Introduction, a concise expose of fracture (including damage zones), fatigue, and fatigue crack growth (high and low-cycle fatigue) is presented and followed by a section on stability and bifurcation analysis. The physical interpretation of the processes in fracture mechanics as given seems to be impossible to improve further. The historical development, however, is described selectively. While the indisputable fathers of fracture mechanics, Griffith and Irwin, are there, others appear to be missing. Similarly, in the section on stability, Poincare would have found a good place beside Lyapunov. But this is not a book on the historic development of the fields. Figures and formulas presented illustrate well the physical background of the state of the art. In particular, the engineering community will be attracted by this Introduction, and this community is responsible for the reliability of structures.

Chapter 2 (out of six), which is 24 pages, comprises the underlying novel theory of analytical mechanics of fracture (the name was chosen in association of Lagrangean analytical mechanics based on generalized coordinates and forces). Fracture is understood in a general sense, usually nonhealing cracks, other kinds of flaws (not necessarily crack-like)—e.g., originating from corrosion, wear, fire damage, etc., even localization of plastic deformation can be modeled analogously within stability theory—then lead to systems with unilateral constraints in such a multiparameter approach. Since Griffith introduced crack length as such a parameter, Bolotin calls the set of generalized coordinates (Griffithian (G-) coordinates, and since the increment of crack length is positive semidefinite, such a unilateral constraint is easily understood (a flat through crack, e.g., has two degrees-of-freedom). The Lagrangean coordinates are assumed holonomic. Generalized forces in virtual work expressions are directly related, e.g., to driving and resistance forces of classical fracture mechanics. A system with unilateral constraints is in equilibrium if the summed work of all active forces is nonpositive (taking into account all possible virtual variations of the G-coordinates). Also the conditions of stability are carefully worked out. Comparison with conventional fracture mechanics rounds off this original chapter solely based on the author's past research.

Chapter 3, on single parameter cracks, Chapter 4, on multiple parameter cracks, illustrate the new procedure, including such topics as branching and kinking of cracks, and Chapter 5 extends the method to fatigue crack propagation. In quasi-stationary approximation, Bolotin (in 1983) showed that a reduction to O.D.E.'s of the latter problem is possible. For a single parameter crack such a reduction is performed in detail.

The final chapter deals with dynamic crack instabilities and exhibits the extension of the principle of virtual work to include inertia, the D'Alembert Principle for cracked bodies.

The theory is well illustrated by applications throughout the text, also including applications to beams.

This monograph may revolutionize the application part of fracture mechanics, with an even greater impact than catastrophe theory had on dynamic stability. The new theory not only unifies the view on nonlinear fracture mechanics, but also has an impact on its computational verification. This book is a source of ideas for engineers and scientists working in all fields of application of reliability of structures. Taking into account the engineering curriculum, which contains a good portion of stability theory but usually provides much less exposure to fracture mechanics, the book may even become a guide to better education.

[1] Professor, Department of Civil Engineering, Technical University of Vienna, Vienna A-1040, Austria. Fellow ASME.

Copyright © 1997 by ASME

Downloaded 04 May 2010 to 171.66.16.34. Redistribution subject to ASME license or copyright; see http://www.asme.org/terms/Terms_Use.cfm